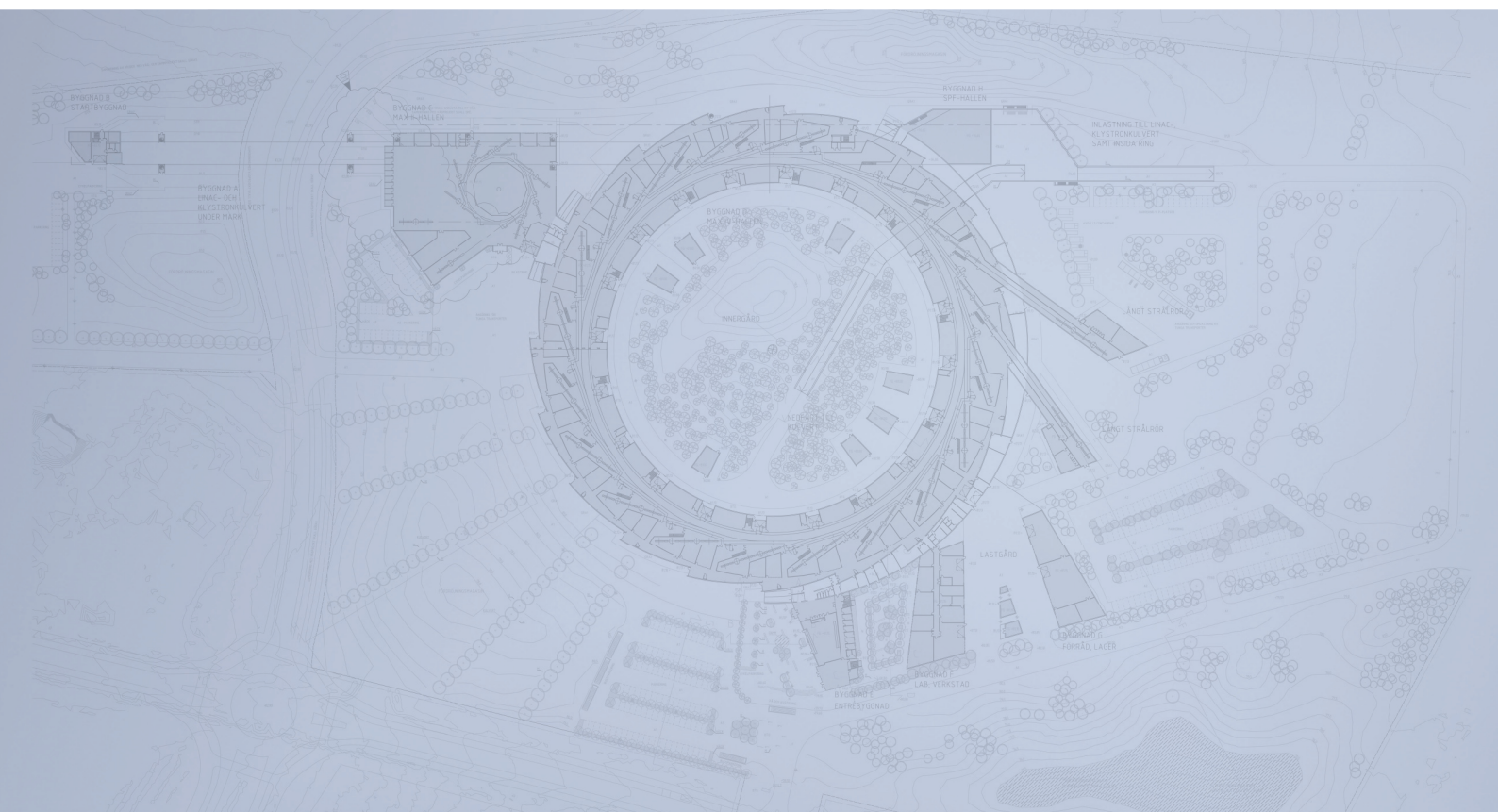


# Detailed Design Report



**MAX IV Facility**





# Table of Contents

---

## **Chapter 1: General Description of the MAX IV Facility**

- 1.1. Introduction
- 1.2. Performance/Cost Considerations
- 1.3. Accelerator Layout

## **Chapter 2: MAX IV 3 GeV Storage Ring**

- 2.1. Introduction
- 2.2. Linear Lattice
- 2.3. Nonlinear Optics
- 2.4. Lattice Errors and Correction
- 2.5. MAX IV Magnets
- 2.6. The Radio Frequency System
- 2.7. Injection
- 2.8. Vacuum System
- 2.9. Diagnostics (RF and vacuum not included)
- 2.10. Beam Lifetime
- 2.11. Collective Effects

## **Chapter 3: MAX IV 1.5 GeV Storage Ring**

- 3.1. Introduction
- 3.2. Linear Lattice
- 3.3. Nonlinear Optics
- 3.4. Lattice Errors and Correction
- 3.5. MAX IV 1.5 GeV Storage Ring Magnets
- 3.6. The Radio Frequency System
- 3.7. Injection
- 3.8. Vacuum System
- 3.9. Diagnostics (RF and vacuum not included)
- 3.10. Beam Lifetime

## **Chapter 4: MAX IV Injector**

- 4.1. General Description and Design Philosophy
- 4.2. Layout, Design Parameters and Optics
- 4.3. Beam Dynamics and Simulations
- 4.4. Electron Gun
- 4.5. Laser System
- 4.6. Acceleration
- 4.7. Magnets
- 4.8. Diagnostics

## **Chapter 5: Insertion Devices**

- 5.1. Introduction
- 5.2. Proposed Beamlines at the MAX IV 3 GeV Storage Ring
- 5.3. Insertion Devices at the MAX IV 3 GeV Ring
- 5.4. Influence from the Insertion Devices on the RF-system the Emittance and Energy Spread of the Stored Electron Beam
- 5.5. The influence on the Brilliance and Angular Spectral Flux from the Number of IDs Installed
- 5.6. Comparison of Specific Undulators at Different Synchrotron Radiation Storage Rings

- 5.7. Acknowledgement
- 5.8. Appendix A: Synchrotron Radiation
- 5.9. Appendix B: Modes of Operation for Elliptically Polarising Undulators
- 5.10. Appendix C: Influence from the Insertion Devices on the Magnetic Optics of the Storage Ring
- 5.11. Appendix D: Influence from the Insertion Devices on the Emittance and Energy Spread of the Stored Beam
- 5.12. Appendix E: Beam Loading of the Radio Frequency System from Insertion Devices
- Bibliography

## **Chapter 6: Stability and Tolerances**

- 6.0. Stability and Tolerances (Vibrations, Settlements and Alignment)
- 6.1. Overall Stability Criteria
- 6.2. Vibration Conventions
- 6.3. Vibration Tolerances
- 6.4. Vibration Measurements
- 6.5. Vibration Management
- 6.6. Alignment, Positional Tolerances
- 6.7. Conclusions
- 6.8. References

## **Chapter 7: MAX IV Shielding**

- 7.1. General
- 7.2. The Linac
- 7.3. The MAX 3 GeV Ring
- 7.4. The Short Pulse Facility
- 7.5. Environmental
- Bibliography
- Appendix A: Source Models
- Appendix B: Material Attenuation Lengths
- Appendix C: Electron Losses
- Appendix D: The Linac
- Appendix E: The The Short Pulse Facility

## **Chapter 8: Commissioning**

- 8.1. Sub-System Commissioning Policy
- 8.2. Time Plan
- 8.3. Organization
- 8.4. 3.0 GeV Storage Ring Commissioning
- 8.5. 1.5 GeV Storage Ring Commissioning
- 8.6. Injector Commissioning

## **Chapter 9: Control System**

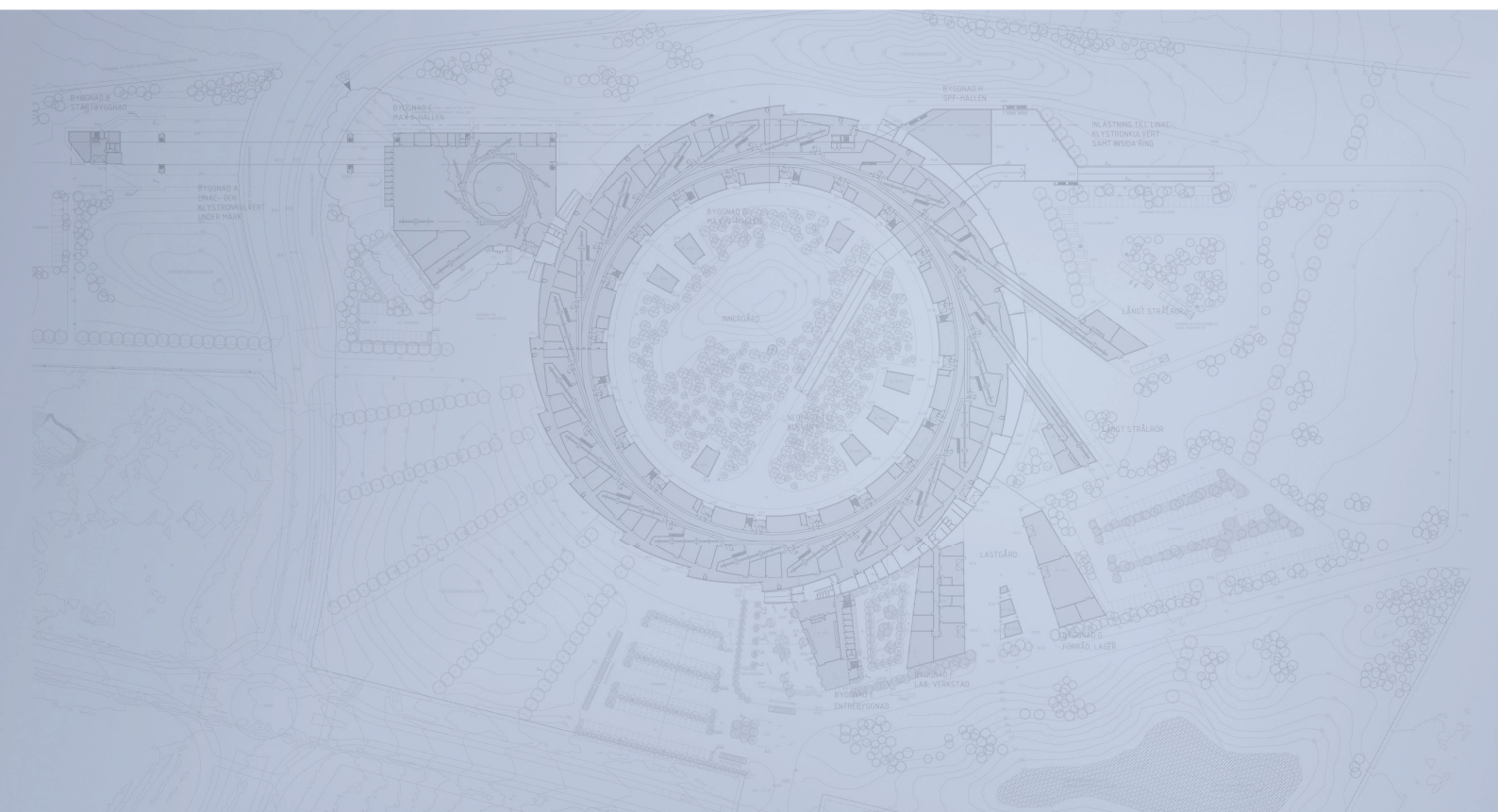
- 9.1. Introduction
- 9.2. Design
- 9.3. Hardware
- 9.4. Connectivity
- 9.5. Software

## **Chapter 10: Short Pulse Facility**

- 10.1. Overview and Layout

## **Chapter 11: The Linac Test Beam (LTB)**

# Detailed Design Report



## Chapter 1

### General Description of the MAX IV Facility

#### 1.1. Introduction

**MAX IV Facility**



## 1.1. Introduction

---

The scientific demands on the MAX IV facility [1-5] call for synchrotron radiation sources giving high quality radiation over a broad spectral and time range. The spectral range stretches from the IR to the hard X-ray regions. The facility should also provide intense, short X-ray pulses in the fs domain.

We have performed a global optimization of a facility design based on these challenging demands. New technical and system solutions had then to be introduced since no existing or planned facility can match the demands imposed. This has optimization resulted in a solution where two storage rings operated at different electron energies will provide spontaneous radiation of high brilliance over the broad spectral range requested and a linear accelerator (linac) working as the injector for the storage rings as well as being the electron source for the generation for the short and intense X-ray pulses. A Short Pulse Facility (SPF) is thus included in the MAX IV project.

*The two storage rings*, operated at different electron energies, will cover a broad spectral range of high quality spontaneous radiation from optimized insertion devices (IDs). The number of radiation sources matches the present and foreseeable future demands in each spectral region.

The prime sources for synchrotron radiation at these rings are optimized IDs spanning the photon energy range from a few eV up to several tens of keVs. The IR spectral range is covered by the ring of lower electron energy. Top-up injection will be used for both storage rings.

These two storage rings will provide electron beams with emittances matching their spectral ranges. The most demanding ring, the X-ray ring, will thus have the smallest horizontal emittance of 0.24 nm rad only. The vertical emittance is adjusted to the diffraction limit for the energy spectrum covered by each ring.

*As injector*, a linac is chosen. Apart from working as an injector for the storage rings, this linac will also be used to generate the short, intense X-ray pulses.

The current need of this kind of radiation sources call for a quick establishment of this SPF. At the first phase, spontaneously radiating sources will thus be used.

The FEL technology has developed remarkably fast and strongly lately. The linac and the building have thus been prepared to take advantage of this FEL development. Different FEL scenarios are now being investigated for a later FEL activity.



## References

### **MAX IV Conceptual Report**

<http://www.maxlab.lu.se/maxlab/publications/max4/MAX-IV-CDR.pdf>

The scientific case and beamline program was further discussed and developed at the well attended MAX-lab user meetings during 2007, 2008 and 2009. During these meetings many parallel workshops were organized addressing special beamlines or experimental techniques.

### **2007 "Science at MAX IV", 345 participants – 12 different sessions**

<http://www.maxlab.lu.se/usermeeting/2007/program.html>

### **2008 "New Directions for MAX IV", 283 participants – 11 different sessions**

<http://www.maxlab.lu.se/usermeeting/2008/program.html>

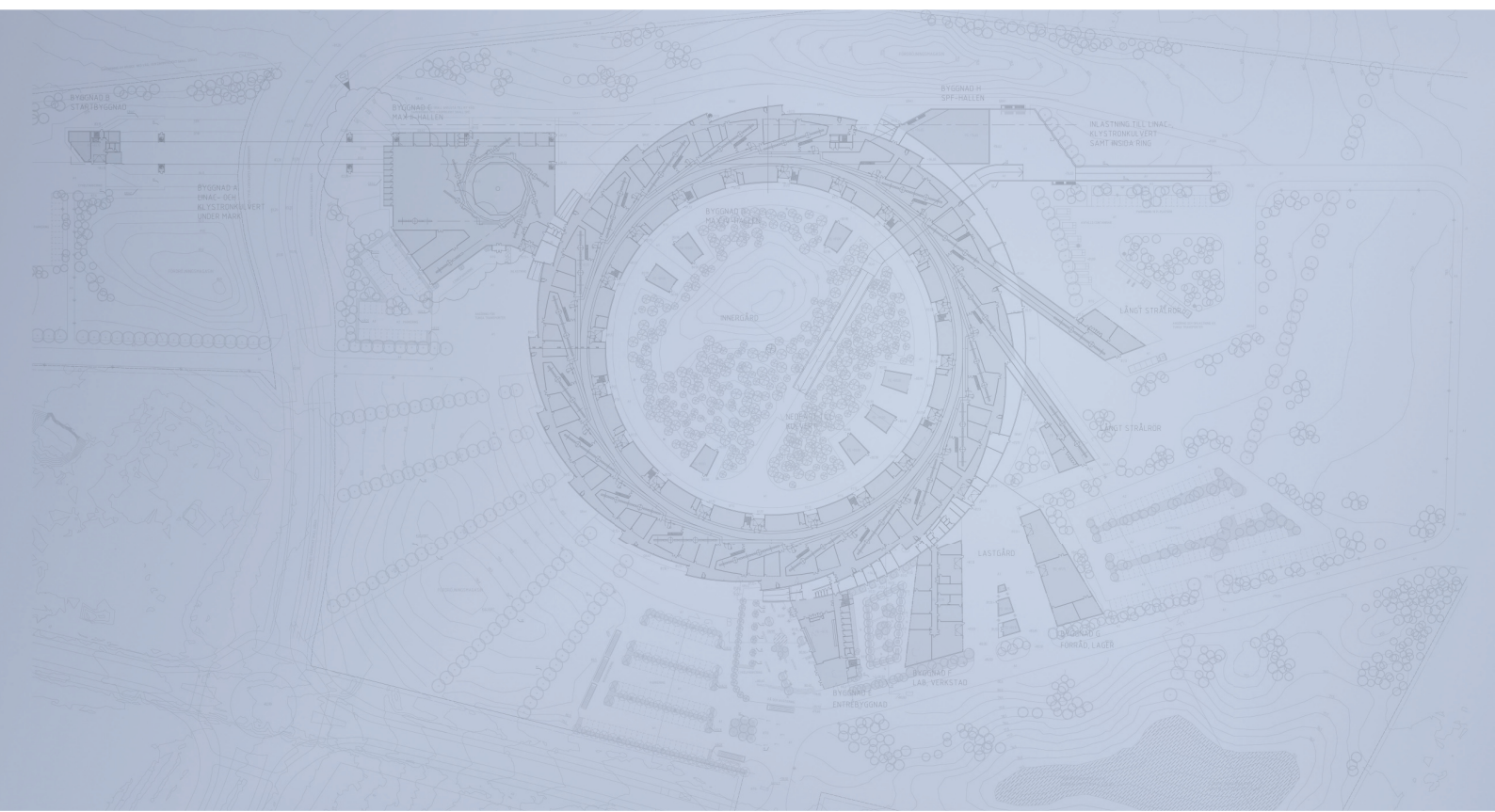
### **2009 22<sup>nd</sup> Annual User Meeting, 301 participants – 14 different sessions**

<http://www.maxlab.lu.se/usermeeting/2009/program.html>

### **Beamlines at MAX IV. Workshop Feb 22-23 2010, 200 participants**

[http://www.maxlab.lu.se/maxlab/workshops/beamlines\\_maxiv/index.html](http://www.maxlab.lu.se/maxlab/workshops/beamlines_maxiv/index.html)

# Detailed Design Report



## Chapter 1

### General Description of the MAX IV Facility

#### 1.2. Performance/Cost Considerations

**MAX IV Facility**



## 1.2. Performance/Cost Considerations

---

The MAX IV facility is a very far reaching project, aiming at a performance approaching the theoretical limits. In the optimization process we have – as is absolutely necessary in a small country – paid high attention to the economical aspects. Both the capital and running costs must be kept at a moderate level. This has to be combined with a high level of performance. The technology used is thus carefully chosen for an optimum performance/cost ratio. Therefore, novel technology had to be developed at the existing MAX laboratory to meet these demands. Some examples are:

***A low frequency 100 MHz RF acceleration system*** will be used for the storage rings. A superconducting system, the choice of many of the new facilities, is considerably more expensive and more complex. The 100 MHz system, developed and implemented at the MAX II and MAX III rings, effectively suppresses the higher order modes in the accelerating cavities and also gives a low electric consumption due to the high efficiency of the tetrode amplifiers and the smaller voltage needed for the large bucket height needed. The small dimensions of the vacuum chamber could cause problems due to the resistive wall instability if short bunches are used. However, the long bunches given by the 100 MHz RF system effectively reduces this problem.

***A harmonic Landau-damping system.*** MAX-lab was the first laboratory to implement this kind of damping system at a third generation storage ring. Apart from damping the coupled bunch instability, the harmonic Landau cavities reduces the heat load on the cold bore superconducting insertion devices by lengthening the bunches. The Touschek losses are also reduced with a factor 3-5. Passive damping systems of this kind have now been installed at several other third generation SR-facilities world-wide.

***The magnet technology*** for MAX IV was pioneered at the present MAX injector and the MAX III storage ring. The technique of machining out complex magnet structures from solid steel blocks yields a very high precision compared to conventional technology, and also leads to a considerably lower price. In the MAX IV case the magnet blocks will also act as girders. This scheme reduces the alignment errors and further reduces the cost. It is furthermore the compact and integrated magnet design that makes it possible to achieve the very small emittance in the relatively small MAX IV rings.

***The magnet apertures*** are much smaller than at conventional facilities. The small dimensions are in fact a necessity for reaching the high performance since very high magnetic field gradients are required to attain a small electron beam emittance. Apart from a low production cost of the small magnets, the operating cost in terms of electric power consumption is reduced compared to conventional magnets. Smaller and lighter magnets

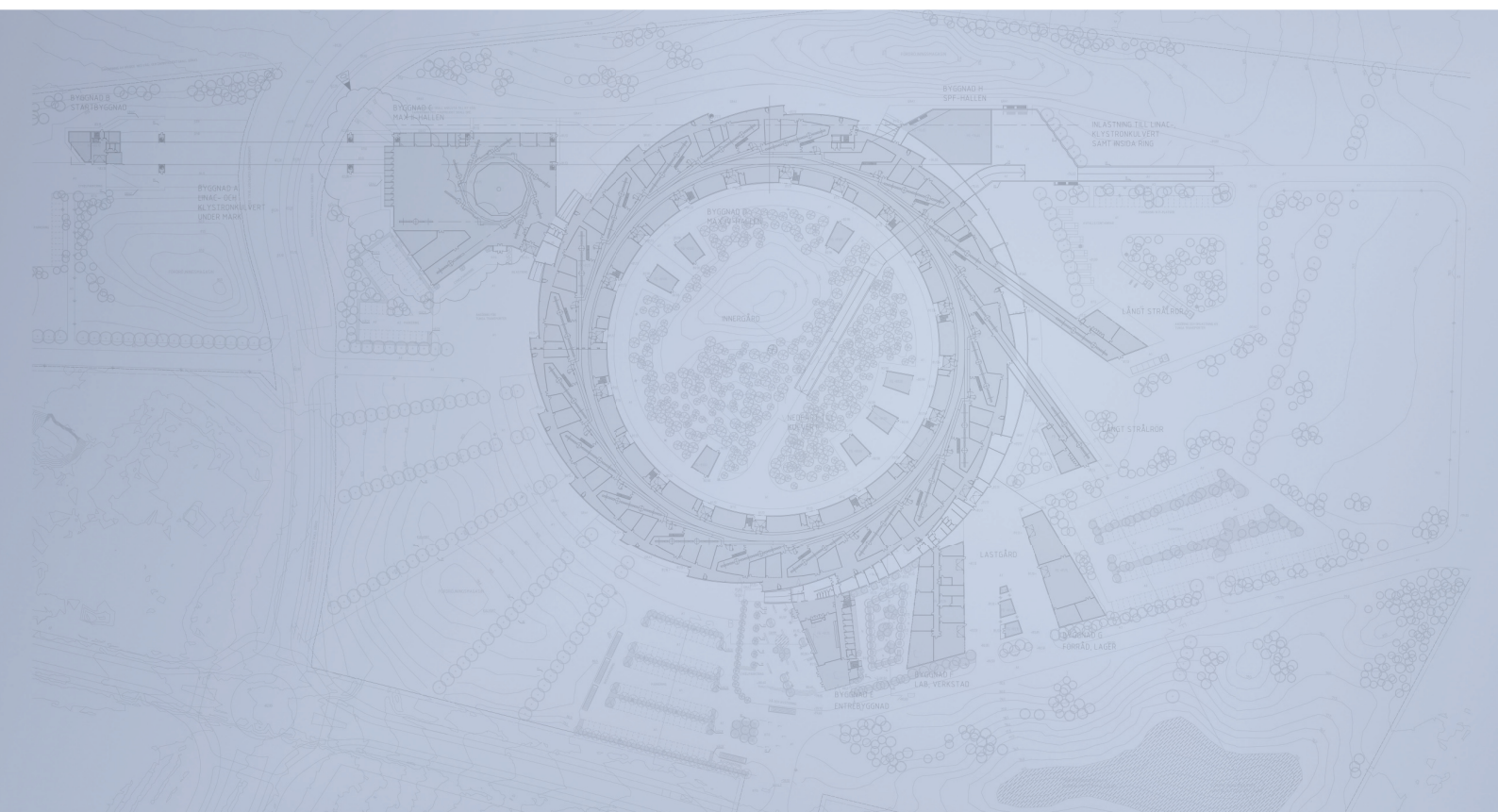
also push up the mechanical eigen-frequency spectrum of the magnets which is of high importance for achieving a beam stability matching the small beam dimensions.

***For the vacuum system*** the new and cost effective technology of NEG-coated vacuum chambers will be used all over the MAX IV rings. This technology enables a much smaller number of discrete pumps to be used and simplifies the design of the heat absorbers.

***The linac injector/Short Pulse Facility.*** The well-known room-temperature 3 GHz linac structure is chosen for this accelerator. New, modern solid state modulators are chosen since these can handle high repetition rates and adjustable pulse lengths and also demonstrates less time jitter. The replacement of the expensive high power thyratrons is avoided with this solid state technology.



# Detailed Design Report



## Chapter 1

### General Description of the MAX IV Facility

#### 1.3. Accelerator Layout

**MAX IV Facility**



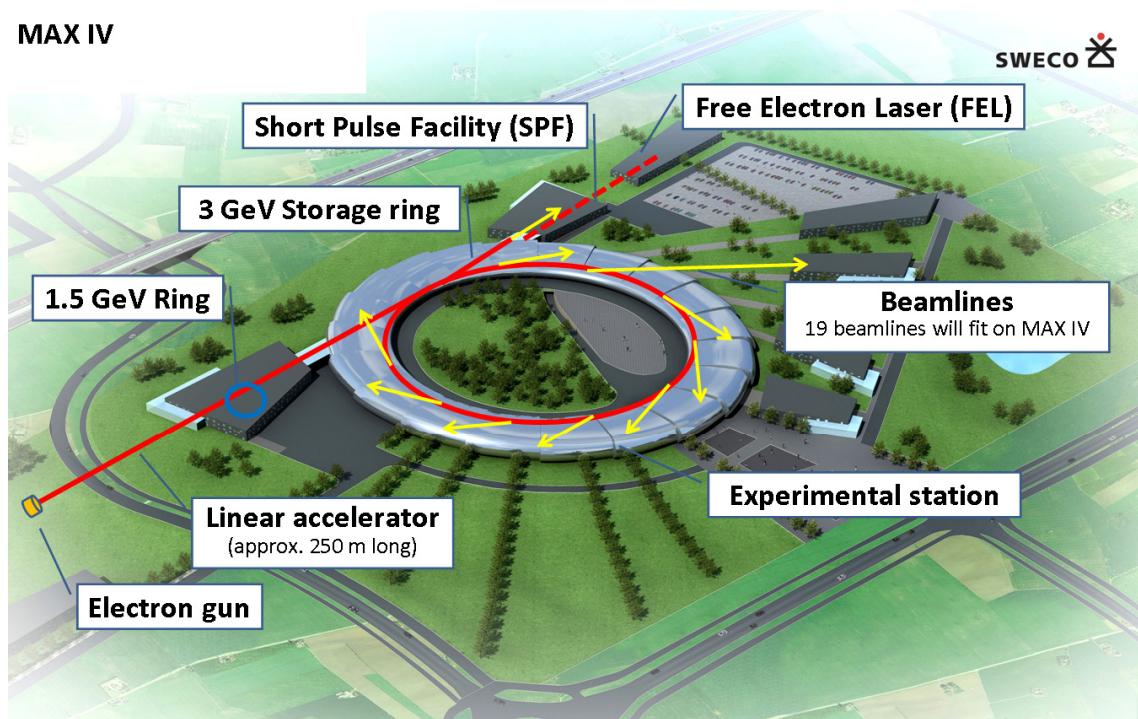
## 1.3. Accelerator Layout

---

The MAX IV accelerator layout is seen below. The electron source is situated in the lower left corner. Following the electron source, a linac is then accelerating the electrons up to the injection energies of the two storage rings. Bunch compressors bring down the bunchlengths to match the SPF needs.

The linac is situated in an underground tunnel. The two storage rings are situated at the ground level. The electron beam is brought up to the rings with kicker systems. The linac settings can thus remain unchanged during operation.

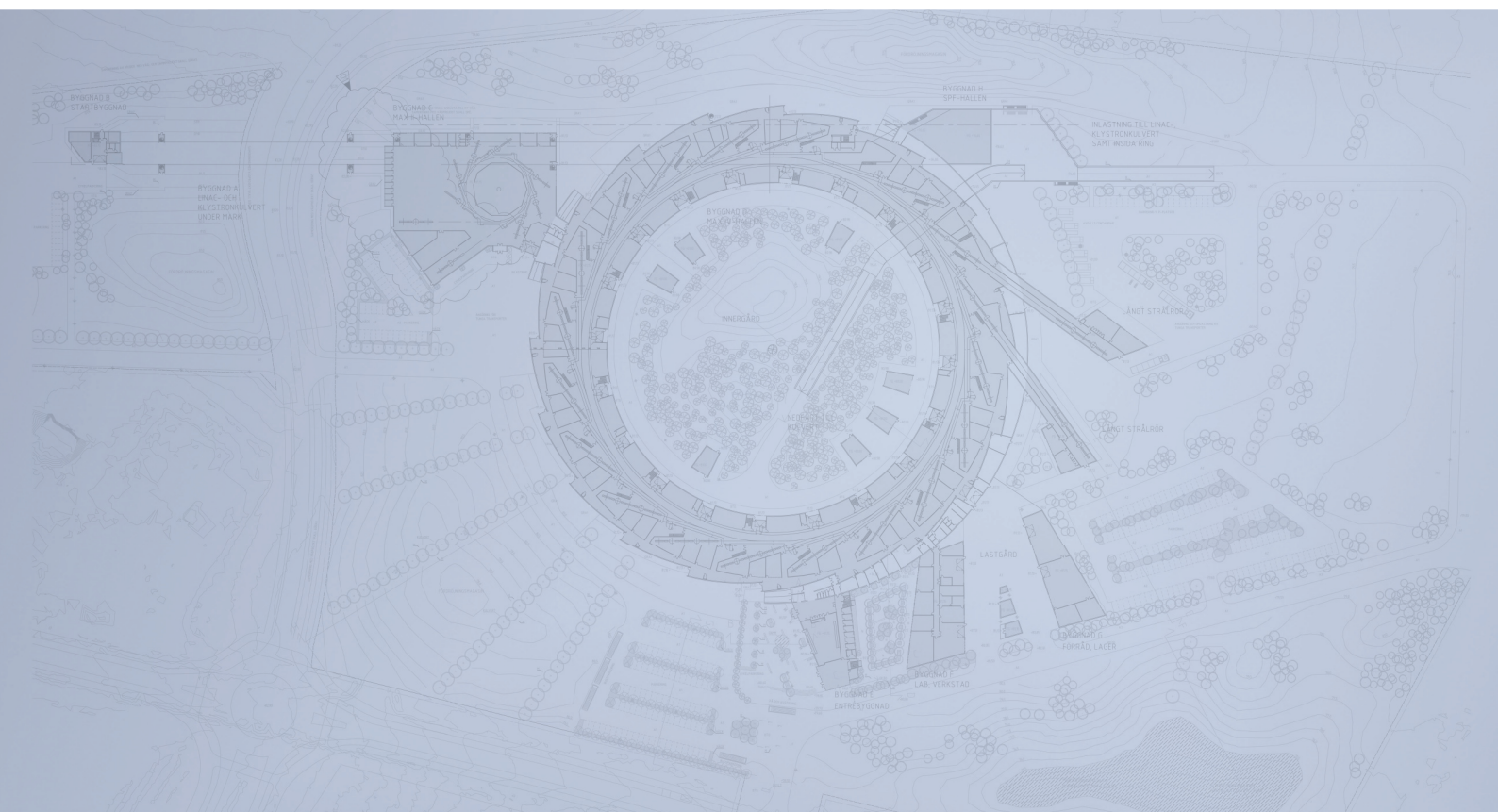
The Short Pulse Facility is placed underground, at the linac level and in the tangent direction of the linac. A later FEL building is foreseen.







# Detailed Design Report



## Chapter 2 MAX IV 3 GeV Storage Ring

MAX IV Facility





# MAX IV Facility



## 2.1. Introduction

---

The design of the MAX IV 3 GeV ring is focused towards achieving a low emittance ring with a sufficient number of ID straight sections to a relatively low cost. The way chosen is to use the 7 bend achromat since this type of lattice demonstrates the necessary stability in terms of dynamic aperture and energy acceptance. The main parameter values are presented in chapter 2.2 table 2.1.

The bare lattice emittance of the storage ring is brought down to 0.33 nm rad. Due to the low dipole fields, the final emittance is quite dependent on the IDs used. The minimum emittance with all ID straight sections filled is just above 0.15 nm rad.

The lattice becomes compact with strong multipole magnets. The Twiss functions are relatively small which results in small apertures. With an inner radius of 11 mm, the lattice energy acceptance is still 4.5 %.

To achieve this large energy acceptance and a sufficient large dynamic aperture, several tricks have to be played. The large number of sextupole magnets within an achromat makes it possible to minimize the Hamiltonian terms driving instabilities within the achromat itself. To minimize the amplitude dependent tune shift, octupoles are added at non-dispersive positions.

To take advantage of the energy acceptance, a low frequency RF system is introduced since this will require a lower RF voltage for given bucket height compared to an RF system of higher frequency. A large energy acceptance is important in this type of low emittance ring to achieve a sufficient long Touschek life-time.

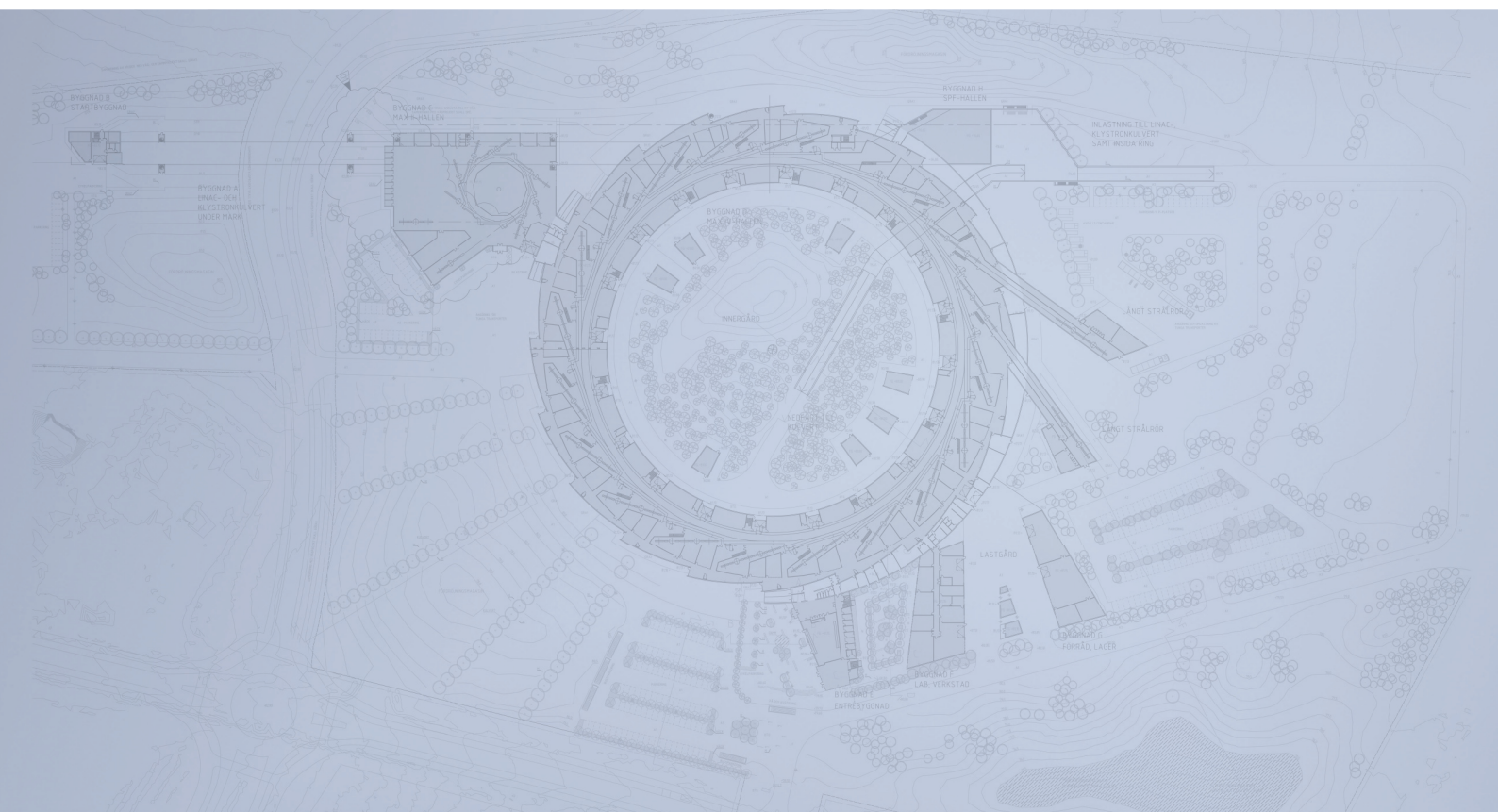
The relatively low RF voltage will permit us to use warm harmonic cavities to stretch the bunches. The bunch lengths are increased a factor of 4 to increase the Touschek life-time further and to reduce the bunch power spectrum which makes the ring more tolerant against Higher Order Mode instabilities. This small bunch power spectrum will also have a positive effect on the resistive wall instability.

The Touschek beam life-time is surprisingly long, considering the small transverse dimensions of the electron and the high circulating current. The slope of the Touschek life-time with respect to the emittance is in fact negative; the Touschek life-time is increasing as the beam emittance shrinks. Although the collision rate between the electrons is increasing, the transverse momentum, which is transformed to longitudinal momentum at Touschek events, becomes smaller so the particles are effectively trapped within the large momentum acceptance of the ring.

The ring is designed to have a low electric consumption. The low field, small aperture dipoles have modest power consumption and the synchrotron radiation losses also become small due to the low dipole fields. The efficiency of the RF tetrode amplifiers is close to 70%. The low RF frequency implies a relatively low RF voltage with a high coupling of the cavities to their transmission lines when matched to the beam load. Close to 60% of the electric power to the transmitters is converted to synchrotron radiation power. The total electric power for operating the 3 GeV ring at 500 mA current is some 1-1.5 MW depending on the IDs chosen.



# Detailed Design Report



## Chapter 2

### MAX IV 3 GeV Storage Ring

#### 2.2. Linear Lattice

MAX IV Facility



# 2.2. Linear Lattice

---

- 2.2. Linear Lattice.....2**
- 2.2.1. Overview ..... 2
- 2.2.2. Achromats ..... 3
- 2.2.3. Bending Magnets..... 5
- 2.2.4. Focussing Magnets..... 9
- 2.2.5. Working Point ..... 11
- 2.2.6. Effects of Insertion Devices.....12
- 2.2.7. Intrabeam Scattering ..... 20
- References ..... 22

## 2.2 Linear Lattice

---

### 2.2.1. Overview

Many of the ideas for the MAX IV 3 GeV storage ring have been inspired by the design of high-energy physics damping rings [1, 2]. These rings are characterized by a very low electron beam emittance, high bunch currents and also by small transverse dimensions regarding apertures and magnet elements. Many of the instability and dynamic aperture-related problems have already been investigated for these lattices. The transformation of a damping ring to a synchrotron radiation storage ring requires the introduction of the straight sections needed for the insertion devices (IDs). This is a delicate problem and the successful combination imposes some restrictions on the length of the straight sections.

Not only is the electron beam emittance essential to achieve a high brilliance, also the optimization of the IDs is very important. The present development of IDs indicates a tendency towards shorter period lengths and smaller gaps. The MAX IV 3 GeV storage ring is matched to these new IDs. The figure of merit of a modern synchrotron radiation facility is a small emittance of the electron beam. The emittance is determined by the competition between quantum heating and damping of the electron beam. The magnet lattice defines the emittance [3]:

$$\varepsilon = C \frac{E^2}{N_d^3} \quad (2.1)$$

where  $E$  is the beam energy,  $N_d$  is the number of dipole magnets, and  $C$  is a constant given by the lattice. The bare lattice emittance is then further reduced by strong IDs (see Section 2.2.6).

A small emittance in a storage ring thus requires a large number of magnet cells or a very low lattice constant  $C$ . The Theoretical Minimum Emittance (TME), resulting in a minimum value of  $C$ , can be achieved for a certain choice of the lattice functions [4]. This approach is however limited by instabilities and requires a complex nonlinear optics design. It has therefore been decided to target a small emittance in the MAX IV 3 GeV storage ring by use of a large number of magnets rather than by pushing towards the TME lattice functions. When reducing the emittance, the ring then easily becomes large

and costly. However, for a given ring size one can increase the number of magnet cells by making the cells shorter. Shorter magnet cells require stronger focusing gradients to keep the electron optics optimized. The strong gradients needed for the MAX IV 3 GeV storage ring are achieved by a reduction of the transverse dimensions of the magnet elements which also results in smaller dimensions of the vacuum chambers. The problems associated with poor vacuum conductance are avoided by introducing a NEG-coated vacuum system (see Chapter 2.8).

The lattice on which this report is based is the 20090601-410 bare lattice and subsequent lattices derived from the 20090601 branch [5]. A summary of the machine parameters for the MAX IV 3 GeV storage ring is given in Table 2.1. Linear optics calculations have been performed with the codes OPA [6] and Tracy-3 [7]. The lattice files for both codes are very similar. For the bare lattice, agreement between the two codes is excellent. Slight differences between the codes are observed when IDs are introduced into the lattice. While OPA has only a simple undulator model, Tracy-3 can also import RADIA kick maps [8]. A quadrupole scaling factor has been introduced to the Tracy-3 lattice file when using kick maps to model IDs in order to set the correct working point. Using these scaling factors Tracy-3 results are in agreement with the OPA results on the sub-percent level.

### 2.2.2. Achromats

The 3 GeV MAX IV storage ring is composed of 20 main cells (achromats). Each achromat consists of five unit cells plus two matching cells (one at each end of the unit cell) to accommodate for IDs in the straight section. A schematic of one achromat is given in Fig. 2.1. The matching cells resembles a “missing magnet” dispersion suppression, that is, they are similar to a unit cell but have only half the dipole magnet strength. An advantage of using this scheme is that a short straight section is provided at the beginning and end of each achromat. This short straight will be used for the accelerating rf cavities thus keeping all but one long straight sections open for IDs. The only long straight section to be occupied for machine purposes is the one used for injection from the linac transfer line to the storage ring. The 20-fold super-periodicity of the storage ring contains an additional seven-fold periodicity (five unit cells plus two matching cells) within the achromats.

Table 2.1: Parameters for the MAX IV 3 GeV storage ring.

Energy [GeV]	3.0
Main radio frequency [MHz]	99.931
Harmonic number	176
Circulating current [mA]	500
Circumference [m]	528
Number of achromats	20
Length of achromat [m]	26.4
Length of long straight sections (BPM to BPM) [m]	4.800
Length of short straight sections (SDend to QFm) [m]	1.302
Number of long straight sections available for IDs	19
Betatron tunes (horizontal / vertical)	42.20 / 14.28
Natural chromaticities (horizontal / vertical)	-49.8 / -43.9
Corrected chromaticities (horizontal / vertical)	+1.0 / +1.0
Momentum compaction factor	$3.07 \times 10^{-4}$
Horizontal emittance (bare lattice) [nm rad]	0.326
Horizontal emittance (with 4 damping wigglers) [nm rad]	0.263
Radiation losses per turn (bare lattice) [keV]	360.0
Radiation losses per turn (with 4 damping wigglers) [keV]	572.1
Natural energy spread (bare lattice)	$7.70 \times 10^{-4}$
Natural energy spread (with 4 damping wigglers)	$9.57 \times 10^{-4}$
Required dynamic acceptance [mm mrad] (horizontal / vertical)	7.1 / 1.3
Required lattice momentum acceptance	$\pm 4.5\%$

In summary, the achromat consists of:

- **LongStr:** a 2.5 m drift section
- **MC:** the matching cell consisting of:
  - OXX, QFend, OXY, QDend, DIPm, OYY, SDend
- **ShortStr:** a 1.3 m drift section
- **UC1:** the unit cell facing the matching section; it consists of:
  - QFm, SFm, QFm, SD, DIP, -DIP, SD
- **UC2:** the outer unit cell consisting of:



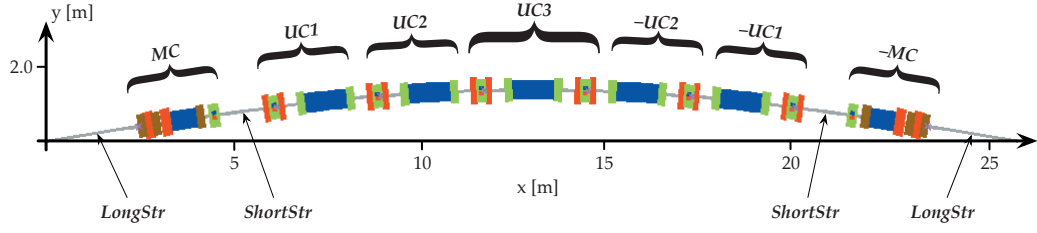


Figure 2.1: Schematic of one achromat of the MAX IV 3 GeV storage ring. The achromat consists of five unit cells and two matching cells. The total bending angle is  $18^\circ$ . The gradient bending magnets (blue) are flanked by sextupoles (green). The bending magnets are interleaved with quadrupoles (red) and sextupoles (green). The final focusing magnets (red) match the beam to the straight section. Octupoles (brown) are installed in the matching section.

– QF, SFo, QF, SD, DIP, –DIP, SD

- **UC3:** the inner unit cell consisting of:

– QF, SFi, QF, SD, DIP, ...

and the mirror of all of the above.

The optical functions for the MAX IV 3 GeV achromat are shown in Fig. 2.2. The compact lattice with strong focusing results in small beta functions and dispersion, reducing the need for large vacuum chamber apertures. For the MAX IV 3 GeV storage ring vacuum chamber a nominal inner diameter of 22 mm has been chosen. The small vacuum chamber cross section allows for small magnet gaps (25 mm full gap). This in turn reduces the required magnet length. By making use of vertically focusing gradient dipoles the lattice becomes even more compact. The vertical acceptance is limited by narrow-gap in-vacuum IDs and not by the lattice design.

### 2.2.3. Bending Magnets

The bending magnets in the five unit cells are sector dipole magnets with a total bending angle of  $3^\circ$  each. Each dipole magnet D consists of two equal half-magnets ( $D = \text{DIP}, -\text{DIP}$ ) where DIP contains the dipole fringe field on one side. The dipole in the matching section, the  $1.5^\circ$  DIPm, consists of a main bending field section (with fringe

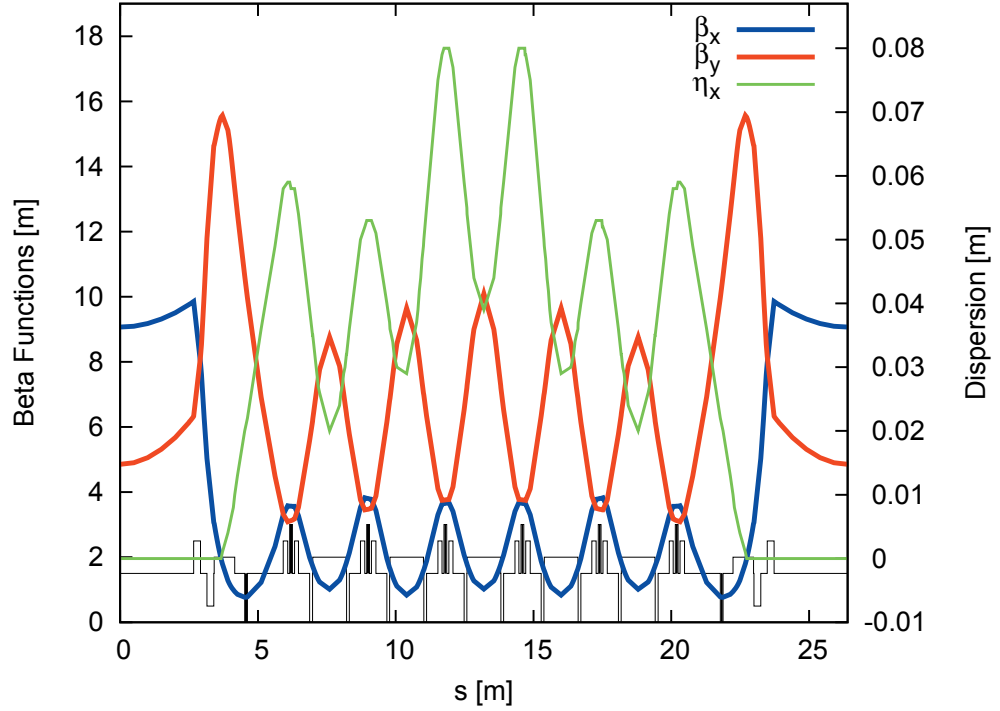


Figure 2.2: One achromat of the MAX IV 3 GeV storage ring. The positions of the magnets are indicated at the bottom in black.

field) and a soft-end section in the direction of the long straight section. The soft-end dipole scheme [9, 10] reduces the amount of synchrotron radiation hitting downstream structures (especially important for the cold bore of super-conducting IDs). A schematic of the bending magnet layout is given in Fig. 2.3.

In addition to the guiding dipole field, the bending magnets contain a vertical focusing gradient. This removes the need for dedicated defocusing quadrupoles making the lattice more compact and at the same time allows for a decrease in horizontal emittance. For beam dynamics studies these dipole magnets have been modeled with several dipole magnet slices (see also Chapter 2.6). The slices have different dipole strengths to model the fringe fields and/or longitudinally varying field strengths as in the actual dipole magnets. The field strengths are plotted in Fig. 2.4 and the parameters given in Table 2.2.

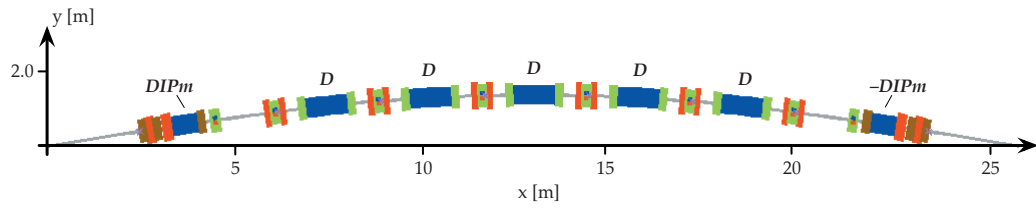


Figure 2.3: Schematic of the bending magnet layout within one achromat of the MAX IV 3 GeV storage ring. The unit cells contain  $3^\circ$  bending magnets ( $D = \text{DIP}, -\text{DIP}$ ). The matching cells contain a  $1.5^\circ$  bending magnet ( $\text{DIPm}$ ) with a soft-end facing the adjacent long straight.

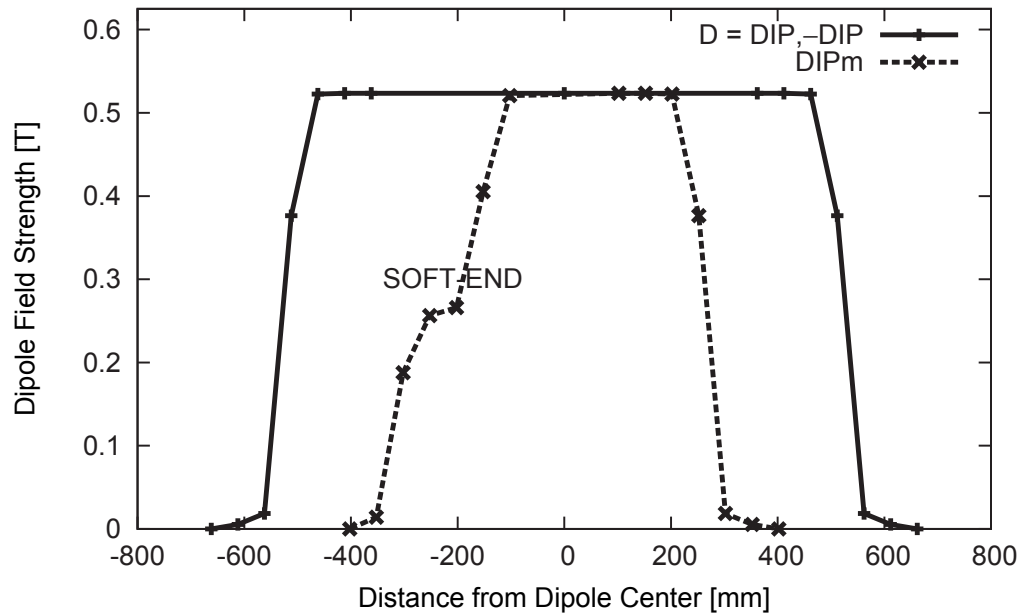


Figure 2.4: Field strength of the different slices used to model the bending magnets (including fringe fields) in the MAX IV 3 GeV storage ring. The soft-end in the matching cell dipole  $\text{DIPm}$  is indicated.

Table 2.2: Parameters for the different slices used to model the bending magnets in the MAX IV 3 GeV storage ring. Slices with 'f' indicate fringe contributions. Slices with 's' indicate soft-end contributions. The main dipole is given by  $D = \text{DIP}, -\text{DIP}$  with  $\text{DIP} = f_6, f_5, f_4, f_3, f_2, f_1, D_0$ . The matching cell soft-end dipole is given by  $\text{DIPm} = f_6, f_5, f_4, f_3, f_2, f_1, D_{m0}, s_1, s_2, s_3, s_4, s_5, s_6$ .

Magnet Slice	Dipole Field [T]	Gradient [T/m]	Length [mm]	Bend Angle [°]
f5	0.005385	0.001212	50.00	0.001543
f4	0.018679	0.064422	50.00	0.005351
f3	0.376410	-5.931011	50.00	0.107834
f2	0.522500	-8.683296	50.00	0.149685
f1	0.523390	-8.690806	50.00	0.149940
D0 / Dm0	0.523600	-8.694711	361.89 / 204.32	1.085673 / 0.612961
s1	0.520680	-8.691507	50.00	0.149164
s2	0.405334	-6.084524	50.00	0.116120
s3	0.265973	-4.240015	50.00	0.076196
s4	0.256269	-4.183135	50.00	0.073416
s5	0.187622	-0.288492	50.00	0.053750
s6	0.014171	-0.006915	50.00	0.004060

### 2.2.4. Focussing Magnets

There are in total five quadrupole families providing the focusing in the MAX IV 3 GeV storage ring. A summary of the focusing magnet parameters is given in Table 2.3. A schematic of the focusing magnet layout is given in Fig. 2.5.

Table 2.3: Quadrupole magnet parameters for the bare lattice.

<i>Unit Cell Focusing Magnets (QF)</i>	
Type	Dedicated quadrupole
Minimum bore radius [mm]	12.5
Length [m]	0.15
Quadrupole gradient [T/m]	40.38
<i>Matching Cell Focusing Magnets (QFm)</i>	
Type	Dedicated quadrupole
Minimum bore radius [mm]	12.5
Length [m]	0.15
Quadrupole gradient [T/m]	37.80
<i>Final Focusing Magnets (QFend, QDend)</i>	
Type	Dedicated quadrupole
Minimum bore radius [mm]	12.5
Length [m]	0.25 / 0.25
Quadrupole gradient [T/m]	35.37 / $-22.40$
<i>Defocusing Magnets (QD)</i>	
Type	Gradient integrated in dipoles
Minimum full gap height [mm]	28.0
Length [m]	0.650
Quadrupole gradient [T/m]	$-8.69$ (max.)

The original design foresaw the use of combined function quadrupoles-sextupole magnets between the unit cells in order to integrate sextupole focusing and achieve a more com-

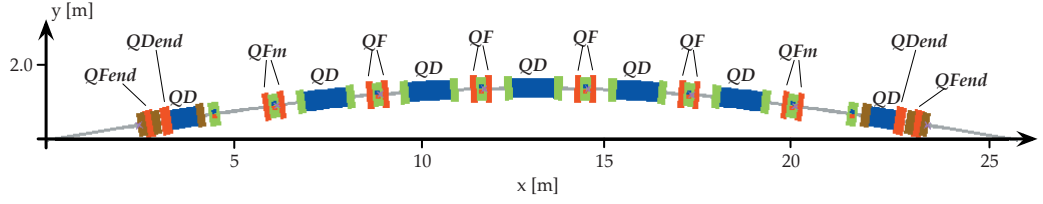


Figure 2.5: Schematic of the quadrupole magnet layout within one achromat of the MAX IV 3 GeV storage ring.

pact lattice. A thorough investigation revealed however that the 300 mm long magnets were the source of strong nonlinearities and limited dynamic aperture due to their long sextupole component. Another concern was that the focusing strength and sextupole setting were tied to each other in the combined function design. It was feared that the lack of tuning options could become a problem during commissioning and possibly beyond.

It was therefore decided to split up these long quadrupole magnets into two 150 mm long quadrupoles of equal strength and insert a dedicated thin sextupole at the center. A drift space of 50 mm was left between the magnets to provide space for the coils. There are six such “magnet sandwiches” flanking the unit cells. The inner four contain pairs of the QF family while the outer two use pairs of the QFm family. The QFm family is most efficient to adjust the dispersion in the straight section. The quadrupoles in the QF and QFm family are 150 mm long each and have a minimum bore radius is 12.5 mm.

The defocusing quadrupole family (QD) is given by the gradient in the bending magnets. Pole-face strips will be included to allow for tuneability of the QD component. A few percent tuning range should be sufficient to move the tunes adequately (see Table 2.6).

Finally two quadrupole families QFend and QDend are introduced for matching in the straight section. They have the same 12.5 mm minimum bore radius as the other quadrupoles. Due to the required focusing strength and tuneability their length was extended to 250 mm. They are positioned downstream of the matching bend with the QFend closest to the straight section.



### 2.2.5. Working Point

The linear optics of the MAX IV 3 GeV storage ring have been tuned in such a way to achieve a working point at tunes  $\nu_x = 42.20$  and  $\nu_y = 14.28$ . This puts both fractional tunes below the half integer (this is necessary to damp transverse resistive wall instability [11]). In order to make the machine less sensitive to misalignments the tunes should stay clear of the integer (closed orbit instability due to dipole errors) and half integer (beam blow-up due to gradient errors) [12]. It is however not feasible to put them both at 0.25 because this would lead to a working point on the linear coupling resonance which is driven by skew quadrupolar fields that are always present in real machines. The choice of working point for the MAX IV 3 GeV storage ring close but not on the quarter-integer reflects this.

The choice of the working point was however also heavily influenced by the nonlinear dynamics, specifically by the tune footprint for amplitude-dependent tune shifts and chromaticity. These issues are described in more detail in Section 2.3.4.

With the achromat tuned in this way the horizontal beta function oscillates between 0.8 m and 3.8 m within the cells and reaches a maximum of 9.8 m in the QFend before the straight. The vertical beta function oscillates between roughly 3.1 m and 10.1 m within the cells. The maximum vertical beta function is 15.5 m and is reached in the bending magnet of the matching cell. Therefore these final elements of the achromat (QFend, QDend, and matching cell bend) will be most sensitive to misalignment errors; accordingly this is also the area where orbit correctors are most efficient (see Section 2.4.4).

In the straight sections the vertical beta function is reduced to 4.8 m. This corresponds roughly to the maximum ID length which assures that the vertical acceptance is not reduced by the ID aperture. Increasing the vertical beta function is not desirable because of the elastic scattering lifetime. For a typical undulator beamline the diffraction limit is  $\varepsilon_\gamma = \lambda/4\pi = 8$  pmrad. Therefore we require betatron coupling to remain below  $\kappa < \varepsilon_\gamma/\varepsilon_x = 2.4\%$ . At this coupling the vertical source size would be  $\sigma_y = \sqrt{\varepsilon_y\beta_y} = 6.2$   $\mu\text{m}$ . In order to improve matching of the electron beam to the photon beam emerging from the ID (and hence increase the photon brightness), it can be of interest to further reduce the emittance coupling. Other modern light sources routinely

operate with  $\kappa \ll 1\%$  so we anticipate low coupling. In addition, since we plan to match the achromat optics locally to strong IDs (cf. Section 2.2.6), vertical beta functions in the IDs will be reduced to  $\beta_y^* \geq 1$  m. In summary, the vertical source at the center of the ID can be expected to be as low as  $2 \mu\text{m}$ .

At a horizontal beta function of 9 m in the straights the horizontal rms beam size for is  $54 \mu\text{m}$ . A further reduction of this value is not feasible because it would require increasing the vertical betatron in the straight section. Maximum values for the dispersion of 8 cm are found at the QF magnets flanking the center unit cell. This gives a horizontal orbit offset of 3.6 mm for a  $\pm 4.5\%$  off-momentum particle (and a maximum excursion of 7 mm for a Touschek-scattered particle). Dispersion reduces to zero in the matching bending magnet and remains zero in the straight section.

Ideally all beamlines should operate in a vertically diffraction-limited regime. However, it is not advisable to chose a vertical beam size far below the diffraction limit because of intrabeam scattering and lifetime concerns. It is therefore desirable to exercise tight coupling control. A set of non-dispersive skew quadrupoles can be used to minimize betatron coupling. Together with orbit correction with respect to sextupole magnet centers this should minimize spurious vertical dispersion. If the resulting very low coupling leads to lifetime issues, a set of dedicated dispersive skew quadrupoles will be used to introduce local vertical dispersion in the achromats [13].

### 2.2.6. Effects of Insertion Devices

A strong undulator or wiggler will have a net vertical focusing effect on the stored electron beam. Without further correction this causes a vertical tune shift

$$\Delta\nu_y \approx \frac{\pi L \langle \beta_y \rangle K^2}{2\lambda_u^2 \gamma^2} \quad (2.2)$$

and a vertical beta beat

$$\frac{\Delta\beta_y}{\beta_y} \approx \frac{2\pi\Delta\nu_y}{\sin(2\pi\nu_y)} \quad (2.3)$$

where  $L$  is the length of the ID,  $\lambda_u$  its period length [3]. These perturbations of the design optics can lead to a reduction of dynamic aperture and lifetime.

From a linear optics standpoint this effect therefore needs to be compensated in two steps:

- ensure that the ID is matched to the adjacent achromats,
- restore the original machine working point.

Matching of the ID to the adjacent straight sections can be accomplished by tuning the final focusing magnets QFend and QDend. In principle this can be one in two ways: the strength of the QDend can be reduced in order to compensate for the vertical focusing of the ID (“compensation”) or it can be increased in order to compress the beam vertically thus reducing the vertical focusing effect of the undulator or wiggler magnetic field (“mitigation”). A comparison of both methods has been performed. It has been observed that while the “mitigation” approach results in a larger change in total phase advance, the “compensation” approach leads to comparably high values for the vertical beta function ( $\sim 6$  m) in the ID. An example of these two adjustments is displayed in Fig. 2.6 where the final focusing magnets have been tuned to match to the adjacent achromats to a 2.22 T permanent magnet damping wiggler (PMDW).

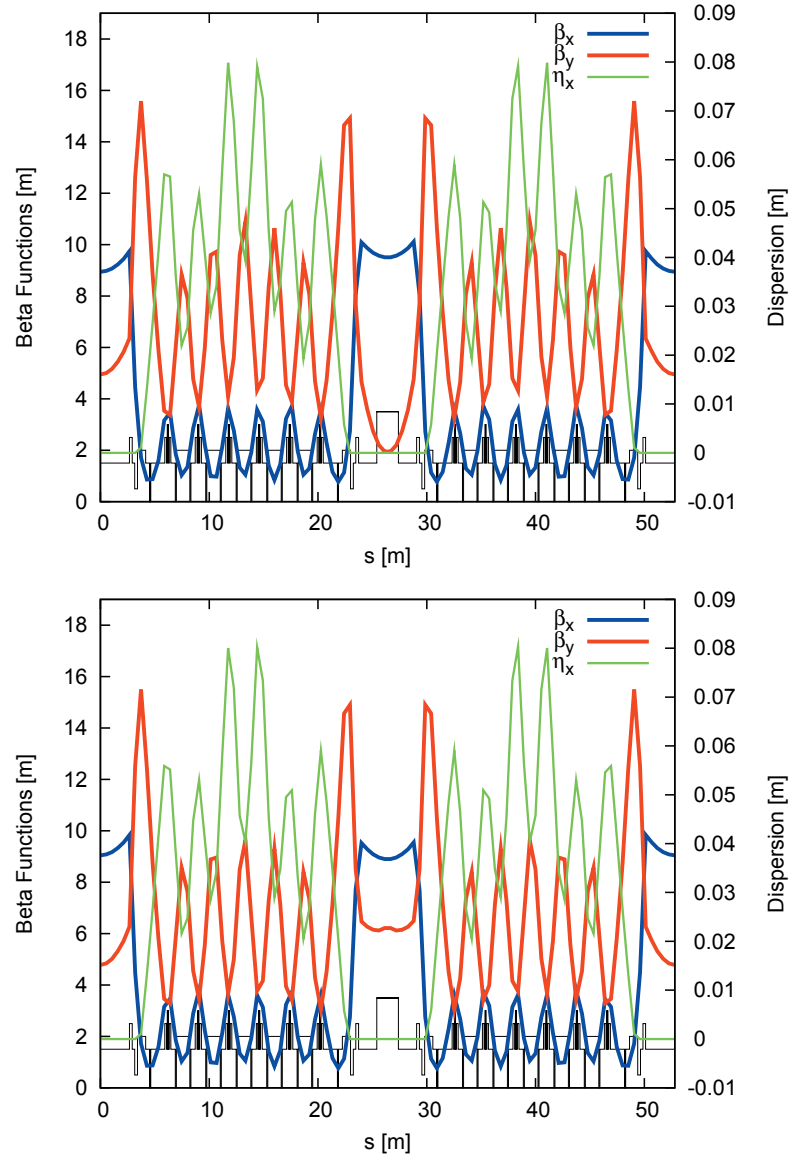


Figure 2.6: Two achromats of the MAX IV 3 GeV storage ring with a 2.22 T PMDW installed in the long straight section between the two achromats. The positions of the magnets are indicated at the bottom in black. The wiggler is also indicated. The final focusing magnet have been tuned to match the ID to the adjacent achromats. The upper plot shows the preferred “mitigation” approach. The lower plot shows the “compensation” approach.

The PMDW parameters are summarized in Table 2.4. This wiggler type has been chosen as a test case because it represents the strongest vertically focusing ID to be installed in the MAX IV 3 GeV storage ring. It is foreseen to install four such devices to act as damping wigglers. This reduces the emittance from the bare lattice value of 0.336 nm rad to a value of 0.299 nm rad.<sup>1</sup>

Table 2.4: Parameters of the 2.22 T PMDW.

Length [m]	2.0
Number of periods	25
Period length [mm]	80
Peak magnetic field strength [T]	2.22
Full gap height [mm]	4
Radiated energy per turn (at peak strength) [keV]	53
Reduction of overall emittance (at peak strength) [nm rad]	0.016

For the reasons mentioned above it is advisable to use the “mitigation” approach to match IDs to adjacent achromats in the MAX IV 3 GeV storage ring. In the case of the 2.22 T PMDWs installed in a long straights of the MAX IV 3 GeV storage ring, the tuning required is shown in Table 2.5.

As a result of matching the adjacent achromats to an ID, the phase advance over these achromats is changed and thus the global machine working point is shifted. This can be corrected by a slight global tuning of the main quadrupoles in the storage ring. In this example the gradient strengths in the dipole slices have been scaled together in order to adjust the defocusing strength. This illustrates the necessity for additional pole-face strips on the dipoles. These windings act as a tuning knob for the defocusing strength of the entire lattice. Table 2.6 shows the required tuning for the example case of a 2.22 T PMDW installed in the MAX IV 3 GeV storage ring.

Another important example is a typical undulator to be installed into the MAX IV 3 GeV storage ring. These devices are 1.27 T in-vacuum undulators (IVUs) with a total length of just over 3 m. The key parameters are given in Table 2.7. The adjustments

---

<sup>1</sup>An option to install more PMDWs in order to reduce the emittance even further is being investigated. If budget allows one could contemplate filling up all free straight sections with PMDWs. Such PMDWs would only be removed to make space for the installation of new user IDs.

Table 2.5: Adjustments required to match the adjacent achromats to a 2.22 T PMDW installed in the long straight section of the MAX IV 3 GeV storage ring. In the “mitigation” approach the relevant change is the increase in defocusing magnet strength (15% here) to reduce vertical beam size within the ID. As a result of this matching, the beta function values at the far ends of the adjacent long straights are matched to those of a bare achromat. This ensures that the PMDW does not cause a beta beat throughout the rest of the storage ring.

Before Adjustment		After Adjustment
$k_{\text{QFend}} = 35.34 \text{ T/m}$	$\longrightarrow$	36.58 T/m
$k_{\text{QDend}} = -22.40 \text{ T/m}$	$\longrightarrow$	-25.77 T/m
$\Downarrow$		$\Downarrow$
$\beta_x^* = 9.000 \text{ m}$	$\longrightarrow$	9.000 m
$\beta_y^* = 3.436 \text{ m}$	$\longrightarrow$	4.800 m

made to match the IVU to the achromats along with the resulting tune shift are shown in Table 2.8.

Although these devices each have a weaker overall effect on the storage ring optics compared to the PMDWs, roughly a dozen IVUs will be installed. This means that the resulting storage ring emittance and radiated energy per turn (and hence the damping time) will be heavily influenced by the IVUs. The emittance of a storage ring with IDs can be expressed as [3]

$$\varepsilon_{\text{ID}} = \varepsilon_0 \frac{1 + \frac{2\sqrt{2}\pi^3 \rho_0^3 K^3 \langle H_{\text{ID}} \rangle}{\lambda_{\text{ID}}^3 \gamma^3 \langle H_0 \rangle}}{1 + \frac{\pi N \rho_0 K^2}{\lambda_{\text{ID}} \gamma^2}} \quad (2.4)$$

where

$$\langle H_i \rangle = \frac{1}{C} \int \frac{ds}{\beta} \left[ \eta^2 + \left( \beta \eta' - \frac{1}{2} \beta' \eta \right)^2 \right] \quad (2.5)$$

with  $C = \oint ds$  the machine circumference and the expression evaluated either for the bare lattice (dipoles)  $H_0$  or for an ID  $H_{\text{ID}}$ .

While four PMDWs increase the radiated energy of the bare lattice from 360 keV to



Table 2.6: Adjustments required to re-establish the original working point after insertion of a single 2.22 T PMDW in the MAX IV 3 GeV storage ring. The largest change is the compensation of an excess 1% vertical phase advance. Note that the tune shift shown here corresponds to one PMDW installed in an otherwise bare lattice. In order to correct for all four PMDWs in the storage ring, we require a reduction of the dipole gradient by 0.8%.

Before Adjustment		After Adjustment
$k_{\text{QF}} = 40.38 \text{ T/m}$	$\longrightarrow$	40.33 T/m
Dipole Gradient Scaling = 1.000	$\longrightarrow$	0.998
$\Downarrow$		$\Downarrow$
$\nu_x = 42.194$	$\longrightarrow$	42.200
$\nu_y = 14.428$	$\longrightarrow$	14.280

Table 2.7: Parameters of the 1.27 T in-vacuum undulators.

Length [m]	3.002
Number of periods	158
Period length [mm]	19
Peak magnetic field strength [T]	1.27
Full gap height [mm]	4
Radiated energy per turn (at peak strength) [keV]	27.3
Reduction of overall emittance (at peak strength) [nm rad]	0.013

572 keV, adding ten IVUs will push radiated energy loss to a total of 845 keV. Meanwhile the bare lattice emittance of 0.326 nm rad is reduced to 0.263 nm rad by four PMDWs, but finally reaches a minimum of 0.201 nm rad when the ten IVU are added. This is summarized in Table 2.9 and plotted in Fig. 2.7.

Equation 2.4 also illustrates how IDs installed in dispersive sections can blow up the emittance and hence the beam size in all other insertion devices. It is for this reason that **IDs are not foreseen to be installed in the short straight sections of the MAX IV 3 GeV storage ring**. The installation of such devices can be considered once all dispersion-free long straights have been occupied with IDs. However, as long as dispersion-free long straight sections remain available, no ID should be installed in a short straight as this would dilute the photon intensity in all beamlines.

Table 2.8: Adjustments required to match the adjacent achromats to a 1.27 T IVU installed in the long straight section of the MAX IV 3 GeV storage ring. This corresponds to the “mitigation” approach. The main change is increasing the QDend strength by 14%. Note that the tune shift shown here corresponds to one IVU installed in an otherwise bare lattice.

Before Adjustment	After Adjustment
$k_{\text{QFend}} = 35.34 \text{ T/m}$	$\longrightarrow 36.52 \text{ T/m}$
$k_{\text{QDend}} = -22.40 \text{ T/m}$	$\longrightarrow -25.60 \text{ T/m}$
	$\Downarrow$
	$\Delta\nu_x = -5.67 \times 10^{-3}$
	$\Delta\nu_y = +1.38 \times 10^{-1}$

Table 2.9: Budget for different ID configurations of the MAX IV 3 GeV storage ring. The calculations have been done assuming each ID is at running at peak field strength. The last case corresponds to a fully loaded storage ring with ten in-vacuum undulators and all remaining straights filled with damping wigglers. Given are radiated energy per turn  $\Delta E$ , horizontal emittance  $\varepsilon_x$ , energy spread  $\sigma_\delta$ , horizontal damping time  $\tau_x$ , and longitudinal damping time  $\tau_\delta$ . As a reference, the synchrotron period is for the bare lattice is roughly 0.75 ms and the revolution period is 1.76  $\mu\text{m}$ .

	$\Delta E$ [keV]	$\varepsilon_x$ [nm rad]	$\sigma_\delta$ [%]	$\tau_x$ [ms]	$\tau_\delta$ [ms]
Bare lattice	360.0	0.326	0.077	15.8	25.8
4 PMDWs	572.1	0.263	0.096	12.0	12.6
4 PMDWs and 10 IVUs	845.4	0.201	0.091	9.2	7.6
4 PMDWs and 15 IVUs	982.0	0.179	0.090	8.2	6.4
9 PMDWs and 10 IVUs	1264.8	0.169	0.103	6.8	4.7

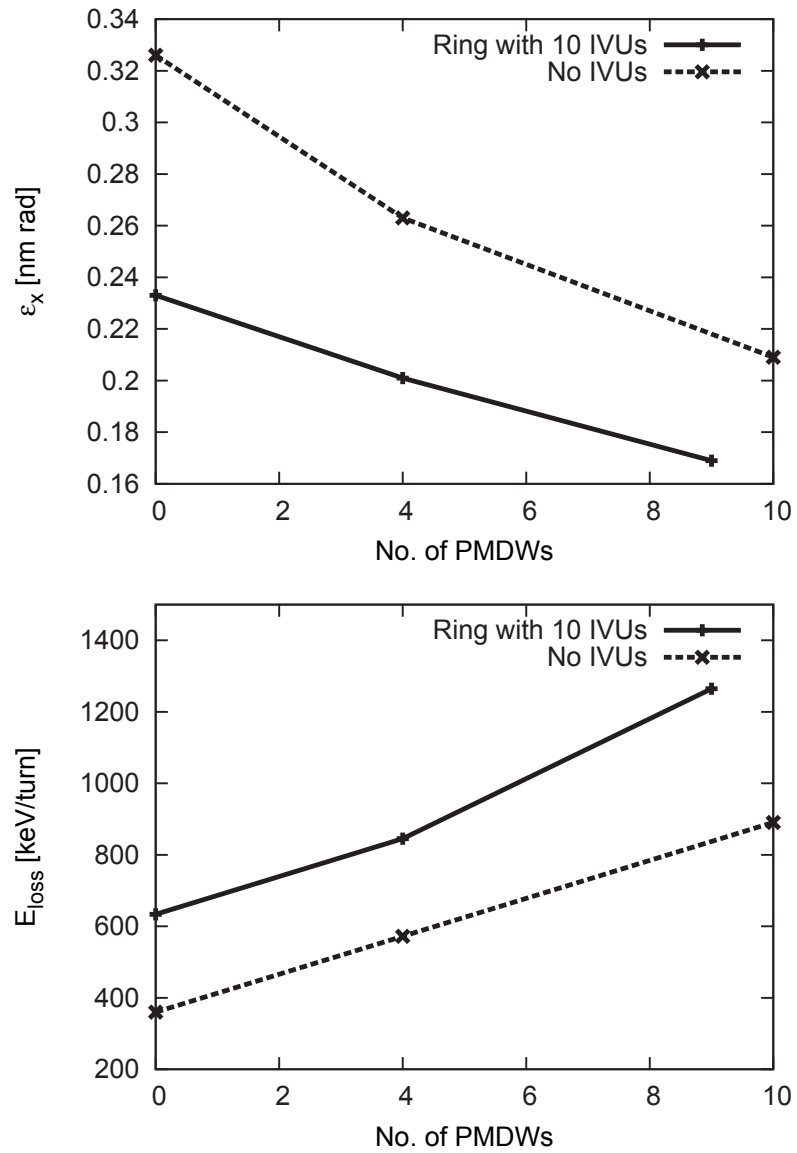


Figure 2.7: Horizontal lattice emittance (top) and energy loss per turn (bottom) for different numbers of PMDWs installed in the MAX IV 3 GeV storage ring.

### 2.2.7. Intrabeam Scattering

Because the transverse emittance of the MAX IV 3 GeV storage ring lattice is so small, intrabeam scattering (IBS) is expected to have a significant influence on the overall equilibrium emittance. Emittance values given so far take into account the emission of synchrotron radiation and quantum emission fluctuations, but not IBS.

In order to quantify the effect of IBS calculations have been performed in Tracy-3 and verified with ZAP [14]. The results calculated for a total stored current of 500 mA and expected rf parameters are summarized in Table 2.10. The emittance is significantly underestimated when IBS is not taken into account in the case of the bare lattice (the inclusion of IBS leads to a 39% increase of the equilibrium emittance). However, once the harmonic Landau cavities and IDs are added, the influence of IBS becomes small ( $< 15\%$ ) as can be seen in Fig. 2.8. In the case of a storage ring with damping wigglers, IDs, and Landau cavities the equilibrium emittance including IBS remains well below 0.3 nm rad.

Table 2.10: Equilibrium values for the horizontal emittance of the MAX IV 3 GeV storage ring calculated with (right) and without (left) IBS. The influence of the harmonic Landau cavities (LC) is also shown.

	$\varepsilon_x$ [nm rad]	
Bare Lattice	0.326	0.453
Bare Lattice with LC	0.326	0.372
Lattice with 4 PMDWs and LC	0.263	0.297
Lattice with 4 PMDWs, 10 IVUs, and LC	0.201	0.231

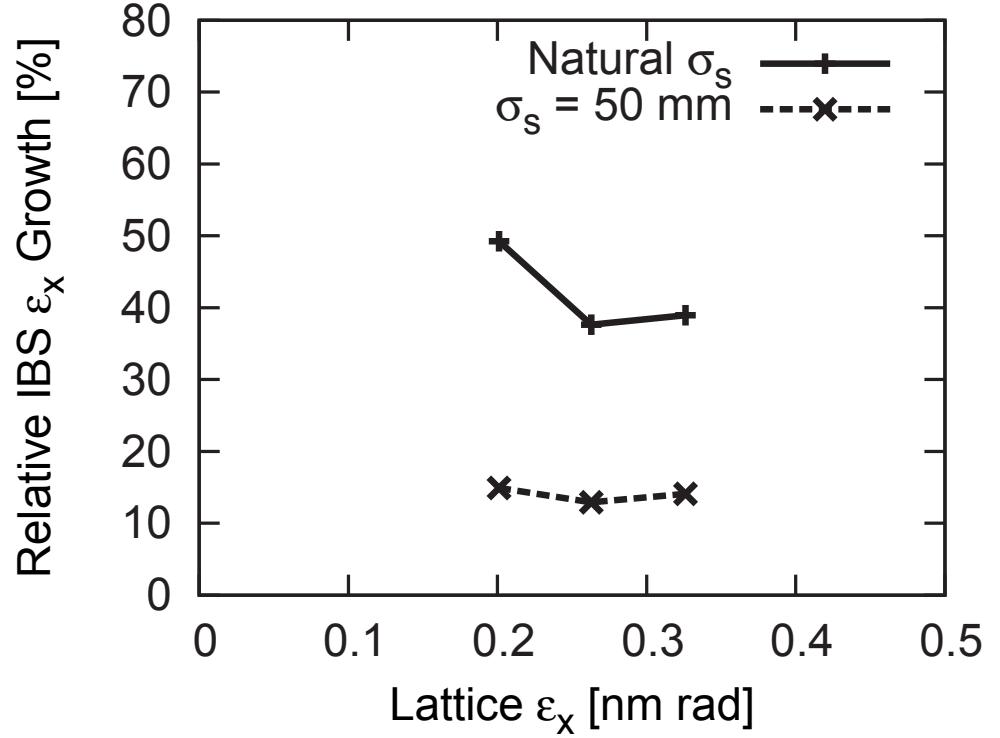


Figure 2.8: Relative growth of the horizontal emittance when IBS is included vs. the horizontal lattice emittance without IBS. The data has been calculated with ZAP assuming a single bunch charge of  $Q_b = 5$  nC and a vertical emittance held constant at  $\epsilon_y = 8$  pm rad for three configurations (see Table 2.10). The calculation has been performed for two different bunch lengths: the natural bunch length and  $\sigma_s = 50$  mm to illustrate the effect of the Landau cavities. With stretched bunches, including IBS adds roughly 15% to the horizontal emittance regardless of the configuration. Without bunch lengthening, emittance growth from IBS is significantly larger and becomes even stronger for ultra-low emittance configurations.

## References

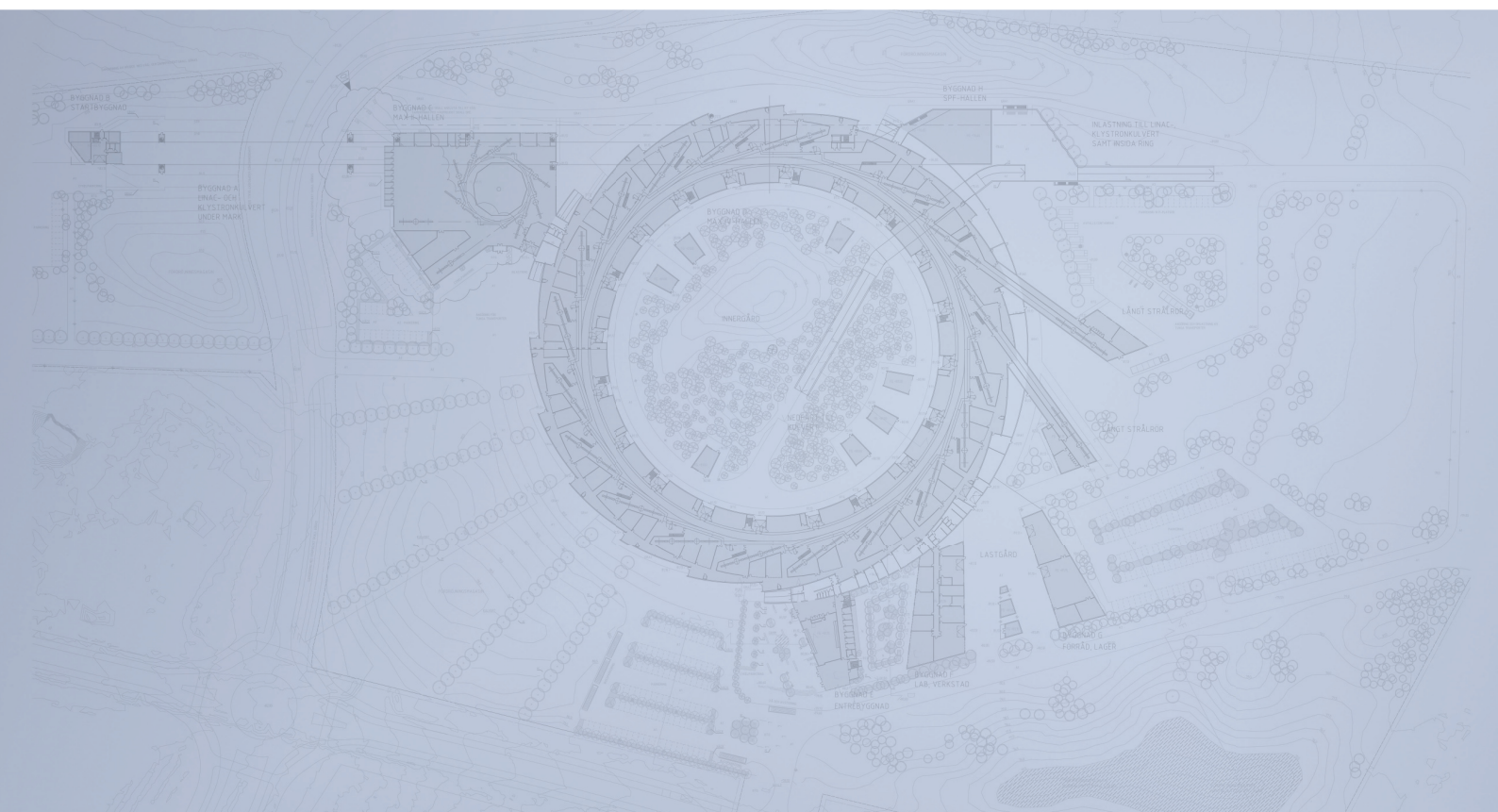
- [1] M. Korostelev, F. Zimmermann, *Optimization of CLIC Damping Ring Design Parameters*, Proceedings of EPAC 2002, Paris, France.
- [2] A. Wolski, J. N. Corlett, *The Next Linear Collider Damping Ring Lattices*, Proceedings of PAC 2001, Chicago, USA.
- [3] J.B. Murphy, *Synchrotron Light Source Data Book*, available at <http://www.nsls.bnl.gov/newsroom/publications/otherpubs/dbook>
- [4] S.Y. Lee, L. Teng, Theoretical Minimum Emittance Lattice for an Electron Storage Ring, in: Proceedings of PAC 1991, May 6–9, San Francisco CA, USA, 2007, pp. 2679–2681.
- [5] Lattice files can be obtained at [http://www.maxlab.lu.se/local/maxiv\\_reports/accelerators\\_machine/3GeV/Lattice/index.html](http://www.maxlab.lu.se/local/maxiv_reports/accelerators_machine/3GeV/Lattice/index.html)
- [6] A. Streun, *OPA*, code and documentation available at <http://slsbd.psi.ch/~streun/opa>
- [7] J. Bengtsson, *Tracy-2 User's Manual*, unpublished
- [8] P. Elleaume, A New Approach to the Electron Beam Dynamics in Undulators and Wigglers, in: Proceedings of 3rd European Particle Accelerator Conference (EPAC-92), March 24–28, Berlin, Germany, 1992, pp. 661–663.
- [9] R. Nagaoka, A. F. Wrulich, *Emittance minimisation with longitudinal dipole field variation*, Nucl. Instr. Meth. A 575 (2007) 292.
- [10] *MAX IV Conceptual Design Report*, available at <http://www.maxlab.lu.se/maxlab/publications/max4/MAX-IV-CDR.pdf>



- [11] A. Hofmann, *Beam Instabilities*, Proceedings of the CERN Accelerator School on Synchrotron Radiation and Free-electron Lasers 2003, Brunnen, Switzerland
- [12] A. Streun, *Lattices for Light Sources*, Proceedings of the CERN Accelerator School on Synchrotron Radiation and Free-electron Lasers 2003, Brunnen, Switzerland
- [13] C. Steier, D. Robin, A. Wolski, G. Portmann, J. Safranek, *Coupling Correction and Beam Dynamics at Ultralow Vertical Emittance in the ALS*, Proceedings of PAC 2003, Portland OR, USA, 2003, pp. 3213–3215.
- [14] M.S. Zisman, S. Chattopadhyay, J.J. Bisognano, ZAP User's Guide, LBL 21270, December 1986.



# Detailed Design Report



## Chapter 2

### MAX IV 3 GeV Storage Ring

#### 2.3. Nonlinear Optics

MAX IV Facility



# 2.3. Nonlinear Optics

---

- 2.3. Nonlinear Optics .....2
- 2.3.1. Overview ..... 2
- 2.3.2. Sextupoles ..... 3
- 2.3.3. Octupoles ..... 6
- 2.3.4. Dynamic Aperture..... 11
- 2.3.5. Energy Acceptance .....16
- 2.3.6. Effects of Insertion Devices..... 22
- References ..... 34

## 2.3. Nonlinear Optics

---

### 2.3.1. Overview

In order to correct the large natural negative chromaticity to slightly positive values, two families of strong chromatic sextupoles are required for the MAX IV 3 GeV storage ring. Because of their nonlinear nature, chromatic sextupoles lead to a variation of the tune with betatron amplitude. Particle motion can become unstable above certain amplitudes in such a way that a particle can no longer be stored within the machine. The maximum amplitude at which a particles can be stored is called the dynamic aperture (DA). Obviously this DA can vary around the storage ring. If not otherwise specified, DA refers to the DA at the center of the injection straight.

Ideally the DA would be as large as the physical aperture, but due to the nonlinear effects this is usually not the case.<sup>1</sup> In order to enlarge the DA compensation sextupoles are installed in the storage ring. If this is done in zero-dispersion areas the sextupoles are referred to as harmonic sextupoles because they have no chromatic effect on the beam. The primary goal of the nonlinear lattice design is then to ensure that the DA is sufficient to achieve the required beam lifetime and increase injection efficiency.

Second-order effects of the sextupoles cause large amplitude-dependent tune shifts and non-linear chromatic tune shifts. Both can reduce DA significantly which leads to low injection efficiency and bad lifetime. Conventional sextupole optimization puts a lot of weight on amplitude-dependent tune shifts. The very strong sextupoles in MAX IV make such corrections an absolute necessity. Octupoles are the obvious choice here since amplitude-dependent tune shifts and quadratic chromaticity are first-order effects of an octupole. Several families of weak octupoles placed at suitable locations can therefore be used to efficiently restore DA and increase injection efficiency.

---

<sup>1</sup>It is important to note here that even a storage ring consisting only of linear elements (bending magnets, quadrupoles) will show nonlinear effects due to magnet fringe fields, magnet imperfections, misalignments, etc. It is therefore imperative to design a storage ring with nonlinear optics in mind from the start. As correctly pointed out by others [1, 2], there is no such thing as a purely linear optics design. Linear and nonlinear lattice design are interleaved and have to be treated together.

### 2.3.2. Sextupoles

The MAX IV 3 GeV storage ring has five sextupole families. There are two defocusing sextupole families and three focusing sextupole families. Although one family is at low-dispersion location, none of the five families is purely harmonic. A schematic of the sextupole magnet layout is given in Fig. 2.1. The position of the sextupoles is also indicated in the plot showing the optical functions for one achromat (Fig. 2.2). A summary of the sextupole parameters is given in Table 2.1.

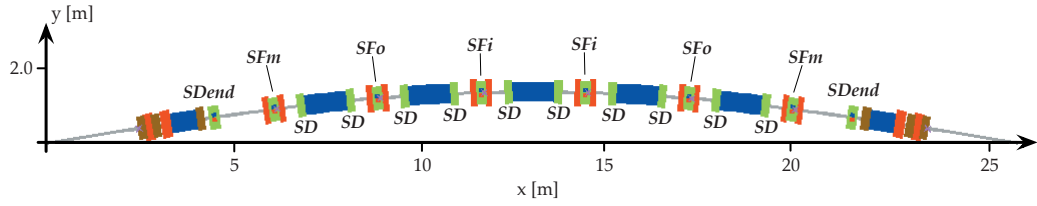


Figure 2.1: Schematic of the sextupole magnet layout within one achromat of the MAX IV 3 GeV storage ring. Sextupoles are indicated in green.

There are three focusing sextupole families per achromat (SFi, SFo, SFm). All focusing sextupoles are flanked by focusing quadrupoles (QF, QFm) so they are located at local dispersion maxima. Each achromat also contains two defocusing sextupole families.

The main defocusing family (SD) consists of five pairs of sextupole magnets so that each unit cell dipole is flanked by a defocusing sextupole. Because their position is close to the unit cell bending magnets they are at locations of relatively low dispersion. The second defocusing family is installed in the matching cell (SDend) at the minimum of the horizontal beta function. There is a 36 cm gap between the matching cell dipole and the defocusing sextupole in which dispersion increases a bit (the matching cell dipole opens up dispersion within the achromat).

The sextupole strengths have been calculated with OPA. Two families were designated to correct the natural chromaticities to  $\xi_{x,y} = +1.0$ . SD and SFi were chosen because they are the most efficient family (located at highest dispersion) of each type. OPA was then used to optimize the strengths of all sextupole families in such a way as to minimize the first order chromatic and geometric driving terms of the sextupole Hamiltonian plus the three second order terms for amplitude-dependent tune shift [2]. In addition



Table 2.1: Sextupole magnet parameters for the five sextupole families in the bare lattice (without octupoles).

<i>Focusing Sextupoles</i> (SF <sub>i</sub> , SF <sub>o</sub> , SF <sub>m</sub> )	
Number per achromat	$2 \times 3$
Minimum bore radius [mm]	12.5
Length [m]	0.100
Sextupole field [T/m <sup>2</sup> ]	2216 / 1738 / 1509
<i>Defocusing Sextupoles</i> (SD)	
Number per achromat	$5 \times 2$
Minimum bore radius [mm]	12.5
Length [m]	0.100
Sextupole field [T/m <sup>2</sup> ]	−1204
<i>Matching Cell Defocusing Sextupoles</i> (SD <sub>end</sub> )	
Number per achromat	$2 \times 1$
Minimum bore radius [mm]	12.5
Length [m]	0.100
Sextupole field [T/m <sup>2</sup> ]	−1226

there are several more terms available for optimization (two quadratic chromaticities, eight octupolar resonances, two cubic chromaticities) and also the weights for each of the driving terms can be varied. Finding more refined sextupole settings is ongoing work.

OPA is then used to calculate amplitude-dependent tune shifts and chromatic tune shifts from tracking. This gives a first impression of the tune footprint. An example is given in Fig. 2.2. The optimized sextupole settings found with OPA are then transferred to the Tracy-3 lattice file. Tracy-3 is used to confirm and the non-linear chromaticity (shown in Fig. 2.3) and the amplitude-dependent tune shifts (shown in Fig. 2.4). Agreement between the two codes regarding tunes, chromaticities, and amplitude-dependent tune shifts is excellent for the bare lattice.

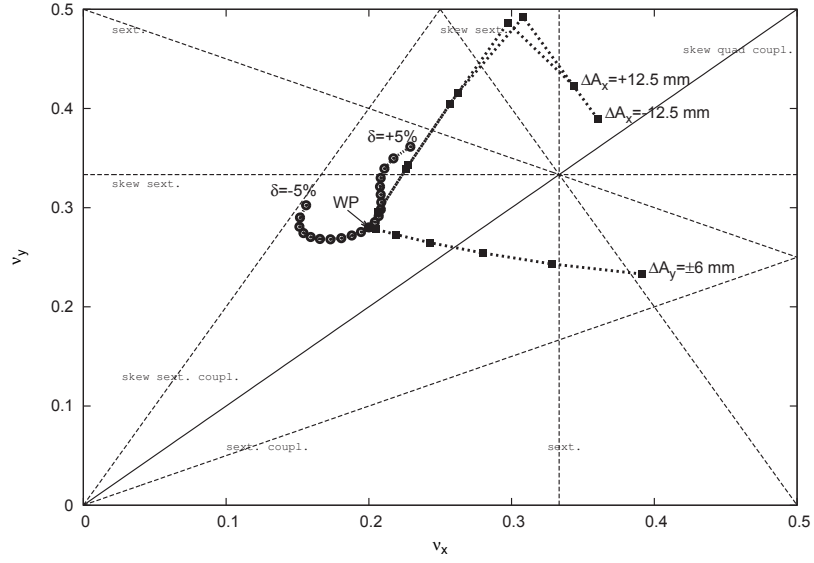


Figure 2.2: A plot of fractional tune space for the MAX IV 3 GeV storage ring bare lattice (without octupoles) as calculated by OPA. Resonance and skew resonance lines have been included up to third order. WP indicates the working point. The step size chosen for the chromatic tune shift is 0.5% and 2.5 mm [1.0 mm] for the horizontal [vertical] amplitude-dependent tune shift.

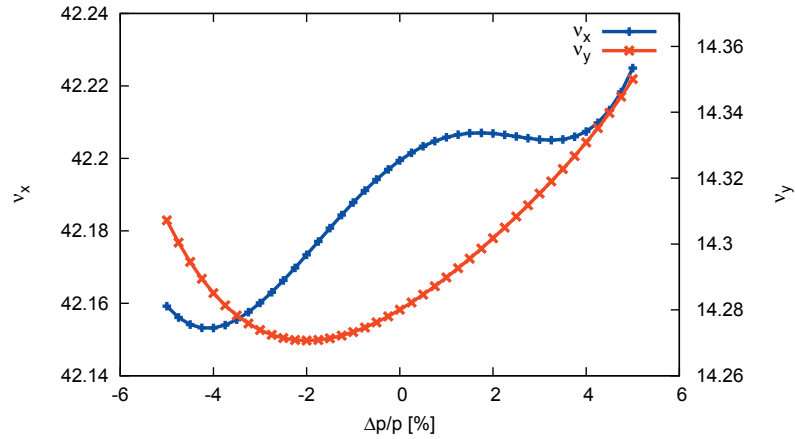


Figure 2.3: Chromatic tune shift for the MAX IV 3 GeV storage ring bare lattice (without octupoles) as calculated by Tracy-3. Agreement with results given by OPA is excellent.

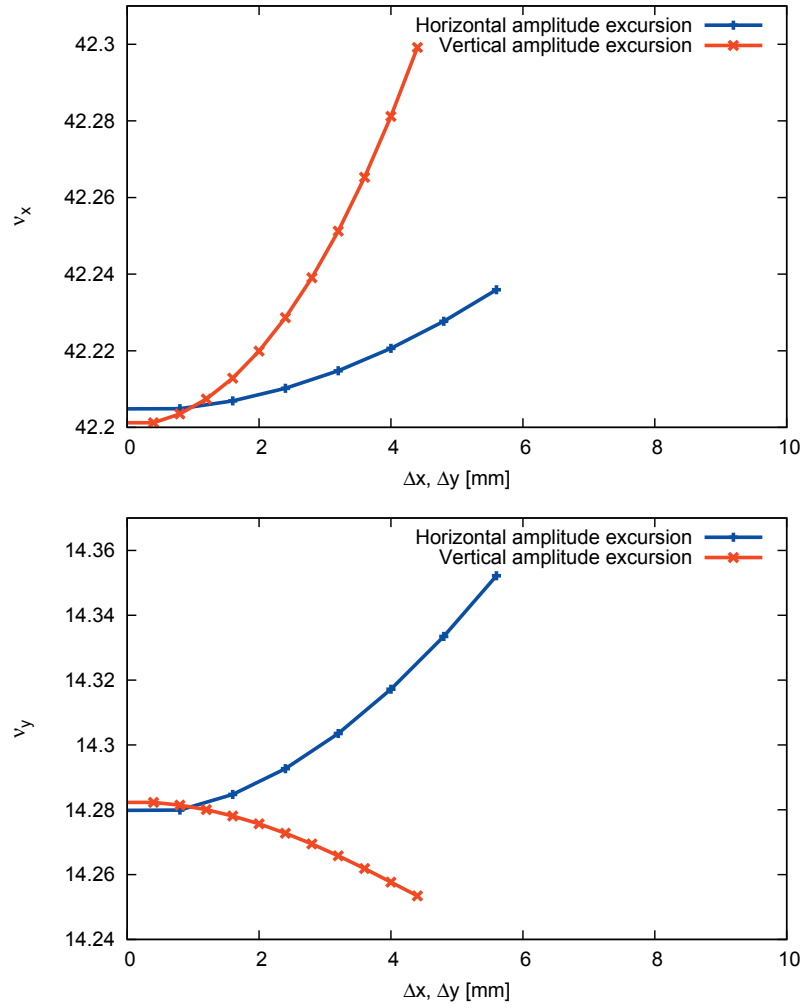


Figure 2.4: Plots showing the amplitude-dependent tune shift for the MAX IV 3 GeV storage ring bare lattice (without octupoles) as calculated by Tracy-3. Agreement with results given by OPA is excellent.

### 2.3.3. Octupoles

Originally a strategy was pursued where all three first-order octupole driving terms for amplitude-dependent tune shifts and both first-order driving terms for quadratic chromaticity were cancelled by using up to five families of harmonic and chromatic

octupoles. An SVD optimizer was written<sup>2</sup> in order to find octupole settings that would cancel specific driving terms. Several different locations and optimization schemes were investigated. However, it quickly became clear that the damage caused by higher-order chromatic terms outweighed the benefits of using chromatic octupoles.

Therefore a new approach was taken in which only three harmonic octupole families were used to cancel the three first-order octupole driving terms for amplitude-dependent tune shifts. The sextupole optimization was changed accordingly so the sextupole settings minimize the quadratic chromaticity. The net effect of these sextupole and octupole tunings is that amplitude-dependent and chromatic tune shifts are both effectively minimized. It was also noticed that an overall optimization does not call for complete cancellation of the first-order driving terms. Instead, a reduced octupole strength allowing for a small residual driving term for first-order amplitude-dependent tune shift helped reduce the quadratic chromaticity while it did not noticeably increase the amplitude-dependent tune shift.

The MAX IV 3 GeV storage ring has three octupole families. The octupoles have been placed where they are most efficient for each driving term: OXX where  $\beta_x \gg \beta_y$ , OXY where  $\beta_x \simeq \beta_y$ , and OYY where  $\beta_x \ll \beta_y$  (see Fig. 2.2). OYY sees a very small amount of dispersion but its chromatic contribution is negligible. Predominantly, all octupole families are acting as harmonic octupoles. Due to this choice of octupole locations the required octupole strengths are very low and a magnet length of only 100 mm is sufficient (including 100% tuning range). The inner bore radius is 12.5 mm as for the sextupoles. A schematic of the octupole magnet layout is given in Fig. 2.5. The octupole strengths are shown in Table 2.2.

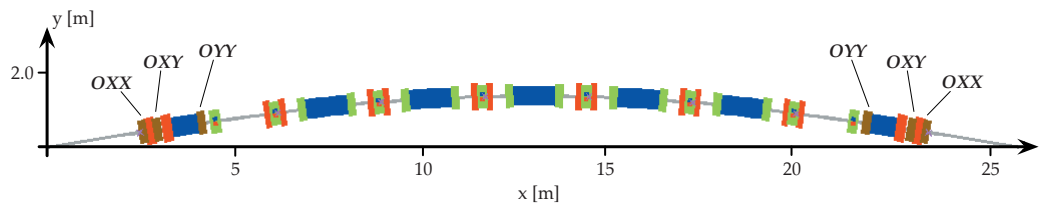


Figure 2.5: Schematic of the octupole magnet layout within one achromat of the MAX IV 3 GeV storage ring.

<sup>2</sup>In the meantime, the SVD optimizer has been included in OPA.

Table 2.2: Strengths for the octupole families in the MAX IV 3 GeV storage ring (bare lattice). The optics parameters at the location of the octupoles are also shown.

	$m_4$ [T/m <sup>3</sup> ]	$\beta_x$ [m]	$\beta_y$ [m]	$\eta_x$ [mm]
OXX	−13144	9.75	6.21	0.0
OXY	21816	6.87	9.25	0.0
OYY	−6886	0.90	12.89	11.2

With the octupoles, the sextupoles no longer have to be used to cancel amplitude-dependent tune shift driving terms. Instead a new sextupole optimization can be chosen where the sextupoles are mainly tuned to cancel first-order nonlinearities as well as quadratic chromaticity; the result is that the chromatic tune shift is “wrapped up” around the working point. The change in sextupole strengths is shown in Table 2.3. The biggest change is the 9% increase of sextupole strength of the SDend family.

Table 2.3: Results of the sextupole optimizations done with and without octupoles in the MAX IV 3 GeV storage ring lattice.

	Original Settings without Octupoles	Settings with Octupoles
SFi	2216 T/m <sup>2</sup>	2148 T/m <sup>2</sup>
SFo	1738 T/m <sup>2</sup>	1700 T/m <sup>2</sup>
SFm	1509 T/m <sup>2</sup>	1600 T/m <sup>2</sup>
SD	−1204 T/m <sup>2</sup>	−1179 T/m <sup>2</sup>
SDend	−1226 T/m <sup>2</sup>	−1340 T/m <sup>2</sup>

The harmonic octupoles are optimized to reduce the amplitude-dependent tune shifts. A comparison of the amplitude-dependent tune shifts with and without sextupoles is shown in Fig. 2.6. The dramatic decrease due to efficient first-order octupole cancelation is clearly seen. The optimized chromatic tune shift is displayed in Fig. 2.7.

Figure 2.8 shows the tune foot print for the bare lattice with octupoles and the new sextupole optimization. A clear improvement can be seen in comparison to the tune foot print displayed in Fig 2.2.

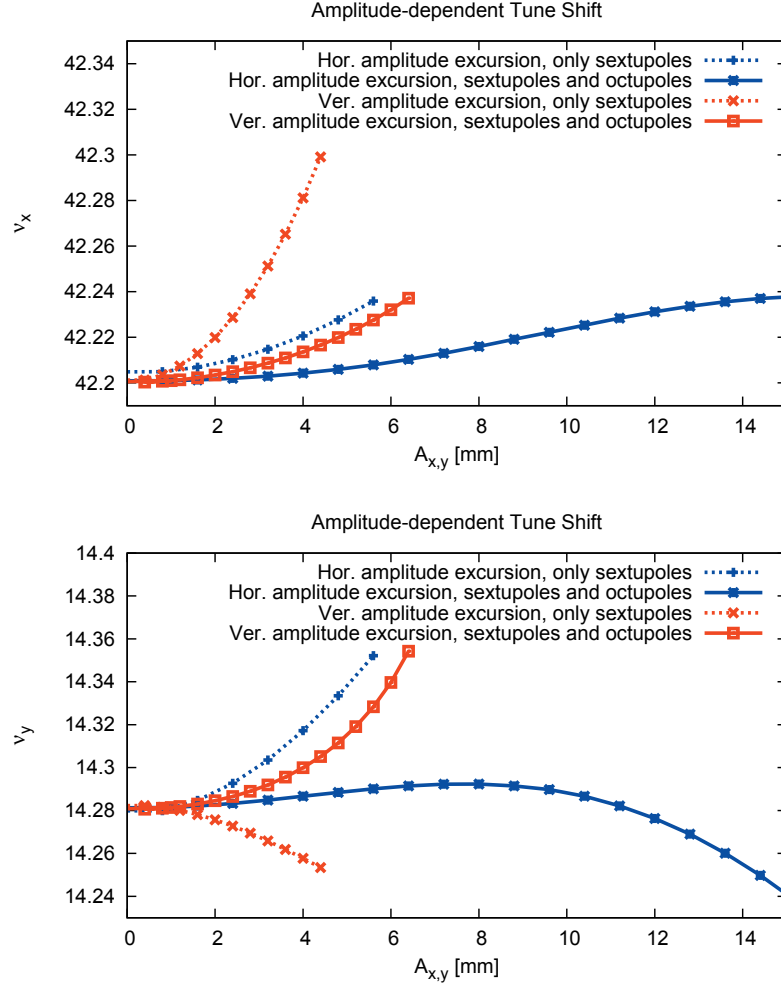


Figure 2.6: Plots showing the amplitude-dependent tune shifts for the MAX IV 3 GeV storage ring bare lattice with and without octupoles as calculated by Tracy-3. The dramatic decrease due to efficient first-order octupole cancelation is clearly seen.

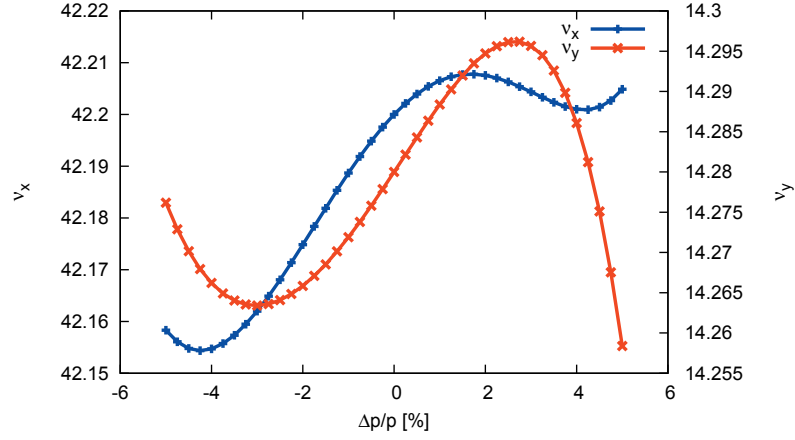


Figure 2.7: Chromatic tune shift for the MAX IV 3 GeV storage ring bare lattice with octupoles as calculated by Tracy-3. Agreement with results given by OPA is excellent.

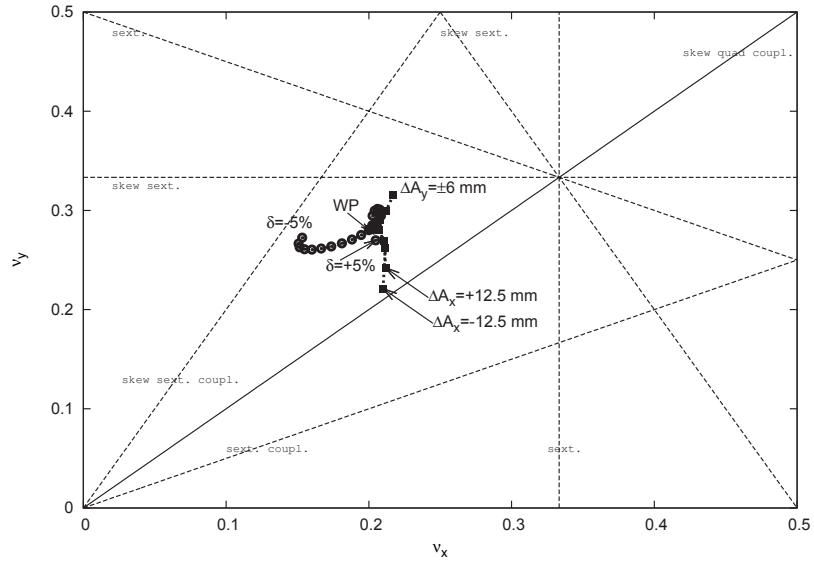


Figure 2.8: A plot of fractional tune space for the MAX IV 3 GeV storage ring bare lattice (with octupoles) as calculated by OPA. Resonance and skew resonance lines have been included up to third order. WP indicates the working point. The step size chosen for the chromatic tune shift is 0.5% and 2.5 mm [1.0 mm] for the horizontal [vertical] amplitude-dependent tune shift.

### 2.3.4. Dynamic Aperture

As pointed out in the overview, the MAX IV 3 GeV storage ring requires a sufficiently large DA in order to achieve high injection efficiency and long Touschek lifetime. A high injection efficiency is necessary in order to reduce the time required for injection (number of shots required from the linac) and to reduce the amount of radiation at injection. Touschek lifetime is of great importance because in modern light sources it usually dominates lifetime and hence defines the brightness at the beamlines (decaying beam mode) or the required injection rate (top-up mode). In addition, Touschek scattering is usually the main source of the overall radiation background and hence it is imperative to achieve a high Touschek lifetime even when operating in top-up mode.

The required physical acceptance for the MAX IV 3 GeV storage ring has been specified at 7.1 mm mrad in the horizontal and 1.3 mm mrad in the vertical plane. In the center of the straight sections this corresponds to a required aperture of  $\pm 8$  mm in the horizontal and  $\pm 2.5$  mm in the vertical plane. The reasoning behind the required vertical aperture is that narrow-gap in-vacuum IDs in the MAX IV 3 GeV storage ring will reduce the vertical physical aperture in the straight sections to  $\pm 2$  mm. The horizontal aperture requirement is motivated by the injection process (see also Chapter 2.7):

- septum thickness is 2.5 mm (Lambertson septum),
- stored beam moved to within 2 mm of the septum (a stored beam has a size of  $\sigma_x = \sqrt{\varepsilon\beta_x^*} \approx 54 \mu\text{m}$  in the injection straight where dispersion is zero) by the injection bump,
- injected bunch brought to within 1 mm of the septum (assuming the injector linac delivers a beam with an normalized transverse emittance of  $12 \mu\text{m rad}$  we get a injected beam size of  $\sigma_x = \sqrt{\varepsilon\beta_x^*} \approx 136 \mu\text{m}$ ).

This gives a separation of 5.5 mm between the bumped stored beam and the injected beam at the septum. We add a 2.5 mm safety margin and arrive at a total required aperture of 8 mm for capture.

An example for the DA of the MAX IV 3 GeV storage ring bare lattice is given in Fig. 2.9 where Tracy-3 has been used to calculate DA for on and off-momentum particles with 6D tracking. It is clear that even for off-momentum particles the acceptance requirements



are fulfilled. If the physical boundaries are included in the lattice file, the DA extends to these boundaries confirming that nonlinearities are very small within the physical aperture.

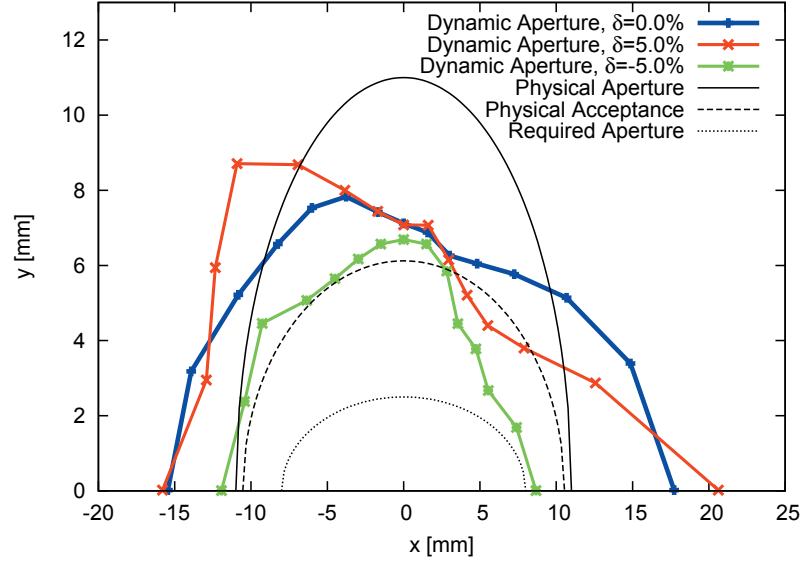


Figure 2.9: Dynamic aperture at the center of the long straight section in the MAX IV 3 GeV storage ring (bare lattice). Tracking was performed with Tracy-3 in 6D for one synchrotron period. Physical aperture and acceptance are also indicated in the plot.

This picture however lacks dynamics information and it does not reveal where the limitations of the DA come from. In order to get a better idea of what governs the DA, frequency map analysis (FMA) can be performed [3]. For a given initial position in transverse phase space, Tracy-3 tracks the particle for a certain number of turns ( $N_t = 2064$  chosen for most studies) in the storage ring and calculates the diffusion rate

$$D = \log \sqrt{(\Delta\nu_x)^2 + (\Delta\nu_y)^2} \quad (2.1)$$

where

$$\Delta\nu_i = \nu_{i,0} - \nu_{i,N_t}, \quad i = x, y. \quad (2.2)$$

This is done for on and off-momentum particles. In addition to calculating the diffusion

rate as a function of initial conditions, Tracy-3 also plots diffusion as a function of the initial tunes. These so-called frequency maps — using a modified definition of diffusion  $D = \min(-2, \log \sqrt{(\Delta\nu_x)^2 + (\Delta\nu_y)^2})$  — show which areas of tune space correspond to stable motion, diffusion, and particle loss. Through particle tracking, areas of interest in the diffusion map can be linked to locations in frequency space. The frequency map then helps identify sources of particle loss. Since diffusion and frequency maps can be used to understand beam loss mechanisms, they are valuable tools to optimize nonlinear optics.

Figure 2.10 shows a first example of a diffusion map for the bare lattice. Clearly the DA shown in Fig. 2.9 is consistent with this diffusion map.

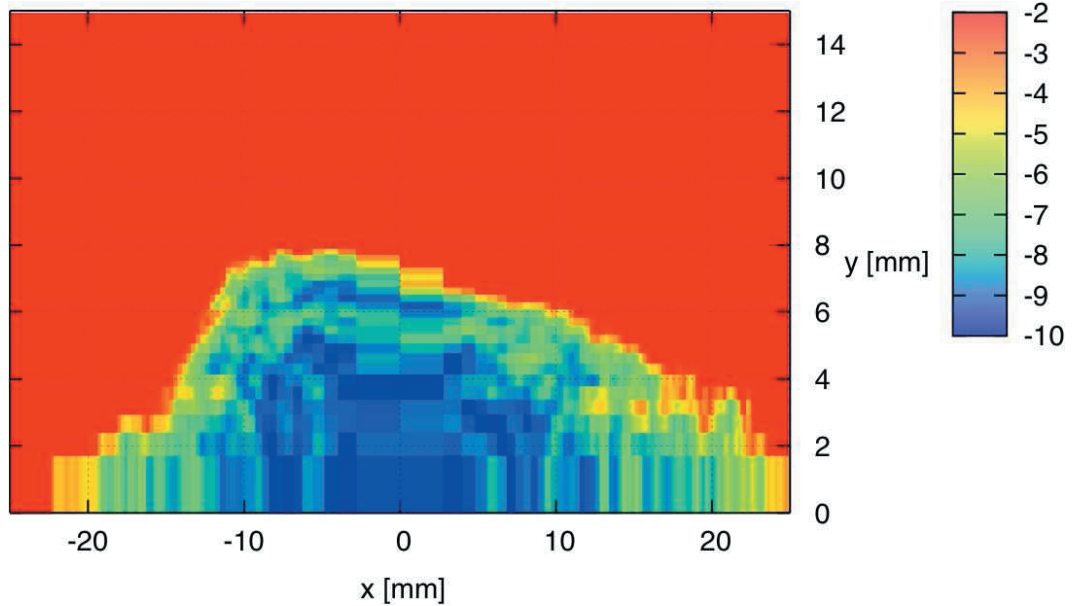


Figure 2.10: Diffusion map for the MAX IV 3 GeV storage ring bare lattice taken at the center of the straight section. Blue areas show small tune shifts, red areas show large tune shifts and particle loss. The plot has been generated with Tracy-3 by scanning transverse configuration space on-momentum and tracking for 2048 turns.

To get a better idea of the dynamics within the required aperture a magnified view of this diffusion map along with the corresponding frequency map are given in Fig. 2.11. Increased tune shifts are observed in a band-like structure around the origin starting at  $\Delta x = \pm 6$  mm. This is caused by the  $2\nu_x + 2\nu_y = 113$  resonance which can easily be

identified as a pronounced band in the frequency map (around  $[0.209, 0.291]$ ). There is also some structure further inside, but these are very low diffusion rates.

Common to this resonant behavior is that it is very weak. The chosen working point is away from harmful resonances. Frequency map analysis confirms that because of the small amplitude-dependent tune shift, the tune footprint remains confined in a very limited area. The relatively large distance to potentially harmful lower-order resonances and the small tune footprint justify the choice of this working point for the MAX IV 3 GeV storage ring from a nonlinear optics point of view (assuming that once the storage ring includes PMDWs the behavior will deteriorate, see Section 2.3.6).

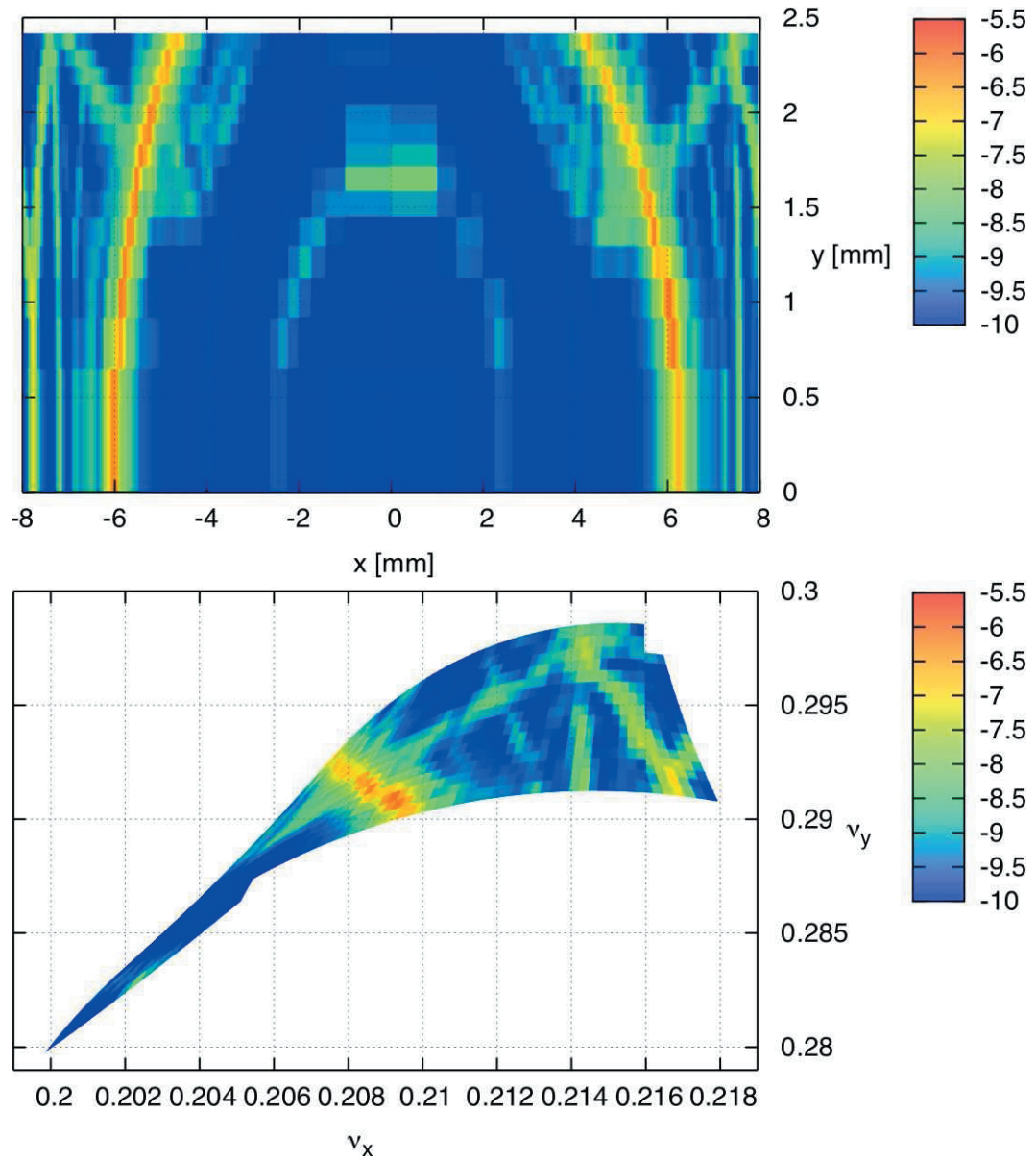


Figure 2.11: Magnified diffusion map (top) and corresponding frequency map (bottom) for the MAX IV 3 GeV storage ring bare lattice taken at the center of the straight section. Note that compared to Fig. 2.10 the scale has shifted to significantly lower diffusion values.

### 2.3.5. Energy Acceptance

The ultimate energy acceptance of the MAX IV 3 GeV storage ring will be given by several factors. While the energy acceptance defined by the rf bucket (the “rf acceptance”<sup>3)</sup> needs to be sufficient, the ultimate energy acceptance of the storage ring will be determined by the dynamic momentum acceptance of the lattice. More specifically, what is the maximum energy Touschek scattering event allowed so that both Touschek-scattered electrons can be stored in storage ring until their betatron motion around the dispersive orbit has damped down to betatron motion around the design orbit. In this sense a large lattice momentum acceptance will ensure a good Touschek lifetime.

The amplitude of a Touschek-scattered particle on its dispersive orbit is

$$x_\delta = \sqrt{A_x \beta_x(s)} + |\eta(s)\delta| = \left( \sqrt{\mathcal{H}_0 \beta_x(s)} + |\eta(s)| \right) \times |\delta| \quad (2.3)$$

where we have used the chromatic invariant and so-called “dispersion’s emittance”

$$\mathcal{H}_0 = \gamma_0 \eta_0^2 + 2\alpha_0 \eta_0 \eta'_0 + \beta_0 \eta_0'^2 = \frac{A_x}{\delta^2} \quad (2.4)$$

where the subscript <sub>0</sub> indicates that the functions have been evaluated at the location of the Touschek scattering event<sup>4</sup>. The local momentum acceptance of the lattice in  $s_0$  is therefore given by

$$\delta_{\text{acc}}(s_0) = \pm \min_{\forall s} \left( \frac{a_x(s)}{\sqrt{\mathcal{H}(s_0) \beta_x(s)} + |\eta(s)|} \right) \quad (2.5)$$

where  $\alpha_x(s)$  is the horizontal half-aperture at location  $s$ .

Two simple cases can be recognized:

---

<sup>3</sup>The rf bucket can also be distorted due to high-order contributions to longitudinal motion. The very low nonlinear momentum compaction in MAX IV ( $\alpha_2 \approx 3 \times 10^{-4}$ ) indicates rf buckets in MAX IV should show only little distortion.

<sup>4</sup>For Touschek scattering events one can assume that the scattering takes place at the core of the bunch (greatest charge density) and that the particles are located at  $(0, 0, 0, 0, \pm\delta)$  in phase space immediately after scattering.

- In dispersion-free sections  $\mathcal{H}(s) = 0$  and therefore

$$\delta_{\text{acc}} = \pm \min_{\forall s} \left( \frac{a_x(s)}{\eta(s)} \right) \quad (2.6)$$

- At the location of maximum dispersion  $\mathcal{H}(s) = \gamma_0 \eta_{\text{max}}^2 = \eta_{\text{max}}^2 / \beta_0(s)$  and therefore

$$\delta_{\text{acc}} = \pm \min_{\forall s} \left( \frac{a_x(s)}{2\eta(s)} \right) \quad (2.7)$$

For the MAX IV 3 GeV storage ring this means the lattice momentum acceptance in the long straights is 14% and about 7% in the achromat at the location of maximum dispersion. From these calculations it becomes clear that even for large-energy Touschek events the vacuum chamber could be restricted to a horizontal half-aperture of 10 mm without negative impact on lifetime. In fact, to ensure a lattice momentum acceptance of no less than 4.5%, a horizontal vacuum chamber half-aperture of 7.2 mm would be sufficient.

However, containing the dispersive orbits within the physical aperture boundaries does not take into account the dynamics of the Touschek scattering process. One has to consider that an electron, after undergoing Touschek scattering, will oscillate around many dispersive orbits while damping down longitudinally. A synchrotron period in the MAX IV 3 GeV storage ring (without Landau cavities) is  $\approx 880 \mu\text{s}$  ( $\approx 500$  turns). Longitudinal damping time is on the order of 20 ms (11,364 turns). Touschek-scattered electrons will cover many dispersive orbits corresponding to their momentary energy while damping down. During this entire longitudinal and transverse damping process, it is therefore required that the Touschek-scattered electrons encounter no harmful resonances (a schematic of this process is given in Fig. 2.12).

As shown in Fig. 2.3 the chromatic tune shift is “wrapped up” around the working point thus strongly reducing the chromatic tune footprint (see Fig. 2.8). However as noted in the previous section, the dynamics are not fully depicted by this simple tune footprint plot. It is rather necessary to again investigate results from FMA for off-energy particles and identify resonances in the frequency maps in order to understand limitations of the lattice momentum acceptance. Tracy-3 has again been used for this purpose. Scans have been performed where particles were given a certain initial horizontal amplitude (the initial vertical offset was fixed at +1 mm) and momentum offset. After 2048 turns

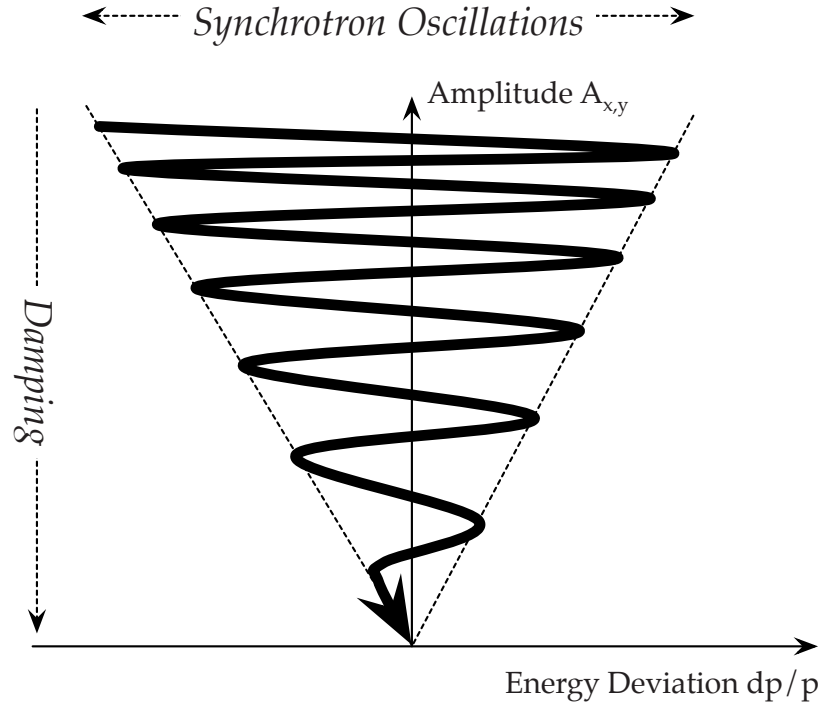


Figure 2.12: A schematic depicting the motion of a Touschek-scattered electron in momentum-amplitude space. While the particle damps down it covers many dispersive orbits corresponding to its momentary energy. In addition, it will perform betatron oscillations around these orbits. In order to increase Touschek lifetime it has to be ensured that the particle encounters no destructive resonance on its path. This implies particles should spend only little time in the vicinity of strong resonances but also that resonances in the vicinity of where the particle remains for long periods of time must be weak.

the tunes and diffusion were calculated resulting in diffusion and frequency maps for different energy and amplitude offsets. An example of such a diffusion map for off-momentum particles is given in Fig. 2.13. From this first scan it appears a bare lattice momentum acceptance of at least  $\pm 8\%$  can be achieved.

A more detailed understanding can be gained from the magnified view shown in Fig. 2.14 along with the corresponding frequency map. It is important to keep in mind that the source of most off-momentum particles are Touschek scattering events. Touschek-scattering occurs at the core of the beam where particle density is highest. Consequently, particles with large momentum offset will have a small initial amplitude (therefore the

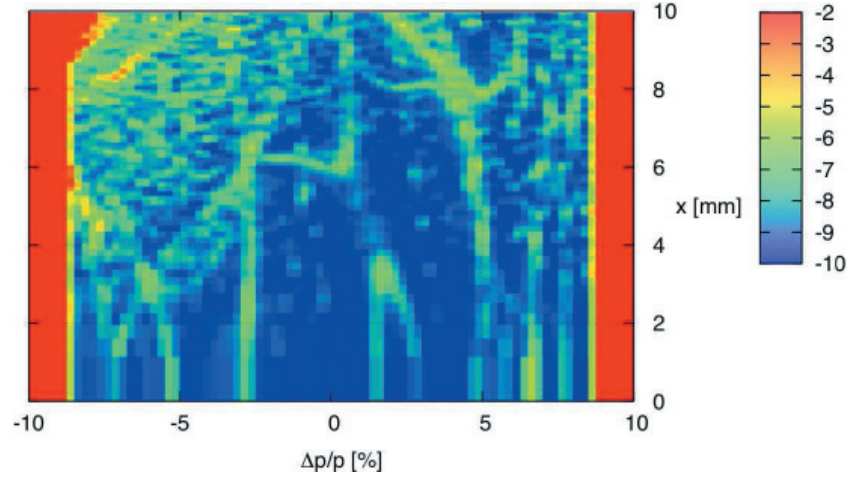


Figure 2.13: Diffusion map for the MAX IV 3 GeV storage ring bare lattice taken at the center of the straight section for off-momentum particles. Blue areas show small tune shifts, red areas show large tune shifts and particle loss. The plot has been generated with Tracy-3 by scanning the horizontal coordinate and momenta and tracking for 2048 turns. The initial vertical amplitude was +1 mm.

horizontal scale in the magnified view of Fig. 2.14 only extends to 3 mm).

The “wrap-up” of the chromatic tune shift around the working point is clearly recognized. Particles with energy above design ultimately experience a reduction of vertical tune. Particles with energy below design first see a reduction of horizontal tune followed by and an increase together with an increase of vertical tune. In frequency space a few distinct lines appear:

- The resonance  $6\nu_x = 253$  which causes the two bands seen in the diffusion map at  $\delta = -3\%$  and  $\delta = -5.25\%$
- The skew sextupole resonance  $3\nu_y = 43$  which amplifies the tune shift seen for  $\delta > 4\%$ ,  $\Delta x > 2$  mm
- The resonance  $2\nu_x + 2\nu_y = 113$  giving rise to elevated tune shifts at  $\delta = +1.5\%$
- The skew octupolar resonance  $4\nu_y = 57$  giving rise to elevated tune shifts at  $\delta = +5\%$
- The octupolar resonance  $4\nu_x = 169$  giving rise to elevated tune shifts at  $\delta = +6.5\%$



The conclusion that can be drawn from these plots is that for particles within the design lattice momentum acceptance of  $\pm 4.5\%$  no particle loss can be observed due to resonances. There are however some slightly elevated levels of tune shift in the vicinity of the working point. This behavior should be evaluated again for a lattice with PMDWs (see Section 2.3.6).

Finally, we note that knowledge of local lattice momentum acceptance around the entire machine is required to make accurate estimates of Touschek lifetime. Results of this “Touschek tracking” are given in Section 2.10.3. In rigorous measurement, modeling, and optimization campaigns, modern light sources have shown that by correct modeling (6D Touschek tracking including magnet and misalignment errors, actual apertures, non-linear betatron coupling, etc.), restoring of the design linear optics, and symmetrization of the nonlinear optics correction, good agreement can be achieved between predicted momentum acceptance and measured lifetime [4, 5, 6, 7, 8, 9, 10].

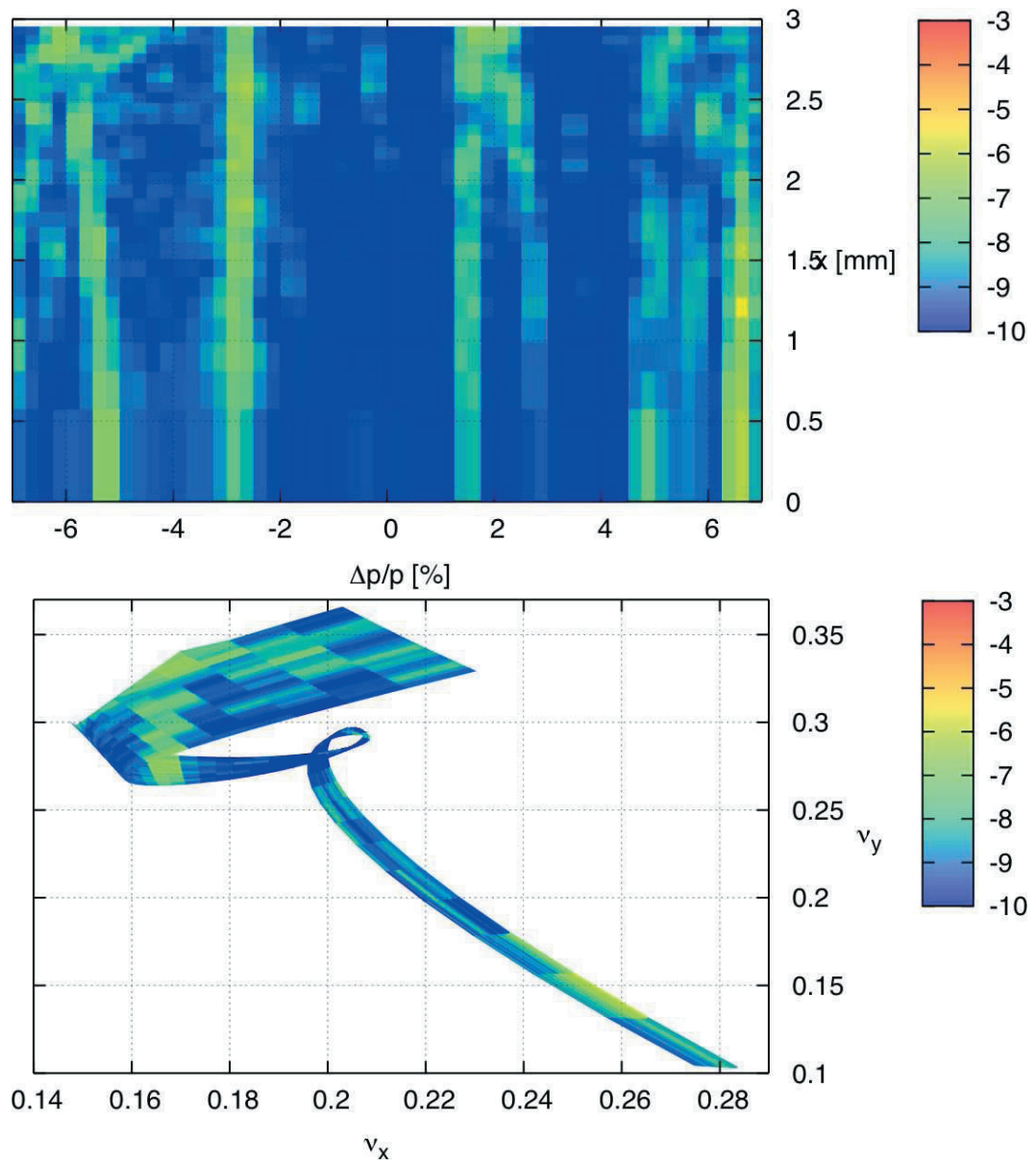


Figure 2.14: Magnified diffusion map (top) and corresponding frequency map (bottom) for the MAX IV 3 GeV storage ring bare lattice taken at the center of the straight section for off-momentum particles. Note that compared to Fig. 2.13 the scale has shifted to lower diffusion values.

### 2.3.6. Effects of Insertion Devices

Similar to the disturbances to the linear lattice as described in Section 2.2.6, IDs can perturb the nonlinear storage ring optics. Two simple aspects can be considered to demonstrate this.

- Firstly, aside from the additional vertical focusing of a strong ID, there is an amplitude-dependent effect: away from the mid-plane where the undulator or wiggler field is sinusoidal, the electron experiences a step-like focusing force.
- Secondly, the over-focusing of the ID is quadratic rather than linear in energy because the entrance angle of the particle in the undulator or wiggler period and the bending angle both scale inversely with energy.

Therefore, it's important to investigate the nonlinear behavior of the MAX IV 3 GeV storage ring lattice with one or several IDs installed. Obviously this should happen in addition to ensuring that the linear optics have been properly matched to the IDs.

It was decided to add four 2.22 T PMDWs to the MAX IV 3 GeV storage ring lattice in order to assess changes of DA and momentum acceptance. The parameters of these devices have been given in Table 2.4. It is expected that these very strong wigglers will have the largest vertical focusing effect of any ID in MAX IV. In addition, by installing four such wigglers the radiated energy is heavily increased thus giving a better picture of the dynamics of a “loaded” storage ring (see also Table 2.9). The four devices were installed in opposing straight sections as they would be in the real machine due to periodicity concerns. However it was later also verified that the DA or momentum acceptance did not change substantially for only a single super-conducting wiggler or an asymmetric placement of two of these devices.

In OPA the devices are modeled by using the built-in undulator model. In Tracy-3 the devices have been modeled using the built-in wiggler model as well as imported kick maps. The advantage of the kick maps is that the actually calculated kicks outside of the horizontal plane are applied to the particles with vertical amplitude oscillations rather than just assuming a mean vertical beta function in the device and calculating a mean vertical focusing force for the entire device. The one disadvantage of the using kick maps in Tracy-3 (apart from the increased runtime) is that the DA information is no longer truly a DA but is skewed by acceptance limits. This is because Tracy-3 assumes

a particle is lost if its tracked position is ever outside of the kick map. The kick maps used for these studies covered  $\pm 20$  mm in the horizontal (81 mesh points) and  $\pm 3.5$  mm in the vertical plane (15 mesh points). Since the vertical dimension of these kick maps is larger than the required vertical aperture this does not invalidate the studies, but is important to keep in mind when interpreting vertical DA results.

OPA and Tracy-3 results showed excellent agreement using the built-in models. The sextupole and octupole settings were optimized with OPA for the bare lattice. These settings were then transferred to Tracy-3 and applied to the lattice for wiggler model and wiggler kick map studies. The plots in Figs. 2.15 and 2.16 show the influence of the four PMDWs on the storage ring optics if the sextupoles and octupoles are left unchanged.

The amplitude-dependent shift of the horizontal tune is changed significantly for vertical offsets. However, in a favorable fashion since the resulting shift with the four PMDWs is smaller. The vertical tune shift is changed for amplitude excursions in both planes. And in both cases the shift is larger when the four PMDWs are inserted.

The chromatic tune shift is changed more dramatically by the insertion of the four PMDWs. For the horizontal tune there is a change mainly for positive momentum deviations. However, for the vertical tune the difference is observed for negative momentum deviations and is actually quite considerable. Where as the nonlinear optics settings kept the vertical tune shift almost unchanged for  $-6\% < \delta < 0\%$  for the bare lattice, it shows a strong positive correlation when the four PMDWs are inserted into the machine. This is problematic because it pushes the tunes toward the  $4\nu_y = 57$  resonance.

This results in the tune footprint shown in Fig. 2.17. It is debatable if the increased tune footprint warrants a re-adjustment on the nonlinear optics settings. It is evident that momentum acceptance could be improved by a nonlinear re-optimization resulting in a reduced chromatic tune shift. On the other hand, tracking data shows that it is not imperative to modify the nonlinear settings once the four PMDWs are added to the bare lattice. It is suggested that both configurations are benchmarked with respect to actual lifetime and injection efficiency during commissioning and the final decision on which strategy to follow is postponed until then.

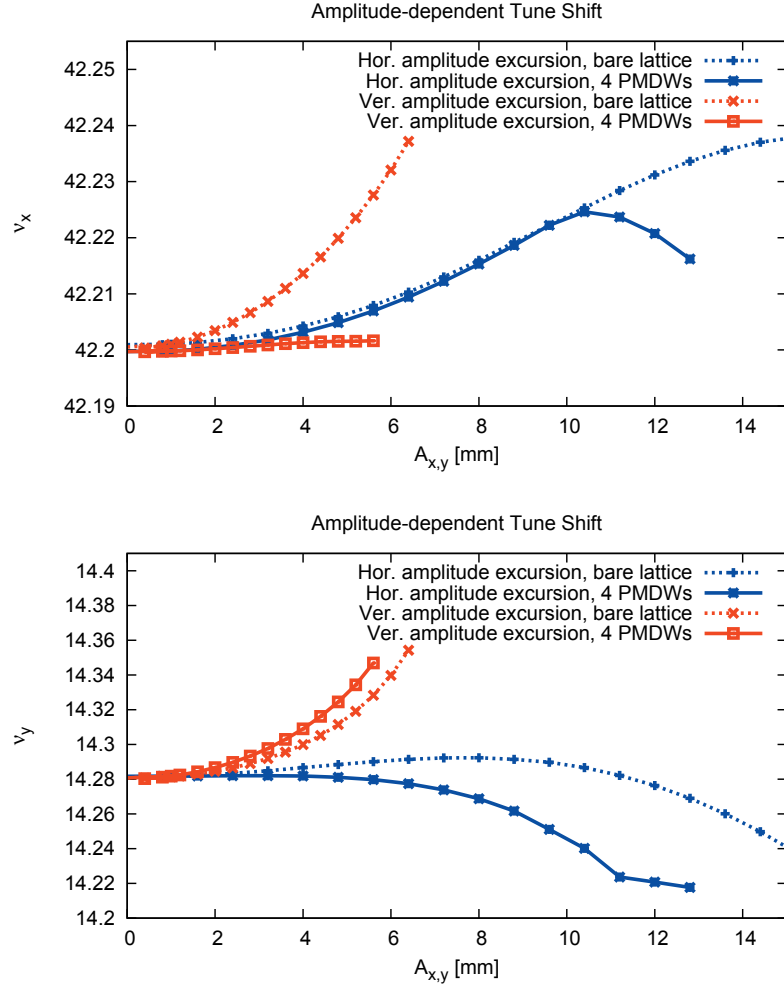


Figure 2.15: Plots showing the amplitude-dependent tune shift for the MAX IV 3 GeV storage ring as calculated by Tracy-3. The tune shifts are compared for the bare lattice and the lattice containing four PMDWs. The sextupole and octupole settings are equal in both cases.

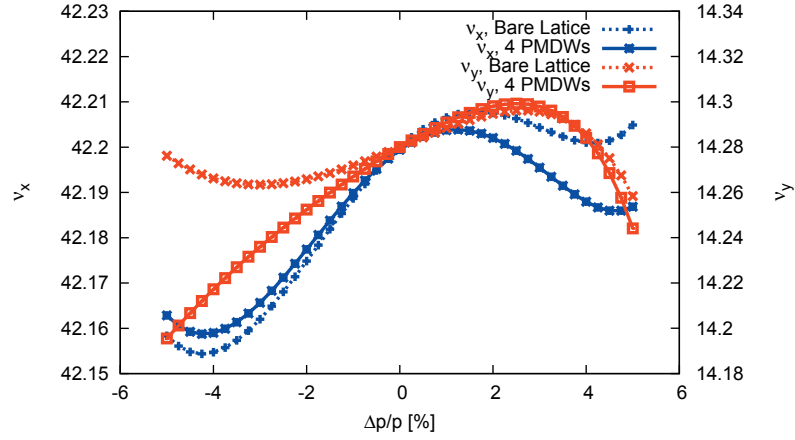


Figure 2.16: Chromatic tune shift for the MAX IV 3 GeV storage ring as calculated by Tracy-3. The chromaticity is compared for the bare lattice and the lattice containing four PMDWs. The sextupole and octupole settings are equal in both cases.

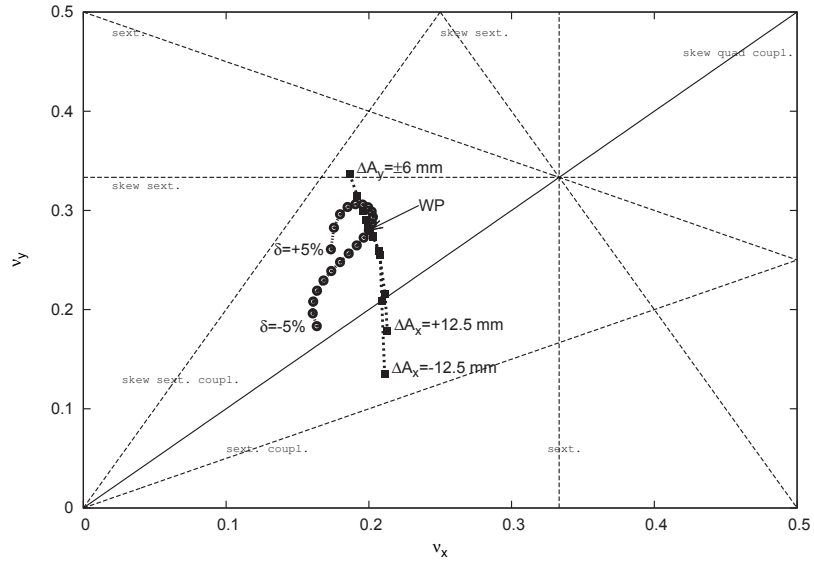


Figure 2.17: A plot of fractional tune space for the MAX IV 3 GeV storage ring with four PMDWs as calculated by OPA. The sextupole and octupole settings are the same as those calculated for the bare lattice (compare Fig. 2.8).

In this report the nonlinear re-optimization for a lattice with four PMDWs shall be demonstrated to give an idea of what kind of improvement can be expected if indeed nonlinear re-adjustment is applied in the actual machine. New sextupole and octupole settings calculated by the SVD optimizer in OPA for a ring including four PMDWs are displayed in Table 2.4. As expected, the proposed changes are mostly very small.

Table 2.4: A comparison of sextupole and octupole optimizations performed with OPA for the bare lattice and a lattice with four PMDWs installed.

Alternate magnet settings for PMDWs		
Sextupoles	SFi:	+1.0%
	SFo:	+0.0%
	SFm:	−2.5%
	SD:	−1.4%
	SDend:	+6.0%
Octupoles	OXX:	+3.2%
	OXY:	−0.9%
	OYY:	+24.2%
Resulting linear chromaticity		
Bare lattice settings, bare lattice	$\xi_x = 1.00,$	$\xi_y = 1.00$
Bare lattice settings, four PMDWs installed	$\xi_x = 0.60,$	$\xi_y = 1.45$
New settings, four PMDWs installed	$\xi_x = 1.00,$	$\xi_y = 1.00$

Figures 2.18–2.20 show tune shifts and the tune footprint for a storage ring with four PMDWs installed and with re-optimized nonlinear optics settings. The results are evident: the original bare lattice “wrap-up” of the chromatic tune shift around the WP has been restored for the lattice with four PMDWs. The amplitude-dependent tune shifts have been restored as well. In the case of tune shifts for vertical amplitude excursions the re-optimization has led to even smaller shifts than for the original bare lattice case.

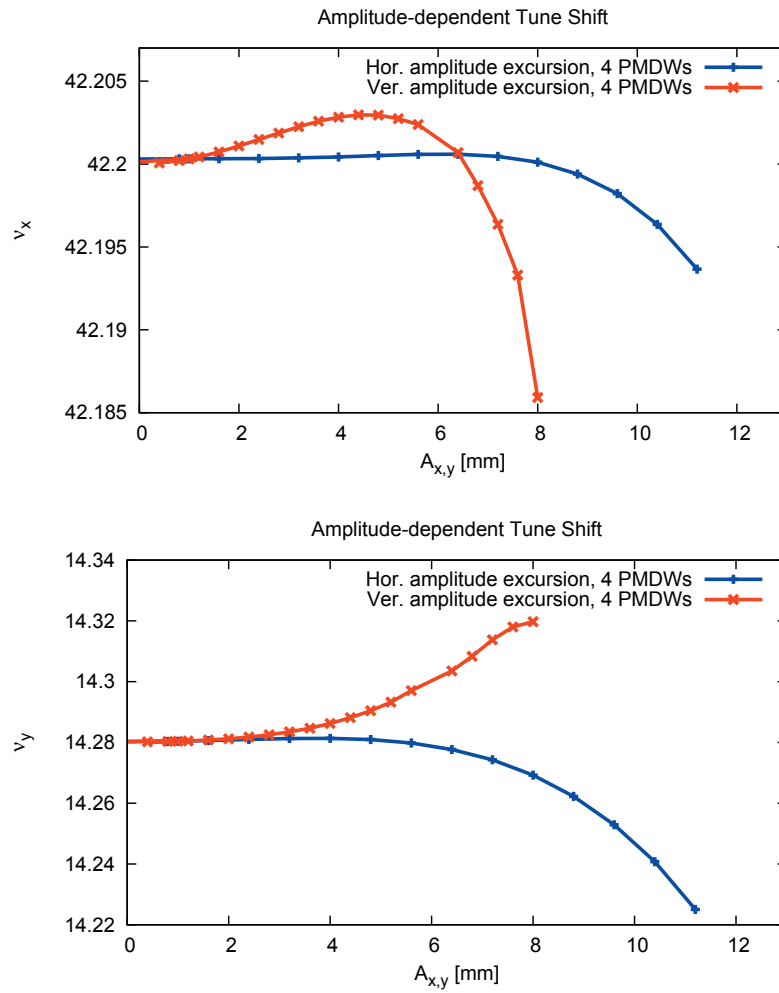


Figure 2.18: Plots showing the amplitude-dependent tune shift for the MAX IV 3 GeV storage ring with four PMDWs as calculated by Tracy-3. The sextupole and octupole settings have been optimized for this configuration.



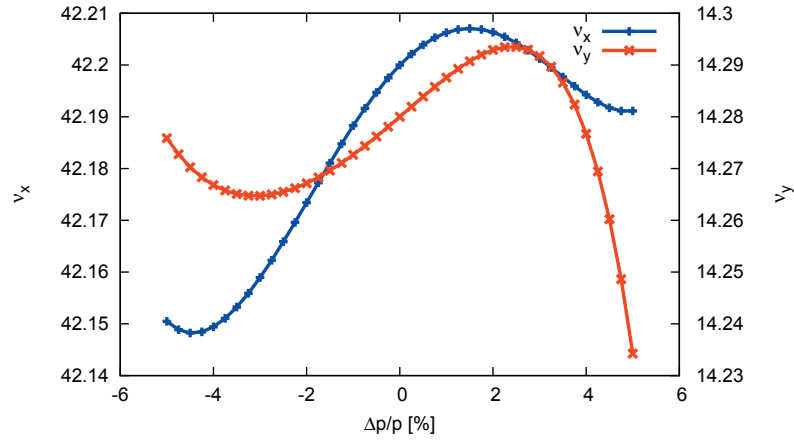


Figure 2.19: Chromatic tune shift for the MAX IV 3 GeV storage ring with four PMDWs as calculated by Tracy-3. The sextupole and octupole settings have been optimized for this configuration.

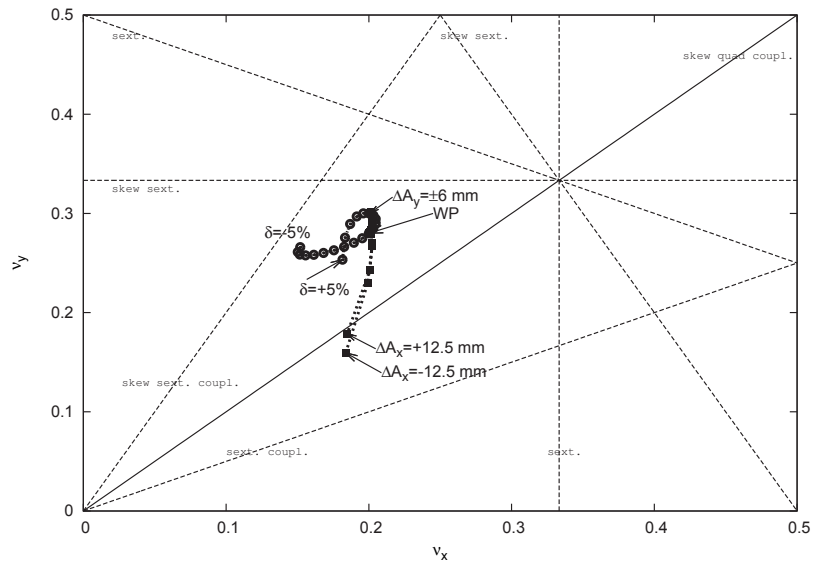


Figure 2.20: A plot of fractional tune space for the MAX IV 3 GeV storage ring with four PMDWs as calculated by OPA. The sextupole and octupole settings have been optimized for this configuration (compare Fig. 2.17).

Finally the DA was calculated with Tracy-3 using the sextupole and octupole settings optimized for a machine configuration with four PMDWs installed. It is shown in Fig 2.21. A comparison with the bare lattice (in Fig. 2.9) shows that while the DA has decreased, the aperture requirement is still fulfilled for off-momentum particles with the exception of large positive horizontal offsets at momenta far below design. As in previous sections this DA can be verified and understood by performing FMA. A diffusion map calculated by Tracy-3 is displayed in Fig. 2.22. Again, good agreement between the two plots is observed.

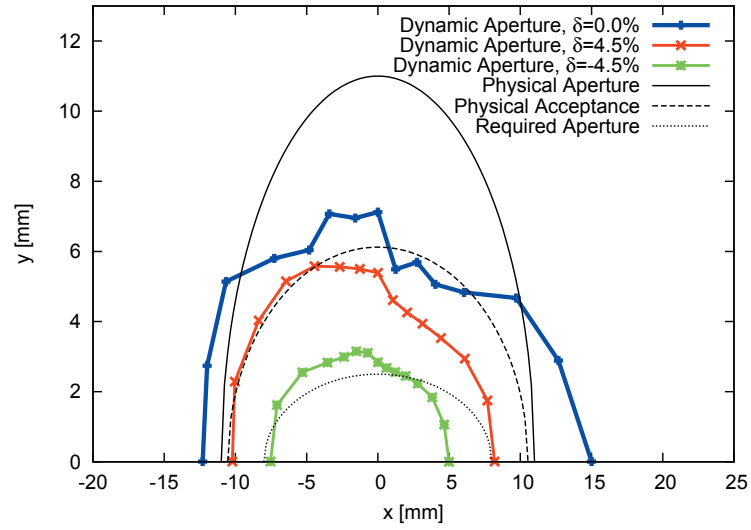


Figure 2.21: Dynamic aperture at the center of the long straight section in the MAX IV 3 GeV storage ring with four PMDWs installed. Tracking was performed with Tracy-3 in 6D for one synchrotron period. Physical aperture and acceptance are also indicated in the plot.

A magnified view of the diffusion map shown in Fig. 2.22 is given in Fig. 2.23 along with the corresponding frequency map. A comparison with Fig. 2.11 reveals the effect of the four PMDWs. The banding originally caused by  $2\nu_x + 2\nu_y = 113$  has disappeared due to a different tune footprint. The amplitude-dependent tune shift away from the fractional working point 0.20/0.28 can be clearly recognized. Highest diffusion (roughly  $10^{-6}$ ) is encountered as the tune shift reaches  $5\nu_x = 211$ ; this corresponds to the bands seen in the top of Fig. 2.23 for  $|\Delta x| \geq 4$  mm,  $|\Delta y| > 1$  mm. But overall the tune footprint of the lattice with four PMDWs is very small (for excursions within the required aperture it is  $< [0.01 \times 0.01]$ ). there is no resonant particle loss for particles within the required aperture.

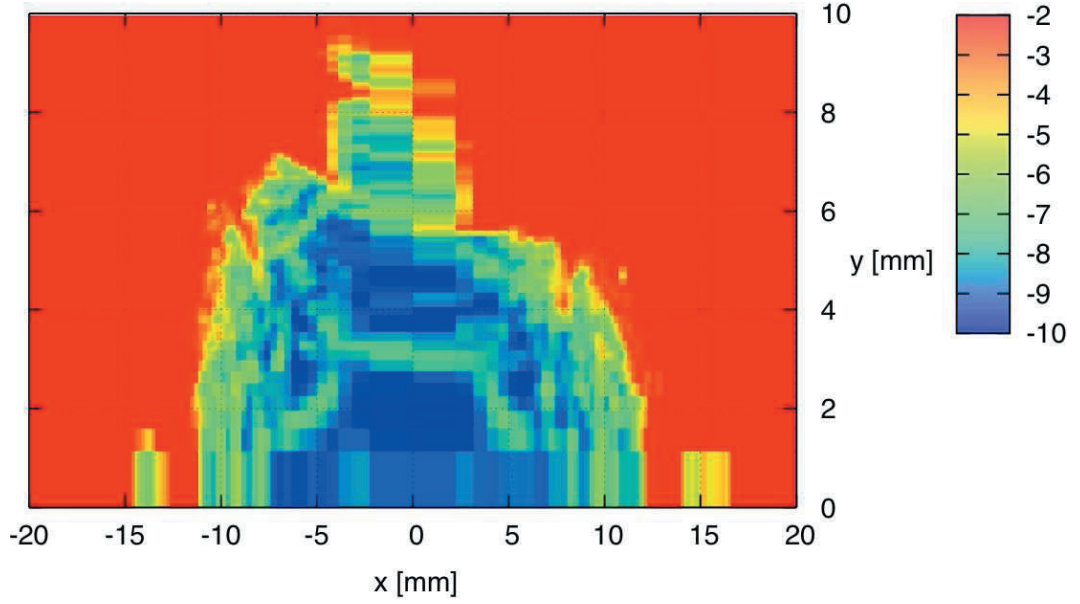


Figure 2.22: Diffusion map for the MAX IV 3 GeV storage ring with four PMDWs taken at the center of the straight section. Blue areas show small tune shifts, red areas show large tune shifts and particle loss. The plot has been generated with Tracy-3 by scanning transverse configuration space on-momentum and tracking for 2048 turns.

The momentum acceptance of the storage ring with four PMDWs installed does not seem to differ on as large scale from that of the bare lattice. A more detailed view (shown in Fig. 2.24) reveals a couple of differences compared to the magnified bare lattice plots (see Fig. 2.14). There is a stop band for large momentum deviations ( $\delta > +6\%$ ) caused by the integer resonance  $\nu_y = 14$ . Otherwise, slightly elevated tune shifts are recognized for particles below design energy ( $\delta < -2\%$ ) caused mainly by  $6\nu_x = 253$  and  $3\nu_y = 43$ . The resonances can both be identified in the frequency map. Frequency map analysis demonstrates that the chromatic tune shifts in the MAX IV 3 GeV storage ring with four PMDWs are very small. Horizontal tune excursions remain well below 0.1 for all energies within the RF momentum acceptance; the overall vertical tune shift is no larger than 0.3. This shows that even for extreme Touschek events no dangerous low-order resonances will be encountered ensuring good Touschek lifetime and large momentum acceptance.

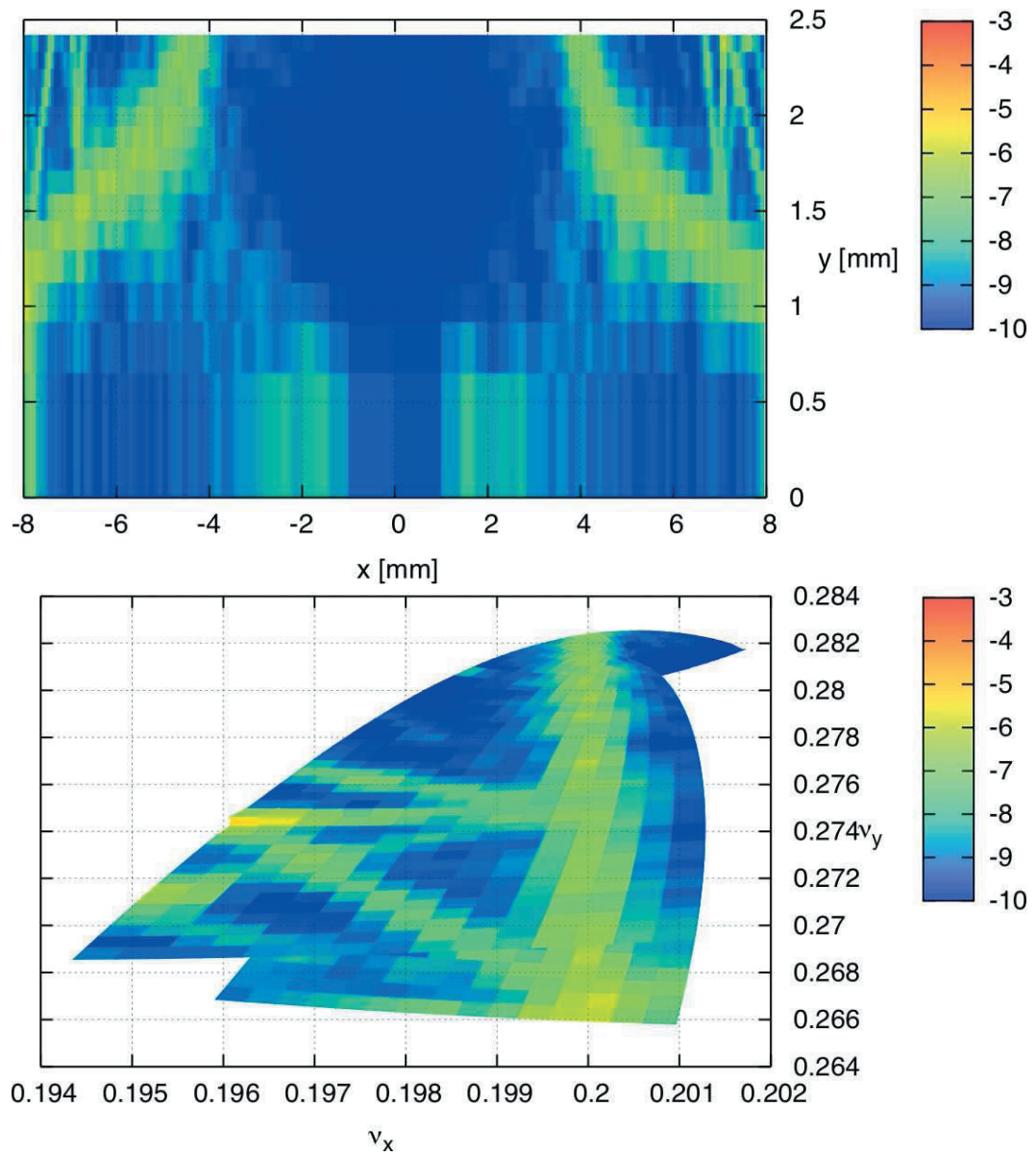


Figure 2.23: Magnified diffusion map (top) and corresponding frequency map (bottom) for the MAX IV 3 GeV storage ring with four PMDWs taken at the center of the straight section. Note that compared to Fig. 2.22 the scale has shifted to lower diffusion values.

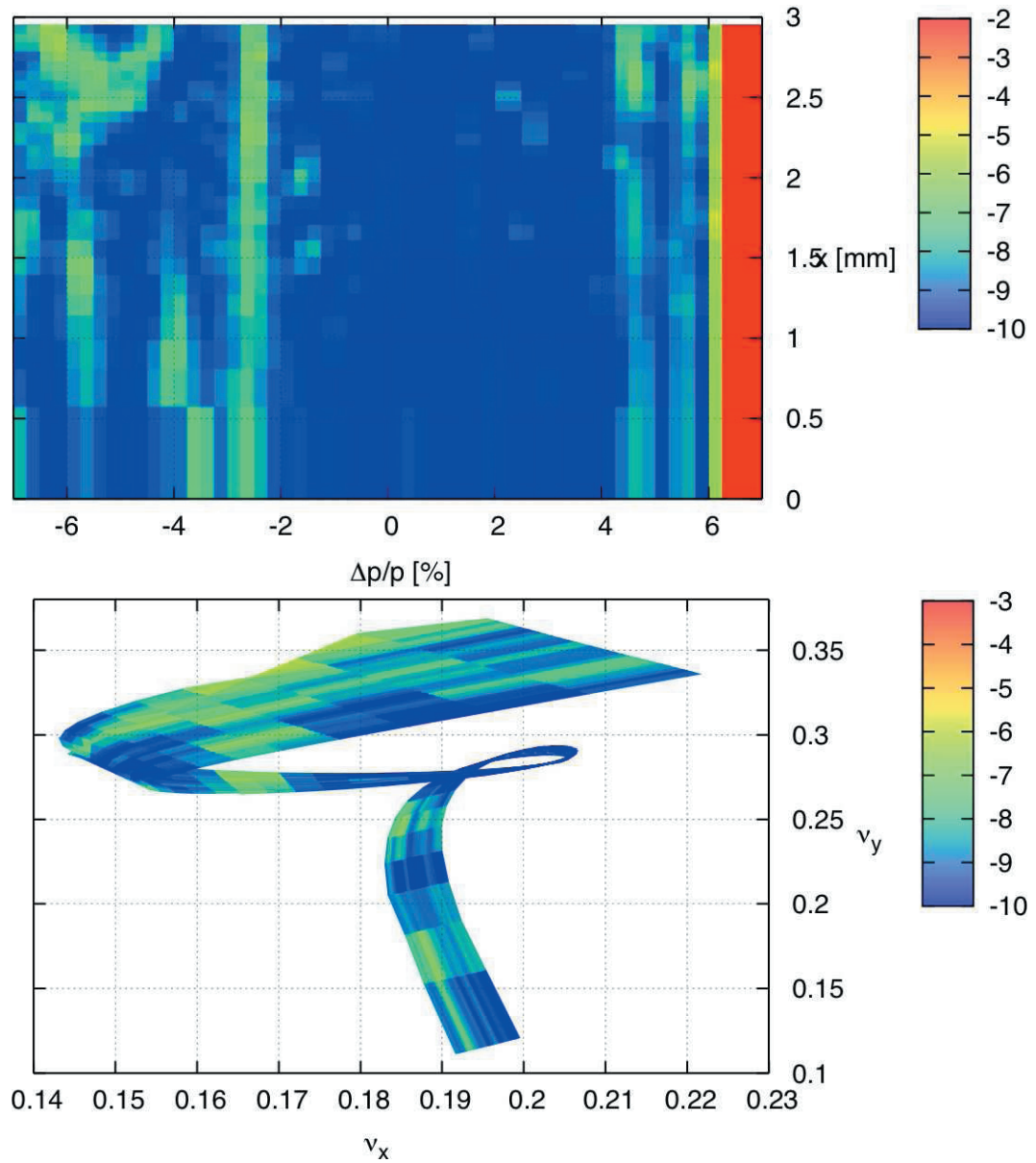


Figure 2.24: Magnified diffusion map (top) and corresponding frequency map (bottom) for the MAX IV 3 GeV storage ring with four PMDWs taken at the center of the straight section for off-momentum particles.

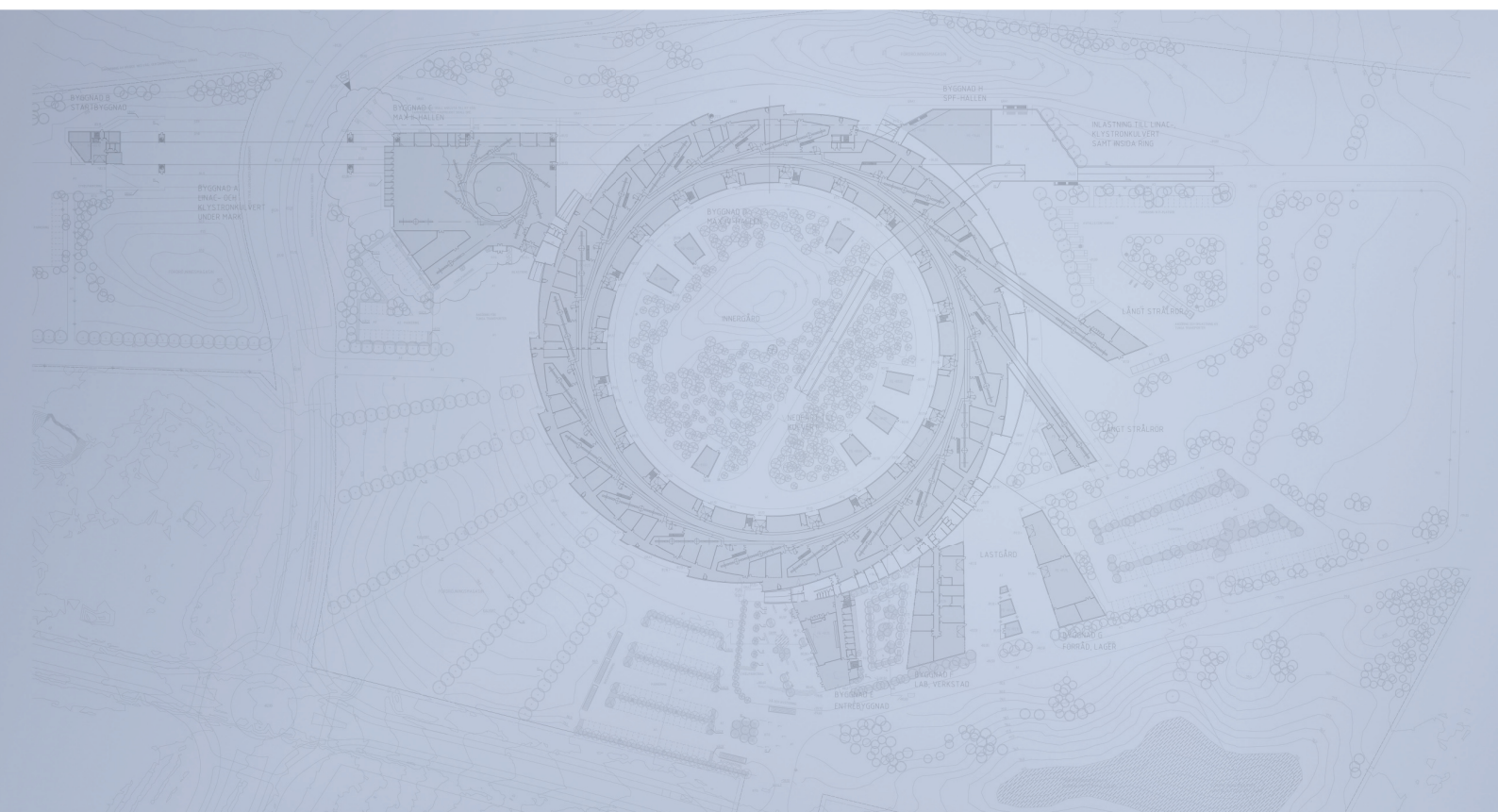
One distinct advantage of the MAX IV 3 GeV storage ring's multibend achromat over conventional DBA or TBA lattices is that resonance driving terms are reduced by the sextupoles locally within the achromat. Rather than rely on elaborate interleaving schemes between achromats, the multibend achromat uses the many sextupoles within every achromat to minimize resonance driving terms within the achromat. Hence, when IDs are introduced to the lattice and the optics are locally matched to make the ID transparent to the rest of the machine, the perturbation of the nonlinear optics correction remains very small (note the only minor adjustment to the nonlinear correction scheme proposed above in order to accommodate four strong damping wigglers). In this way the nonlinear optics of the multibend achromat become very robust even in the presence of phase errors introduced by IDs.

## References

- [1] É. Forest, *Beam Dynamics: A New Attitude and Framework*, Hardwood Academic, Amsterdam, 1998
- [2] J. Bengtsson, *The Sextupole Scheme for the Swiss Light Source (SLS): An Analytic Approach*, SLS Internal Report SLS-TME-TA-1997-0009, available at <http://slsbd.psi.ch/pub/slsnotes/sls0997.pdf>
- [3] L. Nadolski, J. Laskar, Phys. Rev. ST Accel. Beams 6, 114801, 2003.
- [4] D. Robin, J. Safranek, W. Decking, Phys. Rev. ST Accel. Beams, 2, 044001, 1999.
- [5] C. Steier, D. Robin, L. Nadolski, W. Decking, Y. Wu, J. Laskar, Phys. Rev. E, 65, 056506, 2002.
- [6] J. Safranek, Nucl. Instr. and Meth. A, 388, 27, 1997.
- [7] R. Bartolini, I. P. S. Martin, J.H. Rowland, P. Kuske, F. Schmidt, Phys. Rev. ST Accel. Beams, 11, 104002, 2008.
- [8] Å. Andersson, M. Böge, A. Lüdeke, V. Schlott, A. Streun, Nucl. Instr. and Meth. A, 591, 437, 2008.
- [9] Å. Andersson, M. Böge, A. Lüdeke, A. Streun, *Coupling Control at the SLS*, Proceedings of 11th European Particle Accelerator Conference (EPAC-08), Genova, Italy, pp. 1983–1985, 2008.
- [10] M. Böge, A. Lüdeke, A. Streun, *Correction of Imperfections in the SLS Storage Ring*, Proceedings of PAC09, Vancouver, Canada, 2009.



# Detailed Design Report



## Chapter 2

### MAX IV 3 GeV Storage Ring

#### 2.4. Lattice Errors and Correction

MAX IV Facility





# 2.4. Lattice Errors and Correction

---

- 2.4. Lattice Errors and Correction .....2**
  - 2.4.1. Overview ..... 2
  - 2.4.2. Magnet Errors ..... 2
  - 2.4.3. Misalignment Errors .....21
  - 2.4.4. BPM and Correction Pattern ..... 37
  - 2.4.5. Orbit Correction..... 40
  - 2.4.6. Coupling and Higher-order Correction.....61
  - References ..... 66

## 2.4. Lattice Errors and Correction

---

### 2.4.1. Overview

The previous chapters introduced the design optics for the MAX IV 3 GeV storage ring. In the final machine there will be deviations between the design magnet parameters (strength, higher-order field contributions) and the parameters of the actually installed magnets; in addition, alignment of the magnets will not be identical with the ideal design alignment.

This chapter will discuss influence of such errors on the design optics and correction of the deviations with the goal to make the real machine resemble the ideal design as well as possible. The first two sections deal with error sources: field errors and misalignment errors. The third section introduces the correction pattern and discusses methods to restore the design optics in the real machine. Finally, the fourth section is dedicated to coupling and higher-order correction.

### 2.4.2. Magnet Errors

#### 2.4.2.1. Field Strength Errors

The actually installed gradient dipoles and quadrupoles will contain gradient errors. These errors have an immediate effect on the linear optics. Additionally, the sextupole and octupole magnets will show deviations between the actual and the designed sextupole and octupole component strength. These errors will influence the nonlinear optics, namely chromaticity shifts (in the case of the sextupole errors) and a reduction of the dynamic aperture. This section will first introduce field error estimates for quadrupoles, sextupoles, and octupoles, and close with a brief outline of correction possibilities for these errors included in the magnet design.

**2.4.2.1.1 Quadrupole Errors** A first study investigates the sensitivity of the linear optics on gradient errors of a single magnet. A gradient error of a single magnet will cause a beta beat and change the phase advance which results in a tune shift. The tune shift is given by [1]

$$\Delta\nu_{x,y} = \frac{1}{4\pi} \int \beta_{x,y}(s) \Delta k(s) ds \quad (2.1)$$

and the beta beat can be expressed as [1]

$$\Delta\beta_{x,y}(s) = \frac{\beta_{x,y}(s)}{2 \sin 2\pi\nu_{x,y}} \int \beta_{x,y}(\tilde{s}) \Delta k(\tilde{s}) \cos [\phi_{x,y}(s) - \phi_{x,y}(\tilde{s}) - \pi\nu_{x,y}] d\tilde{s} \quad (2.2)$$

where  $\Delta k(s)$  is the normalized gradient error.

According to these expressions, the most sensitive magnets can be identified. For horizontal tune shifts and beta beats, QFend is the most sensitive magnet because of the large  $\beta_x$ . In the vertical plane, the most sensitive magnet will be the center unit cell dipole. The  $\beta_y$  is larger in the matching cell dipole than in the unit cell dipoles, but the unit cell dipoles are longer. A summary is given in Table 2.1.

Table 2.1: Resulting tune shift and maximum beta beat observed with Tracy-3 for a 1% gradient error in a single quadrupole or dipole (QD). The most significant contributions in either plane have been underlined.

Family	$\Delta\nu_x$	$\Delta\nu_y$	$ \Delta\beta_x/\beta_x $	$ \Delta\beta_y/\beta_y $
QF	0.002	0.002	0.013	0.012
QFm	0.002	0.001	0.012	0.010
QFend	<u>0.006</u>	0.005	<u>0.045</u>	0.032
QDend	0.002	0.006	0.012	0.038
DIP	0.001	<u>0.006</u>	0.005	<u>0.042</u>
DIPm	0.001	0.005	0.004	0.034

Certain errors could affect entire magnet families. Examples for this are magnet fabrication errors, calibration errors, or errors of the power supply powering a certain family. For quadrupoles this will lead to a strong distortion of the linear optics, namely the beta functions and tunes. For quadrupole magnet families Eq. 2.1 points to the QF family (for disturbances in the horizontal plane) and the main dipole magnet family (for disturbances in the vertical plane) because of the large number of magnets belonging to both families. Table 2.2 summarizes the effect of a gradient error for an entire magnet family.

Table 2.2: Resulting tune shifts observed with Tracy-3 for a 0.05% gradient error in all magnets of a certain quadrupole or dipole (QD) family. The most significant contributions in either plane have been underlined.

Family	$\Delta\nu_x$	$\Delta\nu_y$
QF	<u>0.014</u>	0.014
QFm	0.006	0.006
QFend	0.013	0.010
QDend	0.003	0.012
DIP	0.004	<u>0.030</u>
DIPm	0.001	0.010

Finally, it is of interest to investigate the impact manufacturing tolerances on individual magnets have on the overall performance. For this purpose Tracy-3 studies are carried out to determine the dynamic aperture of a machine with random gradient errors corresponding to the manufacturing tolerance which is expected to be 0.2% rms (before calibrating and shunting individual magnets) [4]. The variation in gradient leads to a beta beating around the ring which perturbs the sextupole correction hence spoiling the DA. Figure 2.1 shows the results of these studies for 20 error seeds for on and off energy dynamic aperture.

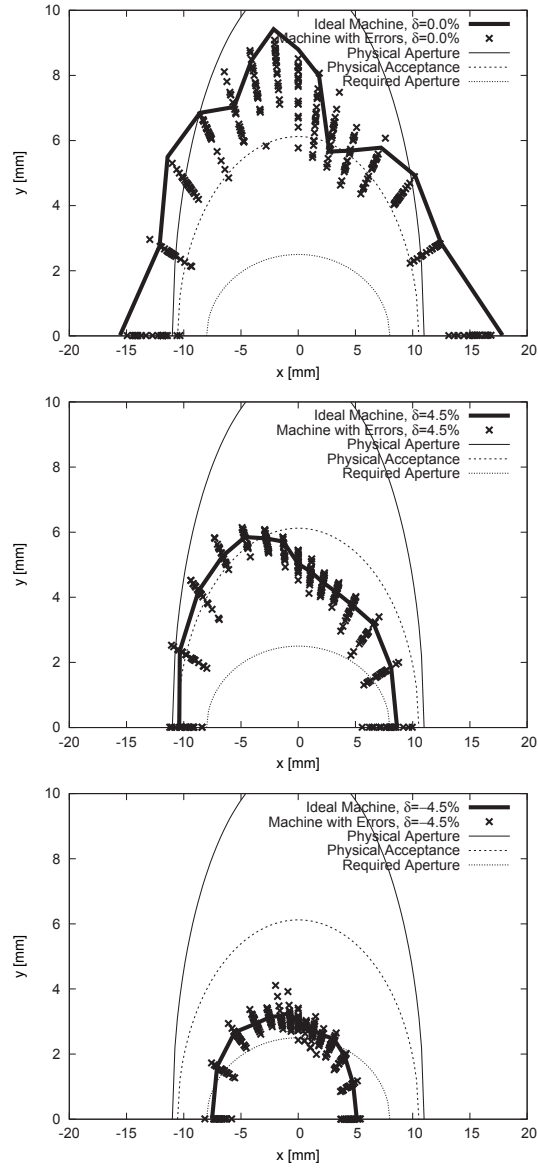


Figure 2.1: Dynamic aperture at the center of the long straight section as calculated by Tracy-3 on and off energy ( $\delta = \pm 4.5\%$ ) for a machine configuration with 4 PMDWs. The solid line shows the dynamic aperture for the ideal machine. The crosses show results for 20 error seeds. For the error seeds a 0.2% rms gradient variation across all dipole and quadrupole magnets was assumed with a cutoff at  $2\sigma$ .

**2.4.2.1.2 Sextupole Errors** For sextupole magnet families an error will cause a degradation of the chromaticity correction and spoil the dynamic optimization. Similar to Eq. 2.1, the change of chromaticity resulting from a sextupole error can be expressed as [2]

$$\Delta\xi_{x,y} = \frac{1}{4\pi} \int \beta_{x,y}(s)\eta_x(s)\Delta m(s) ds \quad (2.3)$$

where  $\Delta m(s)$  is the normalized sextupole strength error.

For disturbance of the horizontal chromaticity the obvious candidate is the SFi family because of the large product  $\beta_x\eta_x$  and the strong sextupole strength of the family. Table 2.3 summarizes the effect of sextupole gradient variations within an entire family on chromaticity.

Table 2.3: Resulting tune shifts observed for a 0.05% sextupole gradient error in all magnets of a certain sextupole family. The most significant contributions in either plane have been underlined.

Family	$ \Delta\xi_x $	$ \Delta\xi_y $
SFi	<u>0.020</u>	0.020
SFo	0.011	0.010
SFm	0.011	0.009
SD	0.015	<u>0.053</u>
SDend	0.001	0.009

The dynamic aperture also shows sensitivity on sextupole gradient errors because of the change in the underlying dynamics. The chosen sextupole settings have been optimized in order to minimize driving terms in the sextupole Hamiltonian. If this delicate balance is perturbed certain resonances could as a result be strongly driven which will have an detrimental influence on lifetime and injection efficiency. Therefore, Tracy-3 studies were carried out to determine the dynamic aperture of a machine with random sextupole errors according to manufacturing tolerances which are expected to be 0.2% rms (before calibrating and shunting individual magnets) [4]. Figure 2.2 shows the results of these studies for 20 error seeds for on and off energy dynamic aperture.

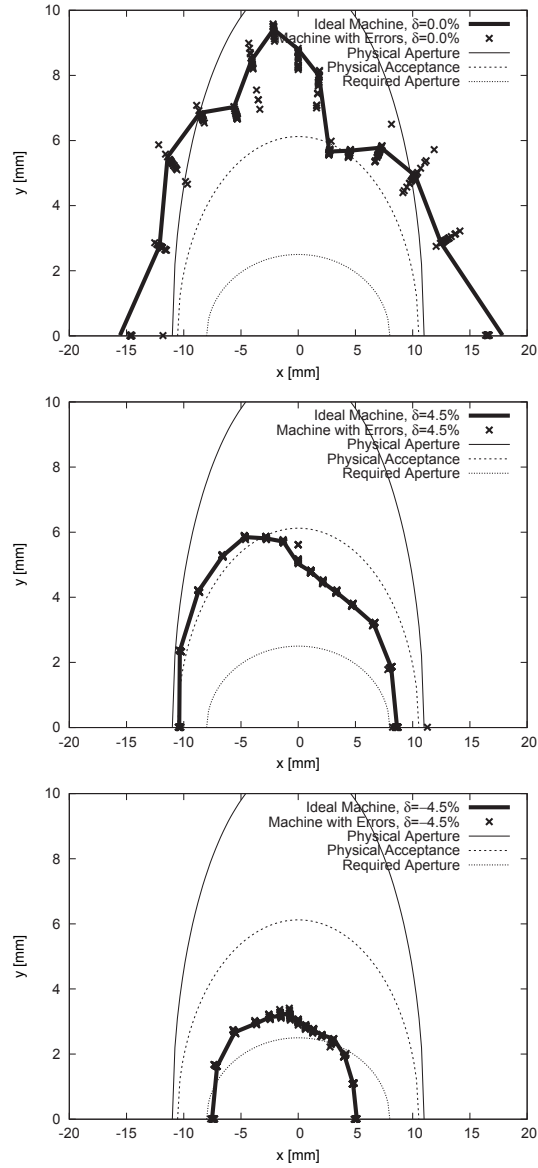


Figure 2.2: Dynamic aperture at the center of the long straight section as calculated by Tracy-3 on and off energy ( $\delta = \pm 4.5\%$ ) for a machine configuration with 4 PMDWs. The solid line shows the dynamic aperture for the ideal machine. The crosses show results for 20 error seeds. For the error seeds a 0.2% rms sextupole gradient variation across all sextupole magnets was assumed with a cutoff at  $2\sigma$ .



**2.4.2.1.3 Octupole Errors** Finally, influence of errors of octupole families are investigated. These errors change chromatic and amplitude-dependent tune shifts and therefore they influence dynamic behavior for particles away from the design orbit and design momentum. Table 2.4 gauges this effect by showing how much the dynamic aperture is reduced by detuning a single octupole family. Obviously, OXX and OXY show the strongest influence.

Table 2.4: Sensitivity to errors for each octupole family. The values given are the maximum changes of dynamic aperture in the horizontal and vertical planes for on-momentum particles.

Family	Error	$\Delta DA_{\text{hor}}$ [mm]	$\Delta DA_{\text{ver}}$ [mm]
OXX	$\Delta m_4/m_4 = \pm 5\%$	-1.9	—
OXY	$\Delta m_4/m_4 = \pm 5\%$	-0.4	-0.3
OYY	$\Delta m_4/m_4 = \pm 5\%$	—	-0.3

Figure 2.3 then shows dynamic aperture results for 20 error seeds with random octupole errors on the order of 0.2% rms.

From a comparison of Figs. 2.1–2.3 it becomes quite clear that most of the dynamic aperture reduction is caused by a variation of the quadrupole gradient strengths. Overall, the dynamic aperture reduction caused by the 0.2% rms gradient variations that are assumed to result from regular magnet manufacturing (without extra shunting) [4] is a very large effect (see Fig. 2.4). Compared to the dynamic aperture reduction expected from multipole errors (see Section 2.4.2.2, Fig. 2.6) and misalignment errors (see Section 2.4.3, Fig. 2.16), the reduction caused by a 0.2% rms variation of the main component strength is significant.

If additional calibration measurements and shunting of the magnets are performed after manufacturing so that the resulting variation becomes as low as 0.02% rms, the dynamic aperture reduction becomes comparable to the reduction from multipole errors and negligible compared to the reduction from misalignments. For comparison, Fig. 2.5 shows dynamic aperture assuming all gradients show a 0.02% rms variation.

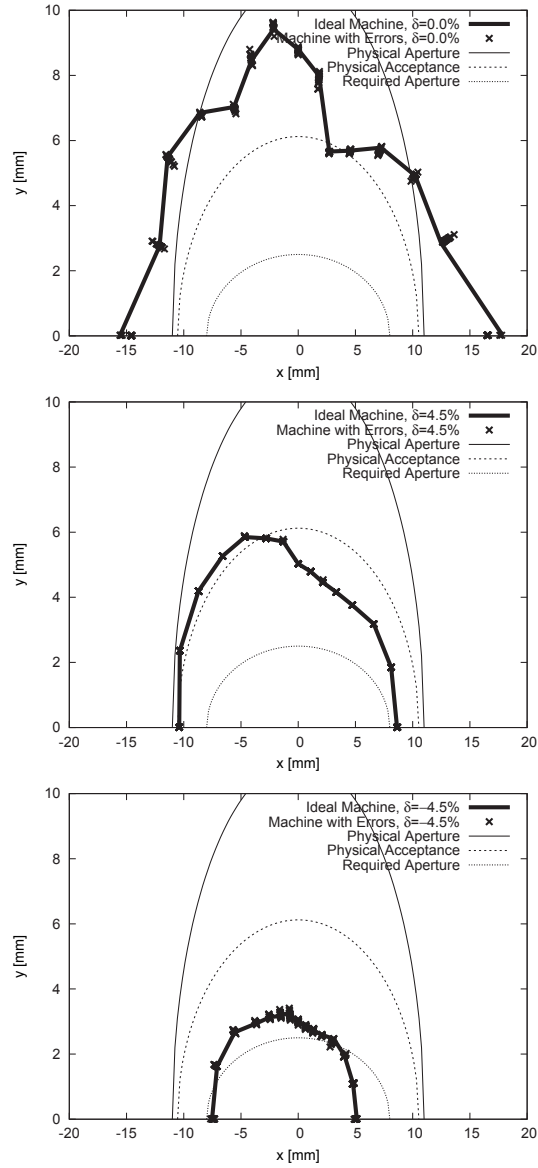


Figure 2.3: Dynamic aperture at the center of the long straight section as calculated by Tracy-3 on and off energy ( $\delta = \pm 4.5\%$ ) for a machine configuration with 4 PMDWs. The solid line shows the dynamic aperture for the ideal machine. The crosses show results for 20 error seeds. For the error seeds a 0.2% rms octupole gradient variation across all octupole magnets was assumed with a cutoff at  $2\sigma$ .

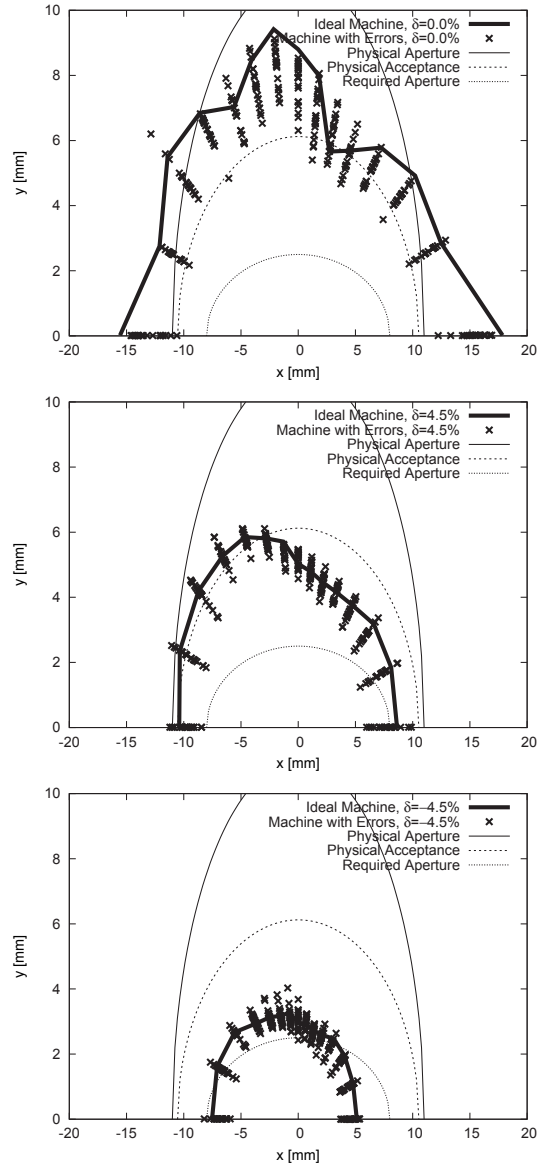


Figure 2.4: Dynamic aperture at the center of the long straight section as calculated by Tracy-3 on and off energy ( $\delta = \pm 4.5\%$ ) for a machine configuration with 4 PMDWs. The solid line shows the dynamic aperture for the ideal machine. The crosses show results for 20 error seeds. For the error seeds a 0.2% rms gradient variation across all dipole, quadrupole, sextupole, and octupole magnets was assumed with a cutoff at  $2\sigma$ .

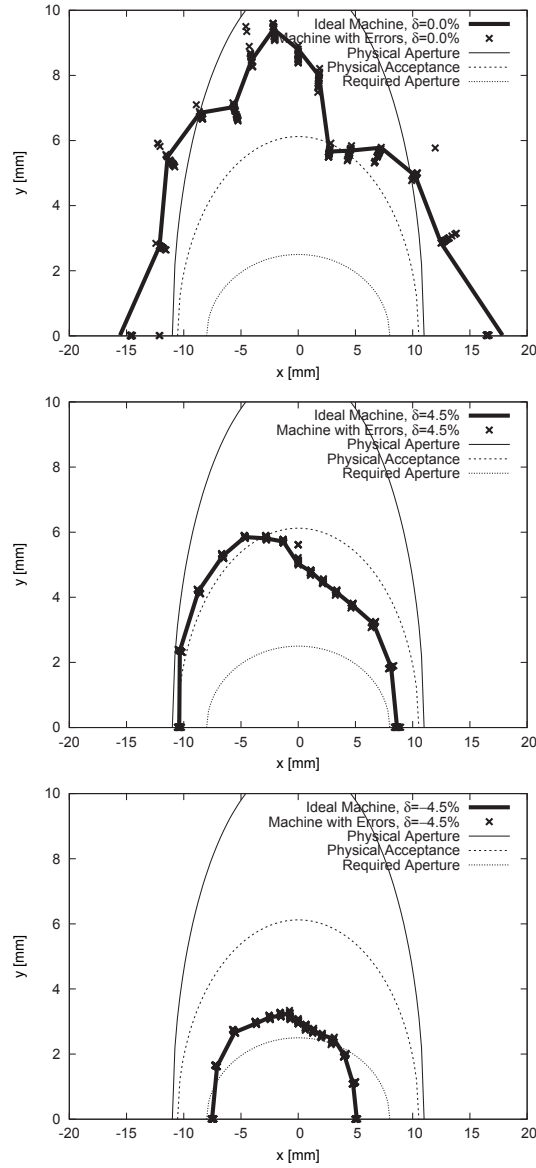


Figure 2.5: Dynamic aperture at the center of the long straight section as calculated by Tracy-3 on and off energy ( $\delta = \pm 4.5\%$ ) for a machine configuration with 4 PMDWs. The solid line shows the dynamic aperture for the ideal machine. The crosses show results for 20 error seeds. For the error seeds a 0.02% rms gradient variation across all dipole, quadrupole, sextupole, and octupole magnets was assumed with a cutoff at  $2\sigma$ .

**2.4.2.1.4 Shunting** As mentioned above shunting of individual magnets will be used to assure the rms deviations from the design field values are kept at an acceptable level. This allows powering magnets in families rather than having individual powering and cabling for every magnet. Dipoles, quadrupoles, and sextupoles will contain shunts. The shunts are to be implemented as binary resistor batteries thus allowing fine adjustment over a comparably large range with few inexpensive and standardized/modular parts.

Dipoles and quadrupoles will be shunted in two stages. A first stage should be performed by the manufacturer as a result of magnetic field measurements. This coarse shunting should assure deviations from design values below 0.2% rms [4]. After the magnets have been installed and machine commissioning has started, LOCO analysis will deliver the necessary results for the second stage of shunting that will be performed on site by the machine group. This shunting should then assure deviations from design approach a level of roughly 0.02% rms [4].

Sextupoles will be shunted in a single stage only. In order to detect deviations in the sextupole pattern from design, nonlinear optics (e.g. spectral components in betatron motion excited by resonance driving terms) have to be measured and analyzed (cf. e.g. [5] and Section 2.9.11.2). This measurement campaign depends on the quality of the available BPM system and is expected to take place in a later stage of commissioning. Hence, a single shunting stage will be performed by the machine group once this campaign has delivered the necessary results.

Note however, that the auxiliary sextupole powering of the secondary windings on certain sextupoles cannot be viewed as an alternative to individual sextupole corrections with shunts. The auxiliary sextupoles are required for nonlinear corrections that have to be applied outside of symmetric families (degeneration of driving terms). Sextupole shunting on the other hand ensures that symmetric sextupole families exist in the first place.

We assume that shunting of the octupole magnets will not be necessary. Because of the relaxed octupole design and the comparably low main field, rms deviations from design are expected to remain low enough so as not to drive strong octupolar resonances.

### 2.4.2.2. Higher-order and Multipole Errors

**2.4.2.2.1 Analytic Studies** Each magnet and ID installed in the MAX IV 3 GeV storage ring will have non-zero higher-order magnetic field components. While quadrupole components will lead to beta beats and tune shifts (or vertical dispersion in the case of skew quadrupole components), sextupole and octupole components will change the dynamic behavior: chromatic tune shift and amplitude-dependent tune shift behavior is changed. Since the chromaticity is corrected with a dedicated sextupole layout and settings, and the second-order chromaticity and amplitude-dependent tune shift driving terms are optimized with the octupoles, any additional sextupole or octupole components added to the design lattice will disturb the delicate balance that results from the dynamic optimization. Therefore it is essential to gauge the sensitivity of the lattice and the optimization to such perturbations. The result of such studies gives a specification for the higher-order field components of installed magnets and IDs.

While it is relatively difficult to specify boundary conditions for changes in the dynamic behavior, changes of the corrected chromaticity  $\xi_{x,y}$  can be measured (see Eq. 2.3). Likewise changes of the driving terms for second-order chromaticity and amplitude-dependent tune shifts [6]

$$\xi_{x,y}^{(2)} = \pm \frac{3}{4\pi} b_4 \eta^2 \beta_{x,y} \quad (2.4)$$

$$dQ_{xx} = \frac{\partial \Delta\nu_x}{\partial J_x} = \frac{3}{8\pi} b_4 \beta_x^2 \quad (2.5)$$

$$dQ_{xy} = \frac{\partial \Delta\nu_x}{\partial J_y} = \frac{\partial \Delta\nu_y}{\partial J_x} = -\frac{3}{4\pi} b_4 \beta_x \beta_y \quad (2.6)$$

$$dQ_{yy} = \frac{\partial \Delta\nu_y}{\partial J_y} = \frac{3}{8\pi} b_4 \beta_y^2 \quad (2.7)$$

can be measured for a set of higher-order perturbations. For the studies presented here thin sextupole and octupole kicks were added to different magnet families and their effect on these driving terms was gauged. A typical strength to apply is given by assuming that a 2 G residual pole tip field is always present. According to the multipole order, magnet length, and magnet gap this translates to a specific integrated multipole strength. Assuming such a multipole be added to every magnet of a specific family, the overall change of the dynamic properties can be assessed.

Another way to attack the multipole problem is to derive the multipole field strength

that can be applied to each member of a magnet family until the changes in chromaticity or higher-order driving terms (Eqs. 2.5–2.7) reach a specific level. For example, when the driving terms change by more than 10% of the correction applied to these terms as a result of the original octupole optimization.

Table 2.5 shows the result of such a study done for sextupole components in quadrupole and dipole magnets. For each family the integrated normalized sextupole strength ( $b_3l$ ) equivalent of a residual 2 G pole tip field is calculated. For each family, the resulting change in linear chromaticity  $\xi_{x,y}$  can be calculated according to Eq. 2.3. In a second step the influence of such an additional sextupole component on second-order chromaticity  $\xi_{x,y}^{(2)}$  is observed. For this purpose, a thin sextupole with the calculated strength is integrated into each of the quadrupole and dipole magnets in the OPA model. For quadrupoles, the thin sextupole was added at the center of the quadrupole magnet. For dipole magnets, the sextupole component was added as thin sextupole kicks between individual dipole slices. For each magnet family, the resulting change in second-order chromaticity  $\xi_{x,y}^{(2)}$  is then recorded.

Table 2.5: Sensitivity to sextupole components for each quadrupole and dipole family. The second column shows the equivalent sextupole strength of a residual pole tip field of 2 G. The last two columns show the change in (corrected) linear and second-order chromaticity resulting from such a sextupole component in the different magnet families. This specification allows a direct comparison with the sextupole magnet strengths given in Table 2.1 in Section 2.3.2.

Family	$(b_3l)$ equiv. of 2G	$ \Delta\xi_{x,y}/\xi_{x,y} $	$ \Delta\xi_{x,y}^{(2)}/\xi_{x,y}^{(2)} $
QFend	$0.0320 \text{ m}^{-2}$	—, —	$4.7 \times 10^{-2}, 2.4 \times 10^{-1}$
QDend	$0.0320 \text{ m}^{-2}$	—, —	$1.2 \times 10^{-2}, 3.0 \times 10^{-1}$
QFm	$0.0192 \text{ m}^{-2}$	$4.9 \times 10^{-2}, 4.7 \times 10^{-2}$	$2.3 \times 10^{-3}, 8.0 \times 10^{-2}$
QF	$0.02083 \text{ m}^{-2}$	$1.2 \times 10^{-1}, 1.2 \times 10^{-1}$	$4.2 \times 10^{-3}, 1.1 \times 10^{-1}$
DIPm	$0.0770 \text{ m}^{-2}$	$1.6 \times 10^{-3}, 2.1 \times 10^{-2}$	$8.2 \times 10^{-3}, 4.7 \times 10^{-1}$
DIP	$0.1249 \text{ m}^{-2}$	$9.8 \times 10^{-2}, 5.7 \times 10^{-1}$	$1.1 \times 10^{-2}, 7.9 \times 10^{-1}$

A similar study was conducted for octupolar field components in sextupole, quadrupole, and dipole magnets. Table 2.6 summarizes the results. For each magnet family the 2 G equivalent octupole strength was calculated and applied to the magnet family as an

additional octupole kick. The resulting change of the second-order chromaticity  $\xi_{x,y}^{(2)}$  as well as the relative change in amplitude-dependent tune shift driving terms  $\Delta dQ_{ij}/dQ_{ij}$  was noted.

Table 2.6: Sensitivity to octupole components for each sextupole, quadrupole, and dipole family. The second column shows the equivalent octupole strength of a residual pole tip field of 2 G. The third and fourth columns show the change in chromatic and amplitude-dependent tune shift driving terms resulting from such an octupole component in the different magnet families. Note that the indices  $ij$  stand for  $xx, xy, yy$ . The octupole strength specification allows a direct comparison with the octupole magnet strengths given in Table 2.2 in Section 2.3.3.

Family	$(b_4l)$ equiv. of 2G	$\Delta\xi_{x,y}^{(2)}/\xi_{x,y}^{(2)}$ [%]	$\Delta dQ_{ij}/dQ_{ij}$ [%]
SFi	$1.024 \text{ m}^{-3}$	2.1, 9.3	8.6, 3.9, 0.4
SFo	$1.024 \text{ m}^{-3}$	0.8, 3.5	7.4, 3.3, 2.7
SFm	$1.024 \text{ m}^{-3}$	0.8, 3.8	6.1, 2.8, 2.1
SD	$1.024 \text{ m}^{-3}$	1.0, 20.1	6.8, 13.3, 34.7
SDend	$1.024 \text{ m}^{-3}$	< 0.1, 1.7	0.2, 1.8, 19.5
QFend	$2.560 \text{ m}^{-3}$	—, —	61.8, 31.6, 14.3
QDend	$2.560 \text{ m}^{-3}$	—, —	10.4, 26.0, 57.3
QFm	$1.536 \text{ m}^{-3}$	1.5, 9.3	10.4, 6.7, 3.9
QF	$1.536 \text{ m}^{-3}$	4.0, 28.8	22.7, 16.2, 10.3
DIPm	$5.497 \text{ m}^{-3}$	—, 0.6	5.2, 28.0, 148.0
DIP	$8.920 \text{ m}^{-3}$	3.3, 130.5	24.0, 92.7, 329.6

Finally, it must also be assumed that IDs installed in the long straight sections will contain high-order field components as well. To gauge this effect a typical ID with a length of 2 m was assumed and given quadrupole, sextupole, and octupole moments. The quadrupole contribution was modeled as a long hard-edge quadrupole at the center of the straight. It was found that for only one such device installed in the storage ring, an integrated normalized contribution of  $(b_2l) = 0.1123 \text{ m}^{-1}$  will result in a horizontal tune shift of  $\Delta\nu_x = 0.1$  (cf. Eq. 2.1). To obtain a vertical tune shift of  $\Delta\nu_y = 0.1$  an integrated normalized contribution of  $(b_2l) = 0.2369 \text{ m}^{-1}$  is required. If one assumes that ten such devices are installed in the storage ring and operated at the same time,



the maximum allowable gradient error per ID is  $(b_2l) = 0.0136 \text{ m}^{-1}$  for  $\Delta\nu_x = 0.1$  and  $(b_2l) = 0.0244 \text{ m}^{-1}$  for  $\Delta\nu_y = 0.1$ . Similar studies have been performed for the sextupole and octupole contributions: long hard-edge sextupoles and octupoles have been applied to the center of a straight section and the effect on linear chromaticity  $\xi_{x,y}$  (cf. Eq. 2.3), second-order chromaticity  $\xi_{x,y}^{(2)}$  and amplitude-dependent tune shift driving terms  $dQ_{ij}$  observed. Assuming again that the maximum tolerable contribution should amount to no more than 10% of the correction applied by the dedicated sextupoles and octupoles, an upper limit for high-order field contributions in an ID can be specified.

Finally, from all of the above mentioned studies, one can gather a set of maximum higher-order field components for each type of magnet and ID. The assumption made here is that the multipole contribution should amount to no more than 10% of the corrections applied by the design optics. These figures can be seen as beam dynamics tolerance limits on magnet and ID quality. The values are given in Table 2.7. The magnets have been grouped by manufacturing types.

Table 2.7: Tolerances of different magnet types and IDs for higher-order field components. The underlying condition is that the multipole contribution should amount to no more than 10% of the corrections applied by the design optics.

Magnet type	Maximum allowable multipole components		
	$(b_2l) [\text{m}^{-1}]$	$(b_3l) [\text{m}^{-2}]$	$(b_4l) [\text{m}^{-3}]$
DIP	—	0.016	0.271
DIPm	—	0.016	0.371
QF, QFm	—	0.017	0.533
QDend, QFend	—	0.011	0.414
SFi, SFo, SFm	—	—	1.191
SD, SDend	—	—	0.295
Single ID	0.112	0.170	8.921
10 IDs	0.014	0.018	0.892

**2.4.2.2.2 Tracking Studies** What is missing in this analysis so far is the influence of random multipoles and the overall effect of random and systematic multipoles on the storage ring performance. More specifically, how much reduction of dynamic aperture

is caused by the presence of multipole contributions in the storage ring magnets? One way to gauge this is to compare the dynamic aperture of the ideal machine with that of a machine where field and multipole errors have been added. Since there is presently no measurement data from prototype magnets for MAX IV available, we instead use the magnet errors measured for the SLS storage ring magnets [7]. Table 2.8 lists the assumptions made in this error model.

Table 2.8: Multipole errors used in the MAX IV error model. The data has been taken from magnet measurements of the SLS storage ring magnets [7]. The order column refers to the multipole order defined by 2 = quadrupole, 3 = sextupole, etc.

Magnet family	Error type	Order	Maximum multipole component (relative to main field component)	
			Upright	Skew
Quadrupoles	Systematic	6	$0.5 \times 10^{-4}$	—
		10	$0.5 \times 10^{-4}$	—
		14	$0.1 \times 10^{-4}$	—
Sextupoles	Systematic	9	$0.5 \times 10^{-4}$	—
		15	$0.5 \times 10^{-4}$	—
		21	$0.5 \times 10^{-4}$	—
Quadrupoles	Random (rms)	2	$2.5 \times 10^{-4}$	—
		3	$2.8 \times 10^{-4}$	$2.9 \times 10^{-4}$
		4	$1.9 \times 10^{-4}$	$1.4 \times 10^{-4}$
		6	$1.3 \times 10^{-4}$	—
		10	$3.0 \times 10^{-5}$	—
Sextupoles	Random (rms)	3	$5.0 \times 10^{-4}$	—
		4	$5.2 \times 10^{-4}$	$4.9 \times 10^{-4}$
		5	$3.5 \times 10^{-4}$	—
		9	$8.0 \times 10^{-5}$	—
		15	$5.0 \times 10^{-5}$	—

The dynamic aperture results using the multipole error model are shown in Fig. 2.6. The multipole errors have been applied as detailed above for 20 seeds with a cutoff at  $2\sigma$ .

Figure 2.7 shows the dynamic aperture including both multipole errors and the 0.02% rms field errors expected after calibrating and shunting the newly manufactured MAX IV magnets. The multipole and field errors have been applied for 20 seeds with a cutoff at  $2\sigma$ . As already pointed out in Section 2.4.2.1.3, if calibration and shunting of the magnets after manufacturing can guarantee a main field variation no larger than 0.02% rms, the field errors do not lead to a dynamic aperture reduction significantly beyond that caused by the multipole errors. And as will be demonstrated in the next section, overall dynamic aperture reduction will be dominated by misalignment errors rather than by multipole or field errors.

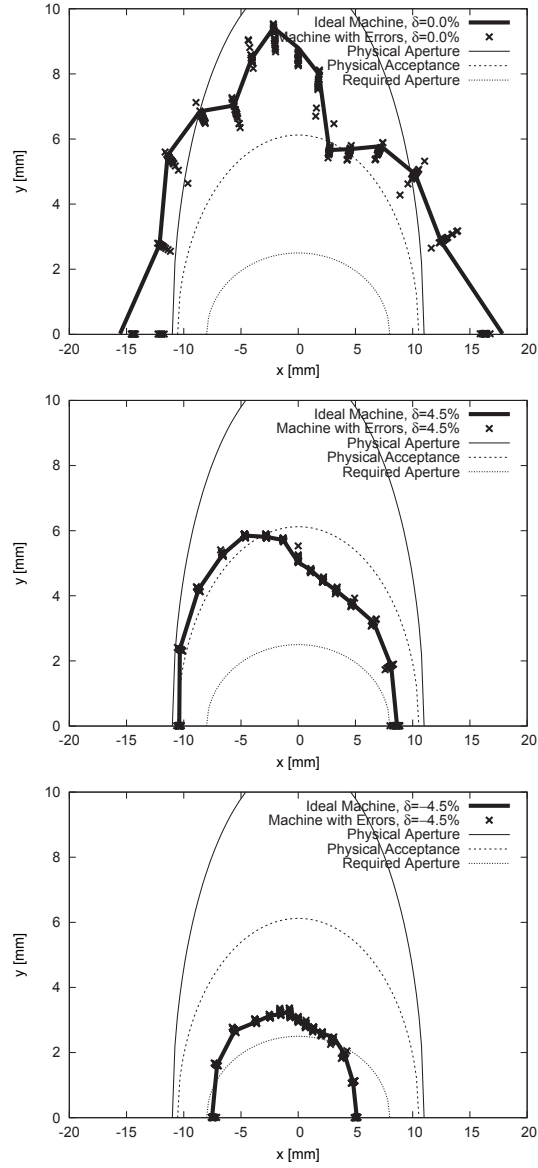


Figure 2.6: Dynamic aperture at the center of the long straight section as calculated by Tracy-3 on and off energy ( $\delta = \pm 4.5\%$ ) for a machine configuration with 4 PMDWs. The solid line shows the dynamic aperture for the ideal machine. The crosses show results for 20 error seeds. For the error seeds the multipole error model was assumed with a cutoff at  $2\sigma$ .

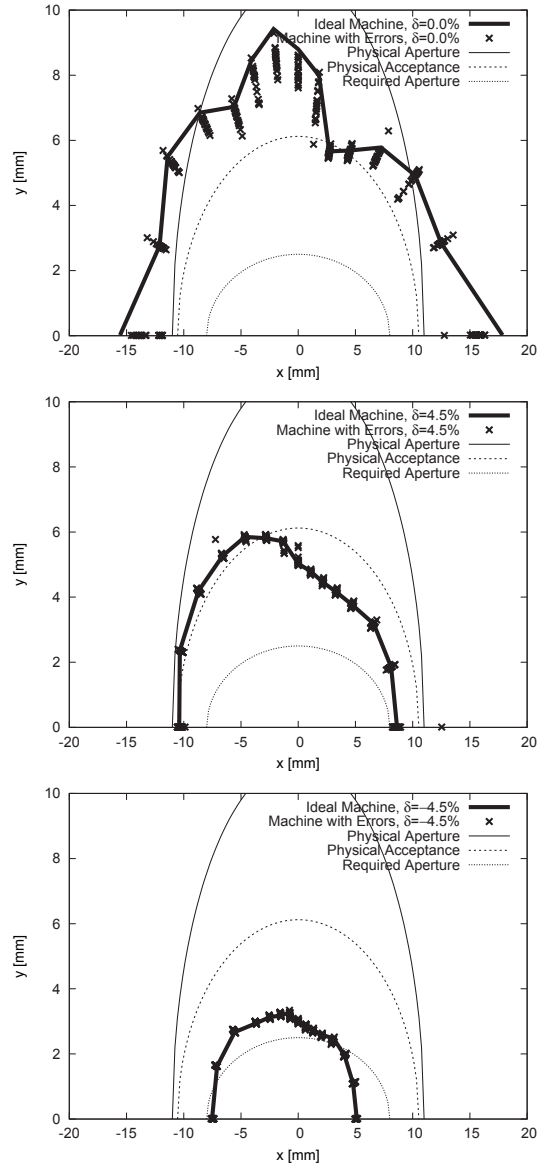


Figure 2.7: Dynamic aperture at the center of the long straight section as calculated by Tracy-3 on and off energy ( $\delta = \pm 4.5\%$ ) for a machine configuration with 4 PMDWs. The solid line shows the dynamic aperture for the ideal machine. The crosses show results for 20 error seeds. For the error seeds the multipole and field error model (0.02% rms field errors) was assumed with a cutoff at  $2\sigma$ .

### 2.4.3. Misalignment Errors

In a real storage ring magnets are always positioned away from their ideal locations. While longitudinal alignment of one element with respect to its upstream and downstream neighbors is facilitated by the use of rigid girders (see Chapter 2.5), magnets can easily be misaligned in the transverse plane. In addition, roll errors generate skew field components which are not present in the theoretical design. Displacements in the transverse direction can be detected by BPMs and corrected by horizontal and vertical corrector coils installed throughout the achromat. A proper correction of these misalignments will lead to a new closed orbit. It then remains to be shown that the deviations of this closed orbit from the ideal orbit can be handled (see Section 2.4.4). Roll errors on the other hand cannot be corrected directly. These roll errors induce spurious dispersion, coupling, and ultimately define the vertical emittance of the machine (see Section 2.4.6).

#### 2.4.3.1. Effects of Misalignment Errors without Coupling

In order to properly model misalignments, the correlations from integrated assembly and girders have to be taken into account. Since no complete set of prototype measurements exists from which misalignment data could be extracted, an error model is defined. In this model two sets of errors are applied: the “required” misalignments and the “challenge” misalignments. The former are considered a pessimistic estimate and should be achieved without any extra effort. The latter is a set of reduced errors which corresponds to what is expected if extra care is taken during manufacturing and alignment. Both models can be compared to gain a feeling for the effect of errors on performance. The error model makes the following assumptions for the “required” misalignments (“challenge” misalignments given in brackets):

- The unit cell dipoles, both adjacent SDs, and one quadrupole/sextupole sandwich are machined from a common solid block of iron. This block also includes one set of hor./ver. correctors and a BPM. The magnetic centers are aligned to within the machining accuracy of  $25\ \mu\text{m rms}$  [ $10\ \mu\text{m rms}$ ] in both planes. Assume a  $0.2\ \text{mrad rms}$  [ $0.1\ \text{mrad rms}$ ] roll error.
- Unlike the outer unit cells, the center unit cell block contains two quadrupole/sextupole

sandwiches two sets of hor./ver. correctors and BPMs. The tolerances within are the same as for the other unit cells: the magnetic centers are aligned to within the machining accuracy of  $25\text{ }\mu\text{m}$  rms [ $10\text{ }\mu\text{m}$  rms] in both planes. Assume a  $0.2\text{ mrad}$  rms [ $0.1\text{ mrad}$  rms] roll error.

- The matching section consists of one solid block containing the the soft-end matching dipole, the final focusing quadrupoles, the SDend, all octupoles, and two pairs of hor./ver. correctors and BPM. Again, this assembly is manufactured from one common solid iron block and therefore the magnetic centers are again aligned to within the machining accuracy of  $25\text{ }\mu\text{m}$  rms [ $10\text{ }\mu\text{m}$  rms] in both planes. Assume a  $0.2\text{ mrad}$  rms [ $0.1\text{ mrad}$  rms] roll error.
- The BPMs are fastened to the adjacent sextupole or octupole magnet. This ensures only a  $25\text{ }\mu\text{m}$  rms [ $10\text{ }\mu\text{m}$  rms] machining accuracy error between the BPM position and the magnetic center in both planes. In addition a BPM calibration accuracy of  $10\text{ }\mu\text{m}$  rms [ $5\text{ }\mu\text{m}$  rms] is assumed ( $3\text{ }\mu\text{m}$  rms calibration has already been achieved at SLS [3]). In total this gives an rms alignment error of  $27\text{ }\mu\text{m}$  [ $11\text{ }\mu\text{m}$ ] in both planes for the BPMs. Assume a  $0.2\text{ mrad}$  rms [ $0.1\text{ mrad}$  rms] roll error.
- The solid iron blocks containing the magnets for the unit and matching cells are assumed to have an alignment error of  $100\text{ }\mu\text{m}$  rms [ $50\text{ }\mu\text{m}$  rms] in both planes along with a  $0.2\text{ mrad}$  rms [ $0.1\text{ mrad}$  rms] roll error.
- The random misalignment of the solid blocks (modeled as the girders) are applied systematically to the elements within. On top of this error the random alignment error for each element is applied.
- One known deficiency of this misalignment error model is that the dipoles are modeled with slices (see Chapter 2.2.3) which each carry their own individual random misalignment. This is a pessimistic model since in reality the dipole magnet within the solid iron block is manufactured as one solid iron yoke. However, since the main contribution to the integrated dipole field strength comes basically from two slices, the discrepancy should not be too large.

Orbit correction finds corrector settings which result in a new closed orbit which lies as close to the design orbit as possible. Obviously this orbit correction relies on the underlying BPM and corrector pattern (see Section 2.4.4). Tracy-3 has been used to simulate

this process for a machine configuration with 4 PMDWs. The code first calculates an orbit response matrix which is then inverted using SVD. This inverted response matrix is then used to calculate corrector settings for an arbitrary set of beam position readings. Tracy-3 performs this correction in three iterations and then returns a final closed-orbit as a set of deviations from the design orbit around the ring.

The overall effect of misalignments is the closed orbit resulting from orbit correction; this is shown in Figs. 2.8 and 2.9. The applied misalignments correspond to the misalignments specified in the “required” alignment error model above. For rms misalignments a  $2\sigma$ -cutoff was assumed. Results are shown for 100 seeds. For the misalignments calculated and displayed in Figs. 2.8 and 2.9, the required corrector strengths have also been recorded. Figures 2.10 and 2.11 show these mean and rms corrector strengths (using a three-step correction).

For comparison, Figs. 2.12, 2.13, 2.14 and 2.15 show the closed orbit deviations and required corrector strength for the “challenge” alignment error model. It appears that both closed orbit distortions and corrector strengths scale roughly linearly with the girder misalignment which apparently dominates over the misalignment of the elements within a girder.

One may also ask what influence these misalignments have on the dynamic performance of the storage ring. One way to gauge this is to investigate the dynamic aperture for a misaligned and corrected machine. These results are shown in Fig. 2.16 for the “required” alignment error model and in Fig. 2.17 for the “challenge” model.

Finally, dynamic aperture including all modeled error sources (0.02% rms field errors, multipole errors, and “required” alignment errors) is displayed in Fig. 2.18. It is of interest to note that the combined dynamic aperture reduction from all error sources is not significantly larger than that of only the misalignment errors. It is the latter that presents the dominating source of dynamic aperture reduction.

For comparison, dynamic aperture including all modeled error sources (0.02% rms field errors, multipole errors, and “challenge” alignment errors) is displayed in Fig. 2.19.



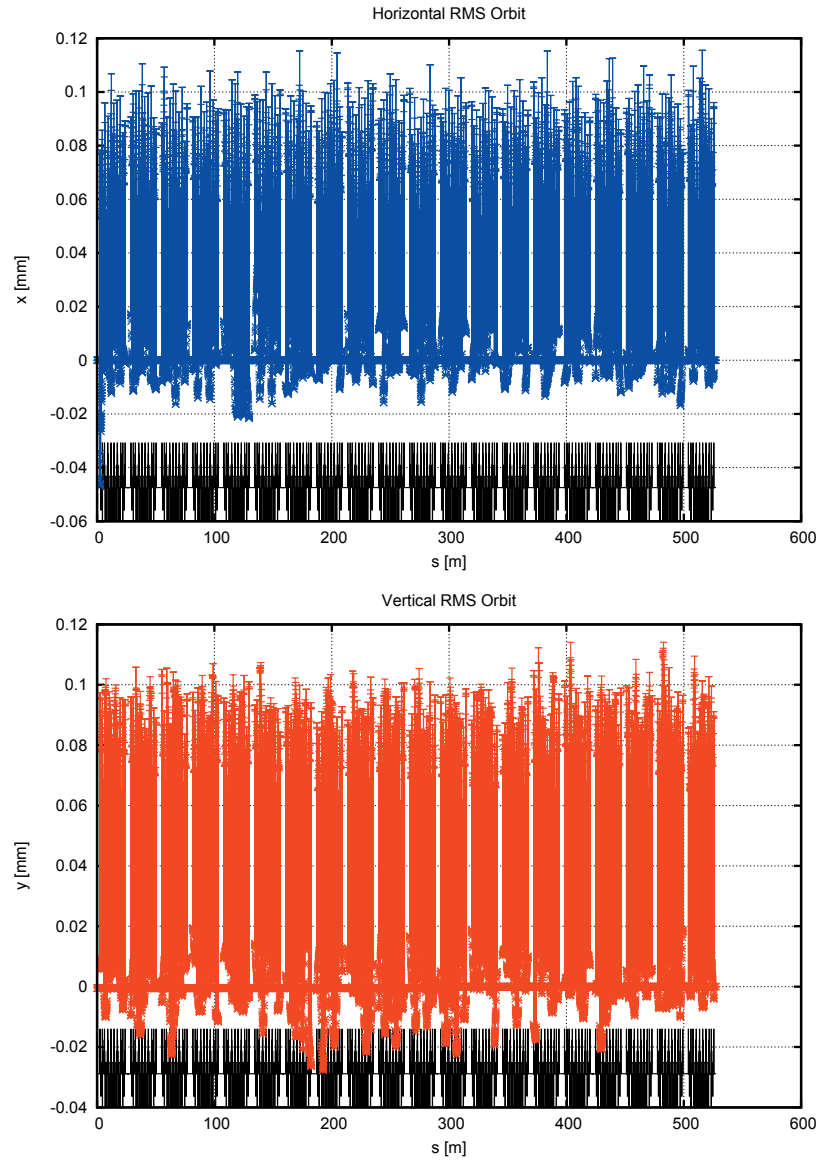


Figure 2.8: Closed-orbit deviations from the design orbit after applying misalignments (“required” model) and correcting the orbit. The dot shows the mean deviation for all seeds and the “error bar” depicts the deviation corresponding to 1 standard deviation across all seeds. 100 seeds were used.

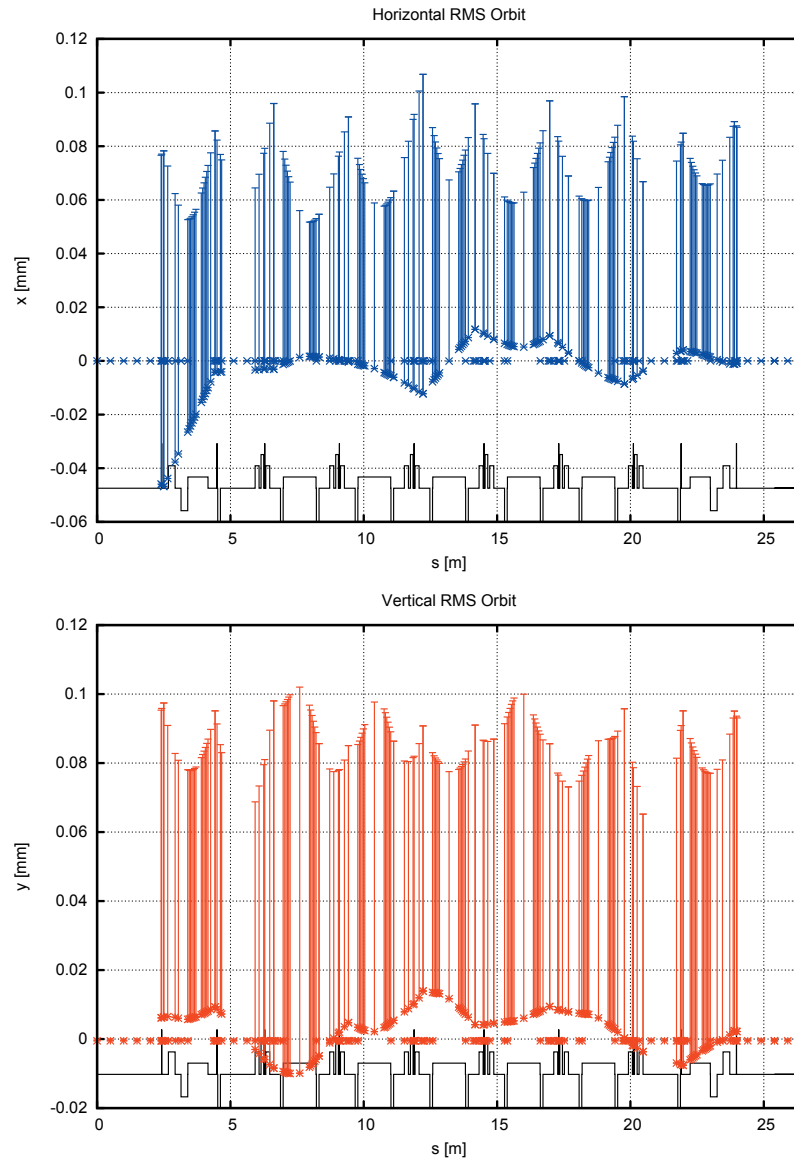


Figure 2.9: Magnification of Fig. 2.8 showing results for only one achromat.

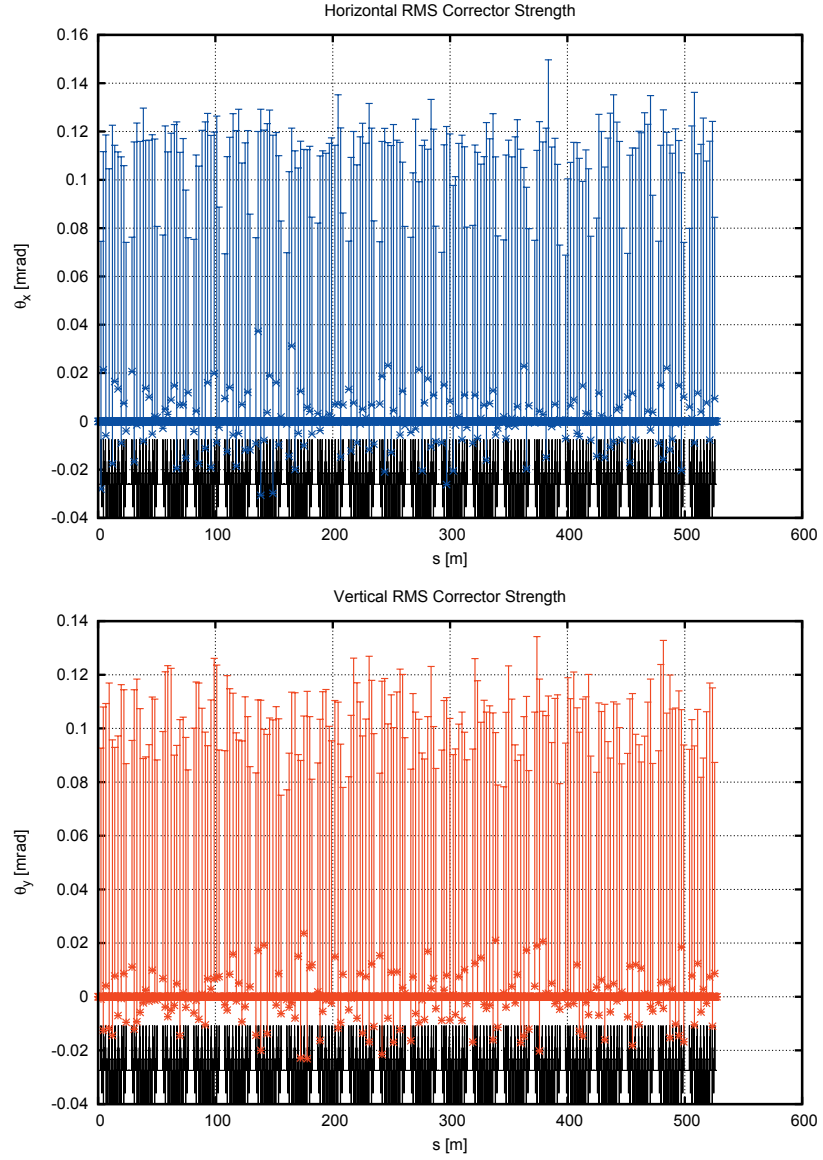


Figure 2.10: Corrector strengths required for the orbit correction displayed in Fig. 2.8. The dot shows the mean corrector strength for all seeds and the “error bar” depicts the deviation corresponding to 1 standard deviation across all seeds. 100 seeds were used.

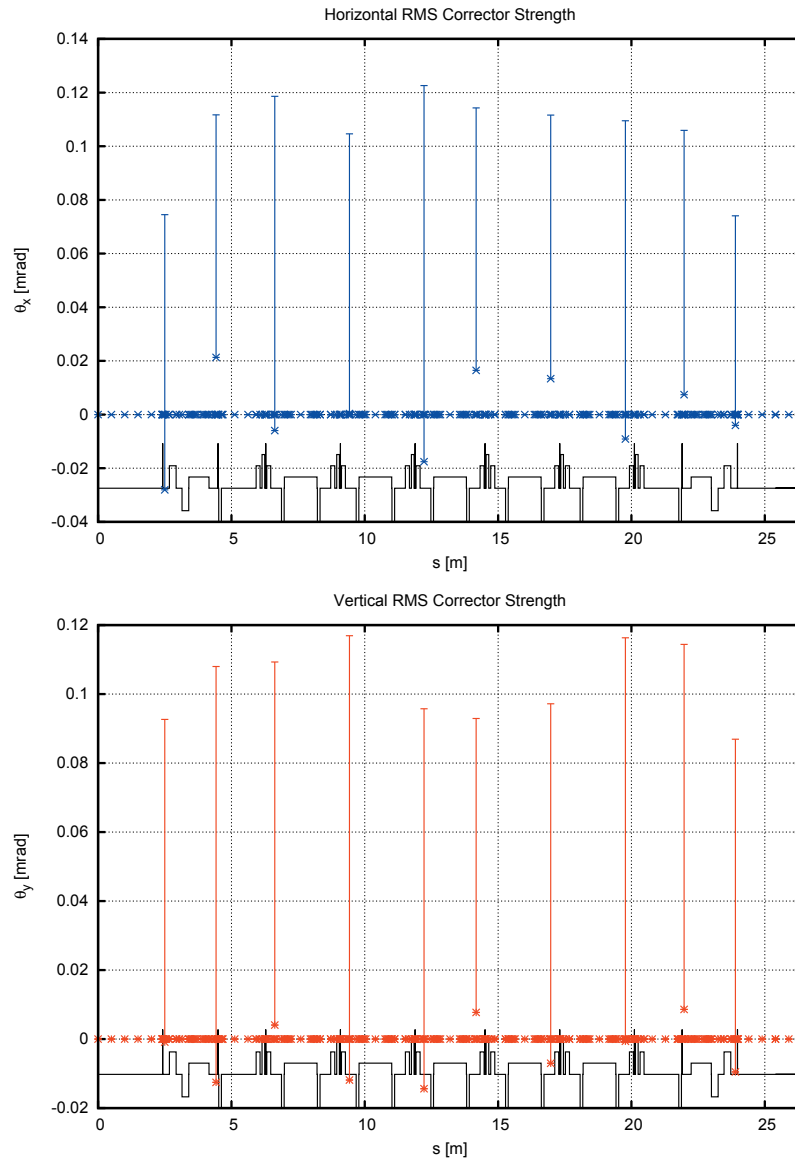


Figure 2.11: Magnification of Fig. 2.10 showing results for only one achromat.

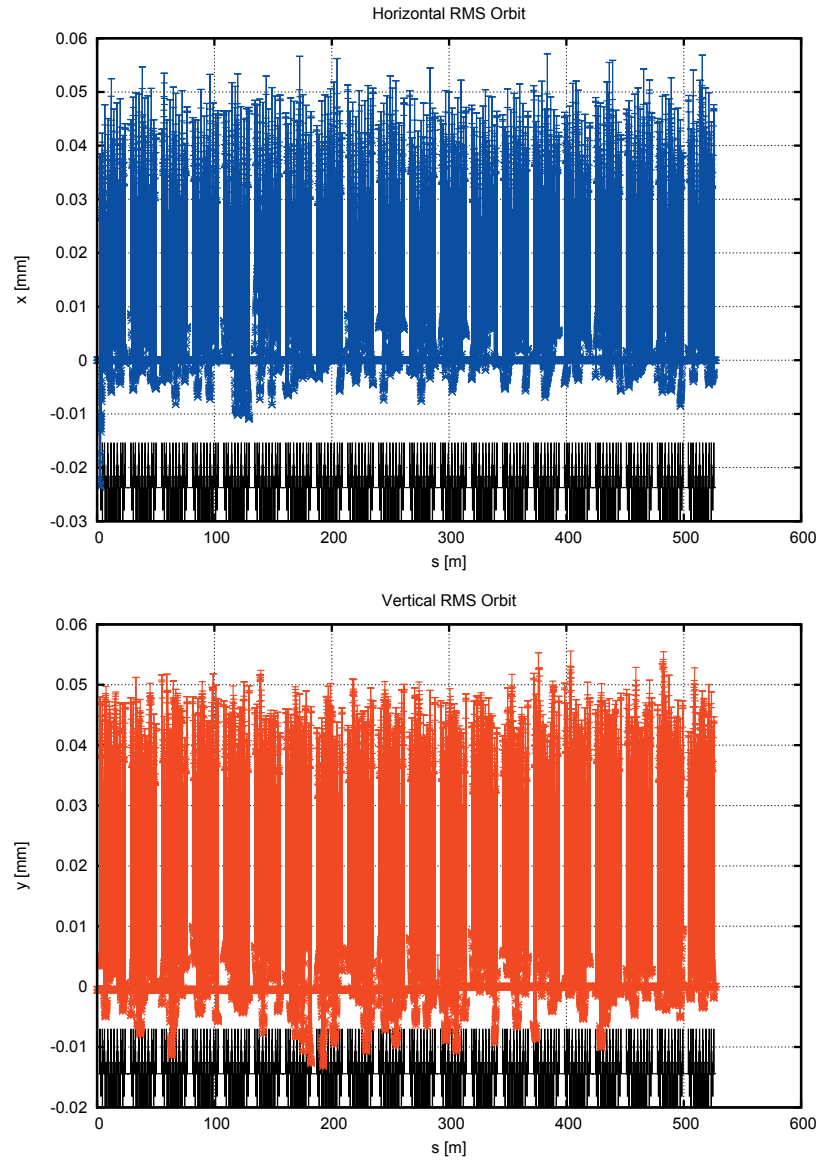


Figure 2.12: Closed-orbit deviations from the design orbit after applying misalignments (“challenge” model) and correcting the orbit. The dot shows the mean deviation for all seeds and the “error bar” depicts the deviation corresponding to 1 standard deviation across all seeds. 100 seeds were used.

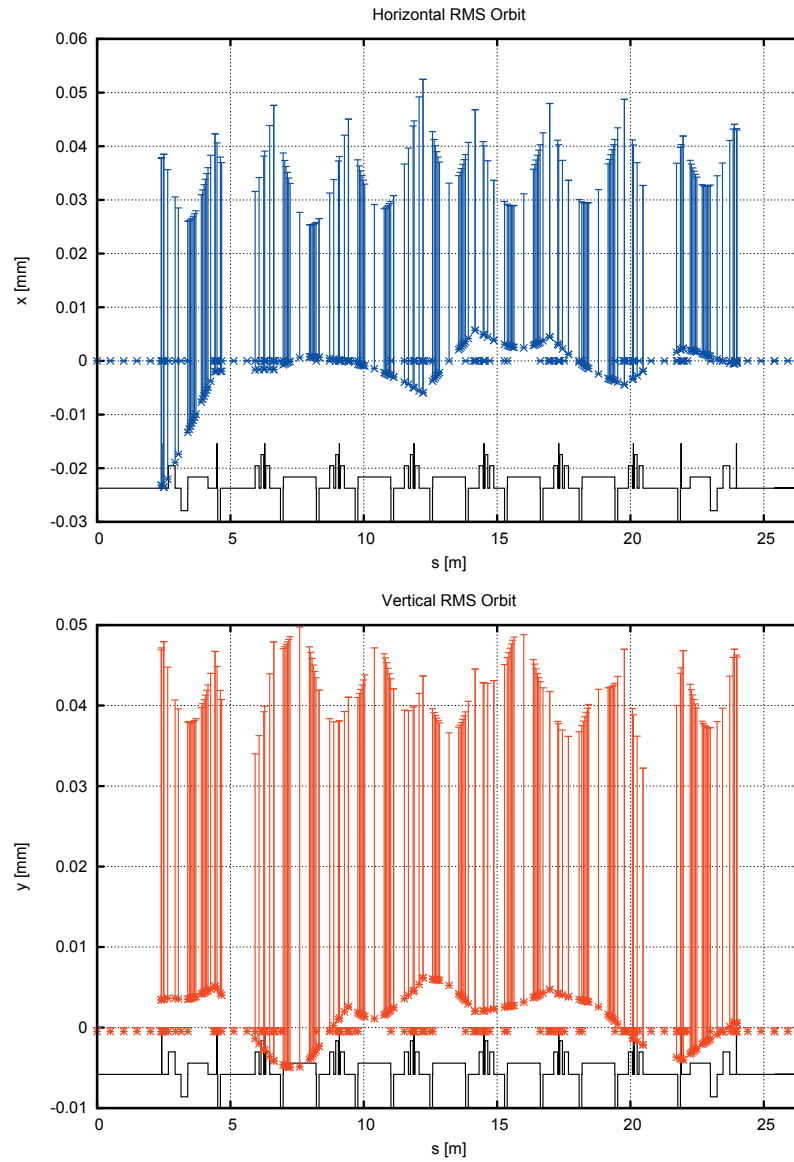


Figure 2.13: Magnification of Fig. 2.12 showing results for only one achromat.

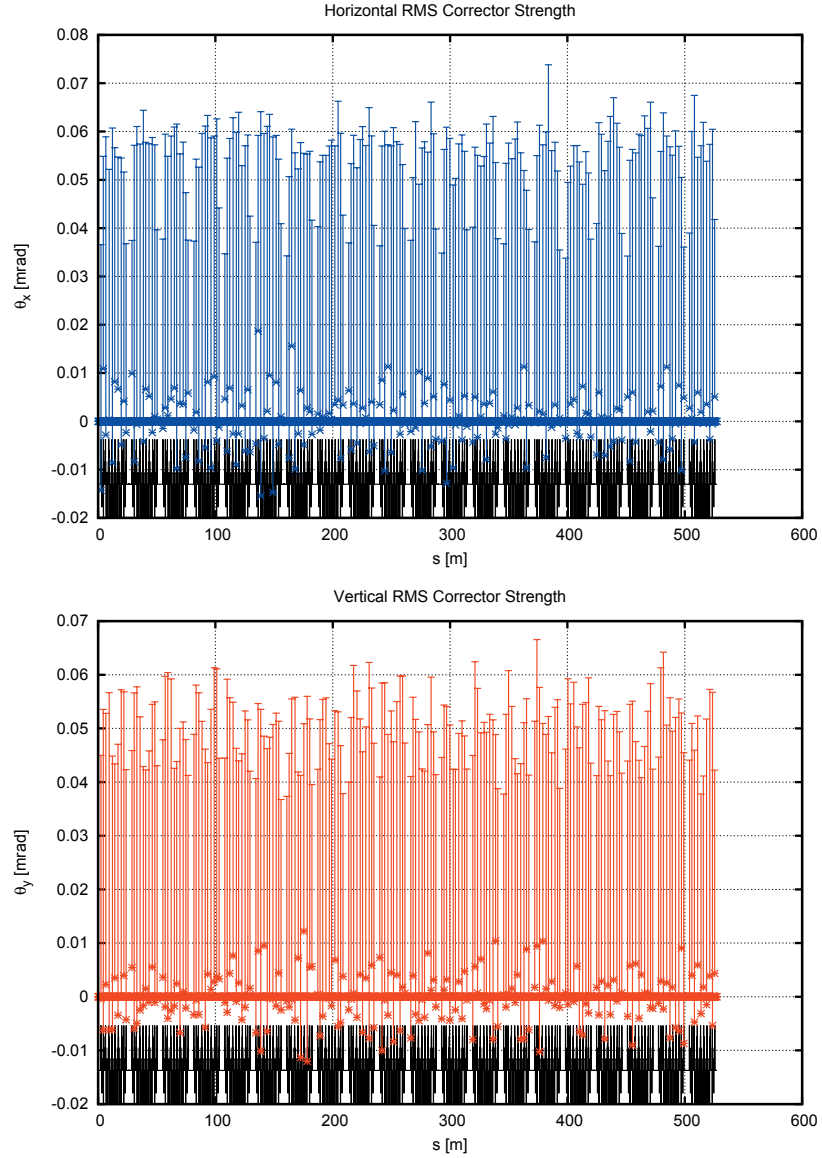


Figure 2.14: Corrector strengths required for the orbit correction displayed in Fig. 2.12. The dot shows the mean corrector strength for all seeds and the “error bar” depicts the deviation corresponding to 1 standard deviation across all seeds. 100 seeds were used.

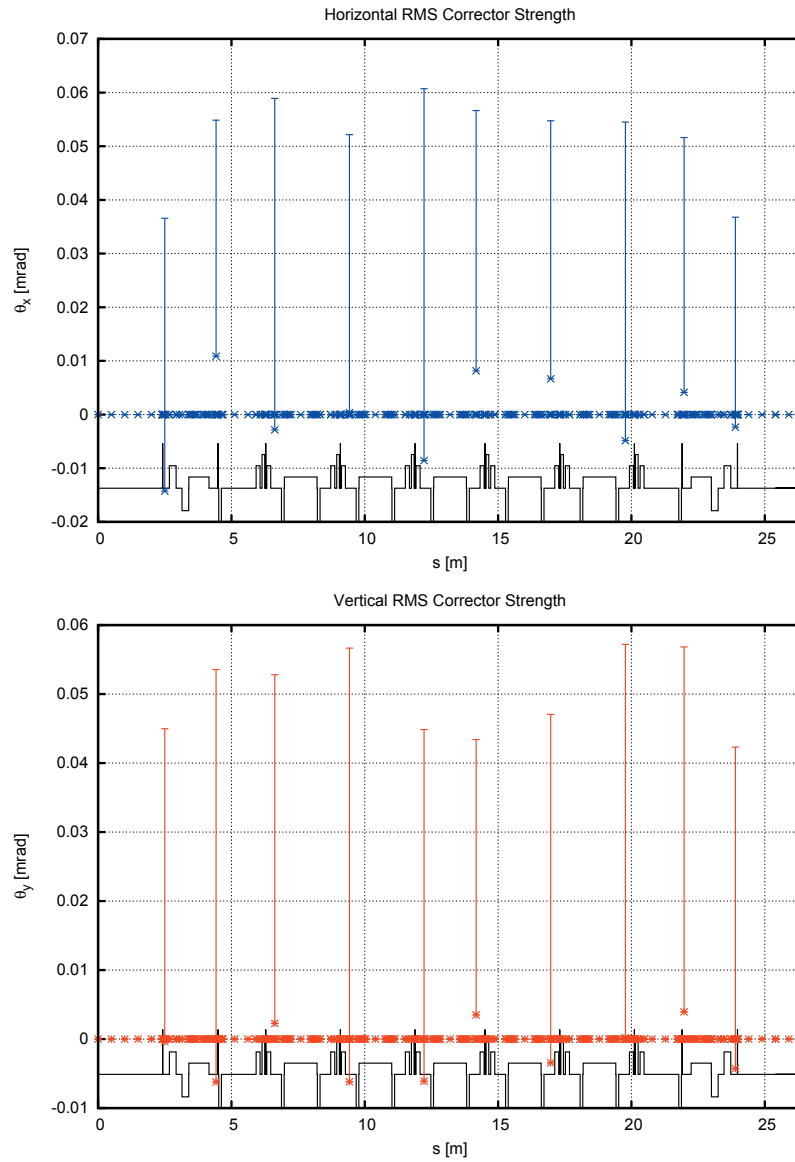


Figure 2.15: Magnification of Fig. 2.14 showing results for only one achromat.



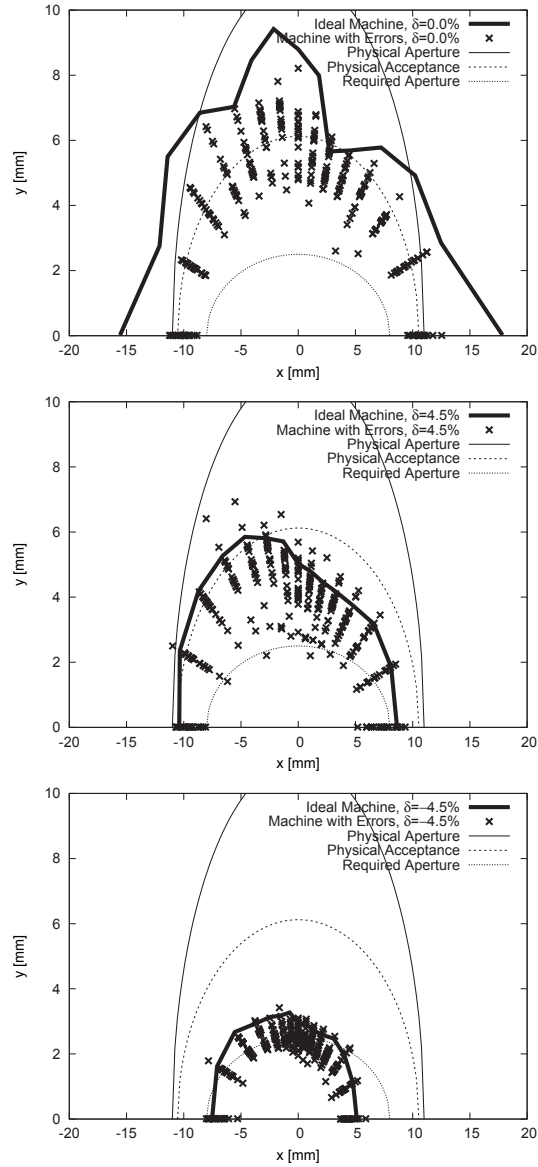


Figure 2.16: Dynamic aperture at the center of the long straight section as calculated by Tracy-3 on and off energy ( $\delta = \pm 4.5\%$ ) for a machine configuration with 4 PMDWs. The solid line shows the dynamic aperture for the ideal machine. The crosses show results for 20 error seeds. For the error seeds the “required” alignment error model was assumed with a cutoff at  $2\sigma$ .

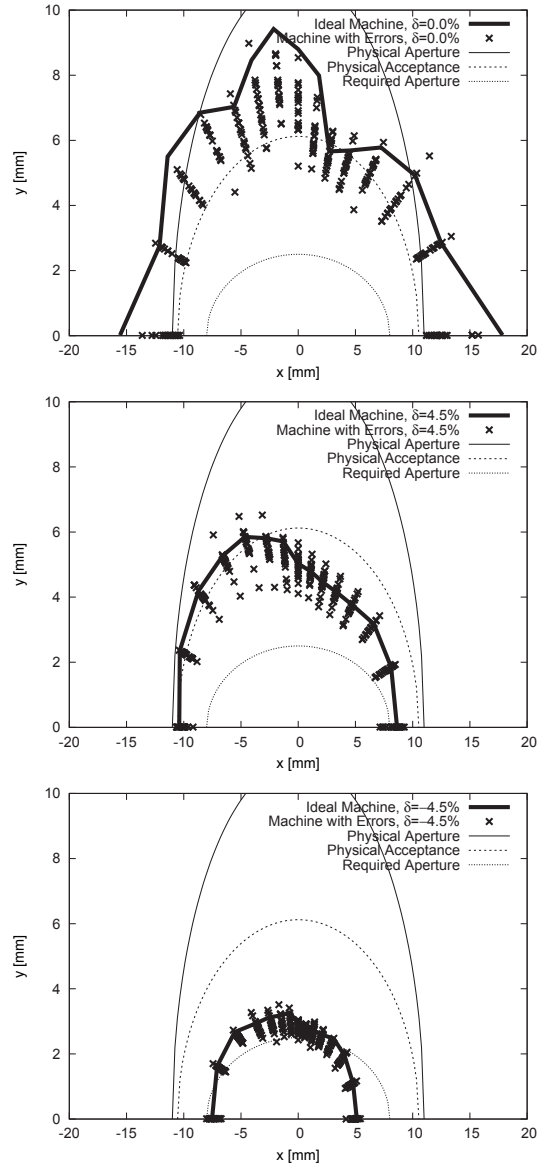


Figure 2.17: Dynamic aperture at the center of the long straight section as calculated by Tracy-3 on and off energy ( $\delta = \pm 4.5\%$ ) for a machine configuration with 4 PMDWs. The solid line shows the dynamic aperture for the ideal machine. The crosses show results for 20 error seeds. For the error seeds the “challenge” alignment error model was assumed with a cutoff at  $2\sigma$ .

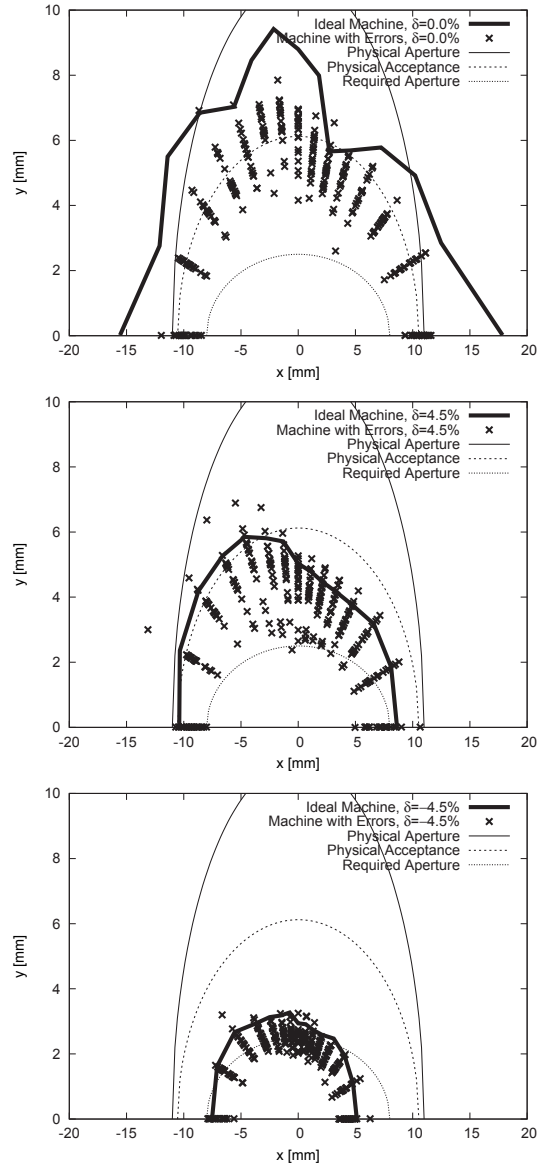


Figure 2.18: Dynamic aperture at the center of the long straight section as calculated by Tracy-3 on and off energy ( $\delta = \pm 4.5\%$ ) for a machine configuration with 4 PMDWs. The solid line shows the dynamic aperture for the ideal machine. The crosses show results for 20 error seeds. For the error seeds the “required” alignment, multipole, and field error models were assumed with a cutoff at  $2\sigma$ .

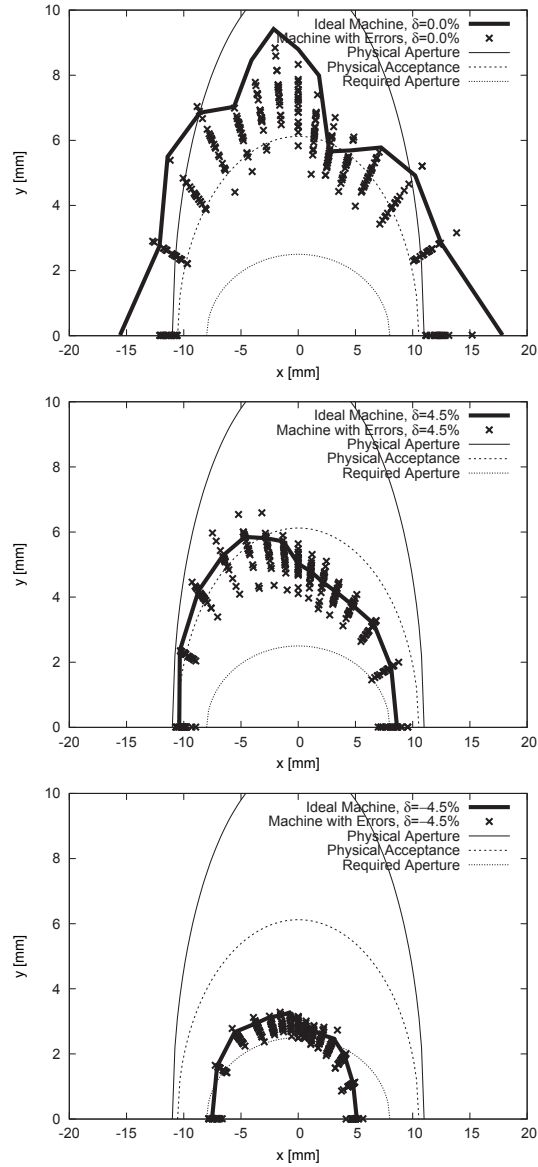


Figure 2.19: Dynamic aperture at the center of the long straight section as calculated by Tracy-3 on and off energy ( $\delta = \pm 4.5\%$ ) for a machine configuration with 4 PMDWs. The solid line shows the dynamic aperture for the ideal machine. The crosses show results for 20 error seeds. For the error seeds the “challenge” alignment, multipole, and field error models were assumed with a cutoff at  $2\sigma$ .

### 2.4.3.2. Coupling from Misalignment Errors

Finally, a study has been performed to assess the amount of linear betatron coupling that results from the multipole and misalignment errors in the model given above. For each seed with random errors applied with a  $2\sigma$ -cutoff we derive the betatron coupling as the ratio of the normal-mode emittances  $\kappa = \varepsilon_{\text{II}}/\varepsilon_{\text{I}}$ ; we also note the tilt angle of the beam.

*This is ongoing work...*

### 2.4.4. BPM and Corrector Pattern

The MAX IV 3 GeV storage ring will be equipped with ten BPMs and ten horizontal/vertical corrector pairs per achromat. The average phase advance between BPMs is  $26^\circ$  in the vertical plane and  $76^\circ$  in the horizontal. These phase advances are sufficient to sample betatron motion around the ring. BPM buttons are installed as close as possible to window-frame corrector magnets (which correct both the horizontal and the vertical beam position) in order to minimize the phase advance in between.

Within the unit cells the BPMs are placed adjacent to the focusing sextupoles because this is the location where orbit offsets in the magnets give the largest contribution to betatron coupling. In the matching section one BPM is installed immediately next to the SDend magnet and one BPM is installed as the very last element in the long straight. Calibration of the BPMs to the adjacent sextupole magnet centers can be achieved by exciting a secondary winding in the sextupoles that generates a quadrupolar field (see Section 2.4.6). The correctors are realized as dedicated window-frame magnets that are installed close to the BPMs. Within the unit cells this means that the corrector is separated from the BPM (which is between the sextupole and the quadrupole) only by a focusing quadrupole. In the matching cell the correctors are placed immediately next to the BPMs. The result is a very diagonal form of the inverted response matrix. If the response matrix is given by  $\mathcal{M}$  and the kicks by all correctors in the machine are denoted as  $\vec{\theta}$ , the resulting orbit relative to the magnet centers is given by  $\vec{\mathcal{X}} = \mathcal{M}\vec{\theta}$ . After the response matrix has been calculated or measured, it can be inverted with SVD thus giving the well-known equation for orbit correction  $\vec{\theta} = \mathcal{M}^{-1}\vec{\mathcal{X}}$ . If the inverted response matrix has diagonal form, global correction requires only knowledge of the adjacent correctors, in essence reducing global correction to local correction by means of the three or four kicker bump.

In the model the space reserved for the correctors is a 100 mm drift section and a 50 mm drift section for the BPMs. The presently foreseen positions of the BPMs and correctors are indicated in Fig. 2.20. The BPMs are symbolized by magenta crosses. Blue and red bars indicate horizontal and vertical correctors, respectively. A plot of the inverted response matrices (a  $200 \times 200$  matrix both for the horizontal and the vertical plane; coupling has been disregarded here) for the bare machine is shown in Fig. 2.21. The diagonal form can be easily recognized.

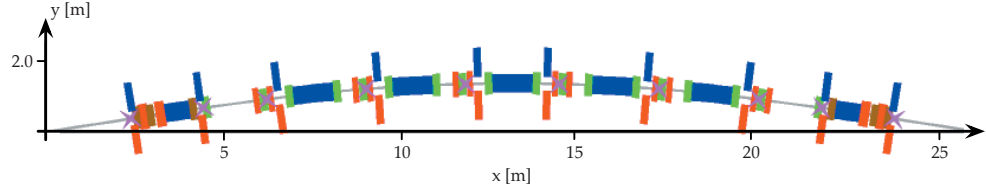


Figure 2.20: Positions of BPMs and correctors in the MAX IV 3 GeV storage ring achromat. The magenta crosses indicate locations of the BPMs. The blue and red strips indicate the position of the correctors.

As will be explained further below, two correction systems are planned for the 3 GeV storage ring. The fast system (FOFB) will make use of the four correctors and BPMs in the matching section in order to correct the beam inside the ID in the long straight. Therefore these correctors need to be laminated and the BPM electronics capable of reading beam positions at a rate on the order of 100 Hz <sup>1</sup>. The remaining six BPM and corrector pairs in every achromat are not required to be very fast. Acquisition of position data and application of corrections at roughly 2 Hz is deemed sufficient (SOFB).

Originally it was foreseen to not operate the two systems at the same time in closed-feedback mode to prevent crosstalk which would necessitate a frequency deadband. Instead, it was planned to run the SOFB during injection and top-up shots and apply corrections globally. After injection (or a single top-up shot) has completed, the SOFB is switched off and the FOFB turned on. From then on (and until the next top-up shot), the FOFB will apply local corrections to the four fast correctors around long straight sections at a high rate while retaining the SOFB settings on the other correctors.

In the meantime, we believe both SOFB and FOFB can actually be operated at the same time without a frequency deadband. The key to such an operation mode lies in communication between the FOFB and SOFB. As long as the FOFB always receives the information about what the correction goal of the current SOFB correction is, crosstalk between the two systems can be avoided. The application of this scheme [8] at MAX IV is currently under investigation.

<sup>1</sup>As there is basically no power in the vibration spectrum above 100 Hz, we believe correction of such high frequency (noise!) is actually not required to reach our beam stability requirements.

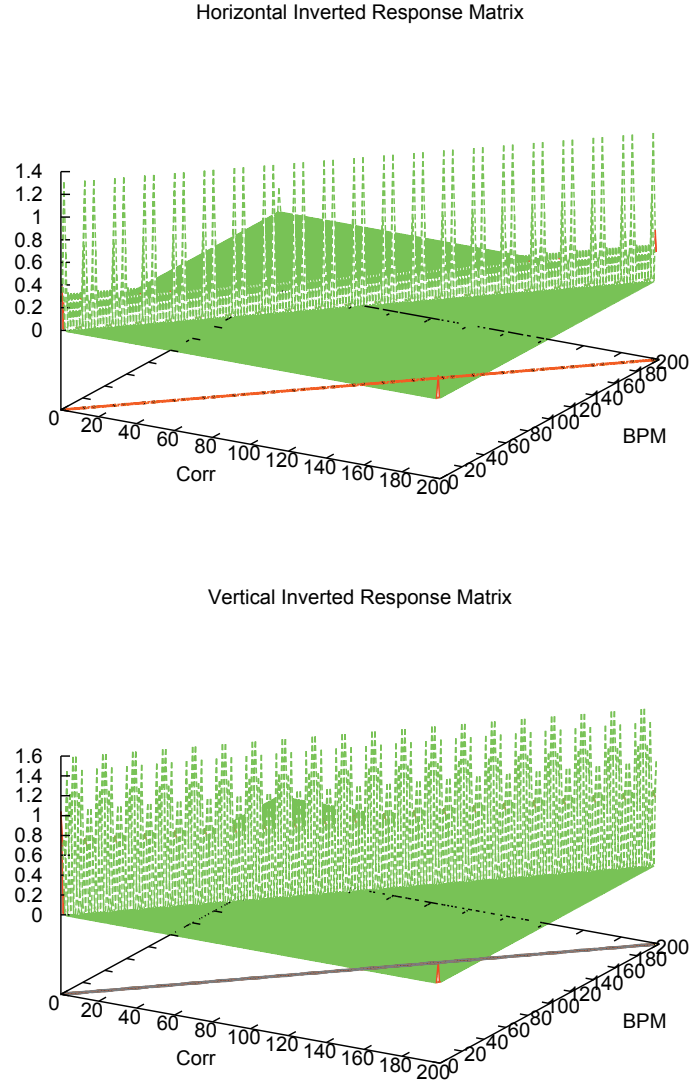


Figure 2.21: Plot of the inverted response matrices for the bare lattice. As there are 200 BPMs and 200 correctors in the storage ring each matrix consists of  $200 \times 200$  elements. The diagonal form can be easily recognized. In general a coupled  $400 \times 400$  matrix should be given, however for clarity a perfect lattice is assumed and coupling disregarded.



### 2.4.5. Orbit correction

The MAX IV 3.0 GeV storage ring will be equipped with 200 BPM, ten per achromat, covering the entire circumference of the ring. This will allow more than adequate sampling of orbit betatron oscillations given a horizontal and vertical tune of 42.2 and 14.28, respectively.

Of these, a decision is yet to be taken regarding how many will be equipped with fast electronics in the sense that they will be able to provide both single-pass capability for commissioning purposes as well as a 10 kHz data acquisition mode for the stored beam.

The following sections will study a possible orbit correction scheme for the 3.0 GeV ring where the orbit is corrected globally at all BPM at a low rate, as well as corrected locally at the straight sections at a high rate. It is assumed that two BPM per achromat, i.e. 40 in total, will have fast electronics. The fast electronics will be installed for BPM flanking the straight sections. There will additionally be ten spare sets of fast electronics available should they be necessary during commissioning. This should be considered the minimum amount of fast electronics required for a FOFB system.

The philosophy for this minimum solution will be to correct the orbit globally at low correction frequencies using a standard response matrix method. This will be referred to as the SOFB system. Simultaneously another faster orbit correction algorithm will be implemented at the long straights, referred to as the FOFB system. This fast correction will also be global in the sense that orbit data from all BPM will be available at the controllers for the local orbit bumps. This is motivated by the worry that purely local FOFB controllers will excite noise elsewhere in the storage ring, as the four-kicker bumps used for the local correction of orbit position and angle will not be perfect in the real world. Dissemination of BPM orbit data to each FOFB controller will allow them to minimize their effect on other locations, using the pseudo-inverse of the response matrix obtained via SVD. Mathematically this solution should be equivalent to a fully global correction system, albeit with a distributed calculation of the new corrector settings.

For this solution to be feasible, some effort has to go into preventing the two correction systems from working at cross-purposes, i.e. fighting one another. Traditionally this has been achieved by keeping the two systems separate in what orbit oscillation

frequencies they will correct by introducing a deadband [9]. For MAX IV a different system is envisaged based on the solutions at ALS [10] and later SOLEIL [11] among others where communication between a fast and slow correction system was successfully used to prevent escalating control signals being sent out to the corrector magnets. This approach is becoming common at modern lightsources.

### 2.4.5.1. System dynamics

The dynamics of the plant, i.e. the MAX IV ring, is highly linear in the vicinity of the design orbit. The linearized dynamics are well described by

$$y_k = R(z)(\mathbf{U}\Sigma\mathbf{V}^T)P(z)u_k + d_k \quad (2.8)$$

where

$y_k$  represent the BPM outputs.

$P(z)$  is a diagonal matrix with elements  $p_j(z)$  containing the corrector magnet dynamics for magnet  $j$ . These are unfortunately not identical for all correctors.

$R(z)$  is a diagonal matrix with elements  $r_i(z)$  containing the sensor dynamics, such as latency, for BPM  $i$ .

$\mathbf{U}\Sigma\mathbf{V}^T$  is the Singular Value Decomposition of the linear response matrix  $\mathbf{M}$ , seen in Figure 2.22.

$u_k$  represent the corrector magnet set values.

$d_k$  represent disturbances. This will include BPM noise, thermal beam motion, as well as various modes of beam oscillation.

$k$  is the iteration number.

For the SOFB, where sample times are much greater than the system delays, the actuator dynamics in  $p_j(z)$  may be safely ignored which greatly simplifies the controller design. However, this is not possible for the FOFB controller where bandwidth limitations enter the picture.

The dynamics of the actuators, i.e. the corrector magnet field response at the beam location to a change in the control value  $u_k$ , is influenced by the power supply rise time,

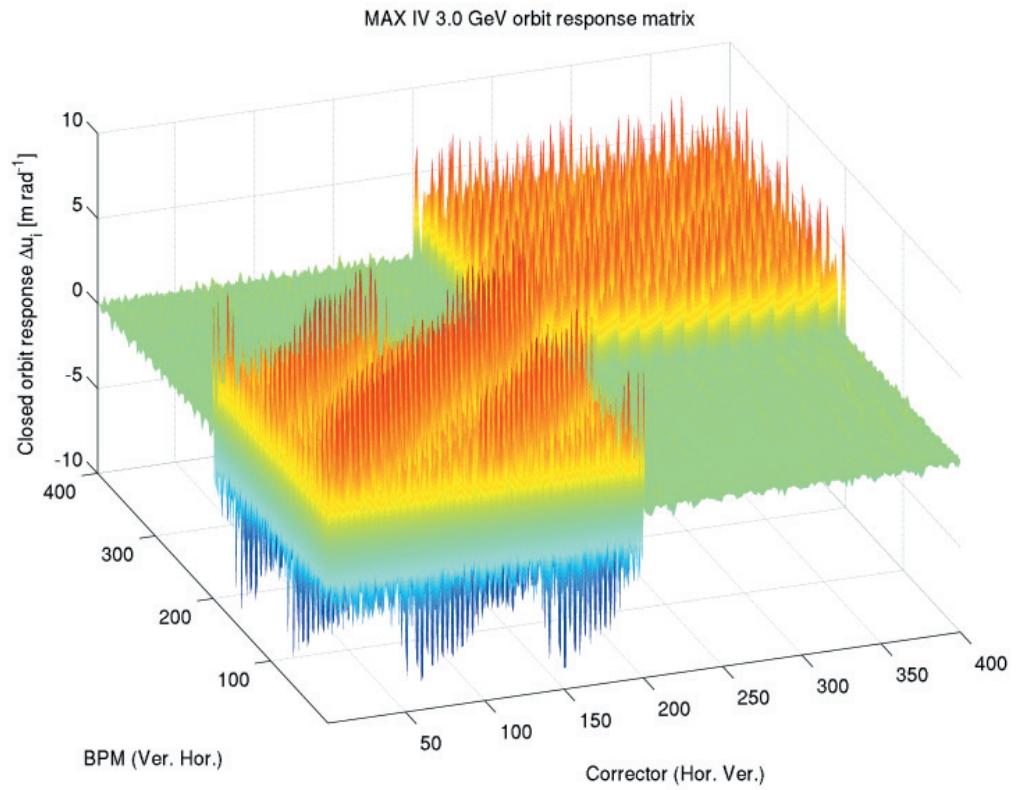


Figure 2.22: Graphical representation of the orbit response to a change in correction magnet field, i.e. the response matrix  $M$ .

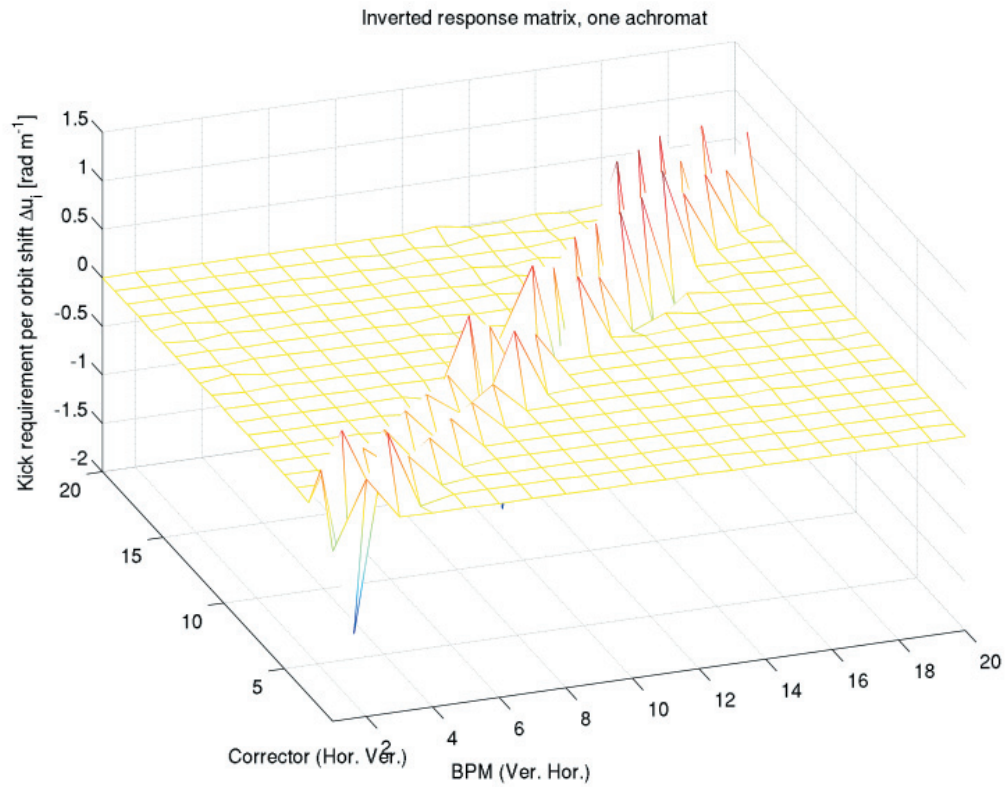


Figure 2.23: Graphical representation of a section of the inverted response matrix corresponding to one achromat. Note that for an orbit change in one BPM only the three closest corrector magnets are necessary.

the magnet construction, and the vacuum chamber.

**Power supply rise time:** More information is needed regarding the power supply rise times: the closed loop behaviour for the power supply controller will vary between manufacturers as well as with the magnet design, due to the inductive load. It is expected that the power supply rise time will be negligible for the current design though they may well play a role for solutions where other actuator components are more responsive, such as air coils placed over ceramic chambers.

The rise time will include a pure delay however, due to the communication delay between the controller and the power supplies.

**Magnet design:** The preliminary design for the MAX IV 3.0 GeV storage ring corrector magnets calls for dedicated biplanar corrector magnets made out of laminated iron with a 0.5 mm laminate thickness in order to limit eddy currents. There will be ten such correction magnets per achromat. Out of the 10, four corrector magnets in each achromat are intended for use by both the FOFB and the SOFB system. Hence they will be installed over a Steel vacuum chamber in order not to limit the total actuator bandwidth, while the remaining six corrector magnets in the achromat will be installed over a Cu chamber in order to keep the vacuum system complexity down.

**Vacuum chamber:** Changes in the corrector magnet field will give rise to eddy currents in the vacuum chamber wall which will counteract the field change. Mathematically, the transfer function for the vacuum chamber eddy currents is given by

$$P_{vac}(z) = \frac{1 - e^{-h/\tau}}{z - e^{-h/\tau}} \quad (2.9)$$

where  $h$  is the sampling time and  $\tau$  is the time required for the eddy currents to decay by a factor  $e$ . This is arrived at by starting in the time domain and assuming a simple exponential decay of the eddy currents. The field response  $y(t)$  to a signal  $u(t)$  is governed by

$$\dot{y}(t) = -\frac{1}{\tau}y + u(t) \quad (2.10)$$

$$u(t) = A\theta(t) \quad (2.11)$$

$$y(0) = 0 \quad (2.12)$$

$$\lim_{t \rightarrow \infty} y(t) = A \quad (2.13)$$

which has the solution

$$y(t) = Cy(0)e^{-t/\tau} + AC\tau\theta(t)(1 - e^{-t/\tau}) \quad (2.14)$$

Assuming no eddy currents before the field change, the initial condition  $y(0) = 0$  can be imposed and the homogenous part of the solution is eliminated. Using Equation 2.13,  $C = 1/\tau$ . Using the one-sided Z-transform on the remainder then yields

$$Y(z) = \mathcal{Z}\{A\theta(t)(1 - e^{-t/\tau})\} \quad (2.15)$$

$$\begin{aligned} &= \mathcal{Z}\{A(\theta(nh) - \theta(nh)e^{-nh/\tau})\} \\ &= A\left(\mathcal{Z}\{(\theta(nh))\} - \mathcal{Z}\{\theta(nh)e^{-nh/\tau}\}\right) \\ &= A\left(\frac{z}{z-1} - \frac{z}{z-e^{-h/\tau}}\right) \\ &= \left(\frac{1-e^{-h/\tau}}{z-e^{-h/\tau}}\right)A\left(\frac{z}{z-1}\right) \\ &= \left(\frac{1-e^{-h/\tau}}{z-e^{-h/\tau}}\right)U(z) \end{aligned} \quad (2.16)$$

from which the stated transfer function in Equation 2.9 is easily seen. The region of convergence for the Z transform is given by  $|z| > 1$  and  $|z| > |e^{-h/\tau}|$ . As the region of convergence includes infinity, the transfer function is casual.

In the MAX IV 3.0 GeV storage ring, vacuum chamber material and cross-section will vary between corrector magnet locations. For the 80 corrector magnets used for both FOFB and SOFB, the material will be Steel 304 which yields a  $\tau$  of

roughly  $80\mu\text{s}$  for a circular chamber. Vacuum chamber design at these locations is not yet done: efforts are underway to standardize the cross-section and material in order to obtain identical frequency responses for all fast correctors.

For the 120 SOFB corrector magnets, the vacuum chamber will be made out of OFHC Cu with considerable variations in cross-section at different locations. In addition, the Cu cooling channel running on the outside of the vacuum chamber will result in different dynamical response in the horizontal and vertical plane as the extra Cu in the cooling channel will increase  $\tau$  for the vertical direction. However, the differences in dynamics are not expected to be problematic due to the low correction frequencies used in the SOFB system.

Field simulations indicate a  $\tau$  of roughly 2 ms for the horizontal SOFB correctors and a circular Cu chamber. The simulated response for the circular chamber is shown in Figure 2.24: the response for the non-circular chamber is expected to be somewhat worse at higher frequencies. Hence the effective bandwidth of the corrector magnets is expected to be 0-250 Hz (see DDR chapter 2.8 Vacuum System), as at higher correction frequencies the field attenuation will be severe. A 1 kHz signal is expected to be attenuated by 75%.

More thorough calculations of the eddy current decay time will be carried out once a more detailed vacuum system design becomes available.

Note that if the final vacuum system design does not have identical vacuum chamber cross-sections for all corrector magnets in the FOFB system, the closed four-kicker bumps used to correct the orbit on the straight sections will *not* be closed for higher frequencies. To ensure closed four-kicker bumps regardless, model reference control techniques will have to be implemented in the individual corrector magnet power supplies to ensure similar dynamics for the different FOFB actuators. Another consequence is that it will not be possible to move into the 'mode space' of the SVD where the different modes are fully decoupled and the MIMO system may be treated as a number of independent SISO systems.

The BPM or sensor dynamics  $r_i(z)$  in Equation 2.8 will pre-dominantly appear through the delay introduced by the time needed for data processing in the BPM electronics and data transfer to the controller, i.e. the latency. As the data transfer structure design is

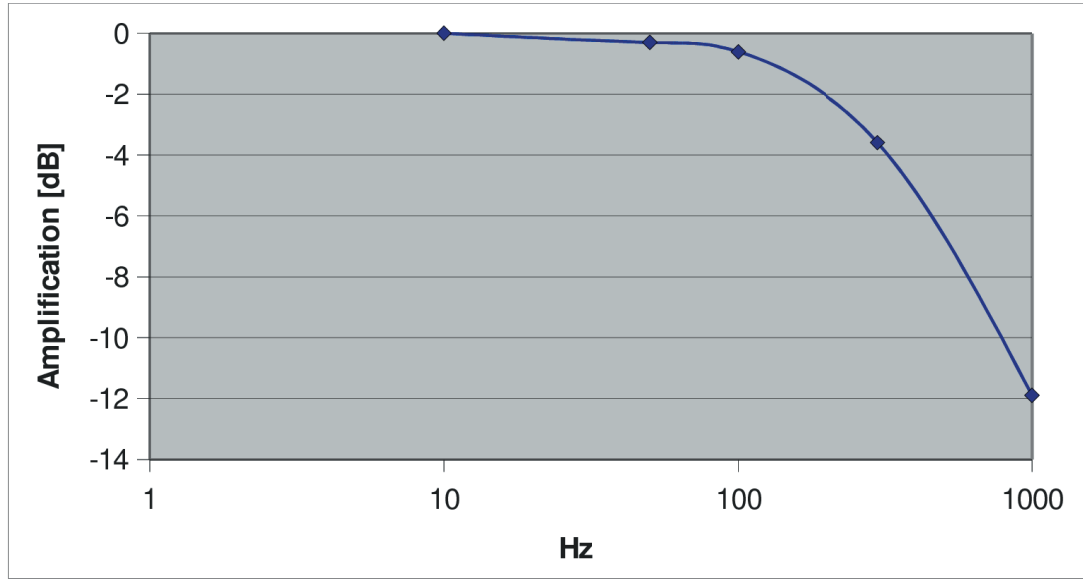


Figure 2.24: The simulated frequency response for the corrector magnet iron and Cu vacuum chamber.

not yet complete, results will be presented for both an ideal system with no latency as well as for latency values corresponding to those of a global system where data from all sensors must be available at each local controller. The latency value for SOLEIL of 360  $\mu\text{s}$  has been used [12], which will correspond to a time delay of  $n = 4$  sampling periods at 10 kHz sampling frequency. At lower sampling frequencies,  $n$  will approach 1.

$$r_i(z) = \frac{1}{z^n} \quad \text{for all } i \quad (2.17)$$

### 2.4.5.2. Controller dynamics

The global SOFB controller will attempt to correct the global orbit  $y_k$  as read from all 200 BPM. To prevent it from fighting the FOFB controllers the influence of the FOFB control signals must be removed beforehand: this is done by taking in the FOFB signals  $u_k^f$  and computing an estimate of the orbit effect via response matrix multiplication. The result can then be subtracted from the BPM readings and standard feedback may be applied to the filtered signal.



The SOFB controller used in this design study is a standard PI controller. It is assumed that the SOFB controller only acquires data at 10 Hz: a running mean is taken for the fast BPM. Using  $k$  as the iteration variable for the SOFB controller, the PI feedback structure is given by

$$u_k^s = \left( K + I \frac{1}{z-1} \right) \mathbf{M}^{-1} (r + \mathbf{M} u_k^f - y_k) \quad (2.18)$$

with  $K$  as the proportional gain and  $I$  as the integration gain. The controller uses the inverted linear response matrix  $\mathbf{M}^{-1}$  is used as an internal model to compensate for the plant dynamics. No effort has been made to include an internal model of actuator or sensor dynamics due to the sampling period being much longer than the relevant decay times or delays.

The FOFB controllers have as their primary goal to reject orbit disturbances, of which induced orbit oscillations and noise are two concerns. Standard PI controllers were assumed.

At large orbit deviations from the reference the FOFB will be disconnected. The global SOFB will be relied upon to reduce the DC orbit error. Once the DC error is below  $100\mu\text{m}$  on all BPM controlled by the fast controllers they will activate at 10 kHz correction frequency to reduce orbit oscillations.

Given the approximate transfer functions for the actuators ( $p_j(z) \approx P_{vac}$  for all  $j$ , see Equation 2.16), the beam (the response matrix  $\mathbf{M}$ ) and the sensors (Equation 2.17), the closed loop system for the plant and the FOFB controller is given by

$$y_k = r_i(z) \mathbf{M} P_{vac}(z) u_k + d_k \quad (2.19)$$

$$u_k = \left( K + I \frac{1}{z-1} \right) \mathbf{M}^{-1} (r - y_k) \quad (2.20)$$

Eliminating  $u_k$  the closed loop is described by

$$y_k = H(z)r + G(z)d_k \quad (2.21)$$

$$H(z) = \frac{r_i(z)P_{vac}(z)\left(K + I\frac{1}{z-1}\right)}{1 + r_i(z)P_{vac}(z)\left(K + I\frac{1}{z-1}\right)} \quad (2.22)$$

$$G(z) = \frac{1}{1 + r_i(z)P_{vac}(z)\left(K + I\frac{1}{z-1}\right)} \quad (2.23)$$

where  $H(z)$  is the system response to a change in the reference value and  $G(z)$  the system response to a disturbance on the output. While the former contains information about how quickly and in what manner the system will approach a new set value for the orbit, the latter contains information regarding how output disturbances will be attenuated.

It should again be noted that there is an implicit assumption above that all actuators and sensors, i.e. corrector magnets and BPM, have identical dynamics. This is not strictly true, as there will be individual variations between them due to the aforementioned differences in vacuum chamber material and cross-section.

### 2.4.5.3. Simulation results

In order to test the correction system design and verify that SOFB and FOFB controllers are capable of working together a SimuLink simulation was set up according to Figure 2.25. In lieu of a real ring, an Accelerator Toolbox model with approximate corrector and BPM dynamics is used as the plant. As the corrector magnet design is not yet finalized, the corrector magnet dynamics are assumed to be wholly determined by the vacuum chamber eddy currents according to Equation 2.9, while the BPM dynamics are treated as a pure delay.

The Accelerator Toolbox model of the 3.0 GeV MAX IV storage ring includes a misalignment data model with resulting betatron coupling. The misalignment data model takes the girder and block structure of the MAX IV 3.0 GeV ring into account. An approximate response matrix was 'measured' from the model and noise added.

In order to verify that the SimuLink model results are reliable the individual noise attenuation function for the FOFB closed loop systems was first compared to theory.

Both SOFB and FOFB controllers were then activated at the same time to obtain results for the total transfer function as well as to verify that cross-talk between them would not pose a problem. This was determined through study of the controller output and the orbit error.

Three different sampling frequencies were investigated for the FOFB PI controller: 100 Hz, 1 kHz and 10 kHz. At the higher sampling frequencies the sensor and actuator dynamics, the latter dominated by the vacuum chamber eddy currents, had a significant impact on the result.

Due to a lack of time, no attempt was made to include a model of the actuator dynamics in the FOFB PI controller. Some tweaking of the proportional and integration gain was however required for the 10 kHz PI controller in order to avoid significant noise amplification in specific frequency bands. Additionally, only a single long straight was controlled by the FOFB. The simulation will be expanded to include all long straights in the near future.

Finally, note that some care should be taken when interpreting the simulation results as the plant model used in lieu of a true ring does not correctly reflect the temporal dynamics: it is merely an approximation.

**2.4.5.3.1 SOFB controller performance** A standard PI controller was used for the SOFB, although the input had to be adjusted by the estimated orbit effect from the FOFB controller. The flowchart is shown in Figure 2.26.

The theoretical noise amplification for the SOFB controller is shown in Figure 2.27. No SimuLink simulation was done for the case with only SOFB running for two reasons: first, the design follows the one in use at the MAX II and MAX III rings where it is known to work. Second, if the FOFB is not active the case with SOFB only is identical to the case with only FOFB save for the sampling time.

**2.4.5.3.2 FOFB controller performance** A standard PI controller was used for the FOFB, connected according to the scheme in Figure 2.28.

**Noise attenuation** The noise amplification for the FOFB controlled straight section is shown in Figure 2.29 for the ideal case. As can be seen higher correction frequency

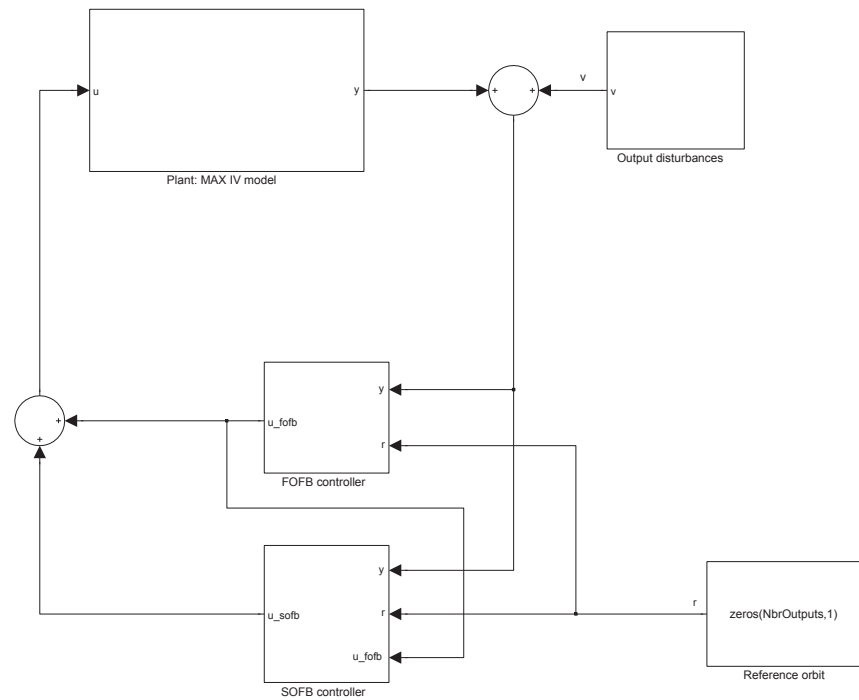


Figure 2.25: The closed loop including an SOFB controller for global orbit correction, a FOFB controller for local fast correction on the second straight section, and an Accelerator Toolbox model acting as an approximation of the plant.

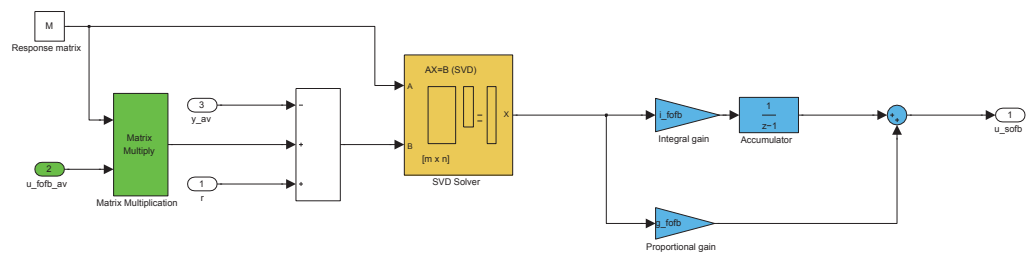


Figure 2.26: The SOFB PI controller flowchart.

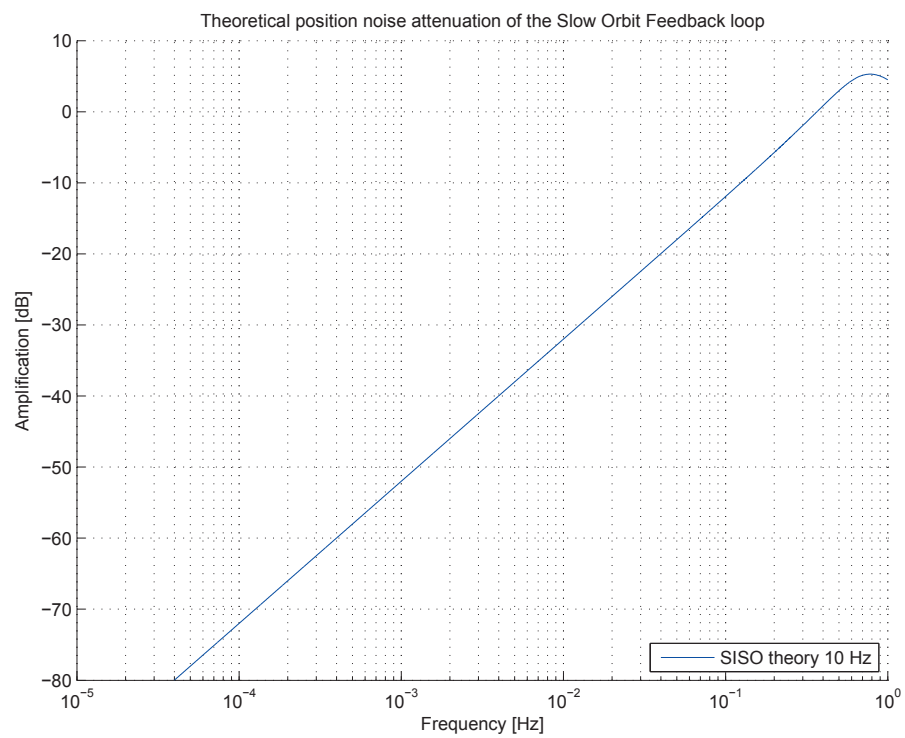


Figure 2.27: Noise attenuation plot for the plant regulated by the SOFB controller.

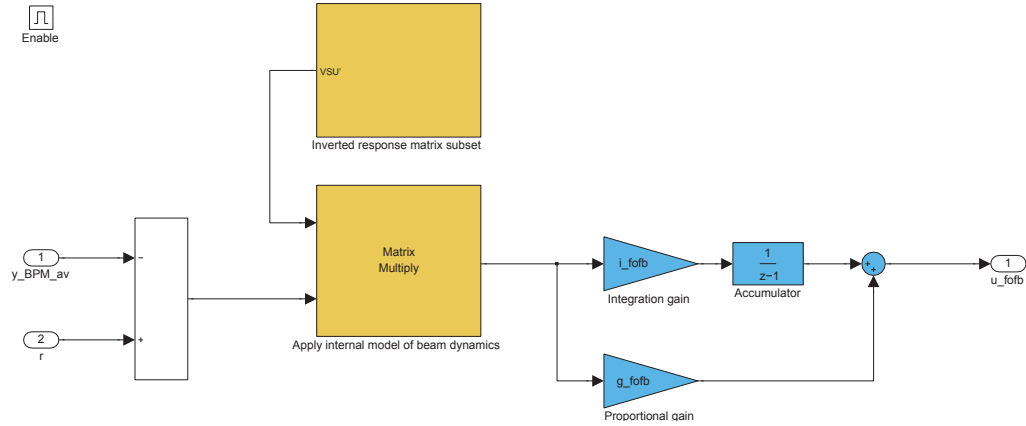


Figure 2.28: The FOFB PI controller block diagram, taken from the SimuLink model.

results in improved noise attenuation.

For the more realistic plant model taking the vacuum chamber material into account it becomes significantly more difficult to improve the noise attenuation for higher frequencies by simply increasing the FOFB sampling frequency, as indicated in Figure 2.30 and 2.31. Here the difference between the use of OFHC Cu and Steel 304 for the vacuum chamber material is also clearly demonstrated.

It should be noted that the 'break-even' noise frequency, where the FOFB controller instead starts to amplify noise, is significantly lower than the correction frequency. In order to achieve 10 dB damping at 75 Hz, 10 kHz correction frequency is needed along with Steel 304 vacuum chambers. This result is in line with results from Fast-Orbit-Correction systems already online at different electron storage ring facilities [13][14].

**Cross-talk** A simulation of correcting the orbit for a misaligned lattice to the reference orbit indicated that there is no detrimental interaction between the SOFB and FOFB controller. The results can be seen in Figure 2.32 and Figure 2.33. After the FOFB controller activated at the set limit of  $< 100\mu\text{m}$  orbit error at the relevant straight section it rapidly corrected the orbit error. Subsequent iterations of the SOFB controller then reduced the FOFB RMS corrector strengths, although a transient behaviour of the FOFB controller output could be observed after each

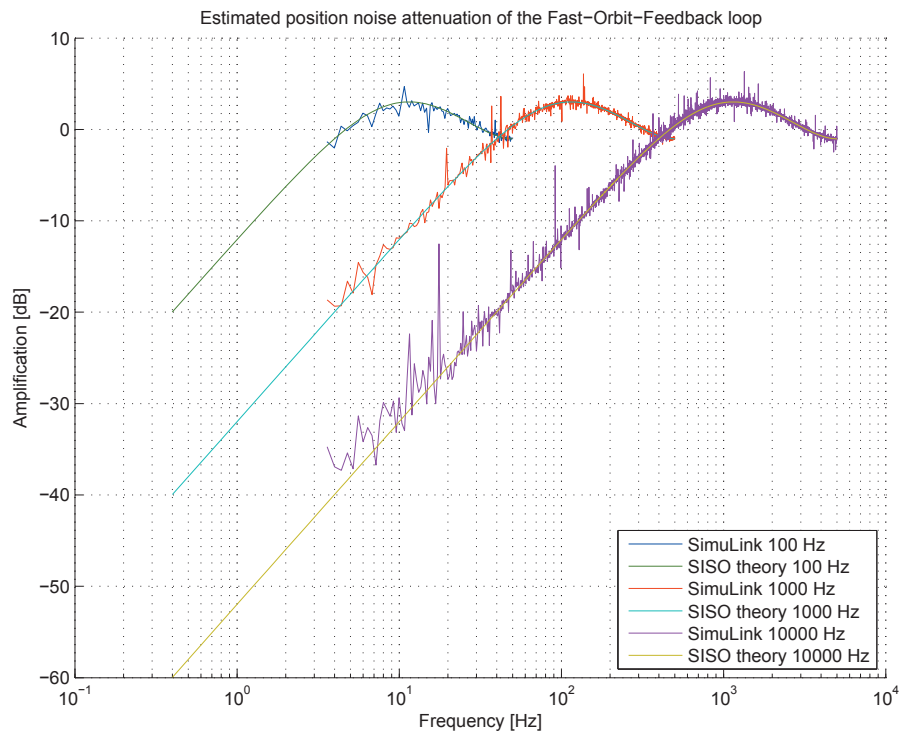


Figure 2.29: Noise amplification for the closed loop containing the ideal 3.0 GeV ring plant and the FOFB controller. Different curves show the amplification variation with FOFB correction frequency. Identical controller parameters were used in all cases.

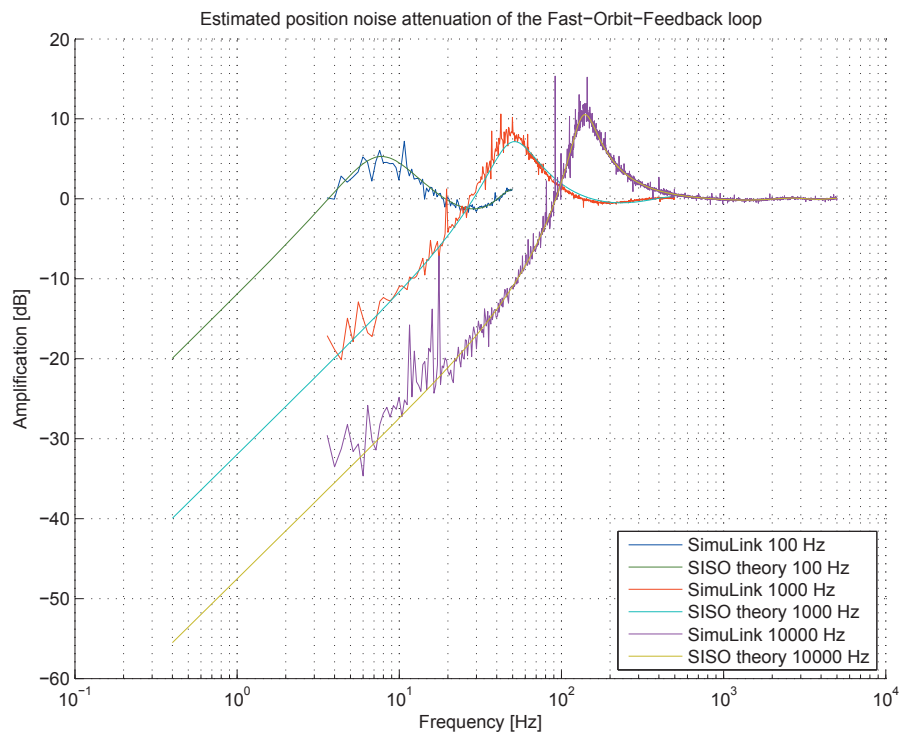


Figure 2.30: Noise amplification for the closed loop containing the 3.0 GeV ring plant and the FOFB controller. Sensor and actuator dynamics include processing delay and eddy currents, respectively. A vacuum chamber made out of Cu was assumed. Different curves show the amplification variation with FOFB correction frequency. PI controller parameters differ between cases.



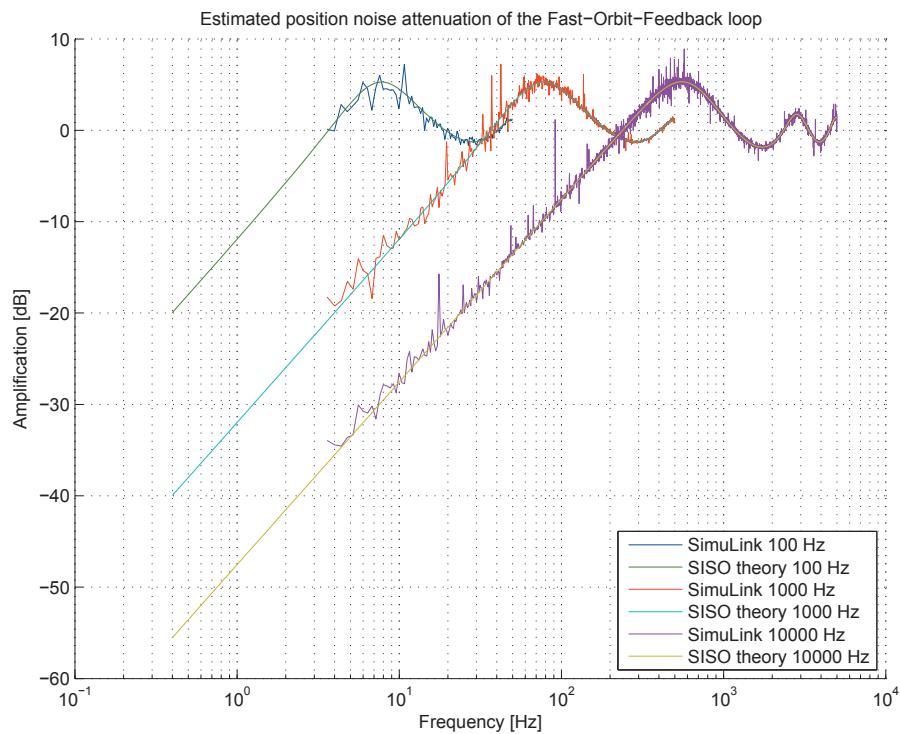


Figure 2.31: Noise amplification for the closed loop containing the 3.0 GeV ring plant and the FOFB controller. Sensor and actuator dynamics include processing delay and eddy currents, respectively. A vacuum chamber made out of Steel 304 was assumed. Different curves show the amplification variation with FOFB correction frequency. PI controller parameters differ between cases.

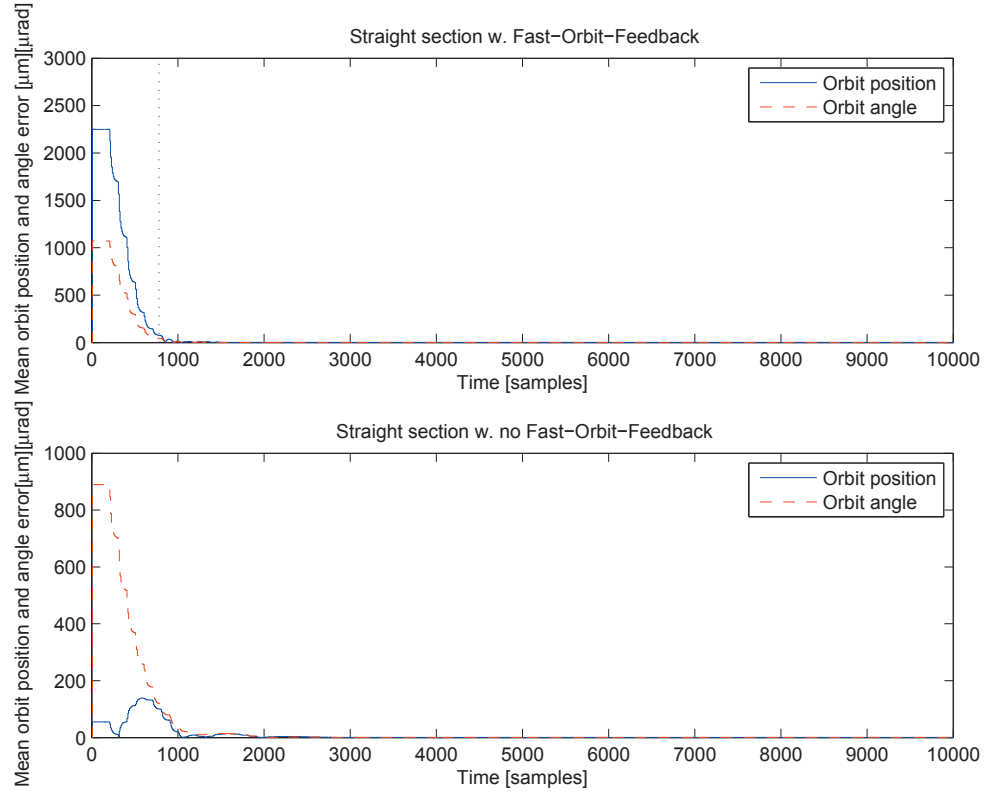


Figure 2.32: The development of the residual orbit error on the straight sections when correcting from the nominal orbit for a misaligned MAX IV 3.0 GeV ring lattice, using both the global SOFB and one local FOFB controller. The dotted vertical line indicates the activation of the FOFB controller.

SOFB iteration.

#### 2.4.5.4. Hardware requirements

**2.4.5.4.1 Correction magnet powersupplies** In addition to rise times, which affects the bandwidth of the fast orbit correction system, the current stability must be considered as otherwise corrector magnets may themselves act as a noise source. Finally, the DAC granularity must also be considered as the power supplies must be able to alter the current with high enough precision.

As a high degree of modularity is desired in order to limit the amount of different systems

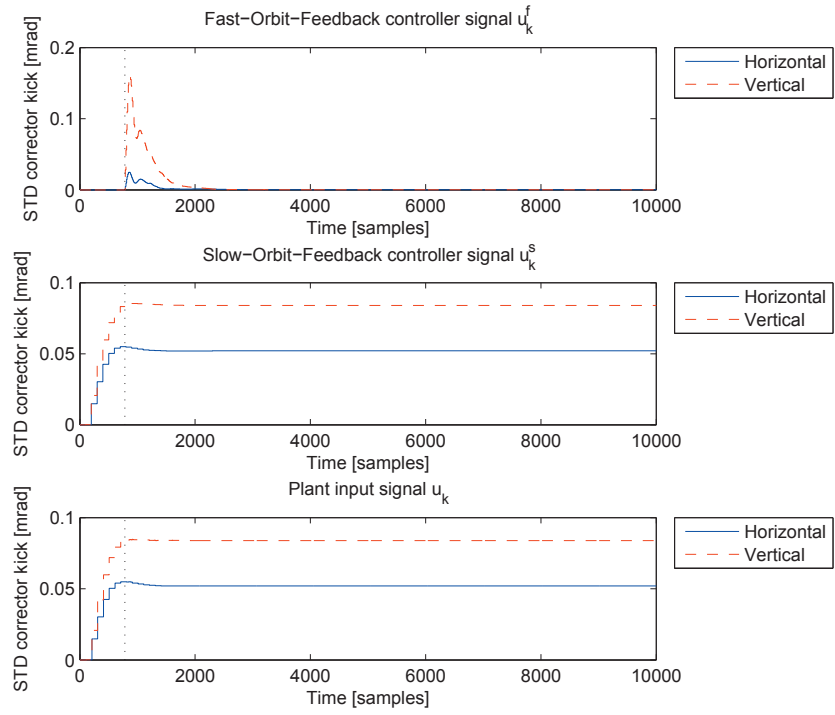


Figure 2.33: The development of the global SOFB and local FOFB controller control signals,  $u_k^s$  and  $u_k^f$  respectively, when correcting from the nominal orbit for a misaligned MAX IV 3.0 GeV ring lattice. The dotted vertical line indicates the activation of the FOFB controller.

in need in maintenance, it is assumed that all correctors will be equipped with identical power supplies.

**Stability:** The relevant expression to determine the required power supply stability is

$$\sigma_y|_i = \sqrt{\sum_j M_{ij}^2 \sigma_\theta^2} < 230 \text{ nm for all } j \quad (2.24)$$

$$(2.25)$$

where  $i$  are the indices for BPM flanking the straight sections. For the MAX IV 3.0 GeV storage ring this results in a maximum permitted kick  $\sigma_\theta$  of 5.4 nrad. Given the maximum corrector kick amplitude of 0.25 mrad this corresponds to a field and current stability of  $2.1 \cdot 10^{-5}$  for the approximate range  $10^{-1} - 10^3$  Hz in order to avoid transferring sufficient noise power to the beam that it will be visible to the users. At lower frequencies the orbit correction feedback loops should be able to compensate while at higher frequencies the magnet iron response and in particular the vacuum chamber conductance will limit the noise transferred to the beam.

However, as there are other sources of noise some safety margin should be considered and a  $10^{-6}$  current stability for the range 100 mHz to 1 kHz for the corrector magnet power supplies will be highly recommended.

**DAC granularity:** The maximum kick of the MAX IV 3.0 GeV storage ring corrector magnets is 0.25 mrad. The greatest tolerance requirements on orbit stability are in the vertical plane, where the rule-of-thumb 10% of beam size requirement on stability yields an orbit stability of 230 nm.

Viewing the orbit correction system as a source of orbit noise once the orbit has been corrected to the limit of the power supply DAC, the 5.4 nrad limit on the maximum permitted kick for each corrector magnet derived previously may also be considered the required DAC precision. This then corresponds to a bit depth of 16 for the 3.0 GeV storage ring corrector magnets. Including a bit for the sign, the minimum DAC bit depth is 17.

**2.4.5.4.2 BPM requirements** In order for the described orbit correction system to function the BPM must be able to

- Be able to deliver orbit data at a minimum of 10 kHz
- Deliver orbit data to individual controllers around the entire ring. The time allocated for the data transport should be kept shorter than the sampling period  $100\mu s$  to avoid significant delays.
- BPM orbit data accuracy should be better than 230 nm for the 10% beam size criteria for orbit stability to be achievable.

Note that additional requirements on the BPM may enter due to other considerations, such as single-pass capability during beam commissioning.

## 2.4.6. Coupling and higher-order Correction

In addition to correcting the uncoupled linear optics and running an orbit feedback, the nonlinear optics will need to be corrected to restore design settings. Also, transverse betatron motion needs to be uncoupled in order to achieve flat beams with minimum beam height in the IDs.

### 2.4.6.1. Betatron Coupling

A set of skew quadrupoles will be used to minimize any remaining betatron coupling after the orbit has been corrected to the sextupole magnet centers. For this purpose one to two such skew quadrupoles should be provided in every achromat of the storage ring. In principle four skew quadrupoles (two for control of  $h_{10100} \rightarrow \nu_x + \nu_y$  and two for control of  $h_{10010} \rightarrow \nu_x - \nu_y$ ) at a location with high  $\sqrt{\beta_x \beta_y}$  should be sufficient [15].

It has been shown at SLS using eight skew quadrupoles that minimizing vertical beam size at one location is equivalent to a global minimization of vertical beam size [16]. It remains to be shown in Tracy-3 simulations that the same holds for the MAX IV 3 GeV storage ring.

*This is ongoing work...*

It should also be noted that minimizing the overall betatron coupling might not be required. The vertical beam size should be lower than the diffraction limit for the most demanding beamline, but not lower for lifetime reasons. Therefore, the skew quadrupoles should be tuned in such a way to reduce the betatron coupling to this required level, but not necessarily any further. From the combined alignment and field error models we acquire ???% rms betatron coupling for a machine configuration with 4 PMDWs. This corresponds to a vertical emittance of  $\varepsilon_y = ???$  pmrad or a diffraction limit of  $\lambda_\gamma < ???$  Å. This can be seen as the minimum achievable coupling without additional (corrector-based) realignment and skew quadrupole correction.

### 2.4.6.2. Vertical Dispersion Bumps

After betatron coupling has been minimized in the storage ring the vertical beam size should be minimized globally. In principle two skew quadrupoles for control of  $h_{00101}$  at a location with high  $\eta_x\sqrt{\beta_x}$  should be sufficient [15]. If the vertical beam is minimized, Touschek lifetime will reduce as well. However, the low vertical beam size is only required in the long straights where the IDs are located, but not within the achromats. Therefore it is foreseen to drive vertical dispersion bumps within the achromats once the global betatron coupling has been minimized. This has the benefit of increasing Touschek lifetime without increasing the source size for beam line users.

For this purpose at least four dispersive skew quadrupoles are required within the achromat; as has been demonstrated at ALS [17] additional skew quadrupoles are required to minimize betatron coupling within the vertical dispersion bump.

*This is ongoing work...*

### 2.4.6.3. Sextupole Corrections

In the MAX IV 3 GeV storage ring all sextupoles are powered in families. In order to correct for local distortions of the sextupole pattern and to restore the nonlinear design optics auxiliary sextupoles are required.

Each achromat requires one to two of these sextupoles. However, since the required strength is only very weak they can be implemented as secondary windings on existing sextupoles. It is however important that they are not implemented on the same magnet and family in every achromat (degeneration of terms in the first-order sextupole Hamiltonian).

### 2.4.6.4. Requirements for Secondary Sextupole/Octopole Windings

Nondispersive skew quads can be implemented as one secondary winding on the OXX and OXY family. The same secondary winding on OXX can be used to calibrate the adjacent (and final) BPM. This gives four nondispersive skew quadrupoles per achromat.

An secondary winding on the SDend, SFm, SFo, and SFi families implemented as a skew quadrupole winding could be used to calibrate the BPMs adjacent to these sextupole magnets. Once this calibration is complete this secondary winding can be used as a nondispersive skew quad (on SDend) or as dispersive skew quad (on SFm, SFo, and SFi). Not all SF families need to be used as skew quadrupoles in every achromat though. One family can instead be used to implement the auxiliary sextupole of which at least one per achromat is required.

For the auxiliary sextupoles it is however important that they are not implemented on the same magnet and family in every achromat. Therefore a secondary winding on the SD family could be used in some achromats as an auxiliary sextupole in lieu of (or in addition to) using a winding on one of the SF magnets.

Finally, we note that use of skew quadrupoles for BPM calibration is rather uncommon; normally upright quadrupoles are used. Also, because of hysteresis, during BPM calibration a tune response from an upright quadrupole variation is of advantage; it is however unclear if a sufficient such response can also be achieved when using skew quadrupoles for BPM calibration. Hence, we need the option to power the extra windings installed in magnets adjacent to BPMs (OXX, SDend, SFm, SFo, SFi) as upright quadrupoles for BPM calibration (“beam-based calibration” often referred to as beam-based alignment).



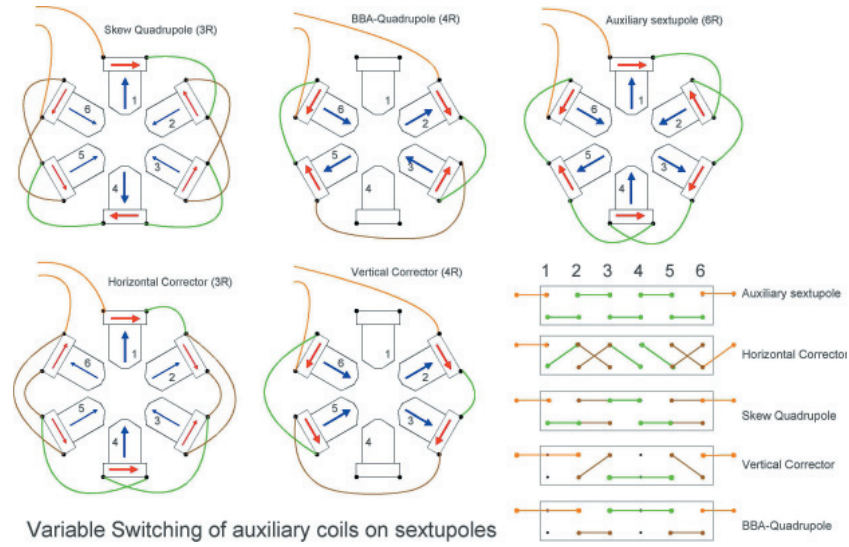


Figure 2.34: Illustration of the per-pole wiring and switchboard required to exchange the purpose of an auxiliary winding on a sextupole between skew quad and auxiliary sextupole. Note how the resistance of the circuit (indicated as 3R, 4R, 6R) changes depending on the chosen function. Courtesy of Andreas Streun (SLS/PSI).

All of these different powerings can however all be provided for the same secondary winding provided a “switchboard” (see Fig. 2.34) is installed between the secondary winding on each yoke and the power supply. Throughout commissioning, but also later during machine shifts it will be necessary to switch between different powerings on the secondary coils. For example, for beam-based calibration all windings on OXX, SDend, SFm, SFo, and SFI will be switched to upright quadrupoles. But as soon as calibration is completed, these windings should be switched back to powering for skew quadrupoles or auxiliary sextupoles; during commissioning it might also be of interest to power some as additional dipole correctors. Because of the very large number of secondary windings and the expected frequent changes between how these windings are powered, remote control of the “switchboard” should be possible for those windings that are used for beam-based calibration.

We therefore summarize the requirements:

- Secondary windings are installed on all **OXX**, **OXY**, **SD**, **SDend**, **SFm**, **SFo**, **SFi** magnets.
- The windings can be powered as follows:
  - **OXX**: upright quadrupole (“BBA quad”), skew quadrupole, horizontal corrector, vertical corrector
  - **OXY**: skew quadrupole, horizontal corrector, vertical corrector
  - **SD**: skew quadrupole, auxiliary sextupole, horizontal corrector, vertical corrector
  - **SDend**: upright quadrupole (“BBA quad”), skew quadrupole, auxiliary sextupole, horizontal corrector, vertical corrector
  - **SFm**, **SFo**, **SFi**: upright quadrupole (“BBA quad”), skew quadrupole, auxiliary sextupole, horizontal corrector, vertical corrector
- All secondary windings are connected through a local switchboard to the power supply; the switchboard is remote-controlled for **OXX**, **SDend**, **SFm**, **SFo**, **SFi**.
- Skew quadrupole strength  $\geq 1.6$  T/m (3% of reg. quadr. strength over 10 cm) [18]
- Auxiliary sextupole strength  $\geq 100$  T/m<sup>2</sup> (5% of reg. sext. strength over 10 cm) [18]

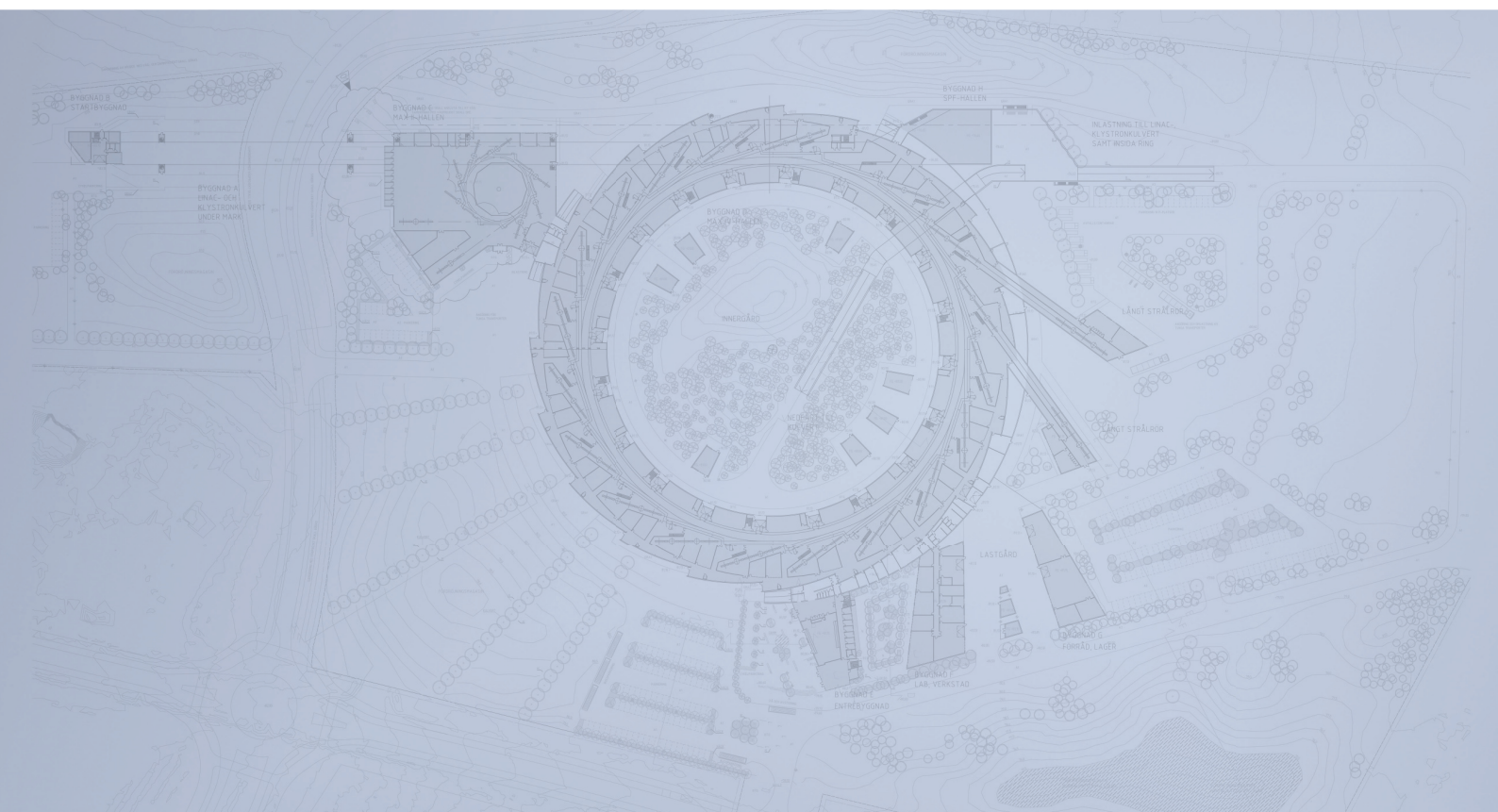
## References

- [1] J.B. Murphy, *Synchrotron Light Source Data Book*, available at <http://www.nsls.bnl.gov/newsroom/publications/otherpubs/dbook>
- [2] H. Wiedemann: *Particle Accelerator Physics I, Basic Principles and Linear Beam Dynamics*, 2<sup>nd</sup> Ed., Springer, Berlin, 1999.
- [3] M. Böge, private communication.
- [4] L.-J. Lindgren, private communication.
- [5] R. Bartolini, I. P. S. Martin, J.H. Rowland, P. Kuske, F. Schmidt, Phys. Rev. ST Accel. Beams, 11, 104002, 2008.
- [6] S.C. Leemann, A. Streun, Unusual magnets in storage ring-based synchrotron light sources, under review.
- [7] E.I. Antokhin, I.N. Churkin, V.V. Demenev, O.B. Golubenko, V.N. Korchuganov, A.B. Ogurtsov, E.P. Semenov, A.G. Steshov, S.F. Mikhailov, L. Rivkin, Ch. Vollenweider, J.A. Zichy, *Precise Magnetic Measurements of the SLS Storage Ring Multipoles: Measuring System and Results*, Proceedings of the Second Asian Particle Accelerator Conference, Beijing, China, 2001, p. 209–211.
- [8] N. Hubert, L. Cassinari, J.-C. Denard, A. Nadji, L. Nadolski, *Global Orbit Feedback Systems Down to DC Using Fast and Slow Correctors*, Proceedings of DIPAC09, Basel, Switzerland, p. 27–31.
- [9] C. Schwartz and L. Emery, Compensating the frequency deadband of the APS real-time and DC transverse orbit correction systems, in Proceedings of the 2001 Particle Accelerator Conference, PAC 2001, volume 2, pages 1234–1236, 2001.

- [10] Christoph Steier, Edward E. Domning, Tom Scavie, Eric Williams, Operational Experience Integrating Slow and Fast Orbit Feedbacks at the ALS, 2004.
- [11] N. Hubert et al. Design of a fast orbit feedback for SOLEIL, Prepared for 7th European Workshop on Beam Diagnostics and Instrumentation for Particle Accelerators (DIPAC 2005), Lyon, France, 6-8 Jun 2005.
- [12] N. Hubert, L. Cassinari, J.C. Denard, J.M. Filhol, N. Leclercq, A. Nadji, L.S. Nadolski, D. Pedeau, Commissioning of SOLEIL Fast Orbit Feedback system, EPAC'08, 11th European Particle Accelerator Conference, 23–27 June 2008, Genoa, Italy.
- [13] M.T. Heron et al. Performance and Future Developments of the Diamond Fast Orbit Feedback System, EPAC'08, 11th European Particle Accelerator Conference, 23–27 June 2008, Genoa, Italy.
- [14] Thomas Schilcher, Michael Böge, Boris Keil, Patrick Pollet, Volker Schlott. Commissioning and Operation of the SLS Fast Orbit Feedback, 2004.
- [15] J. Bengtsson, I. Pinayev, *NSLS-II: Control of Vertical Beam Size*, NSLS-II Technical Note, No. 7, Jan 31, 2007.
- [16] Å. Andersson, M. Böge, A. Lüdeke, V. Schlott, A. Streun, Nucl. Instr. and Meth. A, 591, p.437, 2008.
- [17] C. Steier, E. Forest, L. Nadolski, H. Nishimura, D. Robin, W. Wan, Y. Wu, A. Zholents, *Accelerator Physics Challenges of the fs-slicing Upgrade at the ALS*, Proceedings of the 2003 Particle Accelerator Conference, Portland OR, USA, p. 397–399.
- [18] A. Streun, private communication.



# Detailed Design Report



## Chapter 2

### MAX IV 3 GeV Storage Ring

#### 2.5. MAX IV Magnets

MAX IV Facility



## 2.5. MAX IV Magnets

---

- 2.5. MAX IV Magnets.....2**
- 2.5.1. Dipole Magnets..... 2
- 2.5.2. Quadrupole Magnets .....14
- 2.5.3. Sextupole Magnets..... 20
- 2.5.4. Octupoles Magnets ..... 26
- 2.5.5. Correction Magnets .....31



## 2.5. MAX IV Magnets

---

### MAX IV Magnets (figure of one full cell)

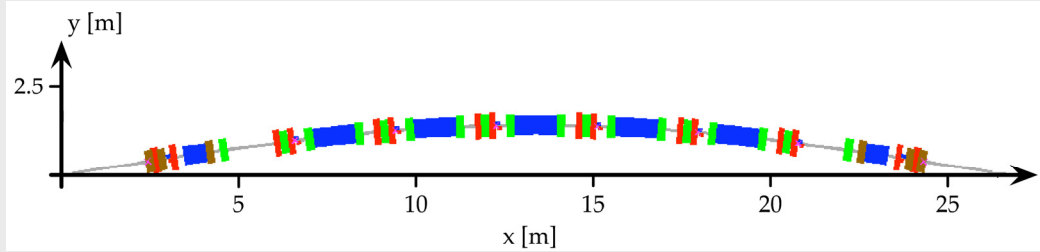


Figure 1: Schematic of one achromat of the MAX IV 3 GeV storage ring. The achromat consists of five unit cells and two flanking matching cells. The total bending angle is  $18^\circ$ . The gradient bending magnets (blue) are flanked by sextupoles (green). The bending magnets are interleaved with quadrupoles (red) and sextupoles (green). The final focusing magnets (red) match the beam to the straight section. Octupoles (brown) are installed in the matching section.

### 2.5.1. Dipole Magnets

In the MAX IV ring lattice we use gradient bending magnets. The end dipoles also have special features as soft ends where the bending field decreases to half value. The transition from full field to half end field and finally to zero field is handled in the 3d calculations and then used as input for the lattice calculations.

#### 2.5.1.1. 2d-Calculations

In this section the results from the 2d-calculation of the bending magnets are given. A transverse cut of the magnet is used as input for the calculation. All bending magnets of the lattice have the same transverse pole profile. The calculations are made in the program FEMM. The upper half of the dipole with calculated field lines is shown in fig. 2.

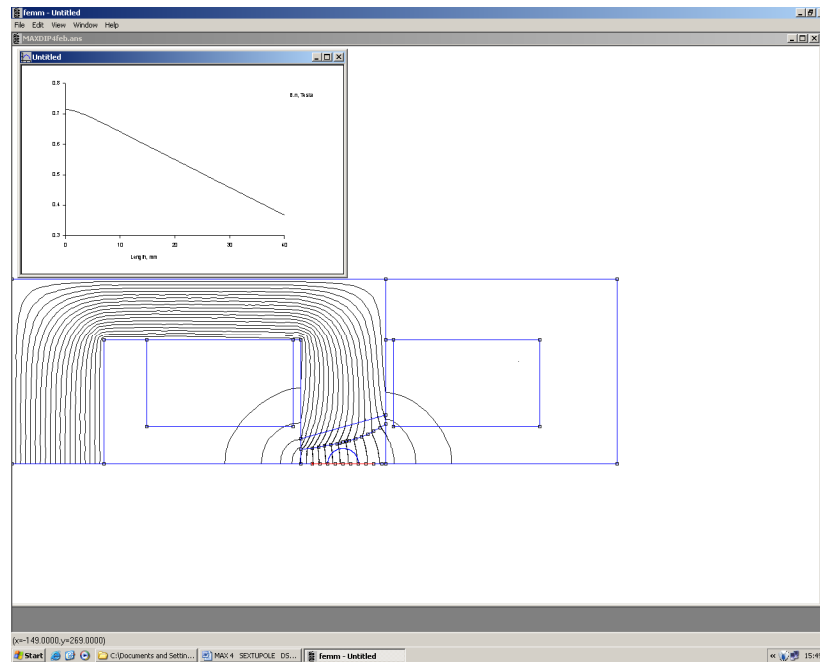


Figure 2.

The coordinates for the pole region are given in Table 1 below.  
The result of the calculation is:

Dipole field	0.5236 T	(0.52395T calculated)
Gradient	8.619 T/m	(8.603 T/m calculated)
Current	6118 At	

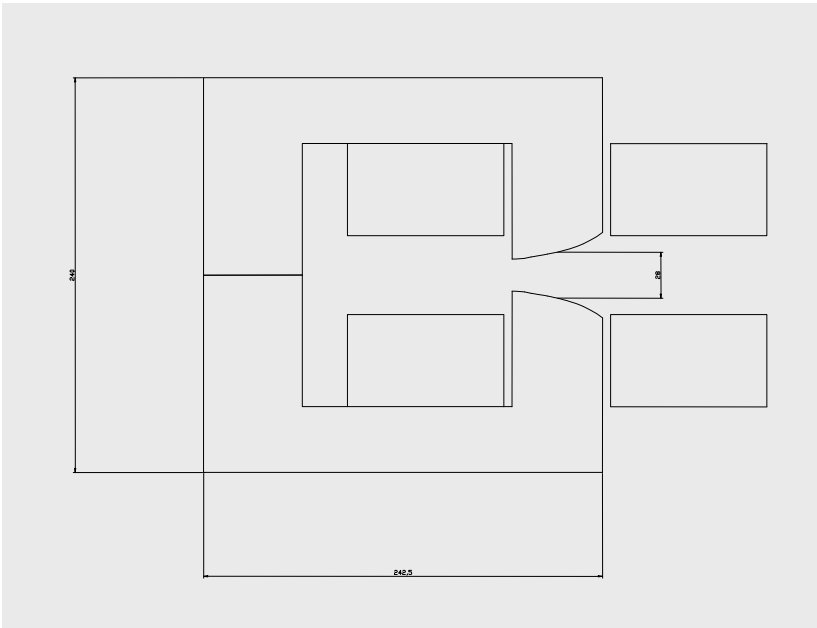
In the calculations above the good field region is -12.5 to +15 mm.

The good field region is defined where the residual field variation is less than +1Gauss see figure 5.

Table 1.

X [mm]	Y[mm]
-27.5	9.765
-25.5	9.765
-20.6189	10.1704
-19.3911	10.3489
-16.2838	11.0064
-15.7135	11.107
-14	11.3627
-12	11.6765
-10	12.007
-8	12.3617
-6	12.7344
-4	13.1298
-2	13.5517
0	14
2	14.4826
4	14.9978
6	15.5453
8	16.1423
10	16.7798
12	17.4824
14	18.2338
16	19.0669
20	21.074
24	23.36
27.5	25.95

Figure 3: Transverse dimensions of the dipole.



Plots of “dipole field” and residual field along the horizontal axis. The ripple in the calculated points is partly due to the mesh size (25um).

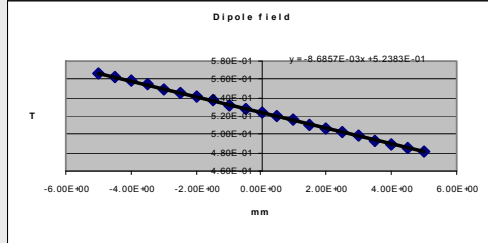


Figure 4.

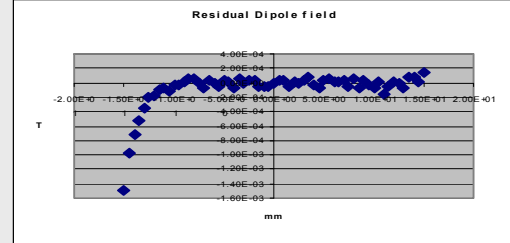


Figure 5.

### 2.5.1.2. 3d-Calculations

The dipole is well calculated in 2D to get the desired dipole and gradient in the bulk of the bending-magnets.

There are two types of dipoles in the lattice the main dipoles inside the cell and the softended dipoles facing the long straight sections. The softended dipole is used to protect insertion devices in the long straight sections from high thermal load.

The aim of the 3d calculations is to determine the field profile in the fringe field region and also in the transition region from main field to soft field. The relative contributions of gradient field and dipole field is important to calculate. All the dipoles have magnetic shunts on each end to shorten the fringe fields.

When the magnets are calculated the resulting field map is divided in a number of slices that will become the new magnet. When this extended magnet is put into the lattice program we find that the tune might not be correct. The lattice is retuned and new slices are calculated. The process converges quickly and results in bending-magnets that reflects the calculated field map.

### 2.5.1.3. Slicing and Lattice Iteration

The picture below shows the lower half of the model for the softended dipole used in 3D calculations.

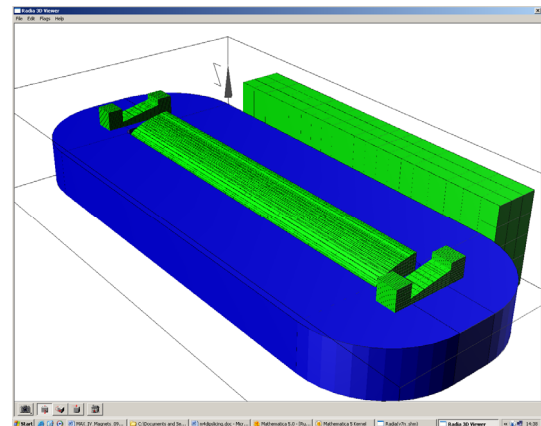
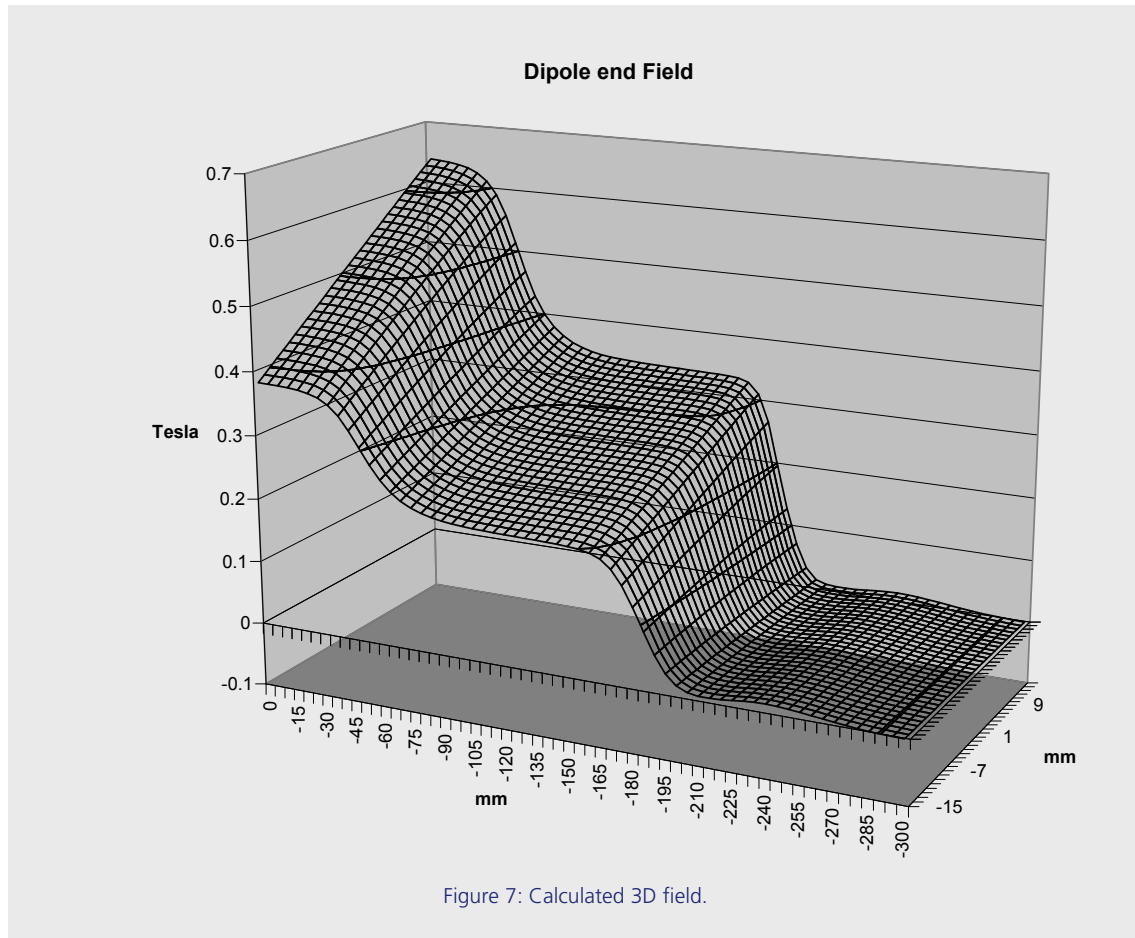


Figure 6: The model magnet.



The field calculated from the model cover regions of the main magnet, the soft end region and the end fields. As can be seen in figure 7. The gradient is present in the soft region but disappears quickly in the end field region. A magnetic shunt is cutting off the end fields.

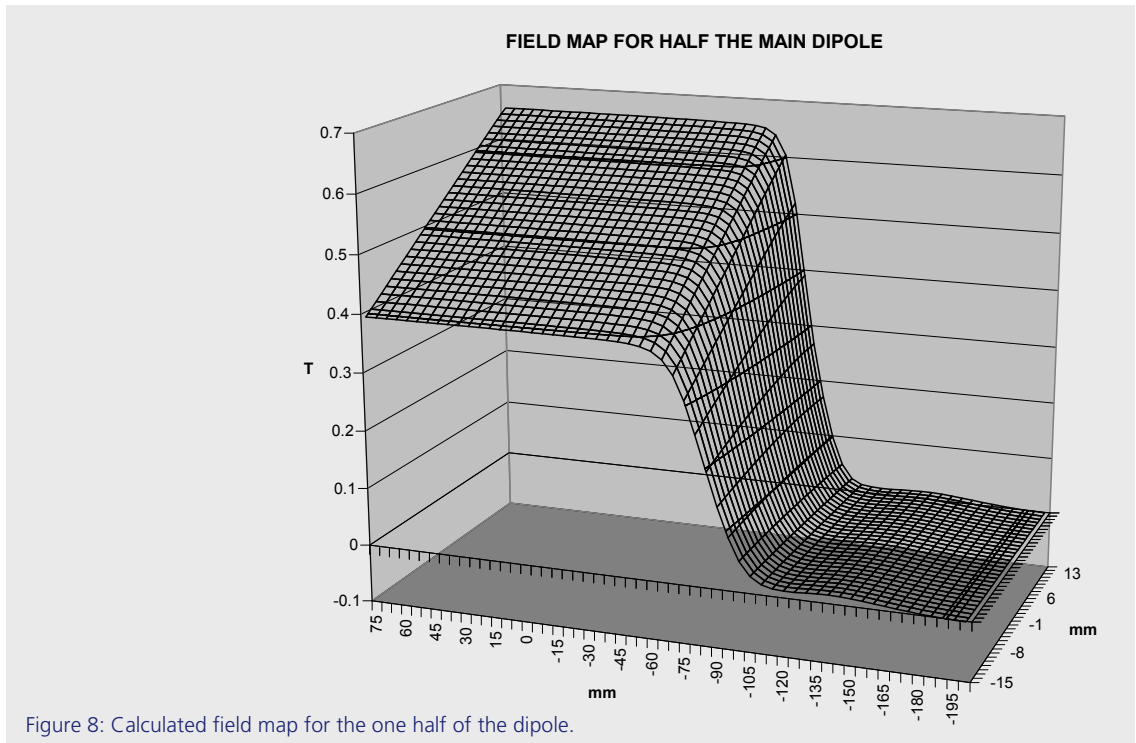
The softended dipole is divided into twelve slices. The first one is the main part with constant longitudinal field. The second part is the first one seen in the figure above. The other slices follows each being 50mm long. The other side of the magnet is the region facing the hard edge part. The fringe field region of this part have five slices that are the same as for the main hard edge magnet. All slices are considered as longitudinally constant in field given by the average from the calculations.

Data for the final iteration are given below.

SOFT SLICE	BEND	L[mm]	B[T]	Q[T/m]	RHO	ang[mrad]	ang[deg]
Ds6	50	50	0.007738	0.005164	1292.324	0.03869	0.002217
Ds5	100	50	0.18697	2.932271	53.48452	0.93485	0.053563
Ds4	150	50	0.259229	4.234943	38.57593	1.296145	0.074264
Ds3	200	50	0.269543	4.299814	37.09983	1.347715	0.077218
Ds2	250	50	0.406663	6.082495	24.59039	2.033315	0.1165
Ds1	300	50	0.520683	8.562347	19.20554	2.603415	0.149165
Ds0	504.24	204.24	0.5236	8.66874	19.09855	10.69401	0.612721
D1	554.24	50	0.52339	8.6798	19.10621	2.61695	0.14994
D2	604.24	50	0.5225	8.6723	19.13876	2.6125	0.149685
D3	654.24	50	0.37641	5.9235	26.56678	1.88205	0.107834
D4	704.24	50	0.018679	-0.06434	535.3606	0.093395	0.005351
D5	754.24	50	0.005385	-0.00121	1856.976	0.026926	0.001543
							1.500001

#### 2.5.1.3.1. Main Bending Magnet

The bending magnets inside the cell are normal sector magnets with a gradient equal to the softended magnet. The same procedure is used for this magnet and the result is a number of slices given in the table below. Only one half of the magnet is calculated as it is symmetric. (Figure 8)



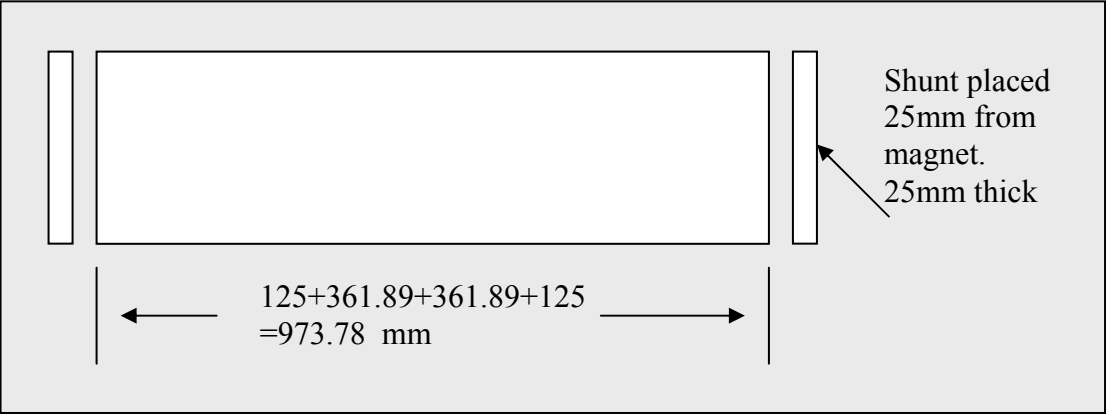
The calculated slices are found in table 2. Below.

Hard edge							
slice	L[mm]	B[T]	Q[T/m]	RHO	ang[mrad]	ang[deg]	
0	361.89	0.5236	8.6837	19.09855	18.94856	1.085673	
1	50	0.52339	8.6798	19.10621	2.61695	0.14994	
2	50	0.5225	8.6723	19.13876	2.6125	0.149685	
3	50	0.37641	5.9235	26.56678	1.88205	0.107834	
4	50	0.018679	-0.06434	535.3606	0.093395	0.005351	
5	50	0.005385	-0.00121	1856.976	0.026926	0.001543	
						1.500025	

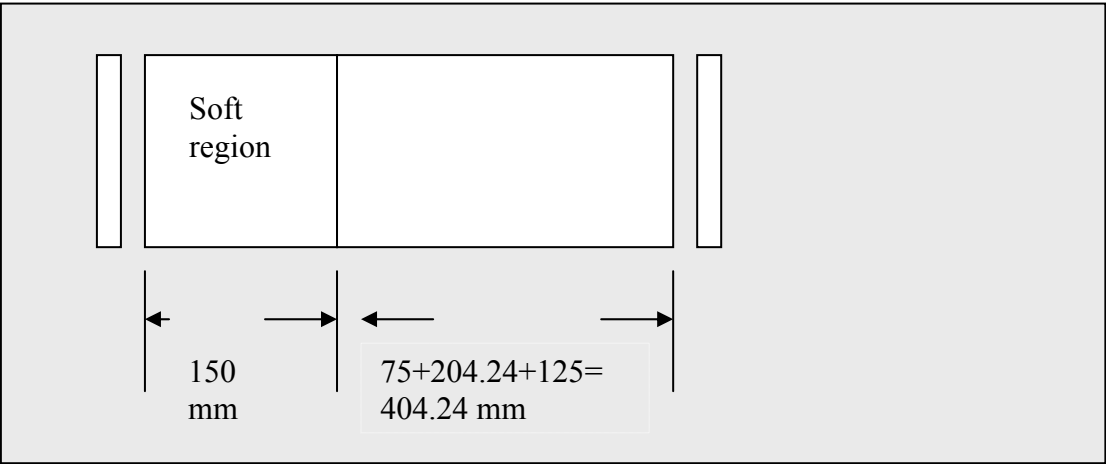
Table 2: Slices for half dipole.

Schematic view of the dipoles with iron length given

Main dipole



2 Softended





### 2.5.1.4. Coil Currents and Cooling Data for Bending Magnets

			dip-dip		dipm	(-dipm)
Conductor		Antal	100		20	20
	Energi	GeV	3		3	3
	BR	Tm	10		10	10
	B	Tesla	0.523		0.523	0.523
	Grad	T/m	8.68		8.68	8.68
	Sext.	T/m^2				
	Oct.	T/m^3				
	R	m	19.1		19.1	19.1
	L	m	1		0.567	0.567
	Gap	m	0.028		0.028	0.028
	NI	At	12236		12236	12236
	Pole width	m	0.055		0.055	0.055
	Coil length	m	2.428451		1.562451	1.562451302
	Width	mm	8		8	8
	Hole	mm	3.5		3.5	3.5
	No of	Layers	6		6	6
	turns	per layer	9		5	5
	Res. Per coil	Ohm	0.045819		0.016378	0.016377633
	Current	Amp	116.1287		209.0317	209.0316667
	Voltage per coil	V	5.320913		3.423444	3.42344402
dT=10C	Power per coil	kW	0.617911		0.715608	0.715608209
	Power per magnet	kW	1.235821		1.431216	1.431216418
	Water	Bar	0.813312		0.375858	0.375857795
	Water circ.	per magnet	6		6	6
6 circuits	Total power	kW	123.5821		28.62433	28.62432837
	Voltage	V	1064.183		136.9378	136.9377608
	Voltage	V	177.3638	2 parallel:	68.46888	68.4688804
dT=10C	Current	A	696.7722		418.0633	418.0633333
	Water/magnet	lit/min	1.770932		2.050933	2.050933128
dT=10C	Total water	lit/min	177.0932		41.01866	41.01866255
2	Bar	lit/min/magnet	2.961399		5.330999	5.330999331
	Total water	lit/min	296.1399		106.62	106.6199866
2	Bar	Deg C	5.980052		3.847183	3.84718324
			1770.932		410.1866	410.1866255
		PS V	177.3638			136.9377608
		PS A	696.7722			418.0633333
	Tot	kW	123.5821			57.24865674
	Number	of PS	1			1
	Possible	PS type				

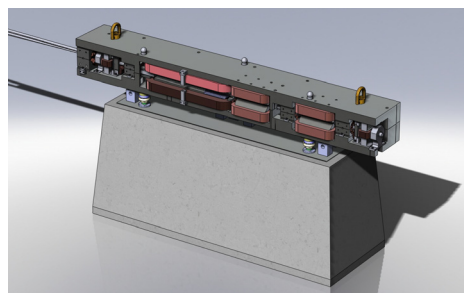
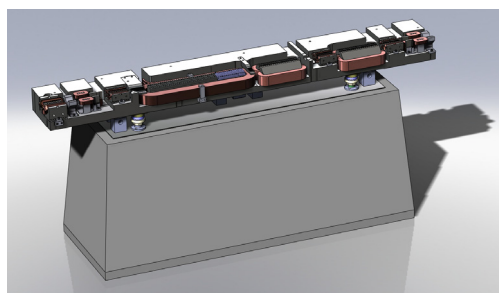
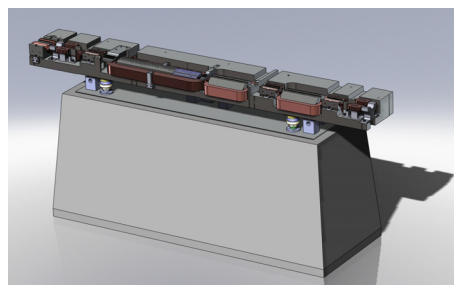
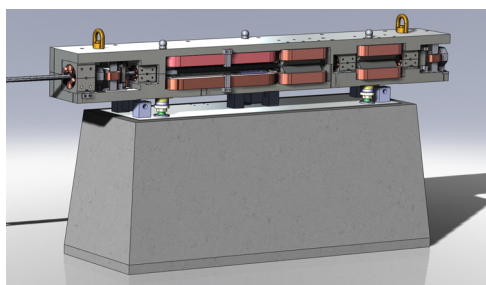
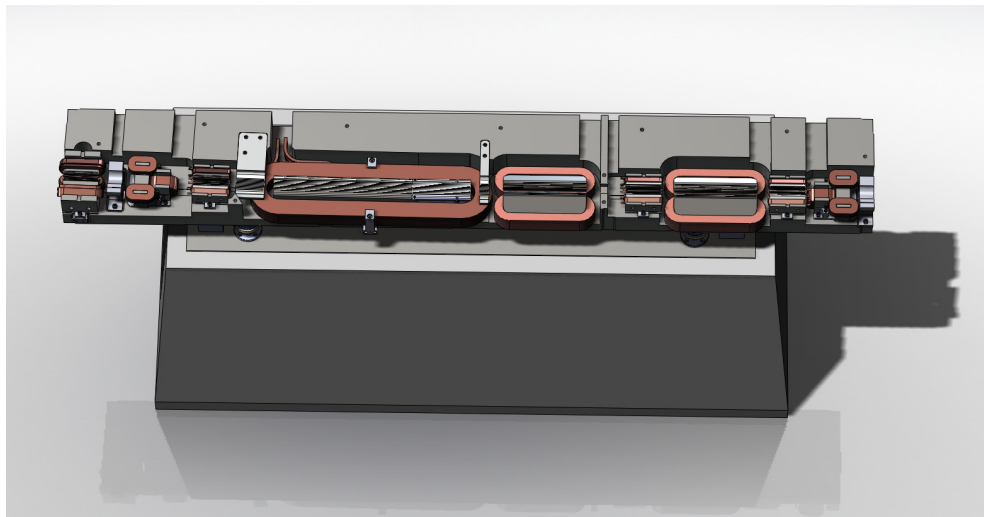
2.5.1.5. Magnet Material Data

The steel for the magnets will have an analysis similar to the following: The steel will be delivered normalized from the steel work and then treated for optimum magnetic characteristics by heating to 700C for 10h and cooled slowly (10C/h) to 300C.

C	.001%
Si	.02%
Mn	.14%
P	.008%
S	.008%
Al	.032%

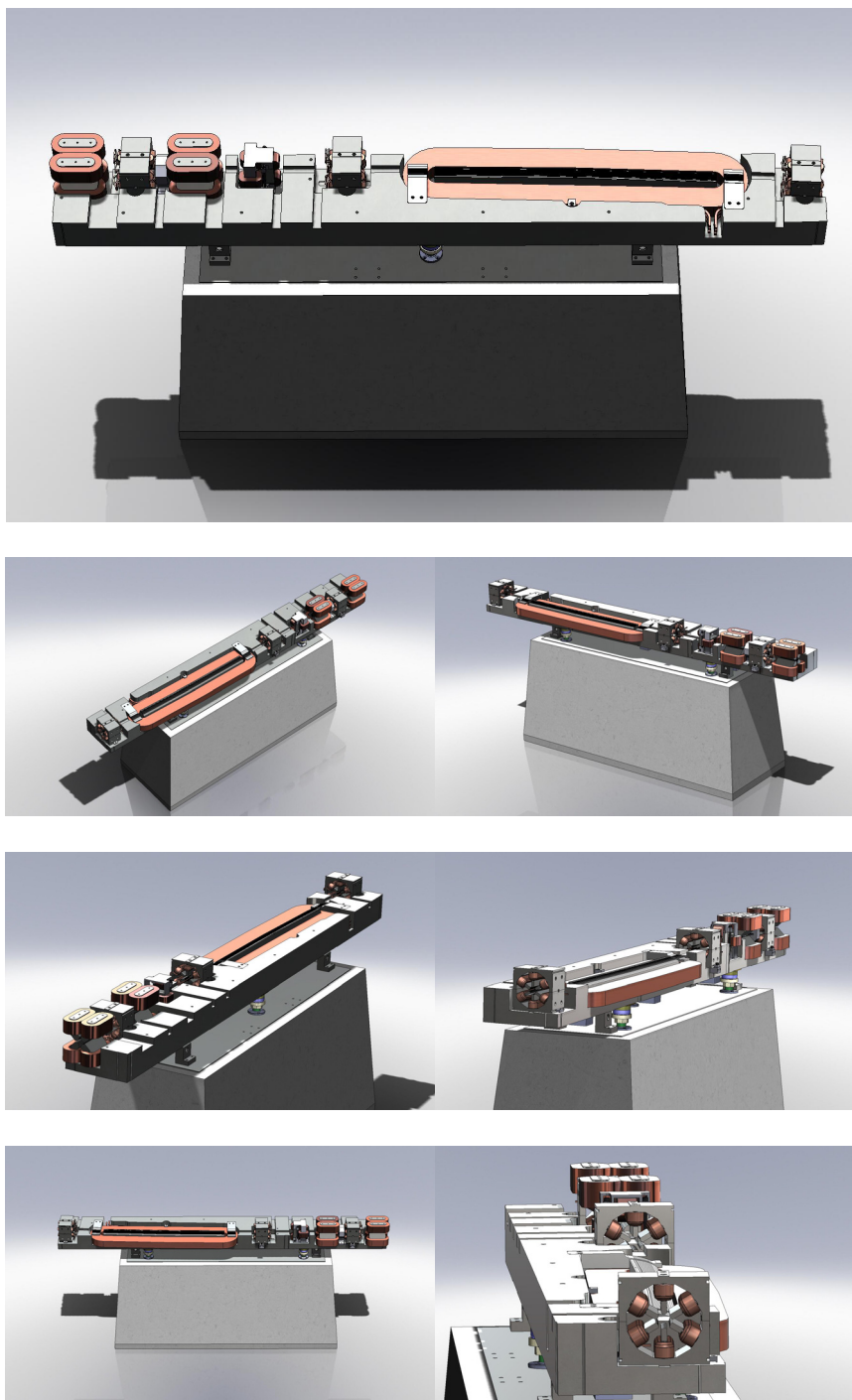
### 2.5.1.6. The Matching Cell

The softended dipole is part of the matching cell. The softended part is seen in the drawing below as the right part of the dipole followed by two quadrupoles Q<sub>dend</sub> and Q<sub>fend</sub>. The other elements in the cell are type sextupoles and octupoles.



### 2.5.1.7. The Unit Cell

The normal dipoles are included in the unit cells. In the upper drawing below the 3 deg. dipole is shown to the right and the split focusing cell to the left with a sextupole insertion. The other type of sextupole is found one on each side of the dipole.



## 2.5.2. Quadrupole

The dipole gradient is focusing in the vertical direction and normal quadrupoles are used for the horizontal plane. The normal quads range from 30 to about 40 T/m in strength. An additional quadrupole is used in the end section for the vertical plane. The quadrupoles are named qf, qfm, qfend, and qdend.

The magnets differ in length but will all have the same transverse profile as used in the 2d design below.

### 2.5.2.1. 2d-Calculations

The figure to the left (figure 9) shows one quarter of the quadrupole. The designed strength is about 43 T/m.

The requirements for all quadrupoles are lower than this design value.

The full sized magnet with its final pole coordinates is shown in figure 10. The pole coordinates are given for a pole that is rotated 45 degrees around the centre. When rotated, the pole face is symmetric around line  $x=0$ .

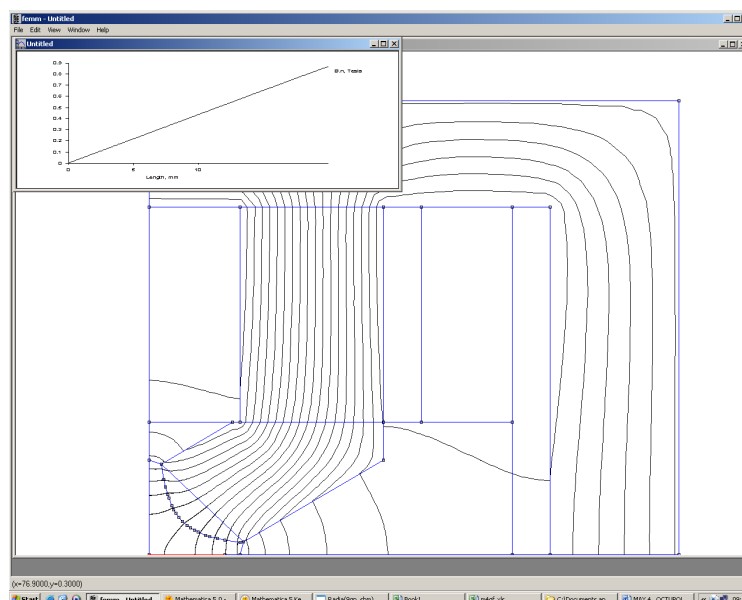
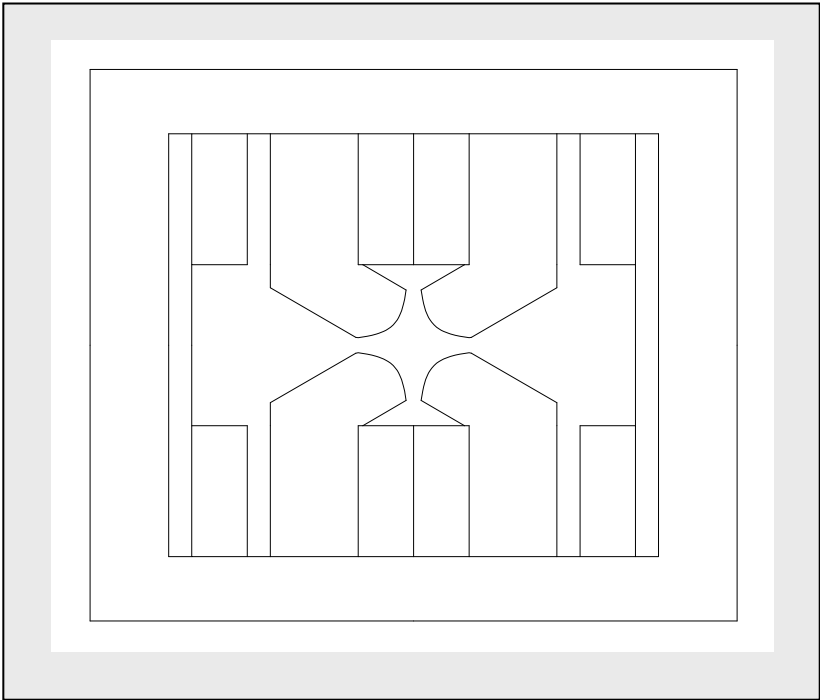


Figure 9.

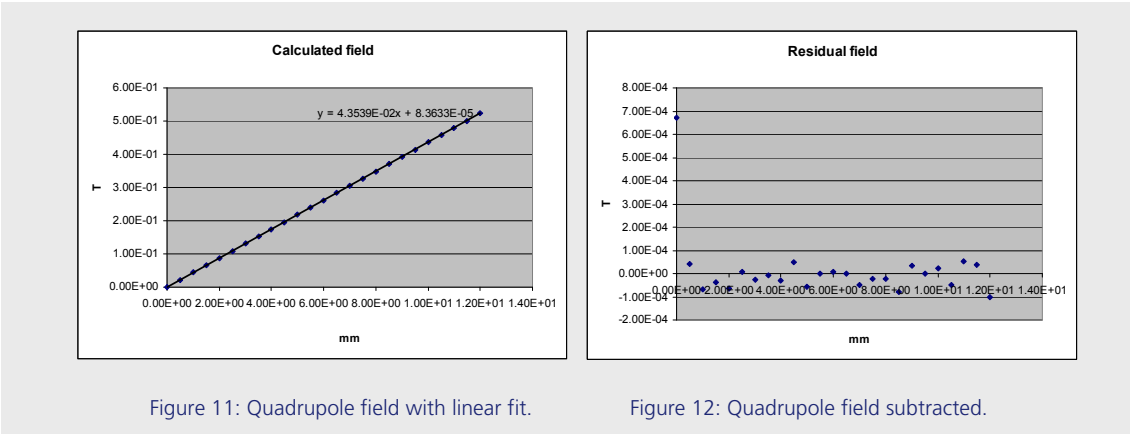
Table 3: Pole coordinates (pole vertical).

X [mm]	Y[mm]
0	12.5
1.5468	12.5953
2.75611	12.8002
3.88172	13.0888
4.94295	13.4418
6.92376	14.2894
7.86104	14.7664
9.65888	15.797
11.38	16.9043
14.6688	19.2723

Figure 10.



The magnet field and the quality of the field are shown in figure 11 and figure 12 respectively. The insertion in figure 3 shows a linear fit to the calculated points



**Quadrupole field**43.55 T/m  
**Radius** 12.5 mm  
**Current** 2900 At

### 2.5.2.2. 3d-Calculations

A model for the Quadrupole is set up in “Radia” (figure 13.).

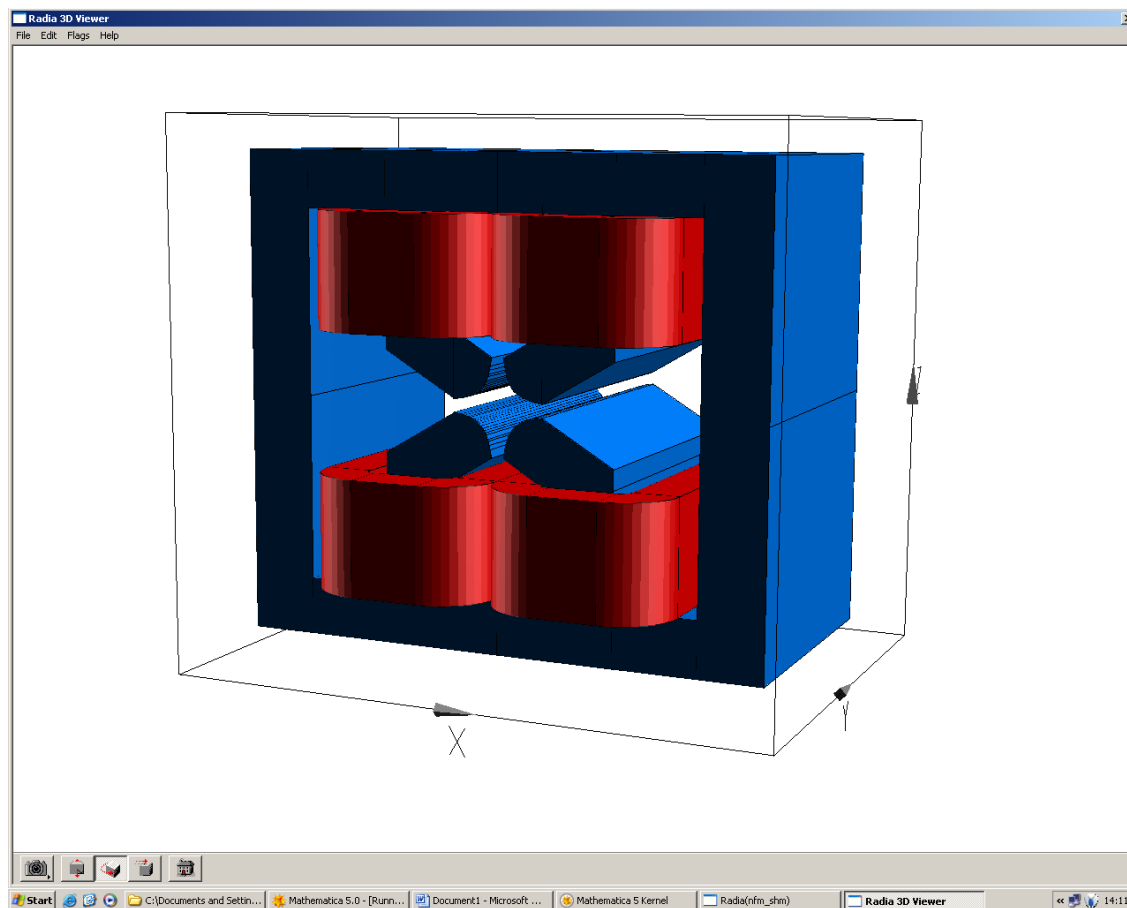


Figure 13: Model magnet.

Fields for the magnet are calculated from the middle of the magnet and far out until the fields have decreased to zero. The calculated field map is found in figure 14.

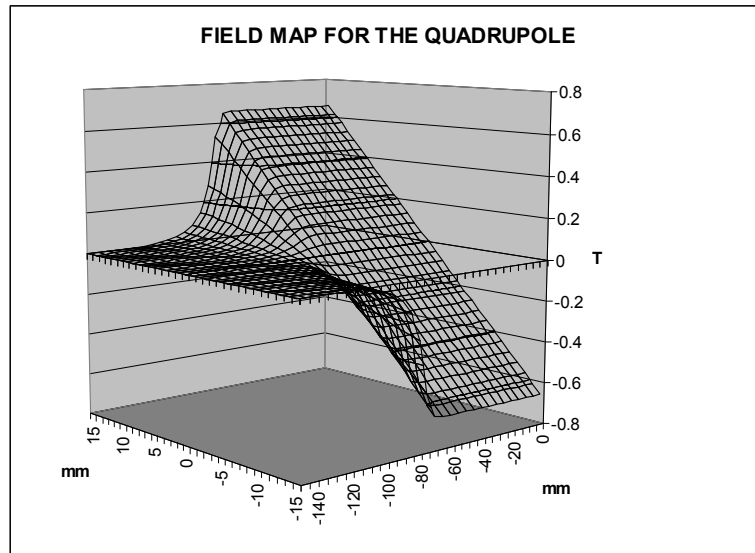


Figure 14: Calculated field map.

From the field map the longitudinal field integral is determined. The integral field is found in figure 15.

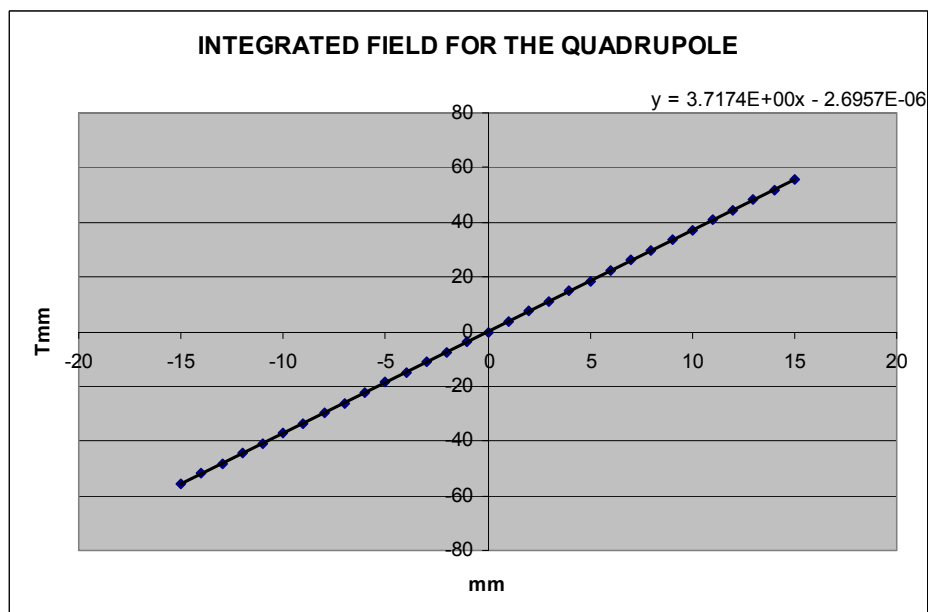


Figure 15.



When subtracting the quadrupole part from the integral the residual fields remain showing the quality of the integrated field. Figure 16.

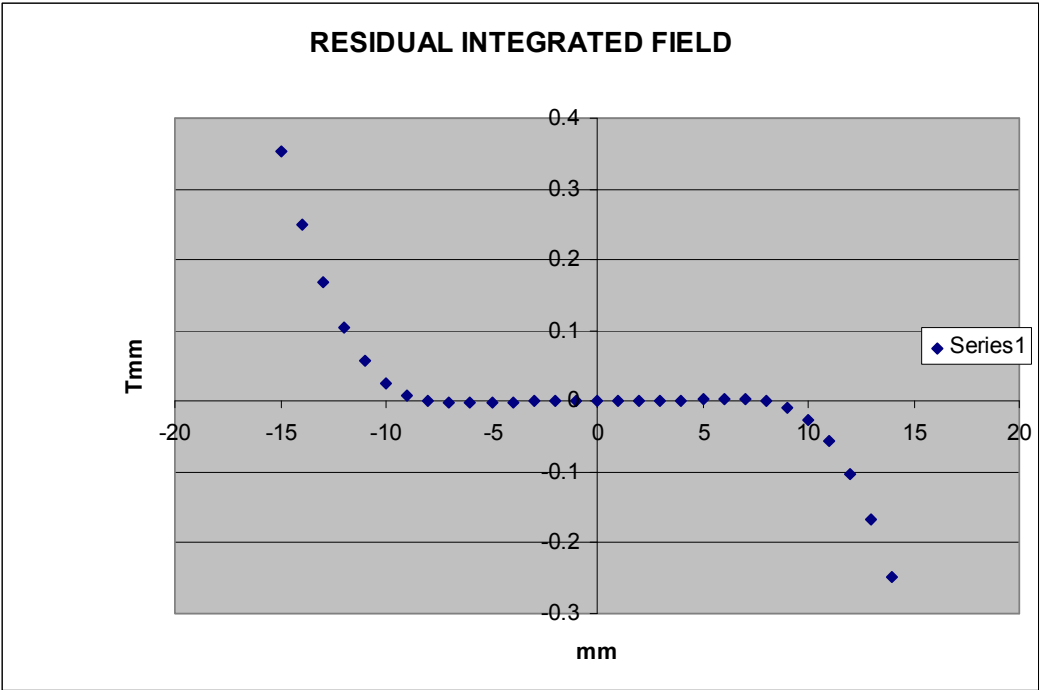


Figure 16.

The effective length of the quadrupole is calculated by dividing the integral value by the gradient value extracted from the main part of the magnet.

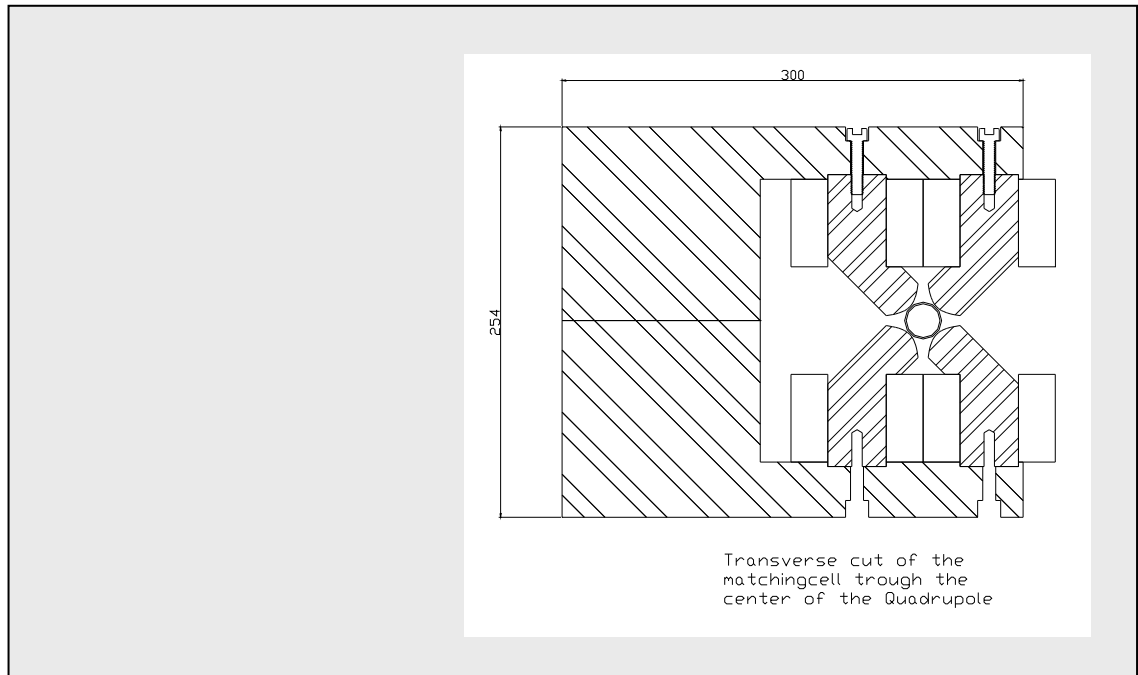
DATA FOR THE MODEL MAGNET	
HALF GAP	12.5 mm
IRON LENGTH	150 mm
CAL. GRAD	44.0 T/M
CAL.INT.GRAD	
FOR HALF MAGNET	3.728 T
CALC. MAGNETIC	
LENGTH	84.7 mm
EFB	+9.5 mm on each side
EXCITATION	3100 At

### 2.5.2.3. Coil Currents and Cooling Data Quadrupoles

				qf	qfm	qfend	qdend	
	Conductor		Antal	160	80	40	40	
		Energi	GeV	3	3	3	3	
		BR	Tm	10	10	10	10	
		B	Tesla					
		Grad	T/m	40.38	37.8	35.22	21.76	
		Sext.	T/m^2	0	0	0	0	
		Oct.	T/m^3					
		L	m	0.15	0.15	0.25	0.25	
		Gap	m	0.025	0.025	0.025	0.025	
		NI	At	3012.505	2820.027	2189.624	1352.817	
		Pole width	m	0.038	0.038	0.038	0.038	
		Coil length	m	0.438832	0.438832	0.638832	0.638832	
		Width	mm	5	5	5	5	
		Hole	mm	3	3	3	3	
		No of	Layers	4	4	4	4	
		turns	per layer	10	10	10	10	
		Res. Per coil	Ohm	0.018599	0.018599	0.027076	0.027076	
		Current	Amp	75.31262	70.50067	54.7406	33.82043	
		Voltage per coil	V	1.400764	1.311265	1.48216	0.915724	
		Power per coil	kW	0.105495	0.092445	0.081134	0.03097	
	Power per magnet	kW	0.421981	0.36978	0.324537	0.123881		
	dT=10C	Water	Bar	1.41691	1.124557	1.302812	1.624642	
		Water circ.	per magnet	2	2	2	1	
		Total power	kW	67.51691	14.79121	12.98149	4.955228	
		Voltage	V	896.4888	209.8023	237.1456	146.5158	
	dT=10C	Water/magnet	lit/min	0.604698	0.529895	0.465062	0.177521	
	dT=10C	Total water	lit/min	96.75174	21.1958	18.60248	7.100842	
	Water if	2	Bar	lit/min/magnet	0.736327	0.736327	0.594125	0.199908
			Total water	lit/min	117.8124	29.45309	23.76498	7.996323
	Temp rise if	2	Bar	Deg C	8.212359	7.19646	7.827684	8.880134
					967.5174	211.958	186.0248	71.00842
				PS V	224.1222	52.45059	59.2864	36.62896
			PS A	75.31262	70.50067	54.7406	33.82043	
		Tot	kW	67.51691	14.79121	12.98149	4.955228	
		Number	of PS	4	4	4	4	
		Possible	PS type		SM 70-90	SM 70-90	SM 70-90	

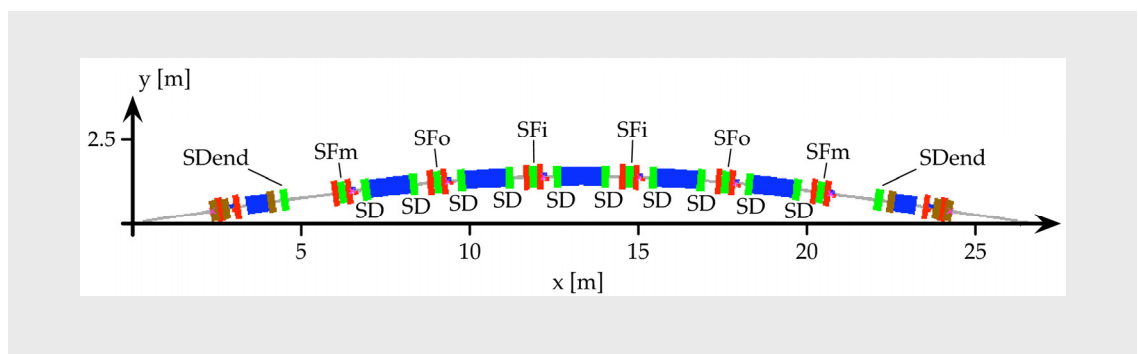
### 2.5.2.4. Drawing of Qpole-Magnet

Figure 17.



### 2.5.3. Sextupole Magnets

Chromatic corrections are made by five families of sextupoles. Two families are used in the vertical plan and three in the horizontal plane.



### 2.5.3.1. 2d-Calculations

Close to the ends of the dipoles a special sextupole SD is positioned. The design of SD follows below.

#### 2.5.3.1.1. SD(END) Design

Figure 18 below shows the symmetric part of SD used in the calculations, and table 4 gives pole coordinates for the vertical pole. (Symmetry around  $x=0$ )

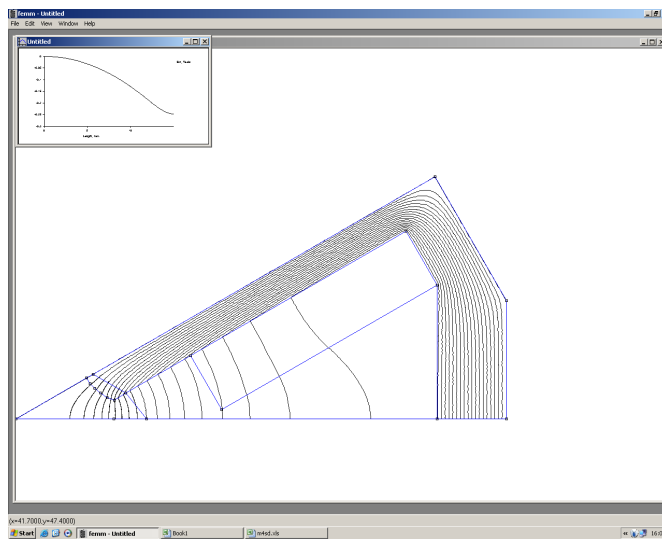


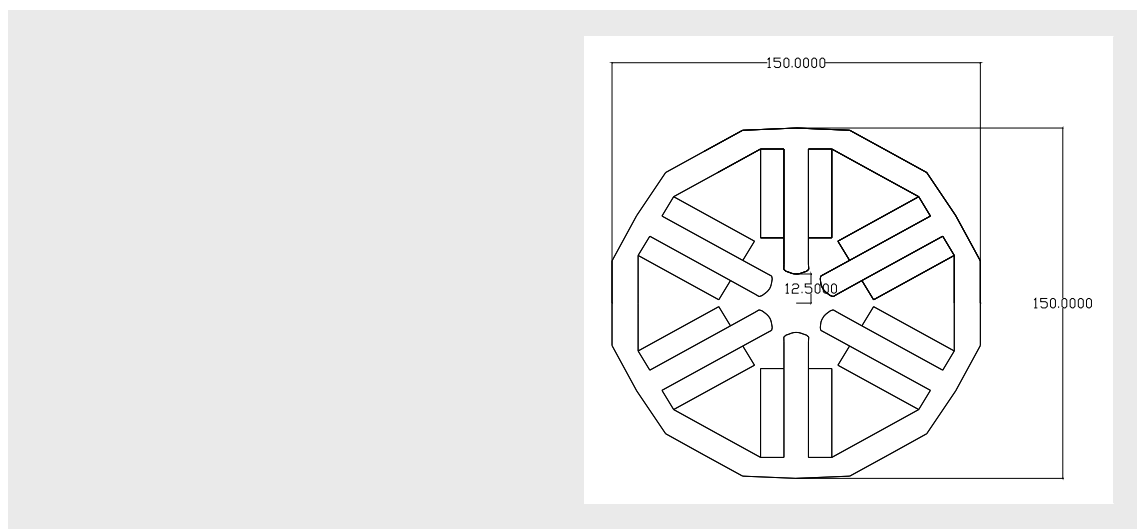
Figure: 18.

x[mm]	y[mm]
0	12.5
1	12.5812
2	12.825
3	13.23
4.17321	13.7
5.0866	14.478

Tabel: 4.

The complete magnet with dimensions is shown in figure 19.

Figure 19.



SD field map on the median plane, a polynomial fit is shown (figure 20.).

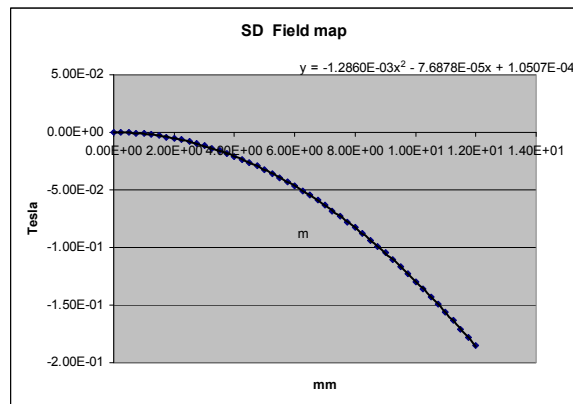


Figure 20.

Residual SD field (figure 21.) when the sextupole component is extracted. The good field region is defined as the part where the residual field is below one Gauss. In the figure this region is  $\pm 11$ mm.

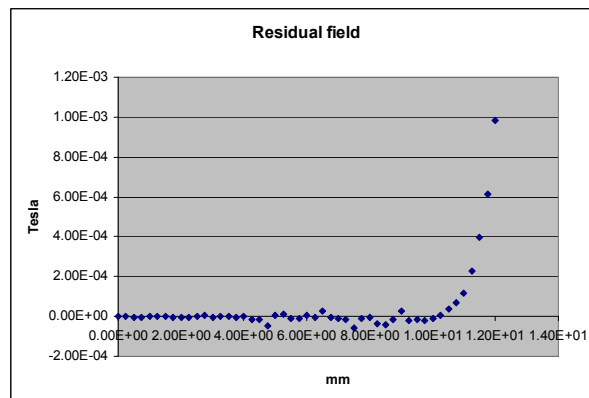


Figure 21.

The same magnet as designed above is used for SDeud with lower excitation or shorter length

**FIELD DATA:**  
**1294.2T/m<sup>2</sup>**  
**707.56 AT**  
**Radius 12.5 mm**

### 2.5.3.1.2. SF0,SFi,SFm Design

The three families are represented by the same magnet design. SF0 and SFi have about the same strength and SFm is about half that value. Either SFm is made shorter or is excited by a lower current.

#### MAX 4 SEXTUPOLE SF0 2D Calculations

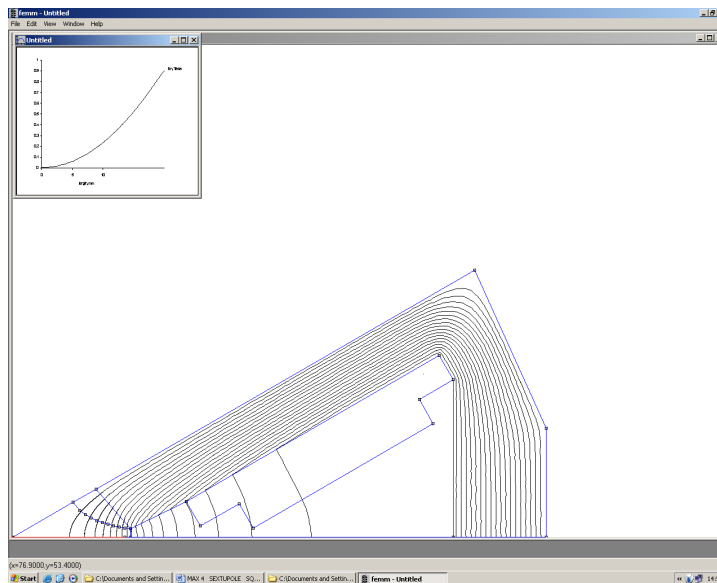


Figure 22.

X [mm]	Y[mm]
0	12.5
1.83529	12.7968
3.01847	13.2684
4.02615	13.8413
4.92182	14.4789
5.73952	15.1615
6.50006	15.8771
7.21722	16.6177
7.90061	17.3779
8.55721	18.1535
9.19225	18.9416

Table 5.

Figure 22 shows the symmetric part of SF0 used in the calculations, and table 5 gives pole coordinates for the vertical pole. (Symmetry around  $x=0$ )

The complete sextupole with dimensions is shown in figure 23.

Calculated field with a nonlinear fit is found in figure 24. After extraction of the sextupole part of the field the residual field remain which is found in figure 25.

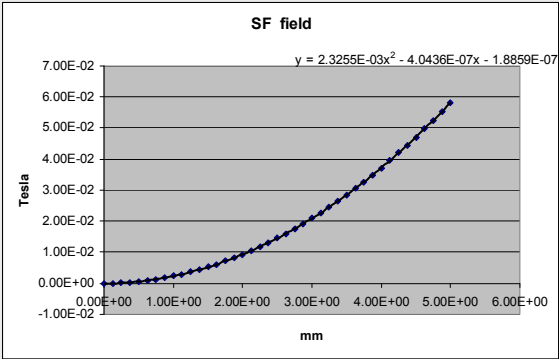


Figure 24.

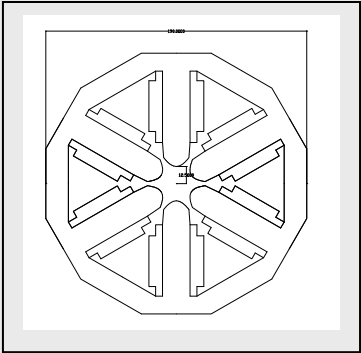


Figure 23.

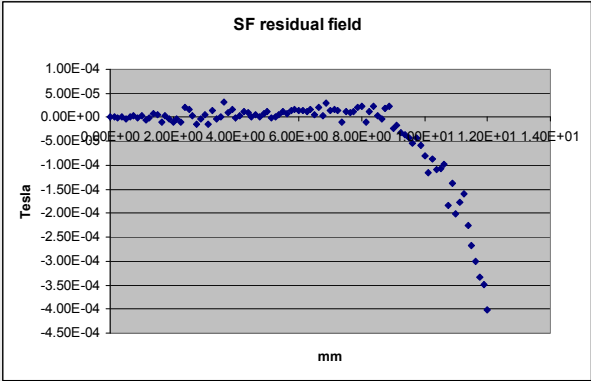


Figure 25. Good field region is slightly above 10mm (within one gauss).

Magnet Data:

Field:	2325 T/m2
Exc:	1379.5 AT
Radius:	12.5 mm

### 2.5.3.2. 3d-Calculations

### 2.5.3.3. Coil Currents and Cooling Data

#### SEXTUPOLES 2009

				sd	sdends	sfms	sfos	sfis	
If parallel	6 circuits		Antal	200	40	40	40	40	
		Energi	GeV	3	3	3	3	3	
		BR	Tm	10	10	10	10	10	
		B	Tesla						
		Grad	T/m						
		Sext.	T/m^2	1179	1340	1600	1700	2148	
		Oct.	T/m^3						
		R	m						
		L	m	0.1	0.1	0.1	0.1	0.1	
		Gap	m	0.025	0.025	0.025	0.025	0.025	
		NI	At	665	800	935	1020	1310	
		Pole width	m	0.01	0.01	0.02	0.02	0.02	
		Coil length	m	0.24513	0.24513	0.26513	0.26513	0.26513	
		Width	mm	4	4	4	4	4	
		Hole	mm	2.5	2.5	2.5	2.5	2.5	
		No of	Layers	2	2	2	2	2	
		turns	per layer	5.5	8	8	6.5	8	
		Res. Per coil	Ohm	0.00462	0.00672	0.00727	0.0059	0.00727	
		Current	Amp	60.4545	50	58.4375	78.4615	81.875	
		Voltage per coil	V	0.27925	0.33594	0.42467	0.46327	0.59499	
		Power per coil	kW	0.01688	0.0168	0.02482	0.03635	0.04871	
		Power per magnet	kW	0.10129	0.10078	0.1489	0.21809	0.29229	
		dT=10C	Water	Bar	0.42984	0.61973	1.32708	2.10277	4.32024
		Water circ.	per magnet	1	1	1	1	1	
		Total power	kW	20.2584	4.0313	5.95594	8.72377	11.6915	
		Voltage	V	335.102	80.626	101.92	111.185	142.797	
		Voltage	V						
		Current	A						
	dT=10C	Water/magnet	lit/min	0.14515	0.14442	0.21337	0.31253	0.41885	
	dT=10C	Total water	lit/min	29.0303	5.77685	8.53487	12.5012	16.7539	
Water if	2	Bar	lit/min/magnet	0.34944	0.28209	0.26973	0.3037	0.26973	
		Total water	lit/min	69.8881	11.2836	10.789	12.1482	10.789	
Temp rise if	2	Bar	Deg C	4.15383	5.11971	7.91069	10.2905	15.5287	
				290.303	57.7685	85.3487	125.012	167.539	
			PS V	83.7755	80.626	25.48	27.7963	35.6992	
			PS A	60.4545	50	58.4375	78.4615	81.875	
		Tot	kW	20.2584	4.0313	5.95594	8.72377	11.6915	
		Number	of PS	4	1	4	4	4	
		Possible	PS type	SM 120-50	SM 120-50	SM 70-90	SM 70-90	SM 70-90	
				Modifierat?					



## 2.5.4. Octupoles Magnets

Three families of octupoles are used for higher orders of correction. The families are named Oyyo, oxxo, and oxyo respectively. For oxxo and oxyo the same design is used, but the weak oyyo is positioned close to a dipole and need special design.

### 2.5.4.1. 2d-Calculations

#### OXYO, OXXO design

Figure 26 shows the symmetric part of Oxyo used in the calculations, and table 1 gives pole coordinates for the vertical pole. (Symmetry around  $x=0$ )

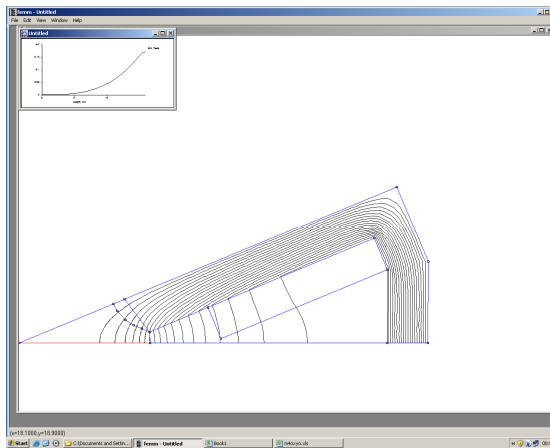
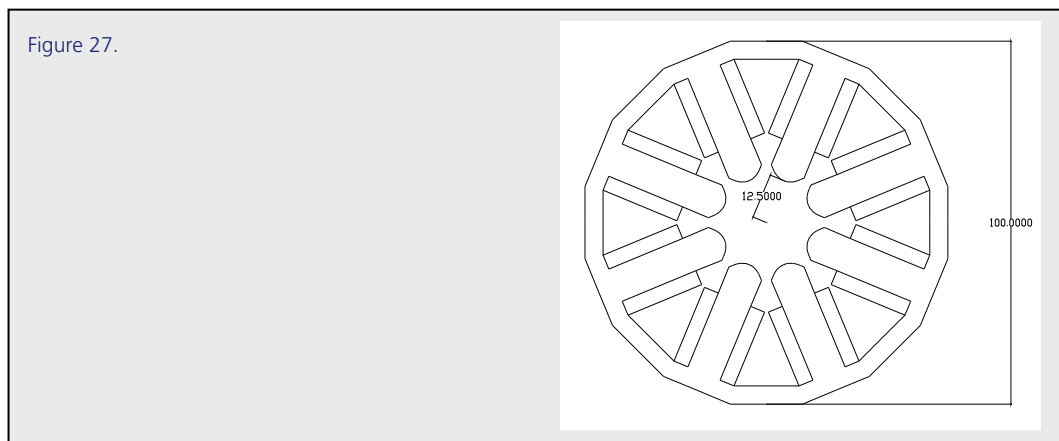


Figure 26.

X mm	Y mm
0	12.5
0.989524	12.5788
2.35846	13.0942
3.3392	13.7704
4.13751	14.5221
4.89239	15.281

Table 6.

The complete magnet with dimensions is shown in figure 27.



Calculated field with a nonlinear fit is found in figure 28. After extraction of the octupole part of the field the residual field remain and is found in figure 29.

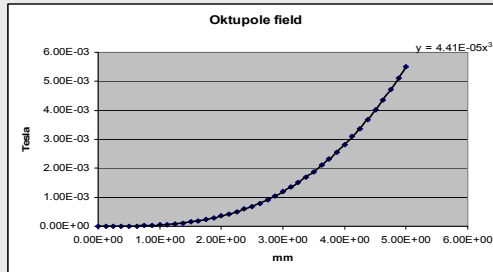


Figure 28.

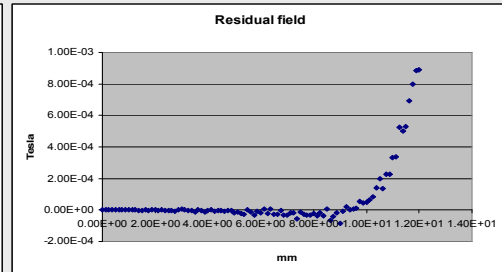


Figure 29.

#### Magnet data

Octupole field                      44100 T/m<sup>3</sup>            (2\*nominal value)

Excitation                            221 AT

Radius                                12.5 mm

#### OYYO design

Figure 30 shows the symmetric part of Oyyo used in the calculations, and table 7 gives pole coordinates for upright pole. (Symmetry around x=0).

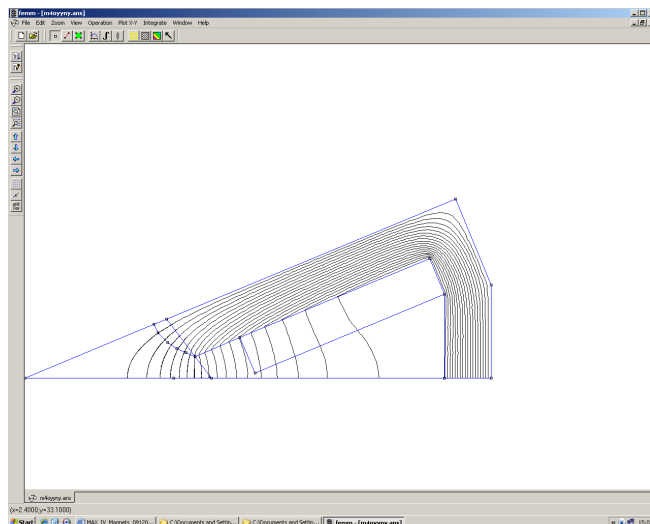


Figure 30.

X[mm]	y[mm]
Xmm	Ymm
0	15
0.989524	15.0788
2.35846	15.5942
3.3392	16.2704
4.13751	17.0221
4.89239	17.781

Table 7.

The complete magnet with dimensions is shown in figure 31. The magnet is like oxyo but with radius increased to 15 mm.

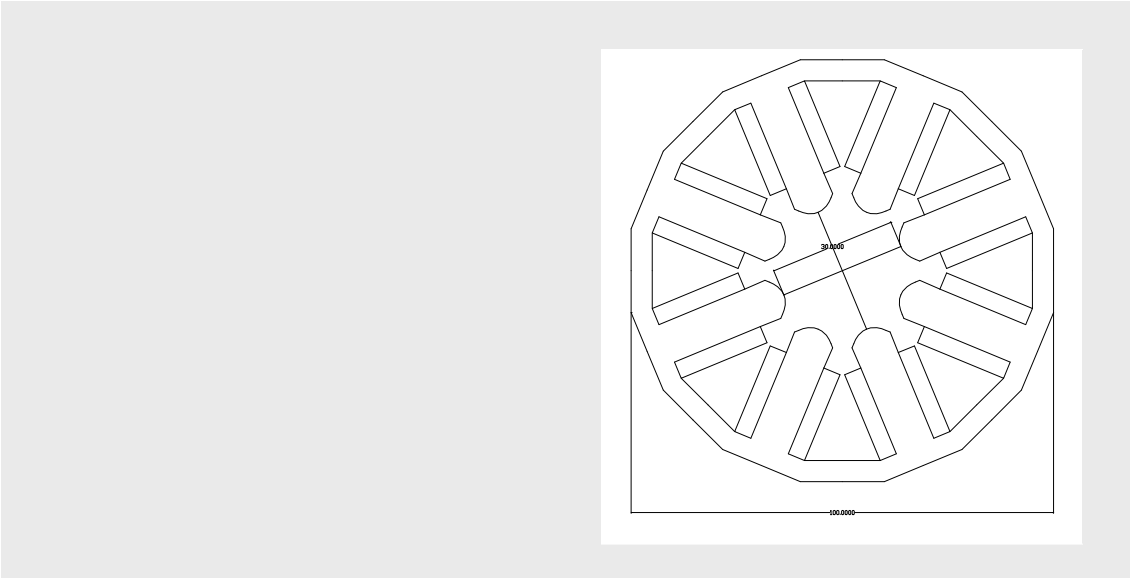
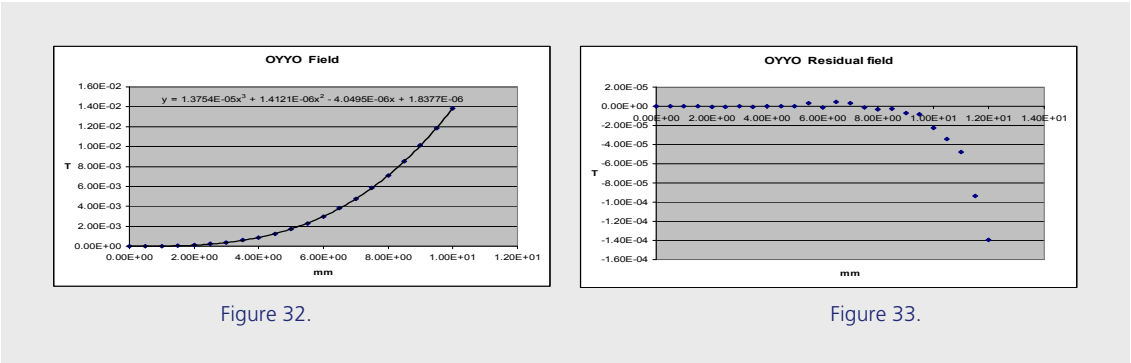


Figure 31.

Calculated field with a nonlinear fit is found in figure 32. After extraction of the octupole part of the field the residual field remain and is found in figure 4.



Magnet Data		
Octupole field	13874 T/m <sup>3</sup>	(2*nominal value)
Excitation	145.2 AT/coil	
Radius	15 mm	

### 2.5.4.2. 3d-Calculations

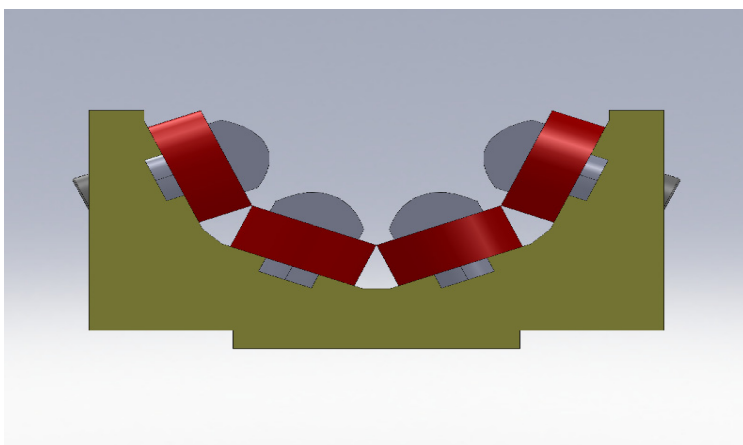
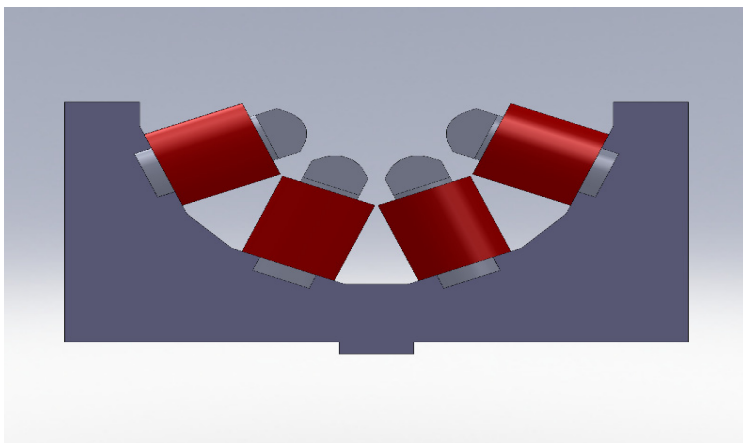
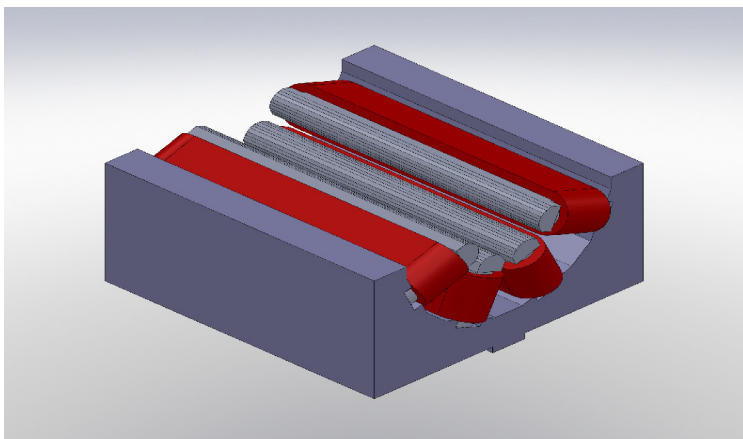
### 2.5.4.3. Coil Currents and Cooling Data

#### OCTUPOLES

				oxxo	oxyo	oyyo
If parallel	nominal max		Antal	40	40	40
		Energi	GeV	3	3	3
		BR	Tm	10	10	10
		B	Tesla			
		Grad	T/m			
		Sext.	T/m^2			
		Oct.	T/m^3	13142	21814	6886
				44100	44100	17265
		R	m			
		L	m	0.1	0.1	0.1
	nominal max	Gap	m	0.025	0.025	0.03
		NI	At	63.831	105.9511	69.0
				221	221	173
		Pole width	m	0.01	0.01	0.01
		Coil length	m	0.232566	0.232566	0.232566
	Conductor	Width	mm	4	4	4
		Hole	mm	2.5	2.5	2.5
		No of turns	Layers	1	1	1
			per layer	3	3	3
		Res. Per coil	Ohm	0.001195	0.001195	0.001195
	dT=10C	Current	Amp	73.66667	73.66667	57.6666
		Voltage per coil	V	0.088046	0.088046	0.03984
		Power per coil	kW	0.006486	0.006486	0.001328
		Power per magnet	kW	0.051889	0.051889	0.010624
		Water	Bar	0.034499	0.034499	0.00215
		Water circ.	per magnet	1	1	1
		Total power	kW	2.075548	2.075548	0.42496
		Voltage	V	28.17486	28.17486	12.74881
	6 circuits	Voltage	V			
		Current	A			
	dT=10C	Water/magnet	lit/min	0.074357	0.074357	0.015224
	dT=10C	Total water	lit/min	2.974261	2.974261	0.608968
Water if	2	Bar	lit/min/magnet	0.756613	0.756613	0.756613
		Total water	lit/min	30.26453	30.26453	30.26453
Temp rise if	2	Bar	Deg C	0.982755	0.982755	0.201215
				29.74261	29.74261	6.08968
			PS V	28.17486	28.17486	12.74881
			PS A	73.66667	73.66667	33.33333
		Tot	kW	2.075548	2.075548	0.42496
		Number	of PS	1	1	1
		Possible	PS type	SM 70-90	SM 70-90	SM 1540-D

#### 2.5.4.4. Drawing of Octupole Magnet

Some construction drawings for the Octupoles.

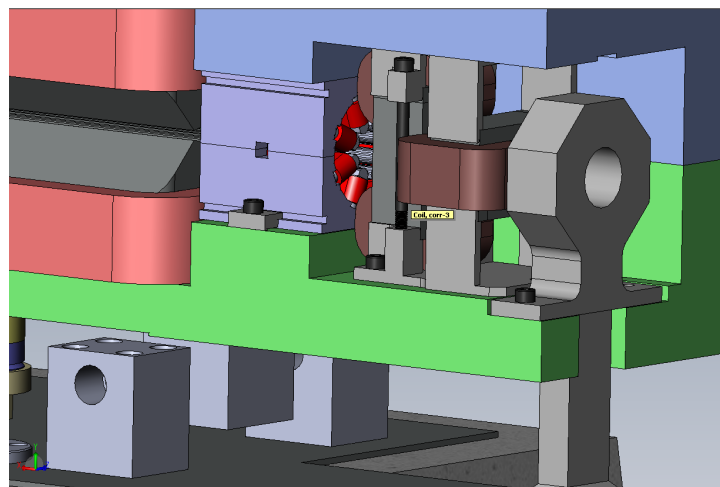
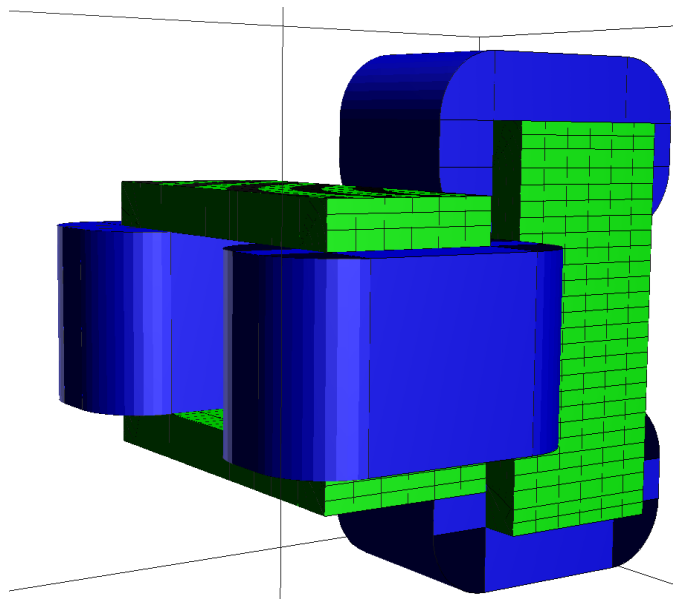


## 2.5.5. Correction Magnets

### 2.5.5.1. Steering Magnets

In each of the 20 supercells of the ring there are 10 orbit correctors for each transverse plane. The correctors are made from thin laminates of steel to allow for fast orbit corrections. The correctors are designed as separate elements of window frame type. There is one element for each plane.

A view of the model magnets is found below.

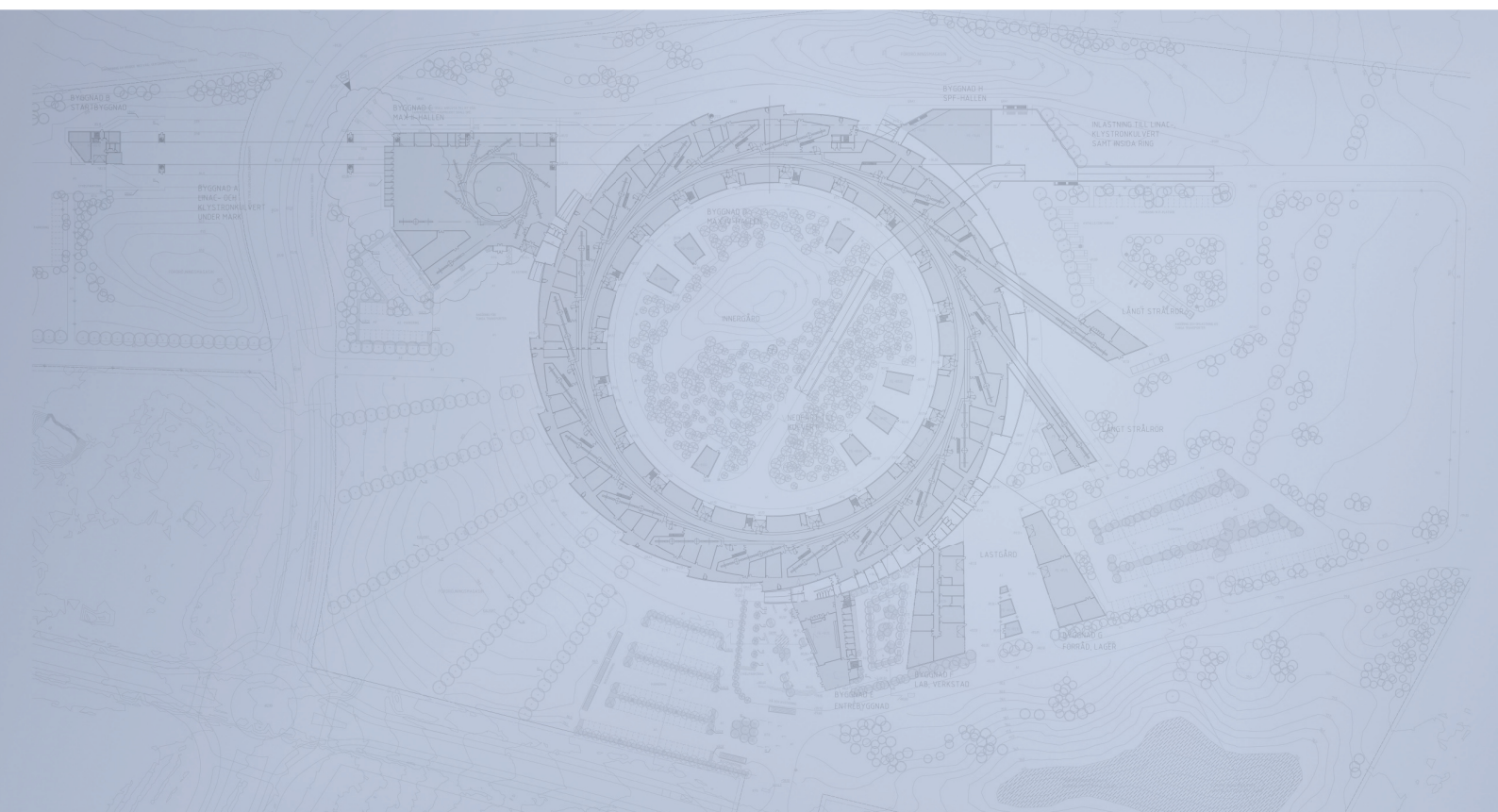


## 2.5.5.2. Coil Currents and Cooling Data

## CORRECTORS

				corr x fast	corr y fast	corr y spec
			Antal	200	199	1
		Energi	GeV	3	3	3
		BR	Tm	10	10	10
		B	Tesla	0.025	0.025	0.025
		Grad	T/m			
		Sext.	T/m^2			
		Oct.	T/m^3			
		R	m			
		L	m	0.04	0.04	0.04
		Gap	m	Injection:	0.04	0.04
		NI	At	100	1082.254	1082.254
		Pole width	m	0.01	0.01	0.01
		Coil length	m	0.162832	0.162832	0.162832
	Conductor	Width	mm	1.420421	1.420421	1.420421
		Hole	mm	0	0	0
		No of	Layers	13	13	13
		turns	per layer	26	26	26
		Res. Per coil	Ohm	0.659912	0.659912	0.659912
		Current	Amp	3	3	3
		Voltage per coil	V	1.979735	1.979735	1.979735
		Power per coil	kW	0.005939	0.005939	0.005939
		Power per magnet	kW	0.011878	0.011878	0.005939
		dT=10C	Water			
	If parallel		Water circ.			
			per magnet	0	0	0
			Total power	2.375682	2.363804	0.005939
			Voltage			
		6 circuits	Voltage			
			Current			
		dT=10C	Water/magnet			
		dT=10C	Total water			
		Water if	2			
			Bar			
	Temp rise if		Total water			
		2	Bar			
			Deg C			
			PS V	3.95947	3.95947	1.979735
			PS A	3	3	3
			Tot	2.375682	2.363804	0.005939
			Number	200	199	1
			Possible			
			PS type	Electrofinn	Electrofinn	Electrofinn

# Detailed Design Report



## Chapter 2

### MAX IV 3 GeV Storage Ring

#### 2.6. The Radio Frequency System

MAX IV Facility





## 2.6. The Radio Frequency System

---

<b>2.6.</b>	<b>The Radio Frequency System.....</b>	<b>2</b>
2.6.1.	General Discussion Motivating the 100 MHz System.....	2
2.6.2.	The 100 MHz RF System.....	4
2.6.3.	Description of the 100 MHz Cavities.....	5
2.6.4.	RF Station Structure.....	10
2.6.5.	Reliability .....	11
2.6.6.	HOM Suppression .....	12
2.6.7.	Control Loops .....	12
2.6.8.	300 MHz Higher Harmonic Cavities .....	13
2.6.9.	Description of Prototype Higher Harm. Cavity .....	14
	References	

## 2.6. The Radio Frequency System

### 2.6.1. General Discussion Motivating the 100 MHz System

The Radio Frequency (RF) system is of vital importance for the performance of the storage rings. It must provide the voltage necessary for the required beam lifetime and it should not induce Higher Order Mode (HOM) instabilities. Other important aspects are the capital and running costs.

Super Conducting (SC) cavities offer a high shunt impedance and a very small contribution of HOM. In order to achieve the necessary voltage and power two cavities have to be used. One spare cavity may be needed for operation safety. One straight section with isolation valves between the cavities is needed in this case. The RF amplifiers could be of the newly developed Inductive Output Tube (IOT) type. These tubes can have a very high efficiency ( $>60\%$ ) and a typical power of 80 kW. Four tubes can be combined to a 320 kW amplifier unit. Special cryogenic knowledge and infrastructure is needed to operate these cavities.

Higher Order Mode-Damped Cavities (Euro cavities) as developed in the EU project HPRI-CT1999-50011 offer a high degree of HOM damping. These cavities can be housed in the short straight sections and the same type of amplifiers as in the SC case can be used.

100 MHz capacity loaded cavities as developed for MAX II and MAX III are also HOM-damped. These can be housed in the short straight sections. The amplifiers are of the tetrode type which offer quite a high efficiency when operated in the class C mode (appr. 70%).

Any of these three systems are able to carry out the function of the RF system needed and the final choice among these will require some additional detailed studies. In Table 1 the characteristics of the three systems are given for reaching an RF-acceptance of 4.5% in a 60% ID equipped ring (energy loss of 756keV/turn) at 500mA. Notable is the fact that to reach 4.5 % energy acceptance, both the SC cavity case and the “Euro” cavity case requires higher electric power than the 100 MHz Capacity loaded cavity case. Bunch length calculations assume a HHC system, which seems to be more complicated for the 500 MHz cases.

Table 1: Comparison of different RF systems for the MAX IV storage ring.

	SC	“Euro”	Cap.loaded
<b>Operating frequency [MHz]</b>	500	500	100
<b>Nr of cavities</b>	2	6	6
<b>Shunt impedance [M<math>\Omega</math>]</b>		<sup>1)</sup> 6.2	3.2
<b>Cooling @ 4 K [W]</b>	200	-	-
<b>Refrigerator power [kW]</b>	200	-	-
<b>Amplifier type</b>	IOT	IOT	Tetrode
<b>Voltage [MV] for 4.5% bucket height</b>	3.5	3.5	1.5
<b>Total RF power [kW]</b>	378	710	500
<b>Electric power [kW]</b>	840	1180	670
<b>Nr of RF amplifiers</b>	2	6	6
<b>Rms bunch length [mm]</b>	15	15	70
<b>Cost</b>	High	Medium	Low
<b>Ease of operation</b>	-	++	++
<b>Resistive wall effect</b>	-	-	+
<b>Higher order mode spectrum</b>	Good	Medium	Good

In the following we study only the 100 MHz Capacity loaded cavity case.

### 2.6.2. The 100 MHz RF System

Table 2 presents the data for two alternative 100 MHz configurations. Both alternatives are for 4.5% RF energy acceptance, however alt I is for a 60% ID equipped ring (360 keV+396 keV per turn), and alt II is for a fully ID equipped machine(360keV+660keV per turn). The reason to study the 60 % case is that for a quite long time after commissioning, the ring will not be fully equipped. However, we must keep in mind that a solution for the 100% equipped case should be in reach after this intermediate stage.

Table 2: Alternative 100 MHz configurations for reaching 4.5% RF energy acceptance.

Alternative	I	II
Energy loss with Ids	756keV	1020keV
Circulating current	0.5A	0.5A
Total beam power	378kW	510kW
Total RF voltage	1.5MV	1.8MV
Number of cavities	6	6
Cavity shunt impedance	3.2Mohm	3.2Mohm
Cu losses	117kW	169kW
Total RF power needed	495kW	679kW

Nr of RF stations	6	6
Nr of transmitters	12	12
Transmitter power	41.5kW	56kW
Power to cavity	83kW	113kW
Cu losses/cav	20kW	28kW
Coupling (beta)	4.2	4.0
Cavity voltage	250kV	300kV
Cavity gap	4cm	5cm
Kilp. Limit	260kV	310kV

**Alt I:** Represents a solution for a 60% ID equipped ring, with the present MAX II/ MAX III cavities.

**Alt II:** Represents a solution for a fully ID equipped ring, with slightly modified MAX II/MAX III cavities.

It has been decided to go for an upgrade of the present 100 MHz main cavity design, that is **alternative II**. By improving the cavity design, we are confident to reach 300 kV in each cavity. This in turn implies that only six cavities are needed to cover the case of a fully ID equipped ring: 1.8 MV equivalent to 4.5 % RF energy acceptance (see table). With the old cavity design we would have needed eight cavities. With the new cavity design five cavities will be sufficient to reach 4.5% RF EA for the intermediate stage of a 60 % ID equipped ring. Two major advantages can be seen: 1) The HOM shunt impedances are reduced 2) the coupling (beta) is reduced.

#### **Some more comments:**

In the chosen alternative II, the natural choice of transmitter power is 60 kW. However, the individual transmitter powers can in principle be halved, by combining four transmitters instead of two, as indicated in the table. There would thus be the possibility to use transmitters of exactly the same type as for MAX II and III. Likewise can the power to the cavity be halved, by splitting up power line somewhere after the circulator (see below) into two branches feeding two coupling loops. In this way the demands on the RF power feed-through to the cavity can be relaxed, if needed.

We have also studied the case where the cavities are made double-sided. One reason to go from single- to double-sided RF cavities is the possibility to decrease the number of cavities and in this way lower the shunt impedance of HOMs. However, it turns out that while the number of HOMs is scaled down a factor of two, their strengths are roughly doubled. That is, no dramatic gain can be expected.

### **2.6.3. Description of the 100 MHz Cavities**

The cavity design for the MAX II/MAX III rings (Alt I) is seen in Fig 1. It is of the capacitor loaded type. Tuning of the cavity is accomplished by changing its capacitance by a slight movement of the left (front) sidewall of the cavity. The stepper motor is seen on top of the cavity and the mechanical transmission system is indicated to the left. Three cavities of this type are currently in operation at the MAX II storage ring and another one is placed in the MAX III ring [1]. The cavities have been conditioned to an accelerating voltage of about 250 kV. The inner profile of this cavity is given in Fig. 2. Its theoretical shunt impedance is 3.5 Mohm and the theoretical Q value is 20500. However surface roughness and ports on the cavity body lower these values by roughly 7%.

The characteristics of this type of cavity have been mapped and the parameter values are presented in Table 3. The fundamental accelerating mode of the electric field is concentrated to the capacitor part at one end of the cavity. This mode has a very small electric field at the other side of the cavity. However, some of the longitudinal HOM:s has a substantial electric field at this back-plate. Damping (capacitive) antennas are introduced at this position to damp the HOM:s while keeping the shunt impedance of the fundamental mode intact. Other HOMs which cannot easily be damped by the capacitive couplers, are planned to be inductively coupled out via one or two loops penetrating from the mantle surface. The input coupler loop was used as such a damping antenna (50 Ohm terminated) when performing the low power HOM measurements presented in Table 3.

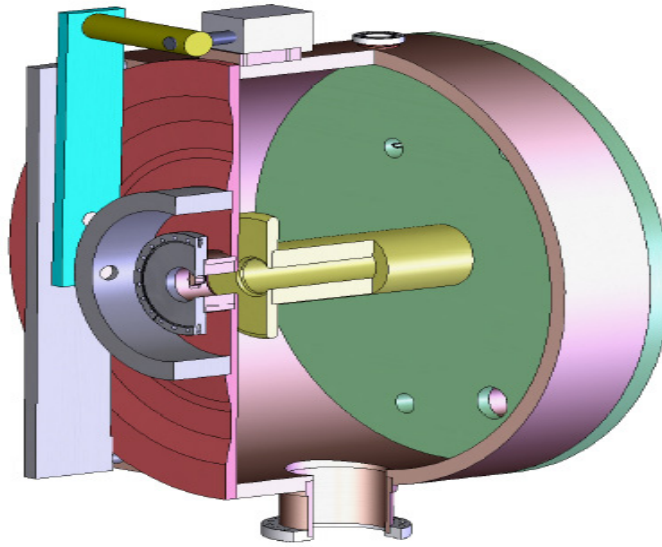


Figure 1: The 100 MHz capacity loaded cavity.

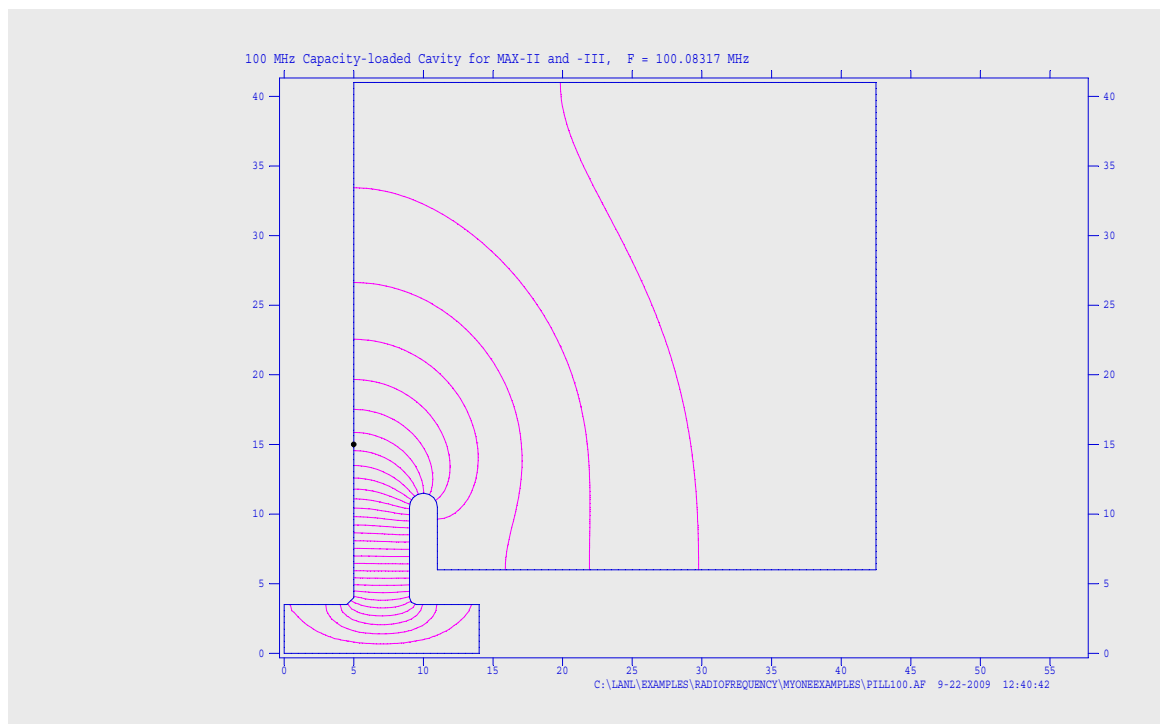


Figure 2: Superfish geometry of the MAX II &amp; III cavity.

Measured Frequency [MHz]	Qtheory	Qmeasured	Rtheory [ $\Omega$ ]	Rscaled [ $\Omega$ ]
<b>100</b>	20500	19000	$3.5 \cdot 10^6$	$3.2 \cdot 10^6$
<b>406.26</b>	32873	300	16000	146
<b>451.99</b>	35980	320	251000	2232
<b>605.79</b>	29680	300	73000	738
<b>801.77</b>	43924	1250	224000	6375
<b>847.01</b>	51080	5750	11000	1238
<b>907.20</b>	39510	700	98000	1736
<b>1187.53</b>	42680	3880	247000	22455
<b>1251.66</b>	57093	1400	29000	711
<b>1435.89</b>	45320	4860	452000	48471

Table 3: MAX II/MAX III type 100 MHz cavity parameters for longitudinal modes.  
Measured Q-values are for the case of two capacitive and one inductive damping antenna.

It is noticeable that the first longitudinal HOM appears at such a high frequency, compared to a usual pillbox cavity where it appears only at a frequency 1.4 times the fundamental. This is achieved by the fact that a capacity loaded cavity is “compressed” in volume. The price to be paid is a lower shunt impedance compare to a pillbox cavity. The longitudinal HOM:s have been mapped up to 1500 MHz. Modes above this frequency will not be activated because of the poor form factor, less than approx. 0.1, given by the long bunch length. Four of the measured modes are still possible candidates to drive coupled bunch mode instabilities (see instability chapter), even with the present damping scheme. Intended enhanced damping of these modes is described below under HOM suppression.

The slightly improved cavities which we are considering in alternative II will have an inner profile shown in Figure 3. They will have an acceleration gap of 5 cm, and dimensions of the inner profile as described in Table 4. The theoretical shunt impedance is 3.5 Mohm and the theoretical Q value is 21000. However surface roughness and ports on the cavity body will lower these values by roughly 7 %.

The cavities should withstand 30 kW of Cu losses, giving a peak acceleration voltage of 300 kV. The deposited power, that has to be cooled away by cooling channels within the copper material, is given in Table 4, for the different surfaces.



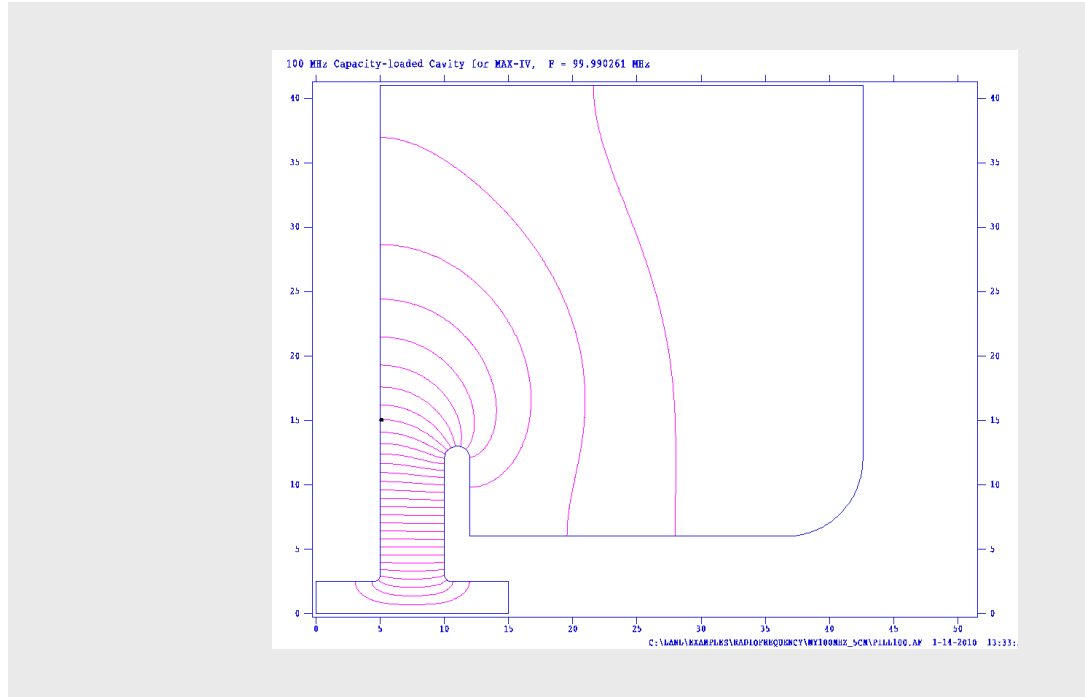


Figure 3: Superfish geometry of the MAX IV cavity.

The cavities should have six extra ports (apart from the two rotational axis ports) with Conflat® type UHV flanges on the mantle surface for pumping, high order mode (HOM) damping coupler and input power coupler. Two measurement ports should be positioned on the back plate. The ports are specified in Table 5.

The tuning mechanism will be of the same type as for our present cavities, with some modifications. The tuning range should be within the reversible deformation region of the copper of the cavity front end plate (minimum  $\pm 1\text{mm}$ ).

Table 4: Inner dimensions and power deposition in the rotationally symmetric 100 MHz cavities.

Surface nr	Z (along axis) [mm]	R (radius) [mm]	P (Deposited power) [kW]
1	0 -> 45	25	0
2	45 -> 50	25 -> 30	0
3	50	30 -> 410	2.5
4	50 -> 426	410	3.1
5	426	410 -> 120	4.7
6	426 -> 366	120 -> 60	4.4
7	366 -> 120	60	13.0
8	120	60 -> 120	1.8
9	120 -> 100	120 -> 120	0.36
10	100	120 -> 30	0.14
11	100 -> 105	30 -> 25	0
12	105 -> 500	25	0

Table 5: Specifications for the cavity ports.

Port type	Diameter [mm]	Flange type	Total length [mm] from Ri	Position Z (or R) [mm]	Position $\phi$ [°], $\phi=0$ is downward*
Slotted, Pump	180	CF 200	100	238	30
Slotted, Pump	180	CF 200	100	238	-30
Open, Power	140	CF 150	60	238	-90
Open, Power	90	CF 100	60	238	90
Open, HOM	90	CF 100	80	238	60
Open, HOM	90	CF 100	80	330	120
Open, Beam	50	CF 63	70 (from Zi)	-20	-
Open, Beam	50	CF 63	-	480	-
Open, Probe	30	CF 40	60 (from Zi)	200 (R)	30
Open, Probe	30	CF 40	60 (from Zi)	200 (R)	-30

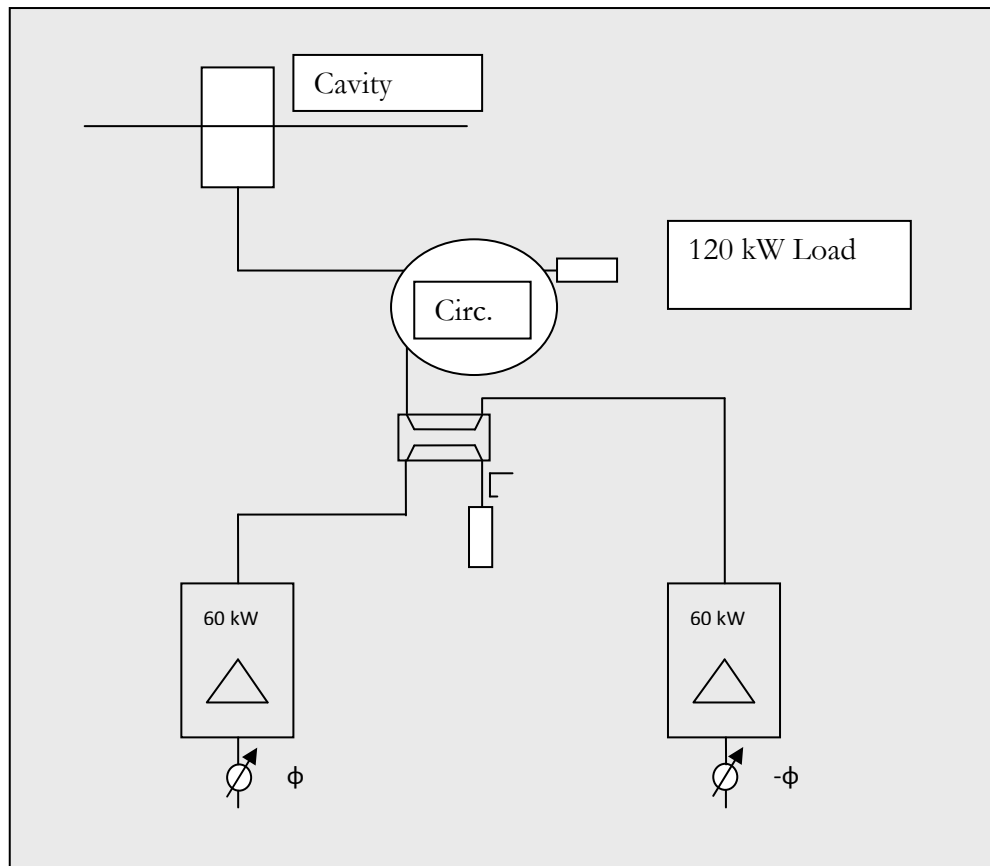
\*When looking from the front end side, positive angles are at positions reached counterclockwise.

## 2.6.4. RF Station Structure

### 2.6.4.1. RF Station

It has been decided to abandon the principle of “pair” cavities, which would allow operating without a circulator. However this scheme is not yet fully tested and, most important, it decreases the RF station modularity (a station would consist of two cavities and four transmitters). The plan is now to combine two 60 kW transmitters to a 120 kW transmission line, equipped with a circulator and a load, and couple this power into one (improved) cavity. As mentioned above, only five such stations will suffice for a 60 % ID equipped machine. Even four stations, giving 1.2 MV will suffice for quite a time. The major advantages are: 1). We will finally have six independent RF stations, which means increased modularity compared to the “pair” cavity case. 2). The advantage of power regulation with phasing can still be utilized, which means higher reliability since the transmitters can run at constant power.

The MAX IV storage ring RF system will consist of six 120 kW RF stations, each one feeding one cavity. The available power from the net should be 200 kW per station, in order to allow for an overall efficiency of 60 %. The output power is fed via a circulator to the cavity. A 120 kW load is connected to the circulator. A 120 kW load is connected to the circulator.



Amplitude and phases of the cavity fields must be kept stable during different steps of machine operations. These require different power levels from the tetrode amplifiers and different tuning of the cavities. The low level RF system will include a frequency loop for each of the six cavities, amplitude and phase loop for each RF station.

We have chosen class C amplifier because of their high efficiency (70%) but they have a very nonlinear relation between input and output power. This non linearity is biggest at very low output power. This makes it difficult to decrease the power to such low level which is needed when beam loading is very low which the case is when the ring is filled after a shut down. One way to do the power regulation is to let the amplifiers deliver full power but direct some of the output power to the dummy load connected to the fourth port of 3 dB hybrid used for combining the power of the two 60 kW transmitters. This is done by changing the phase of the drive signals feeding the two transmitters an equal amount but with opposite sign in order not to change the phase of the output power delivered to the cavities.

## **2.6.5. Reliability**

### **2.6.5.1. Few or many RF Stations**

Our experience from the present MAX facility is that the user community in a better way accept a running machine but with somewhat reduced intensity, compared to a complete shutdown. Many users perform their measurements during short periods like one or two days, and a shutdown of this length of course strikes hard on some unlucky users. Therefore a modular RF system, with several instead of one RF station, seems to be preferable. In this way a failure in one RF station or one cavity might be relatively harmless considering the possibility to tune away or even remove a cavity from the ring.

### **2.6.5.2. Measures to Increase Reliability**

The anticipated scheme of combining the power from two (or four) tetrode amplifiers by help of a 3 dB hybride will make a power regulation possible by phasing, in contrast to a traditional power regulation loop acting on the drive amplifier. The advantage of this is that the tetrode amplifiers can be run with constant output power. This should improve overall phase stabilities between RF stations, and subsequently the reliability of the whole RF system.

The construction procedure of the present MAX II/III cavities involved a welding seem in the mantle surface, which turned out to be the weakest link regarding vacuum properties. We are considering an electron beam welding for our new cavities. If such a welding could be performed for the entire cavity, we could also solve the problem of the too soft copper properties, which are the result of a final soldering the cavity. These technical solutions are under investigation.

For the probe loops in the cavity we are also considering types that are separated from vacuum via a small ceramic window. This would make it easier to supply calibrated signals to the control system, since the probe coupling could be adjusted without breaking vacuum. Furthermore, we would avoid severe shutdowns due to a probe loop failure.

## 2.6.6. HOM Suppression

### 2.6.6.1. Prototype HOM Couplers

The intention is to refine one or two of the capacitive couplers that are situated at the back plane of the cavity. Furthermore, two additional inductive (loop) couplers will be introduced from the mantel surface of the cavity. In these feed-through it will be necessary to apply some kind of stop-band or high pass filter, since the fundamental mode coupling will be too high. We are considering a kind of  $\lambda/4$  filter integrated in a double coaxial structure [2]. Even for 100 MHz such a filter would not be too space demanding. Since the fundamental carries 20 kW the filter attenuation of the fundamental mode need to be in the order of 20 to 30 dB, in order not to cause thermal problems in the filter. In [3] the measured attenuation of the fundamental mode was 22 dB, for the case where a non-filter loop would give  $\beta=6$  for the fundamental. The coupling of the fundamental mode to the external load was in the order of -50 dB, so the load needed only to be specified for the anticipated HOM power.

We should also keep the possibility to use waveguide dampers as developed for the 500 MHz Euro cavities. Those have also been scaled slightly down in cut-off frequency for a scaled cavity version (352 MHz) to be installed in ESRF. We need a cut-off frequency of roughly 400 MHz. HOM damper ports on the cavity should be designed to handle such dampers if this option is chosen.

## 2.6.7. Control Loops

### 2.6.7.1. Resonant Frequency Control

Six frequency loops, one for each cavity, will keep the cavities tuned by compensating for both beam loading and temperature effects. Cavity tuning is performed by an elastic deformation of the cavity in the direction of its axial length. This is realised by means of a mechanism, driven by a stepper motor, which changes the width of the gap of the capacitor in the cavity and therefore its frequency. The motor is controlled in closed loop with the output signal from a phase detector, which is proportional to the phase difference between the cavity incident signal from a directional coupler and cavity voltage from monitoring pick-up in the cavity. A phase shifter in the control loop makes it possible to adjust the phase offset.

### 2.6.7.2. Phase Control

A phase control loop compensates for phase changes in the amplification chain. The RF signal from the master oscillator and the cavity phase are compared in phase and the error signal drives through a PID regulator an electronic phase shifter. The relative phases between the stations are controlled by a mechanical phase shifter at the input of each of the stations amplifier stages.

### 2.6.7.3. Voltage Control

The amplitude control loop adjusts the relative phase difference between the drive of the two transmitters in the RF system. By this the amplifiers can deliver full power but some fraction of the output power will be directed to the dummy load connected to the fourth port of 3 dB hybrid.

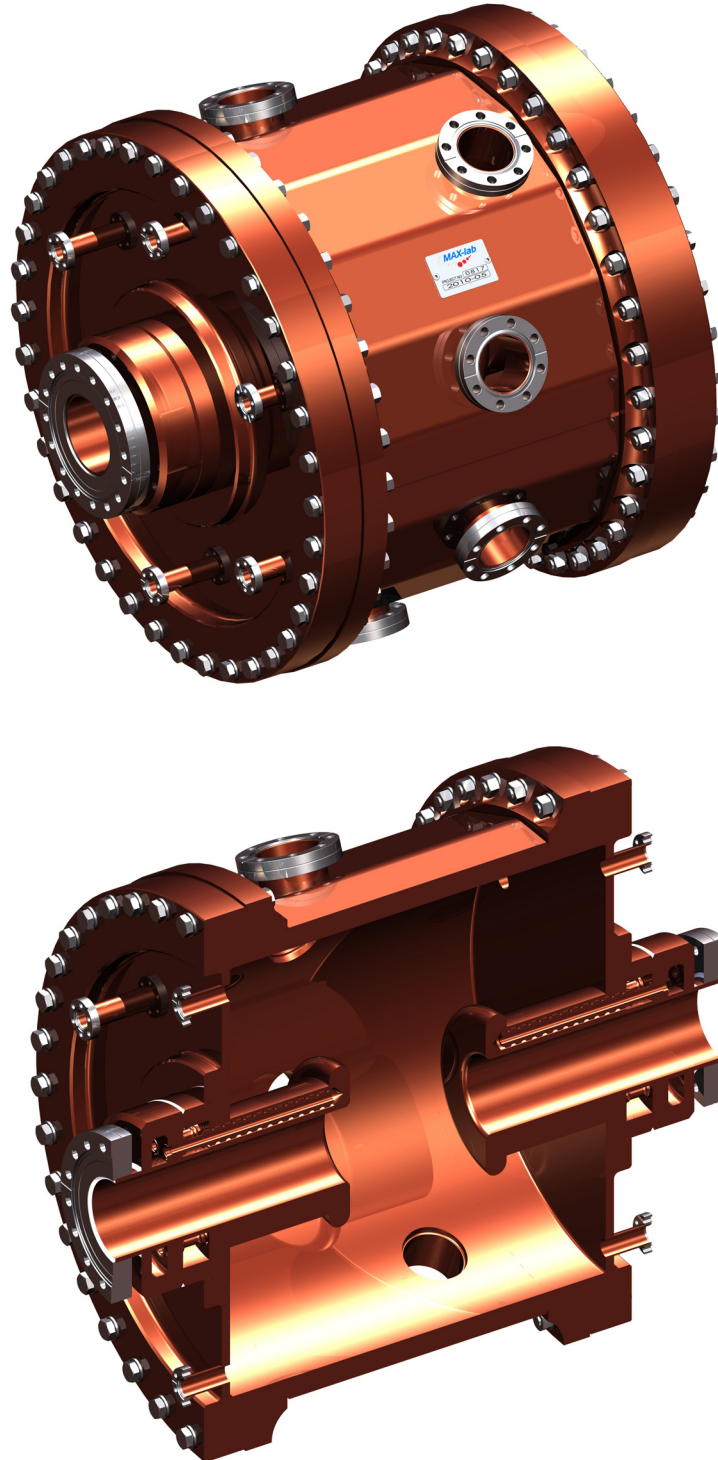
### 2.6.8. 300 MHz Higher Harmonic Cavities

A rough estimate of the required voltage for the higher harmonic cavities (HHC) are 500 kV that is one third of the main cavity voltages. However, due to the synchronous phase angle of 30 degrees in the case of 756 keV losses per turn and a main RF voltage of 1500 kV, a more precise number is 424 kV. This includes the assumption of a total shunt impedance for the HHC of 15 Mohm ( $R=U^2/P$ ), and that they are passively driven by the beam itself (additional 29 keV loss per turn). The form factor influence on the tuning angle of the Landau cavities has been taken into account in a self-consistent way. This gives an rms bunch length of 68 mm, for a symmetric potential well. The bunch shape is rather non-Gaussian, and the  $FWHM/2.355=85$  mm. The achievable rms bunch length increases slightly (2mm/5 Mohm) with increasing shunt impedance, in the 5-20 Mohm range. Above this range, no considerable gain is made. 15 Mohm seems to be a safe choice to stay Robinson stable regarding the double RF system, even for a current of only 200 mA.

The natural rms bunch length for the case studied is 13 mm, and the synchrotron frequency 1.08 kHz. The double RF will create a spread in synchrotron frequencies, thus providing for Landau damping.

The prototype HHC (see below) is of the same capacity loaded type as the main cavities. This is helping us to push up the HOMs in frequency, and making the HOM suppression easier. The shunt impedance for this type of HHCs is 5 Mohm. By choosing three such cavities, each would pull 4 kW out of the beam. We could also think of a higher number (if the HOMs are sufficiently damped) in order to decrease the power consumption, since our experience of several passive cavities are good (phasing problems are not there, because of the passive nature).

### 2.6.9. Description of Prototype Higher Harm. Cavity.



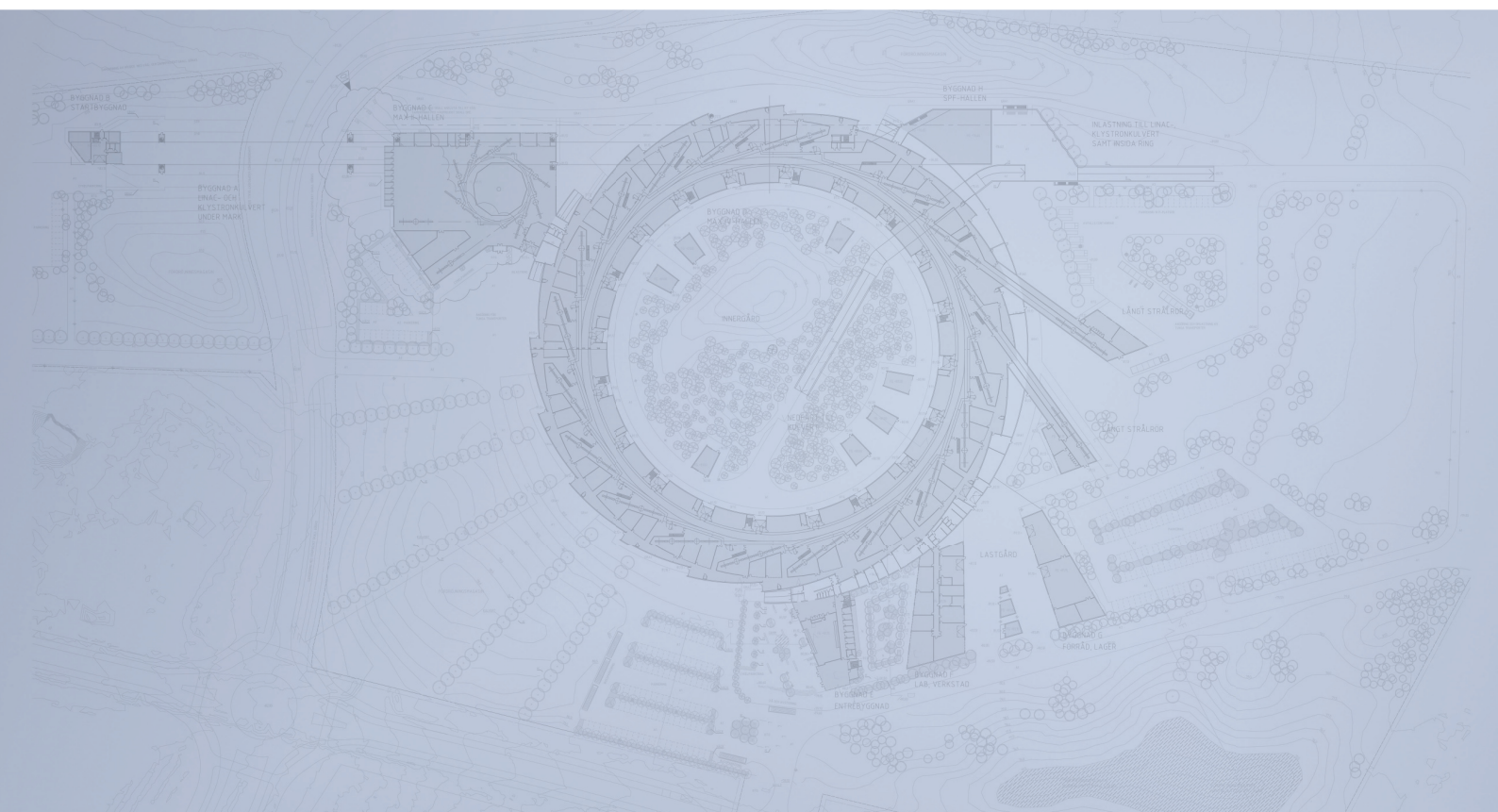
## References

- [1] Andersson et al, "The 100 MHz RF System for MAX-II and MAX-III", EPAC 2002.
- [2] B. Dwersteg et al, "HOM Couplers for normal conducting Doris 5-cell cavities", IEEE Trans. Nucl. Sci. 32, 1985.





# Detailed Design Report



## Chapter 2

### MAX IV 3 GeV Storage Ring

#### 2.7. Injection

MAX IV Facility



## 2.7. Injection

---

<b>2.7.</b>	<b>Injection.....</b>	<b>2</b>
2.7.1.	Septum .....	5
2.7.2.	Transfer Linac M4 Ring .....	10

## 2.7. Injection

---

The beam from the linac is entering the ring tunnel at an vertical angle of 25 deg. Close to the ring a bending magnet reduces the beam angle to 5deg. The septum magnet finally bends the beam into the plane of the ring. At this point the distance from the normal stored beam center and the injected beam is about -13.5 mm.

During injection the stored beam is moved to a position of about -8mm that is 2mm inside the septum at -10 mm. The movement of the stored beam is made by a four kicker system as is shown in figure 1,2 below.

The first kicker is positioned before the half end dipole and the defocusing of this magnet is helpful. The kicker is about 500mm long and kicks the beam about 3 mrad. The beam exits the dipole with a rather large amplitude and turns to a slight focused beam by the end quadrupole. The second kicker in the injection straight now apply a small negative kick to get the beam move at a constant amplitude of about 8mm. This kicker is much shorter (100 mm) and kicks 0.3 mrad. The other two kickers after the septum magnet just invert the process.

The injected beam thus gets oscillation amplitude of 5.5 mm and this amplitude is conserved until damped out. The above discussion applies to the case of a short injected pulse.

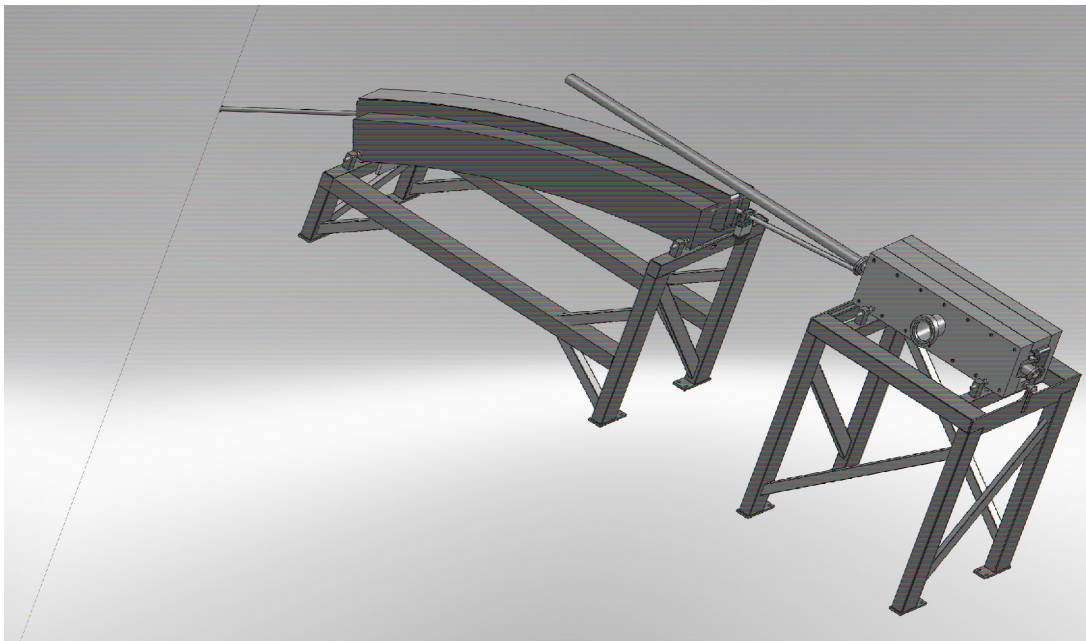
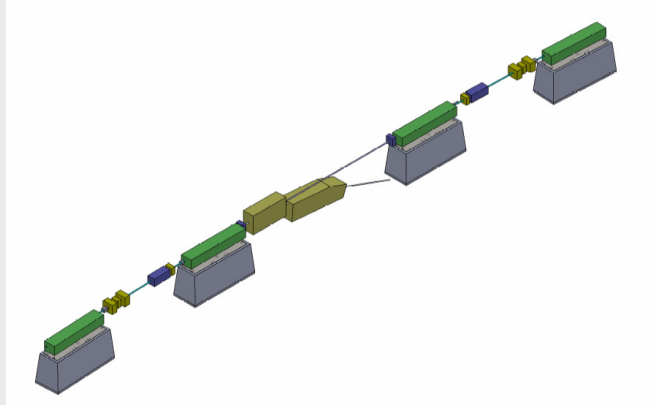


Figure 1.

Figure 2.



The amplitude of the kickers is calculated by tracking the kicked beam through the four kicker system. The result is shown in figure 3.

Amplitudes for the kickers are given for a bump of -8 mm.

K1:	2.688 mrad
K2:	0.180 mrad
K3:	0.180 mrad
K4:	2.688 mrad

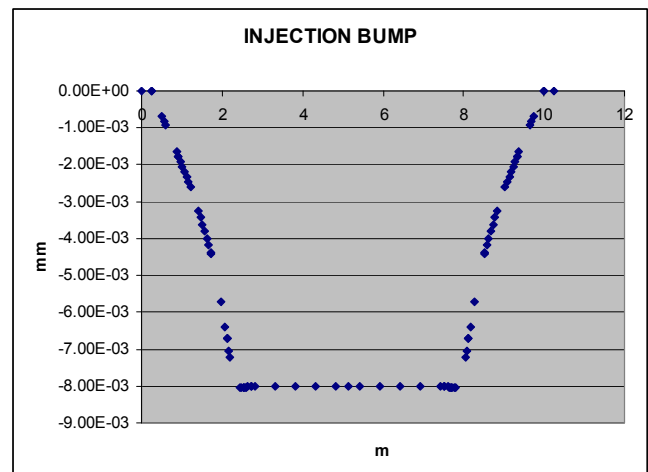


Figure 3.

With the kicker bump set the incoming beam at -13.5 mm is tracked for a full turn around the machine.

When the beam has completed one turn the injection bump is reduced to zero and the beam oscillation will remain at the same amplitude until damped out. The one turn injection is shown in figure 4. As can be seen in the figure the final maximum amplitude is close to 6mm compared to 5.5 mm obtained by the Linear approximation.

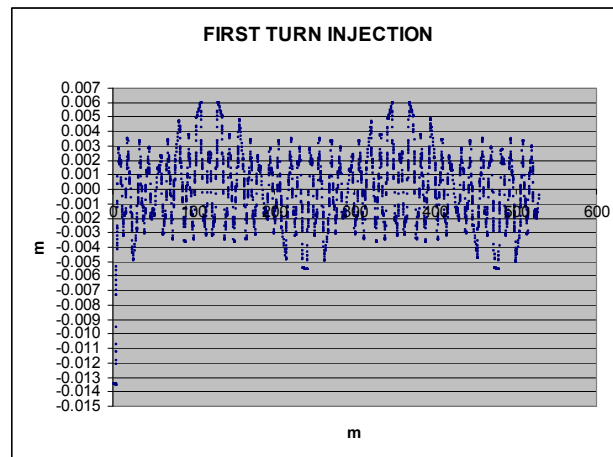


Figure 4.

The incoming beam amplitude of -13.5 mm require special beam tube design for the first few elements.

A closer view for the first 5m is found in figure 5.

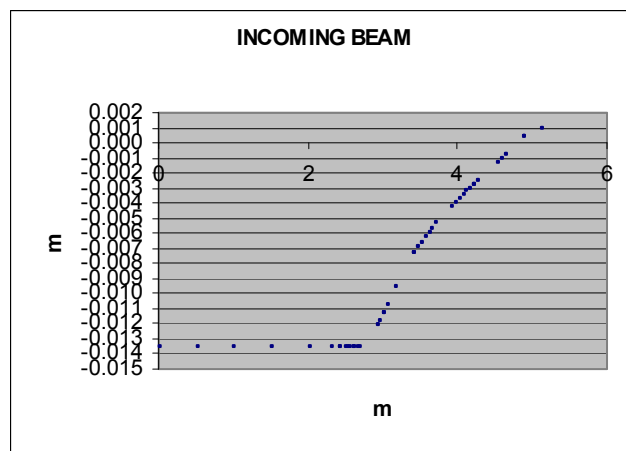


Figure 5.

## 2.7.1. Septum

### 2.7.1.1. MAX IV Injection Septum Magnet

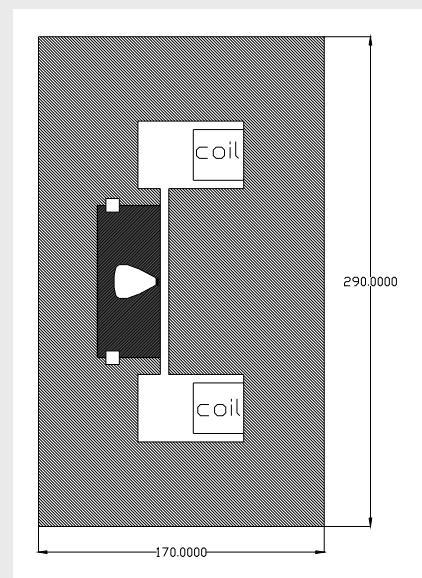
The beam from the linac enters the ring from below by an angle of 25 deg. The electron beam is first bent 20 deg. before the septum by a normal vertical bending magnet. The final 5 deg., to bend into the median plan of the ring is done by the septum magnet. The septum design follows the design used for the MAX I and MAX III rings (Ref .1.).

#### The septum magnet data:

Bending magnetic field	0.85 T
Bend angle	5.0 deg.
Bending radius	11.765 m
Septum straight length	1.02536 m
Injection channel gap	5 mm
Septum thickness	2.5 mm
Septum distance from closed orbit	10 mm
Vertical aperture at closed orbit	+/- 7.5 mm

In figure 6,7 below a transverse cut of the septum is shown with the 5mm injection-channel and the small asymmetric stored beam tube that is part of the ring.

Figure 6: Transverse cut of septum magnet.





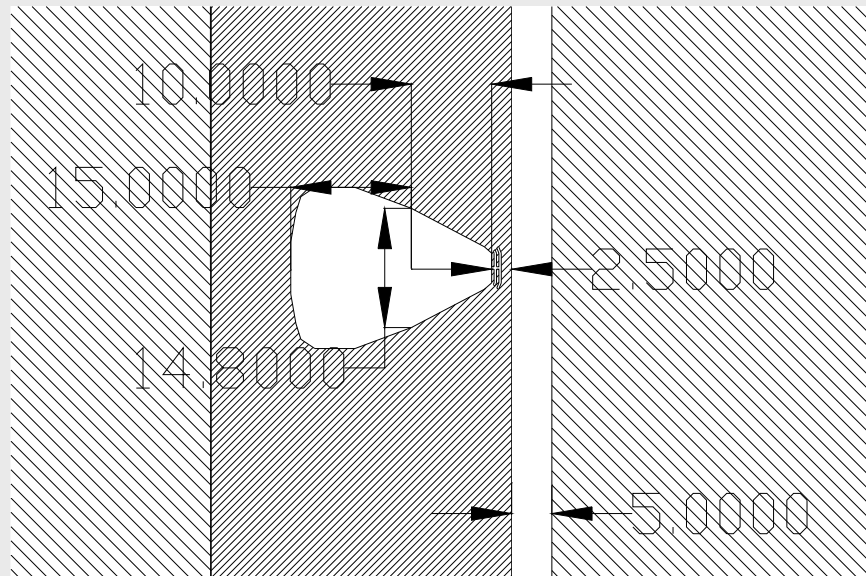


Figure 7: Central part of the septum magnet.

The 2.5 mm septum with filter is designed to give a minimum of leak field into the stored beam tube and the form of the tube is designed to make the leak field dependence linear. A plot of the horizontal leak field (vertical is zero due to symmetry) is found in figure 9.

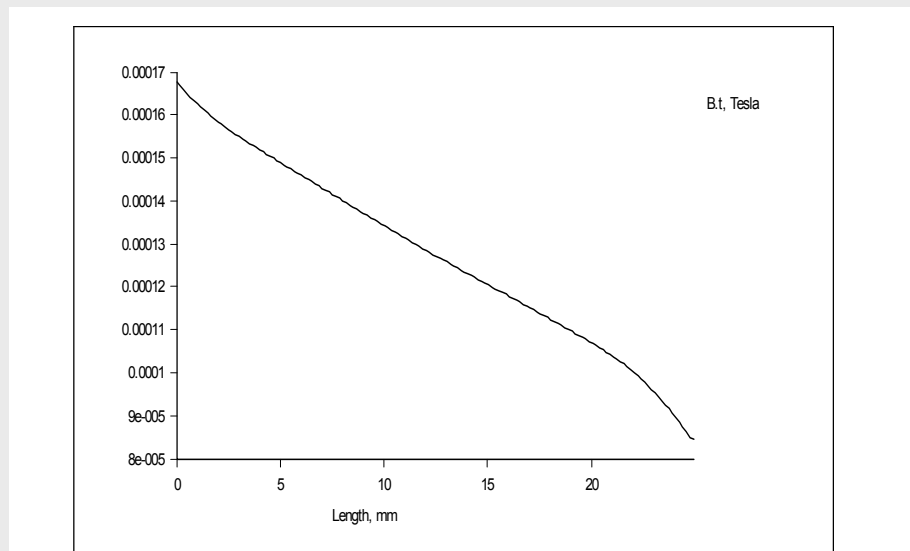


Figure 8: Plot of horizontal leak field ( 25mm is at septum position).

The almost linear leak field shows a dipole part of about 1.2 gauss at the stored beam position. (15 mm). The quadrupole field part is 0.0032 T/m. The effective length of those leak field components are about 0.3 m due to the curvature of the injection channel.

#### 2.7.1.1.1. Experience from MAX I and MAX III Septum Magnets

Figure 9. shows a picture of the central part of the MAX I septum magnet. The leak field from this magnet was carefully measured and it was concluded that the main contribution to the leak field integral was from the ends of the magnet. The total integral was about 0.5 Tmm.

The total kick in case of MAX IV is estimated to 0.05 mrad without any linearization and further shielding.

We will later add a report on 3D calculations for the MAX IV septum magnet, with the intension to be able to further reduce the end fields by shielding.

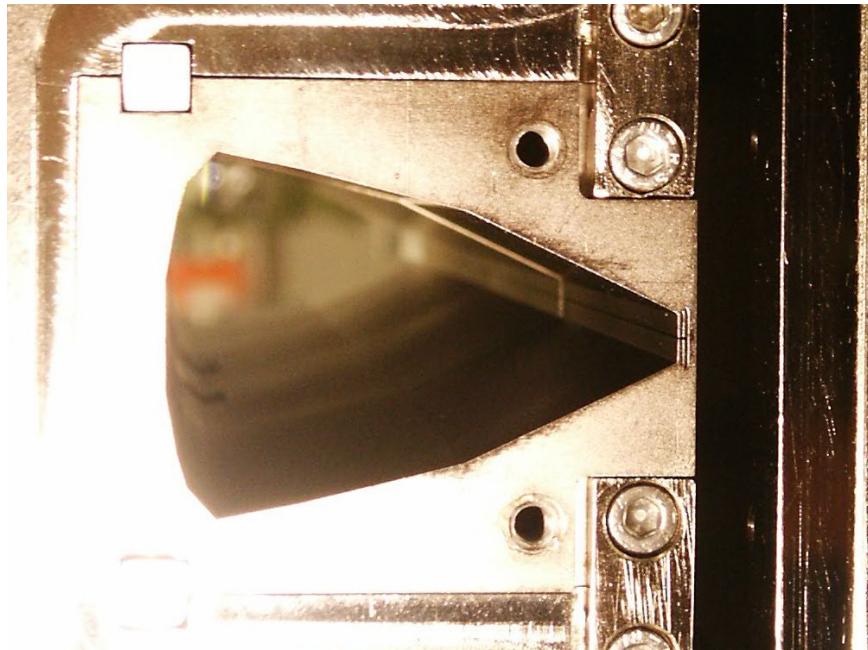


Figure 9: Photo of central part of MAX I septum.

### 2.7.1.2. MAX IV Injection Septum Magnet Leak Fields

As mentioned above the main part of leak fields in the stored beam region comes from the end fields of the magnet.

A 3D model is set up (Figure 10.) to study this effect. The main part of the magnet is simplified resulting in large inside leak fields.

The end fields are however supposed to be well modeled. The results of the calculation show that the leak fields are considerably reduced if the stored beam tube is extended at least 25mm outside the pole, thus shielding the stored beam.

Keeping the septum coil as close as possible to the magnet gap also helps.

The calculations for the magnet are made in a short model magnet where one end of the magnet is not shielded for comparisons. Figure 10. shows the model magnet. The calculated fields are shown for the magnet gap and for the stored beam channel close to the septum respectively.

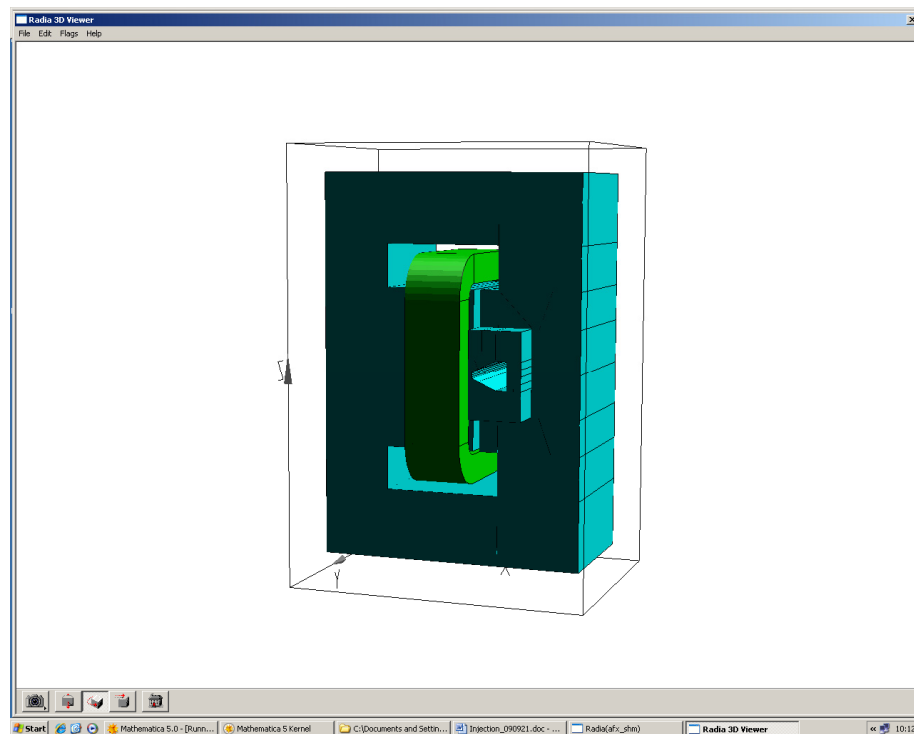


Figure 10: Simplified model magnet without filter in the main magnet region.

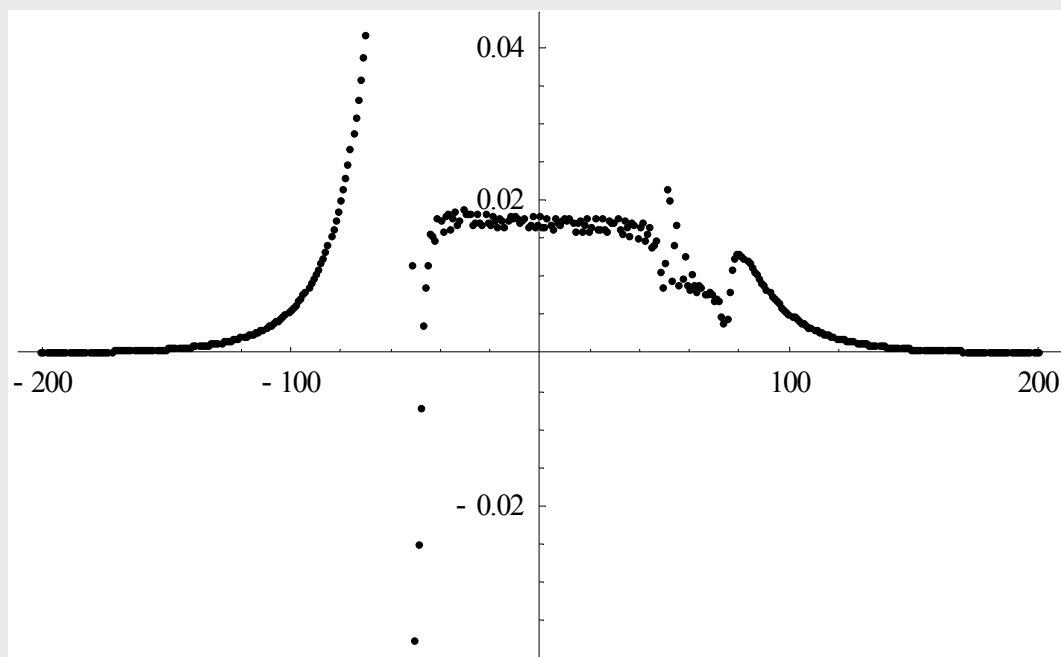


Figure 11: Leak fields on non shielded side, central part and shielded end respectively.

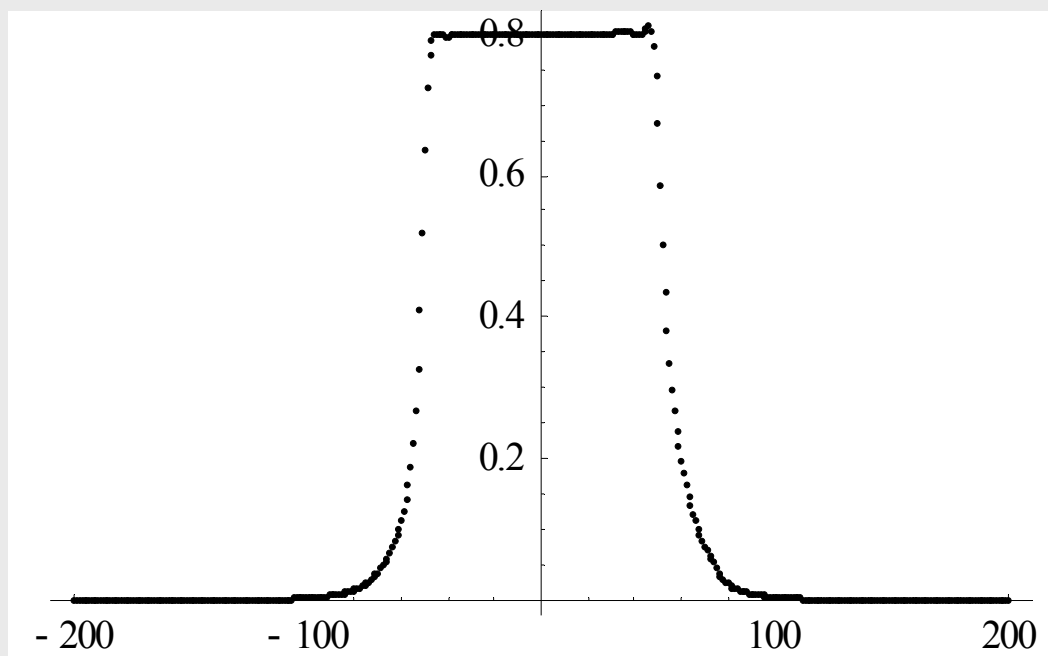


Figure 12: Field in the high field region.

## 2.7.2. Transfer Linac M4 Ring

The beam from the linac is transferred to the ring by an achromatic bend in the vertical plane. The total bend angle is 25 deg. The transport line passes through the 1 meter thick floor between the linac tunnel and the storage ring plane.

The situation is shown in figure 13.

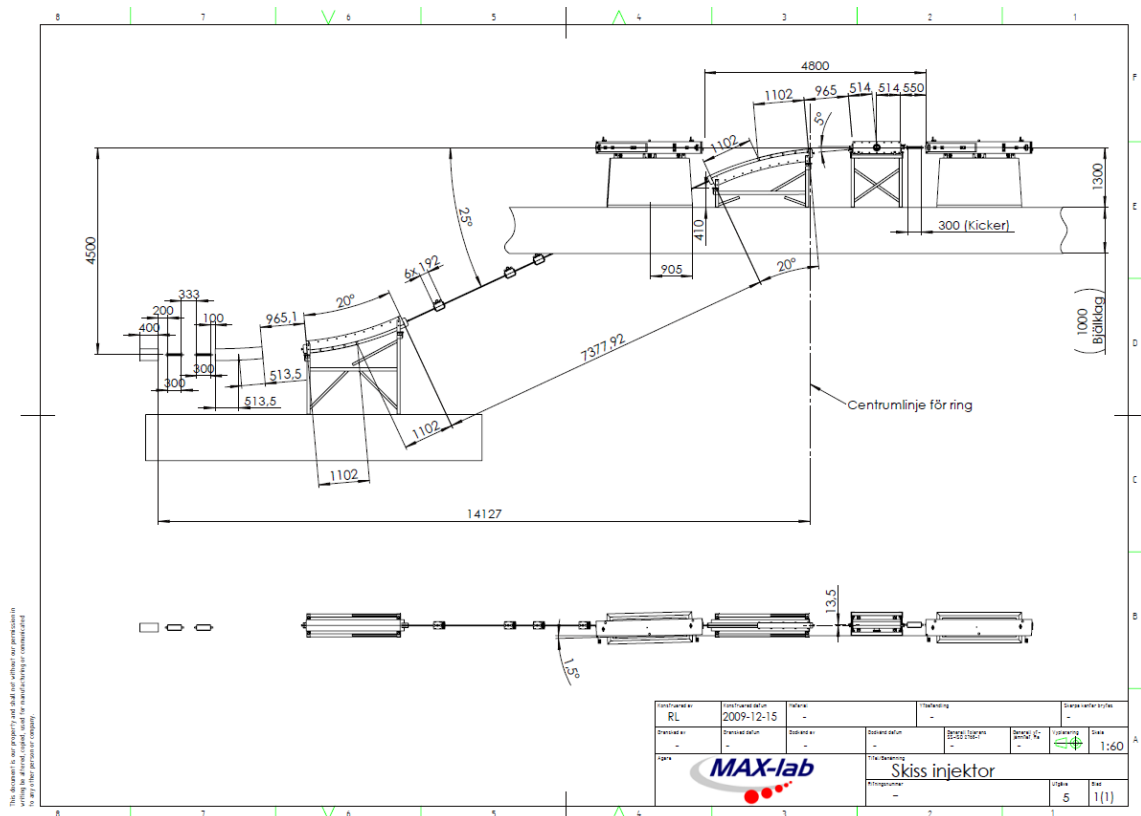


Figure13: Linac- Ring transfer.

It can not be avoided that some of the focusing elements are inside the thick floor. Space enough must be provided for those quadrupoles, not only for the physical size but also for the alignment procedure, cooling water and electrical connections. The optical data for the transfer line are given below.

It is assumed that the beta functions from the linac at the beginning of the transfer are 10 m in both directions. The lattice is rather flexible and beta functions can be changed at least 50%. Presently the lattice is symmetric with three families of quadrupoles.

**Transport section up to m4 25 deg.**

```

TITLE
    TRANSPORT DIPOLUP TO MAX IV
    UTRANSPORT

5
    VSEPS: SBEND,L=1.027,ANGLE=5., E1=0,E2=0,&
    FINTX=0.5,HGAP=0.0025,FINT=0.5,TILT=90
    VDIPS: SBEND,L=2.18167,ANGLE=20., E1=0,E2=0,&
    FINTX=0.5,HGAP=0.0075,FINT=0.5,TILT=90

10    VDIP: SBEND,L=2.18167,ANGLE=-20., E1=0,E2=0,&
    FINTX=0.5,HGAP=0.0075,FINT=0.5,TILT=90
    VSEP: SBEND,L=1.027,ANGLE=-5., E1=0,E2=0,FINT=0.5,HGAP=0.0025,&
    FINTX=0,TILT=90
    QVFD: QUADRUPOLE,L=0.1, K1=-4.3666

15    QHF:QUADRUPOLE,L=0.1, K1=4.92704
    QVF:QUADRUPOLE,L=0.1, K1=-4.8734
    F1: DRIFT,L=1.5
    F2: DRIFT,L=1.5
    F3: DRIFT,L=0.5

20    F4: DRIFT,L=0.48
    F5: DRIFT,L=0.5
    FL: DRIFT, L=0.1
    FD: DRIFT,L=0.25
    FX1: DRIFT,L=-0.000

25    FX2: DRIFT,L=0.000
    BLT: LINE=(F5,QVFD,QVFD,F2,QHF,QHF,F3,QVF,QVF,F4)
    B1: LINE=(VSEPS,F1,VDIPS,BLT)
    B2: LINE=(-BLT,VDIP,F1,VSEP)
    TOT: LINE=(B1,B2)

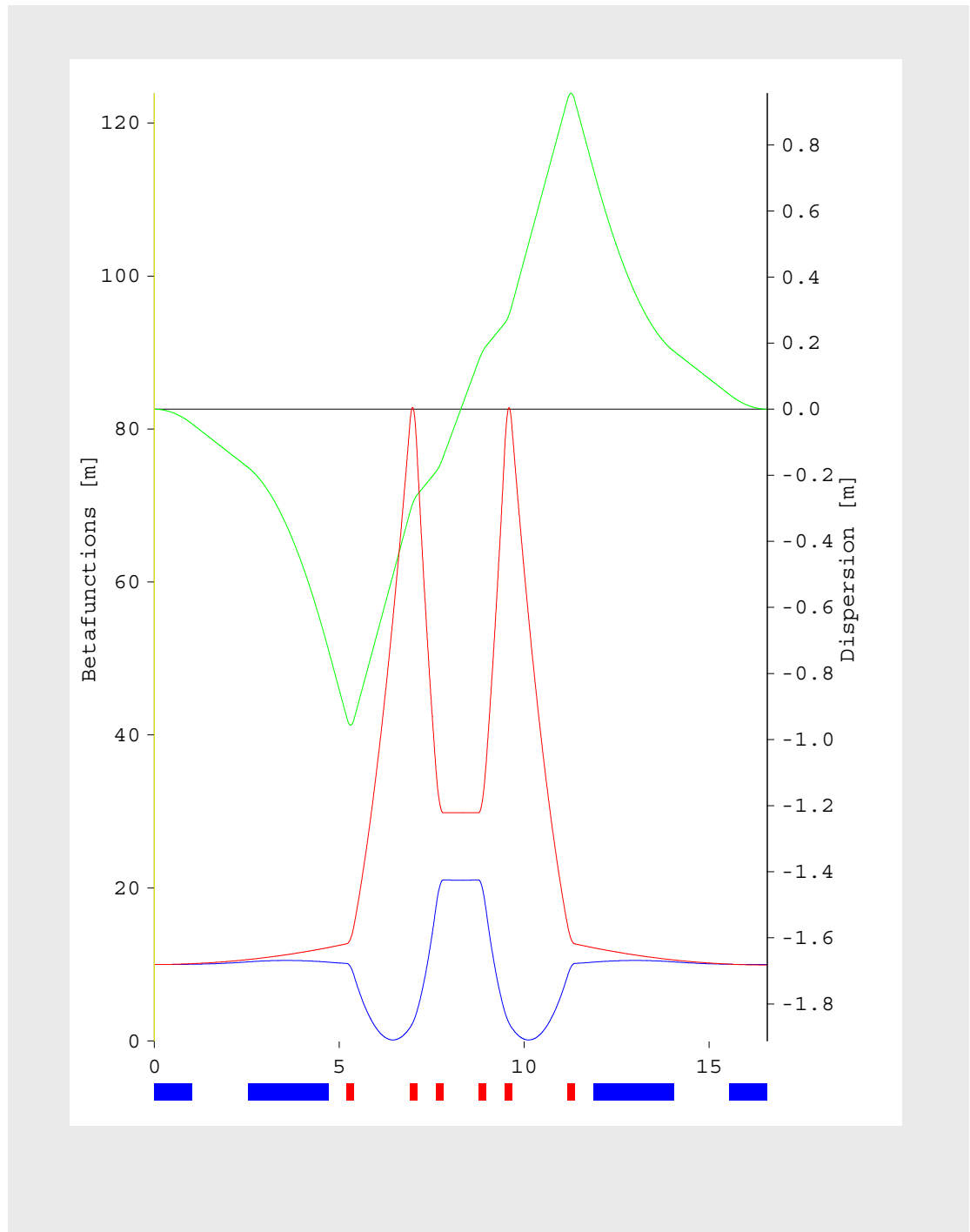
30    USE,TOT
    DIMAT

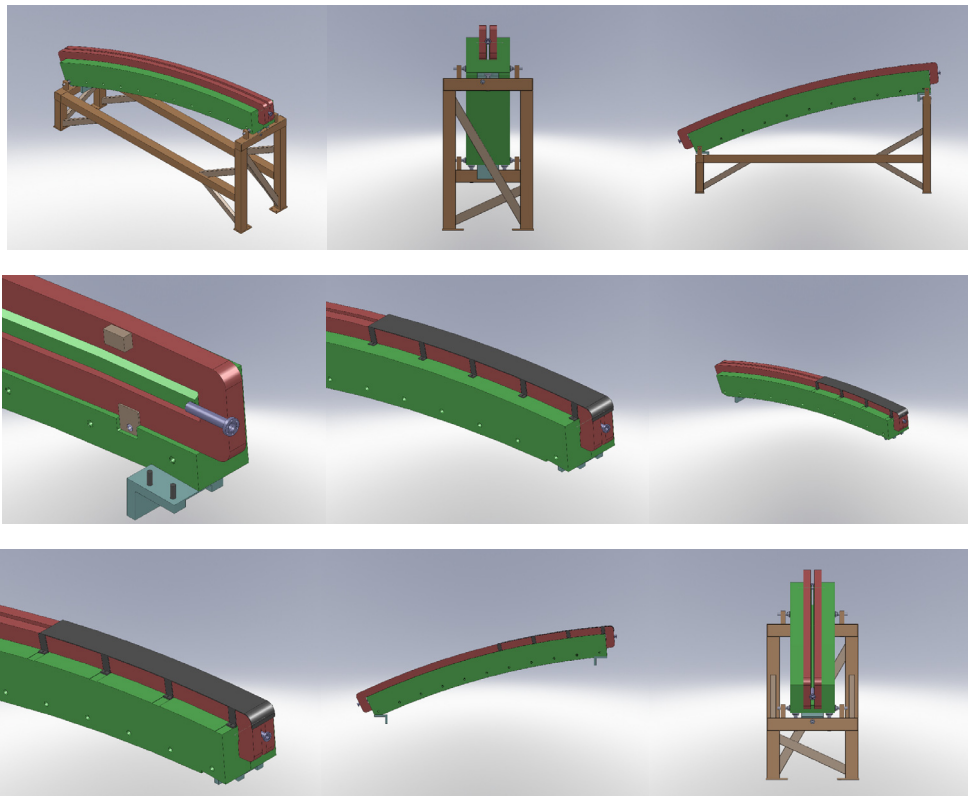
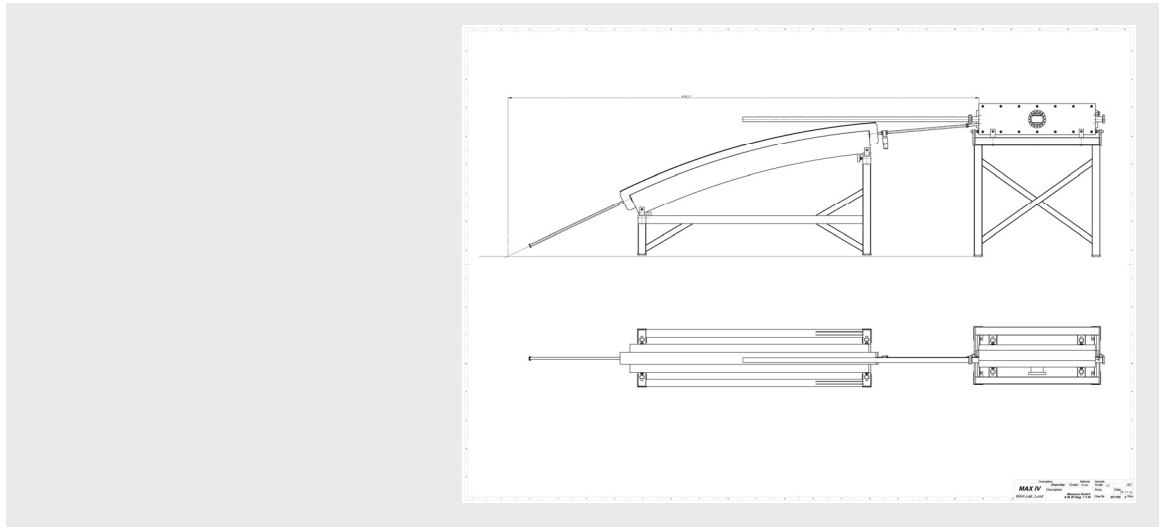
```

ELEMENT	#	BETAX	ALPHAX	BETAY	ALPHAY	ETAX	ETAPX	ETAY	ETAPY			
\$\$INITIAL\$\$	0	10.0000	0.0000	10.0000	0.0000	0.0000	0.0000	0.0000	0.0000	0.00000	0.00000	0.000
VSEPS	1	10.1058	-0.1031	10.0292	-0.0284	0.0000	0.0000	0.0448	0.0872	0.01629	0.01633	1.027
F1	2	10.6400	-0.2531	10.3390	-0.1781	0.0000	0.0000	0.1755	0.0872	0.03939	0.03986	2.527
VDIPS	3	12.2296	-0.4758	10.3010	0.1948	0.0000	0.0000	0.7282	0.4143	0.07002	0.07307	4.709
F5	4	12.7305	-0.5260	10.1314	0.1444	0.0000	0.0000	0.9353	0.4143	0.07640	0.08086	5.209
QVFD	5	13.4039	-6.3051	9.6683	4.4185	0.0000	0.0000	0.9561	-0.0001	0.07763	0.08246	5.309
QVFD	6	15.3266	-13.2016	8.4150	7.9320	0.0000	0.0000	0.9353	-0.4146	0.07874	0.08421	5.409
F2	7	80.6633	-30.3562	1.7090	-3.4614	0.0000	0.0000	0.3134	-0.4146	0.08554	0.51949	6.909
QHF	8	82.7400	9.9304	2.5871	-5.4628	0.0000	0.0000	0.2793	-0.2692	0.08573	0.52712	7.009
QHF	9	76.8203	48.2918	3.9666	-8.5587	0.0000	0.0000	0.2591	-0.1371	0.08593	0.53213	7.109
F3	10	36.1212	33.1064	17.2051	-17.9182	0.0000	0.0000	0.1906	-0.1371	0.08744	0.54177	7.609
QVF	11	31.3805	15.0684	20.0326	-9.8966	0.0000	0.0000	0.1723	-0.2259	0.08791	0.54262	7.709
QVF	12	29.8961	0.0158	21.0364	0.0230	0.0000	0.0000	0.1458	-0.3037	0.08844	0.54339	7.809
F4	13	29.8887	-0.0003	21.0252	0.0002	0.0000	0.0000	0.0000	-0.3037	0.09099	0.54702	8.289
F4	14	29.8967	-0.0164	21.0360	-0.0227	0.0000	0.0000	-0.1458	-0.3037	0.09355	0.55065	8.769
QVF	15	31.3812	-15.0693	20.0323	9.8968	0.0000	0.0000	-0.1724	-0.2258	0.09407	0.55142	8.869
QVF	16	36.1222	-33.1078	17.2047	17.9181	0.0000	0.0000	-0.1906	-0.1370	0.09455	0.55227	8.969
F3	17	76.8232	-48.2941	3.9664	8.5585	0.0000	0.0000	-0.2591	-0.1370	0.09606	0.56191	9.469
QHF	18	82.7433	-9.9313	2.5869	5.4627	0.0000	0.0000	-0.2793	-0.2692	0.09626	0.56692	9.569
QHF	19	80.6665	30.3568	1.7088	3.4613	0.0000	0.0000	-0.3134	-0.4146	0.09645	0.57456	9.669
F2	20	15.3280	13.2022	8.4162	-7.9329	0.0000	0.0000	-0.9353	-0.4146	0.10324	1.00984	11.169
QVFD	21	13.4052	6.3051	9.6697	-4.4188	0.0000	0.0000	-0.9561	-0.0001	0.10436	1.01159	11.269
QVFD	22	12.7319	0.5255	10.1327	-0.1441	0.0000	0.0000	-0.9353	0.4143	0.10559	1.01319	11.369
F5	23	12.2315	0.4754	10.3021	-0.1945	0.0000	0.0000	-0.7281	0.4143	0.11197	1.02098	11.869
VDIP	24	10.6438	0.2527	10.3387	0.1784	0.0000	0.0000	-0.1755	0.0872	0.14259	1.05418	14.050
F1	25	10.1106	0.1028	10.0280	0.0287	0.0000	0.0000	-0.0448	0.0872	0.16568	1.07771	15.550
VSEP	26	10.0053	-0.0001	9.9982	0.0003	0.0000	0.0000	0.0000	0.0000	0.18196	1.09405	16.577

#	NAME	S	X	Y	Z	THETA	PHI	PSI
1	VSEPS	-1.0270000000	0.0007815693	-.0447760770	-1.0256969875	-.0874841538	4.9992365372	1.0038190574
2	F1	-2.5270000000	0.0030631855	-.1754897797	-2.5199890347	-.0874841538	4.9992365372	1.0038190574
3	VDIPS	-4.7086700000	0.0128678666	-0.7371995817	-4.6166378847	-0.4662736907	24.9959308687	1.1033535600
4	F5	-5.2086700000	0.0165557194	-0.9484765292	-5.0697917782	-0.4662736907	24.9959308687	1.1033535600
5	QVFD	-5.3086700000	0.0172932900	-0.9907319187	-5.1604225569	-0.4662736907	24.9959308687	1.1033535600
6	QVFD	-5.4086700000	0.0180308605	-1.0329873082	-5.2510533356	-0.4662736907	24.9959308687	1.1033535600
7	F2	-6.9086700000	0.0290944190	-1.6668181506	-6.6105150162	-0.4662736907	24.9959308687	1.1033535600
8	QHF	-7.0086700000	0.0298319896	-1.7090735401	-6.7011457949	-0.4662736907	24.9959308687	1.1033535600
9	QHF	-7.1086700000	0.0305695602	-1.7513289296	-6.7917765736	-0.4662736907	24.9959308687	1.1033535600
10	F3	-7.6086700000	0.0342574130	-1.9626058770	-7.2449304671	-0.4662736907	24.9959308687	1.1033535600
11	QVF	-7.7086700000	0.0349949836	-2.0048612665	-7.3355612458	-0.4662736907	24.995930868	1.1033535600
12	QVF	-7.8086700000	0.0357325541	-2.0471166560	-7.4261920245	-0.4662736907	24.9959308687	1.1033535600
13	F4	-8.2886700000	0.0392728929	-2.2499425256	-7.8612197623	-0.4662736907	24.9959308687	1.1033535600
14	F4	-8.7686700000	0.0428132316	-2.4527683952	-8.2962475000	-0.4662736907	24.9959308687	1.1033535600
15	QVF	-8.8686700000	0.0435508022	-2.4950237847	-8.3868782787	-0.4662736907	24.9959308687	1.1033535600
16	QVF	-8.9686700000	0.0442883727	-2.5372791741	-8.4775090574	-0.4662736907	24.9959308687	1.1033535600
17	F3	-9.4686700000	0.0479762256	-2.7485561216	-8.9306629510	-0.4662736907	24.9959308687	1.1033535600
18	QHF	-9.5686700000	0.0487137961	-2.7908115111	-9.0212937297	-0.4662736907	24.9959308687	1.1033535600
19	QHF	-9.6686700000	0.0494513667	-2.8330669006	-9.1119245084	-0.4662736907	24.9959308687	1.1033535600
20	F2	-11.1686700000	0.0605149252	-3.4668977430	-10.4713861889	-0.4662736907	24.9959308687	1.1033535600
21	QVFD	-11.2686700000	0.0612524958	-3.5091531325	-10.5620169676	-0.4662736907	24.9959308687	1.1033535600
22	QVFD	-11.3686700000	0.0619900663	-3.5514085220	-10.6526477463	-0.4662736907	24.9959308687	1.1033535600
23	F5	-11.8686700000	0.0656779192	-3.7626854694	-11.1058016399	-0.4662736907	24.9959308687	1.1033535600
24	VDIP	-14.0503400000	0.0754826002	-4.3243952715	-13.2024504899	-0.0874841538	4.9992365372	1.0038190574
25	F1	-15.5503400000	0.0777642164	-4.4551089742	-14.6967425370	-0.0874841538	4.9992365372	1.0038190574
26	VSEP	-16.5773400000	0.0785457857	-4.4998850512	-15.7224395245	0.0000000000	0.0000000000	1.0000000000

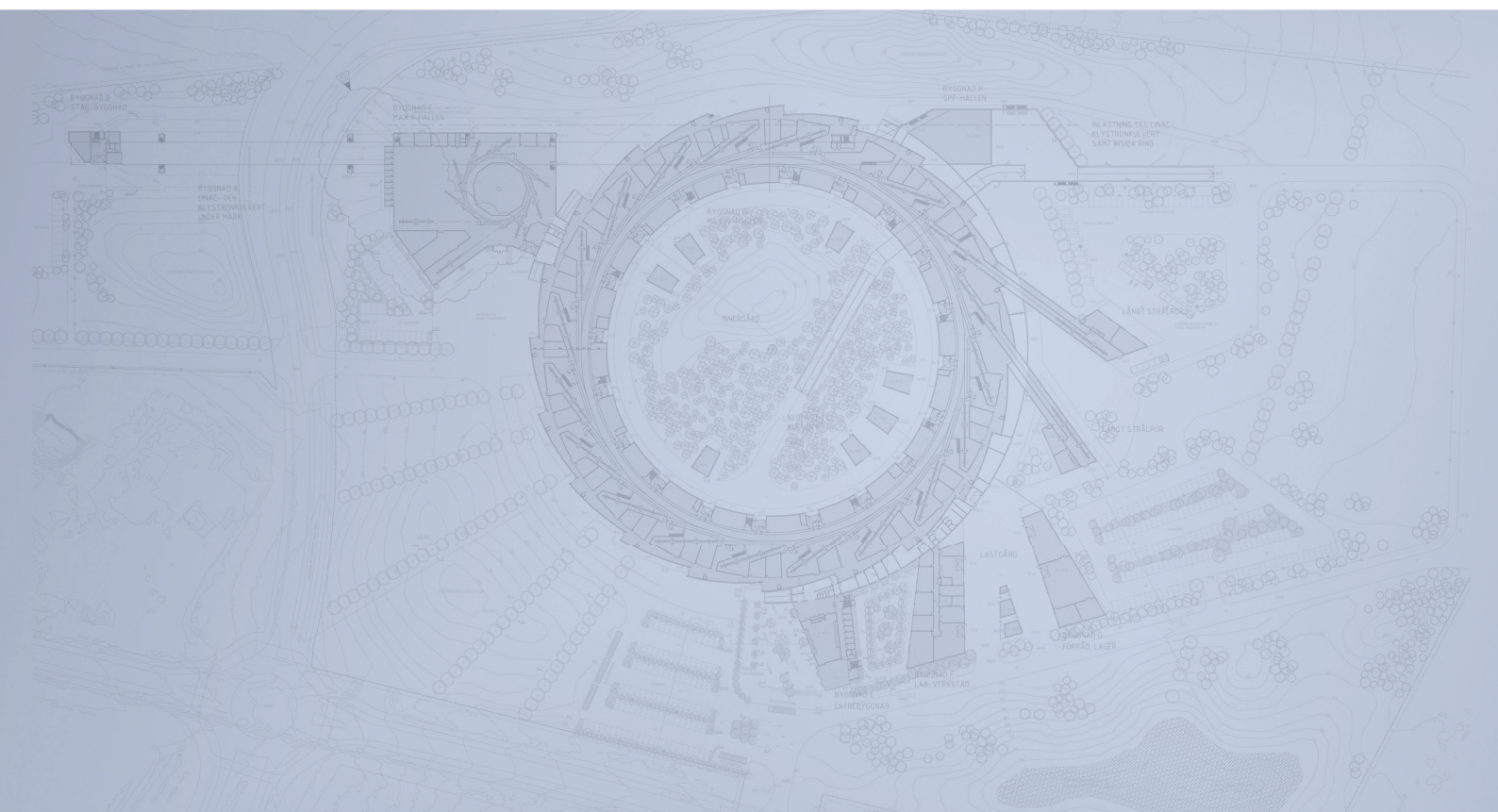




**Some Drawings for the 20deg Bend Section**



# Detailed Design Report



## Chapter 2

### MAX IV 3 GeV Storage Ring

#### 2.8. Vacuum System

MAX IV Facility



## 2.8. Vacuum System

---

<b>2.8.</b>	<b>Vacuum System .....</b>	<b>2</b>
2.8.1.	Design Philosophy and Objectives.....	2
2.8.2.	3GeV Ring Structure .....	3
2.8.3.	Vacuum Diagnostics.....	44
2.8.4.	Installation .....	45
2.8.5.	Pump Down .....	46
2.8.6.	Beam Induced Pressure.....	48
2.8.7.	Venting and Maintenance.....	52
2.8.8.	Conditioning/Performance .....	53
2.8.9.	Synchrotron Heat Load .....	56
2.8.10.	Remarks/Questions.....	57
2.8.11.	Abbreviations Used.....	58

## 2.8. Vacuum System

---

### 2.8.1. Design Philosophy and Objectives

For the vacuum system the cost effective technology of NEG-coated vacuum chambers will be used all over the MAX IV ring. This technology enables a much smaller number of discrete pumps to be used and simplifies the design of the heat-absorbers.

NEG coated chambers has become a well proven reliable technique used in a number of modern synchrotrons such as:

- Soleil (from start 2005 in all straight sections; 200m about 56% of the circumference)
- ESRF (First chamber in 1999 and about 90m (11%) installed in 2006 with plans for more)
- Elettra (First chamber in 2002)
- MAX-II (First chambers in 2005, now 4 straight Al- chambers and 3 dipole Cu-chambers)
- MAX-III (5 of 8 straight chambers, 30% of the ring since 2006)

The development of the NEG technology has mainly been made at CERN. See the report CERN-TS-2006-001(MME); Ti-Zr-V non-evaporable getter films: from development to large scale production for the Large Hadron Collider.

From CERN-TS-Note-2008-006:

*Produced as a thin film by magnetron sputtering, The NEG film combines three favorable characteristics:*

- *High pumping speed for most of the residual gases in vacuum chambers (up to 0.5 l/s/cm<sup>2</sup> for H<sub>2</sub> and 5 l/s/cm<sup>2</sup> for CO and CO<sub>2</sub>)*
- *Low electron and photon induced desorption*
- *Low secondary electron emission*

*These benefits are obtained after in situ heating, in good vacuum, at a temperature higher than 180 °C (activation temperature). The duration of the thermal treatment is also important. It has to be at least one full day at the lowest possible temperature, while a few hours are sufficient for heating temperatures higher than 200 °C.*

The beam lifetime is mainly restricted by losses induced by the rest gas pressure and by the Touschek effect. Gas losses should preferably be smaller than the Touschek losses. This requires a partial pressure lower than 10<sup>-9</sup> mbar for CO-like molecules.

---

Flanges and bellows will be put at each end of long straight sections and around RF cavities.

If flat flanges are used it is possible to make a final machining after welding to adjust length and angle of the chambers.

The building and installation of vacuum chambers will be done in steps:

1. For the first beam tests only circular ID22 tubes will be installed in the straight sections with a few beam exit ports at long straights.
2. Beam lines will be added as insertion devices are installed in the 19 long straights.

Reference labels for machine parts (e.g. 301M1.BPMW1) are used in this document following the convention;

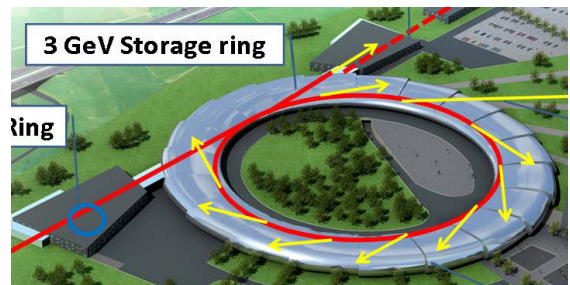
[http://www.maxlab.lu.se/local/maxiv\\_reports/accelerators\\_machine/General\\_description/MAX\\_IV\\_Naming\\_Convention\\_100426.pdf](http://www.maxlab.lu.se/local/maxiv_reports/accelerators_machine/General_description/MAX_IV_Naming_Convention_100426.pdf)

The naming document will be updated whenever new components are defined.

## 2.8.2. 3GeV Ring Structure

The ring is situated above the linac, close to the linac end. It consists of identical achromatic magnet cells with straight sections in between.

One straight section is dedicated for the injection system and the other straight sections may be used for insertion devices.



Gate valves will divide the ring in vacuum system sections. Each such section has a valve for connection to a mobile turbo pump station for roughing.

Number of identical magnet cells	20
Total bending angle per cell	18 degrees (314 mrad)
Length of cell	26.4 m (Lattice 200900909-410)
Length of straight sections for insertion devices	4.8 m; including bellows and gate valves at both ends
Minimum bending radius in dipoles	19.1 m
Beam height over the floor	1.3 m



2.8.2.1. Magnet Cell

Figure 1: Schematic of one achromat (magnet cell).

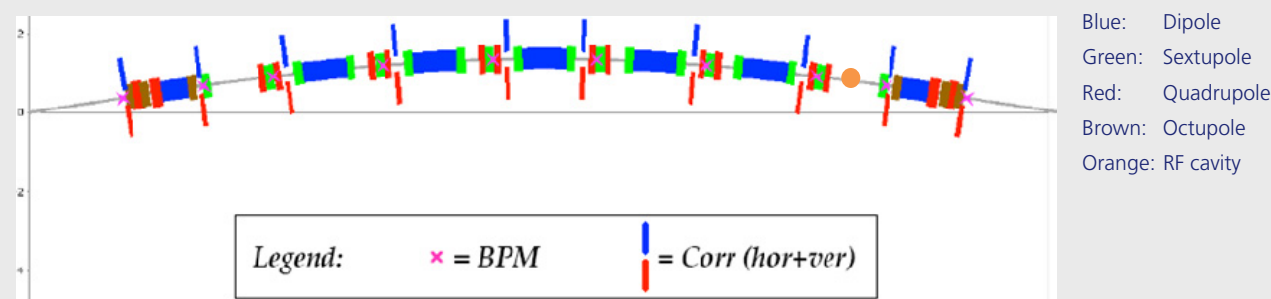
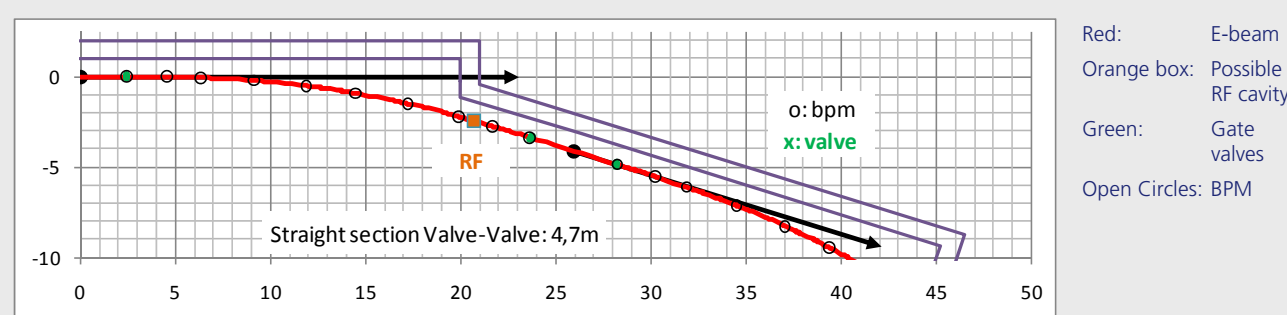


Figure 2: Beam path layout for 1.5 cells



Black: Possible beam path positions (dots) and directions (arrows).  
Purple: Walls similar to the alternative described in figure 3.2 in the DDR §7.3.4.  
The beam lines will have limited apertures, see § 2.8.2.4-2.8.2.11 for details.

The bending radius is large compared to the width of the chamber.  
Conical transitions (10-20°) will be used in order to match different chambers apertures.

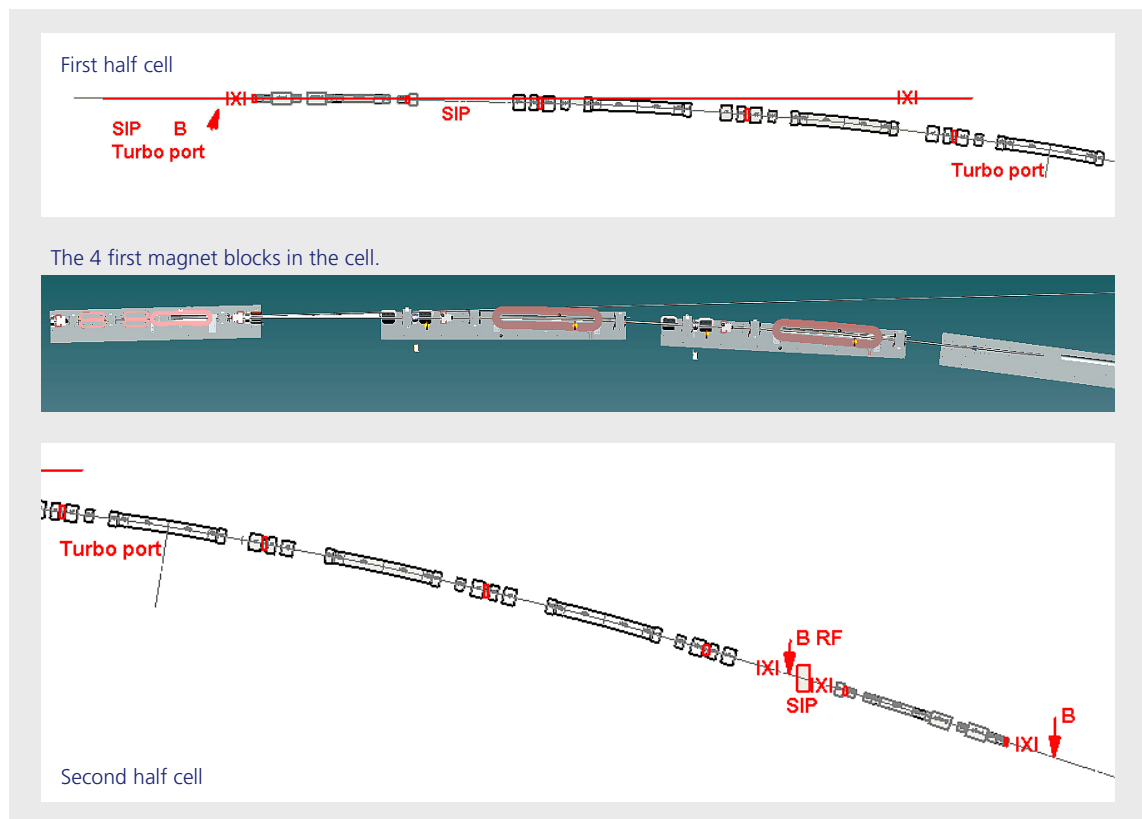
Proposed flange type	ConFlat
Vacuum chambers	NEG-coated OFHC. Possibly GlidCop at high power areas
Pipe ID	22 mm
Pipe OD	24 mm (1 mm wall) + cooling tube
NEG activation	By heating the outside of the chamber, 180-200°C, 24hrs
Dipole width [mm]	300
Dipole height [mm]	240
Table-beam height [mm]	120-24= 96 Close to the dipole 120-43=77 (from iron 100 mm out)
Radial coil extension	About 125 mm from beam path
Full height between coils	About 60 mm
Pole face winding	Conductor plus insulation maximum 1mm thick

Table 1: Some dipole and vacuum chamber data.

All magnets are made in an upper and a lower part. For installation or baking of the vacuum chambers the upper parts may be lifted off and the lower parts moved downwards by 20mm.

The expansion of 3mm/m during baking will cause too high stresses in the chambers. We study the approach to lift the magnet section chambers to be baked separated from the rest of the system. The baking system is described in section 2.8.8.1. See also the bellows paragraph 2.8.2.2.2. and the thermal expansion paragraph 2.8.8.2.

Figure 3: Proposed positions for vacuum components in one section.



<b>B:</b>	<b>Bellows</b>
	<ul style="list-style-type: none"> <li>• on each side of the RF cavity</li> <li>• between the gate valves and the long straight sections</li> </ul>
<b>IXI:</b>	Gate valves <ul style="list-style-type: none"> <li>• at both ends of the long straight section</li> <li>• around the RF cavity</li> </ul>
<b>Red boxes</b>	BPM houses
<b>SIP</b>	Sputter ion pumps. Additional pumps will be placed at positions where the gas load is high; e.g. at chambers without NEG coating.

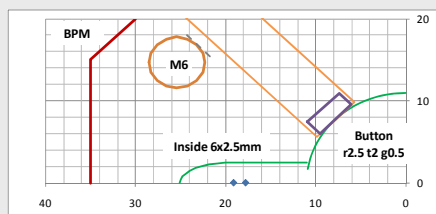
See paragraph 2.8.2.2.5 for the description of vacuum chambers.

## 2.8.2.2. Components in the Cell

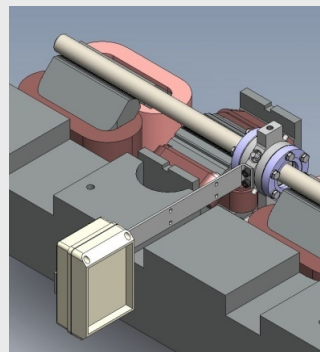
### 2.8.2.2.1. BPM Heads

- The BPM house will be a rigid steel body with CF40-flanges.
- Circular opening inner diameter 22 mm.
- Larger aperture (e.g. a keyhole shape) is needed for the “3\*\*M1.BPMW2” positioned after the first magnet (see Table 7) and “301M1.BPMI1” at the injection straight. The latter unit is turned 180 degrees as seen in §2.8.2.9. The keyhole profile may need to be shallower in order to keep the impedance down. For a pulsed sextupole injection the “301M2.BPMI1” will need the same profile.
- For BPM without the keyhole shape a small taper of 0.5mm in the median plane at the upstream chamber end (on the outer radius ring side) is enough to shadow the BPM house from synchrotron light.
- All blocks NEG coated (Might not be necessary?).
- 4 SLS Alba type buttons per block: BPM button assemblies are mounted in the steel frame.
- Fixation for radial and height positions within  $\pm 0.1$  mm or better(?).
- Cable feedthroughs with rigid cables to a connection box for access to connectors when installed.
- Where the BPM is connected to a gate valve, the bolts needs to go through the BPM-body. A possible geometry for feedthroughs in the body is shown in Figure 4 (compare Table 7):

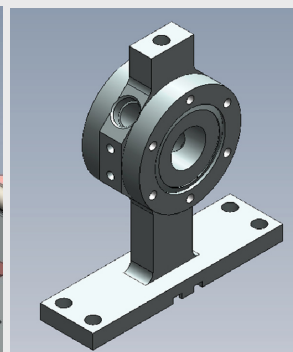
Figure 4: BPM geometry.



Main dimensions; model with a pocket for the photon beamline.



Connectors in a box



Housing

With the shown dimensions the distance M6-hole to button hole is about 1.5mm.

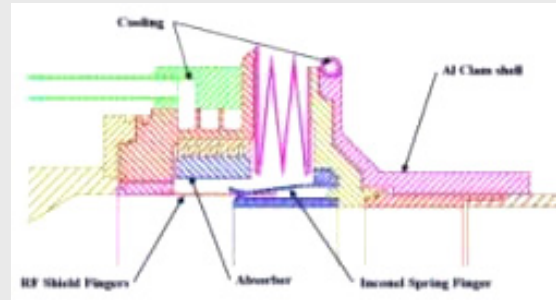
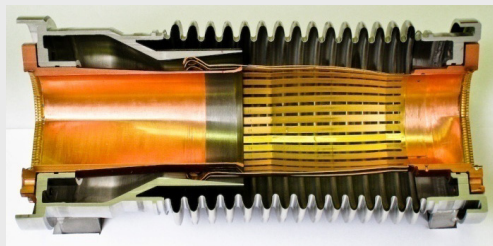
The button surface will have the same radius as the chamber; 11mm.

The rod for signal and fixation of the button in the feedtrough will be covered with an insulator also used for stiffening of the assembly.

### 2.8.2.2.2. Bellows and RF-Shields

In MAX II a simple type of BeCu-shield was used in the bellows. A number of fingers were overheated and bent into the beam. All shields have been removed. In MAX IV shields will be needed, a design similar to the one used in PEP-II will be studied.

Figure 5: LHC (left) and PEP (right) designs.



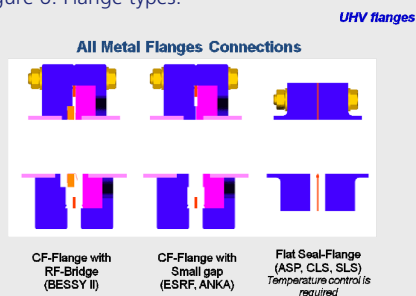
See paragraph 2.8.8.2 for discussion on thermal movements.

The PEP-II design have water cooled HOM-absorbers as the High Energy Ring has been run with 2A 9GeV electrons with 1732 bunches 10-12mm long. In April 7, 2008 PEP-II was closed down. (EPAC08, Last year of PEP-II B-factory operation).

### 2.8.2.2.3. Flanges

Different types used in synchrotrons: ConFlat (CF) or flat (VATSEAL: “at the same time a reliable, low resistance RF contact”) KEK has developed another system (MO-type) were also non circular shapes are possible.

Figure 6: Flange types.



a: modified CF  
c: Modified MAX II CF

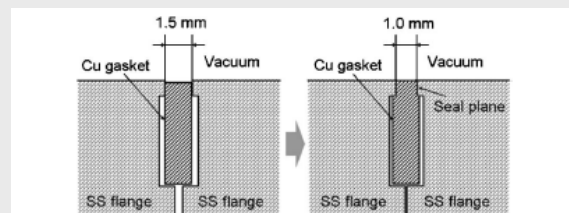
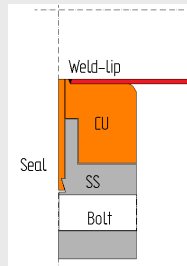


Fig. 2. Conceptual principle of the MO-type flange. The vacuum is sealed by a plane (seal plane) at just the inner surface.

b: MO

Connections between the chambers will likely be made with standard CF40 flanges brazed to a copper ring. A thin lip will be prepared in the ring for welding to the 22/24mm tube (in red) as indicated. An automated welding procedure should be setup to ensure the quality.

CU: Copper ring brazed to the ConFlat flange.

SS: ConFlat flange 12.7mm thick, OD 70mm, ID 38.2/35mm.

Bolt: Opening for M6 (35mm long bolts).

Seal: ConFlat copper seal.

Standard dimensions; 2 x 37 x 48.2mm.

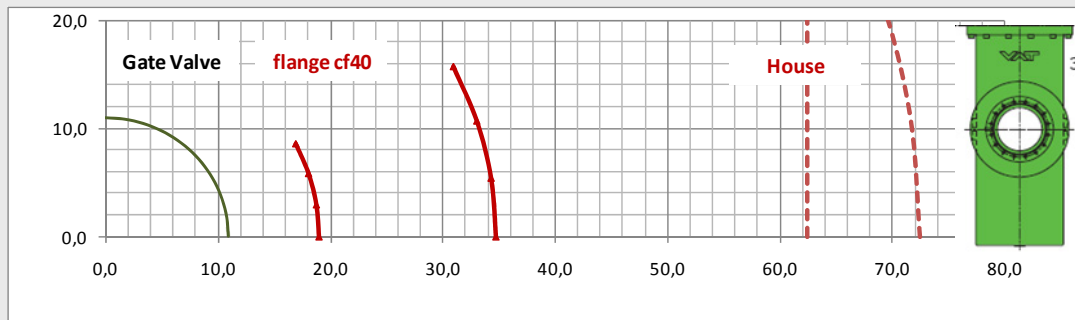
Modification of the seal with the opening matching the chamber aperture simplifies the adaption of valves and other CF components.

#### 2.8.2.2.4. Valves

About 60 RF-shielded CF40 gate valves (VAT Series 47 or similar) will be used in the ring. An option is the VAT/KEK version with a shield.

About 40 gate valves for beam lines and injection will be without RF-shield.

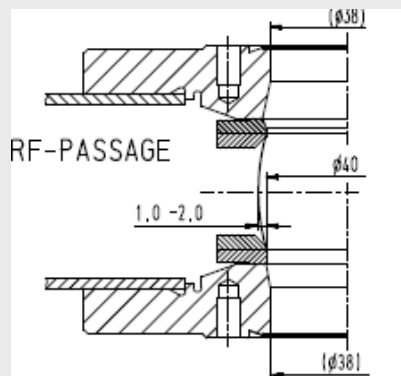
Table 2: Gate valve dimensions.



Standard VAT valve series 47

The length of the valve is 72 mm.

Total 98 mm is needed for the connecting flanges. Screws (33 mm long) are not included.



RF Shield and aperture

The RF shield is made of parallel contact blades where the blades are flexing outwards.

The aperture of the valve should be modified to 22mm ID. At the exit of the injection septum a special aperture is needed as the injected beam position is 13.5 mm from the nominal beam path. See Table 12.

About 40 Right angle valves (CF16 or 40) as roughing ports; one in each section.

### 2.8.2.2.5. Vacuum Chambers in the 3GeV Ring



Chamber part 5 (uc3) is shown twice in the sketch above.  
See also Table 4 for sketches of some chamber sections.

NEG coated and water cooled chambers for each achromat;  
Table 3: Vacuum chambers.

No	Description	Heat load	Connections
<b>1</b> <b>3**M1.VC1*</b>	ID 22mm chamber with a small keyhole extension at the connection to the BPM before chamber 2. About 2m long. Bend 1.5deg. As correction magnet frequency above 100 Hz is needed, the ends of this chamber will be made in stainless steel with CF40 flanges.	0-25 W/mm or more at the downstream end (outer radius); depending on wiggler model	
<b>2</b> <b>3**S1.VC2*</b>	Crotch chamber with tapers. About 1.8m for electrons; about 10m ID14mm for photons to the front end beam stop. Y-shape with 2 almost straight legs.	About 25W/mm over short crotch (<200W) and some 15-20W/mm in the taper before bend (photon inner radius)	Pump ports at the crotch and at the beam stop.
<b>3-4</b> <b>3**U1.VC3*</b> <b>3**U2.VC4*</b>	22/24 mm chamber. About 2.7m. Bend 3deg.	Maximum 2W/mm at the outer radius, falling towards 0 when leaving the bend magnet.	
<b>5</b> <b>3**U3.VC5*</b>	22/24 chamber. About 3.5m. Bend 3deg.	As 3	Turbo pump port in the middle. Might be better to move to the beginning of chamber 6 for better access.
<b>6-9</b> <b>3**U4.VC6*</b> <b>3**U5.VC7*</b> <b>3**S2.VC8*</b> <b>3**M2.VC9*</b>	Similar to chamber 3, lengths and bends mirrors of 4-1. 301M2.VC9T with steel ends and taper for pulsed magnet injection.	As 3	


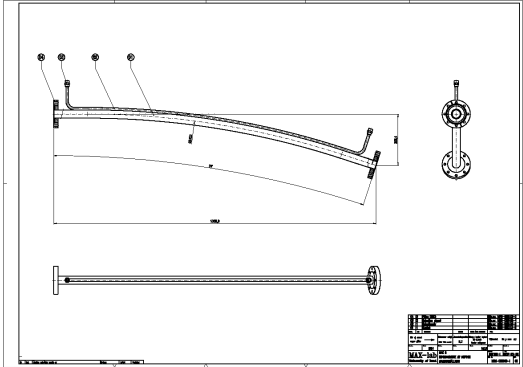
Note: Fast correction magnets have roughly a limit at 100Hz for copper chambers 22/24mm. See the end of Table 7. At the beam exits the vacuum chambers are somewhat wider; at a diagnostic port (after uc5) the correction magnet needs to be wider. Higher frequency magnets will need stainless or ceramic chambers.

Chambers in dipole magnets will need to be stabilized in order to keep the correct bending radius after baking. At MAX II we have seen what we understand as stress relief of the bent copper tube making the radius larger.

A small wedge (0.5-1mm) on the outer wall before the end flange is needed in order to protect the following BPM from synchrotron radiation unless there is a “keyhole”.

Special chambers;

No	Description	Heat load	Connections
<b>BPM (between other chambers)</b>	About 200 units. Short houses (40mm) in stainless steel. About 20 units with keyhole opening for beam exits and injection path. Used as fixation points for the other vacuum chambers and lifting points when lifting the magnet section chambers for baking.	Maybe 20W	CF40 flanges machined in the body. Some units will need bolts to go through the body for connection to gate valves.
<b>Kicker (1, 8)</b>	2 Ceramic chambers with RF-shielded bellows about 0.7m long	Maximum 2W/mm	
<b>Kicker (Long)</b>	2 Ceramic chambers with RF-shielded bellows about 0.35m long	Maximum 2W/mm	
<b>Inj septum (Long)</b>	The injection septum has an integrated vacuum chamber. The inner surface will be nickel coated. A screen for aperture adaption is needed, possibly with NEG coating.	?	100mm pump port on the side of the magnet. Cooling?
<b>RF 100MHz (8)</b>	6 cavities. The cavities need aperture tapers, bellows with RF-screens and a gate valve on each side. Length with tapers about 1m.	About 60W on downstream taper	Pump ports on the cavity. Cooling
<b>RF 300MHz (8)</b>	3 cavities. Shorter than the 100MHz version. Tapers/bellows to give the same total length with cavities as the 100MHz systems?	About 60W on downstream taper	Pump ports on the cavity. Cooling
<b>RF replace (8)</b>	A “dummy” chamber to replace the RF chambers during maintenance and baking of the magnet section chambers	Maximum 2W/mm	Pump port for evacuation.
<b>Strip line (8)</b>	Strip line monitors. One or two units? Dimensions?	Max power?	Adjustments? Cooling?
<b>DCCT (8)</b>	One short chamber 22mm inner diameter. Ceramic chamber. Need bellows?	Maximum 2W/mm	
<b>Emitt (8)</b>	After one uc5. A chamber with a power absorber in the mid plane in front of a mirror for emittance measurements	About 500W on the absorber (350mm) and 300W on the inner chamber wall	Adjustable positions on the absorber and mirror. Water cooling on the absorber and chamber. Pump port.

No	Description	Heat load	Connections
<b>Fill (8)</b>	After one uc5? A chamber with a copper mirror for fill pattern and bunch length measurements. Similar to the "Emitt" chamber above	Similar to the "Emitt" chamber or less if a more narrow beam angle is used	Adjustable positions of the mirror. Water cooling on the mirror and chamber. Pump port.
<b>Scrape (Long / 8)</b>	Beam scrapers. One or two units? Dimensions? May fit above the injection bend magnet?	Max power?	Adjustments?
<b>ID dummies (Long)</b>	5-19 chambers 22/24mm before installation of insertion devices during start up. NEG coated. 4.8m long including bellows and gate valves. The rest Al-chambers?	Maximum 2W/mm	Pump port.
<b>Pulsed sextupole magnet; PSM (Long)</b>	For the pulsed sextupole injection scheme the center of the sextupole will be positioned 523mm from the center of the following BPM in 302L. A ceramic chamber; length?	Maximum 2W/mm	
<b>ID (Long)</b>	Aluminum chamber for magnet gaps larger than 7.8mm. NEG coated. Half axes 15x 2.5mm, wall $\geq 1$ mm	Maximum 2W/mm	
<b>Dipole chamber example</b>			
	<p>Drawing of the MAX-II dipole chamber showing the principle of a simple copper tube with a cooling line along.</p> <p>The 3 GeV dipoles have larger bending radius and the maximum synchrotron radiation power density is the same as for MAX II.</p> 		

Diagnostics that might need special chambers:

**Pinger magnets;** one horizontal and one vertical or a combined magnet. Fast pulses are needed => ceramic chamber(s)? Sizes and needed positions are not known. Combined with other fast magnets?

Information on the fabrication of copper chambers for the SPEAR 3-ring is found at:

[http://ssils.ssrc.ac.cn/symposium/Paper/Storage\\_Ring\\_Technology/copper\\_vacuum.PDF](http://ssils.ssrc.ac.cn/symposium/Paper/Storage_Ring_Technology/copper_vacuum.PDF)

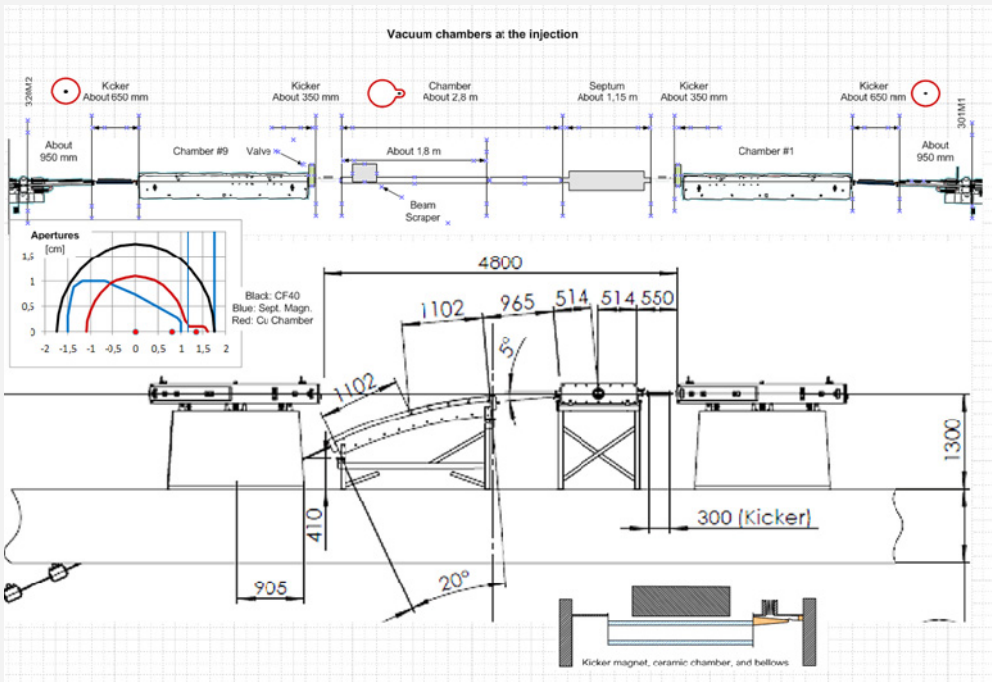
Design of special chambers etc was presented at the Barcelona Vacuum Workshop, September 13, 2005:

<https://www.cells.es/static/Files/ALBA%20vacuum%20workshop%2012-13%20Sep%202005/Kurita%20Spear%20III/>



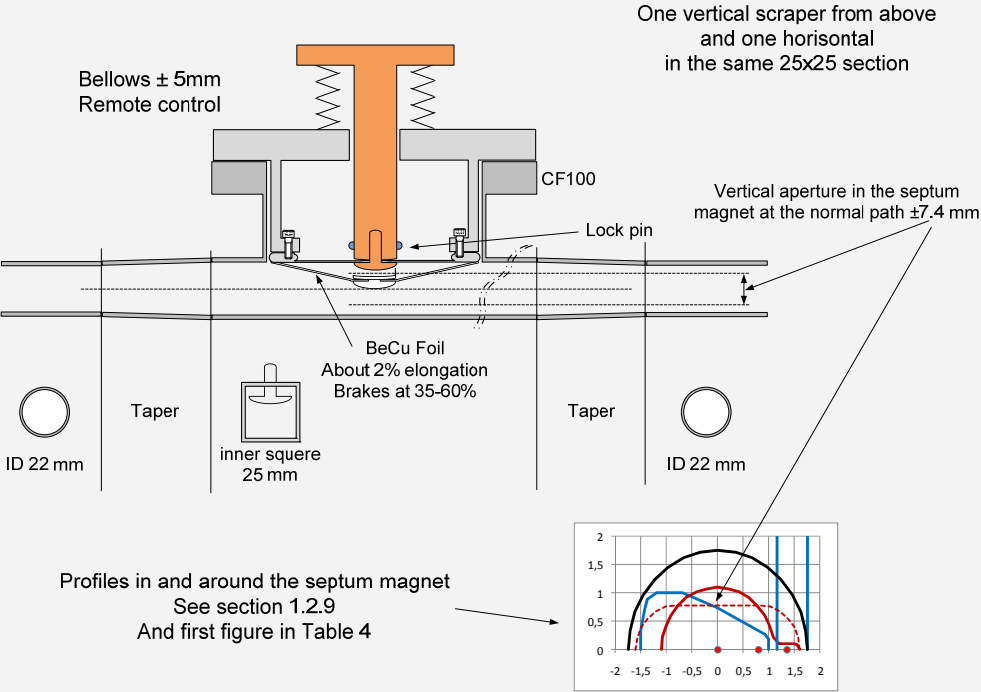
Table 4: Chamber layout for some sections.

1: Injection chambers.

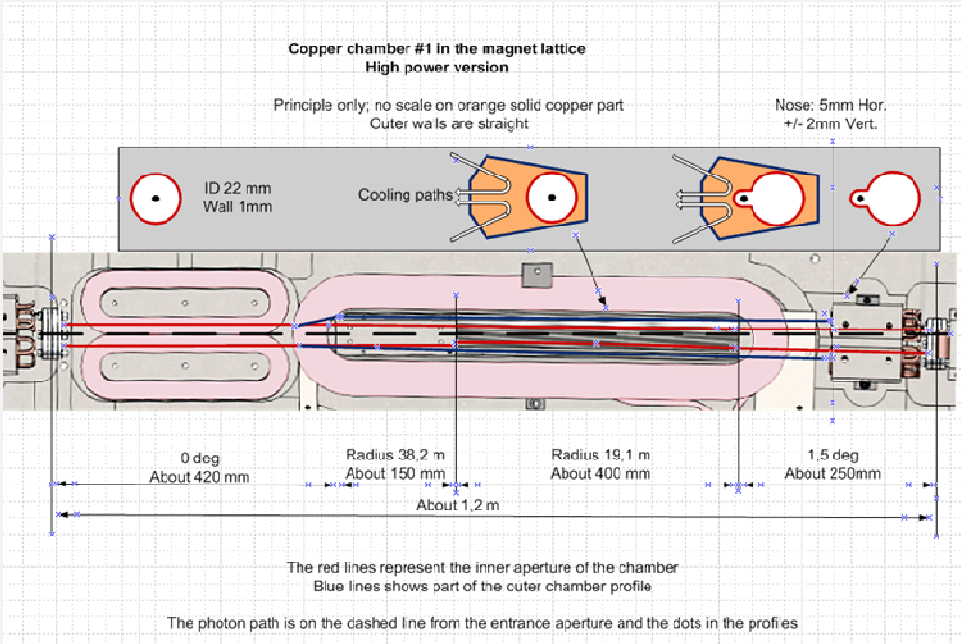


2: Beam scraper proposal.

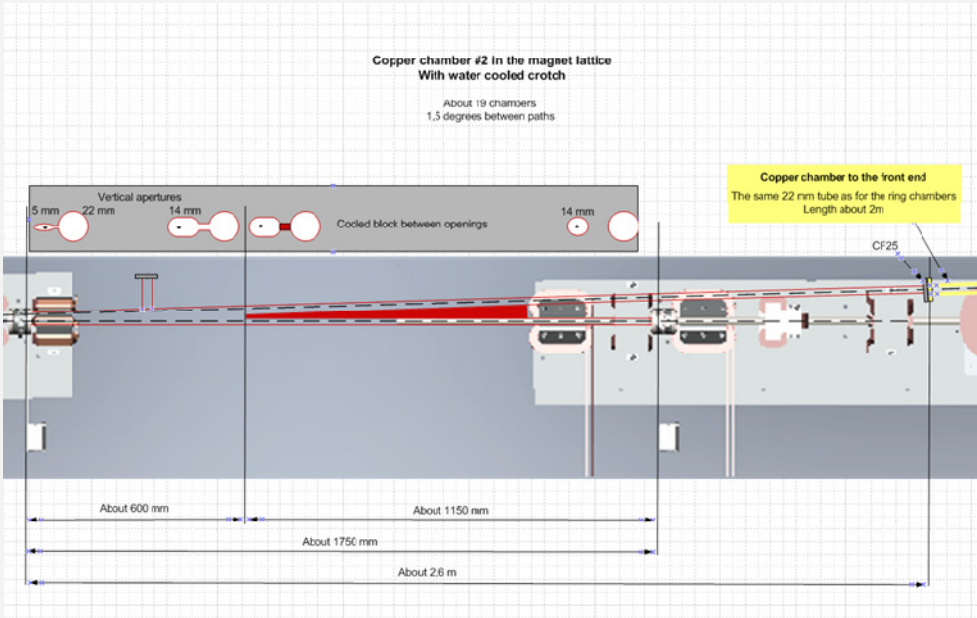
Beam Scraper proposal



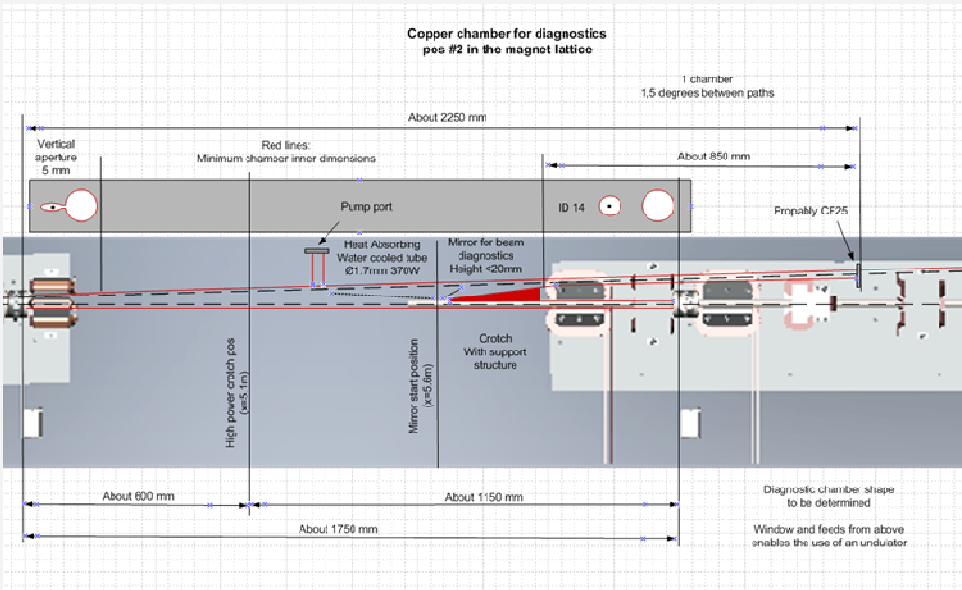
3: Chambers at DIMC1.



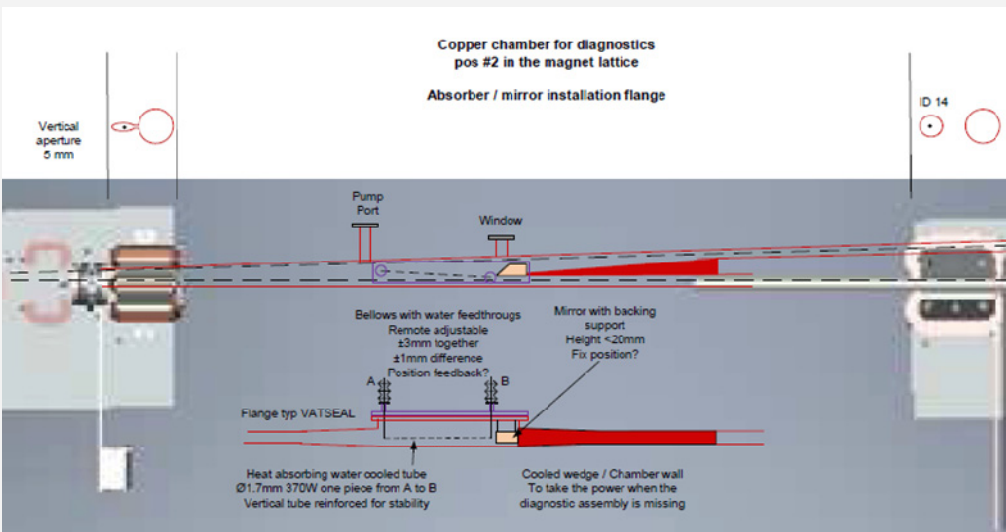
4: High power chamber between DIMC1 and DIP1.



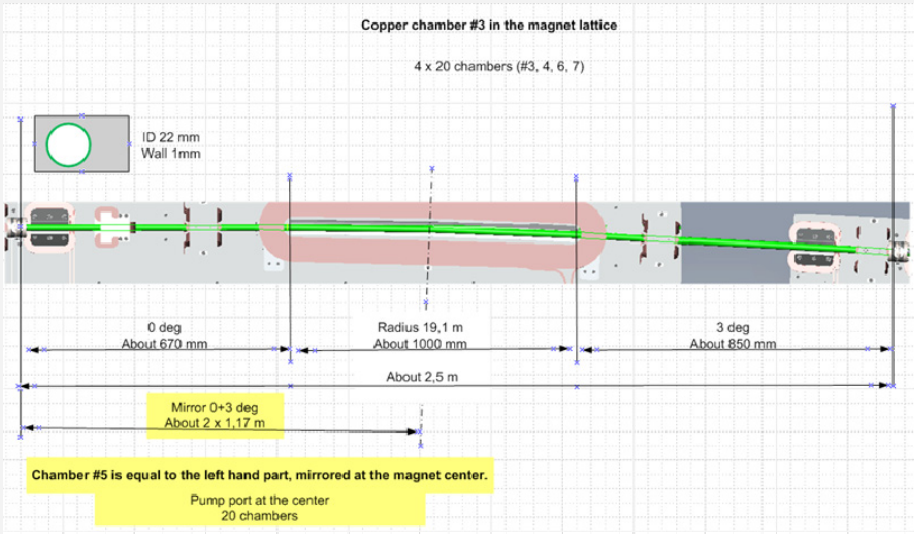
5: Low power/ Diagnostic chamber between DIMC 1and DIP1.



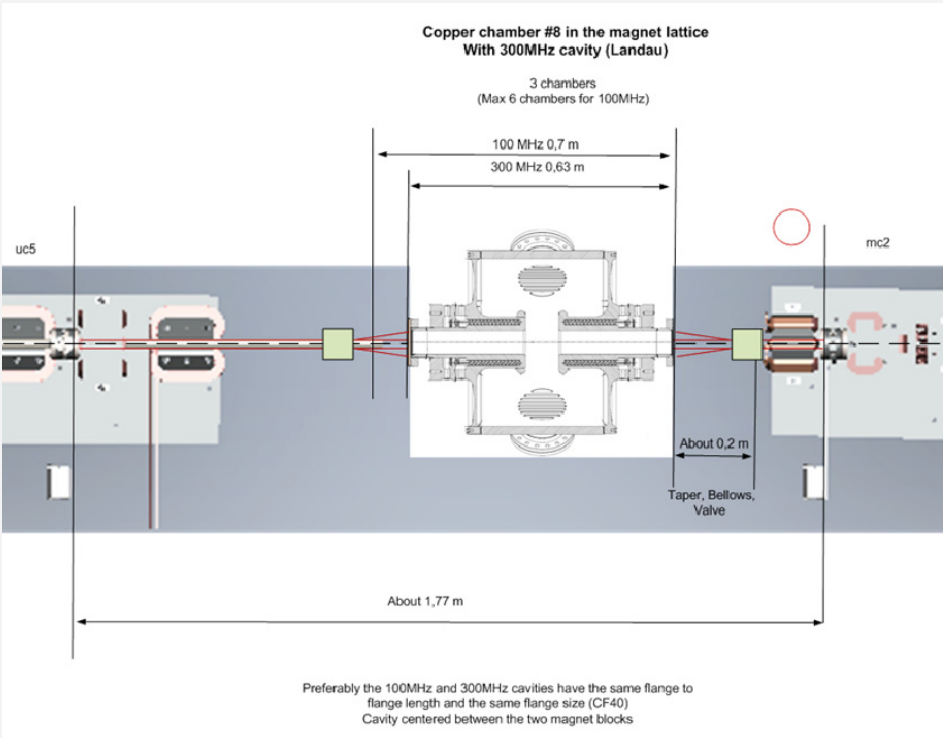
6: Mirror and absorber installation principle.



7: Chamber in DIP1, 2, 4, and 5. Size of chamber #5 in DIP3 in the yellow field.

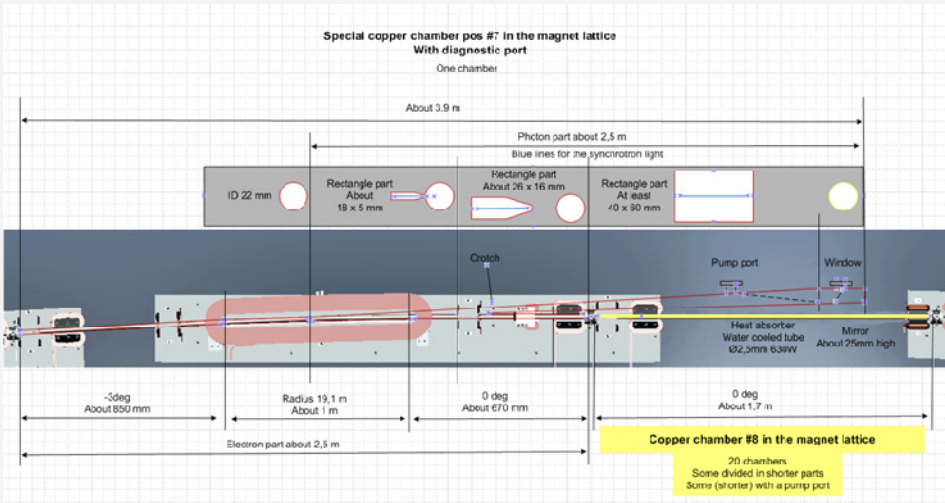


8: Chambers at the RF cavities.



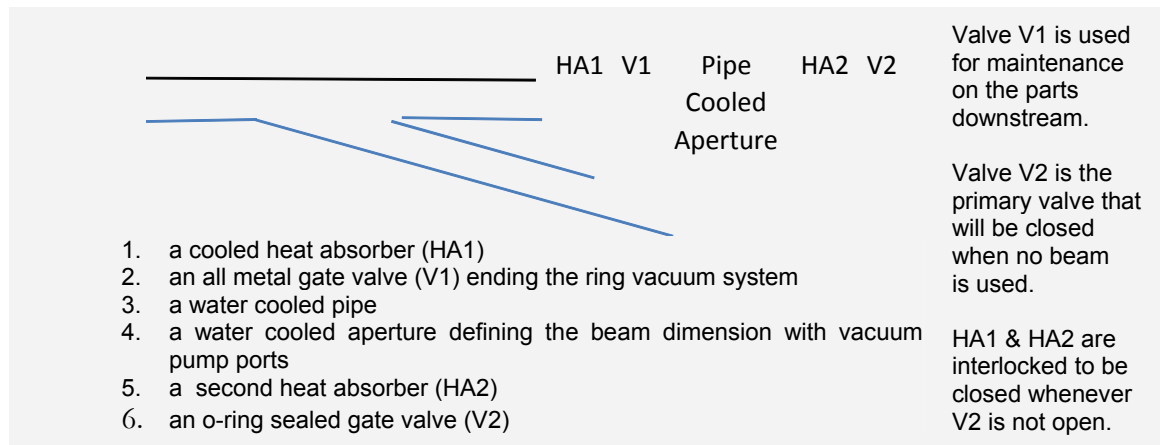
9: Chambers at the diagnostic port after DIP5.

See also row 6 in this table for the mirror absorber.



### 2.8.2.2.6. Photon Beamline Components

Each beamline will be equipped with:



The accelerator vacuum system ends with HA1 and V1 after which the Beamline system takes over.

#### Heat Load on Heat Absorber HA1

Heat loads from two ID's has been estimated from the graphs in DDR chapter 5.

Position: 10m after the center of the insertion device

HA1 surface angle: 1.5 degrees

HA1 surface radius: 10mm

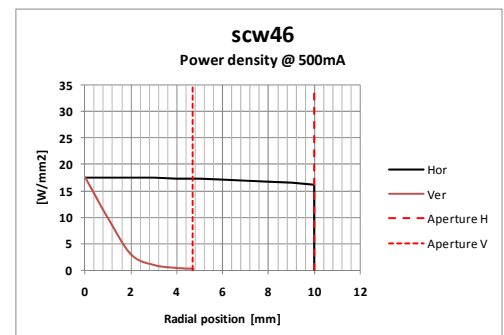
HA1 surface length: 400mm

##### Scw46

The highest total beam power (75kW) and also the widest fan. 20kW on HA1.

About 26 kW each on chambers #1 and #2.

If scw46 will be installed it will most likely be a shorter version with less power.

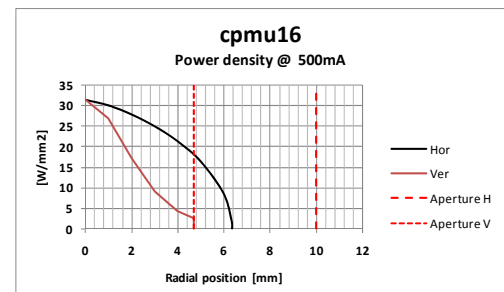


##### Cpmu46

The highest power density (120kW/mrad²), but in a more narrow fan.

Total power is low (15kW).

Only a fraction of the power is collimated by the vacuum chambers.



### 2.8.2.2.7. Beam Interaction with Chamber Dimension Variations

The electron beam will interact with cavities between flanges, bellows, and other geometry variations resulting in both disturbances of the beam and heat load on the vacuum chamber. The effects are studied and described in the chapter 2.11 Beam Instabilities.

### 2.8.2.3. Insertion Devices

The insertion devices in Table 5 are proposed for MAX IV. Path descriptions with formulas for approximations of the power density profiles are given in the indicated paragraphs. The approximations are made from graphs in the Insertion Device chapter and used to estimate the power heating the vacuum chambers.

The devices without reference to a path description will give less power losses to the chamber walls even if the peak power is higher.

Labels in Table 5 on next page:

<b>ID:</b>	ID names according to table 3 in the insertion device chapter 5.3. Names in parentheses refer to the version of September 2009.
<b>Path description:</b>	Sections in this chapter showing power distribution in the vacuum pipes.
<b>Length:</b>	Approximate mechanical length of the ID.
<b>Gap:</b>	Vertical magnet aperture. The chamber profile shown in  Table 3 is valid for gaps larger than 7.8mm. More narrow magnets need to be in vacuum.
<b>Peak:</b>	Maximum power density, not always the on-axis power density.
<b>Total:</b>	Total power radiated from the ID.
<b>Hor/Ver:</b>	Angles of deflection where the power density approaches zero as shown in the power density maps of chapter 5.3. Compare with the apertures shown in paragraphs 2.8.2.4 - 2.8.2.11 and the note after Table 5.



Table 5: Insertion devices.  
The list is not complete; see chapter 5 of the DDR.

ID	Path	Length	Gap	Peak	Total	Hor	Ver
	description	m	mm	kW/mrad <sup>2</sup>	kW	mrاد	mrاد
scw46	§ 2.8.2.4	2	12	67,22	74,28	2,65	0,2
wig80		4	7,8	51,24	45,08	2,38	0,2
(wigD)		4	9	47,75	40,43	2,27	0,23
(wigS)		1	12	8,93	7,28	2	0,23
epu53p6Plan	§ 2.8.2.5	4	9	38,00	16,22	1,1	0,2
epu48Plan		4	9	40,05	14,53	0,9	0,2
epu43p6Plan		4	9	42,13	13,14	0,88	0,2
epu53p6Heli		4	9	13,00	12,93	0,85	0,85
epu48Heli		4	9	13,00	11,18	0,73	0,73
epu43p6Heli		4	9	13,00	9,98	0,65	0,65
(epuA) epu38Plan		4	9	43,89	10,88	0,62	0,23
epul1011Heli		2,1	14	4,70	2,12	0,55	0,55
epul1011Plan		2,1	14	13,96	3,08	0,55	0,2
(pmuC)		3,8	4,2	92,31	16,72	0,42	0,23
(pmuB) pmu20		3,8	4,2	95,82	14,84	0,36	0,23
(pmuA) pmu18p5		3,8	4,2	97,11	13,3	0,32	0,23
(cpmuB)		3,8	4,2	118,75	15,47	0,3	0,2
cpmu16		3,8	4,2	119,22	14,88	0,29	0,2
(cpmuA)		3,8	4,2	119,47	14,26	0,28	0,2
epu48Vert	§ 2.8.2.5	4	9	31,72	9,15	0,2	0,7
epu43p6Vert		4	9	32,46	7,84	0,2	0,58
(epuA) epu38Vert		4	9	32,46	6,01	0,2	0,46

The vacuum chamber apertures are:

Horizontal:  $\pm 1\text{mrad}$

Vertical:  $\pm 0.47\text{mrad}$

Photons outside these values will be lost as heat on the narrow parts of the chambers.

All calculations on heat loads and aperture needs are made for the ID at the center of a long straight section.



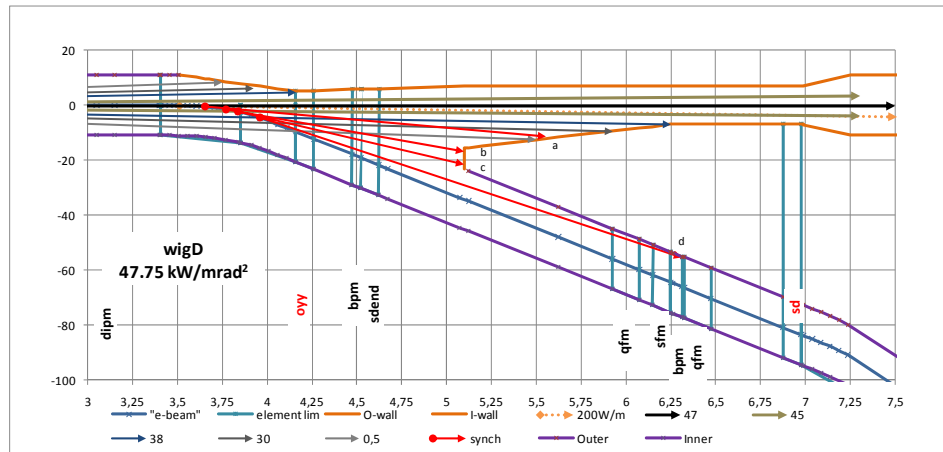
### 2.8.2.4. Port for a 4m Wiggler; wigD or scw46

Two to four long straight sections might be configured with wigglers, giving the widest light fan and the highest thermal load on the vacuum chamber.

Figure 5 shows the position of the extracted photon beam from wigD relative to the electron beam path as black and gray arrows. Numbers in the legend denote the power density in kW/mrad<sup>2</sup>. Positions of labeled elements are shown in blue. Vertical blue lines are drawn up to the photon path for aperture restricting elements. See Table 7 for details.

The photon beam tube (orange) leaves the coil area of the dipole about 8m after the midpoint (x=0). Note the different scales: X in meter and Y in millimeter.

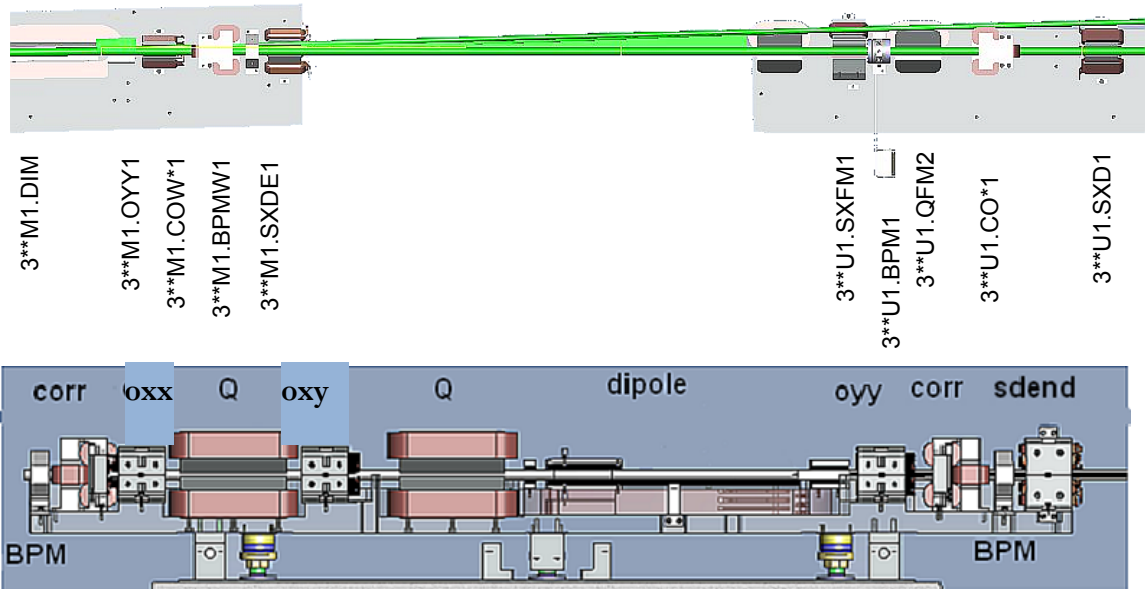
Figure 5: Horizontal vacuum chamber layout with beam power distribution from wigD.



See also chamber #1 in Table 4 row 3.

Top view similar to the graph above.

The labels are according to the component naming convention for drawings and documents.



Side view from the inside of the ring. Upper yoke and dipole are removed.

The aperture in oyy is limited vertically to  $\pm 2\text{mm}$  and horizontally to  $5\text{mm}$  on the left hand side.

Corresponding angles:  $2/4.2 = 0.47\text{mrad}$ ,  $5/4.2 = 1.2\text{mrad}$ .

The narrow vacuum chamber will act as a baffle for the radiation as indicated in the graphs below. A recommendation from ESRF for distributed absorbers is to have a linear power density below 20W/mm (ESRF Thermal absorbers..., MEDSI02).

Nominal size of the beam pipe is 22mm ID. At the chamber crotch the pipe is enlarged to reduce the power density on the walls. The beam aperture is limited at the elements oyy, sdend, and sd.

The crotch between the two beam pipes is shadowed from the insertion device radiation by the curvature of the dipole chamber.

For the elements in front of the crotch the synchrotron light passes through the opening in the median plane as indicated by the red arrows in Figure 5. See also the sketches at the end of Table 7.

The dotted orange arrow shows radiation at 0.2kW/m source power from the beginning of the magnet that might be used during the start up of the system. See § 2.8.4.

### Photons from a 4 m Damping Wiggler

Source position                      Center of straight section (x=0 in Figure 5)

Power density                      [kW/mrad<sup>2</sup>] at 500mA

$$\text{IF } h < A \text{ then PowDen} = P \frac{\sqrt{1 - \left(\frac{h}{A}\right)^B} \left(1 + \frac{5}{7} \frac{C^2 v^2}{1 + C^2 v^2}\right)}{(1 + C^2 v^2)^D}$$

$$\text{else PowDen} = 0$$

h is horizontal and v is vertical angle [mrad].

Constant	A	B	C	D	P
wigD	2.2416	1.4166	5.871	2.5	47.75
scw46	2.6595	1.9542	6.72	2.11	67.22

**For wigD:**

Horizontal	1% level at $\pm 2.24$ mrad; 94% at $\pm 0.5$ mrad High power density areas in the horizontal plane are at the apertures for oyy, sdend, and sd where the apertures are restricted.
Vertical	1% level at $\pm 0.44$ mrad; 90% at $\pm 0.04$ mrad The vertical apertures are limited in the oyy and sdend to a few mm. As seen in Table 7 the beam is vertically smaller than the chamber apertures.
Total power on the walls up to 7m is 18kW.	
Power inside $\pm 0.5$ mrad x $\pm 0.125$ mrad is about 9kW.	

**For scw46** the power load is higher and the photon fan is wider than this; see Table 7.

**Synchrotron Radiation**

The power from synchrotron radiation has a maximum of 1.57kW/m electron path.

The power is radiated vertically inside  $\pm 0.125$  mrad.

Maximum power density is on the chamber crotch with about 23W/mm (170W total).

On the walls parallel to the beam the maximum power density is 1.6W/mm.

Table 6 show the estimated power as seen by the vacuum chamber, using the formulas in §2.8.9 for the red rays in Figure 5: Horizontal vacuum chamber layout with beam power distribution from wigD.

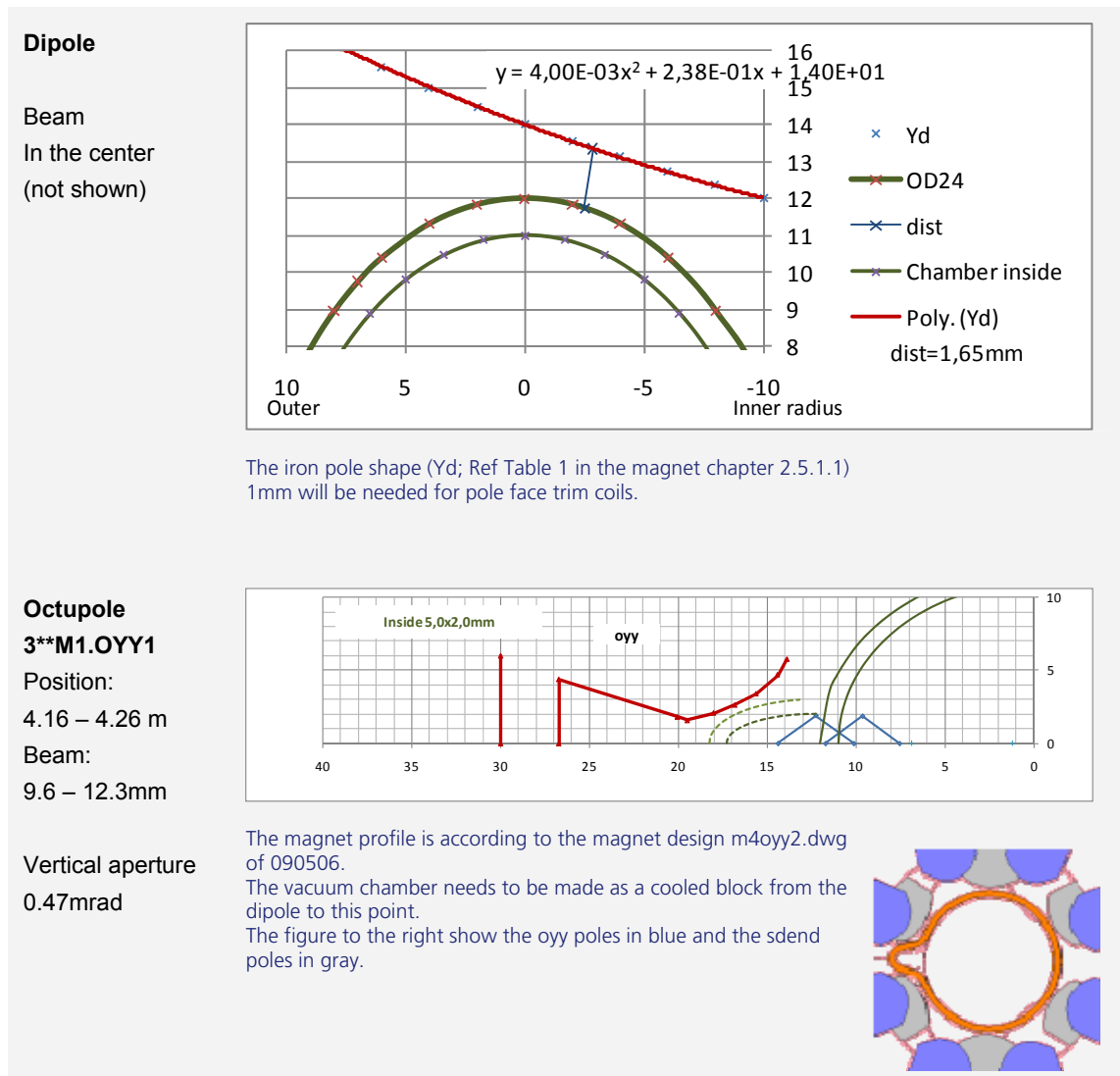
Ray	Produced	Source Distance	Magnet distance	Source radius	Wall Power	Beam height
	W/m	m	m	m	W/m	±mm
<b>a</b>	943	1,9	1,5	24,6	124	0,24
<b>b</b>	1563	1,33	1,1	19,1	205	0,17
<b>c</b>	1563	1,26	1,1	19,1	205	0,16
<b>d</b>	1563	2,35	2,3	19,1	58	0,29

Table 6: Power densities on walls.

Table 7 shows the photon beam position and size relative to the magnets at the entrance and exit of the elements.

- Red: Magnet and coil profile (dimensions from FEM-files).
- Green: Electron beam pipe (solid lines) and photon pipe (dashed). One quarter of the photon pipe envelope is shown for the entrance and exit of each element.
- Blue: Photon beam from ID's at entrance and exit of the elements. 3 points are made for each beam position indicating the “useful” horizontal (0.5mrad) and the “full” vertical (0.44mrad) divergence of the beam.

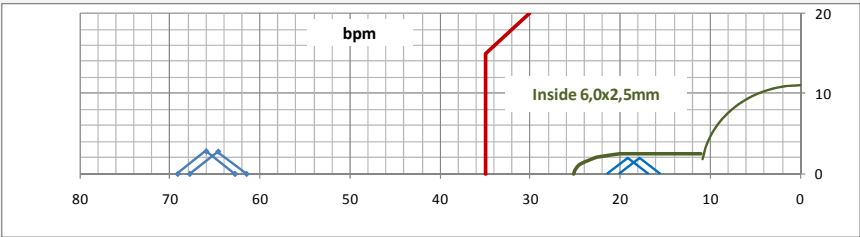
Table 7: Beam from wigglers relative to chambers.



**BPM**  
**3\*\*M1.BPMW1**

Position:  
4.47 – 4.52 m  
In front of sdcnd

Beam:  
17.8 – 19.1mm  
Beam position  
for 3\*\*U1.BPM1  
is indicated

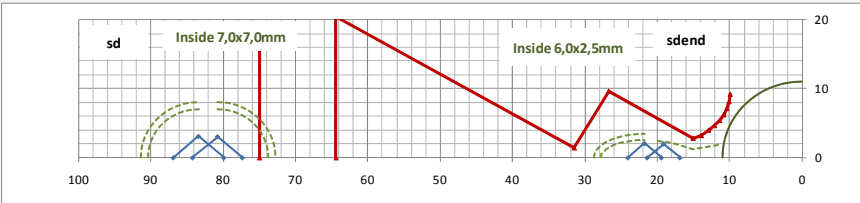


The BPM house 3\*\*M1.BPMW1 will need a "pocket" for the photon beam.  
For the 3\*\*U1.BPM1 the photon beam goes outside of the BPM housing.

**Sextupoles**  
**3\*\*M1.SXDE1**

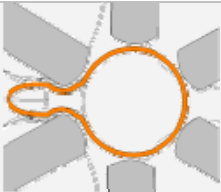
Position sdcnd:  
4.52 – 4.62m  
Beam:  
19.1 - 21.8mm

**3\*\*U1.SXD1**  
Position sd:  
6.88 – 6.98m  
Beam:  
80.8 – 83.4mm



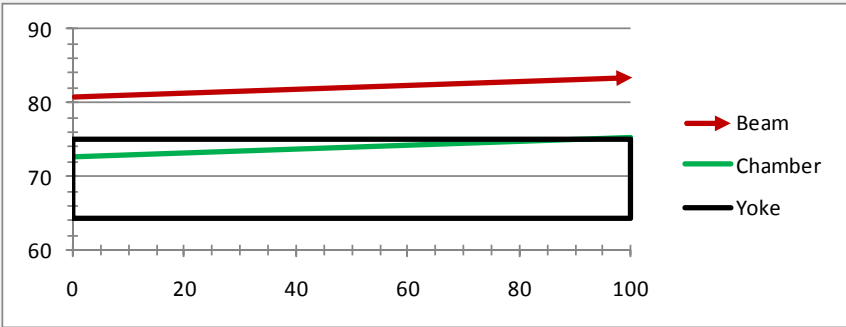
sdcnd: The chamber is open between the electron and the photon beam.

sd: The return yoke needs to be modified in order to reduce the heat load on the chamber wall in front of the magnet.



**Profiles at sd**

Position:  
6.88 – 6.98m  
  
Chamber  
outer wall:  
72.8 – 75.4mm



Horizontal cut of the return yoke at the mid plane [mm].

**Quadrupoles**

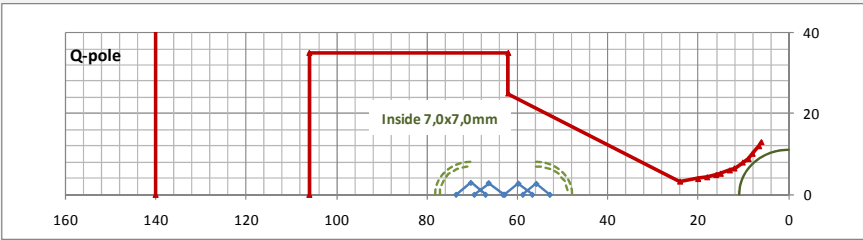
**3\*\*U1.QFM1**

Position:

5.92 – 6.07m

Beam:

55.8 – 59.8mm



The pipe size is for the sextupole (sfm) between the two quadrupoles.

**3\*\*U1.QFM2**

Position:

6.32 – 6.47m

Beam:

66.3 – 70.2mm

**Sextupole**

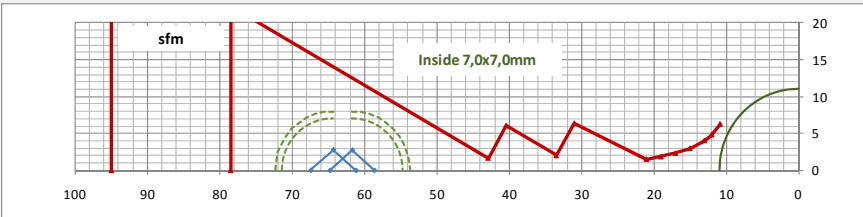
**3\*\*U1.SXFM1**

Position:

6.15 – 6.25m

Beam:

61.7 – 64.3mm



**Heat loads from wigD**

Power density on strips along the chamber. Vertical positions according to legend.

**Inner wall**

horizontal

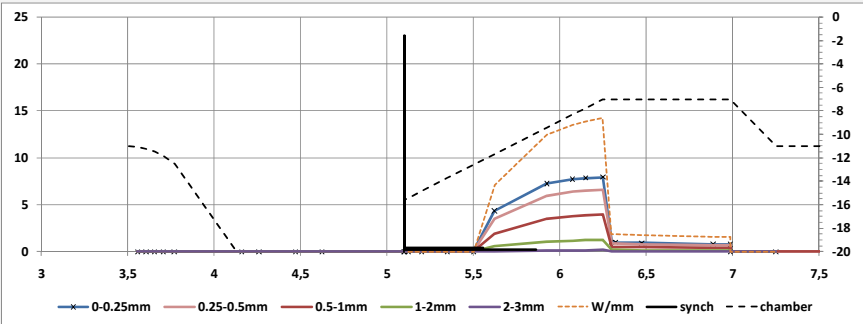
aperture (mm:

right hand scale)

Power density

(W/mm<sup>2</sup>: left

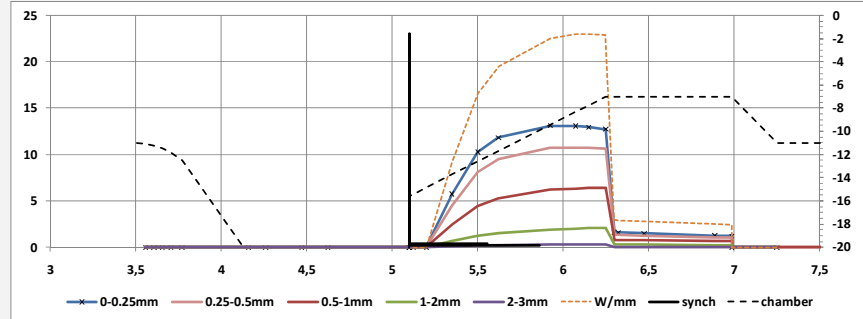
hand side)



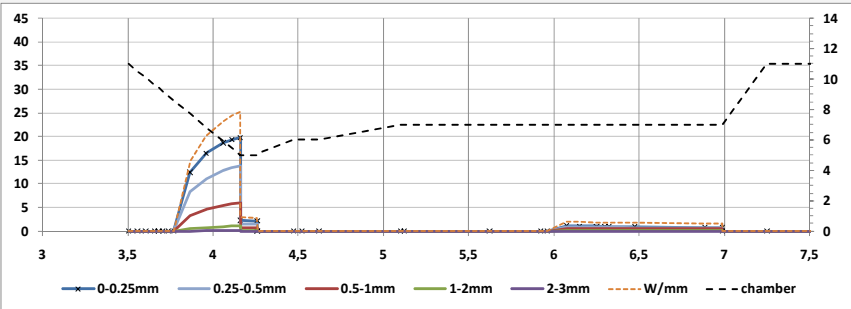
Synch: the average power density from the synchrotron light between the positions indicated by the red arrows in Figure 5 (23W/mm on crotch).

**Heat loads from Scw46**

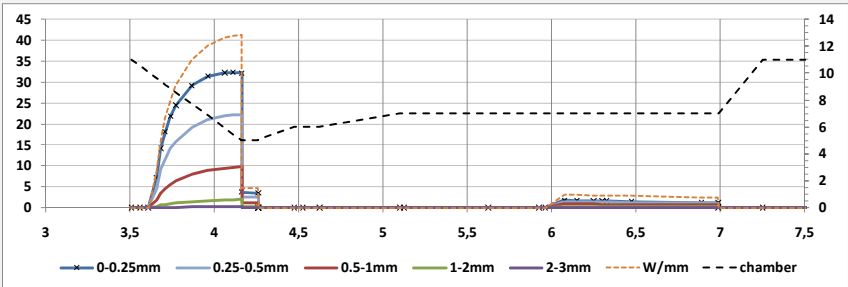
**Inner wall**



Heat loads  
from wigD  
Outer wall

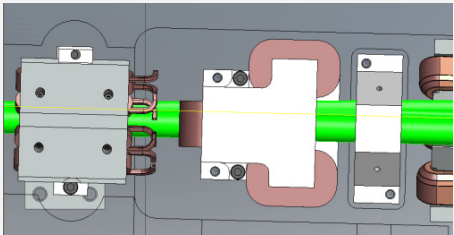


Heat loads  
from Scw46  
Outer wall



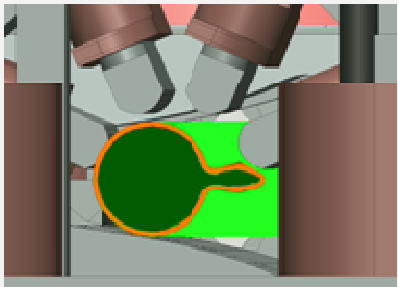
Laminated  
Correction  
Magnet  
3\*\*M1.COL\*1

Magnet  
apertures:  
45 x 25mm  
(Hor. x Vert.)



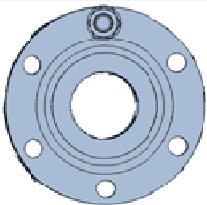
Light green: Chamber outside.  
Dark green: Chamber inside.  
Orange: Chamber profile.

Top view with upper main yoke removed.  
oyy to the left.

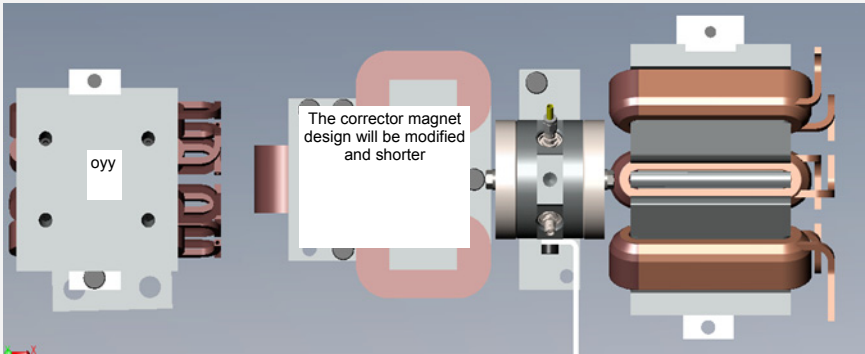


Cut at the end of the correction magnet  
looking towards oyy.

Vacuum flanges  
for a SS304  
chamber at  
3\*\*M1.COL\*2

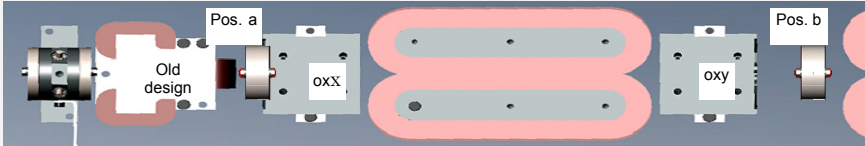


CF40:  
Diam. 70mm  
L 2 flanges;  
25.4mm



The only possible position is after magnet oyy.

Vacuum  
flanges for  
SS304 chamber  
at 3\*\*M1.COL\*1

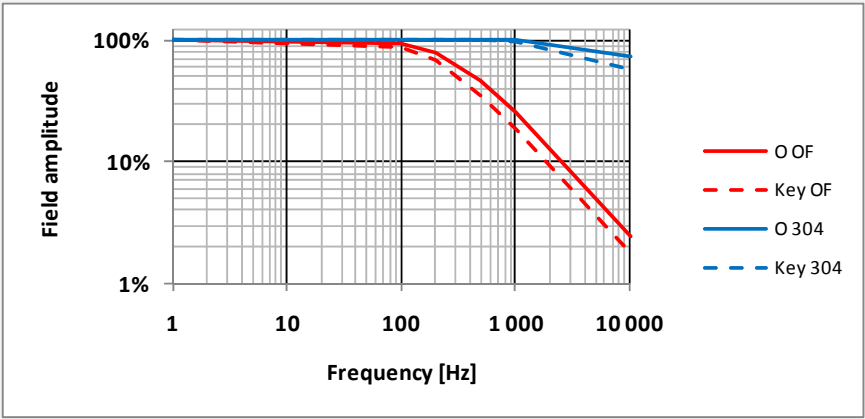


Two positions could be possible;  
a: short chamber; the new corrector design might give space enough.  
b: with a long ss304 chamber. The heat load from scw46 is not hitting this chamber.

Corrector field  
response in  
Chambers:

Shape:  
O: Circular  
Key: Keyhole

Material:  
OF: Oxygen free  
copper  
304: Stainless  
steel



Calculated with FEM 4.2. (Skin depth for copper is 1mm at 4 300Hz).

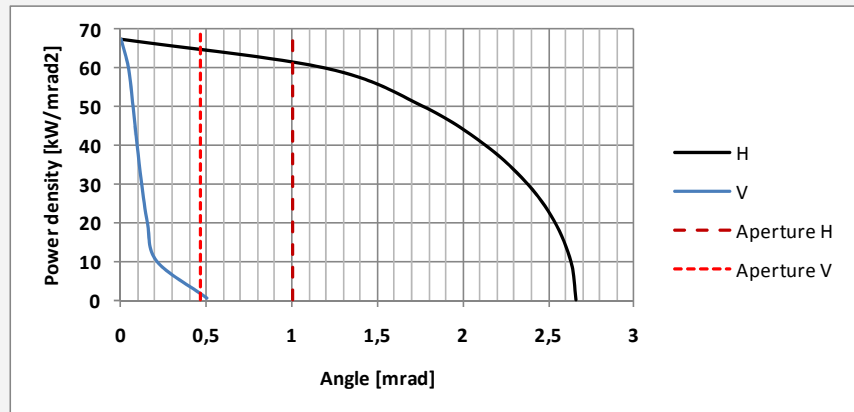


### Power density scw46

Limiting apertures:

Horizontal in the  
tapers before oyy  
and sfm.

Vertical in oyy.



Vertically the power density could be approximated by a straight line from max to zero at 0.3mrad.

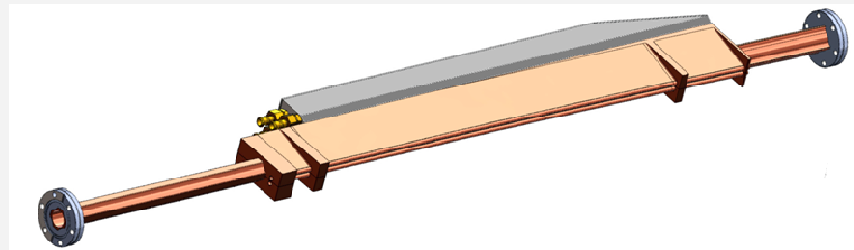
### Power density wigD

The limiting  
apertures are the  
same as for  
scw46.



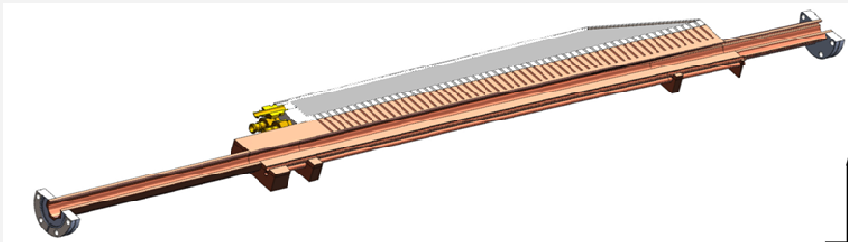
### Water cooled chamber in mc

Copper with  
stainless steel  
water manifold

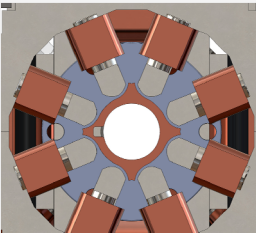


Water cooled chamber in mc

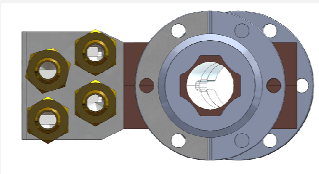
Cut below the median plane showing the cooling channels



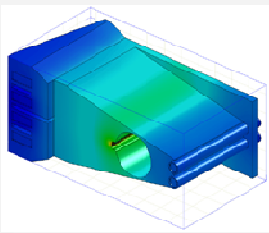
Water cooled chamber in mc



Stiffening ribs and photon opening in oyy.

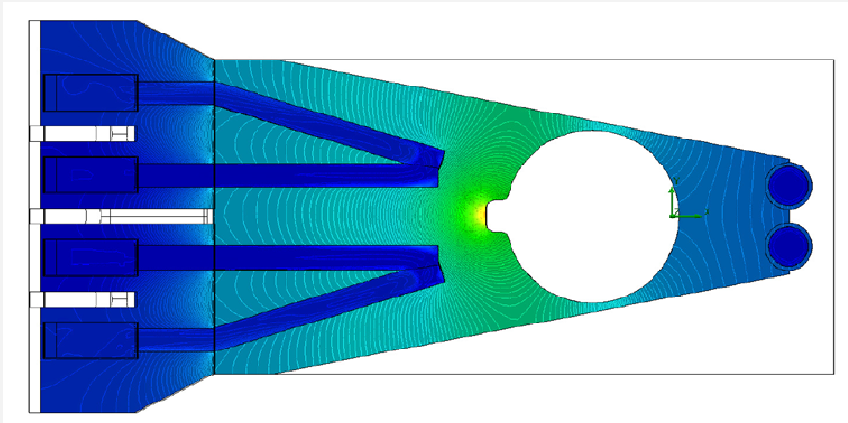
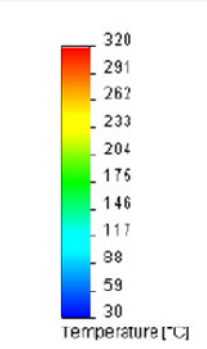


End view.



Modelled block.

Water cooled chamber in mc  
**PRELIMINARY**



Maximum temperature at the photon impact about 320°C. Central part about 200°C.  
Cooling circuits 30-50°C. **PRELIMINARY calculated on 1dm of chamber**

Heat load from  
scw46

Numbers are for wigD and [scw46]  
Wig80 is slightly above wigD

**Maximum power density**

**Maximum linear power density on a 22mm ID pipe after the sd magnet**

**Total power until position 7m.**

**Inner wall**

23W/mm in the crotch  
10W/mm<sup>2</sup> (14W/mm) [about 28W/mm] on the tapers after the corner and before the sd

1W/mm [1.5W/mm] at position 11m

9.3kW [about 26kW] + 0.4kW Synch.

**Outer wall**

20W/mm<sup>2</sup> (25W/mm) [about 55W/mm] in front of magnet oyyo

1W/mm [1.5W/mm] at position 11m

7.3kW [About 27 kW]

### 2.8.2.5. Port for a 4m Undulator; epuA

Undulators have a much narrower beam than the damping wiggler. The horizontally widest beam (1.1mrad) comes from the elliptically polarizing undulator epu53p6Plan in the planar mode. This section describes the distribution from epuAPlan which had the widest beam (0.62mrad) in the first version of the insertion device chapter. epuAVert has a higher beam profile.

The vacuum chamber will only need to handle the bending magnet radiation and may be simplified compared to the chamber needed after the wiggler wigD in paragraph 2.8.2.4. The diagnostic chamber #2 in Table 4 row 5 might be used. As we make the design of the chambers we can select the cheaper one as the “standard”.

#### Photons from the undulator epuAVert

Source position            Center of straight section (x=0)

Power density            [kW/mrad<sup>2</sup>] at 500mA

$$\text{IF } v < 0.4552 \text{ then PowDen} = 32.46 \frac{\sqrt{1 - \left(\frac{v}{0.4552}\right)^{1.5588}} \left(1 + \frac{5}{7} \frac{5.871^2 h^2}{1 + 5.871^2 h^2}\right)}{(1 + 5.871^2 h^2)^{2.5}}$$

**else PowDen = 0**

h is horizontal and v is vertical angle [mrad].

Horizontal            1% level at ±0.44mrad; 90% at ±0.04 mrad

Vertical                1% level at ±0.455mrad; 90% at ±0.16 mrad

The vertical apertures are limited in the oyy (0.47mrad) and sdend (0.54mrad).

As seen in

Figure 8 the beam is vertically about the same size as the chamber apertures except for the helical mode where the beam is higher.

Table 8: Power on the chamber wall above the beam at different polarizations [W/mm<sup>2</sup>].

Position	Helical	Vertical	Inclined
Octupole oyy	0.12	0	0.01
BPM	0.15	0.15	0.01
Sextupole sdend	0.05	0	0

The power densities given in Table 8 are for the wall parallel to the beam above the beam center.

Figure 8 upper show the vertical approximation of the power density for **cpuAVert** (red) and radial approximation for **epuAHeli** (blue) in kW/mrad<sup>2</sup> as a function of direction in mrad.

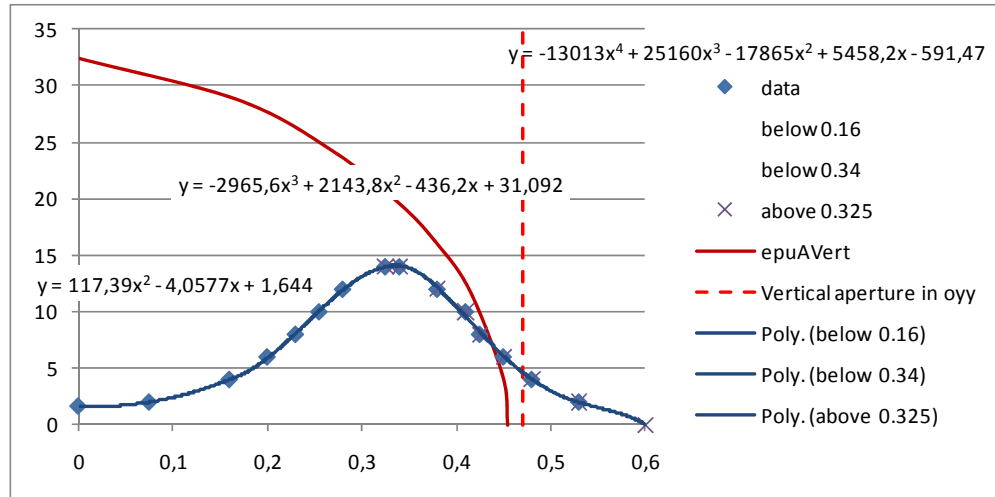
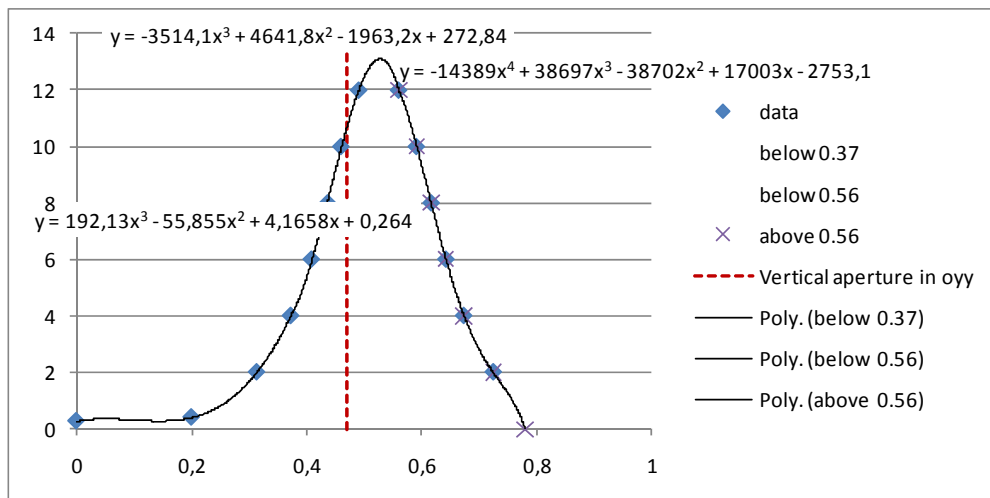


Figure 8: Power density approximations.

The lower graph is for **epu48Heli** having the peak outside of the vertical aperture.

Epu53p6Heli has a somewhat wider photon fan, with the outer 2kW/mrad<sup>2</sup> level at 0.82mrad.

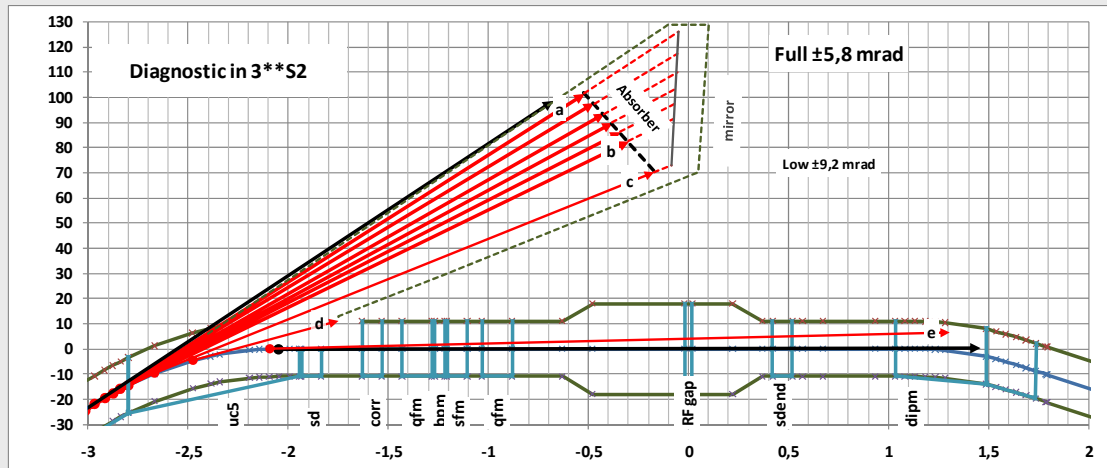


### 2.8.2.6. Diagnostic Port after uc5

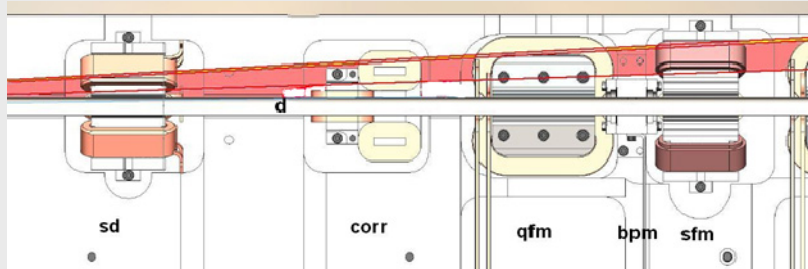
The position could be used for a diagnostic beam going through the end sextupole and be captured on a mirror in the short straight section, where an RF-cavity is placed in some other sections.

Note that the diagnostic port cannot be placed in a section with an RF cavity.

Figure 6: Horizontal vacuum chamber layout with synchrotron light dipole uc5.



See also diagnostic chamber pos #2 in Table 4 rows 5 and 6.



Reddish area: Open photon area in the mid plane.

Yellow area: Margin between the forward line and ray a.

The crotch is just after the sd (d).

The aperture is limited as seen in Table 9.

The red arrows show the directions for the high power flux.

The vertical aperture is  $\pm 4\text{mrad}$  between rays a and b.

The aperture is limited to  $\pm 1\text{mrad}$  between b and c.

The dashed black line is for a  $\pm 0.5\text{mrad}$  high absorber in order to prevent the mirror from high power radiation.

The dotted purple line indicates the inside of the vacuum chamber for the diagnostic beam.

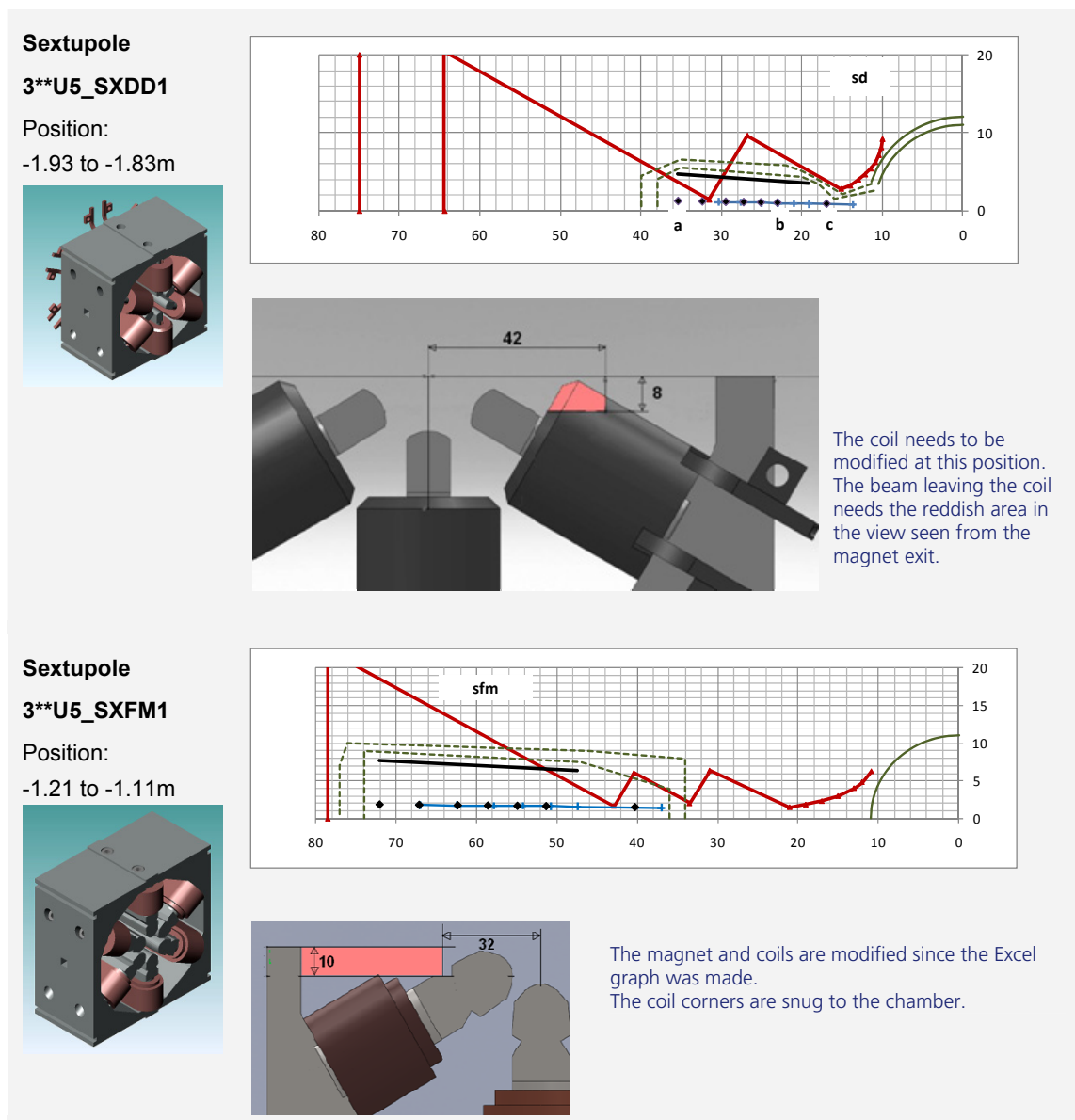
The power dissipation on the wall between rays c and d is about 500W (mainly before point f, about 120W on the crotch if it is 4mm long). (Between rays c and d2 300W and c-d about 200W).

The black arrows indicate the directions of the straight lines at the ends of the bend magnet.

Table 9 shows the radiation position relative to magnets in the following straight section. Positions for the 5 rays shown in Figure 6 going to the absorber are marked.

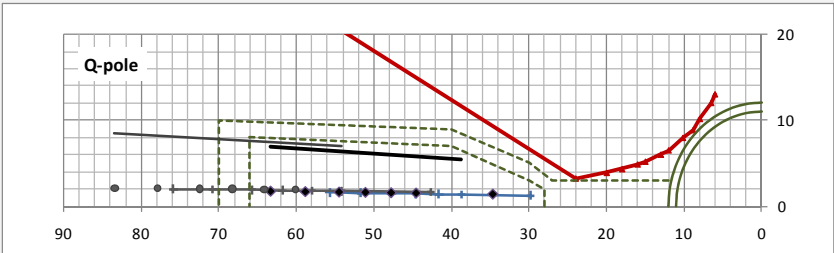
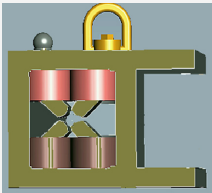
- Red: Magnet and coil profile (dimensions from FEM-files).
- Green: Electron beam pipe.
- Dashed green: Appendix vacuum chamber for the diagnostic beam.
- Black lines: Synchrotron light at 4mrad vertical direction inside the horizontal  $\pm 5\text{mrad}$  segment (a-b) at entrance and exit of the elements.
- Other: Synchrotron light at 1mrad vertical direction inside the horizontal  $\pm 9\text{ mrad}$  segment (a-c) at entrance and exit of the elements.
- Positions are marked for the beams indicated by the red arrows (a-c) in Figure 6.
- The entrance positions in blue are connected with a line.

Table 9: Emitted synchrotron light and chamber geometry.

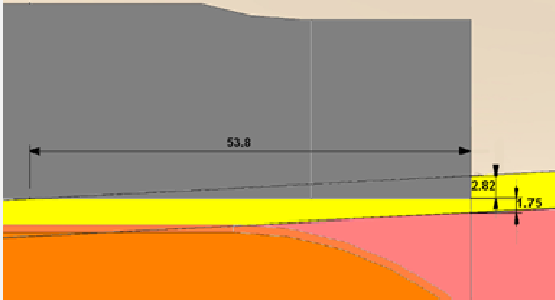


**Quadrupole**  
**3\*\*U5\_QF1**  
-1.43 to -1.28m

**3\*\*U5\_QF2**  
-1.03 to -0.88m  
beam profiles  
shown in gray.

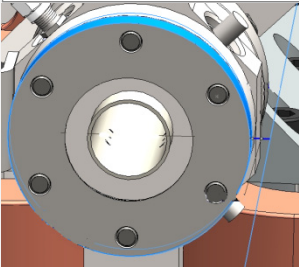
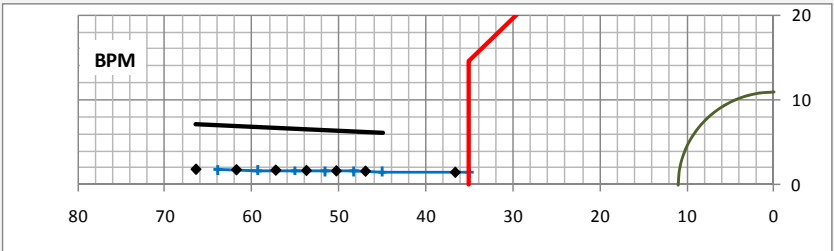
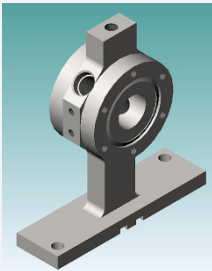


Above; a chamber profile for the first quadrupole. A cooling block at the crotch will be needed.



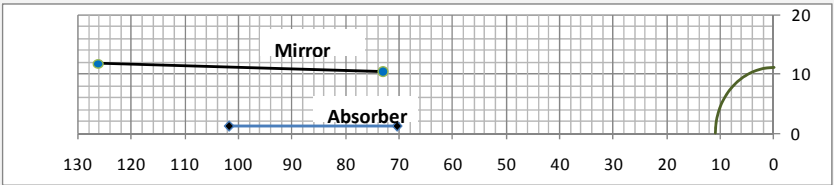
The exit yoke corner of the second quadrupole need to be trimmed 6mm for clearance to the vacuum chamber. Pink and yellow areas as in Figure 6.

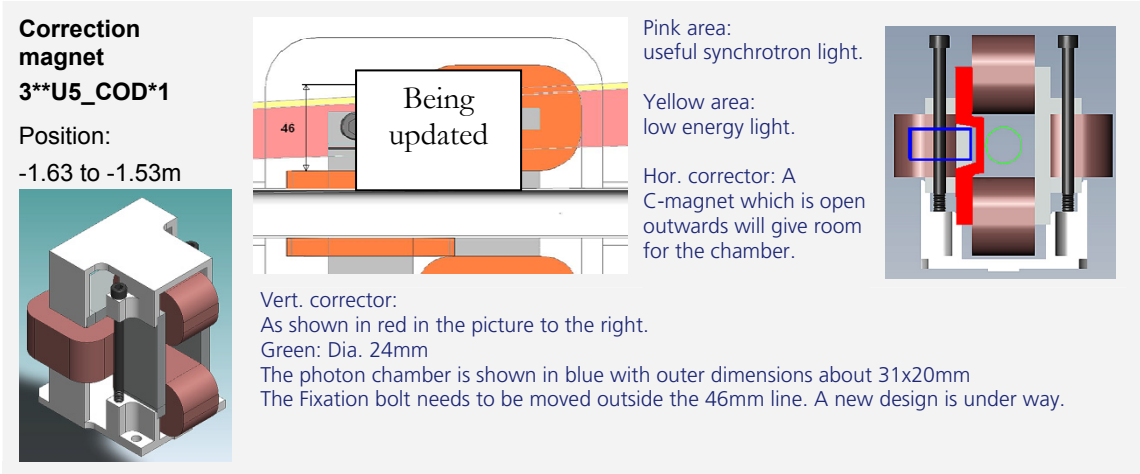
**BPM**  
**3\*\*U5\_BPM1**  
Position:  
-1.27 to -1.22m



Beam "c" leaves the BPM house with 5.2mm clearance and enters the BPM with 3.5mm clearance. The low  $\pm 9\text{mrad}$  radiation angle might be reduced for the vacuum chamber needs.

**Positions of the**  
light on the  
absorber and mirror  
relative to the  
beamline





Dimensions for an absorber and mirror placed according to Figure 6:

	Absorber	Mirror
Material	Copper tube	?
Horizontal length	About 350 mm	About 65mm
Vertical coverage	±0.5 mrad	±4 mrad
Total height	2.5 mm	About 25 mm
Power density	1.8 W/mm	--
Total power	630W	--
Cooling pipe ID; Flow; dP	1.1mm ; 0.25l/min; 1.7bar	--
Temp max	90°C	--
Cooling water temp in-out	30 - 66°C	--
Length expansion	About 0.3mm	--

Table 10: Absorber and Mirror data.





### 2.8.2.8. Diagnostic Port after Matching Dipole mc1

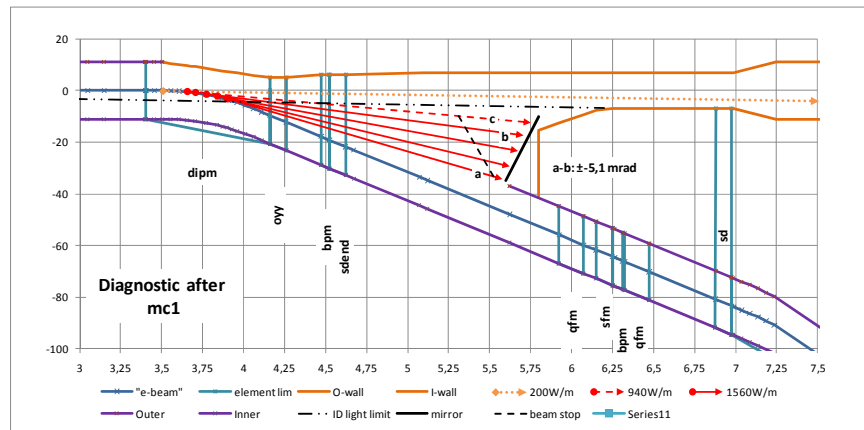
Synchrotron light from the matching magnet after a long straight could be used for diagnostic purposes.

The vertical aperture is limited by the magnet oyy.

If the upstream ID is not a wiggler, then a mirror might be positioned in the tapered part before the crotch. Especially if the feedthroughs for adjustments and cooling are inserted from above, then the beamline could be used for undulators.

The dashed black line in Figure 8 is for the maximum deflection angle as listed in Table 5; i.e. 1.1mrad for epu53p6Plan. The surface “below” this line will receive very low flux of radiation from non-wiggler ID’s.

Figure 8: Horizontal vacuum chamber layout with synchrotron light dipole mc1.



See also “diagnostic chamber #2” in Table 4 rows 5 and 6.

From ray b and upward, the synchrotron light power goes down, between a and b the power is at maximum.

The power labels for the synchrotron light rays indicates W/m electron path.

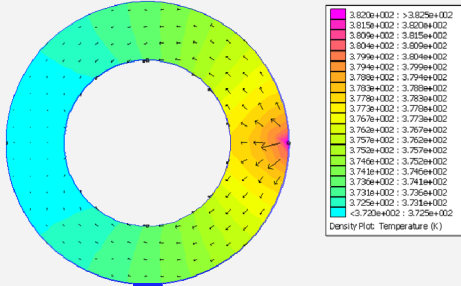
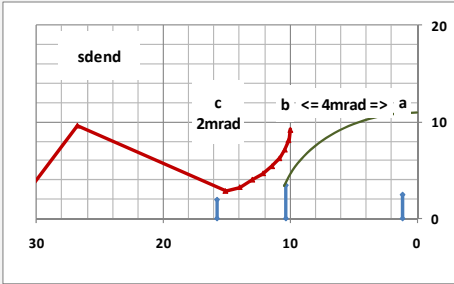
Unless the port is used for an ID the apertures needed in the magnets are the relaxed compared to §2.8.2.4.

The absorber is positioned to give the same distance from the source of radiation along the absorber, thus a constant height for a constant vertical angle.

The crotch is protected by the absorber and need no special cooling. Heat from an ID might fall on the chamber surface in front of the sextupole at about 7m. The crotch geometry should be designed together with the mirror system in order to minimize HOM disturbance.

Dimensions for an absorber and mirror placed according to Figure 8:

Table 11: Absorber and Mirror data.

	Absorber	Mirror
Material	Copper tube	
Horizontal length	About 230 mm	About 50mm
Vertical coverage	$\pm 0.5$ mrad	$\pm 4$ mrad
Total height	1.7 mm	About 13-17mm
Power density	1.6 W/mm	--
Total power	370W	--
Cooling pipe ID; Flow; dP	1mm ; 0.23l/min; 1.6bar	--
Cooling water temp in-out	30 - 53°C	--
Length expansion	About 0.3mm	--
2 dimensional heat flow at the "hot end" of the absorber		--
Copper temperatures 100-110°C will go down somewhat in the 3D		--
Position of rays' a - c at the end of sdend. Outside ray b the vertical aperture is limited.		

2.8.2.9. Injection Straight

This section will have

- Kicker magnets with ceramic chamber (2 short and 2 long magnets).
- a septum magnet in the middle (Lambertson septum, see Max II/III).  
Length about 1m plus flanges, bend radius 11.765 m.  
Ion Pump port on the side and NEG-coating.

Is a tapered chamber adaption at the ends of the septum magnet needed to reduce HOM?

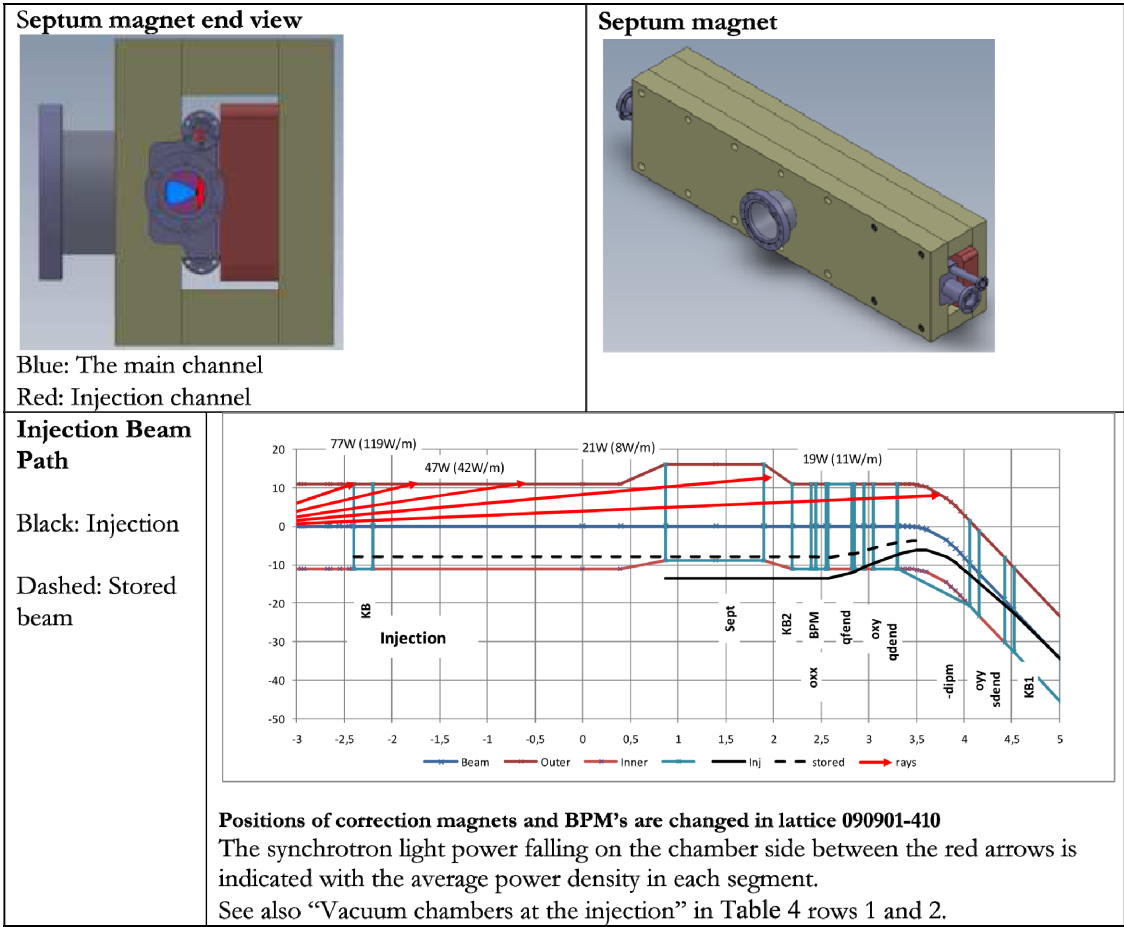
NEG coating of the main channel (shown in blue) is foreseen. The walls seen by the circulating e-beam needs to be copper plated before the NEG coating is applied. As an alternative a NEG coated copper shield with extensions to the beam chambers in front and after the iron part should be studied.

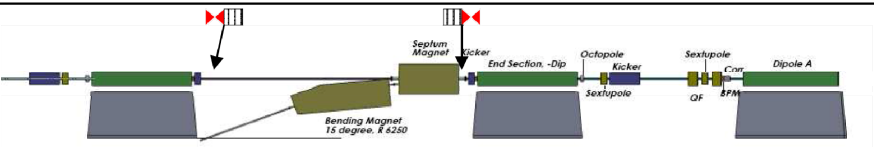
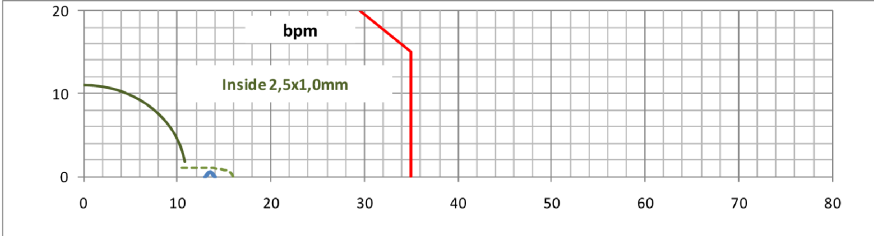
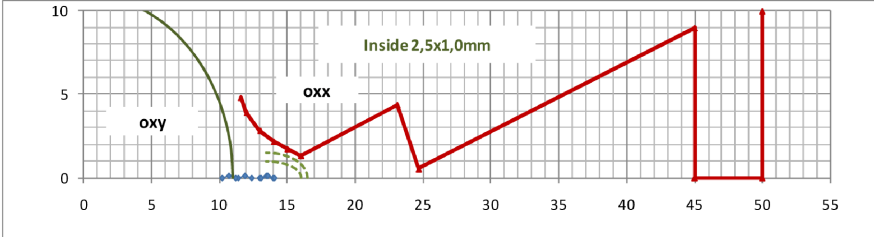
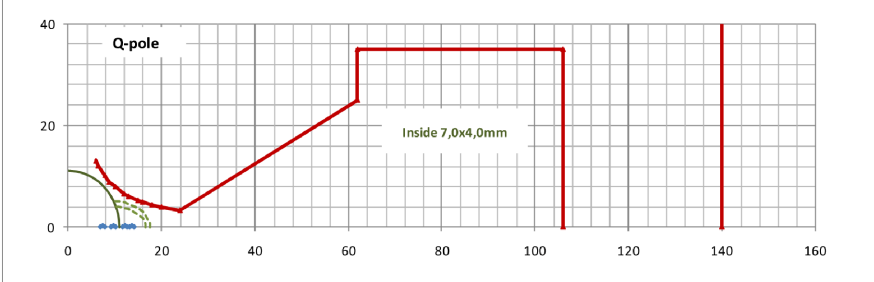
Special vacuum chambers are needed for the elements following the septum magnet.

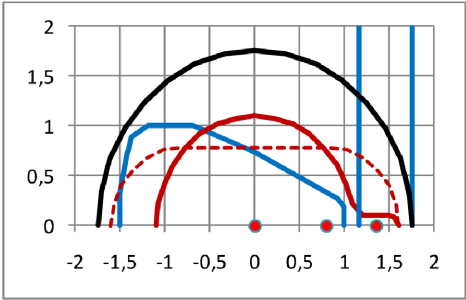
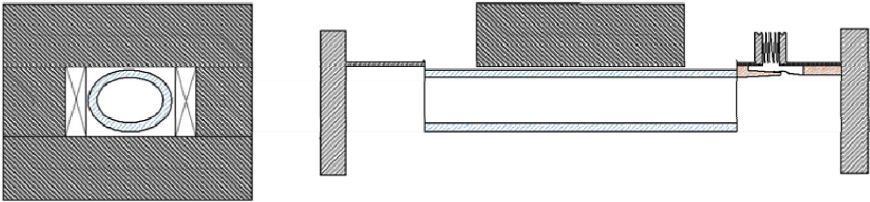
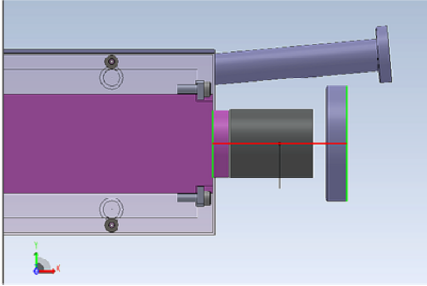
The sketches in

Table 12 are not updated for lattice 090901-410!

Table 12: Layout and beam positions.



<div>Kickers and septum</div> <div>Blue elements: Kickers</div>	<div></div> <div>The bend magnet is changed to 20 degrees (Nov 10) The symbols above indicate the positions for bellows and gate valves needed for the installation and baking of the vacuum sections. The two bellows will together be compressed by about 21mm during baking (worst case with AL-chambers in the long straight)</div>
<div>BPM</div> <div>301M1.BPM11</div> <div>Beam pos 13.5 mm</div> <div>The Gate Valve 301M1.VGR41 in front will need the same opening.</div>	<div></div> <div>The BPM-house in Table 7 may be used, turned 180 degrees but the “pocket” is larger than needed. A shallower version is shown here.</div>
<div>Octupoles</div> <div>301M1.OXX1</div> <div>301M1.OXY1</div> <div>Beam pos 13.5 - 11.3 mm</div>	<div></div>
<div>Quadrupoles</div> <div>301M1.QFE1</div> <div>301M1.QDE1</div> <div>Beam pos 13.5 - 9.1 mm</div>	<div></div>

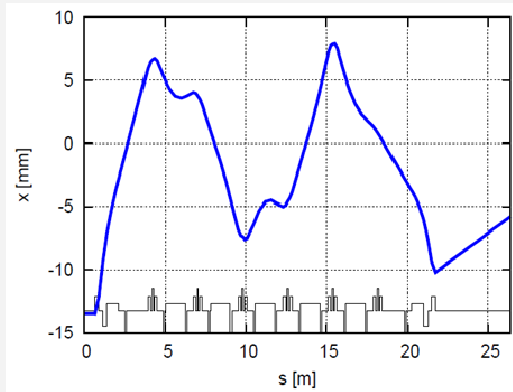
<div><b>Septum apertures</b> Full red: Chamber 22 mm Dashed red: Ceramic profile Black: Flange 36mm Blue: Magnet profile Dots: Beam positions</div>	<div></div> <div>Copper shields at the ends are needed for a smooth transition between the different chamber apertures. A NEG-coated C-shaped screen along the septum magnet connected to the end shields will be studied.</div> <div>The RF gate valve after the short kicker will need a keyhole profile (see the full red line)</div>
<div><b>Short kicker magnet</b> Proposal of layout of ceramic chamber and bellows</div>	<div></div> <div>Nominal length of proposed chamber; 350mm. (play -18 to +4mm) Distance Septum iron (green line to the left) to BPM center is 523mm.</div> <div></div>

### 2.8.2.10. Pulsed Sextupole Magnet Injection

A second method of injection to the ring will be implemented. The horizontal beam position differs from the method used with kicker magnets in §2.8.2.9.

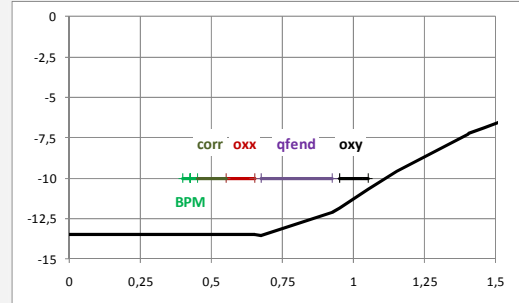
Figure 9 show the orbit of the Injected bunch starting at the injection point and ending at the location of the Pulsed Sextupole Magnet (PSM) at the end of the 2nd long straight; 26.4m downstream of the injection septum end.

Figure 9: Horizontal path.

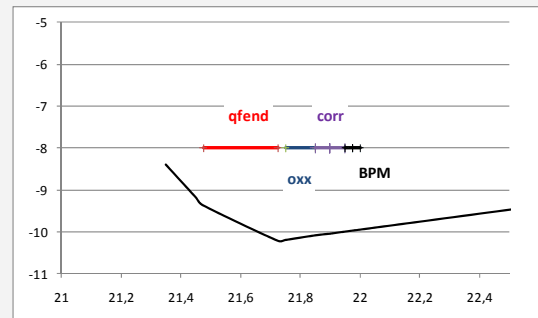


The chambers in the elements with labels (in the close up figures) will need the keyhole apertures as indicated in Table 11.

A ceramic vacuum chamber is needed in the PSM.



Close up at the beginning of the injection path.



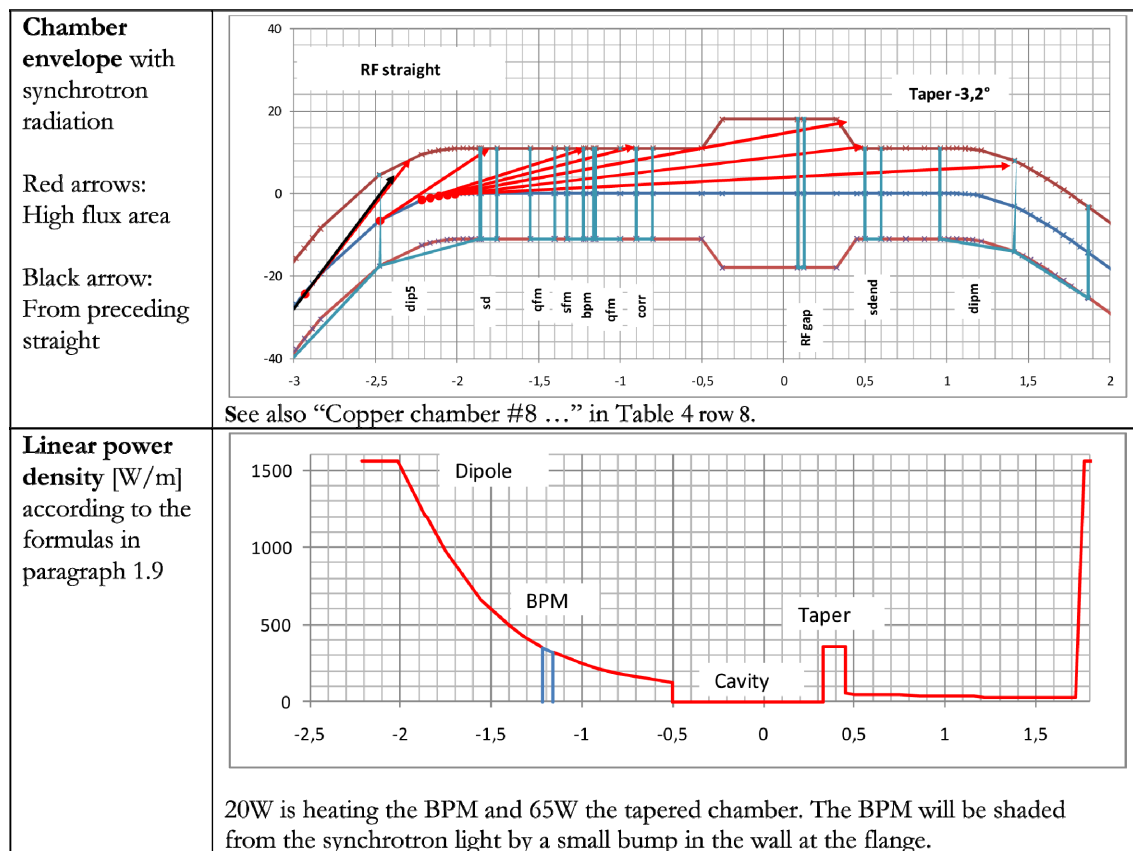
Close up at the end of the injection path.

### 2.8.2.11. RF in Second Short Straight

Maximum 6 sections will have one 100 MHz cavity each. (§3.6 version 091203).

Total cavity length: 700 mm  
 Outer radius: 440 mm  
 Radial aperture: 18 mm (Standard flange CF40 has gasket ID 36.8mm)  
 RF gap: 40 mm  
 Distance gap to exit flange: 200 mm

Table 13: Horizontal vacuum chamber layout.



Tuning of the cavity frequency needs an axial movement of approximately  $\pm 1$ mm.

The tapered parts shall include a set of bellows for the length adjustment of the cavity and the thermal expansion when baking the chambers.

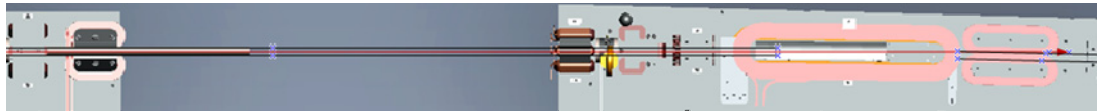
About 3 sections will each have a 300MHz cavity which is smaller.



### 2.8.3. Vacuum Diagnostics

The quality of the vacuum will be read by

- Gamma detection; installed as many as practical. They will serve as the primary tool. A possible position might be at quadrupole after the last matching dipole, where the gammas produced on the last short straight will be detected.



- Ion Sputter pump currents
- Radiation monitors
- RGA; as part of the turbo pump stands.
- Beam loss monitors along the ring as done at DELTA

When the NEG coating is activated the RGA and pressure readings will only “see” the local conditions at the measuring point as the distributed pumping speed is quite high for most gases.

The quality of interest is not the total (nitrogen equivalent) pressure as such but the gas induced losses. The loss is a function of the mass of the gas molecule.

(Anders Hansson and Magnus Lundin are measuring gamma radiation from conventional and NEG chambers in MAX II.)

## 2.8.4. Installation

First installation will be made without insertion devices and with circular 22mm NEG-coated vacuum chambers in the straight sections.

Straight forward ports with windows will be used in order to look at some synchrotron radiation from the bend magnet. See the dotted arrow in Figure 5 where the emitted power in the small opening angle in the beam pipe will be in the order of 20W (at 500mA).

Insertion Devices will successively be installed when the system is tested with beam.

NEG-coated chambers are to be activated prior to installation and then backfilled with nitrogen, sealed off, and protected.

NEG-coating may be made in lengths up to 6 m.

Longer chambers may be welded after coating. E.g. 10 m long aluminum chambers for Soleil are coated in 5m lengths.

### Aluminum chamber for Soleil Jean-Marc FILHOL at EPAC2006: THXPA02\_TALK.pdf

- *Al extruded up to 10 m long*
- *Helical undulator gap 19mm*
- *Water cooled*
- *NEG coated in 2 parts 5m long (SAES)*
- *Welded together (CINEL)*

Figure 10: Welding.



What is the maximum chamber length we can handle/install? (Building layout).

See also “Compatibility of surface treatments and assembling techniques with Ti-Zr-V performances”, P.C. Pinto; CERN, 45<sup>th</sup> IUVSTA meeting, Catania 2006.

As the distances between flanges and magnets are very small it will not be possible to assemble the vacuum system in the final position. All components will be put together in a lifting frame where the BPM's will be fixed to the frame and all heavy components, (e.g. valves, vacuum pumps ...) will need to be supported from above. The weight and rigidity of the individual vacuum chambers will be studied and supports designed where needed. Special consideration will be made regarding how to handle the torque needed for compressing CF-gaskets; about 16Nm for CF40 with M6 bolts.

Starting the beam tuning with simple chambers in the long straights and no ID's is preferred. Adding ID's one at a time and retuning the machine will help understanding the behavior of the machine.

### 2.8.5. Pump Down

- One CF40 valve/port in each section for connection to a mobile Turbo pump unit (50 l/s).
- Sputter Ion Pumps (CF40) with effective pump speed of about 10 l/s will be spaced for a good pressure distribution for the NEG conditioning.

Maximum times:

- Roughing 6 hrs
- High vacuum in 24 hrs
- Activation at 200°C during 24 hrs + temperature ramping

Calculations below are made by iteration of the pressure in discrete points along the cell with the following formula:

$$P_j = \frac{Q_j + \sum_{i \neq j} (P_i \times C_{ij})}{S_j + \sum_{i \neq j} C_{ij}}$$

With:

j	Calculation point		
i	Other points		with direct connection to point j
$P_j$	Pressure in point j	[mbar]	
$Q_j$	Total gas load in point j	[mbar l/s]	Outgassing from surfaces is split equally between adjacent points
$C_{ij}$	Conductance between points i and j	[l/s]	
$S_j$	Pump speed at point j	[l/s]	Effective speed for pump with connection. In §1.6 the distributed pumping is split equally between adjacent calculation points

Vacuum pressure is calculated for one magnet cell with closed gate valves 5cm into the long straight sections.

The calculated section contains one beam port and one RF cavity. A small SIP (40CF) is positioned close to the beam port and a larger (160CF) on the cavity. The inside of the cavity is not NEG coated, nor the beam pipe. The pump speed for the SIP on the cavity is reduced by a screen with 50% opening.

For roughing and during the baking of the chambers the turbo pump at the center of the cell is connected through a 25cm long 40mm flexible tube.

Label Pumps	Effective speed	Gassing rate	Max pressure	Comments
		[mbar l/s/cm <sup>2</sup> ]	[mbar]	
Turbo	10 l/s	10 <sup>-9</sup>	2 · 10 <sup>-4</sup>	One full cell with closed gate valves at each end.
SIP	10 & 220 l/s + turbo	10 <sup>-9</sup>	5 · 10 <sup>-6</sup>	SIP's and turbo pump active
SIP Baked	SIP's	10 <sup>-12</sup>	2 · 10 <sup>-8</sup>	The turbo pump is disconnected
NEG	0.5 l/s/cm <sup>2</sup> + SIP's	10 <sup>-12</sup>	3 · 10 <sup>-10</sup>	NEG-coating activated on surfaces in the electron ring but not in the cavity and beam-line.

Pumping speed of 0.5 l/s·cm<sup>2</sup> for hydrogen and 5 l/s·cm<sup>2</sup> for CO has been reported by the CERN vacuum group at the 45<sup>th</sup> IUVSTA meeting, Catania, 2006.

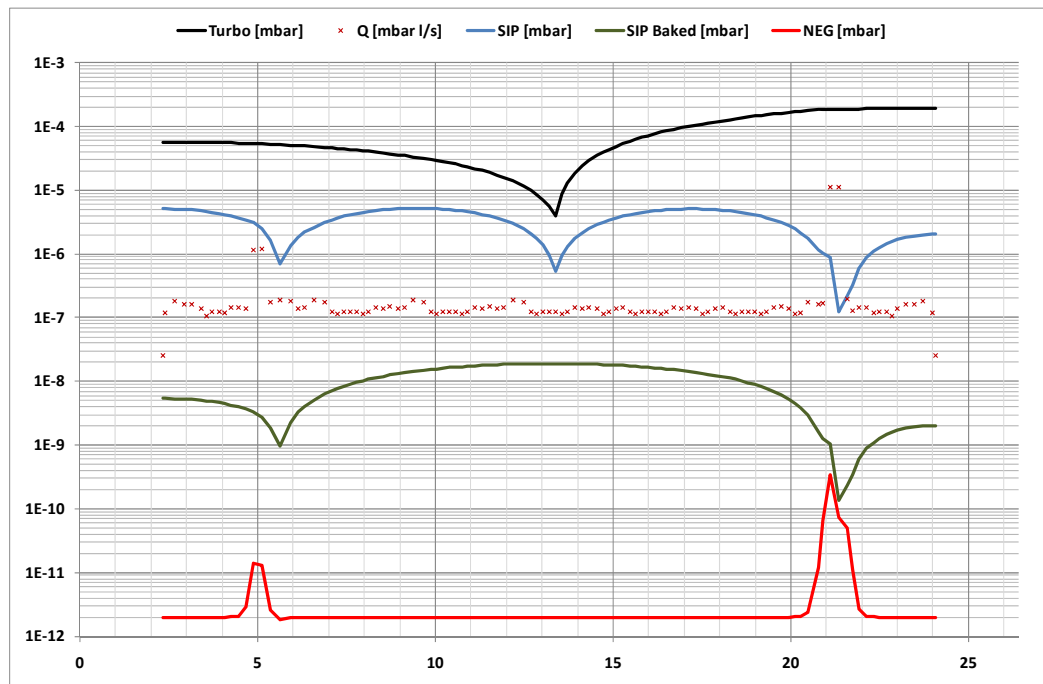


Figure 11: Roughing pressures.

Conductance and pump speeds for mass 28 (CO or N<sub>2</sub>) are used. (NEG pump speed for H<sub>2</sub>)  
 The peak in the curve "NEG" at position 4.5m is for the gases from a 4m beam pipe with average diameter 16mm. At 22m the gas load from the RF cavity (not NEG treated) is shown.

## 2.8.6. Beam Induced Pressure

Beam induced gas load is calculated for the geometry and pump speeds as case “NEG” in paragraph 1.5.

The chamber geometry is the same as in §2.8.5.

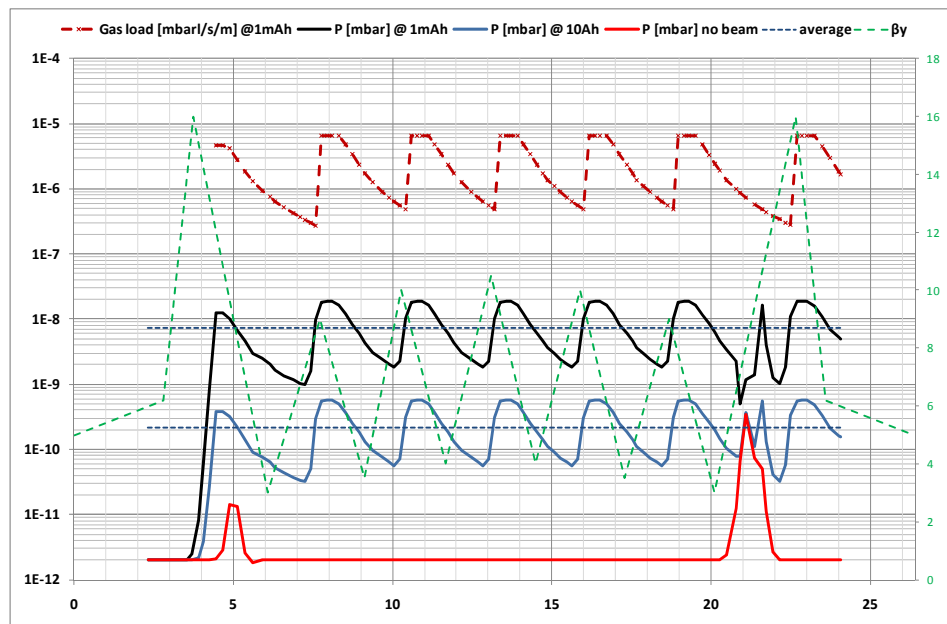
The synchrotron radiation is hitting the vacuum chamber at small angles.

The photon flux is calculated with the formula in §2.8.9.

Vacuum pressure is calculated for one magnet cell at 500mA circulating beam:

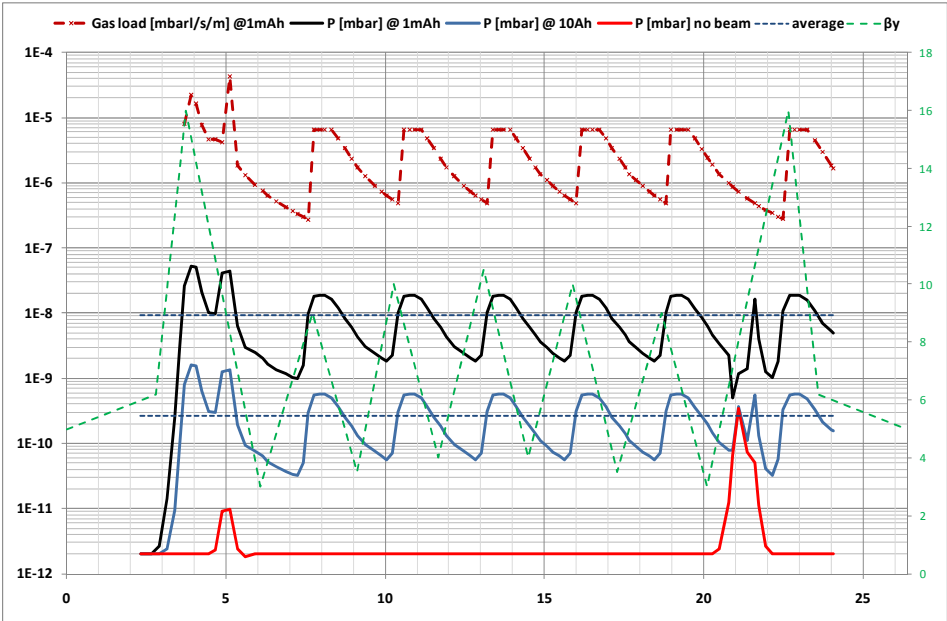
Label	Desorption rate [molecules/ photon]	Max /average pressure [mbar]	Comments
@1mAh	$4.2 \cdot 10^{-5}$	$2 \cdot 10^{-8}$ $7 \cdot 10^{-9}$	Rates for activated NEG surface in Figure 14
@10Ah	$1.3 \cdot 10^{-6}$	$6 \cdot 10^{-10}$ $2 \cdot 10^{-10}$	Rates for activated NEG surface in Figure 14
No beam	-	$3 \cdot 10^{-10}$ $7 \cdot 10^{-12}$	Same as “NEG” in Figure 11

Figure 12: Beam induced pressure.



Induced gas load at 1mAh is shown in the diagram.  
The pressure should be below  $10^{-9}$  mbar especially where the  $\beta_y$ -function is high.  
The beta function is simplified from Figure 3.2. in §2.2. of the DDR.

Figure 13: pressure at 500mA beam with wigD active.



The desorption rate from the surfaces hit by the photons from the wiggler is estimated to be the same as from the synchrotron radiation (scaled with kW)

Label	Desorption rate	Max /average pressure	Comments
	[molecules/ photon]	[mbar]	
@1mAh	4.2 10 <sup>-5</sup>	5 10 <sup>-8</sup> 9 10 <sup>-9</sup>	Rates for activated NEG surface in Figure 14
@10Ah	1.3 10 <sup>-6</sup>	2 10 <sup>-9</sup> 3 10 <sup>-10</sup>	Rates for activated NEG surface in Figure 14
No beam	-	3 10 <sup>-10</sup> 7 10 <sup>-12</sup>	Same as “NEG” in Figure 11

Local sputter ion pumps connected to the vacuum chamber will not lower the maximum pressure at 4m as the conductance is low. Added pumping at 5-5.5m might reduce the peak at 5m.

NOTE:

- Conductance is calculated for mass 28 (N<sub>2</sub> or CO); 3.7 times lower than for molecular hydrogen (H<sub>2</sub>) but the calculated pressure profile will only be marginally changed as the pumping speed of the NEG coating is large.

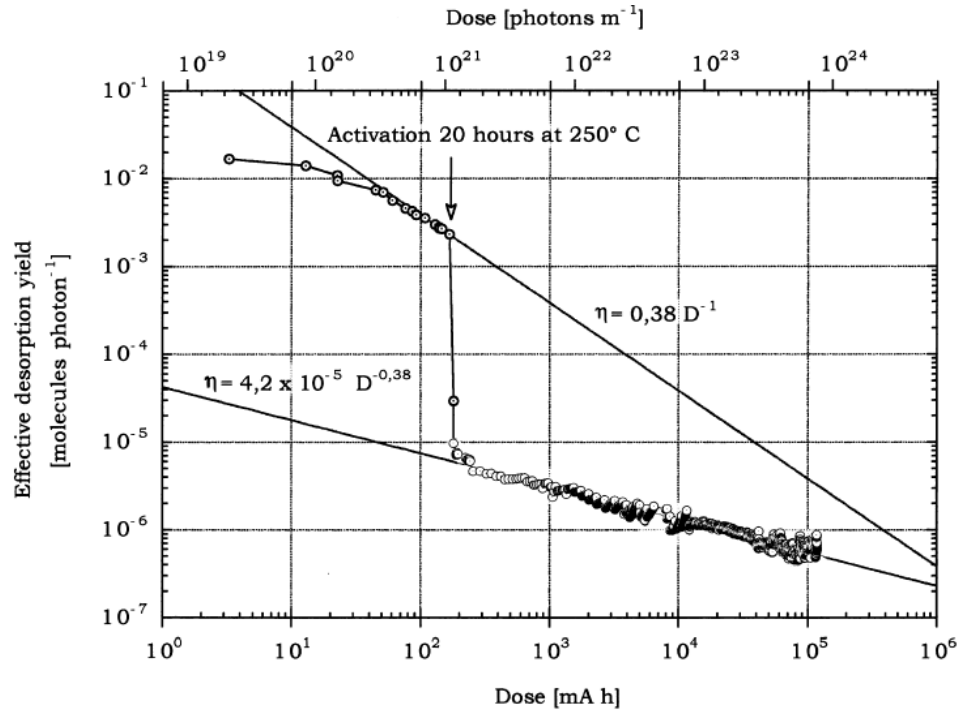


Figure 14: Desorption yields measured on a NEG coated stainless steel chamber at CERN.

[P. Chiggiato, R. Kersevan / Vacuum 60 (2001) 67-72] Desorption yields for NEG coated chambers before and after activation.

By scaling the maximum pressure found in Figure 12 with desorption rate as a function of dose we get the two beam conditioning cases in Table 14.

Beam lifetime is scaled from 6 minutes for 10<sup>-6</sup>mbar (ME).

In chapter 2.10 *Beam Lifetime* the lifetime is calculated for a constant pressure of 2 · 10<sup>-9</sup>mbar.

Elastic 25.4hrs; inelastic 56.1hrs; resulting total lifetime 17.2hrs.

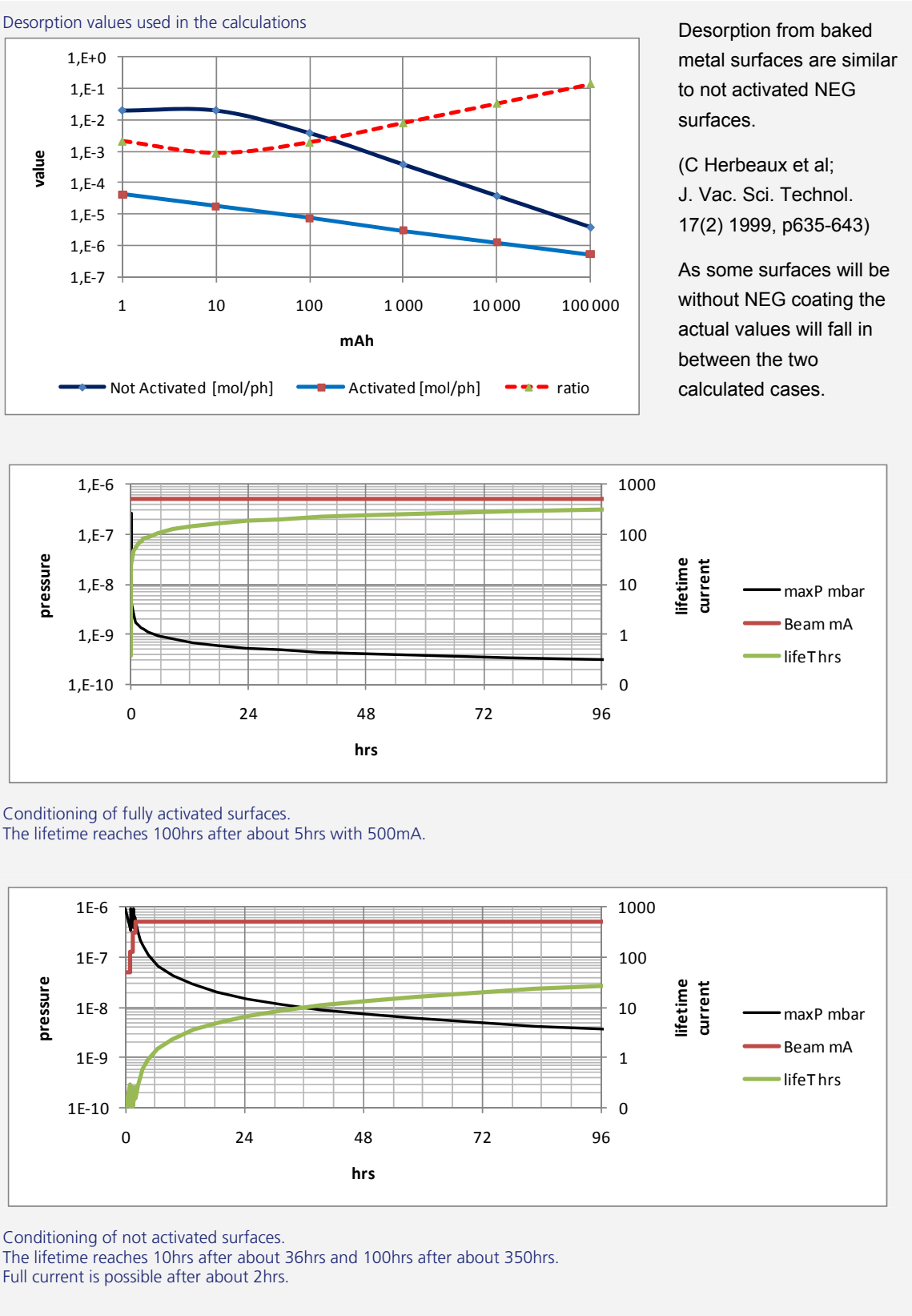
This corresponds to 2 minutes at 10<sup>-6</sup>mbar which is the maximum pressure allowed in the calculations in Table 14.

6 minutes is used as the lifetime calculations are scaled with the maximum pressures while chapter 2.10 is calculated for a constant pressure in the ring.

(The ratio maximum to average pressure is 2.7/1 in Figure 12).

The calculation is done for a coasting beam with no insertion devices.

Table 14: Beam Conditioning.





### 2.8.7. Venting and Maintenance

Erik Wallén got the information about how to vent NEG coated vacuum systems from Vincent Baglin at CERN (Vincent.Baglin@cern.ch). Vincent plans to report about this venting technique at a future vacuum conference.

*Equipment:*

- Argon gas in bottle
- SAES Getter pump (model not reported yet)
- Venting valves and tubes
- Baking heat strips

*NEG coated vacuum systems have a tendency of being large and it may be very difficult to reactivate the NEG coating after the system has been vented due to some minor work like replacing a valve.*

*It is possible to vent NEG coated system without having to reactivate the NEG coating by doing the venting with Argon gas that has passed through a well baked getter pump.*

*The Argon gas pressure in the NEG coated vacuum system should be slightly above atmospheric pressure when opening the vacuum system so that Argon is flowing out when doing the repair work on the vacuum system.*

Figure 15: Vent gas equipment.



Note that argon is heavier than air and will flow like water out of a filled volume.

Most of the argon will be evacuated by the turbo pump system prior to starting the Sputter Ion Pumps.

## 2.8.8. Conditioning/Performance

### 2.8.8.1. Baking System

#### 2.8.8.1.1. General

Vacuum system must be baked at 180°C for 24 hours for the activation of the NEG. Some synchrotron laboratories are using thin (<1mm thick) Kapton insulated heater films for in situ baking (Soleil). Other laboratories use pre-baking in ovens for large sections of the rings (ALBA, SLS, ASP) with final conditioning of the vacuum system with beam.

Figure 16: SLS and ASP ovens.



More pictures showing the handling of chambers during baking and assembly is shown in:

<http://www.fmb-berlin.de/start.php?lang=2&node=30306&lnode=103&mh=0&e>

The same website has also similar pages for SLS and other laboratories with interesting pictures of vacuum chambers and other components.

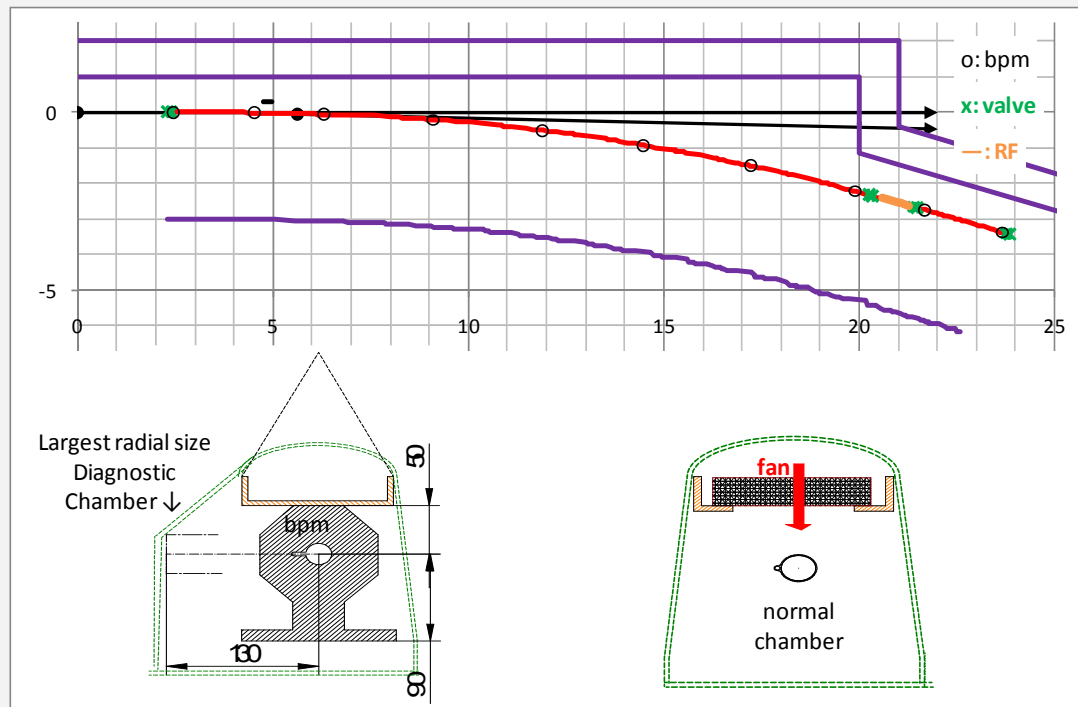
#### 2.8.8.1.2. MAX IV Magnet Sections

The use of copper for the vacuum chambers in the magnets simplifies the baking system.

During baking the magnets will be opened in the mid plane and the upper halves moved away from the chamber. A support is needed that include the heat elements with an insulating hood around as proposed in Figure 17 and Figure 18.

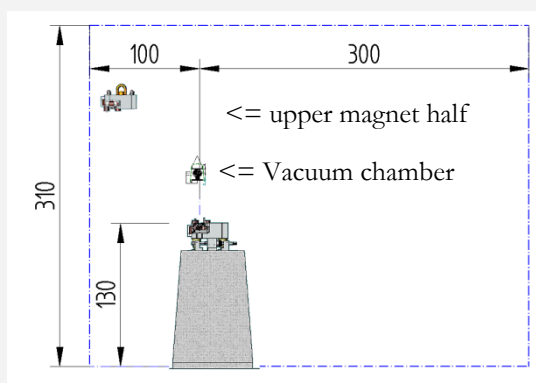
This approach allows a free expansion of the vacuum chambers without bellows in the cells. Also the heater system is simplified as no individual heater elements directly on the chambers and BPM houses are needed.

Figure 17: Heating frame and hood principal layout.



Measures in the graph in meter but mm in the lower sketch.

Figure 18: Baking geometry and tunnel dimensions.



Distances in cm.

The upper magnet halves are put aside secured above the vacuum chamber baking hood as indicated.

The frame with hood as seen in Figure 17 includes heater elements and fans connected to regulation systems in order to keep an even heat distribution during the thermal cycling.

An alternative is to lower the assembly into an oven on the floor in front of the concrete stands. Programming and logging of the procedure is foreseen.

Handling of the frame and hood needs to be investigated.

### 2.8.8.1.3. Straight Sections

Baking of the straight sections and RF cavities are foreseen to be made in place with bellows to compensate for the longitudinal expansion. The heating system for each section depends on the installed components. At the first start of the storage ring a version of the hood could be used.

Cooling of the adjacent vacuum sections during the baking may be needed. Calculation of heat transfer through the gate valves will be done.

See §2.8.8.2 and the bellows paragraph 2.8.2.2.2.

### 2.8.8.2. Length Dimensions at Baking

The path length	Room temperature 20°C	expansion at 200°C
Complete ring	528 m	1.66 m (Cu) dR = 2.64dm if circle
Magnet section	22m	67mm (OFC) 1.76e-5/degC
Straight sections	4.8m	22mm (pure Al) 2.6e-5/degC 15mm (OFC)

The stresses in a 300mm long 24x1mm copper tube with fixed ends have been calculated with Comsol Multiphysics. When heated from 20°C to 200°C the von Mises Stress is 400MPa along the tube and about 700MPa at the ends. The higher value could be a result of the meshing.

The yield strength of OFC is about 40-120MPa annealed and 180-420MPa for cold worked.

The calculated stresses are too high. A test with a 300mm resulted in cracked welds between the flange disc and the tube. Modified weld geometry and e-beam welding will improve the strength and quality. Still the strength will be too low and the baking scheme is altered where the magnet sections are baked when lifted out of the magnets and then only perform beam conditioning in situ, reducing the need for bellows. See § 2.8.2.1, §2.8.2.2.3, and §2.8.8.1. - 2.8.8.2.

Behavior of the straight sections will need a separate review for each type of elements.

Example Injection septum magnet with the centre point fixed:

- The iron ends will move about 1.3mm
- The stainless steel chamber about 1.6mm
- The rest of the straight section (if copper) about 11mm

The result is need for bellows for 14mm compression before the septum magnet and 2mm after the septum chamber. A set of bellows ( $\pm 3$ mm from nominal length) incorporated in the beam exit port of the chamber will facilitate assembly and baking of the section.

## 2.8.9. Synchrotron Heat Load

The heat load at the center of each bend magnet.

Max dipole  
synchrotron  
radiation

$$P[W] = 14079.28 \cdot L[m] \cdot I[A] \cdot \frac{E[GeV]^4}{r[m]^2}$$

1.57 kW/m @ 0.5A, 3GeV, 19.1m

[http://hasylab.desy.de/e70/e6129/e3260/e3262/infoboxContent3265/f2\\_eng.pdf](http://hasylab.desy.de/e70/e6129/e3260/e3262/infoboxContent3265/f2_eng.pdf)

Max II @ 250 mA 1.5 kW/m

Radiated full  
height on  
chamber wall

±0.08mm  
(630 mm tangential from beam; height ±0.125mrad)

Flux dissipation  
in straight  
section after a  
bend magnet

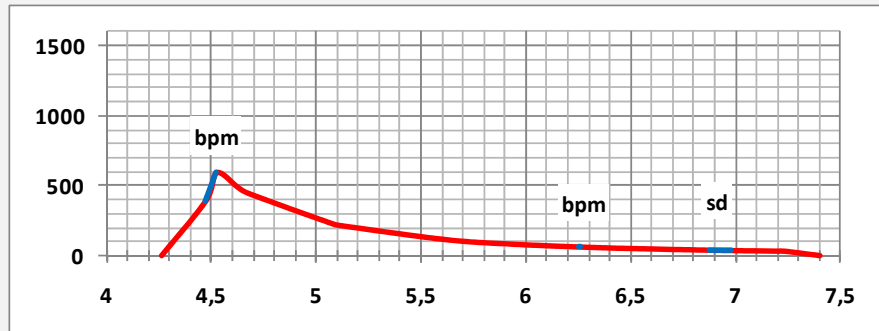
From Diamond Design specification, June 2002, page E5-22:

For practical use it is more convenient to write a formula for the photon flux per meter,  $\Gamma_m$ , as a function of distance,  $z$ , from the end of dipole, which has bending radius  $R_d$ , and horizontal half-aperture of vacuum chamber  $a$  :

$$\Gamma_m(z) = \frac{\Gamma_{tot}}{2\pi} \left( \frac{R_d + a}{(R_d + a)^2 + z^2} - \frac{R_d z}{((R_d + a)^2 + z^2) \sqrt{z^2 + 2 R_d a + a^2}} \right)$$

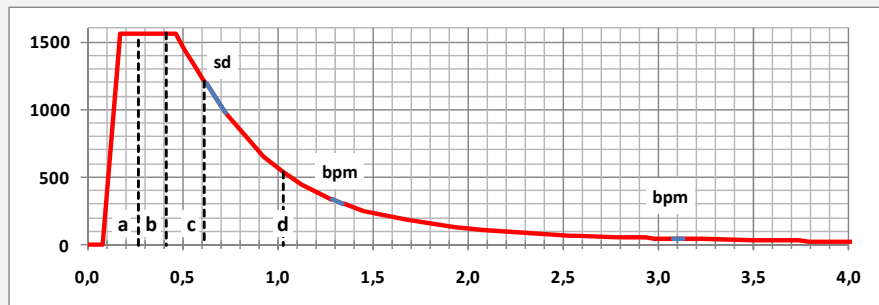
**Radiated power**  
[W/m] on the  
electron beam  
pipe after mc.

The zero  
position is at the  
middle of the  
straight section.



**Radiated power**  
[W/m] on the  
electron beam  
pipe after uc5.

The zero  
position is at the  
middle of the  
dipole.



Positions a-d according to the diagnostic port Figure 6.



### 2.8.9.1. Cooling Water Need

This section is not updated for the new insertion devices.

Points 1 and 2 below are with the 4m damping wiggler. There will be 4 units or less in the ring.

All other insertion devices will put much less power on the chamber walls.

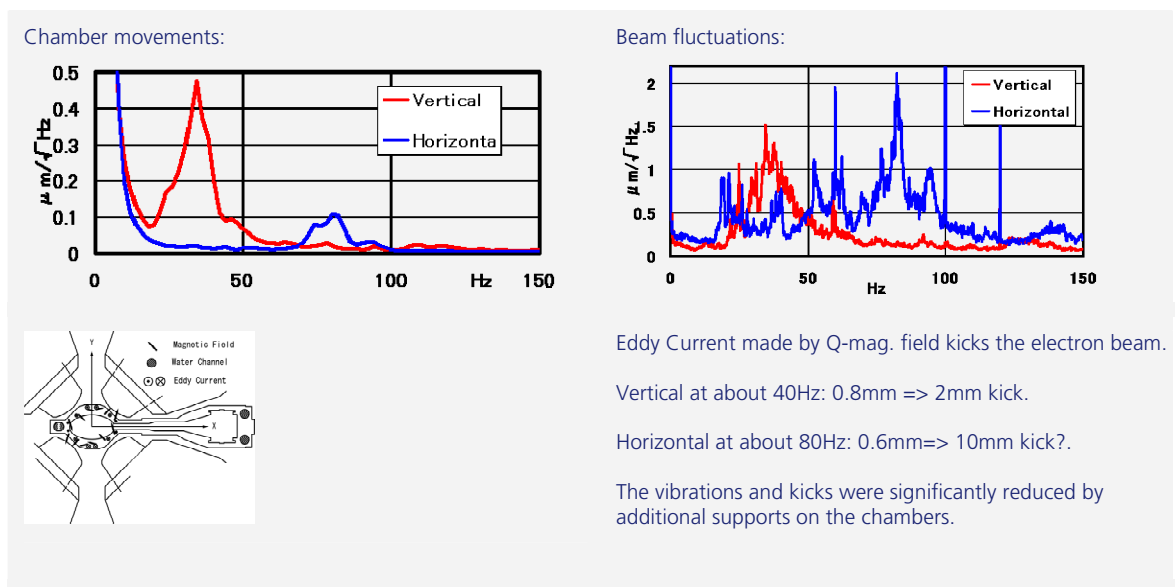
1. The first block at the dipole: 7kW, about 25l/min at pressure drop 1.2bar  
Max 25W/mm over about 1mm height.
2. Second block in/after crotch: 8kW with about 170W around the short crotch end.  
Max 15W/mm. Cooling is not yet studied.
3. General electron beam pipes:  
In bend max 1560W/m, average in ring 355W/m.  
Total 188kW. Cooling is not yet studied. See the power profile at the end of Table 9.

During baking of the straight sections cooling of the ends of connected magnet sections is needed. Pressure relief valves will be used to prevent the circuits from excess pressure.

## 2.8.10. Remarks/Questions

- **Vibrations**

SPring-8 reports about beam position fluctuations caused by vibrations from water cooling (S. Matsui, et al.; Jpn. J. Appl. Phys.; Vol. 42 (2003) pp.L338).



- **Corrosion**

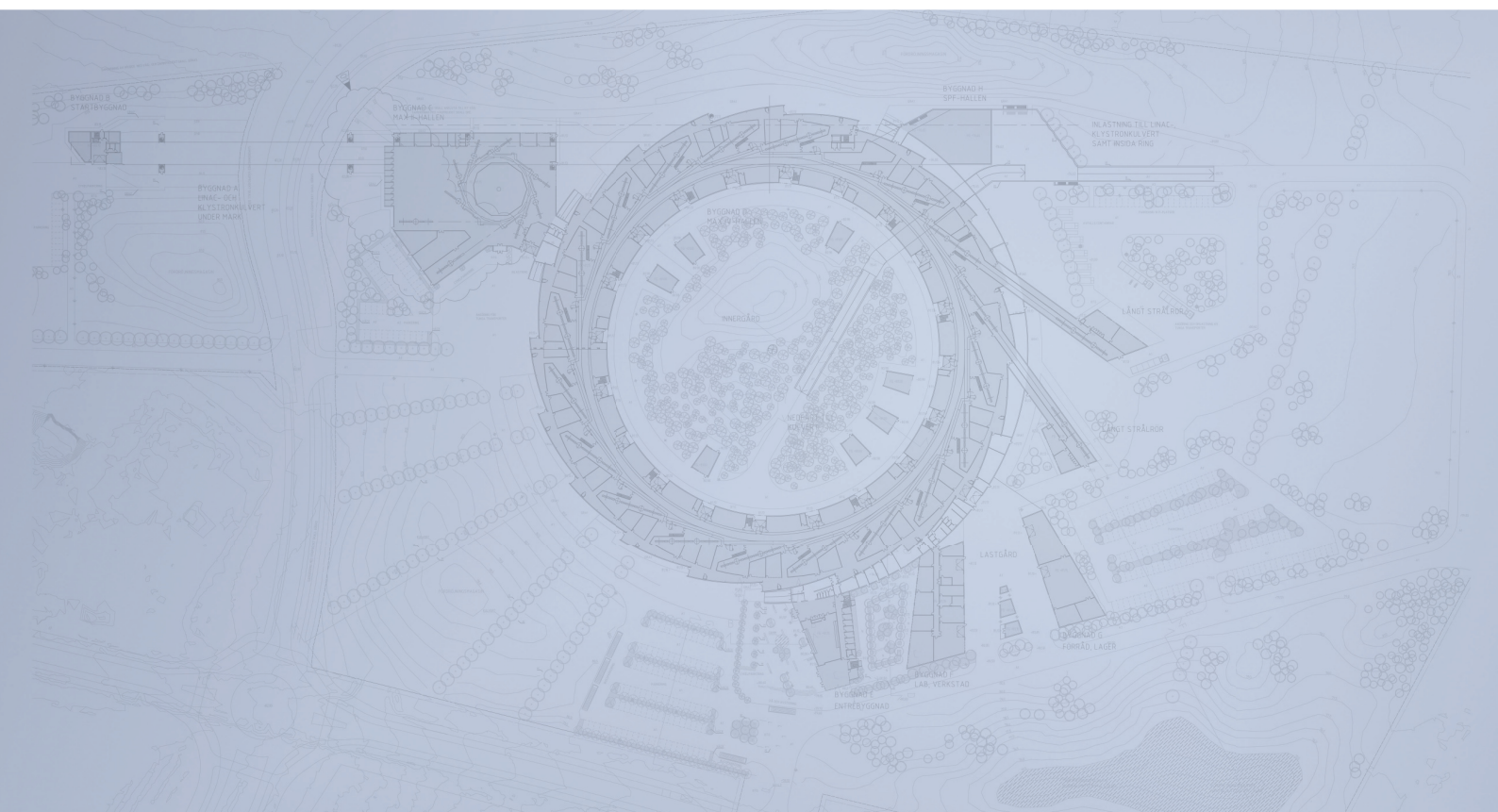
At SPring-8; an absorber at a RF section leaked cooling water. There is a possibility that synchrotron radiation, water, and dissolved oxygen corroded Cu.

### 2.8.11. Abbreviations Used

Abbreviation	Short for	Remark
BPM	Beam Position Monitor	Capacitive pickups
CF	ConFlat	Type of vacuum flange
DIP, dip	Dipole magnet	The 3 degree dipole
DIPm, dipm	Matching dipole magnet	The 1.5 degree dipole at each end of the magnetic cell
ESRF	European Synchrotron Radiation Facility	Grenoble, France
FEM		A finite element program for 2D calculations of magnetic, electrostatic, and thermal fields
GlidCop	Copper mixed with aluminum oxide ceramic particles	increases the copper's resistance to thermal softening and enhances elevated temperature strength
ID	Inner Diameter. Insertion Device.	
KEK	The High Energy Accelerator Research Organization	Tsukuba, Japan
NEG	Non Evaporable Getter	
OD	Outer Diameter	
OFC - OFHC	Oxygen Free Copper where H stands for High conductance	
oxx, oxy		Octupole magnet
oyy, oyyo		Octupole magnet
qf, qfm		Quadrupole magnet, focusing in the mid plane
RGA	Residual Gas Analyzer	
sd		Sextupole magnet, defocusing in the mid plane
sdend		Sextupole magnet at the end of the magnetic cell
sfm		Sextupole magnet, focusing in the mid plane
SIP	Sputter Ion Pump	
SLS	Swiss Light Source	Villigen, Switzerland
VAT		Manufacturer of vacuum valves

To be continued.

# Detailed Design Report



## Chapter 2

### MAX IV 3 GeV Storage Ring

#### 2.9. Diagnostics (RF and vacuum not included)

MAX IV Facility





## 2.9. Diagnostics (RF and vacuum not included)

---

<b>2.9.</b>	<b>Diagnostics (RF and vacuum not included) .....</b>	<b>2</b>
2.9.1.	Beam Position Monitors (BPMs) .....	2
2.9.2.	Tune Measurement: Stripline Monitor and/or Button BPMs .....	17
2.9.3.	Current Measurement: DCCT and BPMs. ....	18
2.9.4.	Emittance Monitor: Pi-Polarization Method .....	18
2.9.5.	Bunch Length Monitor .....	19
2.9.6.	Filling Pattern or Bunch Current Monitor. ....	20
2.9.7.	Scrapers with Possible Function as Dedicated Aperture to Protect IDs ....	20
2.9.8.	Pinger Magnets .....	21
2.9.9.	Beam Loss Monitor System .....	22
2.9.10.	Temperature Sensors .....	23
2.9.11.	Beam Dynamics Measurements/ Control System Applications .....	23
2.9.12.	References .....	26

## 2.9. Diagnostics (RF and vacuum not included)

---

### 2.9.1. Beam Position Monitors (BPMs)

#### 2.9.1.1. BPM Introduction

It has been demonstrated that state of the art BPM and correction performance, including the entire chain from BPM button to a final position correction, at a rate of 100 Hz, lays in the region of 0.3  $\mu\text{m}$  rms at a current of 400 mA. In other words; at a charge of 4 mC the rms position is kept within 0.3  $\mu\text{m}$ . This ensures a maximum position reading rms noise of 0.3  $\mu\text{m}$  for a 10 ms sample time at 400 mA. The vertical beam size in the straight sections will be around 2.5  $\mu\text{m}$  for a 2.5 pmrad vertical emittance beam, corresponding to 1% emittance coupling. The beam should be kept stable to within a tenth of this value at the foreseen 500 mA. This performance is thus almost within reach with present day technology. However, the MAX IV ring will definitely be run at a lower beam current in its initial phase, and an equally good beam position performance need to be achieved at even 200 mA of stored beam. Thus some BPM performance development has to be planned.

Considering the commissioning phase, we need less resolution, but we can only sample a short pulse. The MAX IV ring injector will deliver a 300 pC pulse with a pulse length of 1 ns for commissioning. This will require the electronics to be able to detect and calculate the position from this short pulse. A ringing filter is a way to achieve this, which is used in one commercial unit. This unit reaches quite good position readings using a ringing filter during commissioning.

#### 2.9.1.2. BPM Signals from Pickups

To meet the required performance the BPM pickups need to be sensitive enough to provide the BPM electronics with detectable signals through the entire operating range.

Button radius	$r = 2 \text{ mm}$
BPM RF Frequency	$f = 300 \text{ MHz}$
Button Capacitance	$C_b = 0.6229 \text{ pF}$
Circular Vacuum pipe radius	$b = 11 \text{ mm}$

Table 1: MAX IV Button Parameters.

The dissipated power from a button  $P_{btn}$  to an external load  $Z_0$ , at a beam current of  $I$ , is calculated with [3]:

$$P_{btn} = \frac{1}{2} * I^2 * Z_0 * \varphi^2 * \left( \frac{\omega_1}{\omega_2} \right) * \left( \frac{(\omega/\omega_1)^2}{1 + (\omega/\omega_1)} \right)$$

$$\omega = 2 * \pi * f \quad \omega_1 = \frac{1}{Z_0 * C_b} \quad \varphi = \frac{r}{4 * b}$$

Where  $f$  is the RF frequency,  $C_b$  is the button capacitance,  $r$  is the pickup button radius,  $b$  the beam pipe radius and  $\varphi$  the coverage factor.

Using the properties from table 1 for the MAX IV BPM pickups and  $Z_0=50 \Omega$ , the power at different beam currents is shown in Figure 1.

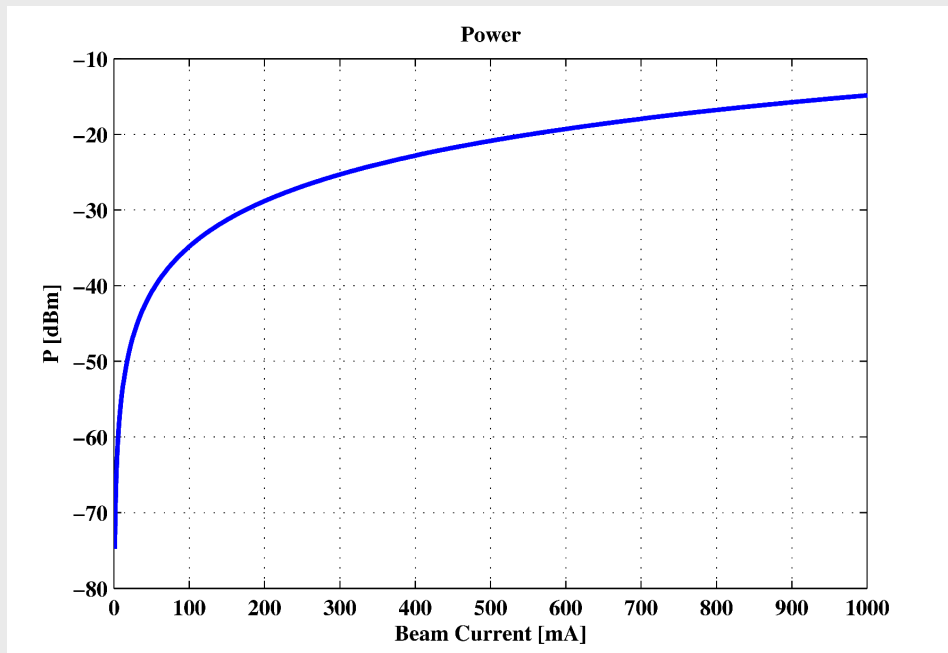


Figure 1: Power at BPM pickups.

At a beam current at 100 mA the power at the pickups  $P_{btm}$  is calculated to  $3.2515 \times 10^{-7}$  watts which equal:

$$P_{btm}(dbm): 10 * \log\left(\frac{3.2515 * 10^{-7}}{1 * 10^{-3}}\right) = -34.9 dBm$$

This is a voltage of:

$$U_{btm} = \sqrt{P_{btm} * 2 * Z_0} = 5.7 mV$$

The *delta-over-sum* sensitivity of the BPM pickups is shown in Figure 2, which is calculated and plotted with the ALBA-CELLS BPM GUI Matlab tool [1].

A 1  $\mu m$  beam displacement corresponds to a delta-over-sum signal change of  $1.25 \times 10^{-4}$

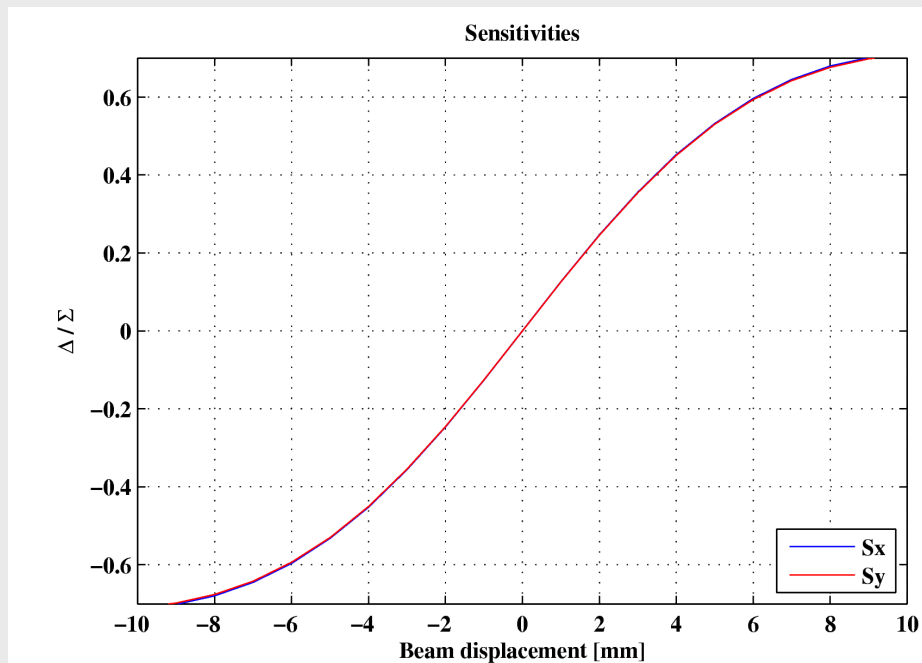


Figure 2: Horizontal and vertical position characteristics.

At 100 mA this signal change equals:

$$U_{change} = 1.25 * 10^{-4} * 5.7 * 10^{-3} = 712.5 \text{ nV}$$

To achieve the required resolution the noise of the BPM electronics must be significantly lower than the difference in voltage to be detected in this case 712.5 nV or -110 dBm. The theoretical noise voltage in an electronics system is calculated by:

$$U_{noise} = \sqrt{4 * kTB R}$$

Where k is Boltzmann's constant ( $1.38 \times 10^{-23}$ ), T is the temperature and B is the systems bandwidth and R is the impedance. As can be seen by the formula the larger the bandwidth of the system is the higher the noise voltage becomes. At room temperature T=298 K with a R=50  $\Omega$  system the theoretical noise floor at a B=10 kHz system bandwidth will be 90.7 nV or -128 dBm. This gives a theoretical Signal-To-Noise ratio of 18dB at a beam current of 100mA.

A 0.3  $\mu\text{m}$  beam displacement corresponds to a delta-over-sum signal change of  $2.5 \times 10^{-5}$ . Using the same calculations as above, but with a beam current of 400 mA and a required resolution of 0.3  $\mu\text{m}$  results in:

$$U_{change} = 2.5 * 10^{-5} * 22.8 * 10^{-3} = 570 \text{ nV} \rightarrow -112 \text{ dBm}$$

Thus at 400 mA and a required resolution of just 0.3  $\mu\text{m}$  the theoretical SNR will be 16 dB and at 200 mA and 0.3  $\mu\text{m}$  the theoretical SNR will only be 10 dB.

### 2.9.1.3. BPM Electronic Systems Introduction

The electronics of the BPM system is required to measure the beam position accurately within the full specified storage ring current range. Position information must be stable and provided at rates up to 10 kHz for Fast-Orbit-Feedback.

The current MAX II BPM receiver electronics has been developed and built in house. MAX-labs BPM receiver electronics would meet the required position resolution for Slow-Orbit-Feedback, but without modifications it can't provide position information faster than 65 Hz, another bottleneck is the time it takes for the PLC system to sample the signals from the BPM receiver and calculate the corrections at a central computer.

Today there are commercial digital BPM electronics systems available for purchase. In MAX IV a total of 200 BPM heads and should be installed for storage ring operations. At least one extra BPM head should be installed for use as a permanent test station.

Preferably the same BPM electronics should be used for commissioning which means that special considerations for this phase should be taken into account.

Temperature stabilization for the BPM electronics racks should be used to avoid temperature drifts in the electronics.

MAX IV will use a RF frequency of 100 MHz (like MAX II and MAX III). Most other synchrotron light sources use a RF frequency of 500 MHz. At MAX II and MAX III we detect the third harmonic with the BPM receivers. For MAX IV we'll most likely want to use the second or third harmonic, although the fifth harmonic could also be used to ease use of commercially available alternatives.

### 2.9.1.4. BPM Electronic Systems Overview

There are at least three main possible electronic solutions for MAX IV. Each of the possible variants will be discussed within the following sub chapters. Cost considerations also play a certain role.

Some hybrid variants are also under discussion, with fast electronics on the flanking BPM pickups and with slow electronics on the rest of the BPM pickups. This would lower the total cost for BPM electronics significantly compared to e.g. equipping the entire MAX IV storage ring with the Libera Brilliance system.

#### 2.9.1.4.1. Commercial Digital BPM System

##### 2.9.1.4.1.1. General Description

The commercially available system is a complete digital BPM receiver. This system is used on several third generation synchrotron light sources and supports Turn-by-Turn acquisition with a bandwidth of 1 MHz and high resolution position measurements with 1 kHz bandwidth. The Turn-by-Turn and high resolution measurements can be done simultaneously.

### 2.9.1.4.1.2. Hardware

The RF frontend of this digital BPM system uses a “Quasi-Crossbar-Switch”, four identical RF channels, with one analogue-to-digital converter for each channel. The analogue board uses undersampling to sample directly on the signal from the BPM buttons.

The signals from the pick-up electrodes first pass through the “Quasi-Crossbar Switch” which is a method to compensate for differences between the four RF signal paths. What the switch does is to make it possible to redirect any of the four input channels to any of the four RF channels and ADC's. This method improves accuracy and reproducibility.

Each RF channel have filter and gain adjustment. The attenuator is controlled digitally and has a range 31 dB (in 1 dB steps). The gain control is handled by the digital board and is adjusted during operation to fit the input amplitude range of the ADC.

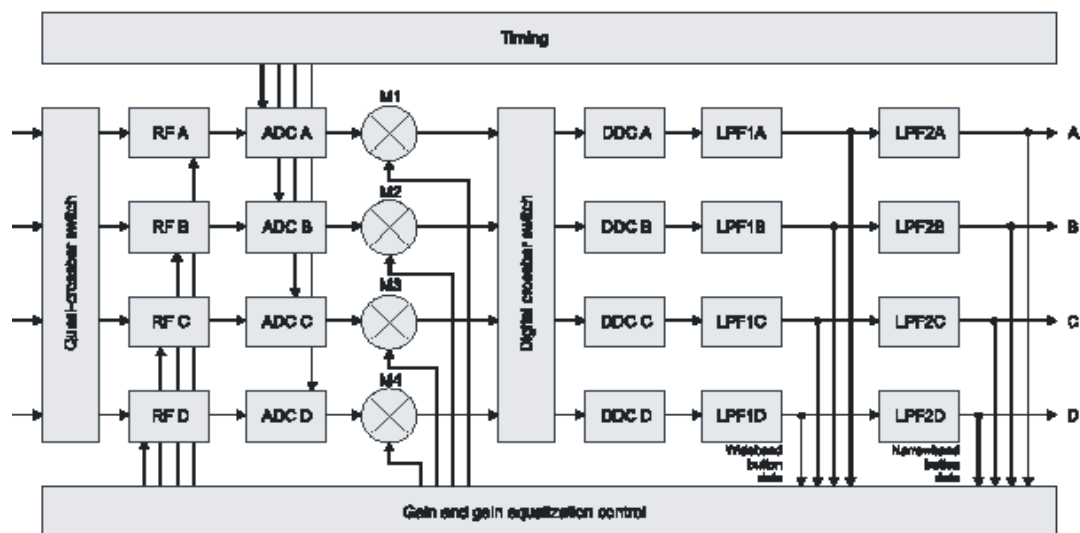


Figure 3: Details of the Digital BPM RF Frontend.

Since the ADC's uses undersampling it is very important to suppress frequency components that are outside the chosen Nyquist zone, which could cause aliasing. Two bandpass filters handle this before the ADC's.

The 16 bit ADC's have a maximum sampling rate of 130 Msps and can sample up to 700 MHz signals directly using the undersampling technique. The data is then decimated with digital downconverters which are implemented in the FPGA. See figure for a detailed block schematic of the RF frontend.

The main digital part of this Digital BPM system is built around a Virtex II Pro FPGA with two PowerPC 405 processor cores. All digital signal processing, communication and timing is done in this FPGA. There is also a SBC (Single Board Computer) which is based around a StrongArm Intel XScale chip. This board is running an embedded Linux operating system



which runs the application software and also handles the bootstrap and configuration of the FPGA.

Communication is available through eight SFP slots which can be equipped with different standard communications protocols (e.g. Gigabit Ethernet, Fibre Channel), the connectors support data rates beyond 5 Gbps.

The Digital BPM system needs a system clock that is derived from the accelerator. This clock is used to time stamp all the data and is required to have meaningful timestamps and for post mortem analysis. This should be either 1 MHz or 10 MHz depending on which frequency is used for the RF.

A Machine Clock is also needed by the Digital BPM system, this clock synchronizes the frontend with the storage ring revolution frequency. When the Machine Clock is absolutely tuned to the revolution frequency a data stream with Turn-by-Turn data is available at that frequency.

A Post Mortem signal input is also available to make analysis of the beam position, just before a beam loss occurs.

The Digital BPM electronics has separate interlock output signal that checks X, Y signals and if it's not within the specified limits an interlock signal can be set. The output data latency is  $\sim 270 \mu\text{s}$  (worst-case), which means that an interlock generated by the Digital BPM system electronics will never take longer than  $270 \mu\text{s}$ . For Fast-Orbit-Feedback the delay in the DSP block is important as this affects how fast the corrections can be output from the hardware. The Digital BPM system Group Delay (how much time it takes for a given signal to propagate through the DSP block) is specified to typically  $150\text{-}160 \mu\text{s}$ .

#### 2.9.1.4.1.3. Software

The Digital BPM system system uses digital processing for the filtering, decimation. These processing algorithms can be tuned for user specific requirements. The SBC runs an embedded GNU/Linux version (Debian) which handles user's customizations and networking.

The Digital BPM system has an API for writing applications which communicate with the system. This is called the Control System Programming Interface (CSPI). The CSPI is a high-level C library that makes it possible to write specific control applications for the Digital BPM system without the need to know all low-level hardware details. The CSPI also has the advantage that changes to the firmware for the Digital BPM system should be transparent to the applications which communicate through the CSPI.

Support for both EPICS and TANGO is available. The system is running with both TANGO and EPICS in storage rings which are in operation.

The possibility to include your own custom software in the Digital BPM system FPGA is available after signing an NDA with manufacturer.

A Generic server is also included that provides access to the Digital BPM system from a remote host across the network. The server uses TCP protocol and it uses the same API as the CSPI mentioned above.

#### 2.9.1.4.1.4. Specifications

The Digital BPM system specifications are summarized in table 2 (information from [9]).

Parameter	Range	Performance	
		TBT = 131 kHz	TBT = 1.15MHz
<b>Resolution (turn-by-turn)</b>	> -28 dBm	1 $\mu\text{m}$	3 $\mu\text{m}$
	-28 dBm < > -44 dBm	5 $\mu\text{m}$	15 $\mu\text{m}$
<b>Beam Current Dependence</b>	0 dBm < > 24 dBm	1 $\mu\text{m}$	1 $\mu\text{m}$
	0 dBm < > -32 dBm	1.5 $\mu\text{m}$	1.5 $\mu\text{m}$
	0 dBm < > -50 dBm	2 $\mu\text{m}$	2 $\mu\text{m}$
<b>Fill pattern dependence</b>	100% $\rightarrow$ 20% duty cycle	1 $\mu\text{m}$	1 $\mu\text{m}$
<b>FA data resolution (2 kHz bandwidth)</b>	0 $\rightarrow$ -20 dBm	0.25 $\mu\text{m}$	
<b>Crosstalk</b>	-45 dB to -70 dB		

Table 2: Digital BPM guaranteed performance.

#### 2.9.1.4.2. Fast “spear-head” Digital BPM

##### 2.9.1.4.2.1. General Description

The Fast “spear-head” Digital BPM electronics system is a FPGA based BPM system under development. The system uses a pilot-tone / calibration tone to calibrate the system for long-term drifts. The platform is designed as a flexible “Software defined instrument” with one Analog board and one Digital board.

##### 2.9.1.4.2.2. Hardware

The Fast “spear-head” Digital BPM consists of two boards, one Analog Front-End (AFE) and one Digital Front-End (DFE). The modular approach has the advantage of easy hardware adoption for specific uses, without actually touching the digital hardware. The partitioning into two boards enables a flexible Software Defined Instrument.

The DFE architecture consists of a Virtex-5 with a MicroBlaze embedded processor. AFE is based on a bandpass sampling architecture utilizing 16-bit ADCs. Long-term drift is corrected by inclusion of an out-of-band calibration tone.

Before the AFE, there is a passive RF processing unit which consists of isolators, Diplexer and four-way splitters. The isolator gives a return loss of 18 dB over a 150 MHz bandwidth centred around 500 MHz. The diplexer is used to combine the pickup-signal with the calibration tone. The high-band of the diplexer is centred at 500 MHz and has a bandwidth of 8.5 MHz with a 3.8dB insertion loss. The low-band is centred at 465 MHz and is used for the calibration tone.

The 8.5 MHz bandwidth of the filter centred on 500 MHz gives a good ringing of the filter when used with short pulses i.e. at commissioning.

The AFE consists of four separate BPM processing channels, which are then feed to the DFE. The signal into the AFE is the combined signal of the pickup signal at 500MHz and the narrowband calibration tone at 465MHz. This signal is then undersampled with four 16 bit ADC's (@  $\sim 117$ MHz). Each channel has one low-noise amplifier and digital attenuators (to increase the dynamic range). A bandpass filter is also fitted to AFE with large enough bandwidth to handle the diplexed signal.

The DFE takes care of all the digital processing and communications with the control system. The Virtex-5 FPGA takes care of the signal processing of the signals from the AFE. While the soft-core MicroBlaze processor handles the communication with the control system.

Slow acquisition data is provided on demand via Ethernet, while fast data is provided at a fixed rate via SFP modules and is provided directly from the FPGA without using the soft-core processor.

The Fast Digital BPM prototype uses a 500 MHz front-end which would mean that we would have to use the fifth harmonic for MAX IV, to avoid developing more than one RF frontend, as the fifth harmonic will be at 500 MHz.

The signal power from the pickup buttons is almost 5 dB higher at 500 MHz in comparison to 300 MHz (with 400 mA beam current) as used today in MAX II and MAX III, so running the BPM system at 500 MHz would actually increase the signal to noise ratio.

A plot of the signal power at 300 MHz is shown in Figure 5, and a plot of signal power at 500MHz is shown in Figure 4. Both plots are generated from the ALBA-CELLS BPM GUI tool [1] which is based on the DAFNE button calculations [2]. The BPM pickups parameters used in the plots can be seen in table 1.

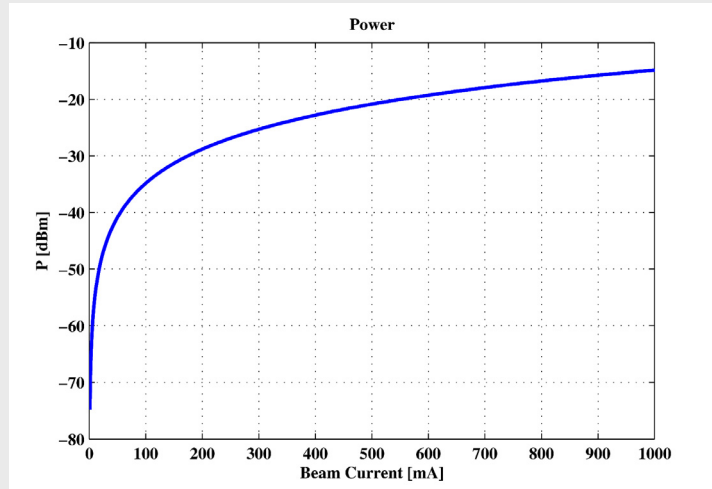


Figure 5: Pickup button power at 300 MHz.

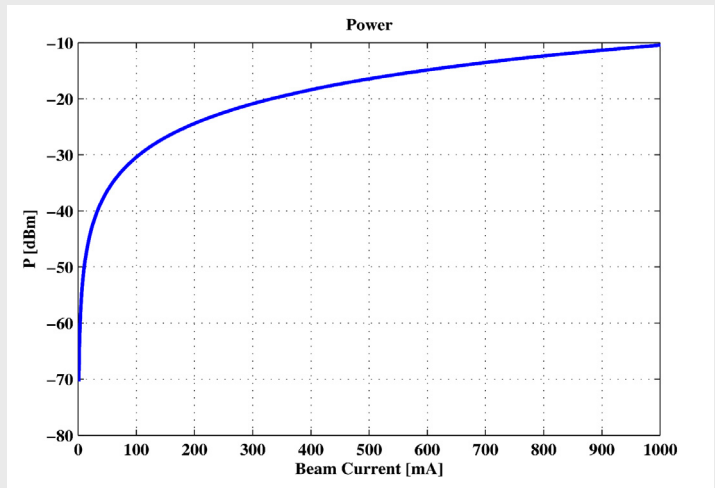


Figure 4: Pickup Button power at 500 MHz.

### 2.9.1.4.2.3. Software

The software will consist of several pieces of code, FPGA code in VHDL, C/C++ code for soft-core processor. The source-code of the software will be available to MAX-lab. TANGO drivers must however be developed by MAX-lab.

### 2.9.1.4.2.4. Specifications

Since the hardware isn't finished yet, final specifications are to be determined, but laboratory tests indicate a rms resolution position of  $>100\text{nm}$  should be possible for stored beam at full energy. Commissioning position resolution should be in the  $5\text{-}10\text{ }\mu\text{m}$  range.

## 2.9.1.4.3. An Improved Version of the MAX II/MAX III BPM Electronics

### 2.9.1.4.3.1. General Description

The in-house developed analogue BPM receiver for MAX II and MAX III is based on the superhetrodyne principle. The electronics achieves sub-micron resolution for the current MAX-lab storage rings.

In its current implementation the hardware can't provide data faster than 65 Hz but with an improved version 1 kHz should be possible. This would of course also need upgrades of the PLC ADC's to cope with the increased data speed.

### 2.9.1.4.3.2. The Current Hardware

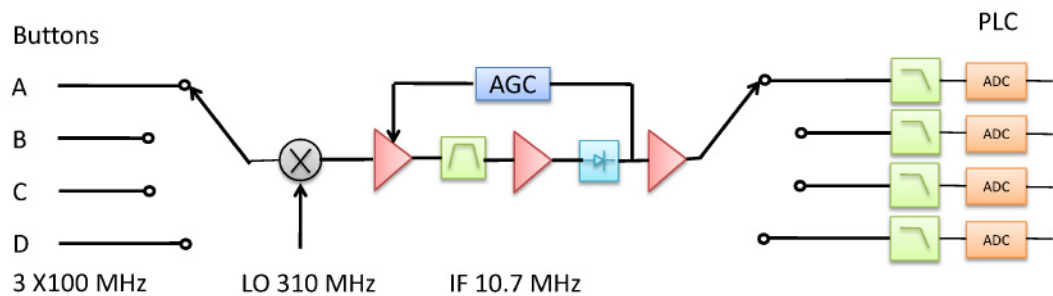


Figure 6: Block schematic of MAX-labs BPM receiver.

The MAX II and MAX III BPM electronics is the designed to use the third harmonic of the storage rings RF frequency ( $3 \times 100\text{ MHz}$ ).

The BPM receivers are of the multiplexed type, which means that all four pickup button signals share the same signal path. The single channel path has the advantage that it eliminates drifts of the individual channels. See Figure 6 for a block schematic of the analog BPM receiver.

Each of the four signals first gets filtered by a bandpass filter and are then feed into the multiplexer which switches between the four channels every 2.5 ms. The multiplexed signal is then feed into a mixer that mixes the button signals with the Local Oscillator frequency (LO) , which is chosen as  $3 \times 100 \text{ MHz} + 10.6937 \text{ MHz}$ . After the multiplexer an amplifier with Automatic Gain Control (AGC) adjusts the gain of the signal before a narrowband bandpass filter with a bandwidth of 15 kHz filters the signal. Another amplifier amplifies the signal once again before the envelope detector. The last amplifier amplifies the envelope detected signal which is then demultiplexed and feed through one low pass filter per channel.

The analogue signal is sampled by a 16 bit analogue-to-digital converter that is connected to the PLC system.

#### **2.9.1.4.3.3. Hardware Improvements**

The analogue BPM receiver described above have some room for improvements. An increase in switching speed of the multiplexer is a possibility. The disadvantage of this would be the decrease of the sampling time. As mentioned above decreasing the sample time a factor  $n$  will increase the position rms noise by a factor  $\sqrt{n}$ , thus an increase in speed of a factor 100, would increase the rms noise by a factor of 10.

A design with adjustable or switch-able bandwidth IF filters, could make it possible to use the receiver with FOFB.

To improve the overall BPM system latency it is possible to sample the multiplexed channels directly on the BPM receiver and also calculate horizontal and vertical positions on the receiver. This would mean less data and calculations at a central computer.

The above improvements would require some development resources/time.

#### **2.9.1.4.3.4. Software**

The software for the MAX II and MAX III is entirely PC-based since the electronics is purely analogue. The software runs on central computer with the Solaris operating system and it reads the data from all the BPM's and calculates the corrections at 0.5 Hz for MAX II. This works well in MAX II which only has 30 BPM pickups, but MAX IV will have 200 of them, so a centralised computer for calculating the corrections will need a fast dedicated network to be able to get all the data fast enough.

#### **2.9.1.4.3.5. Specifications**

The current MAX II/III BPM system achieves sub-micron performance at a correction rate of half a hertz. For Slow-Orbit-Feedback in MAX IV the MAX II/III BPM receiver should achieve position information within the specifications.

#### 2.9.1.4.4. Hybrid BPM Electronics Solution

##### 2.9.1.4.4.1. General Description

One option for the BPM system is to use fast BPM electronics which can handle Fast-Orbit-Feedback on the flanking BPM heads for the straight section, where the demand on the stability is the highest. In the rest of the ring the demands are much lower which means that one could use the slower electronics (like our current electronics used in MAX II / MAX III) for these bpm heads. They would then only be used for the Slow-Orbit-Feedback.

The advantage of this approach is that it only requires 40 units of fast/expensive BPM electronics while the other 160 BPM heads can use much cheaper electronics.

##### 2.9.1.4.4.2. Hardware

This approach will require two different hardware versions one for the Fast-Orbit-Feedback and one for the Slow-Orbit-Feedback. The storage ring should be equipped with the FOFB version at the flanking of the straight sections.

The BPM electronics for the FOFB should be fast Digital BPM system. The rest of the cell should be equipped with MAX-labs current electronics but with some improvements. The improvements required for this would be to sample directly at the intermediate frequency (IF 10.7 MHz). The sampled data would then be processed and an X and Y position would be calculated, and be available from the BPM electronics. The intensity (sum signal) could be made available on demand.

The BPM electronic should also handle commissioning which would require a modification to handle the short pulses that the injector will inject into the ring. A ringing bandpass filter in the front-end with a specific bandwidth will take care of this.

This filter will be fitted even when in the “standard” operating mode and should replace the old analogue front-end filter. See chapter for more details about the commissioning mode.

##### 2.9.1.4.4.3. Software

The embedded software on the electronics will do the necessary signal processing and communication with the control system.

##### 2.9.1.4.4.4. Commissioning

The hardware could be triggered externally or one could sample and buffer and then freeze the buffer once the signal rises above a threshold. Possible solutions for commissioning:

- **The Time-Division Approach:**  
Adjust the data path for each channel to insert the data of each channel after one other and thereby make it possible to use the multiplexing single data path for. This could be done by adding a separate circuit board in front of the electronics when the commissioning is to be used. This would require mounting of the extra PCB when commissioning is needed and then removing them for normal operations. The advantage is that this approach would be fairly easy to

implement and delivers position readings at every shot. The downside is that switching between the two operating mode will require installation/removal of equipment on 160 BPM heads.

- **The Multiplexing with Normalization Approach:**

Sample data from one button at each shot and then normalize the data against the closest FOFB electronics intensity, see Figure 7. One position reading would then require four shots.

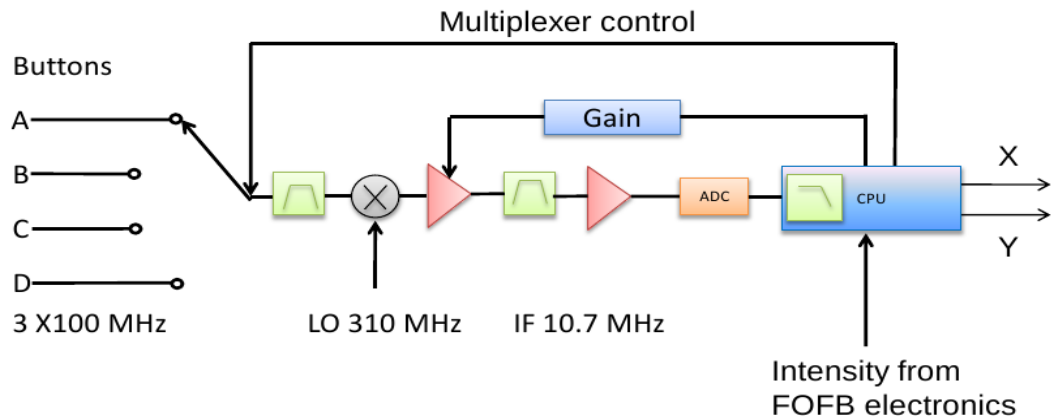


Figure 7: Figure over the multiplexing with normalization approach.

- The redesign of the electronics would in this case be quite moderate, and nothing would have to be installed or removed when shifting between the normal operations mode and the commissioning mode. The downside of this approach is that it requires four shots to get one reading and also that the resolution accuracy will decrease.
- **The Separate Channels Approach:**  
Redesign of the analogue front-end with four separate data paths without multiplexing, this approach would in principle require a total redesign of the entire BPM electronics. This would require some kind of “live” calibration like a pilot tone. The upside is that it would give good resolution accuracy and position readings at every shot. The full redesign would require quite some time/resources.
- **Ten Extra Units of fast Electronics:**  
If ten extra units of fast electronics could be bought they could be moved around the ring during commissioning. If problems getting beam round the storage ring arises one could put in the extra units where needed. This approach would require no hardware development regarding the commissioning for the electronics. This would also give the advantage of having spare units available if a unit will fail for some reason. The main disadvantage is of course that for commissioning one would need to move around the extra units until you get the electron beam through a full turn in the storage ring.



### 2.9.1.5. Infrastructure

The infrastructure for the beam position monitoring system is of high importance to achieve the best possible performance. This includes keeping the BPM electronics at a constant temperature to avoid temperature drifts. For the Digital BPM electronics, it is recommended with an ambient temperature variation of no more than  $\pm 1^\circ\text{C}$  to avoid large temperature drifts. The electronics temperature drift, for the commercial BPM option, is specified to  $0.2\ \mu\text{m}/^\circ\text{C}$ . Temperature controlled electronics racks will be needed to meet these requirements.

An upgraded version of the MAX-lab electronics may relax these requirements due to the multiplexing technology with one signal path for all four BPM signals.

Semi-rigid cables will be used between the pickup buttons and the BPM receivers. The cables will be equipped with high quality SMA connectors.

To ease maintenance, a mounting panel for all four buttons with short cables close to the BPM pickups should be considered. This would avoid mounting and dismounting in the tight area near the BPM pickups.

The BPM system should have dedicated network for Slow-Orbit-Feedback / communications and the Fast-Orbit-Feedback.

### 2.9.1.6. Commissioning

The commissioning scheme will depend on which BPM electronics the storage ring will be equipped with. The Digital BPM electronics systems hardware is fast enough for single-pass capability. A fully equipped MAX IV storage ring with one of these systems would not require any special hardware for commissioning.

It is also possible to equip one cell with fast electronics during commissioning and then move the electronics around the storage ring cell by cell. If the cost-saving option with the Hybrid BPM electronics option will be used, we will get ten extra units of the Fast Digital Electronics to move around during commissioning.

### 2.9.1.7. BPM Electronics Conclusions

The main route will be to equip all the 200 BPM pickups with fast Digital BPM electronics. The BPM system will be able to provide both Slow-Orbit-Feedback and Fast-Orbit-Feedback.

The cost-saving option of the Hybrid BPM electronics described above with 40 Fast Digital BPM systems at the flanking of the straights and 160 “standard” (improved MAX II /MAX III BPM receivers) will be a secondary option. The hybrid solution, although cheaper, will have the disadvantage of the added complexity of two different systems in both terms of installation and maintenance.

## 2.9.2. Tune Measurement: Stripline Monitor and/or Button BPMs

One could either chose to base the tune measurement on a dedicated spectrum analyser with tracking generator, or one could chose a turn by turn mode read-out of one BPM head followed by a fast Fourier transform calculation. In both cases an excitation of the beam is necessary, and one should consider the excitation amplitude in the two cases. In principle, a smaller excitation would be sufficient if a traditional 15 cm quarter wave (fifth harmonic) strip-line detector is used instead of the the button type BPM. This is because the tracking feature used by the spectrum analyzer is inherently more effective in detecting a disturbance (synchronous detection). Actually a counter- example is the SLS, where only the turn by turn data from one BPM is used for tune measurements. In this case the tune measurement is limited to the injection moments in the top-up mode (the kicker excitation of the stored beam), since the necessary excitation between injections would disturb the users. For a strip-line detection system this will not be a limitation, because of the inherently more effective detection.

In conclusion, one should study the possibility of a traditional excitation/detection with quarter wave strip-lines. Such a study would include;

- A mechanical design study of the strip-lines for the unusually small vacuum chamber in MAX IV. If the small vacuum chamber is a problem, two entire short straight sections could be used, and there would be space for decently long tapers.
- Estimation of the impedance contribution from the device.
- A cost estimation of a dedicated spectrum analyser together with power amplifiers.
- Considerations if there might be beneficial effects beside the tune measurement, for example a possibility for slightly larger, frequency controlled, excitation of the beam, which is needed when using the spin polarization method for beam energy calibration. Also the possibility of detection of lower currents than detectable with the button type BPMs should be taken into account.

### **Vacuum System Implications:**

We need to consider where to install the two strip-line pairs (with diagonal pairs it is sufficient with one excitation pair and one detection pair), either in the injection straight (chamber aperture?), or in one or two free short straight section, where the radius of the device may be chosen quite arbitrary since tapers could have quite a considerable length.

## 2.9.3. Current Measurement: DCCT and BPMs.

### 2.9.3.1. Stored Beam

A commercially available DC current transformer should be capable of measuring the stored beam current to a relative precision of at least  $10^{-4}$ . This should be sufficient for both lifetime calculations and current stabilization in the top-up mode. Lifetime measurements may be improved by averaging a large number of BPMs, where the relative strength of the sum signal of all four buttons is being used.

### 2.9.3.2. Commissioning

During the commissioning phase one should use the possibility of monitoring the sum signal from selected BPM heads. This should give a crude measure of the beam current during the first turn in the machine. Also the sum signal from a strip-line pair may be used for relative measurements. This signal should be stronger than the button type sum signals, and may therefore be crucial at commissioning.

#### **Vacuum System Implications:**

We need to consider where to install the DCCT, either in the injection straight (larger chamber aperture?), or in a free short straight section, where the chamber ceramic part need only to be around 25 mm diameter.

## 2.9.4. Emittance Monitor: Pi-Polarization Method

A robust on-line measurement of the beam sizes at one location in the ring, is an extremely versatile tool for a machine operator. Often just the on-line two-dimensional image, even without absolute beam size values, helps in finding the source of different beam instabilities. It is of high importance that this diagnostic device is running already during the commissioning phase, when it is crucial to pinpoint those beam instabilities having a “simple” origin.

The purpose of the beam size measurement is eventually to determine the transverse beam emittances. Usually the vertical emittance is the most interesting since it is given by the machine alignment, and thus difficult to predict. However for the MAX IV ring also the horizontal emittance is non-trivial to predict because it will be operated in such a low emittance regime that intrabeam scattering becomes non-negligible. For the emittance determinations, separate determinations of beta values and dispersion values at the observation point are needed (cf. Section 2.9.11.1). Also a beam energy spread measurement is in principle needed. However, usually one can by different means verify that the beam energy spread is close to the theoretical one, given by the lattice.

For the MAX IV ring the horizontal/vertical emittance is expected to be in the order of 250/8 pmrad. However, we should strive to detect/determine a vertical emittance down to 1 % of the horizontal, or 2.5 pm. We foresee one of two beam size monitors to be situated

in one of the outermost (half) dipoles of the achromat. Here are the beta values approx. 1 m and 15m in x and y respectively. Dispersion values should theoretically be zero. Thus, we want to measure a  $\sigma_x$  of 16  $\mu\text{m}$  and a  $\sigma_y$  of 6  $\mu\text{m}$ . Starting with the vertical beam size measurement it is in magnitude very similar to the one already performed at the SLS, using the so called pi-polarisation method [4]. This method utilizes the vertically polarized UV-Vis synchrotron radiation (SR), and has turned out to have potential to determine vertical emittances in the few pmrad region. With some small improvements, the limit could even be pushed down to 1 pmrad, corresponding to  $\sigma_y$  of about 4  $\mu\text{m}$ .

The recently built third generation sources have a horizontal emittance of around 5 nmrad with quite small betax in the observation point leaving a  $\sigma_x$  of around 50  $\mu\text{m}$  to be measured. In the determination of the horizontal beam size one has thus so far not been able to utilize the diffraction properties of the imaged UV-Vis SR, and the more traditional method of an X-ray pinhole camera have instead been used. However, with the sub-nm horizontal emittance of MAX IV we consider to stay in the UV-Vis region and take advantage of the SR emission and diffraction properties. With the same beam size monitor set-up as for the vertical size, we plan to determine the horizontal beam size by studying the dilution of a zero minimum in the diffraction dominated filament beam image. The only improvement needed compared to the SLS monitor is a somewhat larger horizontal acceptance angle of the SR.

#### **Vacuum System Implications:**

We will need two, dedicated, extraction port of SR from a dipole for this device. One will extract the light from the dipole in UC5 and use the space of the short straight section upstream the long straight. The other will extract light from the matching dipole in MC1 and use the available space in the downstream short straight. Large efforts are made to extract wide enough opening angles of the light and to protect the extraction mirror with a thin horizontal absorber.

### **2.9.5. Bunch Length Monitor**

A conventional choice is here a streak camera. However we should look into the possibility of using fast photodiodes, since the expected bunch rms length is around 170 ps. Photodiodes with rise-times (10-90%) around 80 ps are available for low price and are easy to operate (demonstrated at MAX II). A dedicated fast oscilloscope is of course necessary, but it should anyway be part of the diagnostic equipment, and could be used in various situations. A draw-back is of course the rise-time, but diodes with shorter rise-times may be used at the expense of the easiness of aligning them.

#### **Vacuum System Implications:**

We will need one, simple, extraction port of SR from a dipole for this device. “Simple”, in the meaning that no emphasis has to be put on the wavefront distortion of the extracted light. Most efficient would be to use the same extraction port as for the filling pattern monitor.

### 2.9.6. Filling Pattern or Bunch Current Monitor

A filling pattern monitor will be a crucial device in order to keep the sub-micron stability of the transverse beam position. The reason for this is that the front end electronics of the BPMs are likely to be dependent on the filling pattern. This is envisaged considering the fact that an un-even fill of the ring will result in bunches of different lengths, which in turn induces different signal levels in the BPMs. In order to assure the stability, a reasonably fixed filling pattern is needed. Secondly, even the transverse beam profile and the lifetime will be affected, via intra beam scattering effects.

However, we will have a good possibility to keep a fixed wanted filling pattern, since we will fill individual buckets with the injector. A very effective filling pattern monitor, even used as a feed-back device to generate arbitrary filling patterns, has been realized for at SLS (where RF=500 MHz). It is based on a photodiode detecting the light from individual bunches. This photodiode also gives superior linearity of the output signal to the bunch current, compared to either a sum signal taken from the BPMs, or from a stripline, to a fast oscilloscope (it is clear that these signals are bunch length dependent). Since we use only a 100 MHz RF, there will be good hope to successfully implement the photodiode solution for our filling pattern monitor and feed-back algorithm the for filling.

#### **Vacuum System Implications:**

We will need one, simple, extraction port of SR from a dipole for this device. “Simple”, in the meaning that no emphasis has to be put on the wavefront distortion of the extracted light. Most efficient would be to use the same extraction port as for bunch length measurements.

### 2.9.7. Scrapers with Possible Function as Dedicated Aperture to Protect IDs

A vertical scraper will give valuable information on the average pressure in the machine, that is it will give the possibility to put numbers on elastic and inelastic (gas) lifetime and finally on the Touschek lifetime. Furthermore, with knowledge of the vertical beta function, the vertical acceptance of the ring can be determined. This is crucial information when commissioning different insertion devices. However, this diagnostic device could be designed also to be a dedicated protection of the IDs against radiation. Furthermore, this protection fulfils a third aim, and that is to concentrate all vertical losses from stored beam to a single area where radiation protection walls could be somewhat enhanced in order to cope with this radiation. Not only electrons that are scattered elastically against rest gas atoms, but also Touschek scattered electrons that eventually couple their horizontal motion to a vertical one will be caught in this “bottle neck”, instead of being lost in the IDs.

A horizontal scraper does not necessarily show the horizontal physical acceptance of the machine. It could instead reveal the lattice dynamic energy acceptance, or the RF energy acceptance. A thorough investigation has to be done after the scraper scan is done.

However, correctly interpreted the data should help in determining these important quantities. We should contemplate whether we want to place it at a dispersive or non-dispersive location.

#### **Vacuum System Implications:**

The best place for the vertical scraper should be the injection straight, regarding the fact that the radiation shield anyhow here has to be slightly enforced. If possible one should allocate roughly 1m of the straight section to place this tapered “bottle neck”. Tapers are contemplated for reduction of the impedance, and the length gives a possibility for some radiation shielding (lead) on top and below the chamber. Furthermore one could think of a very simple device, where the entire unit is levelled to the position which just about shadows all the other straight sections and their IDs. Still it will require some kind of bellows at the ends, which probably should incorporate RF shields. However, regarding the fact that IDs are supposed to have gaps of only 4 mm, the movement of the whole device would not have to be more than roughly 2-3 mm. We would still be able to perform the entire scraper scan.

The location of a traditional horizontal scraper should be determined. From radiation point of view it should also be in the injection straight where the radiation shielding is enforced, since it could also serve as a “bottle neck”. At the proper horizontal displacement it will shadow the rest of the ring from softly scattered Touschek particles.

### **2.9.8. Pinger Magnets**

In order to characterize the nonlinear optics in the commissioned storage ring (c.f. Section 2.9.11.2), we foresee use of a pinger magnet. A pinger is basically a strong single-turn dipole kicker installed in a certain location of the storage ring. It allows betatron excitation of the beam with a specific kick strength during a single passage. Single-turn BPMs are then used to measure the coherent betatron response of the beam to this excitation over many turns.

In order to excite uncoupled betatron motion in both planes we would require two separate pingers. They can be placed next to each other. The exact location of the pingers is not crucial. Considering the beta functions, the injection straight would be a good location, however it is usually crowded making it difficult to fit two pinger magnets next to the septum and in between the injection kickers. An alternative would be one of the many free short straight sections. The horizontal beta function is substantially lower there however, thus making a stronger pinger magnet necessary.

In order to sample nonlinear betatron motion, large amplitudes are required. The pinger magnet should therefore allow excitation amplitudes of up to  $\pm 10$  mm. This kick can be unidirectional and the sign is not important. A simple approximation reveals that the pinger requires between 1 and 3.5 mrad kick strength (depending on the location of the pinger) in order to sample the entire acceptance of the machine. A more detailed analysis is ongoing.



The pulse is roughly a half-sine with a base length shorter than a single revolution period (1.7  $\mu$ s). Ideally the trigger to fire the pinger can be delayed so as to set the maximum kick strength to a specific location within the bunch train. Also, the pinger trigger needs to be synchronized with the single-turn BPMs. This synchronization as well as the synchronization of the single-turn BPM read-out at different BPMs along the ring is crucial.

Finally, note that the injection kickers could possibly be used as pinger magnets. Obviously only the horizontal pinger can be replaced this way. The maximum kick and the pulse duration need to be satisfactory, however.

#### **Vacuum System Implications:**

They should be designed with thought on impedance contribution.

### **2.9.9. Beam Loss Monitor System**

During commissioning of the storage ring as well as during later machine studies (momentum acceptance studies, energy calibration, ID commissioning, etc.) it will be of interest to identify locations of elevated beam loss. A simple and inexpensive way to achieve this is the use of optical fibers running along the vacuum chamber. Such a system has already successfully been used at the MAX-FEL experiment. Four fibers run along the vacuum chamber; each fiber covers a 90 degree segment of the chamber. The fibers are taped directly onto the chamber. Since the fibers are very small they can be threaded through magnet apertures or ID gaps.

Bremsstrahlung generated at beam loss creates visible radiation in the fiber at a location close to the loss area. This radiation can be transported by the fiber all the way to one end where the intensity is measured. If this measurement is synchronized with the beam revolution, the time of flight creates a relation between delay of a measured pulse and loss location along the fiber. Therefore if an intensity burst is measured, the delay of this burst with respect to the revolution trigger reveals the location of burst source along the fiber. Since four such fibers are installed with each in a different segment of the chamber, losses above and below the machine midplane can be distinguished from each other as well as losses to the inside and outside of the ring. The latter (if measured in coincidence) can be used to distinguish Touschek losses from gas scattering losses.

If beam loss is to be measured specifically for the purpose of energy calibration (cf. section 2.9.11.3), a measurement that can distinguish Touschek loss pairs from other scattering losses is of advantage. Such a system can be implemented by setting up two scintillators downstream of a dipole magnet on the inside and outside of the storage ring. Or alternatively, downstream of a vertical aperture limitation (for example an in-vacuum ID with closed gap) above and below the vacuum chamber. If the read-out from these scintillators is fed to a comparator and the generated coincidence signal is monitored, Touschek losses can easily be identified.

## 2.9.10. Temperature Sensors

Considering the fact that the vacuum system should cope with the entire heat load, without any separated absorbers, it could be a great advantage to plan for a set of permanent temperature sensors at crucial points around the ring fastened onto the vacuum chamber. Most often storage rings have during (and after) commissioning suffered from unexpected “hot spots” that severely affect the lifetime, and maybe other features of the beam. If temperature sensors will be used at for example front ends and/or beamlines we should strive to standardize them.

## 2.9.11. Beam Dynamics Measurements/ Control System Applications

We list here beam dynamics measurements that need to be automatized.

### 2.9.11.1. Linear Optics Characterization

The MATLAB Middle Layer (MML) software [5] will be used for the MAX IV storage rings. It contains a number of routines and applications for accelerator control, simulation and machine measurements including but not limited to:

- Accelerator Toolbox for machine physics simulations
- Orbit correction application
- Beam Position Monitor (BPM) offset calibration
- Chromaticity measurement
- Dispersion function measurement
- Beta function measurement
- Corrector magnet hysteresis measurement
- Response matrix measurement

As MML is in use at a number of light sources including Diamond, SOLEIL and SSRF, the component routines have been tested extensively for a number of different machines. Setting up the MML software for controlling the MAX IV storage rings during characterization measurements will require a TANGO interface, rather than the EPICS interface. This had been previously done at SOLEIL. Furthermore, Linear Optics from Closed Orbits (LOCO) [6] is integrated in the MML package and will be used extensively for characterization of the linear optics, gain calibration of BPMs, et.c. This will require setting up an accurate Accelerator Toolbox (AT) lattice model for the 3.0 GeV storage ring.



### 2.9.11.2. Non-Linear Optics Characterization

In order to characterize the nonlinear optics in the commissioned storage ring, we foresee use of a pinger magnet (cf. Section 2.9.8) and single-turn BPMs. After exciting coherent betatron motion of the beam with the pinger, the single-turn BPM data around the ring is spectrally analyzed giving amplitudes and phases that can be assigned to resonance driving terms (cf. e.g. [7]). Similar to the LOCO approach for linear optics, this data can then be used to calibrate the nonlinear machine model and hence correct the nonlinear optics in the real machine. The goal is to restore the ideal symmetric nonlinear optics in a first step and to correct for nonlinear perturbations (for example from IDs) in a second step.

An important issue here is the BPM capability. Single-turn BPMs are required to properly resolve the coherent betatron response to the pinger excitation over many turns (a few hundred is usually sufficient). Since betatron motion has to be resolved also the number of BPMs required can be estimated. Similar to what is known in linear optics analysis, each betatron oscillation needs to be observed in at least two separate locations in order to properly resolve the oscillation. This means we need roughly 84 single-turn BPMs in the horizontal and roughly 29 in the vertical plane. Since we expect two fast BPMs per ID straight section, the vertical requirement should be met. In the horizontal plane we clearly cannot fulfill the requirement using only the BPMs in the ID straight. This issue remains to be investigated in further studies.

### 2.9.11.3. Beam Energy Calibration

In order to gain a detailed understanding of the storage ring (e.g. nonlinear momentum compaction) as well as to calibrate ID spectra, precise knowledge of the storage ring energy is required. In order to go beyond the  $10^{-3}$  accuracy achieved with Hall probe measurements of the dipole field, resonant spin depolarization can be used. This method delivers an energy calibration on the  $10^{-5}$  level and has successfully been used at several storage rings (cf. e.g. [8]). Basically, an undisturbed electron beam in the ideal storage ring polarizes anti-parallel to the guiding dipole field after injection through the emission of spin-flip radiation. Once the beam has polarized, excitation of the beam at a specific frequency can be used to depolarize it. The frequency at which the beam depolarizes is directly proportional to the beam energy. If the frequency of the excitation is swept across an interval and the degree of polarization is monitored, the drop of polarization upon hitting the depolarizing resonance can be linked to the exact beam energy.

This measurement does not necessarily require an expensive Compton polarimeter setup, however. Touschek lifetime is polarization-dependent (the higher the polarization the lower the Touschek-scattering cross section and hence the higher the Touschek lifetime) so that monitoring Touschek lifetime can reveal the degree of polarization of the stored beam in the machine. Similarly, the depolarizing resonance can be identified by a sudden drop of Touschek lifetime and/or a sudden increase in Touschek-scattered electron pairs. All that is then needed is a fast kicker (injection kicker, pinger magnet) with a tunable source (e.g. sine generator with settings to sweep the frequency over a predefined range).

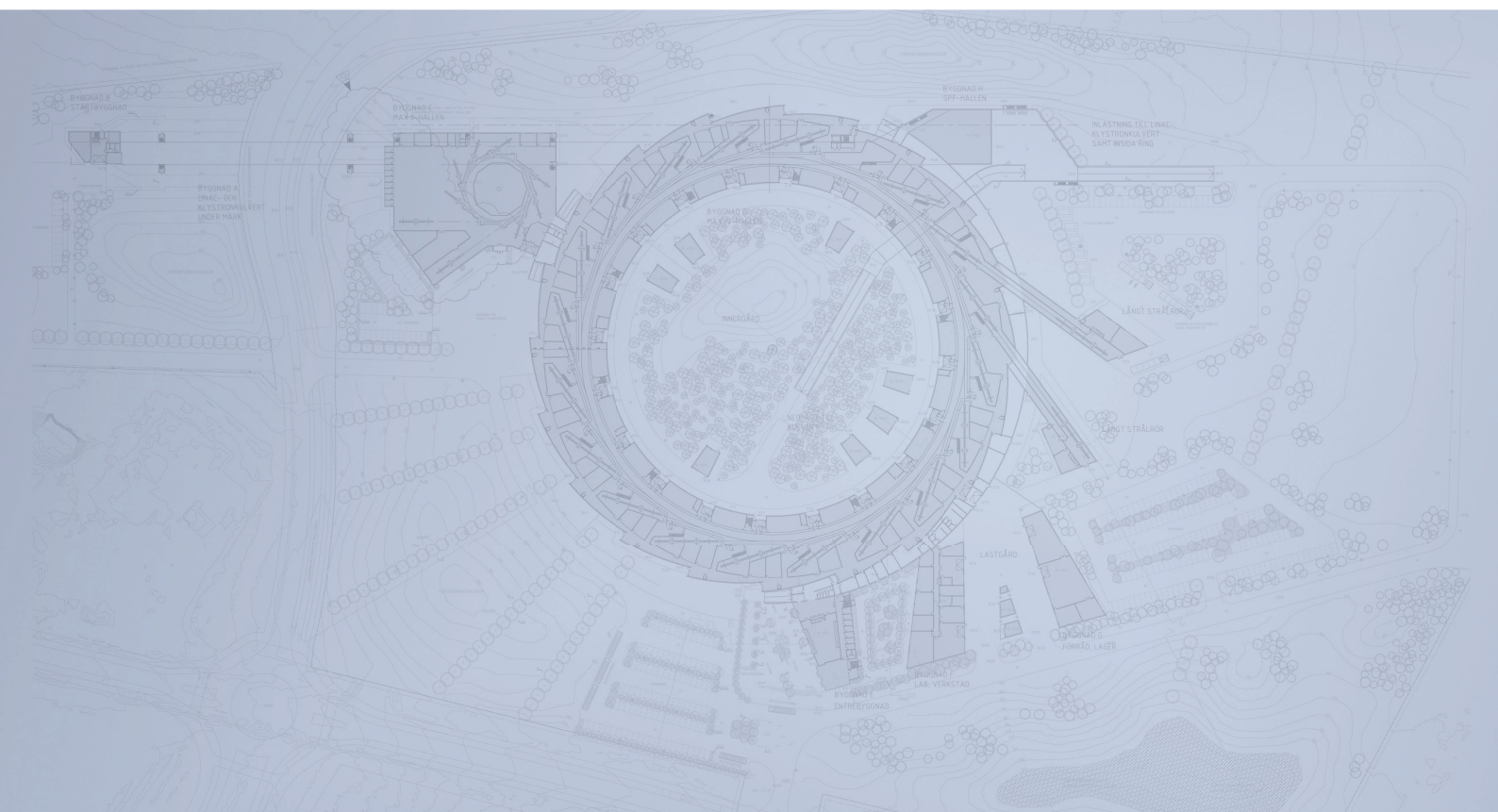
However, certain conditions should be met. Firstly, the lifetime has to be Touschek-dominated in order for lifetime measurements to reveal polarization-dependence. Secondly, high levels of polarization need to be achieved before depolarization can take place and be detected. The first condition is not necessarily given in the MAX IV 3 GeV storage ring. This will depend to a large extent on the achieved scattering lifetime. In the base line design Touschek lifetime and elastic scattering lifetime are roughly equal (see Section 2.10.3.2). The second condition is the more serious obstacle: high degrees of polarization in the stored beam require an excellent machine alignment with a well-corrected orbit. In addition the machine must be left quiet/stable for extended periods of time without orbit feedback or injection in order for polarization to build up. Due to large bending radius of the MAX IV 3 GeV storage ring, polarization build-up time is very long. Compared to the already long 31 minutes at SLS, the MAX IV 3 GeV storage ring will have a polarization build-up time of 54 minutes. This means that the machine must be operated in a completely quiet and stable way without any corrections, top-up injection shots, or ID gap changes for at least two to four hours in order to successfully measure polarization build-up and find the depolarizing resonance.

Finally, we note that the spin tune of the MAX IV 3 GeV storage ring should be around 6.809 (corresponding to a depolarizing resonance around 460 kHz or 109 kHz). The fractional spin tune has a mirror at 0.191 which is fairly close to the fractional horizontal betatron tunes 0.20 (corresponding to 114 kHz). This could prevent higher levels of polarization in the stored beam.

## 2.9.12. References

- [1] A. Olmos, F. Pérez , ALBA-CELLS, Cerdanyola, Barcelona, Spain, G. Rehm, Diamond Light Source, Oxfordshire, U.K. “Matlab code for bpm button geometry computation”, DIPAC07.
- [2] A. Stella, “Analysis of the DAFNE Beam Position Monitor with a Boundary Element Method”, INFNLNF, Accelerator Division, Frascati, December 1997.
- [3] F. Marcellini, “DAFNE broad-band button electrodes”, 1997
- [4] Å. Andersson, M. Böge, A. Lüdeke, V. Schlott, A. Streun, “Determination of a small vertical electron beam profile and emittance at the Swiss Light Source”, Nuclear Instruments and Methods, A 591 (2008) 437–446.
- [5] G J Portmann, Jeff Corbett, and Andrei Terebilo. An accelerator control middle layer using matlab.
- [6] J Safranek, G Portmann, A Terebilo, and C Steier. Matlab-based loco. 2002.
- [7] R. Bartolini, I.P.S. Martin, J.H. Rowland, P. Kuske, F. Schmidt, Phys. Rev. ST Accel. Beams, 11, 104002, 2008.
- [8] S.C. Leemann, M. Böge, M. Dehler, V. Schlott, Proceedings of EPAC 2002, Paris, France, pp 662-664.
- [9] Libera Brilliance Specifications, Instrumentation Technologies

# Detailed Design Report



## Chapter 2

### MAX IV 3 GeV Storage Ring

#### 2.10. Beam Lifetime

MAX IV Facility



## 2.10. Beam Lifetime

---

<b>2.10.</b>	<b>Beam Lifetime .....</b>	<b>2</b>
2.10.1.	Elastic Scattering Lifetime .....	2
2.10.2.	Inelastic Scattering Lifetime.....	3
2.10.3.	Touschek Lifetime .....	3
2.10.4.	Total Lifetime .....	9
2.10.5.	References.....	9

## 2.10. Beam Lifetime

---

The beam lifetime in the MAX IV ring will be limited by elastic and inelastic (Bremsstrahlung) interactions between electrons and the rest gas molecules, and by Touschek (electron-electron) scattering within the bunches, resulting in electron losses from the beam.

The rest gas scattering lifetimes are inversely proportional to the rest gas pressure given a certain rest gas composition. Below is given an assumption for the rest gas pressure, but one should remember that it can easily be wrong by a factor two or three, which then is inversely reflected in the gas lifetimes. However, for a well conditioned machine the assumption below is quite conservative.

The Touschek lifetime follows simple scaling laws for bunch charge,  $q$ , and bunch length,  $\sigma_s$ :  $\tau_{\text{Touschek}} = k/q$  and  $\tau_{\text{Touschek}} = k \cdot \sigma_s$ . However, it has a quite complicated dependence (see for example [1]) on parameters like horizontal beam size,  $\sigma_x$ , horizontal beam divergence,  $\sigma'_x$ , vertical beam size,  $\sigma_y$ , and momentum acceptance,  $\delta_{\text{acc}}$ , all of which varies around the machine lattice. This requires that the Touschek lifetime is calculated as an average of local Touschek loss rates around the entire machine. In particular it is necessary to determine the momentum acceptance for every lattice point. It is the minimum of the RF momentum acceptance (bucket height) and the lattice momentum acceptance at the position of the scattering event. The (local) lattice momentum acceptance is well predicted for a linear machine with the knowledge of the horizontal vacuum chamber dimensions. However for the case of a highly chromaticity corrected (strong sextupoles) machine like MAX IV, this determination is more complex [1] and is safest done by tracking off-momentum particles starting at the event position. In our case we use full 6D tracking with the code Tracy3.

### 2.10.1. Elastic Scattering Lifetime

The assumptions are:

Rest gas pressure and composition equivalent to 2 pbar of CO gas. (2 pbar=1.5 nTorr).

Vertical acceptance: 1.3 mm mrad ( $\beta_y=3\text{m}$  at undulator ends with  $\pm 2\text{mm}$  gap).

Horizontal acceptance: 12 mm mrad ( $\beta_{x\text{max}}=10\text{m}$  and chamber  $\pm 11\text{mm}$ ).

$$\tau_{el} = 25.4 \text{ h}$$

Note: We have made the simplification to assume a pressure which is constant around the machine circumference. Emphasis should be made to decrease the rest gas pressure at locations of high  $\beta_y$ , in which case one would gain in lifetime, still with the same average pressure.

## 2.10.2. Inelastic Scattering Lifetime

The assumptions are:

Rest gas pressure and composition equivalent to 2 pbar of CO gas.

Momentum acceptance:  $\delta_{\text{acc}} = 4.5 \%$

$\tau_{\text{inel}} = 56.1 \text{ h}$

Note: This lifetime is quite insensitive to the momentum acceptance:  $\delta_{\text{acc}} = 4.0 \%$  gives  $\tau_{\text{inel}} = 53.1 \text{ h}$ .

## 2.10.3. Touschek Lifetime

In a first study (Ch 2.10.3.1) Touschek lifetimes are calculated for four main (ID and RF voltage configuration) cases, assuming that horizontal emittance and beam energy spread are being given by the equilibrium from quantum fluctuations and radiation damping. In a second study (Ch 2.10.3.2), Touschek lifetimes are calculated taking into account the effects of Intra Beam Scattering (IBS), that is the effects of weak multiple electron scatterings inside the bunch. They are of the same nature as the Touschek events, though do not lead to electron loss. However, they increase the bunch volume and its energy spread. To more clearly reveal the special features of MAX IV, a limiting RF momentum acceptance of 4.5% is assumed (which actually would be easily realized by varying the RF power from four stations, with respect to SR losses from IDs). This overall momentum acceptance is justified since tracking results for all four cases give a minimum local lattice momentum acceptance larger or equal to 4.5%. Furthermore, we assume a bunch lengthening from the passive Landau cavities resulting in a rms bunch length of 50 mm in all four cases (which is also more realistic than assuming always a factor five lengthening, see RF Chapter). In both studies we assume that the vertical emittance is being adjusted to the diffraction limit of 8 pmrad, by help of a vertically introduced dispersion wave [2]. By this we avoid betatron coupling and the risk of losing Touschek scattered particles vertically in narrow gap IDs.

### 2.10.3.1. Touschek Lifetime without IBS

Dynamic Touschek lifetime [1] has been calculated with Tracy3 in 6D. We assumed 500 mA stored beam current in 176 bunches ( $I_b \approx 5 \text{ nC}$ ). Realistic vacuum chamber dimensions were included in the Tracy3 model, but no errors.

Four main cases were studied. The parameters of these cases are displayed in Table 1. Apart from case D, six RF cavities for a total gap voltage of 1.5 MV were assumed. Case D is identical to case C except for the 2 MV applied RF cavity voltage (eight cavities). The vertical emittance in all cases was set at the 8 pm rad diffraction limit; therefore emittance ratio is not identical in all cases.



Case	Configuration	$\delta_{\text{acc}}^{\text{min}}$	$\delta_{\text{RF}}$	$\sigma_{\delta}$ [ $\times 10^{-4}$ ]	$\sigma_s$ [mm]	$\epsilon_x$ [nm rad]	$\epsilon_y$ [nm rad]
A	bare lattice	5.2%	6.196%	7.70	9.73	0.326	0.008
B	4 PMDW	4.5%	5.285%	9.57	12.39	0.263	0.008
C	4 PMDW & 10 IVU	4.8%	4.046%	9.12	12.50	0.201	0.008
D	4 PMDW & 10 IVU	4.8%	5.786%	9.12	10.33	0.201	0.008

Table 1: Parameters for the cases used to study Touschek lifetime in the MAX IV 3 GeV storage ring. The parameters displayed are the minimum lattice momentum acceptance, the RF acceptance, rms momentum spread of the bunch, rms bunch length, as well as horizontal and vertical emittance.

Each case was tracked for 1.5 synchrotron periods in 6D. The results for the cases with and without Landau cavities (where bunch lengthening by a factor five was assumed) are displayed in Table 2.

	$\delta_{\text{acc}} = \delta_{\text{RF}}$	6D	6D with LC
Case A	23.06	15.03	75.14
Case B	17.79	14.73	73.65
Case C	6.54	6.49	32.44
Case D	27.24	20.06	100.31

Table 2: Touschek lifetime results in hours. Tracking was done with Tracy3. The first column shows results assuming infinite lattice momentum acceptance. The 6D tracking results take into account lattice and RF acceptances. They are displayed for a ring without and with Landau cavities (LC).

In case C there is almost no difference between the results in the first two columns because the overall momentum acceptance is dominated by the RF acceptance. In case A the lattice acceptance cuts into the RF acceptance at certain locations within the achromat and hence there is a much larger difference between the results the first two columns. An example for the overall momentum acceptance along one achromat of the lattice is given in Figure 1. The asymmetry between the positive and negative momentum acceptance reflects the asymmetry in dynamic aperture (caused by the highly nonlinear chromaticity).

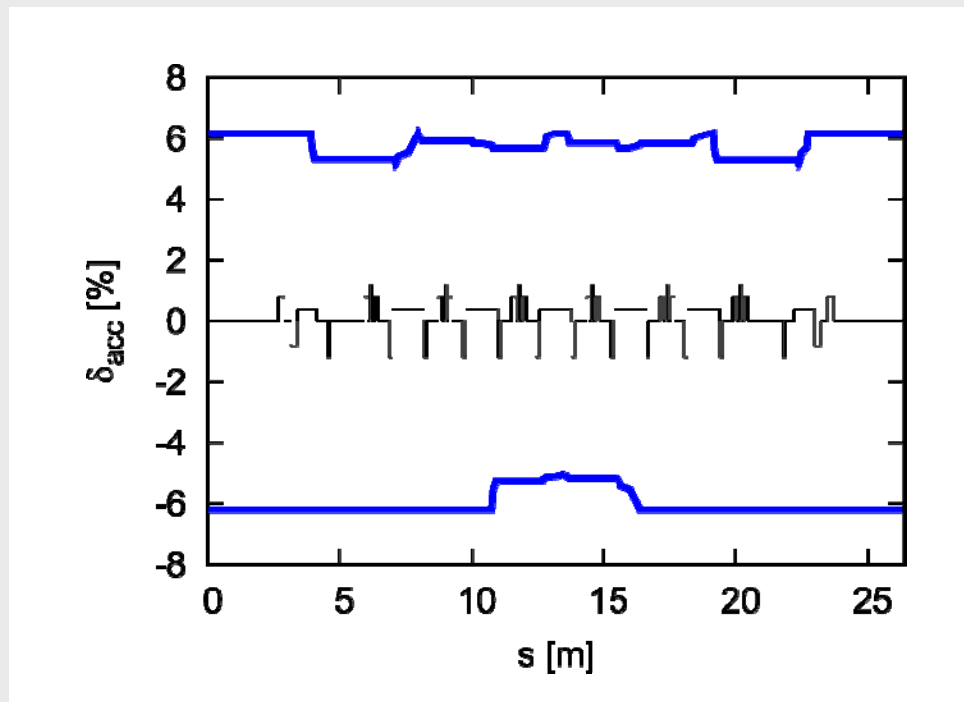


Figure 1: Momentum acceptance for case A (one achromat) with 1.5 MV RF cavity voltage (blue). The lattice is indicated in black. The RF acceptance is 6.2% corresponding to the maximum acceptance observed here.

### 2.10.3.2. Touschek Lifetime with IBS

In a next step, Touschek lifetime was calculated when IBS was taken into account. The code ZAP was used to calculate equilibrium emittance values including IBS. In order to make results comparable, the RF acceptance was set to  $\delta_{\text{rf}} = 4.5\%$  for all cases. Also, it was assumed that bunch lengthening from the Landau cavities resulted in a bunch length of  $\sigma_s = 50$  mm in all cases. Results for Touschek lifetime with and without IBS are shown in Table 3.

	$\tau_{\text{Touschek}}$ [h]	
Bare Lattice	6.96	8.61
Bare Lattice with LC	28.98	29.02
Lattice with 4 PMDWs and LC	35.57	34.52
Lattice with 4 PMDWs, 10 IVUs, and LC	41.54	39.49

Table 3: Touschek lifetime for the MAX IV 3 GeV storage ring calculated with (right) and without (left) IBS using ZAP and Tracy-3. The vertical emittance  $\epsilon_y = 8$  pm rad and RF acceptance

$\delta_{\text{rf}} = 4.5\%$  were kept constant. The influence of the third-harmonic Landau cavities (LC) is also shown.

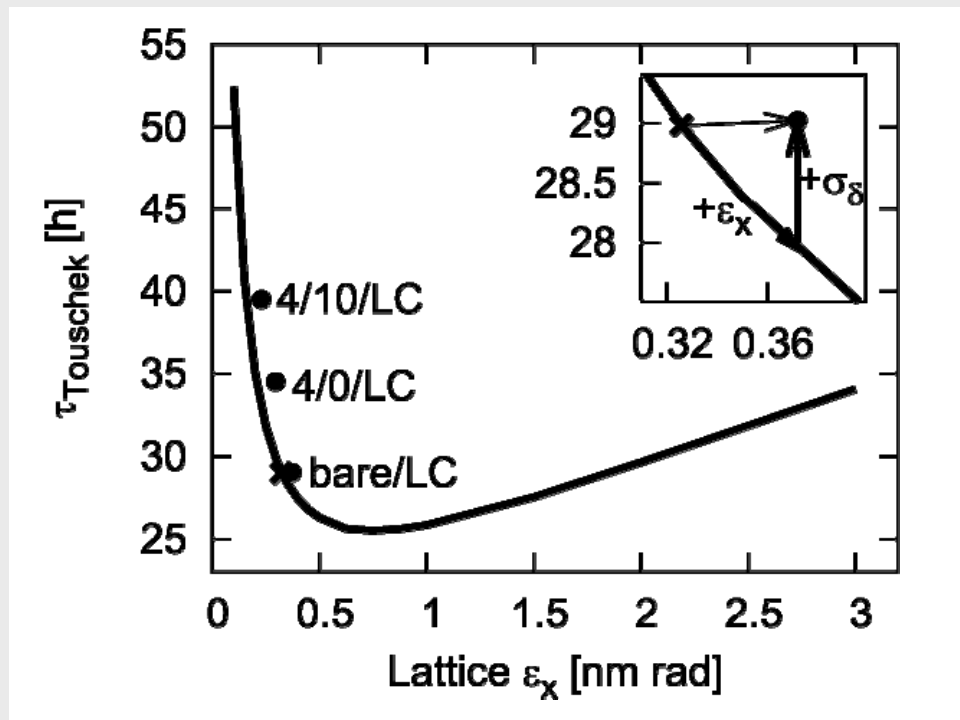


Figure 2: The trend line shows Touschek lifetime for the bare lattice (IBS neglected) if it were possible to vary the lattice emittance while keeping the energy spread constant. Specific configurations (bare lattice, 4 PMDWs, and 4 PMDWs plus 10 IVUs; all including LCs) are indicated by crosses and dots. Crosses indicate IBS neglected, dots indicate IBS included. The enlarged segment illustrates the effect of IBS for the bare lattice configuration: while the IBS emittance growth ( $+\epsilon_x$ ) leads to a decrease of

Touschek lifetime, the IBS energy spread growth ( $+\sigma_\delta$ ) leads to an increase of Touschek lifetime.

It should be pointed out that concerning Touschek lifetime the MAX IV 3 GeV storage ring operates in an atypical regime. As the emittance of the storage ring is further reduced by adding additional IDs, the Touschek lifetime actually improves. This is a unique property among third-generation synchrotron radiation sources and is ultimately a consequence of the ultra-low emittance of the MAX IV 3 GeV storage ring. An evaluation of the Touschek function [1] shows that there is sharp change in behavior once the transverse momenta in the bunch become small compared to the momentum acceptance. The physical explanation is that the transverse momenta in an ultra-low emittance bunch are insufficient to generate scattering events which result in momentum deviations that can no longer be contained by the longitudinal acceptance of the machine, as pointed at by Eriksson at [3]. This leads to overall fewer Touschek losses and hence increased lifetime at lower emittances. A plot showing Touschek lifetime vs. horizontal emittance for the MAX IV 3 GeV storage ring is displayed in Fig. 2. Clearly, further reducing the lattice emittance with additional damping wigglers and insertion devices has a beneficial effect on Touschek lifetime.

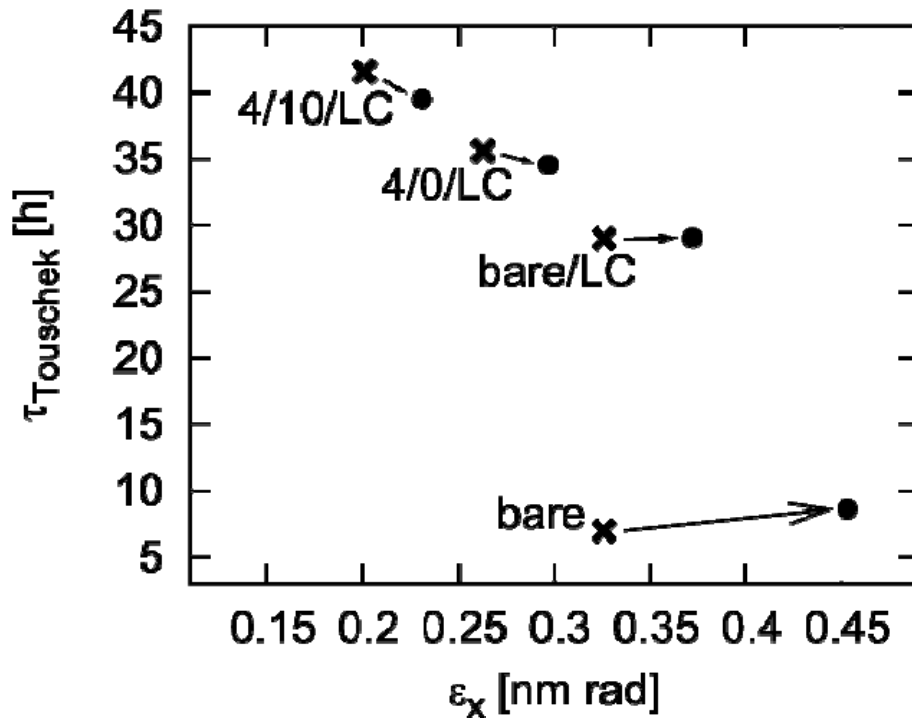


Figure 3: Tauschek lifetime vs. horizontal emittance for different configurations of the MAX IV 3 GeV storage ring: bare lattice, lattice with 4 PMDWs, lattice with 4 PMDWs and 10 IVUs. The vertical emittance  $\epsilon_y = 8$  pm rad and RF acceptance  $\delta_{\text{rf}} = 4.5\%$  were kept constant; the other parameters were changed to match the actual configuration. The effect of IBS is indicated by arrows. Crosses indicate IBS neglected, dots indicate IBS included.

With IBS taken into account, one cannot emphasize the benefits of Landau cavities enough. By increasing the bunch length, and hence decreasing, the charge density in the bunch, the Landau cavities not only increase Tauschek lifetime, they also reduce the horizontal emittance blow-up from IBS, which in the case of the MAX IV 3 GeV storage ring increases the Tauschek lifetime even further. Figures 2 and 3 illustrate this situation.

## 2.10.4. Total Lifetime

For lifetime considerations we define a "worst-case" scenario. Firstly, the configuration with 4 PMDWs and 10 IVUs ensures large radiated energy losses. Secondly, we assume no extra RF stations are added; six cavities will give a maximum total cavity voltage of 1.5 MV. This results in a low RF acceptance of  $\delta_{rf} = 4.0\%$ . The Touschek lifetime including Landau cavities is then 25.5 h.

This "worst-case" scenario Touschek lifetime is combined with the gas scattering lifetimes in Table 4. Note that Touschek lifetime is defined as a half-lifetime, whereas the gas scattering lifetimes are  $1/e$ -lifetimes. However, since we are interested in evaluating the total lifetime at the design current 500 mA, it can simply be derived from the sum of individual loss rates. When the MAX IV 3 GeV storage ring is operated with IDs and Landau cavities, as a consequence of the long Touschek lifetime, overall beam lifetime will no longer be Touschek dominated.

	$\tau$ [h]
Elastic gas scattering	25.4
Inelastic gas scattering	53.1
Touschek scattering (with Landau cavities)	25.5
<b>Total</b>	<b>10.3</b>

Table 4: Contributions to the total MAX IV 3 GeV storage ring lifetime  $\tau$ . The results have been calculated for a "worst-case" scenario: four PMDWs and ten IVUs are installed in the storage ring while the total applied RF voltage is 1.5 MV which corresponds to an RF acceptance of only  $\delta_{rf} = 4.0\%$ .

## 2.10.5. References

- [1] A. Streun, "Momentum acceptance and Touschek lifetime", SLS Note 18/97.
- [2] M.S. Zisman et al. ZAP user's manual LBL-21270, 1986.
- [3] <http://www.maxlab.lu.se/maxlab/conference/small-emittance/>



# MAX IV Facility





## 2.11. Collective Effects

---

<b>2.11. Collective Effects .....</b>	<b>2</b>
2.11.1. Single Bunch Effects.....	4
2.11.2. Multi Bunch Effects.....	5
2.11.3. Higher Order Modes Coupled Bunch Instabilities.....	8

## 2.11. Collective Effects

At higher beam currents, there are several effects which have an impact on beam stability. Many of these are well known and we have quite an empirical knowledge of these effects as well as well-proven theories.

Compared to more conventional synchrotron light sources, the vacuum chamber of the MAX IV ring has a small bore radius (11 mm), NEG-coated copper is proposed as the vacuum chamber material and the RF system is operating at a low frequency of 100 MHz. A harmonic RF system, operating at the 3<sup>rd</sup> harmonic, is also foreseen. The impact of these unconventional items has to be scrutinized.

We can sort the collective affects into two catogories:

- Single bunch effects. The induced fields are fast-decaying and interacts with the inducing bunch only.
- Multi bunch effects. The induced fields are oscillating for a time which is long compared to the time interval between bunches.

The low intensity beam parameters are the following (without/ with harmonic RF system):

<b>C (Ring circumference)</b>	528 m
<b><math>\alpha</math> (momentum compaction)</b>	$3 \cdot 10^{-4}$
<b>E (electron energy)</b>	3 GeV
<b>I<sub>circ</sub></b>	0.5 A
<b>RF</b>	100 MHz
<b>Bunch charge</b>	5 nC
<b><math>\sigma_l</math> (RMS bunch length)</b>	1.1 cm/5.6 cm
<b>I<sub>p</sub> (Peak current)</b>	54 A/10.7 A
<b>f<sub>s</sub> (synchrotron frequency)</b>	1.08 kHz/124 Hz
<b><math>\sigma_{fs}</math></b>	-/213 Hz
<b><math>\tau_{\text{Landaudamp}}</math> (Long Landau damp time)</b>	-/1.24 $10^{-3}$ s
<b><math>\sigma_\delta</math> (Relative enrgy spread)</b>	0.08%

### Landau Damping

The MAX IV ring will be equipped with harmonic passive cavities (HC), operating at the third harmonic. These cavities are driven by the electron beam and tuned in such a way that the RF gradient given by the main 100 MHz cavities and these harmonic cavities will cancel at the bunch position. When the shunt impedance of these harmonic cavities are chosen in an optimal way, both the first total RF field gradient and the second derivative will be zero. The potential well for the electrons in the bunch will then be of fourth order, compared to the second order potential well in the no-harmonic cavity case.

Particles of nominal energy will thus be stationary with zero synchrotron frequency. Particles with deviating energy will get a synchrotron frequency proportional to the energy deviation.

The synchrotron frequency spread within a bunch will thus be substantial and so the Landau damping of coherent synchrotron oscillations. This will obviously have a damping effect of the longitudinal coherent oscillations but also for transverse oscillations with other synchrotron modes than the rigid bunch one.

The bunches are elongated by this fourth order potential well, without an associated increased energy spread. As seen above, this will restrict the bunch power spectrum in frequency, so it will not be necessary to introduce a large chromaticity to fight the transverse resistive wall instability.

The calculations for the bunch properties with a 3<sup>rd</sup> harmonic system give the result presented below

<b>Circulating current (mA)</b>	500
<b>100 MHz RF voltage (MV)</b>	1.5
<b>HC frequency (MHz)</b>	300
<b>Landau damping time (ms)</b>	1.24

## 2.11.1. Single Bunch Effects

### 2.11.1.1. Microwave Instability

The microwave instability is driven by a number of cavity-like objects with a small Q-value. Examples of such objects are BPMs, vacuum flanges, vacuum chambers, kickers, below shielding etc. An impedance budget will be calculated for the MAX IV ring, taking into account the contributions from different items in the vacuum system. At this stage, these impedances are replaced by a single oscillator with  $Q=1$  and the resonating frequency at the cut-off frequency of the vacuum tube. This angular frequency is given by

$$\omega_{co} = \frac{c}{b} \text{ (b is the vacuum chamber radius) which yields the cutoff frequency of 4 GHz.}$$

The longitudinal threshold impedance is given by

$$\left| \frac{Z}{n} \right| = \frac{2\pi\alpha E \delta_\delta^2}{q_e I_{peak}}$$

If the actual ring impedance is higher than the threshold impedance, the bunch will be lengthened, the momentum spread increased until the new threshold impedance equals the ring impedance.

The longitudinal microwave instability threshold impedance for the natural momentum spread is  $0.27 \Omega$  for a mean circulating current of 0.5 A, all bunches equally filled and lengthened a factor 5 by the harmonic cavities.

As a comparison, it should be noted that the longitudinal impedance measured in Soleil [Nagaoka] was  $0.4 \Omega$ . Well shielded flanges are a necessity to achieve this low impedance value.

The transverse peak bunch current threshold is given by

$$Z_{T,MAX} = \frac{4E\nu_s}{q_e I_b \bar{\beta}_{x,y}} \frac{4\sqrt{\pi}}{3} F' \text{ where } \nu_s \text{ is the synchrotron tune, } F' = \sqrt{\pi} R, Z_T \text{ is the}$$

transverse impedance, R the ring radius and  $\bar{\beta}_{x,y}$  the mean Twiss parameters. (A more exact calculation integrating the  $\beta Z_T$  around the ring will be done). The threshold transverse impedance is  $423 \text{ k}\Omega/\text{m}$ .

This value can be compared to the coarse relation

$$Z_T = \frac{2R}{b^2} \frac{Z}{n} \text{ which gives } Z_T = 0.35 \text{ M}\Omega/\text{m}.$$

It is quite clear that a thorough impedance budget has to be performed since these approximations not give some order of magnitude safety margin.

### 2.11.1.2. Coherent Synchrotron Radiation

The threshold for the number of electrons/bunch for coherent synchrotron radiation is given by

$$N_{0,Th} = 3.6 * \frac{C}{4\pi b} \frac{\gamma \alpha \sigma_\delta \sigma_l}{r_e}$$

This yields  $2.3 \cdot 10^{11}$  particles/bunch, to be compared to the actual number of  $3 \cdot 10^{10}$ .

### 2.11.1.3. Space charge tune shift.

The space charge tune shift is given by

$$\delta\nu_y = \frac{N_0 r_e}{(2\pi)^{1.5} \gamma^3 \sigma_l} C \frac{\beta_{y,mean}}{\sigma_y (\sigma_x + \sigma_y)} \text{ which yields the vertical tune shift to } 7 \cdot 10^{-3}.$$

## 2.11.2. Multi Bunch Effects

The longitudinal multi bunch instabilities are driven by the positive, real part of the contributing impedances, while the negative impedances act damping.

The power spectrum of the bunches plays an important role. Short bunches induce high harmonics while the power spectrum of the MAX IV ring with long bunches will have a limited frequency span.

In the transverse direction, the negative, real parts of the transverse impedances induce instabilities, while the positive ones act damping. The angular frequency of the bunch power

spectrum is shifted by  $\frac{\xi}{\alpha} \omega_0$  ( $\xi$  is the chromaticity and  $\omega_0$  is the rotation angular frequency).

The restricted power spectrum of the long bunches and the shift of the spectrum effectively reduces the effect of the transverse coupled bunch instabilities in this case. It should also be noted that higher synchrotron modes than the rigid bunch oscillation, are effectively damped by the Landau damping introduced by the harmonic cavities.

### 2.11.2.1. Resistive Wall Effect

The transverse resistive wall impedance is given by

$$Z_{RW}(\omega) = (1-i) \frac{RZ_0}{b^3} \frac{\sqrt{2c}}{\sqrt{Z_0 \omega \sigma_w}} \quad \text{where } Z_0 \text{ is the free space impedance and } \sigma_w \text{ the vacuum}$$

chamber wall conductance.

The real part of the resistive wall impedance and the power spectra for the first two modes are seen below. As seen, the power spectra hardly overlaps to the negative, unstable impedances.

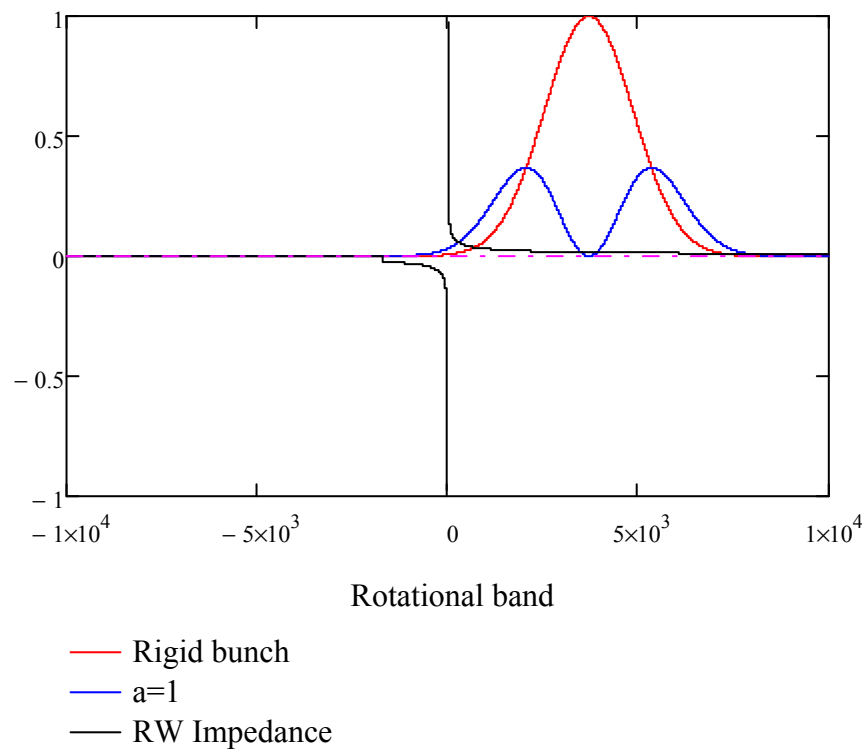


Figure 1

The growth rate of the resistive wall transverse instability can be written as

$$\Delta\omega(s, a) = -i \frac{1}{a+1} \frac{I_b c^2 q_e}{2\nu_y \omega_0 E 2\sqrt{\pi} \sigma_l} Z_T(s, a)$$

where we look at the vertical oscillations which have the fastest growth rate. The effective transverse impedance is given by

$$Z_T(s, a) = \frac{\sum_{p=-\infty}^{\infty} Z_{RW} \left( (pN_b + s + \nu_y + a\nu_s) \omega_0 \right) * h \left( \left( pN_b + s + \nu_y + a\nu_s - \frac{\xi}{\alpha} \right) \omega_0, a \right)}{\sum_{p=-\infty}^{\infty} h \left( \left( pN_b + s + \nu_y + a\nu_s - \frac{\xi}{\alpha} \right) \omega_0 \right)}$$

is the convolution of the impedance and power spectrum.

The growth rates of the first 4 synchrotron modes are seen below. The first two modes are damped, while the next two ones only have small growth rates, much smaller than the synchrotron radiation damping times.

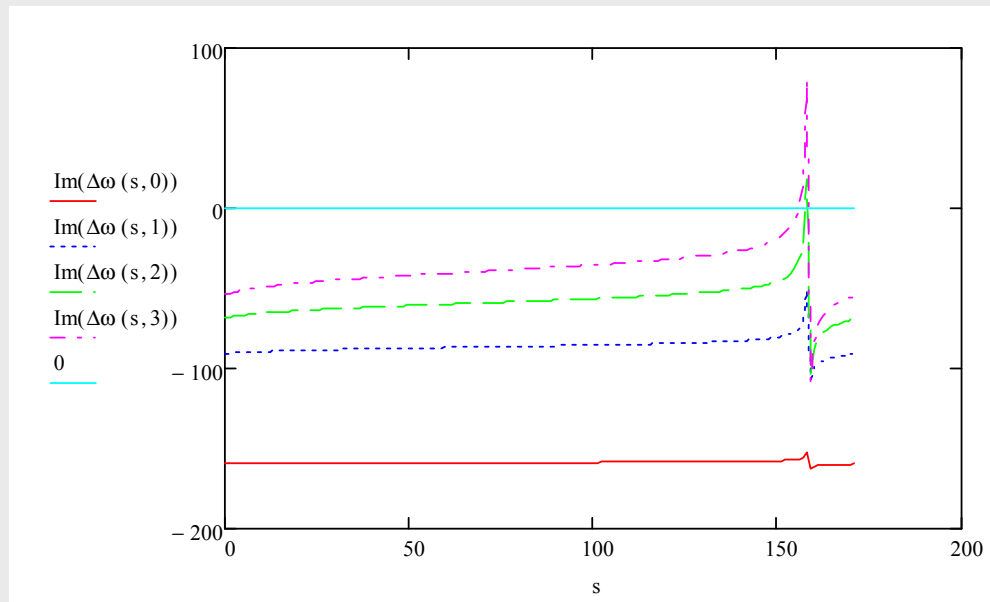


Figure 2



### 2.11.3. Higher Order Modes Coupled Bunch Instabilities

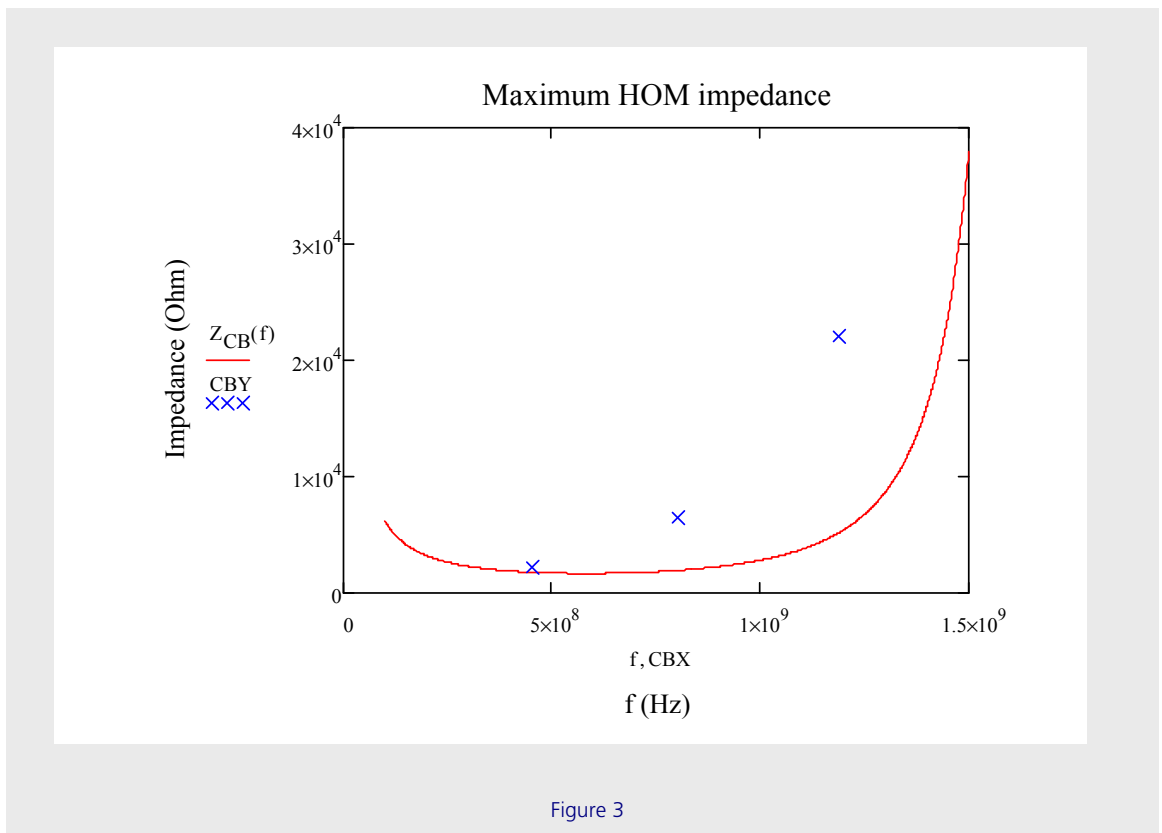
The higher order modes (HOM) in a capacity-loaded 100 MHz RF cavity of the MAX IV type start at 400 Mhz, a factor of 4 higher than the fundamental frequency. In a conventional cavity, this ratio is just 1.5. At frequencies higher than 1 GHz, the form factor of the stretched bunches steeply decrease the sensitivity of higher order modes. We will thus only have to fight a limited number of HOMs.

#### 2.11.3.1. Longitudinal HOM Coupled Bunch Instabilities

The growth rate of the longitudinal HOM instabilities can be calculated for a fourth order potential well as

$$\frac{1}{\tau} = \sqrt{\frac{Z_{CB} q_e I_{mean} \alpha F_{CB}^2 f 2\pi N_c}{ET_0}} \quad \text{where } F_{CB} \text{ is the form factor at frequency } f \text{ and } T_0 \text{ is the revolution time. } N_c \text{ is the number of 100 MHz cavities.}$$

The maximum longitudinal HOM impedance is shown below. There are three modes, so far not sufficiently damped, indicated in the graph.



The harmonic cavities will also contain HOMs. The design of the harmonic cavities are just down-scaled versions of the 100 MHz cavities so the HOM spectrum and impedances will scale accordingly. These HOMs of the harmonic cavities are thus quite insensitive to the long bunches.

#### **2.11.3.2. Transverse HOM Coupled Bunch Instabilities**

In the transverse case, HOMs will have damping effect as seen from fig. 1. The bunch power spectrum will not extend to negative frequencies so only the damping positive impedances will contribute.



# MAX IV Facility



# MAX IV Facility





## 3.1. Introduction

---

The low energy MAX IV 1.5 GeV ring is designed to serve the IR to UV synchrotron radiation user community. A sufficient number of ID straight sections, and a sufficiently low emittance, for a relatively low cost, are the goals. For this, a double bend achromat lattice is chosen. Combined function dipoles are chosen, which, compared to the present MAX II ring at MAX-lab, roughly decrease the emittance a factor two, still keeping the circumference below 100 m. The main parameter values are presented in chapter 3.2 table 3.1.

The lattice becomes compact with combined quadrupole-sextupole magnets. The same magnet technology with several magnets machined into a large iron block. The Twiss functions are relatively small which results in relatively small apertures. With an inner horizontal half width of 20 mm, the minimum lattice energy acceptance is still 3 %.

The same magnet technology as used for the high energy ring, with several magnets machined into a large iron block, will facilitate the alignment procedure. Alignment errors should be less critical for achieving the design dynamic acceptances.

To take advantage of the lattice energy acceptance, a low frequency RF system is introduced since this will require a lower RF voltage for given bucket height compared to an RF system of higher frequency. A large energy acceptance is important in this low energy and moderately low emittance ring to achieve a sufficient long Touschek life-time.

The relatively low RF voltage will permit us to use warm harmonic cavities to stretch the bunches. The bunch lengths are increased a factor of 4 to increase the Touschek life-time further and to reduce the bunch power spectrum which makes the ring more tolerant against Higher Order Mode instabilities. This small bunch power spectrum will also have a positive effect on the resistive wall instability.





# MAX IV Facility



# 3.2. Linear Lattice

---

- 3.2. Linear Lattice.....2**
- 3.2.1. Overview ..... 2
- 3.2.2. Achromats ..... 3
- 3.2.3. Bending Magnets..... 4
- 3.2.4. Focussing Magnets..... 5
- 3.2.5. Working Point ..... 6
- 3.2.6. Effects of Insertion Devices ..... 8
- 3.2.7. Intrabeam Scattering ..... 11
- References .....12

## 3.2. Linear Lattice

---

### 3.2.1. Overview

The MAX IV 1.5 GeV storage ring will accommodate IR and UV beamlines. Some of these beamlines will move from the existing MAX II and MAX III storage rings to the new facility while others will be entirely new beamlines. Additionally, for the *Kraków option*, the possibility to accommodate a superconducting wiggler (SCW) for the generation of soft X-rays in this low-energy storage ring is foreseen.

The lattice design aims therefore at low emittance with zero-dispersion straights of moderate length. The result is a ultra-compact double-bend achromat (DBA) lattice with twelve 3.5 m straight sections and a total circumference of 96 m. Several steps have been taken to achieve the compactness of this lattice:

- the focusing gradient has been integrated into the dipoles (this increases  $J_x$  and hence reduces the emittance)
- the focusing sextupoles have been integrated into the focusing quadrupoles
- all magnets within the DBA are to be integrated into one solid iron block
- a NEG-coated copper vacuum chamber reduces the number of pumps and doesn't require lumped absorbers.

The lattice on which this report is based is the m5-20100325-501 lattice and subsequent lattices derived from the m5-20100325 branch [1]. This is a working draft of the MAX IV 1.5 GeV storage ring lattice; it has so far not been verified that the magnet design for this lattice is feasible and lattice refinement (e.g. slicing of large magnets and fringe fields) has not yet been completed. This is work in progress, however. A summary of the machine parameters for the MAX IV 1.5 GeV storage ring is given in Table 3.1. Linear optics calculations have been performed with the codes OPA [2] and Tracy-3 [3]. The lattice files for both codes are very similar; the main difference being that the Tracy-3 lattice requires girder start and end markers for error studies. The agreement between the two codes is excellent.

Table 3.1: Parameters for the MAX IV 1.5 GeV storage ring.

Energy [GeV]	1.5
Main radio frequency [MHz]	99.931
Harmonic number	32
Circulating current [mA]	500
Circumference [m]	96
Number of achromats	12
Length of straight sections (BPM to BPM) [m]	3.5
Betatron tunes (horizontal / vertical)	11.22 / 3.14
Natural chromaticities (horizontal / vertical)	−22.9 / −17.1
Corrected chromaticities (horizontal / vertical)	+2.0 / +2.0
Momentum compaction factor	$3.04 \times 10^{-3}$
Horizontal emittance (bare lattice) [nm rad]	6.00
Radiation losses per turn (bare lattice) [keV]	117.2
Natural energy spread (bare lattice)	$0.75 \times 10^{-3}$
Required dynamic acceptance [mm mrad] (horizontal / vertical)	17.7 / 5.6
Required lattice momentum acceptance	±3.0%

### 3.2.2. Achromats

The 1.5 GeV MAX IV storage ring is composed of 12 main cells of DBA type. The DBA is built up by joining one half-achromat (a bending magnet flanked by focusing quadrupoles and defocusing sextupoles) with a mirrored half-achromat; in the lattice file however, this symmetry appears broken by the BPM and corrector layout. A schematic of one achromat is given in Fig. 3.1. Twelve straight sections connect the 12 DBAs. Two of these straights are reserved for machine use: the injection straight and a straight to house rf cavities. Ten straight sections remain for insertion devices (IDs).

In summary, each DBA consists of:

- **Straight:** a 1.75 m drift section
- **hACHR:** the half-achromat; it consists of:
  - **SQFo:** the outer focusing quadrupole/sextupole
  - **SCo:** the outer sextupole corrector

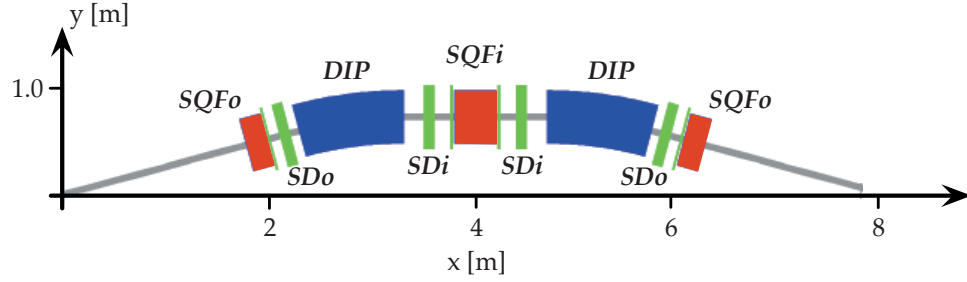


Figure 3.1: Schematic of one of the 12 DBAs of the MAX IV 1.5 GeV storage ring. The total bending angle is  $30^\circ$ . The gradient bending magnets (blue) are flanked by sextupoles (green). The bending magnets are interleaved with combined-function quadrupoles/sextupoles (red). Thin corrector sextupoles are installed throughout the DBA (green, thin).

- **SDo**: the outer defocusing sextupole
- **DIP**: the  $15^\circ$  dipole with focusing gradient
- **SDi**: the inner defocusing sextupole
- **SCi**: the inner sextupole corrector
- **SQFi**: the inner focusing quadrupole/sextupole

and the mirror of all of the above.

The optical functions for the MAX IV 1.5 GeV achromat are shown in Fig. 3.2. The compact lattice with strong focusing results in relatively small beta functions and dispersion, reducing the need for large vacuum chamber apertures. For the MAX IV 1.5 GeV storage ring vacuum chamber an elliptical cross section with inner diameters of 40/20 mm has been chosen. The relatively small vacuum chamber cross section allows for small magnet gaps ( $> 42$  mm full gap). This in turn reduces the required magnet length.

### 3.2.3. Bending Magnets

The bending magnets in the DBA are sector dipole magnets with a total bending angle of  $15^\circ$  each. In this simple lattice model used here this dipole is modeled as a hard-edge magnet without fringes. The magnet is exactly 1 m long and hence the bending magnet field strength is  $\hat{B} = 1.31$  T corresponding to a bending radius of  $\rho = 3.820$  m.

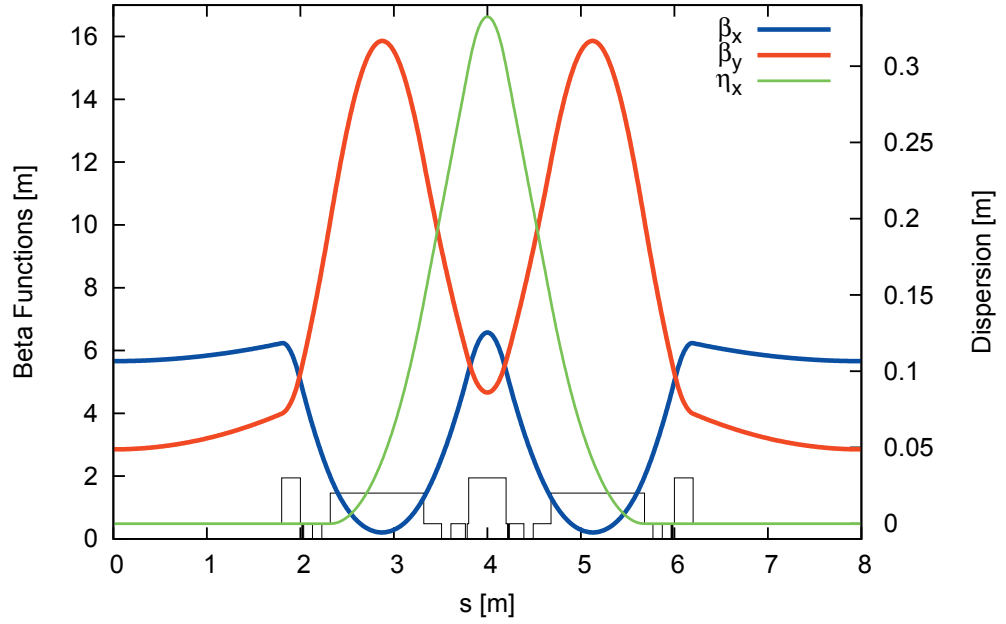


Figure 3.2: One achromat of the MAX IV 1.5 GeV storage ring. The positions of the magnets are indicated at the bottom in black.

In addition to the guiding dipole field, the bending magnets contain a vertical focusing gradient. This removes the need for dedicated defocusing quadrupoles making the lattice more compact and at the same time increases  $J_x$  which allows for a decrease in horizontal emittance. The defocusing gradient is  $k = -1.348 \text{ m}^{-1}$ .

### 3.2.4. Focussing Magnets

In addition to the gradient in the bending magnets, there are two quadrupole families providing the focusing in the MAX IV 1.5 GeV storage ring. The SQFi family is located at the center of the DBA while the SQFo family is installed at both ends of the DBA. The focusing quadrupoles also integrate a sextupole gradient; this will be detailed in Section 3.3.2. A summary of the focusing magnet parameters is given in Table 3.2.

The defocusing quadrupole family (QD) is given by the gradient in the bending magnets. Pole-face strips will be included to allow for tunability of the QD component. In order to move the vertical tune by  $\Delta\nu_y = \pm 0.5$  a tuning of  $\Delta k_{QD} = \pm 1.5\%$  is required (keeping the horizontal tune and dispersion constant). The pole face strips should therefore provide at least  $\pm 2\%$  tuning range.



Table 3.2: Quadrupole magnet parameters for the bare lattice. Note that in the lattice files SQFi is modeled as two half-magnets for symmetry reasons.

<i>Inner Focusing Magnet (SQFi)</i>	
Type	Combined-function quadrupole/sextupole
Length [m]	0.40
Quadrupole gradient [ $\text{m}^{-2}$ ]	4.998
<i>Outer Focusing Magnet (SQFo)</i>	
Type	Combined-function quadrupole/sextupole
Length [m]	0.20
Quadrupole gradient [ $\text{m}^{-2}$ ]	5.737
<i>Defocusing Magnets (QD)</i>	
Type	Gradient integrated in dipole
Length [m]	1.00
Quadrupole gradient [ $\text{m}^{-2}$ ]	-1.348

### 3.2.5. Working Point

The linear optics of the MAX IV 1.5 GeV storage ring have been tuned in such a way to achieve a working point at tunes  $\nu_x = 11.22$  and  $\nu_y = 3.14$ . This puts both fractional tunes below the half integer (this is necessary to damp transverse resistive wall instability [4]). In order to make the machine less sensitive to misalignments the tunes should stay clear of the integer (closed orbit instability due to dipole errors) and half integer (beam blow-up due to gradient errors) [5]. It is however not feasible to put them both at 0.25 because this would lead to a working point on the linear coupling resonance which is driven by skew quadrupolar fields that are always present in real machines. The choice of working point for the MAX IV 1.5 GeV storage ring close but not on the quarter-integer reflects this.

The choice of the working point was however also heavily influenced by the nonlinear dynamics, specifically by the tune footprint for amplitude-dependent tune shifts and chromaticity. These issues are described in more detail in Section 3.3.

With the achromat tuned in this way the horizontal beta function oscillates between 0 m and 6 m within the DBA. It reaches its maximum at the center and edges of the DBA. The vertical beta function oscillates between 4 m and 16 m within the DBA. The maximum vertical beta function is reached in the dipoles, while the local minimum within the DBA is found in the center. In the straight sections the vertical beta function is reduced to 2.85 m which is the global minimum. The horizontal beta function in the straights is 5.66 m, just below the global maximum of 6 m. The vertical beta function in the straights corresponds roughly to the maximum ID length which assures that the vertical acceptance is not reduced by the ID aperture. Increasing the vertical beta function is not desirable because of the elastic scattering lifetime.

Assuming a coupling of  $\kappa = \varepsilon_y/\varepsilon_x \approx 1\%$ , we note that beamlines in the MAX IV 1.5 GeV storage ring will be diffraction limited at  $\lambda_{\min} = 4\pi\varepsilon_y = 7.5 \text{ \AA}$ . At this coupling the vertical source size would be  $\sigma_y = \sqrt{\varepsilon_y\beta_y} = 13.1 \text{ }\mu\text{m}$ . If the beamlines operated on the MAX IV 1.5 GeV storage ring do not require such a low diffraction limit, the coupling can be increased by skew quadrupoles to improve lifetime. But ultimately the goal will be to best match the electron beam to the photon beam emerging from the IDs (and hence increase the photon brightness)

Keeping the *Kraków option* in mind, we note that vertical beta functions as low as 1.2 m can be expected if we match the achromat optics locally to a strong SCW (cf. Section 3.2.6). With such optics, the lowest source size expected at 1% coupling is  $\hat{\sigma}_y = \sqrt{\varepsilon_y\hat{\beta}_y} = 8.5 \text{ }\mu\text{m}$ .

At a horizontal beta function of 5.66 m in the straights the horizontal rms beam size for is  $184 \text{ }\mu\text{m}$ . A further reduction of this value is not feasible because it would require increasing the vertical betatron in the straight section. Maximum values for the dispersion of 33 cm are found at the center of the DBA in SQFi. This gives a horizontal orbit offset of 10 mm for a  $\pm 3\%$  off-momentum particle (and a maximum excursion of 20 mm for a Touschek-scattered particle). Dispersion reduces to zero towards the end of the dipoles and remains zero throughout the straight section.

### 3.2.6. Effects of Insertion Devices

Undulators and wigglers will have a net vertical focusing effect on the stored electron beam. Without further correction this causes a vertical tune shift (cf. Eq. 2.2 in Chapter 2.2.6) and a vertical beta beat (cf. Eq. 2.3 in Chapter 2.2.6). These perturbations of the design optics can lead to a reduction of dynamic aperture and lifetime.

From a linear optics standpoint this effect therefore needs to be compensated in two steps:

- ensure that the ID is matched to the adjacent achromats,
- restore the original machine working point.

In the MAX IV 1.5 GeV storage ring IDs will be installed for the production of UV and IR radiation. Because of the longer periods of such devices and the low ring energy the effect of these IDs on the optics is small compared with the 3 GeV ring (cf. Chapter 2.2.6). Therefore the optics will not be matched to individual IDs in the 1.5 GeV storage ring. This reduces the complexity of the facility considerably because it means all gradient dipoles and quadrupoles can be powered in families and without extra floating power supplies.

The exception here is the installation of a SCW for the *Kraków option*. For such a strong device, local optics adjustments should be performed. We assume a device similar to the superconducting MAX-wigglers installed in MAX II: peak field of  $\hat{B} = 3$  T, period length  $\lambda_w = 61$  mm, and 25 periods. The SCW parameters are summarized in Table 3.3.

Table 3.3: Parameters of the 3 T SCW.

Length [m]	1.525
Number of periods	25
Period length [mm]	61
Peak magnetic field strength [T]	3.0
Full gap height [mm]	10.2
Radiated energy per turn (at peak strength) [keV]	18.5
Reduction of overall emittance (at peak strength) [nm rad]	0.62

Matching of such an ID to the adjacent straight sections can be accomplished by adjusting the gradient in the flanking bending magnets as well as the flanking SQFo. This can be achieved by adding floating power supplies to these two SQFo magnets and the pole face strips on the flanking dipoles. The resulting matched optics are shown in Fig. 3.3.

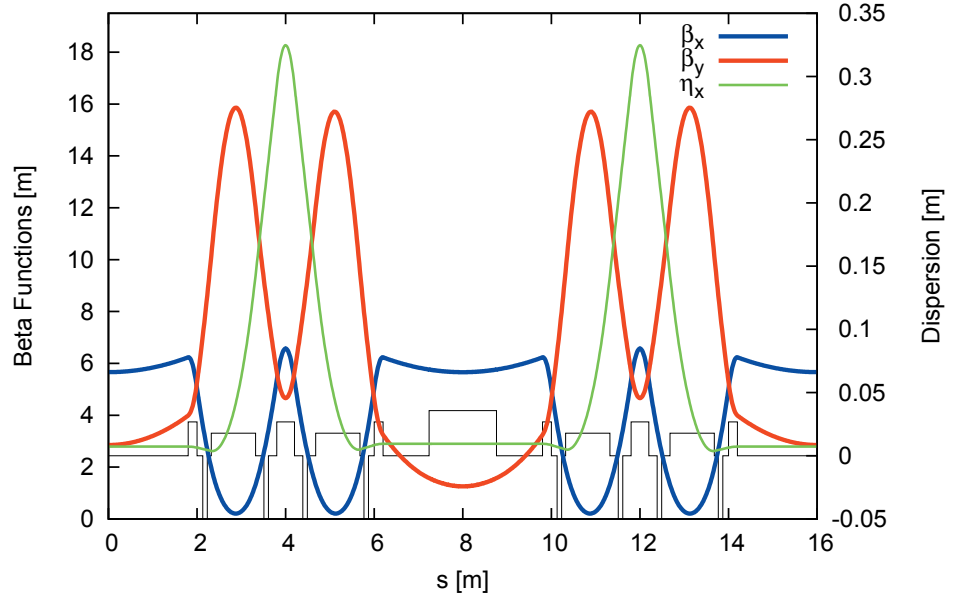


Figure 3.3: Two achromats of the MAX IV 1.5 GeV storage ring with a 3 T SCW installed in the straight section between the two achromats. The positions of the magnets are indicated at the bottom in black. The wiggler is also indicated. The gradient in the dipoles and SQFo magnets flanking the SCW have been adjusted to match the achromat optics to the SCW locally. This type of match leaves a slight dispersion leak which can be seen at the edges ( $\eta_x \approx 7$  mm).

The required gradient changes are summarized in Table 3.4. This match is not perfect because it only partially satisfies the first of the two above mentioned compensation steps. The matching proposed here is simple and requires only little extra hardware, but it leaves an excess phase advance and a small dispersion leak into the rest of the machine. The dispersive beam size contribution is small compared to the natural beam size ( $\sigma_\delta \lesssim 4 \mu\text{m}$  compared to  $\sigma_{x,\beta} = 180 \mu\text{m}$ ) however. Furthermore, the overall tune shift resulting from one such SCW is rather low and hence the working point must not

necessarily be corrected; it is however well within the tuning range of the pole face strips. The tune shifts resulting from this match to the SCW are given in Table 3.5.

Table 3.4: Adjustments required to match the adjacent achromats to a 3 T SCW installed in a straight section of the MAX IV 1.5 GeV storage ring. The largest change is the 4.2% increase in the dipole gradient. As a result of this matching, the beta function values at the ends of the adjacent straights are matched to those of a bare achromat. This ensures that the SCW does not cause a beta beat throughout the rest of the storage ring.

Before Adjustment with 1 SCW		After Adjustment with 1 SCW	
$k_{\text{SQFo}} = 28.68 \text{ T/m}$	$\longrightarrow$	$28.74 \text{ T/m}$	
$k_{\text{DIP}} = -6.74 \text{ T/m}$	$\longrightarrow$	$-7.02 \text{ T/m}$	
$\Downarrow$		$\Downarrow$	
$\beta_x^* = 5.662 \text{ m}$	$\longrightarrow$	$5.662 \text{ m}$	
$\beta_y^* = 6.563 \text{ m}$	$\longrightarrow$	$2.852 \text{ m}$	
$\eta_x^* = 0.0 \text{ mm}$	$\longrightarrow$	$7.2 \text{ mm}$	

Table 3.5: Tune shifts after matching the optics locally to a single 3 T SCW in the MAX IV 1.5 GeV storage ring. The largest difference is an excess 5% vertical phase advance. Note that the tune shift shown here corresponds to one SCW installed in an otherwise bare lattice.

Bare Lattice		After Adjustment with 1 SCW	
$k_{\text{SQFo}} = 28.68 \text{ T/m}$	$\longrightarrow$	$28.74 \text{ T/m}$	
$k_{\text{DIP}} = -6.74 \text{ T/m}$	$\longrightarrow$	$-7.02 \text{ T/m}$	
$\Downarrow$		$\Downarrow$	
$\nu_x = 11.2200$	$\longrightarrow$	$11.2162$	
$\nu_y = 3.1400$	$\longrightarrow$	$3.2955$	

### 3.2.7. Intrabeam Scattering

Because the emittance of the MAX IV 1.5 GeV storage ring lattice is not ultralow, intrabeam scattering (IBS) is not expected to have the significant influence on overall equilibrium emittance that it has for the 3 GeV storage ring. Emittance values given so far take into account the emission of synchrotron radiation and quantum emission fluctuations, but not IBS. We will briefly calculate IBS emittance growth to verify that IBS can be neglected in the case of the 1.5 GeV storage ring.

IBS calculations have been performed with ZAP [7] using expected rf parameters (cf. Section 3.6.2). The results calculated for a total stored current of 500 mA ( $\rightarrow$  bunch charge  $Q_b = 5$  nC), expected rf parameters (radiation losses  $\approx 130$  kV, total cavity voltage 560 kV  $\rightarrow$  rf acceptance  $\sigma_{\text{rf}} = 4.0\%$ , rms bunch length  $\sigma_s = 14.7$  mm), and coupling set to 1% ( $\rightarrow \varepsilon_y = 60$  pm rad) are summarized in Table 3.6. We compare the values for the bare lattice with those for a lattice with harmonic Landau cavity running at 300 MHz ( $\sigma_s = 14.7$  mm  $\rightarrow$  60 mm). The table also shows the results for the *Kraków option* where a superconducting wiggler is included; in this case the rf acceptance is only 3.5% (radiation losses with one superconducting wiggler  $\approx 150$  kV, total cavity voltage 500 kV) and the natural bunch length is 16.3 mm.

As expected, as soon as the harmonic Landau cavity is tuned in, IBS can be neglected in the MAX IV 1.5 GeV storage ring. This also holds for the *Kraków option*. In fact, even without the Landau cavity, the influence of IBS on emittance and bunch length is minute ( $\leq 3\%$ ).

Table 3.6: Effect of IBS on the MAX IV 1.5 GeV storage ring. The bare lattice emittance has been calculated assuming coupling adjusted to give  $\varepsilon_y = 60$  pm rad. The influence of the harmonic Landau cavities (LC) is also shown. Emittance growth and bunch lengthening from IBS become negligible once the LCs are operated.

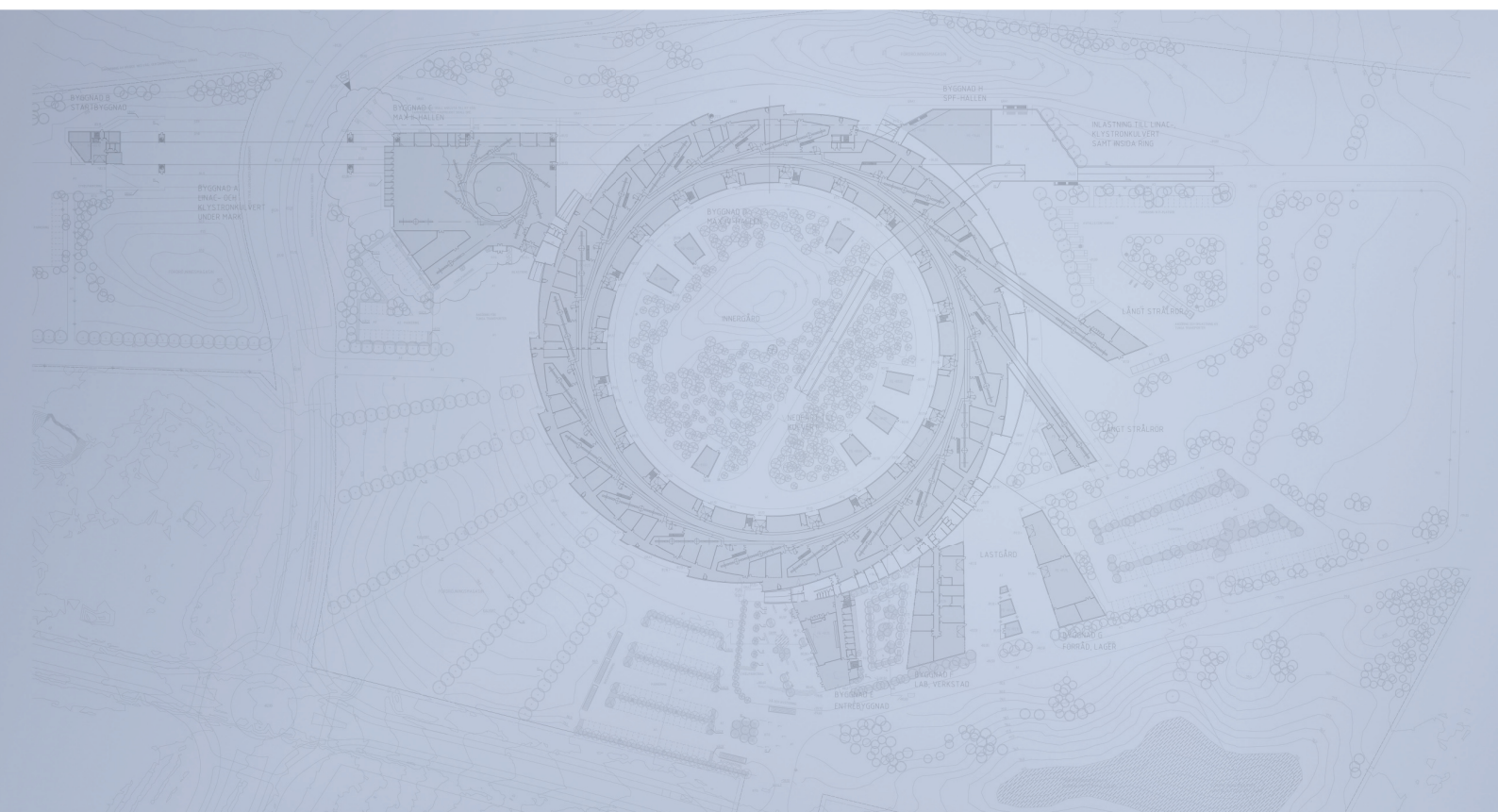
	$\varepsilon_x$ [nm rad]			$\sigma_s$ [mm]		
MAX IV 1.5 GeV	6.00	$\rightarrow$	6.19	14.7	$\rightarrow$	15.0
MAX IV 1.5 GeV with LC	6.00	$\rightarrow$	6.05	60.0	$\rightarrow$	60.2
<i>Kraków option</i>	5.38	$\rightarrow$	5.56	16.3	$\rightarrow$	16.4
<i>Kraków option</i> with LC	5.38	$\rightarrow$	5.45	60.0	$\rightarrow$	60.1

## References

- [1] Lattice files can be obtained at [http://www.maxlab.lu.se/local/maxiv\\_reports/accelerators\\_machine/1.5GeV/Lattice/index.html](http://www.maxlab.lu.se/local/maxiv_reports/accelerators_machine/1.5GeV/Lattice/index.html)
- [2] A. Streun, *OPA*, code and documentation available at <http://slsbd.psi.ch/~streun/opa>
- [3] J. Bengtsson, *Tracy-2 User's Manual*, unpublished
- [4] A. Hofmann, *Beam Instabilities*, Proceedings of the CERN Accelerator School on Synchrotron Radiation and Free-electron Lasers 2003, Brunnen, Switzerland
- [5] A. Streun, *Lattices for Light Sources*, Proceedings of the CERN Accelerator School on Synchrotron Radiation and Free-electron Lasers 2003, Brunnen, Switzerland
- [6] J.B. Murphy, *Synchrotron Light Source Data Book*, available at <http://www.nsls.bnl.gov/newsroom/publications/otherpubs/dbook>
- [7] M.S. Zisman, S. Chattopadhyay, J.J. Bisognano, ZAP User's Guide, LBL 21270, December 1986.



# Detailed Design Report



## Chapter 3

### MAX IV 1.5 GeV Storage Ring

#### 3.3. Nonlinear Optics

MAX IV Facility





# 3.3. Nonlinear Optics

---

- 3.3. Nonlinear Optics .....2**
- 3.3.1 Overview ..... 2
- 3.3.2 Sextupoles ..... 2
- 3.3.3 Dynamic Aperture ..... 9
- 3.3.4 Energy Acceptance .....14
- 3.3.5 Effects of Insertion Devices.....19
- References ..... 38

## 3.3. Nonlinear Optics

---

### 3.3.1. Overview

In order to correct the natural negative chromaticity to slightly positive values, two families of chromatic sextupoles are required for the MAX IV 1.5 GeV storage ring. Because of their nonlinear nature, chromatic sextupoles lead to a variation of the tune with betatron amplitude. Particle motion can become unstable above certain amplitudes in such a way that a particle can no longer be stored within the machine. The maximum amplitude at which a particles can be stored is called the dynamic aperture (DA). Obviously this DA can vary around the storage ring. If not otherwise specified, DA refers to the dynamic aperture at the center of the injection straight.

Ideally the DA would be as large as the physical aperture, but due to the nonlinear effects this is usually not the case.<sup>1</sup> In order to enlarge the DA compensation sextupoles are installed in the storage ring. If this is done in zero-dispersion areas the sextupoles are referred to as harmonic sextupoles because they have no chromatic effect on the beam. The primary goal of the nonlinear lattice design is then to ensure that the DA is sufficient to achieve the required beam lifetime and increase injection efficiency.

### 3.3.2. Sextupoles

In the MAX IV 1.5 GeV storage ring it has been decided to integrate the focusing sextupoles into the focusing quadrupoles in order to make the lattice more compact. The defocusing sextupoles are however inserted into the lattice as dedicated magnets. Since this means the focusing sextupole strength and hence the chromaticity is set in iron, we add weak focusing correction sextupoles to the lattice. These allow adjustment of the chromaticity within a certain range.

The MAX IV 1.5 GeV storage ring therefore ends up with six sextupole families. Two

---

<sup>1</sup>It is important to note here that even a storage ring consisting only of linear elements (bending magnets, quadrupoles) will show nonlinear effects due to magnet fringe fields, magnet imperfections, misalignments, etc. It is therefore imperative to design a storage ring with nonlinear optics in mind from the start. As correctly pointed out by others [1, 2], there is no such thing as a purely linear optics design. Linear and nonlinear lattice design are interleaved and have to be treated together.

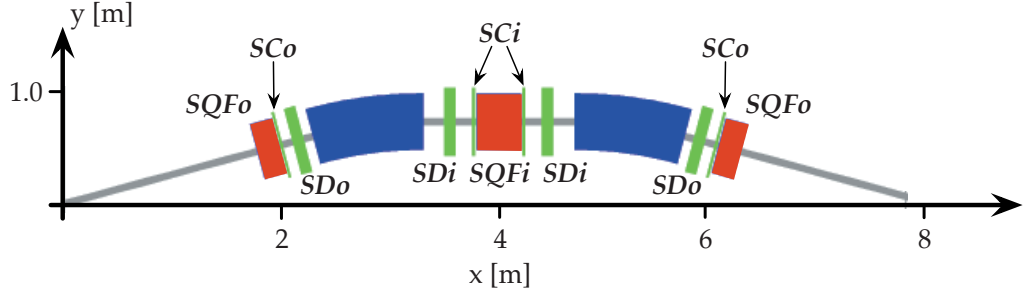


Figure 3.1: Schematic of the sextupole magnet layout within one achromat of the MAX IV 1.5 GeV storage ring. Dedicated sextupoles are indicated in green while sextupole gradients integrated in combined-function magnets are indicated in red.

of these families are defocusing: SDi and SDo. Note that only SDi is chromatic while SDo is purely harmonic. Both families use dedicated sextupole magnets. There are two main focusing sextupole families: SQFi and SQFo. Again only one is chromatic (SQFi) while the other is purely harmonic (SQFo). Since these sextupoles are integrated into quadrupole magnets, their strength cannot be adjusted individually. Therefore, two extra sextupole families are added; we refer to these families as correction sextupoles. Again, one family is chromatic (SCi) while the other is harmonic (SCo). These correction sextupoles are small and weak because they are only required for chromaticity tuning; the bulk of the chromatic correction is taken care of by SDi and SQFi. A schematic of the sextupole magnet layout is given in Fig. 3.1. The position of the sextupoles is also indicated in the plot showing the optical functions for one achromat (Fig. 3.2 in Section 3.2.2). A summary of the sextupole parameters is given in Table 3.1.

The sextupole strengths have been calculated with OPA. The two chromatic families of the regular sextupole magnets were designated to correct the natural chromaticities to  $\xi_{x,y} = +2.0$  (lattice m5-20100325-501). The two harmonic families were tuned to minimize the first order chromatic and geometric driving terms of the sextupole Hamiltonian plus the three second order terms for amplitude-dependent tune shift (ADTS) [2]. For alternative operation at chromaticity  $\xi_{x,y} = +1.0$  (lattice m5-20100325-503) we adjust SDi and power SCi. Accordingly, we then use SDo and power SCo to minimize resonance driving terms and shape the ADTS. The resulting change required for SDi and SDO is  $< 8\%$ . The required integrated gradients for SCi and SCO remain below  $|b_3 L| < 0.3 \text{ m}^{-2}$ .

Table 3.1: Sextupole magnet parameters for six sextupole families. The specified gradients render a corrected chromaticity of  $\xi_{x,y} = +2.0$ . The gradients indicated in brackets are for a corrected chromaticity of  $\xi_{x,y} = +1.0$ .

<i>Focusing Sextupoles</i> (SQFi, SQFo)	
Type	Combined-function magnet
Number per achromat	2 / 1
Minimum bore radius [mm]	> 42
Length [mm]	200 / 400
Sextupole gradient [ $\text{m}^{-3}$ ]	28.040 / 36.677
<i>Defocusing Sextupoles</i> (SDi, SDo)	
Type	Dedicated sextupole magnet
Number per achromat	2 / 2
Minimum bore radius [mm]	> 42
Length [mm]	100
Sextupole gradient [ $\text{m}^{-3}$ ]	−73.226 [−68.176] / −91.922 [−84.763]
<i>Correction Sextupoles</i> (SCi, SCo)	
Type	Dedicated sextupole magnet
Number per achromat	2 / 2
Minimum bore radius [mm]	> 42
Length [mm]	20
Sextupole gradient [ $\text{m}^{-3}$ ]	0.0 [−20.157] / 0.0 [−29.997]

OPA is then used to calculate ADTS and chromatic tune shifts from tracking. This gives a first impression of the tune footprint. An example is given in Fig. 3.2. The optimized sextupole settings found with OPA are then transferred to the Tracy-3 lattice file. Tracy-3 is used to confirm the non-linear chromaticity (shown in Fig. 3.3) and the amplitude-dependent tune shifts (shown in Fig. 3.4). Agreement between the two codes regarding tunes, chromaticities, and amplitude-dependent tune shifts is excellent for the bare lattice.

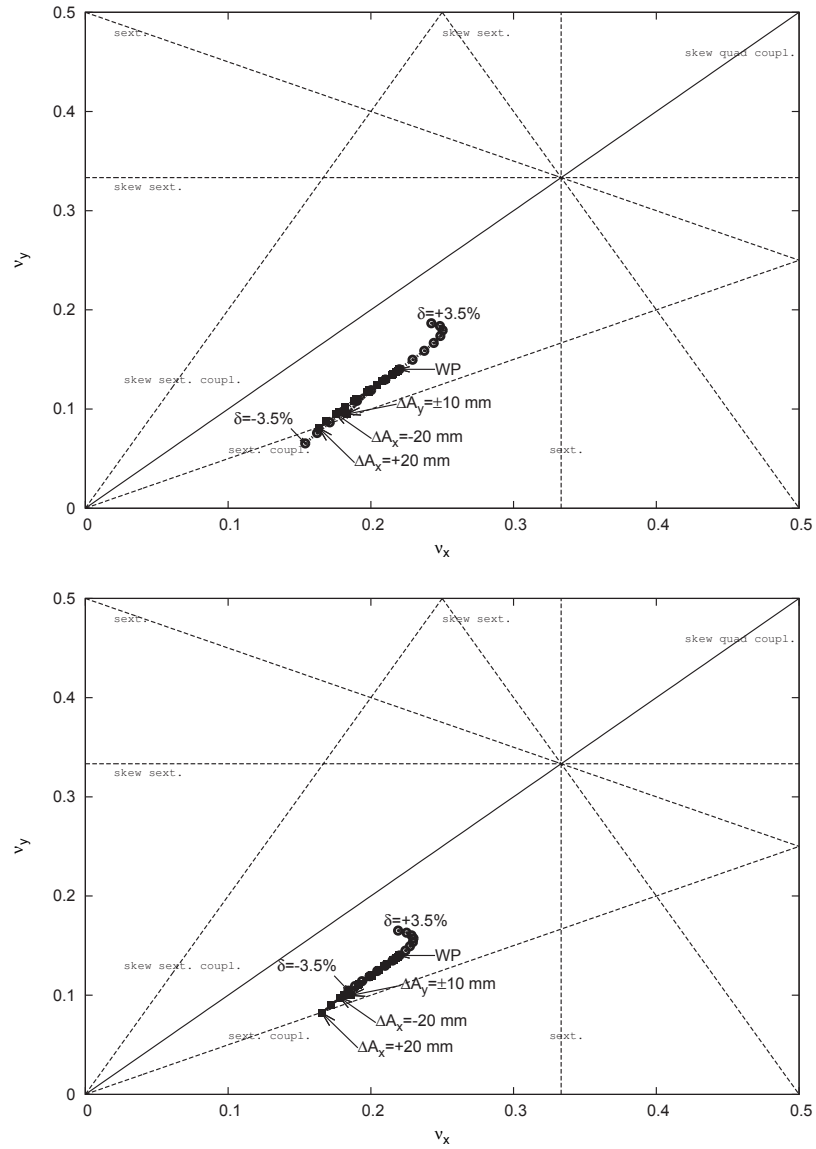


Figure 3.2: A plot of fractional tune space for the MAX IV 1.5 GeV storage ring bare lattice as calculated by OPA. The top plot shows the footprint for the basic optics ( $\xi_{x,y} = +2.0$ ); the lower plot shows the footprint for alternative optics with chromaticity adjusted to  $\xi_{x,y} = +1.0$ . Resonance and skew resonance lines have been included up to third order. WP indicates the working point. The step size chosen for the chromatic tune shift is 0.5% and 2.5 mm for the amplitude-dependent tune shift.

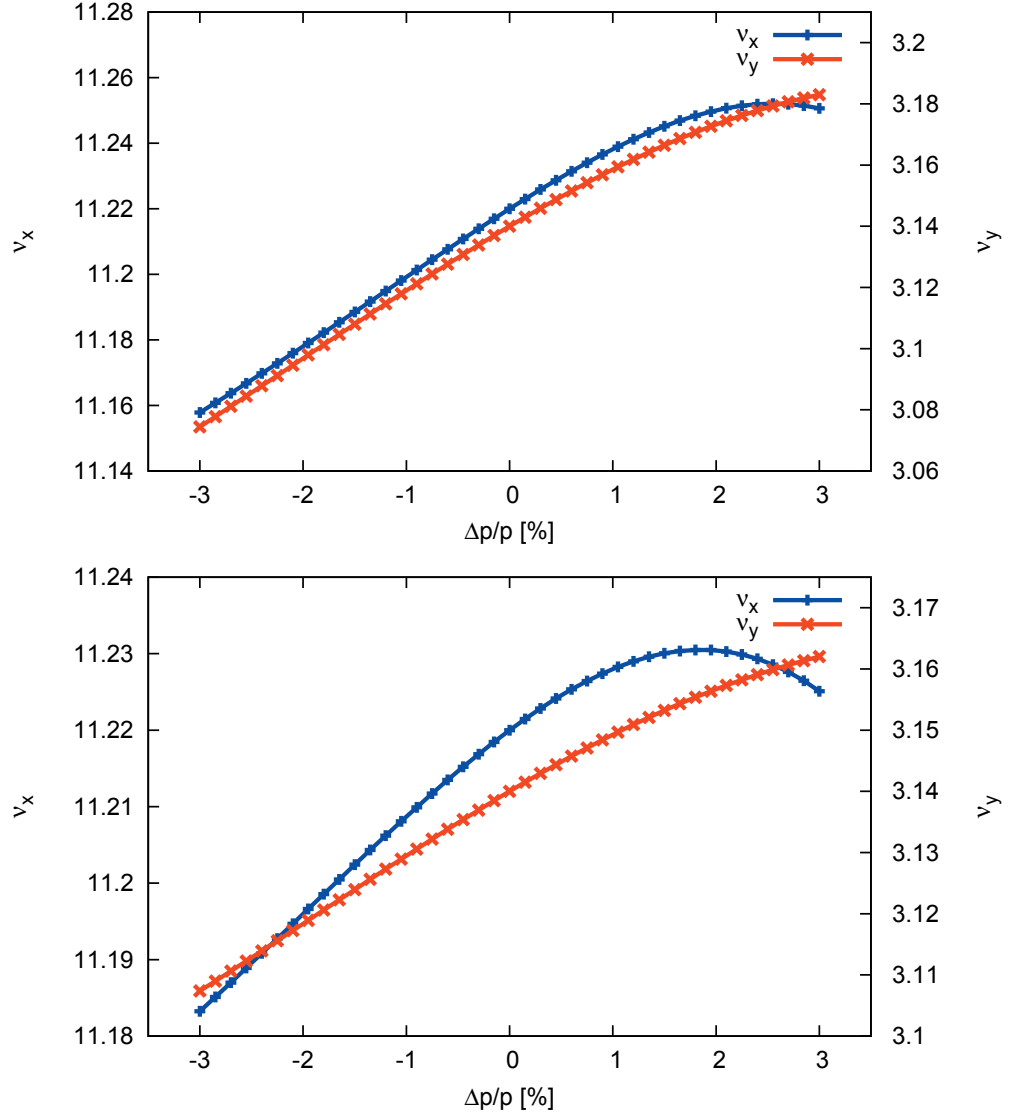


Figure 3.3: Chromatic tune shift for the MAX IV 1.5 GeV storage ring bare lattice as calculated by Tracy-3. The top plot shows the footprint for the basic optics ( $\xi_{x,y} = +2.0$ ); the lower plot shows the footprint for alternative optics with chromaticity adjusted to  $\xi_{x,y} = +1.0$ . Agreement with results given by OPA is excellent.



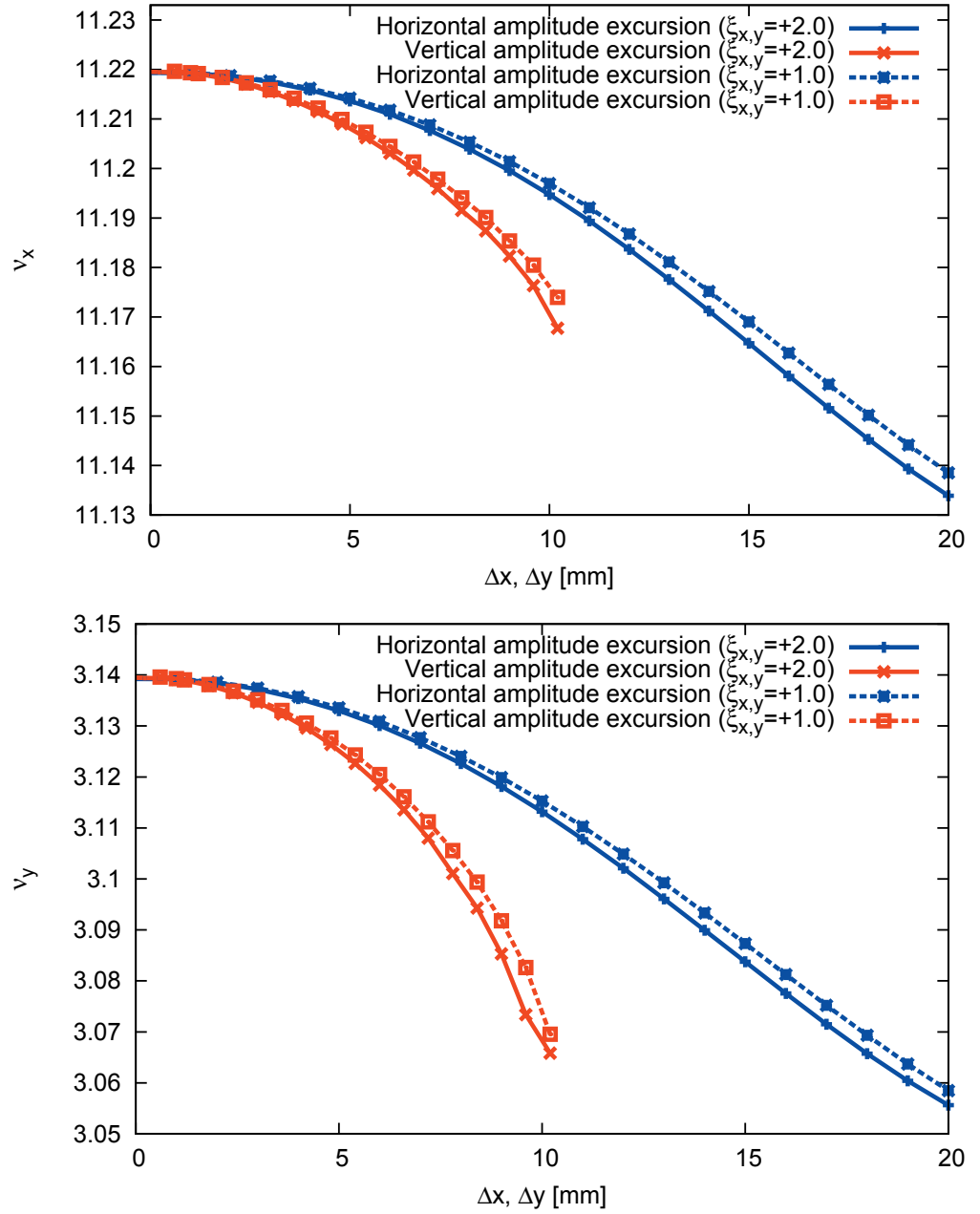


Figure 3.4: Plots showing the amplitude-dependent tune shift for the MAX IV 1.5 GeV storage ring bare lattice as calculated by Tracy-3. The plots show data both for the basic optics ( $\xi_{x,y} = +2.0$ ) and for alternative optics with chromaticity adjusted to  $\xi_{x,y} = +1.0$ . Agreement with results given by OPA is excellent.

### 3.3.3. Dynamic Aperture

As pointed out in the overview, the MAX IV 1.5 GeV storage ring requires a sufficiently large DA in order to achieve high injection efficiency and long Touschek lifetime. A high injection efficiency is necessary in order to reduce the time required for injection (number of shots required from the linac) and to reduce the amount of radiation at injection. Touschek lifetime is of great importance because in modern light sources it usually dominates lifetime and hence defines the brightness at the beamlines (decaying beam mode and *Kraków option*) or the required injection rate (top-up mode). In addition, Touschek scattering is usually the main source of the overall radiation background and hence it is imperative to achieve a high Touschek lifetime even when operating in top-up mode.

The required physical acceptance for the MAX IV 1.5 GeV storage ring has been specified at 17.7 mm mrad in the horizontal and 5.6 mm mrad in the vertical plane. In the center of the straight sections this corresponds to a required aperture of  $\pm 10$  mm in the horizontal and  $\pm 4$  mm in the vertical plane. The reasoning behind the required vertical aperture is that the narrow-gap ID chambers likely to be installed in the MAX IV 1.5 GeV storage ring will reduce the vertical physical aperture in the straight sections to  $\pm 4$  mm. The horizontal aperture requirement is motivated by the injection process (see also Chapter 3.7):

- septum thickness is 2.5 mm (Lambertson septum),
- stored beam moved to within 3.5 mm of the septum (a stored beam has a size of  $\sigma_x = \sqrt{\varepsilon\beta_x^*} \approx 184 \mu\text{m}$  in the injection straight where dispersion is zero) by the injection bump,
- injected bunch brought to within 1 mm of the septum (assuming the injector linac delivers a beam with an normalized transverse emittance of  $12 \mu\text{m rad}$  we get a injected beam size of  $\sigma_x = \sqrt{\varepsilon\beta_x^*} \approx 152 \mu\text{m}$ ).

This gives a separation of 7.0 mm between the bumped stored beam and the injected beam at the septum. We add a 3 mm safety margin and arrive at a total required aperture of 10 mm for capture.

An example for the DA of the MAX IV 1.5 GeV storage ring bare lattice is given in

Fig. 3.5 where Tracy-3 has been used to calculate DA for on and off-momentum particles with 6D tracking. It is clear that even for off-momentum particles the DA requirements are fulfilled. If the physical boundaries are included in the lattice file, the DA extends to these boundaries confirming that nonlinearities are very small within the physical aperture.

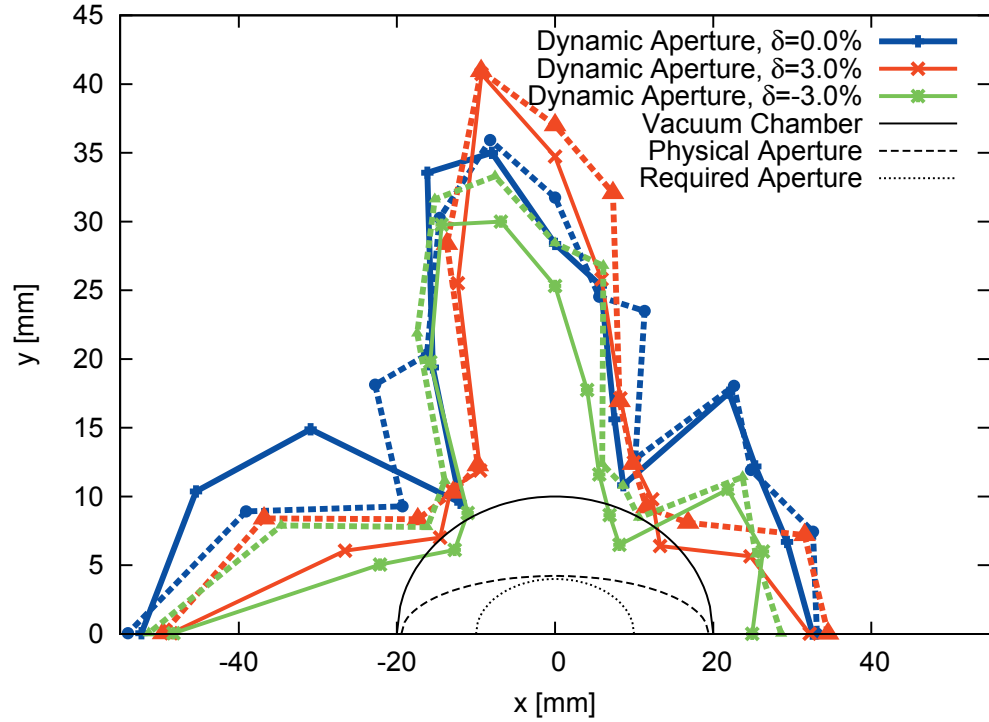


Figure 3.5: Dynamic aperture at the center of the long straight section in the MAX IV 1.5 GeV storage ring. Solid lines correspond to the basic optics ( $\xi_{x,y} = +2.0$ ), dashed lines to the alternative optics ( $\xi_{x,y} = +1.0$ ). Tracking was performed with Tracy-3 in 6D for one synchrotron period. Physical aperture and required aperture are also indicated in the plot.

This picture however lacks dynamics information and it does not reveal where the limitations of the DA come from. In order to get a better idea of what governs the DA, frequency map analysis (FMA) can be performed [3]. For a given initial position in transverse phase space, Tracy-3 tracks the particle for a certain number of turns ( $N_t = 2064$  chosen for most studies) in the storage ring and calculates the diffusion rate

$$D = \log \sqrt{(\Delta\nu_x)^2 + (\Delta\nu_y)^2} \quad (3.1)$$

where

$$\Delta\nu = \nu|_{N=0} - \nu|_{N=N_t}. \quad (3.2)$$

This is done for on and off-momentum particles. In addition to calculating the diffusion rate as a function of initial conditions, Tracy-3 also plots diffusion as a function of the initial tunes. These so-called frequency maps — using a modified definition of diffusion  $D = \min(-2, \log \sqrt{(\Delta\nu_x)^2 + (\Delta\nu_y)^2})$  — show which areas of tune space correspond to stable motion, diffusion, and particle loss. Through particle tracking, areas of interest in the diffusion map can be linked to locations in frequency space. The frequency map then helps identify sources of particle loss. Since diffusion and frequency maps can be used to understand beam loss mechanisms, they are valuable tools to optimize nonlinear optics.

Figure 3.6 shows a diffusion map for the bare lattice for the area within the vacuum chamber. From this diffusion map it becomes clear that the DA shown in Fig. 3.5 gave a too optimistic picture; the extremely large vertical DA for small horizontal amplitudes is actually cut off starting at around  $y = 10$  mm according to the diffusion map. However, the diffusion map does confirm that essentially the entire area within the vacuum chamber is available DA. To get a better idea of the dynamics within the required aperture a frequency map is given in Fig. 3.7. In the diffusion map, increased tune shifts are observed in a semi-circular band-like structure around the origin starting at  $\Delta x \approx -20$  mm, up to  $\Delta y \approx +8$  mm, and finally back down to  $\Delta x \approx +15$  mm. This is caused by the sextupole coupling resonance  $\nu_x - 2\nu_y = 5$  which can easily be recognized as a band in the frequency map (from  $[0.16, 0.08]$  to  $[0.18, 0.09]$ ). The semi-circular structures that appear for larger vertical amplitudes are caused by the resonance  $\nu_x - 2\nu_y = 67$  which can also be recognized in the frequency map as the line at  $\nu_x = 0.166$  (resonance  $6\nu_x = 67$ ). In summary, we note that there is no elevated diffusion from resonant behavior within the physical aperture.

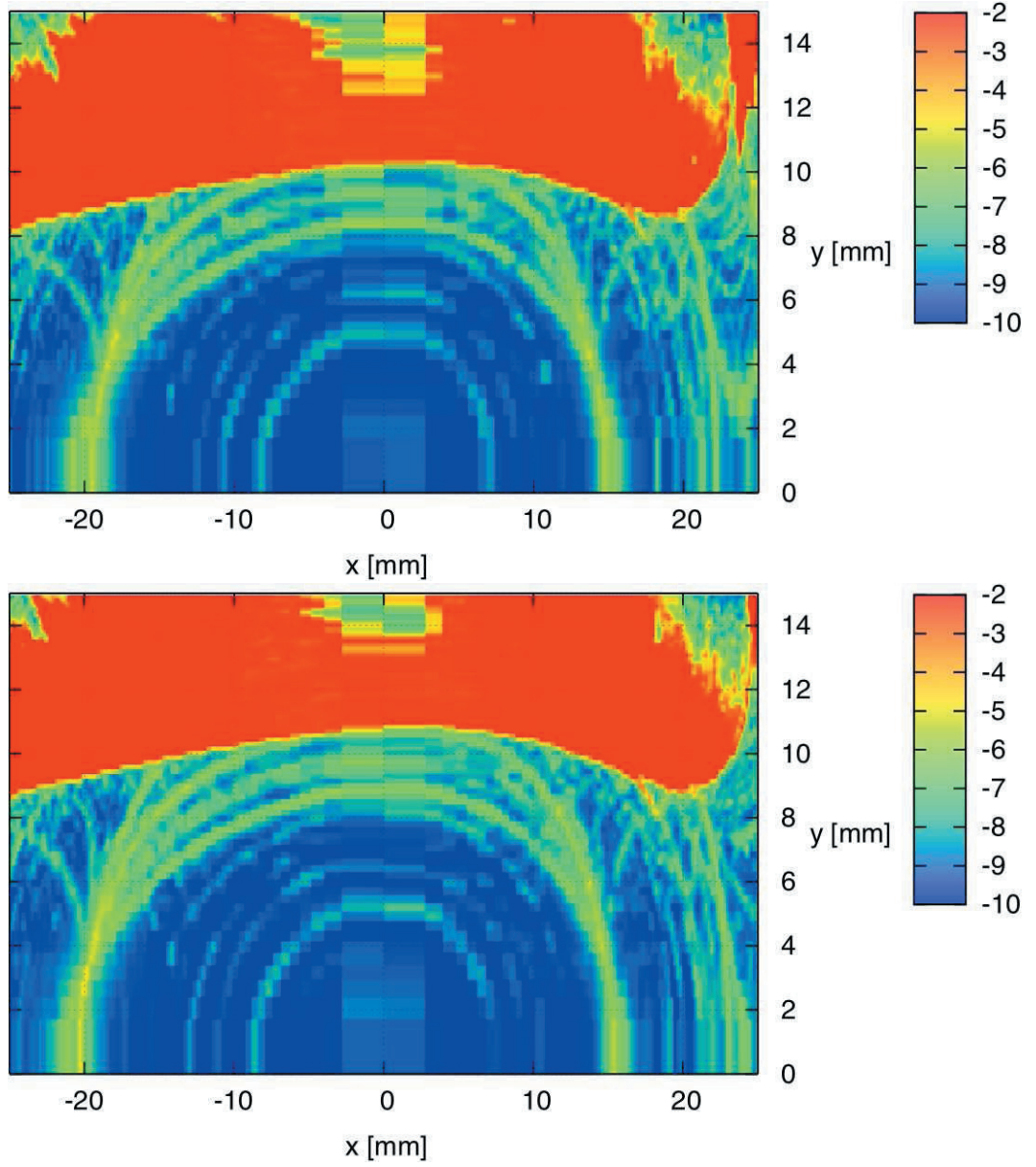


Figure 3.6: Diffusion maps for the MAX IV 1.5 GeV storage ring bare lattice taken at the center of the straight section for on-momentum particles. The top plot corresponds to the basic optics ( $\xi_{x,y} = +2.0$ ), the bottom plot to the alternative optics ( $\xi_{x,y} = +1.0$ ). Blue areas show small tune shifts, red areas show large tune shifts and particle loss. The plot has been generated with Tracy-3 by scanning transverse configuration space on-momentum and tracking for 2048 turns.

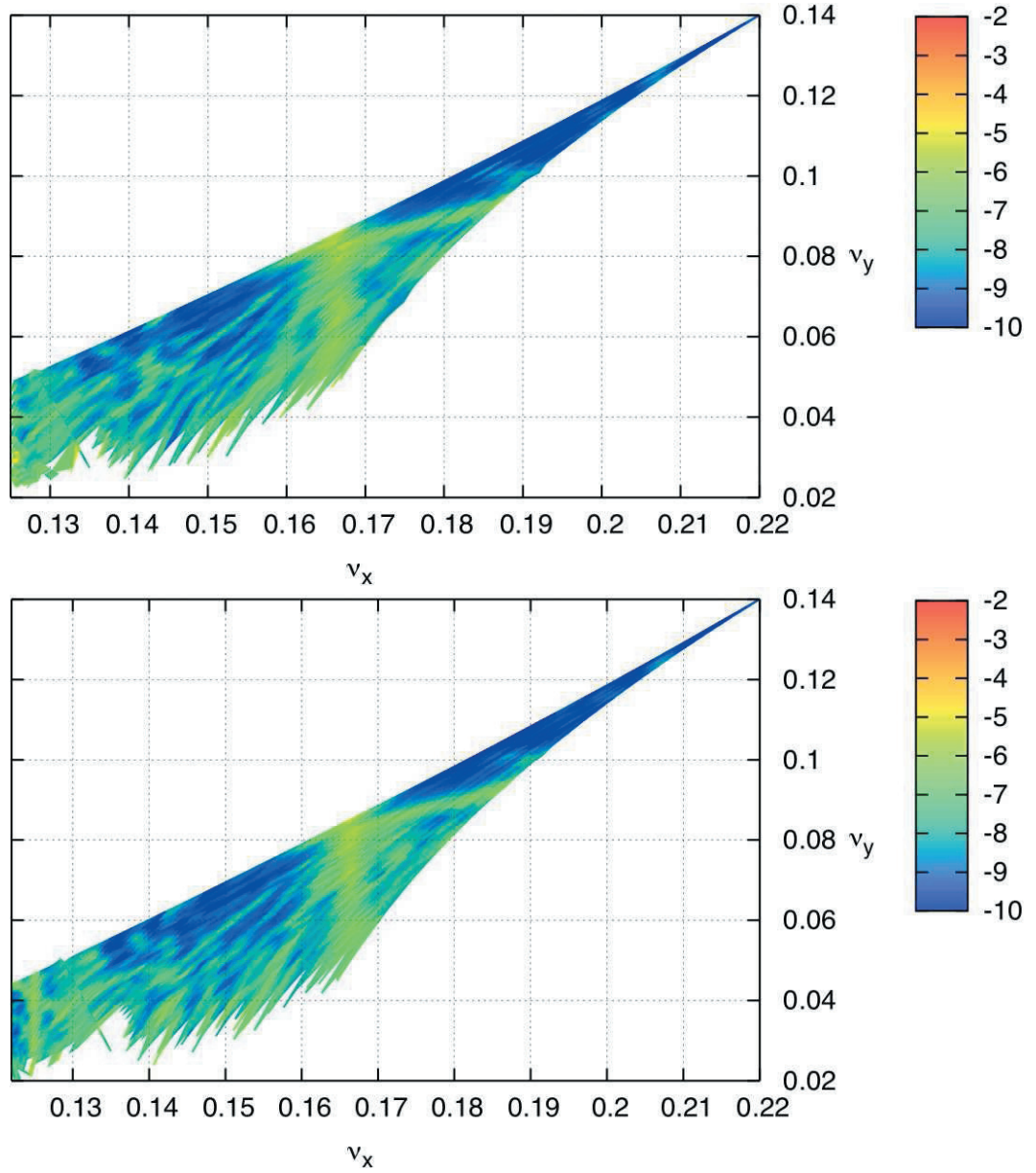


Figure 3.7: Frequency maps for the MAX IV 1.5 GeV storage ring bare lattice taken at the center of the straight section for on-momentum particles. The top plot corresponds to the basic optics ( $\xi_{x,y} = +2.0$ ), the bottom plot to the alternative optics ( $\xi_{x,y} = +1.0$ ). These frequency maps correspond to the diffusion maps shown in Fig. 3.6.

Common to this resonant behavior at the edge of the physical aperture is that it is relatively weak. The chosen working point is away from harmful resonances. Frequency map analysis confirms that because of the small amplitude-dependent tune shift, the tune footprint remains confined in a very limited area. The relatively large distance to potentially harmful lower-order resonances and the small tune footprint justify the choice of this working point for the MAX IV 1.5 GeV storage ring from a nonlinear optics point of view (assuming that once the storage ring includes IDs the behavior will deteriorate, cf. also Section 3.3.5).

### 3.3.4. Energy Acceptance

The ultimate energy acceptance of the MAX IV 1.5 GeV storage ring will be given by several factors. While the energy acceptance defined by the rf bucket (the “rf acceptance”<sup>2</sup>) needs to be sufficient, the ultimate energy acceptance of the storage ring will be determined by the dynamic momentum acceptance (MA) of the lattice. More specifically, what is the maximum energy Touschek scattering event allowed so that both Touschek-scattered electrons can be stored in storage ring until their betatron motion around the dispersive orbit has damped down to betatron motion around the design orbit. In this sense a large lattice MA will ensure a good Touschek lifetime.

As shown in Section 2.3.5, two simple cases for the local lattice MA can be recognized:

- In dispersion-free sections (straights, SQFo)  $\mathcal{H}(s) = 0$ , hence

$$\delta_{\text{acc}} = \pm \min_{\forall s} \left( \frac{a_x(s)}{\eta(s)} \right) \quad (3.3)$$

- At the location of maximum dispersion (SQFi)  $\mathcal{H}(s) = \gamma_0 \eta_{\text{max}}^2 = \eta_{\text{max}}^2 / \beta_0(s)$ , hence

$$\delta_{\text{acc}} = \pm \min_{\forall s} \left( \frac{a_x(s)}{2\eta(s)} \right) \quad (3.4)$$

For the MAX IV 1.5 GeV storage ring this means the lattice MA in the straights is about 6% and about 3% in the achromat center at the location of maximum dispersion. From

---

<sup>2</sup>The rf bucket can also be distorted due to high-order contributions to longitudinal motion. The low nonlinear momentum compaction in MAX IV ( $\alpha_2 \approx 4.8 \times 10^{-3}$  compared to  $\alpha_c \approx 3 \times 10^{-3}$ ) indicates rf buckets in MAX IV should show only little distortion.



these calculations it becomes clear that in order to ensure a lattice MA of no less than 3%, a horizontal vacuum chamber half-aperture of 20 mm is required (at the location of maximum dispersion).

However, containing the dispersive orbits within the physical aperture boundaries does not take into account the dynamics of the Touschek scattering process. One has to consider that an electron, after undergoing Touschek scattering, will oscillate around many dispersive orbits while damping down longitudinally. A synchrotron period in the MAX IV 1.5 GeV storage ring (without Landau cavities) is  $\approx 130\mu\text{s}$  ( $\approx 405$  turns). Longitudinal damping time is on the order of  $\approx 5$  ms ( $\approx 17,000$  turns). Touschek-scattered electrons will cover many dispersive orbits corresponding to their momentary energy while damping down. During this entire longitudinal and transverse damping process, it is therefore required that the Touschek-scattered electrons encounter no harmful resonances (a schematic of this process is given in Fig. 2.12 in Section 2.3.5).

As shown in Fig. 3.3 the chromatic tune shift is minimized around the working point thus strongly reducing the chromatic tune footprint (see Fig. 3.2). However as noted in the previous section, the dynamics are not fully depicted by this simple tune footprint plot. It is rather necessary to again investigate results from FMA for off-energy particles and identify resonances in the frequency maps in order to understand limitations of the lattice MA. Tracy-3 has again been used for this purpose. Scans have been performed where particles were given a certain initial horizontal amplitude (the initial vertical offset was fixed at +1 mm) and momentum offset. After 2048 turns the tunes and diffusion were calculated resulting in diffusion and frequency maps for different energy and amplitude offsets. An example of such a diffusion map for off-momentum particles is given in Fig. 3.8. From this first scan it appears a bare lattice MA of at least  $\pm 8\%$  can be achieved. A more detailed understanding of the limitations can be gained from the corresponding frequency map shown in Fig. 3.9. It is important to keep in mind that the source of most off-momentum particles are Touschek scattering events. Touschek-scattering occurs at the core of the beam where particle density is highest. Consequently, particles with large momentum offset will have a small initial amplitude (therefore the horizontal scale in the magnified view of Fig. 3.9 only extends to 3 mm).



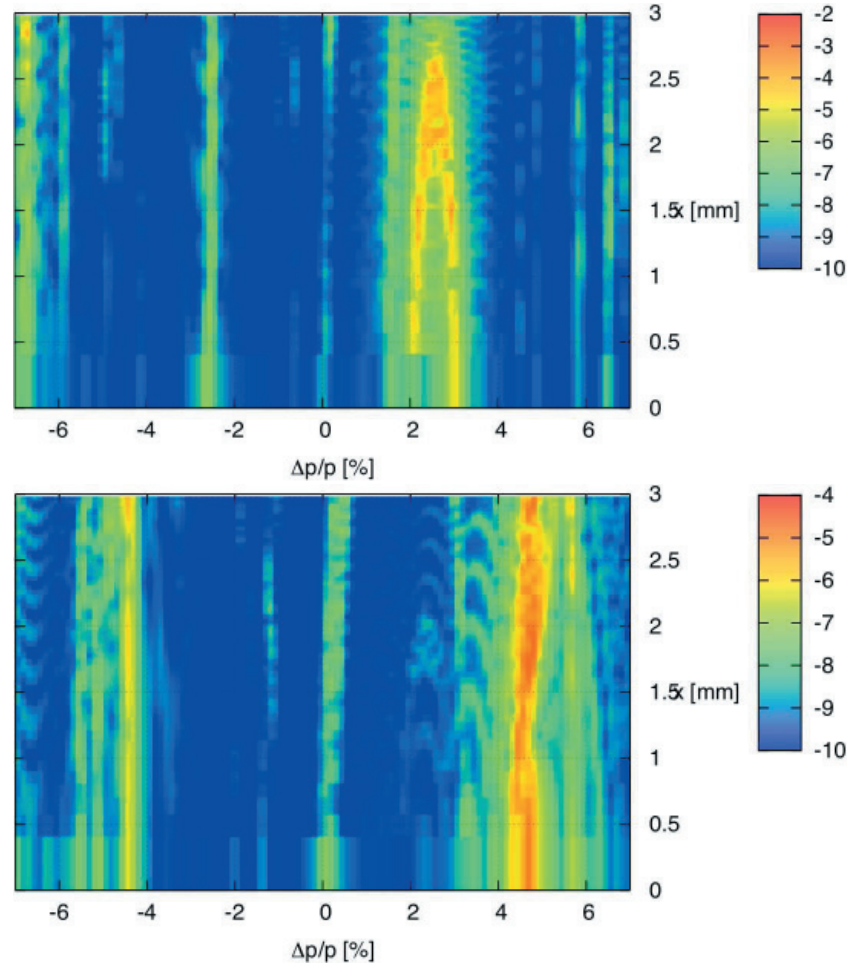


Figure 3.8: Diffusion maps for the MAX IV 1.5 GeV storage ring lattice taken at the center of the straight section for off-momentum particles. The top plot corresponds to the basic optics ( $\xi_{x,y} = +2.0$ ), the bottom plot to the alternative optics ( $\xi_{x,y} = +1.0$ ). Blue areas show small tune shifts, red areas show large tune shifts and particle loss. The plot has been generated with Tracy-3 by scanning the horizontal coordinate and momenta and tracking for 2048 turns. The initial vertical amplitude was +1 mm.

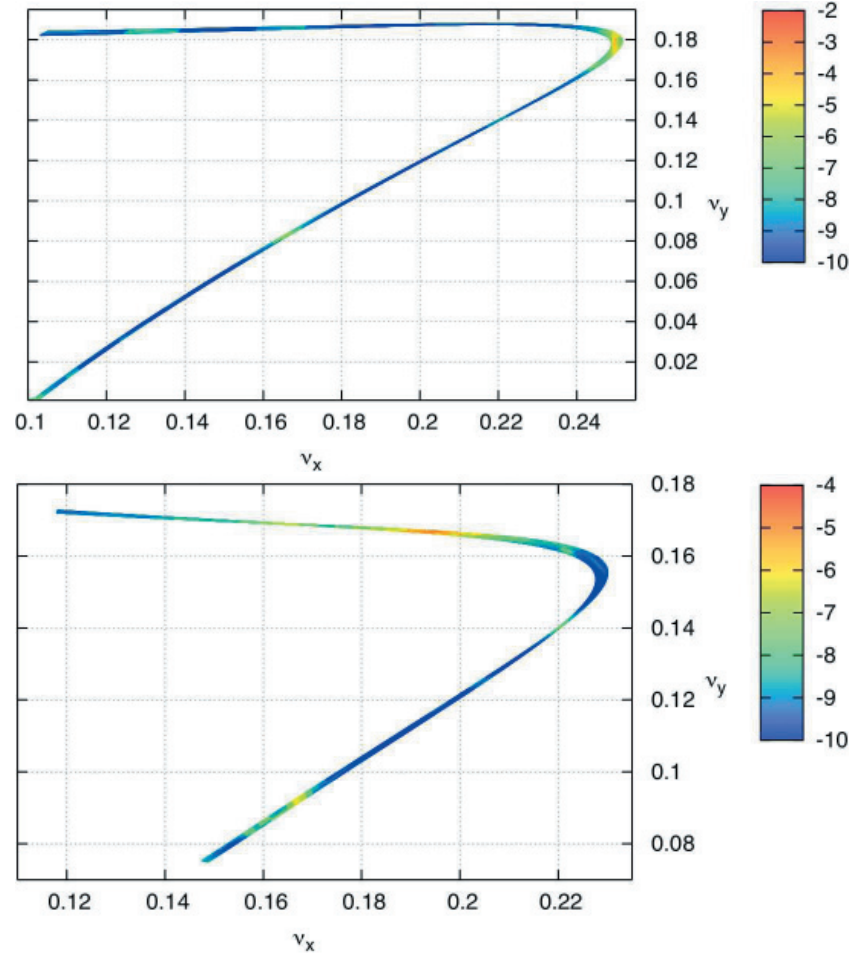


Figure 3.9: Frequency map for the MAX IV 1.5 GeV storage ring lattice taken at the center of the straight section for off-momentum particles. The top plot corresponds to the basic optics ( $\xi_{x,y} = +2.0$ ), the bottom plot to the alternative optics ( $\xi_{x,y} = +1.0$ ). These frequency maps correspond to the diffusion maps shown in Fig. 3.8.

While chromatic tune shifts in the vertical depend on the sign of the momentum deviation (larger vertical tune with positive momentum offset, lower vertical tune with negative momentum offset), the horizontal tune shift is almost only negative regardless of the sign of the momentum deviation. The horizontal fold in the chromatic tune shift around the working point is clearly recognized. It is also easily recognizable that the chromaticity  $\xi_{x,y} = +1.0$  optics reduce the extension of the tune footprint.

In the chromaticity  $\xi_{x,y} = +2.0$  case there is a shift to slightly larger horizontal tunes for positive energy offsets which is more pronounced than in the chromaticity  $\xi_{x,y} = +1.0$  case. In fact, it is pronounced enough to encounter the quarter-integer resonance  $4\nu_x = 45$  which does not occur in the chromaticity  $\xi_{x,y} = +1.0$  case. This resonance is the reason for the increased diffusion seen around  $\delta = +2.5\%$ . On the other hand, in the chromaticity  $\xi_{x,y} = +1.0$  case larger positive momentum offsets lead to tunes close to the area  $6\nu_y = 19$  (well visible in the bottom plot of Fig. 3.9) which causes the increased diffusion around  $\delta = +4.5\%$ .

The resonance  $6\nu_x = 67$  is also crossed for off-energy particles. In the  $\xi_{x,y} = +2.0$  case this happens for  $\delta = +5.8\%$  and  $\delta = -2.6\%$  while in the  $\xi_{x,y} = +1.0$  case the resonance is crossed near  $\delta = +5.6\%$  and  $\delta = -4.4\%$ .

The conclusion that can be drawn from these plots is that for particles within the design lattice MA of  $\pm 3.0\%$  no particle loss can be observed due to resonances if the  $\xi_{x,y} = +1.0$  optics is chosen. For the  $\xi_{x,y} = +2.0$  optics there is some elevated diffusion caused within the required MA by the quarter-integer resonance  $4\nu_x = 45$ .

Finally, we note that knowledge of local lattice MA around the entire machine is required to make accurate estimates of Touschek lifetime. Results of this “Touschek tracking” are given in Section 3.10. In rigorous measurement, modeling, and optimization campaigns, modern light sources have shown that by correct modeling (6D Touschek tracking including magnet and misalignment errors, actual apertures, nonlinear betatron coupling, etc.), restoring of the design linear optics, and symmetrization of the nonlinear optics correction, good agreement can be achieved between predicted MA and measured lifetime [4, 5, 6, 7, 8, 9, 10].

### 3.3.5. Effects of Insertion Devices

Similar to the disturbances to the linear lattice as described in Section 3.2.6, strong IDs like the SCW for the *Kraków option* can perturb the nonlinear storage ring optics. Two simple aspects can be considered to demonstrate this.

- Firstly, aside from the additional vertical focusing of a strong ID, there is an amplitude-dependent effect: away from the mid-plane where the undulator or wiggler field is sinusoidal, the electron experiences a step-like focusing force.
- Secondly, the over-focusing of the ID is quadratic rather than linear in energy because the entrance angle of the particle in the undulator or wiggler period and the bending angle both scale inversely with energy.

Therefore, it's important to investigate the nonlinear behavior of the MAX IV 1.5 GeV storage ring lattice with one SCW installed. Obviously this should happen in addition to ensuring that the linear optics have been properly matched to the ID. For this purpose it was decided to add the 3 T SCW to the MAX IV 1.5 GeV storage ring lattice in order to assess changes of DA and MA. The parameters of the device have been given in Table 3.3 in Section 3.2.6.

In OPA this device is modeled by using the built-in undulator model. In Tracy-3 the device has been modeled using the built-in wiggler model. A kick map could be used, but because of the high level of agreement noted for strong damping wigglers in the 3 GeV storage ring (cf. Section 2.3.6), only the simpler wiggler model is used in Tracy-3.

OPA and Tracy-3 results showed excellent agreement using the built-in models. The sextupole settings were optimized with OPA for the bare lattice. These settings were then transferred to Tracy-3 and applied to the lattice for wiggler model and wiggler kick map studies. The plots in Figs. 3.10 and 3.11 show the influence of the SCW on the storage ring optics if the sextupoles are left unchanged. The chromatic tune shifts are very similar to the bare lattice case (cf. Fig. 3.3), apart from the fact that the working point has drifted mainly in the vertical ( $\Delta\nu_y = 0.16$ ). The ADTS is almost identical to the ADTS for the bare lattice, again apart from the absolute shift of working point.

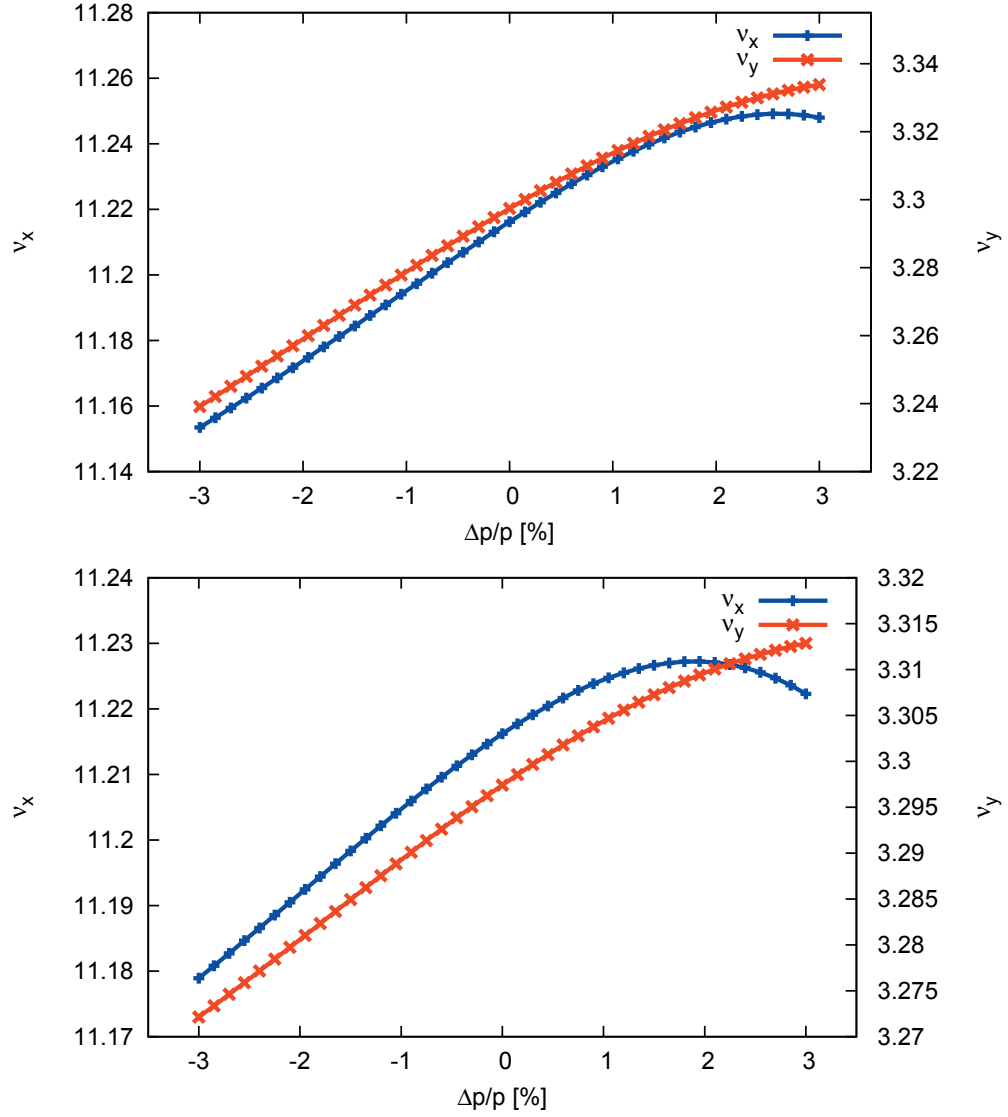


Figure 3.10: Chromatic tune shift for the MAX IV 1.5 GeV storage ring as calculated by Tracy-3. The chromaticity is compared for the bare lattice and the lattice containing a SCW. The sextupole settings are equal in both cases. The top plot corresponds to the basic optics ( $\xi_{x,y} = +2.0$ ), the bottom plot to the alternative optics ( $\xi_{x,y} = +1.0$ ).

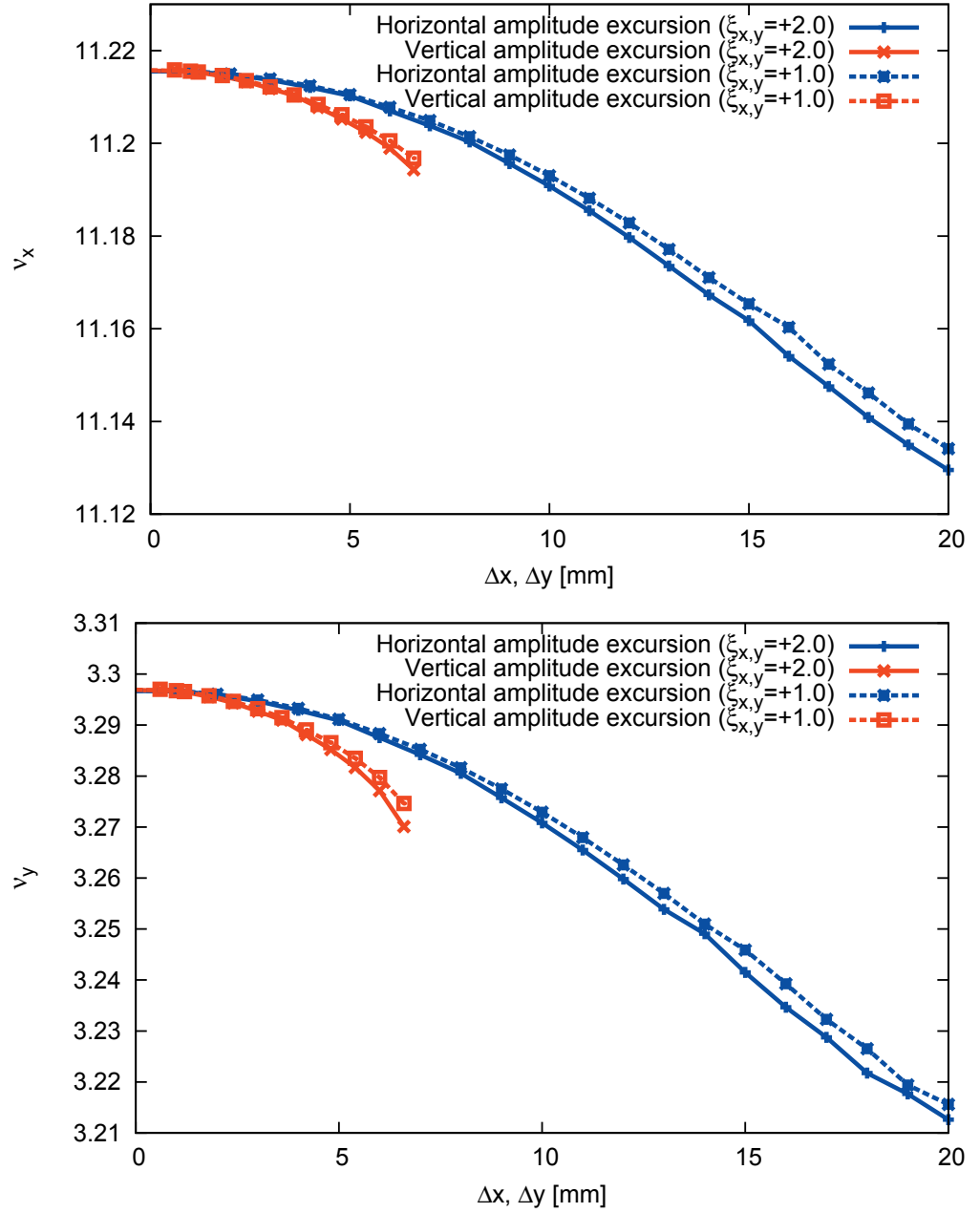


Figure 3.11: Plots showing the amplitude-dependent tune shift for the MAX IV 1.5 GeV storage ring as calculated by Tracy-3. The tune shifts are compared for the bare lattice and the lattice containing a SCW. The sextupole settings are equal in both cases. The top plot corresponds to the basic optics ( $\xi_{x,y} = +2.0$ ), the bottom plot to the alternative optics ( $\xi_{x,y} = +1.0$ ).

This results in the tune footprint shown in Fig. 3.12. After investigating the tune shifts above, it comes as no surprise that the tune footprints are basically shifted versions of the bare lattice footprints (cf. Fig. 3.2). Whereas the bare lattice footprints were wedged in below the linear coupling resonance and above a sextupole coupling resonance, they are now just above the linear coupling resonance and below a skew coupling resonance. Especially in the case of the alternative optics ( $\xi_{x,y} = +1.0$ ) this is very convenient as it appears the tune footprint can be contained within a small and unperturbed area without further adjustments. In the basic optics case ( $\xi_{x,y} = +2.0$ ) the third-integer resonance  $3\nu_y = 10$  is however approached which will most likely limit acceptance at positive momentum offsets. In addition, in the basic optics case the quarter-integer resonances  $4\nu_x = 45$  and  $4\nu_y = 13$  are both approached which needs also to be investigated with FMA.

Diffusion maps and frequency maps for the lattice with one SCW are displayed in Figs. 3.13 and 3.14 as well as Figs. 3.15 and 3.16 for off-momentum particles. Compared to the bare lattice (cf. Fig. 3.6) the main difference observed is the more limited area available in configuration space. The area of low diffusion is now limited to roughly  $\pm 12$  mm in the horizontal and  $\pm 7$  mm in the vertical. However, although this is clearly more limited than in the bare lattice case, it is still more than enough to fulfill the DA requirements. Within that requirement we note that there is an area of somewhat elevated diffusion seen in both optics cases as a circular band around the center starting at  $\Delta x = -6$  mm, proceeding to  $\Delta y = 4$  mm, and ending at  $\Delta x = +5$  mm. This is caused by crossing the resonance  $2\nu_x + 2\nu_y = 29$  which can be seen well in the frequency map ([0.21,0.29] in Fig. 3.14). The next concentric band is located at the edge of the DA requirement and is narrower than the first band. This band comes from the crossing of the resonance  $5\nu_x = 56$  which can also be recognized in the frequency map around [0.20,0.28].

The off-momentum FMA does not reveal any surprises. The basic optics case ( $\xi_{x,y} = +2.0$ ) shows limited MA because it approaches the third-integer resonance  $3\nu_y = 10$  for momentum deviations  $+2\% \leq \delta \leq +2.75\%$  and  $+4.6\% \leq \delta \leq +6\%$ . There is also elevated diffusion at  $\delta = -2.5\%$  caused by the resonance  $6\nu_x = 67$ . For the alternative optics ( $\xi_{x,y} = +1.0$ ) the only substantially elevated diffusion that can be seen is around  $\delta \leq 6\%$  which is caused by the quarter-integer resonance  $4\nu_y = 13$ . The resonance  $6\nu_x = 67$  does however also cause some increased tune diffusion for  $\delta = -4\%$  and  $\delta = +5.6\%$ .

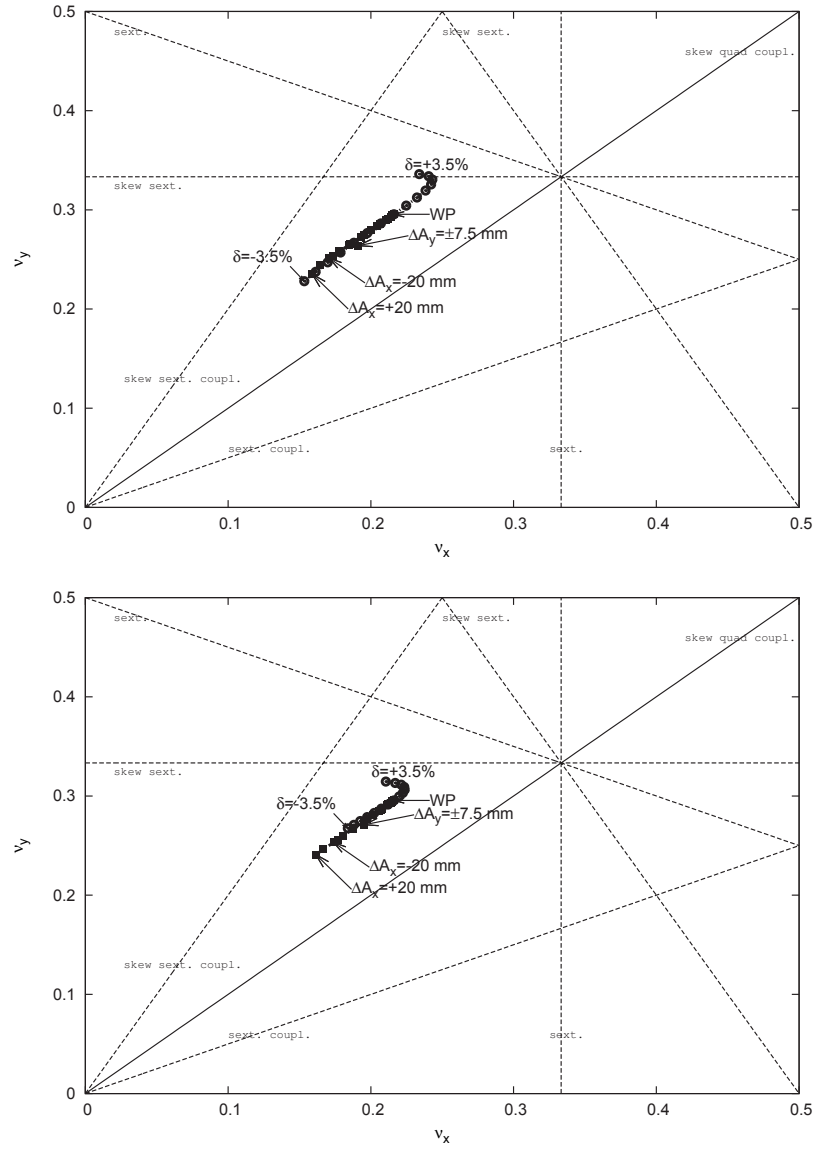


Figure 3.12: A plot of fractional tune space for the MAX IV 1.5 GeV storage ring with a SCW as calculated by OPA. The top plot shows the footprint for the basic optics ( $\xi_{x,y} = +2.0$ ); the lower plot shows the footprint for alternative optics with chromaticity adjusted to  $\xi_{x,y} = +1.0$ . The sextupole settings are the same as those calculated for the bare lattice (cf. Fig. 3.2).



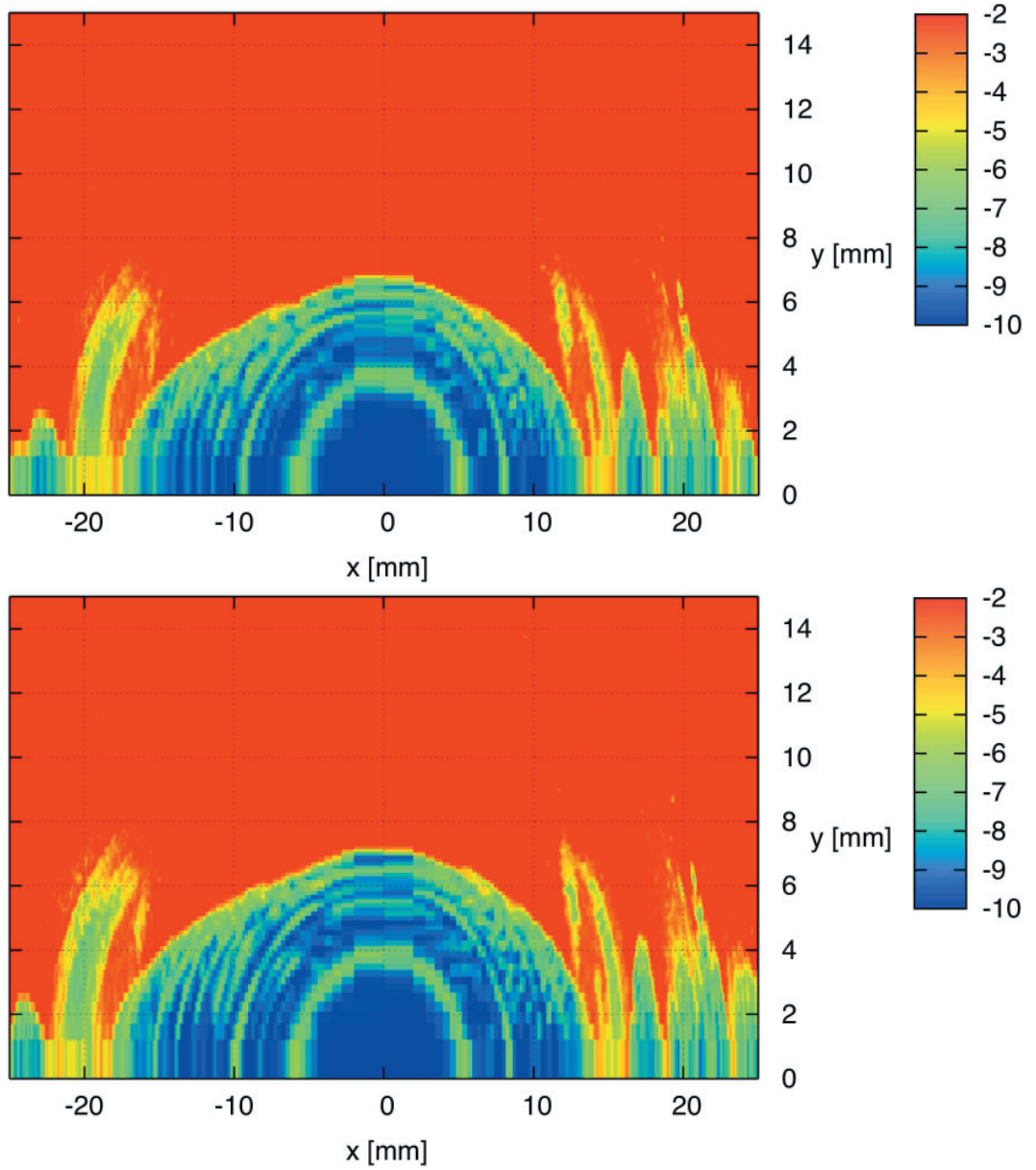


Figure 3.13: Diffusion maps for the MAX IV 1.5 GeV storage ring bare lattice with a SCW taken at the center of the straight section for on-momentum particles. The top plot corresponds to the basic optics ( $\xi_{x,y} = +2.0$ ), the bottom plot to the alternative optics ( $\xi_{x,y} = +1.0$ ). Blue areas show small tune shifts, red areas show large tune shifts and particle loss. The plot has been generated with Tracy-3 by scanning transverse configuration space on-momentum and tracking for 2048 turns.

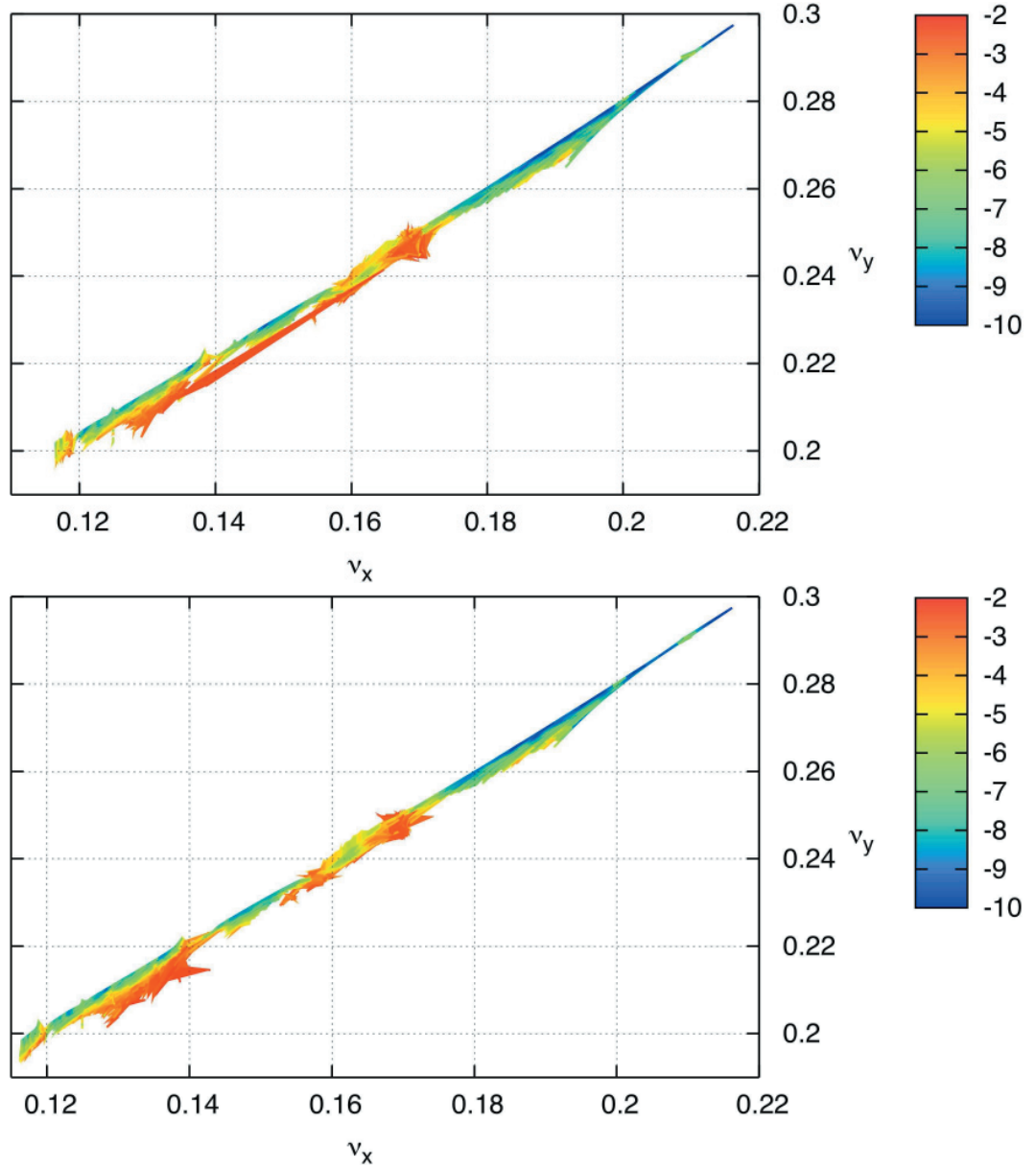


Figure 3.14: Frequency maps for the MAX IV 1.5 GeV storage ring bare lattice with a SCW taken at the center of the straight section for on-momentum particles. The top plot corresponds to the basic optics ( $\xi_{x,y} = +2.0$ ), the bottom plot to the alternative optics ( $\xi_{x,y} = +1.0$ ). These frequency maps correspond to the diffusion maps shown in Fig. 3.6.

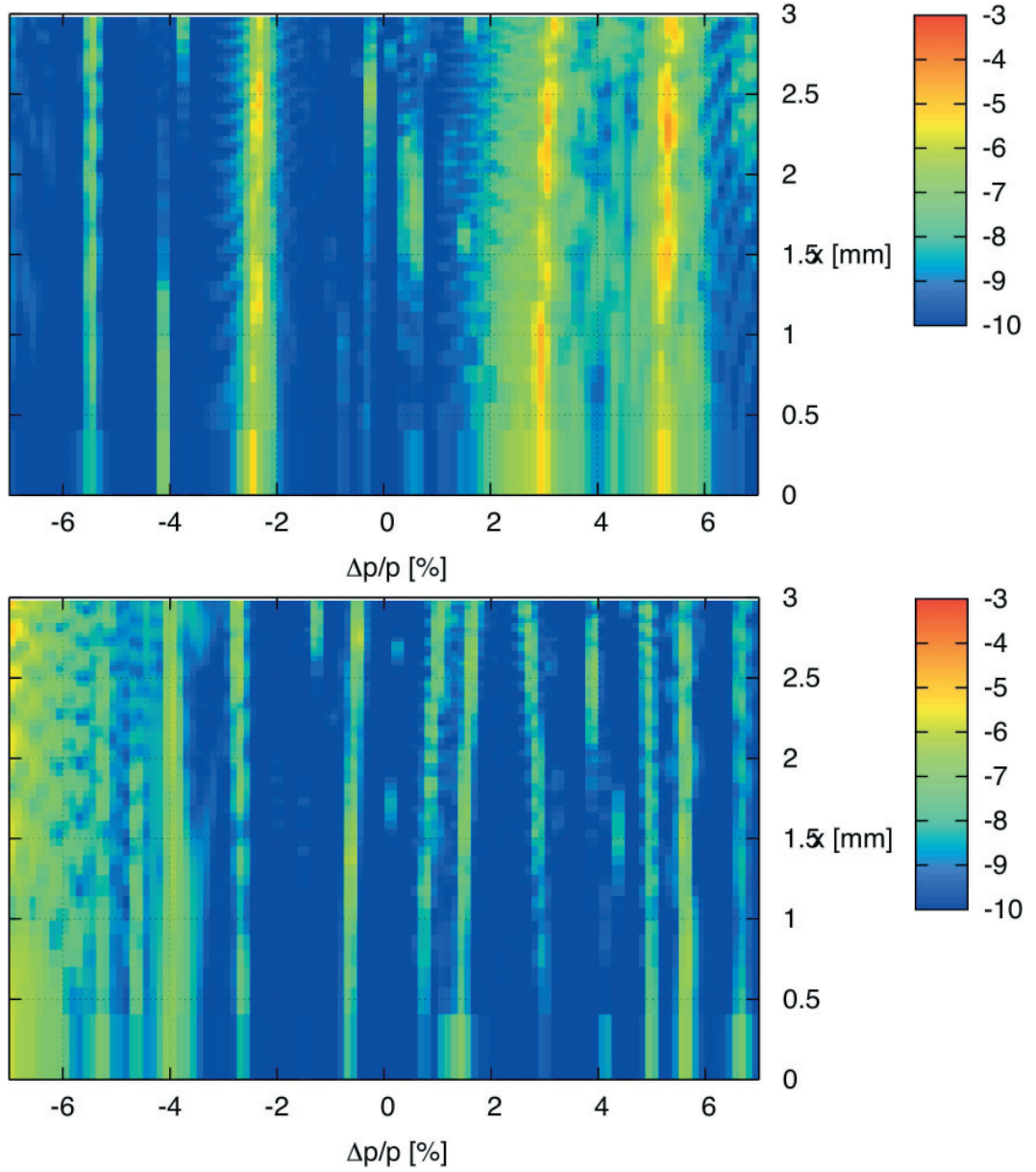


Figure 3.15: Diffusion maps for the MAX IV 1.5 GeV storage ring lattice with a SCW taken at the center of the straight section for off-momentum particles. The top plot corresponds to the basic optics ( $\xi_{x,y} = +2.0$ ), the bottom plot to the alternative optics ( $\xi_{x,y} = +1.0$ ). Blue areas show small tune shifts, red areas show large tune shifts and particle loss. The plot has been generated with Tracy-3 by scanning the horizontal coordinate and momenta and tracking for 2048 turns. The initial vertical amplitude was +1 mm.

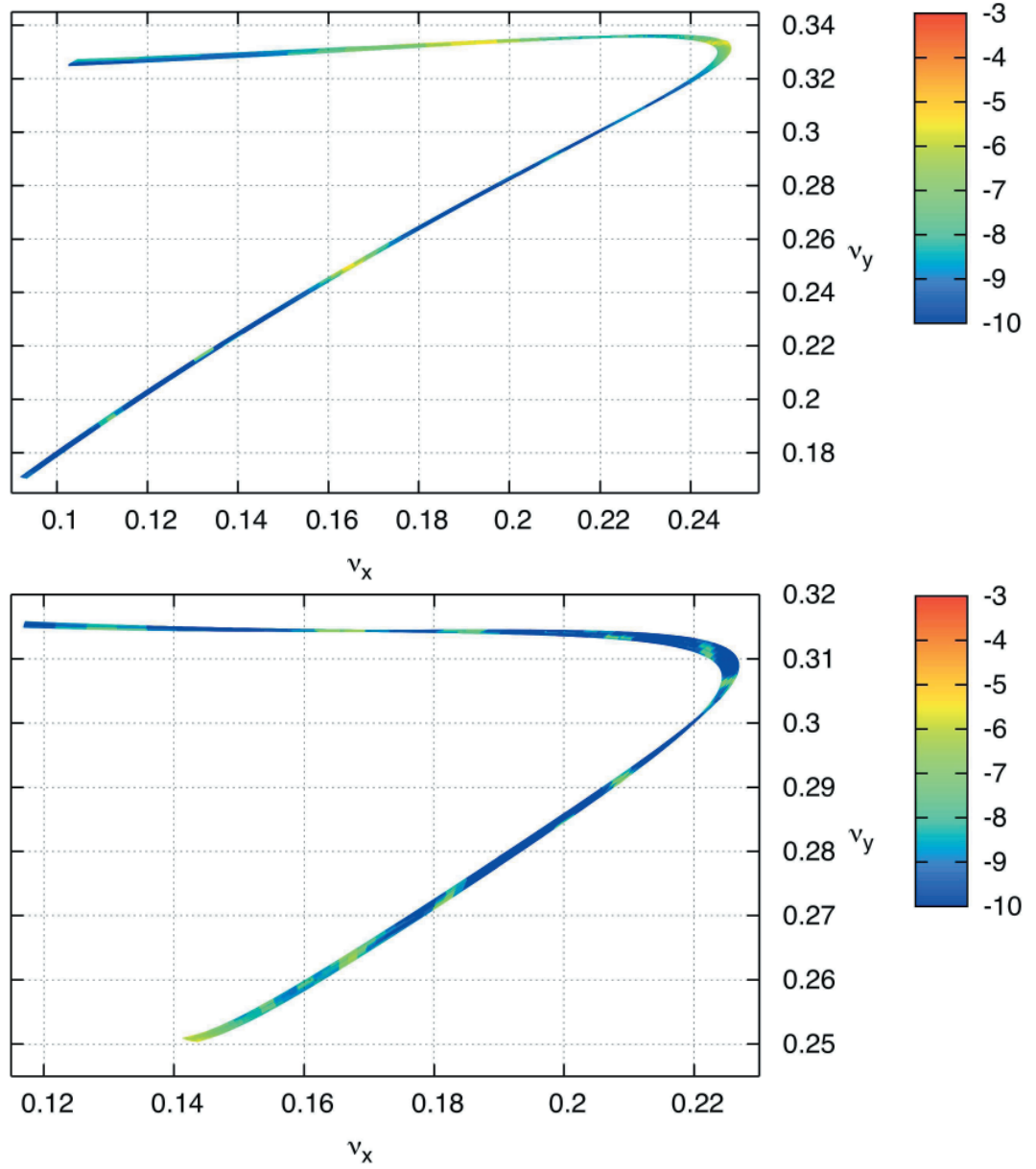


Figure 3.16: Frequency map for the MAX IV 1.5 GeV storage ring lattice with a SCW taken at the center of the straight section for off-momentum particles. The top plot corresponds to the basic optics ( $\xi_{x,y} = +2.0$ ), the bottom plot to the alternative optics ( $\xi_{x,y} = +1.0$ ). These frequency maps correspond to the diffusion maps shown in Fig. 3.8.

Finally, the DA is shown in Fig. 3.17. As already indicated by FMA, the DA requirement is met. However, not a lot of margin is left (especially off-momentum) and it is possible that once errors are included into the lattice (cf. Section 3.4), the DA falls short of the requirements. We shall therefore investigate additional optics adjustments aimed at correcting the nonlinear lattice for the case of a lattice with SCW.

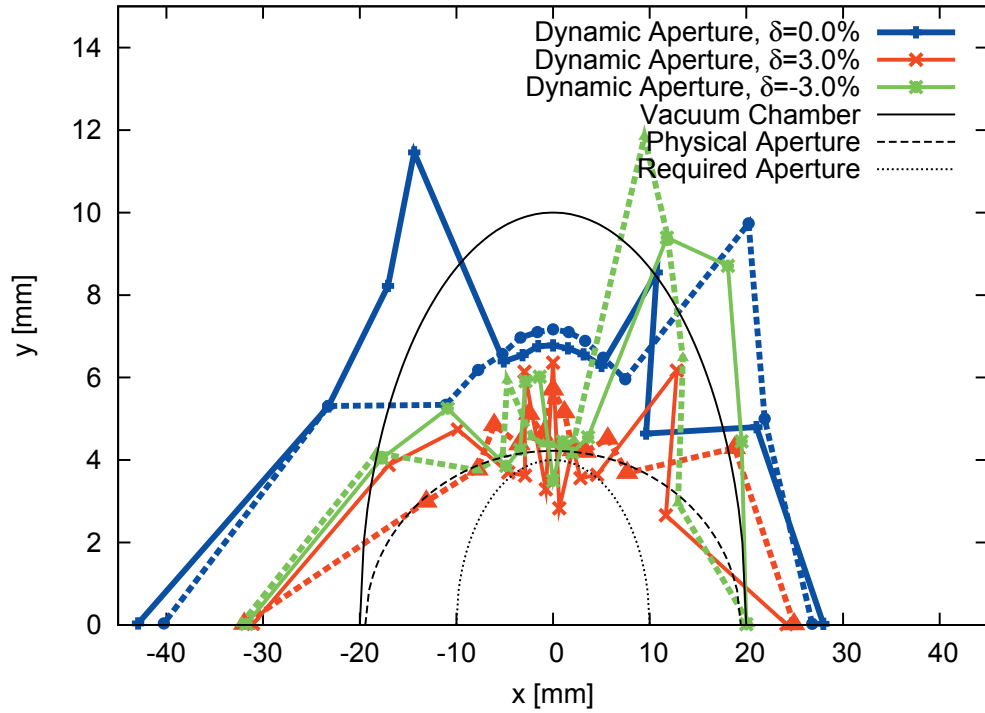


Figure 3.17: Dynamic aperture at the center of the long straight section in the MAX IV 1.5 GeV storage ring with a SCW. Solid lines correspond to the basic optics ( $\xi_{x,y} = +2.0$ ), dashed lines to the alternative optics ( $\xi_{x,y} = +1.0$ ). Tracking was performed with Tracy-3 in 6D for one synchrotron period. Physical aperture and required aperture are also indicated in the plot.

It is important to recall here, that for all the results presented above, the working point had not been restored to the design value when the optics were matched to the SCW. The optics were only matched locally to the SCW to avoid beta-beating, but an overall residual phase advance remained (cf. Section 3.2.6). Hence, the chromaticity did not return to the properly corrected design value either. In the following we shall investigate two cases where, for the lattice with a SCW, the chromaticities have been corrected

to their actual target values of  $\xi_{x,y} = +2.0$  and  $+1.0$  respectively, using the correction sextupoles available in the lattice. Note that in order to keep these optics modifications simple (and because the tune footprints already indicated that the shift of working point does not push the tunes into potentially dangerous areas), we keep the working point shifted. In this way we do not require global gradient corrections to accommodate the SCW; the only required gradient change is local and can be performed with dedicated hardware (cf. Section 3.2.6). Table 3.2 shows the required sextupole setting changes to achieve chromaticity  $\xi_{x,y} = +2.0$  and  $+1.0$  respectively for the lattice with one SCW installed.

Table 3.2: A comparison of sextupole optimizations performed with OPA for the bare lattice and a lattice with one SCW installed. Note that the working point is allowed to drift with the SCW installed.

Sextupole gradient adjustments for one SCW	Basic optics	Alternative optics
SDi:	+1.4%	+1.5%
SDo:	−4.0%	−4.1%
SCi:	+4.1 m <sup>−3</sup>	−20.6%
SCo:	+2.1 m <sup>−3</sup>	−8.8%
Resulting linear chromaticity		
Bare lattice, basic optics	$\xi_x = 2.00,$	$\xi_y = 2.00$
Lattice with SCW, unchanged basic optics	$\xi_x = 1.79,$	$\xi_y = 1.81$
Lattice with SCW, readjusted basic optics	$\xi_x = 2.00,$	$\xi_y = 2.00$
Bare lattice, alternative optics	$\xi_x = 1.00,$	$\xi_y = 1.00$
Lattice with SCW, unchanged alternative optics	$\xi_x = 0.79,$	$\xi_y = 0.81$
Lattice with SCW, readjusted alternative optics	$\xi_x = 1.00,$	$\xi_y = 1.00$

The tune footprints for the two lattices with a SCW and adjusted sextupole gradients are displayed in Fig. 3.18. In comparison with the unadjusted cases (cf. Fig. 3.12) it appears the ADTS has grown while the chromatic footprint could not be further reduced.

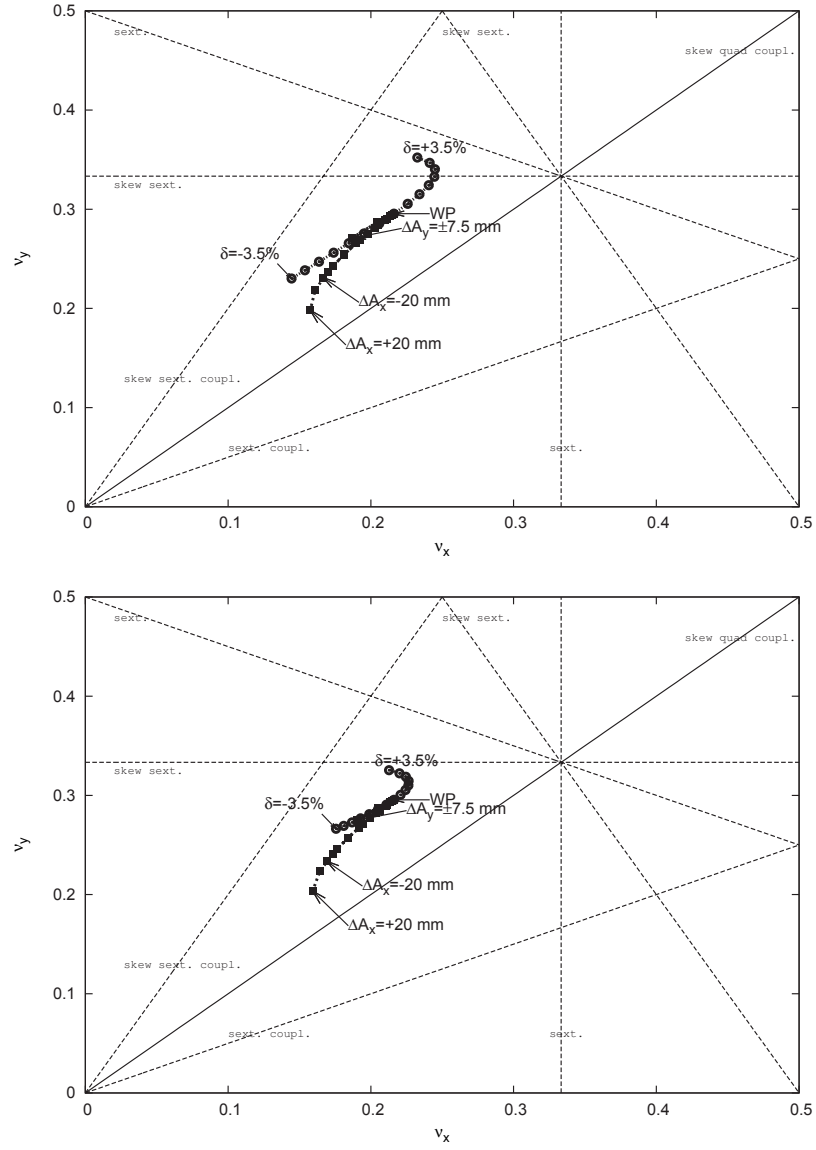


Figure 3.18: A plot of fractional tune space for the MAX IV 1.5 GeV storage ring with a SCW and adjusted sextupole gradients as calculated by OPA. The top plot shows the footprint for the basic optics ( $\xi_{x,y} = +2.0$ ); the lower plot shows the footprint for alternative optics with chromaticity adjusted to  $\xi_{x,y} = +1.0$ .



To further investigate the differences between adjusted and non-adjusted nonlinear optics, we turn to FMA. On-momentum frequency and diffusion maps for the two cases are displayed in Figs. 3.19 and 3.20. For both cases the diffusion maps for the adjusted nonlinear optics appear horizontally a bit more compressed than they were for the unadjusted nonlinear optics (cf. Fig. 3.13). This was to be expected because of the somewhat larger ADTS resulting from the nonlinear adjustment (cf. Figs. 3.12 and 3.18). However, within the required DA the differences are negligible. The two concentric bands caused by crossing the resonance  $2\nu_x + 2\nu_y = 29$  and  $5\nu_x = 56$ , respectively can again be recognized. In the frequency map (cf. Fig. 3.20) both can be recognized at  $[0.21, 0.29]$  and  $[0.20, 0.28]$ , respectively.

Figures 3.21 and 3.22 show the off-momentum maps. For the basic optics ( $\xi_{x,y} = +2.0$ ) case no significant improvement can be seen. The large bands that were located at  $+2\% \leq \delta \leq +6\%$  have been reduced because the adjusted nonlinear optics now let the tune shift cross the third-integer resonance  $3\nu_y = 10$  rather than remain on it. This crossing happens at  $\delta \approx +2\%$  which means the MA is still limited as in the case where the nonlinear optics had not been adjusted to the SCW. In the alternative optics ( $\xi_{x,y} = +1.0$ ) case the area within the required MA is mostly unchanged. With the adjusted nonlinear optics we note that there is slightly more diffusion around  $\delta = +0.9\%$  which is caused by the resonance  $\nu_x - 4\nu_y = -2$  and can be recognized in the frequency map around  $[0.222, 0.306]$ .



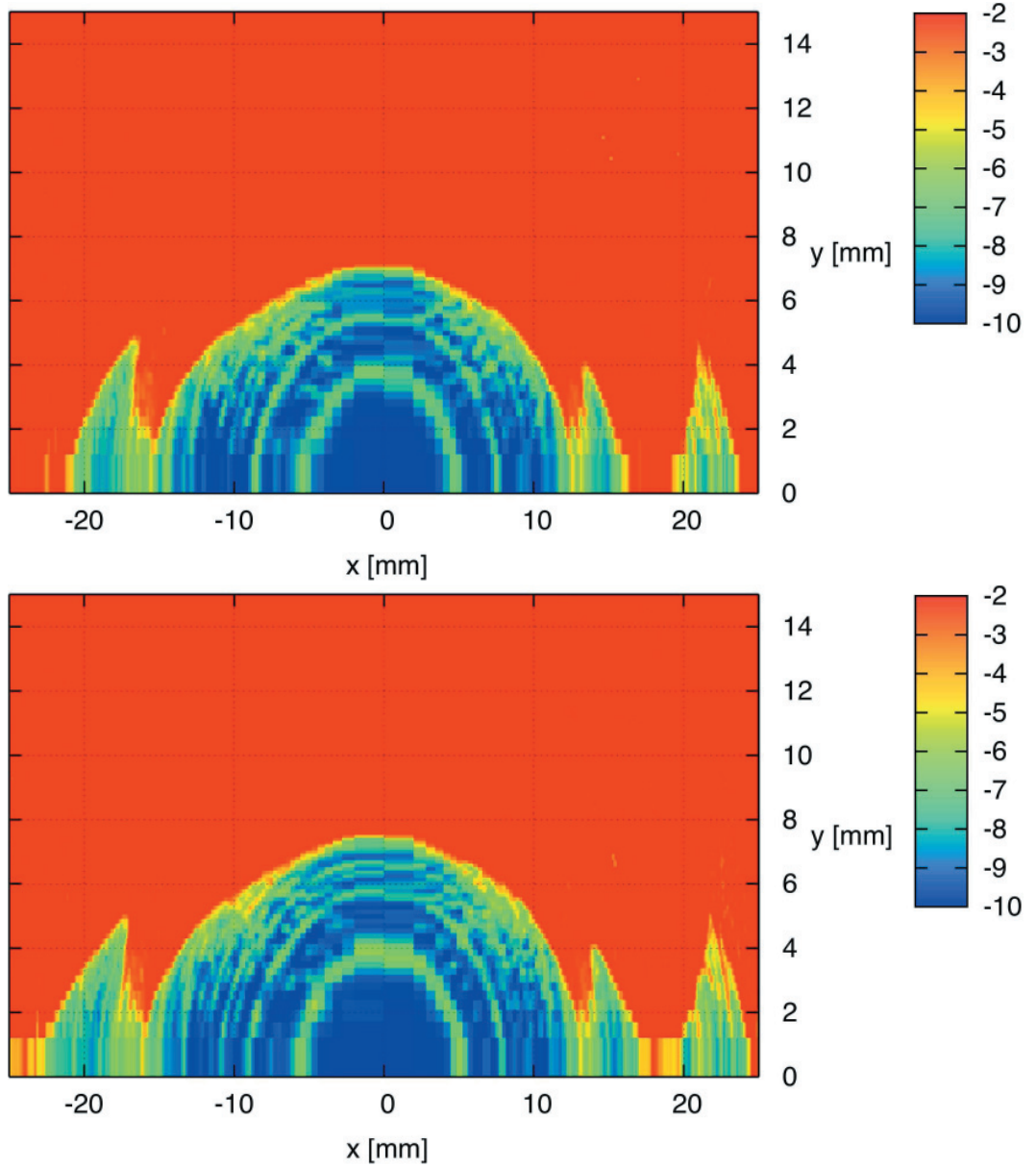


Figure 3.19: Diffusion maps for the MAX IV 1.5 GeV storage ring bare lattice with a SCW taken at the center of the straight section for on-momentum particles and adjusted sextupole gradients. The top plot corresponds to the basic optics ( $\xi_{x,y} = +2.0$ ), the bottom plot to the alternative optics ( $\xi_{x,y} = +1.0$ ). Blue areas show small tune shifts, red areas show large tune shifts and particle loss. The plot has been generated with Tracy-3 by scanning transverse configuration space on-momentum and tracking for 2048 turns.

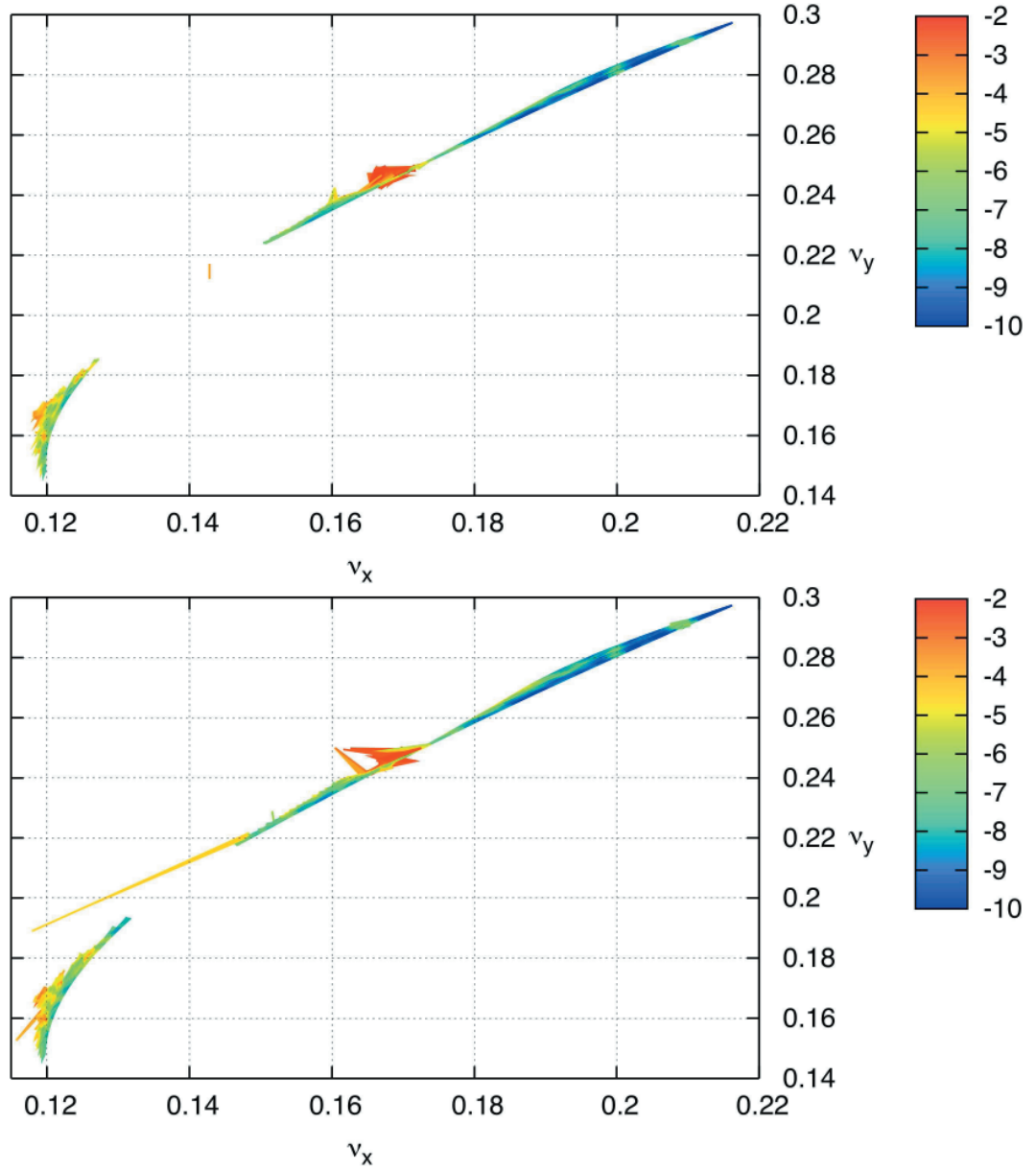


Figure 3.20: Frequency maps for the MAX IV 1.5 GeV storage ring bare lattice with a SCW taken at the center of the straight section for on-momentum particles and adjusted sextupole gradients. The top plot corresponds to the basic optics ( $\xi_{x,y} = +2.0$ ), the bottom plot to the alternative optics ( $\xi_{x,y} = +1.0$ ). These frequency maps correspond to the diffusion maps shown in Fig. 3.6.

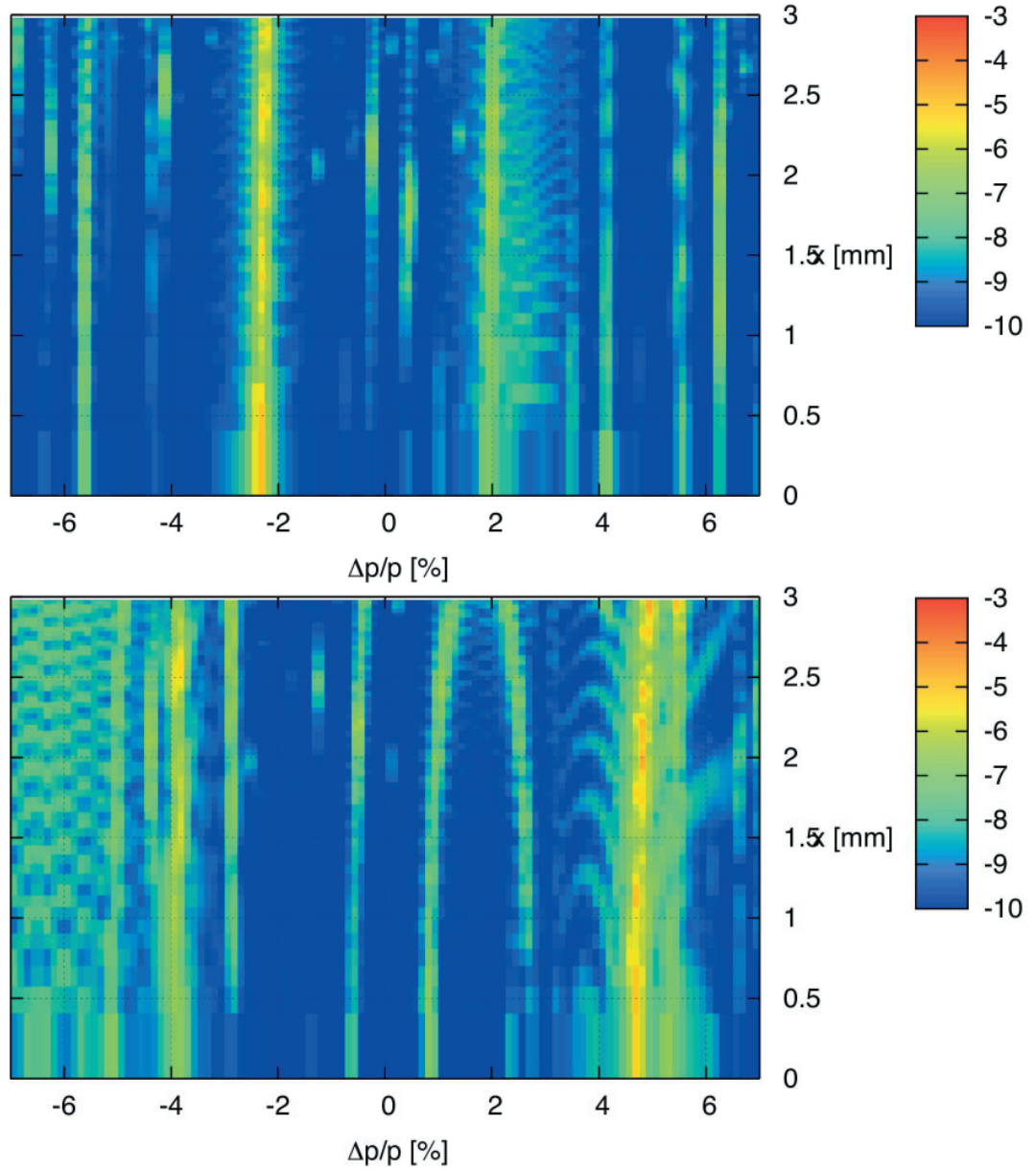


Figure 3.21: Diffusion maps for the MAX IV 1.5 GeV storage ring lattice with a SCW and adjusted sextupole gradients taken at the center of the straight section for off-momentum particles. The top plot corresponds to the basic optics ( $\xi_{x,y} = +2.0$ ), the bottom plot to the alternative optics ( $\xi_{x,y} = +1.0$ ). Blue areas show small tune shifts, red areas show large tune shifts and particle loss. The plot has been generated with Tracy-3 by scanning the horizontal coordinate and momenta and tracking for 2048 turns. The initial vertical amplitude was +1 mm.

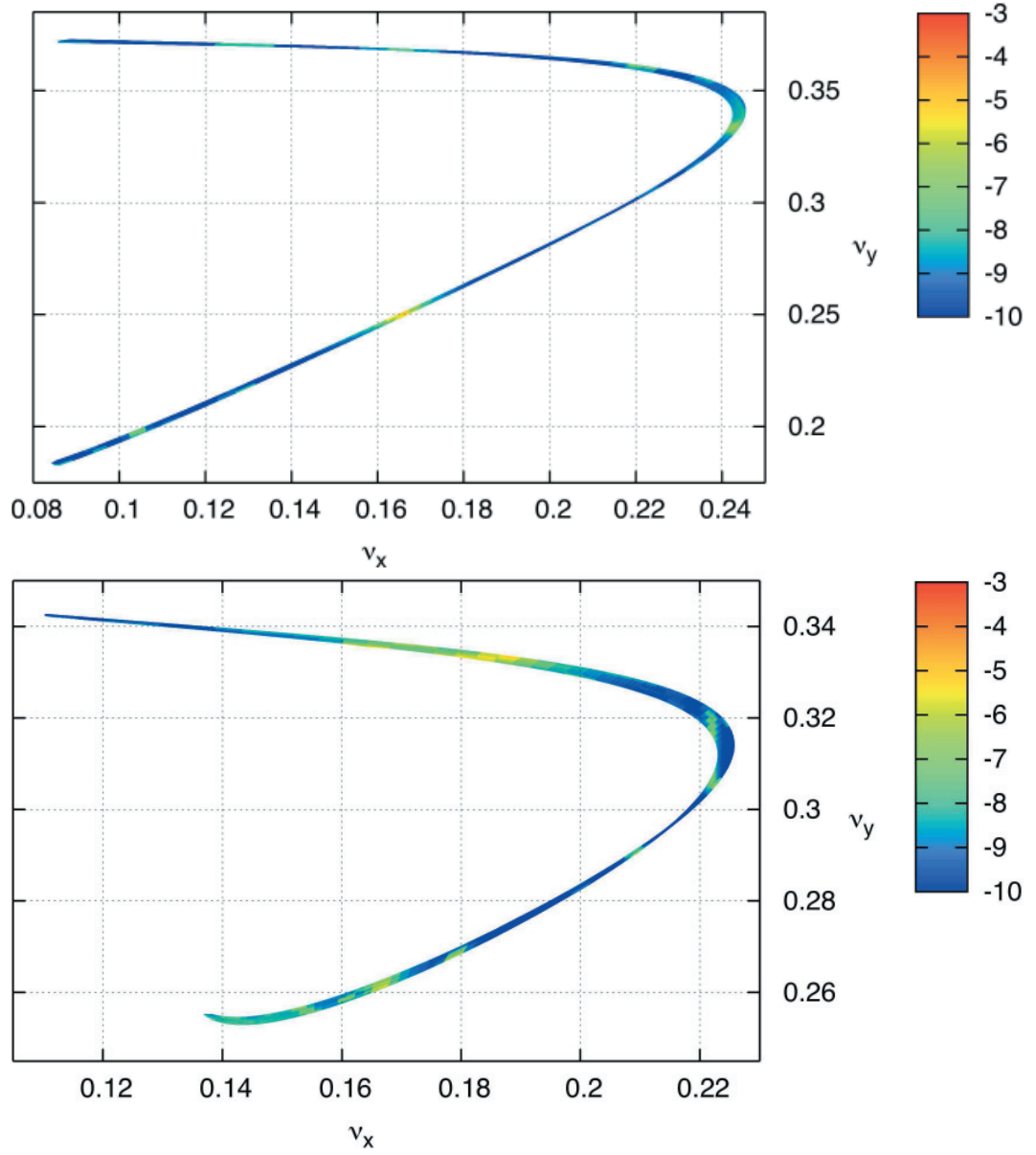


Figure 3.22: Frequency map for the MAX IV 1.5 GeV storage ring lattice with a SCW and adjusted sextupole gradients taken at the center of the straight section for off-momentum particles. The top plot corresponds to the basic optics ( $\xi_{x,y} = +2.0$ ), the bottom plot to the alternative optics ( $\xi_{x,y} = +1.0$ ). These frequency maps correspond to the diffusion maps shown in Fig. 3.8.

Finally, we compare the DA for the adjusted nonlinear optics shown in Fig. 3.23 with the DA of the unadjusted optics (cf. Fig. 3.17). It appears the readjustment has not increased DA significantly. It is still sufficient to fulfill the DA requirements, but there is not much margin left. This is in agreement with the comparison based on FMA.

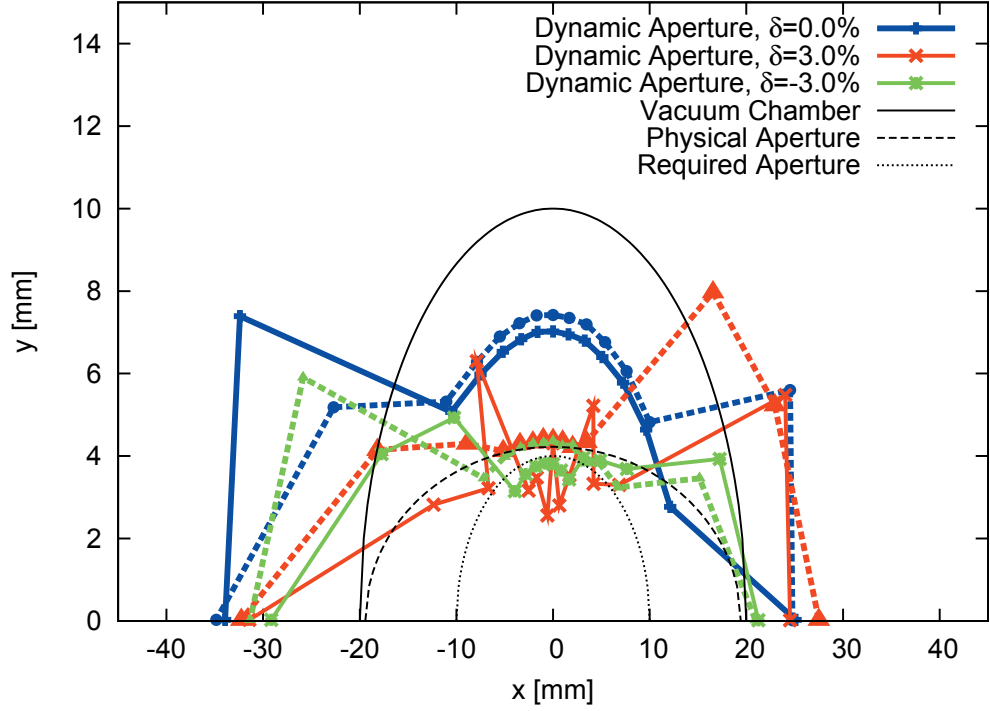


Figure 3.23: Dynamic aperture at the center of the long straight section in the MAX IV 1.5 GeV storage ring with a SCW and adjusted sextupole gradients. Solid lines correspond to the basic optics ( $\xi_{x,y} = +2.0$ ), dashed lines to the alternative optics ( $\xi_{x,y} = +1.0$ ). Tracking was performed with Tracy-3 in 6D for one synchrotron period. Physical aperture and required aperture are also indicated in the plot.

From the comparison of the lattice with nonlinear readjustment for the SCW and the lattice without readjustment, it is debatable if the extra effort is actually warranted. It does not appear that DA or MA is significantly improved with the readjusted sextupole settings. The only possible improvement could be a somewhat better MA in the basic optics ( $\xi_{x,y} = +2.0$ ) case since the tune shift does not lead to a working point stuck around the third-integer resonance  $3\nu_y = 10$ .

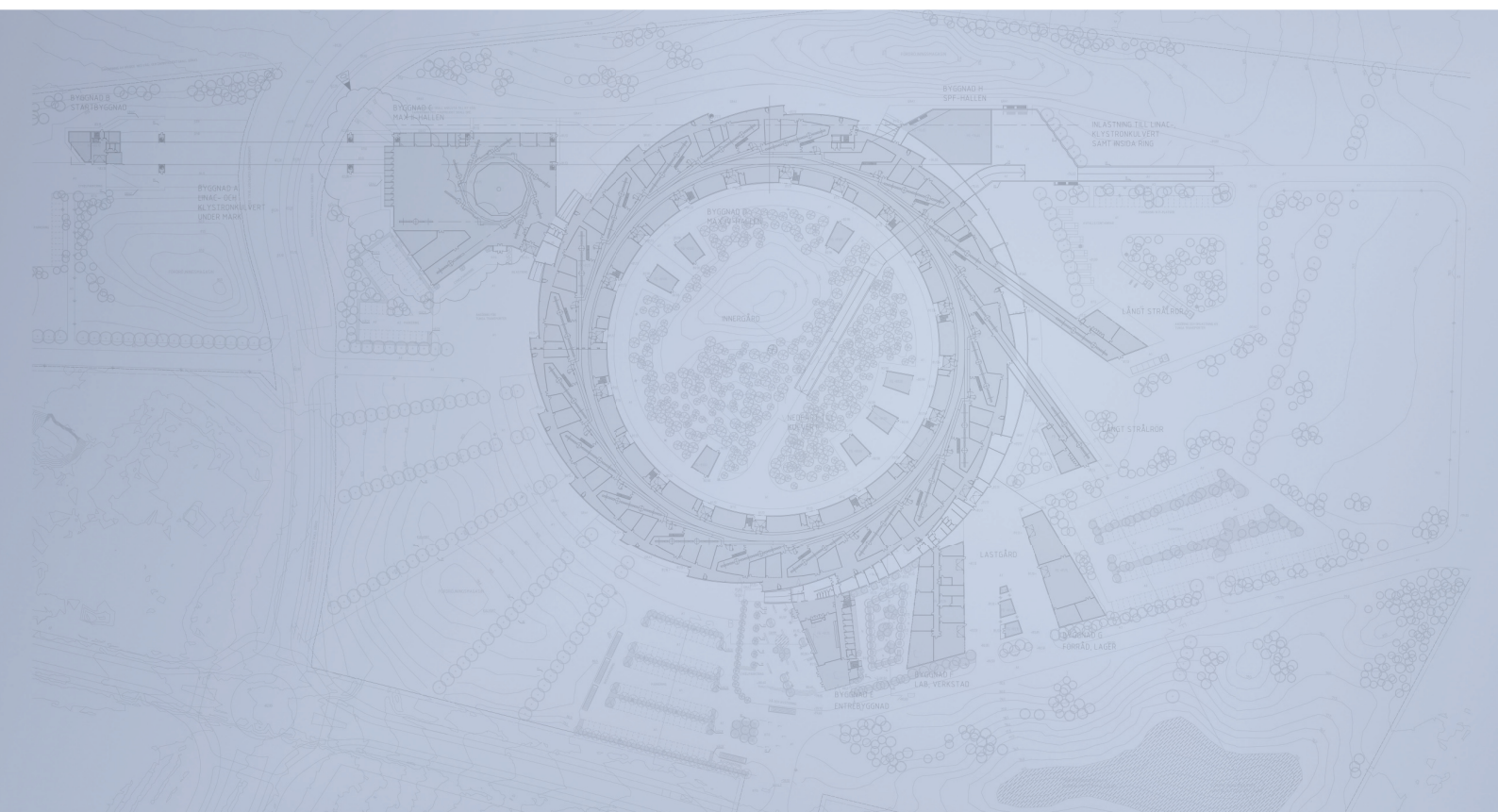
We conclude that once the SCW is added to the bare lattice, running with the alternative optics ( $\xi_{x,y} = +1.0$ ) results in better DA and MA than what can be gained by adjusting the sextupoles for the SCW. It is suggested that both sextupole settings are benchmarked with respect to actual lifetime and injection efficiency during commissioning of the SCW (if time allows) and the final decision on which strategy to follow is postponed until then.

## References

- [1] É. Forest, *Beam Dynamics: A New Attitude and Framework*, Hardwood Academic, Amsterdam, 1998
- [2] J. Bengtsson, *The Sextupole Scheme for the Swiss Light Source (SLS): An Analytic Approach*, SLS Internal Report SLS-TME-TA-1997-0009, available at <http://slsbd.psi.ch/pub/slsnotes/sls0997.pdf>
- [3] L. Nadolski, J. Laskar, Phys. Rev. ST Accel. Beams 6, 114801, 2003.
- [4] D. Robin, J. Safranek, W. Decking, Phys. Rev. ST Accel. Beams, 2, 044001, 1999.
- [5] C. Steier, D. Robin, L. Nadolski, W. Decking, Y. Wu, J. Laskar, Phys. Rev. E, 65, 056506, 2002.
- [6] J. Safranek, Nucl. Instr. and Meth. A, 388, 27, 1997.
- [7] R. Bartolini, I. P. S. Martin, J.H. Rowland, P. Kuske, F. Schmidt, Phys. Rev. ST Accel. Beams, 11, 104002, 2008.
- [8] Å. Andersson, M. Böge, A. Lüdeke, V. Schlott, A. Streun, Nucl. Instr. and Meth. A, 591, 437, 2008.
- [9] Å. Andersson, M. Böge, A. Lüdeke, A. Streun, *Coupling Control at the SLS*, Proceedings of 11th European Particle Accelerator Conference (EPAC-08), Genova, Italy, pp. 1983–1985, 2008.
- [10] M. Böge, A. Lüdeke, A. Streun, *Correction of Imperfections in the SLS Storage Ring*, Proceedings of PAC09, Vancouver, Canada, 2009.



# Detailed Design Report



## Chapter 3

### MAX IV 1.5 GeV Storage Ring

#### 3.4. Lattice Errors and Correction

MAX IV Facility





## 3.4. Lattice Errors and Correction

---

<b>3.4.</b>	<b>Lattice Errors and Correction .....</b>	<b>2</b>
3.4.1.	Overview .....	2
3.4.2.	Magnet Errors .....	2
3.4.3.	Misalignment Errors .....	19
3.4.4.	BPM and Correction Pattern .....	26
3.4.5.	Requirements for Secondary Windings .....	29
3.4.6.	Orbit Correction .....	30
3.4.7.	Coupling and Higher-order Correction .....	31
	References .....	33

## 3.4. Lattice Errors and Correction

---

### 3.4.1. Overview

The previous chapters introduced the design optics for the MAX IV 1.5 GeV storage ring. In the final machine there will be deviations between the design magnet parameters (strength, higher-order field contributions) and the parameters of the actually installed magnets; in addition, alignment of the magnets will not be identical with the ideal design alignment.

This chapter will discuss influence of such errors on the design optics and correction of the deviations with the goal to make the real machine resemble the ideal design as well as possible. The first two sections deal with error sources: field errors and misalignment errors. The third section introduces the correction pattern and discusses methods to restore the design optics in the real machine. Finally, the fourth section is dedicated to coupling and higher-order correction.

### 3.4.2. Magnet Errors

#### 3.4.2.1. Field Strength Errors

The actually installed gradient dipoles and quadrupoles will contain gradient errors. These errors have an immediate effect on the linear optics. Additionally, the sextupole gradients in the quadrupoles and the sextupole magnets will show deviations between the actual and the designed sextupole strength. These errors will influence the nonlinear optics, namely chromaticity shifts and a reduction of the dynamic aperture (DA). This section will first introduce field error estimates for quadrupoles and sextupoles, and close with a brief outline of correction possibilities for these errors included in the magnet design.

**3.4.2.1.1 Quadrupole Errors** A first study investigates the sensitivity of the linear optics on gradient errors of a single magnet. A gradient error of a single magnet will cause a beta beat and change the phase advance which results in a tune shift. The tune shift is given by [1]

$$\Delta\nu_{x,y} = \frac{1}{4\pi} \int \beta_{x,y}(s) \Delta k(s) ds \quad (3.1)$$

and the beta beat can be expressed as [1]

$$\Delta\beta_{x,y}(s) = \frac{\beta_{x,y}(s)}{2 \sin 2\pi\nu_{x,y}} \int \beta_{x,y}(\tilde{s}) \Delta k(\tilde{s}) \cos [\phi_{x,y}(s) - \phi_{x,y}(\tilde{s}) - \pi\nu_{x,y}] d\tilde{s} \quad (3.2)$$

where  $\Delta k(s)$  is the normalized gradient error.

According to these expressions, the most sensitive magnets can be identified. For horizontal tune shifts and beta beats, SQFi is the most sensitive magnet because of its large integrated gradient. In the vertical plane, the most sensitive magnets will be the dipoles. A summary is given in Table 3.1.

Table 3.1: Resulting tune shift and maximum beta beat observed with Tracy-3 for a 1% gradient error in a single quadrupole or dipole (QD). The most significant contributions in either plane have been underlined.

Family	$\Delta\nu_x$	$\Delta\nu_y$	$ \Delta\beta_x/\beta_x $	$ \Delta\beta_y/\beta_y $
SQFi	<u>0.010</u>	0.008	<u>0.064</u>	0.063
SQFo	0.005	0.004	0.035	0.034
DIP	0.001	<u>0.016</u>	0.002	<u>0.134</u>

Certain errors could affect entire magnet families. Examples for this are magnet fabrication errors, calibration errors, or errors of the power supply powering a certain family. For quadrupoles this will lead to a strong distortion of the linear optics, namely the beta functions and tunes. Table 3.2 summarizes the effect of a gradient error for an entire magnet family.

Finally, it is of interest to investigate the impact manufacturing tolerances on individual magnets have on the overall performance. For this purpose Tracy-3 studies are carried

Table 3.2: Resulting tune shifts observed with Tracy-3 for a 0.05% gradient error in all magnets of a certain quadrupole or dipole (QD) family. The most significant contributions in either plane have been underlined.

Family	$\Delta\nu_x$	$\Delta\nu_y$
SQFi	0.0059	0.0048
SQFo	<u>0.0064</u>	0.0049
DIP	0.0009	<u>0.0182</u>

out to determine the DA of a machine with random gradient errors corresponding to the manufacturing tolerance which is expected to be 0.2% rms (before calibrating and shunting individual magnets) [2]. The variation in gradient leads to a beta beating around the ring which perturbs the sextupole correction hence spoiling the DA. Figure 3.1 shows the results of these studies for 20 error seeds for on and off energy DA.

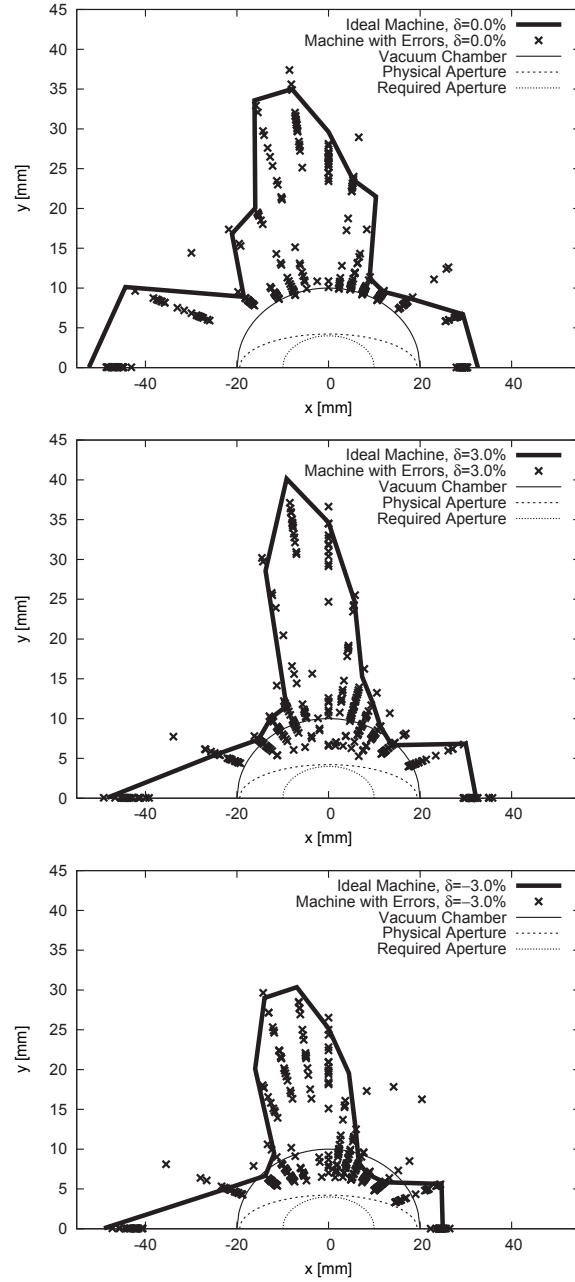


Figure 3.1: Dynamic aperture at the center of the straight section as calculated by Tracy-3 on and off energy ( $\delta = \pm 3.0\%$ ) for the bare lattice. The solid line shows the DA for the ideal machine. The crosses show results for 20 error seeds. For the error seeds a 0.2% rms gradient variation across all dipole and quadrupole magnets was assumed with a cutoff at  $2\sigma$ .

**3.4.2.1.2 Sextupole Errors** For sextupole magnet families an error will cause a degradation of the chromaticity correction and spoil the dynamic optimization. Similar to Eq. 3.1, the change of chromaticity resulting from a sextupole error can be expressed as [3]

$$\Delta\xi_{x,y} = \frac{1}{4\pi} \int \beta_{x,y}(s)\eta_x(s)\Delta m(s) ds \quad (3.3)$$

where  $\Delta m(s)$  is the normalized sextupole strength error. Obviously only the chromatic sextupoles ( $\beta_x\eta_x \neq 0$ ) have an influence on chromaticity. Table 3.3 summarizes the effect of sextupole gradient variations within an entire family on chromaticity.

Table 3.3: Resulting tune shifts observed for a 0.05% sextupole gradient error in all magnets of a certain sextupole family. The most significant contributions in either plane have been underlined.

Family	$ \Delta\xi_x $	$ \Delta\xi_y $
SQFi	<u>0.022</u>	0.018
SQFo	—	—
SDi	0.010	<u>0.027</u>
SDo	—	—

The DA also shows sensitivity on sextupole gradient errors because of the change in the underlying dynamics. For DA, also the harmonic sextupole gradient errors show an effect. The chosen sextupole settings have been optimized in order to minimize driving terms in the sextupole Hamiltonian. If this delicate balance is perturbed certain resonances could as a result be strongly driven which will have an detrimental influence on lifetime and injection efficiency. Therefore, Tracy-3 studies were carried out to determine the DA of a machine with random sextupole errors according to manufacturing tolerances which are expected to be 0.2% rms (before calibrating and shunting individual magnets) [2]. Figure 3.2 shows the results of these studies for 20 error seeds for on and off energy DA.

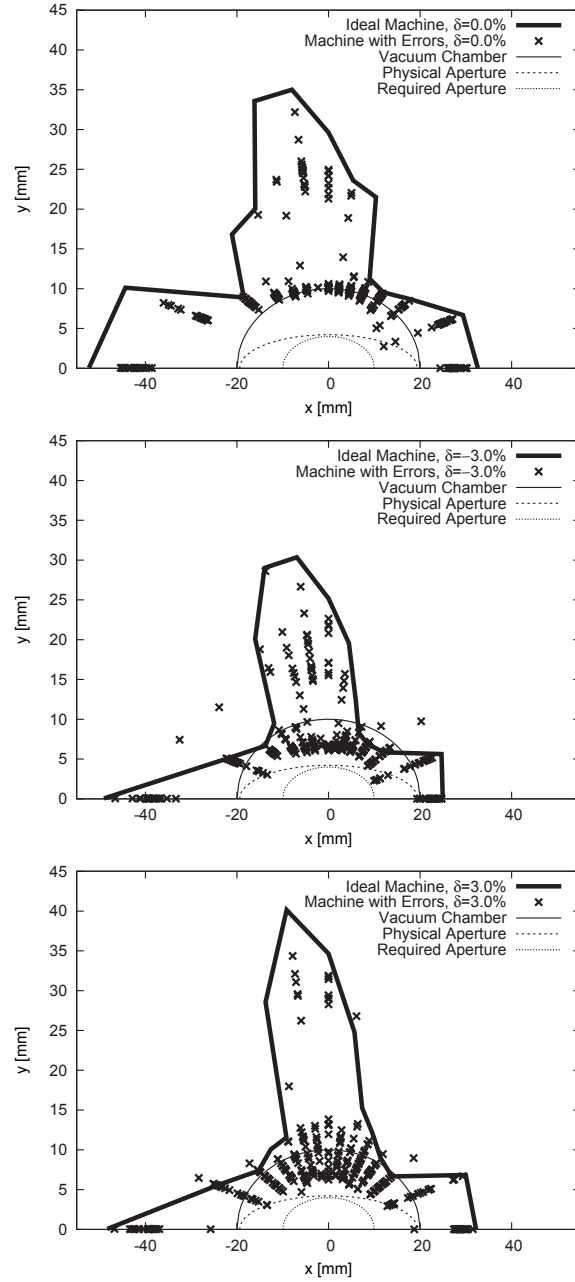


Figure 3.2: Dynamic aperture at the center of the straight section as calculated by Tracy-3 on and off energy ( $\delta = \pm 3.0\%$ ) for the bare lattice. The solid line shows the DA for the ideal machine. The crosses show results for 20 error seeds. For the error seeds a 0.2% rms sextupole gradient variation across all sextupole magnets was assumed with a cutoff at  $2\sigma$ .



From a comparison of Figs. 3.1 and 3.2 it appears that a variation of the sextupole gradient strengths leads to slightly more DA reduction (especially off-energy) than a variation of the quadrupole gradients. Although in both cases the aperture requirement can still be met, there is not much margin left.

The overall DA reduction caused by 0.2% rms gradient variations on both quadrupoles and sextupoles that are assumed to result from regular magnet manufacturing (without extra shunting) [2] is a serious effect (see Fig. 3.3).

If additional calibration measurements and shunting of the magnets are performed after manufacturing so that the resulting variation becomes as low as 0.02% rms, the DA reduction becomes much less severe and aperture requirements are easily met. This also leaves some margin for an additional DA reduction from misalignment and multipole errors. Figure 3.4 shows DA assuming all gradients show a 0.02% rms variation.

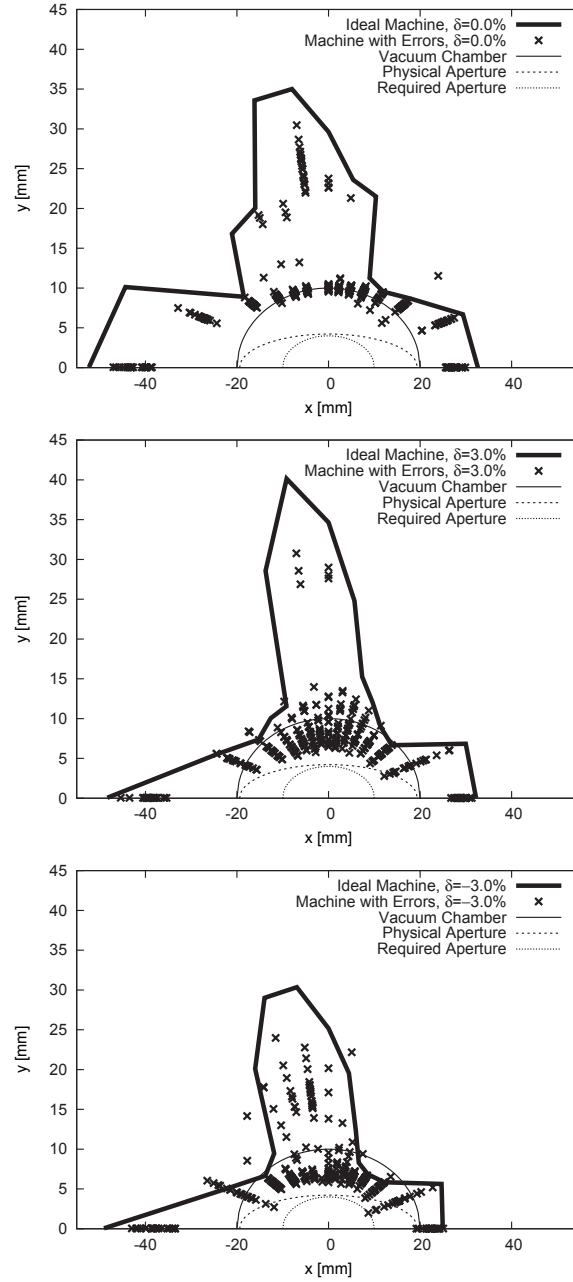


Figure 3.3: Dynamic aperture at the center of the straight section as calculated by Tracy-3 on and off energy ( $\delta = \pm 3.0\%$ ) for the bare lattice. The solid line shows the DA for the ideal machine. The crosses show results for 20 error seeds. For the error seeds a 0.2% rms gradient variation across all dipole, quadrupole, and sextupole magnets was assumed with a cutoff at  $2\sigma$ .

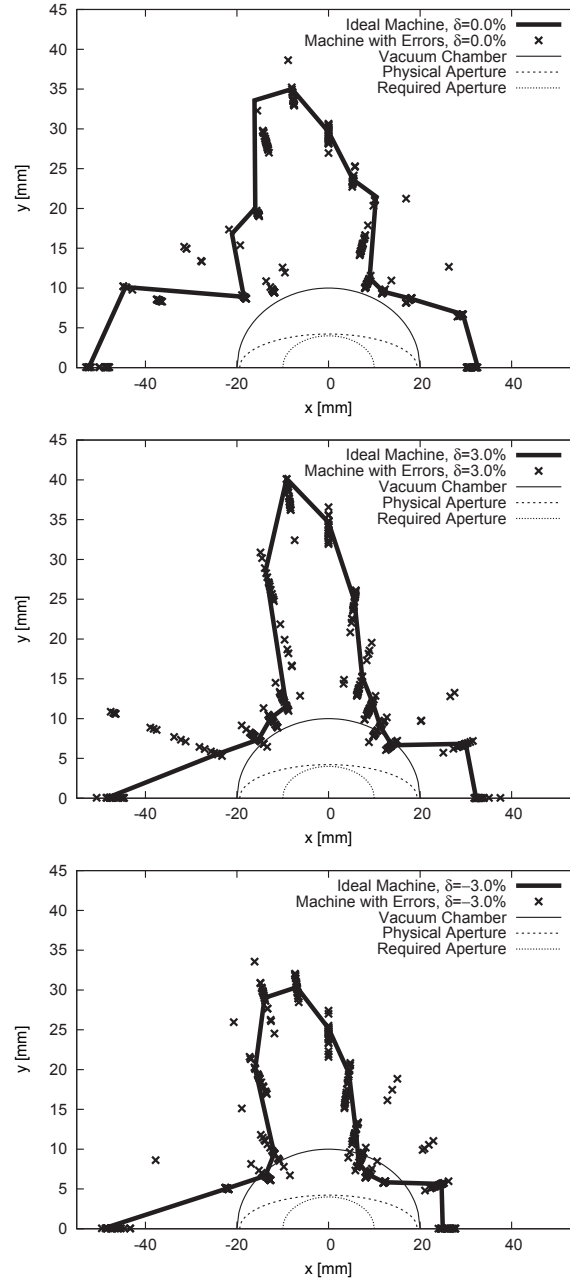


Figure 3.4: Dynamic aperture at the center of the straight section as calculated by Tracy-3 on and off energy ( $\delta = \pm 3.0\%$ ) for the bare lattice. The solid line shows the DA for the ideal machine. The crosses show results for 20 error seeds. For the error seeds a 0.02% rms gradient variation across all dipole, quadrupole, and sextupole magnets was assumed with a cutoff at  $2\sigma$ .

**3.4.2.1.3 Shunting** As mentioned above shunting of individual magnets will be used to assure the rms deviations from the design field values are kept at an acceptable level. This allows powering magnets in families rather than having individual powering and cabling for every magnet. Dipoles, quadrupoles, and sextupoles will contain shunts. The shunts are to be implemented as binary resistor batteries thus allowing fine adjustment over a comparably large range with few inexpensive and standardized/modular parts.

Dipoles and quadrupoles will be shunted in two stages. A first stage should be performed by the manufacturer as a result of magnetic field measurements. This coarse shunting should assure deviations from design values below 0.2% rms [2]. After the magnets have been installed and machine commissioning has started, LOCO analysis will deliver the necessary results for the second stage of shunting that will be performed on site by the machine group. This shunting should then assure deviations from design approach a level of roughly 0.02% rms [2].

The dedicated defocusing sextupoles SDi, SDo will be shunted in a single stage only. In order to detect deviations in the sextupole pattern from design, nonlinear optics (e.g. spectral components in betatron motion excited by resonance driving terms) have to be measured and analyzed (cf. e.g. [4] and Section 3.9.11.2). This measurement campaign depends on the quality of the available BPM system and is expected to take place in a later stage of commissioning. Hence, a single shunting stage will be performed by the machine group once this campaign has delivered the necessary results and the shunting is deemed necessary.

The focusing sextupole component is integrated into focusing quadrupoles (SQFi and SQFo) and hence no individual shunting of these focusing sextupole gradients is possible. Errors in the focusing sextupole gradients will have to be corrected by powering the adjacent correction sextupoles SCi and SCo.

### 3.4.2.2. Higher-order and Multipole Errors

**3.4.2.2.1 Analytic Studies** Each magnet and ID installed in the MAX IV 1.5 GeV storage ring will have non-zero higher-order magnetic field components. While quadrupole components will lead to beta beats and tune shifts (or vertical dispersion in the case of skew quadrupole components), sextupole and octupole components will change the dynamic behavior: chromatic tune shift and amplitude-dependent tune shift (ADTS) behavior is changed. Since the linear and second-order chromaticity as well as the ADTS have been optimized with a dedicated sextupole layout and settings, any additional sextupole or octupole components added to the design lattice will disturb the delicate balance that results from the dynamic optimization. Therefore it is essential to gauge the sensitivity of the lattice and the optimization to such perturbations. The result of such studies gives a specification for the higher-order field components of installed magnets and IDs.

While it is relatively difficult to specify boundary conditions for changes in the dynamic behavior, changes of the corrected chromaticity  $\xi_{x,y}$  can be measured (see Eq. 3.3). Likewise changes of the driving terms for second-order chromaticity and ADTS [5]

$$\xi_{x,y}^{(2)} = \pm \frac{3}{4\pi} b_4 \eta^2 \beta_{x,y} \quad (3.4)$$

$$dQ_{xx} = \frac{\partial \Delta \nu_x}{\partial J_x} = \frac{3}{8\pi} b_4 \beta_x^2 \quad (3.5)$$

$$dQ_{xy} = \frac{\partial \Delta \nu_x}{\partial J_y} = \frac{\partial \Delta \nu_y}{\partial J_x} = -\frac{3}{4\pi} b_4 \beta_x \beta_y \quad (3.6)$$

$$dQ_{yy} = \frac{\partial \Delta \nu_y}{\partial J_y} = \frac{3}{8\pi} b_4 \beta_y^2 \quad (3.7)$$

can be measured for a set of higher-order perturbations. For the studies presented here thin sextupole and octupole kicks were added to different magnet families and their effect on these driving terms was gauged. A typical strength to apply is given by assuming that a 2 G residual pole tip field is always present. According to the multipole order, magnet length, and magnet gap this translates to a specific integrated multipole strength. Assuming such a multipole be added to every magnet of a specific family, the overall change of the dynamic properties can be assessed.

Another way to attack the multipole problem is to derive the multipole field strength that can be applied to each member of a magnet family until the changes in chromaticity

or higher-order driving terms (Eqs. 3.5–3.7) reach a specific level. For example, when the driving terms change by more than 10% of the correction applied to these terms as a result of the original sextupole optimization.

Table 3.4 shows the result of such a study done for sextupole components in quadrupole and dipole magnets. For each family the integrated normalized sextupole strength ( $b_3l$ ) equivalent of a residual 2 G pole tip field is calculated. For each family, the resulting change in linear chromaticity  $\xi_{x,y}$  can be calculated according to Eq. 3.3. In a second step the influence of such an additional sextupole component on second-order chromaticity  $\xi_{x,y}^{(2)}$  is observed. For this purpose, a thin sextupole with the calculated strength is inserted at the center of the quadrupole and dipole magnets in the OPA model. For each magnet family, the resulting change in second-order chromaticity  $\xi_{x,y}^{(2)}$  is then recorded.

Table 3.4: Sensitivity to sextupole components for each quadrupole and dipole family. The second column shows the equivalent sextupole strength of a residual pole tip field of 2 G. The last two columns show the change in (corrected) linear and second-order chromaticity resulting from such a sextupole component in the different magnet families. This specification allows a direct comparison with the sextupole magnet strengths given in Table 2.1 in Section 2.3.2.

Family	$(b_3l)$ equiv. of 2 G	$ \Delta\xi_{x,y}/\xi_{x,y} $ [%]	$ \Delta\xi_{x,y}^{(2)}/\xi_{x,y}^{(2)} $ [%]
SQFi	$0.0363 \text{ m}^{-2}$	7.9, 5.5	5.5, 7.8
SQFo	$0.0181 \text{ m}^{-2}$	—, —	4.9, 2.9
DIP	$0.0907 \text{ m}^{-2}$	—, 9.0	0.3, 7.0

A similar study was conducted for octupolar field components in sextupole, quadrupole, and dipole magnets. Table 3.5 summarizes the results. For each magnet family the 2 G equivalent octupole strength was calculated and applied to the magnet family as an additional octupole kick. The resulting change of the second-order chromaticity  $\xi_{x,y}^{(2)}$  as well as the relative change in ADTS driving terms  $\Delta dQ_{ij}/dQ_{ij}$  was noted.

It must also be assumed that IDs installed in the straight sections will contain high-order field components as well. To gauge this effect a typical ID with a length of 2 m was assumed and given quadrupole, sextupole, and octupole moments. The quadrupole

Table 3.5: Sensitivity to octupole components for each sextupole, quadrupole, and dipole family. The second column shows the equivalent octupole strength of a residual pole tip field of 2 G. The third and fourth columns show the change in chromatic and ADTS driving terms resulting from such an octupole component in the different magnet families. Note that the indices  $ij$  stand for  $xx, xy, yy$ .

Family	$(b_4l)$ equiv. of 2G	$ \Delta\xi_{x,y}^{(2)}/\xi_{x,y}^{(2)} $ [%]	$ \Delta dQ_{ij}/dQ_{ij} $ [%]
SDi	$0.432 \text{ m}^{-3}$	2.9, 9.0	0.5, 2.7, 3.8
SDo	$0.432 \text{ m}^{-3}$	—, —	0.5, 2.6, 3.0
SQFi	$1.728 \text{ m}^{-3}$	32.5, 24.0	4.8, 6.7, 2.5
SQFo	$0.864 \text{ m}^{-3}$	—, —	3.9, 5.4, 2.0
DIP	$4.319 \text{ m}^{-3}$	0.1, 4.2	—, 3.8, 144.2

contribution was modeled as a long hard-edge quadrupole at the center of the straight. It was found that for only one such device installed in the storage ring, an integrated normalized contribution of  $(b_2l) = 0.209 \text{ m}^{-1}$  will result in a horizontal tune shift of  $\Delta\nu_x = 0.1$  (cf. Eq. 3.1). To obtain a vertical tune shift of  $\Delta\nu_y = 0.1$  an integrated normalized contribution of  $(b_2l) = 0.273 \text{ m}^{-1}$  is required. If one assumes that ten such devices are installed in the storage ring and operated at the same time, the maximum allowable gradient error per ID is  $(b_2l) = 0.022 \text{ m}^{-1}$  for  $\Delta\nu_x = 0.1$  and  $(b_2l) = 0.042 \text{ m}^{-1}$  for  $\Delta\nu_y = 0.1$ . Similar studies have been performed for the sextupole and octupole contributions: long hard-edge sextupoles and octupoles have been applied to the center of a straight section and the effect on linear chromaticity  $\xi_{x,y}$  (cf. Eq. 3.3), second-order chromaticity  $\xi_{x,y}^{(2)}$  and ADTS driving terms  $dQ_{ij}$  observed. Assuming again that the maximum tolerable contribution should amount to no more than 10% of the correction applied by the dedicated sextupoles, an upper limit for high-order field contributions in an ID can be specified.

Finally, from all of the above mentioned studies, one can gather a set of maximum higher-order field components for each type of magnet and ID. The assumption made here is that the multipole contribution should amount to no more than 10% of the corrections applied by the design optics. These figures can be seen as beam dynamics tolerance limits on magnet and ID quality. The values are given in Table 3.6.

Table 3.6: Tolerances of different magnet types and IDs for higher-order field components. The underlying condition is that the multipole contribution should amount to no more than 10% of the corrections applied by the design optics.

Magnet type	Maximum allowable multipole components		
	$(b_2l)$ [ $\text{m}^{-1}$ ]	$(b_3l)$ [ $\text{m}^{-2}$ ]	$(b_4l)$ [ $\text{m}^{-3}$ ]
DIP	—	0.101	0.300
SQFi	—	0.046	0.532
SQFo	—	0.037	1.600
SDi	—	—	0.476
SDo	—	—	1.43
Single ID	0.209	1.238	58.5
10 IDs	0.022	0.124	5.85

**3.4.2.2.2 Tracking Studies** What is missing in this analysis so far is the influence of random multipoles and the overall effect of random and systematic multipoles on the storage ring performance. More specifically, how much reduction of DA is caused by the presence of multipole contributions in the storage ring magnets? One way to gauge this is to compare the DA of the ideal machine with that of a machine where field and multipole errors have been added. Since there is presently no measurement data from prototype magnets for MAX IV available, we instead use the magnet errors measured for the SLS storage ring magnets [6]. Table 3.7 lists the assumptions made in this error model.

The DA results using the multipole error model are shown in Fig. 3.5. The multipole errors have been applied as detailed above for 20 seeds with a cutoff at  $2\sigma$ . Figure 3.6 shows the DA including both multipole errors and the 0.02% rms field errors expected after calibrating and shunting the newly manufactured MAX IV magnets. The multipole and field errors have been applied for 20 seeds with a cutoff at  $2\sigma$ .

As already pointed out in Section 3.4.2.1.2, if calibration and shunting of the magnets after manufacturing can guarantee a main field variation no larger than 0.02% rms, the DA reduction from field errors becomes very small. As can be seen here, such field errors certainly do not lead to a DA reduction beyond that caused by the multipole errors alone



Table 3.7: Multipole errors used in the MAX IV error model. The data has been taken from magnet measurements of the SLS storage ring magnets [6]. The order column refers to the multipole order defined by 2 = quadrupole, 3 = sextupole, etc.

Magnet family	Error type	Order	Maximum multipole component (relative to main field component)	
			Upright	Skew
Quadrupoles	Systematic	6	$0.5 \times 10^{-4}$	—
		10	$0.5 \times 10^{-4}$	—
		14	$0.1 \times 10^{-4}$	—
Sextupoles	Systematic	9	$0.5 \times 10^{-4}$	—
		15	$0.5 \times 10^{-4}$	—
		21	$0.5 \times 10^{-4}$	—
Quadrupoles	Random (rms)	2	$2.5 \times 10^{-4}$	—
		3	$2.8 \times 10^{-4}$	$2.9 \times 10^{-4}$
		4	$1.9 \times 10^{-4}$	$1.4 \times 10^{-4}$
		6	$1.3 \times 10^{-4}$	—
		10	$3.0 \times 10^{-5}$	—
Sextupoles	Random (rms)	3	$5.0 \times 10^{-4}$	—
		4	$5.2 \times 10^{-4}$	$4.9 \times 10^{-4}$
		5	$3.5 \times 10^{-4}$	—
		9	$8.0 \times 10^{-5}$	—
		15	$5.0 \times 10^{-5}$	—

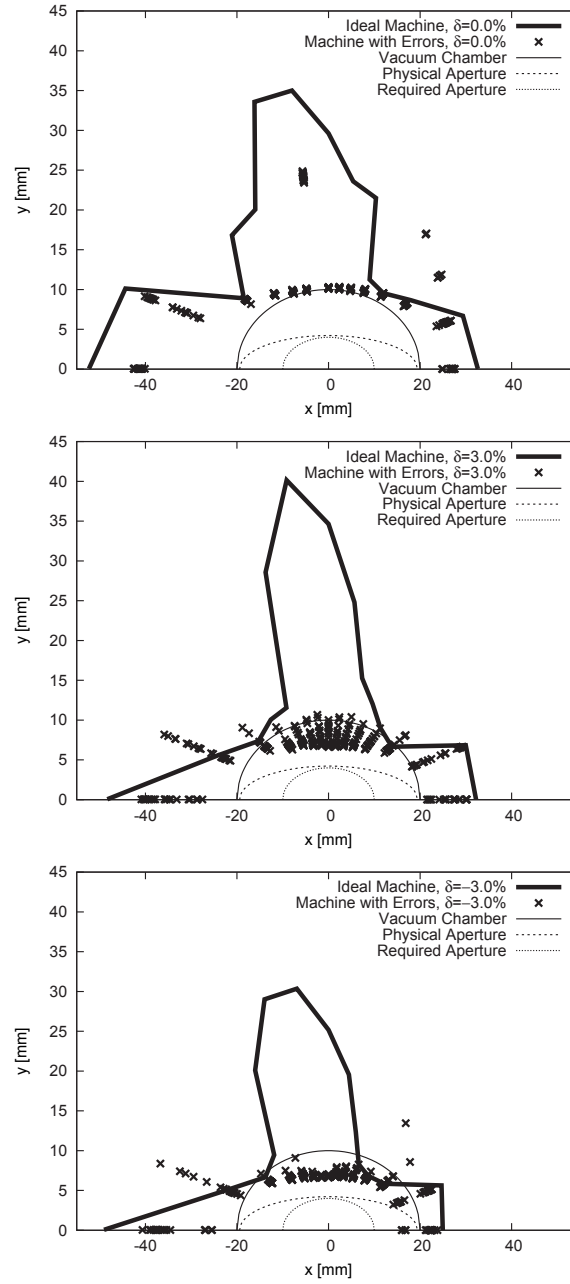


Figure 3.5: Dynamic aperture at the center of the straight section as calculated by Tracy-3 on and off energy ( $\delta = \pm 3.0\%$ ) for the bare lattice. The solid line shows the DA for the ideal machine. The crosses show results for 20 error seeds. For the error seeds the multipole error model was assumed with a cutoff at  $2\sigma$ .

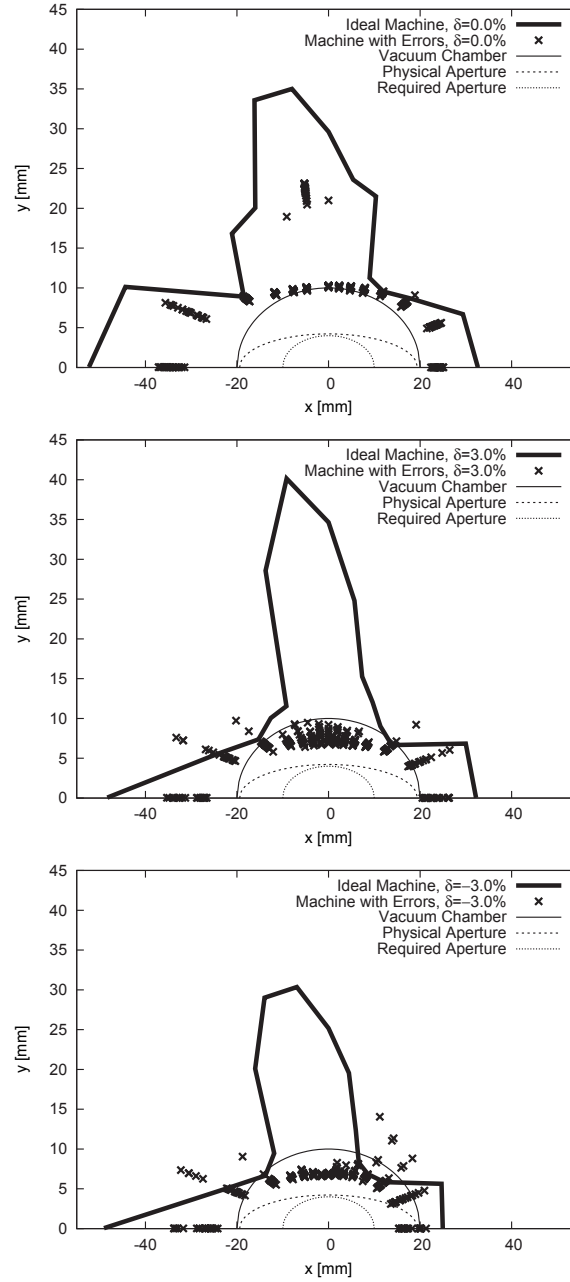


Figure 3.6: Dynamic aperture at the center of the straight section as calculated by Tracy-3 on and off energy ( $\delta = \pm 3.0\%$ ) for the bare lattice. The solid line shows the DA for the ideal machine. The crosses show results for 20 error seeds. For the error seeds the multipole and field error model (0.02% rms field errors) was assumed with a cutoff at  $2\sigma$ .

### 3.4.3. Misalignment Errors

In a real storage ring magnets are always positioned away from their ideal locations. While longitudinal alignment of one element with respect to its upstream and downstream neighbors is facilitated by the use of rigid girders (see Chapter 3.5), magnets can easily be misaligned in the transverse plane. In addition, roll errors generate skew field components which are not present in the theoretical design. Displacements in the transverse direction can be detected by BPMs and corrected by horizontal and vertical corrector coils installed throughout the achromat. A proper correction of these misalignments will lead to a new closed orbit. It then remains to be shown that the deviations of this closed orbit from the ideal orbit can be handled (see Section 3.4.4). Roll errors on the other hand cannot be corrected directly. These roll errors induce spurious dispersion, coupling, and ultimately define the vertical emittance of the machine (see Section 3.4.7).

#### 3.4.3.1. Effects of Misalignment Errors without Coupling

In order to properly model misalignments, the correlations from integrated assembly and girders have to be taken into account. Since no complete set of prototype measurements exists from which misalignment data could be extracted, an error model is defined. In this model a set of misalignment errors are applied that we expect can be achieved after manufacturing and alignment. The error model makes the following assumptions:

- The entire DBA cell is machined from one solid block of iron. This block also includes three sets of hor./ver. correctors and BPMs. The magnetic centers of the magnets within the block (including corrector magnets) are aligned to within the machining accuracy of  $25\text{ }\mu\text{m}$  rms in both planes. Assume a  $0.2\text{ mrad}$  rms roll error.
- The BPMs are fastened to the adjacent sextupole magnet (SDI, SQFo). This ensures only a  $25\text{ }\mu\text{m}$  rms machining accuracy error between the BPM position and the magnetic center in both planes. However, after applying beam-based calibration (BBC<sup>1</sup>) we can achieve a BPM offset of  $5\text{ }\mu\text{m}$  rms ( $3\text{ }\mu\text{m}$  rms calibration

---

<sup>1</sup>Often erroneously referred to as beam-based alignment (BBA).

has already been achieved at SLS [7]). These 5  $\mu\text{m}$  rms is what we set as the total BPM alignment error in both planes. We also assume a 0.2 mrad rms roll error.

- The solid iron blocks containing the magnets for DBA cells are assumed to have an alignment error of 100  $\mu\text{m}$  rms in both planes along with a 0.2 mrad rms roll error.
- The random misalignment of the solid blocks (modeled as the girders) are applied systematically to the elements within. On top of this error the random alignment error for each element within is applied to the element.

Orbit correction finds corrector settings which result in a new closed orbit which lies as close to the design orbit as possible. Obviously this orbit correction relies on the underlying BPM and corrector pattern (see Section 3.4.4). Tracy-3 has been used to simulate this process for the bare lattice. The code first calculates an orbit response matrix which is then inverted using SVD. This inverted response matrix is then used to calculate corrector settings for an arbitrary set of beam position readings. Tracy-3 performs this correction in three iterations and then returns a final closed-orbit as a set of deviations from the design orbit around the ring.

The overall effect of misalignments is the closed orbit resulting from orbit correction; this is shown in Fig. 3.7. The applied misalignments correspond to the misalignments specified in the alignment error model above. For rms misalignments a  $2\sigma$ -cutoff was assumed. Results are shown for 100 seeds. For the misalignments calculated and displayed in Fig. 3.7, the required corrector strengths have also been recorded. Figure 3.8 shows these mean and rms corrector strengths (using two three-step corrections).

One may also ask what influence these misalignments have on the dynamic performance of the storage ring. One way to gauge this is to investigate the DA for a misaligned and corrected machine. These results are shown in Fig. 3.9 for the alignment error model detailed above. Finally, DA including all modeled error sources (0.02% rms field errors, multipole errors, and alignment errors) is displayed in Fig. 3.10. We note that the DA with all error sources combined is worse than the DA including only misalignment errors. Keeping in mind the results shown in Section 3.4.2.2, we conclude that multipole errors dominate over the misalignment errors used in this model.

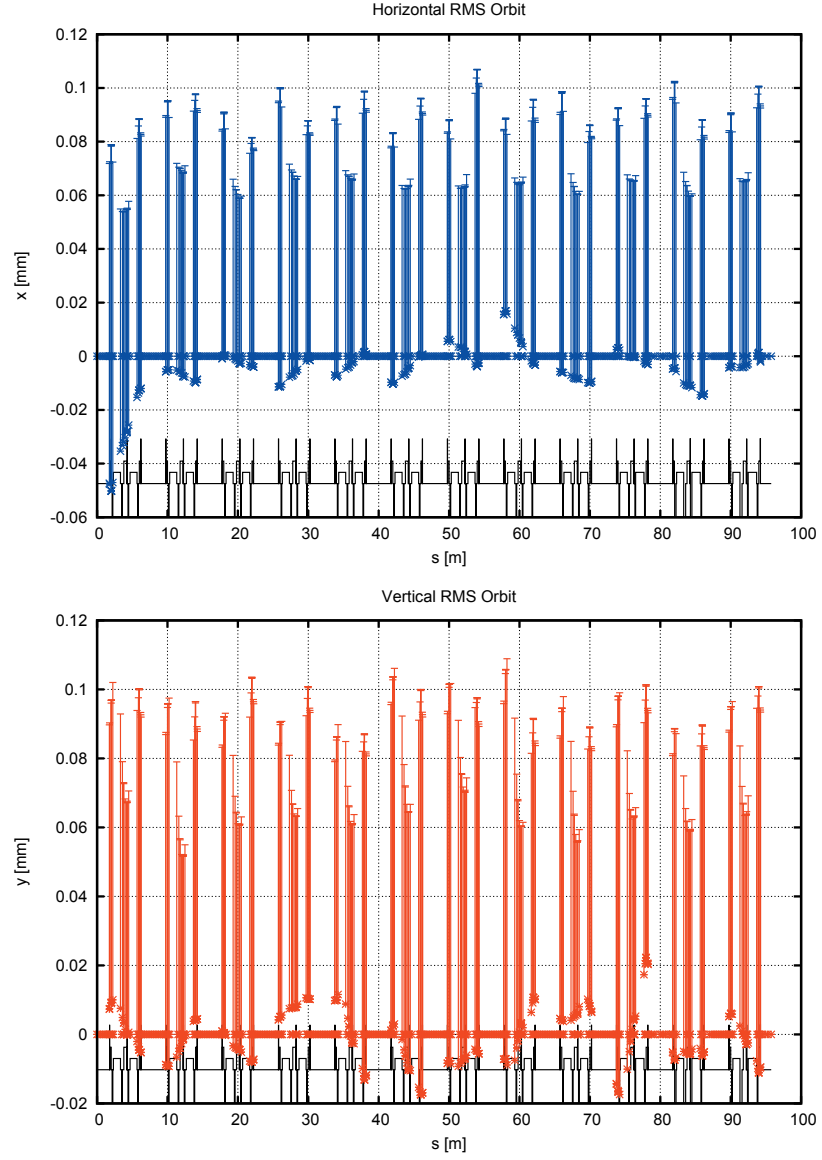


Figure 3.7: Closed-orbit deviations from the design orbit after applying misalignments and correcting the orbit. The dot shows the mean deviation for all seeds and the “error bar” depicts the deviation corresponding to 1 standard deviation across all seeds. 100 seeds were used.

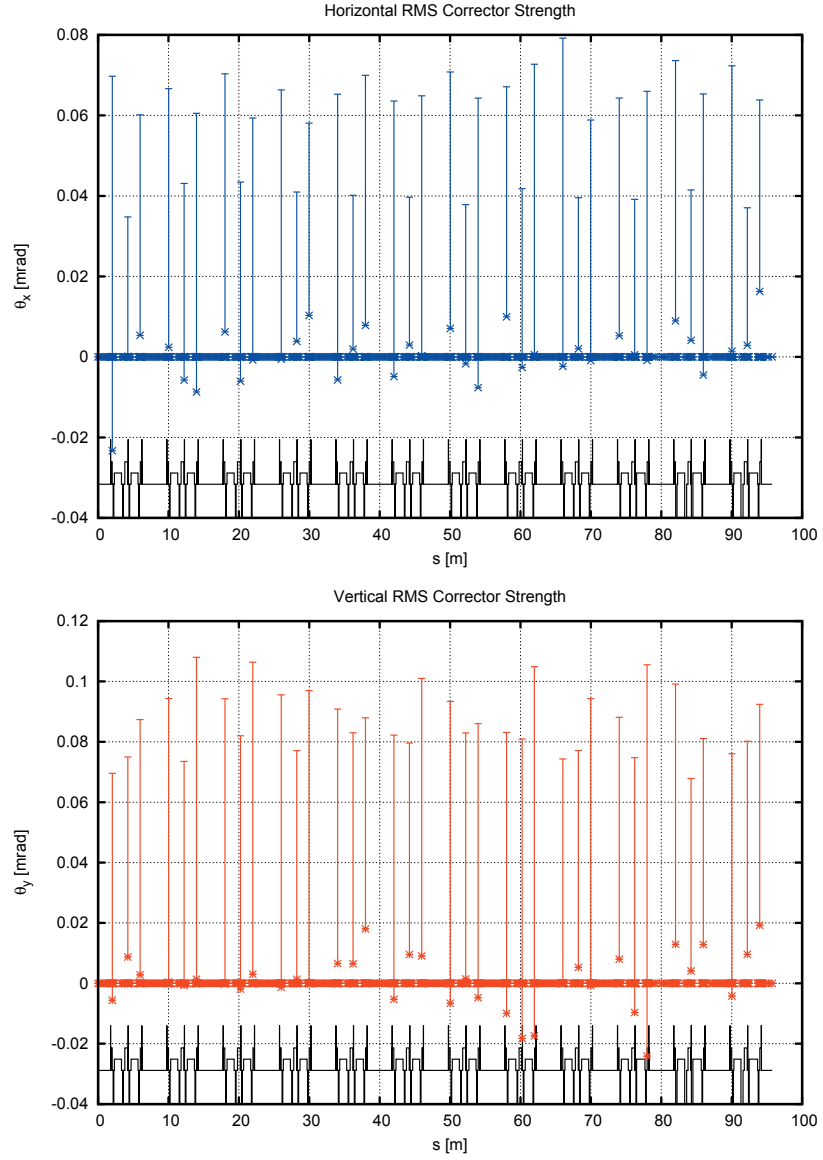


Figure 3.8: Corrector strengths required for the orbit correction displayed in Fig. 3.7. The dot shows the mean corrector strength for all seeds and the “error bar” depicts the deviation corresponding to 1 standard deviation across all seeds. 100 seeds were used.

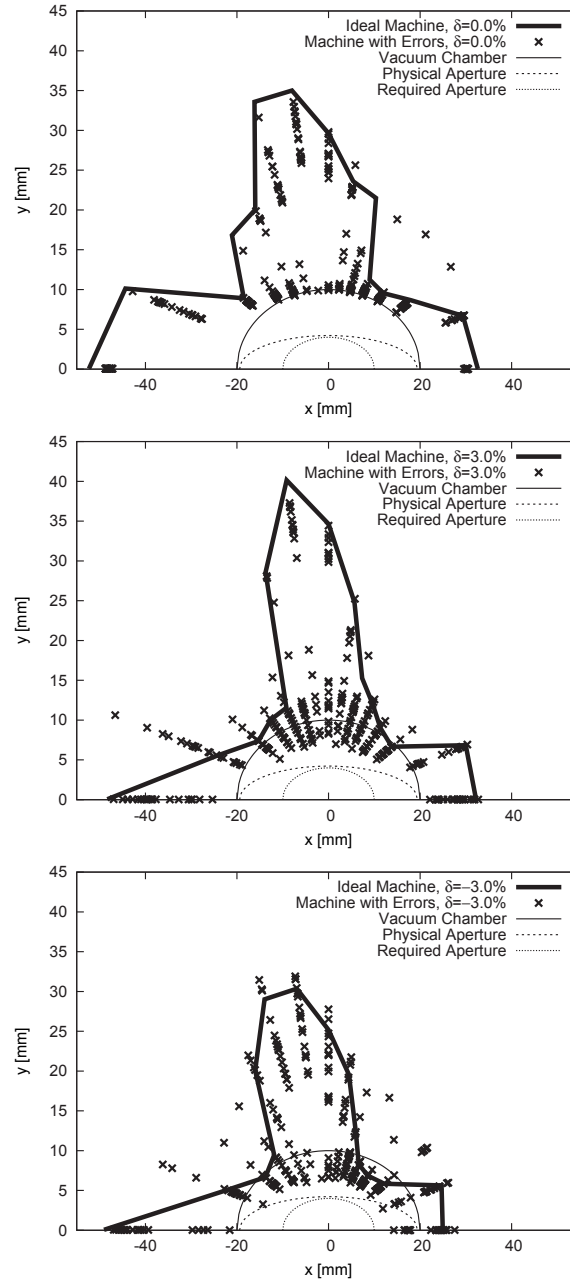


Figure 3.9: Dynamic aperture at the center of the straight section as calculated by Tracy-3 on and off energy ( $\delta = \pm 3.0\%$ ) for the bare lattice. The solid line shows the DA for the ideal machine. The crosses show results for 20 error seeds. For the error seeds the alignment error model was assumed with a cutoff at  $2\sigma$ .



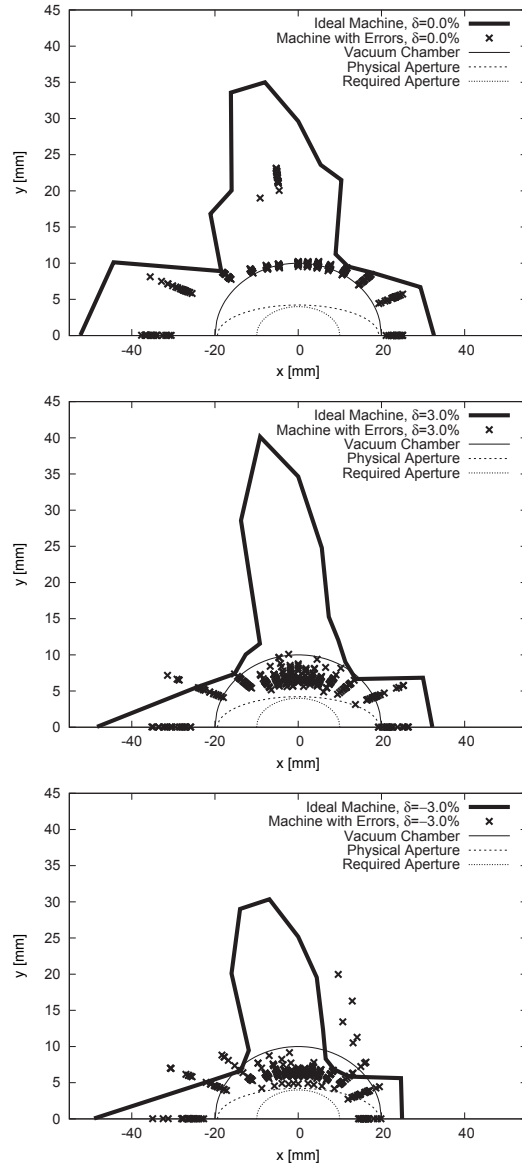


Figure 3.10: Dynamic aperture at the center of the straight section as calculated by Tracy-3 on and off energy ( $\delta = \pm 3.0\%$ ) for the bare lattice. The solid line shows the DA for the ideal machine. The crosses show results for 20 error seeds. For the error seeds the alignment, multipole, and field (0.02% rms) error models were assumed with a cutoff at  $2\sigma$ .

### 3.4.3.2. Coupling from Misalignment Errors

Finally, a study has been performed to assess the amount of linear betatron coupling that results from the multipole and misalignment errors in the model given above. For each seed with random errors applied with a  $2\sigma$ -cutoff we derive the betatron coupling as the ratio of the normal-mode emittances  $\kappa = \varepsilon_{\text{II}}/\varepsilon_{\text{I}}$ ; we also note the tilt angle of the beam.

*This is ongoing work...*

### 3.4.4. BPM and Corrector Pattern

The MAX IV 1.5 GeV storage ring will be equipped with three BPMs and three horizontal/vertical corrector pairs per DBA. The average phase advance between BPMs is  $31^\circ$  in the vertical plane and  $112^\circ$  in the horizontal. These phase advances are sufficient to sample betatron motion around the ring. BPM buttons are installed as close as possible to the dipole correctors (which correct both the horizontal and the vertical beam position) in order to minimize the phase advance in between.

The dipole correctors are implemented as extra windings on the corrector sextupole magnets. One extra winding does horizontal dipole correction, while a second extra winding is used for vertical dipole correction. In the model the space reserved for the the BPMs is a 50 mm drift section.

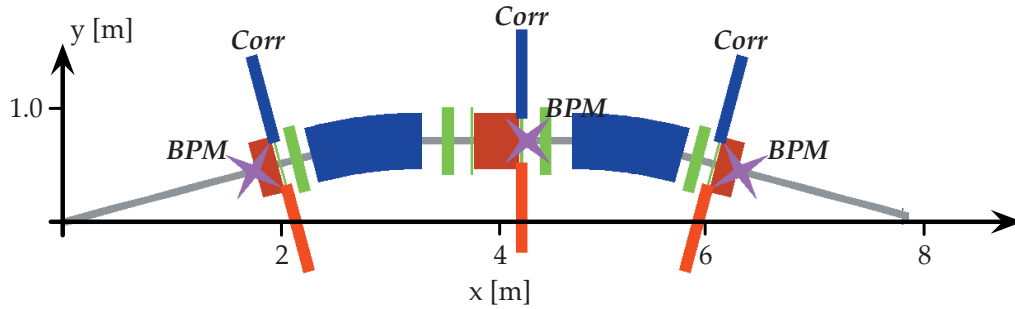


Figure 3.11: Positions of BPMs and correctors in the MAX IV 1.5 GeV storage ring DBA. The magenta crosses indicate locations of the BPMs. The blue and red strips indicate the position of the dipole correctors.

Of the three BPM/corrector pairs in every DBA, one is located at the center of the DBA while the other two are located at the ends of the DBA cell. For the BPM/corrector pair installed at each DBA end, the BPM is positioned as the last element in the DBA facing the straight section. This BPM is followed by the SQFO and SCo magnets. The SCo is a thin corrector sextupole magnet with two extra windings for dipole corrections in both planes. For the BPM/corrector pair located at the center of each DBA, we chose the downstream side of SQFi. The dipole correctors are extra windings on the thin corrector sextupole SCi which is adjacent SQFi. The BPM immediately follows SCi thus minimizing the face advance to the dipole correctors. BPM and corrector positions within the DBA are displayed in Fig. 3.11.

With this placement of BPMs and correctors we make sure the beam position in the ID is always known, the beam position and angle in the ID can be well controlled, and that the orbit offset in the quadrupoles and sextupoles can be minimized by the orbit correction system.

Calibration of the BPMs to the adjacent quadrupole/sextupole magnet centers (SQFi, SQFo) can be achieved by exciting the quadrupole/sextupole magnet while driving orbit bumps through this magnet per the conventional BBC procedure.

The correctors and BPMs are placed close together minimizing the betatron phase advance between these elements. The result is a very diagonal form of the inverted response matrix. If the response matrix is given by  $\mathcal{M}$  and the kicks by all correctors in the machine are denoted as  $\vec{\theta}$ , the resulting orbit relative to the magnet centers is given by  $\vec{\mathcal{X}} = \mathcal{M}\vec{\theta}$ . After the response matrix has been calculated or measured, it can be inverted with SVD thus giving the well-known equation for orbit correction  $\vec{\theta} = \mathcal{M}^{-1}\vec{\mathcal{X}}$ . If the inverted response matrix has diagonal form, global correction requires only knowledge of the adjacent correctors, in essence reducing global correction to local correction by means of the three or four kicker bump.

A plot of the inverted response matrices (a  $36 \times 36$  matrix both for the horizontal and the vertical plane; coupling has been disregarded here) for the bare machine is shown in Fig. 3.12. The diagonal form can be easily recognized.

It has not yet been firmly decided how orbit correction should be implemented. A slow orbit feedback (SOFB) will likely acquire BPM data and set corrector strengths at 10 Hz. The corrector magnets, their power supplies, and the vacuum chamber must be able to support this 10 Hz correction which is not expected to be a problem. Such a SOFB system will be able to counteract long-term drifts ( $\lesssim 0.1$  Hz).

It has not yet been decided if in addition to the SOFB a fast orbit feedback (FOFB) system should be operated to counteract fast disturbances (e.g. gap movement, cultural noise, etc.). In case such a system (running for example at 1 kHz and effectively damping noise up to  $\lesssim 10$  Hz) is required, the BPMs need to support fast data acquisition and the correctors, their power supplies, and the vacuum chamber need to support this faster correction rate.

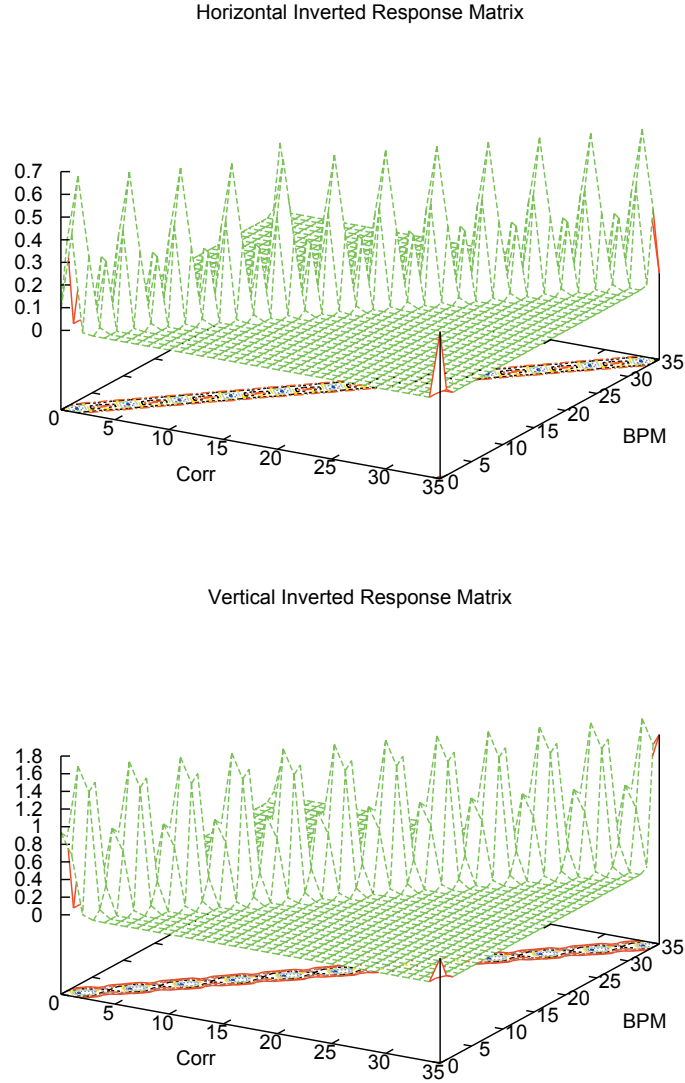


Figure 3.12: Plot of the inverted response matrices for the bare lattice. As there are 36 BPMs and 36 corrector pairs in the storage ring each matrix consists of  $36 \times 36$  elements. The diagonal form can be easily recognized. In general a coupled  $72 \times 72$  matrix should be given, however for clarity a perfect lattice is assumed and coupling disregarded.

### 3.4.5. Requirements for Secondary Windings

The thin sextupole corrector magnets (SCi, SCo) carry two extra windings. Each extra winding is powered individually as a dipole corrector. In this way horizontal and vertical dipole correction is distributed throughout the lattice without taking up much space. Figure 3.13 shows how such windings can be connected and powered to form dipole correctors in both planes.

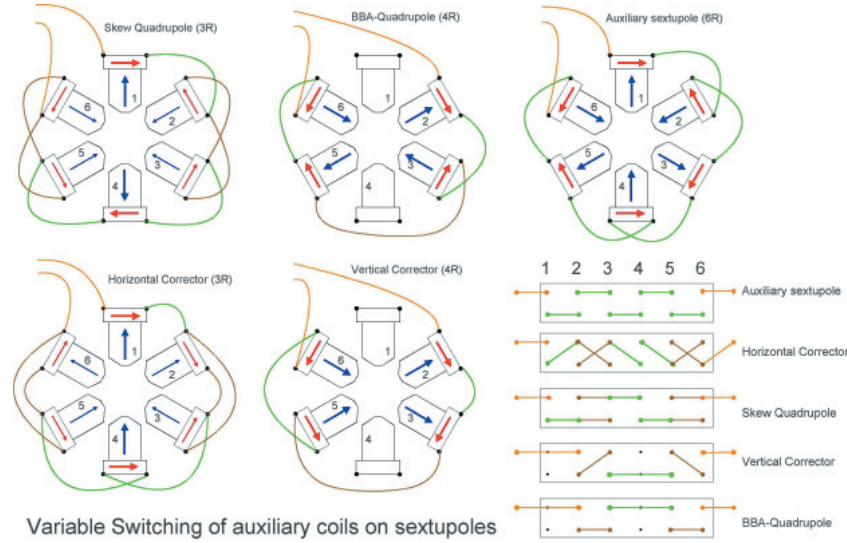


Figure 3.13: Illustration of the per-pole wiring and connections required to create horizontal and vertical dipole correctors using the extra windings on the correction sextupoles. The other applications of the winding can be ignored here. Courtesy of Andreas Streun (SLS/PSI).

From tracking with Tracy-3 using the misalignment error model, orbit correction results have been acquired (cf. Fig. 3.8). These results show that the required rms kick strength is roughly  $80 \mu\text{rad}$  in the horizontal and  $110 \mu\text{rad}$  in the vertical plane. This should serve as a specification for the dipole correctors. The achievable kick angle in both planes should be no less than  $0.25 \text{ mrad}$ ; adding some extra as a safety margin would be advisable.

### 3.4.6. Orbit Correction

The MAX IV 1.5 GeV storage ring will be equipped with 36 beam position monitors (BPMs), 3 per achromat, covering the entire circumference of the ring. This will allow more than adequate sampling of orbit betatron oscillations given a horizontal and vertical tune of 11.22 and 3.14, respectively.

A decision is yet to be taken regarding how many will be equipped with fast electronics in the sense that they will be able to provide both single-pass capability for commissioning purposes as well as a 10 kHz data acquisition mode for the stored beam.

The philosophy for the orbit correction system will be to initially correct the orbit globally at low correction frequencies on the order of 10 Hz, which will be considered a slow orbit feedback (SOFB) system. Such correction can be done asynchronously and does not impose particularly demanding requirements on BPM hardware or corrector magnet power supplies. Post-commissioning the orbit correction system may be upgraded with faster BPM electronics and corrector magnet power supplies, if such are not installed by default, and the orbit correction frequency may be increased towards a 10 kHz level.

In order for this upgrade path to be possible, the vacuum chamber and correction magnets will be designed with future fast orbit feedback (FOFB) requirements in mind. These are a high actuator bandwidth as well as identical actuator response for all actuators in the ring. The latter requirement in practice mean identical corrector magnets as well as identical vacuum chamber cross-section and material at all actuator locations.

The controller used for the feedback will use the standard response matrix inversion via singular value decomposition (SVD) to compensate for the beam dynamics.

### 3.4.7. Coupling and Higher-order Correction

In addition to correcting the uncoupled linear optics and running an orbit feedback, it is in principle possible to correct the nonlinear optics and to restore nonlinear design settings. Also, transverse betatron motion needs to be uncoupled in order to achieve flat beams with minimum beam height in the IDs. On the other hand, reducing vertical beam size beyond the diffraction limit (“what the users can see”) should be avoided for lifetime reasons.

#### 3.4.7.1. Betatron Coupling

A set of skew quadrupoles can be used to minimize any remaining betatron coupling after the orbit has been corrected to the sextupole magnet centers. For this purpose two or more such skew quadrupoles could be added to the bare lattice if required. In principle four skew quadrupoles (two for control of  $h_{10100} \rightarrow \nu_x + \nu_y$  and two for control of  $h_{10010} \rightarrow \nu_x - \nu_y$ ) at a location with high  $\sqrt{\beta_x \beta_y}$  should be sufficient [8].

It has been shown at SLS using eight skew quadrupoles that minimizing vertical beam size at one location is equivalent to a global minimization of vertical beam size [9]. It remains to be shown in Tracy-3 simulations that the same holds for the MAX IV 1.5 GeV storage ring.

*This is ongoing work...*

It should however be noted that minimizing the overall betatron coupling might not be required. The vertical beam size should be lower than the diffraction limit for the most demanding beamline, but not lower for lifetime reasons. Therefore, dedicated skew quadrupoles should only become necessary if the betatron coupling of the well-corrected machine effectively renders too large vertical beam size. Considering the experience gathered at other recently commissioned storage ring sources, such high coupling values are not expected.

From the combined misalignment and field error models we acquire ???% rms betatron coupling for the bare lattice. This corresponds to a vertical emittance of  $\varepsilon_y = ???$  pm rad or a diffraction limit of  $\lambda_\gamma < ???$  Å. This can be seen as the minimum achievable coupling without additional (corrector-based) realignment and skew quadrupole correction.



### 3.4.7.2. Vertical Dispersion Bumps

We do not expect significant vertical dispersion to leak into the straights of the well-corrected machine. Tailoring the vertical dispersion with e.g. vertical dispersion bumps is not foreseen.

### 3.4.7.3. Sextupole Corrections

In the MAX IV 1.5 GeV storage ring all sextupoles are powered in families. In addition, the focusing sextupole gradient is integrated into the focusing quadrupoles (SQFi, SQFo) and hence the focusing sextupole gradient can only be freely adjusted by powering the thin correction sextupoles (SCi, SCo).

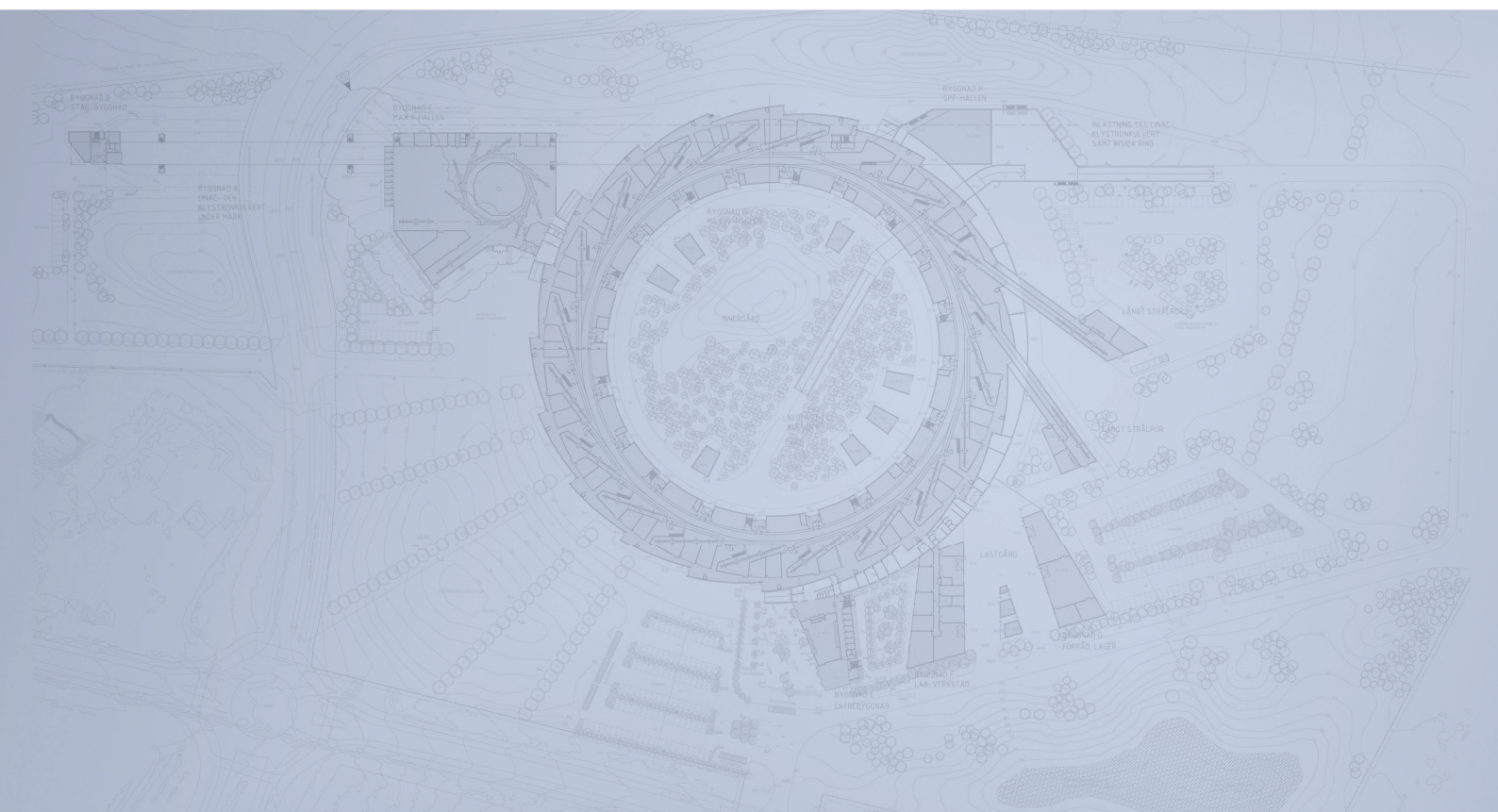
In case it becomes desirable to correct for local distortions of the sextupole pattern and to restore the nonlinear design optics, extra floating power supplies would have to be added to some dedicated sextupoles (SDi, SDo, SCi, SCo).

## References

- [1] J.B. Murphy, *Synchrotron Light Source Data Book*, available at <http://www.nsls.bnl.gov/newsroom/publications/otherpubs/dbook>
- [2] L.-J. Lindgren, private communication.
- [3] H. Wiedemann: *Particle Accelerator Physics I, Basic Principles and Linear Beam Dynamics*, 2<sup>nd</sup> Ed., Springer, Berlin, 1999.
- [4] R. Bartolini, I. P. S. Martin, J.H. Rowland, P. Kuske, F. Schmidt, Phys. Rev. ST Accel. Beams, 11, 104002, 2008.
- [5] S.C. Leemann, A. Streun, Unusual magnets in storage ring-based synchrotron light sources, under review.
- [6] E.I. Antokhin, I.N. Churkin, V.V. Demenev, O.B. Golubenko, V.N. Korchuganov, A.B. Ogurtsov, E.P. Semenov, A.G. Steshov, S.F. Mikhailov, L. Rivkin, Ch. Vollenweider, J.A. Zichy, *Precise Magnetic Measurements of the SLS Storage Ring Multipoles: Measuring System and Results*, Proceedings of the Second Asian Particle Accelerator Conference, Beijing, China, 2001, p. 209–211.
- [7] M. Böge, private communication.
- [8] J. Bengtsson, I. Pinayev, *NSLS-II: Control of Vertical Beam Size*, NSLS-II Technical Note, No. 7, Jan 31, 2007.
- [9] Å. Andersson, M. Böge, A. Lüdeke, V. Schlott, A. Streun, Nucl. Instr. and Meth. A, 591, p.437, 2008.



# Detailed Design Report



## Chapter 3

### MAX IV 1.5 GeV Storage Ring

#### 3.5. MAX IV 1.5 GeV Storage Ring Magnets

MAX IV Facility



# 3.5. MAX IV 1.5 GeV Storage Ring Magnets

---

**3.5. MAX IV 1.5 GeV Storage Ring Magnets.....2**

3.5.1. 2D Design ..... 5

3.5.2. 3D Design .....10

3.5.3. Bibliography.....10

## 3.5. MAX IV 1.5 GeV Storage Ring Magnets

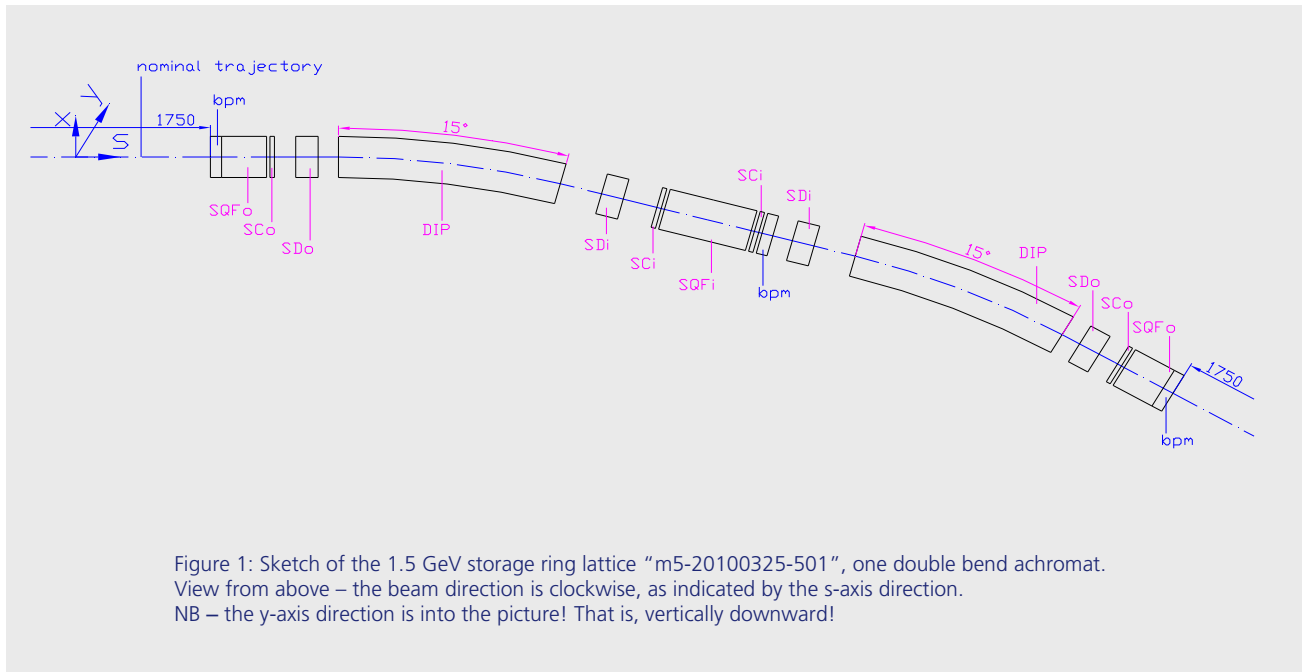
The 1.5 GeV storage ring lattice consists of twelve double bend achromats, with straight sections in between. The starting point for the design of the 1.5 GeV storage ring magnets is the “initial” lattice design “m5-20100325-501” (see chapter 3.2.1). In this lattice, the magnets are defined as hard edge elements. The magnets are designed by performing 3D field simulations and evaluating the integrated field in longitudinal slices. The lattice is refined by replacing the hard edge elements with slices as obtained from the 3D field simulations. A final refined lattice and magnet design is obtained by iterating towards a design which yields the same results in optics calculations as the initial lattice.

The magnet types in the m5-20100325-501 lattice are listed Table 1 and shown schematically in Figure 1. In Figure 1, the direction of the coordinate axes in beam optics calculations are shown. The magnet polarities in the lattice files are to be understood in the sense of this coordinate system.

Table 1: Magnet types in the 1.5 GeV storage ring.

Element	L [m]	Field strength	Comment
<b>SQFo</b>	0.2	$B' = 28.71 \text{ T/m}$ , $B''/2 = 183.6 \text{ T/m}^2$	Combined quadrupole/sextupole
<b>SCo,</b> <b>SCi</b>	0.02		Corrector
<b>SDo,</b> <b>SDi</b>	0.1	$B''/2 = -460.1 \text{ T/m}^2$ , $-366.5 \text{ T/m}^2$	<sup>1</sup>
<b>DIP</b>	1	$B_0 = 1.310 \text{ T}$ , $B' = -6.747 \text{ T/m}$	Gradient dipole
<b>SQFi</b>	0.4	$B' = 25.02 \text{ T/m}$ , $B''/2 = 140.3 \text{ T/m}^2$	Combined quadrupole/sextupole

<sup>1</sup> The lattice elements sdo and sdi differ only in strength, corresponding to one magnet type operated at two field strengths.





In addition to the lattice design, further constraints and specifications for the magnet design are introduced from other aspects of the accelerator design. Such additional specifications are listed in Table 2 and Table 3.

Table 2: Additional specified parameters for magnet design.

Parameter	Value	Unit	Comment
<b>Good field width:</b>			<sup>2</sup>
<b>Dip</b>	$\pm 10$	mm	
<b>Other elements</b>	$\pm 20$	mm	
<b>Vacuum chamber inner dim. (elliptical)</b>	$40 \times 20$	mm	See chapter 3.2.2
<b>Coolant water:</b>			<i>Saknar ref</i>
<b>Pressure drop (<math>\Delta p</math>)</b>	2	bar	
<b>Inlet temperature (<math>T_{in}</math>)</b>	25	°C	
<b>Temperature rise (<math>\Delta T</math>)</b>	$< 10$	°C	

Table 3: Additional specifications for magnet design.

Spec.	Description	Comment
<b>1</b>	All magnets in one double bend achromat are integrated into one solid iron block.	See chapter 3.2.1
<b>2</b>	All magnets of the same type and strength are connected electrically in series.	See chapter 3.2.6
<b>3</b>	Individual magnets shall be shunted electrically, before installation, to within ...	<i>Saknar info</i>
<b>4</b>	In the <i>Kraków option</i> , the magnets will be ramped from 400 MeV to 1.5 GeV. The magnet design shall be optimized for 1.5 GeV operation, but also evaluated for the corresponding field range.	(1)

<sup>2</sup> (4), based on initial lattice  $\beta_x$ , see chapter 3.2.2.

### 3.5.1. 2D Design

The first step of the 1.5 GeV storage ring magnet design was the transverse cross section of each magnet type. In this subchapter, this design step as defined by the initial lattice is presented. The design was performed with the help of 2D field simulations, using the FEMM (2) code. The minimum required transverse cross section dimensions for each magnet type, found by 2D simulations, defines the required dimensions of the magnet block. A sketch of the magnet block is shown in Figure 2.

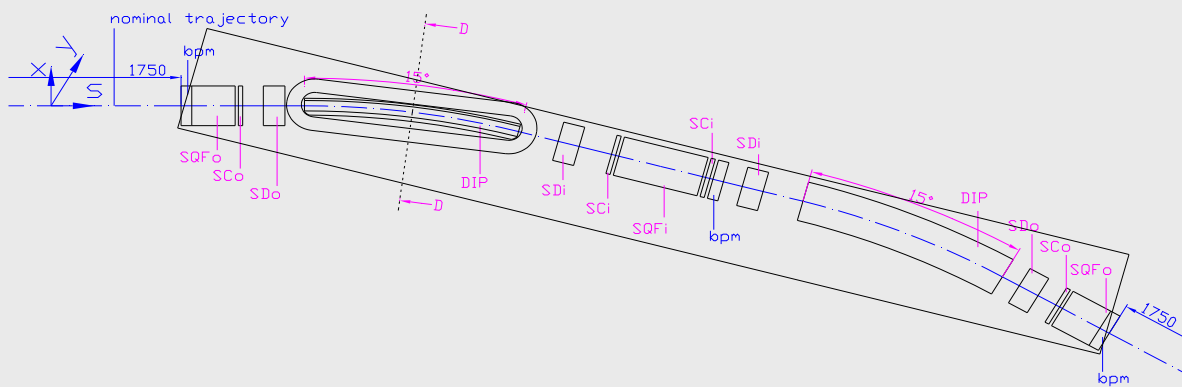


Figure 2: A sketch of the 1.5 GeV storage ring magnet block.

#### 3.5.1.1. Combined Quadrupole/Sextupole “SQFo”

The lattice element “SQFo” is a combined quadrupole/sextupole magnet. The specifications on which the design of this magnet type is based are listed in Table 4.

Table 4:  
Basic specifications for the magnetic element “SQFo”. From lattice design “m5-20100325-501” unless otherwise noted.

Parameter	Value	Unit	Comment
Effective length ( $L_{\text{eff}}$ )	0.2	m	
Quadrupole strength (k)	5.736667	/m <sup>2</sup>	
Sextupole strength (m)	36.676825	/m <sup>3</sup>	

Based on the specified inner size of the vacuum chamber (see Table 2), we estimate that a pole aperture of 44 mm will be sufficient. Another factor which controls the design of this magnet is the close proximity of the adjacent bpm and sextupole corrector “SCo” (see Figure 1.). Due to this, the coil length needs to be  $< 0.2$  m, which in turn requires that the pole root is shorter than the pole face (see Figure 2).

...

### 3.5.1.2. Sextupole Corrector

...

### 3.5.1.3. Sextupole

...

### 3.5.1.4. Gradient Dipole

The lattice element “DIP” is a gradient dipole magnet. The specifications on which the design of this magnet type is based are listed in Table 5.

Table 5:  
Basic specifications for the magnetic element “DIP”. From lattice design “m5-20100325-501” unless otherwise noted.

Parameter	Value	Unit	Comment
Bend angle	15	°	Sector magnet
Entrance/exit angle	0	°	
Effective length ( $L_{\text{eff}}$ )	1	m	
Quadrupole strength (k)	-1.347963	/m <sup>2</sup>	
Pole face strip $\Delta k$	min. $\pm 2$	%	$= \pm 0.026959$ /m <sup>2</sup> , see chapter 3.2.4
Return yoke geometry	C-dipole		(3)

The required pole gap depends on the height of the vacuum chamber and height required for the pole face strips, with some headroom for assembly and manufacturing tolerances. Based on the specified inner height of the vacuum chamber, 20 mm (see Table 2), we estimate that a pole gap of 28 mm (at  $x=0$ ) will be sufficient. The gradient dipole is the magnetic element in this lattice which requires the largest cross section. So, to minimize the height of the iron block<sup>3</sup> we have designed this magnet to be as small as possible in the vertical direction. This means that that the coil was made as wide and low as possible, taking into account the limited space between the gradient dipole and the adjacent sextupole SDo (see Figure 2).

<sup>3</sup> We assume here that the height is the most difficult factor in obtaining low carbon steel plate of the required size.

The resulting magnet design is defined by the FEMM 2D-model “MJ100721-67, DIP.fem” together with the design parameters listed in Table 5. This 2D-model is shown in Figure 3. Simulation results are shown in Figure 4, Table 5 and Figure 5.

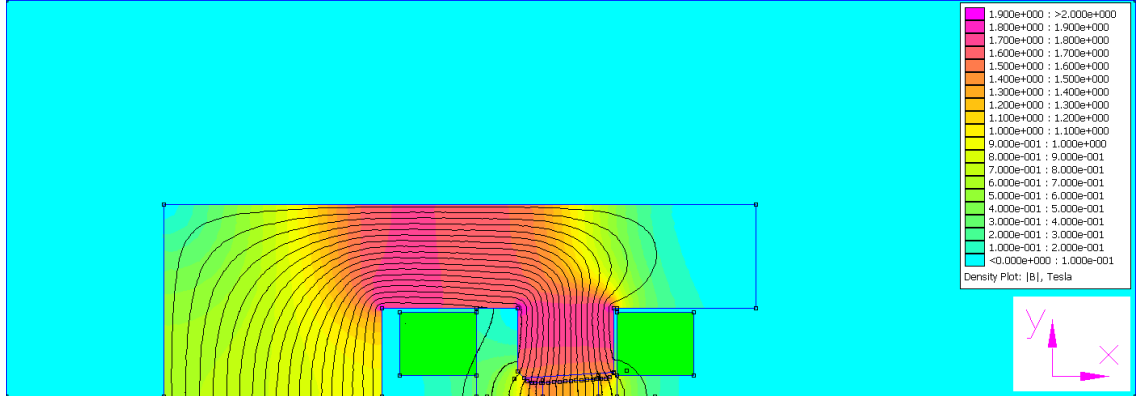


Figure 3: 2D field simulation result for the model “MJ100721-67, DIP.fem”, field distribution in the xy-plane. The colour scale goes from 0 to 2 T. The field in the pole root and middle of the return yoke is 1.7-1.8 T. The coil cross section is marked green. The model geometry corresponds to the cross section view D-D in Figure 2. The directions of the coordinate axes in the model are indicated in the lower right corner.

Table 6: Technical data for the gradient dipole magnet "DIP".

Parameter	Value	Unit	Comment
<b>Magnet type</b>	Gradient dipole		
<b>Pole gap</b>	28	mm	At $x=0$
<b>Nominal field (<math>B_0</math>)</b>	1.31035	T	At $x=0$
<b>Gradient (<math>B'</math>)*</b>	-6.74840	T/m	Corresponds to $k = -1.34829 / \text{m}^2$ , see Table 5
<b>Within gfw, residual field*</b>	$< \pm 1$	G	See Figure 5.
<b>Coils:</b>			
<b>Total current /magnet (NI)*</b>	32116	A	See Table 5
<b>No of coils /magnet</b>	2		
<b>Conductor</b>	OFHC copper, 12×12 mm, Ø7.5 mm internal cooling channel		
<b>Mean length /turn</b>	2.41	m	
<b>No of turns /coil</b>	20		5 turns in width × 4 turns in height direction
<b>No of turns /magnet (N)</b>	40		
<b>Nominal current (I)</b>	803	A	
<b>Resistance/coil at 20°C</b>	8.4	mΩ	
<b>Coil cooling</b>	Water cooled		
<b>No of cooling circuits /coil</b>	2		Coil consists of two double pancakes in parallel
<b>Pressure drop (<math>\Delta p</math>)</b>	2	bar	
<b>Flow /cooling circuit</b>	5.5	l/min	
<b>Temperature rise (<math>\Delta T</math>)</b>	7.5	°C	
<b>Voltage /magnet</b>	14.2	V	= 342 V for all 24 magnets in series, excl cabling
<b>Flow /magnet</b>	22	l/min	
<b>Yoke:</b>			
<b>Yoke geometry</b>	C-dipole		
<b>Material</b>	Armco low carbon steel		
<b>Height</b>	340	mm	= 170 mm per magnet half

- Field simulation results for FEMM 2D-model "MJ100721-67, DIP.fem".

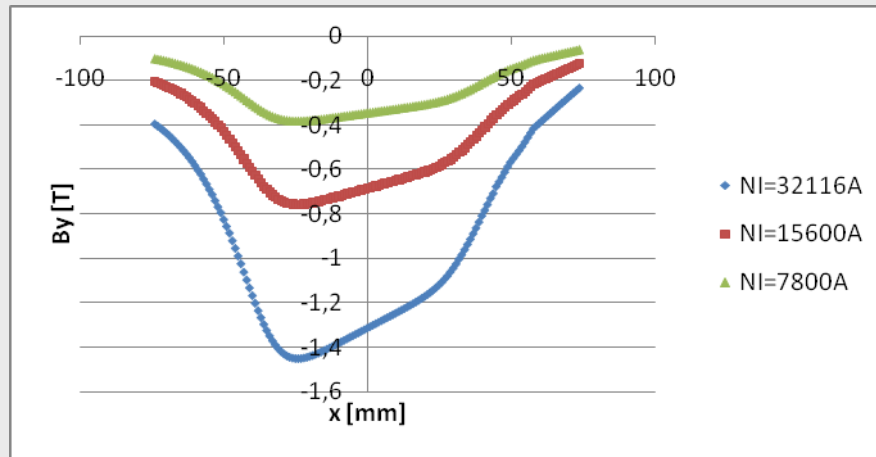


Figure 4: 2D field simulation data for the model "MJ100721-67, DIP.fem,  $B_y(x)$  at  $y=0$ . The simulation was repeated at three different current levels, corresponding to  $I = \text{ca } 400 \text{ MeV}$  to  $1.5 \text{ GeV}$ . The simulated field values are negative, corresponding to the field direction being vertically down, which is the correct polarity for this magnet (cf Figure 1, Figure 3).

Table 5: Results calculated from the simulation data shown in Figure 4.

	NI=32116A	NI=15600A	NI=7800A	Comment
<b><math>B_0</math> [T]</b>	-1.31588	0.68519	0.34435	at $x=0$
<b><math>B'</math> [T/m]</b>	6.77687	3.54736	1.78390	<sup>4</sup>
<b><math>k</math> [/m<sup>2</sup>]</b>	-1.34829	-1.35538	-1.35624	<sup>5</sup>

<sup>4</sup> Calculated as linear fit over  $x=\pm 10 \text{ mm}$ .

<sup>5</sup>  $k = B'/(-B_0)$ , where it is minus  $B_0$  because the y-axis in the FEMM model is opposite to y-axis in the optics calculations. (cf

Figure 1, Figure 3)

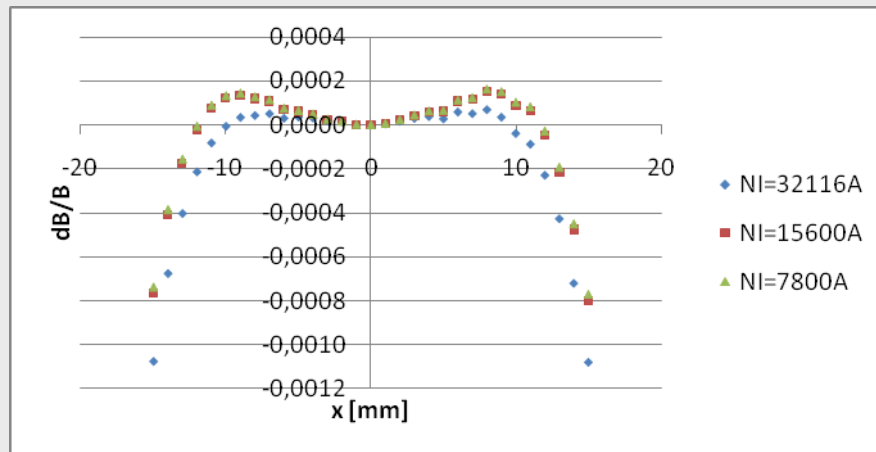


Figure 5:  $dB/B$  calculated from the data shown in Figure 4.  $dB/B(x) = (\text{simulated } B_y(x) - \text{linear fit } B_y(x)) / \text{linear fit } B_y(x)$ , where the linear fit is over  $x = \pm 10$  mm. For the simulation at  $NI = 32116$  A, max-min  $dB/B$  is 0.00011 over  $x = \pm 10$  mm – this corresponds to 1.4 G max-min residual.

### 3.5.1.5. Combined Quadrupole/Sextupole “SQFi”

...

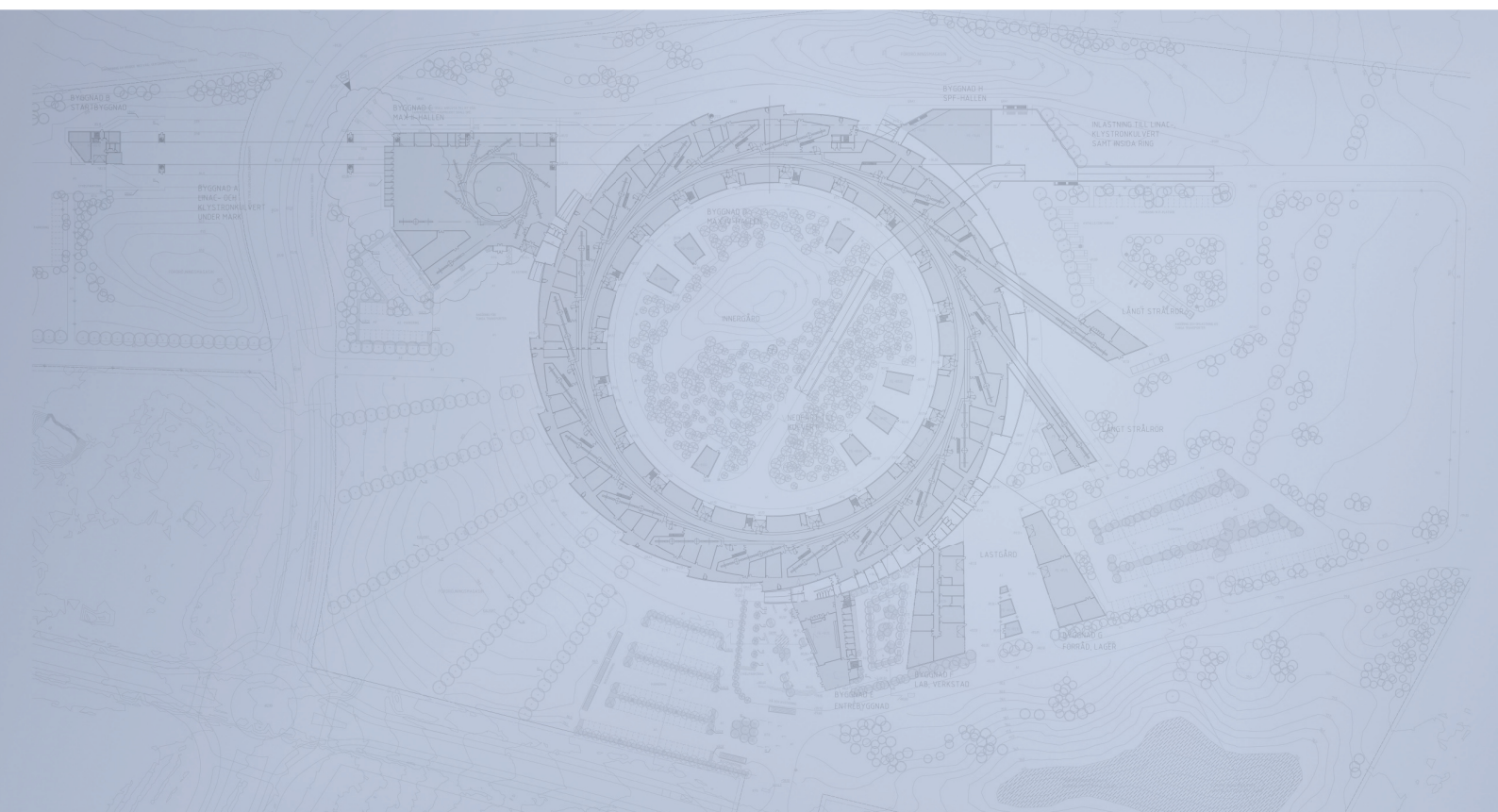
## 3.5.2. 3D Design

...

## 3.5.3. Bibliography

1. M. Eriksson (private communication, 100315).
2. D.C. Meeker, Finite Element Method Magnetics, version 4.2 02Nov2009 (Mathematica Build), <http://www.femm.info>.
3. L.-J. Lindgren (private communication, 100303) .
4. S. Leemann (private communication, 100713).

# Detailed Design Report



## Chapter 3

### MAX IV 1.5 GeV Storage Ring

#### 3.6. The Radio Frequency System

MAX IV Facility





## 3.6. The Radio Frequency System

---

<b>3.6.</b>	<b>The Radio Frequency System.....</b>	<b>2</b>
3.6.1.	General Discussion Motivating the 100 MHz System.....	2
3.6.2.	The 100 MHz RF System.....	3
3.6.3.	Description of the 100 MHz Cavities.....	4
3.6.4.	RF Station Structure.....	4
3.6.5.	Reliability .....	5
3.6.6.	HOM Suppression .....	5
3.6.7.	Control Loops .....	5
3.6.8.	300 MHz Higher Harmonic Cavities .....	6
3.6.9.	Description of Prototype Higher Harm. Cavity.....	7
	References .....	8

## 3.6. The Radio Frequency System

---

### 3.6.1. General Discussion Motivating the 100 MHz System

For reasons described in Chapter 2.6.1, an RF system based on slightly modified MAXII/MAXIII 100 MHz cavities will be chosen. Also a comparison of a 100 MHz and 500 MHz system for the MAX-II ring is performed in [1]. Actually the MAX-II ring, which is very similar to the MAX IV 1.5 GeV ring, has been operated with both RF systems together with passive Higher Harmonic Cavities (HHC) for bunch lengthening, so there is a practical experience in this case.

### 3.6.2. The 100 MHz RF System

Our aim is to use the slightly modified MAXII/MAXIII type cavities, as described in chapter 2.6. These should be able to handle up to 300 kV of accelerating voltage. We consider two cases. The first case is assuming that the ring will be equipped with relatively weak IDs like undulators, which we assume will emit radiation corresponding to a total energy loss per turn of 13 keV, resulting in a total loss of 130 keV per turn. Secondly we consider the Kraków option where one SCW, of similar type as the MAX-II SCWs, is installed. We then anticipate additional radiation emission of 20 keV per turn. Table 1 presents the data for two cases. We aim only for 4 % RF energy acceptance (bucket height), while the lattice energy acceptance is limited to roughly 3 % in the dispersive region.

Case	I	II
Energy loss with Ids	130keV	150keV
Circulating current	0.5A	0.5A
Total beam power	65kW	75kW
Total RF voltage	0.56MV	0.5MV
Number of cavities	2	2
Cavity shunt impedance	3.2Mohm	3.2Mohm
Cu losses	49kW	39kW
Total RF power needed	114kW	114kW
Nr of RF stations	2	2
Nr of transmitters	4	4
Transmitter power	28.5kW	28.5kW
Power to cavity	57kW	57kW
Cu losses/cav	24.5kW	19.5kW
Coupling (beta)	2.3	2.9
Cavity voltage	280kV	250kV
Bucket height	4.0%	3.5%

Table 1: Two anticipated RF scenarios for the 1.5 GeV ring.

**Case I:** Represents a 1.5 GeV ring equipped with only undulators.

**Case II:** Represents a 1.5 GeV ring equipped with additionally one SCW (*Kraków option*).

#### Some comments:

The natural choice of transmitter power is 30 kW. In this way two transmitters will be combined to feed one cavity, and the same principles of power regulation can be used as in the 3 GeV ring. Transmitters of exactly the same type as for MAX II and III may be used. The decrease in RF energy acceptance for the case with one SCW will affect the Touschek lifetime by roughly 20 % (see Ch 3.10). This configuration will be cost saving compared to go for 4.0 % RF EA. However, if this is found to limit the Krakow case performance, there is still room for higher voltage in the cavities, and one could simply install transmitters with slightly higher output.

### 3.6.3. Description of the 100 MHz Cavities

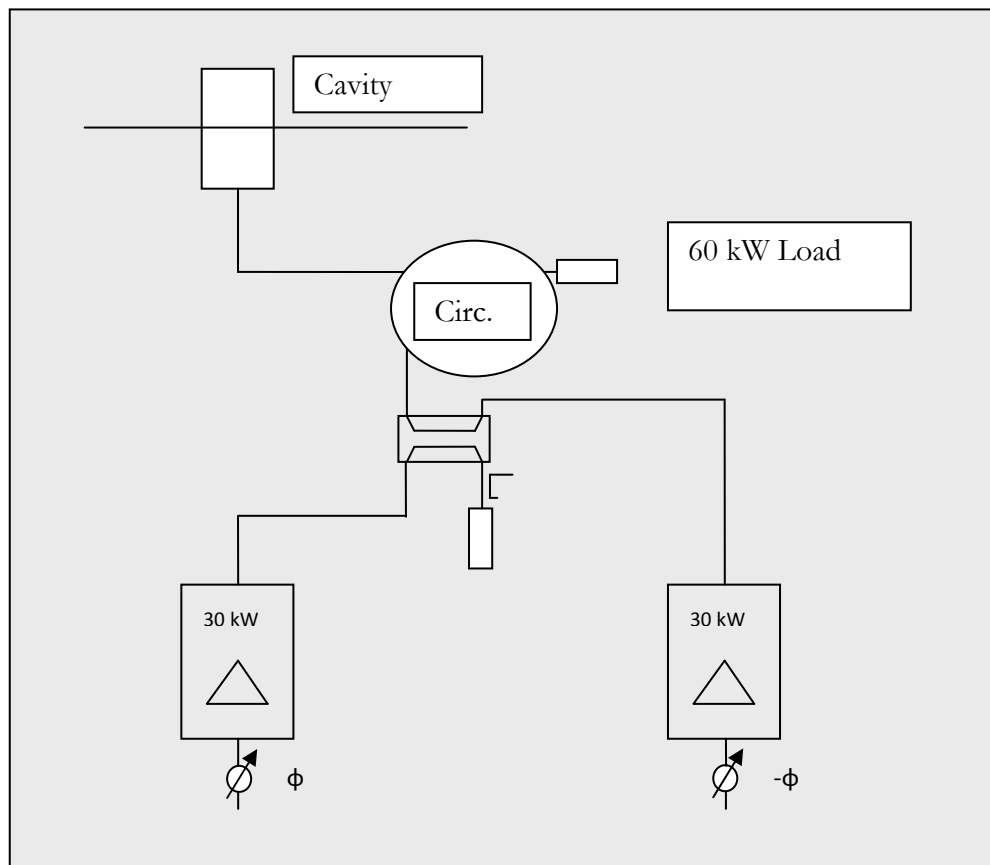
See Chapter 2.6.3.

### 3.6.4. RF Station Structure

#### 3.6.4.1. RF Station

It has been decided to abandon the principle of “pair” cavities, which would allow operating without a circulator. However this scheme is not yet fully tested and, most important, it decreases the RF station modularity (a station would consist of two cavities and four transmitters). The plan is now to combine two 30 kW transmitters to a 60 kW transmission line, equipped with a circulator and a load, and couple this power into one cavity. As mentioned above, two such stations will suffice even for the (*Kraków option*). The advantage of power regulation with phasing can be utilized, which means higher reliability since the transmitters can run at constant power (cf. Ch 2.6.4.1).

The MAX IV 1.5 GeV storage ring RF system will consist of two 60 kW RF stations, each one feeding one cavity. The available power from the net should be 100 kW per station, in order to allow for an overall efficiency of 60 %. The output power is fed via a circulator to the cavity. A 60 kW load is connected to the circulator. Alternatively the same type of circulator and load as in the 3 GeV ring may be used.



## **3.6.5. Reliability**

### **3.6.5.1. Few or many RF Stations**

Our experience from the present MAX facility is that the user community in a better way accept a running machine but with somewhat reduced intensity, compared to a complete shutdown. Many users perform their measurements during short periods like one or two days, and a shutdown of this length of course strikes hard on some unlucky users. Therefore a modular RF system, with two, instead of one, RF station, seems to be preferable. In this way a failure in one RF station or one cavity might be relatively harmless considering the possibility to tune away or even remove a cavity from the ring. The ring could then be operated at half nominal current with an RF energy acceptance exceeding at least 2 %.

### **3.6.5.2. Measures to Increase Reliability**

See Ch. 2.6.5.2

## **3.6.6. HOM Suppression**

### **3.6.6.1. Prototype HOM Couplers**

See Ch 2.6.6.1

## **3.6.7. Control Loops**

### **3.6.7.1. Resonant Frequency Control**

Two frequency loops, one for each cavity, will keep the cavities tuned by compensating for both beam loading and temperature effects. Cavity tuning is performed by an elastic deformation of the cavity in the direction of its axial length. This is realised by means of a mechanism, driven by a stepper motor, which changes the width of the gap of the capacitor in the cavity and therefore its frequency. The motor is controlled in closed loop with the output signal from a phase detector, which is proportional to the phase difference between the cavity incident signal from a directional coupler and cavity voltage from monitoring pick-up in the cavity. A phase shifter in the control loop makes it possible to adjust the phase offset.

### **3.6.7.2. Phase Control**

A phase control loop compensates for phase changes in the amplification chain. The RF signal from the master oscillator and the cavity phase are compared in phase and the error signal drives through a PID regulator an electronic phase shifter. The relative phases between the two stations are controlled by a mechanical phase shifter at the input of each of the stations amplifier stages.

### 3.6.7.3. Voltage Control

The amplitude control loop adjusts the relative phase difference between the drive of the two transmitters in the RF system. By this the amplifiers can deliver full power but some fraction of the output power will be directed to the dummy load connected to the fourth port of 3 dB hybrid.

## 3.6.8. 300 MHz Higher Harmonic Cavities

### Lund case:

A rough estimate of the required voltage for the higher harmonic cavities (HHC) are 187 kV, that is, one third of the sum of main cavity voltages. However, due to the synchronous phase angle of 13 degrees in the case of 130 keV losses per turn and a main RF voltage of 560 kV, a more precise number is 181 kV. This includes the assumption of a total shunt impedance for the HHC of 10 Mohm ( $R=U^2/P$ ), and that they are passively driven by the beam itself (additional 7 keV loss per turn). The form factor influence on the tuning angle of the Landau cavities has been taken into account in a self-consistent way. This gives an rms bunch length of 65 mm, for a symmetric potential well. The bunch shape is rather non-Gaussian, and the  $FWHM/2.355=86$  mm. The achievable rms bunch length is almost insensitive to the chosen shunt impedance, in the 5-20 Mohm range. Also above this range, no considerable gain length is made. 10 Mohm seems to be a safe choice to stay Robinson stable regarding the double RF system, even for a current of only 200 mA.

The natural rms bunch length for the case studied is 14.7 mm, and the synchrotron frequency 7.41 kHz. The double RF will create a spread in synchrotron frequencies, thus providing for Landau damping.

The prototype HHC (see below) is of the same capacity loaded type as the main cavities. This is helping us to push up the HOMs in frequency, and making the HOM suppression easier. The shunt impedance for this type of HHCs is 5 Mohm. By choosing two such cavities, each would pull 1.6 kW out of the beam. We could also think of a higher number (if the HOMs are sufficiently damped) in order to decrease the power consumption, since our experience of several passive cavities are good (phasing problems are not there, because of the passive nature).

### Krakow case:

A rough estimate of the required voltage for the higher harmonic cavities (HHC) are 167 kV, that is, one third of the sum of main cavity voltages. However, due to the synchronous phase angle of 17 degrees in the case of 150 keV losses per turn and a main RF voltage of 500 kV, a more precise number is 158 kV. This includes the assumption of a total shunt impedance for the HHC of 10 Mohm ( $R=U^2/P$ ), and that they are passively driven by the beam itself (additional 5 keV loss per turn). The form factor influence on the tuning angle

of the Landau cavities has been taken into account in a self-consistent way. This gives an rms bunch length of 70 mm, for a symmetric potential well. The bunch shape is rather non-Gaussian, and the  $\text{FWHM}/2.355 = 91$  mm. The achievable rms bunch length is almost insensitive to the chosen shunt impedance, in the 5-20 Mohm range. Also above this range, no considerable gain length is made. 10 Mohm seems to be a safe choice to stay Robinson stable regarding the double RF system, even for a current of only 200 mA.

The natural rms bunch length for the case studied is 16.4 mm, and the synchrotron frequency 6.94 kHz. The double RF will create a spread in synchrotron frequencies, thus providing for Landau damping.

The prototype HHC (see below) is of the same capacity loaded type as the main cavities. This is helping us to push up the HOMs in frequency, and making the HOM suppression easier. The shunt impedance for this type of HHCs is 5 Mohm. By choosing two such cavities, each would pull 1.2 kW out of the beam. We could also think of a higher number (if the HOMs are sufficiently damped) in order to decrease the power consumption, since our experience of several passive cavities are good (phasing problems are not there, because of the passive nature).

### 3.6.9. Description of Prototype Higher Harm. Cavity.

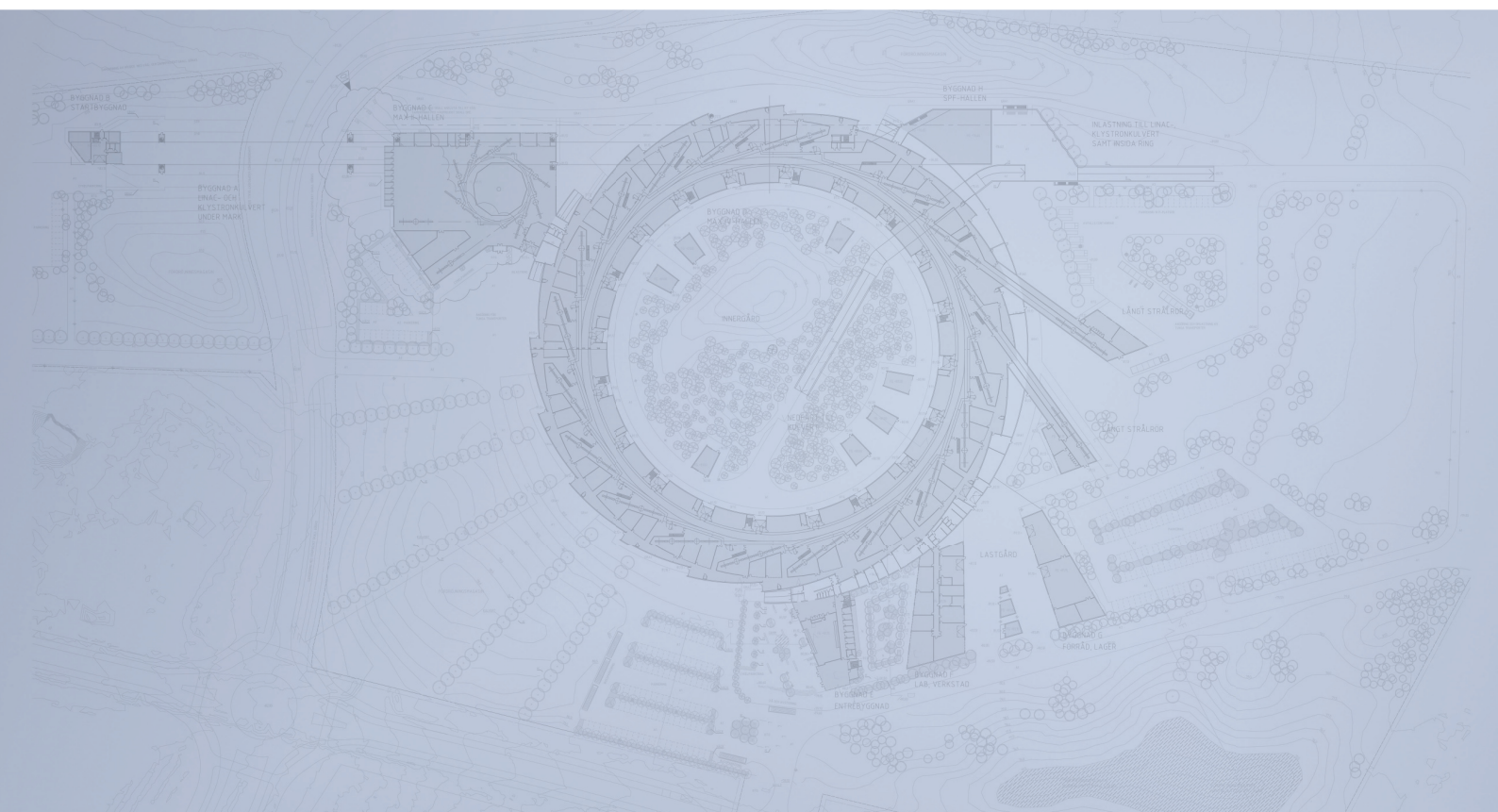
See Ch. 2.6.9.



## References

- [1] Å. Andersson et al, "The 100 MHz RF System for MAX-II and MAX-III", EPAC 2002.
- [2] B. Dwersteg et al, "HOM Couplers for normal conducting Doris 5-cell cavities", IEEE Trans. Nucl. Sci. 32, 1985.

# Detailed Design Report



## Chapter 3

### MAX IV 1.5 GeV Storage Ring

#### 3.7. Injection

MAX IV Facility



## 3.7. Injection

---

<b>3.7.</b>	<b>Injection.....</b>	<b>2</b>
3.7.1.	Transfer Linac to MAX 1.5 Ring.....	2

## 3.7. Injection

---

### 3.7.1. Transfer Linac to MAX 1.5 Ring

The beam from the linac is transferred to the ring by an achromatic bend in the vertical plane. The total bend angle is 30 deg. The transport line passes through the

1 meter thick floor between the linac tunnel and the storage ring plane. The vertical displacement is 4.5 m (figure 1.)

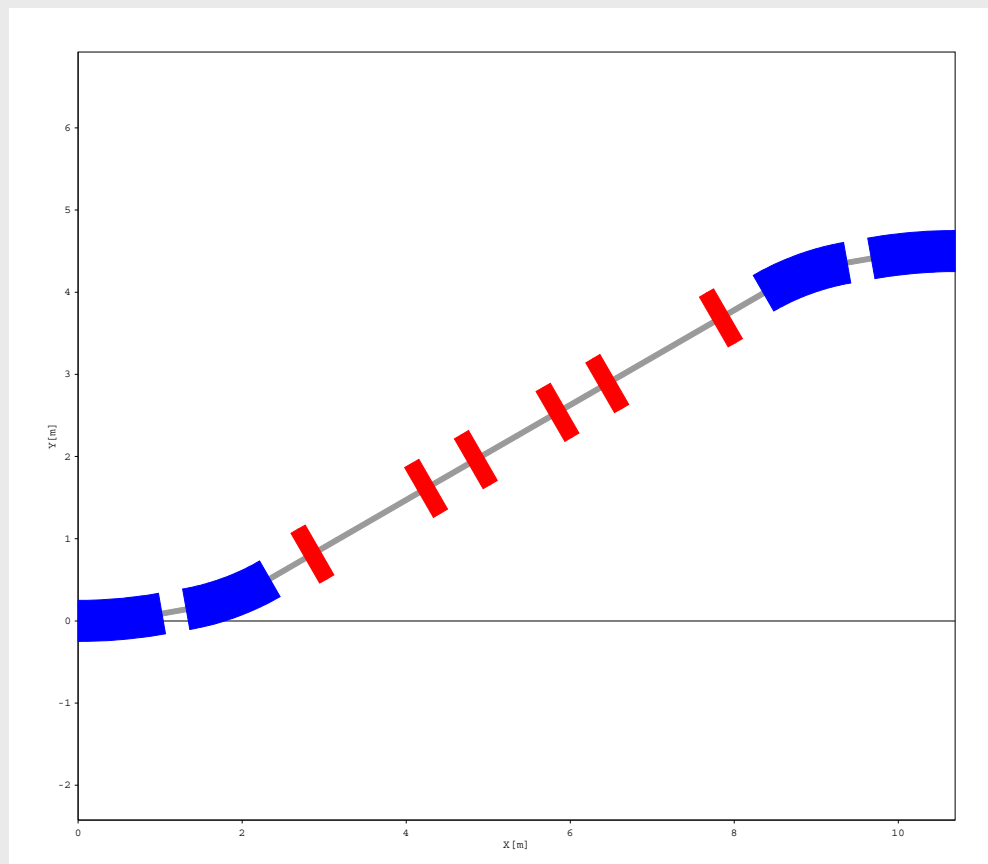


Figure.1: Linac- Ring transfer.

It can not be avoided that some of the focusing elements are inside the thick floor. Space enough must be provided for those quadrupoles, not only for the physical size but also for the alignment procedure, cooling water and electrical connections.

The optical data for the transfer line are given below. It is assumed that the beta functions from the linac at the beginning of the transfer are 10 m in both directions. The lattice is rather flexible and beta functions can be changed at least 50%. Presently the lattice is symmetric with three families of quadrupoles . The lattice should be retuned when the geometric and optical parameters for the extraction point from the linac is known.

**Transport section up to m1.5 30 deg.**

VSEPS: SBEND,L=1.027,ANGLE=10., E1=0,E2=0,&

FINTX=0.5,HGAP=0.0025,FINT=0.5,TILT=90

VDIPS: SBEND,L=1.090835,ANGLE=20., E1=0,E2=0,&

FINTX=0.5,HGAP=0.0075,FINT=0.5,TILT=90

**10VDIP: SBEND,L=1.090835,ANGLE=-20., E1=0,E2=0,&**

FINTX=0.5,HGAP=0.0075,FINT=0.5,TILT=90

VSEP: SBEND,L=1.027,ANGLE=-10., E1=0,E2=0,FINT=0.5,HGAP=0.0025,&

FINTX=0,TILT=90

QVFD: QUADRUPOLE,L=0.1, K1=-5.49005

**15QHF:QUADRUPOLE,L=0.1, K1=5.04897**

QVF:QUADRUPOLE,L=0.1, K1=-4.5761

F1: DRIFT,L=0.3

F2: DRIFT,L=1.4

F3: DRIFT,L=0.5

**20 F4: DRIFT,L=0.475**

F5: DRIFT,L=0.5

BLT: LINE=(F5,QVFD,QVFD,F2,QHF,QHF,F3,QVF,QVF,F4

B1: LINE=(VSEPS,F1,VDIPS,BLT)

B2: LINE=(-BLT,VDIP,F1,VSEP)

**25 TOT: LINE=(B1,B2)**

USE,TOT

DIMAT

ELEMENT	#	BETAX	ALPHAX	BETAY	ALPHAY	ETAX	ETAPX	ETAY	ETAPY	NUX	NUY	ACC.LEN
\$\$INITIAL\$\$	0	10	0	10	0	0	0	0	0	0	0	0
VSEPS	1	10.107	-0.1042	9.8029	0.19	0	0	0.0894	0.1736	0.01629	0.01645	1.027
F1	2	10.1784	-0.1342	9.6984	0.1583	0	0	0.1415	0.1736	0.021	0.02135	1.327
VDIPS	3	10.6074	-0.2595	8.3667	1.0125	0	0	0.507	0.4897	0.03773	0.04028	2.418
F5	4	10.8921	-0.3098	7.4147	0.8915	0	0	0.7519	0.4897	0.04514	0.05039	2.918
QVFD	5	11.5663	-6.5559	6.8455	4.6954	0	0	0.7799	0.0673	0.04657	0.0526	3.018
QVFD	6	13.6115	-14.2683	5.6045	7.4869	0	0	0.7652	-0.3588	0.04785	0.05515	3.118
F2	7	83.022	-35.3107	4.5939	-6.7651	0	0	0.2629	-0.3588	0.05448	0.51066	4.518
QHF	8	85.8749	7.2632	6.3323	-10.9107	0	0	0.2334	-0.234	0.05467	0.51364	4.618
QHF	9	80.2135	48.3948	9.1066	-17.2972	0	0	0.2158	-0.1211	0.05486	0.51575	4.718
F3	10	39.1213	33.7897	34.6448	-33.7793	0	0	0.1552	-0.1211	0.05628	0.52023	5.218
QVF	11	34.2696	15.4652	39.9598	-18.5568	0	0	0.1397	-0.1888	0.05672	0.52066	5.318
QVF	12	32.7447	0.015	41.8432	0.0109	0	0	0.1178	-0.2479	0.0572	0.52104	5.418
F4	13	32.7374	0.0005	41.8383	-0.0005	0	0	0	-0.2479	0.05951	0.52285	5.893
F4	14	32.7438	-0.014	41.8441	-0.0119	0	0	-0.1178	-0.2479	0.06181	0.52466	6.368
QVF	15	34.2684	-15.4637	39.9609	18.5564	0	0	-0.1397	-0.1888	0.06229	0.52504	6.468
QVF	16	39.1197	-33.7873	34.646	33.7794	0	0	-0.1552	-0.1211	0.06273	0.52547	6.568
F3	17	80.2089	-48.391	9.1074	17.2977	0	0	-0.2158	-0.1211	0.06415	0.52995	7.068
QHF	18	85.8697	-7.2618	6.3331	10.911	0	0	-0.2334	-0.234	0.06434	0.53206	7.168
QHF	19	83.0168	35.3094	4.5946	6.7651	0	0	-0.2629	-0.3588	0.06453	0.53504	7.268
F2	20	13.6095	14.2672	5.6023	-7.4849	0	0	-0.7652	-0.3588	0.07116	0.99054	8.668
QVFD	21	11.5645	6.5558	6.843	-4.6946	0	0	-0.7799	0.0673	0.07244	0.99309	8.768
QVFD	22	10.8901	0.3107	7.4121	-0.8921	0	0	-0.7519	0.4897	0.07387	0.9953	8.868
F5	23	10.6046	0.2603	8.3649	-1.0133	0	0	-0.507	0.4897	0.08128	1.00542	9.368
VDIP	24	10.1738	0.135	9.6986	-0.1593	0	0	-0.1415	0.1736	0.09802	1.02435	10.459
F1	25	10.1018	0.1049	9.8037	-0.191	0	0	-0.0894	0.1736	0.10273	1.02924	10.759
VSEP	26	9.9933	0.0014	10.0028	-0.001	0	0	0	0	0.11903	1.04569	11.786

A plot of the twiss functions is given below in figure 2.

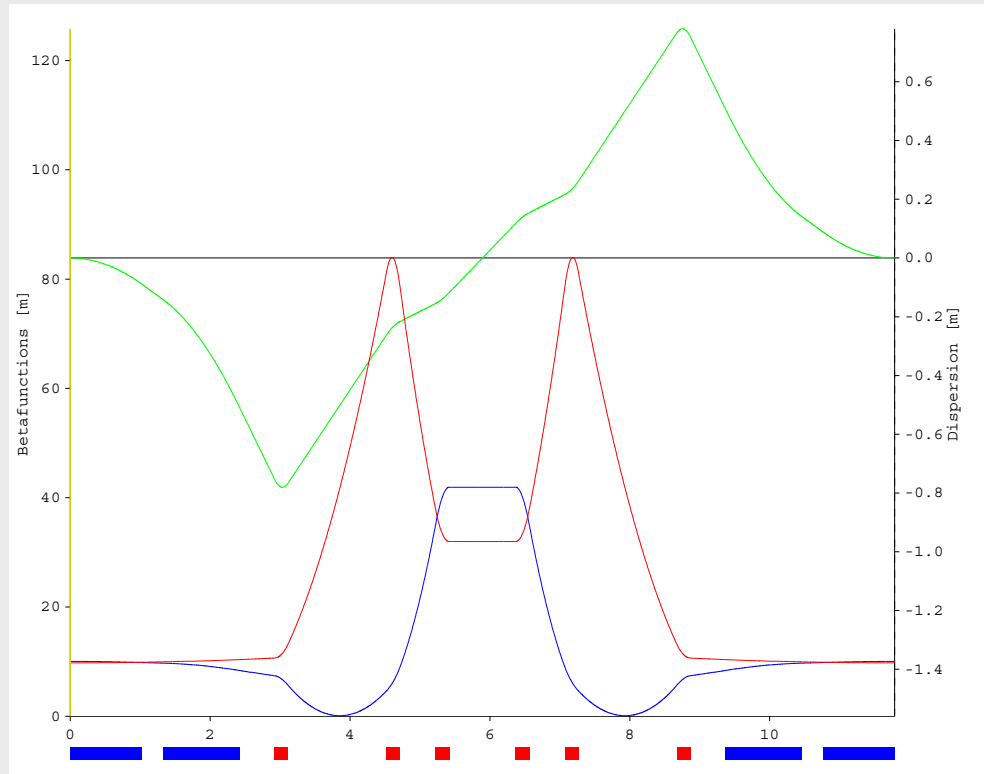


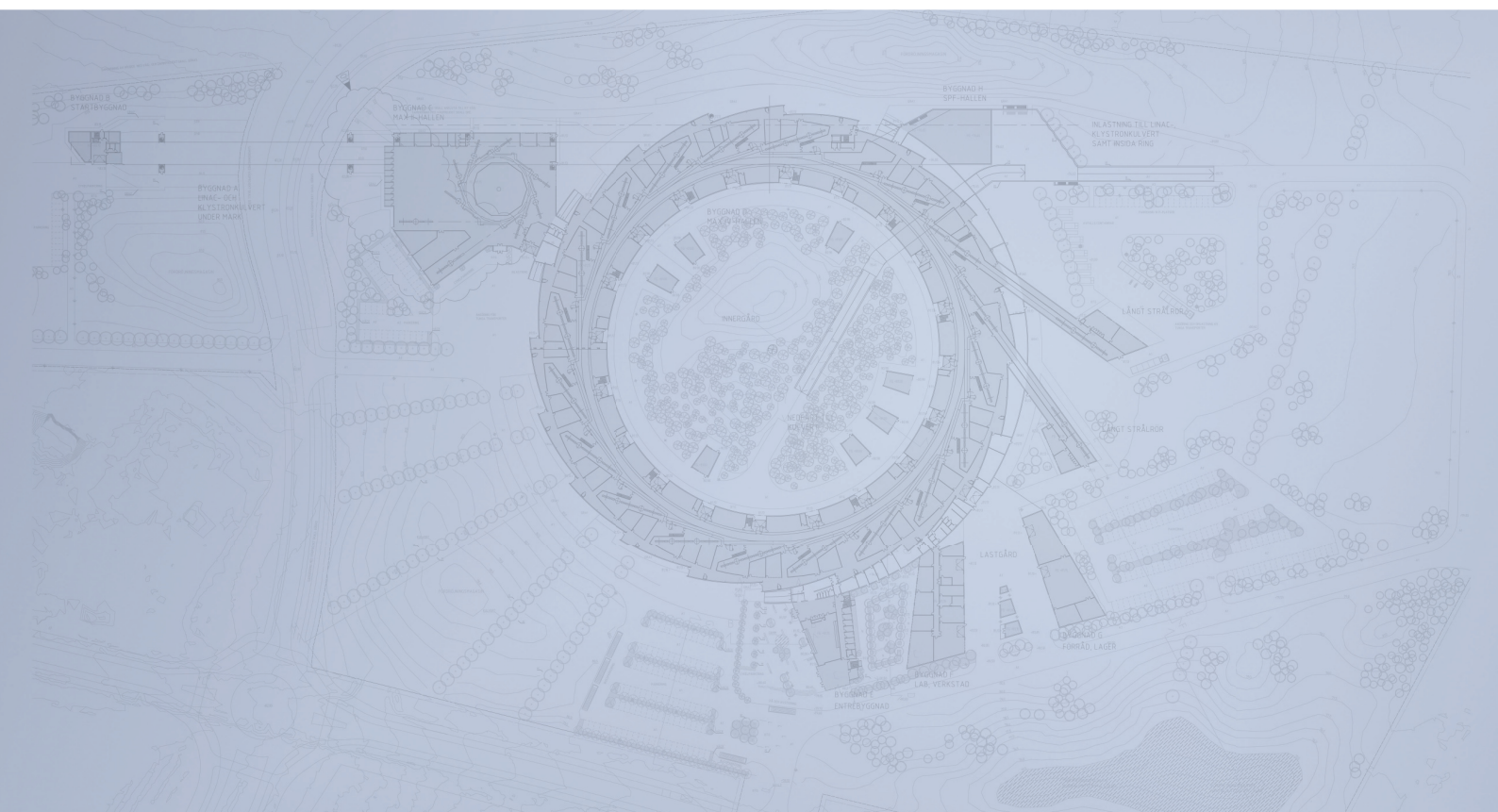
Figure 2: Twiss functions.



The geometric layout of the transferline is found in table below

#	NAME	S	X	Y	Z	THETA	PHI	PSI
1	VSEPS	-1.027	0.00156	-0.08938	-1.02179	-0.17632	9.998461	1.015423
2	F1	-1.327	0.002469	-0.14147	-1.31724	-0.17632	9.998461	1.015423
3	VDIPS	-2.41784	0.008948	-0.51261	-2.33709	-0.5773	29.99496	1.154661
4	F5	-2.91784	0.013311	-0.76257	-2.7701	-0.5773	29.99496	1.154661
5	QVFD	-3.01784	0.014183	-0.81256	-2.8567	-0.5773	29.99496	1.154661
6	QVFD	-3.11784	0.015056	-0.86255	-2.94331	-0.5773	29.99496	1.154661
7	F2	-4.51784	0.027273	-1.56245	-4.15574	-0.5773	29.99496	1.154661
8	QHF	-4.61784	0.028145	-1.61244	-4.24235	-0.5773	29.99496	1.154661
9	QHF	-4.71784	0.029018	-1.66243	-4.32895	-0.5773	29.99496	1.154661
10	F3	-5.21784	0.033381	-1.91239	-4.76196	-0.5773	29.99496	1.154661
11	QVF	-5.31784	0.034254	-1.96239	-4.84856	-0.5773	29.99496	1.154661
12	QVF	-5.41784	0.035126	-2.01238	-4.93517	-0.5773	29.99496	1.154661
13	F4	-5.89284	0.039271	-2.24984	-5.34653	-0.5773	29.99496	1.154661
14	F4	-6.36784	0.043416	-2.48731	-5.75789	-0.5773	29.99496	1.154661
15	QVF	-6.46784	0.044289	-2.5373	-5.84449	-0.5773	29.99496	1.154661
16	QVF	-6.56784	0.045161	-2.58729	-5.9311	-0.5773	29.99496	1.154661
17	F3	-7.06784	0.049524	-2.83725	-6.36411	-0.5773	29.99496	1.154661
18	QHF	-7.16784	0.050397	-2.88725	-6.45071	-0.5773	29.99496	1.154661
19	QHF	-7.26784	0.05127	-2.93724	-6.53731	-0.5773	29.99496	1.154661
20	F2	-8.66784	0.063486	-3.63713	-7.74975	-0.5773	29.99496	1.154661
21	QVFD	-8.76784	0.064359	-3.68712	-7.83635	-0.5773	29.99496	1.154661
22	QVFD	-8.86784	0.065232	-3.73712	-7.92295	-0.5773	29.99496	1.154661
23	F5	-9.36784	0.069595	-3.98708	-8.35597	-0.5773	29.99496	1.154661
24	VDIP	-10.4587	0.076073	-4.35822	-9.37582	-0.17632	9.998461	1.015423
25	F1	-10.7587	0.076982	-4.41031	-9.67126	-0.17632	9.998461	1.015423
26	VSEP	-11.7857	0.078542	-4.49969	-10.6931	0	0	1

# Detailed Design Report



## Chapter 3

### MAX IV 1.5 GeV Storage Ring

#### 3.8. Vacuum System

MAX IV Facility



## 3.8. Vacuum System

---

<b>3.8.</b>	<b>Vacuum System .....</b>	<b>2</b>
3.8.1.	Design Philosophy and Objectives.....	2
3.8.2.	1.5 GeV Ring Structure.....	3
3.8.3.	Injection Straight .....	6
3.8.4.	Vacuum Diagnostics.....	6
3.8.5.	Installation .....	6
3.8.6.	Pump Down .....	6
3.8.7.	Beam Induced Pressure.....	6
3.8.8.	Venting and Maintenance.....	6
3.8.9.	Conditioning/Performance .....	6
3.8.10.	Synchrotron Heat Load .....	7

## 3.8. Vacuum System

---

### 3.8.1. Design Philosophy and Objectives

The vacuum system design follows the principles of the 3 GeV ring system; chapter 2.8. Main differences regarding the vacuum system are:

- Smaller ring radius = larger angles in each section
- Shorter magnet sections
- Larger magnet apertures

The latter two points' result in enhanced conductance compared to the 3 GeV ring.

Detailed design will be made as the details in magnets and diagnostics are known.

BPM's, flanges, and bellows will be put at each end of the straight sections. The building and installation of vacuum chambers will be done in steps:

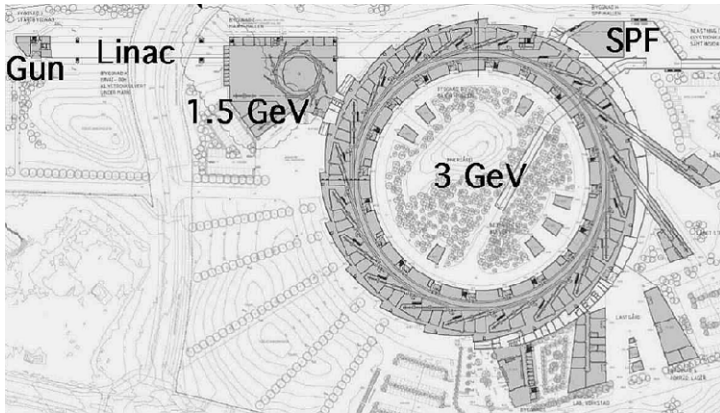
1. For the first beam tests mainly circular tubes will be installed in the straight sections with a few beam exit ports.
2. Beam lines will be added as insertion devices are installed in the straights.

Reference labels for machine parts (e.g. 101\*\*.BPM\*\*) are used in this document following the convention;

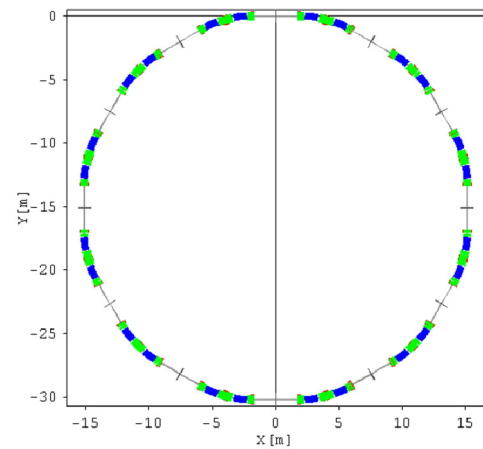
[http://www.maxlab.lu.se/local/maxiv\\_reports/accelerators\\_machine/General\\_description/MAX\\_IV\\_Naming\\_Convention\\_100426.pdf](http://www.maxlab.lu.se/local/maxiv_reports/accelerators_machine/General_description/MAX_IV_Naming_Convention_100426.pdf)

The naming document will be updated whenever new components are defined.

### 3.8.2. 1.5 GeV Ring Structure



The 1.5 GeV ring is placed above the linac before the large 3 GeV ring



Ring lattice, see § 3.8.2.1 for one cell

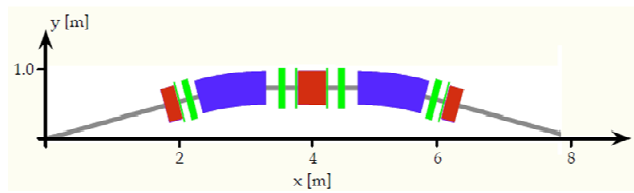
The ring consists of 12 identical achromatic magnet cells with straight sections in between. Gate valves will divide the ring in vacuum system sections. Each section has a valve for connection to a mobile turbo pump station for roughing, one ion pump, and NEG coating as the main pumping system.

One straight section is dedicated for the injection system, one for the RF, and the other 10 straight sections may be used for insertion devices.

<b>Circumference</b>	96 m
<b>Number of identical magnet cells</b>	12
<b>Total bending angle per cell</b>	30 degrees (523.6 mrad)
<b>Length of achromat</b>	8 m
<b>Length of straight sections for insertion devices (BPM to BPM)</b>	3.5 m; including bellows and gate valves at both ends
<b>Minimum bending radius in dipoles</b>	3.82 m
<b>Beam height over the floor</b>	1.3 m

### 3.8.2.1. Magnet Cell

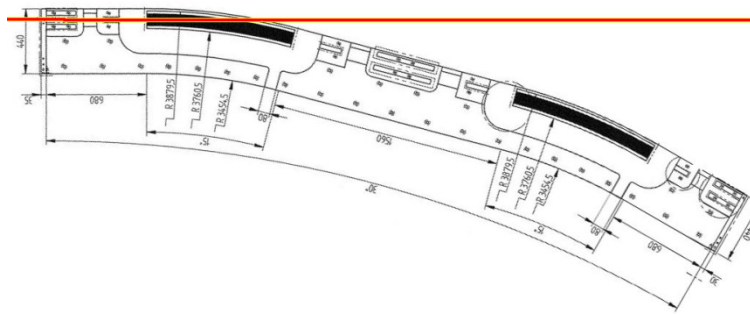
Figure 1: Schematic of one achromat (magnet cell).



Blue: Dipole

Green: Sextupole

Red: Quadrupole



Magnet section

The upper profile of the lower common yoke is shown.

The photon beam (red) leaves the magnet cell at the first dipole section.

Conical transitions (10-20°) will be used in order to match different chambers apertures.

<b>Proposed flange type</b>	ConFlat
<b>Vacuum chambers</b>	NEG-coated OFHC. Possibly GlidCop at high power areas
<b>Dipole vertical aperture</b>	Slanted, 28 mm at the beam path
<b>Pipe ID</b>	40 x 20 mm
<b>Pipe OD</b>	44 x 24 mm (to be confirmed)
<b>NEG activation</b>	By heating the outside of the chamber, 180-200°C, 24hrs
<b>Pole face winding</b>	Conductor plus insulation maximum 1mm thick

Table 1: Some dipole and vacuum chamber data.

All magnets are made in an upper and a lower part. For installation or baking of the vacuum chambers the upper parts may be lifted off.

The expansion of 3 mm/m during baking will cause too high stresses in the chambers. We study the approach to lift the magnet section chambers to be baked separated from the rest of the system. See chapter 2.8.8 for the concept.

### 3.8.2.2. Components in the Cell

#### 3.8.2.2.1. BPM Heads

The BPM will use the same body as for the 3 GeV ring, but with an increased aperture matching the chambers for the quadrupoles.

#### 3.8.2.2.2. Bellows and RF-Shields

Similar to the 3 GeV design.

#### 3.8.2.2.3. Flanges

Similar to the 3 GeV design.

#### 3.8.2.2.4. Valves

Similar to the 3 GeV design.

#### 3.8.2.2.5. Vacuum Chambers in the 1.5 GeV Ring

Magnet section:

NEG coated copper chambers with wall thickness  $\geq 1.5\text{mm}$

Circular ID xx mm in quadrupoles and sextupoles

Elliptical 40 x 30 mm in dipoles

Straight sections:

Depending on insertion device, diagnostics, and injection system

Where nothing is installed; the circular copper chamber

#### 3.8.2.2.6. Photon Beamline Components

Similar to the 3 GeV Ring.

#### 3.8.2.2.7. Beam Interaction with Chamber Dimension Variations

The electron beam will interact with cavities between flanges, bellows, and other geometry variations resulting in both disturbances of the beam and heat load on the vacuum chamber. The effects are studied and described in the chapter 3.11 Beam Instabilities.

### 3.8.2.3. Insertion Devices

Selected data from part 5 Insertion devices will be imported.



### **3.8.3. Injection Straight**

To be written.

#### **3.8.3.1. RF Section**

One 100 MHz cavity and one Landau cavity (300 MHz) will be installed in one straight section.

The cavities have the same design as for the 3 GeV ring.

### **3.8.4. Vacuum Diagnostics**

The concept of the 3 GeV ring will be used.

### **3.8.5. Installation**

Similar to the 3 GeV ring.

### **3.8.6. Pump Down**

Similar to the 3 GeV ring.

### **3.8.7. Beam Induced Pressure**

Similar to the 3 GeV ring.

### **3.8.8. Venting and Maintenance**

Similar to the 3 GeV ring.

### **3.8.9. Conditioning/Performance**

#### **3.8.9.1. Baking System**

Similar to the 3 GeV ring.

##### **3.8.9.1.1. Straight Sections**

Similar to the 3 GeV ring.

### 3.8.9.2. Length Dimensions at Baking

The path length	Room temperature 20°C	Expansion at 200°C
Complete ring	96 m	0.63 m (Cu) dR = 100 mm if circle
Magnet section	4.5 m	14 mm (OFC) 1.76e-5/degC
Straight sections	3.5 m	16 mm (pure Al) 2.6e-5/degC

### 3.8.10. Synchrotron Heat Load

Formulas for the calculations are according to paragraph in chapter 2.8. Heat load on the walls will be of the same order as in MAX II and the 3 GeV ring.

#### 3.8.10.1. Cooling Water Need

Not calculated.



# MAX IV Facility



## 3.9. Diagnostics (RF and Vacuum not Included)

---

<b>3.9.</b>	<b>Diagnostics (RF and Vacuum not Included) .....</b>	<b>2</b>
3.9.1.	BPMs (Required Performance: Stored Beam and Single Beam Passage) ..	2
3.9.2.	Tune Measurement: Stripline Monitor and/or Button BPMs .....	2
3.9.3.	Current Measurement: DCCT and BPMs. ....	3
3.9.4.	Emittance Monitor: Pi-Polarization Method .....	4
3.9.5.	Bunch Length Monitor .....	5
3.9.6.	Filling Pattern or Bunch Current Monitor .....	5
3.9.7.	Scrapers with Possible Function as Dedicated Aperture to Protect IDs .....	6
3.9.8.	Pinger Magnets .....	6
3.9.9.	Beam Loss Monitor System .....	7
3.9.10.	Temperature Sensors .....	7
3.9.11.	Beam Dynamics Measurements/ Control System Applications .....	8
3.9.12.	References .....	10

## 3.9. Diagnostics (RF and Vacuum not Included)

---

### 3.9.1. BPMs (Required Performance: Stored Beam and Single Beam Passage)

Considering the commissioning phase, we need less resolution, but we can only sample a short pulse. The MAX IV ring injector will deliver a 100-300 pC pulse with a pulse length of 1-2ns for commissioning. This will require the electronics to be able to detect and calculate the position from this short pulse. A ringing filter is a way to achieve this, which is used in one commercial unit. This unit reaches quite good position readings using a ringing filter during commissioning.

#### 3.9.1.1. BPM Electronics System for the 1.5 GeV Storage Ring

The 1.5 GeV MAX IV storage ring BPM electronics is required to measure the beam position accurately within the full specified storage ring current range. Position information must be stable and provided at rates up to 10 kHz for Fast-Orbit-Feedback.

The 1.5 GeV storage ring will use 36 BPM button pickups for the beam position monitors.

The BPM electronics for the 1.5 GeV storage ring will be of the same type as the 3GeV MAX IV storage ring. The main route will therefore be to equip all 36 BPM pickups with Fast Digital BPM electronics. The electronics should have single-pass capabilities to help with commissioning. The cost-saving option of Hybrid Electronics is a secondary option.

For more detailed information about the BPM electronics option, refer to the BPM sections in the Diagnostics chapters 2.9.1.2 – 2.9.1.6 for the 3 GeV storage ring.

### 3.9.2. Tune Measurement: Stripline Monitor and/or Button BPMs

One could either chose to base the tune measurement on a dedicated spectrum analyser with tracking generator, or one could chose a turn by turn mode read-out of one BPM head followed by a fast Fourier transform calculation. In both cases an excitation of the beam is necessary, and one should consider the excitation amplitude in the two cases. In principle, a smaller excitation would be sufficient if a traditional 15 cm quarter wave (fifth harmonic) strip-line detector is used instead of the button type BPM. This is because the tracking feature used by the spectrum analyzer is inherently more effective in detecting a

disturbance (synchronous detection). Actually a counter- example is the SLS, where only the turn by turn data from one BPM is used for tune measurements. In this case the tune measurement is limited to the injection moments in the top-up mode (the kicker excitation of the stored beam), since the necessary excitation between injections would disturb the users. For a strip-line detection system this will not be a limitation, because of the inherently more effective detection.

In conclusion, one should study the possibility of a traditional excitation/detection with quarter wave strip-lines. Such a study would include;

- A mechanical design study of the strip-lines for vacuum chamber in the MAX IV 1.5 GeV ring.
- Estimation of the impedance contribution from the device.
- A cost estimation of a dedicated spectrum analyser together with power amplifiers.
- Considerations if there might be beneficial effects beside the tune measurement, for example a possibility for slightly larger, frequency controlled, excitation of the beam, which is needed when using the spin polarization method for beam energy calibration. Also the possibility of detection of lower currents than detectable with the button type BPMs should be taken into account.

#### **Vacuum System Implications**

We need to consider where to install the two strip-line pairs (with diagonal pairs it is sufficient with one excitation pair and one detection pair), either in the injection straight (chamber aperture?), or in the RF straight.

### **3.9.3. Current Measurement: DCCT and BPMs.**

#### **3.9.3.1. Stored Beam**

A commercially available DC current transformer should be capable of measuring the stored beam current to a relative precision of at least  $10E-4$ . This should be sufficient for both lifetime calculations and current stabilization in the top-up mode. Lifetime measurements may be improved by averaging a large number of BPMs, where relative strength of the sum signal of all four buttons is being used.

#### **3.9.3.2. Commissioning**

During the commissioning phase one should use the possibility of monitoring the sum signal from selected BPM heads. This should give a crude measure of the beam current during the first turn in the machine. Also the sum signal from a strip-line pair may be used for relative measurements. This signal should be stronger than the button type sum signals, and may therefore be crucial at commissioning.



### **Vacuum System Implications**

We need to consider where to install the DCCT, either in the injection straight or in the RF straight.

## **3.9.4. Emittance Monitor: Pi-Polarization Method**

A robust on-line measurement of the beam sizes at one location in the ring, is an extremely versatile tool for a machine operator. Often just the on-line two-dimensional image, even without absolute beam size values, helps in finding the source of different beam instabilities. It is of high importance that this diagnostic device is running already during the commissioning phase, when it is crucial to pinpoint those beam instabilities having a “simple” origin.

The purpose of the beam size measurement is eventually to determine the transverse beam emittances. Usually the vertical emittance is the most interesting since it is given by the machine alignment, and thus difficult to predict. For the emittance determinations, separate determinations of beta values and dispersion values at the observation point are needed (cf. Section 3.9.11.1). Also a beam energy spread measurement is in principle needed. However, usually one can by different means verify that the beam energy spread is close to the theoretical one, given by the lattice.

For the MAX IV 1.5 GeV ring the horizontal/vertical emittance is expected to be in the order of 6/0.06 nm rad. However, we should strive to detect/determine a vertical emittance down to 0.1 % of the horizontal, or 6 pm. We foresee one beam size monitor to be observing the central point of one of the achromat dipoles. Here are the beta values approx. 0.25 m and 16m in x and y respectively. Dispersion is ca 40 mm. Thus, we want to measure a  $\sigma_{\text{max}}$  of 49  $\mu\text{m}$  and a  $\sigma_{\text{y}}$  of 10  $\mu\text{m}$ . Starting with the vertical beam size measurement it is in magnitude larger compared to the one already performed at the SLS, using the so called pi-polarisation method [4]. This method utilizes the vertically polarized UV-Vis synchrotron radiation (SR), and has turned out to have potential to determine vertical emittances in the few pmrad region. The horizontal beam size can quite safely be determined by use of either polarization of UV-Vis SR, as demonstrated at SLS.

A second monitor may be positioned observing either the entrance of the first bend or the exit of the second bend in the achromat. In this way a point of almost zero dispersion is observed. Here are  $\beta_{\text{x}} = 2$  m and  $\beta_{\text{y}} = 10$ . Thus,  $\sigma_{\text{max}} = 110$   $\mu\text{m}$  and  $\sigma_{\text{y}} = 8$   $\mu\text{m}$ , for 0.1 % coupling. Both values should be possible to verify utilizing UV-Vis SR and the Pi-polarization method.

### **Vacuum System Implications**

Two ports as described above. Large efforts should be made to extract wide enough opening angles of the light and to protect the extraction mirror with a thin horizontal absorber.

### 3.9.5. Bunch Length Monitor

A conventional choice is here a streak camera. However we should look into the possibility of using fast photodiodes, since the expected bunch rms length is around 170 ps. Photodiodes with rise-times (10-90%) around 80 ps are available for low price and are easy to operate (demonstrated at MAX II). A dedicated fast oscilloscope is of course necessary, but it should anyway be part of the diagnostic equipment, and could be used in various situations. A draw-back is of course the rise-time, but diodes with shorter rise-times may be used at the expense of the easiness of aligning them.

#### **Vacuum System Implications**

We will need one, simple, extraction port of SR from a dipole for this device. “Simple”, in the meaning that no emphasis has to be put on the wavefront distortion of the extracted light. Most efficient would be to use the same extraction port as for the filling pattern monitor.

### 3.9.6. Filling Pattern or Bunch Current Monitor

A filling pattern monitor will be a crucial device in order to keep the micron stability of the transverse beam position. The reason for this is that the front end electronics of the BPMs are likely to be dependent on the filling pattern. This is envisaged considering the fact that an un-even fill of the ring will result in bunches of different lengths, which in turn induces different signal levels in the BPMs. In order to assure the stability, a reasonably fixed filling pattern is needed.

However, we will have a good possibility to keep a fixed wanted filling pattern, since we will fill individual buckets with the injector. A very effective filling pattern monitor, even used as a feed-back device to generate arbitrary filling patterns, has been realized for at SLS (where RF=500 MHz). It is based on a photodiode detecting the light from individual bunches. This photodiode also gives superior linearity of the output signal to the bunch current, compared to either a sum signal taken from the BPMs, or from a stripline, to a fast oscilloscope (it is clear that these signals are bunch length dependent). Since we use only a 100 MHz RF, there will be good hope to successfully implement the photodiode solution for our filling pattern monitor and feed-back algorithm the for filling.

#### **Vacuum System Implications**

We will need one, simple, extraction port of SR from a dipole for this device. “Simple”, in the meaning that no emphasis has to be put on the wavefront distortion of the extracted light. Most efficient would be to use the same extraction port as for bunch length measurements.

### 3.9.7. Scrapers with Possible Function as Dedicated Aperture to Protect IDs

A vertical scraper will give valuable information on the average pressure in the machine, that is it will give the possibility to put numbers on elastic and inelastic (gas) lifetime and finally on the Touschek lifetime. Furthermore, with knowledge of the vertical beta function, the vertical acceptance of the ring can be determined. This is crucial information when commissioning different insertion devices. However, this diagnostic device could be designed also to be a dedicated protection of the IDs against radiation. Furthermore, this protection fulfils a third aim, and that is to concentrate all vertical losses from stored beam to a single area where radiation protection walls could be somewhat enhanced in order to cope with this radiation. Not only electrons that are scattered elastically against rest gas atoms, but also Touschek scattered electrons that eventually couple their horizontal motion to a vertical one will be caught in this “bottle neck”, instead of being lost in the IDs.

A horizontal scraper does not necessarily show the horizontal physical acceptance of the machine. It could instead reveal the lattice dynamic energy acceptance, or the RF energy acceptance. A thorough investigation has to be done after the scraper scan is done. However, correctly interpreted the data should help in determining these important quantities. We should contemplate whether we want to place it at a dispersive or non-dispersive location.

#### Vacuum System Implications

The best place for the vertical scraper should be the injection straight, regarding the fact that the radiation shield anyhow here has to be slightly enforced. If possible one should allocate roughly 1m of the straight section to place this tapered “bottle neck”. Tapers are contemplated for reduction of the impedance, and the length gives a possibility for some radiation shielding (lead) on top and below the chamber. Furthermore one could think of a very simple device, where the entire unit is levelled to the position which just about shadows all the other straight sections and their IDs. Still it will require some kind of bellows at the ends, which probably should incorporate RF shields. However, regarding the fact that IDs are supposed to have gaps of only 10 mm, the movement of the whole device would not have to be more than roughly 6 mm. We would still be able to perform the entire scraper scan.

The location of a traditional horizontal scraper should be determined. From radiation point of view it should also be in the injection straight where the radiation shielding is enforced, since it could also serve as a “bottle neck”. At the proper horizontal displacement it will shadow the rest of the ring from softly scattered Touschek particles.

### 3.9.8. Pinger Magnets

Pinger magnets could require larger efforts to realize in the 1.5 GeV ring compared to the 3 GeV ring due to the shorter revolution time. The issue whether the nonlinear optics

characterisation is needed in the low energy ring is under investigation (c.f. Section 3.9.11.2).

### **Vacuum System Implications**

They should be designed with thought on impedance contribution.

## **3.9.9. Beam Loss Monitor System**

During commissioning of the storage ring as well as during later machine studies (momentum acceptance studies, energy calibration, ID commissioning, etc.) it will be of interest to identify locations of elevated beam loss. A simple and inexpensive way to achieve this is the use of optical fibers running along the vacuum chamber. Such a system has already successfully been used at the MAX-FEL experiment. Four fibers run along the vacuum chamber; each fiber covers a 90 degree segment of the chamber. The fibers are taped directly onto the chamber. Since the fibers are very small they can be threaded through magnet apertures or ID gaps.

Bremsstrahlung generated at beam loss creates visible radiation in the fiber at a location close to the loss area. This radiation can be transported by the fiber all the way to one end where the intensity is measured. If this measurement is synchronized with the beam revolution, the time of flight creates a relation between delay of a measured pulse and loss location along the fiber. Therefore if an intensity burst is measured, the delay of this burst with respect to the revolution trigger reveals the location of burst source along the fiber. Since four such fibers are installed with each in a different segment of the chamber, losses above and below the machine midplane can be distinguished from each other as well as losses to the inside and outside of the ring. The latter (if measured in coincidence) can be used to distinguish Touschek losses from gas scattering losses.

If beam loss is to be measured specifically for the purpose of energy calibration (cf. section 3.9.11.3), a measurement that can distinguish Touschek loss pairs from other scattering losses is of advantage. Such a system can be implemented by setting up two scintillators downstream of a dipole magnet on the inside and outside of the storage ring. Or alternatively, downstream of a vertical aperture limitation (for example an in-vacuum ID with closed gap) above and below the vacuum chamber. If the read-out from these scintillators is fed to a comparator and the generated coincidence signal is monitored, Touschek losses can easily be identified.

## **3.9.10. Temperature Sensors**

Considering the fact that the vacuum system should cope with the entire heat load, without any separated absorbers, it could be a great advantage to plan for a set of permanent

temperature sensors at crucial points around the ring fastened onto the vacuum chamber. Most often storage rings have during (and after) commissioning suffered from unexpected “hot spots” that severely affect the lifetime, and maybe other features of the beam. If temperature sensors will be used at for example front ends and/or beamlines we should strive to standardize them.

### 3.9.11. Beam Dynamics Measurements/ Control System Applications

We list here beam dynamics measurements that need to be automatized.

#### 3.9.11.1. Linear Optics Characterization

The MATLAB Middle Layer (MML) software [5] will be used for the MAX IV storage rings. It contains a number of routines and applications for accelerator control, simulation and machine measurements including but not limited to:

- Accelerator Toolbox for machine physics simulations
- Orbit correction application
- Beam Position Monitor (BPM) offset calibration
- Chromaticity measurement
- Dispersion function measurement
- Beta function measurement
- Corrector magnet hysteresis measurement
- Response matrix measurement

As MML is in use at a number of light sources including Diamond, SOLEIL and SSRF, the component routines have been tested extensively for a number of different machines. Setting up the MML software for controlling the MAX IV storage rings during characterization measurements will require a TANGO interface, rather than the EPICS interface. This had been previously done at SOLEIL. Furthermore, Linear Optics from Closed Orbits (LOCO) [6] is integrated in the MML package and will be used extensively for characterization of the linear optics, gain calibration of BPMs, et.c. This will require setting up an accurate Accelerator Toolbox (AT) lattice model for the 1.5 GeV storage ring.

#### 3.9.11.2. Non-Linear Optics Characterization

The issue whether the nonlinear optics characterisation is needed in the low energy ring is under investigation.

### 3.9.11.3. Beam Energy Calibration

In order to gain a detailed understanding of the storage ring (e.g. nonlinear momentum compaction) as well as to calibrate ID spectra, precise knowledge of the storage ring energy is required. In order to go beyond the  $10^{-3}$  accuracy achieved with Hall probe measurements of the dipole field, resonant spin depolarization can be used. This method delivers an energy calibration on the  $10^{-5}$  level and has successfully been used at several storage rings (cf. e.g. [8]). Basically, an undisturbed electron beam in the ideal storage ring polarizes anti-parallel to the guiding dipole field after injection through the emission of spin-flip radiation. Once the beam has polarized, excitation of the beam at a specific frequency can be used to depolarize it. The frequency at which the beam depolarizes is directly proportional to the beam energy. If the frequency of the excitation is swiped across an interval and the degree of polarization is monitored, the drop of polarization upon hitting the depolarizing resonance can be linked to the exact beam energy.

This measurement does not necessarily require an expensive Compton polarimeter setup, however. Touschek lifetime is polarization-dependent (the higher the polarization the lower the Touschek-scattering cross section and hence the higher the Touschek lifetime) so that monitoring Touschek lifetime can reveal the degree of polarization of the stored beam in the machine. Similarly, the depolarizing resonance can be identified by a sudden drop of Touschek lifetime and/or a sudden increase in Touschek-scattered electron pairs. All that is then needed is a fast kicker (injection kicker, pinger magnet) with a tunable source (e.g. sine generator with settings to sweep the frequency over a predefined range).

However, certain conditions should be met. Firstly, the lifetime has to be Touschek-dominated in order for lifetime measurements to reveal polarization-dependence. Secondly, high levels of polarization need to be achieved before depolarization can take place and be detected. The first condition should be fulfilled for the vacuum conditioned MAX IV 1.5 GeV storage ring. In the base line design Touschek lifetime is dominating if Landau cavities are not operated (see Section 3.10.3). The second condition is the more serious obstacle: high degrees of polarization in the stored beam require an excellent machine alignment with a well-corrected orbit. In addition the machine must be left quiet/stable for extended periods of time without orbit feedback or injection in order for polarization to build up. The build-up time in the MAX IV 1.5 GeV ring is 48 minutes. This means that the machine must be operated in a completely quiet and stable way without any corrections, top-up injection shots, or ID gap changes for at least three to five hours in order to successfully measure polarization build-up and find the depolarizing resonance.

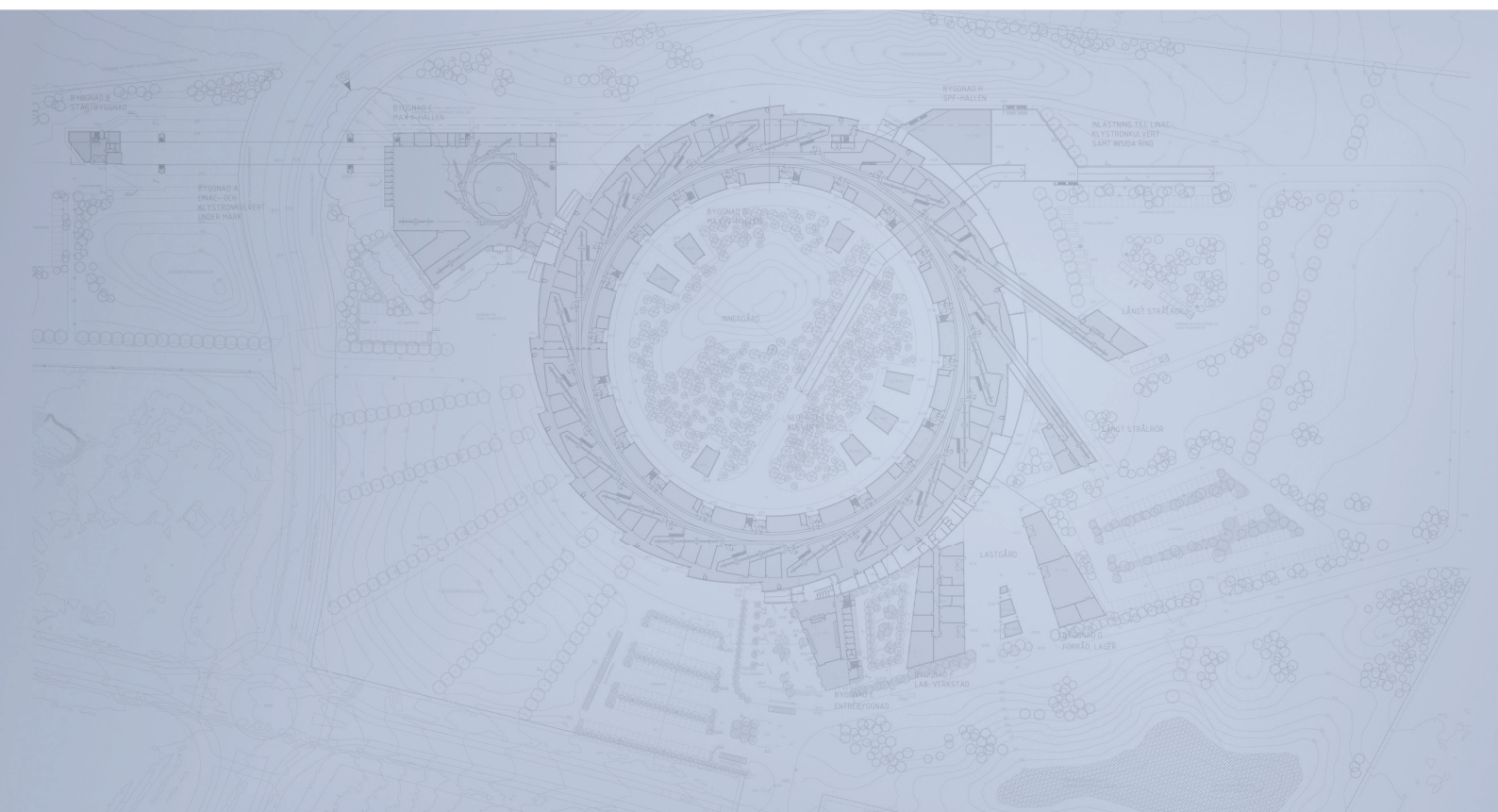
Finally, we note that the spin tune of the MAX IV 3 GeV storage ring should be around 3.405 (corresponding to a depolarizing resonance around 1.265 MHz or 1.857 MHz). The fractional spin tune has a mirror at 0.595. Both are fairly separated from the fractional horizontal and vertical betatron tunes (0.22/0.14). Thus, this should not prevent from reaching higher levels of polarization in the stored beam.

### 3.9.12. References

- [1] A. Olmos, F. Pérez , ALBA-CELLS, Cerdanyola, Barcelona, Spain, G. Rehm, Diamond Light Source, Oxfordshire, U.K. “Matlab code for bpm button geometry computation”, DIPAC07.
- [2] A. Stella, “Analysis of the DAFNE Beam Position Monitor with a Boundary Element Method”, INFNLNF, Accelerator Division, Frascati, December 1997.
- [3] F. Marcellini, “DAFNE broad-band button electrodes”, 1997
- [4] Å. Andersson, M. Böge, A. Lüdeke, V. Schlott, A. Streun, “Determination of a small vertical electron beam profile and emittance at the Swiss Light Source”, Nuclear Instruments and Methods, A 591 (2008) 437–446.
- [5] G J Portmann, Jeff Corbett, and Andrei Terebilo. An accelerator control middle layer using matlab.
- [6] J Safranek, G Portmann, A Terebilo, and C Steier. Matlab-based loco. 2002.
- [7] R. Bartolini, I.P.S. Martin, J.H. Rowland, P. Kuske, F. Schmidt, Phys. Rev. ST Accel. Beams, 11, 104002, 2008.
- [8] S.C. Leemann, M. Böge, M. Dehler, V. Schlott, Proceedings of EPAC 2002, Paris, France, pp 662-664.
- [9] Libera Brilliance Specifications, Instrumentation Technologies



# Detailed Design Report



## Chapter 3

### MAX IV 1.5 GeV Storage Ring

#### 3.10. Beam Lifetime

MAX IV Facility





## 3.10. Beam Lifetime

---

<b>3.10. Beam Lifetime .....</b>	<b>2</b>
3.10.1. Elastic Scattering Lifetime .....	3
3.10.2. Inelastic Scattering Lifetime.....	3
3.10.3. Touschek Lifetime .....	3
3.10.4. Total Lifetime .....	5
3.10.5. References.....	6

## 3.10. Beam Lifetime

---

Just as in the MAX IV 3 GeV ring, the beam lifetime in the MAX IV 1.5 GeV ring will be limited by elastic and inelastic (Bremsstrahlung) interactions between electrons and the rest gas molecules, and by Touschek (electron-electron) scattering within the bunches, resulting in electron losses from the beam. The loss rate from inelastic interactions is independent of beam energy, so we expect a contribution of the same size as for the high energy ring. The loss rate from elastic interactions is inversely proportional to the squared beam energy. For this reason is the minimum ID gap chosen larger in the low energy ring, in order that elastic scattering should not to be the dominating loss mechanism.

The rest gas scattering lifetimes are inversely proportional to the rest gas pressure given a certain rest gas composition. Below is given the same assumption for the rest gas pressure as for the high energy ring, but one should remember that it can easily be wrong by a factor two or three, which then is inversely reflected in the gas lifetimes. However, for a well conditioned machine the assumption below is quite conservative.

The Touschek lifetime follows simple scaling laws for bunch charge,  $q$ , and bunch length,  $\sigma_s$ :  $\tau_{\text{Touschek}} = k/q$  and  $\tau_{\text{Touschek}} = k \cdot \sigma_s$ . However, it has a quite complicated dependence (see for example [1]) on parameters like horizontal beam size,  $\sigma_x$ , horizontal beam divergence,  $\sigma'_x$ , vertical beam size,  $\sigma_y$ , and momentum acceptance,  $\delta_{\text{acc}}$ , all of which varies around the machine lattice. This requires that the Touschek lifetime is calculated as an average of local Touschek loss rates around the entire machine. In particular it is necessary to determine the momentum acceptance for every lattice point. It is the minimum of the RF momentum acceptance (bucket height) and the lattice momentum acceptance at the position of the scattering event. The (local) lattice momentum acceptance is well predicted for a linear machine with the knowledge of the horizontal vacuum chamber dimensions. However for the case of a highly chromaticity corrected (strong sextupoles) machine like the MAX IV 1.5 GeV ring, this determination is more complex [1] and is safest done by tracking off-momentum particles starting at the event position. We have made both simplified (5D) Touschek tracking studies with the code OPA [2], and full 6D tracking with the Tracy3 code. The difference in results are below 5%. Finally it should be pointed out that, while the MAX IV high energy ring operates in the ultra low emittance regime where the Touschek lifetime is increasing with decreasing emittance [3], the MAX IV 1.5 GeV ring will operate in the emittance regime where the reversed (ordinary) dependence governs.

### 3.10.1. Elastic Scattering Lifetime

The assumptions are:

Rest gas pressure and composition equivalent to 2 pbar of CO gas. (2 pbar=1.5 nTorr).

Vertical acceptance: 6 mm mrad ( $\beta_y=4$  m at undulator ends with  $\pm 5$  mm gap).

Horizontal acceptance: 37 mm mrad ( $\beta_x=6$  m at septum wall, at -15 mm).

Result:  $\tau_{el}=30$  h

Note: We have made the simplification to assume a pressure which is constant around the machine circumference. Emphasis should be made to decrease the rest gas pressure at locations of high  $\beta_y$ , in which case one would gain in lifetime, still with the same average pressure.

### 3.10.2. Inelastic Scattering Lifetime

The assumptions are:

Rest gas pressure and composition equivalent to 2 pbar of CO gas.

Average momentum acceptance:  $\delta_{acc}=3.7$  %

Result:  $\tau_{inel}=51$  h

Note: This lifetime is quite insensitive to the average momentum acceptance:  $\delta_{acc}=3.3$  % gives  $\tau_{inel}=49$  h.

### 3.10.3. Touschek Lifetime

We study the two cases described in Ch 2.6. The first case is the “Lund case” with 130 keV energy loss per turn, reflecting a ring equipped with 10 relatively weak IDs. The second case is the Krakow case with one SCW installed, resulting in 150 keV energy loss per turn. In the first case a main cavity total voltage of 560 kV is foreseen, and in the second case a slightly lower cavity voltage of 500 kV is chosen. The resulting RF energy acceptance are 4.0 % and 3.5 % respectively. In neither of the two cases is the Intra Beam Scattering process affecting the equilibrium emittances to a large extent. After introducing the Landau cavities for bunch lengthening, we may simply neglect this effect. Tracking results for the two cases give a local lattice momentum acceptance of approximately 3%, in the dispersive region between the two achromat dipoles. Furthermore, we assume a bunch lengthening from the passive Landau cavities resulting in a rms bunch length of 60 mm in both cases, which is slightly lower than the theoretically achievable (see Ch 3.6.8) rms lengths of 65

mm and 70 mm respectively, for the two cases. In both cases we assume that the vertical emittance is being adjusted to 60 pmrad, by help of a vertically introduced dispersion wave [4]. By this we avoid betatron coupling and the risk of losing Touschek scattered particles vertically in narrow gap IDs.

Dynamic Touschek lifetime [1] has been calculated with OPA and with Tracy3. We assumed 500 mA stored beam current in 32 bunches ( $I_b \approx 5$  nC). Vacuum chamber dimensions and non-linear behavior due to sextupoles were included in the model, but no magnet or misalignment errors. The parameters of the two cases are displayed in Table 1. The vertical emittance in all cases was set at 60 pm rad; therefore emittance ratio is not identical in the two cases.

Case	Configuration	$\delta_{\text{acc}}^{\text{min}}$	$\delta_{\text{RF}}$	$\sigma_{\delta}$ [ $\times 10^{-4}$ ]	$\sigma_s$ [mm]	$\epsilon_x$ [nm rad]	$\epsilon_y$ [nm rad]
I	10 U	3%	4.0%	7.5	14.7	6.0	0.06
II	1 SCW & 9 U	3%	3.5%	7.8	16.4	5.3	0.06

Table 1: Parameters for the cases used to study Touschek lifetime in the MAX IV 1.5 GeV storage ring. The parameters displayed are the minimum lattice momentum acceptance, the RF acceptance, rms momentum spread of the bunch, rms bunch length without LCs, as well as horizontal and vertical emittance.

The results from Tracy, for the two cases with and without Landau cavities (where bunch lengthening to 60 mm was assumed) are displayed in Table 2.

	no LC, $\delta_{\text{acc}} = \delta_{\text{RF}}$	no LC	with LC
Case I	8.3	5.8	23.8
Case II	5.8	5.0	18.4

Table 2: Touschek lifetime results in hours. The first column shows results assuming infinite lattice momentum acceptance. The Tracy results take into account both (nonlinear) lattice and RF momentum acceptances. Those results are displayed for a ring without and with Landau cavities (LC).

In case II there is quite a small difference between the results in the first two columns because the overall momentum acceptance is dominated by the RF acceptance. In case I the lattice acceptance cuts quite deep into the RF acceptance at certain locations within the achromat and hence there is a large difference between the results the first two columns. This is illustrated in Fig. 1. For case II, the RF acceptance is “better matched” to the lattice acceptance, and the lifetimes are more similar.

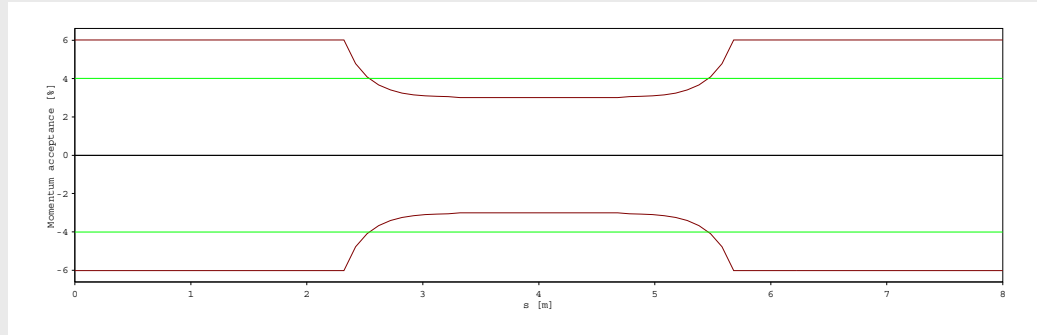


Figure 1: Momentum acceptances for case I (one achromat) with 0.56 MV RF cavity voltage, given by OPA. The RF momentum acceptance is  $\pm 4.0\%$ , indicated by the green lines. The lattice momentum acceptance is given by the brown curves.

### 3.10.4. Total Lifetime

For total lifetime considerations we define the same two cases as given above, the “Lund case” and the “Krakow case”. The Touschek lifetime is combined with the gas scattering lifetimes in Table 4 for the two cases. Note that Touschek lifetime is defined as a half-lifetime, whereas the gas scattering lifetimes are  $1/e$ -lifetimes. However, since we are interested in evaluating the total lifetime at the design current 500 mA, it can simply be derived from the sum of individual loss rates.

Lifetime	Lund	Krakow
Elastic gas scattering [h]	30	30
Inelastic gas scattering [h]	51	49
Touschek scattering (with Landau cavities) [h]	24	18
<b>Total [h]</b>	<b>11</b>	<b>9.3</b>

Table 4: Contributions to the total MAX IV 1.5 GeV storage ring lifetime  $\tau$ , in hours. The results have been calculated for the “Lund case” and the “Krakow case”, where the RF voltage is 0.56 MV and 0.50 MV, and total energy loss per turn is 130 keV and 150 keV, respectively.

### 3.10.5. References

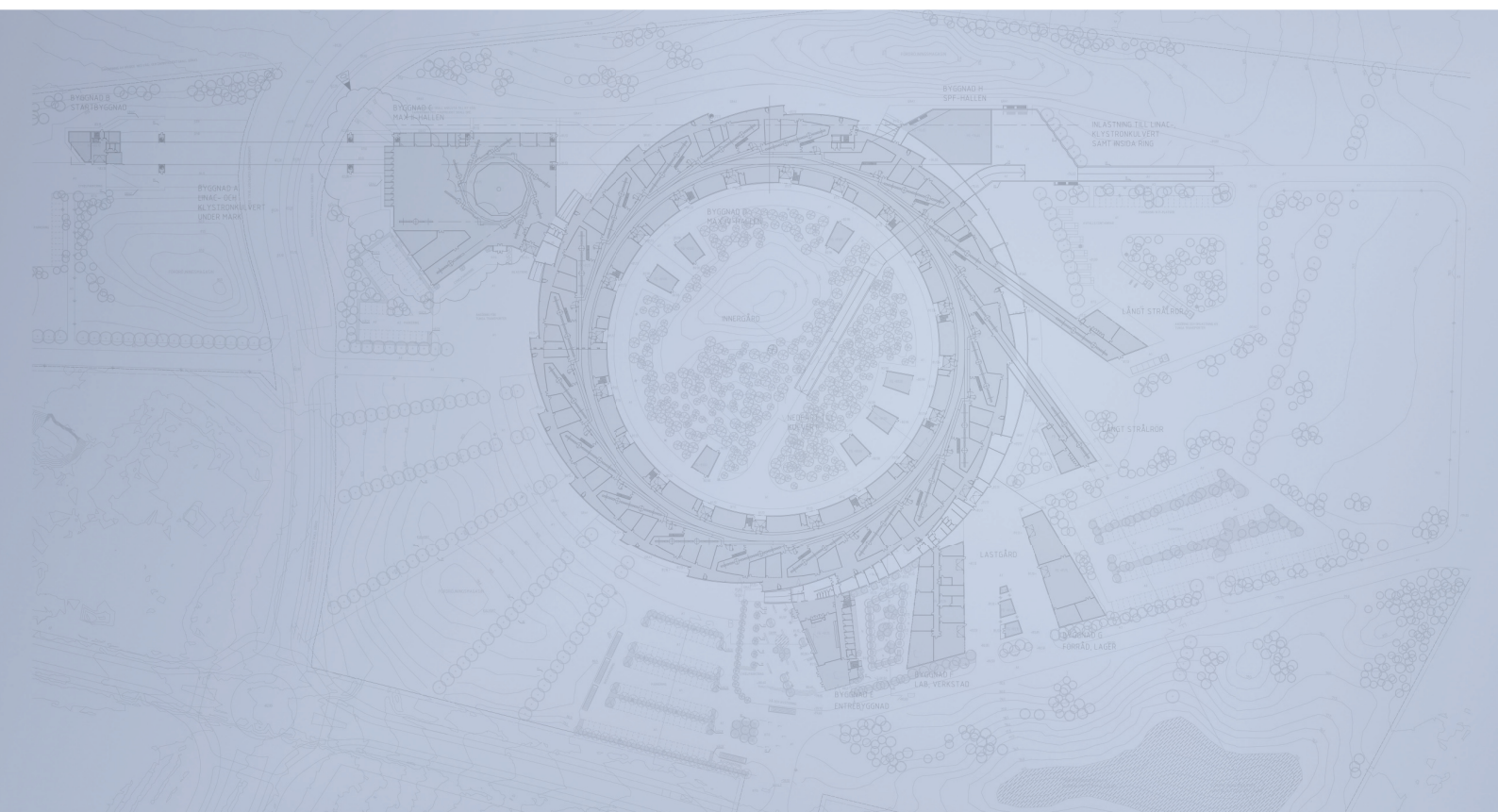
- [1] A. Streun, “Momentum acceptance and Touschek lifetime”, SLS Note 18/97.
- [2] A. Streun, *OPA*, code and documentation available at <http://slsbd.psi.ch/~streun/opa>
- [3] <http://www.maxlab.lu.se/maxlab/conference/small-emittance/>
- [4] J. Bengtsson, I Pinayev, “NLSL-II: Control of Vertical Beam Size”, NLSL-II Technical Note, No. /, Jan 31, 2007.

# MAX IV Facility





# Detailed Design Report



## Chapter 4

### MAX IV Injector

#### 4.1. General Description and Design Philosophy

MAX IV Facility



## 4.1. General Description and Design Philosophy

---

The linac injector will deliver electrons for full energy top-up injection into the two storage rings as well as delivering short and intense electron bunches to the Short Pulse Facility (SPF). A high degree of robustness and availability is a very important feature for the linac, especially for the top-up injection mode. Although of interest, the linac emittance is not of that vital importance for neither injection into the storage rings nor for the SPF operation. For a possible later FEL operation however, the demands on electron beam quality are much higher. In chapter 4.3 simulations for both the relaxed SPF operation and a possible low emittance operation can be found.

The linac will accelerate one bunch in one 3 GHz bucket per RF pulse for the SPF. It will also be possible to accelerate 3 bunches in 3 adjacent 3 GHz-buckets per RF pulse for ring injection. These 3 bunches with a total charge of 300 pC will give a sufficient large signal of the ring BPM systems, filtered at 500 MHz, to facilitate single turn characterization.

The injector will be adjusted to 3 GeV. Some redundancy is available; the maximum electron energy is 3.7 GeV at crest.

In normal operation, the injector is running at 100 Hz with one 100 pC bunch/RF pulse. When injecting to either of the storage rings, the gun laser will deliver 3 bunches separated by 1 dm. Since beam-loading is negligible, the linac electron beam optics can remain unchanged. A semi-fast kicker magnet (10 ms) will deflect these three bunches into the injection transfer line to the relevant storage ring. Two such extraction systems are thus needed, one operated at 1.5 GeV and the other one at 3 GeV. These extraction systems can be operated at 10 Hz to facilitate a fast filling of the rings.

The linac injector is constructed in a very modular way. One accelerating unit consists of one RF unit and one accelerating unit. The RF unit consists of a 35 MW klystron fed by a solid state modulator. These kinds of modulators demonstrate a very low jitter of the HV to the klystrons and thus a low RF phase jitter. The accelerating unit consists of two 5.2 m long S-band room-temperature linac structures fed from a SLED cavity. The on crest energy gain of each structure is 95 MeV.

17 such units will form the main part of the linac injector. One RF unit will feed the electron gun and the first accelerating structure. To cost optimize the injector system, the last two RF units will feed 4 accelerating structures each.

The electron gun is a copy of the FERMI gun. By feeding the gun with a SLED pulse and by overcoupling the gun to the wave-guide, a minimum of heat energy will be deposited in the gun for a given gun gradient and the gun voltage will be kept constant for the last 50 ns of the SLED pulse.

The bunch compression will take place in two stages, one compressor operated at 260 MeV and one at full energy.

The bunch compressors are of the dog-leg type. Each dog-leg consists of two achromats. Each achromat has four identical bending magnets. By a proper choice of the electron-optical parameters, first order as well as second order path length dependence on energy can be adjusted to suitable values. No harmonic accelerator is thus needed for linearization.

The Low Level RF is very simple and robust. In principle, a Main Drive Line (MDL) is connected to the first klystron, prior the SLED cavity. Some 30 kW are tapped out from the wave-guide. This MDL is then running through the linac tunnel and some 200 watts are tapped off to each klystron. Length variations of linac tunnel will be automatically compensated for since the MDL, consisting of a rigid coaxial waveguide with sliding joints, also will follow these length variations.

The main linac parameters are shown below.

<b>Operating energy</b>	3 GeV
<b>Maximum on-crest energy</b>	3.7 GeV
<b>Max RF rep rate</b>	100 Hz
<b>Bucket charge</b>	100 pC
<b>Normalized emittance</b>	<1 mm mrad
<b>Bunch length @ 3 GeV</b>	<100 fs
<b>Peak current</b>	>3 kA
<b>Operating RF</b>	3 GHz
<b>Linac gradient</b>	20 MV/m
<b>No of klystrons</b>	18
<b>No of acc structures</b>	39
<b>Injector length</b>	300 m
<b>Electron gun</b>	FERMI type

# Detailed Design Report



## Chapter 4

### MAX IV Injector

#### 4.2. Layout, Design Parameters and Optics

MAX IV Facility





# 4.2. Layout, Design Parameters and Optics

---

- 4.2. Layout, Design Parameters and Optics .....2
  - 4.2.1. General Layout..... 2
  - 4.2.2. Design Parameters and Operation Modes ..... 4
  - 4.2.3. Bunch Compressors and Linearisation ..... 6
  - 4.2.4. Main Linac .....12



## 4.2. Layout, Design Parameters and Optics

---

### 4.2.1. General Layout

The pre-injector consists of a photo cathode RF gun and a 100 MeV linac where emittance compensation is performed. The electrons then pass a double linac section and a matching section before entering the first double achromat bunch compressor at approximately 260 MeV. After BC1 is a 4 quadrupole section to match into the main linac.

The lattice in the main linac is done as a FODO lattice with focusing quadrupole, linac section, defocusing quadrupole, and linac. At 1.5 GeV the beam is kicked out from the linac for injection into the 1.5 GeV storage ring. The kick from the linac is done in a drift section with a length corresponding to the linac length in order to keep the modularity and the FODO lattice in the whole main part of the injector. At 3 GeV the beam is kicked out again for injection into the 3 GeV storage ring. Since the beam quality is high, with low emittance and energy spread, even for the ring-electrons, no matching have to be done in the linac before the injection transfer lines. The beam is simply extracted with the beta functions it gets from the normal FODO lattice in the main linac.

After the injection extraction at 3 GeV the beam is matched into the second double achromat bunch compressor, which also acts as part of the beam delivery system to the Short Pulse Facility (SPF). When the beam energy is optimised for running SPF, the electron energy at BC2 will be 3.5-3.6 GeV. A schematic view of the injector can be seen in figure 4.2.1. An overview of beta functions from 100 MeV to the end of BC2 can be seen in figure 4.2.2.

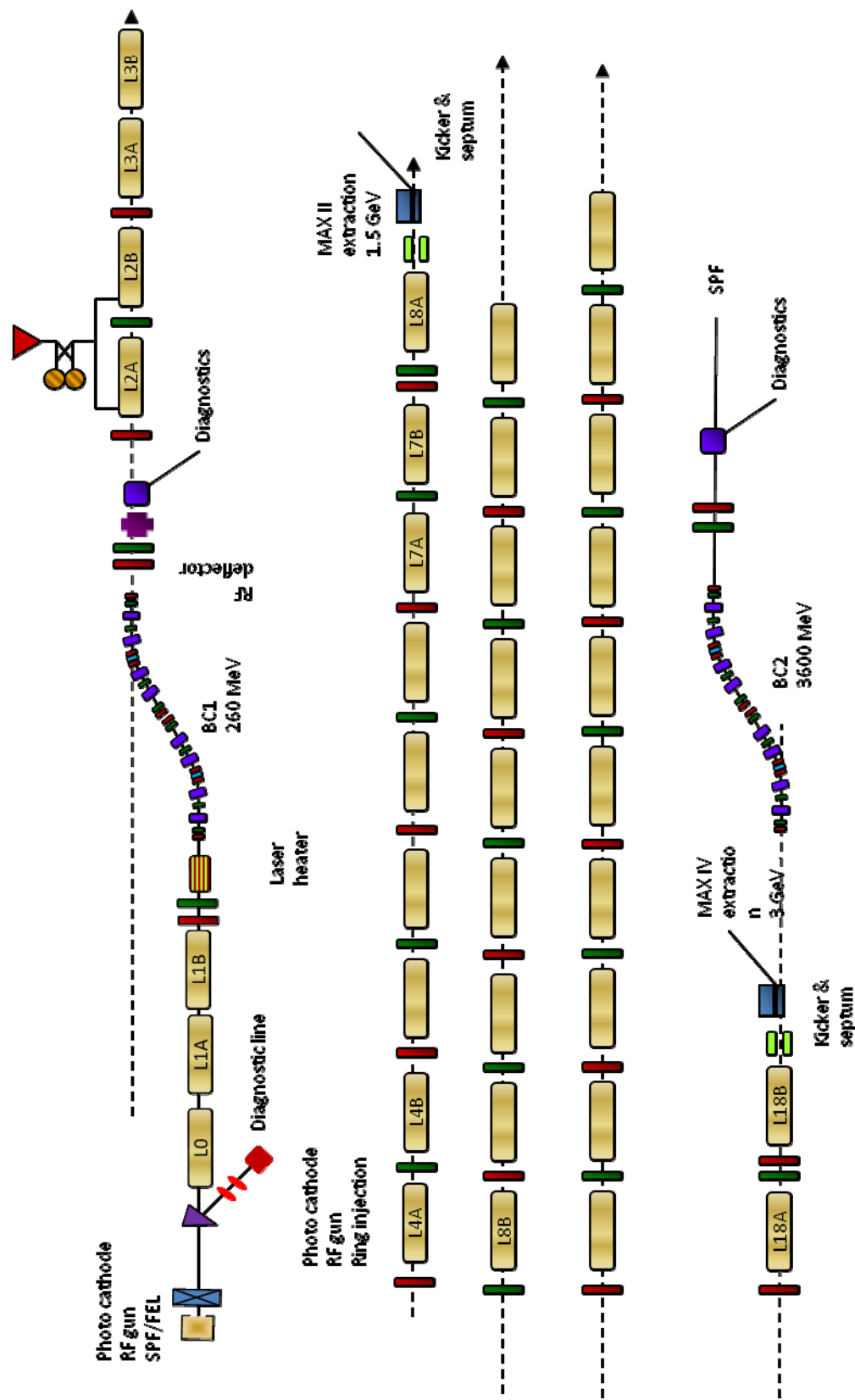


Figure 4.2.1: Schematic overview of the MAX IV injector.

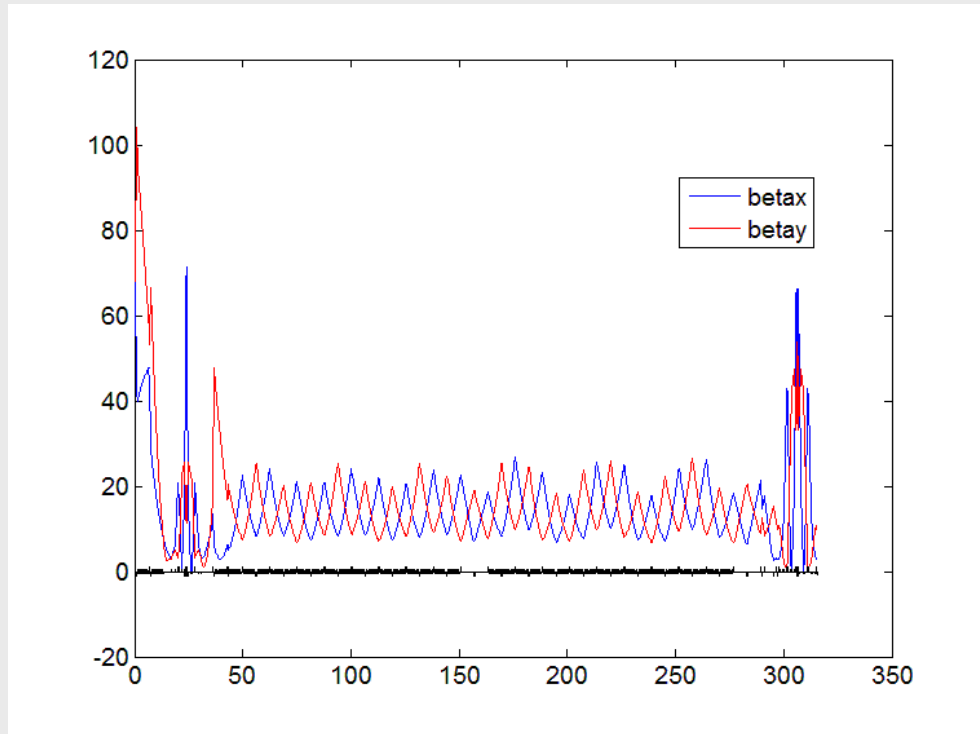


Figure 4.2.2: Optics from 100 MeV to the end of the linac, including BC2.

### 4.2.2. Design Parameters and Operation Modes

The electron bunches produced by the MAX IV Injector will be used both for producing short bursts of spontaneous X-ray radiation in the SPF and for injection and top-up in the two storagerings. This means that the linac will be switched between different energies, RF-phases and repetition rates. Since only one electron gun is used, the storage rings will be injected with the same high brightness beam as the SPF, only with less compression and a different time structure.

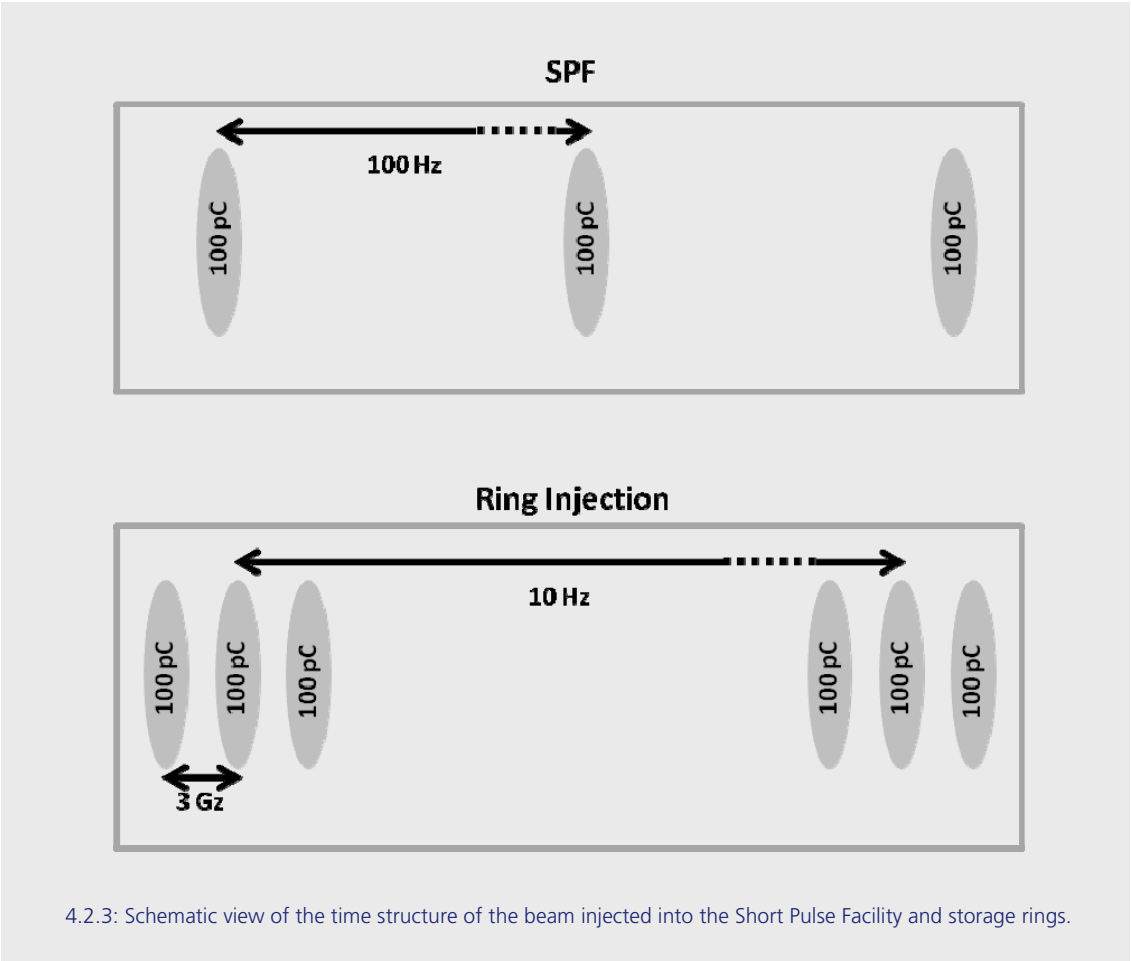
During SPF operation the injector will produce single 100 pC pulses at 100 Hz. Top up and injection in the storage rings will have a repetition rate of 10 Hz, with 100 pC in three adjacent RF buckets in each shot, effectively a 300 pC, 660 ps long pulse.

Top-up into both rings will happen during a period of a few seconds every few minutes. The SPF will receive pulses in between top-up periods.

Table 4.2-1 shows the design electronbunch properties for the three operation modes. In figure 4.2.3 a schematic sketch of the SPF and injection time structures can be seen.

Table 4.2-1: Design properties for the electron bunch.

	1.5 GeV injection	3 GeV injection	SPF mode
Charge (pC)	300	300	100
Bunch length (ps)	660	660	< 0.1fwhm
Energy (GeV)	1.5	3	3.6
Norm. emittance (mm mrad)	< 1	< 1	< 10
Repetition rate (HZ)	10	10	100
Time structure	3×3GHz×10Hz	3×3GHz×10Hz	1×3GHz×100Hz



With a total of 39 linac structures with an effective energy gain of 95 MeV and suitable off crest acceleration the maximum energy for the SPF could be up to 3.6 GeV. But in order to have some energy redundancy, it will be designed for 3.5 GeV. To reach the right energy for injection into the 1.5 and 3 GeV rings, a few linac sections can be turned off and/or the modulator energy reduced.

The injector will be running at a repetition rate of 100 Hz during all operation to ensure temperature and running stability. To reduce the repetition rate to 10 Hz during injection, the beam is simply kicked out from the main linac at that rate. The triple pulse mode is accomplished with the gun laser and will not affect the linac stability.

In chapter 4.3 results of beam dynamics simulations of the injector shows that the design parameters are easily obtained with the MAX IV Injector.

### 4.2.3. Bunch Compressors and Linearisation

Compression of the electron bunches is done in double achromats at 260 MeV and 3.6 GeV.

To reach the highest possible momentum in a linac, the electron bunches need to be accelerated on the crest of the RF pulse. This way the electrons feel the peak amplitude of the high voltage and collect the maximum energy boost in the acceleration.

In order to operate a bunch compressor, the pulses are instead injected with an offset from peak value in the RF phase making the longitudinal position of the electrons in the bunch correlated with energy deviation. The correlated energy spread induced in the bunch is called an energy chirp where the high energy part of the bunch either comes first or last depending on the sign of the RF phase offset. The sign of the chirp depends on the specific type of bunch compressor used. After the energy chirp has been created, some sort of compression is needed to make the bunch short.

Through a dispersive magnetic system, electrons with different energies will not have the same path lengths. High energy electrons are influenced less by the magnetic field in a dipole and thus get a smaller angular kick than low energy electrons will. Depending on the configuration of the magnetic system this will lead to an increase or decrease of path length for electrons with negative or positive energy deviation (momentum compaction, R56). When an electron bunch with an energy chirp of proper sign pass through a dispersive magnet system, the electrons that were in the tail of the bunch will catch up with electrons in the head, leading to longitudinal compression. In longitudinal phase space this looks like a rotation of the beam around the central momentum. Figure 4.2.4 shows a schematic sketch of longitudinal phase space before and after a bunch compressor together with the projected current histogram showing the decrease in bunch length and increase in peak current.

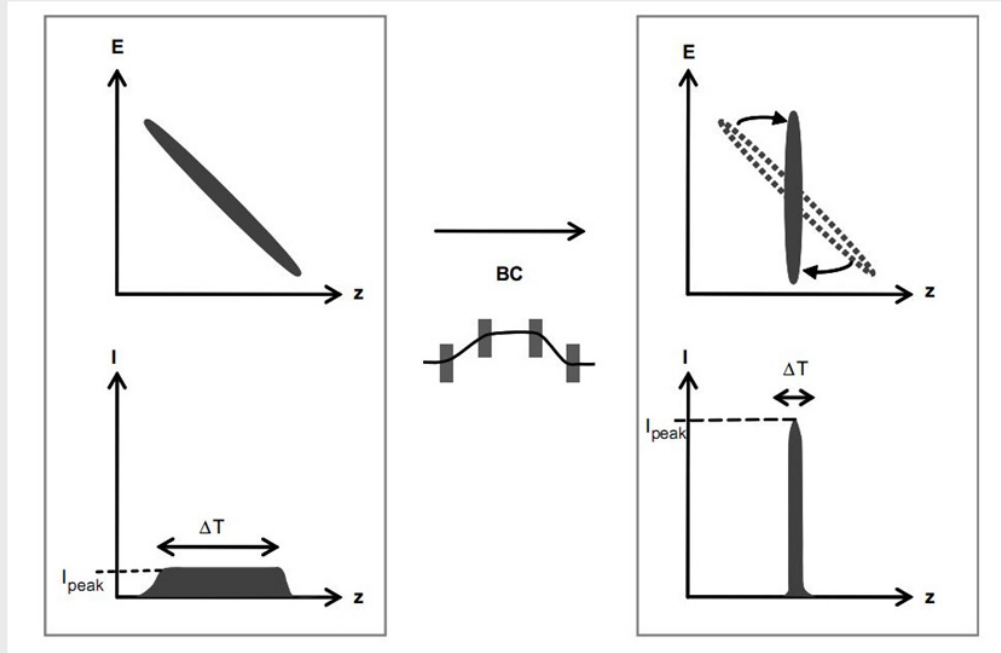


Figure 4.2.4: Schematic view of longitudinal compression on an electron bunch.

When the correlated energy spread required for bunch compression is created, the chirp is not linear, but inherits the curvature from the sinusoidal accelerating field. This curvature limits how short the bunches can be made through compression and gives a bunch shape with a very short high-current peak in one end of the bunch and a long low-current tail.

One way of influencing non-linearities in longitudinal phase space is through the use of sextupole magnets in the electron transport. Sextupole magnets can have a great impact on the second order transfer matrix, and when they are placed in a dispersive section, they will add second order momentum compaction,  $T_{566}$ , which means that both the electrons with positive and negative energy deviation will take a longer path through the compressor. This can effectively help compensate the nonlinearities from acceleration. A schematic view on how sextupole linearisation works on the beam can be seen in figure 4.2.5.

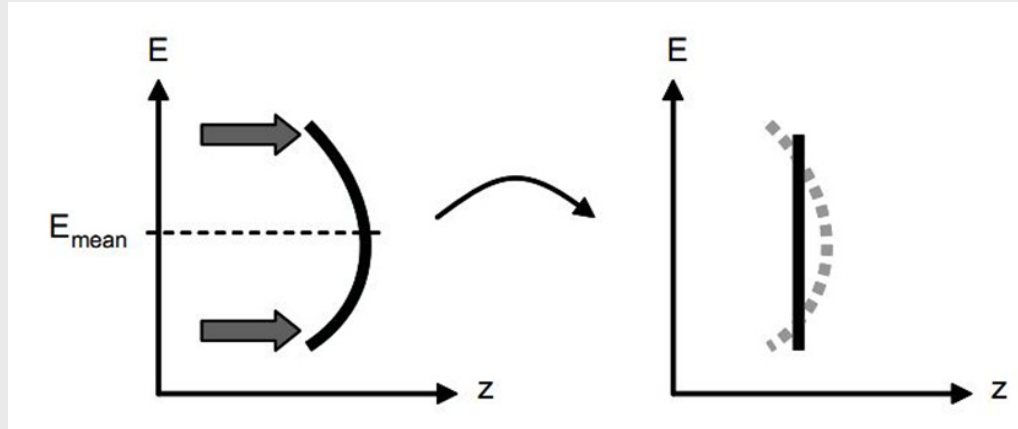


Figure 4.2.5: Schematic view of longitudinal linearisation by adjusting the second order momentum compaction T566.

The magnetic double achromats used as bunch compressors in the MAX IV injector has a positive R56 unlike the commonly used magnetic chicane which has a negative R56. We have thus to work on the falling slope of the RF voltage. Both types of bunch compressors naturally have a positive T566 and a positive T566 has a linearising effect in the achromat case. We can thus choose the optical parameters in the achromat to get optimum linearization without needing to have a harmonic linac for this purpose.

A sextupole is needed to minimize the second order dispersion at the end of the achromat. This sextupole, positioned at the achromat middle, is rather weak and could be compared with the chromaticity compensating sextupoles in a storage ring.

The natural T566 of the double achromats is actually over-linearising the RF induced curvature and the sextupoles work in the opposite direction of the natural T566, to compensate for the over-linearisation. To achieve full linearisation of longitudinal phase space, the sextupole strength has to be increased. This can be done in such a way that second order dispersion still is closed at the end of the BC, but the energy derivative of dispersion becomes large, leading to increased emittance. For a spontaneous source like the SPF this is however not a problem. As can be seen in chapter 4.3 peak currents of up to 20 kA and fwhm bunch length of less than 20 fs can be achieved at the cost of normalised emittance increasing to 2.5 mm mrad, which far exceeds the specifications for the SPF in beam quality.

One single achromat will also induce some other second-order effects acting in the transverse direction. The relevant ones are energy-dependent and thus linear in angle or position. The introduction of a double achromat, the achromats bending in opposite directions, will cancel these terms. We will also effectively get a translation of the beam instead of a change of angle, which eases the construction of the linac hall.

Since the R56 of the double achromats is fixed, the off crest RF phase is used to vary the compression factor.

A schematic view of the double achromat bunch compressors and the corresponding beta and dispersion functions can be seen in figures 4.2.6 to 4.2.9. Table 4.2-2 lists the compression and linearisation parameters used to achieve a short bunch with high peak current for the Short Pulse Facility. Note that the T566 for BC2 in the SPF optimised case is actually negative, contrast to what would be expected for linearisation of the RF induced curvature. This is thought to be due to the bunch being over linearised already in the first BC and the fact that wakefields in the long main linac before BC2 has a strong linearising effect. Table 4.2-2 also gives too high energy values at the BC's since the 95 % efficiency of the linacs was not taken into account during this simulation.

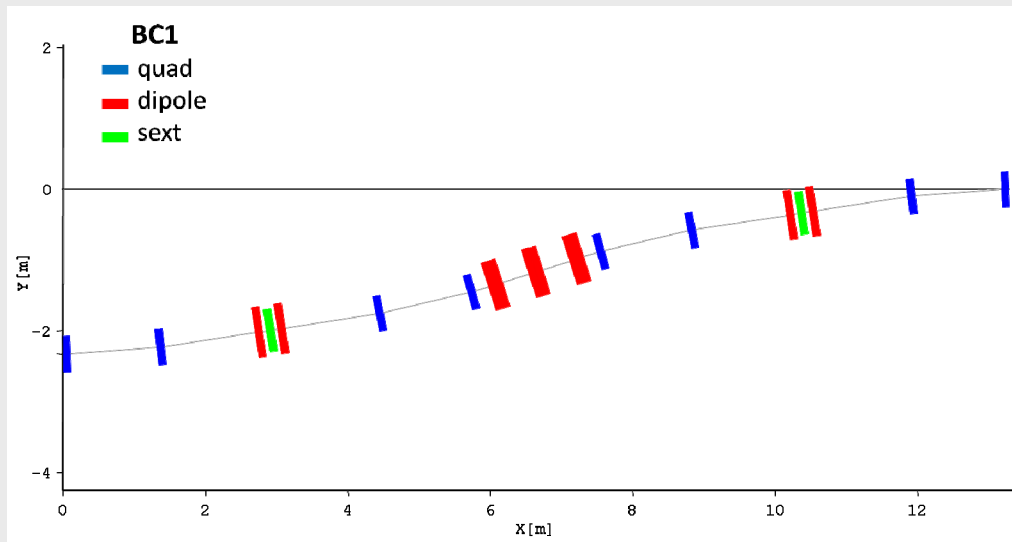


Figure 4.2.6: Layout of double achromat bunch compressor 1.



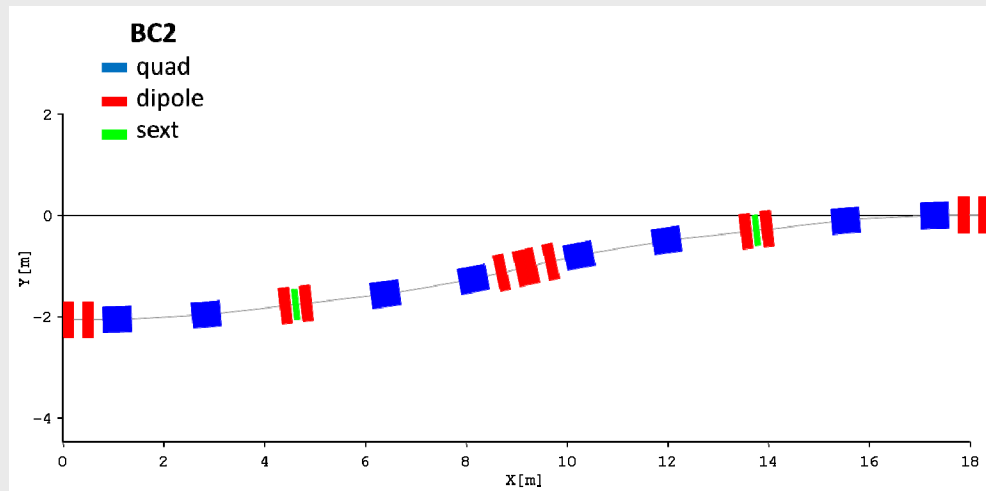


Figure 4.2.7: Layout of double achromat bunch compressor 2.

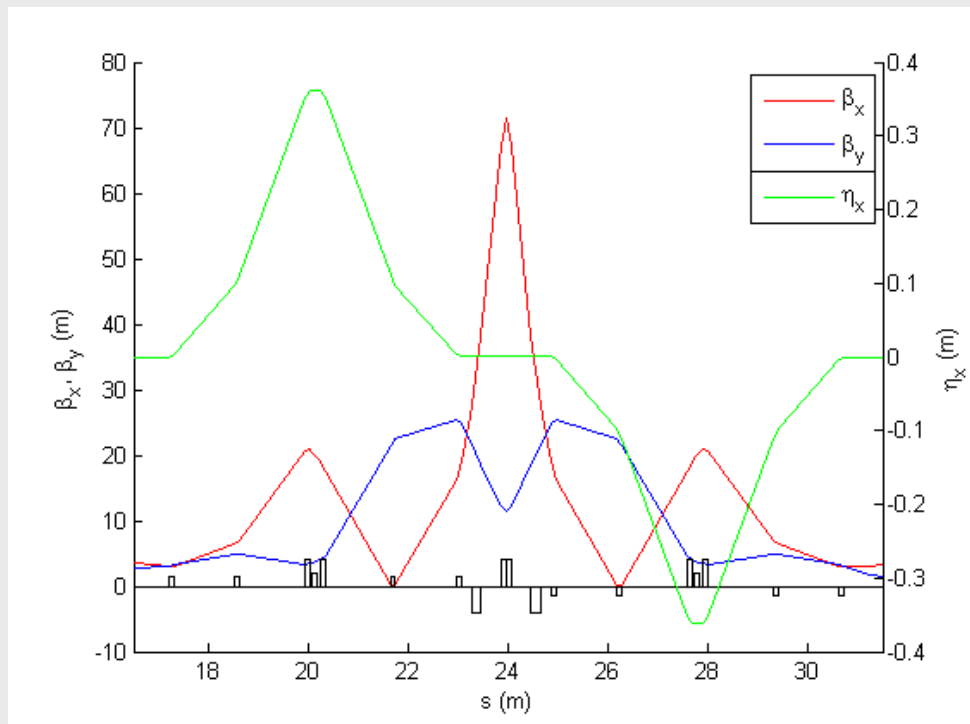


Figure 4.2.8: Optics and dispersion in bunch compressor 1.

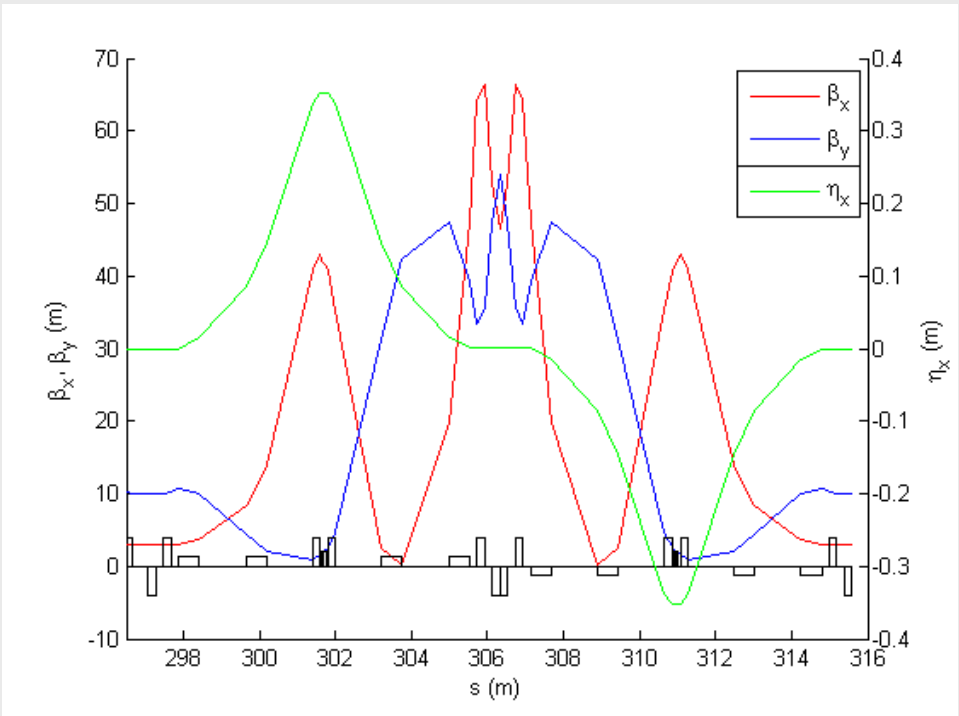


Figure 4.2.9: Optics and dispersion in bunch compressor 2.

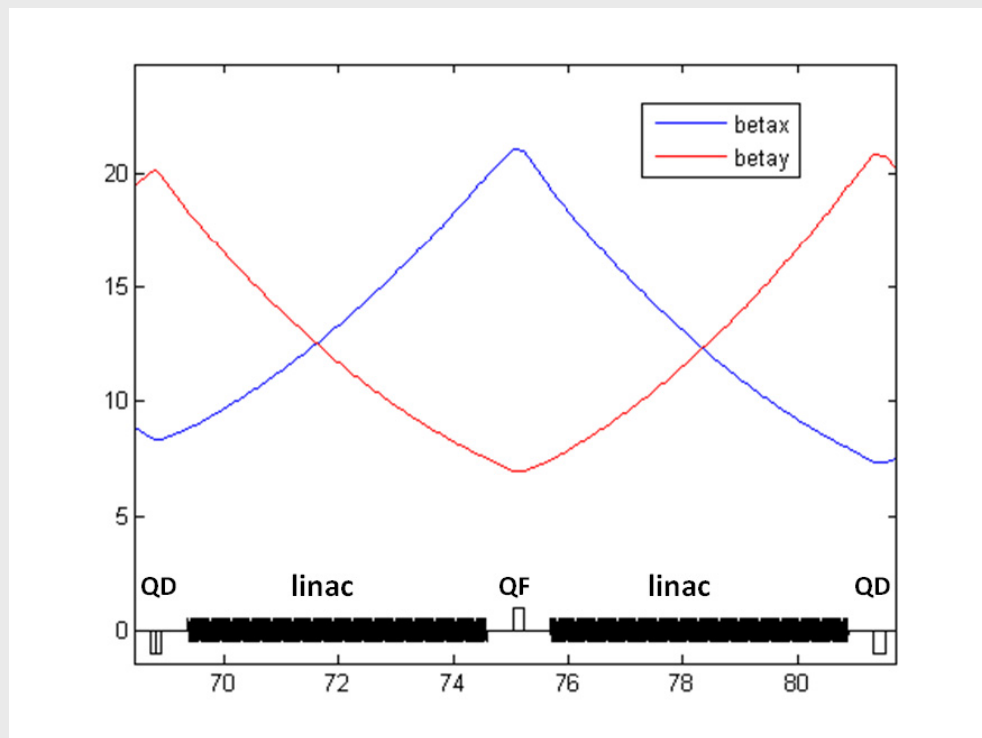
Table 4.2-2: Compression and linearisation parameters.

Lattice: 100623_MAXIV_SPF.lte	BC1	BC2
$R_{56}$	3.23 cm	2.6 cm
$T_{566}$	9.26 cm	-17.8 cm
Energy	275 MeV	3700 MeV
Linac phase	32°	17.5°
Integrated sextupole strength	$\pm 5 \text{ m}^{-2}$	$\pm 10 \text{ m}^{-2}$

#### 4.2.4. Main Linac

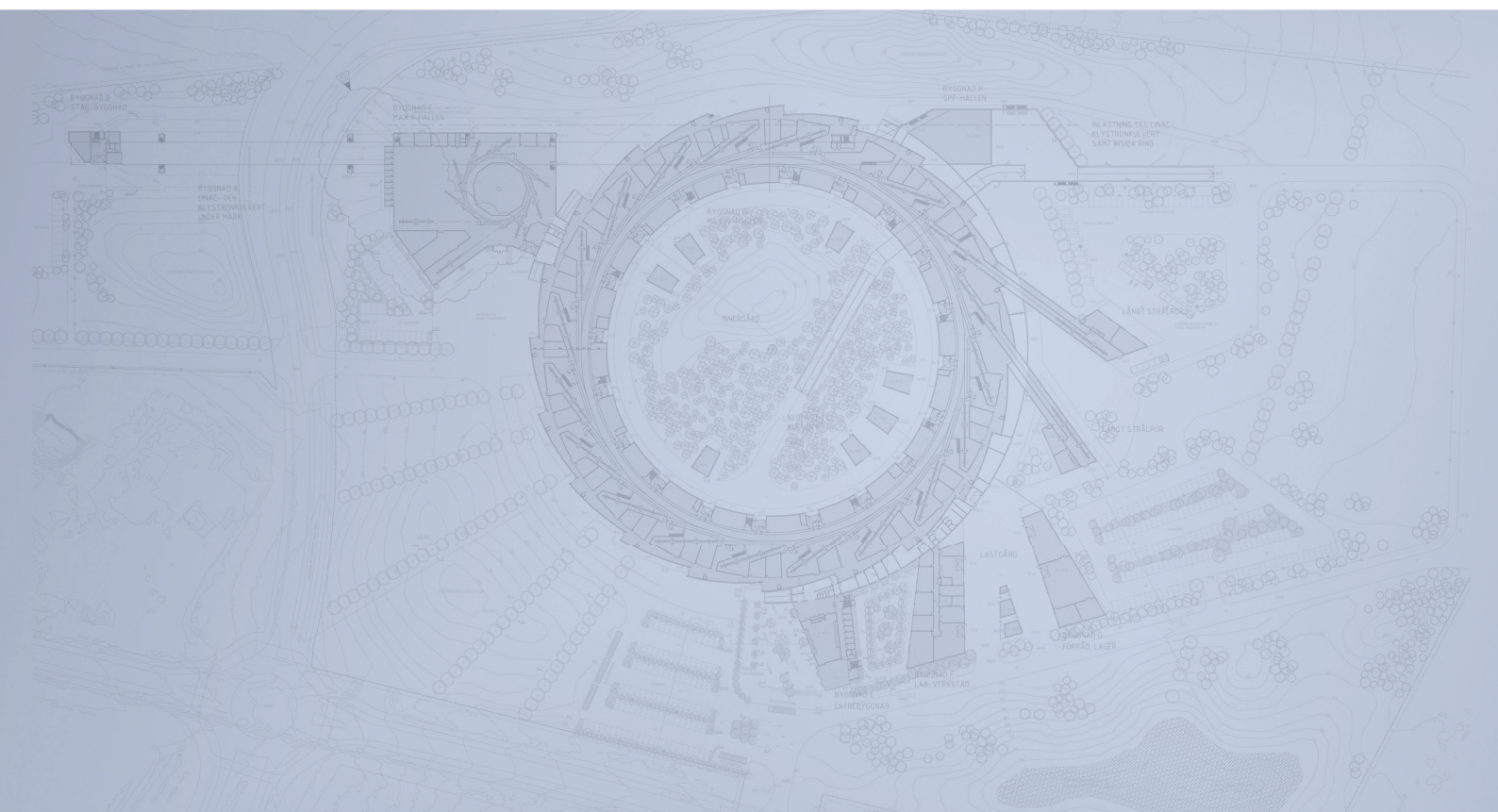
The linacs sections are paired up to make a 200 MeV accelerating unit powered by one klystron. Between the linacs is an intrasection containing vacuum pump, diagnostics, a quadrupole and corrector magnets. The linac modules and quadrupole magnets make up a FODO lattice as seen in figure 4.2.10.

At two points in the accelerator the beam is kicked out to be transferred and injected into the two storage rings. The extraction to the 1.5 GeV ring happens after 17 linac structures which gives a maximum energy of 1.7 GeV. This means we have some redundancy in electron beam energy. The 3 GeV beam is extracted at the end of the accelerator, before BC2 with an energy redundancy of 900 MeV (totally 39 linacs). More about the transfer lines and ring injection can be found in chapters 2.7 and 3.7.



4.2.10: Optics of the FODO lattice in the main linac.

# Detailed Design Report



## Chapter 4

### MAX IV Injector

#### 4.3. Beam Dynamics and Simulations

MAX IV Facility



## 4.3. Beam Dynamics and Simulations

---

<b>4.3.</b>	<b>Beam Dynamics and Simulations .....</b>	<b>2</b>
4.3.1.	ASTRA Simulations .....	2
4.3.2.	MAX IV Linac Beam Dynamics Simulations.....	10
4.3.3.	Phase Stability .....	17

## 4.3. Beam Dynamics and Simulations

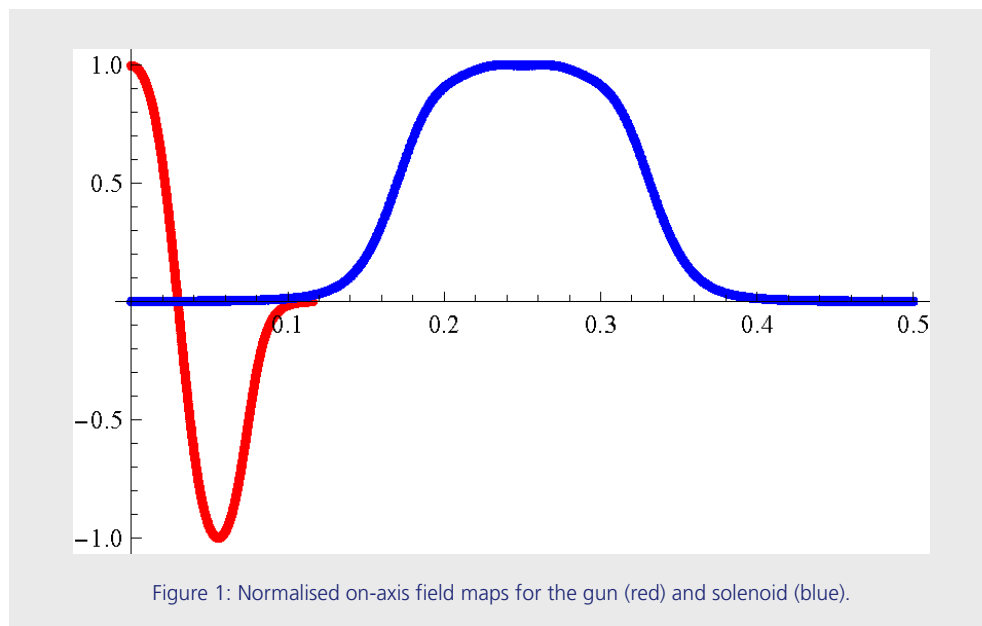
This section deals with the simulations of the optics and optimisation. The section is divided into “Electron guns” which includes the pre-injector up to 100 MeV and the remaining system up to full energy.

### 4.3.1. ASTRA Simulations

#### 4.3.1.1. Astra Simulations

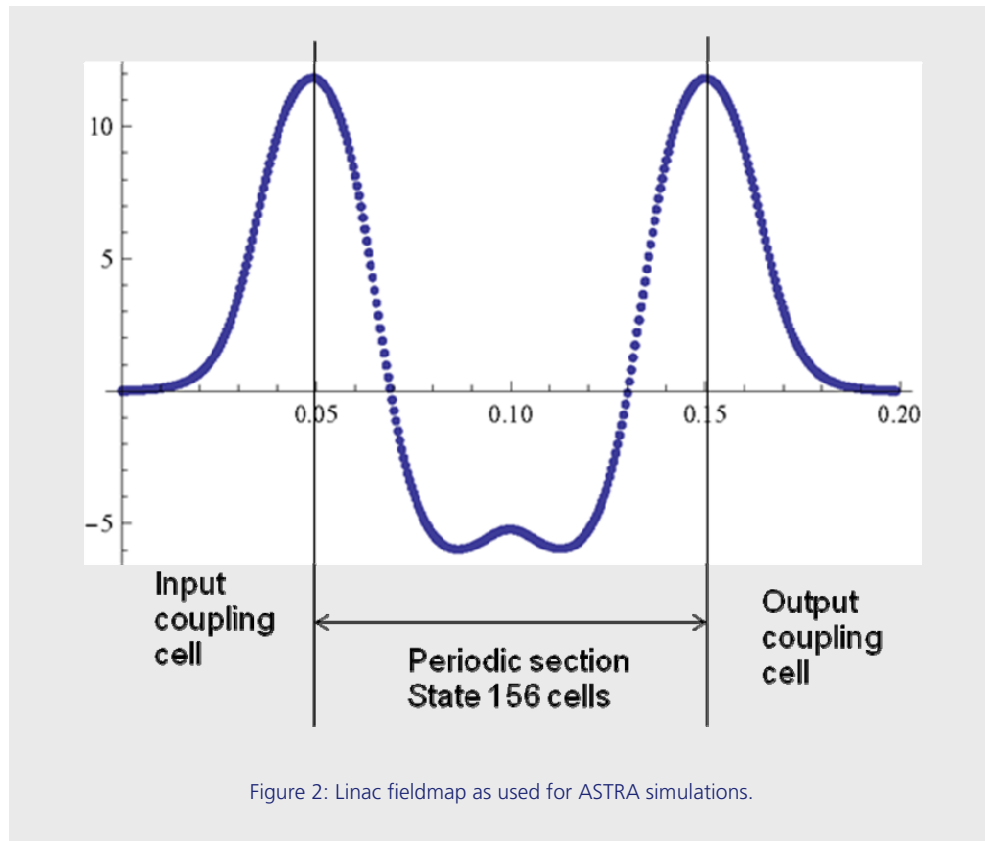
ASTRA [1] was used to model the beam dynamics from the cathode up to the end of the first linac module, L0. ASTRA is nominally a cylindrically symmetric code and tracks particles taking into account space charge. 1D fieldmaps for each beamline element are read in and expanded into 2D to third order within the code.

The gun and solenoid fieldmaps are shown in Figure 1. For more information on these systems, see Section 4.4. For the initial ASTRA simulations it was assumed that the gun will be operated with an on-axis peak field of 100 MV/m. Further simulations are necessary to see the reduction in beam quality with lower field strength. Since the solenoid field is zero at the cathode, no bucking coil is needed.



The laser pulse was modelled with a 5 ps flat-top distribution with 1 ps rise and fall times. The transverse distribution was also given as flat-top. An initial thermal energy of 0.75 eV, isotropically distributed in  $2\pi$ , was given to the emitted 100 pC bunch.

Figure 2 shows the fieldmap used for the  $2\pi/3$  mode travelling-wave linac section. The input and output coupling cells are treated as standing waves and the periodic section treated as a travelling wave, which was stated to repeat for 156 cells. A constant gradient was assumed for the entire linac section, with a peak electric field of 26.25 MV/m which roughly translates to an average accelerating gradient of 20 MeV/m.



All initial ASTRA simulations were carried out with 1000 macroparticles with the space-charge mesh size set to 10x15. More detailed simulations were then carried out, to investigate slice parameters and for importing into ELEGANT, with 100,000 macroparticles with a grid size of 30x45. Finer mesh settings were tested but found to be unnecessary.

#### 4.3.1.2. Laser Spot Size

Initial parameter scans were carried out with the linac entrance positioned at 1.4 m from the cathode. The laser spot diameter was varied from 0.5 to 3 mm. These are summarised in Figure 3. It was found that laser diameters of 0.5 mm and 1 mm gave the lowest emittance, with less variation with solenoid strength compared to the larger laser spots. The 1 mm diameter laser produced beams with far smaller energy spread and bunch length than the 0.5 mm case so was selected for further simulations.



The thermal emittance from a photocathode is given as

$$\epsilon_{th} = \frac{r}{2} \sqrt{\frac{3 k_B T}{2 m_0 c^2}} \quad (1)$$

where  $r$  is the hard-edge radius of the laser spot [2]. Given an initial thermal energy  $k_B T$  of 0.75 eV, the thermal emittance for a 1 mm diameter laser beam is 0.37 mm mrad. Due to Liouville's theorem, this is the lowest emittance achievable for the injector.

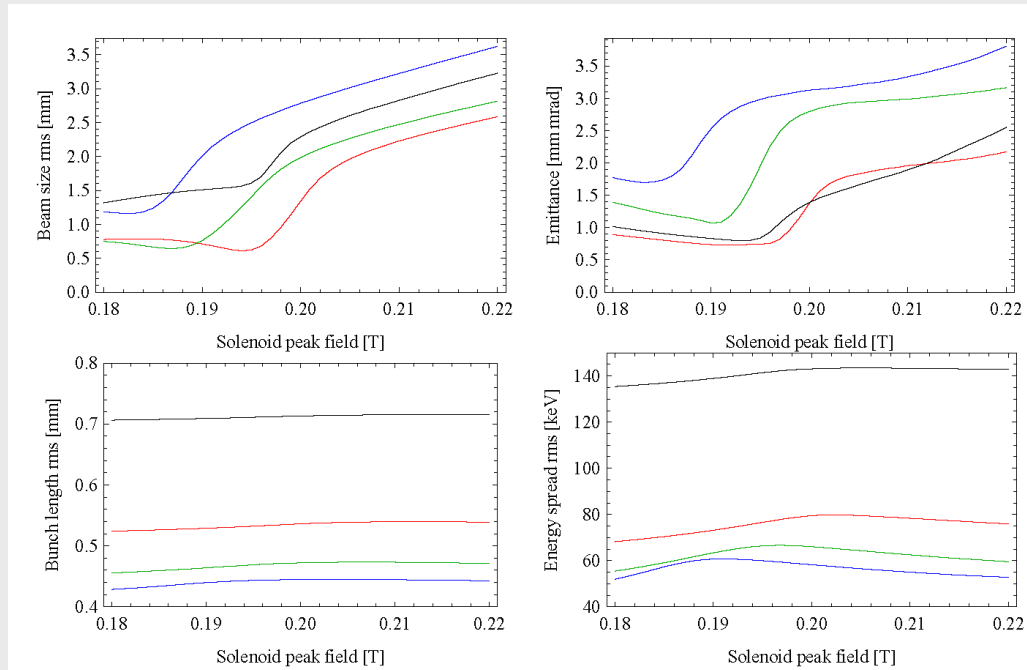


Figure 3: Beam properties at the exit of L0 at various solenoid strengths for laser spot diameters of 0.5 mm (black), 1 mm (red), 2 mm (green), and 3 mm (blue).

### 4.3.1.3. Invariant Amplitude Matching

In order to achieve a constant transverse beam size and low emittance throughout the linac structure, the invariant amplitude condition

$$\sigma_i = \frac{2}{\gamma' \sqrt{\frac{I}{3I_c \gamma_i}}} \quad (2)$$

should be met [3]. This relates the initial beam size  $\sigma_i$  and linac accelerating gradient  $\gamma'$  for a beam of current  $I$  and initial energy  $\gamma_i$ . For a beam of initial energy of 4.5 MeV, linac gradient of 26.25 MV/m, current of 15 A (approximately equal to the peak current of the bunch, see Figure 6), this condition is met with  $\sigma_i = 0.21$  mm. This beam size can easily be met by adjusting the solenoid strength. However, for the condition to hold, the beam should enter the linac at the position where the beam has zero divergence. This occurs when the position of the beam size minimum and the position of the local emittance maximum (between the two minima) meet. This only happens at certain solenoid strengths and therefore for a linac of a certain gradient, the solenoid strength and linac position need to be carefully matched. Figure 4 shows that the condition is met if the linac is positioned at  $\sim 1.8$  m from the cathode for a solenoid with peak field of 0.193 T. It should be noted that changing the gun phase will also affect this condition due to different transverse focussing and slightly different beam energy. Therefore, the three parameters of gun phase, solenoid strength and linac position have to be altered together.

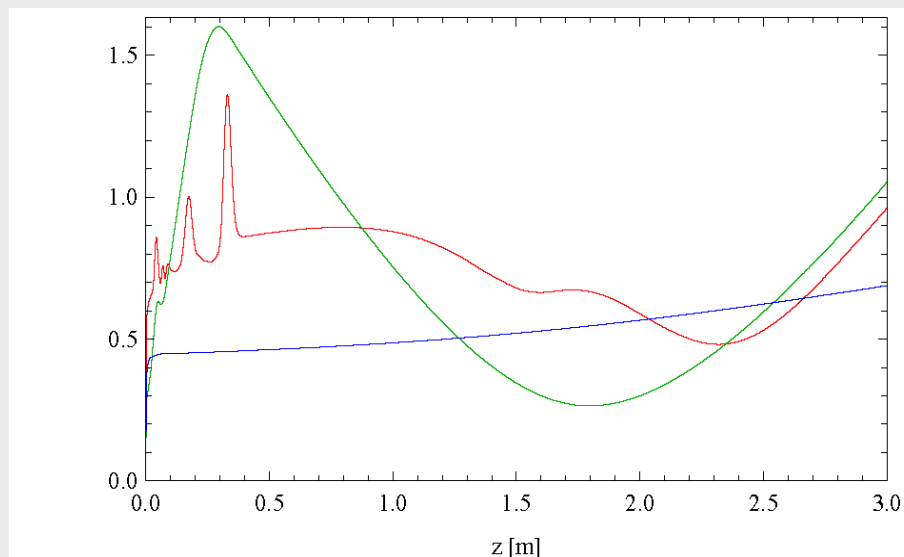


Figure 4: Evolution of rms beam size [mm] (green), transverse emittance [mm mrad] (red), and rms bunch length [mm] (blue) for the gun on crest at 100 MV/m and a solenoid with peak field 0.193 T.

#### 4.3.1.4. Initial Bunch

An initial bunch was produced with both the gun and linac operating on-crest, the linac positioned at 1.8 m from the cathode, and a solenoid peak field of 0.193 T. Figure 5 shows the evolution of rms beam parameters throughout the beamline and Figure 6 shows the bunch profiles. A constant emittance, just above the thermal emittance, is achieved, however the beam is slightly divergent and the longitudinal phase space is highly curved.

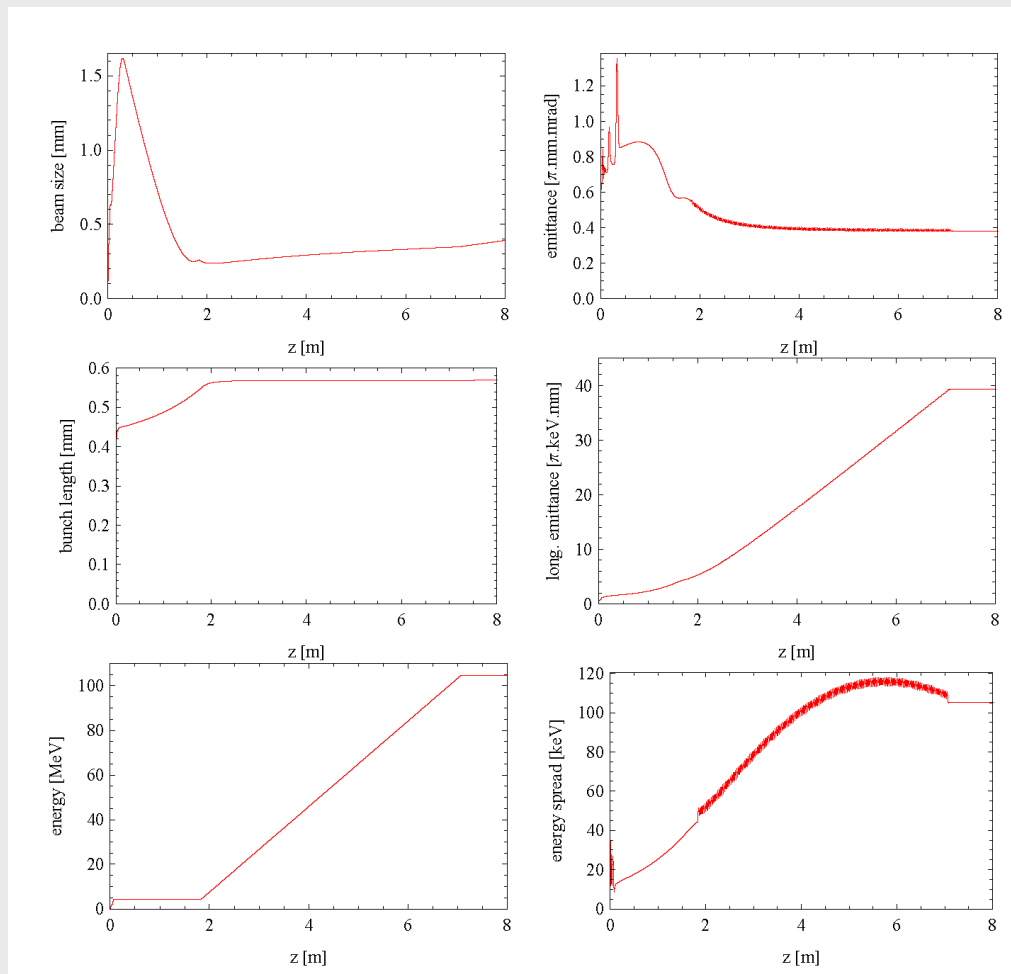


Figure 5: Evolution of rms beam parameters along the beamline.

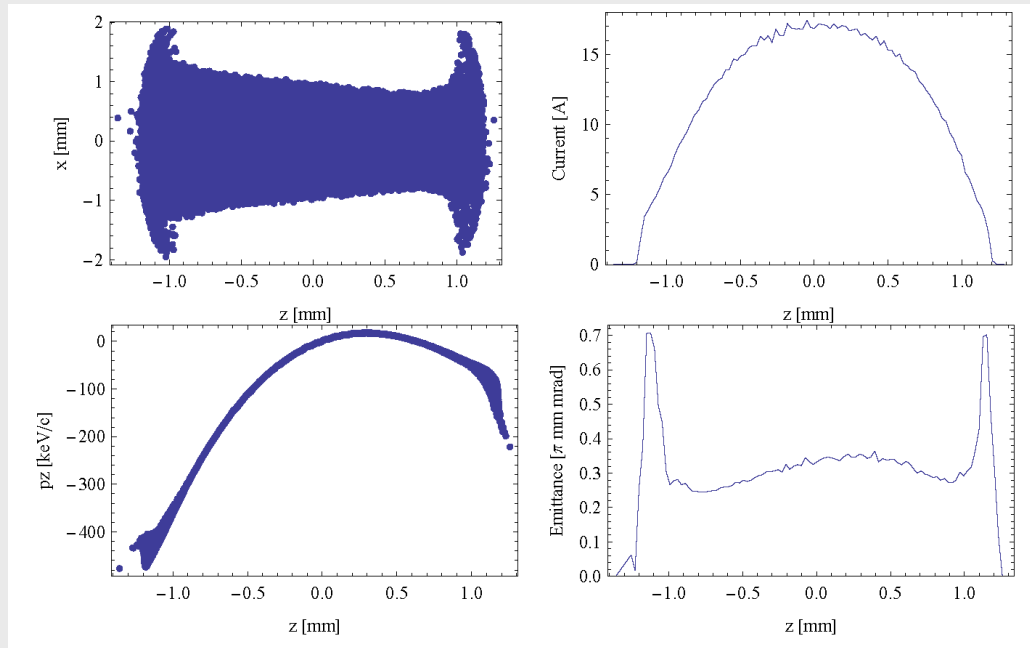


Figure 6: Bunch profiles.

#### 4.3.1.5. Final Bunch

To adjust for the curvature in longitudinal phase space seen in Figure 6, the linac should be operated off-crest. For the compression in BC1 (see Section 4.2.3.), a bunch with a constant energy chirp is desired, with the head of the bunch having higher energy. To investigate the achievable shapes of phase-space, solenoid scans were carried out at various gun phases to find the optimum position of the linac, then the linac phase was scanned. The final bunch input parameters are summarised in Table 1. The evolution of rms beam parameters throughout the beamline is shown in Figure 7. In Figure 8 shows the profiles of the optimised bunch. The final beam parameters are summarised in Table 2. Initial tracking of this bunch through the rest of the injector is detailed in Section 4.3.2.

Bunch charge	100	pC
Laser spot diameter	1	mm
Laser pulse width	5	ps
Laser rise/fall times	1	ps
Initial thermal energy	0.75	eV
Gun peak field	100	MV/m
Gun phase	- 5	°
Solenoid peak field	0.192	T
Linac entrance position	1.85	m
Linac peak field	26.25	MV/m
Linac phase	+ 5	°

Table 1: ASTRA input parameters.

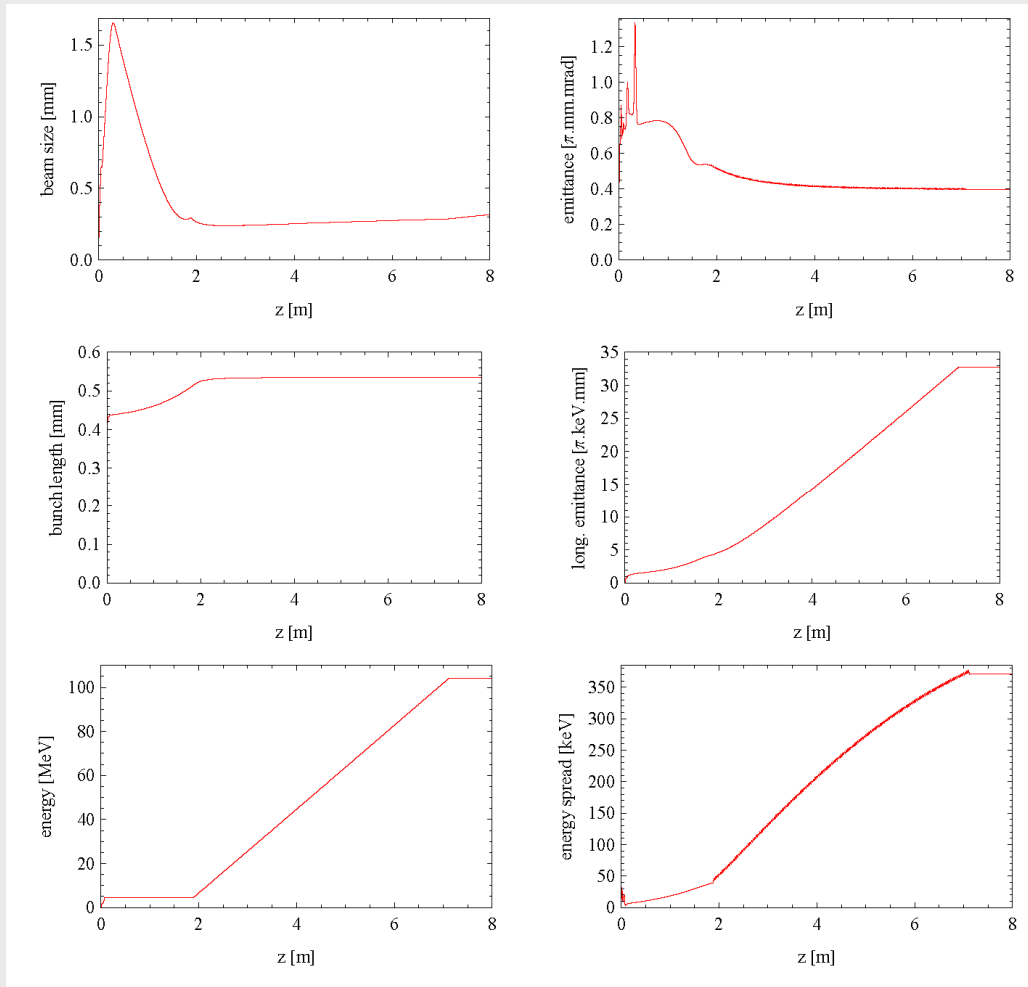


Figure 7: Evolution of rms beam parameters along the final optimised beamline.

Beam size (rms)	0.317	mm
Projected emittance	0.396	mm mrad
Average slice emittance	0.350	mm mrad
Peak current	19	A
Bunch length (rms)	1.79	ps
Bunch length (full)	7.87	ps
Energy spread (full)	1.59	MeV
Energy	104.2	MeV

Table 2: Final bunch parameters.

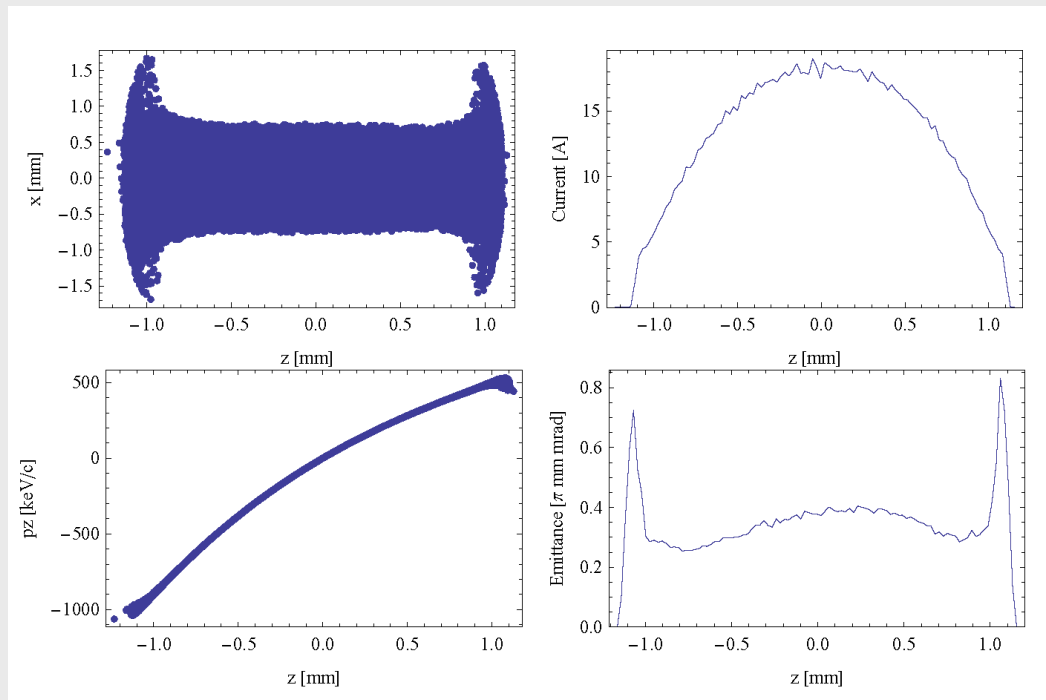


Figure 8: Profiles of the final optimised bunch.

#### 4.3.1.6. References

- [1] K. Flöttmann, ASTRA homepage, <http://www.desy.de/~mpyflo>
- [2] K. Flöttmann, “Note on the thermal emittance of electrons emitted by Cesium Telluride photo cathodes”, TESLA-FEL report 1997-01
- [3] L. Serafini & J.B. Rosenzweig, “*Envelope analysis of intense relativistic quasilaminar beams in rf photoinjectors: A theory of emittance compensation*”, Phys. Rev. E, 55 (6) p7565-7590 (1997)

### 4.3.2. MAX IV Linac Beam Dynamics Simulations

A realistic bunch distribution was generated using ASTRA to optimise parameters up to the end of the first linac module L0. See chapter 4.3.1. for details of this.

The bunch was then converted and read into Elegant for tracking through the linac and the bunch compressors.

At the start of the Elegant tracking the bunch had the properties shown in Figure 6.

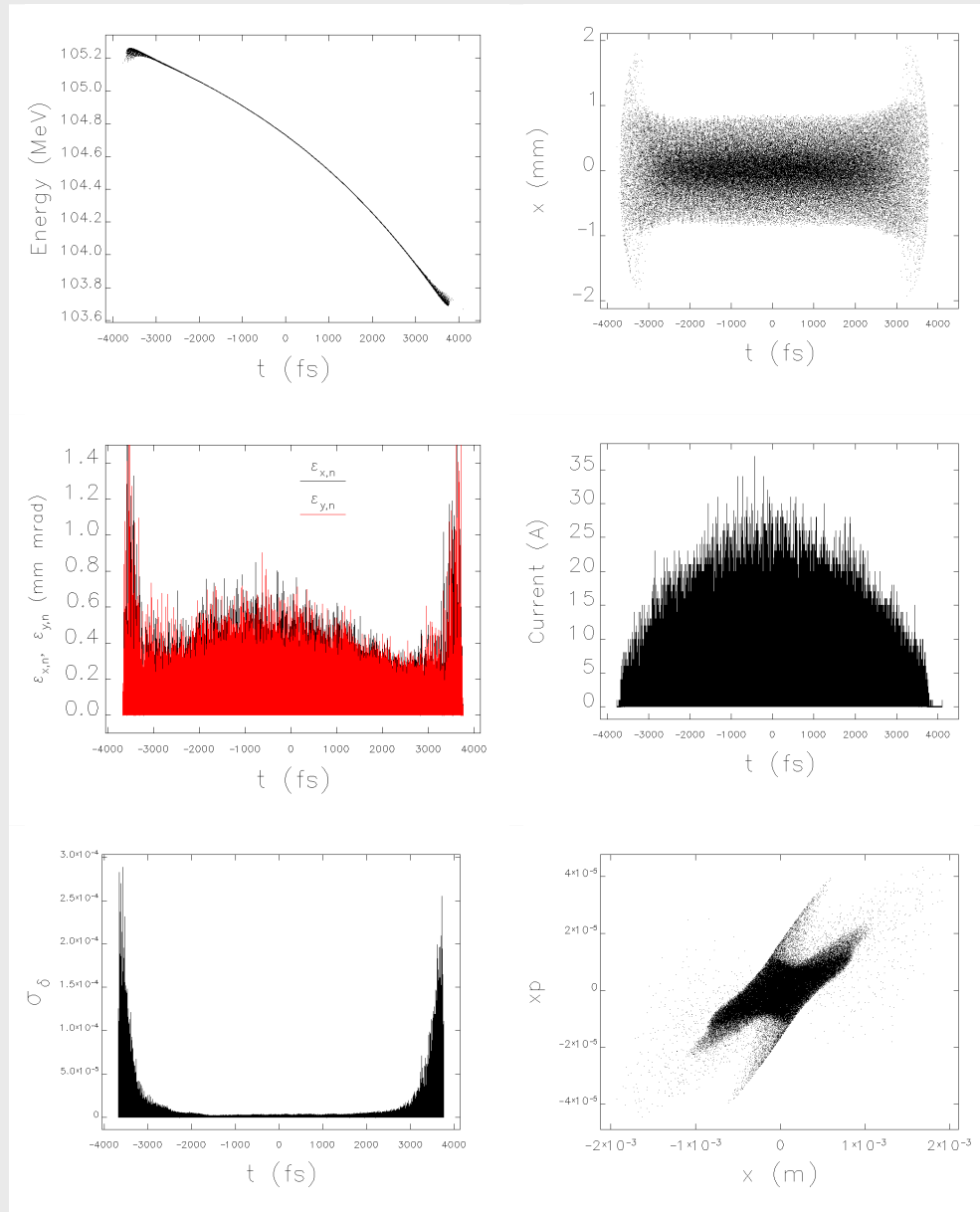


Figure 6: Properties of bunch at start of Linac 1; Longitudinal phase space, horizontal position offset, slice emittances (binned in 1 fs slices), current profile, slice energy spread and horizontal phase space.

### 4.3.2.1. Peak Current Optimisation

The bunch was then tracked through the linac. The effects of transverse and longitudinal wakefield impedance were included, as was longitudinal space charge and coherent synchrotron radiation. Due to the fixed R56 of the achromat compressors, compression was achieved by varying linac phases only. These were found to be optimal at values of 32 degrees beyond crest in the linac section prior to the first compressor, and 17.5 degrees beyond crest in that after the first compressor. Sextupoles in the achromats were tuned such that longitudinal phase space curvature was minimised, this set up is optimal for the short pulse facility where emittance degradation is not of great concern and has second order longitudinal dispersion ( $T_{566}$ ) of opposite sign to first order longitudinal dispersion ( $R_{56}$ ). Figure 7 shows  $R_{56}$  and  $T_{566}$ , chromatic amplitude functions and chromatic derivative of dispersion for the second bunch compressor where the sextupole pair have integrated strength of  $\pm 10. \text{ m}^{-2}$ .

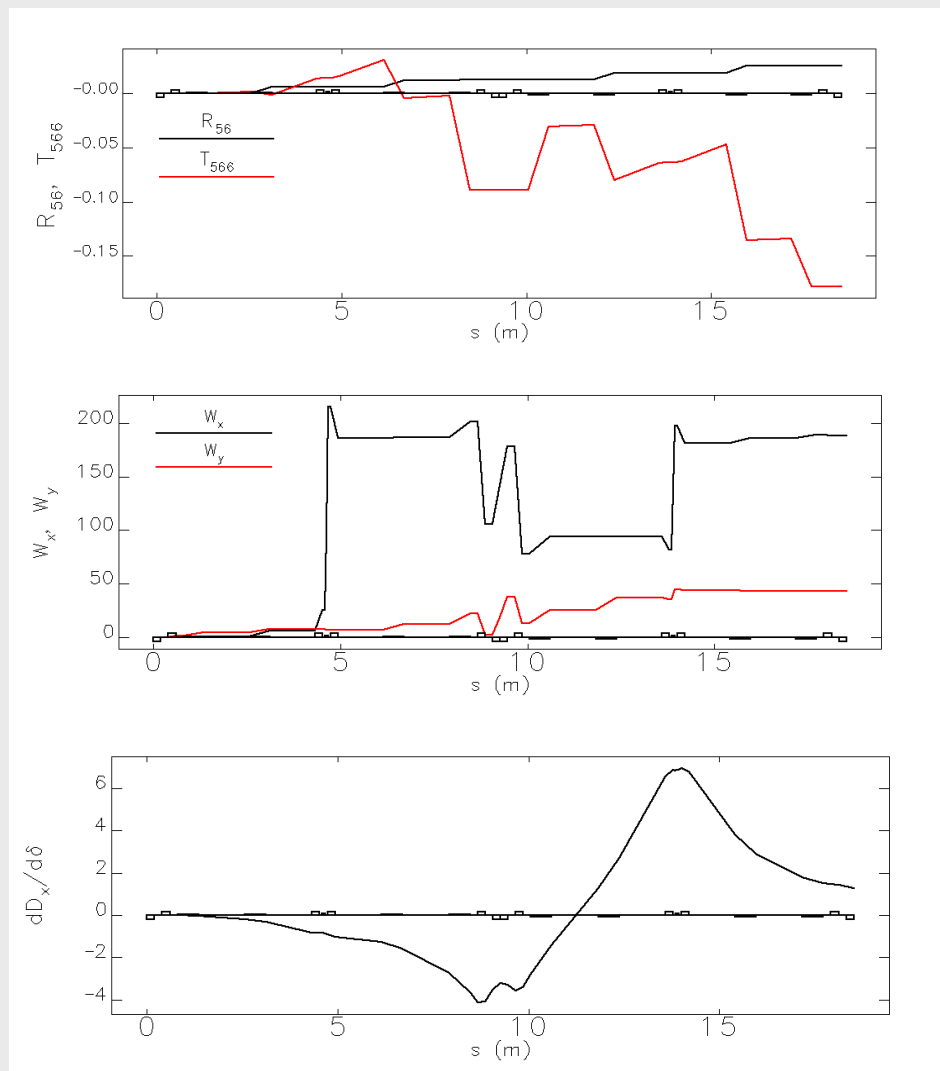


Figure 7: Properties of bunch compressor 2 when tuned for the short pulse facility: First and second order longitudinal dispersion, chromatic amplitude functions and chromatic derivative of dispersion.



Figure 8 shows the evolution of longitudinal phase space through the first and second compressors respectively.

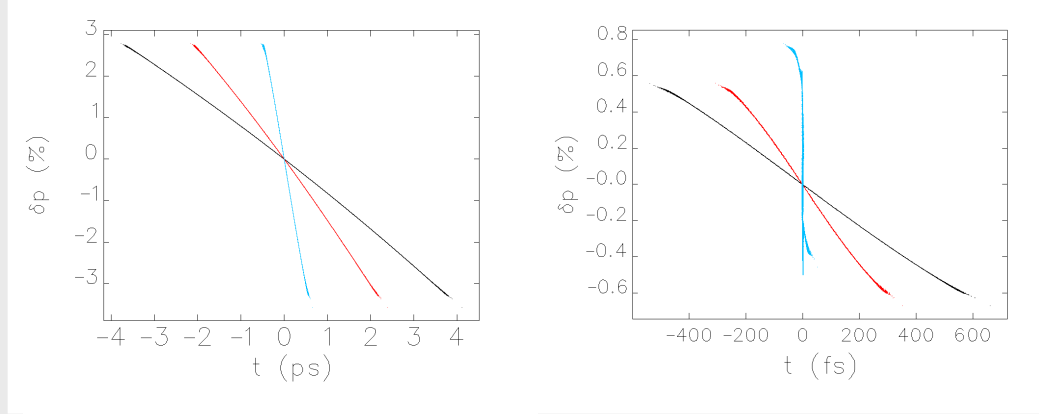


Figure 8: Longitudinal phase space for bunch compressor 1 (left) and bunch compressor 2 (right). Black denotes that on entry, red at the halfway point, and blue at the exit. Mean energy at compressor 1 is 275 MeV, and at compressor 2 is 3720 MeV.

Figure 9 shows the projected, normalised transverse emittances (less dispersive contributions) for the bunch as a function of distance through the linac. It can be seen that the emittance is somewhat degraded as the bunch becomes short in the second compressor. This is due to CSR and leads to the final horizontal emittance value of 2.5 mm mrad.

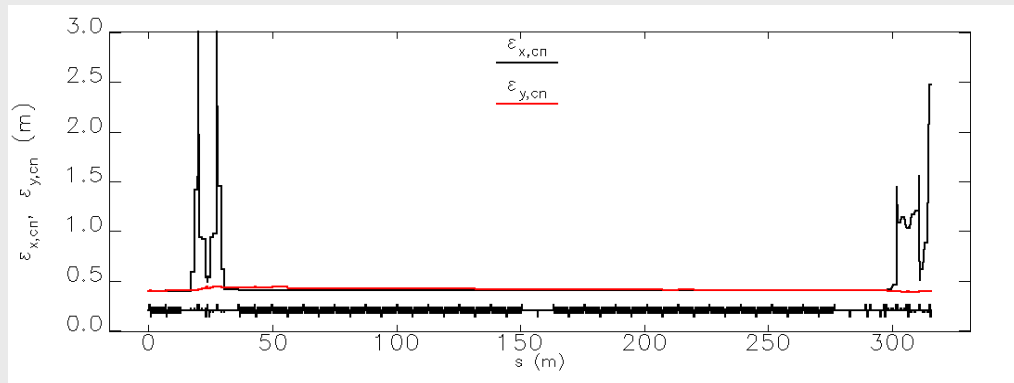


Figure 9: Projected, normalised transverse emittances through the linac. These are plotted without contributions due to dispersion of a Gaussian beam, as the beam is non-Gaussian there are residual "jumps" in dispersive sections, these are a purely calculational artifact.

Figure 10 shows the properties of the bunch at the exit of the second compressor. It can be seen that compression and linearisation is effective and that a peak current of 20kA is achieved. This is done at the expense of both projected and slice emittance. Coherent synchrotron radiation has the effect of shifting trailing particles transversely with respect leading particles.

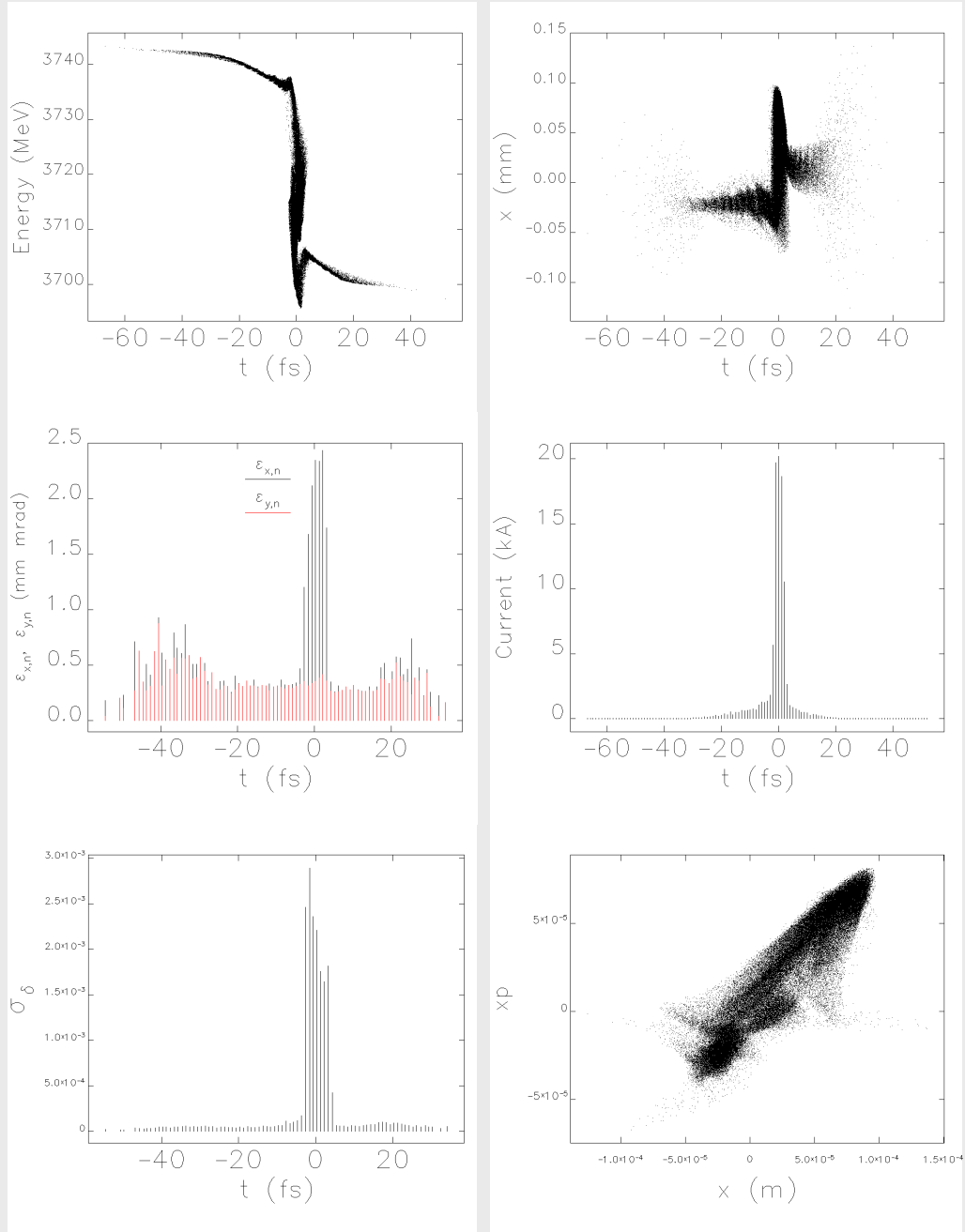


Figure 10: Bunch properties at exit of bunch compressor 2; Longitudinal phase space, horizontal position offset, slice emittances (binned in 1 fs slices), current profile, slice energy spread and horizontal phase space.

#### 4.3.2.2. Low Emittance Optimisation

In order to provide a bunch suitable to drive a free-electron laser we must suppress transverse emittance degradation as much as practicable. This is achieved by tuning the sextupoles in bunch compressor 2 to minimise the chromatic amplitude functions and chromatic derivative of dispersion, in exchange for relaxing the longitudinal linearisation of the bunch. In addition we do not compress as aggressively, thereby trading peak current

against final projected and slice emittance. Figure 11 shows  $R_{56}$  and  $T_{566}$ , chromatic amplitude functions and chromatic derivative of dispersion for bunch compressor 2 when the sextupole pair is tuned for the FEL and have integrated strength of  $\pm 4 \text{ m}^{-2}$ . The latter are much reduced with respect to the short pulse facility tuning, however  $T_{566}$  has changed sign and is now not fully linearising longitudinal phase space.

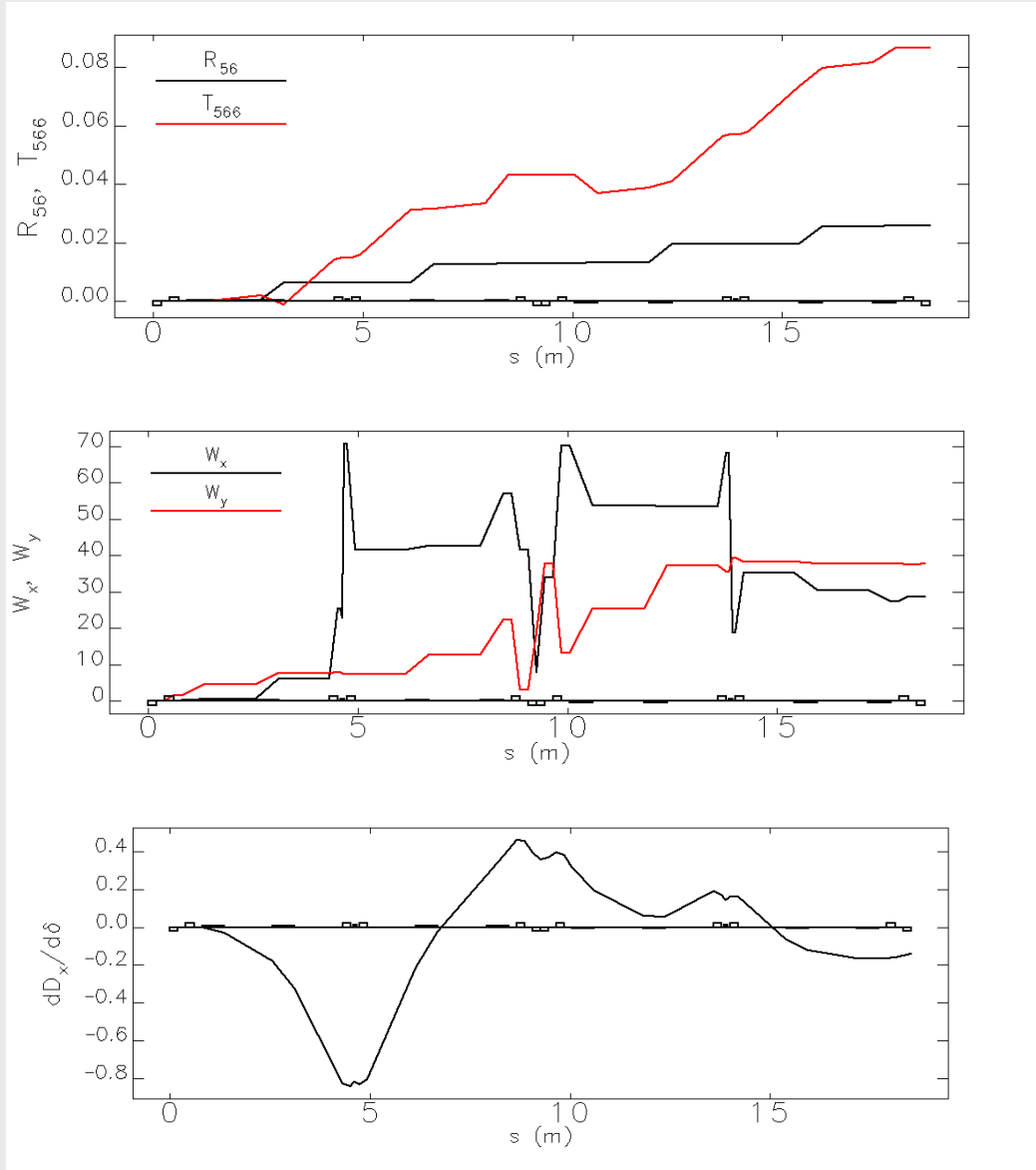


Figure 11: Properties of bunch compressor 2 when tuned for the free-electron laser: First and second order longitudinal dispersion, chromatic amplitude functions and chromatic derivative of dispersion.

We then track through the linac and optimise the phases to produce a reasonable peak current, whilst maintaining small projected and slice horizontal normalised emittance. The phase before bunch compressor 1 is unchanged at +32 degrees from crest, the phase after bunch compressor 1 is reduced to +15.5 degrees from crest.

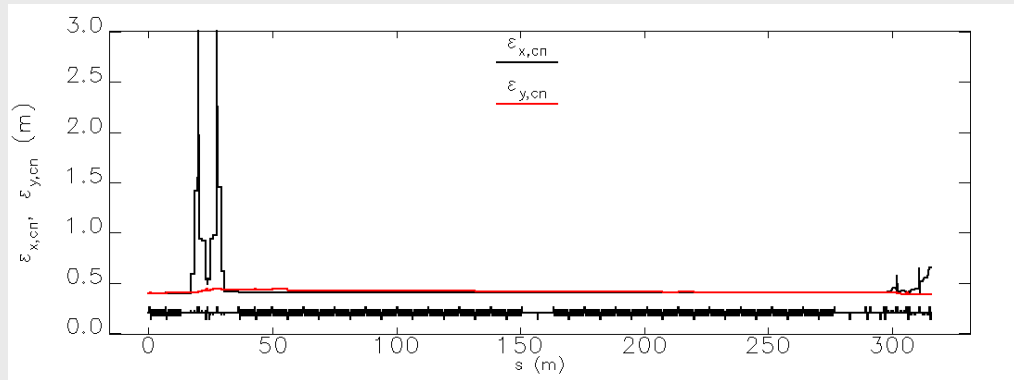


Figure 12: Projected, normalised transverse emittances through the linac. These are plotted without contributions due to dispersion of a Gaussian beam, as the beam is non-Gaussian there are residual "jumps" in dispersive sections, these are a purely calculational artefact.

Figure 12 shows the projected normalised emittance through the linac. We see that in contrast to the short pulse facility tuning, the horizontal emittance only increases to 0.65 mm mrad at the exit of the second compressor.

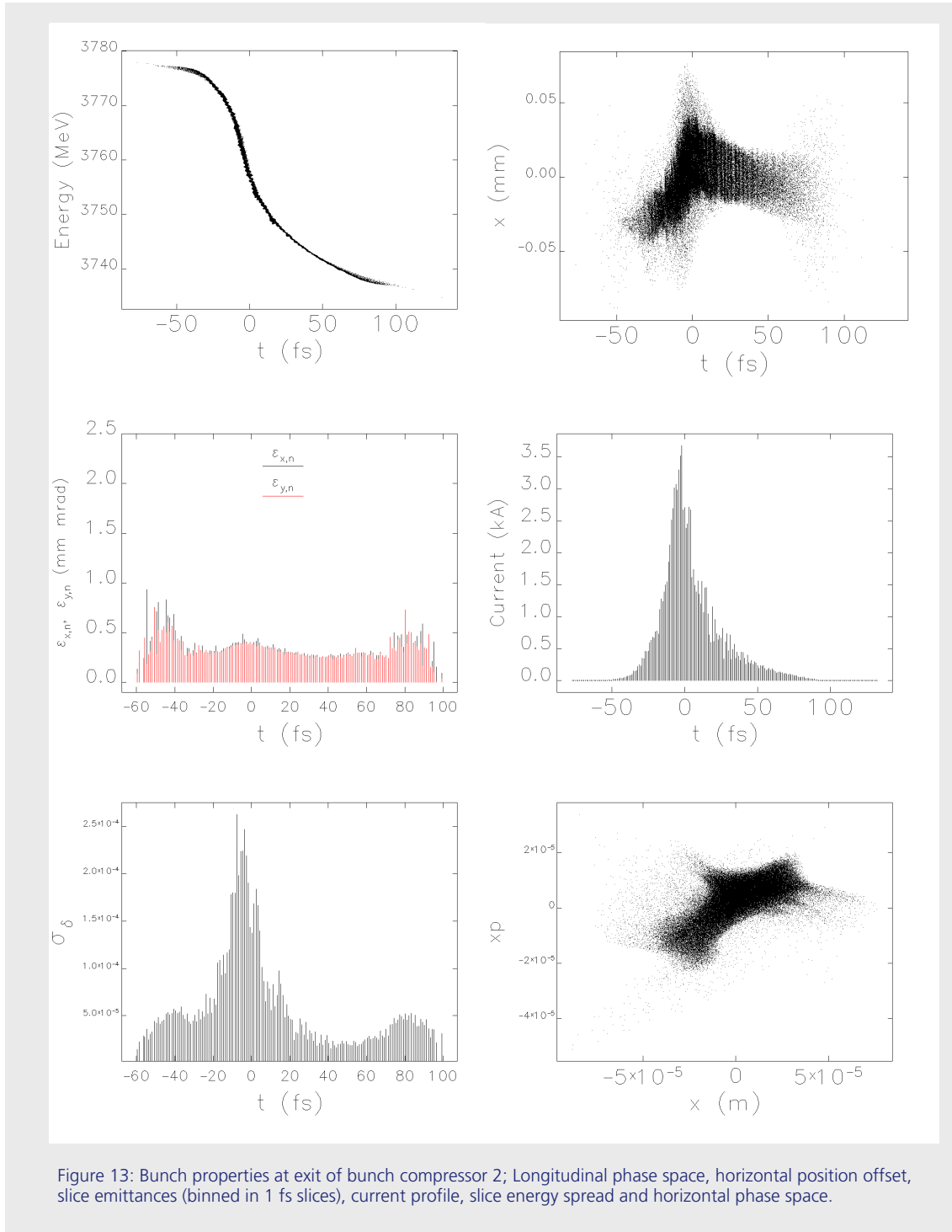
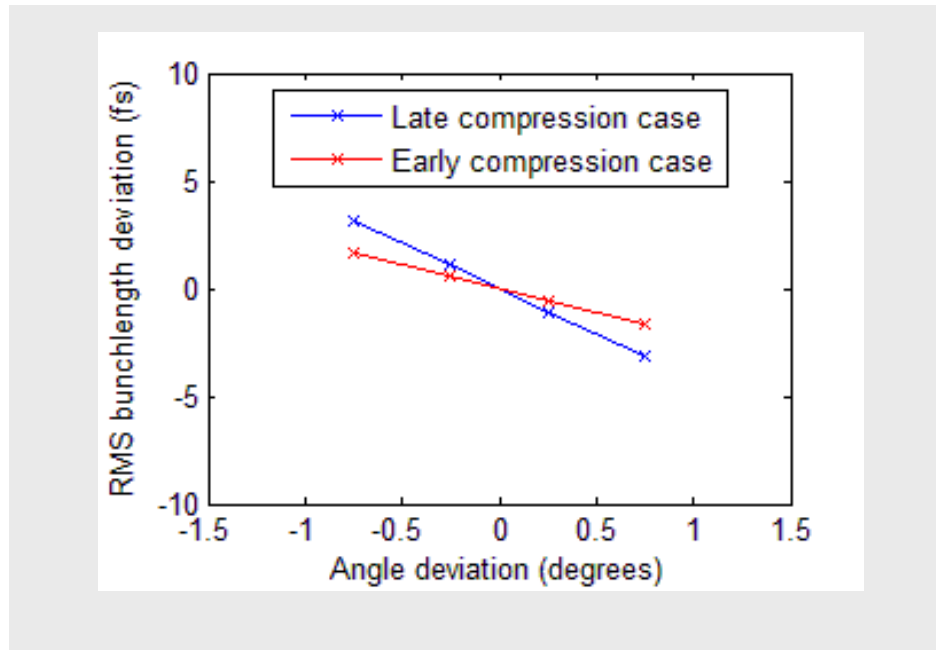


Figure 13 shows the bunch properties at the exit of bunch compressor 2. We see that the bunch slice properties are well preserved. The peak current is reduced, however studies at similar facilities suggest that 3kA would be sufficient to drive an FEL. Of course this should be confirmed through dedicated FEL simulations in the future.

### 4.3.3. Phase Stability

In the following figure I4 have plotted results from simulations where the RF phase in the main linac is scanned 1.5 degrees. The main linac is the 31 accelerator structures between BC1 and BC2.



The case described above is called *late compression* since the beam is “only” compressed to 160 fs in the first bunch compressor and then a factor of almost 5 more in the second bunch compressor. With a jitter of  $\pm 0.75$  degrees in the main linac, the RMS bunchlength jitters with 6.3 fs.

This jitter can be reduced by compressing the bunch more in the first bunch compressor (*early compression case*). The linac phase before BC1 is then 37 degrees, and 3 degrees in the main linac and the bunch is compressed to 95 fs RMS in BC1. The projected emittance is then slightly higher (1.11 mm mrad) and the energy spread lower (0.12 %) and with a phase jitter of 1.5 degrees, the time jitters with 3.3 fs.

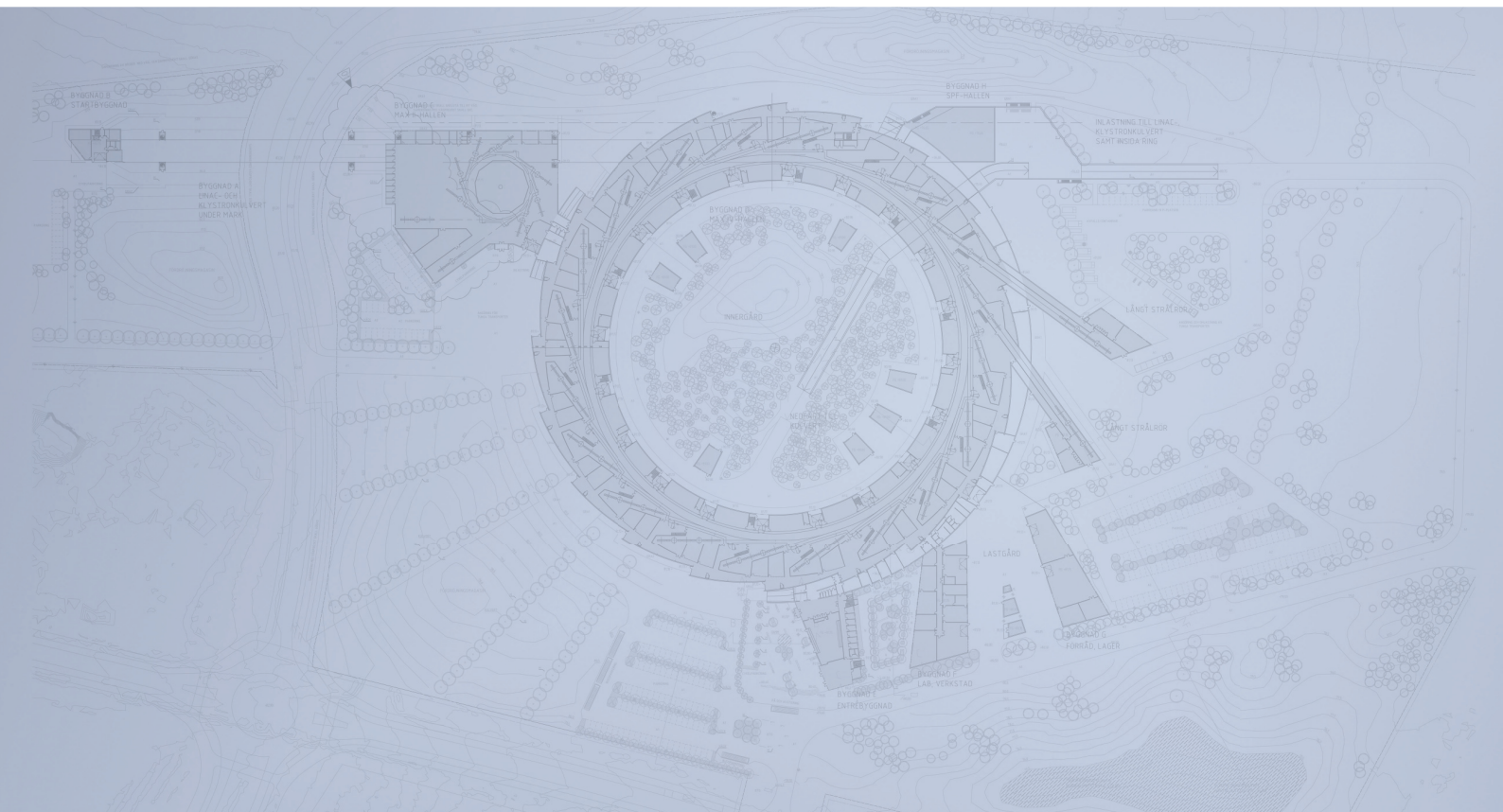
This “stability” comes from the fact that the chirp before the BC2 is determined a lot by the wakefield in the main linac. The higher the compression is in BC1 the higher is the influence from the wake on the chirp. At 37 degrees in the pre BC1 linac the chirp at BC2 is totally dominated by the wakefield and thus not so sensitive to phase jitter in the main linac.

The corresponding arrival time jitter for the high current peak is approximately 3 fs in both cases.

A jitter of 1.5 degrees in the pre BC1 linac causes a bunchlength jitter of almost 20 fs, so here the linac phase needs to be very stable.



# Detailed Design Report



## Chapter 4

### MAX IV Injector

#### 4.4. Electron Guns

MAX IV Facility





# 4.4. Electron Guns

---

- 4.4. Electron Guns .....2**
- 4.4.1. SPF/FEL RF Photo Cathode Gun ..... 2
- 4.4.2. Solenoid Magnet ..... 5
- 4.4.3. Additional Photo Cathode RF Gun ..... 8
- 4.4.4. DC Gun ..... 8
- 4.4.5. Note on the Need for a Solenoid Around the First Linac in the Injector .....12

## 4.4. Electron Guns

---

Several solutions for the MAX IV electron source have been discussed.

In the current solution one single photo cathode RF gun will drive both the ring injection and the SPF mode of the injector. The system will be prepared to complement the operation either by an additional photo cathode RF gun and/or a DC gun system.

For the pre injector the solution is the following:

- One main Photo Cathode RF gun for both ring injection and SPF operation.
- Preparation for a DC gun for ring injection.
- Preparation for an improved Photo Cathode RF gun for FEL operation.

Another approach is the SCSS gun system which still carries several unknown factors. It should be able to deliver the frequency needed. The slice parameters are excellent, but what about projected? How much development is needed?

Thermionic RF gun (similar to current MAX-lab solution) have difficulties with bunching.

### 4.4.1. SPF/FEL RF Photo Cathode Gun

The SPF and the FEL have similar, but not identical, demands on the injector. It can be assumed that both of these modes are achievable by a 3 GHz RF photo cathode gun. These devices are becoming a standard piece of equipment in FEL designs presented worldwide and the systems are also available commercially in more or less complete solutions.

The RF photocathode is followed by an emittance compensation solenoid which matches the system into the pre injector linac. This “locks” the emittance at the exit of the pre-injector linac. Additional focusing at this point is not foreseen to be needed.

A RF photocathode gun can provide the necessary electrons. Running this kind of gun at 100 Hz is challenging (LCLS 120 Hz, FERMI@Elettra 50 Hz in version 2). The laser can rather easily provide the rep rate. The gun structure will have difficulties to house the power. One way is by reducing the maximum fields from 120 MV/m to 80 MV/m the power dissipation will decrease. This might save the case, but there might be a cost in emittance. The solution provided is to power the gun by RF pulses compressed by the SLED system. The shorter pulses will reduce the average power and with a maintained energy deposition a higher rep rate can be achieved. This requires a modified coupling of the gun structure, to rapidly enough couple the RF power into the structure.

The gun structure will be built with an exchangeable backplane. This can either be fitted with a flat Copper surface (Cu-cathode) or a backplane similar to the RF-gun in operation at MAX-lab. This latter backplane can fit a removable cathode assembly which can be of varying materials. Foreseen are BaO (tungsten substrate impregnated with BaO). To mount such a cathode the backplane provides a  $\frac{1}{2}$ -wavelength choke (see Fig).

Laser systems for LCLS have been operated with 99.5% reliability [ref???]. A pair of correctors might be used to assure the beam transport.

(Here fits a description of the FERMI gun system)

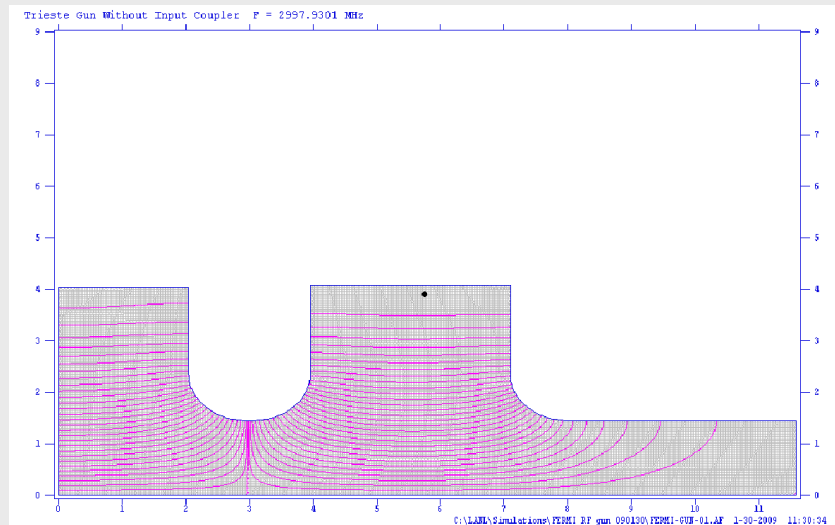


Figure 1: The FERMI gun run in Superfish. (Geometry supplied by Mauro Trovo').

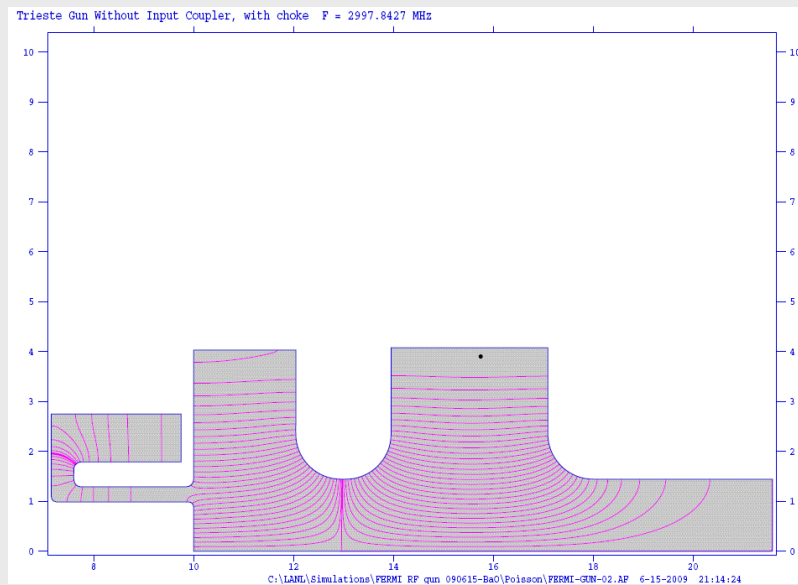


Figure 2: The FERMI gun with an added choke to mount a BaO cathode assembly of the type used at MAX-lab.

The gun geometry as a Superfish [xx] input file is given in Appendix YY for the FERMI gun and in Appendix ZZ for the gun with choke.

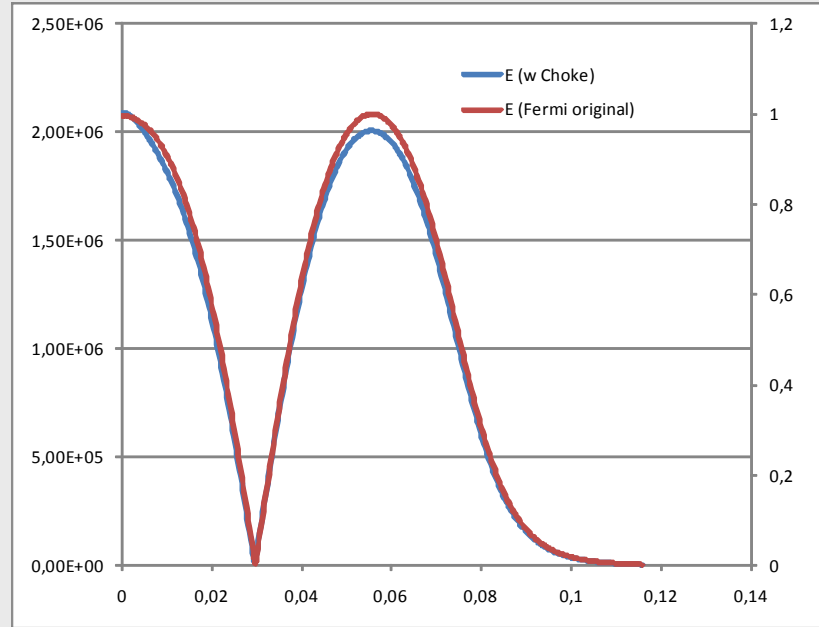


Figure 3: Comparison of the longitudinal E-fields on axis in the two geometries.

#### 4.4.1.1. Cathode Material, Layout, Cu Problems, BaO Type, Pumping Efficiency

It is foreseen to utilise a BaO impregnated Tungsten cathode similar to the currently used cathode at MAX-lab supplied by Spectra-Mat Inc. This gun delivers the charge, stable operation and reliability needed for both guns.

A point of concern is the emittance and rise time of the pulses. At the moment there is no indications that the gun would not perform according to needs. The BaO cathode can always be exchanged for a Cu cathode via the simple exchange mechanism where the cathode holder is kept in place by a spring and inserted from the backside.

#### 4.4.1.2. Coupling and Repetition Frequency

The coupling of the FERMI@Elettra gun is too low to operate well with the short SLED pulses that will be used at MAX IV. These short pulses are needed to easily reach a repetition rate of 100 Hz without special care of the cooling of the gun. The Coupling will be adjusted to around 3 via a post in the waveguide. A redesign of the coupling hole would be possible, but more work has to be put into 3D calculations of the geometry. A post in the waveguide is believed not to disturb the field geometry and resonance frequency of the system, but will be tested on an early built first version of the gun.

### 4.4.2. Solenoid Magnet

The solenoid magnet design is based on the FERMI solenoid.

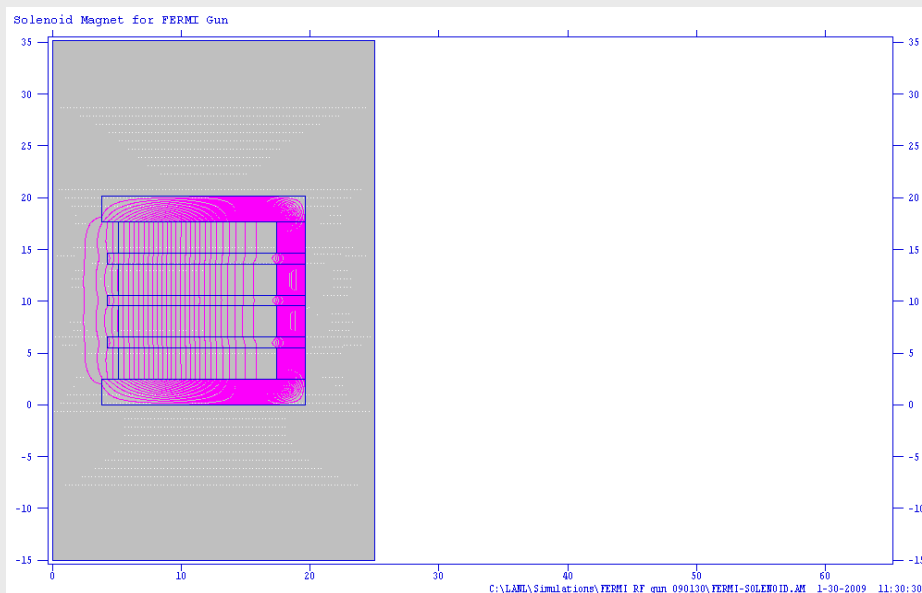


Figure 5: The FERMI solenoid run in Poisson. (Geometry supplied by Mauro Trovo')

Data table

(This table is not edited, but just pasted from the output, not everything is relevant or in relevant form)

Superfish output summary for problem description:

Trieste Gun Without Input Coupler, with choke

Problem file: C:\LANL\Simulations\FERMI RF gun 090615-

BaO\Poisson\FERMI-GUN-02.AF 6-15-2009 21:14:24

-----  
**All calculated values below refer to the mesh geometry only.**

Field normalization (NORM = 0): EZERO = 1.00000 MV/m

Frequency = 2997.84270 MHz

Particle rest mass energy = 0.511000 MeV

Beta = 1.0000000

Normalization factor for E0 = 1.000 MV/m = 13606.061

Transit-time factor = 0.7607960

Stored energy = 0.0017428 Joules

Using standard room-temperature copper.

Surface resistance = 14.28452 milliOhm

Normal-conductor resistivity = 1.72410 microOhm-cm

Operating temperature = 20.0000 C

Power dissipation = 2511.1113 W

Q = 13072.9

Shunt impedance = 46.155 MOhm/m

Rs\*Q = 186.740 Ohm

Z\*T\*T = 26.715 MOhm/m

r/Q = 236.845 Ohm

Wake loss parameter = 1.11530 V/pC

Average magnetic field on the outer wall = 3471.95 A/m, 8.60957 W/cm<sup>2</sup>Maximum H (at Z,R = 17.093,3.29915) = 3809.51 A/m, 10.3651 W/cm<sup>2</sup>

Maximum E (at Z,R = 9.99401,0.913722) = 2.6614 MV/m, 0.056894 Kilp.

Ratio of peak fields Bmax/Emax = 1.7987 mT/(MV/m)

Peak-to-average ratio Emax/E0 = 2.6614

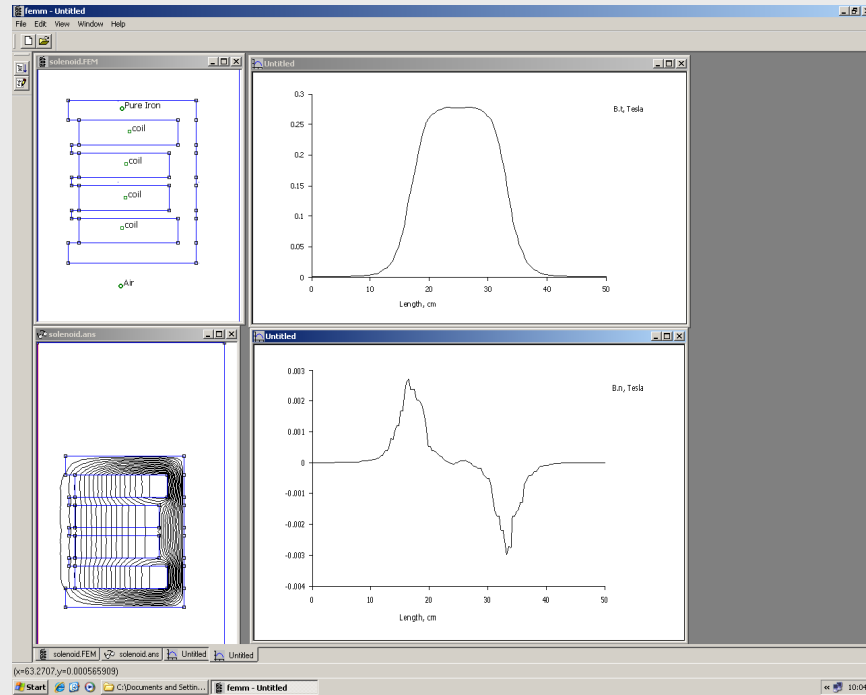


Figure 6: Adapted solenoid design with different coils.  
 (COIL OUTER=23\*6\*70.65=9750 At; COIL INNER=21\*6\*70.65=8909.3 At)

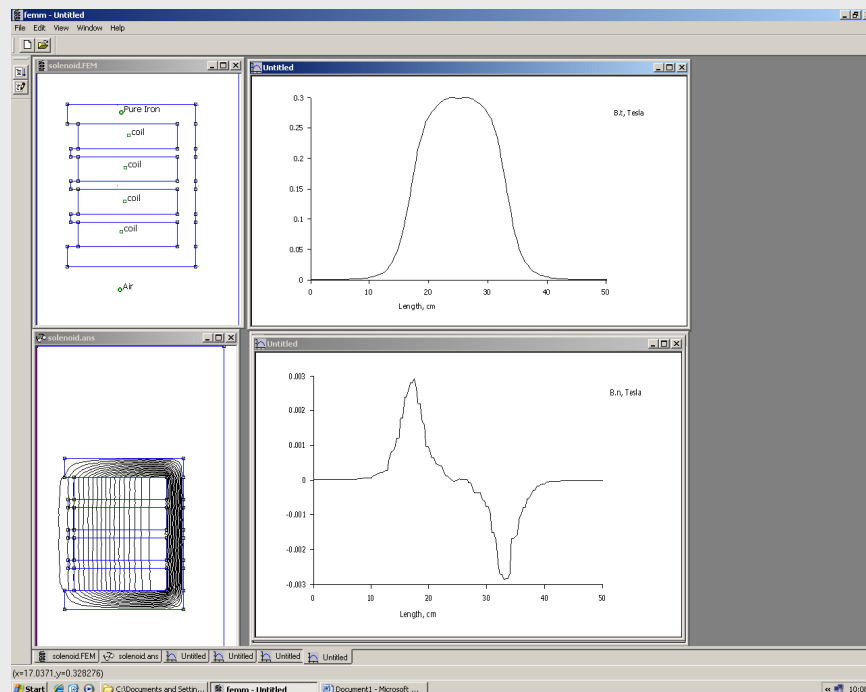


Figure 7: Adapted solenoid design with identical coils.  
 (COIL OUTER= COIL INNER =23\*6\*70.65=9750 At)



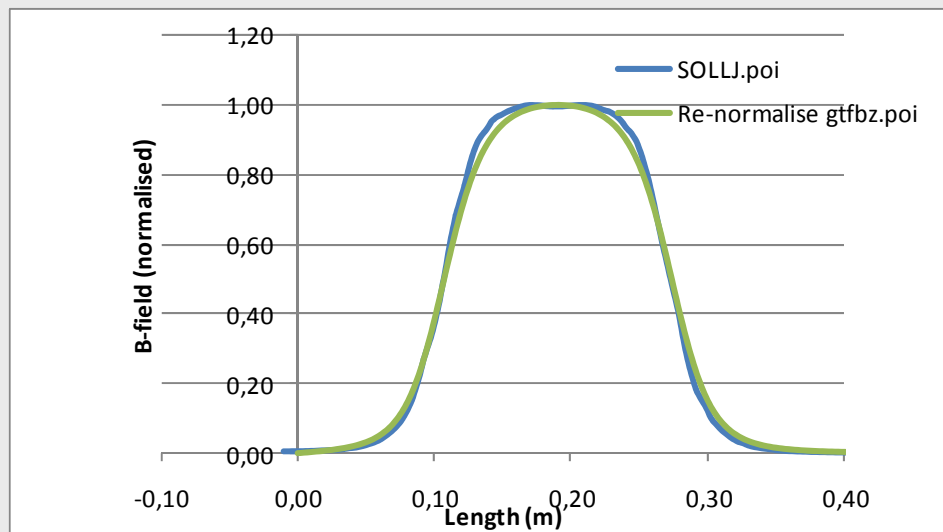


Figure 8: Comparison of solenoid excitation between the Fermi type and the adapted design. (Unclear which magnet is which. Drawings from Mauro Trovo, adaption by LIL/Bengt Anderberg and finally the magnet by Martin)

### 4.4.3. Additional Photo Cathode RF Gun

An additional photo cathode RF gun can most probably be placed at a small angle, if operated with a short pulse ( $<10$  ps) drive laser providing a beam for ring injection.

The straight forward line will then be free for an improved gun solution suitable for FEL operation, if necessary.

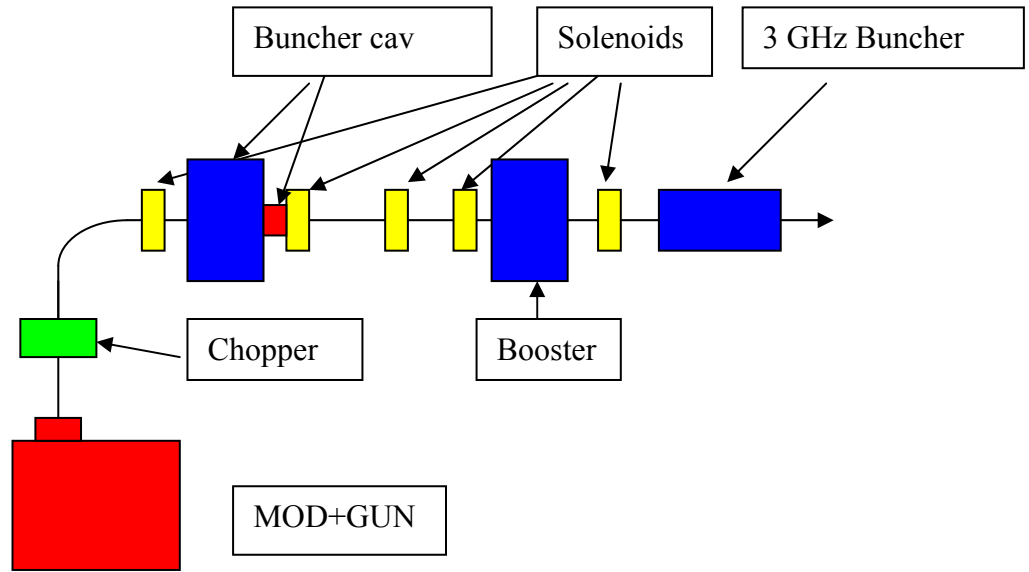
### 4.4.4. DC Gun

The possibility to include a traditional DC gun into the design is being considered. Such a gun will be placed pointing upwards, followed by a 90 degree bend magnet (see fig). How this gun will be fit into the injection line between the photo cathode RF gun and the linac-0 still has to be solved.

(Mikael's previous text)

The electron source is as mentioned above similar to the one used at the SCSS [xxx] project. The kind of device is more bulky than a photo-cathode RF gun, but the system is quite reliable and stable. A closer look at the subsystems of this injector shows that all components used here are reliable, stable, well-known and not that expensive.

The system is shown schematically in fig. 2.3 below.



A thermionic cathode gun is used as the electron source since these cathodes are quite reliable and last for years without any maintenance. Carefully designed, the gun can deliver an electron beam with an emittance close to the one defined by the thermal one

$$\epsilon_n = \frac{r_c}{2} \sqrt{\frac{kT}{m_e c^2}}$$

A BaO cathode of 7 mm diameter will provide an electron beam of 4 A at 1 mm mrad normalised emittance. This electron beam is chopped and then gently compressed ballistically to a 100 A current pulse of a total length of 10 ps.

When the electron bunch is compressed, the longitudinal electric fields tend to stretch the bunch. This stretching effect is proportional to the current gradient, a constant current yields no longitudinal fields. The local compression is given by

$$COMPR = \frac{1}{1 - \frac{L}{c} \beta^2 \frac{d\beta}{dt}}$$

Where  $L$  is the drift length,  $\beta c$  the electron velocity and  $\frac{d\beta}{dt}$  is the  $\beta$  time derivative at the bunching moment.

Even if  $\frac{d\beta}{dt}$  could be kept constant, the  $\beta^2$  dependence tends to give overbunching at the low energy end (leading electrons) and to little bunching at the high energy (trailing electrons). The introduction of an extra buncher cavity, operated at the third harmonic of the main buncher, will effectively decrease this effect.

The next effect counteracting an even current distribution is that the field variation in the buncher cavity no are linear in time, but sine-shaped, which yield a too small energy deviation for large phase angles. The operating frequency of the main buncher cavity should thus be sufficiently low.

The electron beam is chopped two times. The 4 A current from the gun is chopped into 400 ps slices just after the gun. 250 ps pulse length will be necessary to achieve 1 nC/3 GHz bunch. The head and tail of the bunches are kept during the bunching process to avoid debunching current gradients. The head and tail are finally scraped off after the 3 GHz buncher when the electron energy is sufficiently high to avoid de-compression.

The electron beam radius is kept rather large ( $r=10$  mm) to decrease the space charge effects. This radius is kept until the beam enters the 3 GHz buncher, where it is decreased to 3 mm.

---

**Electron gun**

Voltage	500 kV
Pulse length	0.5 $\mu$ s
Current	4 A

**Chopper 1**

Bunch length	800 ps
Nr of bunches	1-10

**Main Buncher**

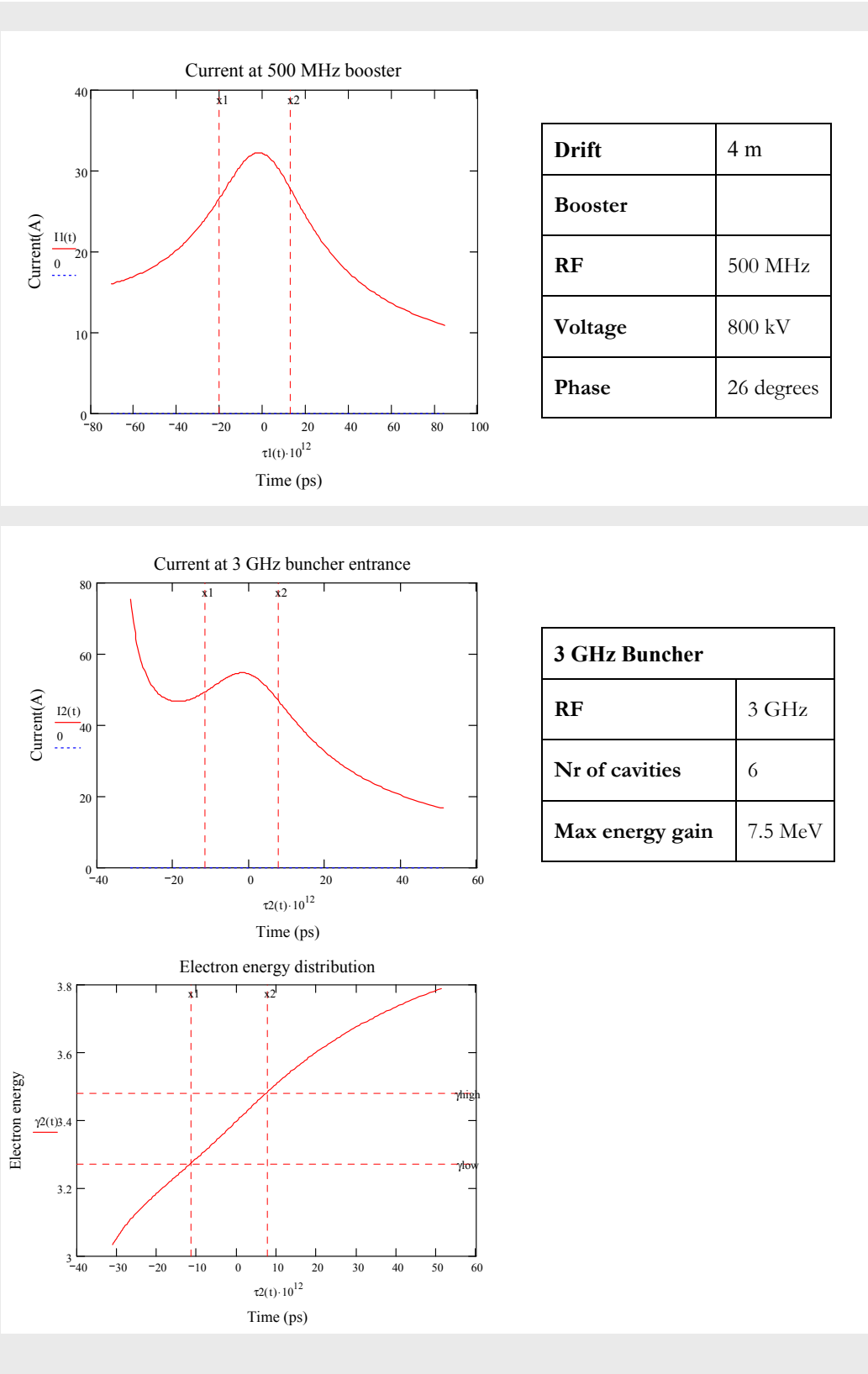
RF	200 MHz
Voltage	230 kV
Phase	0 degrees ( $E(t)=E_0 \sin(\omega t - \theta)$ )

**Harmonic buncher**

RF	600 MHz
Voltage	23 kV
Phase	180 degrees
Drift length	2.2 m

---

The current distribution at the booster entrance is shown below. The vertical markers indicate the electrons preserved through the linac acceleration.



#### 4.4.5. Note on the Need for a Solenoid around the First Linac in the Injector

SW 091111

Several designs of injectors (like LCLS) utilizes a solenoid around the first linac. According to the LCLS design report this is due to the fact that the accelerating fields in the linac are not high enough to give the focusing strong required for the emittance compensation scheme to work until the beam has left the space charge dominated region (around 150 MeV in the LCLS case). (LCLS designreport p 6-7).

The energy gain necessary is given by eq. 6.3 (LCLS design report)

$$\gamma' = \frac{2}{\sigma} \sqrt{\frac{\hat{I}}{2I_0 \gamma}}$$

At the entrance of the first linac in the LCLS case:

$\hat{I}=100$  A,  $\gamma=10$ ,  $\sigma=0.4$  mm,  $I_0=17000$ A

giving  $\gamma'=86$  or  $E=43$  MV/m. This is not within range of the SLAC linacs.

In the Max injector case at 0.25 nC the  $\hat{I}=34$  A (other parameters similar)

Giving  $\gamma'=50$  or  $E=25$  MV/m

This is very close to the nominal field of the MAX IV linacs. With a charge of 0.1 nC the emittance compensation should easily work with the available fields, and no solenoid should be needed.

# MAX IV Facility



# 4.5. Laser System

---

- 4.5. Laser System .....2**
- 4.5.1. Frequency Standard.....2
- 4.5.2. Trigger Pulse Distribution.....4
- 4.5.3. Photocathode Drive Laser.....4
- 4.5.4. Seed Laser Option .....8
- 4.5.5. Laser System Diagnostics.....9



## 4.5. Laser System

---

### 4.5.1. Frequency Standard

Synchronization on the sub-picosecond level is required for stable generation of the short pulses at the SPF. It is also of interest for synchronizing lasers for pump-probe experiments and linac beam diagnostics, such as electro-optic sampling.

Current state of the art systems aim at having a few tens of fs jitter (Winter-Nucl Inst Meth-2006). They rely on a stabilized fiber based link between the signal generator and experimental stations. The signal chain starts with an ultra-low noise RF generator, the performance of which is critical for the achievable jitter level. A fiber laser is locked to this low-noise signal and distributed to wherever it is needed. The optical path length of the fiber changes with temperature and cause jitter in the distributed pulses. This jitter source can be eliminated by inserting a fiber stretcher, controlled by a feedback loop driven by the phase error between the laser pulses and a small back-reflection at the end of a fiber link.

Many fibers are radiation sensitive, so they should not be placed in an environment where they would be exposed to large dose. It is therefore recommended to put the fibers in the same tunnel as the Klystrons and not in the linac tunnel itself.

By using a wavelength common in the telecom industry, 1550 nm, a large inventory of relatively inexpensive components can be used.

The robustness of the system would benefit from having two fibers laid out for redundancy. To retain the short laser pulses after propagation in a long fiber, dispersion compensated fiber must be used.

A problem with the fiber based synchronization scheme is that even though thermal effects on the fiber are compensated by the feedback system, the linac itself will change in length. That means that the laser pulses will arrive at a fixed time, but electrons will drift and the synchronization is lost. This must be monitored by measuring the electron arrival time with respect to the laser with high precision ( $\sim 10$  fs), suggesting electro-optical means.

An alternative approach is to let the laser pulses propagate in low vacuum along the full length of the linac. When the linac cave changes length due to thermal effects, the mirrors for the laser will also move by the same amount, ensuring a more stable synchronization. There are other problems with this technique, such as maintaining a 300 m long vacuum system. It would have to be sectioned into  $\sim 10$  m parts for initial alignment.

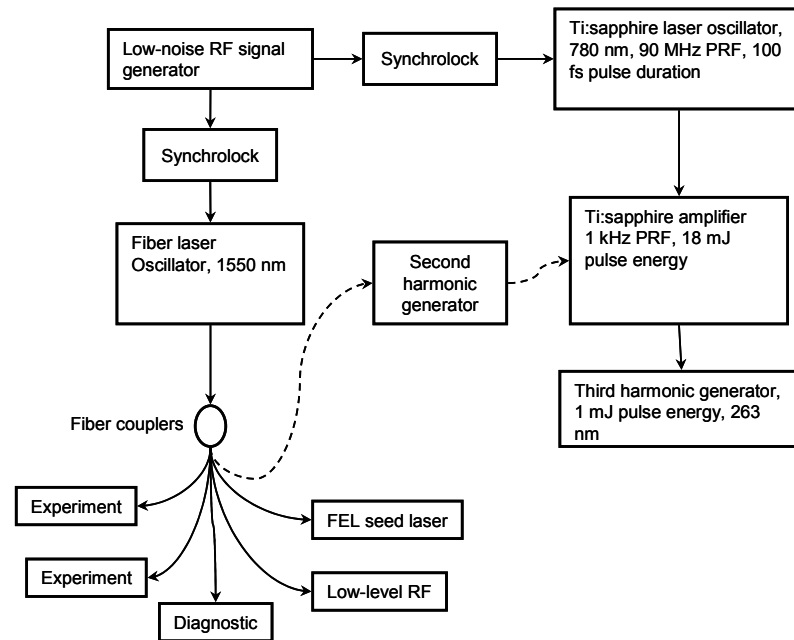


Figure 1: Overview of a fiber based synchronization system. A mode locked fiber laser is locked to a low-noise microwave oscillator. The pulses are distributed through length stabilized fibers to various stations needing a stable frequency. The pulses from the fiber laser could also be frequency doubled and amplified directly for use as photocathode drive laser.

## 4.5.2. Trigger Pulse Distribution

There are three different clocks for the trigger generator, depending on the mode of operation. When the SPF is running, the trigger can use a clock derived from the 3 GHz reference. For ring injections, the trigger must be synchronized to the frequency of the rings (different for 1.5 GeV and 3 GeV rings due to thermal effects) for single bunch injection. 100 MHz bunch clocks from the rings are then selectable clock inputs for trigger generation.

The trigger pulses have more relaxed jitter and drift requirements than the synchronization signal. The laser can handle jitter of  $\sim 100$  ps, limited by the Pockel's cells. The amount of drift that can be tolerated is mostly limited by the requirement for single bunch injection, which means on the order of a ns.

These trigger signals need to be distributed to a large number of devices, e.g. Klystrons, magnets, diagnostics. The system needs to be flexible, easy to maintain and expandable. By including a time stamp in the pulse distribution, various diagnostics throughout the machine can be correlated for each shot.

## 4.5.3. Photocathode Drive Laser

An RF photocathode system is planned for the generation of electrons to be accelerated. This is to ensure low emittance operation of the short pulse facility. For ring injections, emittance is not so much a concern as the ability to provide single bunch electron pulses timed to the ring bunches. Both of these modes will be provided with a single gun and a versatile laser system.

### 4.5.3.1. Overview

The RF photocathode gun works by photo emission of electrons from the cathode illuminated by a short laser pulse. The photon energy of the laser must then be higher than the work function of the cathode material. It should, however, not be much higher, as the additional energy of the released electrons will show up as increased transverse thermal emittance (see Yamamoto-J Appl Phys 102, 024904 (2007)):

$$\varepsilon_{n,\text{rms}} = \frac{R}{2} \sqrt{\frac{2\Delta E}{3m_e c^2} + \frac{2k_B T}{m_e c^2}}$$

A common photocathode material (FERMI, LCLS) is copper, with a work function of  $\sim 4.7$  eV (the value is sensitive to surface conditions, see e.g. Li-Phys Stat Sol 201, 2005-2012 (2004)). The laser wavelength then needs to be below 264 nm, but 266 nm should work albeit at lower quantum efficiency.

Around  $10^{-5}$  quantum efficiency is normally achieved with a copper cathode, but variations of more than a factor of two (up or down) is possible due to a large sensitivity to surface conditions.

The pulse duration should be short enough that the fields in the RF cycle do not change appreciably during the laser pulse, but still long enough that the space charge of the released electrons do not blow the beam up. In practice, this means  $\sim 10$  ps for a 3 GHz RF system.

To synchronize the laser with the RF cycle, the oscillator is locked to an RF source. The current system at the MAX-lab testFEL with a FemtoLock from Femto Lasers works well, with the time jitter determined largely by the quality of the RF source. Jitter down to 50 fs is possible (LCLS), with 0.2 ps being achieved at the testFEL at MAX-lab.

#### 4.5.3.2. Drive Laser Specification

The two modes of operation (SPF, ring injection) require quite different laser performance. For ring injection, the critical parameter is the total charge per shot. 300 pC would be enough for the single pass BPMs to give good signal during commissioning. For the laser that translates into 300  $\mu$ J at 266 nm, including a factor two safety margin. The pulse duration should be less than 1 ns to excite the ringing filter in the BPM electronics substantially. The repetition rate is limited to 10 Hz during initial injection due to the damping time of the injected electrons and more or less single shot during top-up. The SPF on the other hand only needs 100 pC of charge, but during  $< 10$  ps to avoid energy spread of the accelerated electrons. Another point of interest is the ability, at a later stage, to shape the laser pulse intensity longitudinally to e.g. a ramp with sharp edges instead of the usual Gaussian distribution. The repetition rate is set to 100 Hz continuously, limited by the power draw of the Klystrons.

All of these requirements can be met with a single CPA (chirped pulse amplification) Ti:sapphire laser system. With a fundamental wavelength of 780-800 nm, the third harmonic is at 260-266 nm and suitable for a copper cathode. The laser energy is set by the ring injection charge requirement. With an approximate 10% conversion efficiency into the third harmonic, the laser needs  $\sim 5$  mJ per pulse in the fundamental after compression. A 10 nm bandwidth of the laser should be sufficient for any subsequent pulse shaping.

The photocathode laser will operate around the clock at a remote location (beginning of linac). To minimize the maintenance personnel needed it is very important that the laser is robust and reliable. Diode pumped solid state (DPSS) lasers are then required for pumping the Ti:sapphire crystals. The diodes typically have lifetimes rated at  $\sim 10000$  h, giving a service interval of around one year. It would be advantageous to use the same type of pump laser for as many lasers throughout the facility as possible (several similar lasers are e.g. planned at the experimental stations of the SPF). They could then swap parts and the knowledge for servicing the lasers would increase.

With a laser pulse repetition frequency of 1 kHz (a standard for this type of laser) the average power is  $\sim 10$  W. High average power means significant thermal loading of the amplifier crystals, giving rise to thermal lensing. To combat this, cryo cooling of at least the power amplifier- but preferably all- crystals is needed. When Ti:sapphire is cooled down to cryogenic ( $<100$  K) the thermal conductivity increases dramatically and problems with thermal lensing are eliminated. The average power on the cathode is 50 mW with 100 pC charge generation, corresponding to an irradiance of  $6 \text{ W/cm}^2$  if a 1 mm diameter spot is assumed. This should be low enough to not cause thermal damage to the cathode. The peak irradiance is more critical at  $\sim 1 \text{ GW/cm}^2$  with 10 ps pulse duration.

In case of laser failure, complete redundancy is advisable, with two identical systems in parallel. It should be possible to switch between the lasers remotely. Maintenance and testing could then also be done without stopping operations. It is important that there are ample online diagnostics. All diagnostics should interface directly with the Tango control system.

#### 4.5.3.3. Generation of three Photocathode Laser Pulses

During top-up a single (or a few) shots will be fired into the rings once per minute or so. To minimize the disturbance this creates for the SPF experiments, switching mode should be done from one shot to the next. It is difficult to change the laser energy in this short (ms) time and it would probably reduce both the stability and lifetime of the laser. The focusing on the cathode surface would also have to be enlarged to avoid space charge effects. These problems can be avoided if the laser pulse is split up into a pulse train, with each sub-pulse delayed to adjacent 3 GHz RF cycles. With three pulses, giving 100 pC each, the total pulse duration would be 660 ps and the BPMs would still have good response.

Two methods for splitting and recombining a laser pulse are presented here. In the first, two beam splitters are followed by delay stages and the pulses are then focused to a common point which is then relay imaged at the cathode surface. The losses in this case would be small and the system passive and quite robust. The difficulty is that the aperture of the relay imaging system needs to be big and if the cathode is moved out of focus, three spots on the cathode surface are used, possibly changing the emittance and charge of the electron beams. In principle the pulses could be made to overlap by monitoring a virtual cathode plane and having individual motorized steering mirrors for the beams.

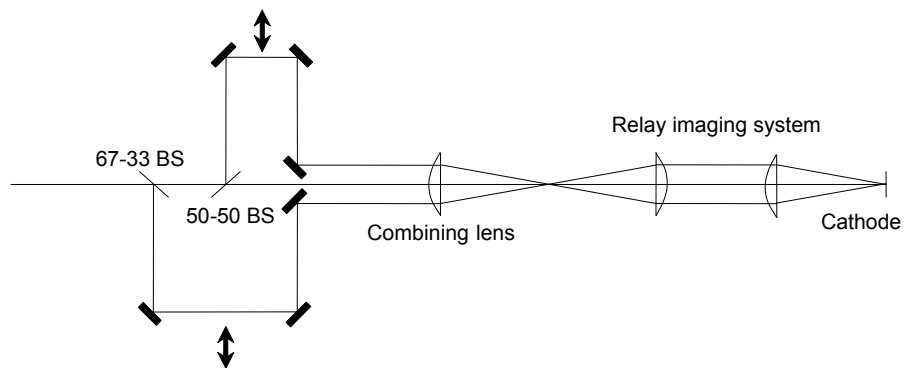


Figure 2: Schematic of the spatial beam combining technique.  
The beams are spatially separated on the combining lens and then focussed onto the same spot.

The second method relies on combination of pulses with different polarization. If the laser is normally incident on the cathode surface, the polarization of the laser is not important for the photoelectron generation process. Polarizing beam splitters and combiners give a collinear pulse train. In the case of a passive system 40 % of the laser energy is lost (since there are only two independent polarization directions). The option is then to twist the polarization of the second pulse after the first two are combined. This can be done with a Pockel's cell. BBO crystals work at 266 nm and drivers with ns rise times exists. In this case the setup can be of low loss. Using a Pockel's cell means the system is no longer passive and not as robust. If the loss can be tolerated (amounting to a few 100  $\mu\text{J}$ ), the passive system would be preferred. An advantage with the polarizer technique is that it would be easy to adjust the energy in every pulse individually by adding half-wave plates in the delay lines.

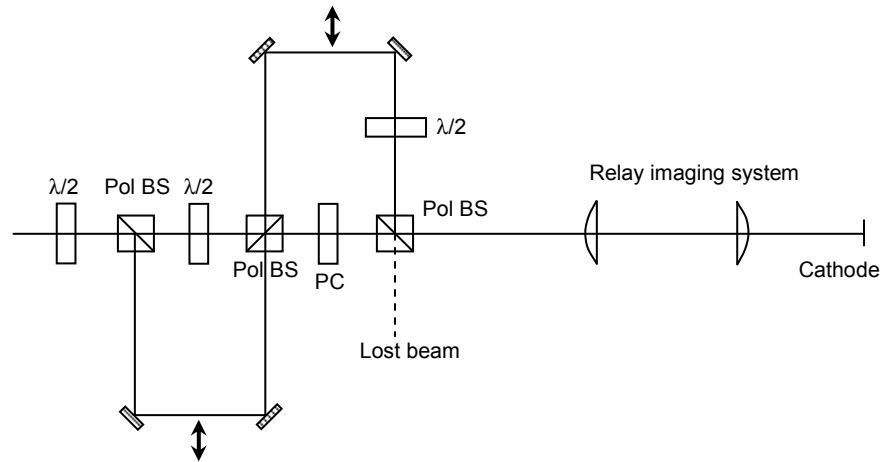


Figure 3: Schematic of the polarization combining technique. The beams are split into orthogonal polarization directions and combined using polarizers. If the Pockel's cell (PC) is not used, 40 % of the energy is lost in the last combination stage.

Another way to use a triple pulse is to supply all three end stations of the short pulse facility with electrons on every shot. It would be possible to use a 100 MHz cavity to deflect three electron pulses differently depending on where in the RF cycle they enter the cavity. To get maximum deviation they should enter at 90 degree intervals (max positive field, zero field, max negative field), or 2.5 ns in the case of a 100 MHz cavity. These three electron bunches are generated at the photocathode by laser pulses. The charge in each bunch should be some 100 pC, which means 0.05 mJ 266 nm laser energy (assuming a  $1e-5$  quantum efficiency copper cathode) per bunch. In addition to setting the 2.5 ns timing of the pulses, fine tuning of the laser arrival time in the phase of the 3 GHz accelerating RF fields in the linac is needed on a ps time scale.

#### 4.5.4. Seed Laser Option

At a later stage, a seeded FEL could be constructed using the electron beam after the linac. To set up the microbunching in the beam, a seed laser is made to overlap the electron bunch in space and time. Since the electron bunches are very short, the timing requirements are particularly strict - typically  $\sim 10$  fs. To achieve such low timing jitter the synchronization pulses from the fiber system could be used to lock a local Ti:sapphire oscillator at the FEL site. It could also be possible to send actual oscillator pulses from the RF photo cathode driver through a separate stabilized fiber to the seed laser and amplify them locally. This scheme is what the testFEL at MAX-lab is using (without the fiber stabilization).

The seed wavelength could be the tripled Ti:sapphire ( $\sim 266$  nm) for easy handling in air and relatively high pulse energy. The final wavelength of the FEL is then  $>50$  nm for a single stage (5<sup>th</sup> harmonic of the seed wavelength). Alternatively, the seed laser could drive high harmonic generation (HHG) in a gas jet, allowing seeding with much shorter wavelengths. A single stage FEL could then reach  $<10$  nm (using the 5<sup>th</sup> harmonic of the 15<sup>th</sup> harmonic of the laser). The disadvantage is setup complexity and laser pulse energy; the conversion efficiency is in the range  $10^{-4}$ - $10^{-5}$ . To get the seed energy up, the drive laser must have much higher pulse energy. This limits the repetition rate to maybe 10-100 Hz.

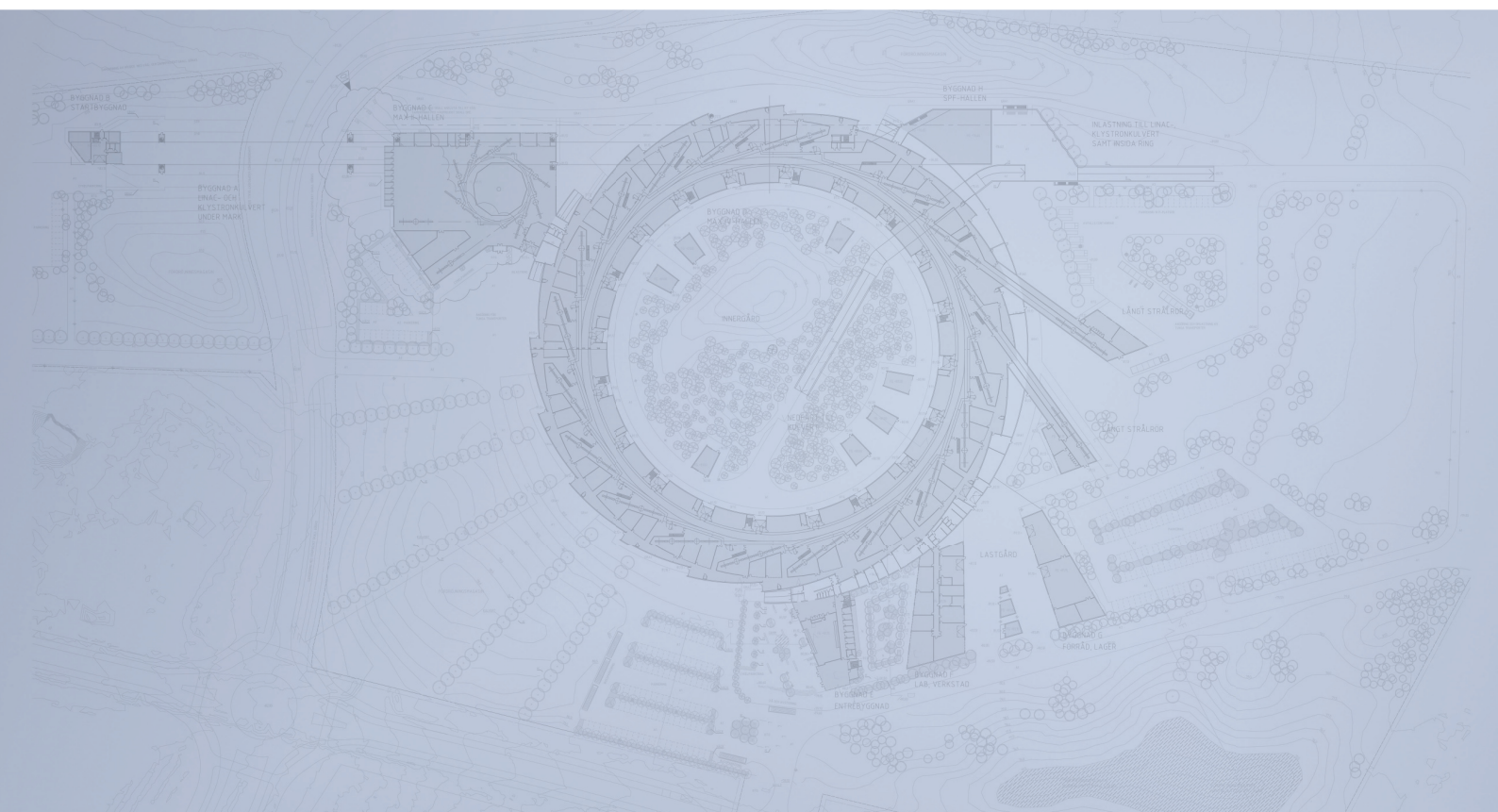
#### 4.5.5. Laser System Diagnostics

A number of diagnostics are needed to ensure that the laser system is running optimally. They include energy meters, auto correlators (2<sup>nd</sup> and 3<sup>rd</sup> order), cross correlator (for UV beam pulse time distribution) and beam profiler. A virtual cathode is important to check what is actually delivered to the cathode. As much as possible should be available online, and logged, to system operators in the control room.





# Detailed Design Report



## Chapter 4

### MAX IV Injector

#### 4.6. Acceleration

MAX IV Facility



# 4.6. Acceleration

---

- 4.6. Acceleration .....2**
- 4.6.1. RF Units ..... 2
- 4.6.2. Accelerator Units ..... 4
- 4.6.3. RF Distribution and Synchronisation..... 7
- 4.6.4. Waveguide System ..... 9
- 4.6.5. Temperature Stabilisation ..... 9

## 4.6. Acceleration

The MAX IV linear accelerator will be constructed in a very modular way. 17 stations are foreseen, each with a high power RF unit and a number of linear accelerator structures. In addition, an 18th high power RF unit will provide RF power to the electron sources and the first Linac section. All 18 RF units are to be constructed in an identical way.

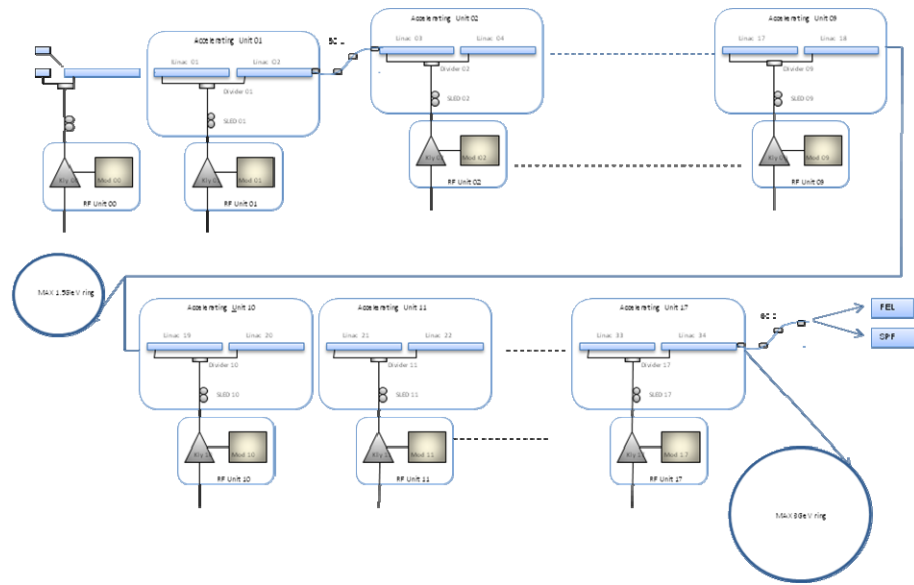
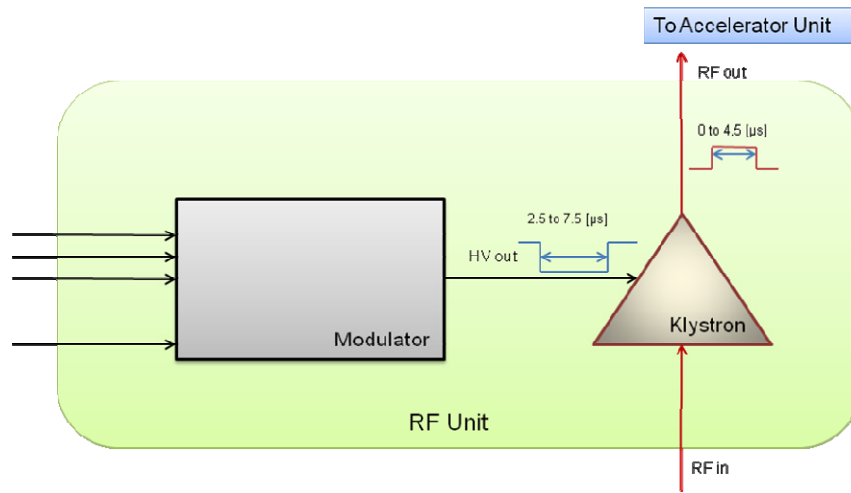


Figure 4.6.1: Block diagram showing the major components of the MAX IV linac RF system.

### 4.6.1. RF Units

The MAX IV linear accelerator will be divided into 18 RF stations. Each station consists of an S-band klystron with modulator and electronics for control and interlock. The klystron generates pulsed RF power from high voltage power delivered by the modulator. The modulator converts AC line power into high voltage pulse power. Its main components are a high voltage power supply, a high voltage pulse unit and a pulse transformer. An interlock system protects the RF unit and the linac in case of failure.

To achieve the MAX IV energy stability the RF accelerating fields must be stable. Pulse to pulse random variations can not be corrected by feedback and therefore gives the upper limits on the phase and amplitude noise levels of individual components such as klystrons and modulators. The jitter tolerance specifies the pulse-to-pulse variations that are acceptable in the linac phase and amplitude parameters. For the Thales klystron TH2100, as an example, the phase jitter is  $4^\circ$  for 1 % variation of klystron voltage (280 kV).



Figur.4.6.2: Schematic layout of RF Unit.

RF unit	Symbol	$ \Delta I/I_0  < \%$	$ \langle \Delta E/E_0 \rangle  < 0.1\%$	Unit
mean rf phase rf unit 0	$\varphi_0$			S-band deg
mean rf phase rf unit1	$\varphi_1$			S-band deg
mean rf phase rf unit 2	$\varphi_x$			S-band deg
mean rf phase rf unit 3-9	$\varphi_2$			S-band deg
mean rf phase rf unit 10-17	$\varphi_3$			S-band deg
mean rf voltage rf unit 0	$\sqrt{V_0/V_0}$			%
mean rf voltage rf unit 1	$\sqrt{V_1/V_1}$			%
mean rf voltage rf unit 3	$\sqrt{V_x/V_x}$			%
mean rf voltage rf unit 3-9	$\sqrt{V_2/V_2}$			%
mean rf voltage rf unit 10-17	$\sqrt{V_3/V_3}$			%

Tabell 4.6.1: The voltage and phase tolerances per rf unit for unit 3-9 and 10-17 are  $\sqrt{8}$ , larger assuming random errors. All tolerances are rms values.

Solid state switching technology will be used for the klystron high voltage pulse unit to achieve the desired demands on stability and low operational cost. The pulse shape must be as rectangular as possible. The raise and fall time should be as short as possible to maximize the total efficiency. The pulse to pulse stability must be better than  $\pm 0.01\%$ .

An output RF power of 35 to 37 MW with a pulse length of 4,5  $\mu$ s and a repetition rate of 100 Hz is needed.

All klystrons can be operated in saturation, with no low level RF amplitude control, and having global phase control.

Total klystron power margin is 1-2 RF units to allow for klystron failure and maintenance.

A comprehensive interlock system is required for the reliable and safe operation of the RF system. Internal protection interlocks must be provided for each RF unit that fully ensures safe operation of the equipment. External interlock connection(s) as part of the protection chain of the RF unit must be provided for use in the MAX-lab installation. External interlock(s) will operate at the level of switching off completely the pulsed high voltage from the RF unit, and could be used for example, from a remote emergency stop button or from a klystron waveguide arc detector.

The control system for the RF unit will include an API for the complete control and status including interlock signals of the equipment and a TANGO ([www.tango-controls.org](http://www.tango-controls.org)) device server/servers for GNU/Linux or Windows XP. The source code for the TANGO device serves will be included and will have all necessary commands and attributes for the complete remote control of the RF unit.

The control interface and protection of each RF unit will be made using the Ethernet protocol having minimum 10ms response time. There will be a local control and display panel showing operational data and the interlock status of a RF unit under all operating conditions.

The RF unit shall be designed for compact size, but still keeping a reasonable level of serviceability. One side of the unit will be placed close to a tunnel wall, so all parts needing service must be accessible from the other three sides. Compact RF units with easy access of replaceable units are preferred. An oil tray must be included that fits below the high voltage pulse transformer tank and has a minimum volume 105 % of the tank oil volume so that all oil will be collected in case of a leak.

## 4.6.2. Accelerator Units

The MAX IV linear accelerator will be constructed in a modular way. The 18 RF stations are foreseen to feed 35 linear structures and two RF guns. See the fig.xx. , each consisting of a high power RF unit followed by a SLED unit, Power divider and two Linac sections. The 35 Linac sections will serve as a full energy injector with electron beam energy in excess of 3 GeV. 17 of all 18 Accelerating units are to be constructed in an identical way. The first one will have some differences.

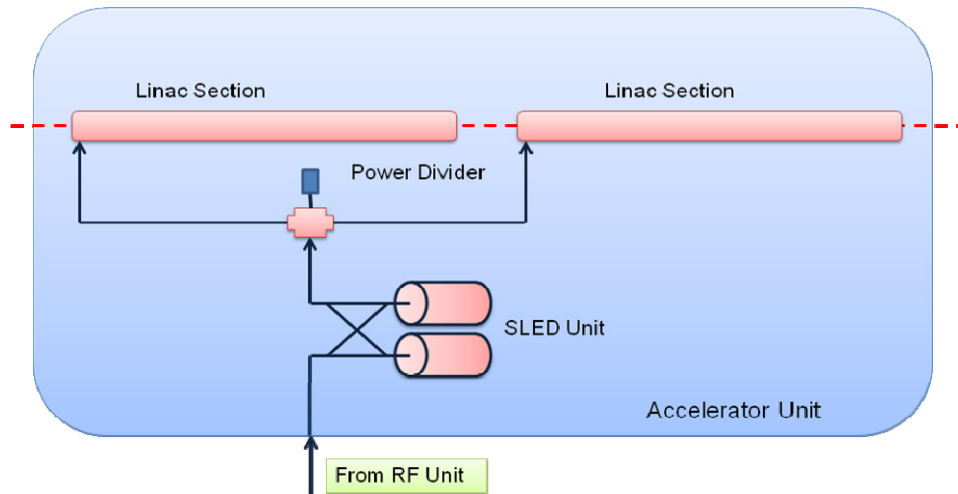


Figure 4.6.3: Schematic layout of one accelerator unit.

The linac sections are 5.2 m long travelling wave S-band structures, operating at 2.998 GHz. They are constant gradient structures with an on-axis load. Therefore the last six of their 154 cells are coated with an absorbing material and add little to the total accelerating voltage. The fill-time of the structures is 740 ns.

The reason to choose 5.3 m long accelerating sections as compared to the well know 3 m structure, is to reduced number of couplers, input windows or valves and a simpler power distribution system.

Basic parameters		
Length	5.2	m
Shunt Impedance	51.5	M $\Omega$ /m
Attenuation	0.4343	dB
Frequency	2.997912 +/- .03	GHz
Mode	2 $\pi$ / 3	
Typ	constant gradient	



SLED system will be used to provide the necessary accelerating gradient. SLED has the advantage that it will not increase the average power consumed by the accelerator. A relatively long output power pulse of  $4,5 \mu\text{s}$  from each klystron is feeding a SLED system that deliver a short high power RF pulse to two linac structures. Each SLED system consists of two cylindrical cavities in the high  $Q$   $\text{TE}_{015}$  mode. The theoretical value of  $Q_0$  for copper cavities is 108000, and values around 100000 have been achieved in practice.

Basic parameters	
Operating Frequency	$2.997912 \pm 0.5 \text{ MHz}$
Cavity Resonant Mode	$\text{TE}_{015}$
Measured Unloaded $Q$	$98000 \pm 5000$
Coupling Value ( $\beta$ )	5
Input power (peak)	40 MW max
Input power (average)	36 kW (PRF 200 Hz, $4.5 \mu\text{s}$ )
Cooling	Water circuit
Operating Temperature	$40 \pm 2^\circ\text{C}$
Input VSWR	1.10:1 with matched load on output port

The RF power delivered from the SLED cavities to the linac structures is seen in Fig 4.6.4. The RF power is normalised to the klystron power.

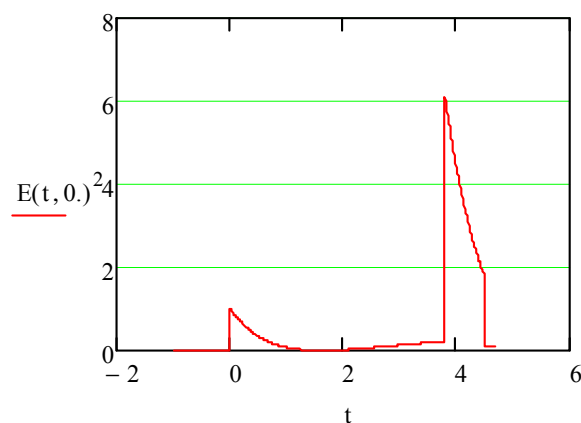


Figure 4.6.4: RF output power delivered to the linac structures normalised to the klystron power for the parameters above.

### 4.6.3. RF Distribution and Synchronisation

The beam energy spread is related to RF phase and amplitude variations. Cooling temperature, air condition and modulator high voltage jitter changes the beam energy. The long term beam energy drift and phase drift will be reduced by using accurate cooling and air conditioning control system. Short term jitter will be reduced by putting high demands on the modulators.

The injector RF distributions system should be designed for maximal phase stability relative to the bunches in the linac. The average position of the beam near crest of the accelerating voltage must be kept stable to a fraction of an S-band wavelength or about  $1^\circ$  (rms). This is achieved by couple out RF power from the first klystron before the SLED cavities which is distributed along an nitrogen-filled rigid coaxial transmission line mechanically attached to the linac supports at each coupling points. About 300W RF power are coupled out at the positions of each klystron for driving the klystrons. A remote controlled phase shifter is needed at each klystron to adjust the RF phase. When the linac tunnel changes length due to temperature, both the linac and the transmission line changes the same length. At each coupling point there is an expansion joint that absorbs the length changes.

This design is based on the fact that the RF wave propagates with almost the same speed (0.25 % difference) in an nitrogen-filled coaxial transmission line as the electron bunches in the linac. When the linac tunnel changes length the RF phase will follow the bunches. Changes in the coaxial line's dielectric constant are the primary cause of phase length variation. Using an approximate equation from SLAC for their 3 km long linac scaled to a 300 m long line the change in phase length relative to the beam is given by:

$$d\theta_r(^{\circ}\theta) = -2.5dT_e(^{\circ}C) + 0.34dp_e(Torr)$$

where  $\theta_r$  is the total equivalent phase length at S-band in degrees of electrical phase,  $\epsilon$  is the relative dielectric constant (teflon supports plus nitrogen gas)  $T_e$  is the temperature of the dielectric and  $p_e$  is the  $N_2$  gas pressure inside the coaxial line. To achieve the demanded phase stability a temperature stability of  $<\pm 0,13^{\circ}C$  and pressure stability of  $>\pm 0,5$  Torr are needed.

In order to minimize losses due to skin depth we want to use a coaxial line with a diameter as large as possible without supporting the  $TE_{11}$  mode (a higher-order mode will increase loss and VSWR and has a different propagation velocity than the TEM mode). Only the

TEM wave can propagate when the wavelengths is longer than  $\lambda_c = \pi\left(\frac{a+b}{2}\right)$  where a is the inner and b the outer radius of the line. If we use the EIA 1 5/8" (a=16,87 and b=38,79 mm) standard coaxial rigid line, the cut off wavelength is 0,087 m (3,43 GHz) which is lower than 0,01m (3 GHz), only the TEM mode will propagate.

The maximum power that could be distributed along the line is 2,35 MW. With 20 linac units of 12,6 meter length and 545 W coupled out from the line at each klystron position a

power of 20 kW is needed from the first klystron. Assuming a 10 m long low loss coaxial cables (Aircom plus™) with an attenuation of 2,6 dB there will be 300 W available at each klystron.

At each klystron input there are remote controlled variable phase shifters and attenuators.

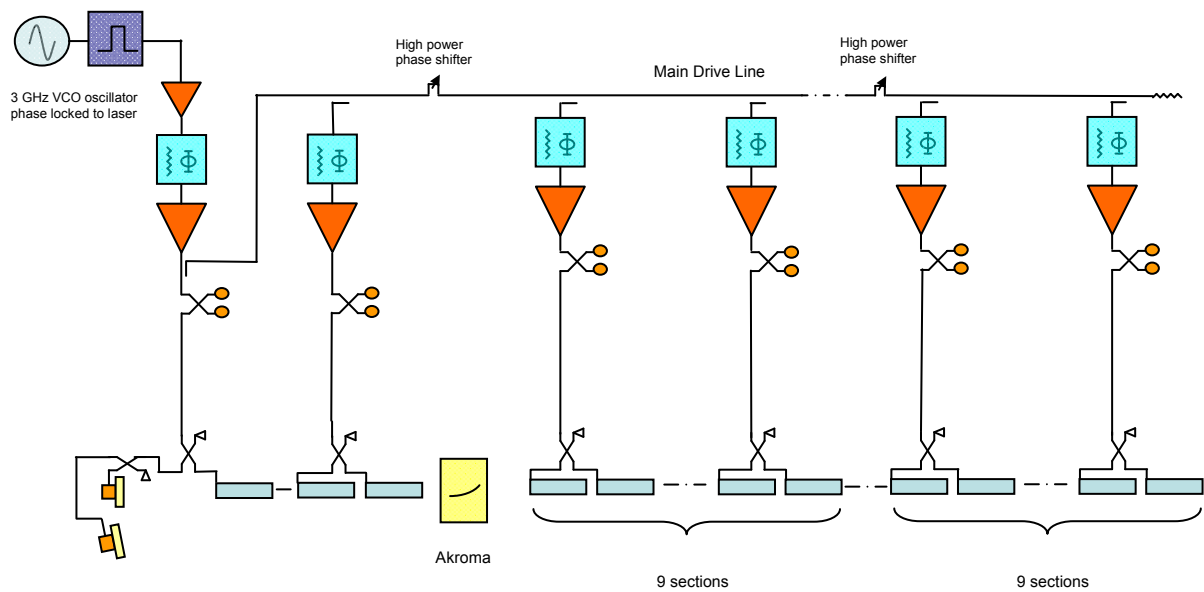


Figure 4: Blockdiagram of the linac RF system showing the main drive line that supplies the klystrons with drive power.

RF unit	Coupling factor [dB]	RF unit	Coupling factor [dB]
0		10	11.9
1	15.4	11	11.4
2	15.1	12	10.8
3	14.7	13	10.3
4	14.4	14	9.6
5	14	15	8.9
6	13.6	16	8.1
7	13.2	17	7.1
8	12.8	19	6
9	12.4	20	4.5

Table 4.1: The coupling factors for the couplers placed along the main drive line is shown in this table.

The master oscillator is the heart of the linac which determines its performance. It should be a RF source with long term frequency stability and low phase noise. Femtosecond lasers push the limits of the phase noise spectrum.

#### 4.6.4. Waveguide System

Because of the very high microwave power used in the linac feeding system the waveguides must be placed under vacuum ( $<10^{-8}$  bar). The high power waveguide network must be adjusted to be equal in phase length, or to differ by only integral numbers of wavelengths.

#### 4.6.5. Temperature Stabilisation

As a general design goal energy stability should be achieved by putting high demands on temperature stability on critical RF components and using klystron modulators with high pulse to pulse voltage stability. To meet the different demands on temperature stability the water temperature control in the linac tunnels will consist of two regulation systems, a

klystron gallery secondary system and a linac station fine cooling system. The RF system including accelerating structures and SLED cavities require a stability of  $\pm 0.05^\circ\text{C}$  at a water temperature of  $39\text{--}41^\circ\text{C}$ . This stability is achieved using a closed-loop water system at each station that provides constant water temperature to the SLED, accelerating structures, waveguides and loads. The klystron gallery secondary system supplies  $25^\circ\text{C}$  temperature regulated water with a stability of  $\pm 0.5^\circ\text{C}$  to components in the klystron gallery such as klystron collector, - body, and focusing coils and other RF devices that needs cooling. Also cooling water for the magnet power supplies and beam focusing magnets are supplied from this system.

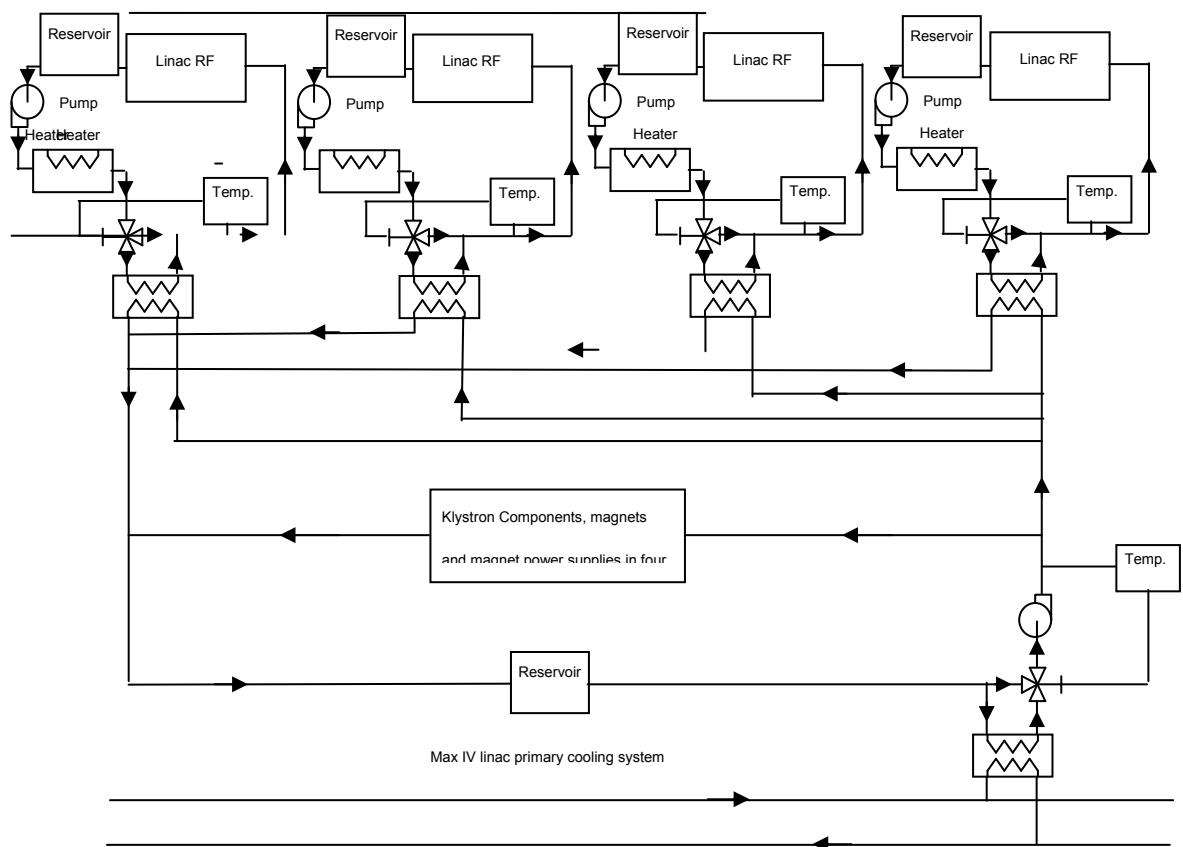
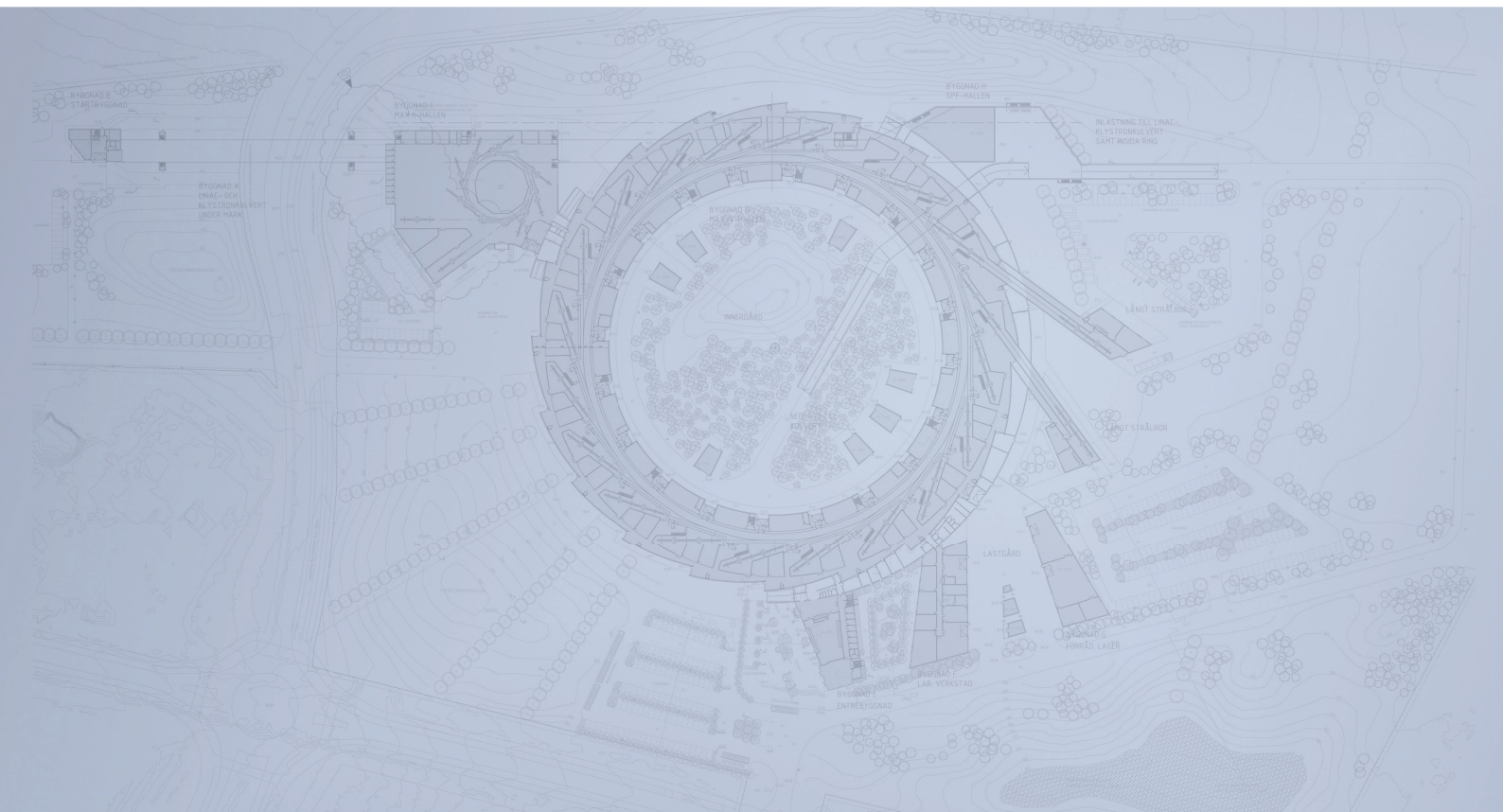


Figure 1: Block diagram showing one water cooling block consisting of four linac stations. Each acceleration station, consisting of SLED, accelerating structures, waveguides and loads, has its own fine cooling system and the other devices have a common temperature regulation system.

To avoid that fast temperature changes on the primary water supply is affecting the fine cooling temperature stability reservoir tanks have to be added in the cooling system, see figure 1.

# Detailed Design Report



## Chapter 4

### MAX IV Injector

#### 4.7. Magnets

MAX IV Facility



# 4.7. Magnets

---

- 4.7. Magnets .....2**
  - 4.7.1. Quadrupole Type A ..... 2
  - 4.7.2. Quadrupole Type B ..... 2
  - 4.7.3. Dipole Type A..... 3
  - 4.7.4. Sextupoles (SXL & SXH)..... 6
  - 4.7.5. Dipole Type B..... 6
  - 4.7.6. Quadrupole Type C ..... 6
  - 4.7.7. Bibliography..... 6



# 4.7. Magnets

The magnetic elements in the injector are defined by the injector lattice (1). Based on this, a few different magnet types have been designed. These magnet types are listed in Table 1. Where possible, the same magnet type is used repeatedly in the machine, operated at different field strength.

Table 1: magnet types in the injector.

Item	Qty	Description	L [m]	Field strength <sup>1</sup>	Comment
QA	12	Quadrupole type A	0.1	1.525 – 7.996 T/m	B''
QB	43	Quadrupole type B	0.2	0.559 – 9.369 T/m	
DIA	8	Dipole type A	0.1	0.67 T, -2.61 T/m	
SXL	2	sextupole, low energy	0.1	48.87 T/m <sup>2</sup>	
DIB	8	Dipole type B	0.35	1.26 T, -9.31 T/m	Gradient dipole
QC	14	Quadrupole type C	0.2	12.226 – 75.601 T/m	B''
SXH	2	sextupole, high energy	0.2	1241 T/m <sup>2</sup>	

## 4.7.1. Quadrupole Type A

...

## 4.7.2. Quadrupole Type B

...

<sup>1</sup> Assuming 100 MeV from gun + each linac section adds 95 MeV.

### 4.7.3. Dipole Type A

The dipole type A has been designed for use in bunch compressor 1. The specifications on which the design is based are listed in Table 2.

Table 2: dipole type A basic specifications. From lattice file (1) unless otherwise noted.

Parameter	Value	Unit	Comment
Beam energy (T)	260	MeV	
Bend angle	4.4	°	
Entrance/exit angle	2.2	°	
Effective length ( $L_{\text{eff}}$ )	0.1	m	
Quadrupole strength	-3	/m <sup>2</sup>	
Good field width	±5	mm	(2)
Pole gap (g)	15	mm	(3)

The magnet was designed with the help of 2D and 3D field simulations, which were performed with the FEMM (4) and Opera3D (5) codes. The final version of the Opera3D-model, “I\_dia\_MJ100601-01.opc”, is shown in Table 1. This model, together with the design parameters listed in Table 3 constitute the basic design upon which manufacturing drawings for this magnet are based.

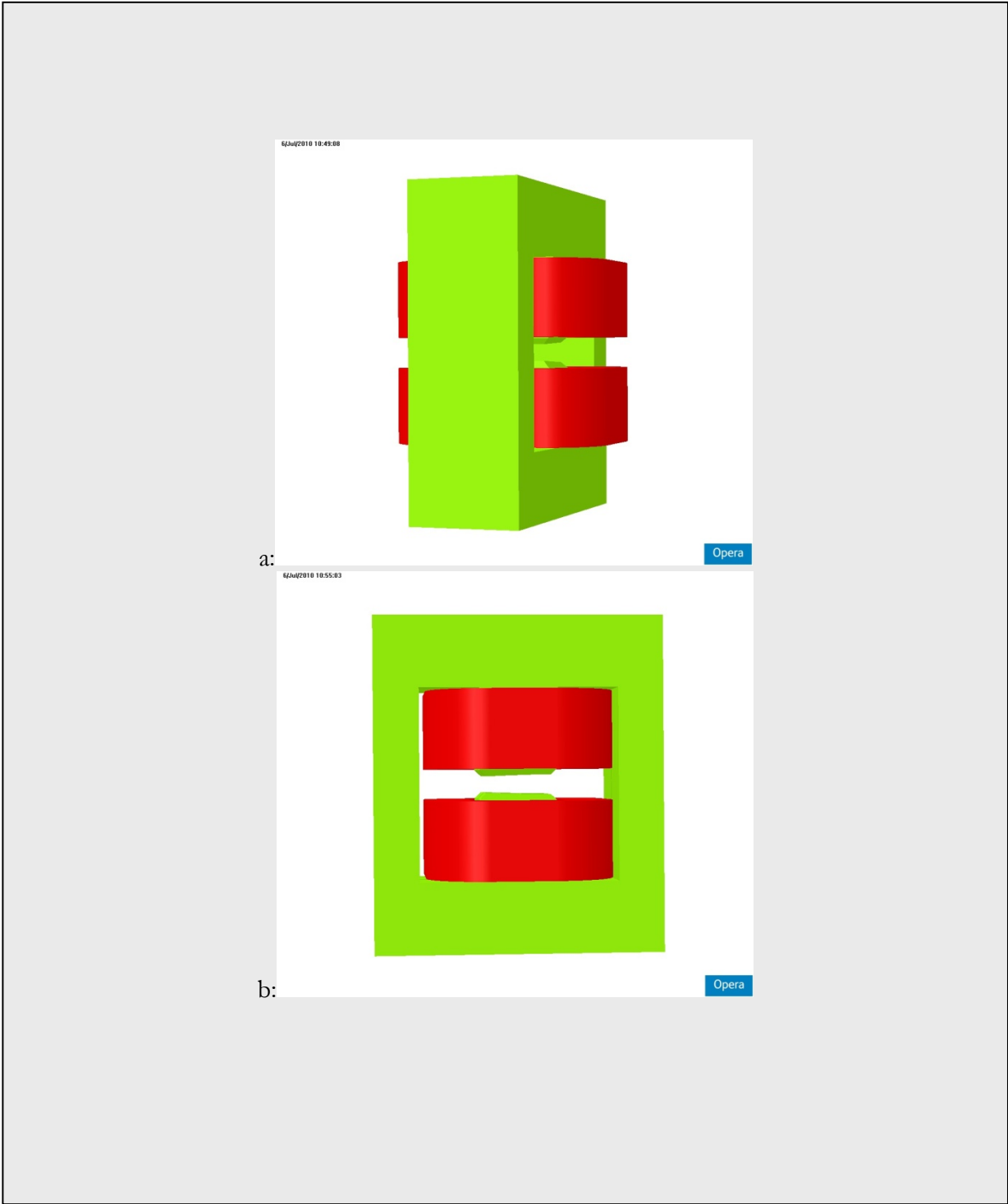


Figure 1: Opera3D model "I\_dia\_MJ100601-01.opc". a: view from left. b: view from front.

Table 3: Technical data for dipole magnet type A.

Parameter	Value	Unit	Comment
Magnet type	Gradient dipole		
Nominal field (B <sub>0</sub> )	0.6673	T	At magnet centre (x,s = 0,0)
Gradient*	-2.6083	T/m	
L <sub>eff</sub> (dipole)*	100.01	mm	
L <sub>eff</sub> (quadrupole)*	100.00	mm	
Integrated dB/B*	0.00005		
Coils:			
Total current /magnet (NI)*	8149.7	A	At nom. B <sub>0</sub>
No of coils /magnet	2		
Conductor	OFHC copper, 5×5 mm, Ø3 mm internal cooling channel		
No of turns /coil	60		Winding = 6 layers, 10 turns /layer
No of turns /magnet (N)	120		
Nnominal current	68	A	
Resistance/coil at 20°C	25	mΩ	
Coil cooling	Water cooled		
No of cooling circuits /coil	1		
Pressure drop (Δp)	2	bar	
Flow /cooling circuit	0.43	l/min	
Temperature rise (ΔT)	4.4	°C	
Voltage /magnet	3.7	V	= 29.6 V for 8 magnets in series, excl. cabling
Flow /magnet	0.86	l/min	
Yoke:			
Yoke geometry	H-dipole, splittable at mid plane		
Material	Armco low carbon steel		
Magnet weight	~45	kg	

\* Field simulation results for Opera3D-model, "I\_dia\_MJ100601-01.opc".

<sup>2</sup> Within  $x=\pm 5\text{mm}$ , in magnet mid plane. Calculated as ("simulated  $\int B(x,s)ds$ "-"nominal  $\int B(x,s)ds$ ")/"nominal  $\int B(x,s)ds$ ", where simulated  $\int Bds$  values are scaled by nominal/simulated  $B_0$  and nominal  $\int Bds$  values are defined from Table 2.

#### 4.7.4. Sextupoles (SXL & SXH)

...

#### 4.7.5. Dipole Type B

...

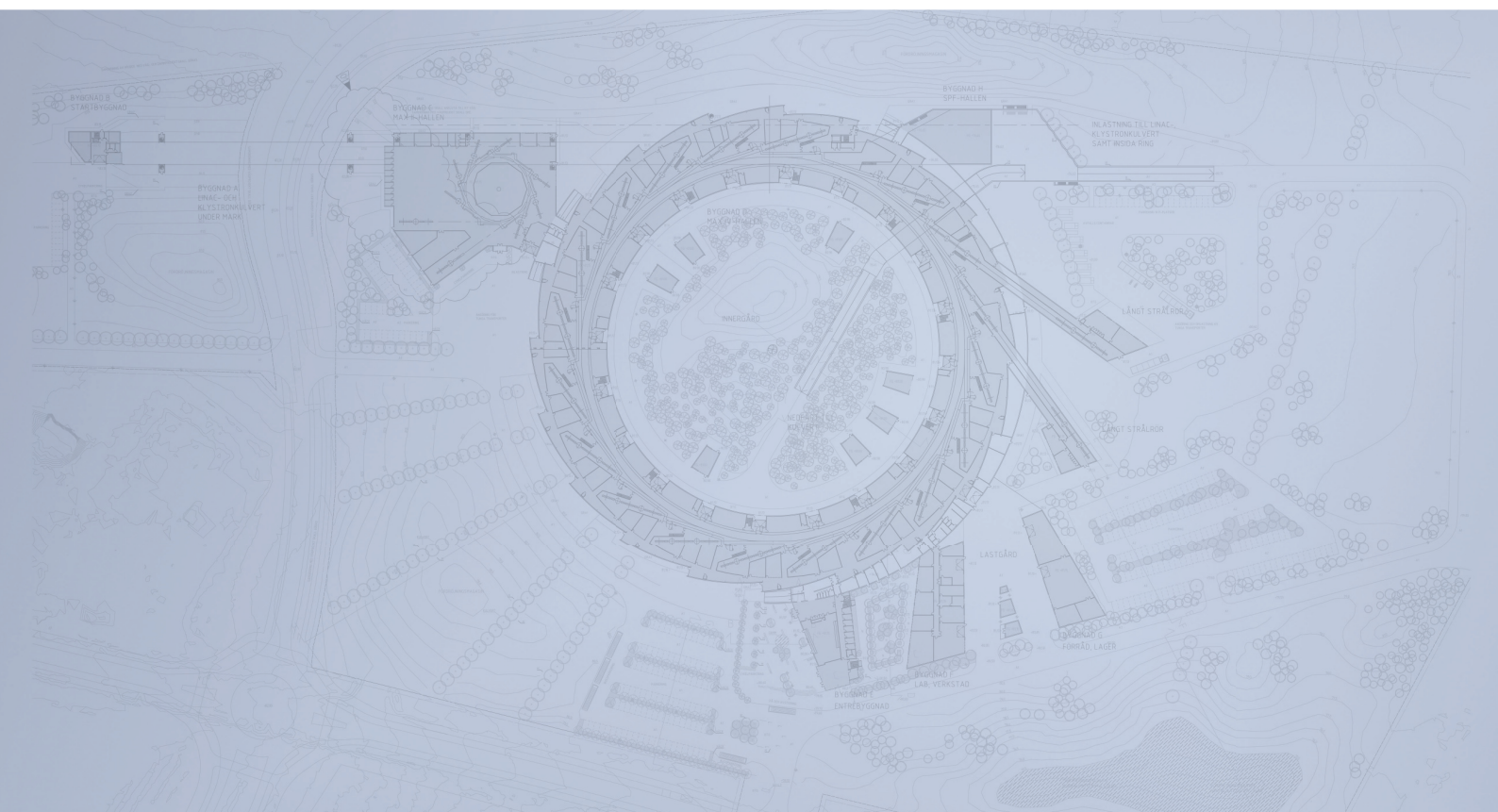
#### 4.7.6. Quadrupole Type C

...

#### 4.7.7. Bibliography

1. S. Thorin (private communication, 100812).
2. S. Thorin (private communication, 100426).
3. B. Anderberg (private communication, 100426).
4. D.C. Meeker, Finite Element Method Magnetics, version 4.2 02Nov2009 (Mathematica Build), <http://www.femm.info>.
5. Opera Version 13.034 Professional Edition x64, <http://www.vectorfields.com/>.

# Detailed Design Report



## Chapter 4

### MAX IV Injector

#### 4.8. Diagnostics

MAX IV Facility



# 4.8. Diagnostics

---

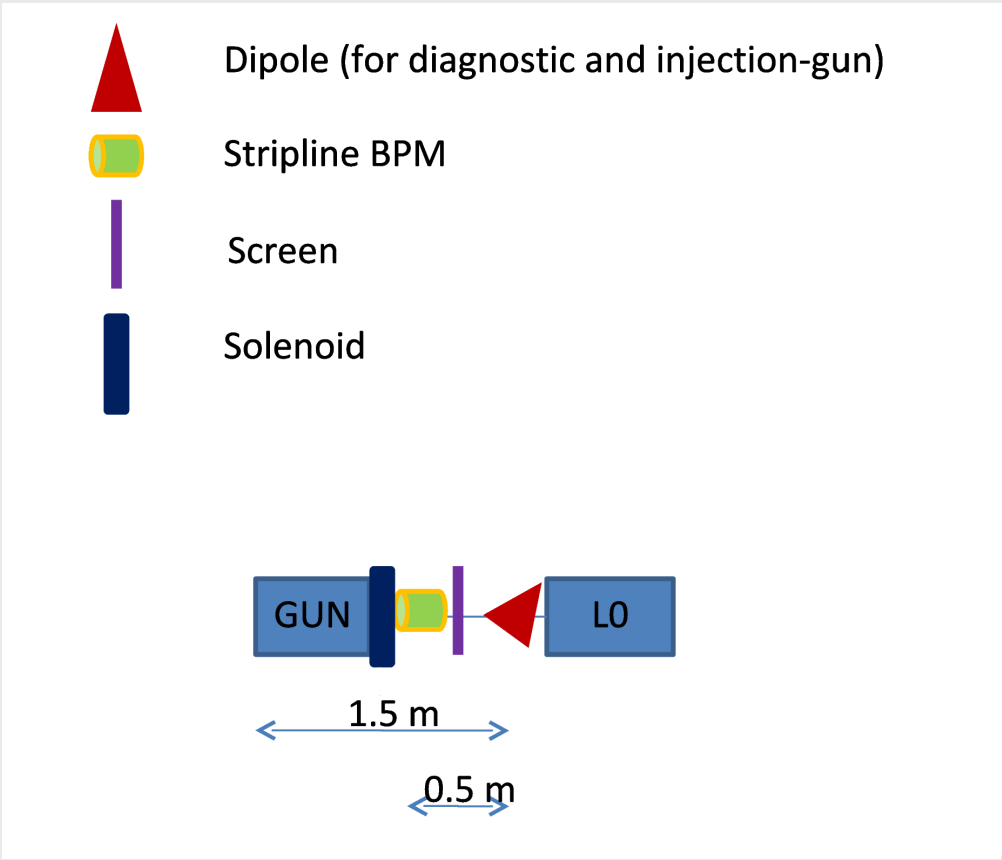
- 4.8. Diagnostics.....2**
- 4.8.1. Linac Diagnostics Placing ..... 2
- 4.8.2. Beam Position Monitors ..... 5
- 4.8.3. Current Transformers ..... 8
- 4.8.4. Screens ..... 8
- 4.8.5. Wire Scanners..... 8
- 4.8.6. References..... 8



# 4.8. Diagnostics

## 4.8.1. Linac Diagnostics Placing

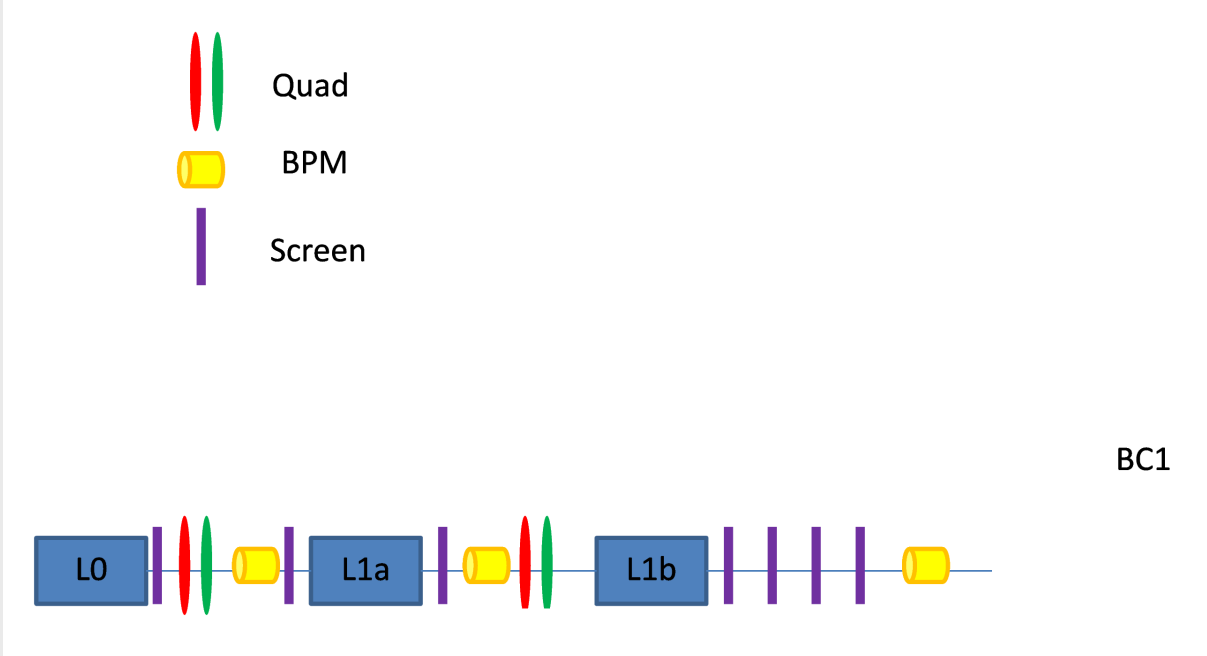
### 4.8.1.1. Gun to L0



Position	Diagnostic	Type
Gun → L0	BPM	Stripline
	Screen	YAG

Table 1 Gun to LINAC 0 diagnostics.

4.8.1.2. L0 to BC1



Position	Diagnostic	Type	Purpose
L0 → BC1	Beam Based Alignment		
L0 → L1a	Screen	YAG	For measuring $\alpha$ and $\beta$ . Emittance measuring for checking L0 matching
	BPM	Stripline	Position
	Screen	YAG	For measuring $\alpha$ and $\beta$ . Emittance measuring for checking L0 matching
L1a → L1b	Screen	YAG	
	BPM	Stripline	Position
L1b → BC1	Screen (x4)	YAG	Setup diagnostics 3x for $\epsilon$ -measuring 1x for error estimation
	BPM	Stripline	Position

Table 2: LINAC 0 to Bunch Compressor 1.

### 4.8.1.3. Intersection Diagnostics

The intersections will be 1.05 m long and they will have the equipment shown in Table 3.

Intersection content	Length (mm)
Screen / Wire scanner	150
Stripline / (Cavity) BPM	200
Vacuum Pump (pipe)	40
Valves (x2)	160
Quad	300
Correctors	130
<b>Total length</b>	<b>980</b>

Table 3: Intersections diagnostics.

Not all intersections will be equipped with the same diagnostics. Screens or wire scanners can be used in different intersections. Wire scanners will be used for on-line beam profile measurements and fitted where needed.

There need to be at least one valve in each intersection. In the intersections that contain a wire scanner there needs to be two valves since the wires in the wire scanners will need replacing on a regular basis. The wire scanner will be designed with a valve in the module.

All intersections can be equipped with Beam Position Monitors, although we could also opt for equipping each third of the intrasections. By equipping each third intersection with BPM's we will be able to the position correctly.

## 4.8.2. Beam Position Monitors

### 4.8.2.1. Cavity BPM Compared to Stripline BPM Parameters

BPM Type	Charge	Typical Position Resolution (RMS)
Spring-8 Cavity tested at SCSS	300 pC	0.2 $\mu\text{m}$
LCLS Cavity	200 pC	0.2 $\mu\text{m}$
Libera Brilliance Single-Pass with stripline	280 pC	3 $\mu\text{m}$
	98 pC	4 $\mu\text{m}$
	31 pC	9 $\mu\text{m}$
	10 pC	33 $\mu\text{m}$

Table 4: Cavity versus Stripline BPM.

The above values are from reports publicized by the labs.

### 4.8.2.2. BPM Requirements

Parameters	Required performance
Min bunch charge	100 pC
Position resolution (RMS)	10 $\mu\text{m}$
RF Frequency	3 GHz
MAX pulse repetition rate	100 Hz
Bunch lengths (RMS)	3 ps – 31 fs

Table 5: BPM requirements.

### 4.8.2.3. BPM Introduction

The BPM electronics for the LINAC is highly dependent on the choice of cavity / stripline BPM. In the case of strip-line BPM's there are commercially available electronics which is not the case for cavity BPM's. The BPM electronics for the stripline BPM's are similar to the storage ring BPM's with the added functionality to detect short single pulses, by the use of a ringing filter. Cavity BPM's requires a different approach for the electronics and cannot use the same or modified storage ring BPM electronics.

### 4.8.2.4. Cavity BPM

Advantages:

- Can achieve much higher position resolution
- Better at low charges
- Radial symmetry, which allows more precise manufacturing
- Dipole mode is excited when beam is off-centred, i.e. a centred beam doesn't give any signal.
- The BPM's can be used at commissioning for alignment.  
(When the signal passed through the cavity is zero the signal passes its centre).

### 4.8.2.5. Stripline BPM

Advantages:

- Widely used and well tested
- Commercially available electronics
- Can use the same electronics as used in the storage ring, if a ringing filter is used in the analog front-end.

### 4.8.2.6. BPM Technology Choice

The primary route for the LINAC BPMs will be the quarter wave directional stripline. The stripline will use electronics with a ringing filter in the front-end to detect the short pulses. As seen in Table 4 the position resolution achieved with this option is less than 10  $\mu\text{m}$ . When compared to the requirements in Table 5 this performance should be sufficient. Since the same type of electronics used in the 1.5 GeV / 3 GeV can be used this makes maintenance easier with only one type of electronics. Another advantage with the same electronics as in the storage rings is that the same control system software can be used without any major modifications.

#### 4.8.2.7. BPM Electronics for Striplines

The Single Pass BPM electronics consists of an analog front-end and one digital back-end. The electronics contain four identical signal processing chains. The input signal is first passed through an analog processing stage, and then it's digitized with fast ADC's and finally the signal passes through the digital signal processing stage.

The single bunch signals from the stripline excite the 500 MHz SAW band-pass filters in the analog front-end. The band-pass filter has a relatively narrow bandwidth which creates a ringing from the filter which gives a lengthened signal. Therefore the ADCs can get a lot more samples out of this long signal. See Figure 1 for an example of how the signals from the stripline (on the left) looks like and how the digitized signal from the electronics looks. The images are from [1].

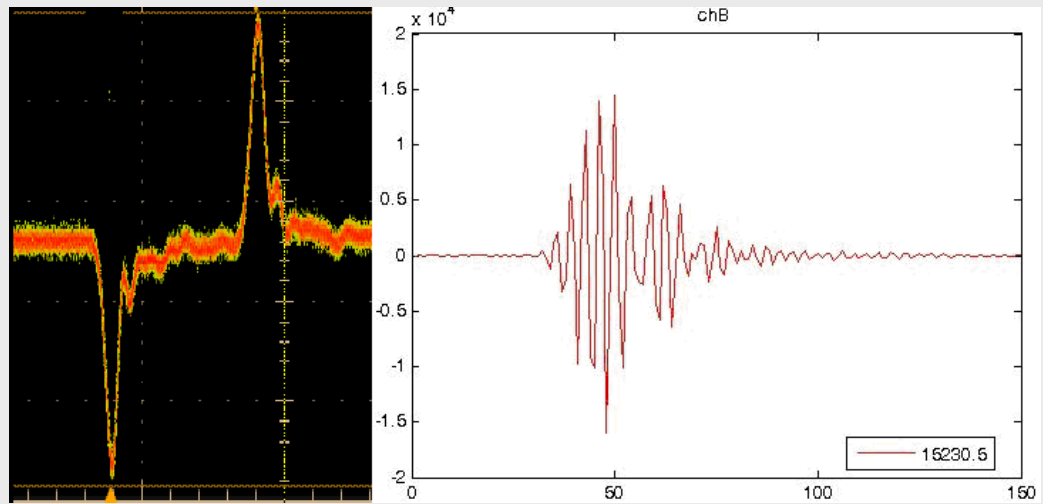


Figure 1: Signal from a stripline (left) and the digitized signal after the analog chain from the electronics.

Furthermore the signal is filtered and amplified in the analog stage. There is also a variable attenuator in the front-end to increase the dynamic range of the electronics.

Once the signal is digitized with the ADCs, the signal is processed by the digital signal processing algorithm which is implemented in the FPGA on the digital back-end. The data is only processed on a trigger event. Therefore the electronics must be triggered by an external trigger source. At a trigger event the first 150 samples from each channel ADC will be processed. (It's possible to delay the trigger event internally in the electronics for about 1.5  $\mu$ s). It's vital that the signal from the stripline is within these first 150 samples, otherwise nothing will be processed.

### 4.8.3. Current Transformers

Standard current transformers are commercially available. They have relatively high accuracy and can resolve low bunch charges. With short pulses it will be hard to detect an oblique angle from the current transformer, but can be useful as bunch charge monitors at strategic places.

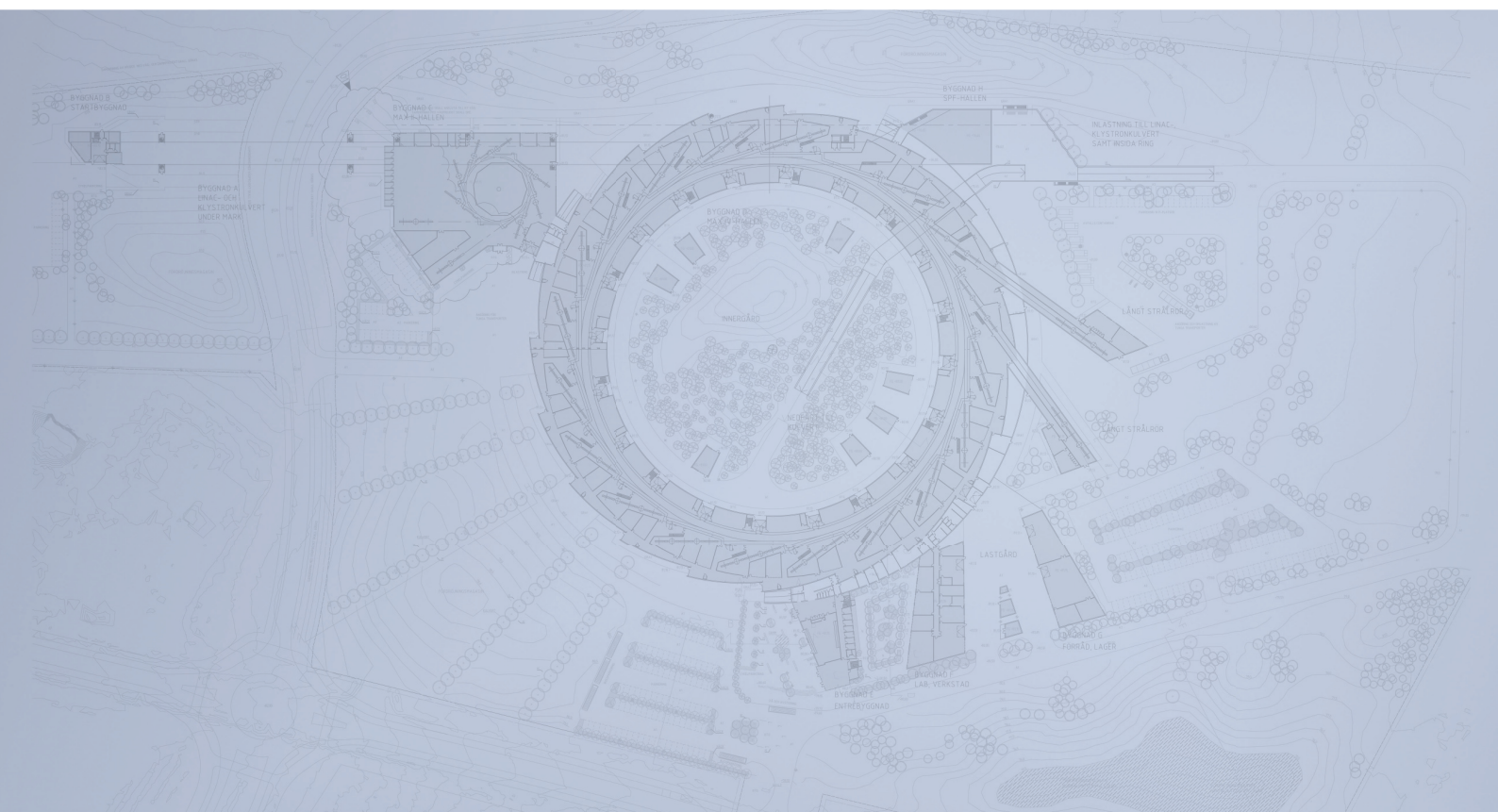
### 4.8.4. Screens

### 4.8.5. Wire Scanners

### 4.8.6. References

- [1] WEPC78 Proceedings of FEL2009, Liverpool, UK, M. Znidarcic, M. Oblak, A. Kosicek, Instrumentation Technologies ,“REAL -TIME FPGA SIGNAL PROC

# Detailed Design Report



## Chapter 5 Insertion Devices

MAX IV Facility





# Contents

<b>Contents</b>	<b>1</b>
5.1 Introduction . . . . .	3
5.1.1 Physical limits for the insertion devices . . . . .	4
5.1.2 Parameters of the stored beam in the MAX IV 3 GeV ring . . . . .	4
5.1.3 Undulators . . . . .	4
5.1.4 Elliptically polarizing undulators . . . . .	6
5.1.5 Wigglers . . . . .	6
5.2 Proposed beamlines at the MAX IV 3 GeV ring . . . . .	8
5.2.1 PX1 . . . . .	9
5.2.2 PX2 . . . . .	9
5.2.3 NANO-1 . . . . .	9
5.2.4 NANO-2 . . . . .	9
5.2.5 SAXS/WAXS . . . . .	9
5.2.6 XDIF . . . . .	9
5.2.7 TOM . . . . .	9
5.2.8 HIKE . . . . .	9
5.2.9 XAFS . . . . .	9
5.2.10 MATERIAL . . . . .	10
5.2.11 BL3-I1011 . . . . .	10
5.2.12 BL4-Gas . . . . .	10
5.2.13 BL5-Spect . . . . .	10
5.3 Insertion devices at the MAX IV 3 GeV ring . . . . .	10
5.3.1 The pmu18p5 ID . . . . .	12
5.3.2 The cpmu16 ID . . . . .	28
5.3.3 The pmu20 ID . . . . .	44
5.3.4 The scw46 ID . . . . .	60
5.3.5 The wig80 ID . . . . .	69
5.3.6 The elliptically polaraising undulator epuI1011 . . . . .	77
5.3.7 The elliptically polaraising undulator epu38 . . . . .	143
5.3.8 The elliptically polaraising undulator epu43p6 . . . . .	208
5.3.9 The elliptically polaraising undulator epu48 . . . . .	274
5.3.10 The elliptically polaraising undulator epu53p6 . . . . .	340
5.3.11 Summary of the magnet model calculations . . . . .	405
5.4 Influence from the insertion devices on the RF-system, the emittance, and the energy spread of the stored electron beam . . . . .	407
5.5 The influence on the brilliance and angular spectral flux from the number of IDs installed . . . . .	416
5.6 Comparison of specific undulators at different synchrotron radiation storage rings	421
5.7 Acknowledgement . . . . .	432
5.8 Appendix A: Synchrotron radiation . . . . .	433

5.8.1	Synchrotron radiation from a single electron moving along an arbitrary trajectory . . . . .	433
5.8.2	Polarisation of the emitted synchrotron radiation . . . . .	434
5.8.3	Angular spectral flux from periodic undulators with sinusoidal field and a filament current . . . . .	435
5.8.4	On axis angular spectral flux from an undulator and a filament current . .	436
5.8.5	On axis spectral flux in the central cone of radiation from an undulator and a filament current . . . . .	437
5.8.6	On axis brilliance from an undulator and a filament current . . . . .	437
5.8.7	Approximative expressions for the on axis angular spectral flux and brilliance including the finite emittance and energy spread of the beam . . .	437
5.8.8	Degree of spatial coherence in the emitted synchrotron radiation on axis .	439
5.8.9	Flux of coherent photons on axis . . . . .	439
5.8.10	Numerical calculation of synchrotron radiation . . . . .	440
5.9	Appendix B: Modes of operation for elliptically polarising undulators . . . . .	441
5.10	Appendix C: Influence from the insertion devices on the magnetic optics of the storage ring . . . . .	443
5.10.1	Beam deflection . . . . .	443
5.10.2	Simple approximations for focusing effect from planar field insertion devices	443
5.10.3	Focusing potential and kick maps for arbitrary types of periodic insertion devices . . . . .	444
5.10.4	Other methods . . . . .	445
5.11	Appendix D: Influence from the insertion devices on the emittance and energy spread of the stored beam . . . . .	446
5.11.1	Synchrotron radiation integrals, momentum compaction, emittance, and energy spread . . . . .	446
5.11.2	Influence from insertion devices on the synchrotron radiation integrals, momentum compaction, emittance, and energy spread . . . . .	447
5.12	Appendix E: Beam loading of the radio frequency system from insertion devices .	450
5.12.1	The network model of an RF system . . . . .	450
5.12.2	The phasor diagram for the RF system of the MAX IV 3 GeV ring a typical running situation . . . . .	451
5.12.3	RF acceptance . . . . .	452

<b>Bibliography</b>	<b>453</b>
---------------------	------------

## 5.1. Overview

The synchrotron radiation used at the experimental stations at MAX IV is created in insertion devices on the straight sections. The insertion devices could be either of undulator or wiggler type. Both wigglers and undulators consist of a periodic arrangement of magnet poles that forces the stored electron beam to oscillate transversely to the direction of motion of the beam and synchrotron radiation is emitted as illustrated in Figure 5.1.

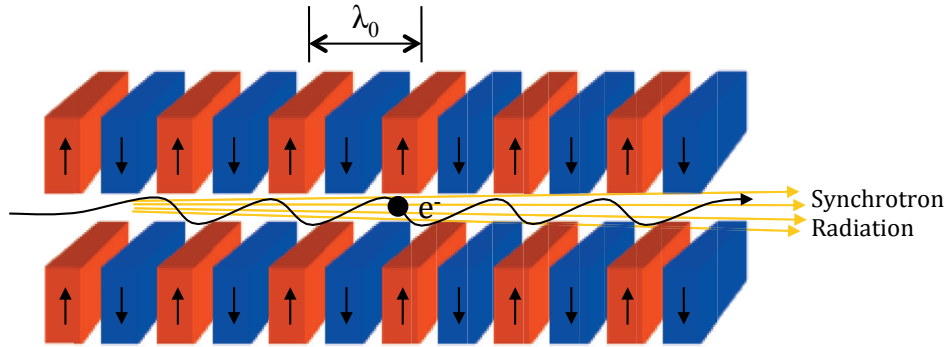


Figure 5.1: Illustration of the emission of synchrotron radiation in a periodic insertion device.

A wiggler has stronger magnetic fields than an undulator and the synchrotron radiation from a wiggler is in principle a superposition of the bending magnet radiation of the poles in the wiggler. In an undulator the emitted light from the consecutive undulator poles is added up to a Fourier sum, which results in an amplification of the light at certain resonance wavelengths in the radiation spectrum. The basic resonance wavelength and the wavelength of the higher harmonics at odd multiples of the basic wavelength are determined by the undulator period length  $\lambda_0$ , the undulator peak field  $B_0$ , and the relativistic factor  $\gamma$  of the stored electron beam in the storage ring.

The wavelength  $\lambda_n$  of the  $n$ :th harmonic of the radiation emitted on axis from the undulator is

$$\lambda_n = \frac{\lambda_0}{2n\gamma^2} \left( 1 + \frac{K^2}{2} \right) \quad (5.1)$$

$K$  is the amplitude of oscillation for the transverse velocity of the stored beam when passing through the undulator in units of  $1/\gamma$ . Instead of wavelength it may be of interest to know the energy of the emitted photons, which is given by the relation  $E_n[\text{keV}] = 12.4/\lambda_n [\text{\AA}]$ . For the special case of a sinusoidal field in the undulator the  $K$ -value is given by

$$K = 0.934\lambda_0[\text{cm}]B_0[\text{T}] \quad (5.2)$$

By varying the peak field  $B_0$  in the undulator it is possible to change the resonance wavelengths. The variation of the peak field in a permanent magnet undulator or wiggler is done by varying the magnetic gap and in a superconducting undulator or wiggler, the peak field is varied by varying the current in the superconducting coils. To have an overlap between the first and third harmonic in the emission spectrum from an undulator, the maximum  $K$ -value has to be larger than 2. If a lower limit of the  $K$ -value of 0.5 is assumed, the maximum  $K$ -value that should be obtained in the undulator must be 2.18 in order to get overlapping between the first and third

harmonics. If there is no need of an overlap between the first and third harmonic it is sufficient to obtain a maximum  $K$ -value of 1.5. A wiggler has a  $K$ -value considerably larger than 1.

There is a general interest in the synchrotron radiation community in producing undulator radiation with as short a wavelength as possible, also using the higher harmonics of the fundamental wavelength. The period length of the undulator should hence be as small as possible. A small period length in combination with a high peak field requires that the magnetic gap of the undulator is small. Small gaps require in turn that the stored electron beam in the accelerator has small dimensions at the position of the insertion device. The search for high brilliance also requires that the beam has a low emittance, i.e. that the beam is well collimated with the electrons in the beam travelling as parallel as possible. The development of the insertion device technology has together with the development of low emittance storage rings designed for the production of synchrotron radiation been the key to the enormous increase in brilliance of the synchrotron light sources over the past decades. The brilliance of an undulator increases with the square of the number of periods in the undulator but the always existing energy spread in storage rings of about 0.1 % has a broadening effect on the peaks in the undulator spectrum and there is no gain in brilliance by increasing the number of periods to more than about 250 periods. Long straight sections on the expense of having a large minimum vertical aperture are hence not beneficial for the performance of the light source.

### 5.1.1. Physical limits for the insertion devices

The straight section length available for insertion devices at the 3 GeV MAX IV storage ring is 4.8 m and the minimum vertical beam stay clear aperture in the middle of the straight sections is 4 mm.

In-vacuum undulators are assumed to have a minimum magnetic gap of 4.2 mm and the magnetic length can be up to 3.8 m since approximately 500 mm are needed at the entrance and exit for valves, absorbers, flanges and tapers.

Elliptically polarising undulators and out of vacuum undulators are assumed to have a minimum magnetic gap of 9 mm and a maximum length of 4 m. The thickness of the NEG coated Al vacuum chamber is assumed to be 7 mm. Current strips to compensate for dynamic multipoles will occupy 1.2 mm of aperture and an additional 0.8 mm is needed for clearance.

Wigglers are assumed to have a minimum magnetic gap of 9 mm and a maximum length of 4 m. The gap may be decreased to 7.8 mm if the same vacuum chamber as for the elliptically polarising undulators is used.

### 5.1.2. Parameters of the stored beam in the MAX IV 3 GeV ring

The beam parameters in the middle of the straight sections the 3 GeV MAX-IV storage ring are given below in Table 5.1 [1]. The parameters in Table 5.1 have been used for the brilliance and angular spectral flux calculations in this report.

### 5.1.3. Undulators

The undulators for high energy photons will by necessity be in-vacuum insertion devices since a small magnetic gap is needed in order to obtain a high undulator peak field in combination with a short period length. The first set of beam lines will use today's state of the art technology with in-vacuum undulators of hybrid type. Cryogenically cooled in-vacuum undulators may also

Table 5.1: Beam parameters in the middle of the straight sections of the MAX IV 3 GeV Ring [1]

Beam Energy	3.0	GeV
Beam Current	500	mA
Energy Spread (rms)	0.0010	
Horizontal Beta Function	9.00	m
Horizontal Emittance	0.263	nmrad
Vertical Beta Function	4.80	m
Vertical Emittance	0.008	nmrad
$\sigma_h$ rms horizontal beam size	48.65	$\mu\text{m}$
$\sigma_{h'}$ rms horizontal beam divergence	5.406	$\mu\text{rad}$
$\sigma_v$ rms vertical beam size	6.197	$\mu\text{m}$
$\sigma_{v'}$ rms vertical beam divergence	1.291	$\mu\text{rad}$

be considered for installation at some of the initial beam lines at the MAX IV 3 GeV ring. The promising but not yet mature technique with superconducting undulators is however not considered for the initial set of beam lines since the fundamental problems with large phase error and field integrals as well as the heat load problems not yet have been solved for this technique. The 3 GeV MAX IV ring is however well suited for the installation of superconducting undulators since the soft end bending magnets flanking the straight sections and the long bunch length in the stored beam will give a moderate heat load to the cold mass of the superconducting undulator.

The three different techniques in-vacuum undulators (PMU), cryogenically cooled in-vacuum undulators (CPMU), and superconducting undulators (SCU) have been compared for the same boundary condition of 4 mm vertical stay clear aperture. The result in the form of a plot of the minimum required period length for a given K-value is shown in Figure 5.2.

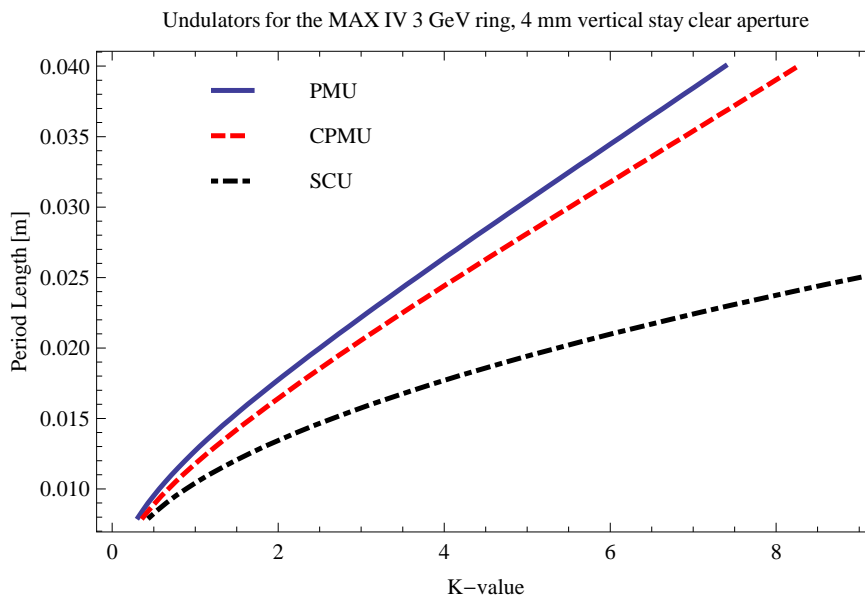


Figure 5.2: Minimum required period length for a given K-value for the undulator techniques in-vacuum undulators (PMU), cryogenically cooled in-vacuum undulators (CPMU), and superconducting undulators (SCU).

The in-vacuum undulators used for the comparison are of hybrid type with  $\text{Sm}_2\text{Co}_{17}$  ( $B_r = 1.05 \text{ T}$ ) as the magnetic material and pure iron as pole material. The peak field is found by magnetic model calculations with the geometry of the iron poles and magnet material in the

undulator using the computer code Radia [2]. The vertical physical aperture is 4 mm and there is a 0.1 mm thick sheet covering the pole faces, which results in magnetic aperture of 4.2 mm. The magnetic material  $\text{Sm}_2\text{Co}_{17}$  is used as the permanent magnet material and iron is used as the pole material. The transverse dimensions of the magnet material are  $50 \times 30 \text{ mm}^2$  and the pole material  $32 \times 24 \text{ mm}^2$ . The longitudinal length, or thickness, of the iron pole disk is 13.6 % of the period length and the longitudinal length, or thickness, of the magnet material disk is 36.4 % of the period length.

The peak field in the cryogenically cooled in-vacuum undulator operating at a temperature of 140 K in the comparison is found by carrying out an identical calculation as for the in-vacuum undulator except for that the magnetic material has been changed to NdFeB (  $B_r = 1.35 \text{ T}$  at 140 K,  $B_r = 1.18 \text{ T}$  at 293 K ), the pole longitudinal length has been increased to 15 % of the period length, and the longitudinal length of the magnet material has been decreased to 35 % of the period length.

The peak field  $B_0$  of the superconducting undulator with a magnetic gap of 4.4 mm and period length  $\lambda_0$  in the comparison is found by using a generalised expression [3] of the peak field in a superconducting undulator using NbTi coils and iron poles

$$B_0[\text{T}] = (1.85 + 0.194\lambda_0) e^{-\frac{\pi g}{\lambda_0}} \quad (5.3)$$

The brilliance limit for the 3 GeV MAX IV has been calculated from the performance limit of the different undulator techniques shown in Figure 5.2 and assuming an undulator length of 3 m. The result is shown in Figure 5.3 and the corresponding spectral flux density is shown in Figure 5.4. The value shown in Figure 5.3 represents the limit of the brilliance at peak energy that can be obtained for a given photon energy. The brilliance plotted in Figure 3 is the brilliance at peak energy and not the maximum brilliance which is found at slightly lower photon energy than the peak energy. It is believed that for a low emittance light source like the 3 GeV MAX IV ring, it is more interesting to use the point like cone of the synchrotron radiation produced at the peak energy than the circular cone of radiation which gives a slightly higher brilliance. The undulator period length, peak field strength, and harmonic has been optimised for each given photon energy value in the plot shown in Figure 3.

A real undulator that will be used over a larger photon energy range by changing the peak field will be slightly lower than brilliance limit shown in Figure 5.3 except for the point where the undulator reaches the brilliance limit of the undulator technique.

### 5.1.4. Elliptically polarizing undulators

The MAX IV 3 GeV storage ring will be an excellent storage ring for the installation of elliptically polarizing undulators since the vertical outer dimension of the vacuum tube is as small as 9 mm. It will be possible to reach as high as 2 keV photon energy with 100 % circularly polarized light using an elliptically polarizing undulator with 38 mm period length.

### 5.1.5. Wigglers

The function of the wigglers at the 3 GeV storage ring is twofold, to act as damping wigglers to decrease the emittance of the stored beam and to be photon sources for experimental stations. The wigglers will also increase the energy spread of the stored beam.

The wigglers may either be hybrid type wigglers using permanent magnet material in combination with soft magnetic materials in the pole centres or superconducting wigglers. The hybrid wiggler

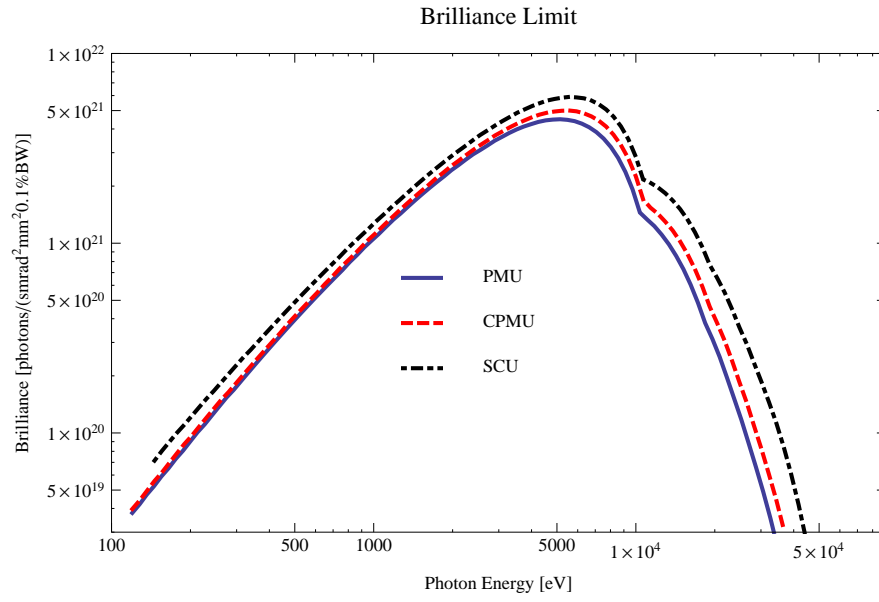


Figure 5.3: Brilliance limit for the 3 GeV MAX IV for the undulator techniques in-vacuum undulators (PMU), cryogenically cooled in-vacuum undulators (CPMU), and superconducting undulators (SCU). The undulators are assumed to be 3 m long.

type have the advantages of e.g. lower running costs and lower technical risks compared to superconducting wigglers. On the other hand, the peak performance of superconducting wigglers is superior to hybrid type wigglers.



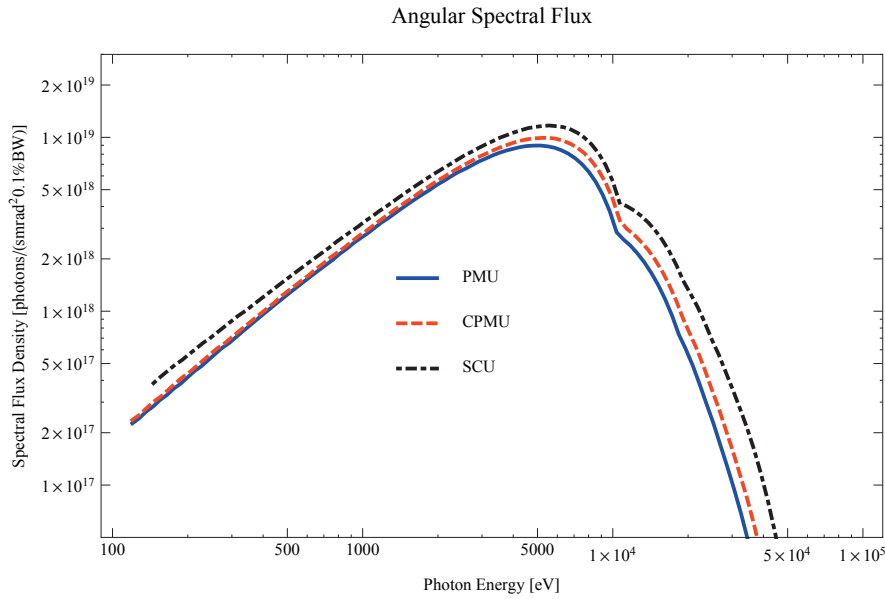


Figure 5.4: Angular spectral flux for the 3 GeV MAX IV for the undulator techniques in-vacuum undulators (PMU), cryogenically cooled in-vacuum undulators (CPMU), and superconducting undulators (SCU). The undulators are assumed to be 3 m long.

## 5.2. Proposed beamlines at the MAX IV 3 GeV ring

No decisions have yet been made on what beamlines should be built on the MAX IV facility and below list should only be regarded as examples on beamlines that could be built. It has been produced to give a possible scenario on what insertion devices that are being considered to be placed around the 3 GeV ring for the Detailed Design Report (DDR) of the accelerator. All of the insertion device based beamlines may not be possible to incorporate in Phase 1, also they are not listed in a priority order. The beamlines are shortly described in Table 5.2 and in the sub-sections below.

Table 5.2: Proposed insertion device based beamlines at the MAX IV 3 GeV ring

	Activity	Photon Energy	Source	Polarisation
PX1	Protein Crystallography	5 - 25 keV	Undulator	Horizontal
PX2	Protein Crystallography	5 - 25 keV	Undulator	Horizontal
NANO-1	Nanofocus	5 - 40 keV	Undulator	Horizontal
NANO-2	Nanofocus	5 - 40 keV	Undulator	Horizontal
SAXS/WAXS	Multipurpose SAXS/WAXS	5 - 30 keV	Undulator	Horizontal
XDIFF	X-ray Diffraction	5 - 30 keV	Undulator	Horizontal
TOM	Tomography/Imaging	10 - 100 keV	Wiggler	Horizontal
HIKE	Photoemission HIKE	2 - 15 keV	Undulator	Horizontal
XAFS	XAFS Spectroscopy	4- 30 keV	Undulator	Horizontal
MATERIAL	High energy XAS and XRD	30 - 100 keV	Wiggler	Horizontal
BL3-I1011	Magnetic Surfaces	300 - 1500 eV	Undulator	All
BL4-Gas	Gas Phase Studies	300 - 2000 eV	Undulator	All
BL5-Spect	Soft X-ray Spectroscopy	200 - 1200 eV	Undulator	All

### 5.2.1. PX1

A high-throughput macromolecular crystallography beamline based on an in-vacuum undulator.

### 5.2.2. PX2

A microfocus beamline for macromolecular crystallography based on an in-vacuum undulator.

### 5.2.3. NANO-1

A beamline with nano-focus capacity for mainly microscopy and spectroscopy applications based on an in-vacuum undulator.

### 5.2.4. NANO-2

A beamline with nano-focus capacity for mainly diffraction and imaging applications based on an in-vacuum undulator.

### 5.2.5. SAXS/WAXS

An in-vacuum undulator based multipurpose SAXS/ WAXS beamline for small angle X-ray scattering (SAXS) experiments with simultaneous wide angle X-ray scattering (WAXS) capacity.

### 5.2.6. XDIFF

X-ray diffraction beamline for x-ray diffraction on powders and single crystals, surface diffraction, and thin-film diffraction based on an in-vacuum undulator.

### 5.2.7. TOM

A tomography/imaging beamline based on a superconducting wiggler with a peak field of 3.5 - 4 T.

### 5.2.8. HIKE

A beamline for HIKE (High Energy Photo Emission) experiments based on an in-vacuum undulator.

### 5.2.9. XAFS

A beamline based on an in-vacuum undulator for bulk-XAFS spectroscopy and micro-XAFS spectroscopy divided at two endstations.

## 5.2.10. MATERIAL

Material Science beam line for high energy x-ray absorption spectroscopy (XAS) and x-ray diffraction (XRD) based on a superconducting wiggler a peak field of 3.5 - 4 T.

## 5.2.11. BL3-I1011

Beamline based on the existing elliptically polarising undulator and equipment at I1011 at the time of the move to the new MAX IV facilities.

## 5.2.12. BL4-Gas

Beam line for gas phase studies, x-ray emission, and photon fluorescence based on an elliptically polarising undulator.

## 5.2.13. BL5-Spect

Beam line for very high resolution soft x-ray spectroscopy in the photon energy range 250 - 1000 eV based on an elliptically polarising undulator.

To summarise, of the 13 beamlines in Table 5.2, 8 will use planar field in-vacuum undulators, 3 will use elliptically polarizing undulators, and 2 will use wigglers. All insertion devices will be placed in the middle of a long straight section of the MAX IV 3GeV ring.

# 5.3. Insertion devices at the MAX IV 3 GeV ring

The beam lines described in Table 5.2 may use the insertion devices shortly described in Table 5.3, where several options have been included.

The lengths given are the maximum lengths of the IDs and it is possible to make them shorter to decrease the heat loads to the optical systems of the beamlines.

The interested reader may read the previous version of this report, with date 2009-09-22, where in addition to the IDs in Table 5.3, 5 additional optional IDs for the MAX IV 3 GeV ring were described.

The 5 additional IDs described in the previous report were: wigS, a 1 m long hybrid type wiggler with 80 mm period length and 1.87 T peak field; wigD, a 4 m long hybrid type wiggler with 80 mm period length and 2.22 T peak field; pmuC, an in-vacuum undulator with 22 mm period length and 1.24 T efficient field, cpmuA, a cryo-cooled in-vacuum undulator with 15.6 mm period length and 1.15 T efficient field; cpmuB, a cryo-cooled in-vacuum undulator with 16.4 mm period length and 1.20 T efficient field.

pmu18p5, pmu20, and epu38 in this version of the report are identical to pmuA, pmuB, and epuA, respectively, in the previous version of the report. wig80 is identical, except for the magnetic gap, compared to the wigD in the previous version of the report. The magnetic gap for wig80 has been decreased to 7.8 mm compared to the 9 mm gap of wiggler wigD.

The insertion devices in Table 5.3 have been modelled in Radia [2] and in the following sections details of the magnet models, magnetic fields, photon energy ranges, emitted power, photon flux, brilliance, kick maps, and tune shifts are described.

Table 5.3: Insertion devices at the MAX IV 3 GeV storage ring

ID	Beamlines	Type	Length	Period
pmu18p5	PX1	In-vacuum undulator	3.8 m	18.5 mm
	PX2			
	NANO-1			
	NANO-2			
	SAXS/WAXS			
	XDIF			
cpmu16	NANO-1, Optional	Cryo-cooled in-vacuum undulator	3.8 m	16.0 mm
	NANO-2, Optional			
pmu20	XAFS	In-vacuum undulator	3.8 m	20.0 mm
	HIKE			
scw46	MATERAIL	Superconducting wiggler	2.0 m	46.0 mm
	TOM			
wig80	MATERAIL, Optional	Wiggler of hybrid type	4.0 m	80.0 mm
	TOM, Optional			
epuI1011	BL3-I1011	Elliptically polarising undator	2.1 m	46.6 mm
epu38	BL4-Gas	Elliptically polarising undator	4.0 m	38.0 mm
	BL5-Spect			
epu43p6	BL4-Gas, Optional	Elliptically polarising undator	4.0 m	43.6 mm
	BL5-Spect, Optional			
epu48	BL4-Gas, Optional	Elliptically polarising undator	4.0 m	48.0 mm
	BL5-Spect, Optional			
epu53p6	BL4-Gas, Optional	Elliptically polarising undator	4.0 m	53.6 mm
	BL5-Spect, Optional			

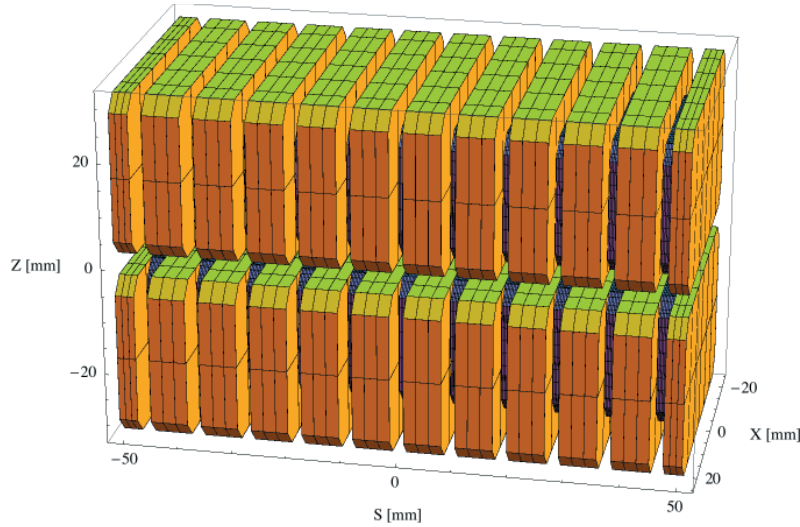


Figure 5.5: Magnetic model of the pmu18p5 ID. The magnet has been modelled with Radia [2].

### 5.3.1. The pmu18p5 ID

#### Magnet model of the pmu18p5 ID

The pmu18p5 is an in-vacuum undulator of hybrid type and the magnetic model of the pmu18p5 is shown in Figure 5.5. The magnet has been modelled with Radia [2]. The magnet blocks, which are yellow in Figure 5.5, are made of the magnetic material  $\text{Sm}_2\text{Co}_{17}$  with a magnetic remanence of 1.05 T at ambient temperature. The dimensions of the magnet blocks are  $50.00 \times 6.73 \times 30.00 \text{ mm}^3$  and there is a 4 mm chamfer at the corners of the magnet blocks. The poles, which are grey in Figure 5.5, are made of pure iron. The dimensions of the poles are  $32.00 \times 2.52 \times 24.00 \text{ mm}^3$  and there is a 3 mm chamfer at the corners of the poles.

#### Analysis of the magnetic field of the pmu18p5 ID

The vertical magnetic field in a central pole of the pmu18p5 ID along the ID axis,  $X = Z = 0$  is shown in Figure 5.6. The vertical magnetic field in a central pole of the pmu18p5 ID in the horizontally transverse direction to the ID axis,  $S = Z = 0$ , is shown in Figure 5.7.

A Fourier analysis of the magnetic field along the axis of the ID gives the higher harmonic contents in the magnetic field. A non-sinusoidal magnetic field profile along the ID would give a large higher harmonics contribution and it would no longer be possible to calculate the K-value of the ID from the peak field only. Also the higher harmonic contribution must be included to get the correct efficient magnetic field and efficient K-value. The higher harmonic contribution to the magnetic field is given in in Table 5.4.

A tranverse field roll-off may pose a problem to the storage ring since it gives a horizontal tune shift. The transverse field roll-off for the pmu18p5 for different horizontal positions out from the ID axis is shown in Figure 5.7 and numbers are given in Table 5.5.

The paremeters of the pmu18p5 are summarised in Table 5.6.

The critical energy of the emitted radiation will vary with the horizontal angle out from the axis of the ID as shown in Figure 5.8.

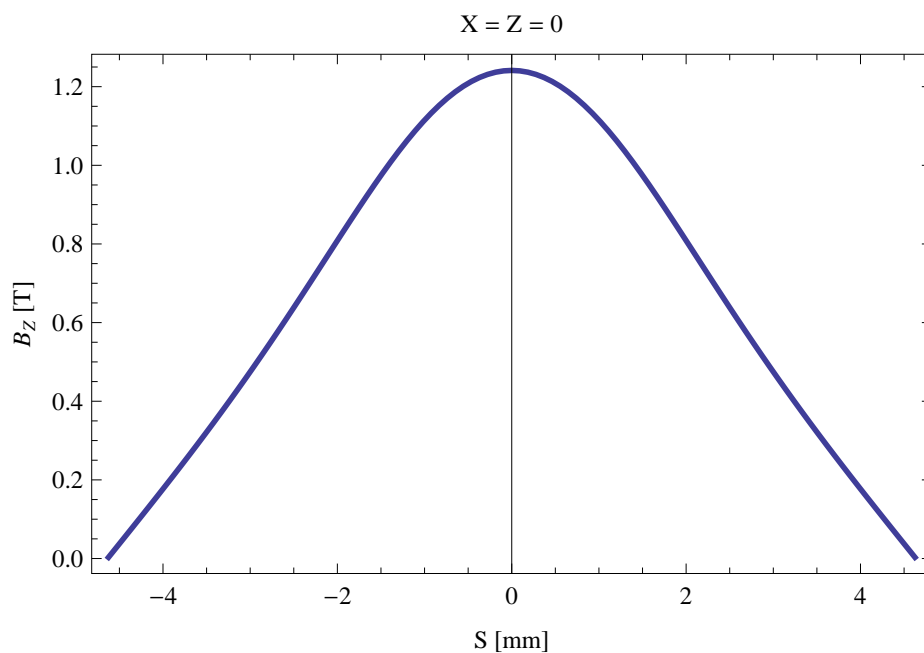


Figure 5.6: Vertical magnetic field in a central pole of the pmu18p5 ID along the ID axis,  $X = Z = 0$

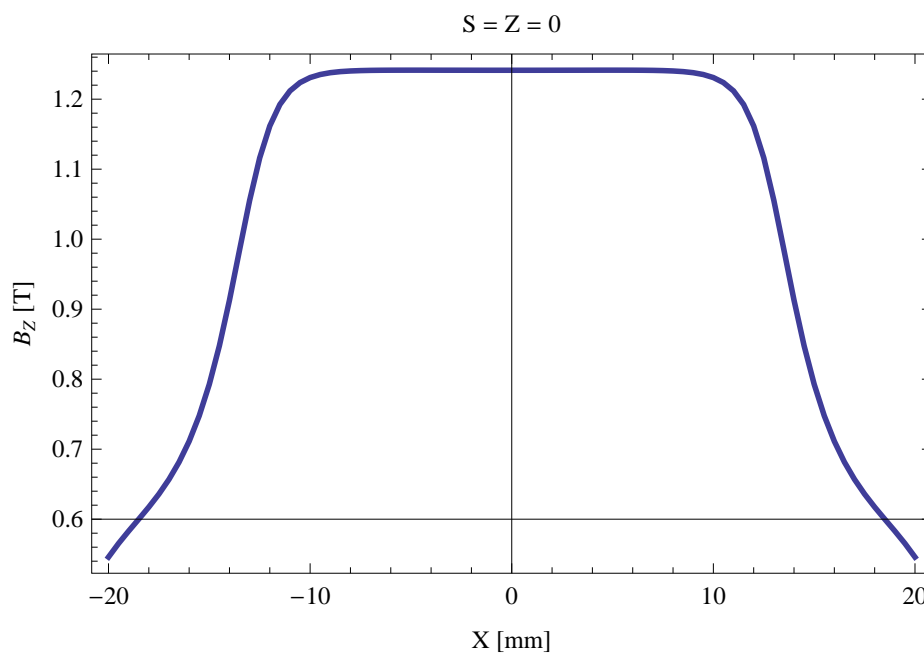


Figure 5.7: Vertical magnetic field in a central pole of the pmu18p5 ID along the horizontally transverse direction to the ID axis,  $S = Z = 0$

Table 5.4: Fourier Analysis of the magnetic field of the pmu18p5 ID

Term	Strength
Harm. Nr. 1	1.111 T
Harm. Nr. 3	0.114 T
Harm. Nr. 5	0.008 T
Harm. Nr. 7	-0.001 T
Harm. Nr. 9	-0.001 T
Harm. Nr. 11	-0.000 T

Table 5.5: Transverse field roll-off for the pmu18p5 ID

X-Position	$B_Z$ Field	Roll-off
$\pm 0$ mm	1.241 T	
$\pm 5$ mm	1.241 T	-0.01 %
$\pm 10$ mm	1.231 T	0.84 %
$\pm 15$ mm	0.793 T	36.14 %
$\pm 20$ mm	0.546 T	56.03 %

Table 5.6: Summary of the pmu18p5 ID parameters

Period	18.5	mm
Gap	4.2	mm
Peak Field	1.241	T
Effective Field	1.111	T
Peak k-value	2.145	
Effective k-value	1.920	
Higher Order Contr.	10.33	%
Maximum e-beam deflection	0.32	mrاد
Electron Beam Energy	3.0	GeV
Electron Beam Current	500	mA
Max Critical Energy	7.429	keV
Emitted Power	13.306	kW
Photon Energy, $n = 1$	1.625	keV
Total Length	3783.3	mm

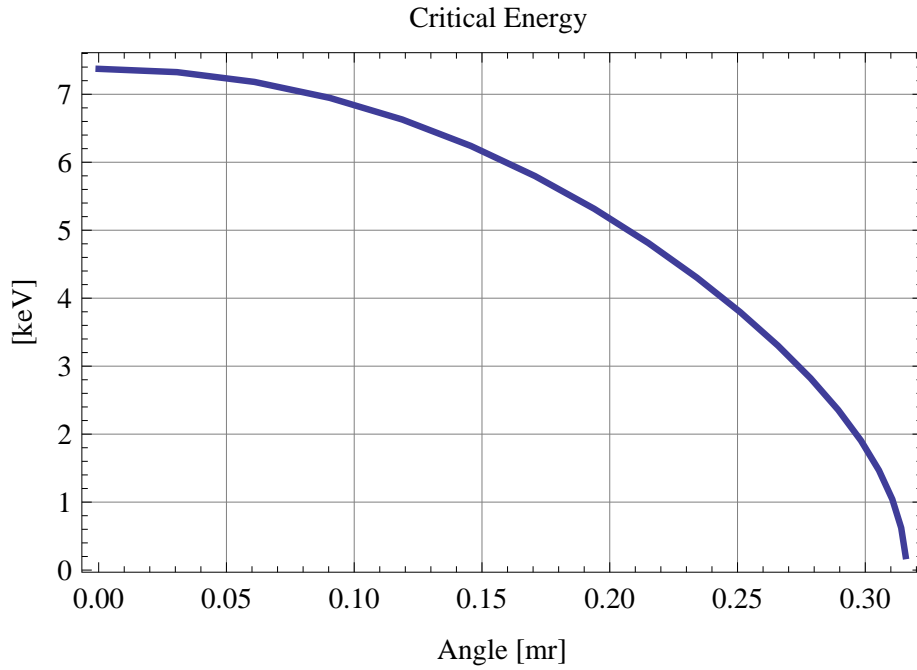


Figure 5.8: Variation of the critical energy with horizontal angle for the emitted synchrotron radiation from the pmu18p5 ID

### Synchrotron radiation from the pmu18p5 ID

The power map of the emitted synchrotron radiation by the pmu18p5 ID, assuming a 0.5 A filament beam with an energy of 3 GeV and undulator properties of the synchrotron radiation, is shown in Figure 5.9. The on-axis power density is 97.108 kW/mrad<sup>2</sup>

A map of the degree of linear polarisation of the fundamental harmonic of the synchrotron radiation emitted by the pmu18p5 ID over the angle of observation is shown in Figure 5.10.

A map of the degree of 45 degree polarisation of the fundamental harmonic of the synchrotron radiation emitted by the pmu18p5 ID over the angle of observation is shown in Figure 5.11.

A map of the degree of circular polarisation of the fundamental harmonic of the synchrotron radiation emitted by the pmu18p5 ID over the angle of observation is shown in Figure 5.12.

The on axis brilliance at peak energy, the angular spectral flux, the flux in the harmonics, the power in the harmonics, the ratio of coherence, the coherent flux in the harmonics, and the power of coherent radiation in the harmonics from the pmu18p5 ID have been calculated and the resulting plots are found in this section of the document. The beam parameters used for the calculation are 0.5 A of stored current,  $\beta_H = 9$  m,  $\varepsilon_H = 0.263$  nmrad,  $\beta_V = 4.8$  m,  $\varepsilon_V = 8$  pmrad, and an energy spread of 0.001.

The brilliance at peak energy and the angular spectral flux density from the pmu18p5 ID for different harmonics at maximum K-value (1.920) are given in Table 5.7 and for minimum K-value (0.400) these values are given in Table 5.8.



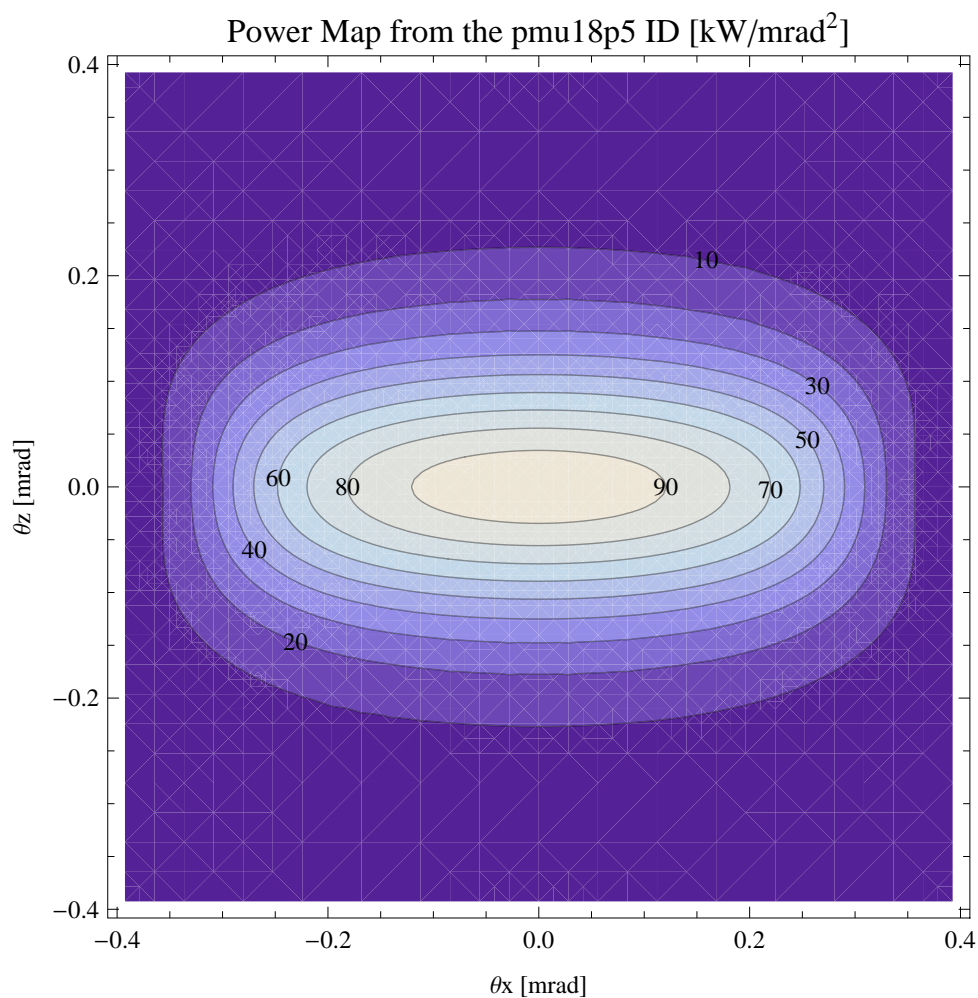


Figure 5.9: Map of the power distribution of the emitted synchrotron radiation by the pmu18p5 ID

Table 5.7: The brilliance at peak energy and the angular spectral flux density from the pmu18p5 ID for different harmonics at maximum K-value (1.920)

Harmonic	Photon Energy [eV]	Brilliance [Ph./s/mrad <sup>2</sup> /mrad <sup>2</sup> /0.1%BW]	Angular Spectral Flux [Ph./s/mrad <sup>2</sup> /0.1%BW]
1	1624.35	$2.23 \times 10^{21}$	$4.8 \times 10^{18}$
3	4873.04	$1.6 \times 10^{21}$	$2.92 \times 10^{18}$
5	8121.74	$9.72 \times 10^{20}$	$1.71 \times 10^{18}$
7	11370.4	$5.91 \times 10^{20}$	$1.02 \times 10^{18}$
9	14619.1	$3.61 \times 10^{20}$	$6.2 \times 10^{17}$
11	17867.8	$2.22 \times 10^{20}$	$3.78 \times 10^{17}$

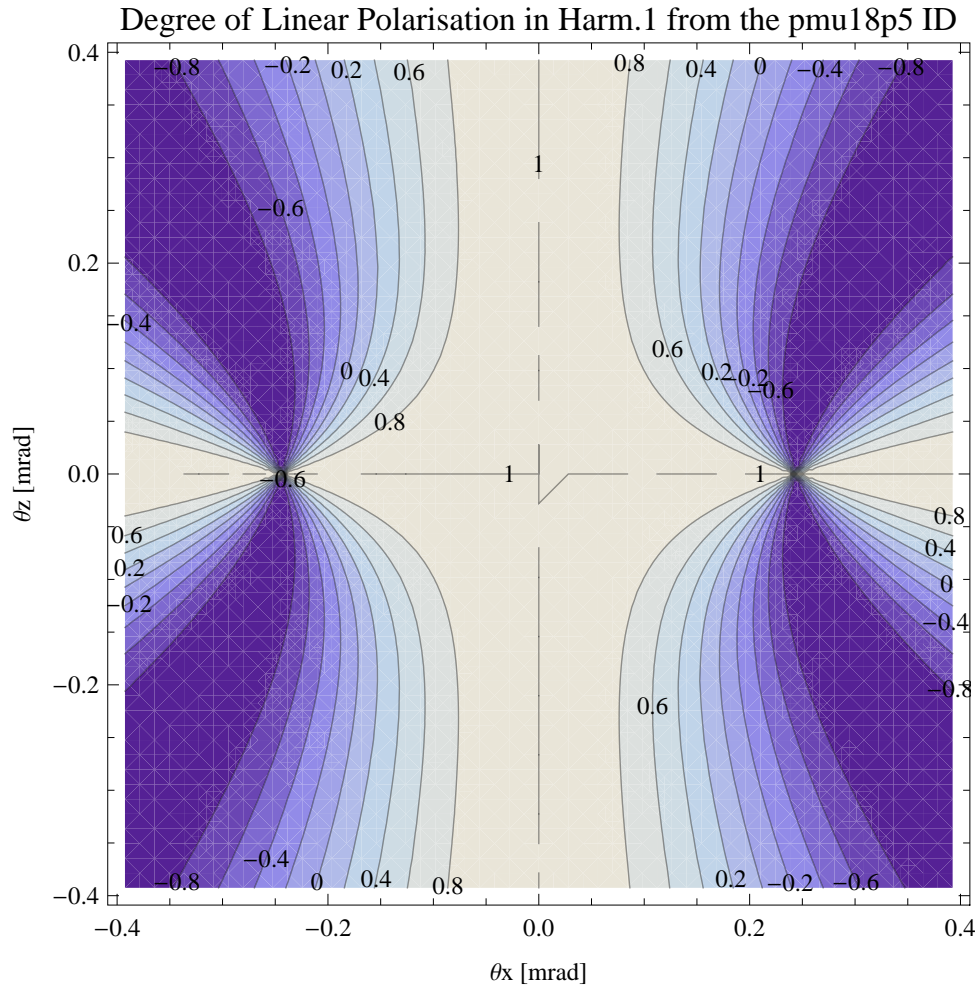


Figure 5.10: Map of linear polarisation in the fundamental harmonic of the synchrotron radiation emitted by the pmu18p5 ID

Table 5.8: The brilliance at peak energy and the angular spectral flux density from the pmu18p5 ID for different harmonics at minimum K-value (0.4)

Harmonic	Photon Energy [eV]	Brilliance [Ph./s/mrad <sup>2</sup> /mrad <sup>2</sup> /0.1%BW]	Angular Spectral Flux [Ph./s/mrad <sup>2</sup> /0.1%BW]
1	4277.66	$1.04 \times 10^{21}$	$1.94 \times 10^{18}$
3	12833.	$1.26 \times 10^{19}$	$2.24 \times 10^{16}$
5	21388.3	$1.3 \times 10^{17}$	$2.28 \times 10^{14}$
7	29943.6	$1.31 \times 10^{15}$	$2.31 \times 10^{12}$
9	38498.9	$1.33 \times 10^{13}$	$2.33 \times 10^{10}$
11	47054.2	$1.34 \times 10^{11}$	$2.36 \times 10^8$

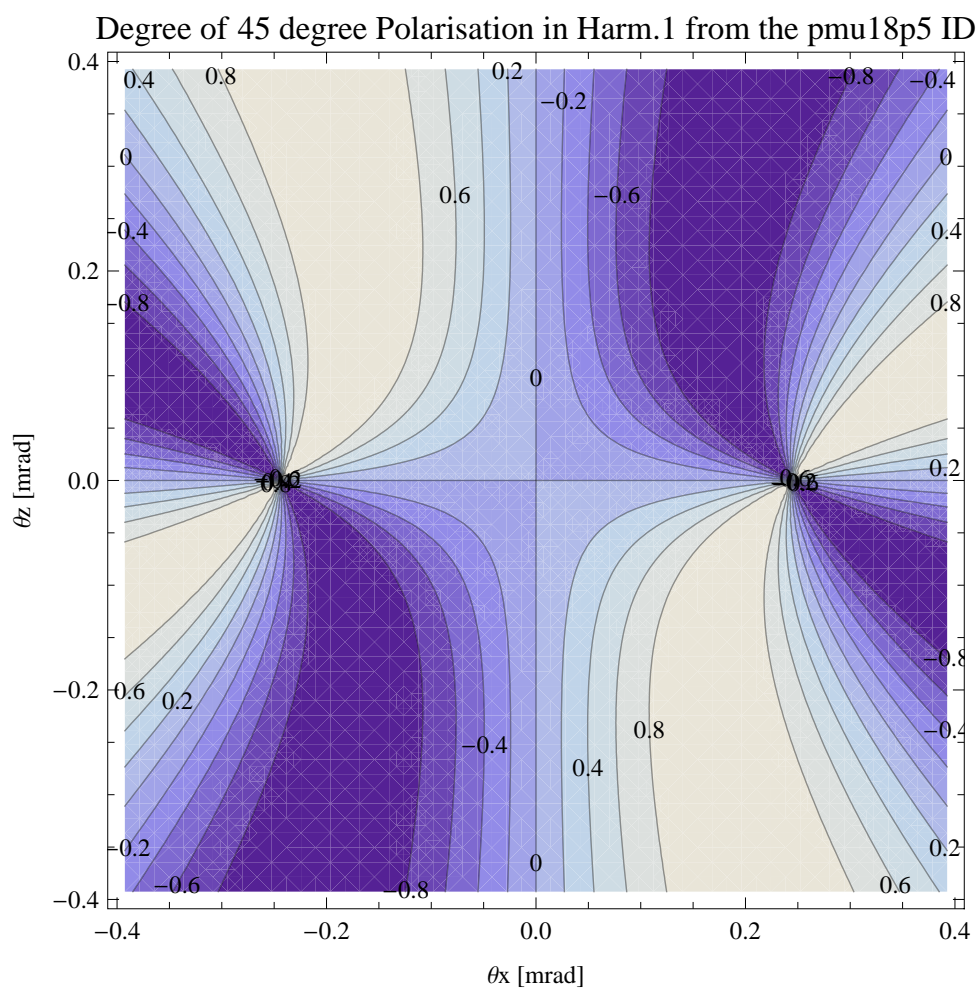


Figure 5.11: Map of 45 degree polarisation in the fundamental harmonic of the synchrotron radiation emitted by the pmu18p5 ID

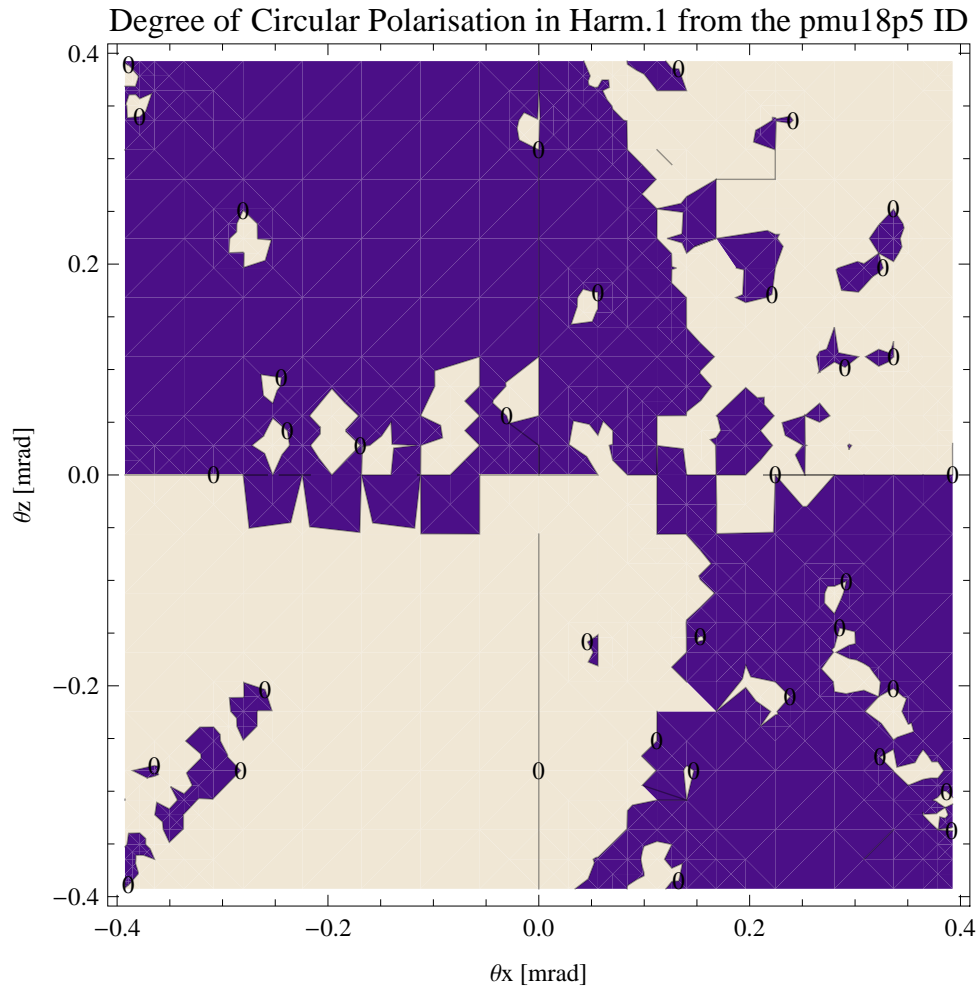


Figure 5.12: Map of circular polarisation in the fundamental harmonic of the synchrotron radiation emitted by the pmu18p5 ID

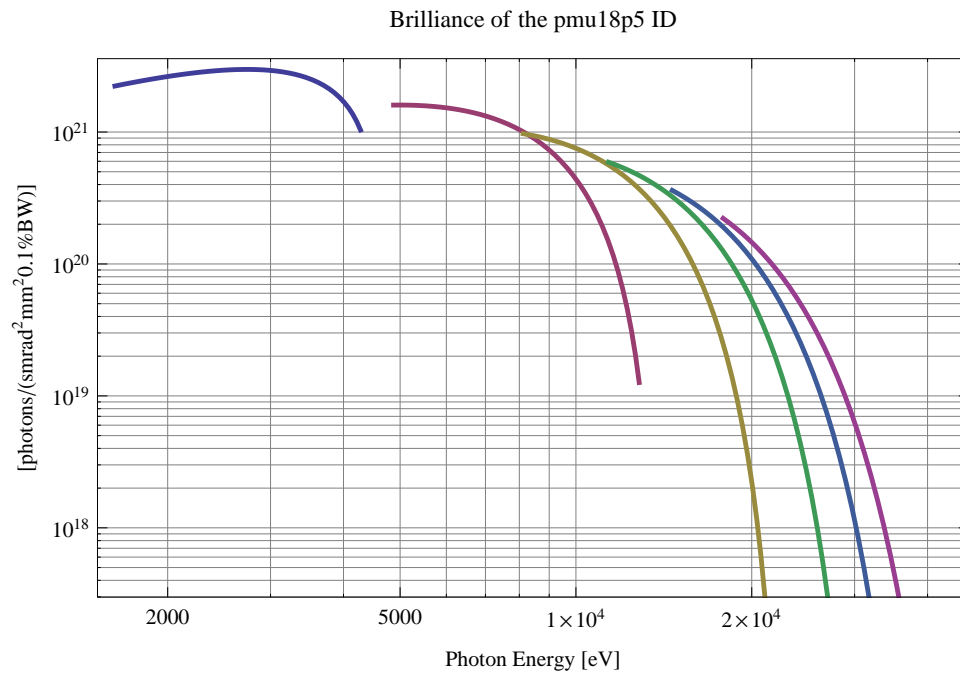


Figure 5.13: The brilliance at peak energy from the pmu18p5 ID

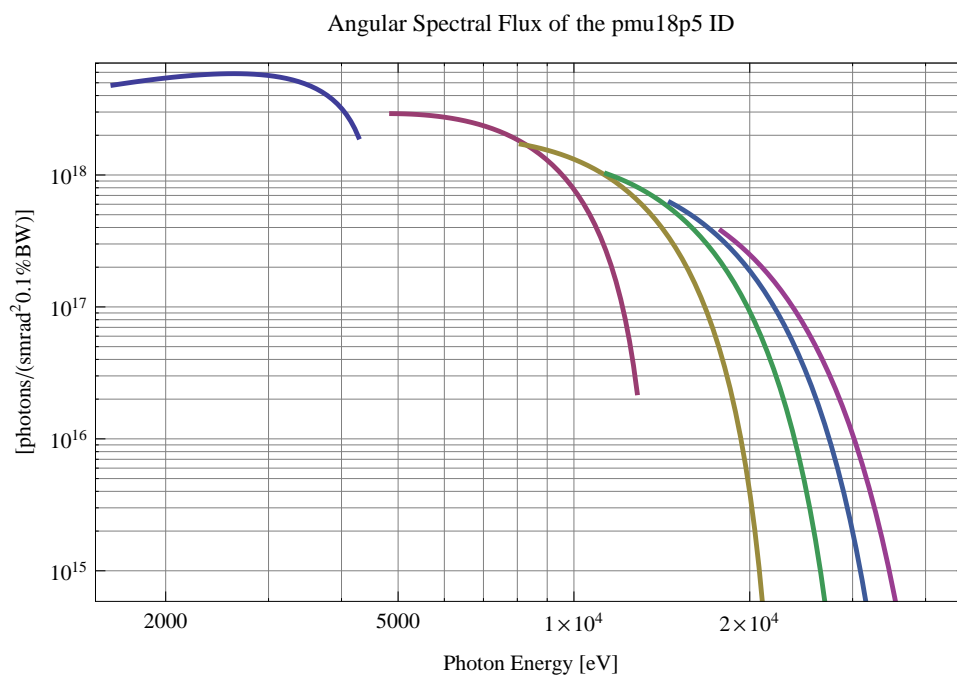


Figure 5.14: The angular spectral flux from the pmu18p5 ID

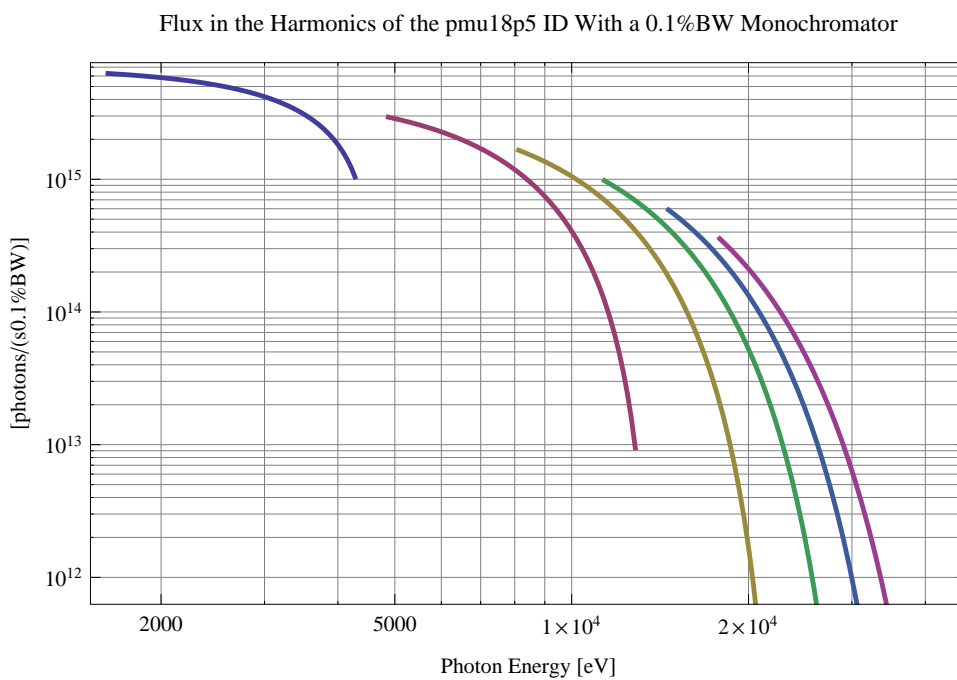


Figure 5.15: The flux of photons in the harmonics from the pmu18p5 ID using a 0.1%BW monochromator

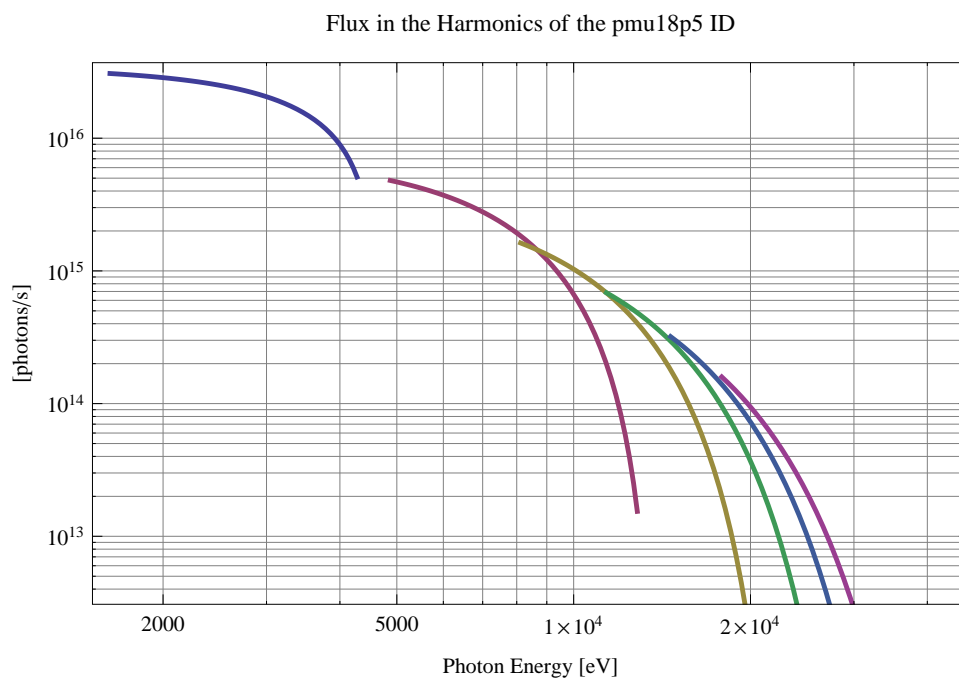


Figure 5.16: The flux of photons in the harmonics from the pmu18p5 ID

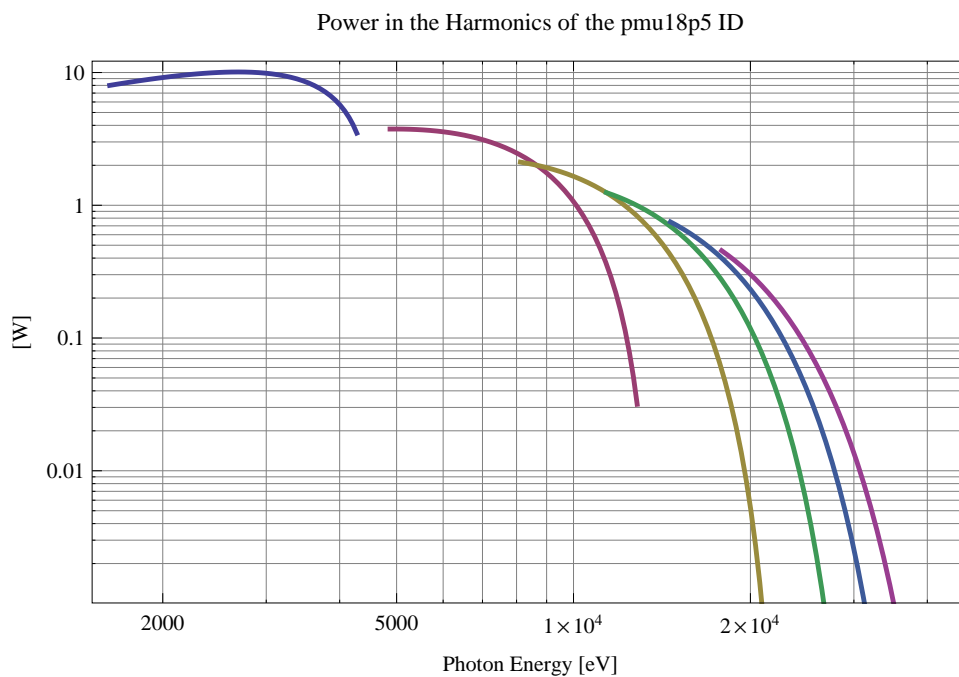


Figure 5.17: The power in the harmonics from the pmu18p5 ID

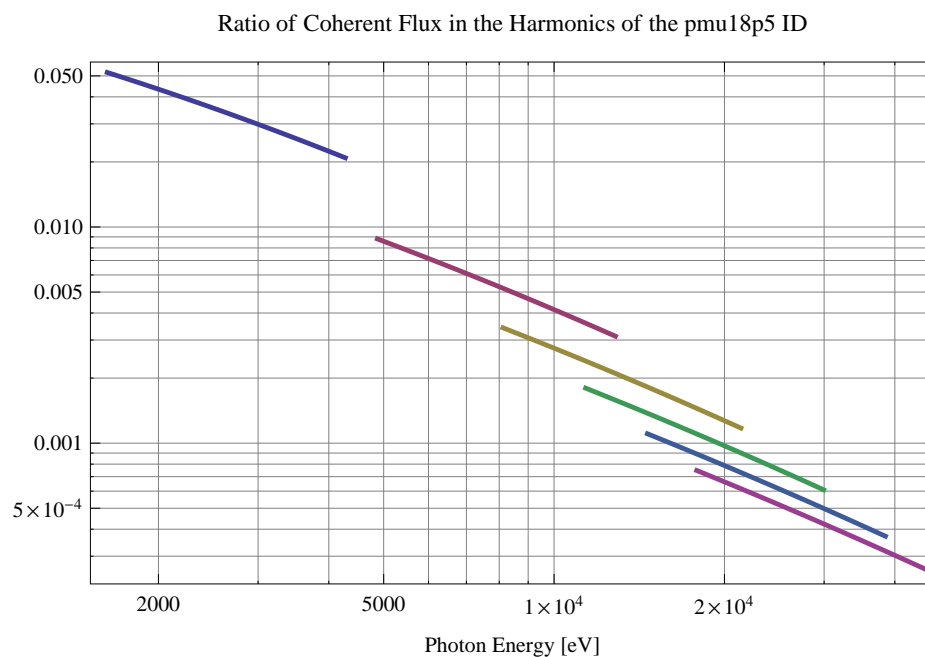


Figure 5.18: The ratio of coherent flux in the harmonics from the pmu18p5 ID

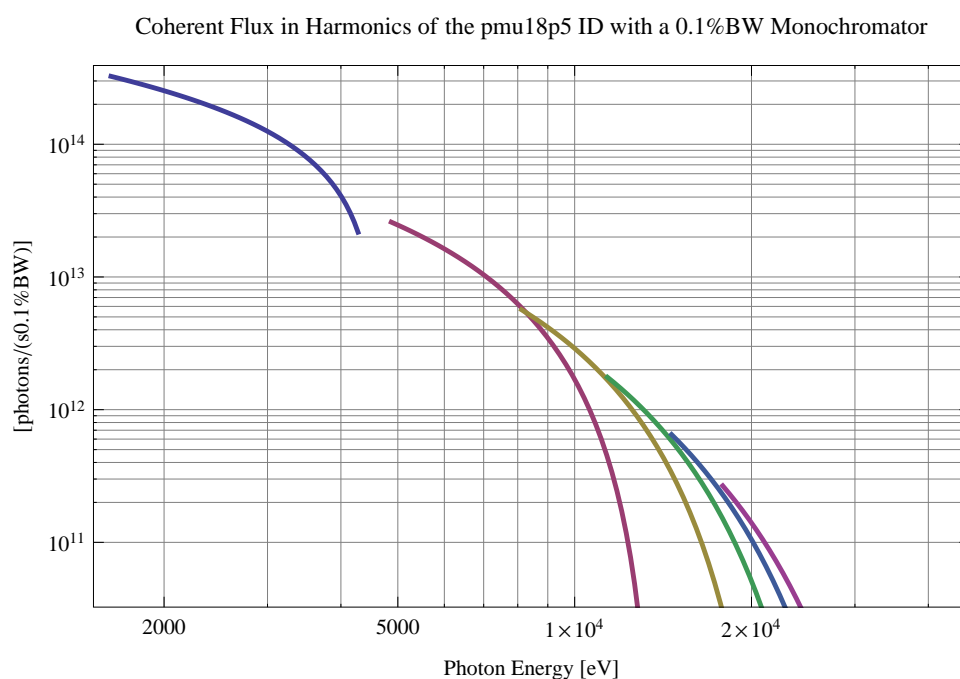


Figure 5.19: The coherent flux in the harmonics of the pmu18p5 ID using a 0.1%BW Monochromator

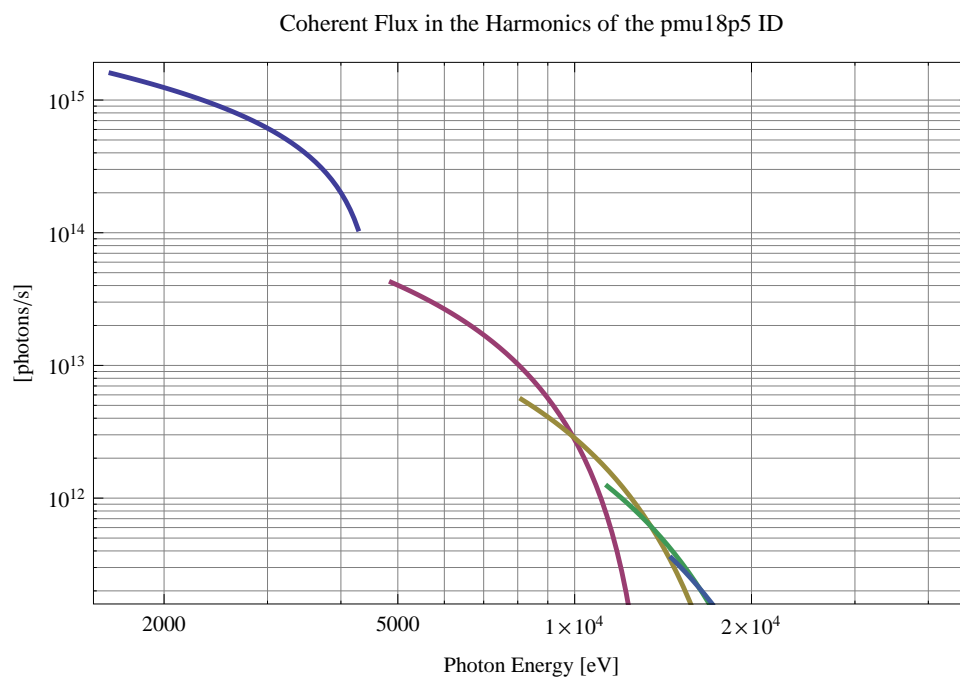


Figure 5.20: The coherent flux in the harmonics of the pmu18p5 ID

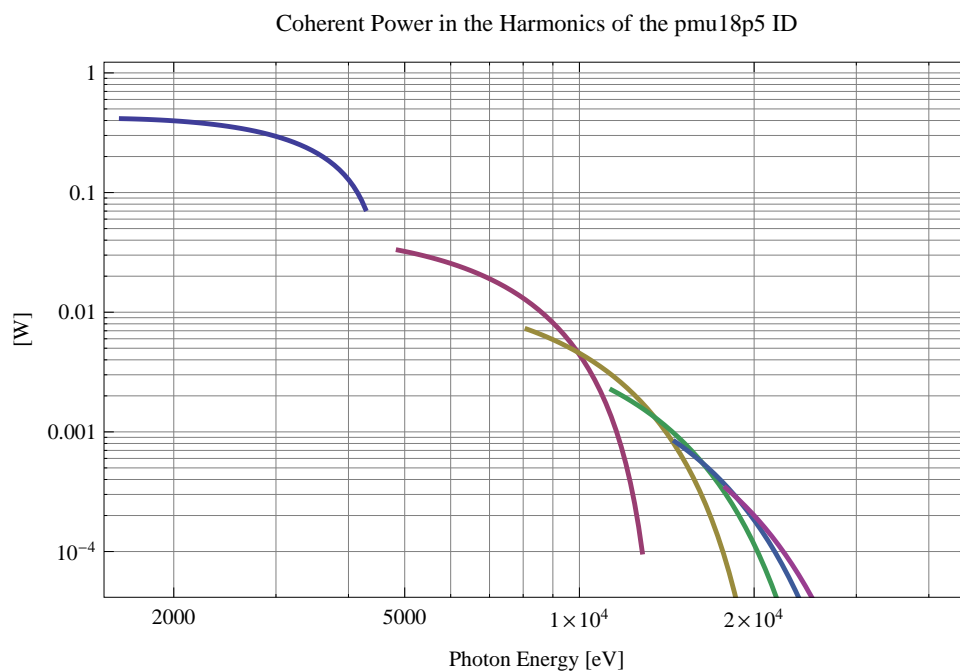


Figure 5.21: The power of coherent synchrotron radiation in the harmonics of the pmu18p5 ID



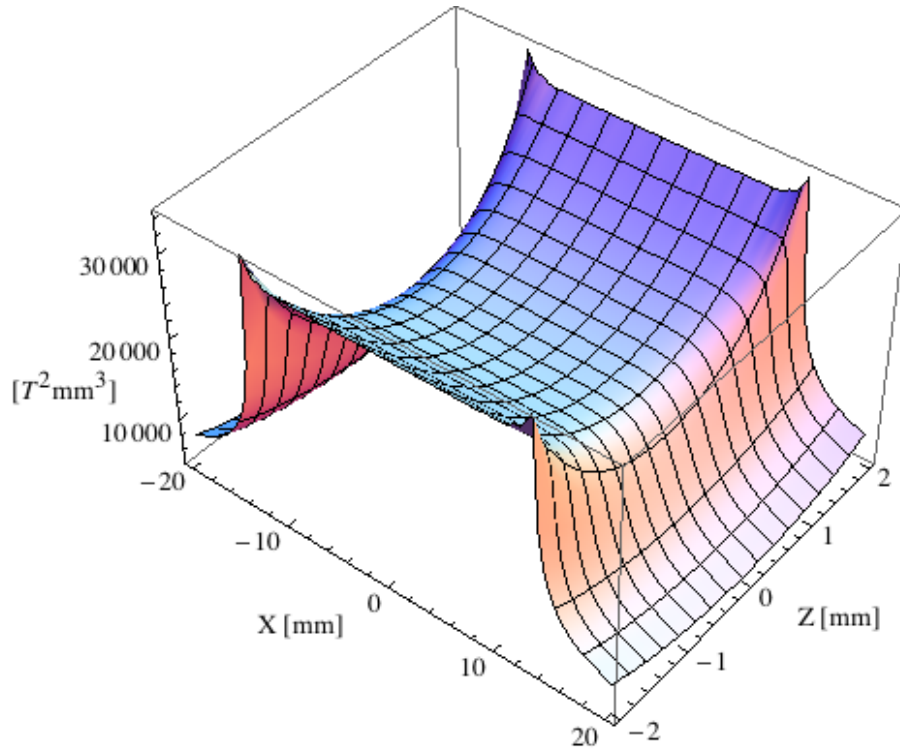


Figure 5.22: Focusing potential from the pmu18p5 ID over the beam stay clear aperture.

### Influence from the pmu18p5 ID on the optics of the stored beam

Figure 5.22 shows the focusing potential from the pmu18p5 over the beam stay clear aperture of the ring aperture.

Figure 5.23 shows the kick map in the beam energy independent unit  $T^2 m^2$  of the kicks induced by the pmu18p5 ID over the beam stay clear aperture.

Figure 5.24 shows the induced angular kick on the stored beam from the pmu18p5 ID as a function of the vertical distance to the axis of the ID.

Figure 5.25 shows the induced angular kick on the stored beam from the pmu18p5 ID as a function of the horizontal distance to the axis of the ID.

Figure 5.26 shows tune shift induced by the pmu18p5 ID over the beam stay clear aperture. Note that the tune shift depends on the beam size at the ID.

Figure 5.27 shows the induced tune shift from the pmu18p5 ID as a function of the vertical distance to the axis of the ID.

Figure 5.28 shows the induced tune shift from the pmu18p5 ID as a function of the horizontal distance to the axis of the ID.

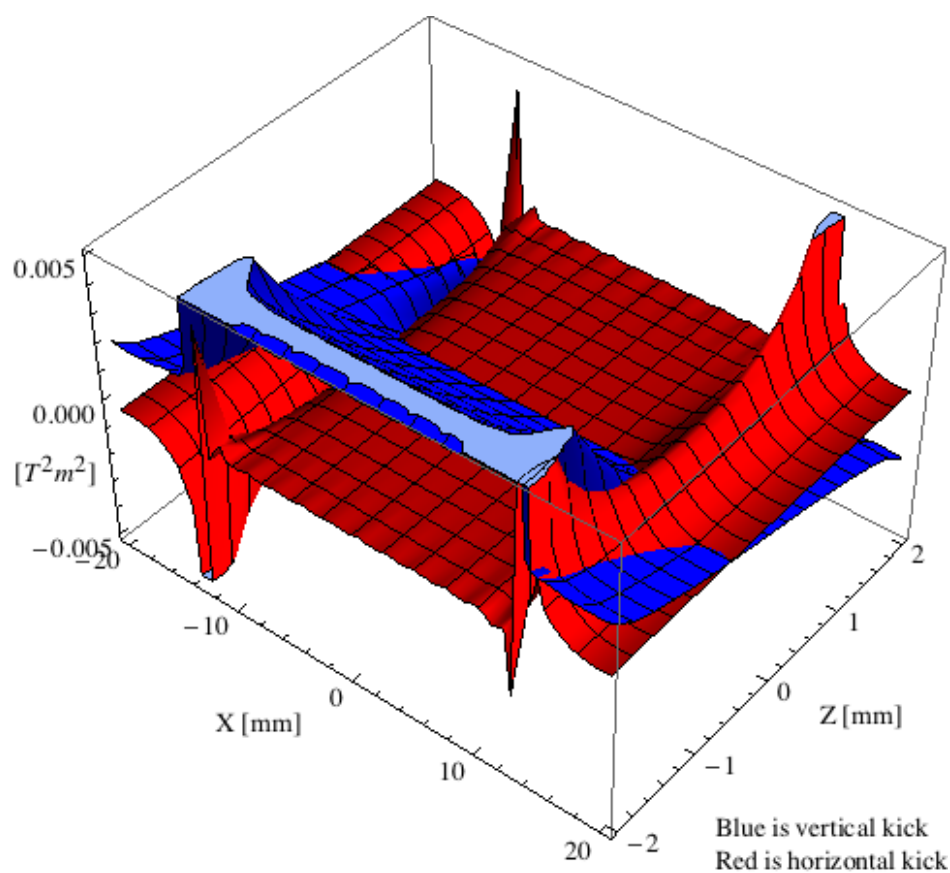


Figure 5.23: Kick map in the beam energy independent unit  $T^2m^2$  of the kicks induced by the pmu18p5 ID over the beam stay clear aperture.

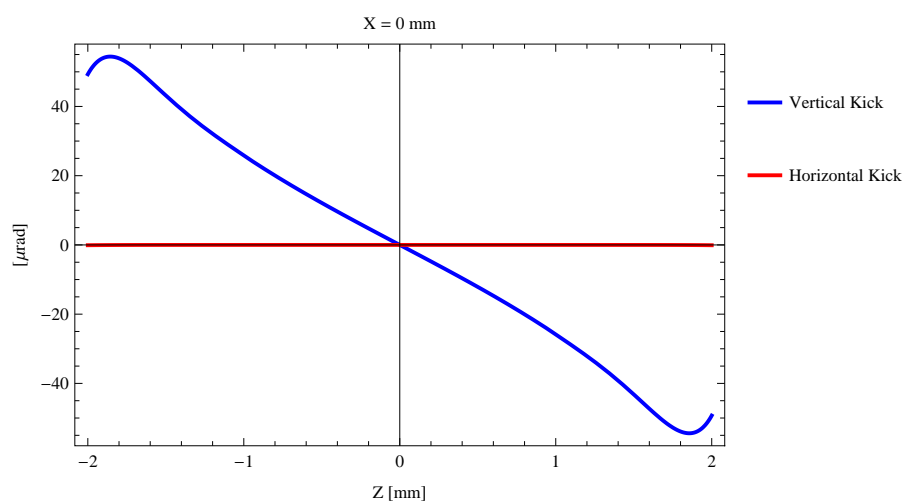


Figure 5.24: Induced angular kick on the stored beam from the pmu18p5 ID as a function of the vertical distance to the ID axis.

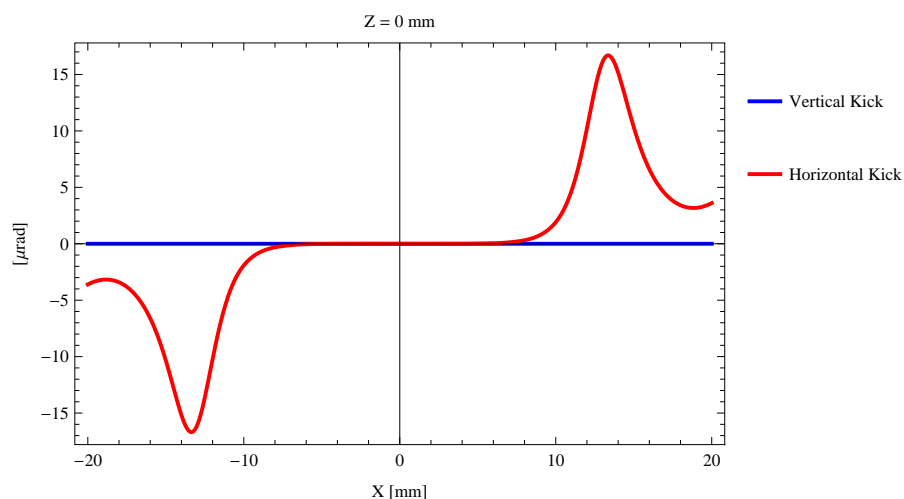


Figure 5.25: Induced angular kick on the stored beam from the pmu18p5 ID as a function of the horizontal distance to the ID axis.

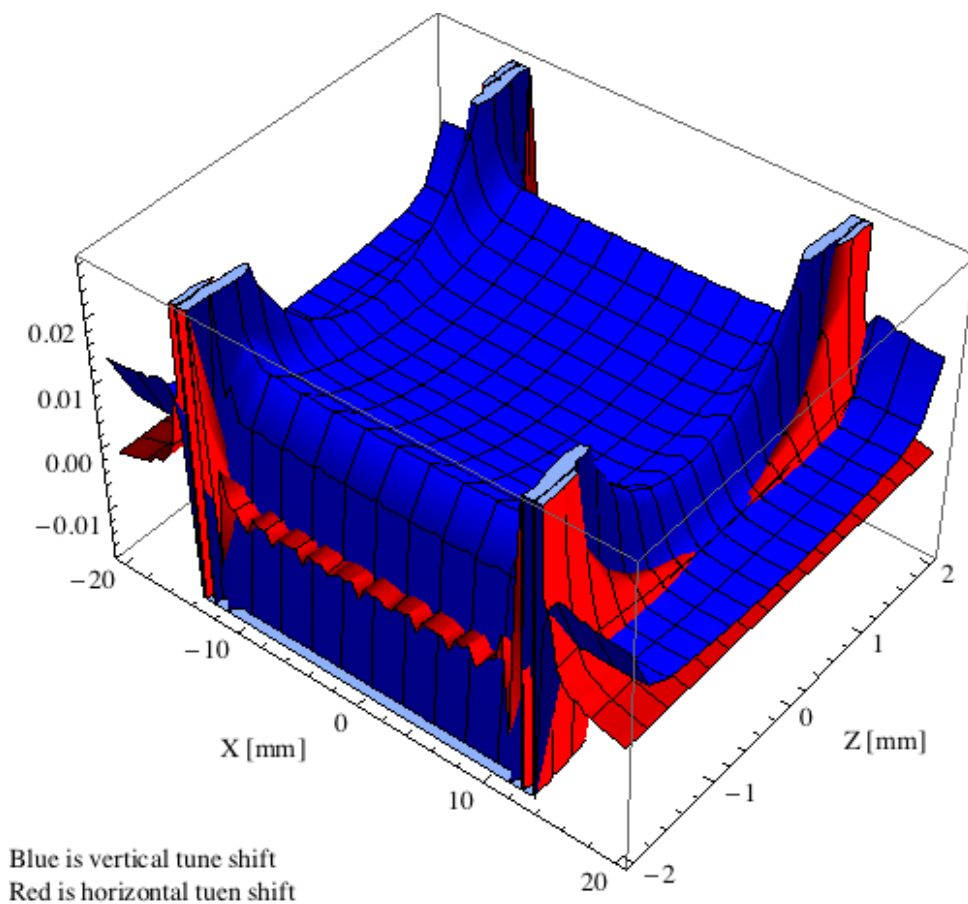


Figure 5.26: Tune shift induced by the pmu18p5 ID over the beam stay clear aperture.

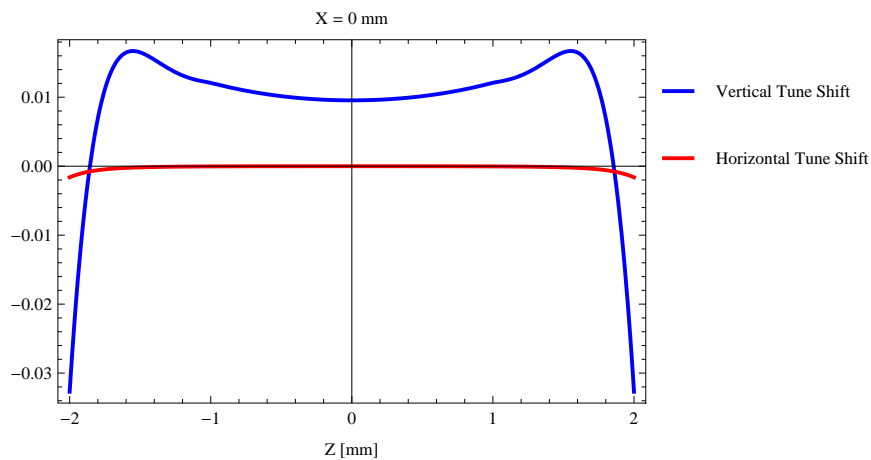


Figure 5.27: Induced tune shift from the pmu18p5 ID as a function of the vertical distance to the axis of the ID.

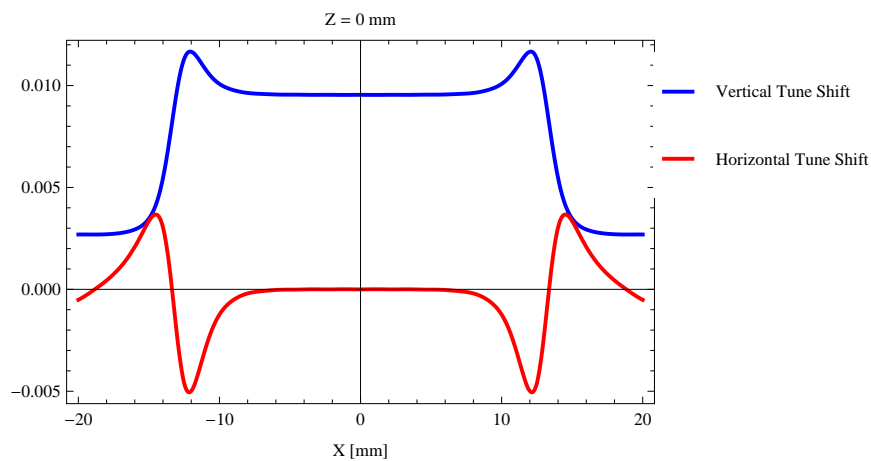


Figure 5.28: Induced tune shift from the pmu18p5 ID on the stored beam from the ID as a function of the horizontal distance to the axis of the ID.

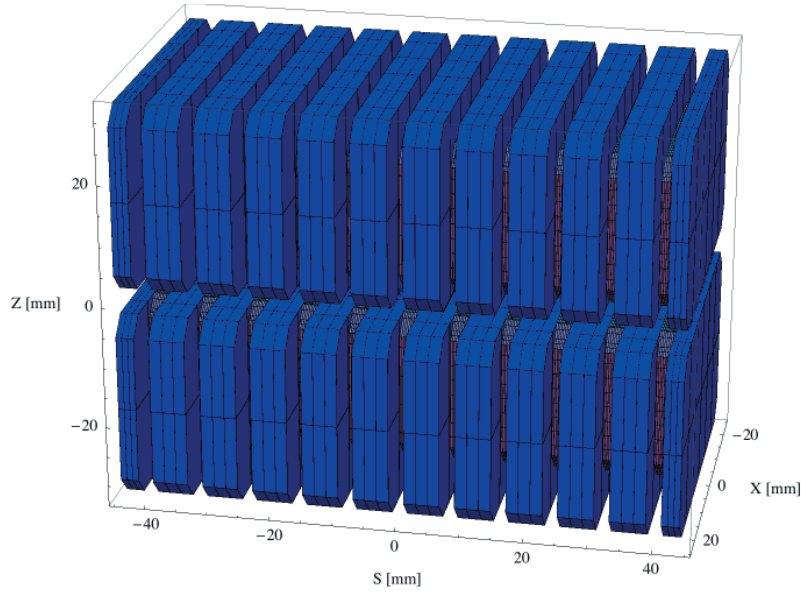


Figure 5.29: Magnetic model of the cpmu16 ID. The magnet has been modelled with Radia [2].

### 5.3.2. The cpmu16 ID

#### Magnet model of the cpmu16 ID

The cpmu16 is a cryogenically cooled in-vacuum undulator of hybrid type and the magnetic model of the cpmu16 is shown in Figure 5.29. The magnet has been modelled with Radia [2]. The magnet blocks, which are blue in Figure 5.29, are made of NdFeB material with a magnetic remanence of 1.35 T at 140 K. The dimensions of the magnet blocks are  $50.00 \times 5.60 \times 30.00 \text{ mm}^3$  and there is a 4 mm chamfer at the corners of the magnet blocks. The poles, which are grey in Figure 5.29, are made of pure iron. The dimensions of the poles are  $32.00 \times 2.40 \times 24.00 \text{ mm}^3$  and there is a 3 mm chamfer at the corners of the poles.

#### Analysis of the magnetic field of the cpmu16 ID

The vertical magnetic field in a central pole of the cpmu16 ID along the ID axis,  $X = Z = 0$  is shown in Figure 5.30. The vertical magnetic field in a central pole of the cpmu16 ID in the horizontally transverse direction to the ID axis,  $S = Z = 0$ , is shown in Figure 5.31.

A Fourier analysis of the magnetic field along the axis of the ID gives the higher harmonic contents in the magnetic field. A non-sinusoidal magnetic field profile along the ID would give a large higher harmonics contribution and it would no longer be possible to calculate the K-value of the ID from the peak field only. Also the higher harmonic contribution must be included to get the correct efficient magnetic field and efficient K-value. The higher harmonic contribution to the magnetic field is given in Table 5.9.

A transverse field roll-off may pose a problem to the storage ring since it gives a horizontal tune shift. The transverse field roll-off for the cpmu16 for different horizontal positions out from the ID axis is shown in Figure 5.31 and numbers are given in Table 5.10.

The parameters of the cpmu16 are summarised in Table 5.11.

The critical energy of the emitted radiation will vary with the horizontal angle out from the axis

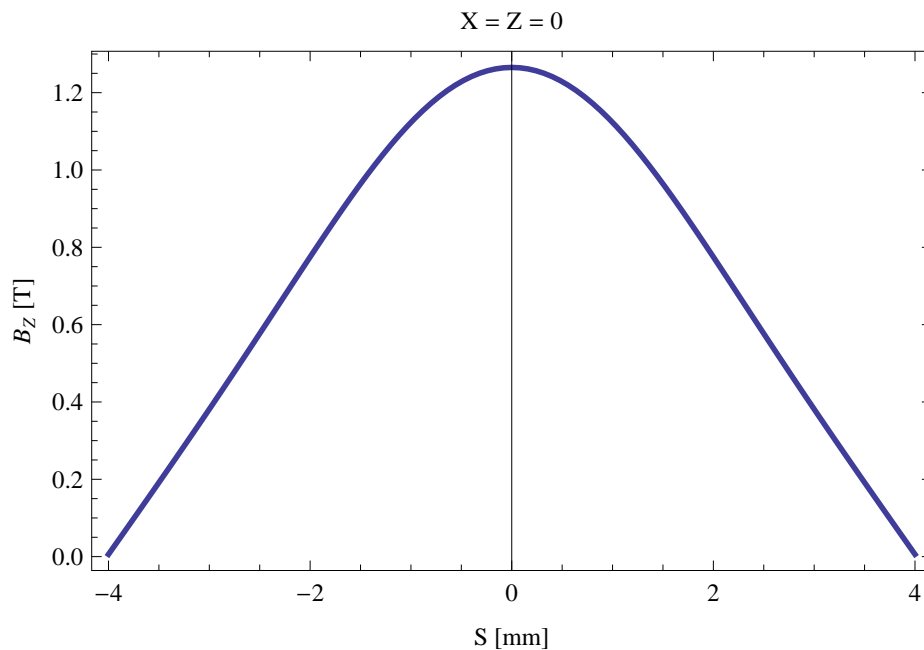


Figure 5.30: Vertical magnetic field in a central pole of the cpmu16 ID along the ID axis,  $X = Z = 0$

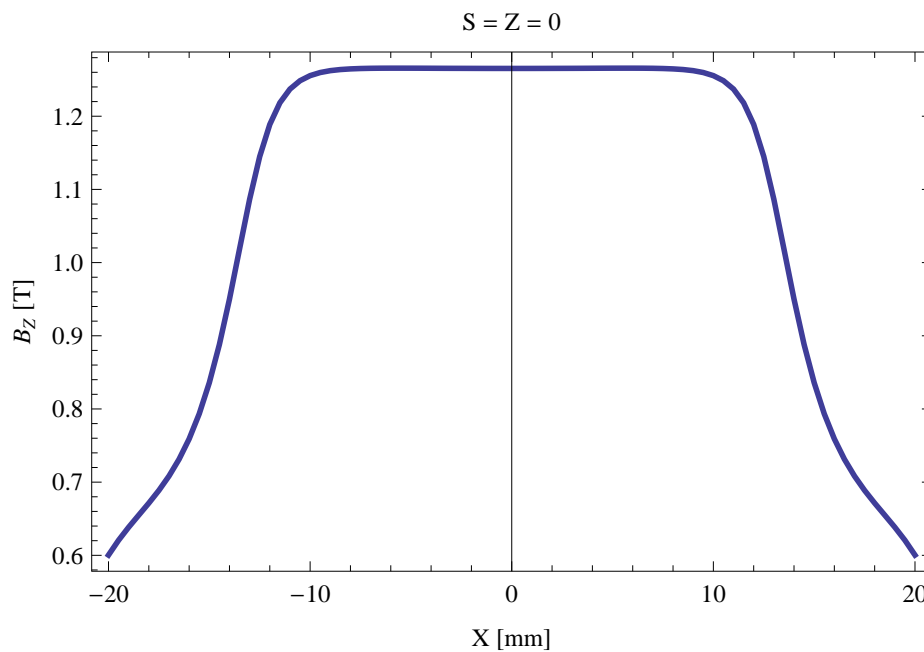


Figure 5.31: Vertical magnetic field in a central pole of the cpmu16 ID along the horizontally transverse direction to the ID axis,  $S = Z = 0$

Table 5.9: Fourier Analysis of the magnetic field of the cpmu16 ID

Term	Strength
Harm. Nr. 1	1.172 T
Harm. Nr. 3	0.082 T
Harm. Nr. 5	0.002 T
Harm. Nr. 7	-0.001 T
Harm. Nr. 9	-0.000 T
Harm. Nr. 11	-0.000 T

Table 5.10: Transverse field roll-off for the cpmu16 ID

X-Position	$B_Z$ Field	Roll-off
$\pm 0$ mm	1.265 T	
$\pm 5$ mm	1.266 T	-0.03 %
$\pm 10$ mm	1.255 T	0.78 %
$\pm 15$ mm	0.836 T	33.94 %
$\pm 20$ mm	0.600 T	52.55 %

Table 5.11: Summary of the cpmu16 ID parameters

Period	16.0	mm
Gap	4.2	mm
Peak Field	1.265	T
Effective Field	1.173	T
Peak k-value	1.891	
Effective k-value	1.753	
Higher Order Contr.	7.02	%
Maximum e-beam deflection	0.29	mrاد
Electron Beam Energy	3.0	GeV
Electron Beam Current	500	mA
Max Critical Energy	7.573	keV
Emitted Power	14.880	kW
Photon Energy, $n = 1$	2.107	keV
Total Length	3800.0	mm

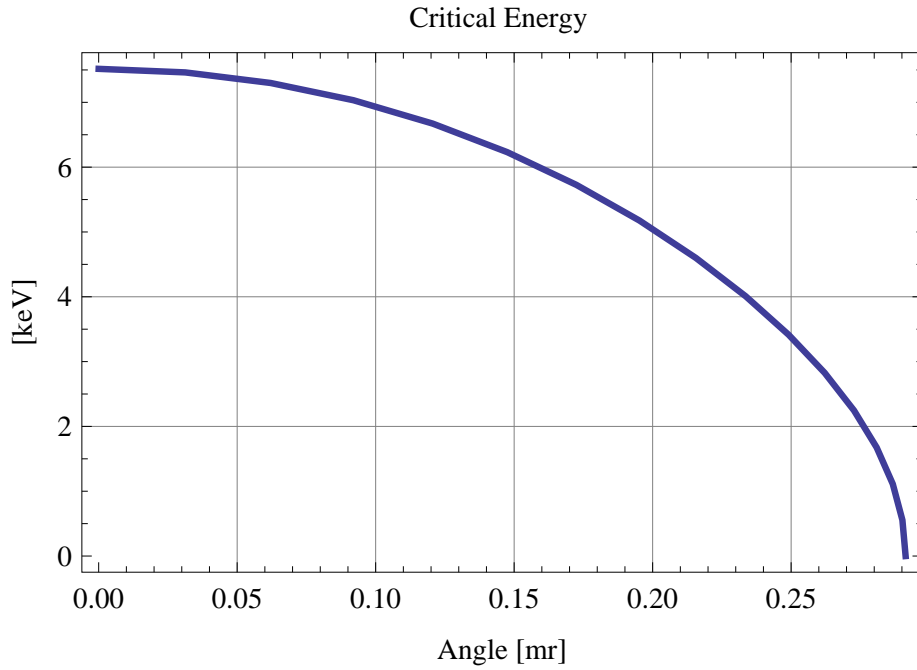


Figure 5.32: Variation of the critical energy with horizontal angle for the emitted synchrotron radiation from the cpmu16 ID

of the ID as shown in Figure 5.32.

### Synchrotron radiation from the cpmu16 ID

The power map of the emitted synchrotron radiation by the cpmu16 ID, assuming a 0.5 A filament beam with an energy of 3 GeV and undulator properties of the synchrotron radiation, is shown in Figure 5.33. The on-axis power density is 119.220 kW/mrad<sup>2</sup>

A map of the degree of linear polarisation of the fundamental harmonic of the synchrotron radiation emitted by the cpmu16 ID over the angle of observation is shown in Figure 5.34.

A map of the degree of 45 degree polarisation of the fundamental harmonic of the synchrotron radiation emitted by the cpmu16 ID over the angle of observation is shown in Figure 5.35.

A map of the degree of circular polarisation of the fundamental harmonic of the synchrotron radiation emitted by the cpmu16 ID over the angle of observation is shown in Figure 5.36.

The on axis brilliance at peak energy, the angular spectral flux, the flux in the harmonics, the power in the harmonics, the ratio of coherence, the coherent flux in the harmonics, and the power of coherent radiation in the harmonics from the cpmu16 ID have been calculated and the resulting plots are found in this section of the document. The beam parameters used for the calculation are 0.5 A of stored current,  $\beta_H = 9$  m,  $\varepsilon_H = 0.263$  nmrad,  $\beta_V = 4.8$  m,  $\varepsilon_V = 8$  pmrad, and an energy spread of 0.001.

The brilliance at peak energy and the angular spectral flux density from the cpmu16 ID for different harmonics at maximum K-value (1.753) are given in Table 5.12 and for minimum K-value (0.400) these values are given in Table 5.13.



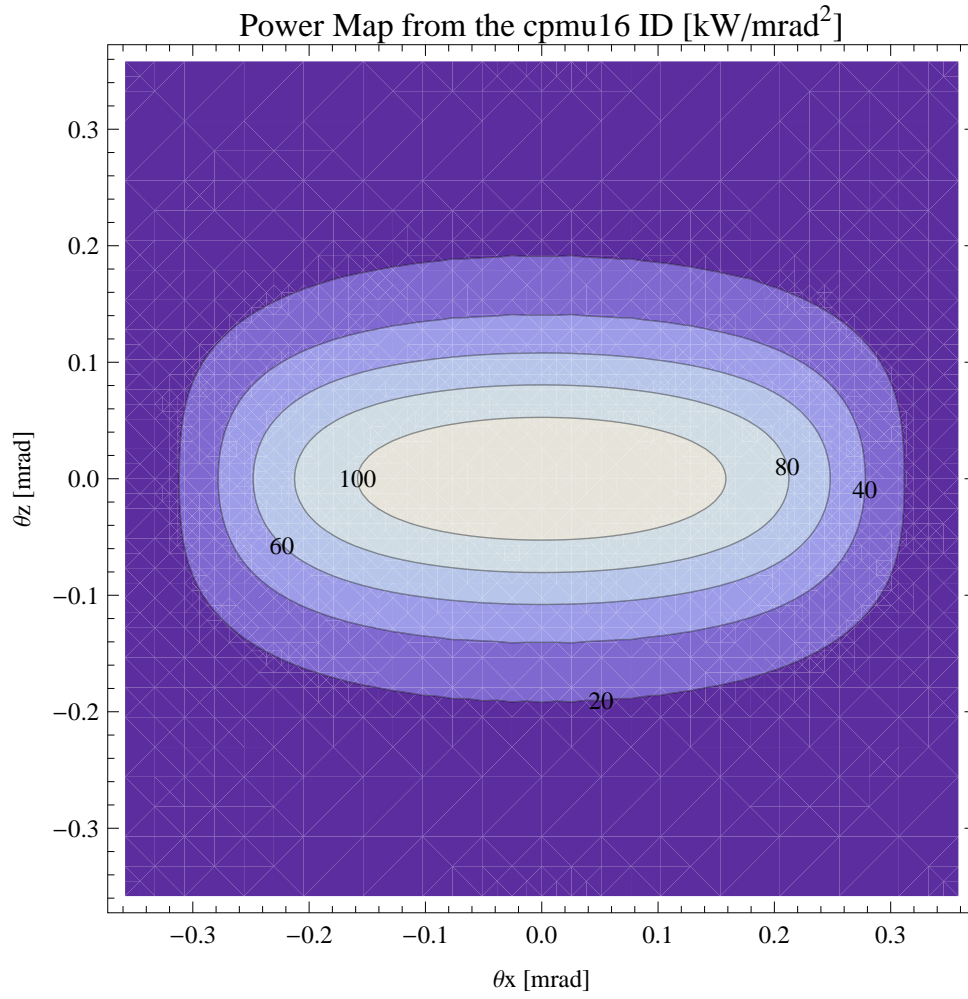


Figure 5.33: Map of the power distribution of the emitted synchrotron radiation by the cpmu16 ID

Table 5.12: The brilliance at peak energy and the angular spectral flux density from the cpmu16 ID for different harmonics at maximum K-value (1.753)

Harmonic	Photon Energy [eV]	Brilliance [Ph./s/mrad <sup>2</sup> /mrad <sup>2</sup> /0.1%BW]	Angular Spectral Flux [Ph./s/mrad <sup>2</sup> /0.1%BW]
1	2106.59	$3.13 \times 10^{21}$	$6.4 \times 10^{18}$
3	6319.76	$1.89 \times 10^{21}$	$3.39 \times 10^{18}$
5	10532.9	$1.03 \times 10^{21}$	$1.79 \times 10^{18}$
7	14746.1	$5.6 \times 10^{20}$	$9.64 \times 10^{17}$
9	18959.3	$3.08 \times 10^{20}$	$5.26 \times 10^{17}$
11	23172.5	$1.7 \times 10^{20}$	$2.89 \times 10^{17}$

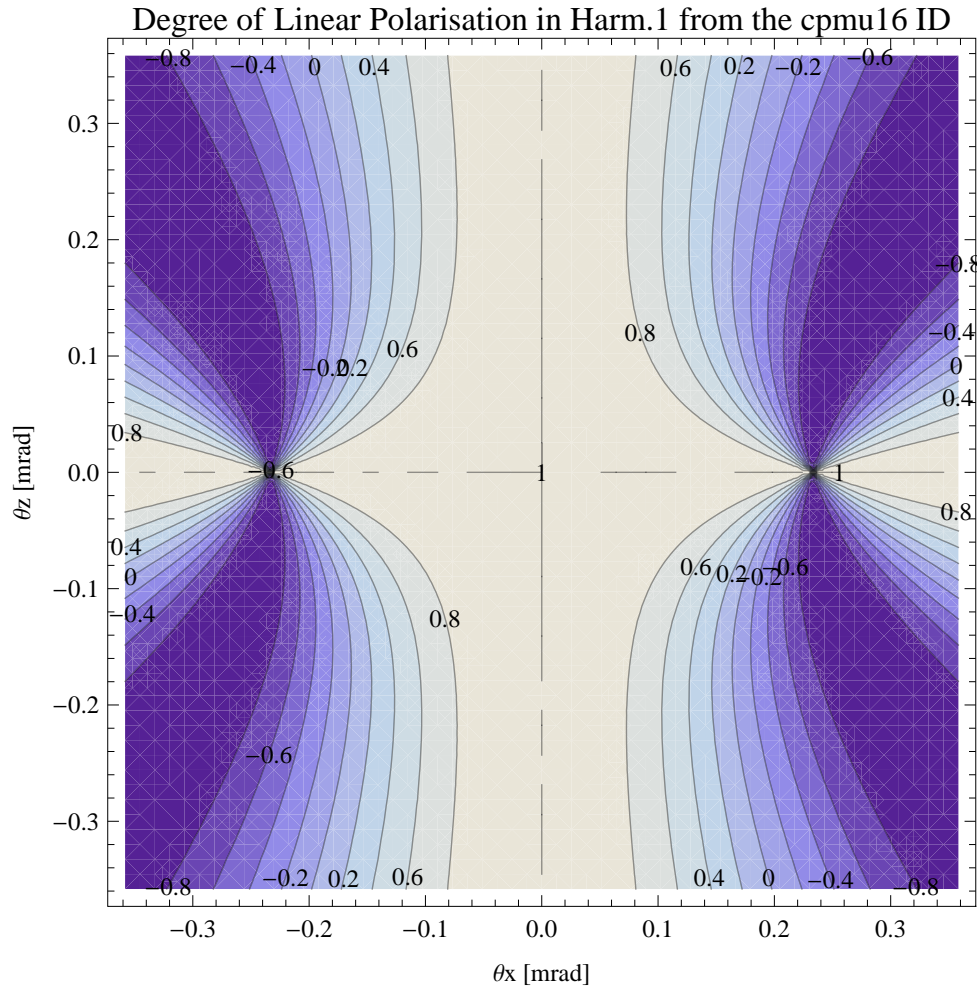


Figure 5.34: Map of linear polarisation in the fundamental harmonic of the synchrotron radiation emitted by the cpmu16 ID

Table 5.13: The brilliance at peak energy and the angular spectral flux density from the cpmu16 ID for different harmonics at minimum K-value (0.4)

Harmonic	Photon Energy [eV]	Brilliance [Ph./s/mrad <sup>2</sup> /mrad <sup>2</sup> /0.1%BW]	Angular Spectral Flux [Ph./s/mrad <sup>2</sup> /0.1%BW]
1	4946.04	$1.29 \times 10^{21}$	$2.39 \times 10^{18}$
3	14838.1	$1.5 \times 10^{19}$	$2.64 \times 10^{16}$
5	24730.2	$1.52 \times 10^{17}$	$2.68 \times 10^{14}$
7	34622.3	$1.54 \times 10^{15}$	$2.7 \times 10^{12}$
9	44514.4	$1.56 \times 10^{13}$	$2.73 \times 10^{10}$
11	54406.5	$1.57 \times 10^{11}$	$2.76 \times 10^8$

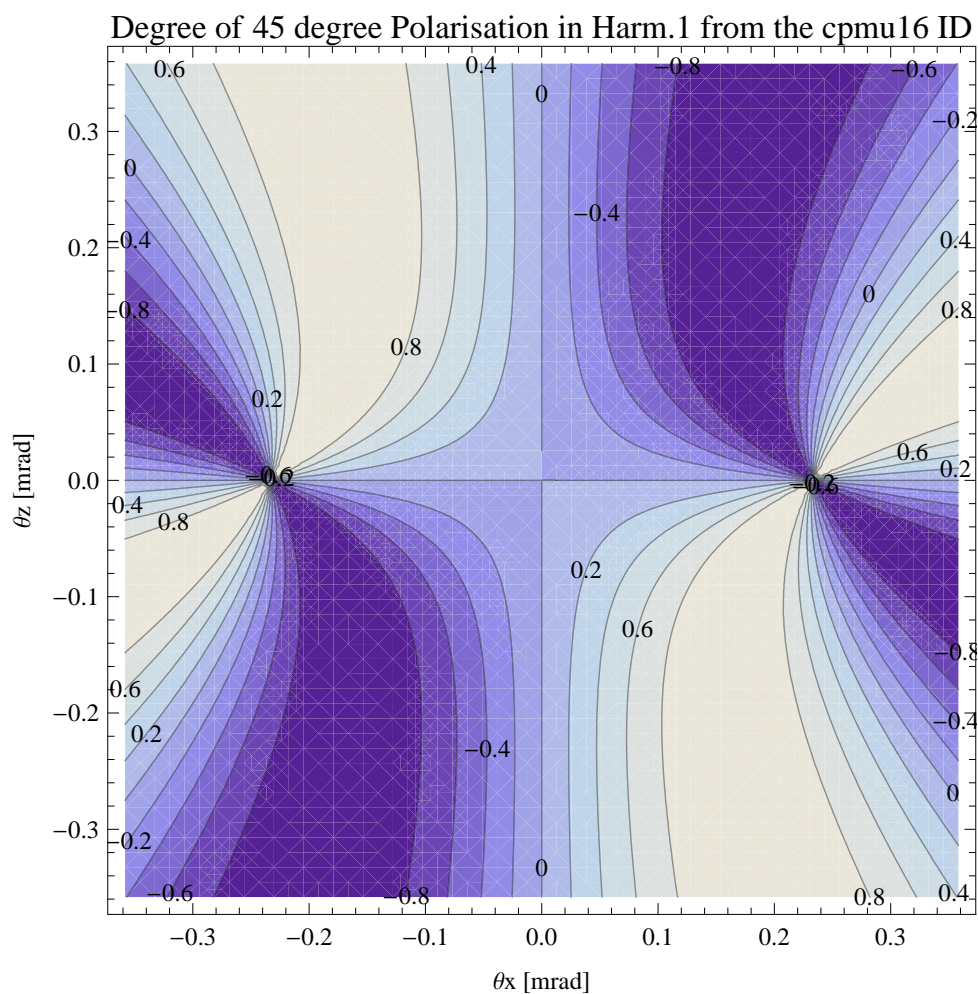


Figure 5.35: Map of 45 degree polarisation in the fundamental harmonic of the synchrotron radiation emitted by the cpmu16 ID

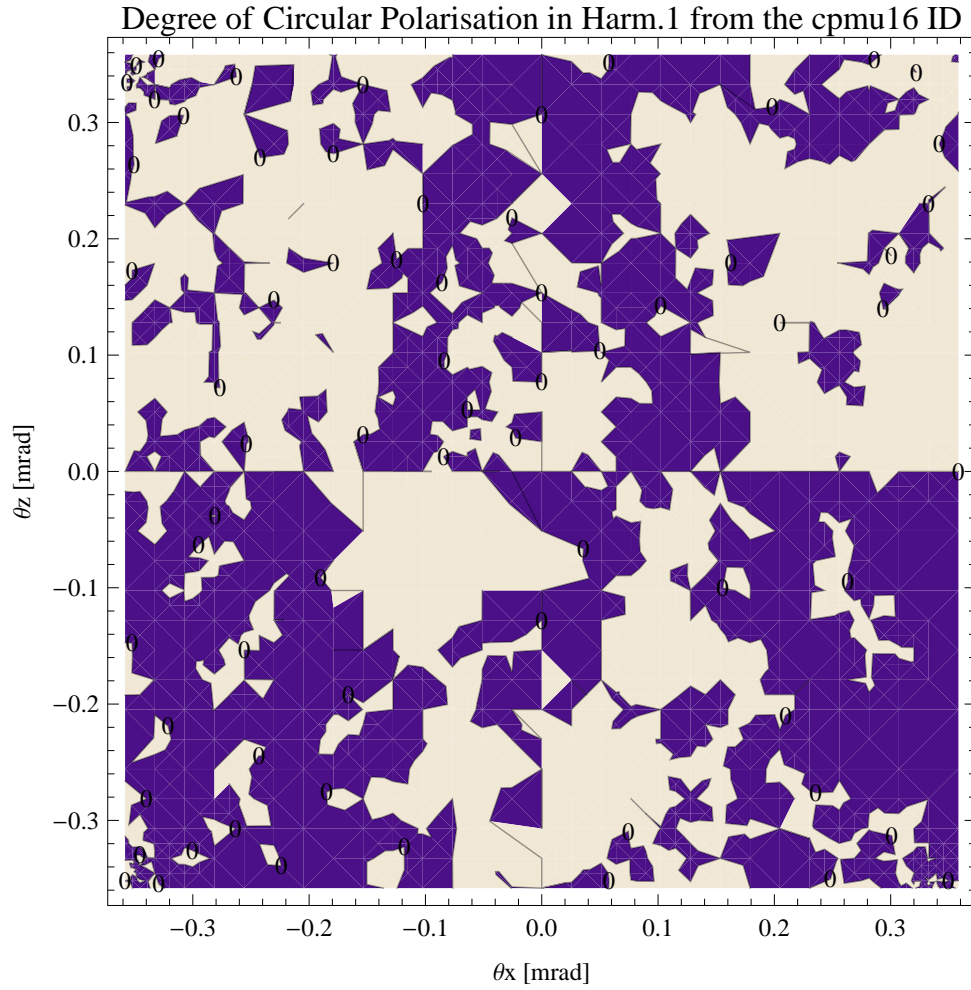


Figure 5.36: Map of circular polarisation in the fundamental harmonic of the synchrotron radiation emitted by the cpmu16 ID

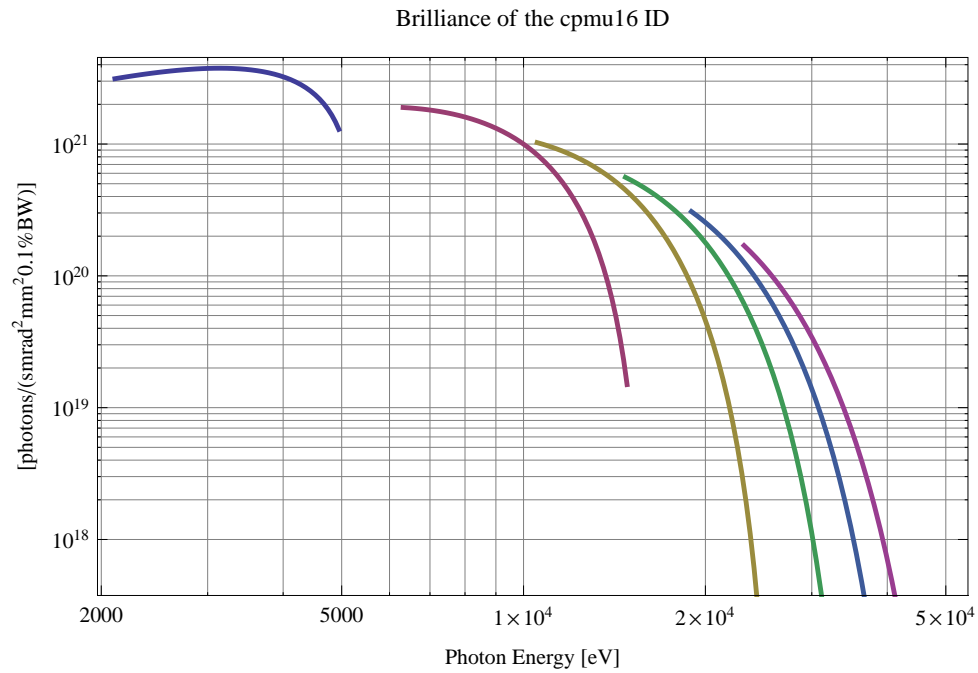


Figure 5.37: The brilliance at peak energy from the cpmu16 ID

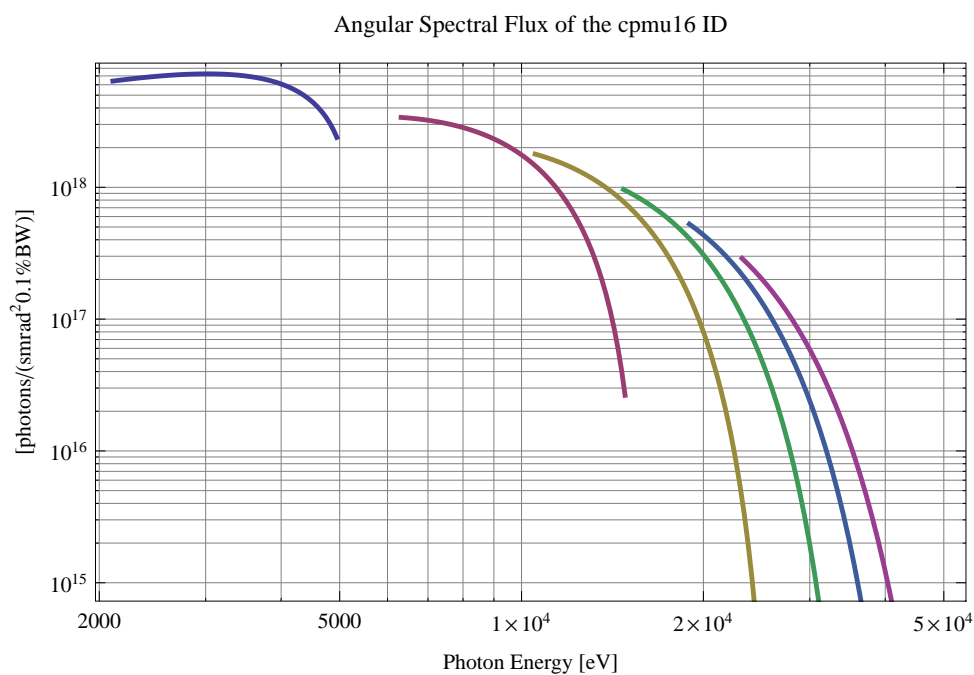


Figure 5.38: The angular spectral flux from the cpmu16 ID

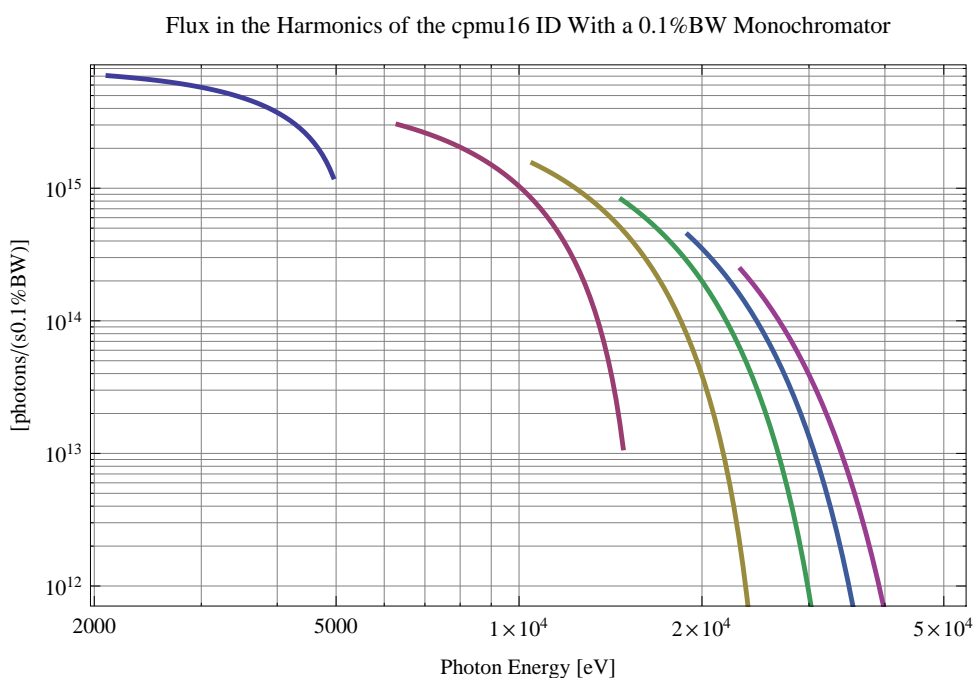


Figure 5.39: The flux of photons in the harmonics from the cpmu16 ID using a 0.1%BW monochromator

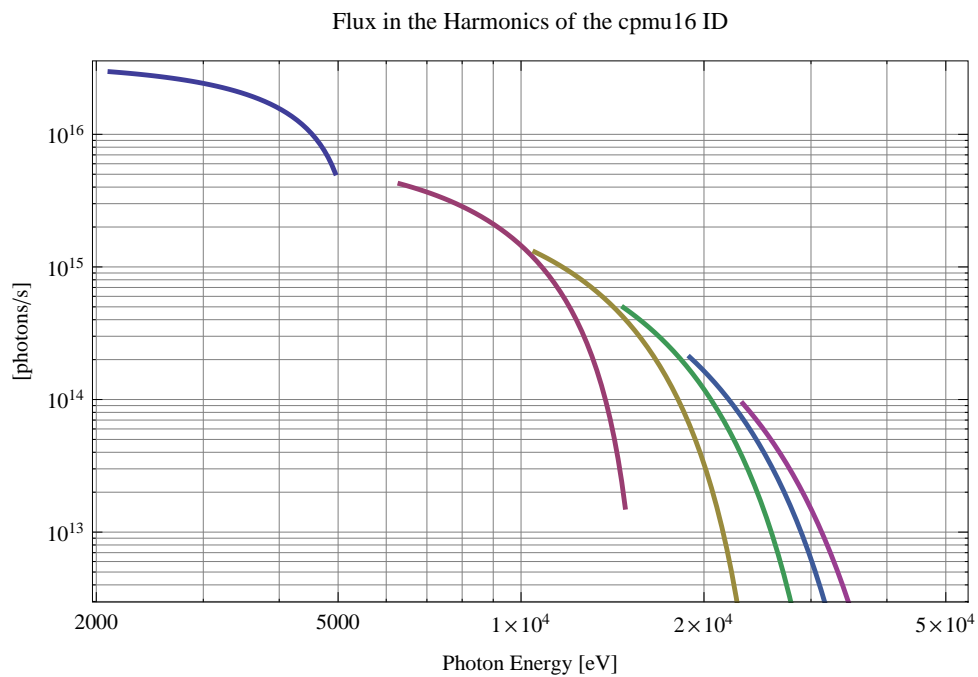


Figure 5.40: The flux of photons in the harmonics from the cpmu16 ID

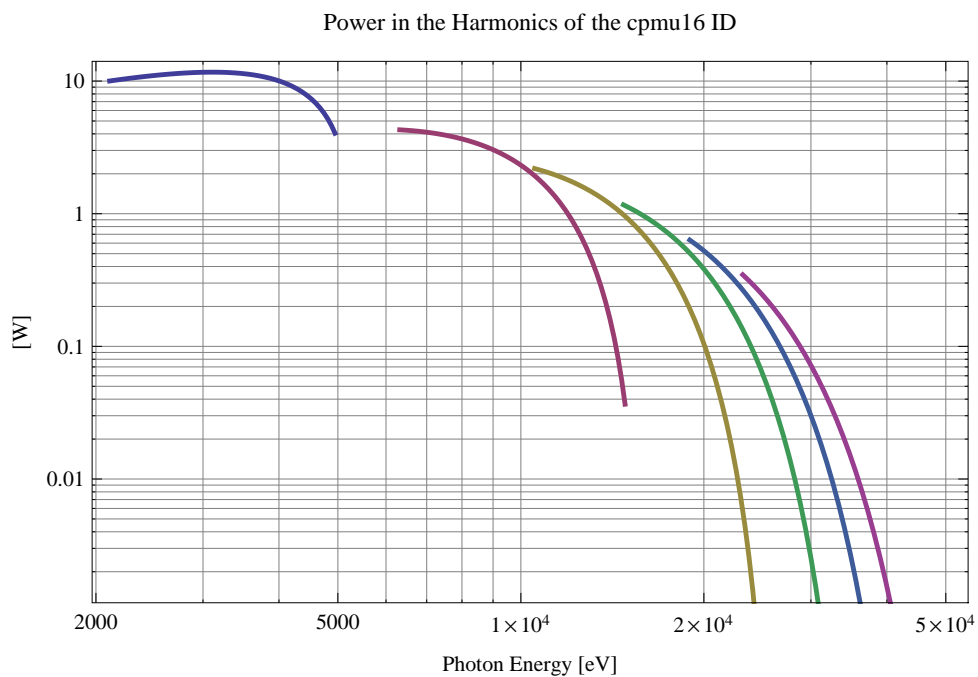


Figure 5.41: The power in the harmonics from the cpmu16 ID

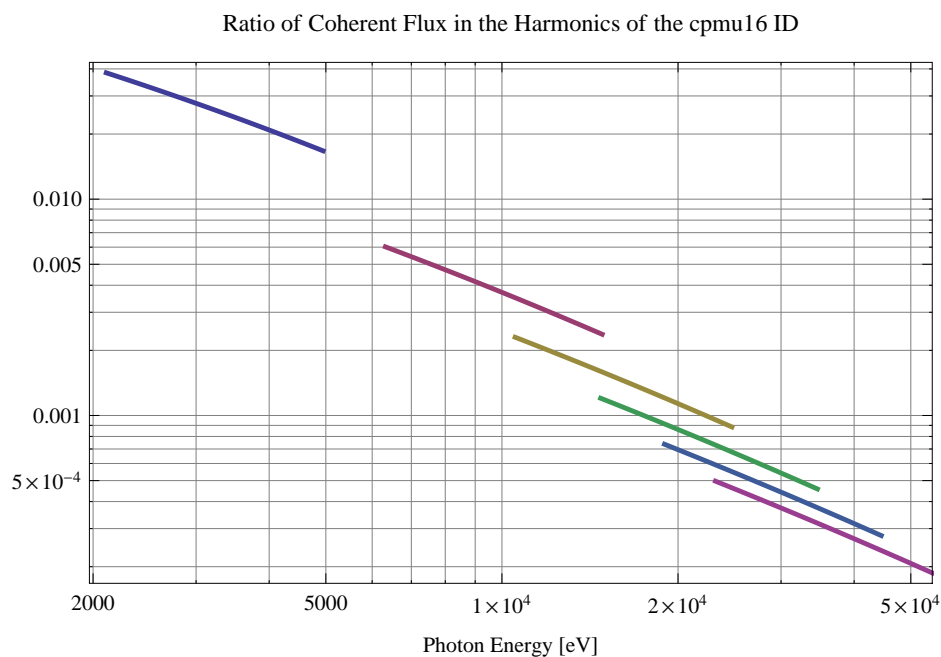


Figure 5.42: The ratio of coherent flux in the harmonics from the cpmu16 ID

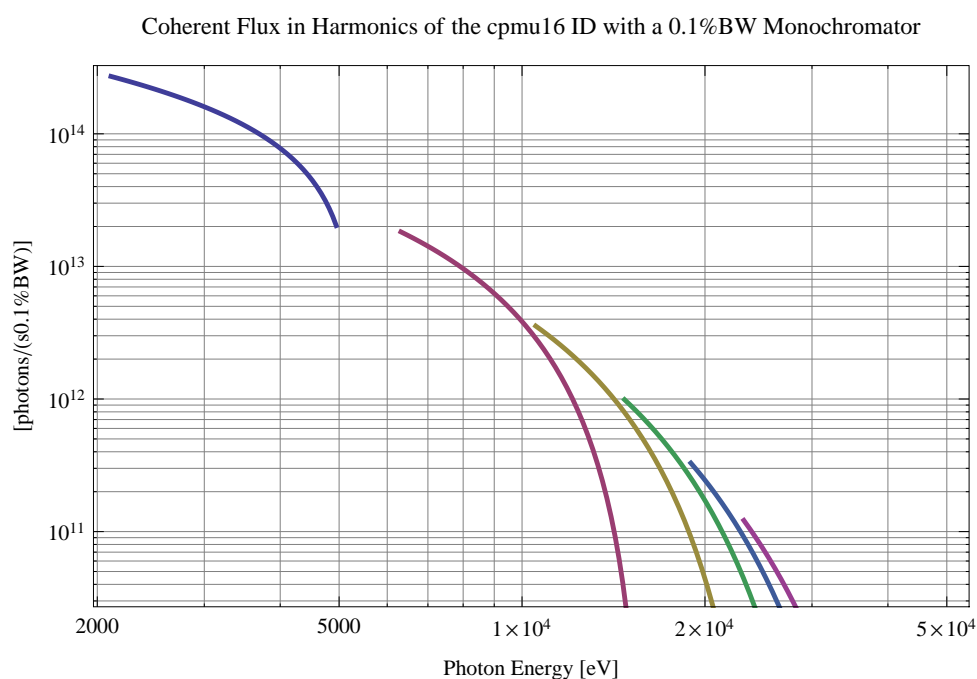


Figure 5.43: The coherent flux in the harmonics of the cpmu16 ID using a 0.1%BW Monochromator

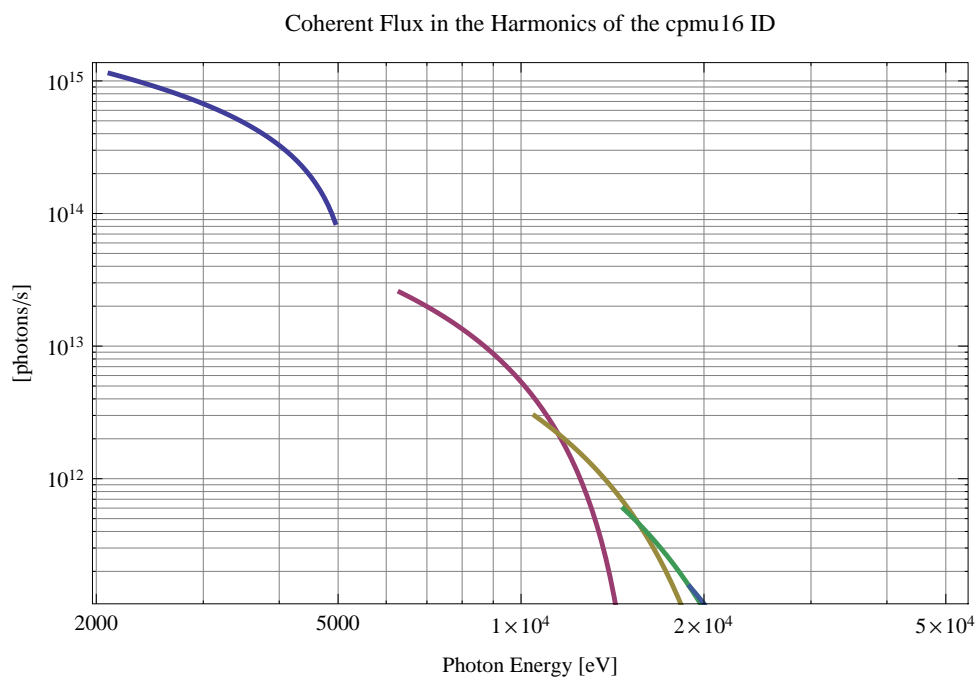


Figure 5.44: The coherent flux in the harmonics of the cpmu16 ID

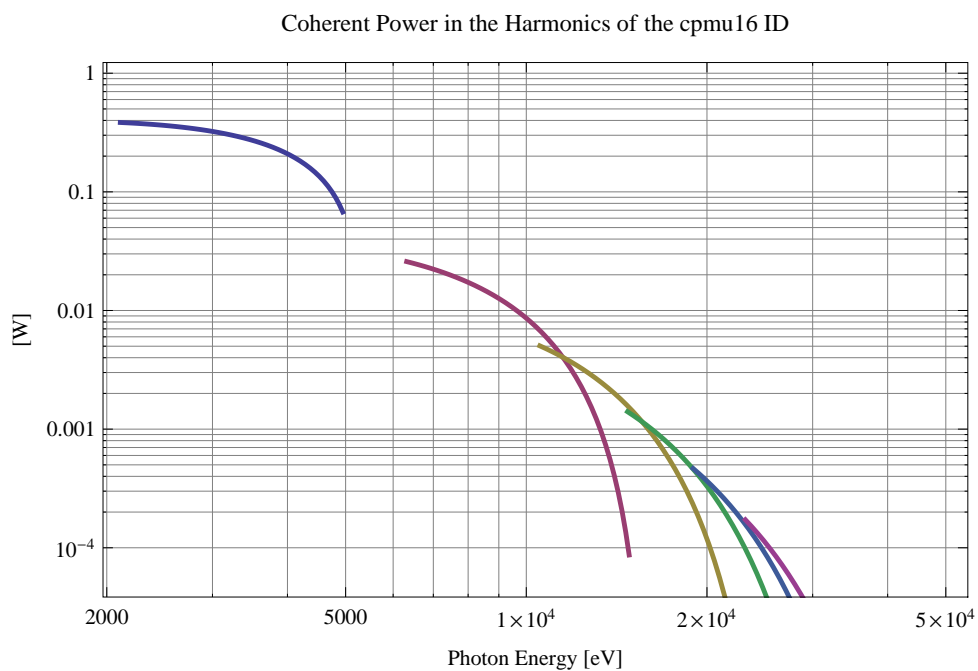


Figure 5.45: The power of coherent synchrotron radiation in the harmonics of the cpmu16 ID



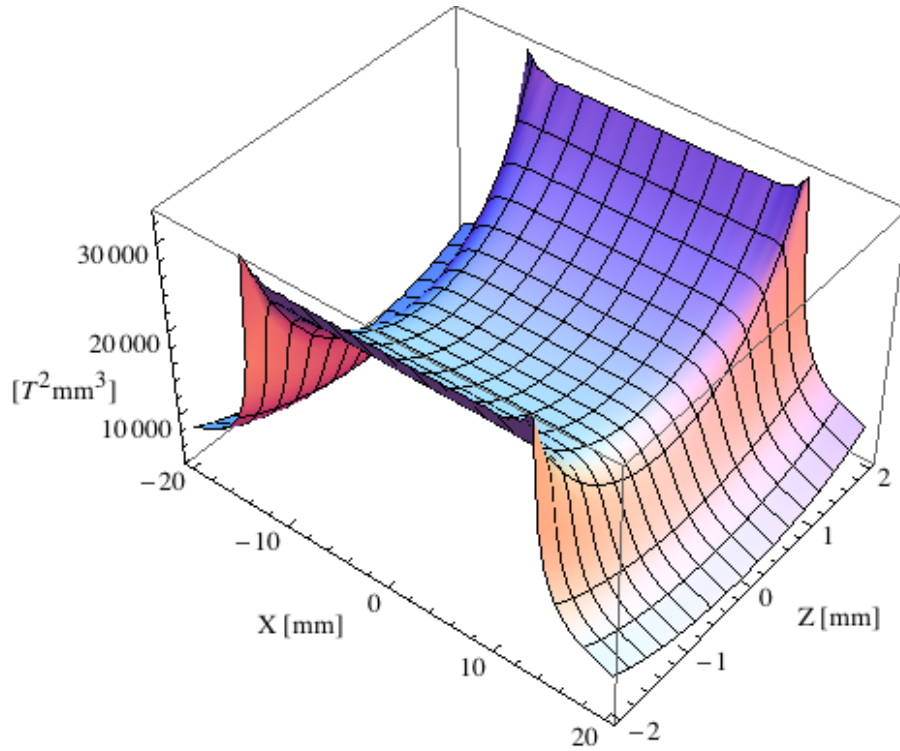


Figure 5.46: Focusing potential from the cpmu16 ID over the beam stay clear aperture.

### Influence from the cpmu16 ID on the optics of the stored beam

Figure 5.46 shows the focusing potential from the cpmu16 over the beam stay clear aperture of the ring aperture.

Figure 5.47 shows the kick map in the beam energy independant unit  $T^2 m^2$  of the kicks induced by the cpmu16 ID over the beam stay clear aperture.

Figure 5.48 shows the induced angular kick on the stored beam from the cpmu16 ID as a function of the vertical distance to the axis of the ID.

Figure 5.49 shows the induced angular kick on the stored beam from the cpmu16 ID as a function of the horizontal distance to the axis of the ID.

Figure 5.50 shows tune shift induced by the cpmu16 ID over the beam stay clear aperture. Note that the tune shift depends on the beam size at the ID.

Figure 5.51 shows the induced tune shift from the cpmu16 ID as a function of the vertical distance to the axis of the ID.

Figure 5.52 shows the induced tune shift from the cpmu16 ID as a function of the horizontal distance to the axis of the ID.

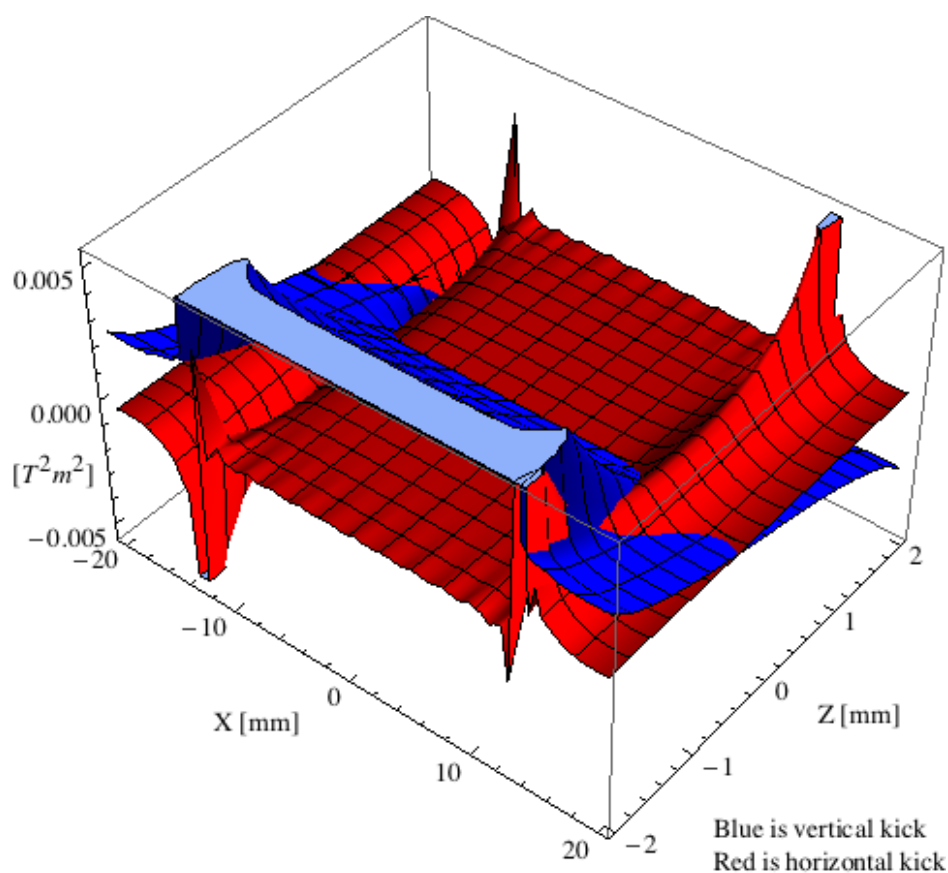


Figure 5.47: Kick map in the beam energy independent unit  $T^2m^2$  of the kicks induced by the cpmu16 ID over the beam stay clear aperture.

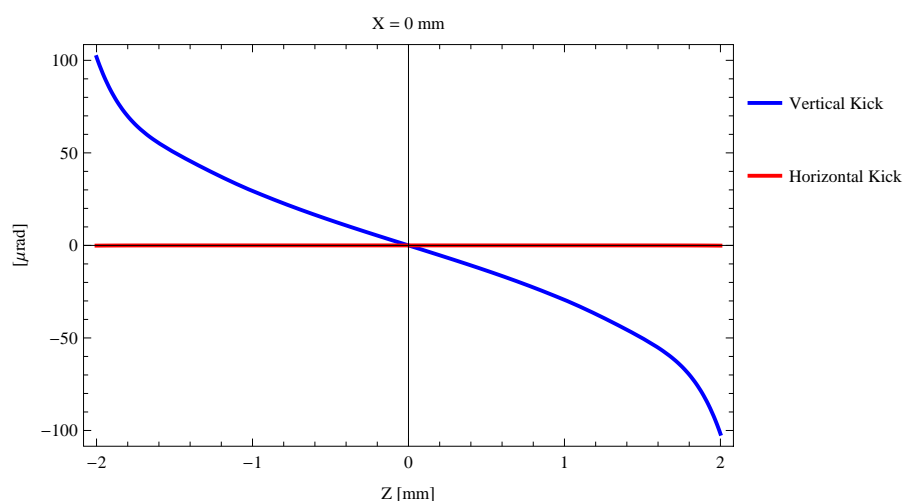


Figure 5.48: Induced angular kick on the stored beam from the cpmu16 ID as a function of the vertical distance to the ID axis.

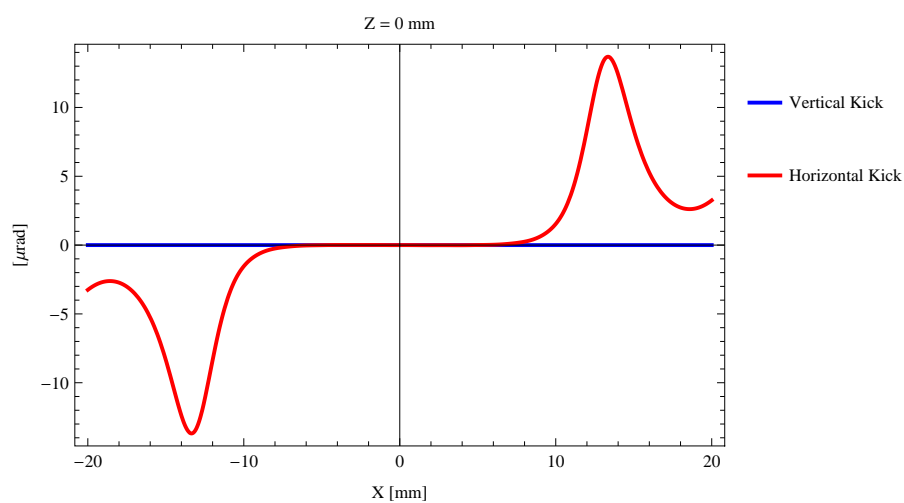


Figure 5.49: Induced angular kick on the stored beam from the cpmu16 ID as a function of the horizontal distance to the ID axis.

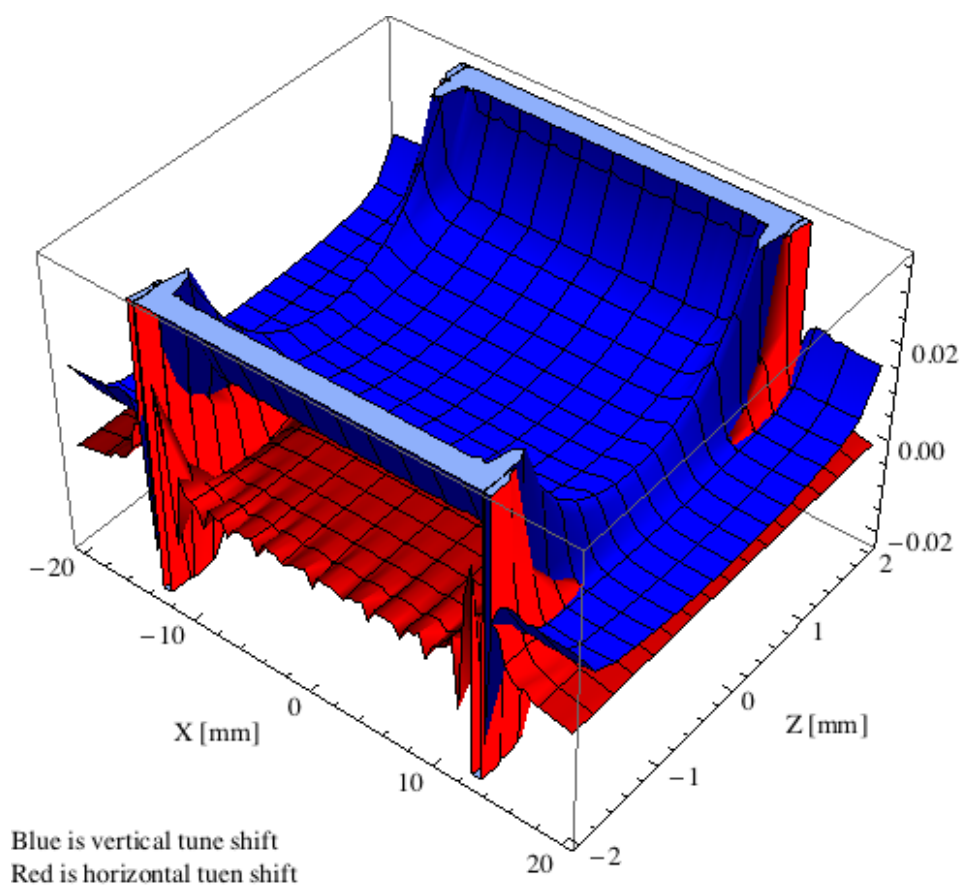


Figure 5.50: Tune shift induced by the cpmu16 ID over the beam stay clear aperture.

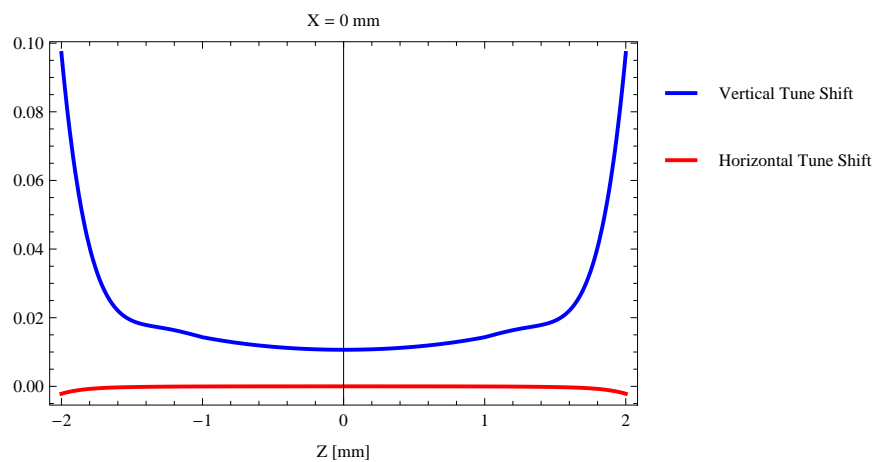


Figure 5.51: Induced tune shift from the cpmu16 ID as a function of the vertical distance to the axis of the ID.

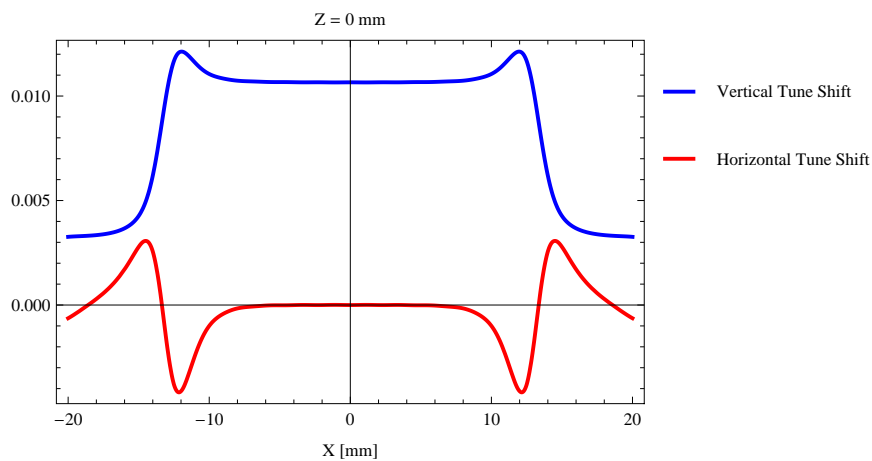


Figure 5.52: Induced tune shift from the cpmu16 ID on the stored beam from the ID as a function of the horizontal distance to the axis of the ID.

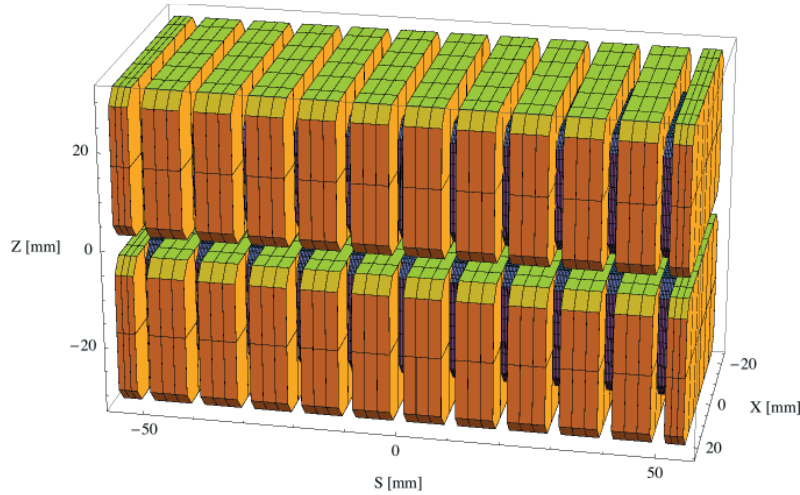


Figure 5.53: Magnetic model of the pmu20 ID. The magnet has been modelled with Radia [2].

### 5.3.3. The pmu20 ID

#### Magnet model of the pmu20 ID

The pmu20 is an in-vacuum undulator of hybrid type and the magnetic model of the pmu20 is shown in Figure 5.53. The magnet has been modelled with Radia [2]. The magnet blocks, which are yellow in Figure 5.53, are made of the magnetic material  $\text{Sm}_2\text{Co}_{17}$  with a magnetic remanence of 1.05 T at ambient temperature. The dimensions of the magnet blocks are  $50.00 \times 7.28 \times 30.00 \text{ mm}^3$  and there is a 4 mm chamfer at the corners of the magnet blocks. The poles, which are grey in Figure 5.53, are made of pure iron. The dimensions of the poles are  $32.00 \times 2.72 \times 24.00 \text{ mm}^3$  and there is a 3 mm chamfer at the corners of the poles.

#### Analysis of the magnetic field of the pmu20 ID

The vertical magnetic field in a central pole of the pmu20 ID along the ID axis,  $X = Z = 0$  is shown in Figure 5.54. The vertical magnetic field in a central pole of the pmu20 ID in the horizontally transverse direction to the ID axis,  $S = Z = 0$ , is shown in Figure 5.55.

A Fourier analysis of the magnetic field along the axis of the ID gives the higher harmonic contents in the magnetic field. A non-sinusoidal magnetic field profile along the ID would give a large higher harmonics contribution and it would no longer be possible to calculate the K-value of the ID from the peak field only. Also the higher harmonic contribution must be included to get the correct efficient magnetic field and efficient K-value. The higher harmonic contribution to the magnetic field is given in in Table 5.14.

A tranverse field roll-off may pose a problem to the storage ring since it gives a horizontal tune shift. The transverse field roll-off for the pmu20 for different horizontal positions out from the ID axis is shown in Figure 5.55 and numbers are given in Table 5.15.

The paremeters of the pmu20 are summarised in Table 5.16.

The critical energy of the emitted radiation will vary with the horizontal angle out from the axis of the ID as shown in Figure 5.56.

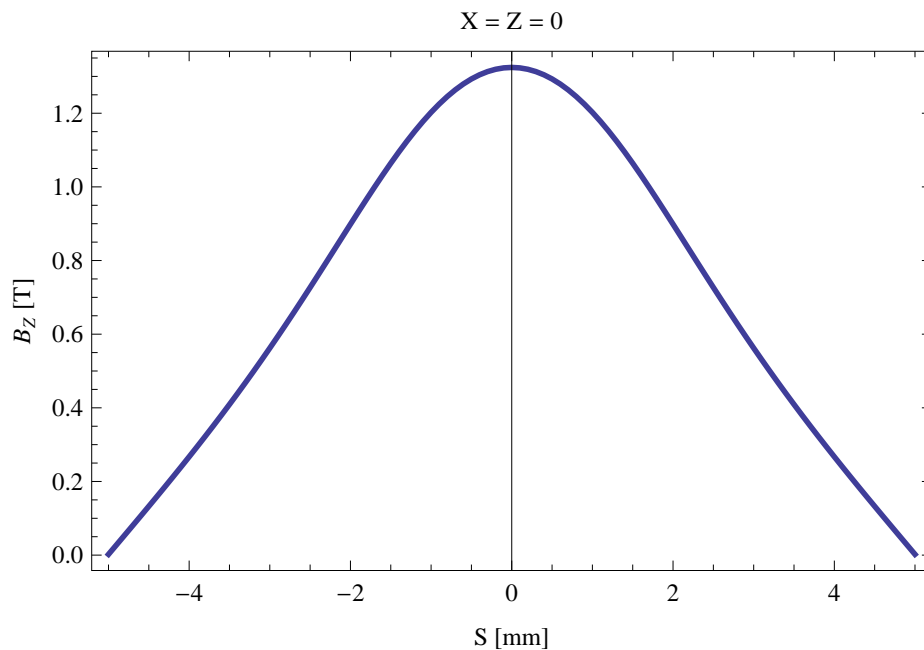


Figure 5.54: Vertical magnetic field in a central pole of the pmu20 ID along the ID axis,  $X = Z = 0$

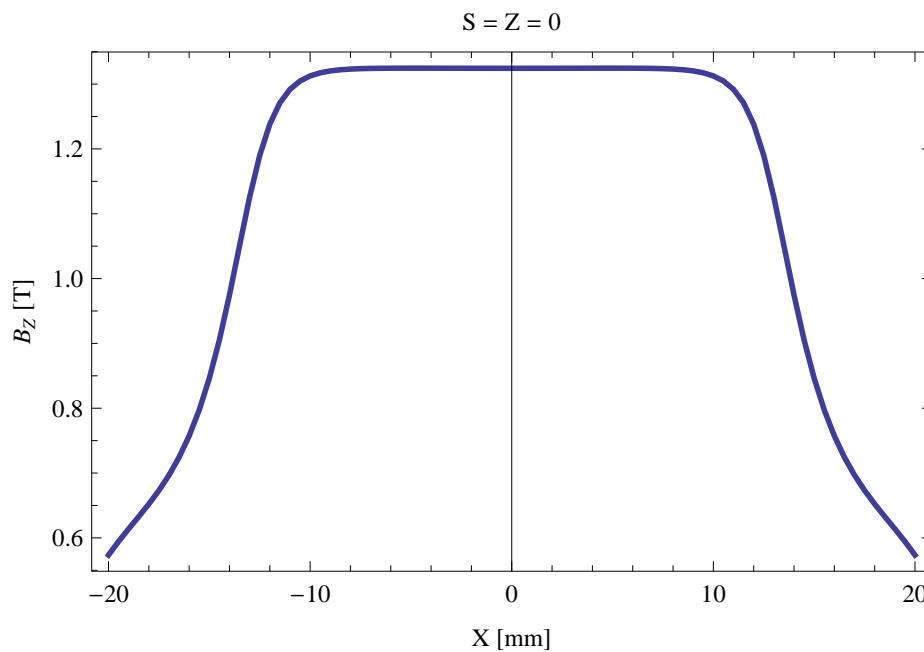


Figure 5.55: Vertical magnetic field in a central pole of the pmu20 ID along the horizontally transverse direction to the ID axis,  $S = Z = 0$

Table 5.14: Fourier Analysis of the magnetic field of the pmu20 ID

Term	Strength
Harm. Nr. 1	1.172 T
Harm. Nr. 3	0.135 T
Harm. Nr. 5	0.011 T
Harm. Nr. 7	-0.001 T
Harm. Nr. 9	-0.001 T
Harm. Nr. 11	-0.000 T

Table 5.15: Transverse field roll-off for the pmu20 ID

X-Position	$B_Z$ Field	Roll-off
$\pm 0$ mm	1.324 T	
$\pm 5$ mm	1.325 T	-0.01 %
$\pm 10$ mm	1.313 T	0.89 %
$\pm 15$ mm	0.846 T	36.11 %
$\pm 20$ mm	0.573 T	56.70 %

Table 5.16: Summary of the pmu20 ID parameters

Period	20.0	mm
Gap	4.2	mm
Peak Field	1.324	T
Effective Field	1.173	T
Peak k-value	2.474	
Effective k-value	2.191	
Higher Order Contr.	11.56	%
Maximum e-beam deflection	0.36	mrاد
Electron Beam Energy	3.0	GeV
Electron Beam Current	500	mA
Max Critical Energy	7.927	keV
Emitted Power	14.845	kW
Photon Energy, $n = 1$	1.257	keV
Total Length	3790.0	mm

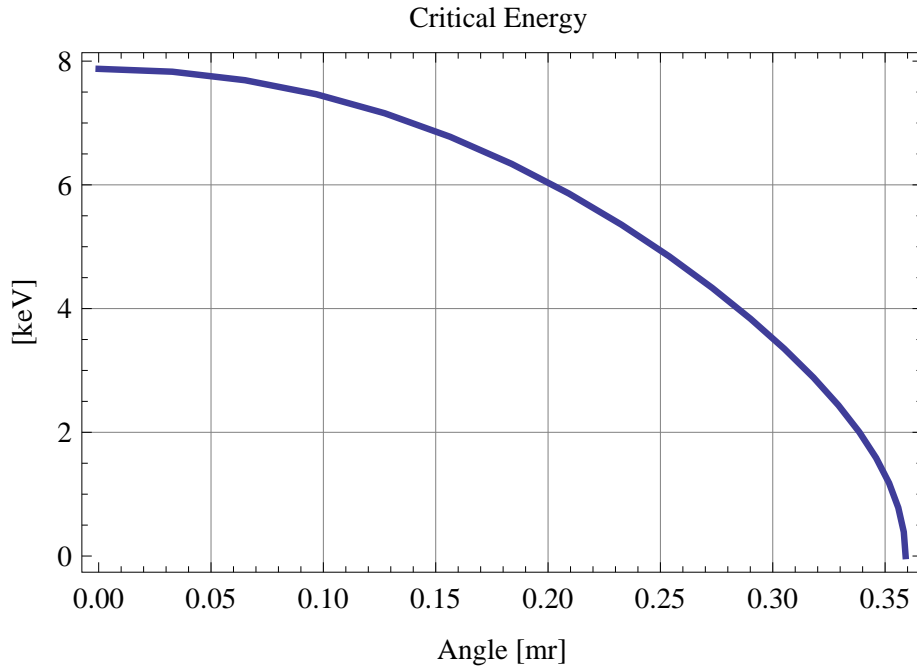


Figure 5.56: Variation of the critical energy with horizontal angle for the emitted synchrotron radiation from the pmu20 ID

### Synchrotron radiation from the pmu20 ID

The power map of the emitted synchrotron radiation by the pmu20 ID, assuming a 0.5 A filament beam with an energy of 3 GeV and undulator properties of the synchrotron radiation, is shown in Figure 5.57. The on-axis power density is 95.818 kW/mrad<sup>2</sup>

A map of the degree of linear polarisation of the fundamental harmonic of the synchrotron radiation emitted by the pmu20 ID over the angle of observation is shown in Figure 5.58.

A map of the degree of 45 degree polarisation of the fundamental harmonic of the synchrotron radiation emitted by the pmu20 ID over the angle of observation is shown in Figure 5.59.

A map of the degree of circular polarisation of the fundamental harmonic of the synchrotron radiation emitted by the pmu20 ID over the angle of observation is shown in Figure 5.60.

The on axis brilliance at peak energy, the angular spectral flux, the flux in the harmonics, the power in the harmonics, the ratio of coherence, the coherent flux in the harmonics, and the power of coherent radiation in the harmonics from the pmu20 ID have been calculated and the resulting plots are found in this section of the document. The beam parameters used for the calculation are 0.5 A of stored current,  $\beta_H = 9$  m,  $\varepsilon_H = 0.263$  nmrad,  $\beta_V = 4.8$  m,  $\varepsilon_V = 8$ . pmrad, and an energy spread of 0.001.

The brilliance at peak energy and the angular spectral flux density from the pmu20 ID for different harmonics at maximum K-value (2.191) are given in Table 5.17 and for minimum K-value (0.400) these values are given in Table 5.18.



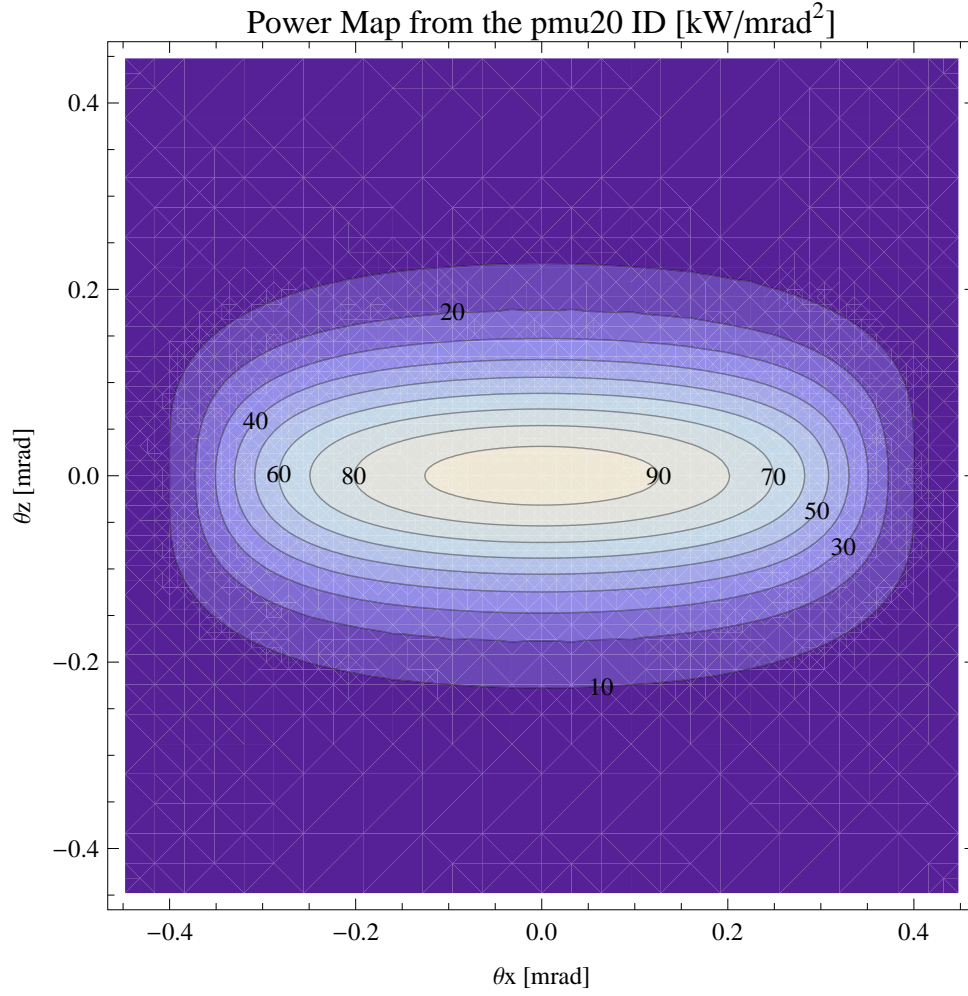


Figure 5.57: Map of the power distribution of the emitted synchrotron radiation by the pmu20 ID

Table 5.17: The brilliance at peak energy and the angular spectral flux density from the pmu20 ID for different harmonics at maximum K-value (2.191)

Harmonic	Photon Energy [eV]	Brilliance [Ph./s/mrad <sup>2</sup> /mrad <sup>2</sup> /0.1%BW]	Angular Spectral Flux [Ph./s/mrad <sup>2</sup> /0.1%BW]
1	1256.75	$1.66 \times 10^{21}$	$3.8 \times 10^{18}$
3	3770.25	$1.4 \times 10^{21}$	$2.63 \times 10^{18}$
5	6283.74	$9.69 \times 10^{20}$	$1.73 \times 10^{18}$
7	8797.24	$6.67 \times 10^{20}$	$1.17 \times 10^{18}$
9	11310.7	$4.62 \times 10^{20}$	$7.98 \times 10^{17}$
11	13824.2	$3.21 \times 10^{20}$	$5.5 \times 10^{17}$

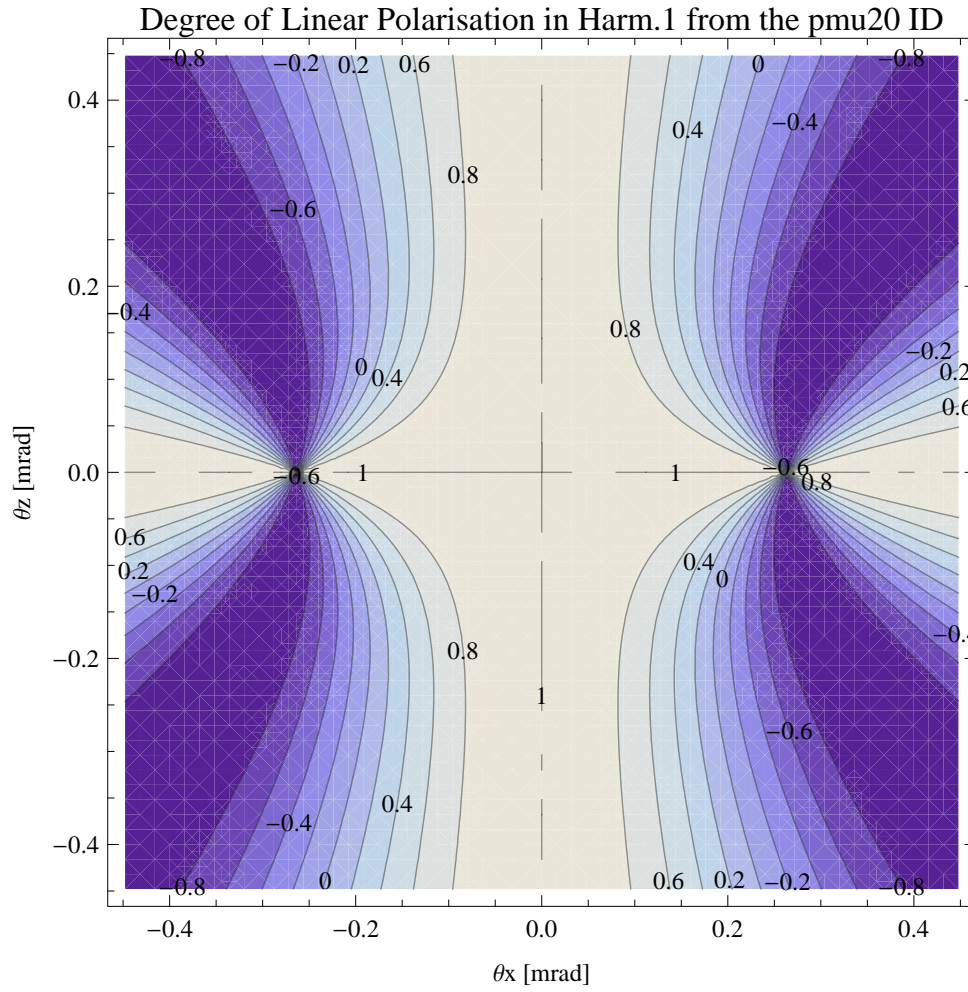


Figure 5.58: Map of linear polarisation in the fundamental harmonic of the synchrotron radiation emitted by the pmu20 ID

Table 5.18: The brilliance at peak energy and the angular spectral flux density from the pmu20 ID for different harmonics at minimum K-value (0.4)

Harmonic	Photon Energy [eV]	Brilliance [Ph./s/mrad <sup>2</sup> /mrad <sup>2</sup> /0.1%BW]	Angular Spectral Flux [Ph./s/mrad <sup>2</sup> /0.1%BW]
1	3956.83	$9.28 \times 10^{20}$	$1.75 \times 10^{18}$
3	11870.5	$1.17 \times 10^{19}$	$2.07 \times 10^{16}$
5	19784.2	$1.2 \times 10^{17}$	$2.12 \times 10^{14}$
7	27697.8	$1.22 \times 10^{15}$	$2.14 \times 10^{12}$
9	35611.5	$1.24 \times 10^{13}$	$2.17 \times 10^{10}$
11	43525.2	$1.25 \times 10^{11}$	$2.19 \times 10^8$

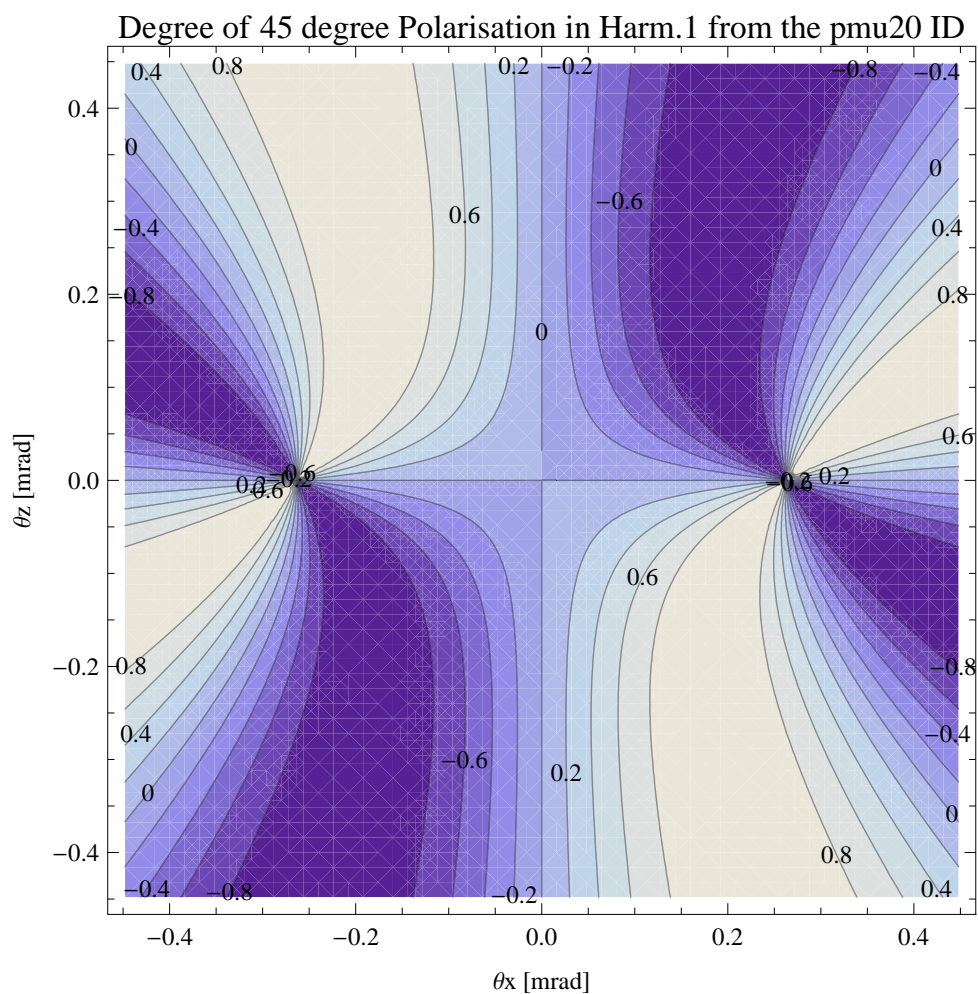


Figure 5.59: Map of 45 degree polarisation in the fundamental harmonic of the synchrotron radiation emitted by the pmu20 ID

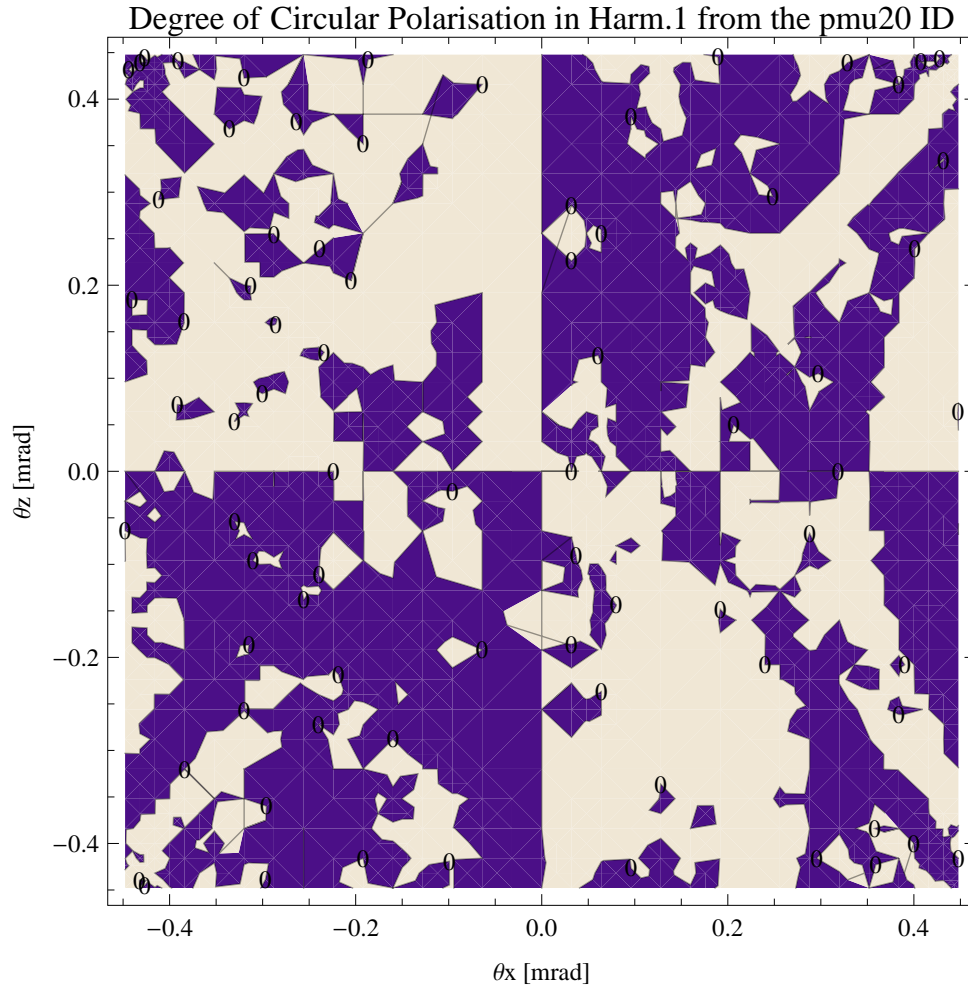


Figure 5.60: Map of circular polarisation in the fundamental harmonic of the synchrotron radiation emitted by the pmu20 ID

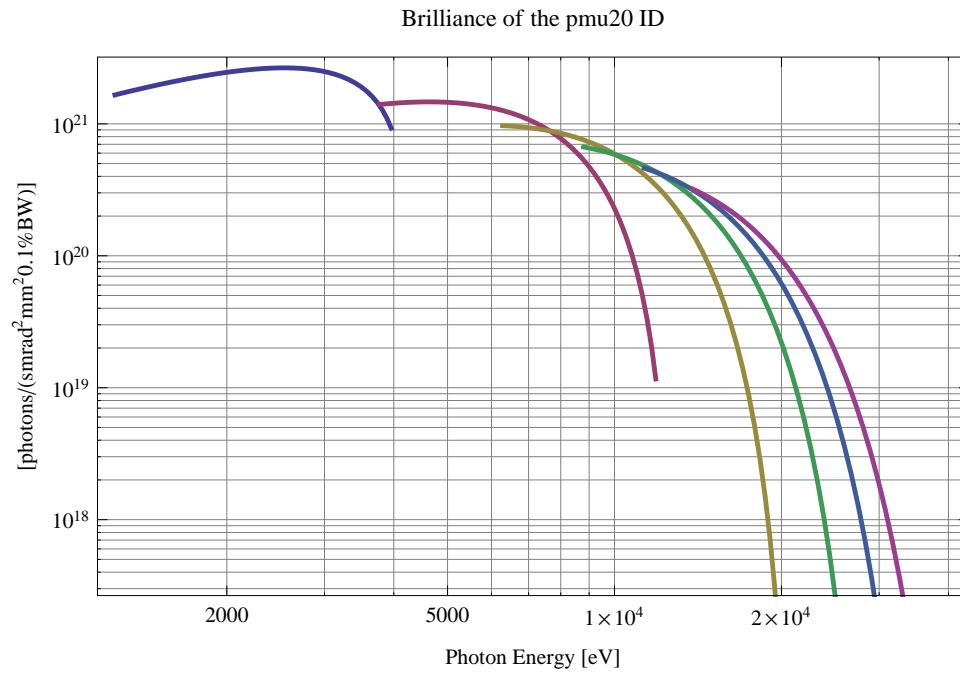


Figure 5.61: The brilliance at peak energy from the pmu20 ID

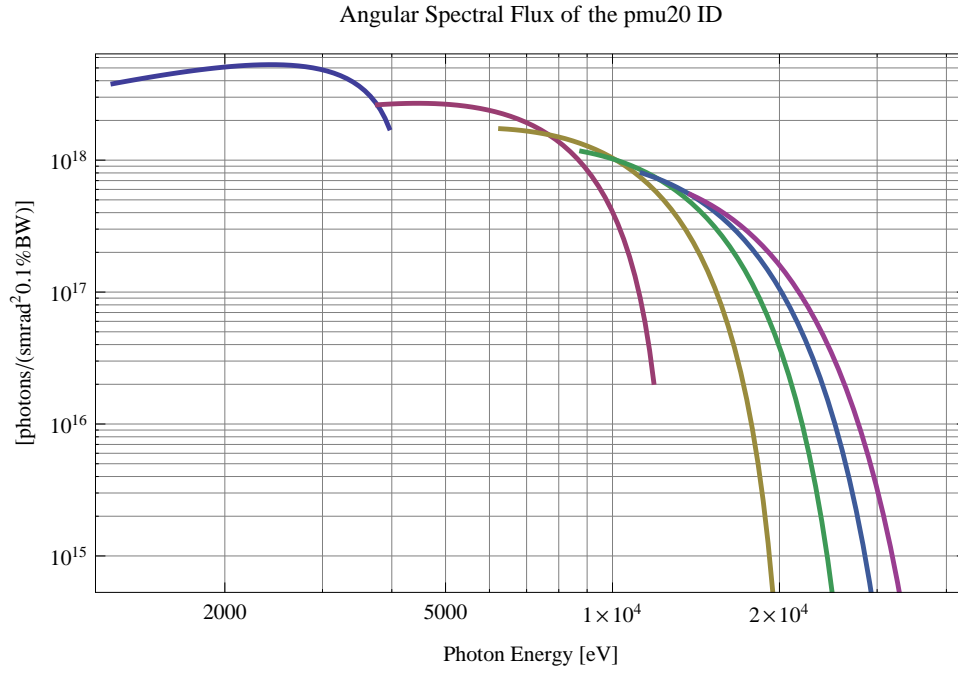


Figure 5.62: The angular spectral flux from the pmu20 ID

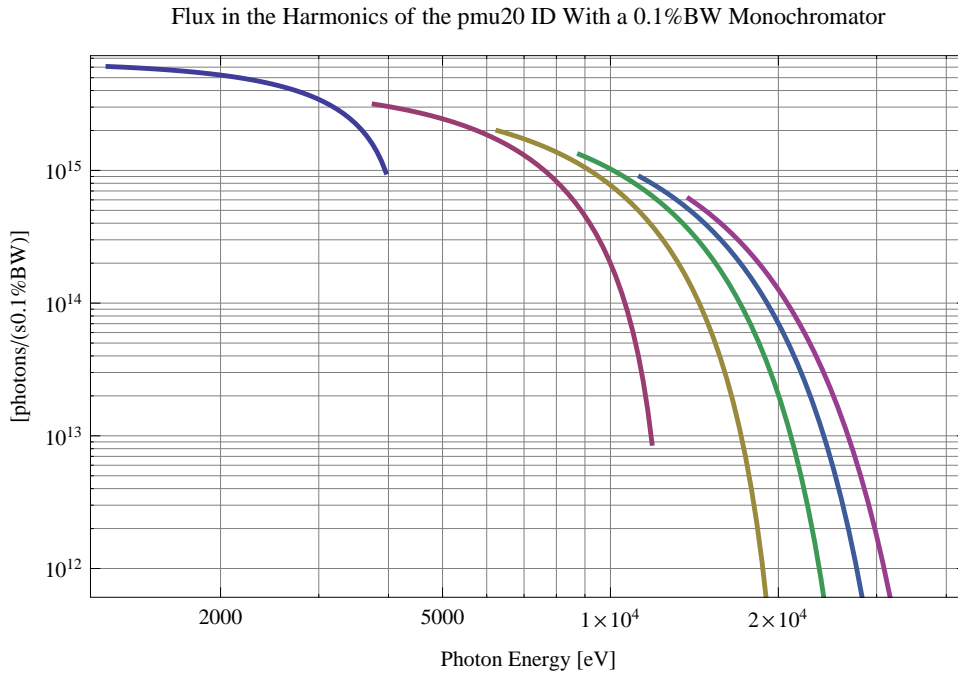


Figure 5.63: The flux of photons in the harmonics from the pmu20 ID using a 0.1%BW monochromator

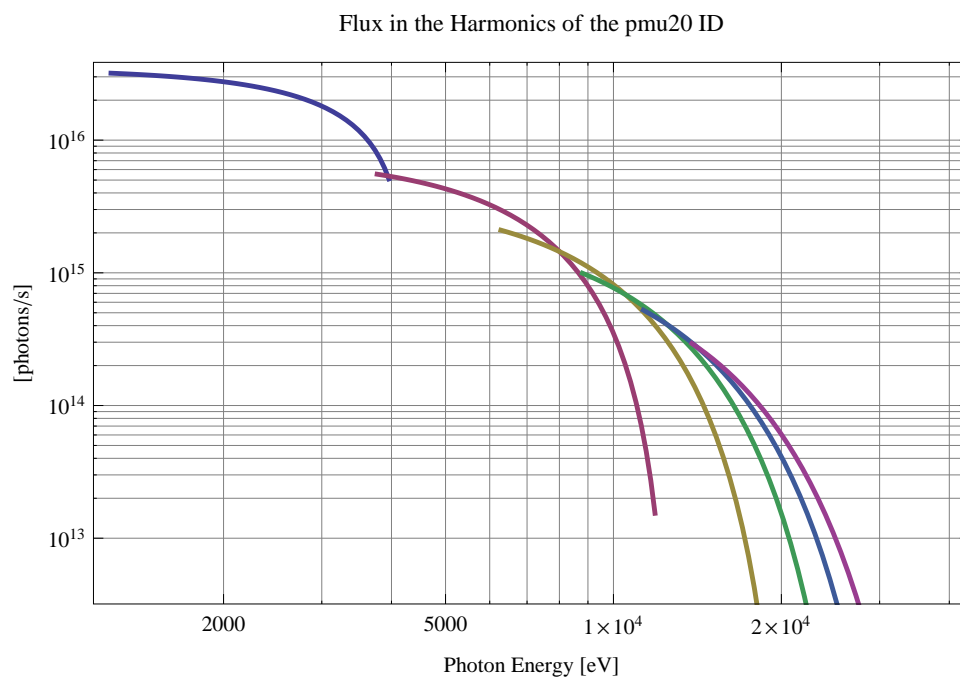


Figure 5.64: The flux of photons in the harmonics from the pmu20 ID

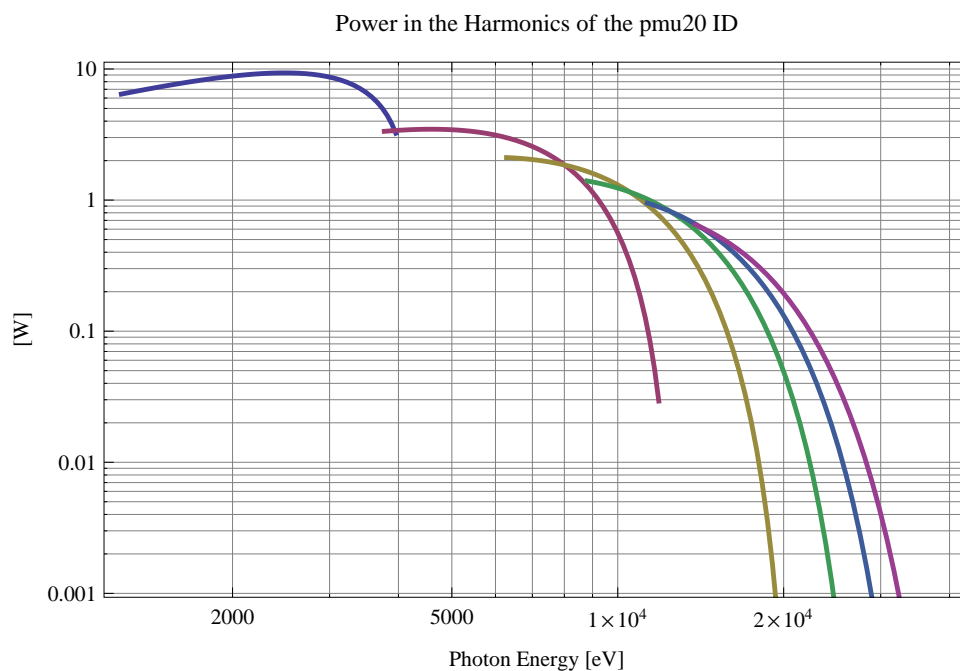


Figure 5.65: The power in the harmonics from the pmu20 ID

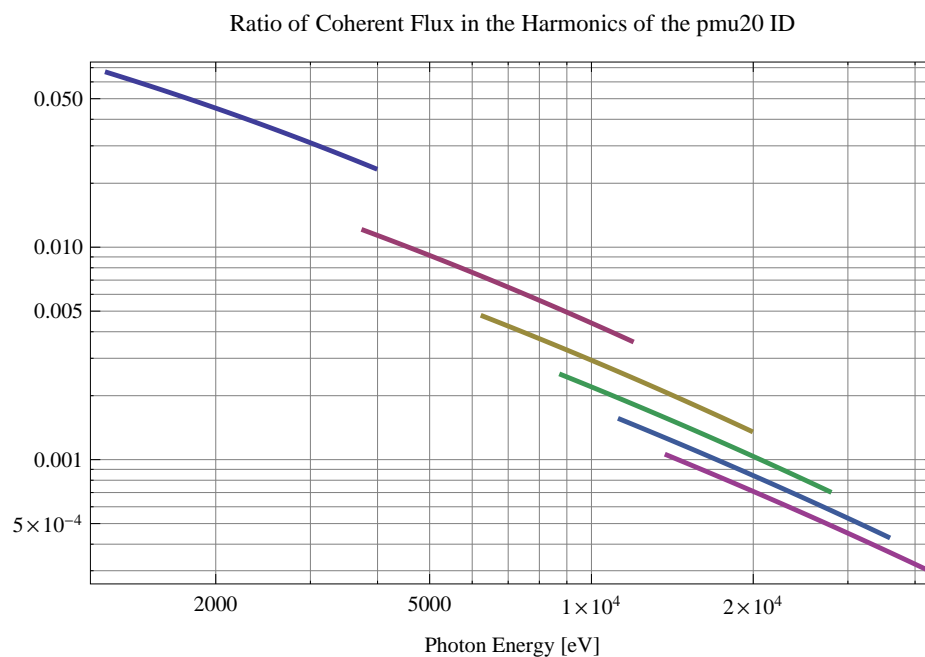


Figure 5.66: The ratio of coherent flux in the harmonics from the pmu20 ID

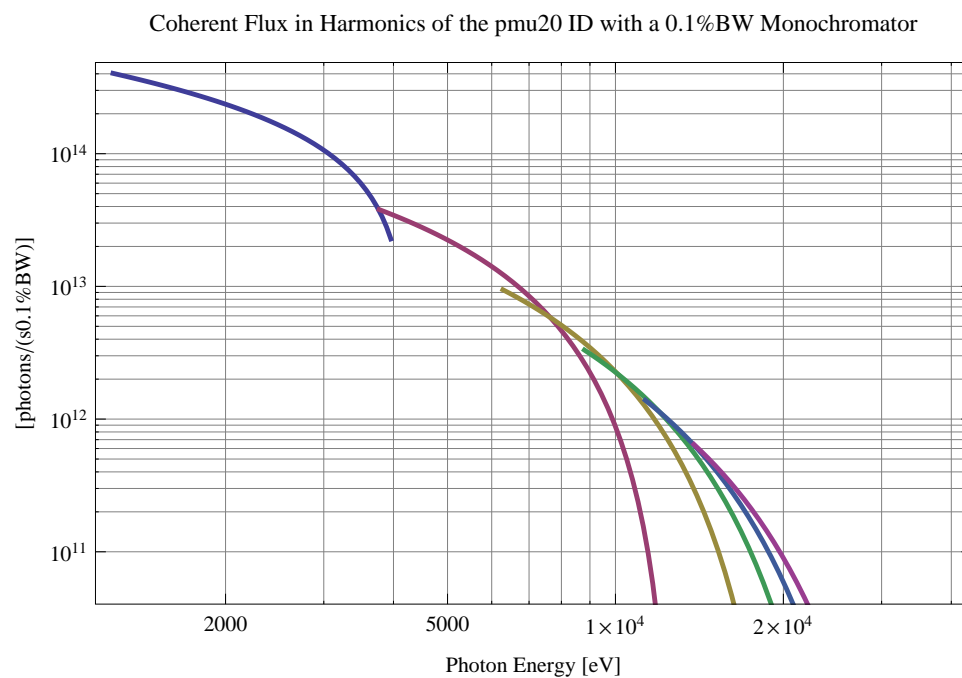


Figure 5.67: The coherent flux in the harmonics of the pmu20 ID using a 0.1%BW Monochromator

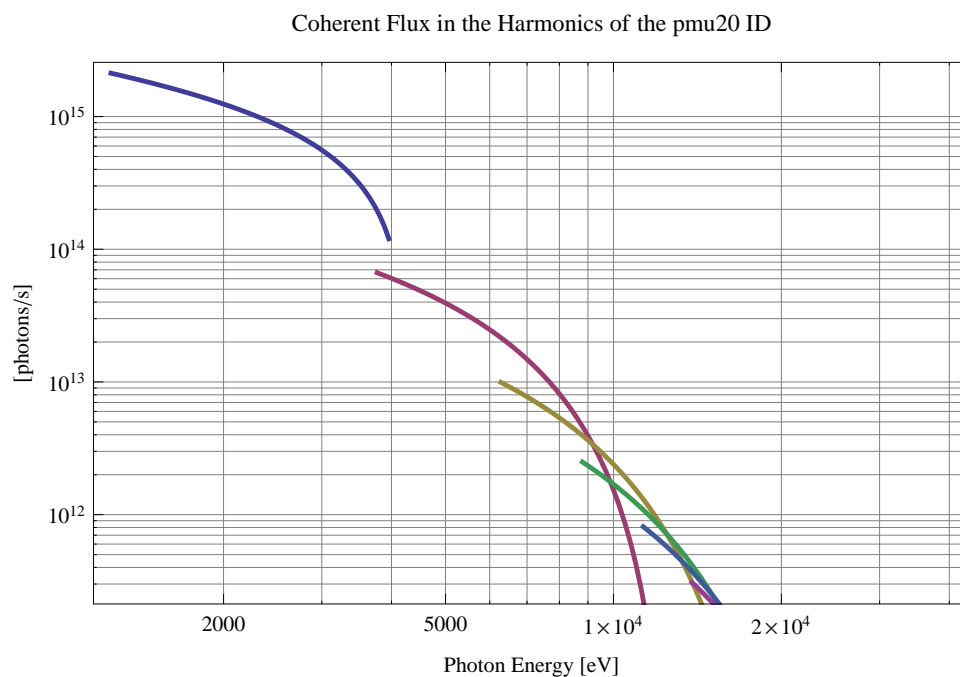


Figure 5.68: The coherent flux in the harmonics of the pmu20 ID

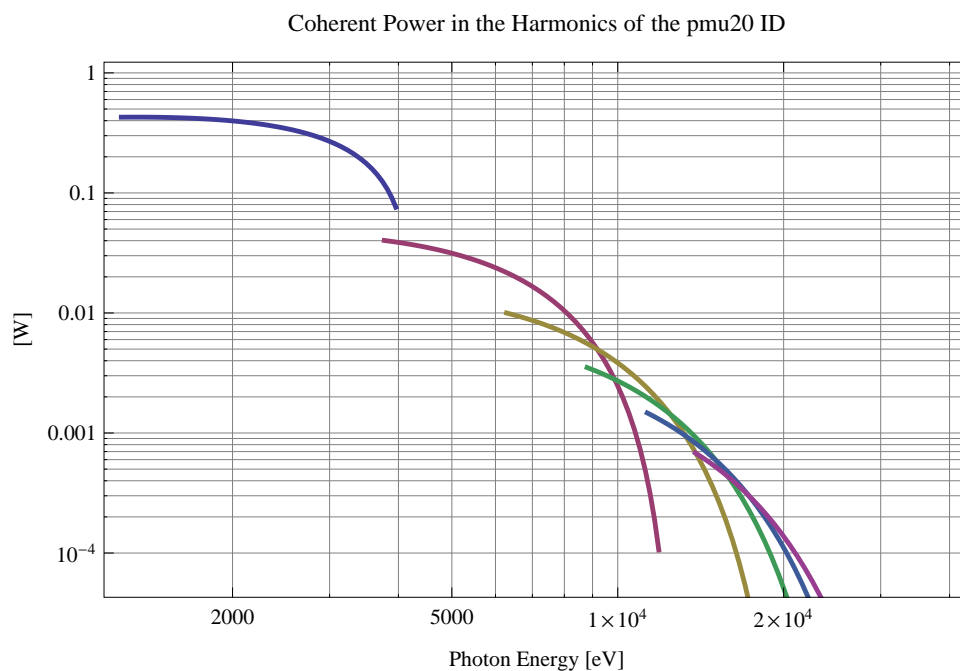


Figure 5.69: The power of coherent synchrotron radiation in the harmonics of the pmu20 ID



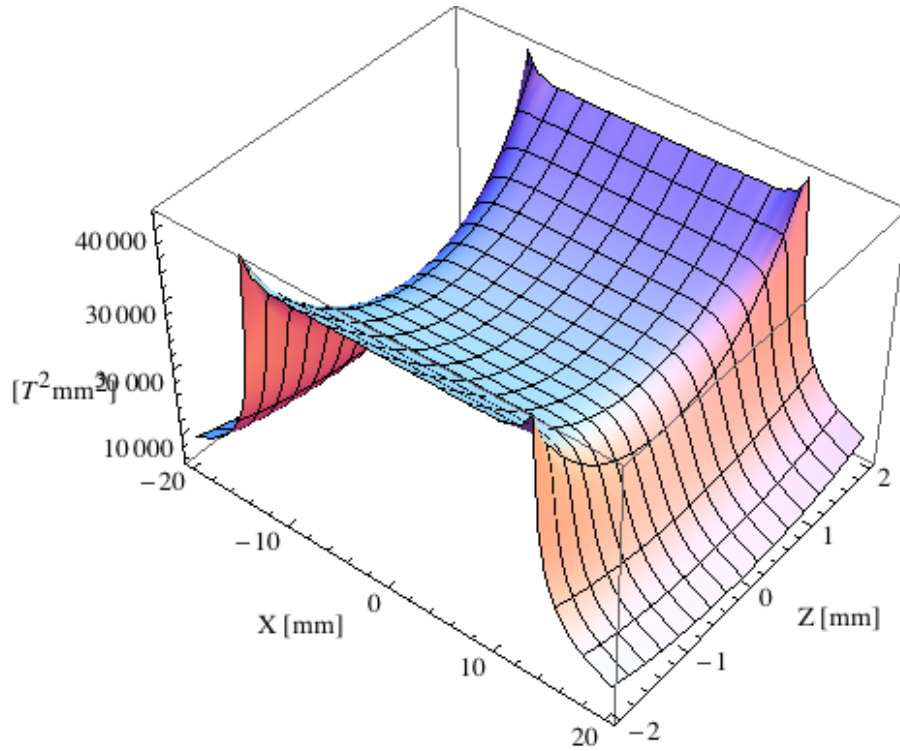


Figure 5.70: Focusing potential from the pmu20 ID over the beam stay clear aperture.

### Influence from the pmu20 ID on the optics of the stored beam

Figure 5.70 shows the focusing potential from the pmu20 over the beam stay clear aperture of the ring aperture.

Figure 5.71 shows the kick map in the beam energy independent unit  $T^2 m^2$  of the kicks induced by the pmu20 ID over the beam stay clear aperture.

Figure 5.72 shows the induced angular kick on the stored beam from the pmu20 ID as a function of the vertical distance to the axis of the ID.

Figure 5.73 shows the induced angular kick on the stored beam from the pmu20 ID as a function of the horizontal distance to the axis of the ID.

Figure 5.74 shows tune shift induced by the pmu20 ID over the beam stay clear aperture. Note that the tune shift depends on the beam size at the ID.

Figure 5.75 shows the induced tune shift from the pmu20 ID as a function of the vertical distance to the axis of the ID.

Figure 5.76 shows the induced tune shift from the pmu20 ID as a function of the horizontal distance to the axis of the ID.

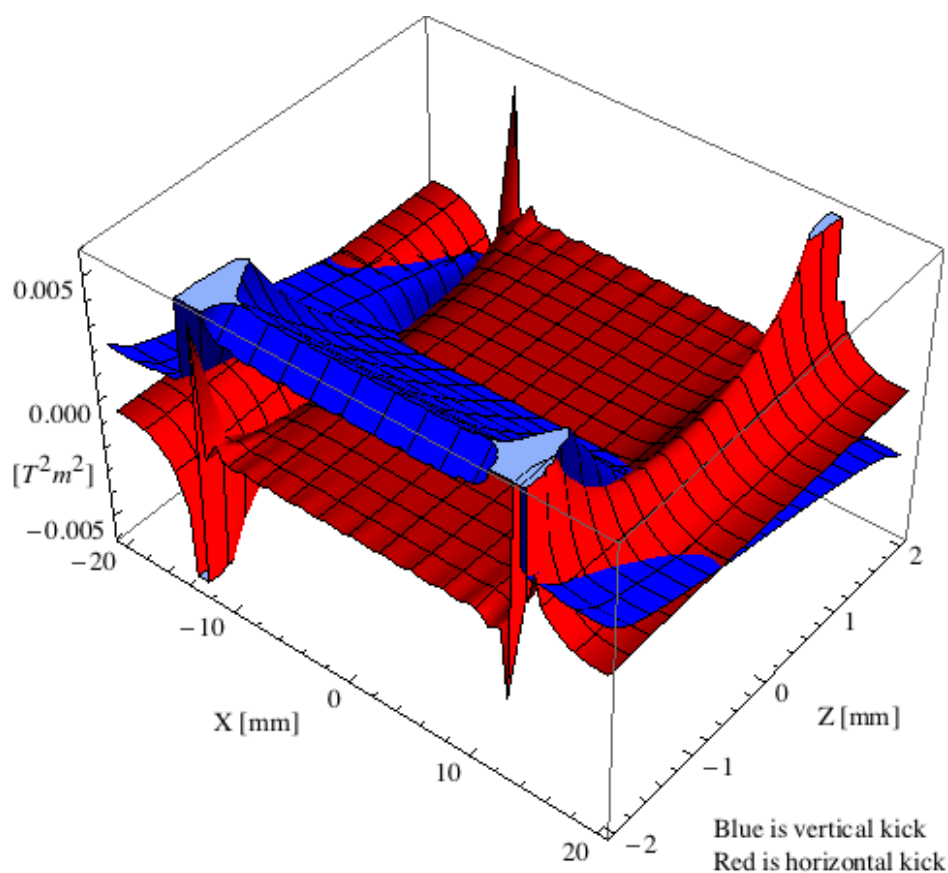


Figure 5.71: Kick map in the beam energy independent unit  $T^2m^2$  of the kicks induced by the pmu20 ID over the beam stay clear aperture.

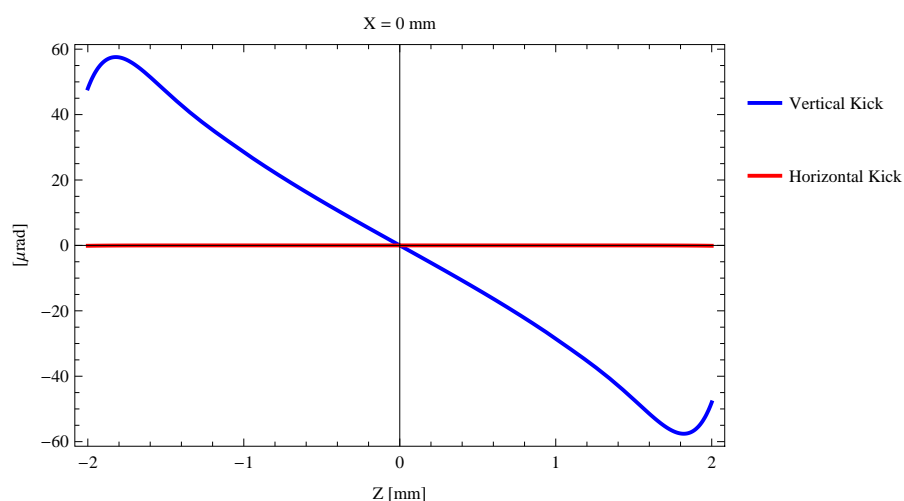


Figure 5.72: Induced angular kick on the stored beam from the pmu20 ID as a function of the vertical distance to the ID axis.

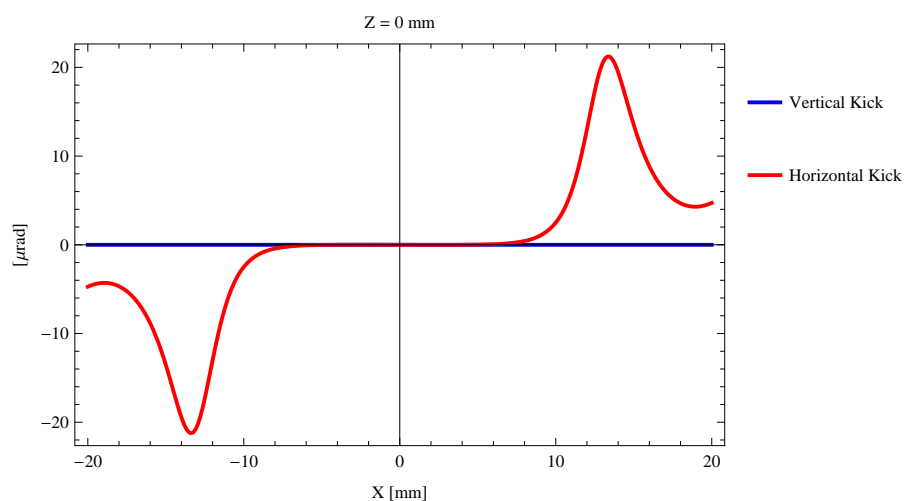


Figure 5.73: Induced angular kick on the stored beam from the pmu20 ID as a function of the horizontal distance to the ID axis.

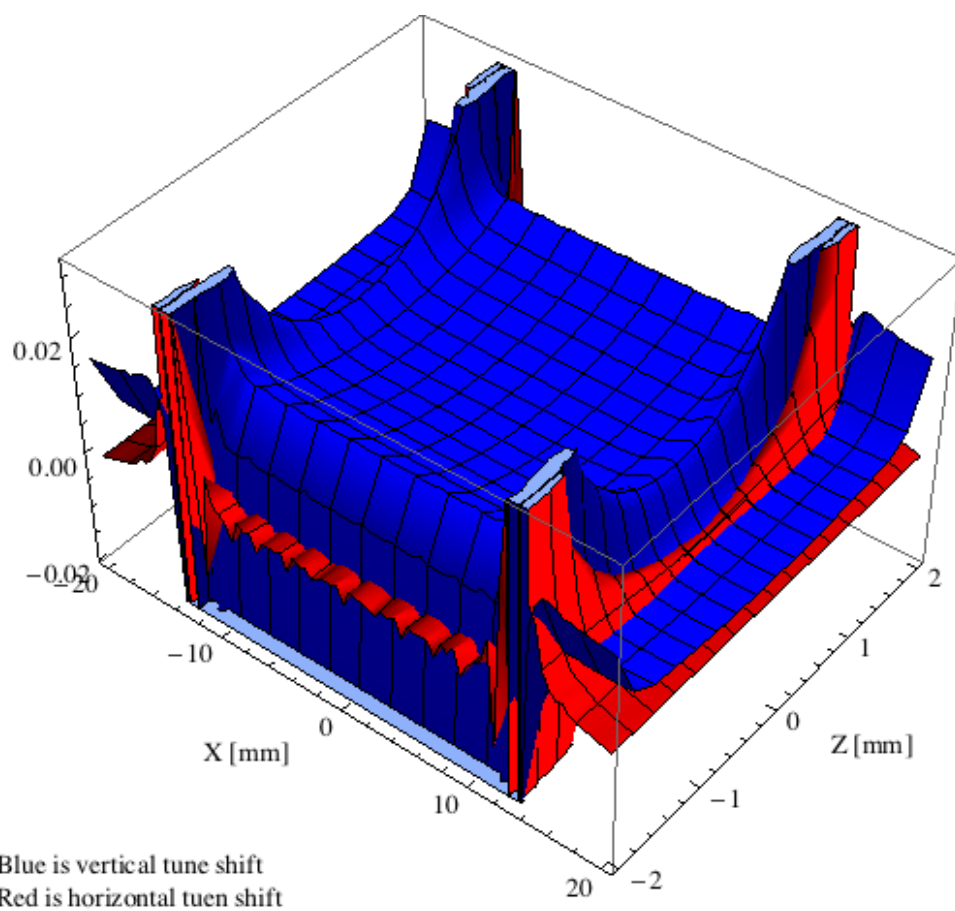


Figure 5.74: Tune shift induced by the pmu20 ID over the beam stay clear aperture.

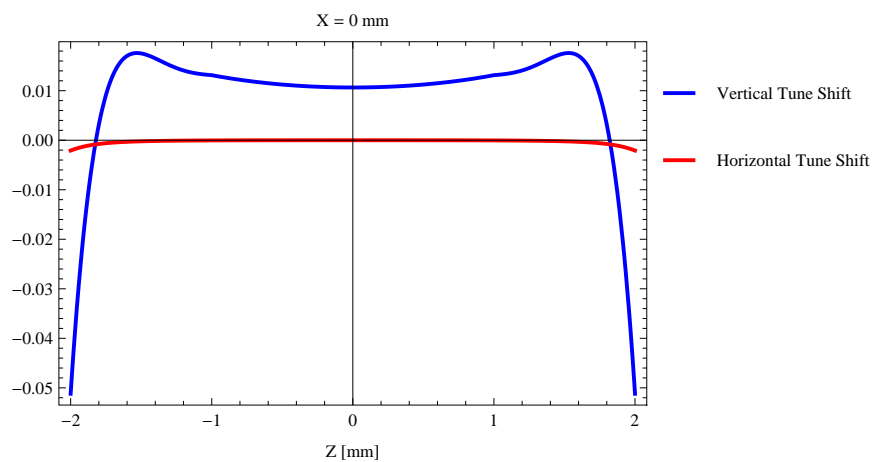


Figure 5.75: Induced tune shift from the pmu20 ID as a function of the vertical distance to the axis of the ID.

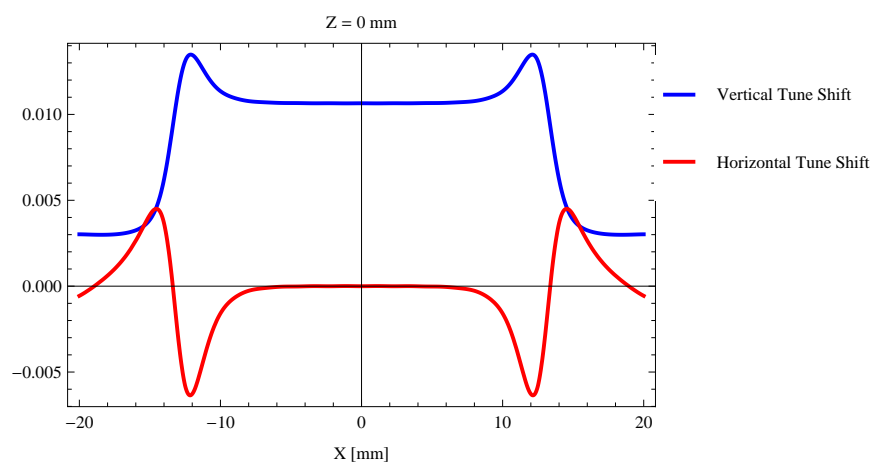


Figure 5.76: Induced tune shift from the pmu20 ID on the stored beam from the ID as a function of the horizontal distance to the axis of the ID.

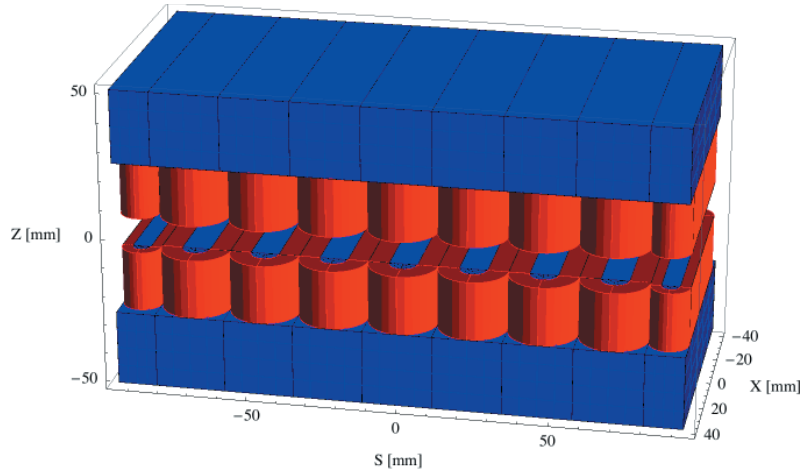


Figure 5.77: Magnetic model of the scw46 ID. The ID has been modelled with Radia [2].

### 5.3.4. The scw46 ID

#### Magnet model of the scw46 ID

The scw46 is a superconducting wiggler with NbTi coils operating at 4.2 K. The magnetic model of the scw46 is shown in Figure 5.77. The ID has been modelled with Radia [2]. The total length of the magnet model is 175.479 mm. The magnet model consists of the standing racetrack coils, which are red in Figure 5.77, the iron pole cores and iron return yokes. The parts made of iron are blue in Figure 5.77. The current density in the coils is  $750 \text{ A/mm}^2$ . The period length is 46 mm. The magnetic gap is 12 mm, which should give enough room for a liner for the beam induced heat loads. The poles are 9.2 mm thick, 20 mm high, and 60 mm wide. The coils are 6.9 mm thick and have the same height as the poles. The return field yoke on top and bottom is 25 mm thick.

#### Analysis of the magnetic field of the scw46 ID

The vertical magnetic field in a central pole of the scw46 ID along the ID axis,  $X = Z = 0$  is shown in Figure 5.78. The vertical magnetic field in a central pole of the scw46 ID in the horizontally transverse direction to the ID axis,  $S = Z = 0$ , is shown in Figure 5.79.

A Fourier analysis of the magnetic field along the axis of the ID gives the higher harmonic contents in the magnetic field. A non-sinusoidal magnetic field profile along the ID would give a large higher harmonics contribution and it would no longer be possible to calculate the K-value of the ID from the peak field only. Also the higher harmonic contribution must be included to get the correct efficient magnetic field and efficient K-value. The higher harmonic contribution to the magnetic field is given in in Table 5.19.

A tranverse field roll-off may pose a problem to the storage ring since it gives a horizontal tune shift. The transverse field roll-off for the scw46 for different horizontal positions out from the ID axis is shown in Figure 5.79 and numbers are given in Table 5.20.

The paremeters of the scw46 are summarised in Table 5.21.

The critical energy of the emitted radiation will vary with the horizontal angle out from the axis of the ID as shown in Figure 5.80.

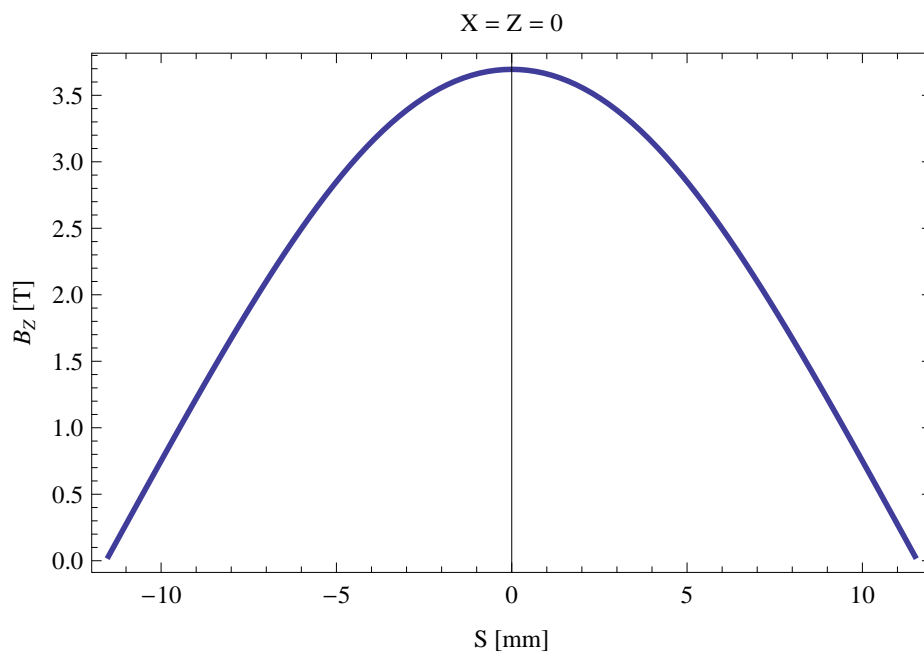


Figure 5.78: Vertical magnetic field in a central pole of the scw46 ID along the ID axis,  $X = Z = 0$

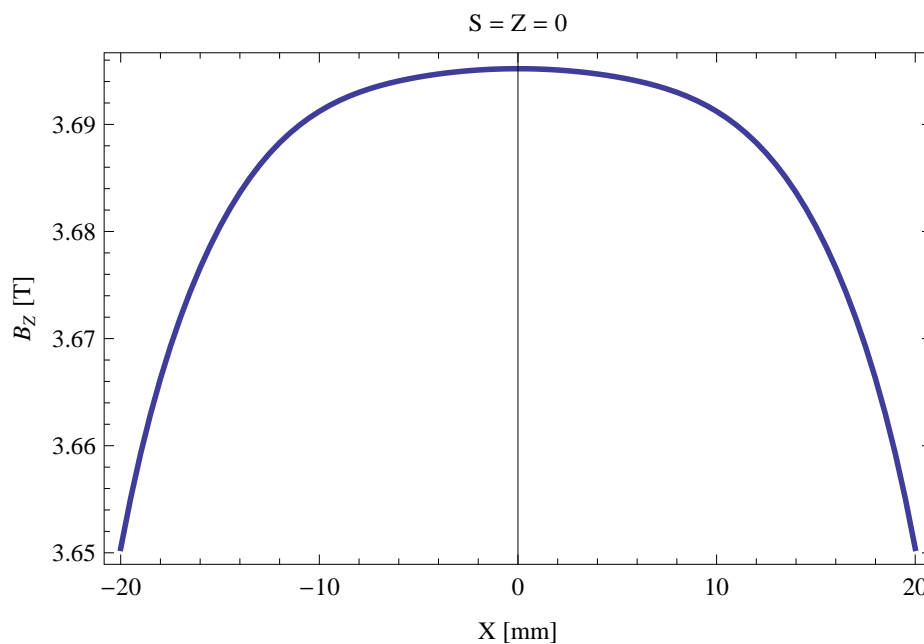


Figure 5.79: Vertical magnetic field in a central pole of the scw46 ID along the horizontally transverse direction to the ID axis,  $S = Z = 0$

Table 5.19: Fourier Analysis of the magnetic field of the scw46 ID

Term	Strength
Harm. Nr. 1	3.639 T
Harm. Nr. 3	0.031 T
Harm. Nr. 5	-0.008 T
Harm. Nr. 7	-0.001 T
Harm. Nr. 9	-0.000 T
Harm. Nr. 11	0.000 T

Table 5.20: Transverse field roll-off for the scw46 ID

X-Position	$B_Z$ Field	Roll-off
$\pm 0$ mm	3.695 T	
$\pm 5$ mm	3.694 T	0.02 %
$\pm 10$ mm	3.691 T	0.11 %
$\pm 15$ mm	3.680 T	0.40 %
$\pm 20$ mm	3.650 T	1.21 %

Table 5.21: Summary of the scw46 ID parameters

Period	46.0	mm
Gap	12.0	mm
Peak Field	3.695	T
Effective Field	3.640	T
Peak k-value	15.876	
Effective k-value	15.637	
Higher Order Contr.	0.88	%
Maximum e-beam deflection	2.65	mrاد
Electron Beam Energy	3.0	GeV
Electron Beam Current	500	mA
Max Critical Energy	22.116	keV
Emitted Power	74.275	kW
Photon Energy, $n = 1$	0.015	keV
Total Length	1969.5	mm

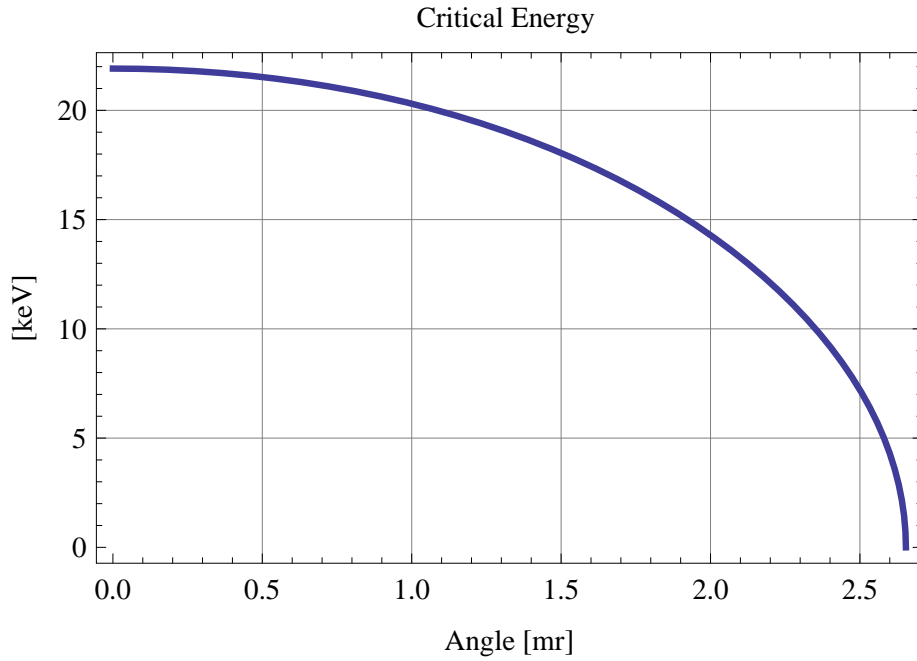


Figure 5.80: Variation of the critical energy with horizontal angle for the emitted synchrotron radiation from the scw46 ID

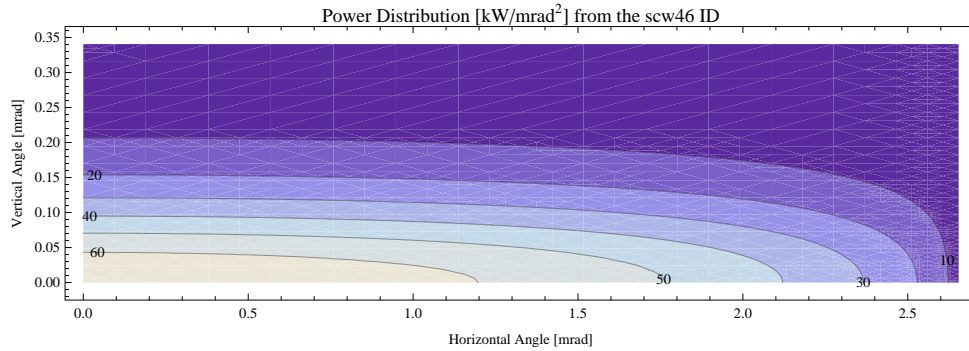


Figure 5.81: Map of the emitted power in the scw46 ID

### Synchrotron radiation from the scw46 ID

The power map of the emitted synchrotron radiation by the scw46 ID, assuming a 0.5 A filament beam with an energy of 3 GeV and bending magnet properties of the synchrotron radiation, is shown in Figure 5.81. The on-axis power density is 67.221 kW/mrad<sup>2</sup>. The angular spectral flux density on axis is shown in Figure 5.82. Detailed calculations of the emitted synchrotron radiation is better carried out with dedicated software packages.



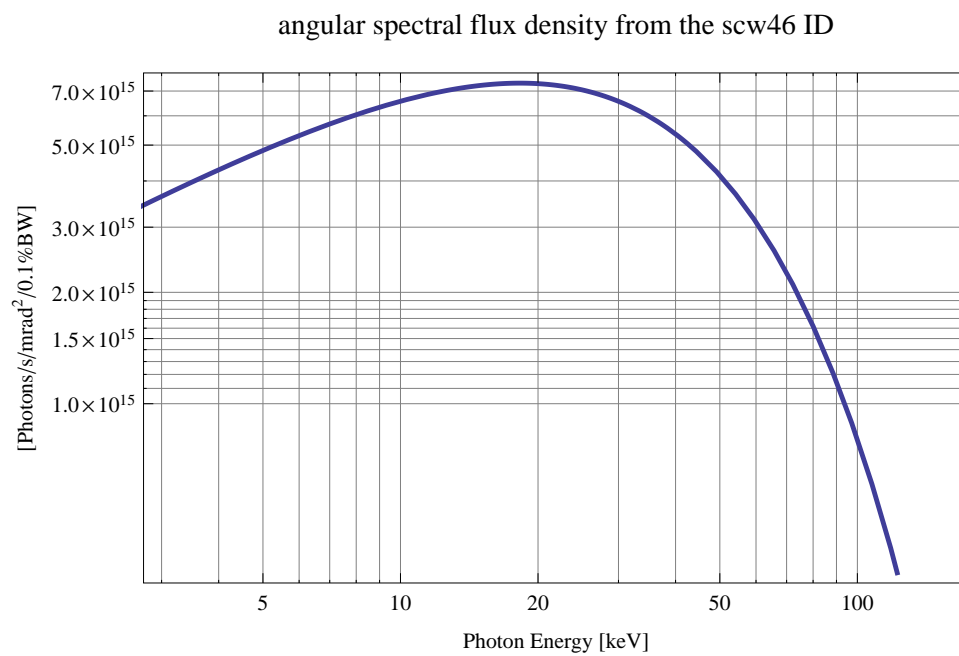


Figure 5.82: angular spectral flux density of the scw46 ID

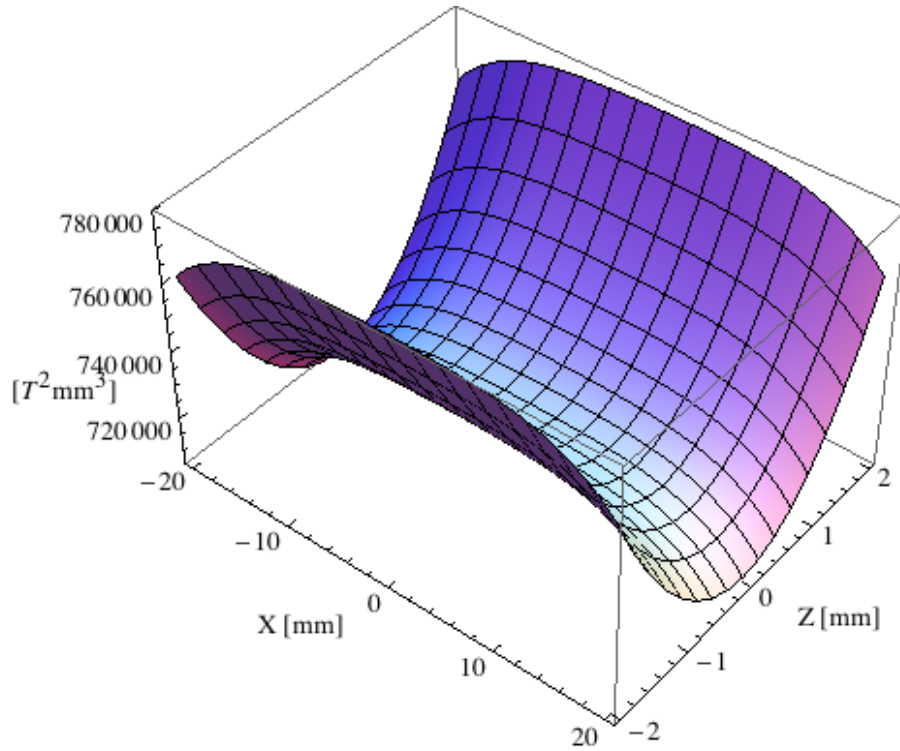


Figure 5.83: Focusing potential from the scw46 ID over the beam stay clear aperture.

### Influence from the scw46 ID on the optics of the stored beam

Figure 5.83 shows the focusing potential from the scw46 over the beam stay clear aperture of the ring aperture.

Figure 5.84 shows the kick map in the beam energy independent unit  $T^2 m^2$  of the kicks induced by the scw46 ID over the beam stay clear aperture.

Figure 5.85 shows the induced angular kick on the stored beam from the scw46 ID as a function of the vertical distance to the axis of the ID.

Figure 5.86 shows the induced angular kick on the stored beam from the scw46 ID as a function of the horizontal distance to the axis of the ID.

Figure 5.87 shows tune shift induced by the scw46 ID over the beam stay clear aperture. Note that the tune shift depends on the beam size at the ID.

Figure 5.88 shows the induced tune shift from the scw46 ID as a function of the vertical distance to the axis of the ID.

Figure 5.89 shows the induced tune shift from the scw46 ID as a function of the horizontal distance to the axis of the ID.

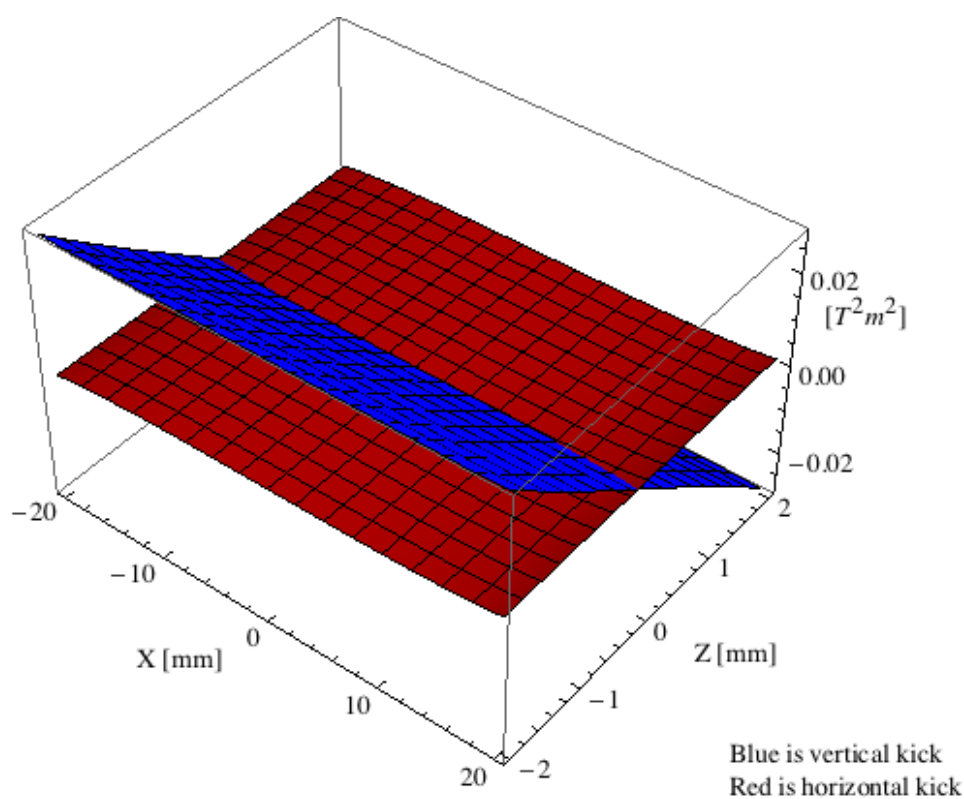


Figure 5.84: Kick map in the beam energy independent unit  $T^2m^2$  of the kicks induced by the scw46 ID over the beam stay clear aperture.

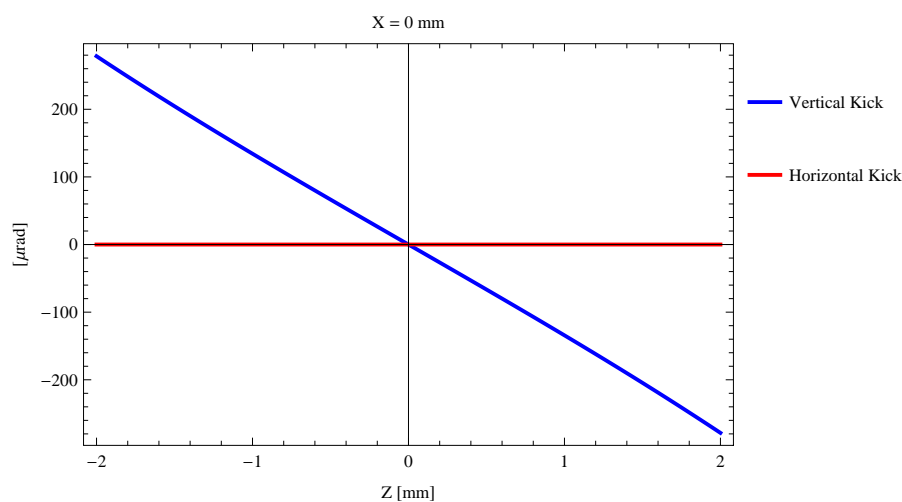


Figure 5.85: Induced angular kick on the stored beam from the scw46 ID as a function of the vertical distance to the ID axis.

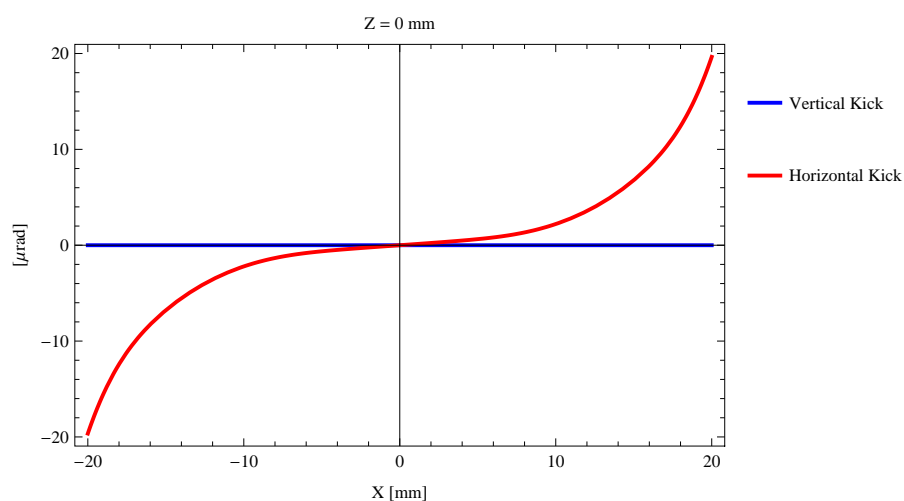


Figure 5.86: Induced angular kick on the stored beam from the scw46 ID as a function of the horizontal distance to the ID axis.

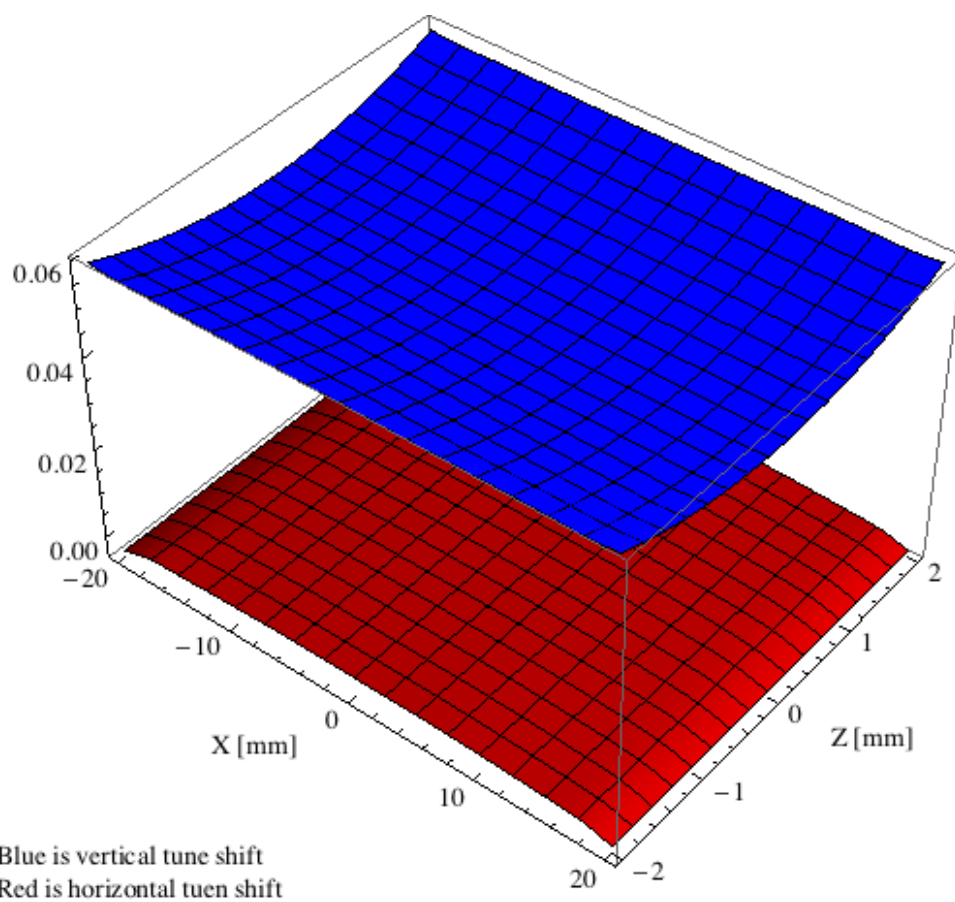


Figure 5.87: Tune shift induced by the scw46 ID over the beam stay clear aperture.

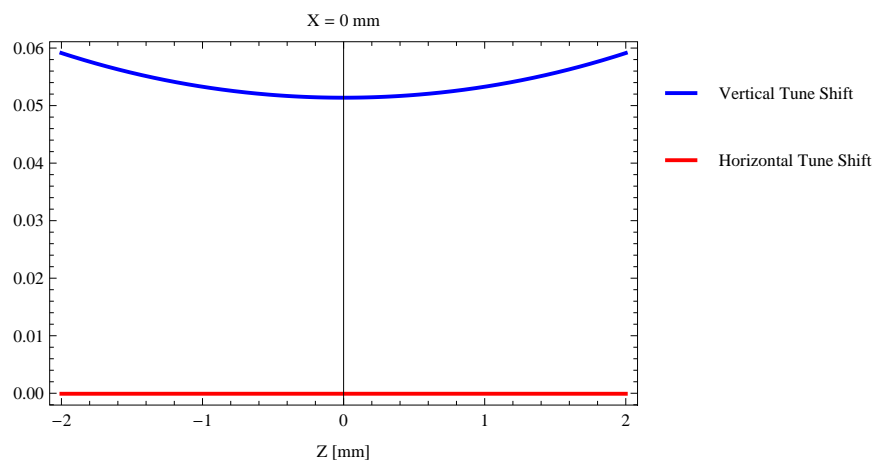


Figure 5.88: Induced tune shift from the scw46 ID as a function of the vertical distance to the axis of the ID.

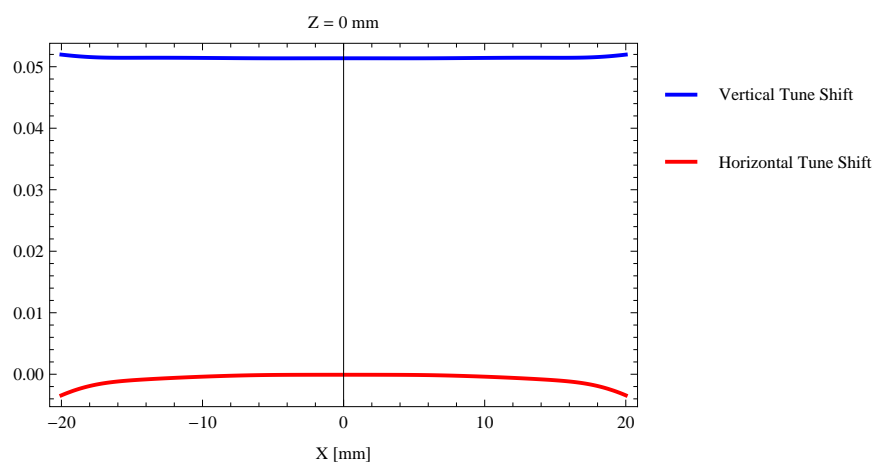


Figure 5.89: Induced tune shift from the scw46 ID on the stored beam from the ID as a function of the horizontal distance to the axis of the ID.

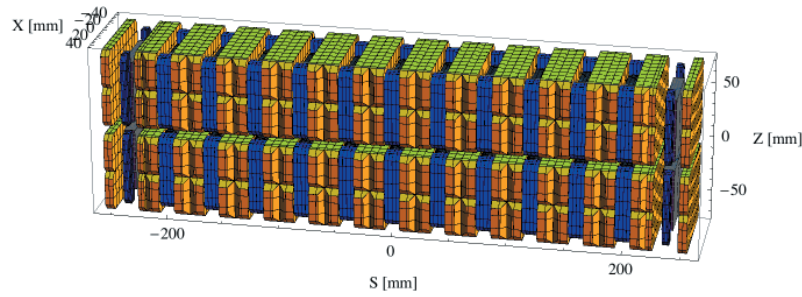


Figure 5.90: Magnetic model of the wig80 ID. The ID has been modelled with Radia [2].

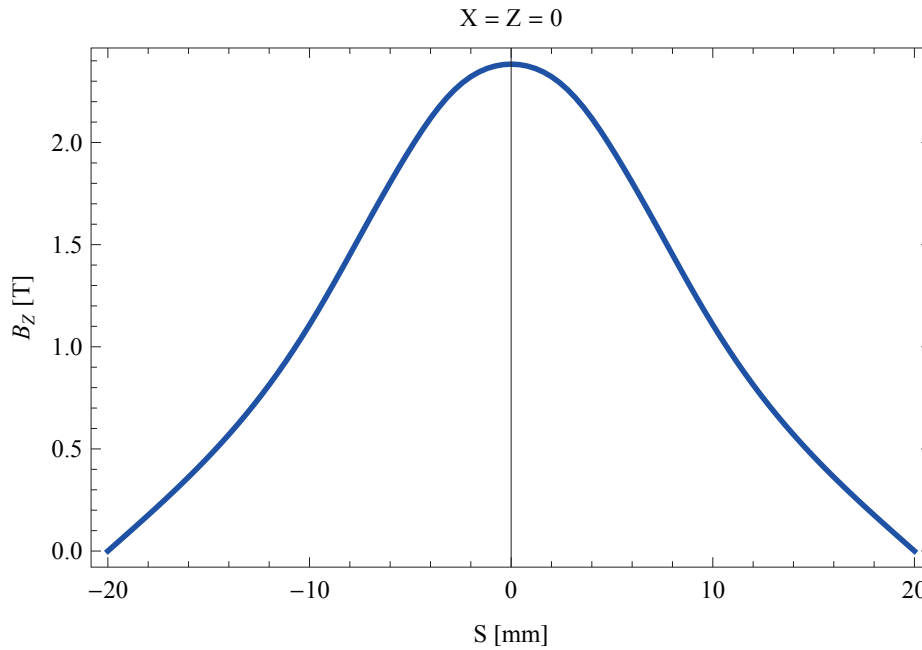


Figure 5.91: Vertical magnetic field in a central pole of the wig80 ID along the ID axis,  $X = Z = 0$

### 5.3.5. The wig80 ID

#### Magnet model of the wig80 ID

The wig80 is a wiggler of hybrid type and the magnetic model of the wig80 is shown in Figure 5.90. The ID has been modelled with Radia [2]. The total length of the magnet model is 510.7 mm. The magnet model is built from three basic building blocks, which are the main blocks, the side blocks, and the poles. The main blocks, which are yellow in Figure 5.90, are made of an NdFeB material with a remanence of 1.25 T and an intrinsic coercivity of 25 kOerstedt. The main block material is similar to the material VACODYM 863 TP from Vacuumschmelze. The side blocks, which are blue in Figure 5.90, are made of an NdFeB material with a remanence of 1.28 T and an intrinsic coercivity of 21 kOerstedt. The side block material is similar to the material VACODYM 776 TP from Vacuumschmelze. The poles, which are grey in Figure 5.90, are made of a Vanadium Permendur type material from MetallImphy (Fe : 49%, Co: 49%, V: 2%), a material similar to VACOFLUX 50 from VacuumSchmelze.

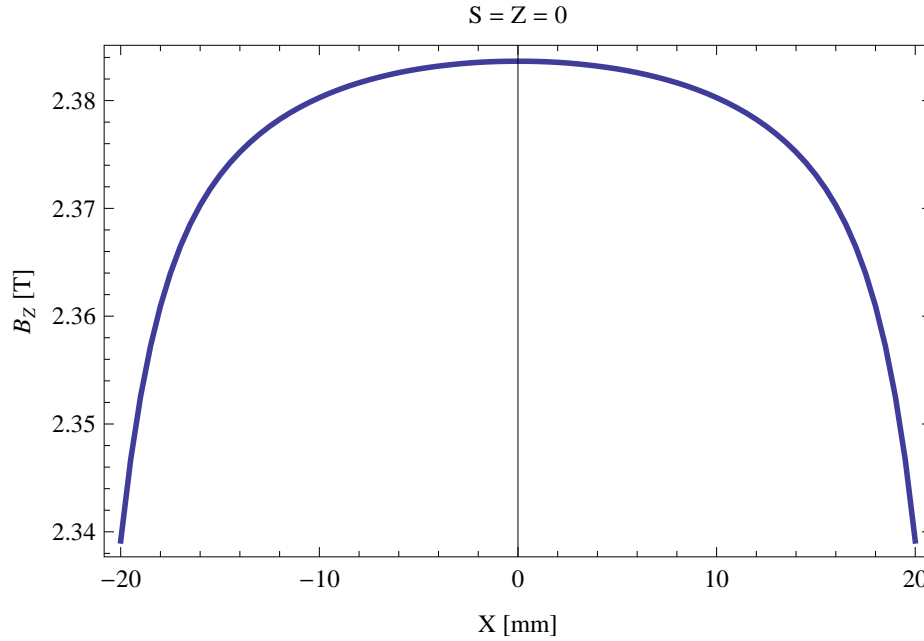


Figure 5.92: Vertical magnetic field in a central pole of the wig80 ID along the horizontally transverse direction to the ID axis,  $S = Z = 0$

### Analysis of the magnetic field of the wig80 ID

The vertical magnetic field in a central pole of the wig80 ID along the ID axis,  $X = Z = 0$  is shown in Figure 5.91. The vertical magnetic field in a central pole of the wig80 ID in the horizontally transverse direction to the ID axis,  $S = Z = 0$ , is shown in Figure 5.92.

A Fourier analysis of the magnetic field along the axis of the ID gives the higher harmonic contents in the magnetic field. A non-sinusoidal magnetic field profile along the ID would give a large higher harmonics contribution and it would no longer be possible to calculate the K-value of the ID from the peak field only. Also the higher harmonic contribution must be included to get the correct efficient magnetic field and efficient K-value. The higher harmonic contribution to the magnetic field is given in in Table 5.22.

Table 5.22: Fourier Analysis of the magnetic field of the wig80 ID

Term	Strength
Harm. Nr. 1	1.988 T
Harm. Nr. 3	0.369 T
Harm. Nr. 5	0.043 T
Harm. Nr. 7	-0.007 T
Harm. Nr. 9	-0.005 T
Harm. Nr. 11	-0.002 T

A tranverse field roll-off may pose a problem to the storage ring since it gives a horizontal tune shift. The transverse field roll-off for the wig80 for different horizontal positions out from the ID axis is shown in Figure 5.92 and numbers are given in Table 5.23.

The paremeters of the wig80 are summarised in Table 5.24.

The critical energy of the emitted radiation will vary with the horizontal angle out from the axis of the ID as shown in Figure 5.93.

Table 5.23: Transverse field roll-off for the wig80 ID

X-Position	$B_z$ Field	Roll-off
$\pm 0$ mm	2.384 T	
$\pm 5$ mm	2.383 T	0.03 %
$\pm 10$ mm	2.380 T	0.14 %
$\pm 15$ mm	2.373 T	0.44 %
$\pm 20$ mm	2.339 T	1.87 %

Table 5.24: Summary of the wig80 ID parameters

Period	80.0	mm
Gap	7.8	mm
Peak Field	2.384	T
Effective Field	1.992	T
Peak k-value	17.811	
Effective k-value	14.883	
Higher Order Contr.	18.71	%
Maximum e-beam deflection	2.38	mrad
Electron Beam Energy	3.0	GeV
Electron Beam Current	500	mA
Max Critical Energy	14.266	keV
Emitted Power	45.078	kW
Photon Energy, $n = 1$	0.010	keV
Total Length	3990.7	mm

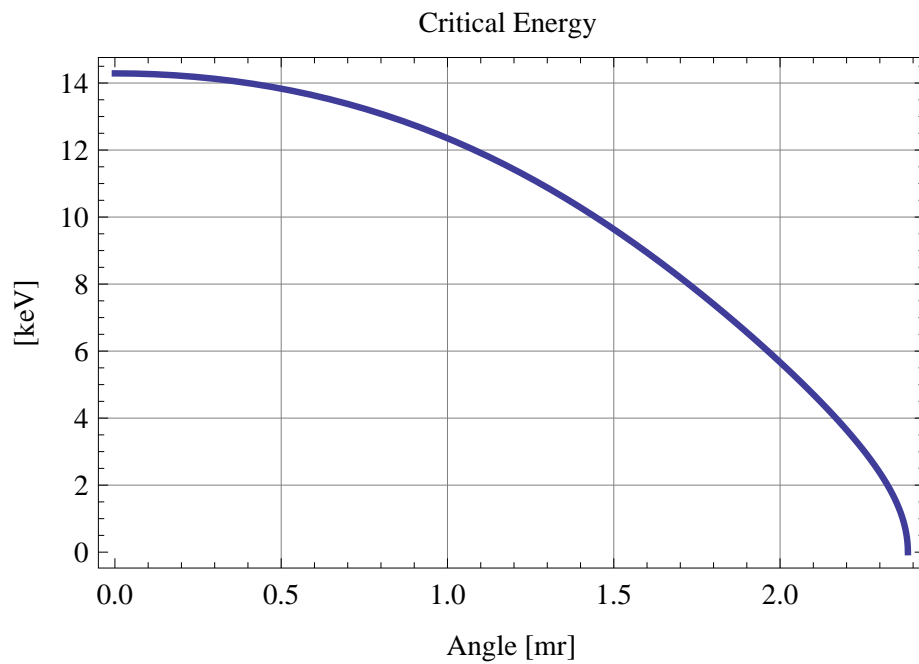


Figure 5.93: Variation of the critical energy with horizontal angle for the emitted synchrotron radiation from the wig80 ID



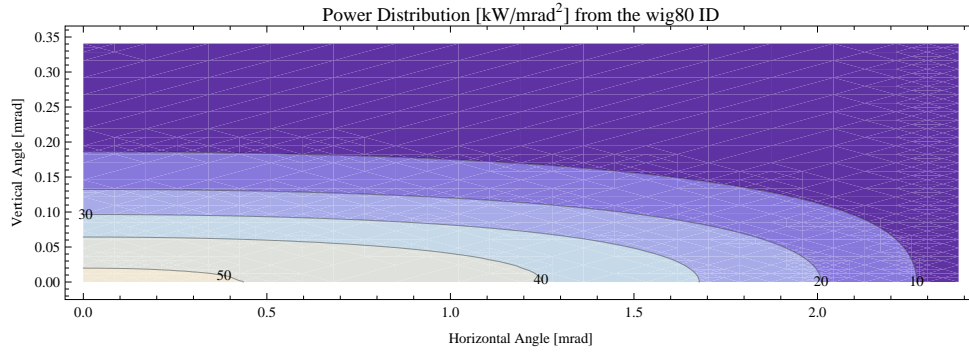


Figure 5.94: Map of the emitted power in the wig80 ID

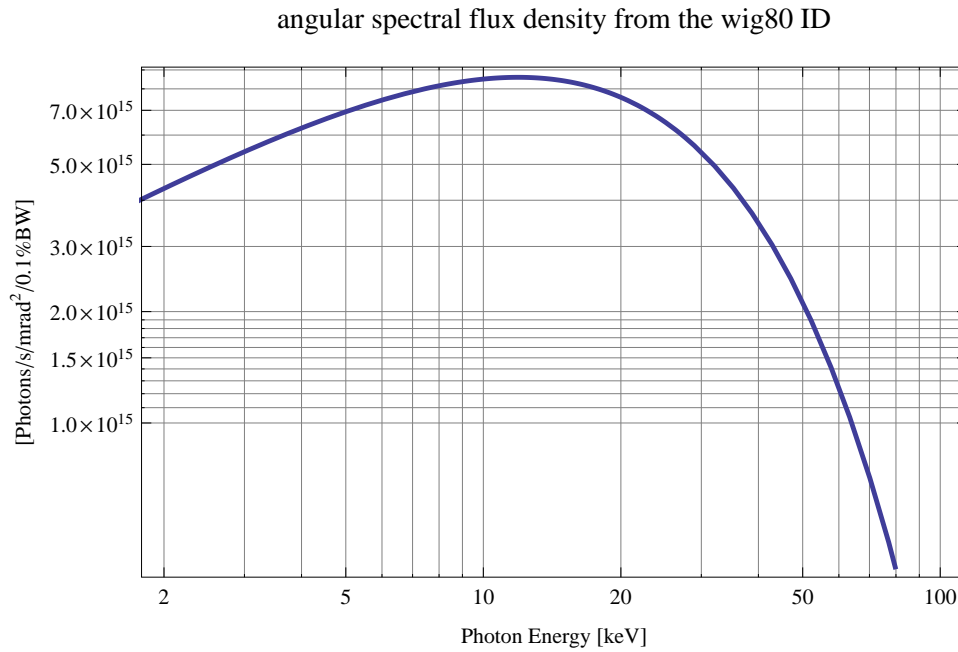


Figure 5.95: angular spectral flux density of the wig80 ID

### Synchrotron radiation from the wig80 ID

The power map of the emitted synchrotron radiation by the wig80 ID, assuming a 0.5 A filament beam with an energy of 3 GeV and bending magnet properties of the synchrotron radiation, is shown in Figure 5.94. The on-axis power density is 51.241 kW/mrad<sup>2</sup>. The angular spectral flux density on axis is shown in Figure 5.95. Detailed calculations of the emitted synchrotron radiation is better carried out with dedicated software packages.

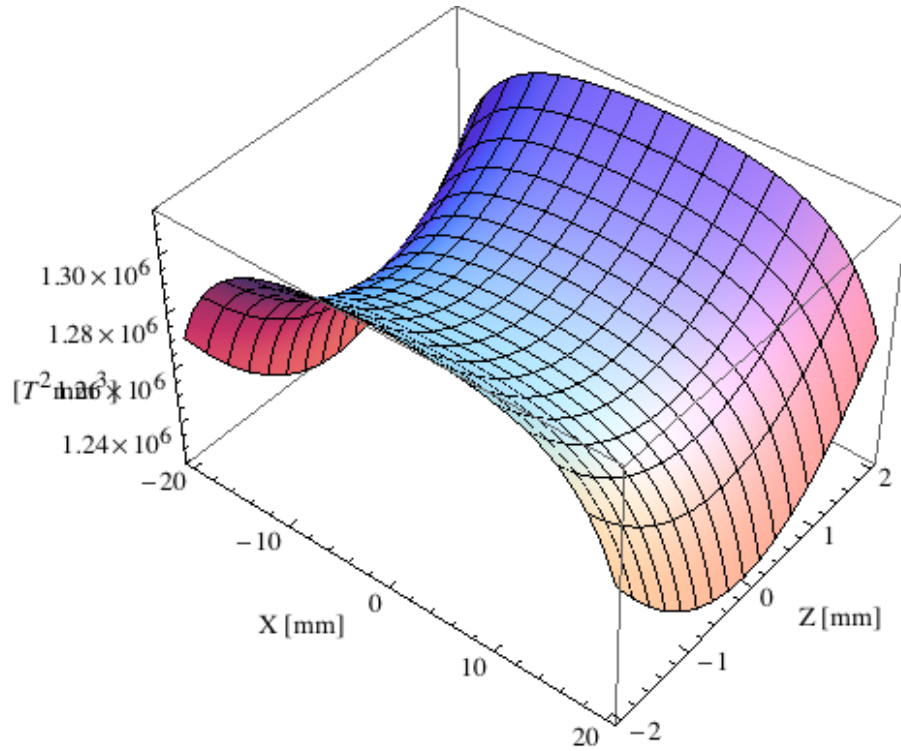


Figure 5.96: Focusing potential from the wig80 ID over the beam stay clear aperture.

### Influence from the wig80 ID on the optics of the stored beam

Figure 5.96 shows the focusing potential from the wig80 over the beam stay clear aperture of the ring aperture.

Figure 5.97 shows the kick map in the beam energy independent unit  $T^2 m^2$  of the kicks induced by the wig80 ID over the beam stay clear aperture.

Figure 5.98 shows the induced angular kick on the stored beam from the wig80 ID as a function of the vertical distance to the axis of the ID.

Figure 5.99 shows the induced angular kick on the stored beam from the wig80 ID as a function of the horizontal distance to the axis of the ID.

Figure 5.100 shows tune shift induced by the wig80 ID over the beam stay clear aperture. Note that the tune shift depends on the beam size at the ID.

Figure 5.101 shows the induced tune shift from the wig80 ID as a function of the vertical distance to the axis of the ID.

Figure 5.102 shows the induced tune shift from the wig80 ID as a function of the horizontal distance to the axis of the ID.

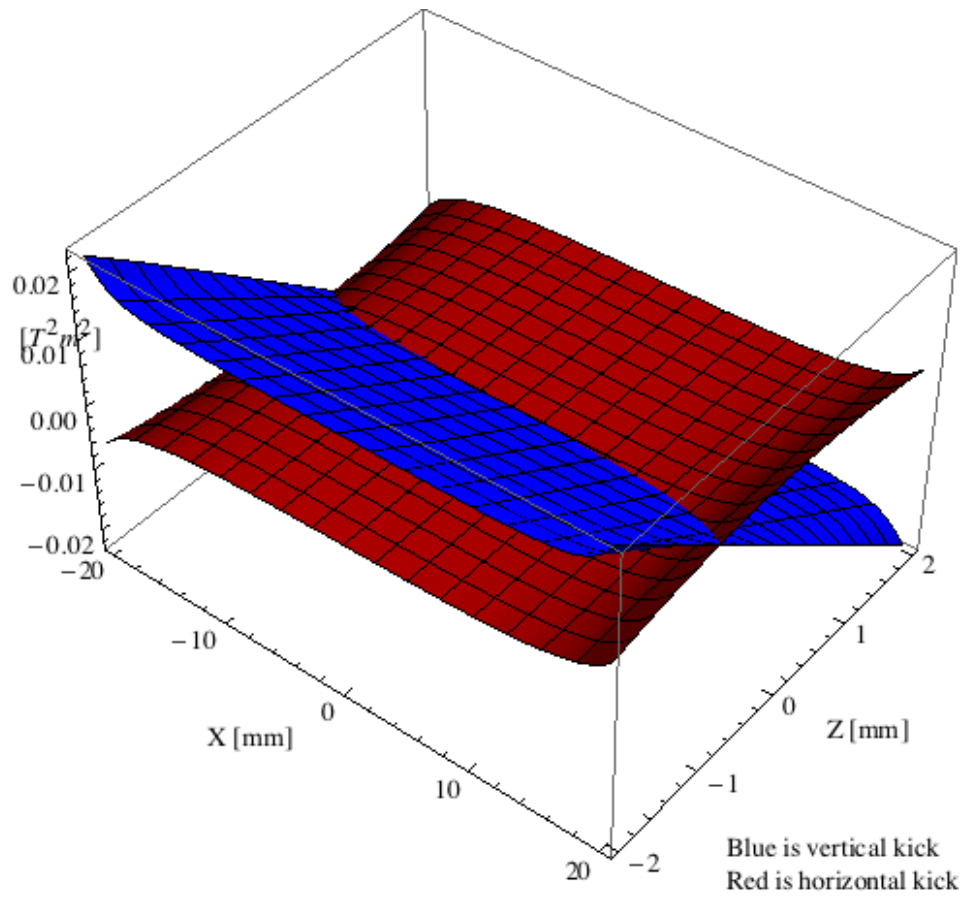


Figure 5.97: Kick map in the beam energy independent unit  $T^2m^2$  of the kicks induced by the wig80 ID over the beam stay clear aperture.

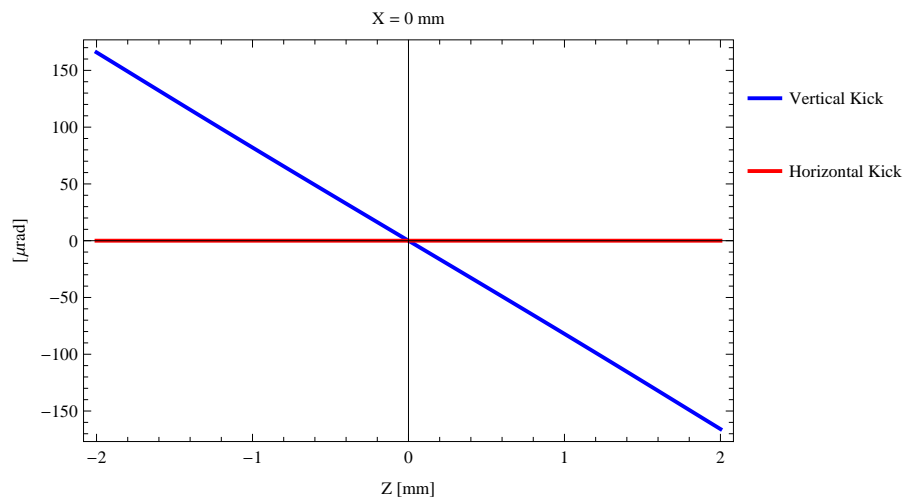


Figure 5.98: Induced angular kick on the stored beam from the wig80 ID as a function of the vertical distance to the ID axis.

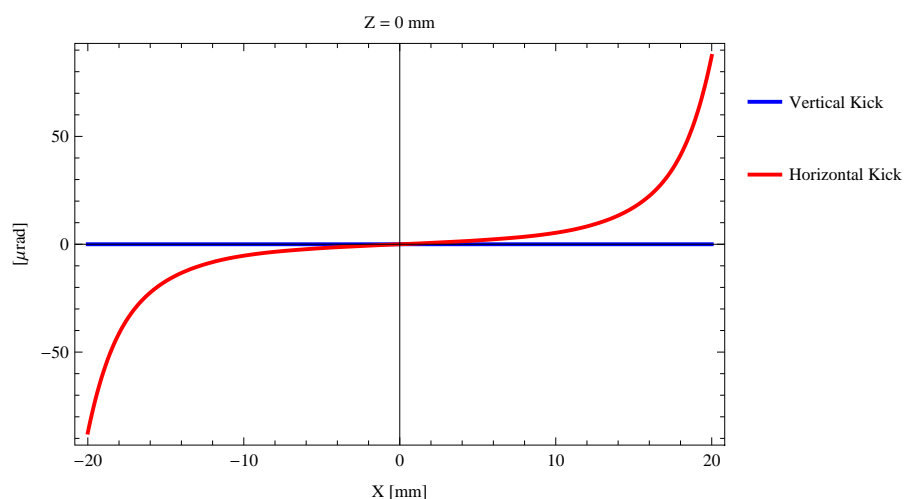


Figure 5.99: Induced angular kick on the stored beam from the wig80 ID as a function of the horizontal distance to the ID axis.

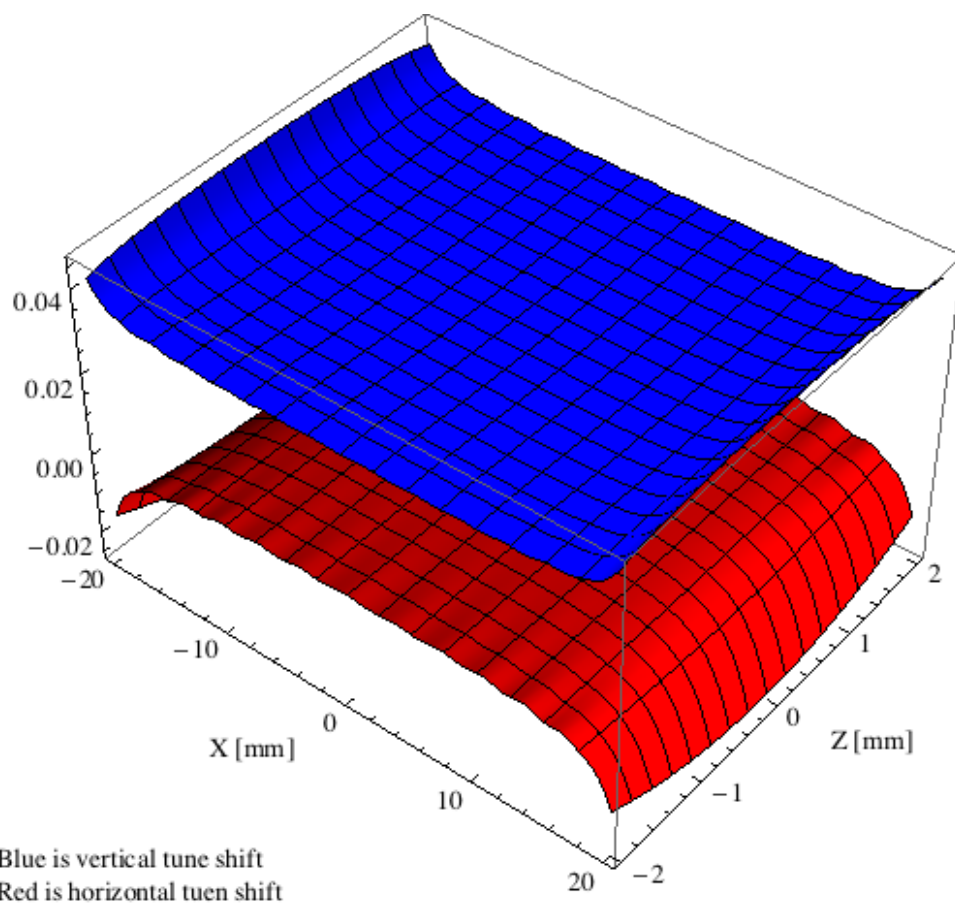


Figure 5.100: Tune shift induced by the wig80 ID over the beam stay clear aperture.

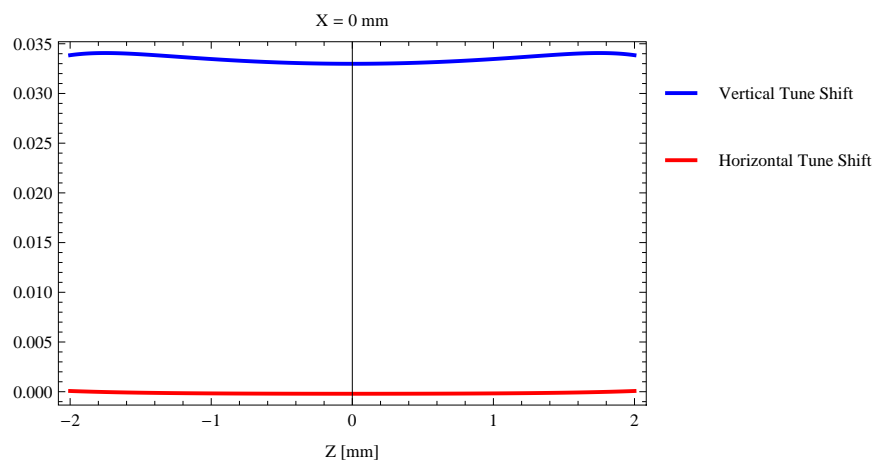


Figure 5.101: Induced tune shift from the wig80 ID as a function of the vertical distance to the axis of the ID.

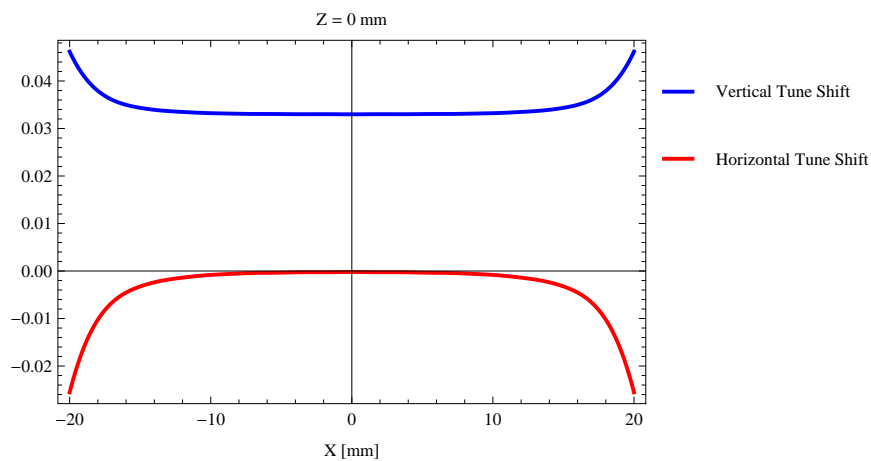


Figure 5.102: Induced tune shift from the wig80 ID on the stored beam from the ID as a function of the horizontal distance to the axis of the ID.

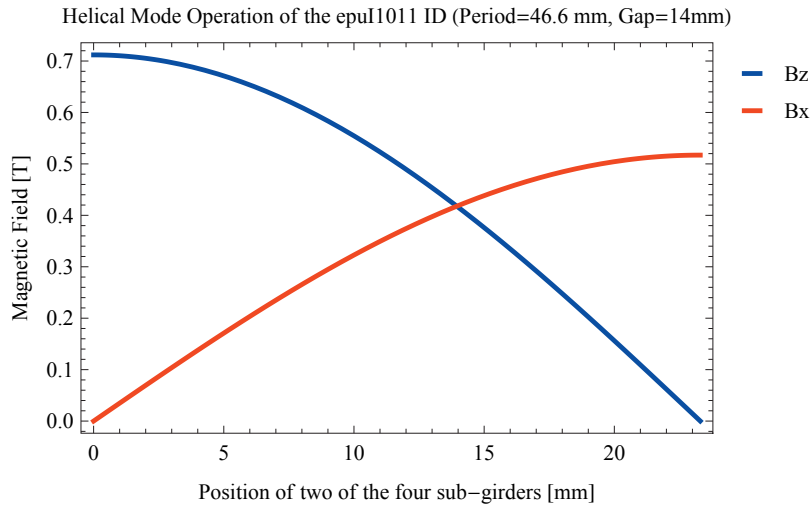


Figure 5.103: Vertical and horizontal magnetic field for the the epul1011 ID when operating in the helical mode for different positions for two of the four sub-girders

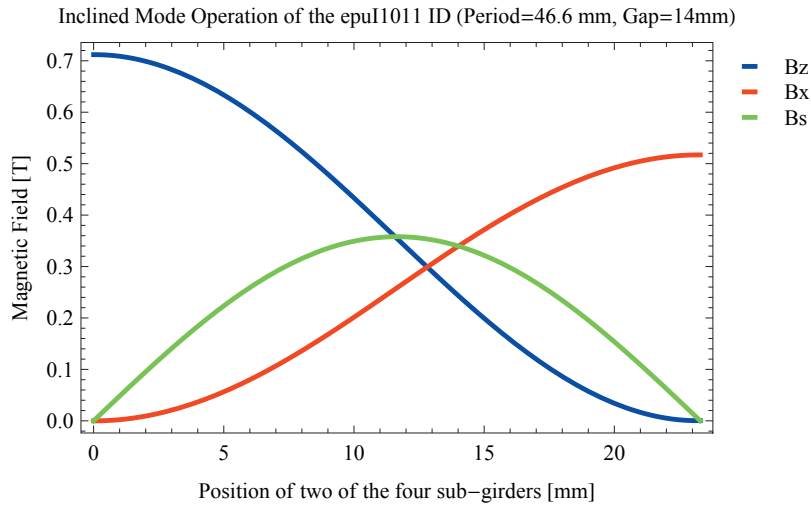


Figure 5.104: Vertical, horizontal, and longitudinal magnetic field for the the epul1011 ID when operating in the inclined mode for different positions for two of the four sub-girders

### 5.3.6. The elliptically polarising undulator epul1011

#### Modes of operation in the elliptically polarising undulator epul1011

Horizontal polarisation of the emitted synchrotron radiation from the epul1011 ID (Period=46.6 mm, Gap=14mm) is found in the planar mode when there is no movement of the sub-girders.

Circular polarisation is found in the elliptical mode of operation for a symmetric sub-grider movement of 13.9494 mm. Figure 5.103 shows the vertical and horizontal magnetic field for the epul1011 ID when operating in the helical mode.

45 degree polarisation is found in the inclined mode of operation for an assymetric sub-grider movement of 12.8128 mm. Figure 5.104 shows the vertical and horizontal magnetic field for the epul1011 ID when operating in the inclined mode.

The following sub-sections will cover four different situations: The epul1011 operating in the

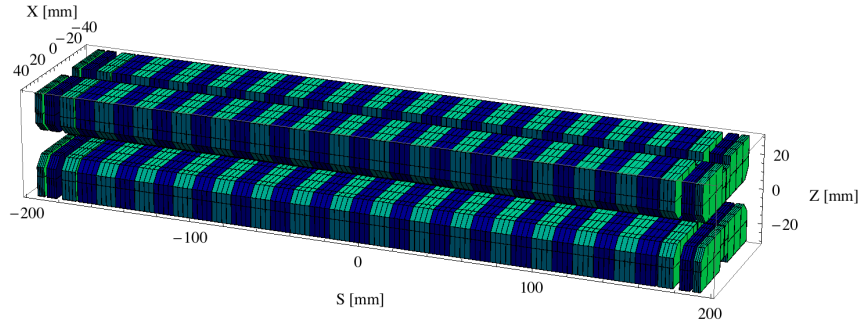


Figure 5.105: Magnetic model of the epuI1011Plan ID. The ID has been modelled with Radia [2]

planar mode for horizontal polarisation (epuI1011Plan); The epuI1011 operating in the helical mode for circular polarisation (epuI1011Heli), the epuI1011 operating in the inclined mode for 45 degree polarisation (epuI1011Incl); and The epuI1011 operating in the vertical mode for vertical polarisation (epuI1011Vert).

### Magnet model of the elliptically polaraising undulator epuI1011Plan

The Radia [2] magnet model of the epuI1011Plan ID is shown in Figure 5.105. The length of the magnet model is 387.26 mm. The magnetic material in the model is NdFeb with a remanence of 1.22 T. Blocks with vertical magnetisation are blue and blocks with horizontal magnetisation are green. This is the existing undulator at the I1011 beamline at the MAX II storage ring. The total length of the epuI1011Plan ID is 2134.76 mm.

### Analysis of the magnetic field of the epuI1011Plan ID

The effective magnetic fields on axis and the fundamental photon energy of the epuI1011Plan ID are shown in Table 5.25. The higher harmonic contents in the magnetic field of an elliptically polarising undulator made of permanent magnets is negligible and the efficient field has about the same strength as the peak field.

Table 5.25: Effective Fields on axis and Fundamental Photon Energy of the epuI1011Plan ID

Undulator Period	46.6	mm
Undulator Gap	14	mm
Undulator Mode	Planar	
Undulator Phase	0.000	mm
Vertical Peak Field	0.707	T
Efficient Vertical Field	0.712	T
Kx (from vert. field)	3.099	
Horizontal Peak Field:	0.000	T
Efficient Horizontal Field	0.000	T
Kz (from hor. field)	0.000	
Photon Energy, Harm.1	0.316	keV
Emitted Power	3.081	kW
Total Length	2134.8	mm

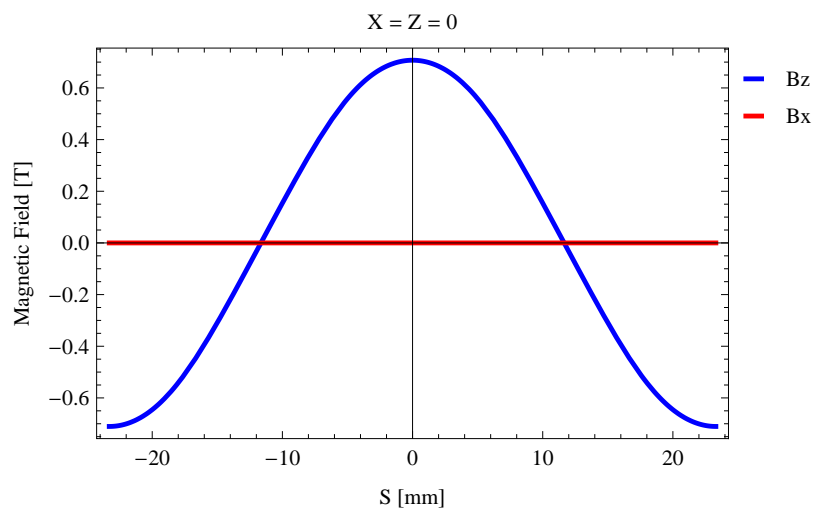


Figure 5.106: Vertical magnetic field in a central pole of the epuI1011Plan ID along the ID axis,  $X = Z = 0$

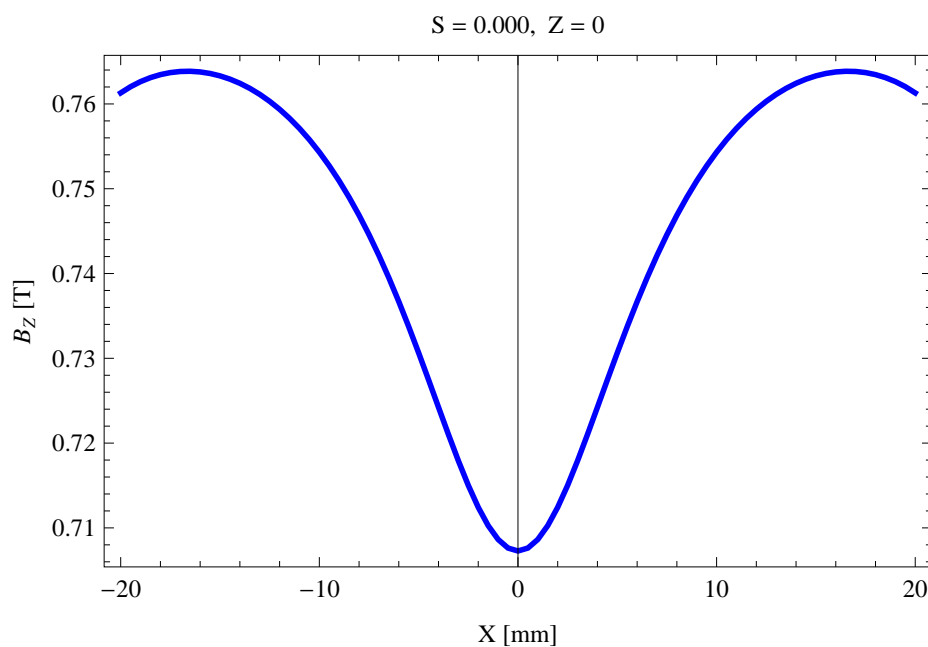


Figure 5.107: Vertical magnetic field in a central pole of the epuI1011Plan ID along the horizontally transverse direction to the ID axis,  $S = 0.000$ ,  $Z = 0$



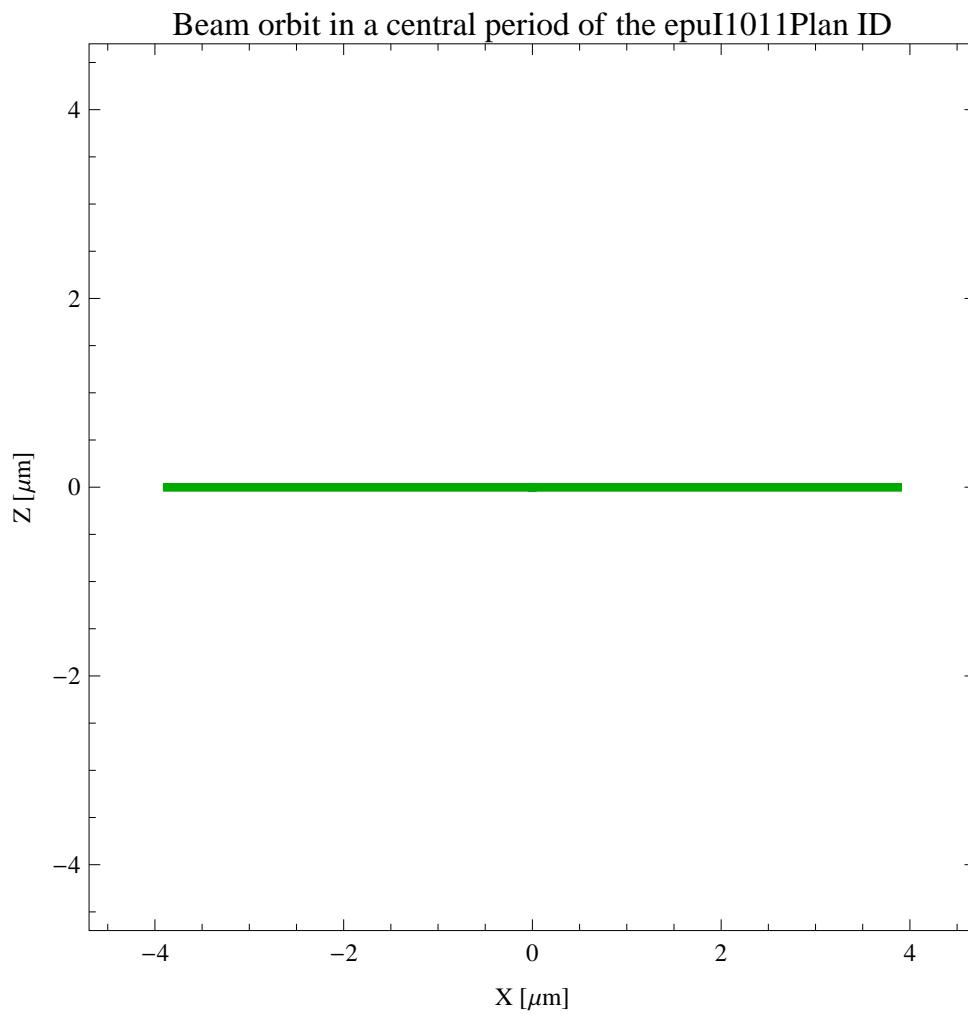


Figure 5.108: The beam orbit of the electron beam through a central period of the epuI1011Plan ID

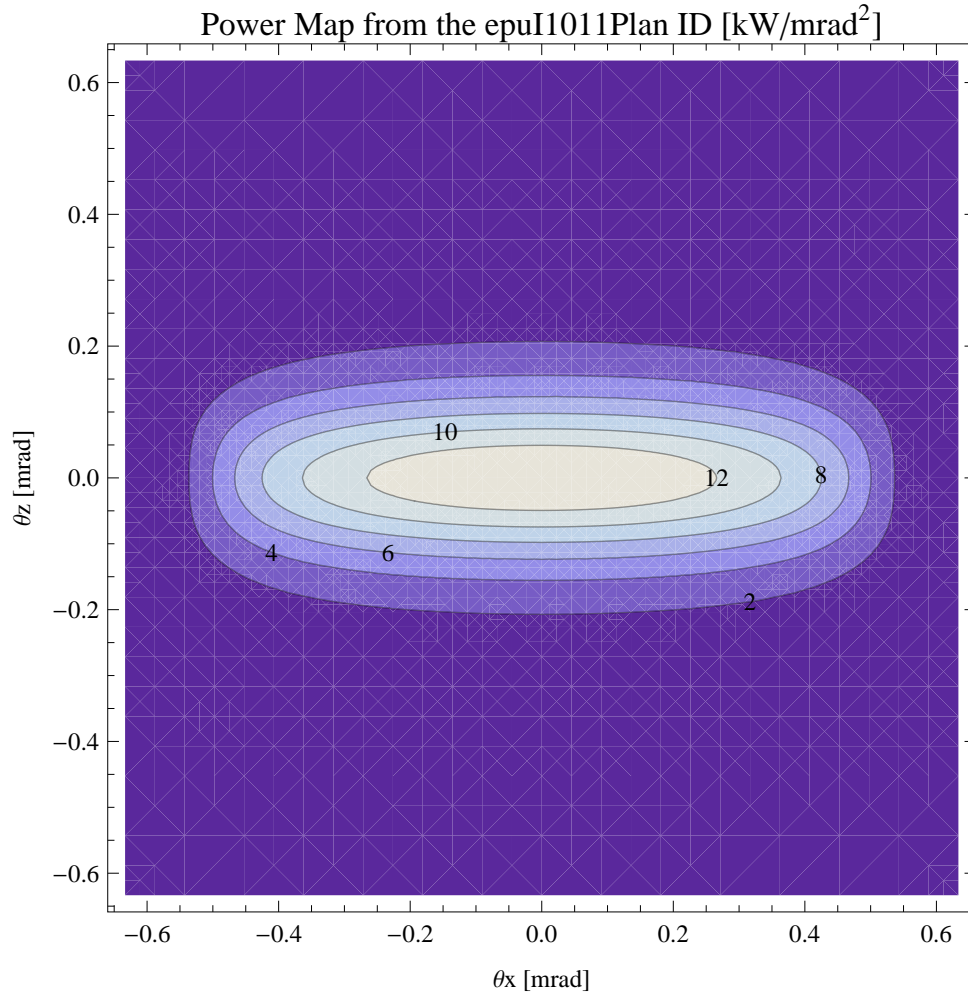


Figure 5.109: Map of the power distribution of the emitted synchrotron radiation by the epuI1011Plan ID

### Synchrotron radiation from the epuI1011Plan ID

The power map of the emitted synchrotron radiation by the epuI1011Plan ID, assuming a 0.5 A filament beam with an energy of 3 GeV and undulator properties of the synchrotron radiation, is shown in Figure 5.109. The on-axis power density is 13.958 kW/mrad<sup>2</sup>

A map of the degree of linear polarisation of the fundamental harmonic of the synchrotron radiation emitted by the epuI1011Plan ID over the angle of observation is shown in Figure 5.110.

A map of the degree of 45 degree polarisation of the fundamental harmonic of the synchrotron radiation emitted by the epuI1011Plan ID over the angle of observation is shown in Figure 5.111.

A map of the degree of circular polarisation of the fundamental harmonic of the synchrotron radiation emitted by the epuI1011Plan ID over the angle of observation is shown in Figure 5.112.

The on axis brilliance at peak energy, the angular spectral flux, the flux in the harmonics, the power in the harmonics, the ratio of coherence, the coherent flux in the harmonics, and the power of coherent radiation in the harmonics from the epuI1011Plan ID have been calculated and the resulting plots are found in this section of the document. The beam parameters used for the calculation are 0.5 A of stored current,  $\beta_H = 9$  m,  $\varepsilon_H = 0.263$  nmrad,  $\beta_V = 4.8$  m,  $\varepsilon_V = 8$ .

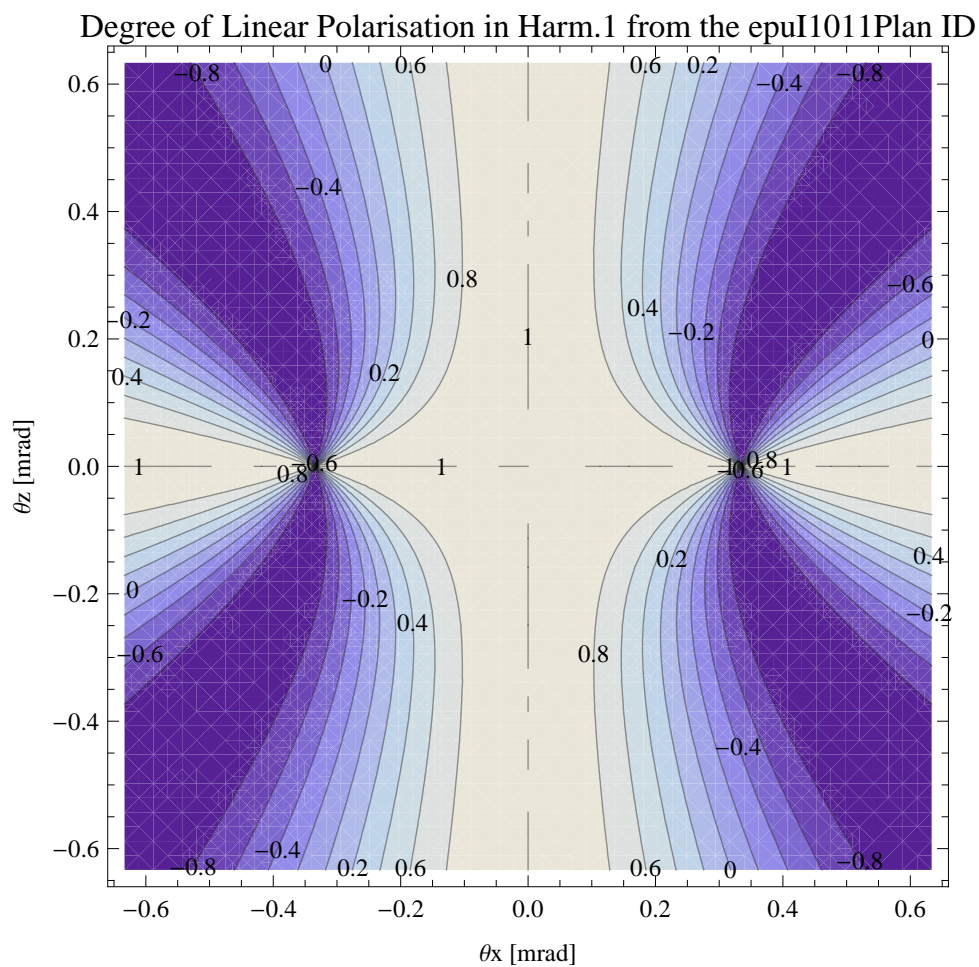


Figure 5.110: Map of linear polarisation in the fundamental harmonic of the synchrotron radiation emitted by the epuI1011Plan ID

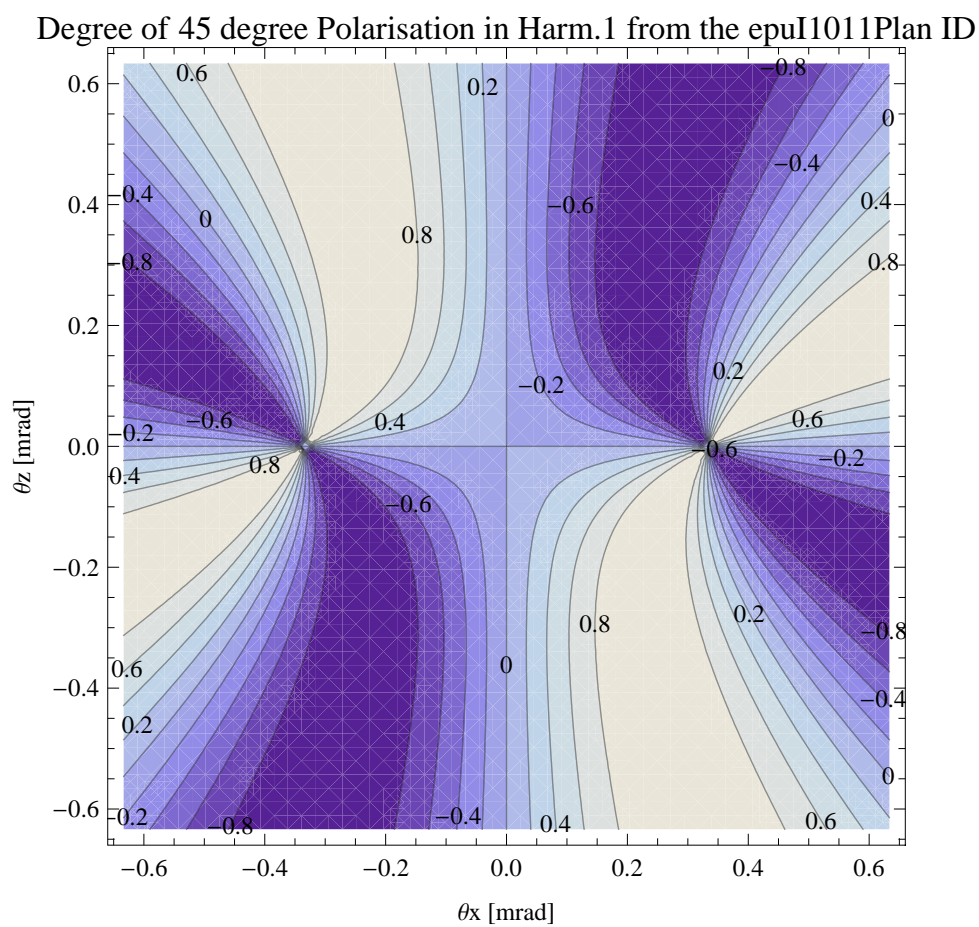


Figure 5.111: Map of 45 degree polarisation in the fundamental harmonic of the synchrotron radiation emitted by the epul1011Plan ID

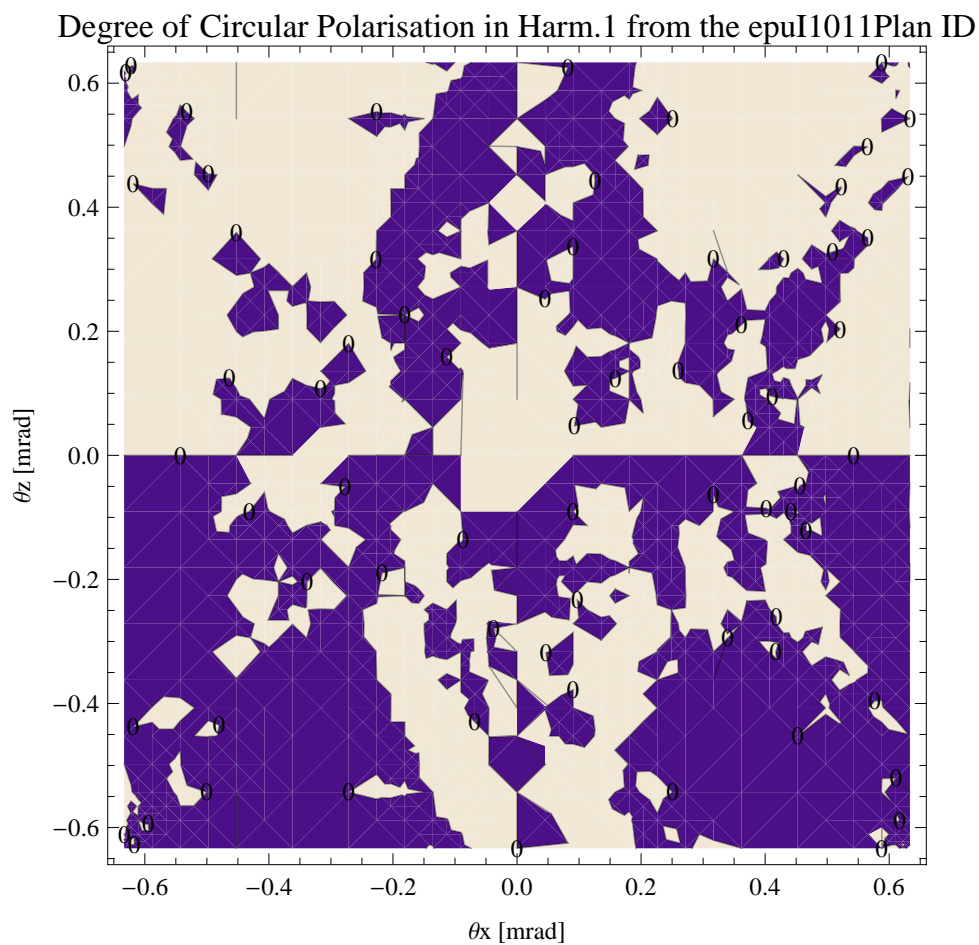


Figure 5.112: Map of circular polarisation in the fundamental harmonic of the synchrotron radiation emitted by the epuI1011Plan ID

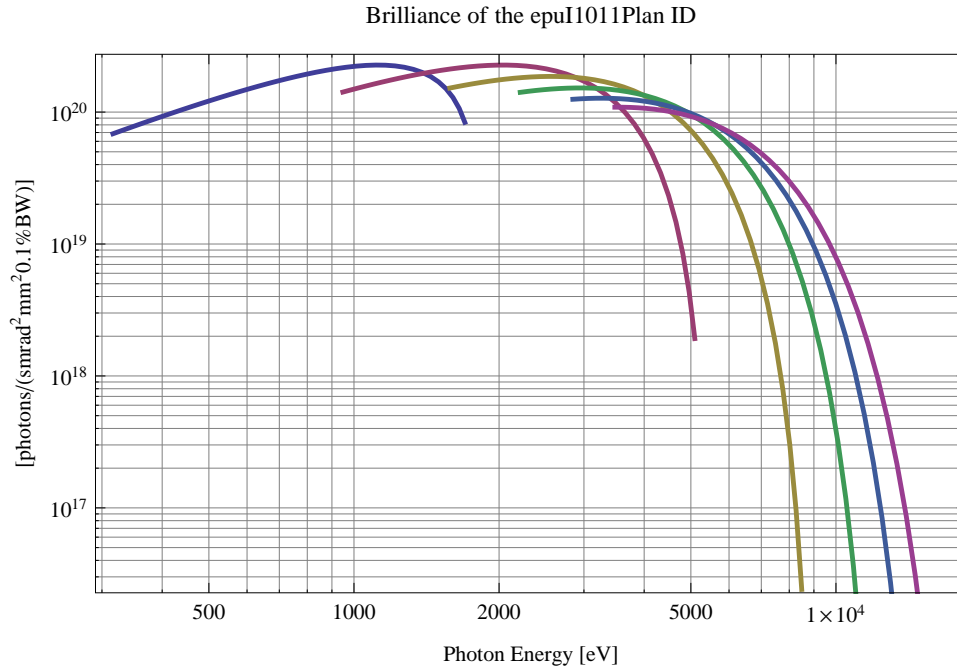


Figure 5.113: The brilliance at peak energy from the epuI1011Plan ID

pmrad, and an energy spread of 0.001.

The brilliance at peak energy and the angular spectral flux density from the epuI1011Plan ID for different harmonics at maximum K-value (3.099) are given in Table 5.26 and for minimum K-value (0.400) these values are given in Table 5.27.

Table 5.26: The brilliance at peak energy and the angular spectral flux density from the epuI1011Plan ID for different harmonics at maximum K-value (3.099)

Harmonic	Photon Energy [eV]	Brilliance [Ph./s/mrad <sup>2</sup> /mrad <sup>2</sup> /0.1%BW]	Angular Spectral Flux [Ph./s/mrad <sup>2</sup> /0.1%BW]
1	316.126	$6.85 \times 10^{19}$	$2. \times 10^{17}$
3	948.377	$1.42 \times 10^{20}$	$2.95 \times 10^{17}$
5	1580.63	$1.52 \times 10^{20}$	$2.86 \times 10^{17}$
7	2212.88	$1.41 \times 10^{20}$	$2.54 \times 10^{17}$
9	2845.13	$1.25 \times 10^{20}$	$2.19 \times 10^{17}$
11	3477.38	$1.09 \times 10^{20}$	$1.88 \times 10^{17}$

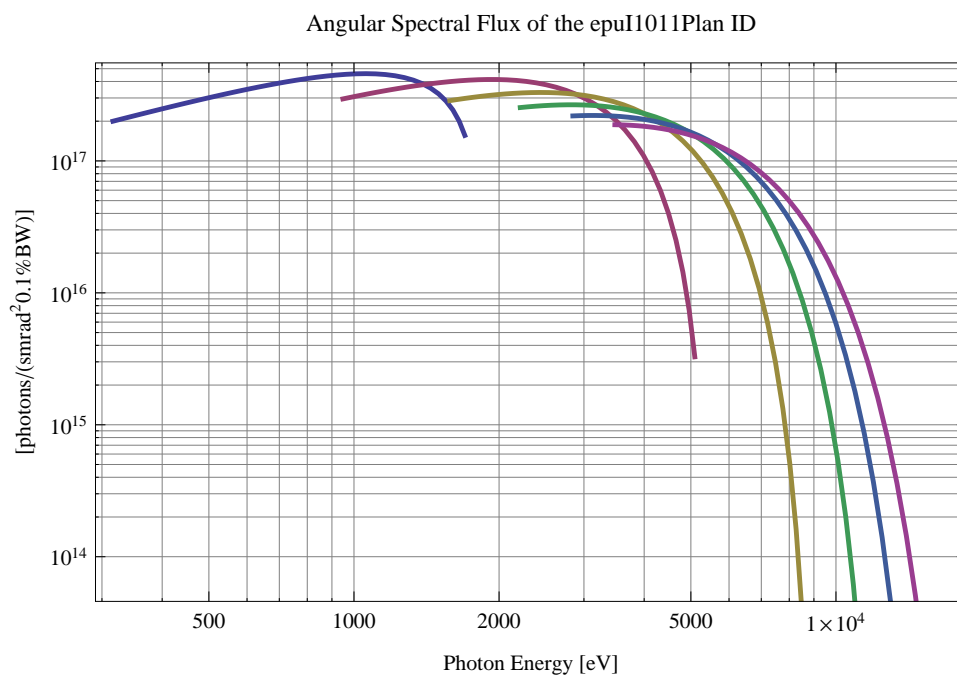


Figure 5.114: The angular spectral flux from the epuI1011Plan ID

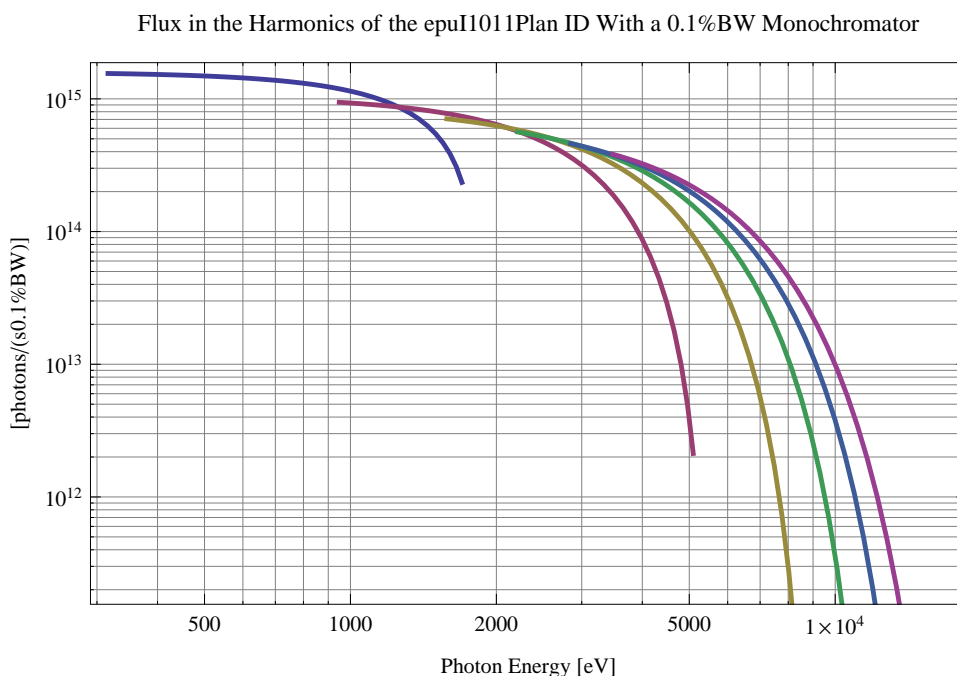


Figure 5.115: The flux of photons in the harmonics from the epuI1011Plan ID using a 0.1%BW monochromator

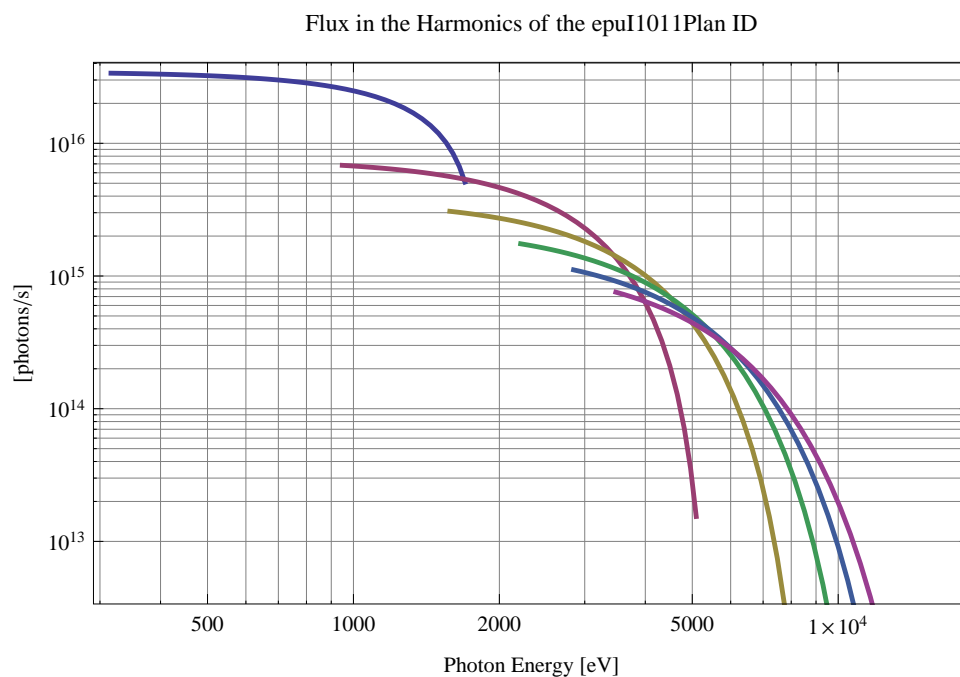


Figure 5.116: The flux of photons in the harmonics from the epuI1011Plan ID

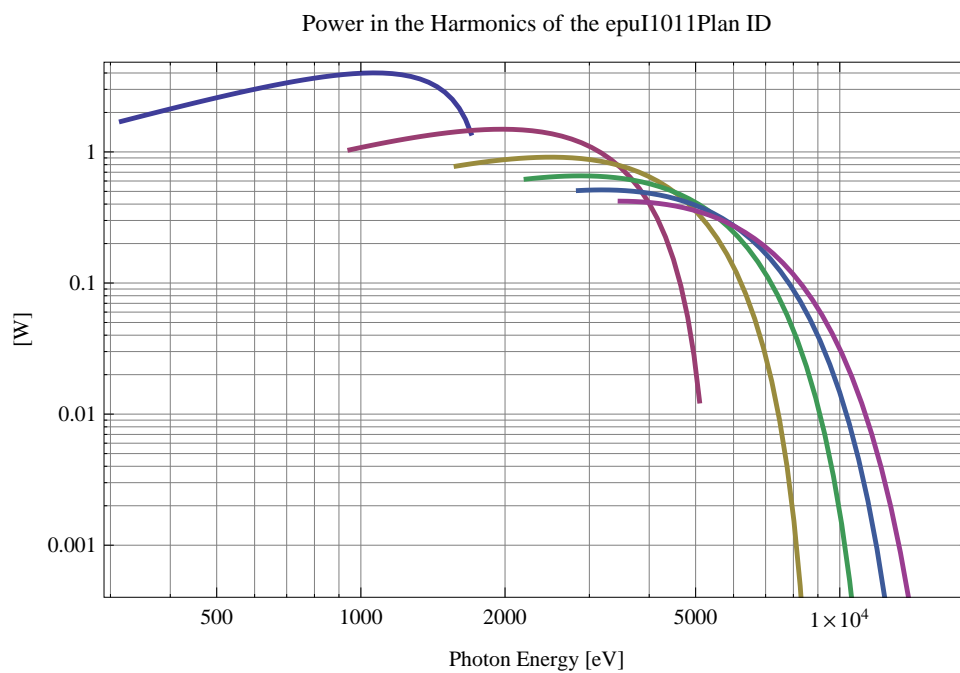


Figure 5.117: The power in the harmonics from the epuI1011Plan ID



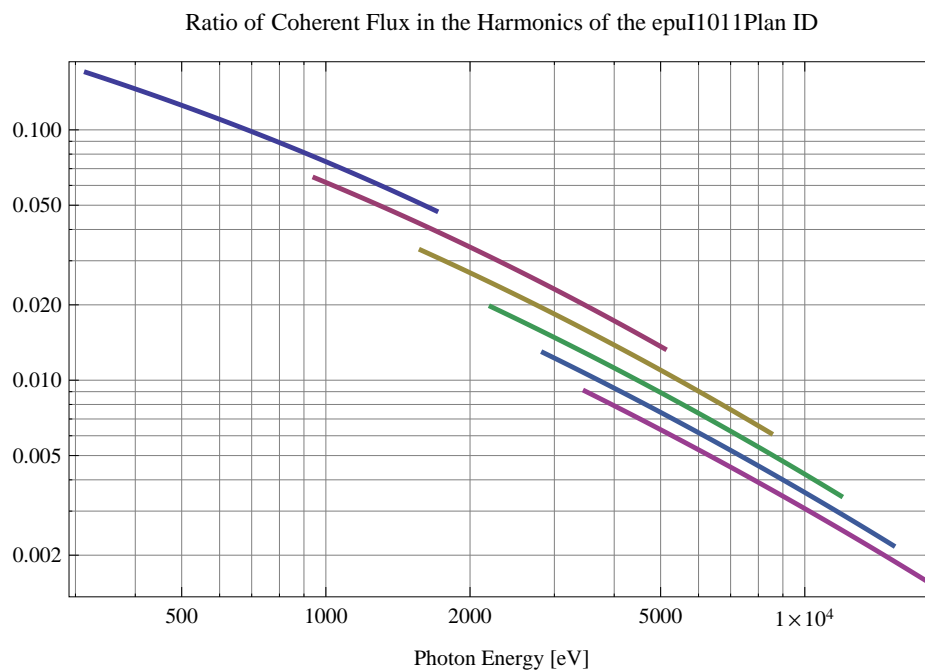


Figure 5.118: The ratio of coherent flux in the harmonics from the epuI1011Plan ID

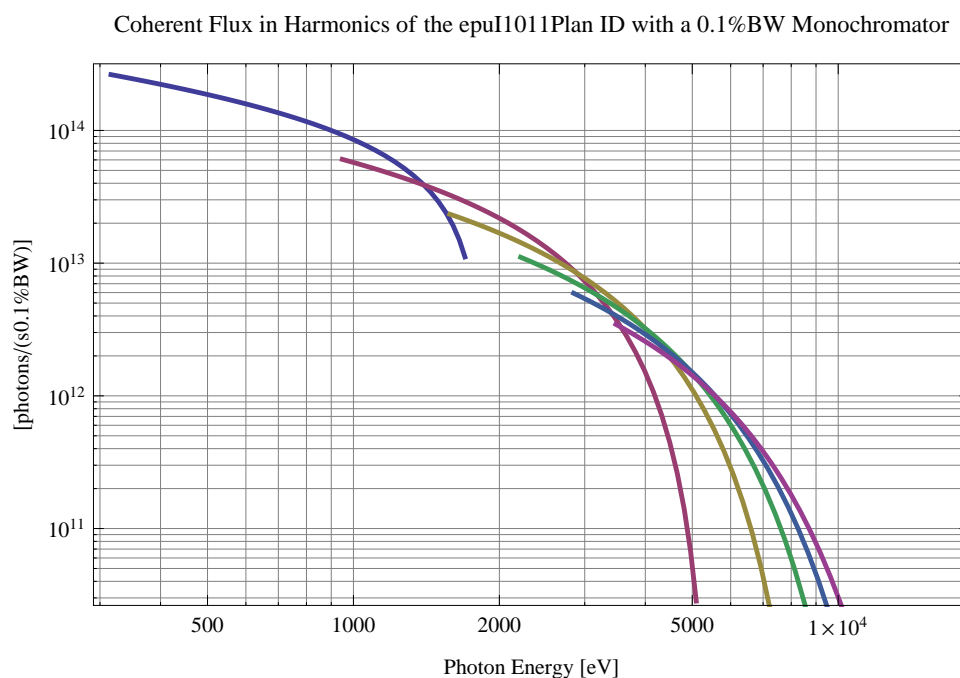


Figure 5.119: The coherent flux in the harmonics of the epuI1011Plan ID using a 0.1%BW Monochromator

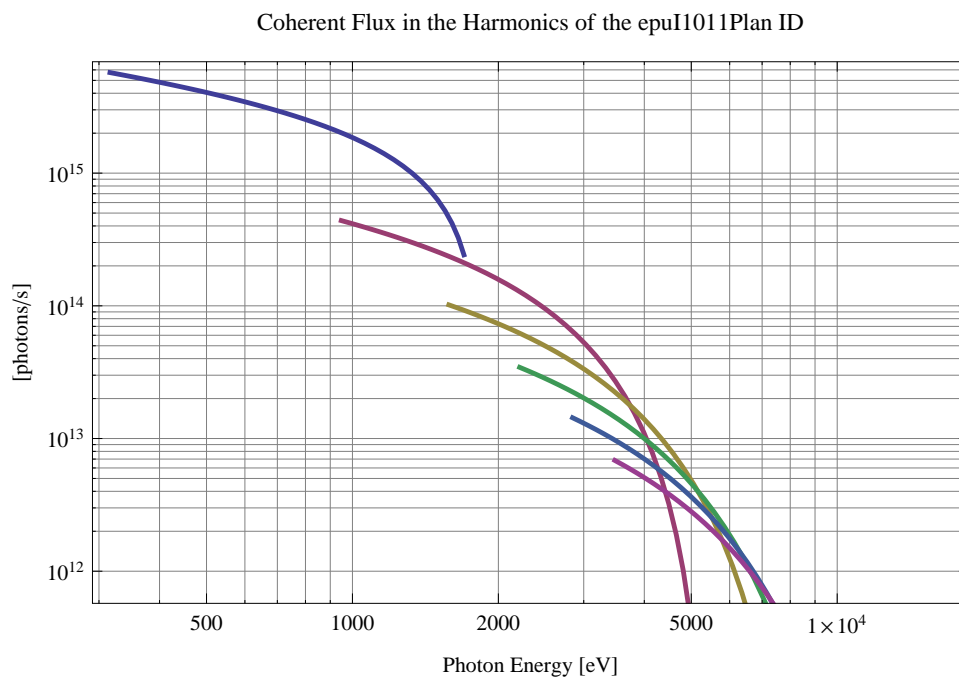


Figure 5.120: The coherent flux in the harmonics of the epuI1011Plan ID

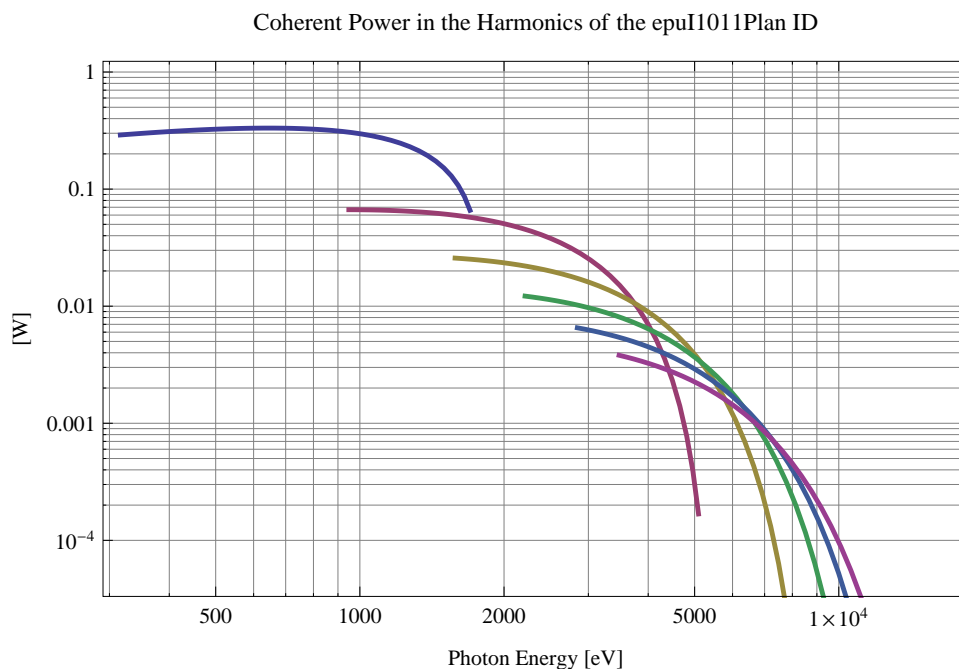


Figure 5.121: The power of coherent synchrotron radiation in the harmonics of the epuI1011Plan ID

Table 5.27: The brilliance at peak energy and the angular spectral flux density from the epuI1011Plan ID for different harmonics at minimum K-value (0.4)

Harmonic	Photon Energy [eV]	Brilliance [Ph./s/mrad <sup>2</sup> /mrad <sup>2</sup> /0.1%BW]	Angular Spectral Flux [Ph./s/mrad <sup>2</sup> /0.1%BW]
1	1698.21	$8.36 \times 10^{19}$	$1.56 \times 10^{17}$
3	5094.63	$1.92 \times 10^{18}$	$3.27 \times 10^{15}$
5	8491.06	$2.41 \times 10^{16}$	$4.07 \times 10^{13}$
7	11887.5	$2.65 \times 10^{14}$	$4.48 \times 10^{11}$
9	15283.9	$2.79 \times 10^{12}$	$4.72 \times 10^9$
11	18680.3	$2.88 \times 10^{10}$	$4.89 \times 10^7$

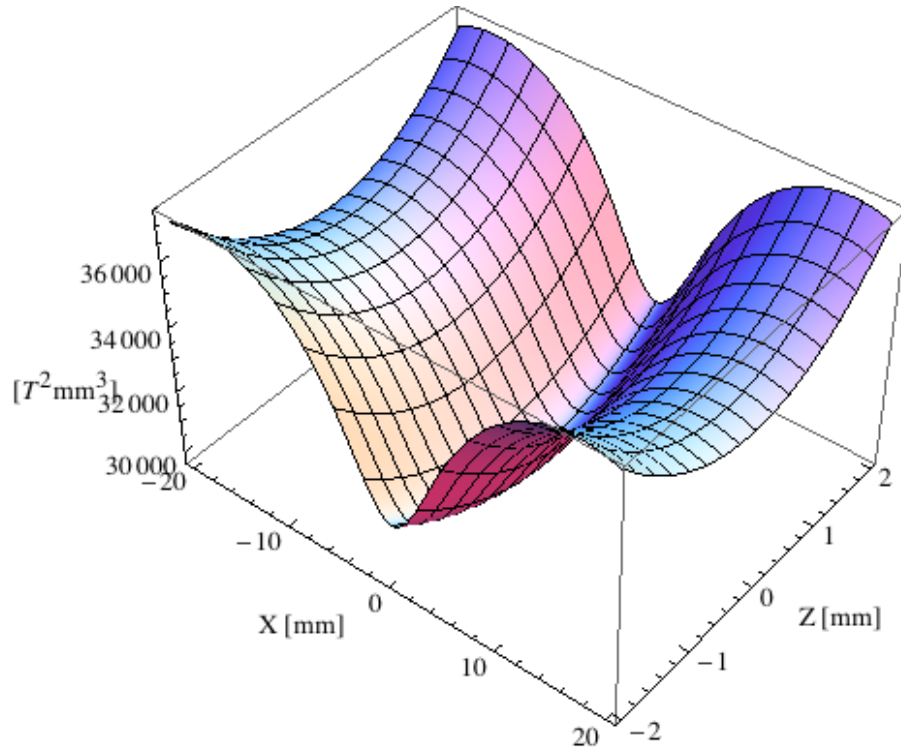


Figure 5.122: Focusing potential from the epuI1011Plan ID over the beam stay clear aperture.

### Influence from the epuI1011Plan ID on the optics of the stored beam

Figure 5.122 shows the focusing potential from the epuI1011Plan over the beam stay clear aperture of the ring aperture.

Figure 5.123 shows the kick map in the beam energy independent unit  $T^2 m^2$  of the kicks induced by the epuI1011Plan ID over the beam stay clear aperture.

Figure 5.124 shows the induced angular kick on the stored beam from the epuI1011Plan ID as a function of the vertical distance to the axis of the ID.

Figure 5.125 shows the induced angular kick on the stored beam from the epuI1011Plan ID as a function of the horizontal distance to the axis of the ID.

Figure 5.126 shows tune shift induced by the epuI1011Plan ID over the beam stay clear aperture. Note that the tune shift depends on the beam size at the ID.

Figure 5.127 shows the induced tune shift from the epuI1011Plan ID as a function of the vertical distance to the axis of the ID.

Figure 5.128 shows the induced tune shift from the epuI1011Plan ID as a function of the horizontal distance to the axis of the ID.

### Magnet model of the elliptically polarising undulator epuI1011Heli

The Radia [2] magnet model of the epuI1011Heli ID is shown in Figure 5.129. The length of the magnet model is 387.26 mm. The magnetic material in the model is NdFeb with a remanence of 1.22 T. Blocks with vertical magnetisation are blue and blocks with horizontal magnetisation

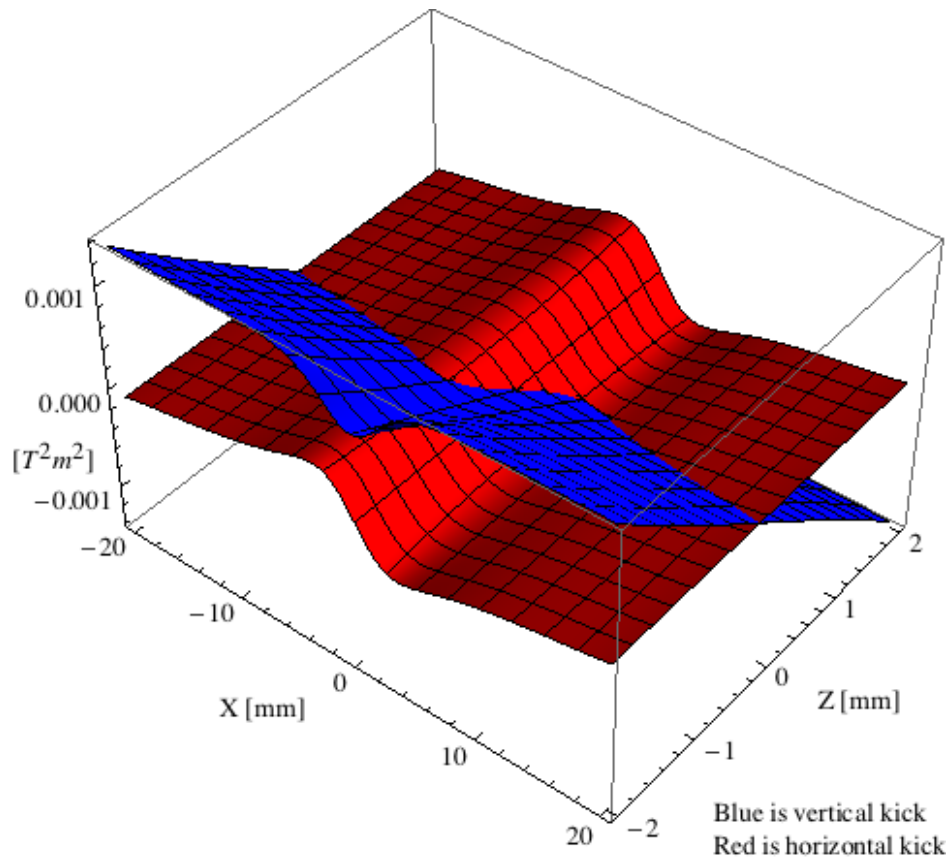


Figure 5.123: Kick map in the beam energy independent unit  $T^2m^2$  of the kicks induced by the epuI1011Plan ID over the beam stay clear aperture.

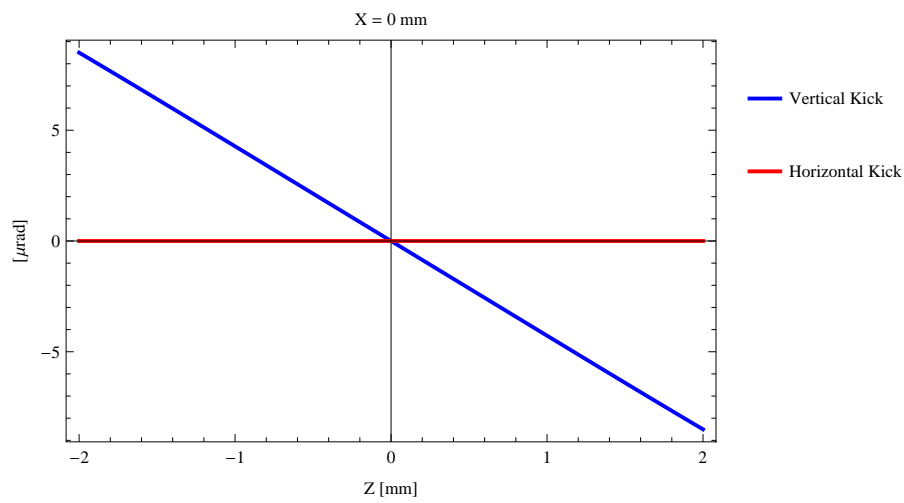


Figure 5.124: Induced angular kick on the stored beam from the epuI1011Plan ID as a function of the vertical distance to the ID axis.

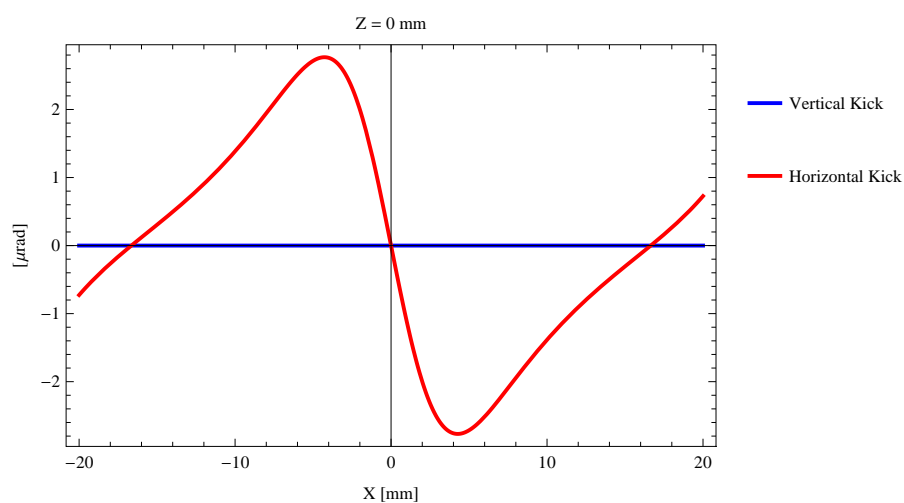


Figure 5.125: Induced angular kick on the stored beam from the epuI1011Plan ID as a function of the horizontal distance to the ID axis.

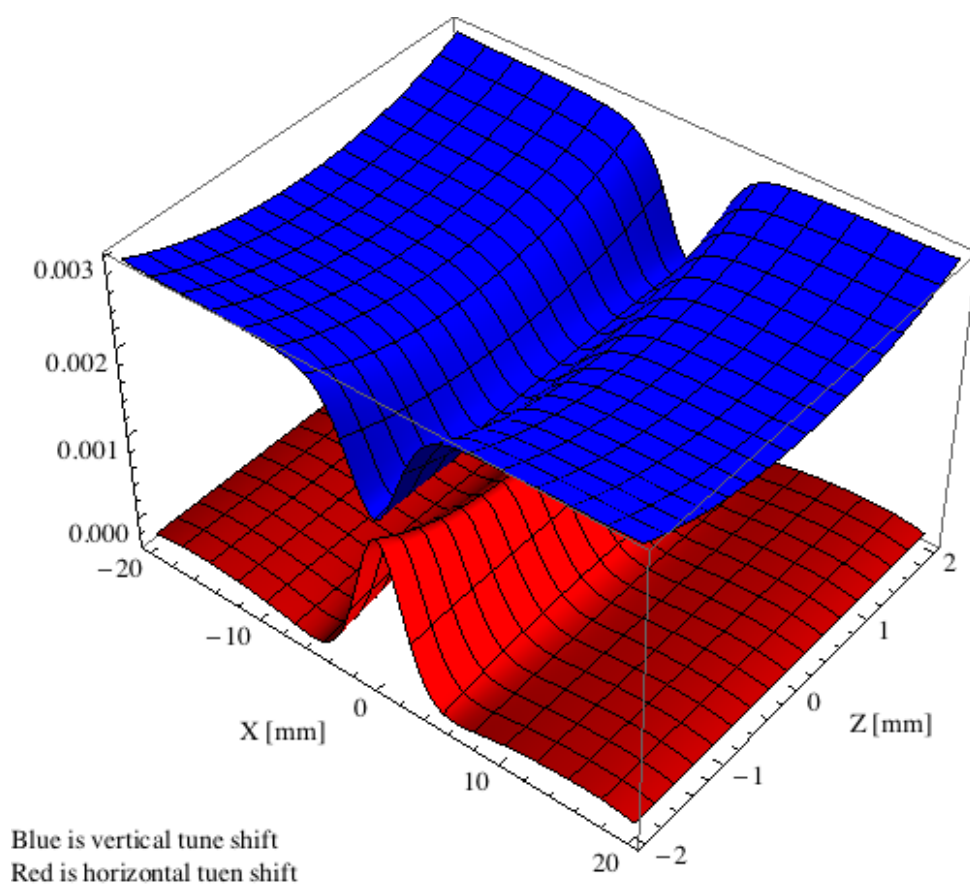


Figure 5.126: Tune shift induced by the epuI1011Plan ID over the beam stay clear aperture.

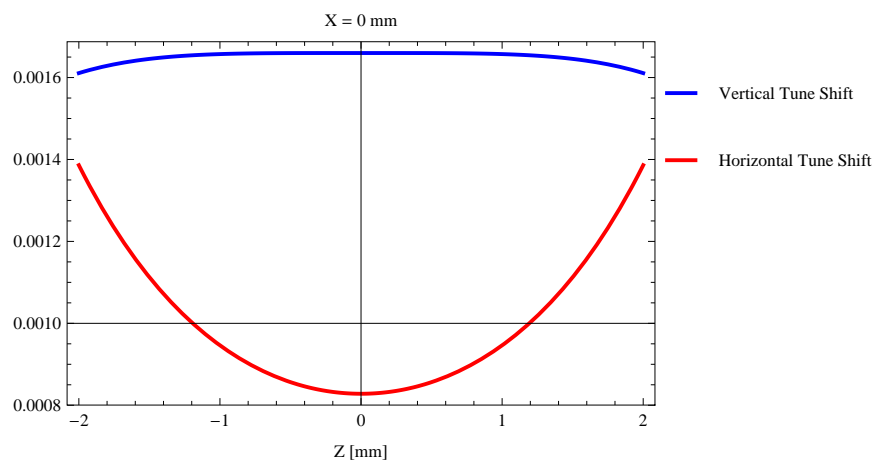


Figure 5.127: Induced tune shift from the epuI1011Plan ID as a function of the vertical distance to the axis of the ID.

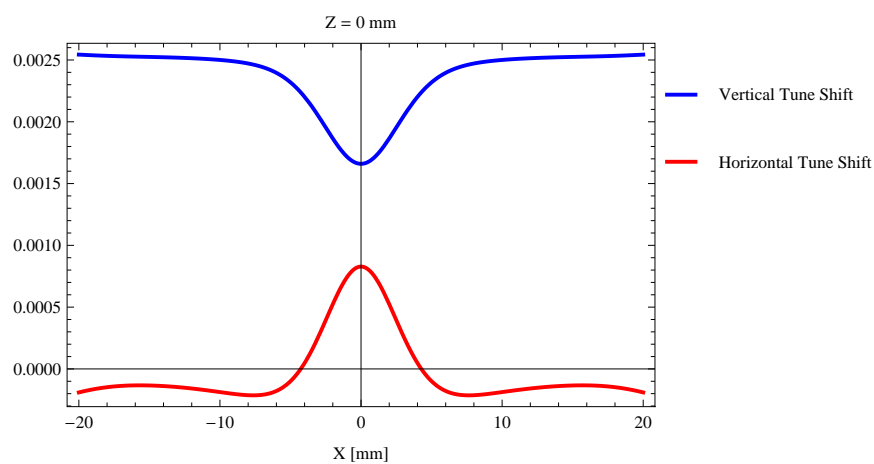


Figure 5.128: Induced tune shift from the epuI1011Plan ID on the stored beam from the ID as a function of the horizontal distance to the axis of the ID.

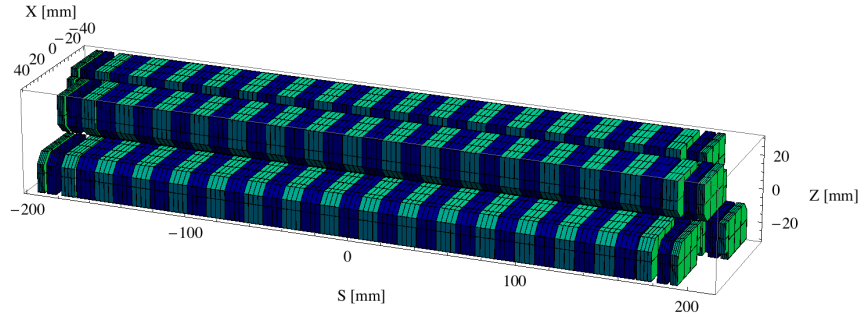


Figure 5.129: Magnetic model of the epuI1011Heli ID. The ID has been modelled with Radia [2]

are green. This is the existing undulator at the I1011 beamline at the MAX II storage ring. The total length of the epuI1011Heli ID is 2134.76 mm.

### Analysis of the magnetic field of the epuI1011Heli ID

The effective magnetic fields on axis and the fundamental photon energy of the epuI1011Heli ID are shown in Table 5.28. The higher harmonic contents in the magnetic field of an elliptically polarising undulator made of permanent magnets is negligible and the efficient field has about the same strength as the peak field.

Table 5.28: Effective Fields on axis and Fundamental Photon Energy of the epuI1011Heli ID

Undulator Period	46.6	mm
Undulator Gap	14	mm
Undulator Mode	Helical	
Undulator Phase	13.949	mm
Vertical Peak Field	0.417	T
Efficient Vertical Field	0.418	T
K <sub>x</sub> (from vert. field)	1.819	
Horizontal Peak Field:	0.418	T
Efficient Horizontal Field	0.418	T
K <sub>z</sub> (from hor. field)	1.819	
Photon Energy, Harm.1	0.426	keV
Emitted Power	2.124	kW
Total Length	2134.8	mm

### Synchrotron radiation from the epuI1011Heli ID

The power map of the emitted synchrotron radiation by the epuI1011Heli ID, assuming a 0.5 A filament beam with an energy of 3 GeV and undulator properties of the synchrotron radiation, is shown in Figure 5.134. The on-axis power density is 0.858 kW/mrad<sup>2</sup>

A map of the degree of linear polarisation of the fundamental harmonic of the synchrotron radiation emitted by the epuI1011Heli ID over the angle of observation is shown in Figure 5.135.

A map of the degree of 45 degree polarisation of the fundamental harmonic of the synchrotron radiation emitted by the epuI1011Heli ID over the angle of observation is shown in Figure 5.136.



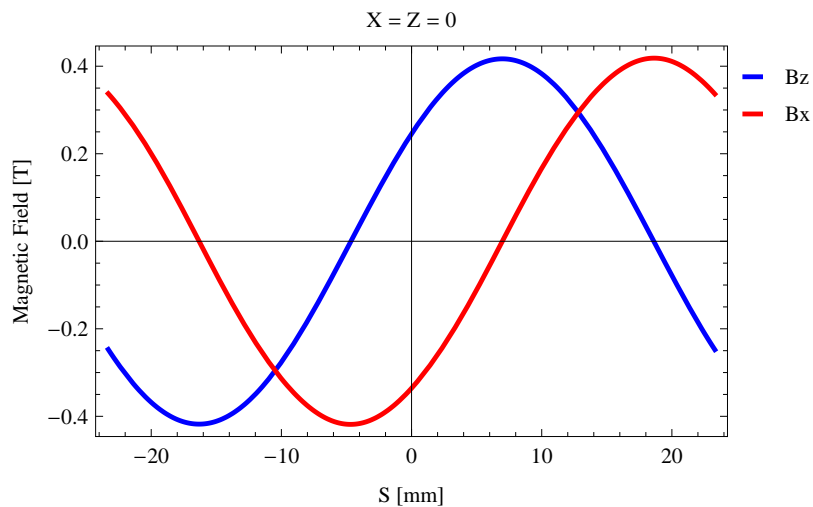


Figure 5.130: Vertical magnetic field in a central pole of the epuI1011Heli ID along the ID axis,  $X = Z = 0$

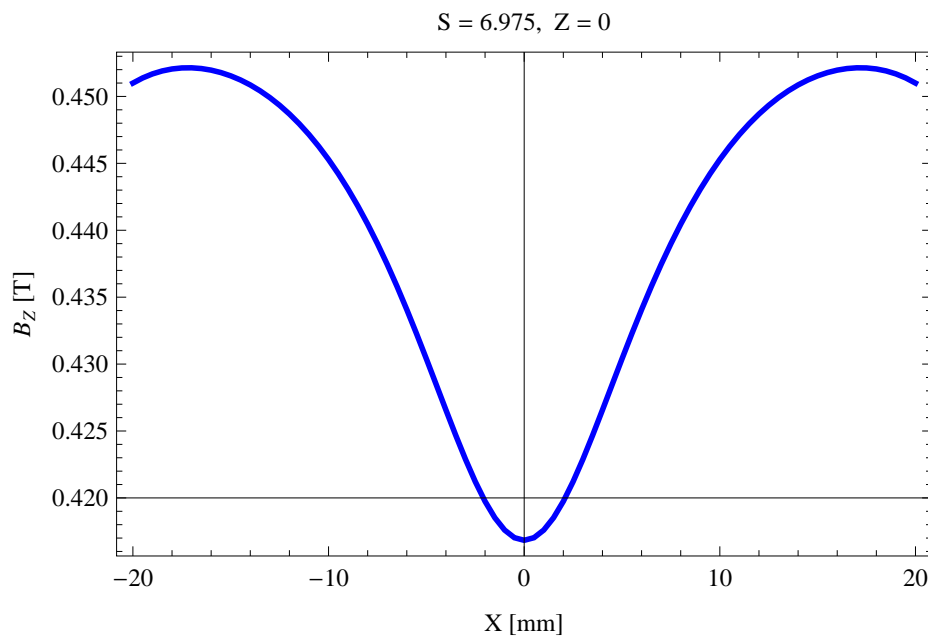


Figure 5.131: Vertical magnetic field in a central pole of the epuI1011Heli ID along the horizontally transverse direction to the ID axis,  $S = 6.975$ ,  $Z = 0$

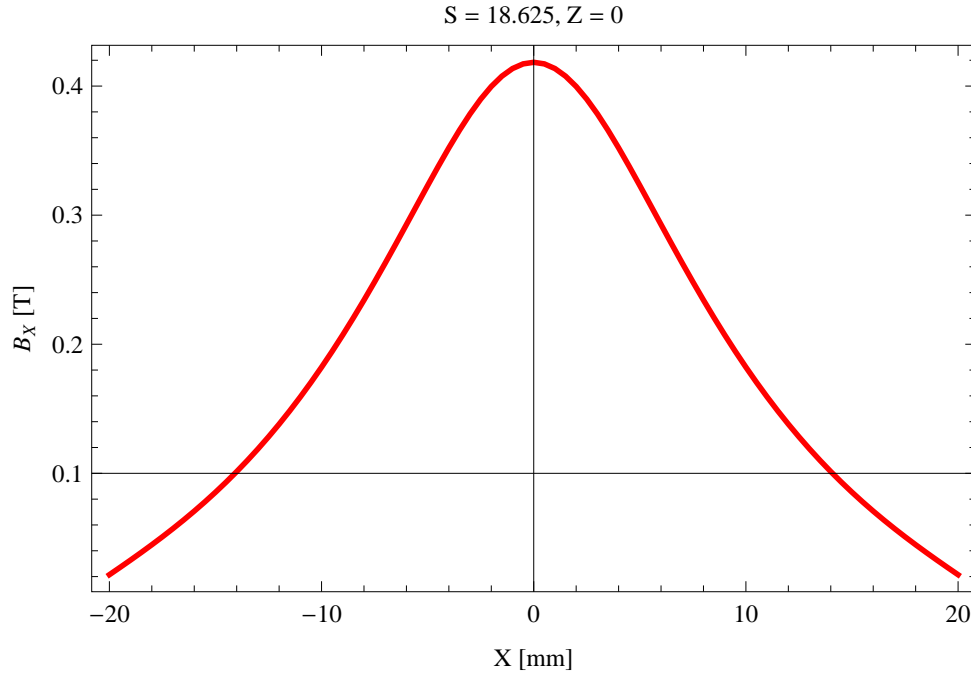


Figure 5.132: Horizontal magnetic field in a central pole of the epuI1011Heli ID along the horizontally transverse direction to the ID axis,  $S = 18.625$ ,  $Z = 0$

A map of the degree of circular polarisation of the fundamental harmonic of the synchrotron radiation emitted by the epuI1011Heli ID over the angle of observation is shown in Figure 5.137.

The on axis brilliance at peak energy, the angular spectral flux, the flux in the harmonics, the power in the harmonics, the ratio of coherence, the coherent flux in the harmonics, and the power of coherent radiation in the harmonics from the epuI1011Heli ID have been calculated and the resulting plots are found in this section of the document. The beam parameters used for the calculation are 0.5 A of stored current,  $\beta_H = 9$  m,  $\varepsilon_H = 0.263$  nmrad,  $\beta_V = 4.8$  m,  $\varepsilon_V = 8$  pmrad, and an energy spread of 0.001.

The brilliance at peak energy and the angular spectral flux density from the epuI1011Heli ID for different harmonics at maximum K-value (2.573) are given in Table 5.29 and for minimum K-value (0.400) these values are given in Table 5.30.

Table 5.29: The brilliance at peak energy and the angular spectral flux density from the epuI1011Heli ID for different harmonics at maximum K-value (2.573)

Harmonic	Photon Energy [eV]	Brilliance [Ph./s/mrad <sup>2</sup> /mrad <sup>2</sup> /0.1%BW]	Angular Spectral Flux [Ph./s/mrad <sup>2</sup> /0.1%BW]
1	425.545	$1. \times 10^{20}$	$2.62 \times 10^{17}$

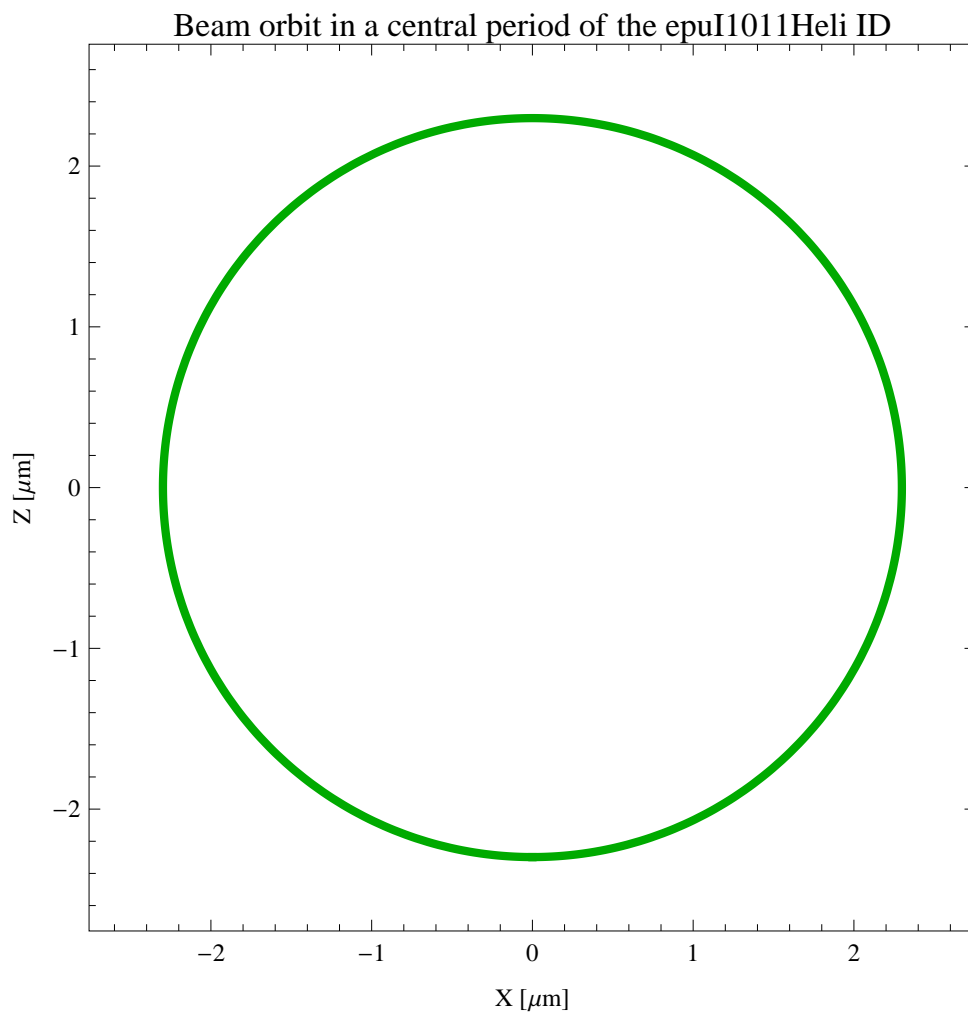


Figure 5.133: The beam orbit of the electron beam through a central period of the epuI1011Heli ID

Table 5.30: The brilliance at peak energy and the angular spectral flux density from the epuI1011Heli ID for different harmonics at minimum K-value (0.4)

Harmonic	Photon Energy [eV]	Brilliance [Ph./s/mrad <sup>2</sup> /mrad <sup>2</sup> /0.1%BW]	Angular Spectral Flux [Ph./s/mrad <sup>2</sup> /0.1%BW]
1	1698.21	$8.36 \times 10^{19}$	$1.56 \times 10^{17}$

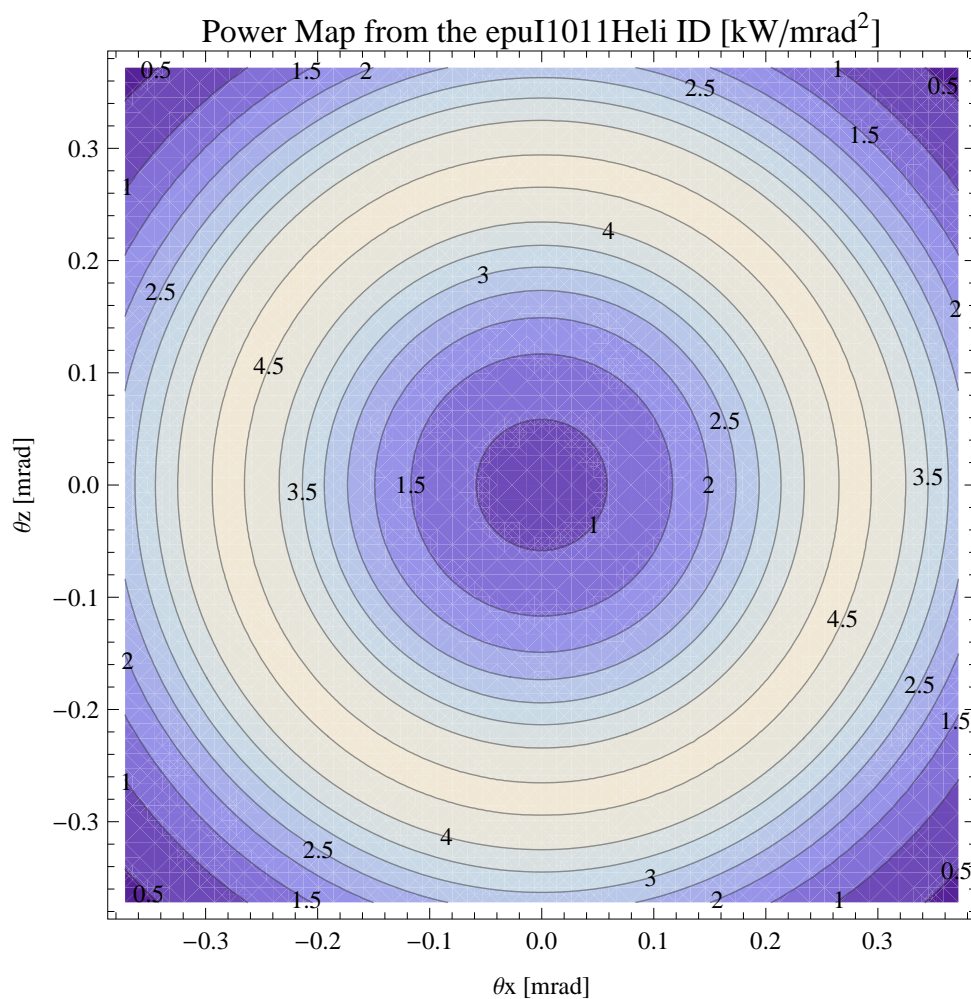


Figure 5.134: Map of the power distribution of the emitted synchrotron radiation by the epuI1011Heli ID

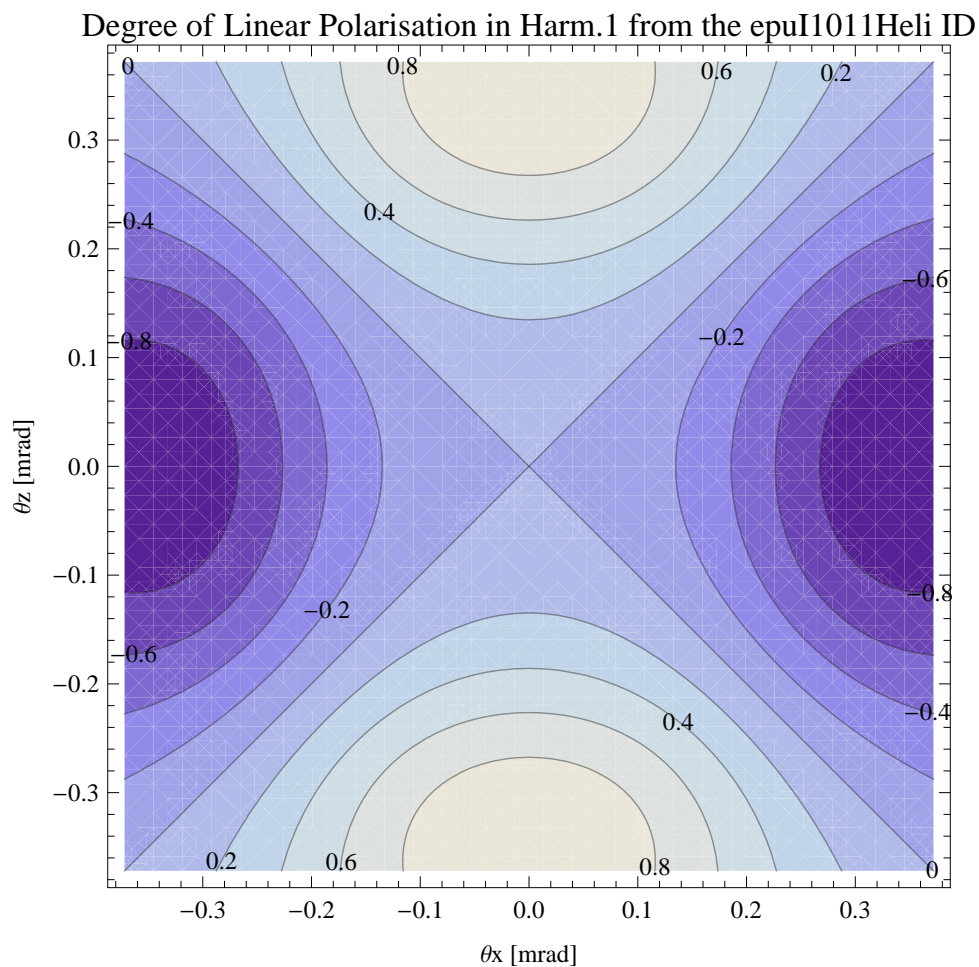


Figure 5.135: Map of linear polarisation in the fundamental harmonic of the synchrotron radiation emitted by the epuI1011Heli ID

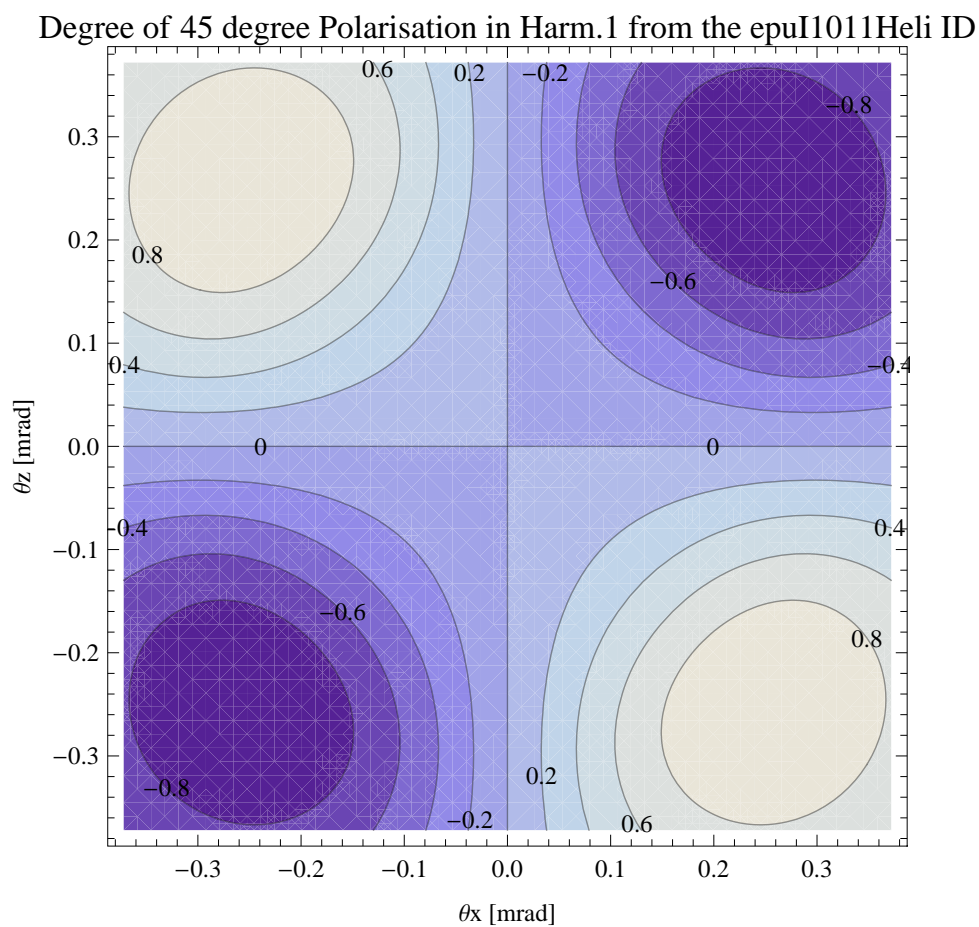


Figure 5.136: Map of 45 degree polarisation in the fundamental harmonic of the synchrotron radiation emitted by the epul1011Heli ID

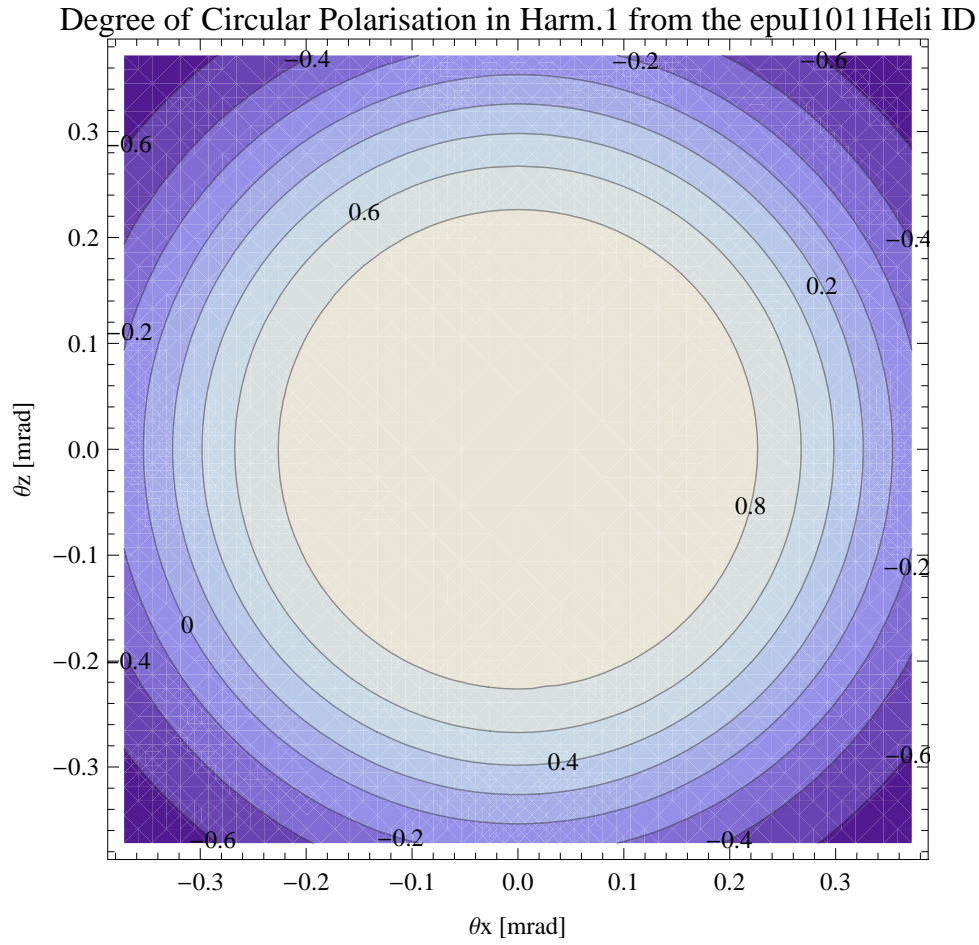


Figure 5.137: Map of circular polarisation in the fundamental harmonic of the synchrotron radiation emitted by the epuI1011Heli ID

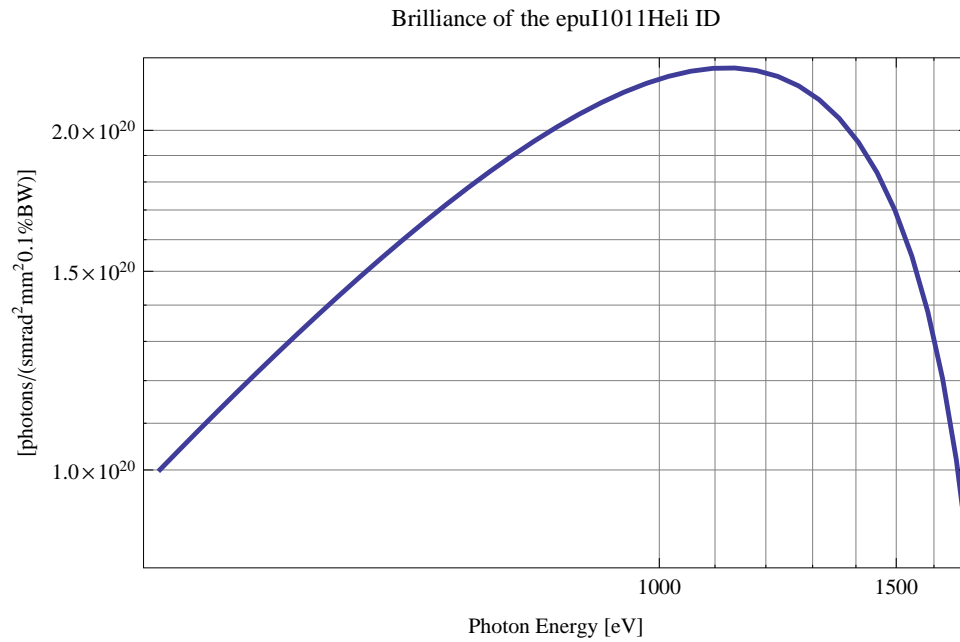


Figure 5.138: The brilliance at peak energy from the epuI1011Heli ID

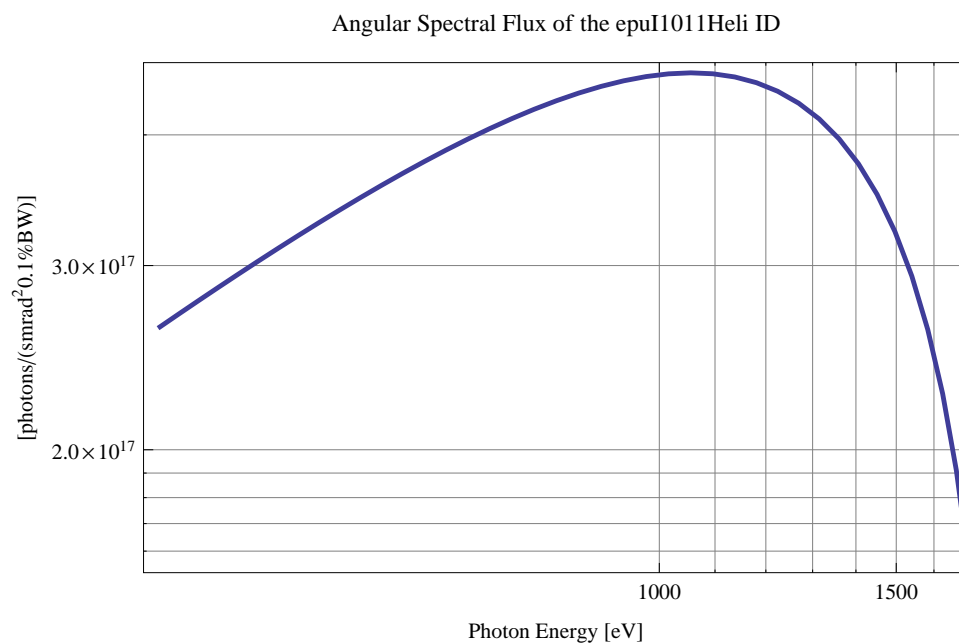


Figure 5.139: The angular spectral flux from the epuI1011Heli ID

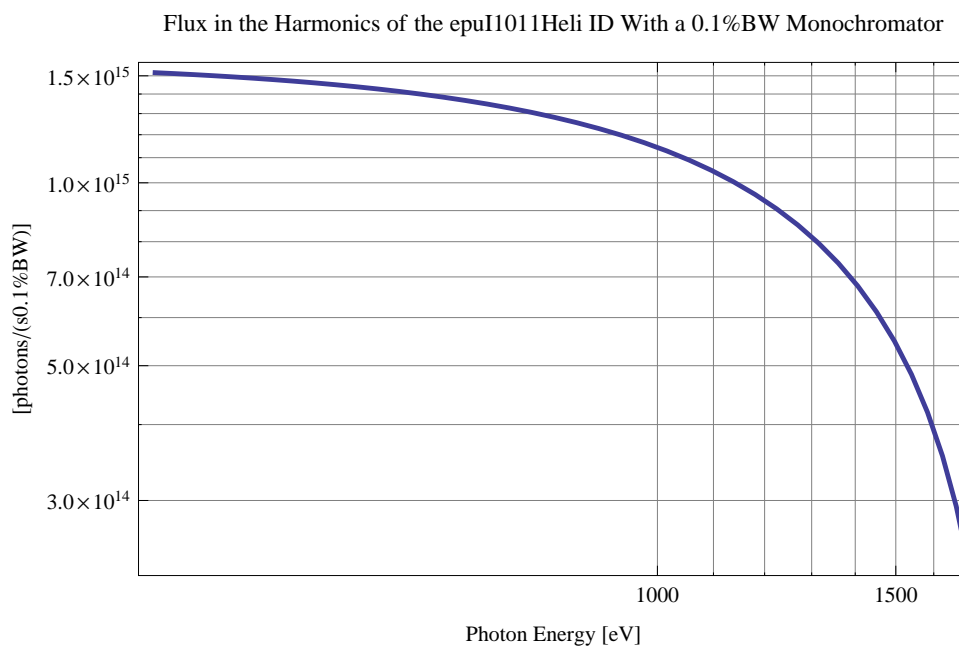


Figure 5.140: The flux of photons in the harmonics from the epuI1011Heli ID using a 0.1%BW monochromator



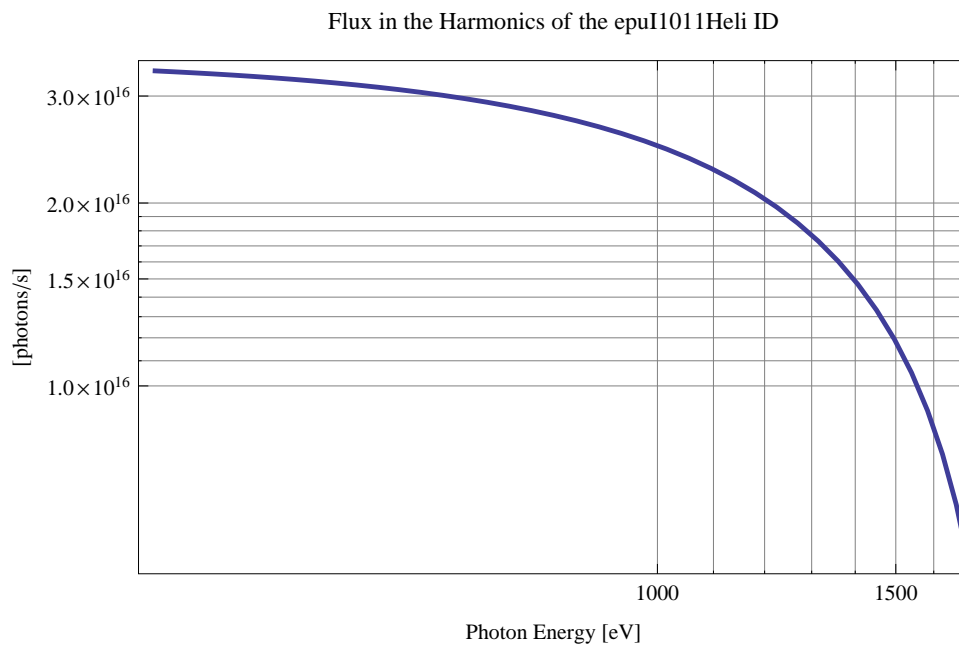


Figure 5.141: The flux of photons in the harmonics from the epuI1011Heli ID

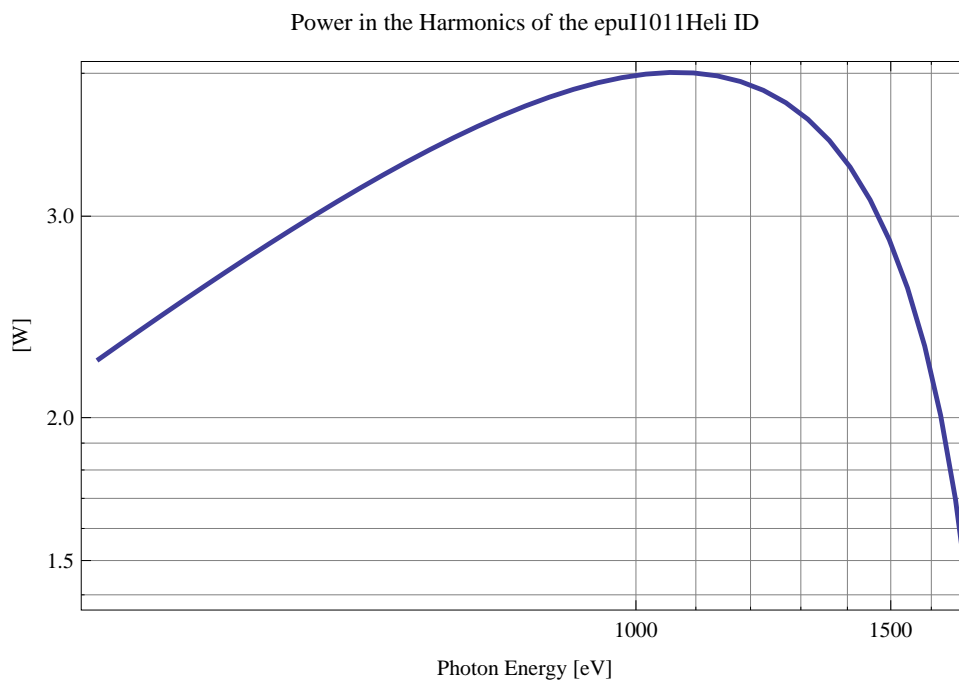


Figure 5.142: The power in the harmonics from the epuI1011Heli ID

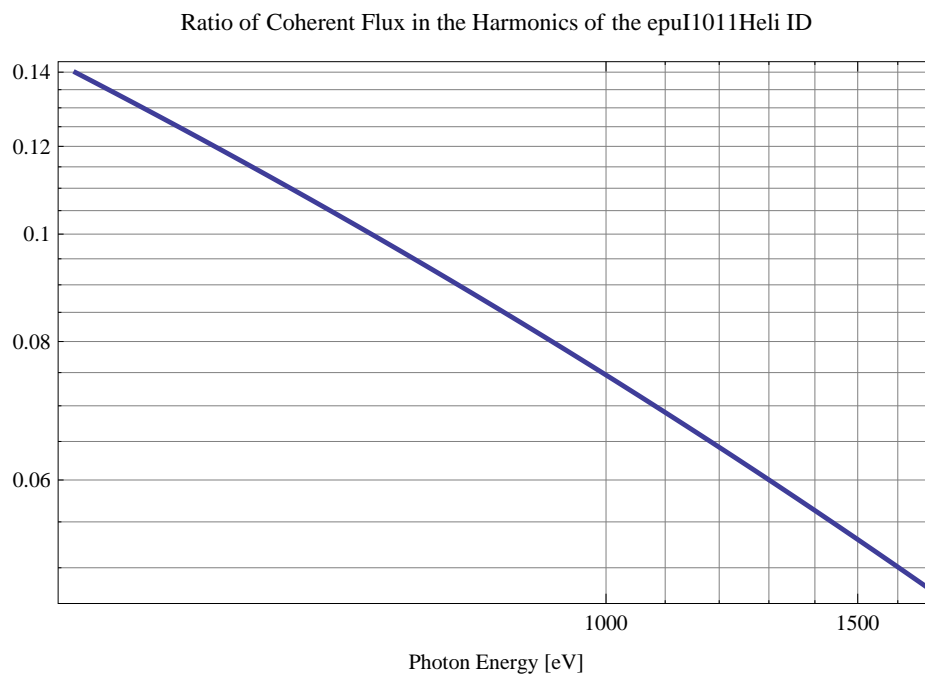


Figure 5.143: The ratio of coherent flux in the harmonics from the epuI1011Heli ID

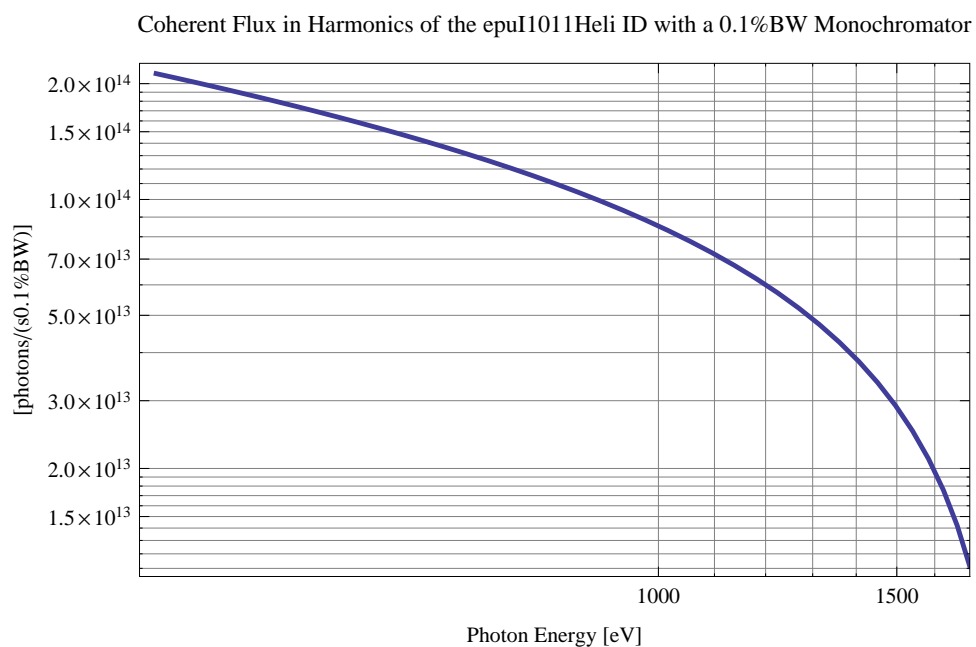


Figure 5.144: The coherent flux in the harmonics of the epuI1011Heli ID using a 0.1%BW Monochromator

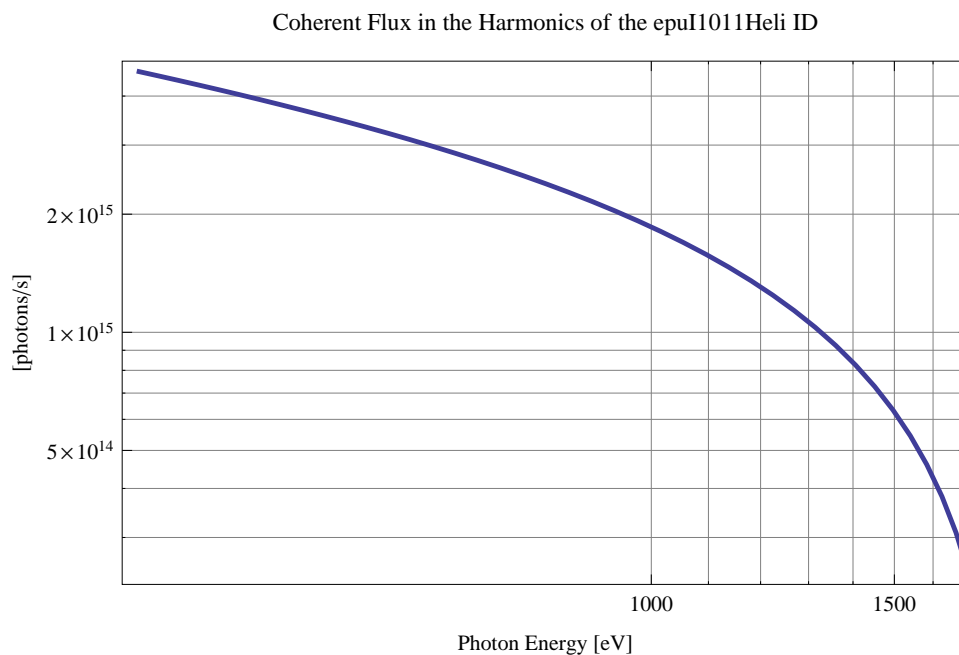


Figure 5.145: The coherent flux in the harmonics of the epuI1011Heli ID

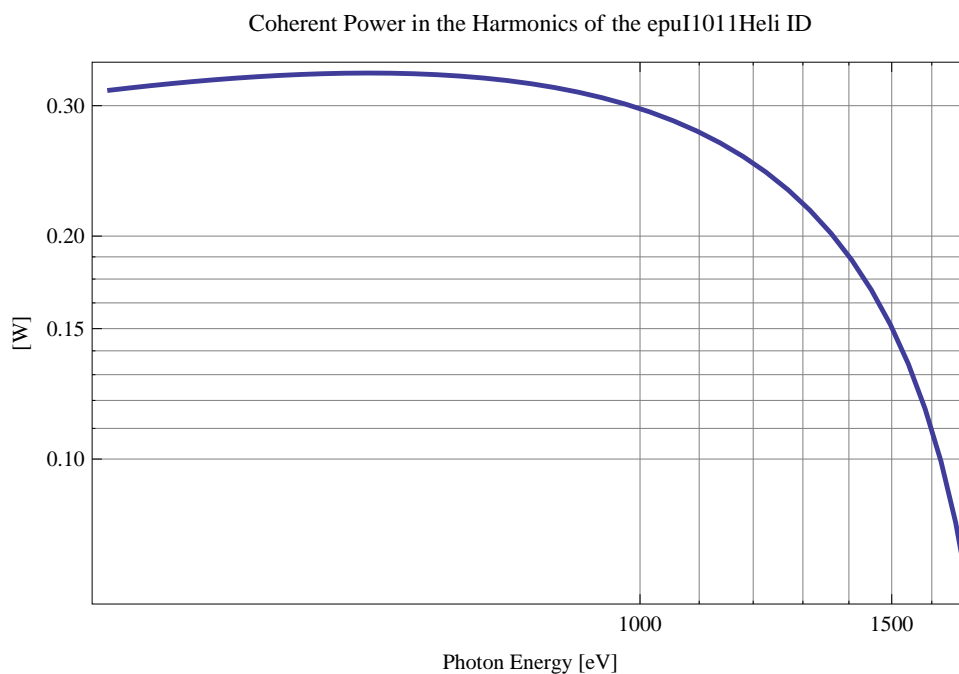


Figure 5.146: The power of coherent synchrotron radiation in the harmonics of the epuI1011Heli ID

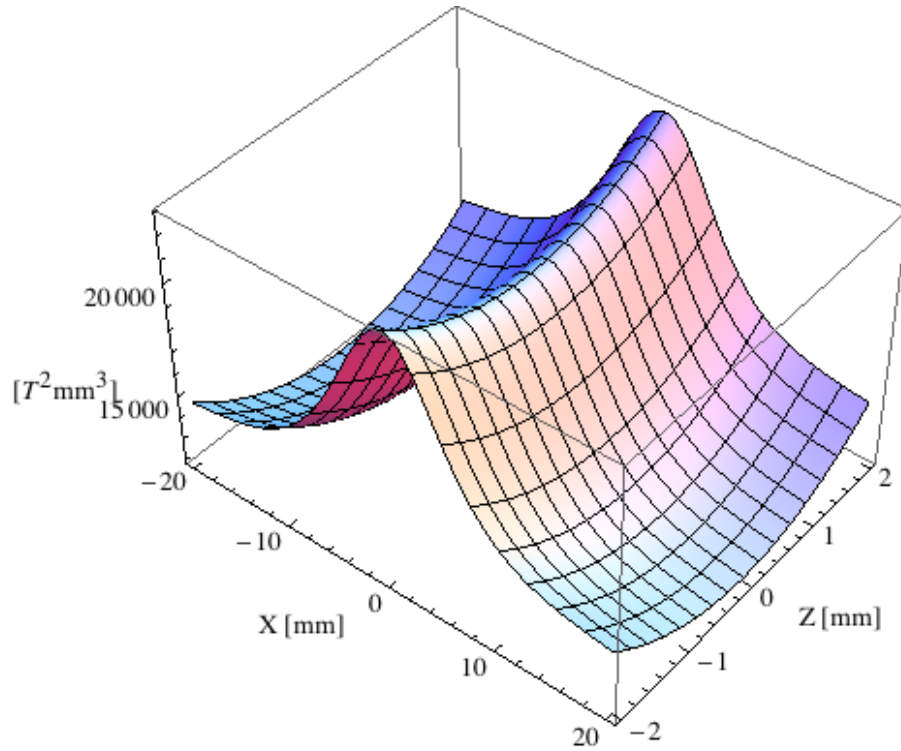


Figure 5.147: Focusing potential from the epuI1011Heli ID over the beam stay clear aperture.

### Influence from the epuI1011Heli ID on the optics of the stored beam

Figure 5.147 shows the focusing potential from the epuI1011Heli over the beam stay clear aperture of the ring aperture.

Figure 5.148 shows the kick map in the beam energy independent unit  $T^2 m^2$  of the kicks induced by the epuI1011Heli ID over the beam stay clear aperture.

Figure 5.149 shows the induced angular kick on the stored beam from the epuI1011Heli ID as a function of the vertical distance to the axis of the ID.

Figure 5.150 shows the induced angular kick on the stored beam from the epuI1011Heli ID as a function of the horizontal distance to the axis of the ID.

Figure 5.151 shows tune shift induced by the epuI1011Heli ID over the beam stay clear aperture. Note that the tune shift depends on the beam size at the ID.

Figure 5.152 shows the induced tune shift from the epuI1011Heli ID as a function of the vertical distance to the axis of the ID.

Figure 5.153 shows the induced tune shift from the epuI1011Heli ID as a function of the horizontal distance to the axis of the ID.

### Magnet model of the elliptically polarising undulator epuI1011Incl

The Radia [2] magnet model of the epuI1011Incl ID is shown in Figure 5.154. The length of the magnet model is 387.26 mm. The magnetic material in the model is NdFeb with a remanence of 1.22 T. Blocks with vertical magnetisation are blue and blocks with horizontal magnetisation

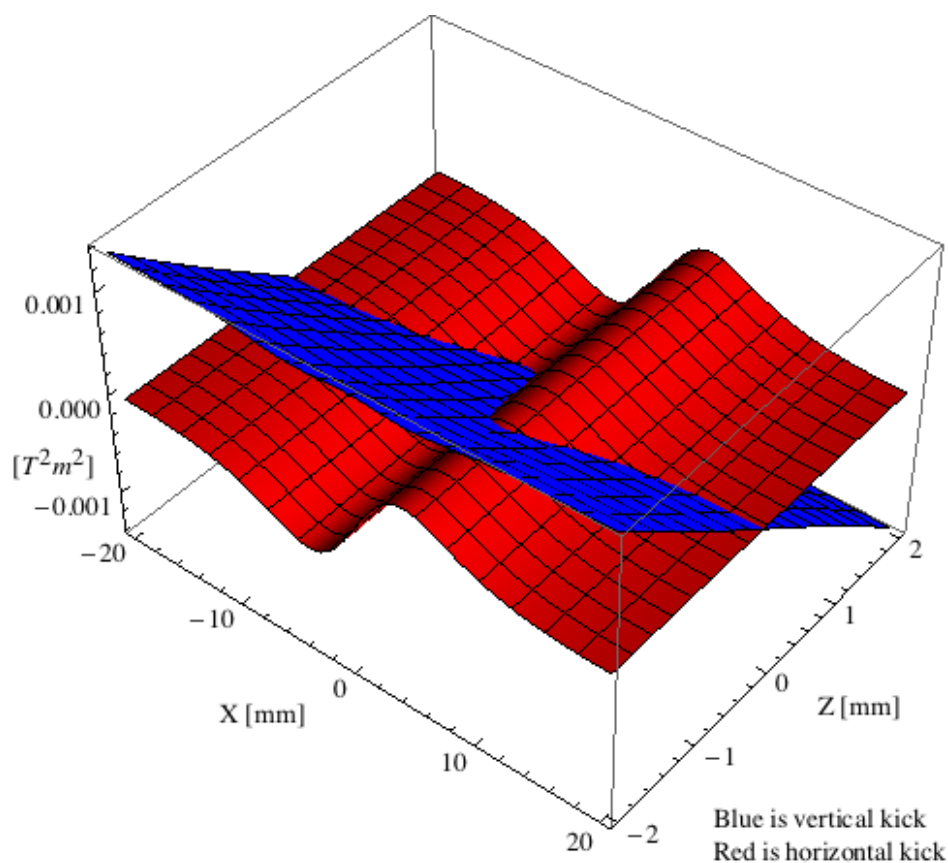


Figure 5.148: Kick map in the beam energy independent unit  $T^2m^2$  of the kicks induced by the epuI1011Heli ID over the beam stay clear aperture.

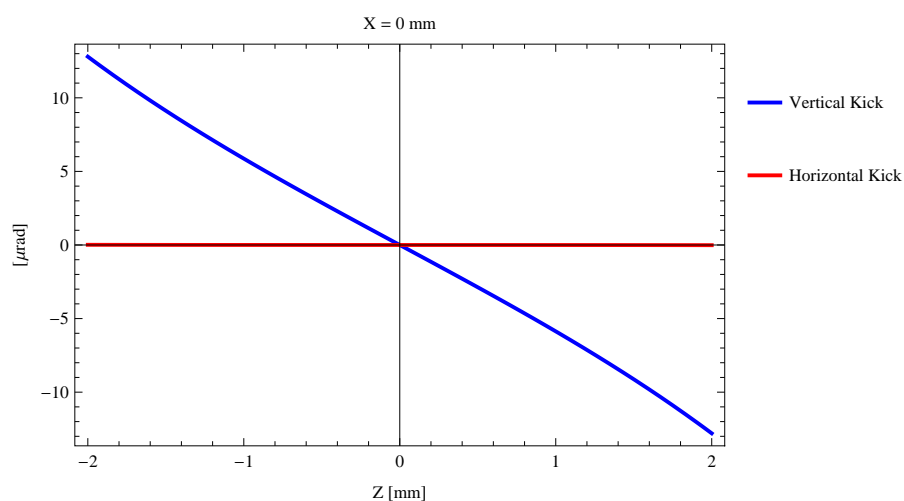


Figure 5.149: Induced angular kick on the stored beam from the epuI1011Heli ID as a function of the vertical distance to the ID axis.

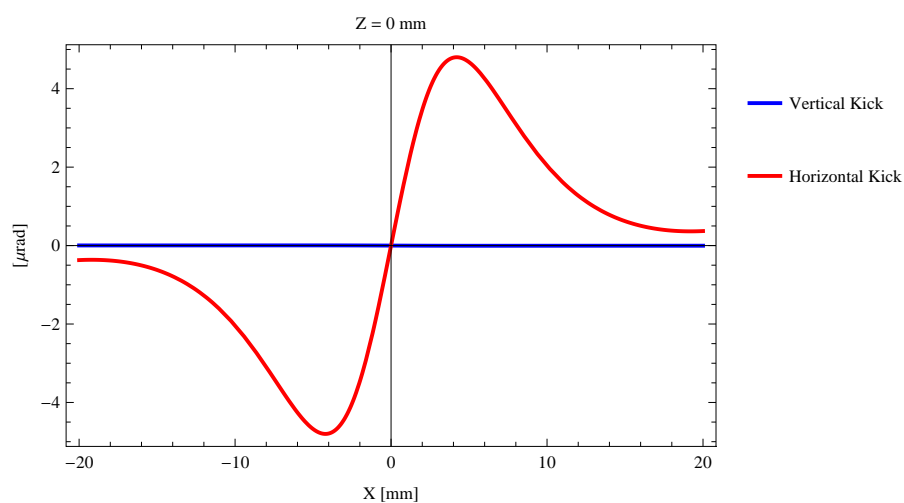


Figure 5.150: Induced angular kick on the stored beam from the epuI1011Heli ID as a function of the horizontal distance to the ID axis.

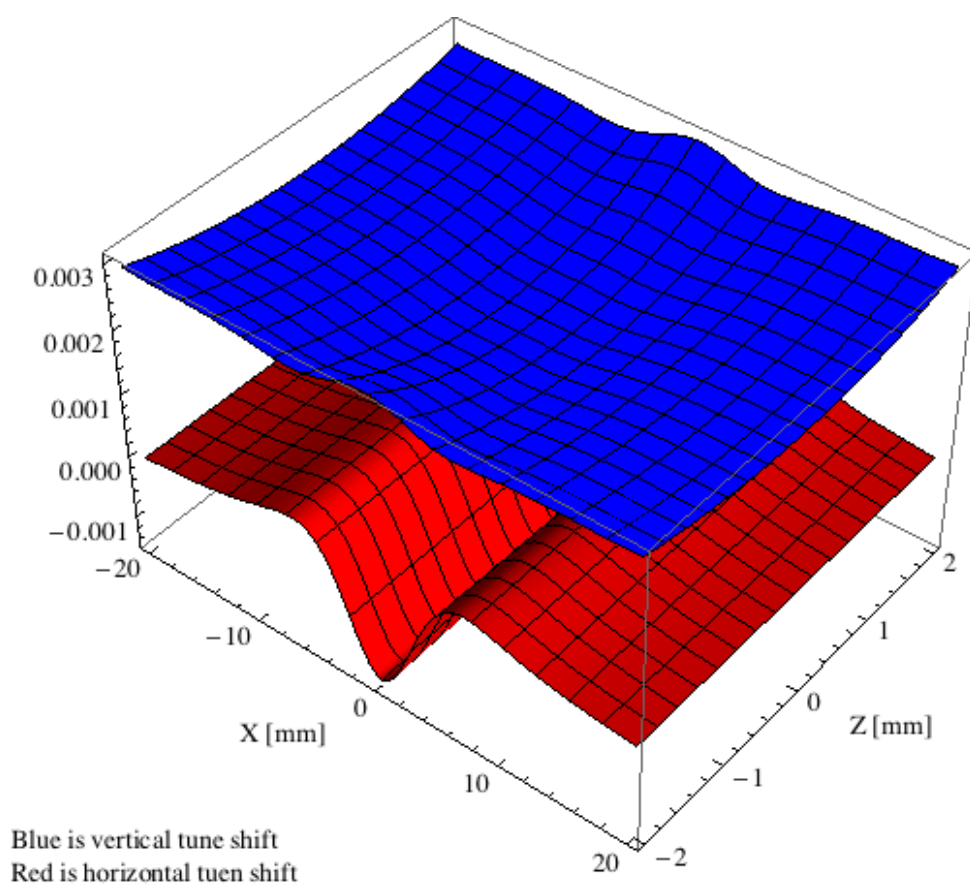


Figure 5.151: Tune shift induced by the epuI1011Heli ID over the beam stay clear aperture.

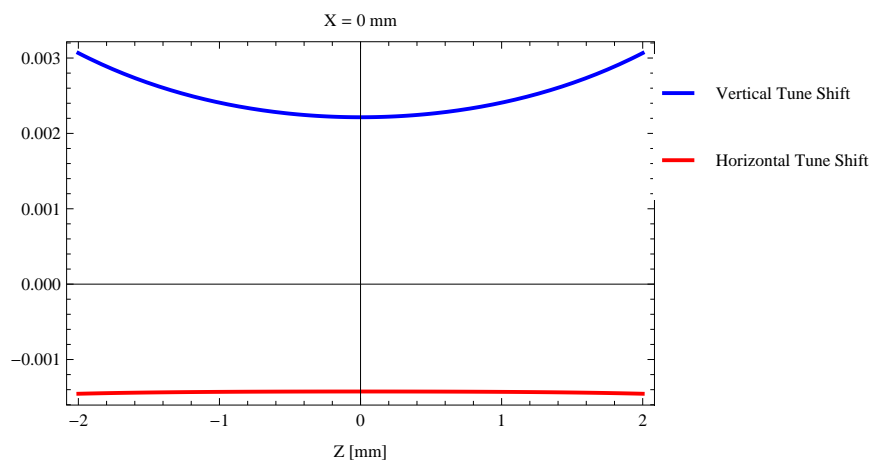


Figure 5.152: Induced tune shift from the epuI1011Heli ID as a function of the vertical distance to the axis of the ID.

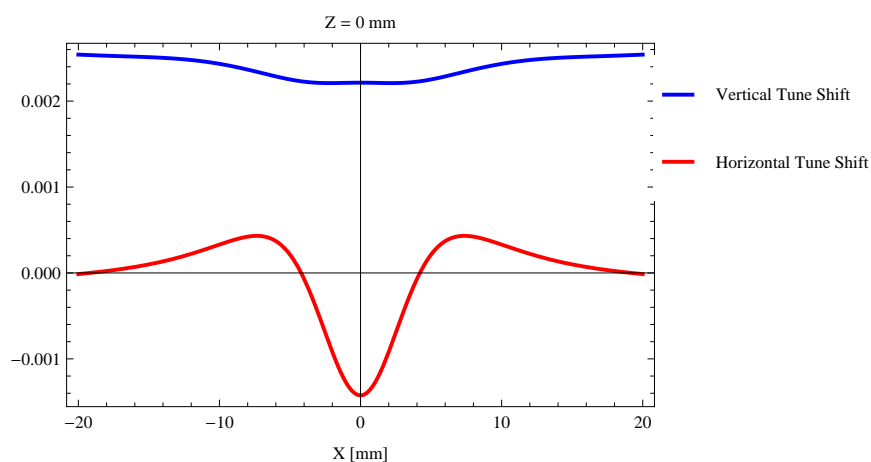


Figure 5.153: Induced tune shift from the epuI1011Heli ID on the stored beam from the ID as a function of the horizontal distance to the axis of the ID.

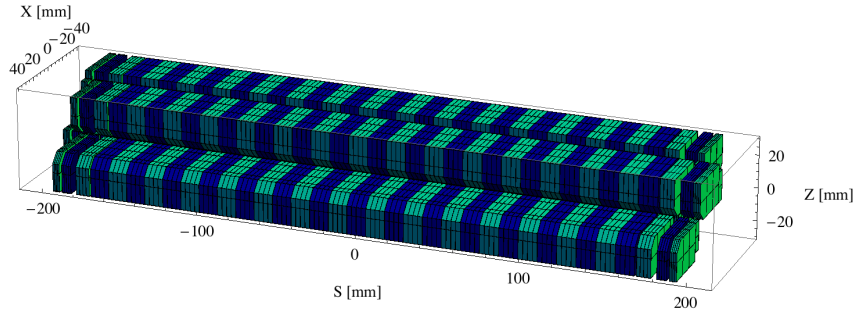


Figure 5.154: Magnetic model of the epuI1011Incl ID. The ID has been modelled with Radia [2]

are green. This is the existing undulator at the I1011 beamline at the MAX II storage ring. The total length of the epuI1011Incl ID is 2134.76 mm.

### Analysis of the magnetic field of the epuI1011Incl ID

The effective magnetic fields on axis and the fundamental photon energy of the epuI1011Incl ID are shown in Table 5.31. The higher harmonic contents in the magnetic field of an elliptically polarising undulator made of permanent magnets is negligible and the efficient field has about the same strength as the peak field.

Table 5.31: Effective Fields on axis and Fundamental Photon Energy of the epuI1011Incl ID

Undulator Period	46.6	mm
Undulator Gap	14	mm
Undulator Mode	Inclined	
Undulator Phase	12.813	mm
Vertical Peak Field	0.298	T
Efficient Vertical Field	0.299	T
K <sub>x</sub> (from vert. field)	1.301	
Horizontal Peak Field:	-0.298	T
Efficient Horizontal Field	0.299	T
K <sub>z</sub> (from hor. field)	1.301	
Photon Energy, Harm.1	0.681	keV
Emitted Power	1.087	kW
Total Length	2134.8	mm

### Synchrotron radiation from the epuI1011Incl ID

The power map of the emitted synchrotron radiation by the epuI1011Incl ID, assuming a 0.5 A filament beam with an energy of 3 GeV and undulator properties of the synchrotron radiation, is shown in Figure 5.159. The on-axis power density is 8.177 kW/mrad<sup>2</sup>

A map of the degree of linear polarisation of the fundamental harmonic of the synchrotron radiation emitted by the epuI1011Incl ID over the angle of observation is shown in Figure 5.160.

A map of the degree of 45 degree polarisation of the fundamental harmonic of the synchrotron radiation emitted by the epuI1011Incl ID over the angle of observation is shown in Figure 5.161.



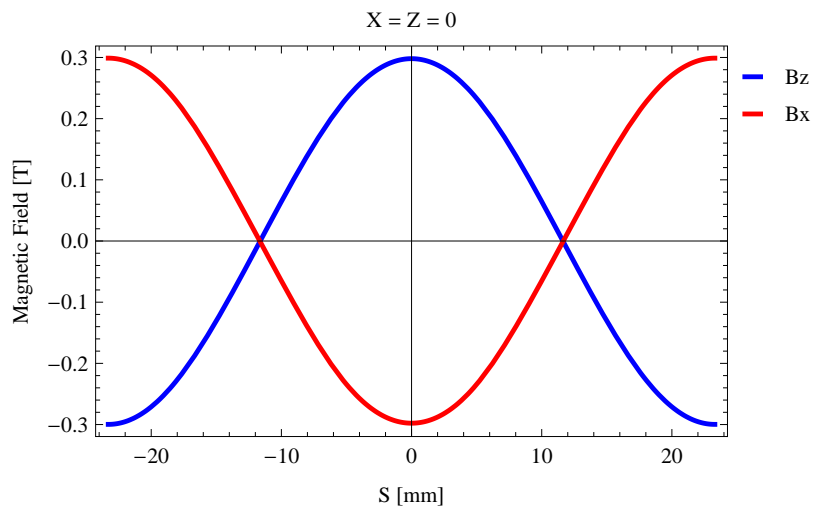


Figure 5.155: Vertical magnetic field in a central pole of the epuI1011Incl ID along the ID axis,  $X = Z = 0$

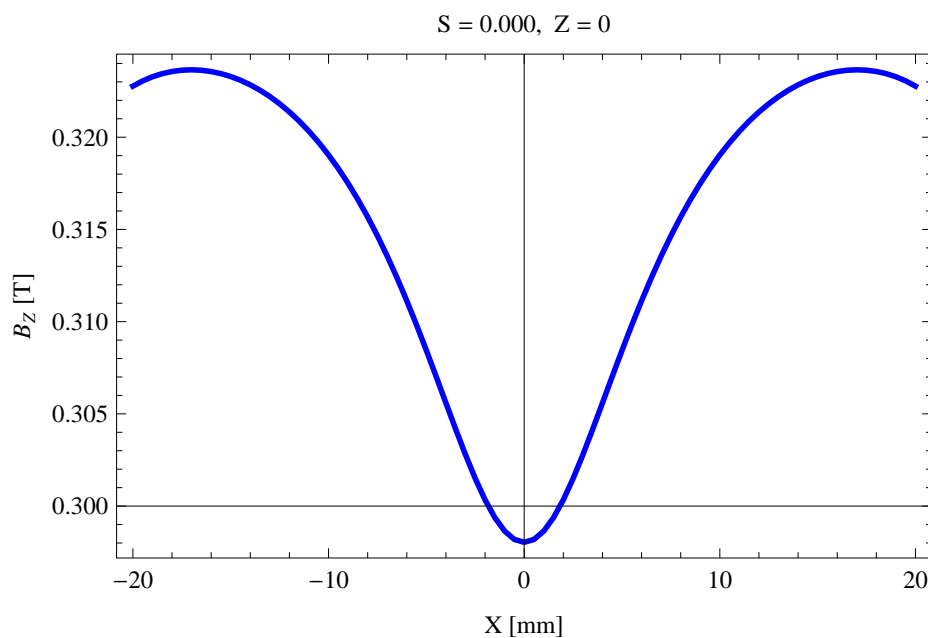


Figure 5.156: Vertical magnetic field in a central pole of the epuI1011Incl ID along the horizontally transverse direction to the ID axis,  $S = 0.000$ ,  $Z = 0$

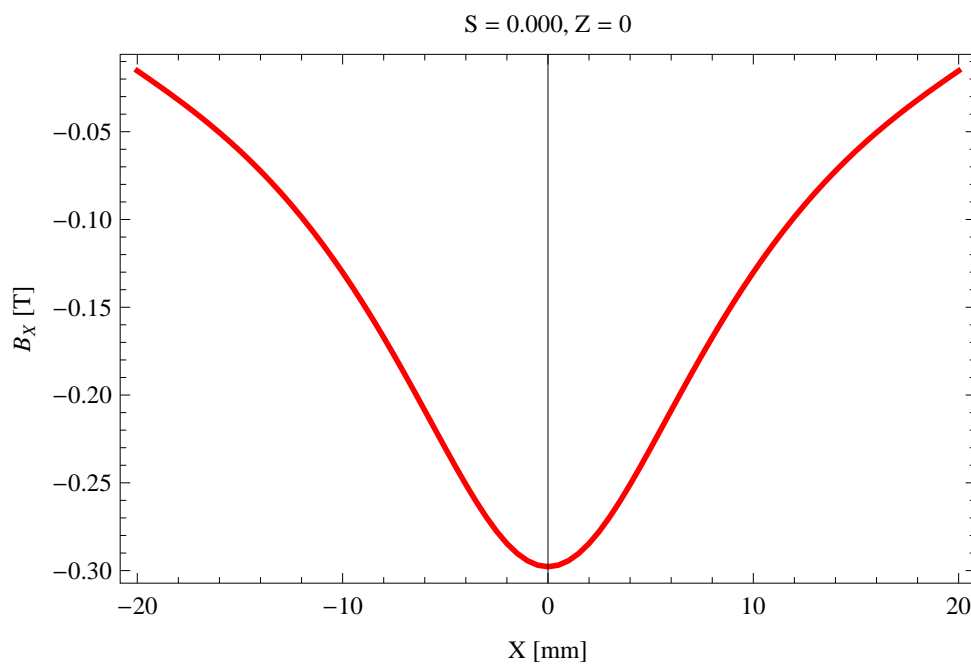


Figure 5.157: Horizontal magnetic field in a central pole of the epuI1011Incl ID along the horizontally transverse direction to the ID axis,  $S = 0.000$ ,  $Z = 0$

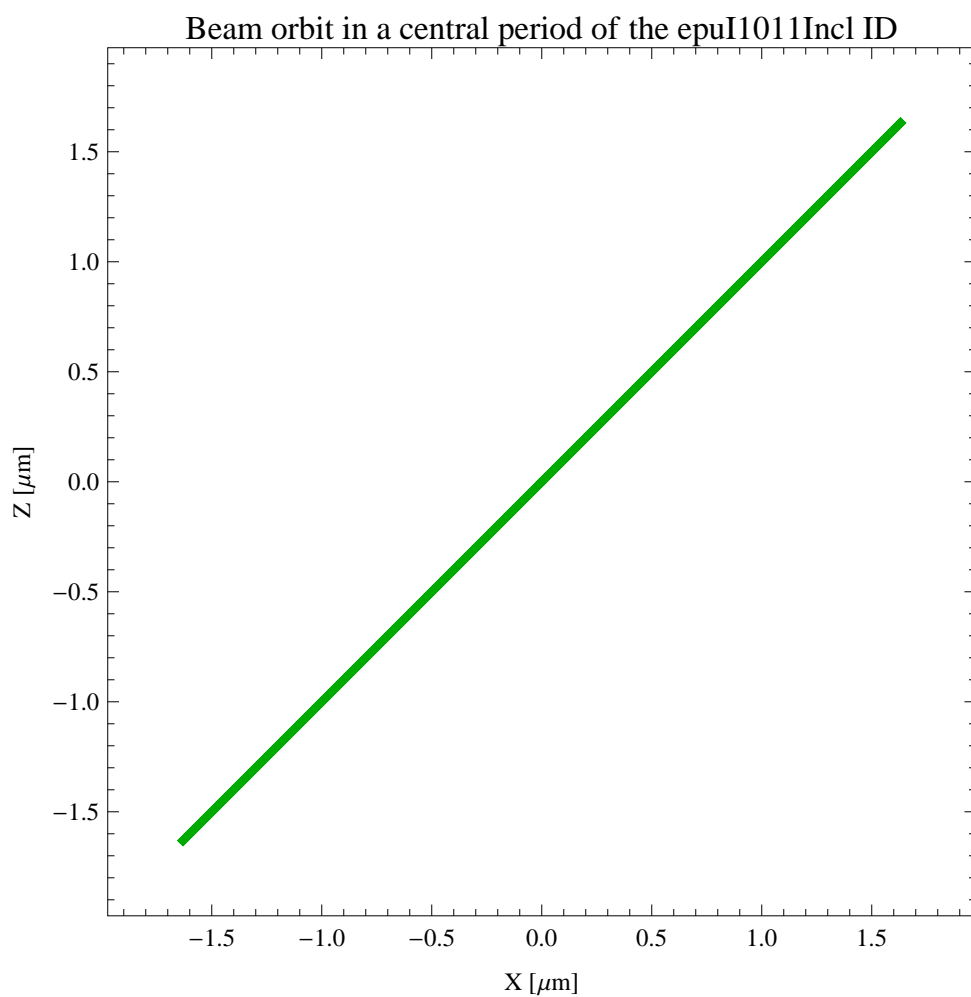


Figure 5.158: The beam orbit of the electron beam through a central period of the epuI1011Incl ID

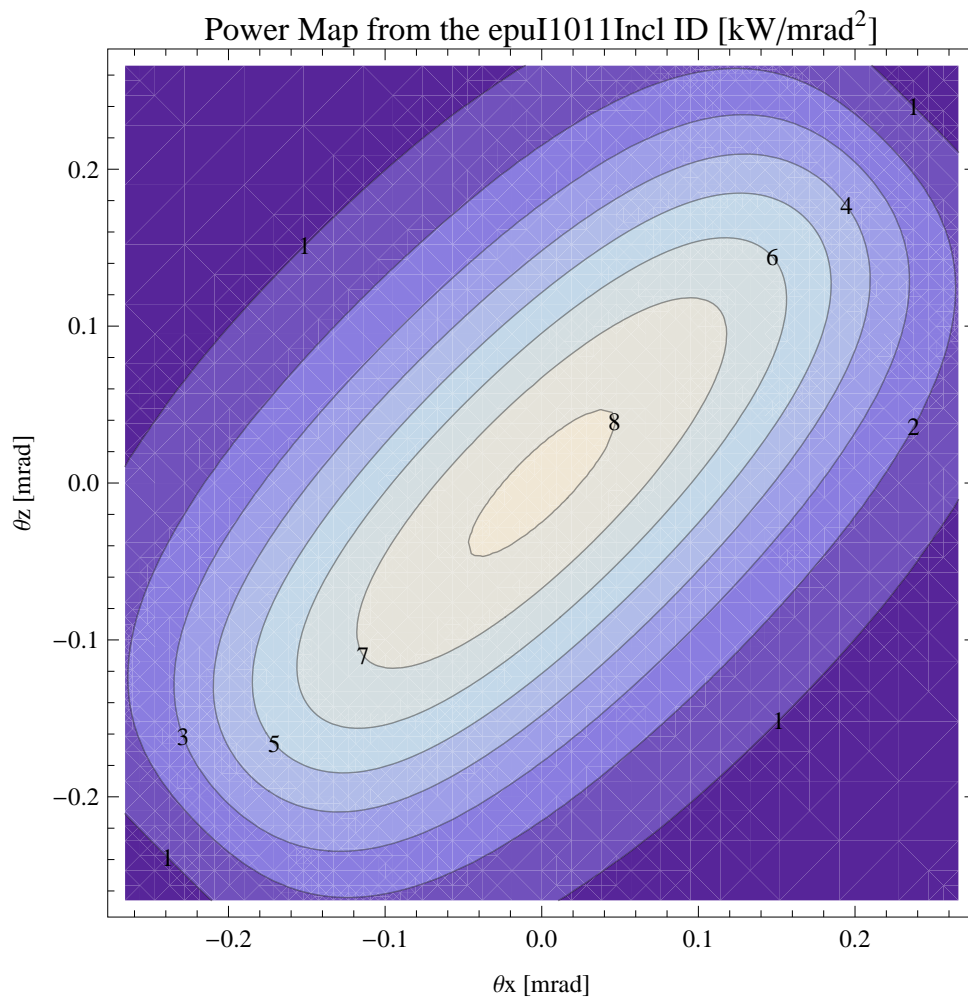


Figure 5.159: Map of the power distribution of the emitted synchrotron radiation by the epuI1011Incl ID

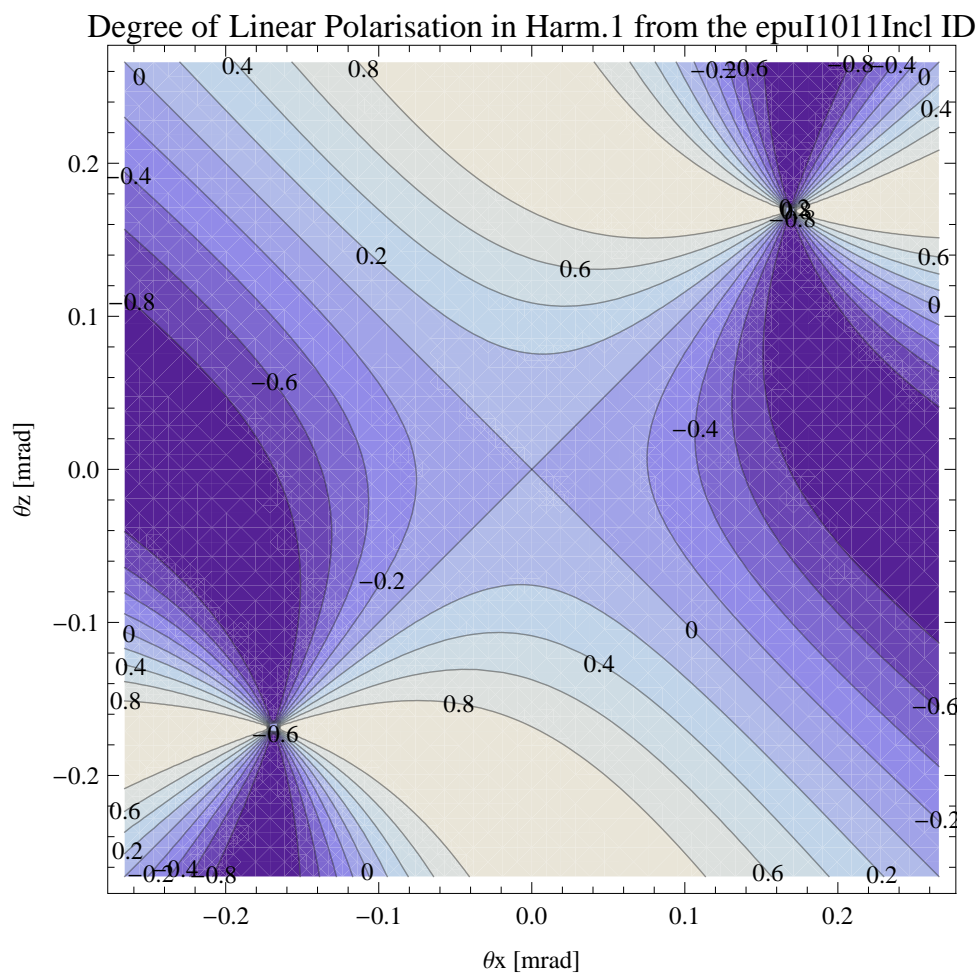


Figure 5.160: Map of linear polarisation in the fundamental harmonic of the synchrotron radiation emitted by the epuI1011Incl ID

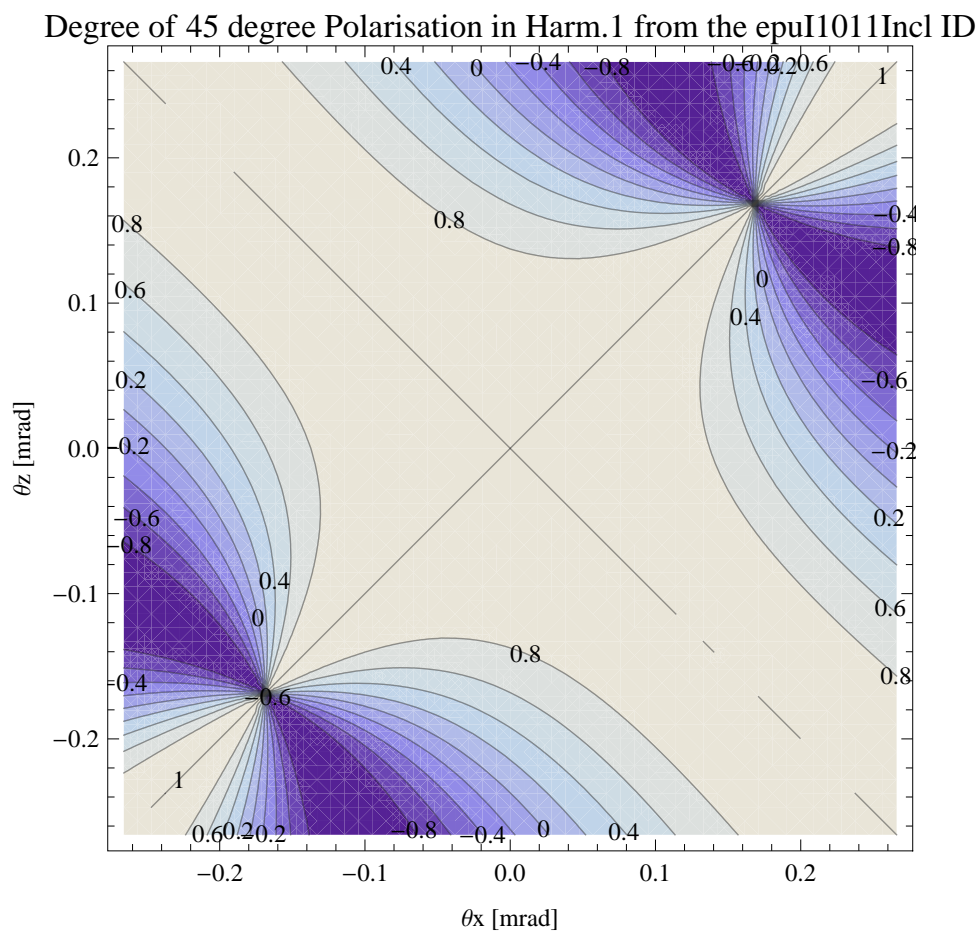


Figure 5.161: Map of 45 degree polarisation in the fundamental harmonic of the synchrotron radiation emitted by the epuI1011Incl ID

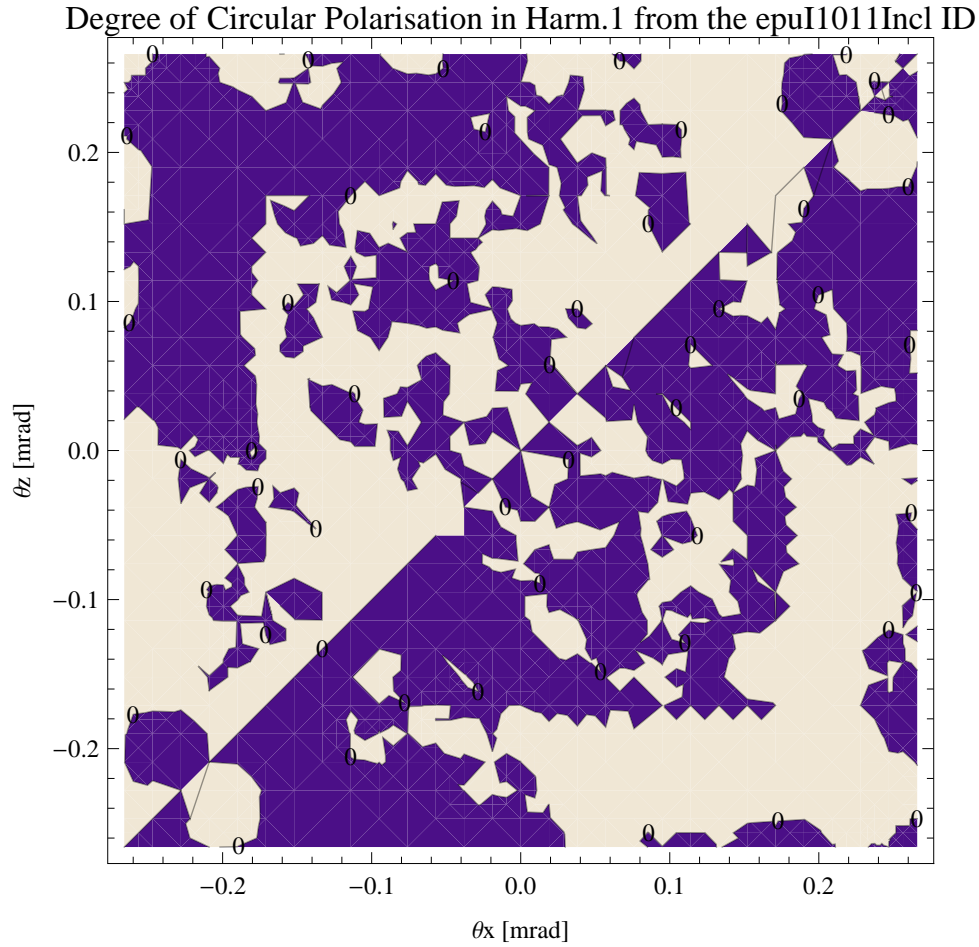


Figure 5.162: Map of circular polarisation in the fundamental harmonic of the synchrotron radiation emitted by the epuI1011Incl ID

A map of the degree of circular polarisation of the fundamental harmonic of the synchrotron radiation emitted by the epuI1011Incl ID over the angle of observation is shown in Figure 5.162.

The on axis brilliance at peak energy, the angular spectral flux, the flux in the harmonics, the power in the harmonics, the ratio of coherence, the coherent flux in the harmonics, and the power of coherent radiation in the harmonics from the epuI1011Incl ID have been calculated and the resulting plots are found in this section of the document. The beam parameters used for the calculation are 0.5 A of stored current,  $\beta_H = 9$  m,  $\varepsilon_H = 0.263$  nmrad,  $\beta_V = 4.8$  m,  $\varepsilon_V = 8$  pmrad, and an energy spread of 0.001.

The brilliance at peak energy and the angular spectral flux density from the epuI1011Incl ID for different harmonics at maximum K-value (1.840) are given in Table 5.32 and for minimum K-value (0.400) these values are given in Table 5.33.

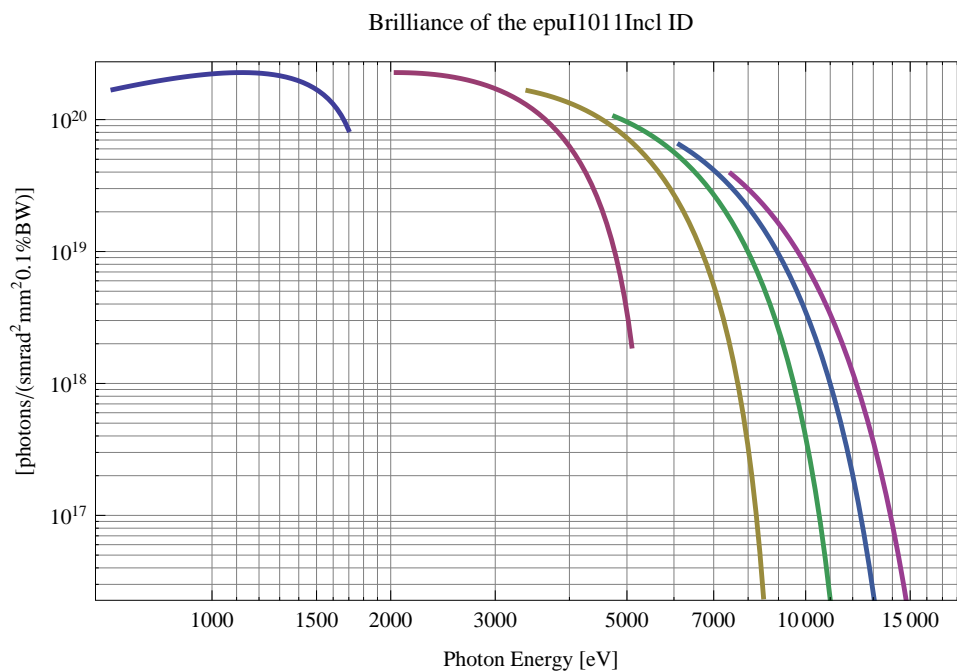


Figure 5.163: The brilliance at peak energy from the epuI1011Incl ID

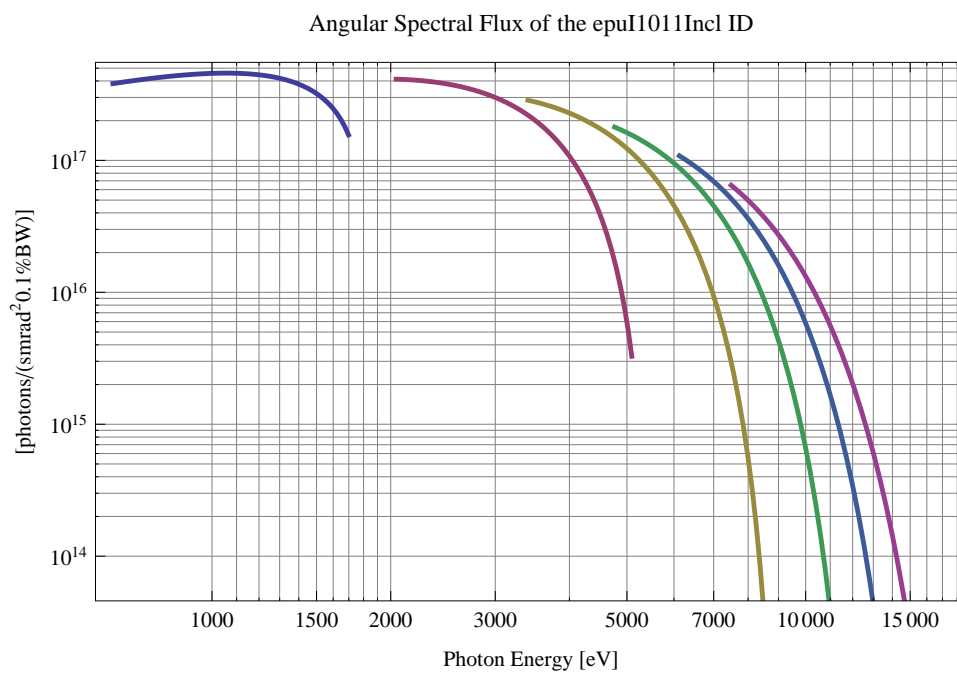


Figure 5.164: The angular spectral flux from the epuI1011Incl ID

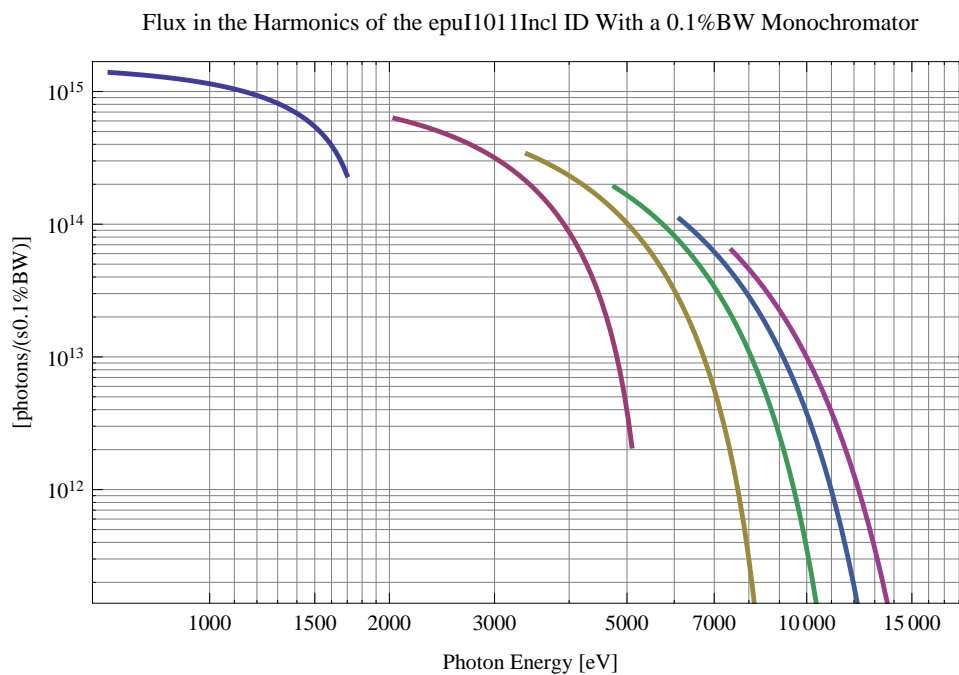


Figure 5.165: The flux of photons in the harmonics from the epuI1011Incl ID using a 0.1%BW monochromator

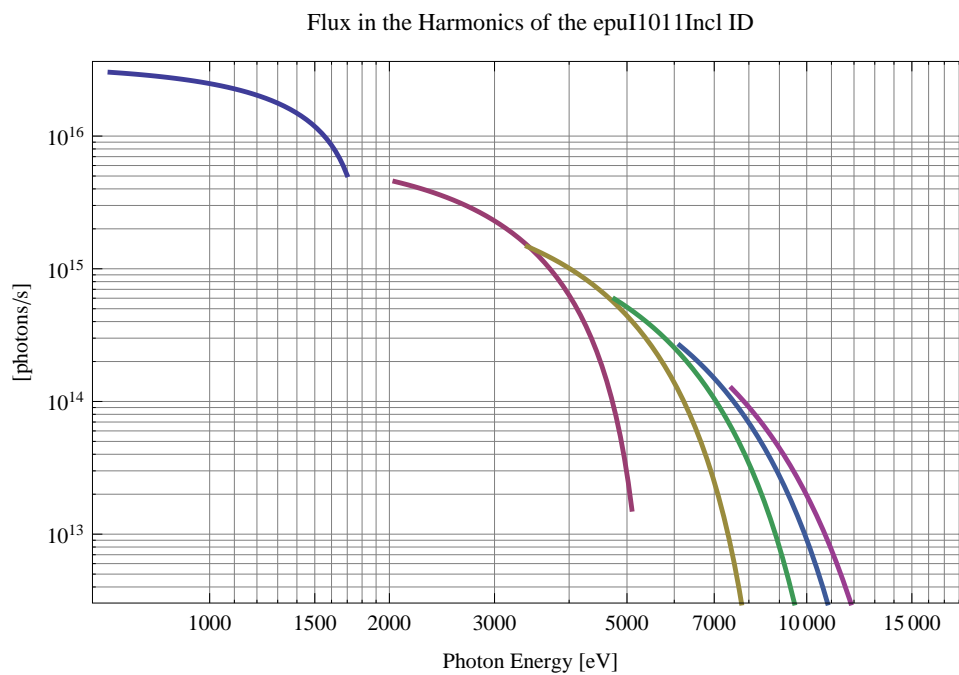


Figure 5.166: The flux of photons in the harmonics from the epuI1011Incl ID



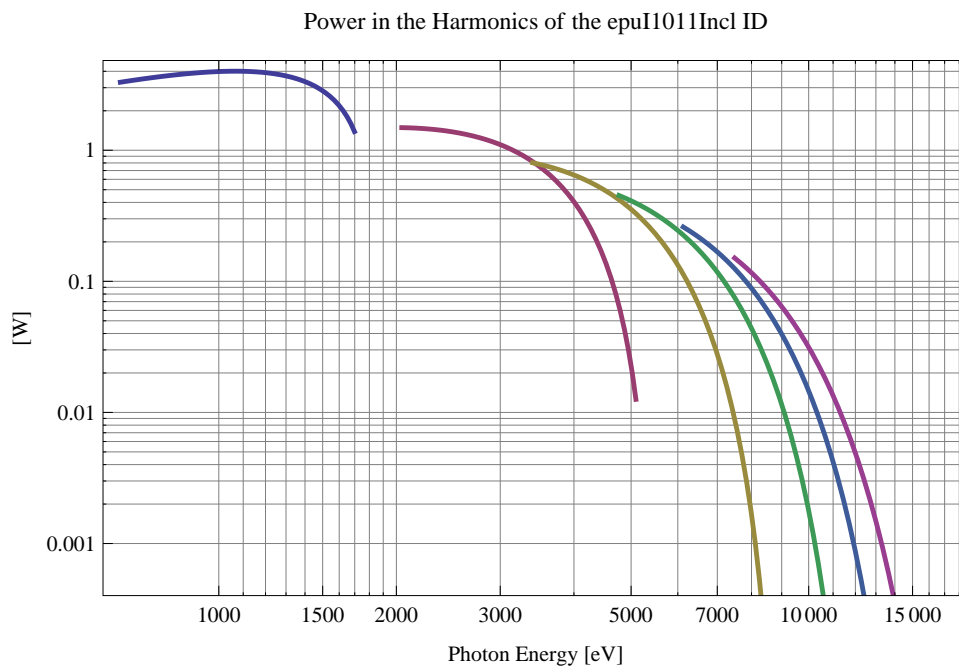


Figure 5.167: The power in the harmonics from the epuI1011Incl ID

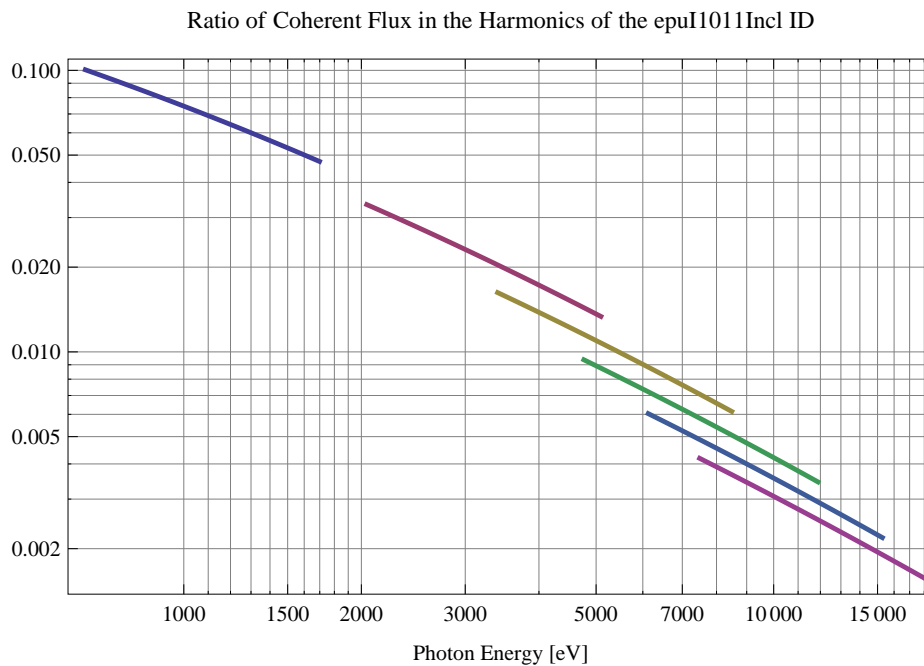


Figure 5.168: The ratio of coherent flux in the harmonics from the epuI1011Incl ID

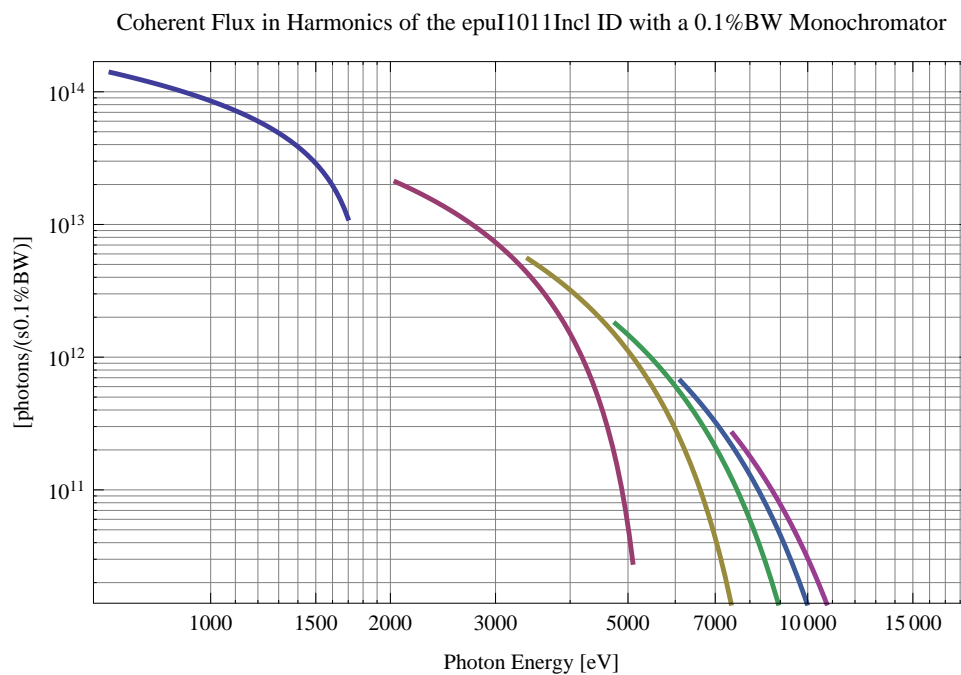


Figure 5.169: The coherent flux in the harmonics of the epuI1011Incl ID using a 0.1%BW Monochromator

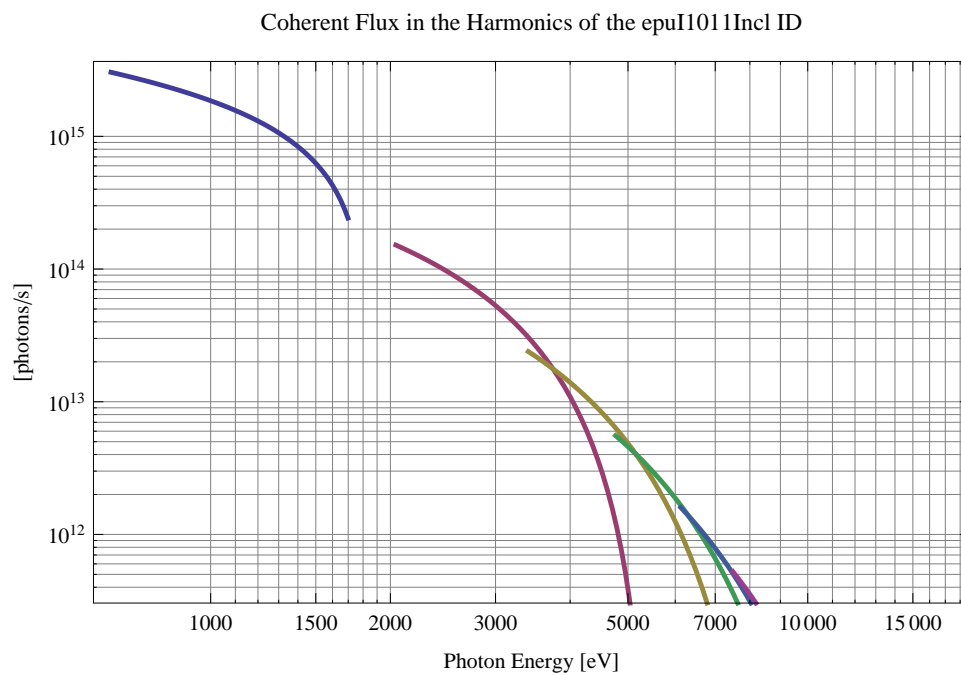


Figure 5.170: The coherent flux in the harmonics of the epuI1011Incl ID

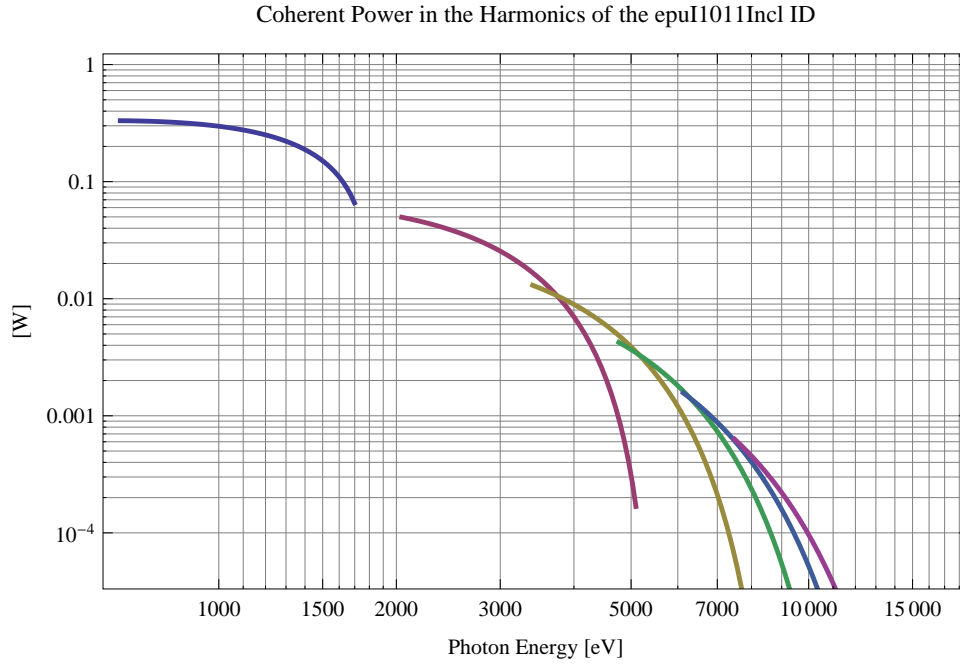


Figure 5.171: The power of coherent synchrotron radiation in the harmonics of the epuI1011Incl ID

Table 5.32: The brilliance at peak energy and the angular spectral flux density from the epuI1011Incl ID for different harmonics at maximum K-value (1.840)

Harmonic	Photon Energy [eV]	Brilliance [Ph./s/mrad <sup>2</sup> /mrad <sup>2</sup> /0.1%BW]	Angular Spectral Flux [Ph./s/mrad <sup>2</sup> /0.1%BW]
1	680.901	$1.69 \times 10^{20}$	$3.82 \times 10^{17}$
3	2042.7	$2.27 \times 10^{20}$	$4.13 \times 10^{17}$
5	3404.51	$1.66 \times 10^{20}$	$2.86 \times 10^{17}$
7	4766.31	$1.06 \times 10^{20}$	$1.79 \times 10^{17}$
9	6128.11	$6.46 \times 10^{19}$	$1.08 \times 10^{17}$
11	7489.92	$3.88 \times 10^{19}$	$6.48 \times 10^{16}$

Table 5.33: The brilliance at peak energy and the angular spectral flux density from the epuI1011Incl ID for different harmonics at minimum K-value (0.4)

Harmonic	Photon Energy [eV]	Brilliance [Ph./s/mrad <sup>2</sup> /mrad <sup>2</sup> /0.1%BW]	Angular Spectral Flux [Ph./s/mrad <sup>2</sup> /0.1%BW]
1	1698.21	$8.36 \times 10^{19}$	$1.56 \times 10^{17}$
3	5094.63	$1.92 \times 10^{18}$	$3.27 \times 10^{15}$
5	8491.06	$2.41 \times 10^{16}$	$4.07 \times 10^{13}$
7	11887.5	$2.65 \times 10^{14}$	$4.48 \times 10^{11}$
9	15283.9	$2.79 \times 10^{12}$	$4.72 \times 10^9$
11	18680.3	$2.88 \times 10^{10}$	$4.89 \times 10^7$

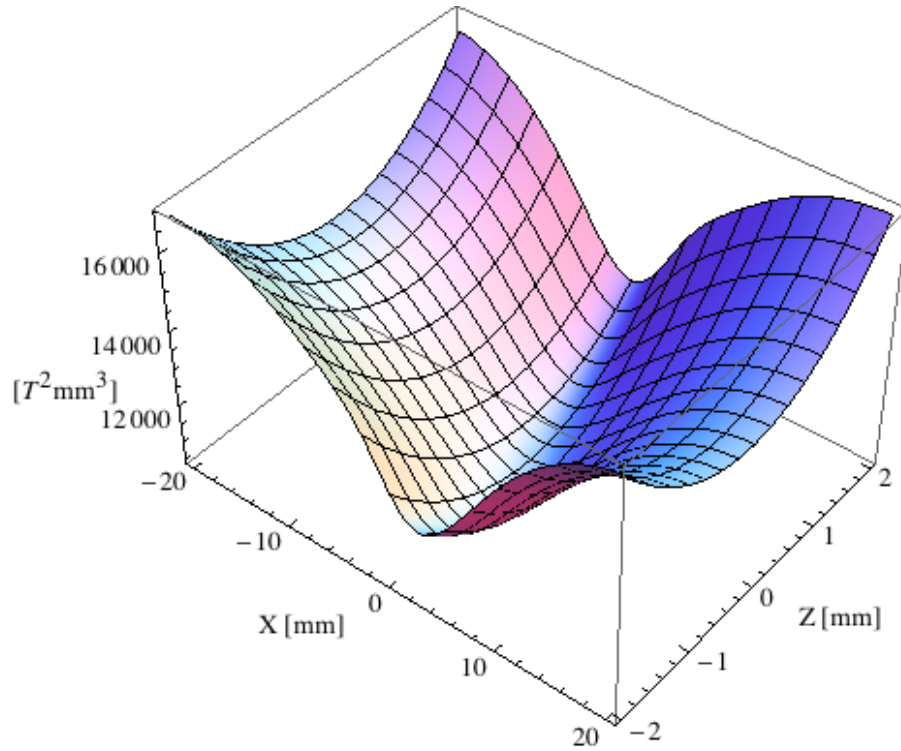


Figure 5.172: Focusing potential from the epuI1011Incl ID over the beam stay clear aperture.

### Influence from the epuI1011Incl ID on the optics of the stored beam

Figure 5.172 shows the focusing potential from the epuI1011Incl over the beam stay clear aperture of the ring aperture.

Figure 5.173 shows the kick map in the beam energy independant unit  $T^2 m^2$  of the kicks induced by the epuI1011Incl ID over the beam stay clear aperture.

Figure 5.174 shows the induced angular kick on the stored beam from the epuI1011Incl ID as a function of the vertical distance to the axis of the ID.

Figure 5.175 shows the induced angular kick on the stored beam from the epuI1011Incl ID as a function of the horizontal distance to the axis of the ID.

Figure 5.176 shows tune shift induced by the epuI1011Incl ID over the beam stay clear aperture. Note that the tune shift depends on the beam size at the ID.

Figure 5.177 shows the induced tune shift from the epuI1011Incl ID as a function of the vertical distance to the axis of the ID.

Figure 5.178 shows the induced tune shift from the epuI1011Incl ID as a function of the horizontal distance to the axis of the ID.

### Magnet model of the elliptically polaraising undulator epuI1011Vert

The Radia [2] magnet model of the epuI1011Vert ID is shown in Figure 5.179. The length of the magnet model is 387.26 mm. The magnetic material in the model is NdFeb with a remanence of 1.22 T. Blocks with vertical magnetisation are blue and blocks with horizontal magnetisation

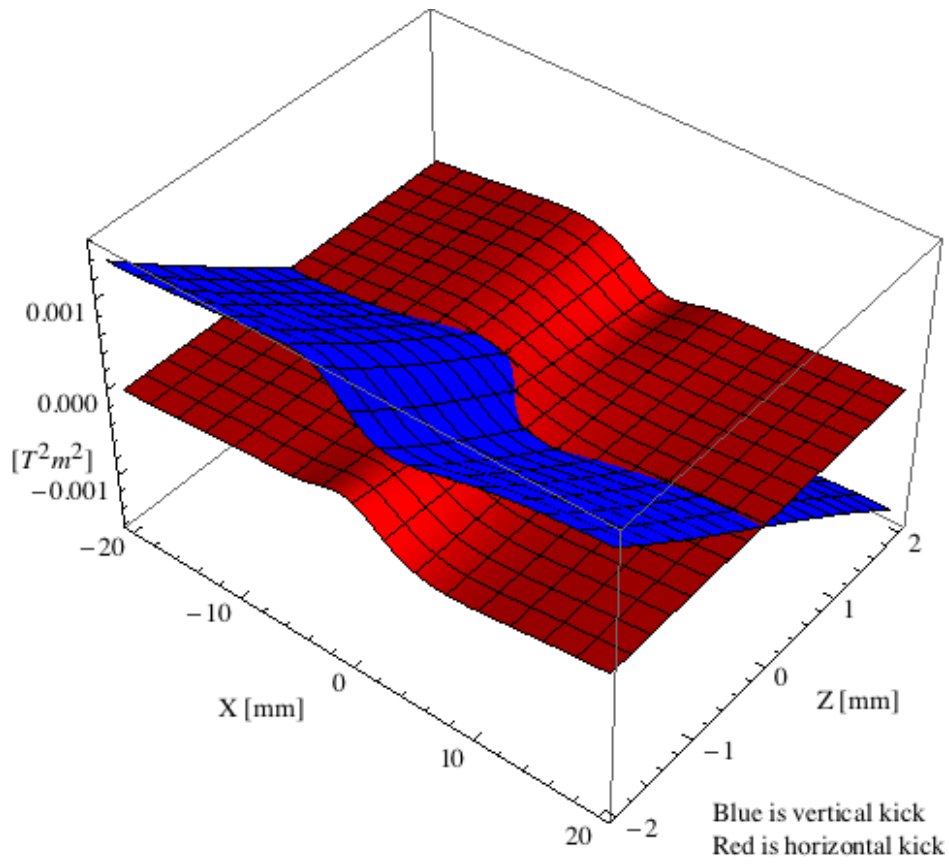


Figure 5.173: Kick map in the beam energy independent unit  $T^2m^2$  of the kicks induced by the epuI1011Incl ID over the beam stay clear aperture.

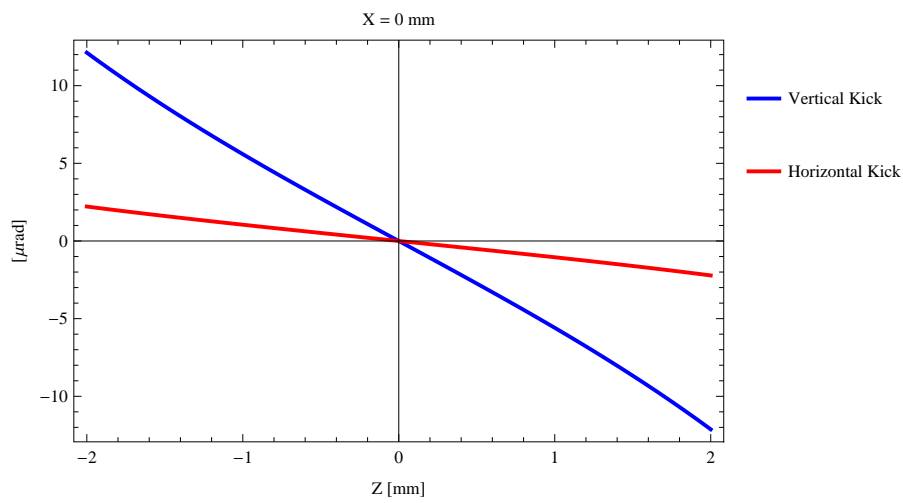


Figure 5.174: Induced angular kick on the stored beam from the epuI1011Incl ID as a function of the vertical distance to the ID axis.

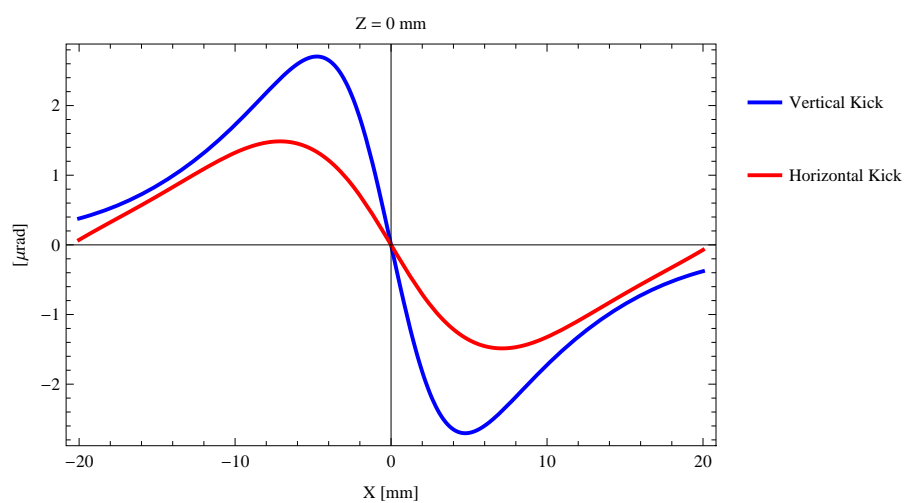


Figure 5.175: Induced angular kick on the stored beam from the epuI1011Incl ID as a function of the horizontal distance to the ID axis.

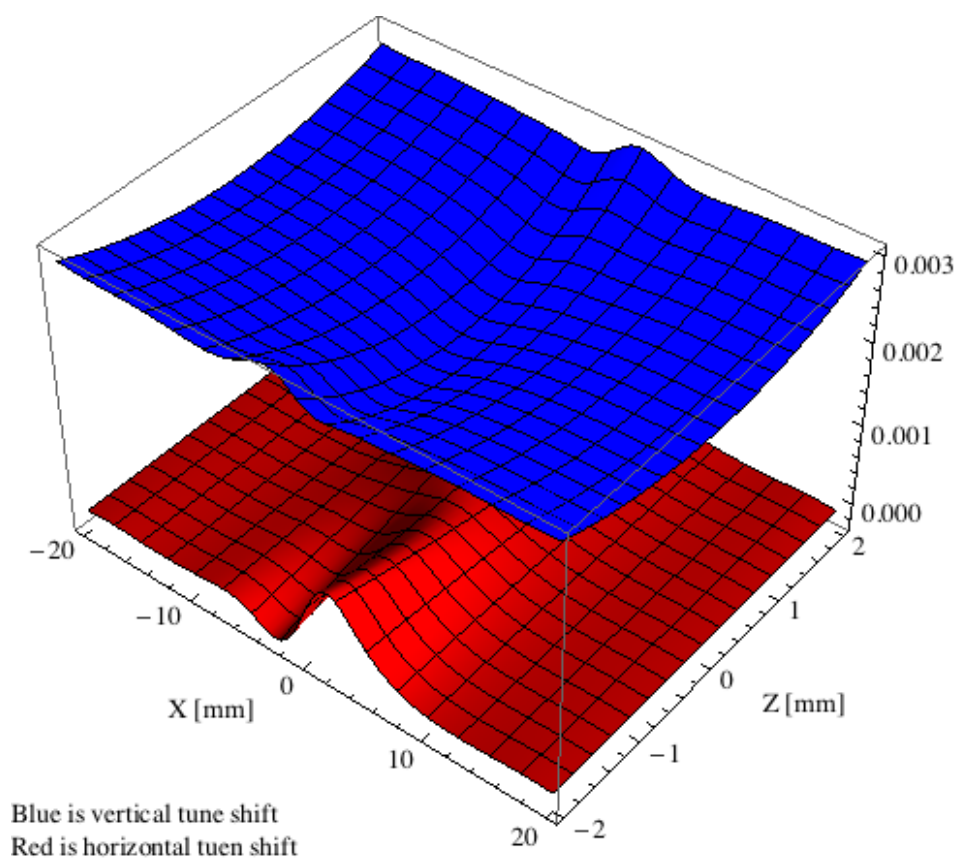


Figure 5.176: Tune shift induced by the epuI1011Incl ID over the beam stay clear aperture.

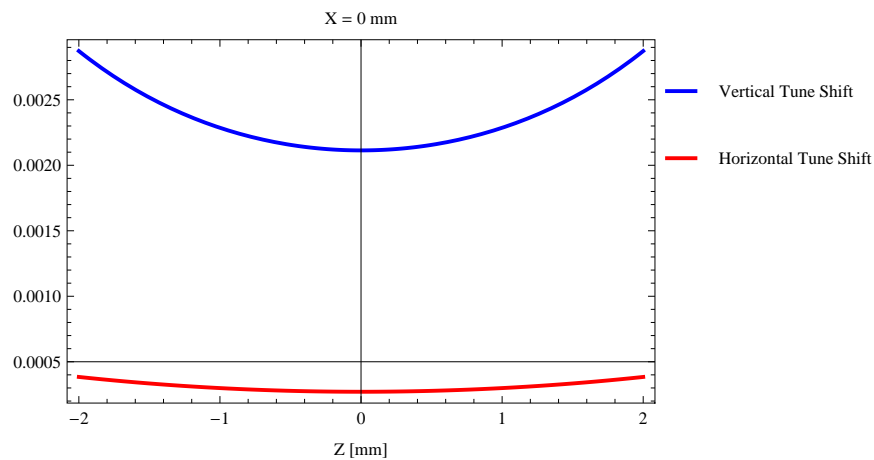


Figure 5.177: Induced tune shift from the epuI1011Incl ID as a function of the vertical distance to the axis of the ID.

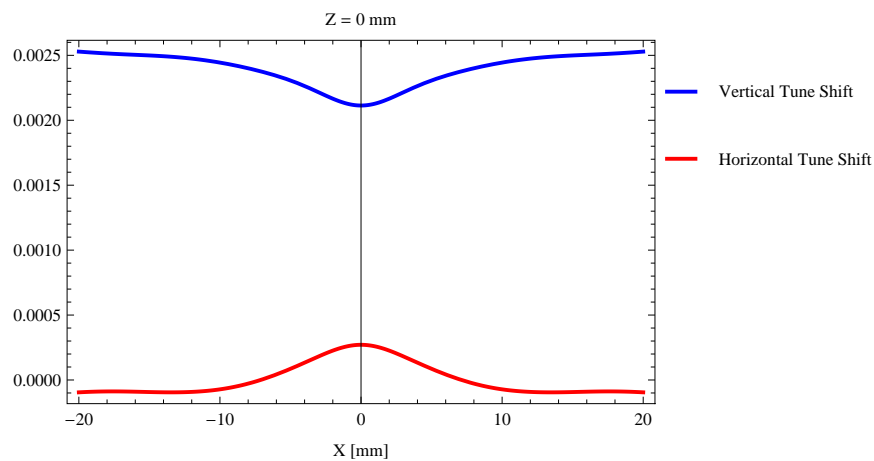


Figure 5.178: Induced tune shift from the epuI1011Incl ID on the stored beam from the ID as a function of the horizontal distance to the axis of the ID.

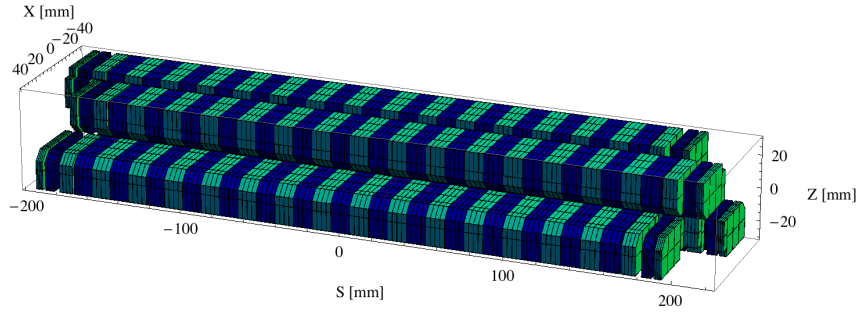


Figure 5.179: Magnetic model of the epuI1011Vert ID. The ID has been modelled with Radia [2]

are green. This is the existing undulator at the I1011 beamline at the MAX II storage ring. The total length of the epuI1011Vert ID is 2134.76 mm.

### Analysis of the magnetic field of the epuI1011Vert ID

The effective magnetic fields on axis and the fundamental photon energy of the epuI1011Vert ID are shown in Table 5.34. The higher harmonic contents in the magnetic field of an elliptically polarising undulator made of permanent magnets is negligible and the efficient field has about the same strength as the peak field.

Table 5.34: Effective Fields on axis and Fundamental Photon Energy of the epuI1011Vert ID

Undulator Period	46.6	mm
Undulator Gap	14	mm
Undulator Mode	Vertical	
Undulator Phase	23.300	mm
Vertical Peak Field	0.000	T
Efficient Vertical Field	0.000	T
Kx (from vert. field)	0.000	
Horizontal Peak Field:	0.517	T
Efficient Horizontal Field	0.517	T
Kz (from hor. field)	2.250	
Photon Energy, Harm.1	0.520	keV
Emitted Power	1.625	kW
Total Length	2134.8	mm

### Synchrotron radiation from the epuI1011Vert ID

The power map of the emitted synchrotron radiation by the epuI1011Vert ID, assuming a 0.5 A filament beam with an energy of 3 GeV and undulator properties of the synchrotron radiation, is shown in Figure 5.183. The on-axis power density is 10.064 kW/mrad<sup>2</sup>

A map of the degree of linear polarisation of the fundamental harmonic of the synchrotron radiation emitted by the epuI1011Vert ID over the angle of observation is shown in Figure 5.184.

A map of the degree of 45 degree polarisation of the fundamental harmonic of the synchrotron radiation emitted by the epuI1011Vert ID over the angle of observation is shown in Figure



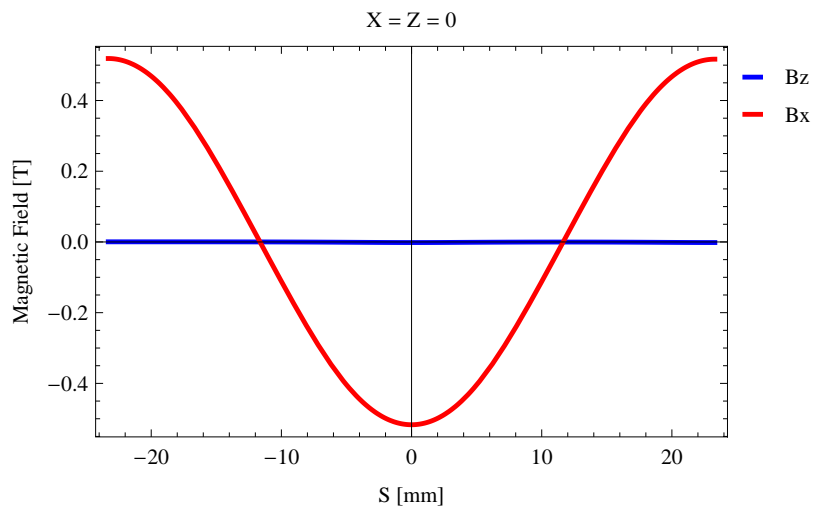


Figure 5.180: Vertical magnetic field in a central pole of the epuI1011Vert ID along the ID axis,  $X = Z = 0$

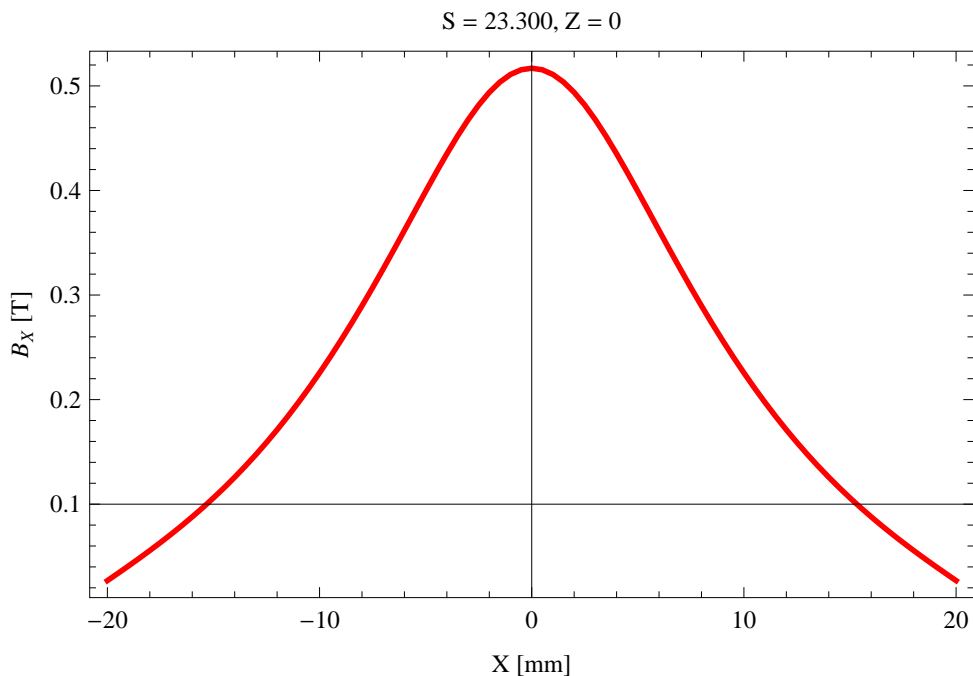


Figure 5.181: Horizontal magnetic field in a central pole of the epuI1011Vert ID along the horizontally transverse direction to the ID axis,  $S = 23.300$ ,  $Z = 0$

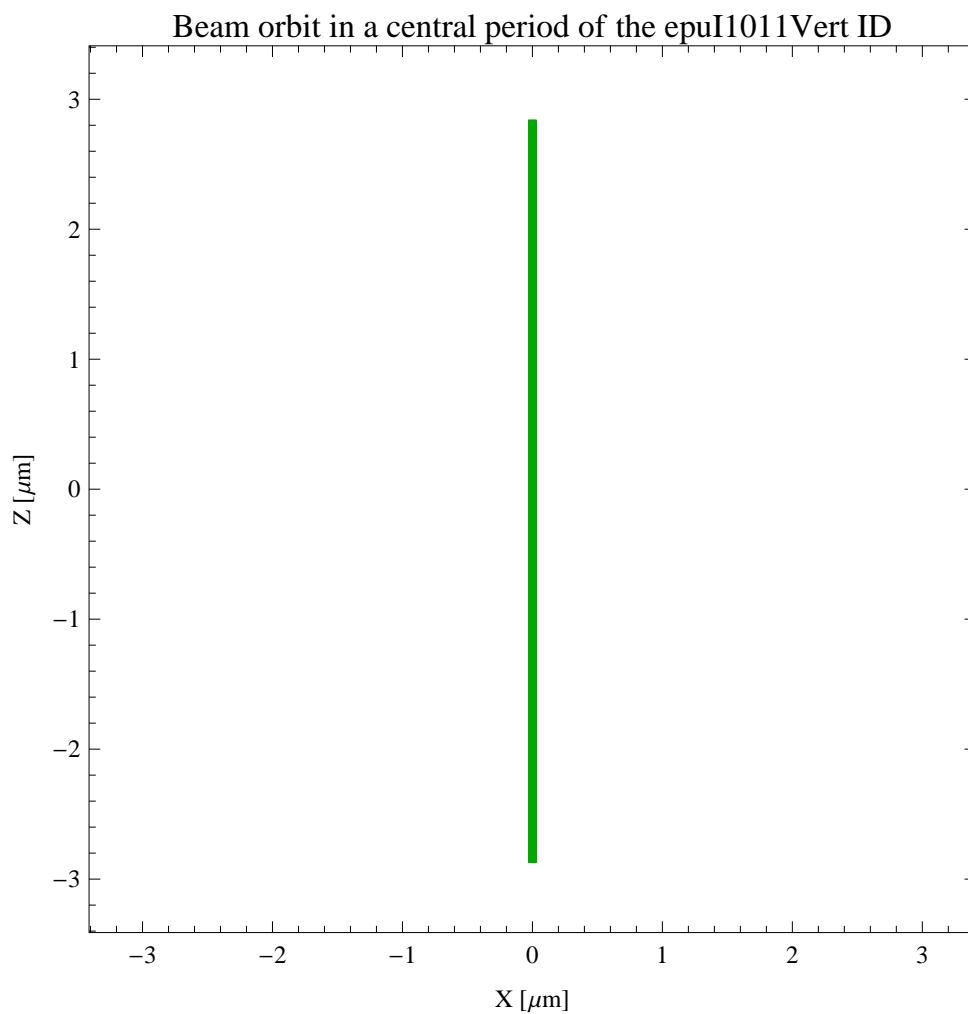


Figure 5.182: The beam orbit of the electron beam through a central period of the epuI1011Vert ID

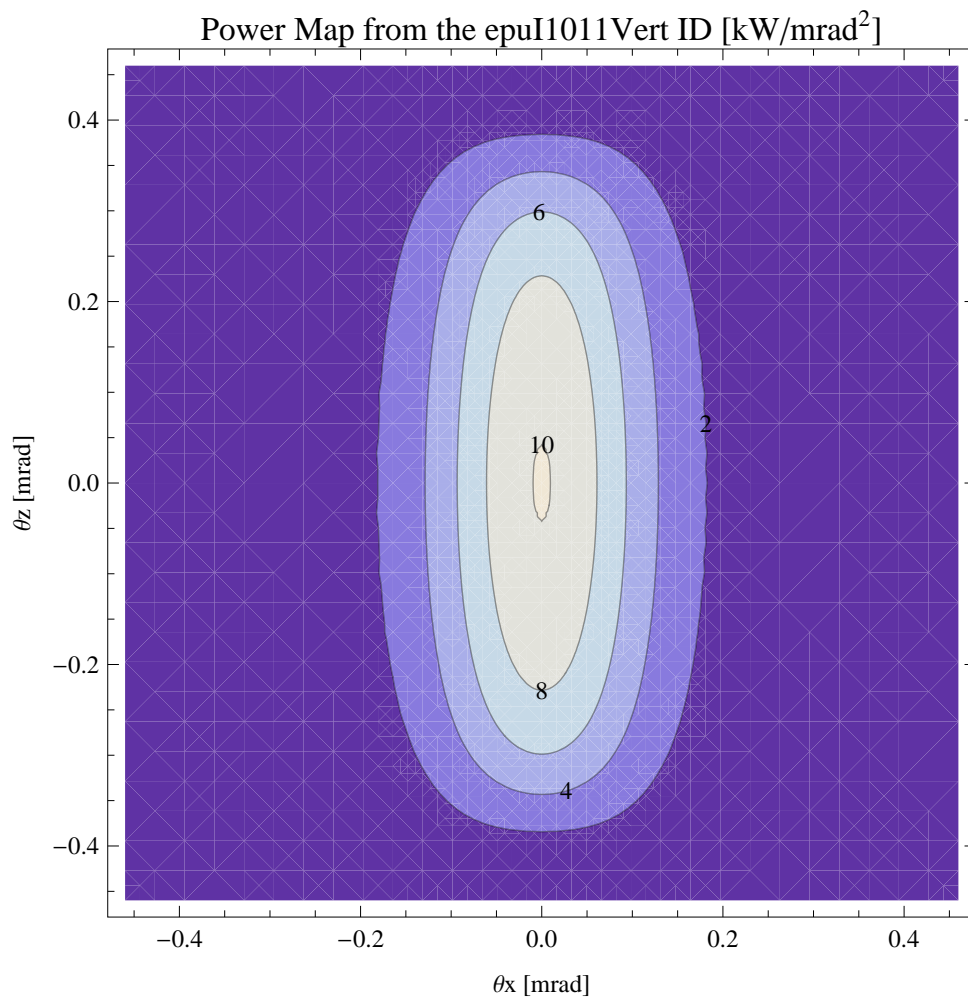


Figure 5.183: Map of the power distribution of the emitted synchrotron radiation by the epuI1011Vert ID

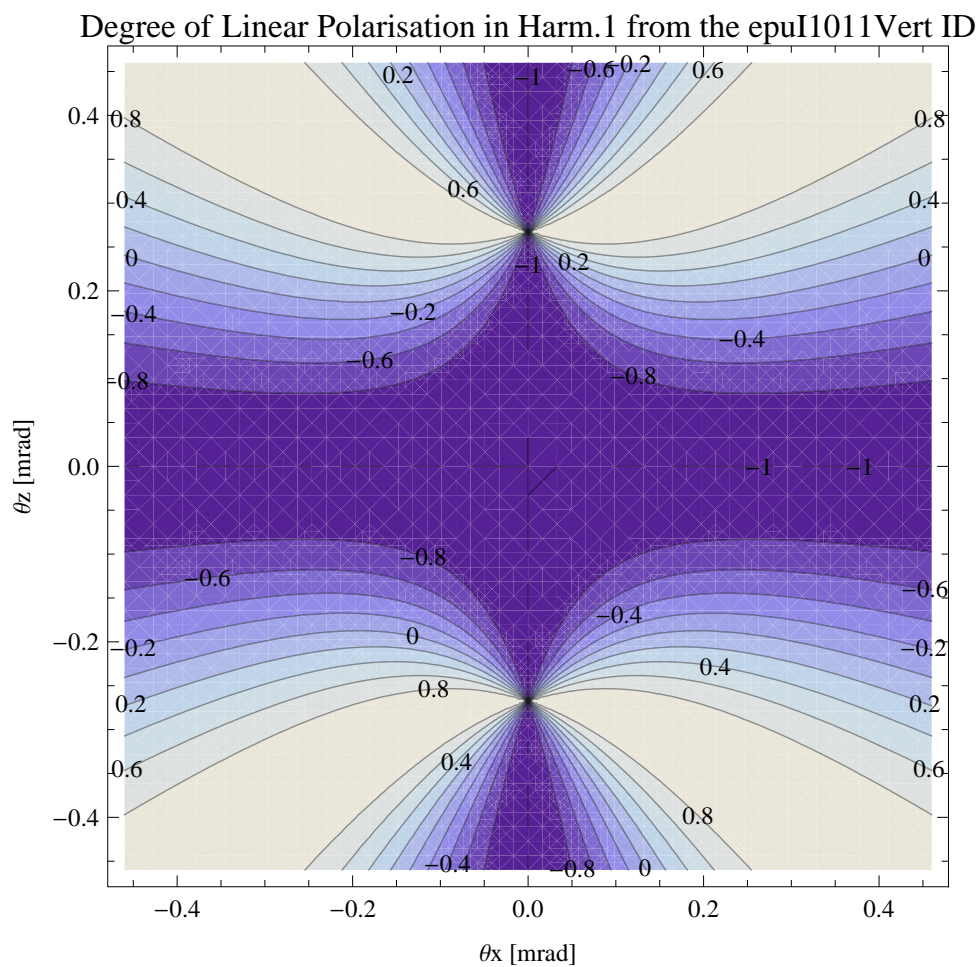


Figure 5.184: Map of linear polarisation in the fundamental harmonic of the synchrotron radiation emitted by the epuI1011Vert ID

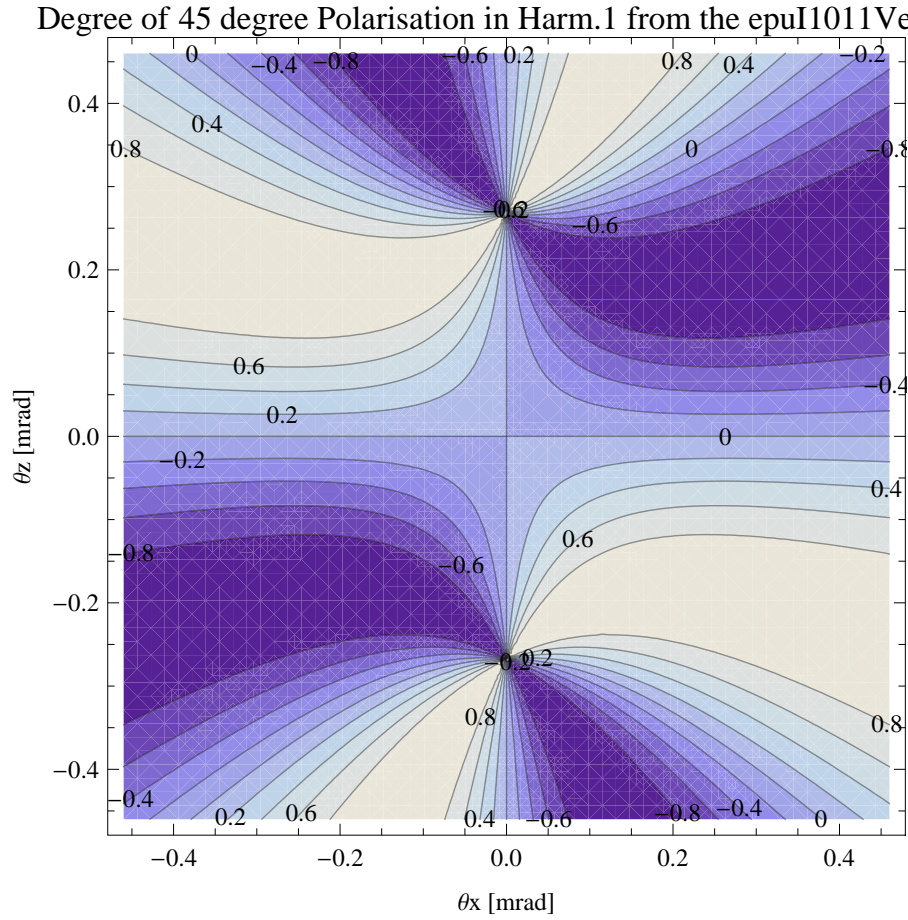


Figure 5.185: Map of 45 degree polarisation in the fundamental harmonic of the synchrotron radiation emitted by the epuI1011Vert ID

5.185.

A map of the degree of circular polarisation of the fundamental harmonic of the synchrotron radiation emitted by the epuI1011Vert ID over the angle of observation is shown in Figure 5.186.

The on axis brilliance at peak energy, the angular spectral flux, the flux in the harmonics, the power in the harmonics, the ratio of coherence, the coherent flux in the harmonics, and the power of coherent radiation in the harmonics from the epuI1011Vert ID have been calculated and the resulting plots are found in this section of the document. The beam parameters used for the calculation are 0.5 A of stored current,  $\beta_H = 9$  m,  $\varepsilon_H = 0.263$  nmrad,  $\beta_V = 4.8$  m,  $\varepsilon_V = 8$  pmrad, and an energy spread of 0.001.

The brilliance at peak energy and the angular spectral flux density from the epuI1011Vert ID for different harmonics at maximum K-value (2.250) are given in Table 5.35 and for minimum K-value (0.400) these values are given in Table 5.36.

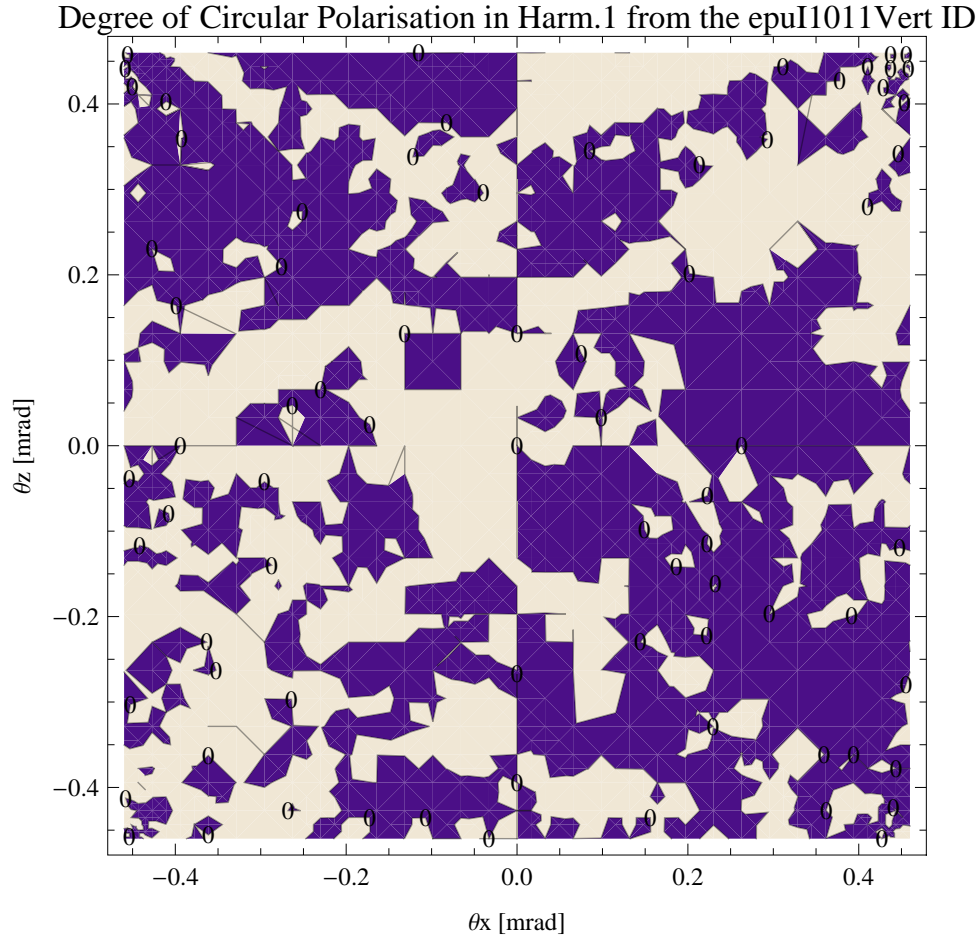


Figure 5.186: Map of circular polarisation in the fundamental harmonic of the synchrotron radiation emitted by the epuI1011Vert ID

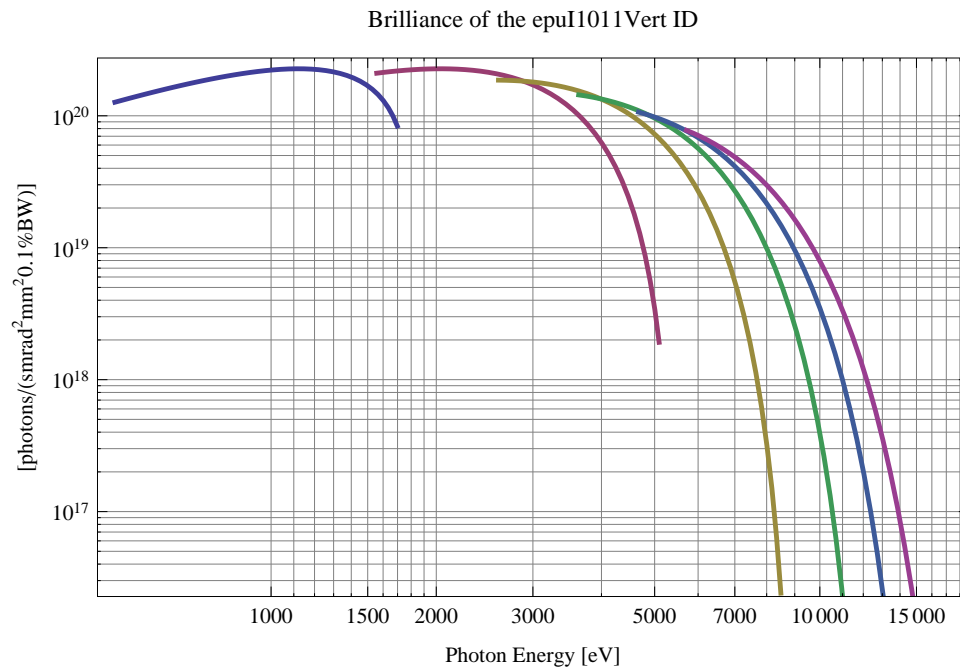


Figure 5.187: The brilliance at peak energy from the epuI1011Vert ID

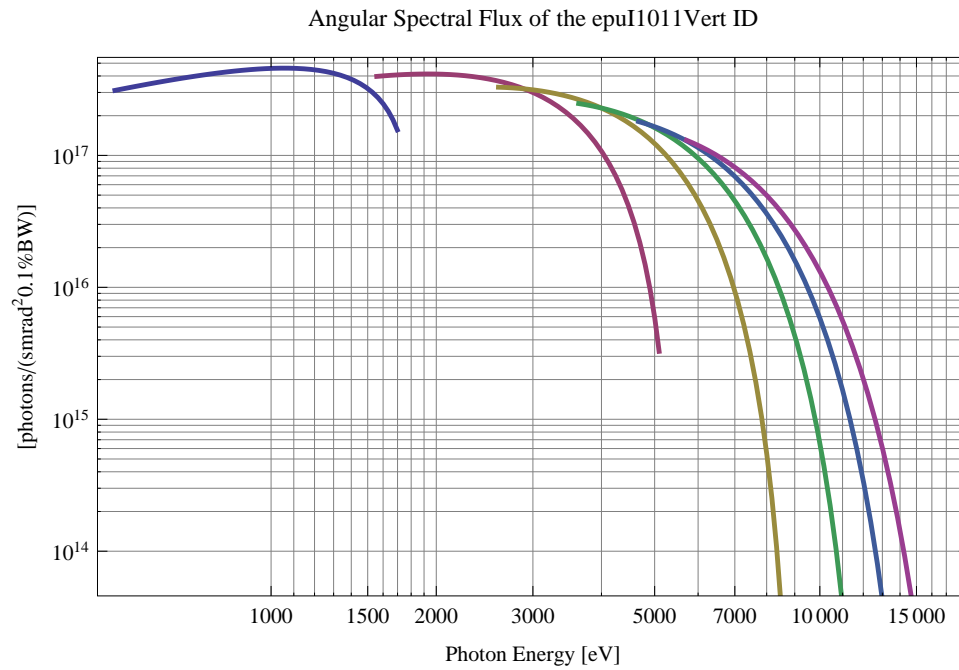


Figure 5.188: The angular spectral flux from the epuI1011Vert ID

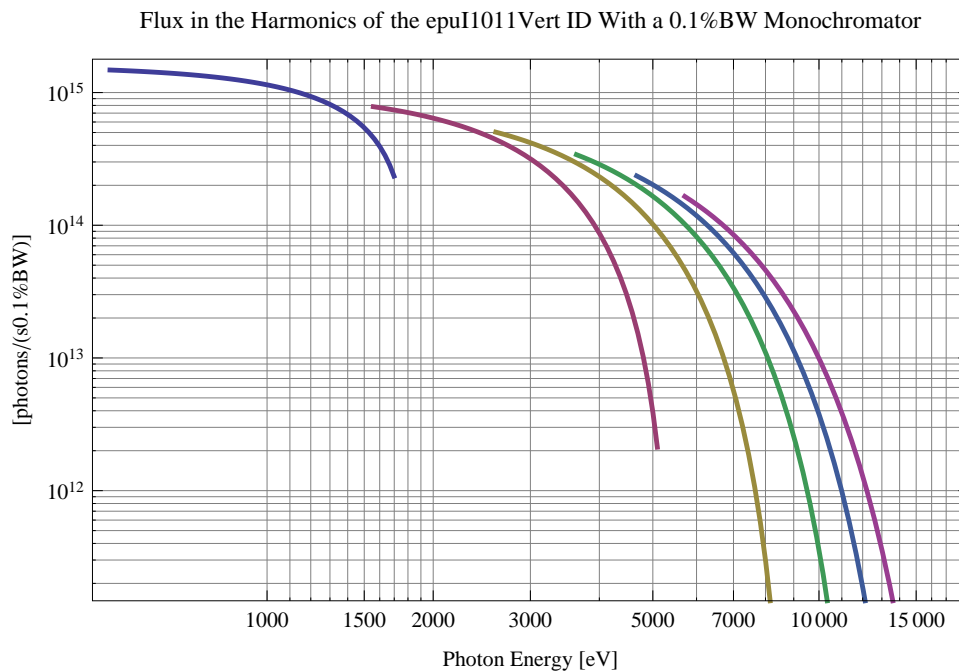


Figure 5.189: The flux of photons in the harmonics from the epuI1011Vert ID using a 0.1%BW monochromator

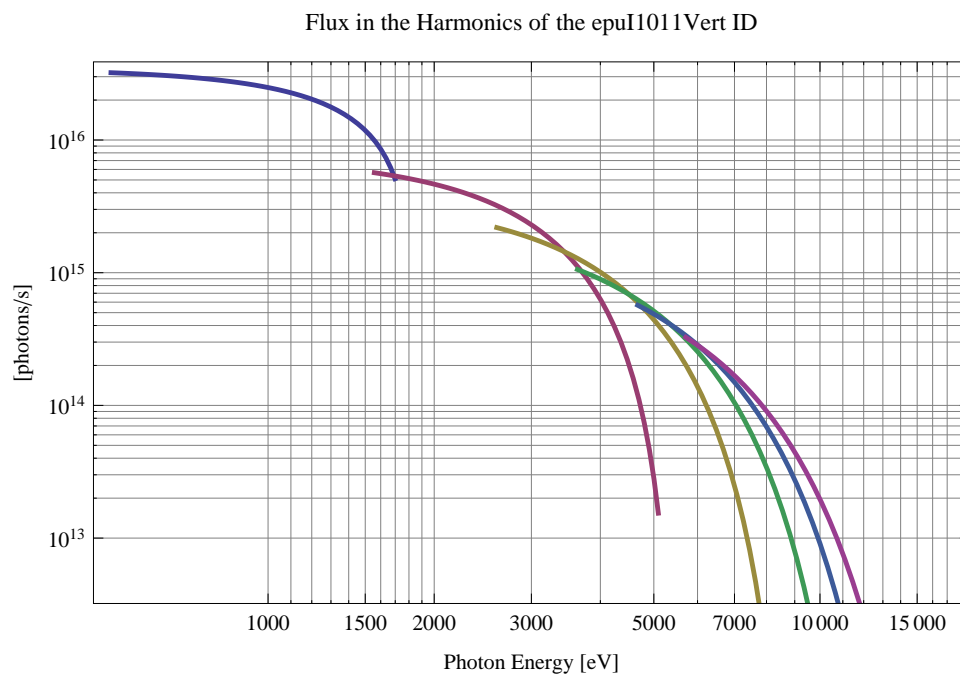


Figure 5.190: The flux of photons in the harmonics from the epuI1011Vert ID

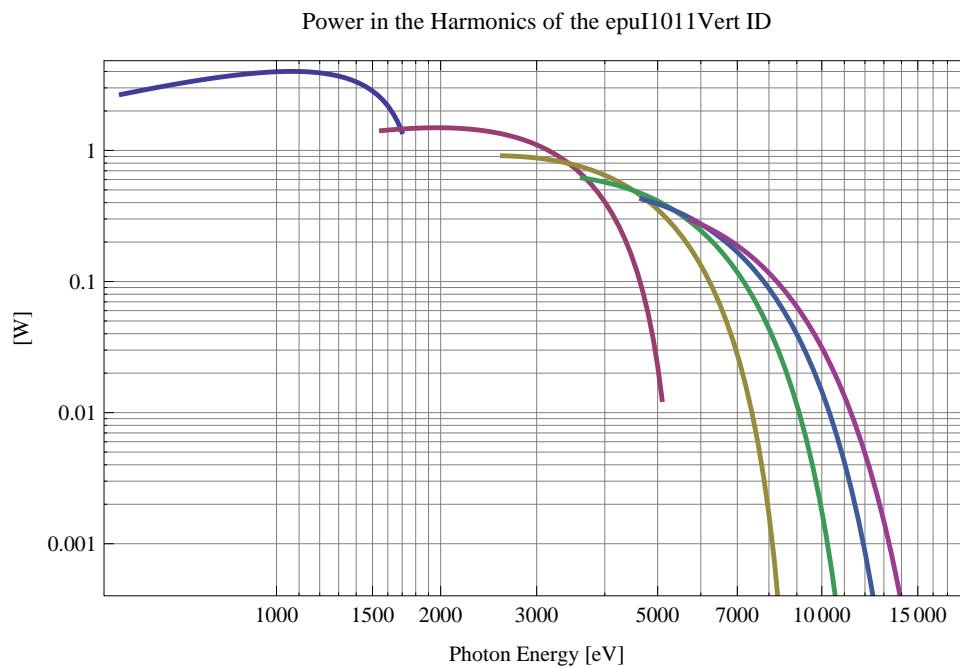


Figure 5.191: The power in the harmonics from the epuI1011Vert ID



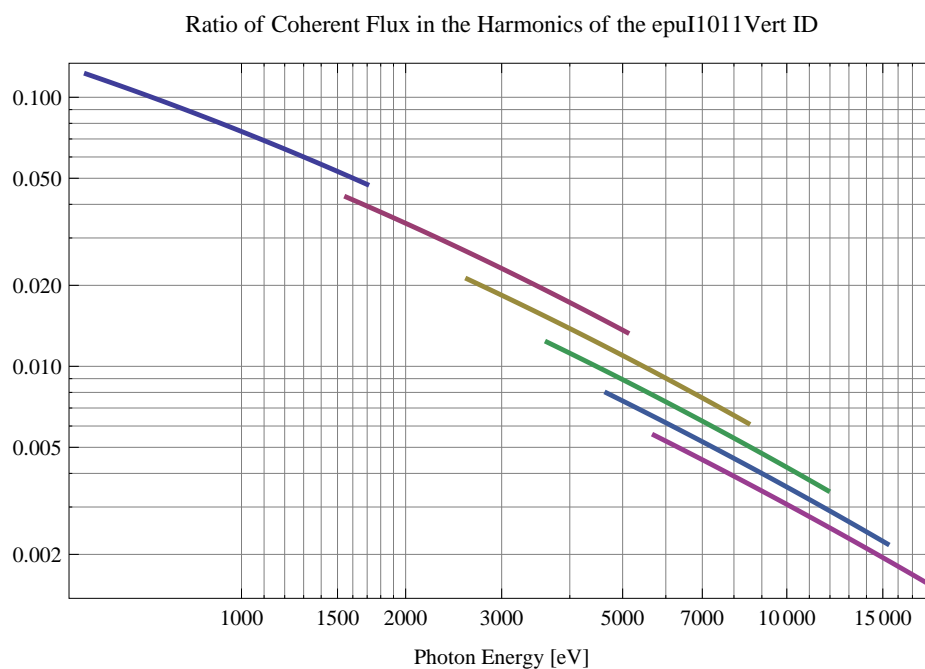


Figure 5.192: The ratio of coherent flux in the harmonics from the epuI1011Vert ID

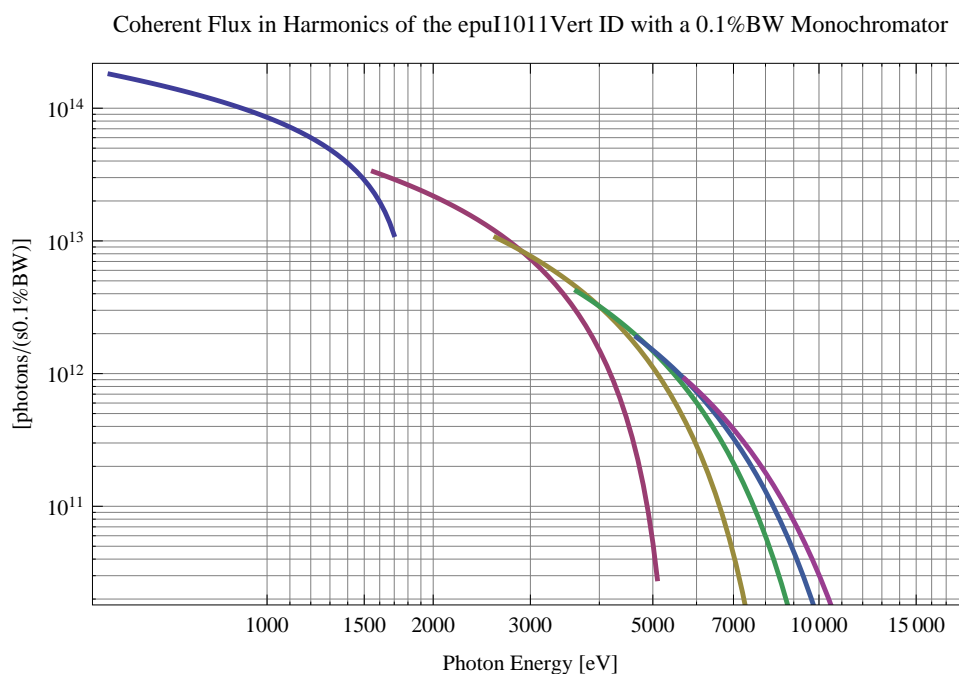


Figure 5.193: The coherent flux in the harmonics of the epuI1011Vert ID using a 0.1%BW Monochromator

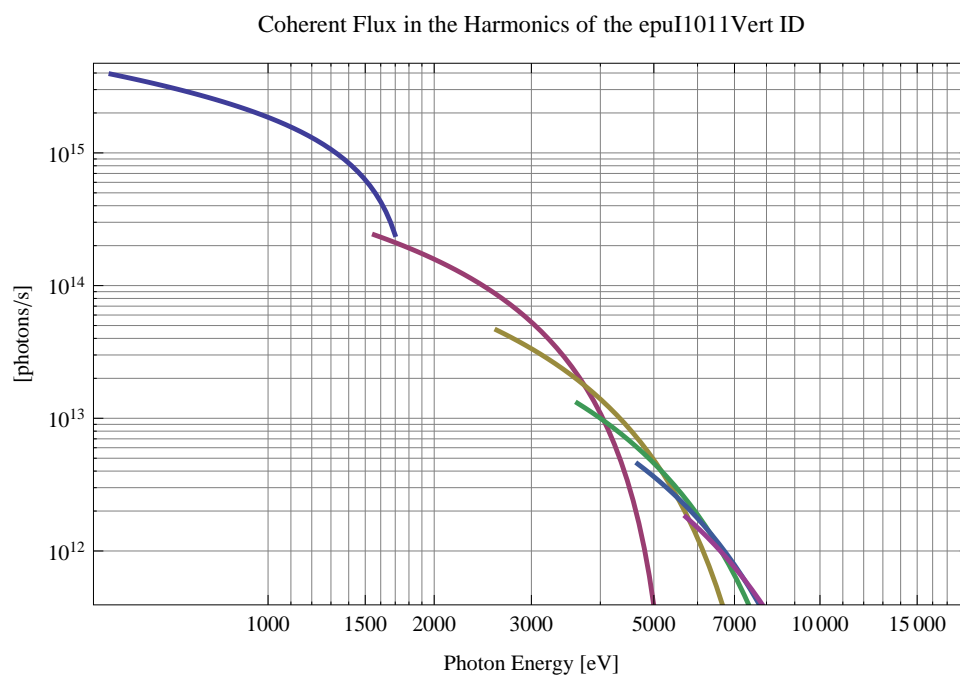


Figure 5.194: The coherent flux in the harmonics of the epuI1011Vert ID

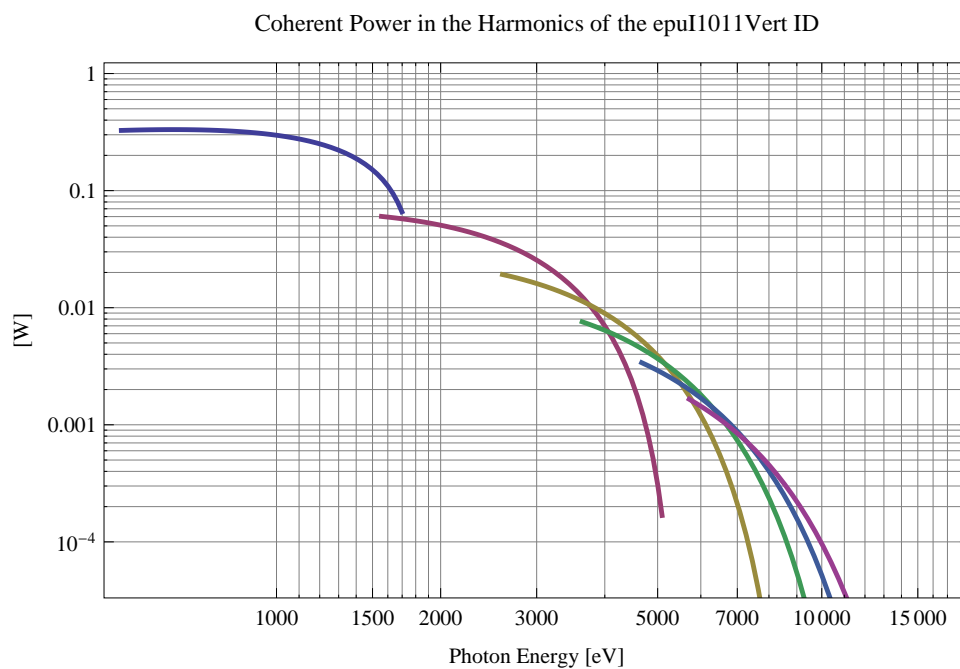


Figure 5.195: The power of coherent synchrotron radiation in the harmonics of the epuI1011Vert ID

Table 5.35: The brilliance at peak energy and the angular spectral flux density from the epuI1011Vert ID for different harmonics at maximum K-value (2.250)

Harmonic	Photon Energy [eV]	Brilliance [Ph./s/mrad <sup>2</sup> /mrad <sup>2</sup> /0.1%BW]	Angular Spectral Flux [Ph./s/mrad <sup>2</sup> /0.1%BW]
1	519.312	$1.27 \times 10^{20}$	$3.11 \times 10^{17}$
3	1557.94	$2.1 \times 10^{20}$	$3.97 \times 10^{17}$
5	2596.56	$1.86 \times 10^{20}$	$3.29 \times 10^{17}$
7	3635.19	$1.44 \times 10^{20}$	$2.47 \times 10^{17}$
9	4673.81	$1.07 \times 10^{20}$	$1.8 \times 10^{17}$
11	5712.43	$7.76 \times 10^{19}$	$1.3 \times 10^{17}$

Table 5.36: The brilliance at peak energy and the angular spectral flux density from the epuI1011Vert ID for different harmonics at minimum K-value (0.4)

Harmonic	Photon Energy [eV]	Brilliance [Ph./s/mrad <sup>2</sup> /mrad <sup>2</sup> /0.1%BW]	Angular Spectral Flux [Ph./s/mrad <sup>2</sup> /0.1%BW]
1	1698.21	$8.36 \times 10^{19}$	$1.56 \times 10^{17}$
3	5094.63	$1.92 \times 10^{18}$	$3.27 \times 10^{15}$
5	8491.06	$2.41 \times 10^{16}$	$4.07 \times 10^{13}$
7	11887.5	$2.65 \times 10^{14}$	$4.48 \times 10^{11}$
9	15283.9	$2.79 \times 10^{12}$	$4.72 \times 10^9$
11	18680.3	$2.88 \times 10^{10}$	$4.89 \times 10^7$

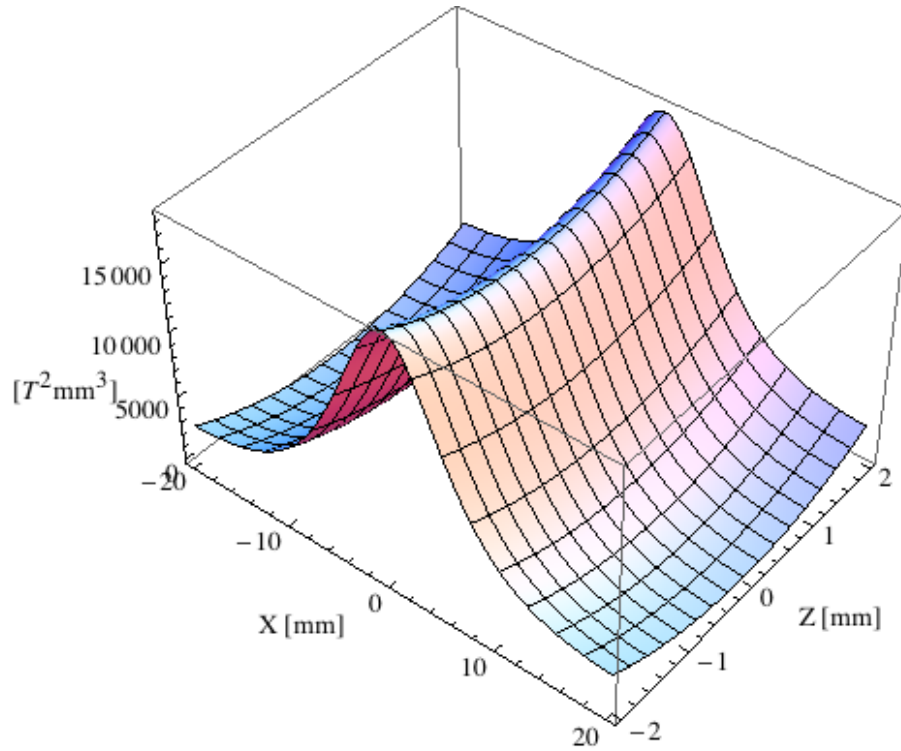


Figure 5.196: Focusing potential from the epuI1011Vert ID over the beam stay clear aperture.

### Influence from the epuI1011Vert ID on the optics of the stored beam

Figure 5.196 shows the focusing potential from the epuI1011Vert over the beam stay clear aperture of the ring aperture.

Figure 5.197 shows the kick map in the beam energy independent unit  $T^2 m^2$  of the kicks induced by the epuI1011Vert ID over the beam stay clear aperture.

Figure 5.198 shows the induced angular kick on the stored beam from the epuI1011Vert ID as a function of the vertical distance to the axis of the ID.

Figure 5.199 shows the induced angular kick on the stored beam from the epuI1011Vert ID as a function of the horizontal distance to the axis of the ID.

Figure 5.200 shows tune shift induced by the epuI1011Vert ID over the beam stay clear aperture. Note that the tune shift depends on the beam size at the ID.

Figure 5.201 shows the induced tune shift from the epuI1011Vert ID as a function of the vertical distance to the axis of the ID.

Figure 5.202 shows the induced tune shift from the epuI1011Vert ID as a function of the horizontal distance to the axis of the ID.

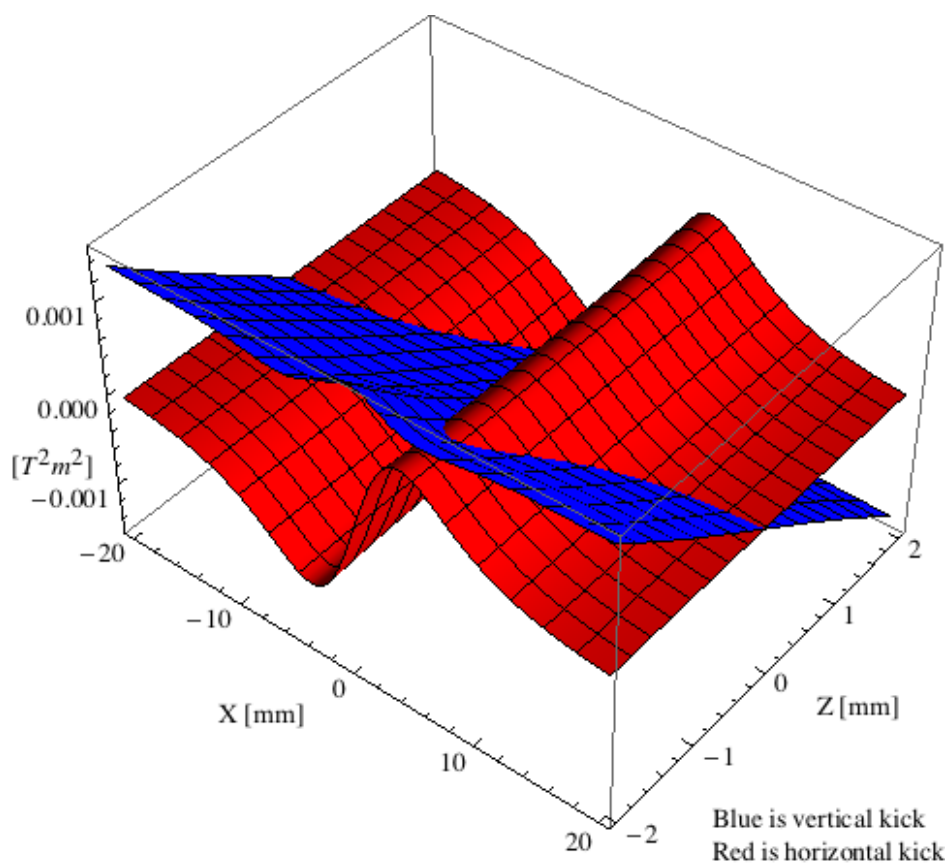


Figure 5.197: Kick map in the beam energy independent unit  $T^2 m^2$  of the kicks induced by the epul1011Vert ID over the beam stay clear aperture.

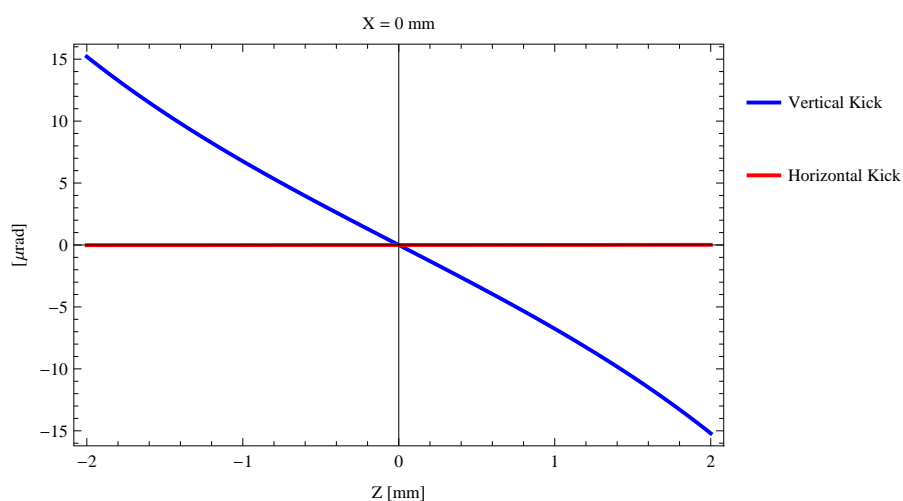


Figure 5.198: Induced angular kick on the stored beam from the epul1011Vert ID as a function of the vertical distance to the ID axis.

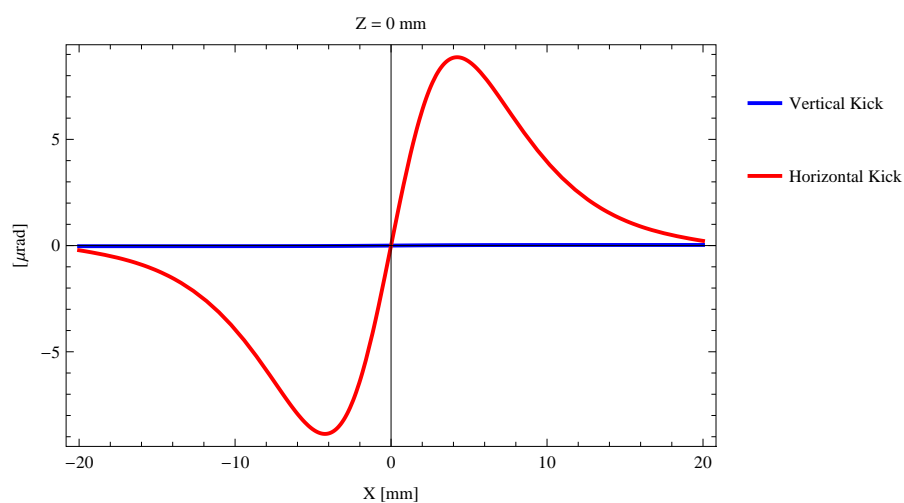


Figure 5.199: Induced angular kick on the stored beam from the epuI1011Vert ID as a function of the horizontal distance to the ID axis.

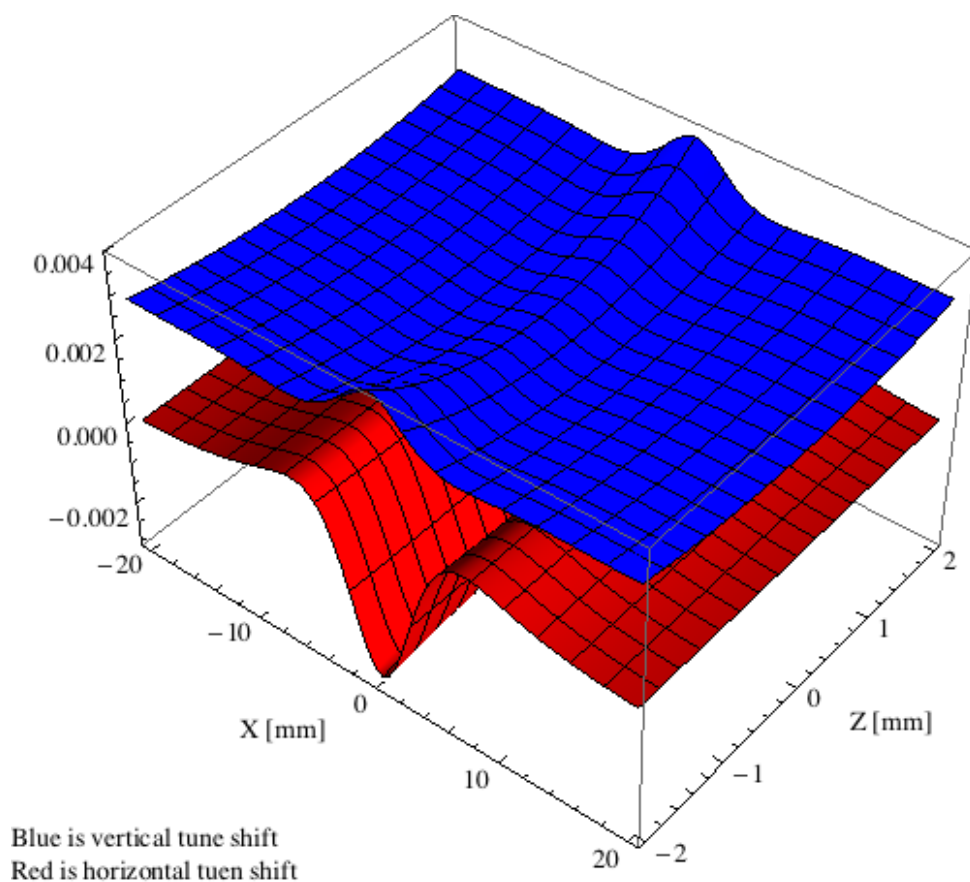


Figure 5.200: Tune shift induced by the epuI1011Vert ID over the beam stay clear aperture.

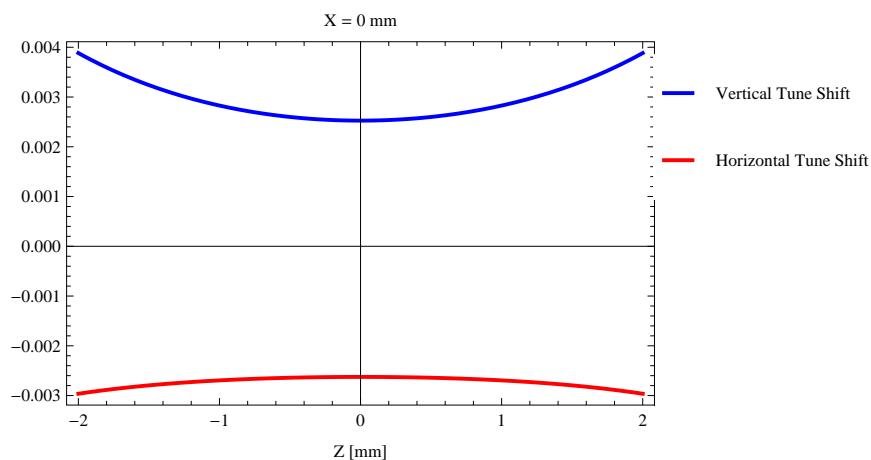


Figure 5.201: Induced tune shift from the epuI1011Vert ID as a function of the vertical distance to the axis of the ID.

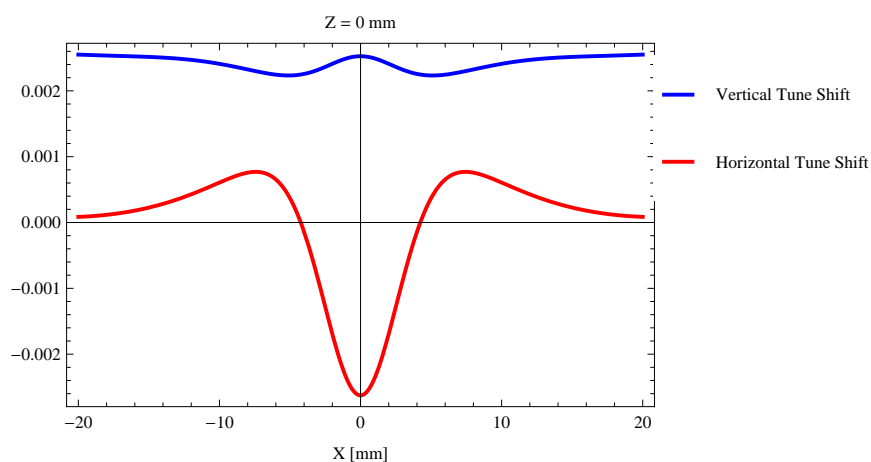


Figure 5.202: Induced tune shift from the epuI1011Vert ID on the stored beam from the ID as a function of the horizontal distance to the axis of the ID.

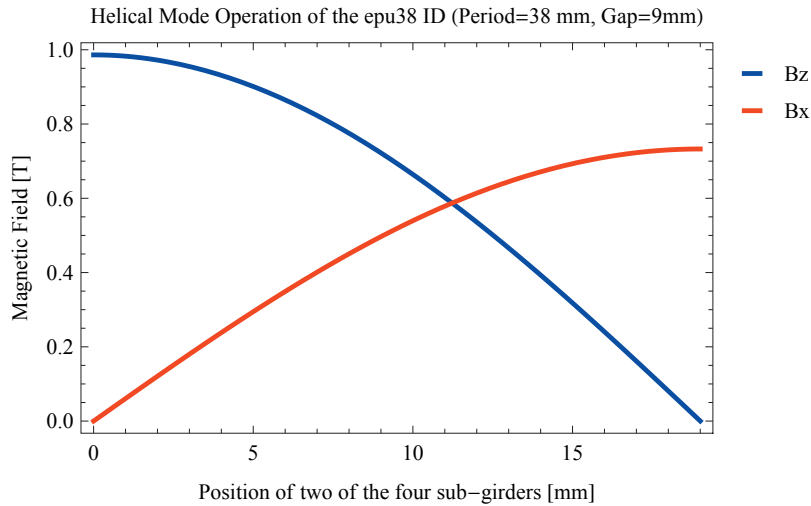


Figure 5.203: Vertical and horizontal magnetic field for the the epu38 ID when operating in the helical mode for different positions for two of the four sub-girders

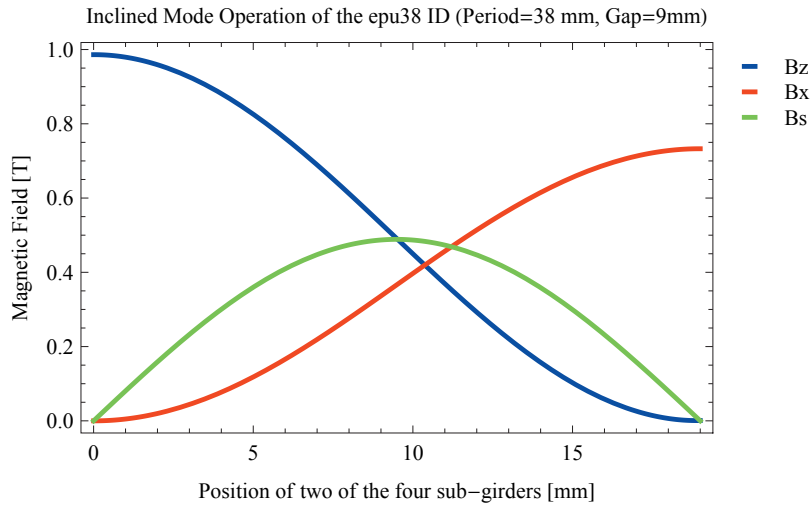


Figure 5.204: Vertical, horizontal, and longitudinal magnetic field for the the epu38 ID when operating in the inclined mode for different positions for two of the four sub-girders

### 5.3.7. The elliptically polarising undulator epu38

#### Modes of operation in the elliptically polarising undulator epu38

Horizontal polarisation of the emitted synchrotron radiation from the epu38 ID (Period=38 mm, Gap=9mm) is found in the planar mode when there is no movement of the sub-girders.

Circular polarisation is found in the elliptical mode of operation for a symmetric sub-grider movement of 11.229 mm. Figure 5.203 shows the vertical and horizontal magnetic field for the epu38 ID when operating in the helical mode.

45 degree polarisation is found in the inclined mode of operation for an assymetric sub-grider movement of 10.3735 mm. Figure 5.204 shows the vertical and horizontal magnetic field for the epu38 ID when operating in the inclined mode.

The following sub-sections will cover four different situations: The epu38 operating in the pla-



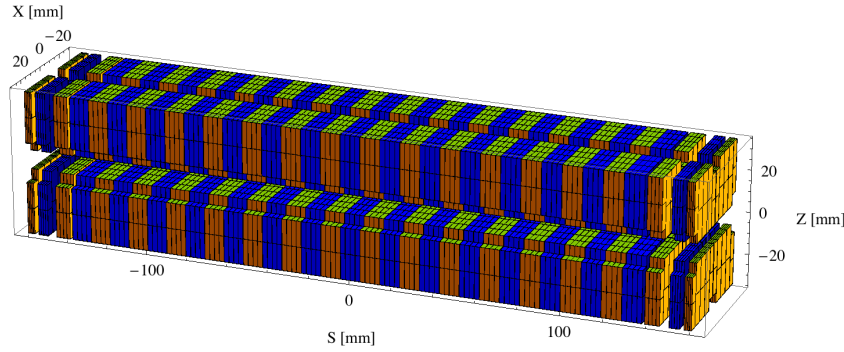


Figure 5.205: Magnetic model of the epu38Plan ID. The ID has been modelled with Radia [2]

nar mode for horizontal polarisation (epu38Plan); The epu38 operating in the helical mode for circular polarisation (epu38Heli), the epu38 operating in the inclined mode for 45 degree polarisation (epu38Incl); and The epu38 operating in the vertical mode for vertical polarisation (epu38Vert).

### Magnet model of the elliptically polarising undulator epu38Plan

The Radia [2] magnet model of the epu38Plan ID is shown in Figure 5.205. The length of the magnet model is 320.976 mm. The magnetic material in the model is NdFeb with a remanence of 1.28 T, a material similar to VACODYM 776 TP from Vacuumschmelze. Blocks with vertical magnetisation are blue and blocks with horizontal magnetisation are yellow. The block size is 30.x30.x9.5 mm<sup>3</sup> and there is a 5. mm cut-out in two of the corners of the blocks. The total length of the epu38Plan ID is 3930.98 mm.

### Analysis of the magnetic field of the epu38Plan ID

The effective magnetic fields on axis and the fundamental photon energy of the epu38Plan ID are shown in Table 5.37. The higher harmonic contents in the magnetic field of an elliptically polarising undulator made of permanent magnets is negligible and the efficient field has about the same strength as the peak field.

### Synchrotron radiation from the epu38Plan ID

The power map of the emitted synchrotron radiation by the epu38Plan ID, assuming a 0.5 A filament beam with an energy of 3 GeV and undulator properties of the synchrotron radiation, is shown in Figure 5.209. The on-axis power density is 43.893 kW/mrad<sup>2</sup>

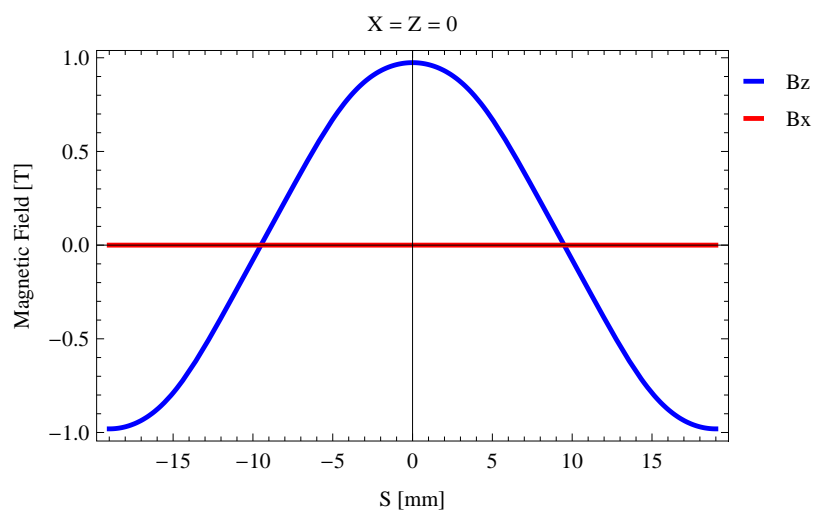
A map of the degree of linear polarisation of the fundamental harmonic of the synchrotron radiation emitted by the epu38Plan ID over the angle of observation is shown in Figure 5.210.

A map of the degree of 45 degree polarisation of the fundamental harmonic of the synchrotron radiation emitted by the epu38Plan ID over the angle of observation is shown in Figure 5.211.

A map of the degree of circular polarisation of the fundamental harmonic of the synchrotron radiation emitted by the epu38Plan ID over the angle of observation is shown in Figure 5.212.

Table 5.37: Effective Fields on axis and Fundamental Photon Energy of the epu38Plan ID

Undulator Period	38	mm
Undulator Gap	9	mm
Undulator Mode	Planar	
Undulator Phase	0.000	mm
Vertical Peak Field	0.974	T
Efficient Vertical Field	0.986	T
Kx (from vert. field)	3.500	
Horizontal Peak Field:	0.000	T
Efficient Horizontal Field	0.000	T
Kz (from hor. field)	0.000	
Photon Energy, Harm.1	0.316	keV
Emitted Power	10.881	kW
Total Length	3931.0	mm

Figure 5.206: Vertical magnetic field in a central pole of the epu38Plan ID along the ID axis,  $X = Z = 0$

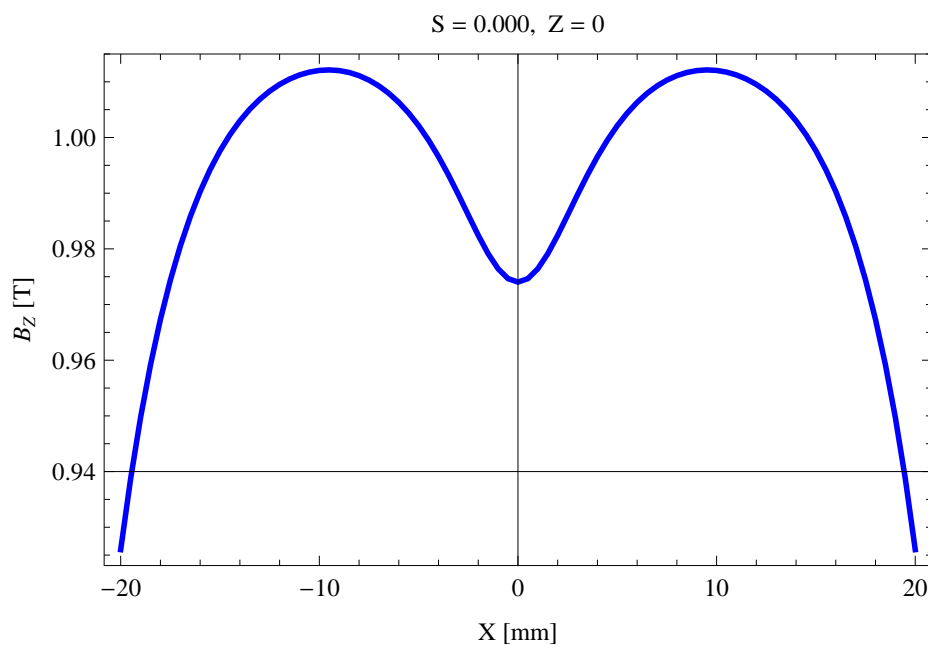


Figure 5.207: Vertical magnetic field in a central pole of the epu38Plan ID along the horizontally transverse direction to the ID axis,  $S = 0.000, Z = 0$

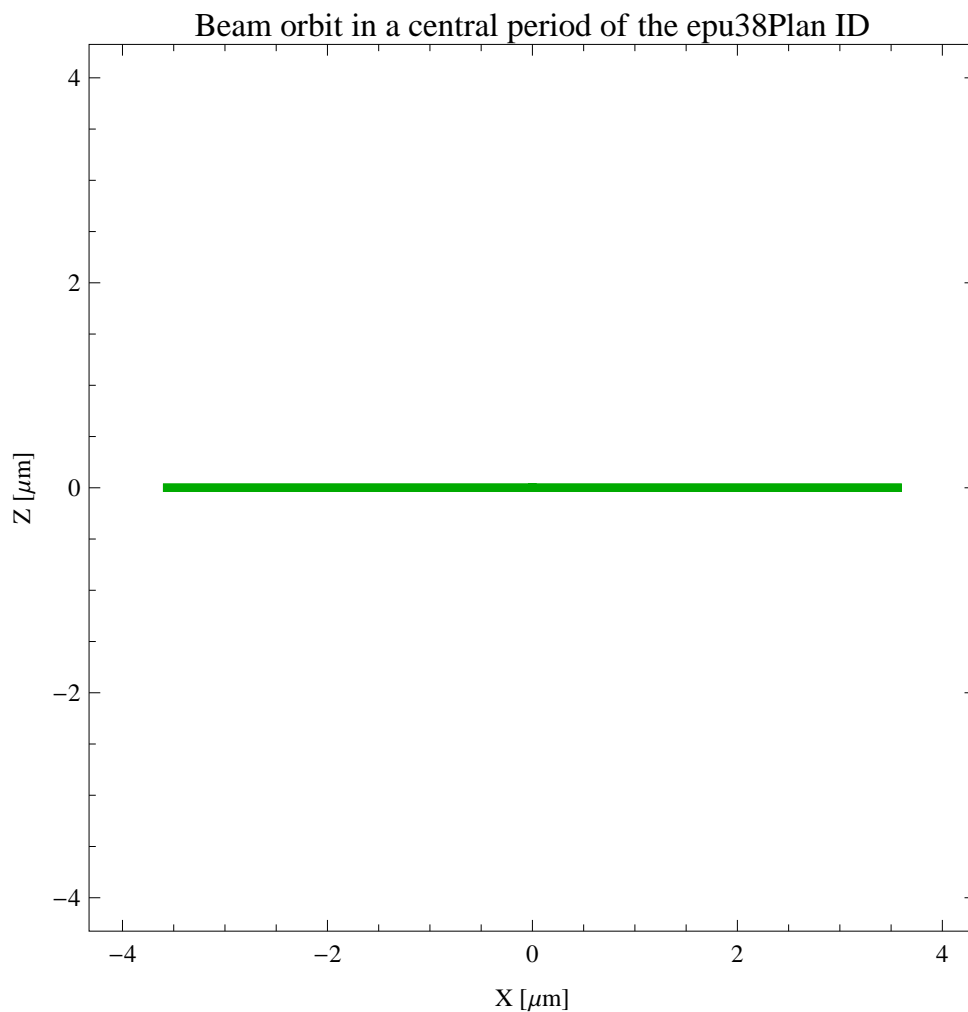


Figure 5.208: The beam orbit of the electron beam through a central period of the epu38Plan ID

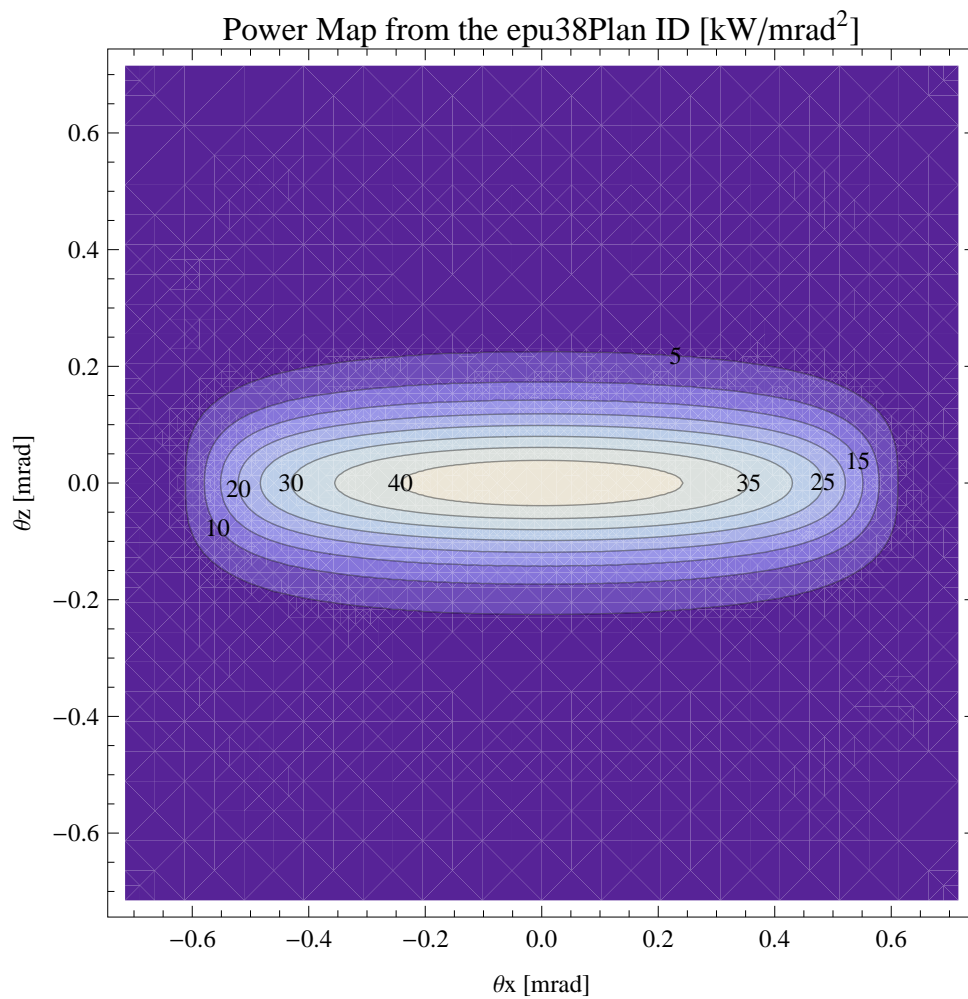


Figure 5.209: Map of the power distribution of the emitted synchrotron radiation by the epu38Plan ID

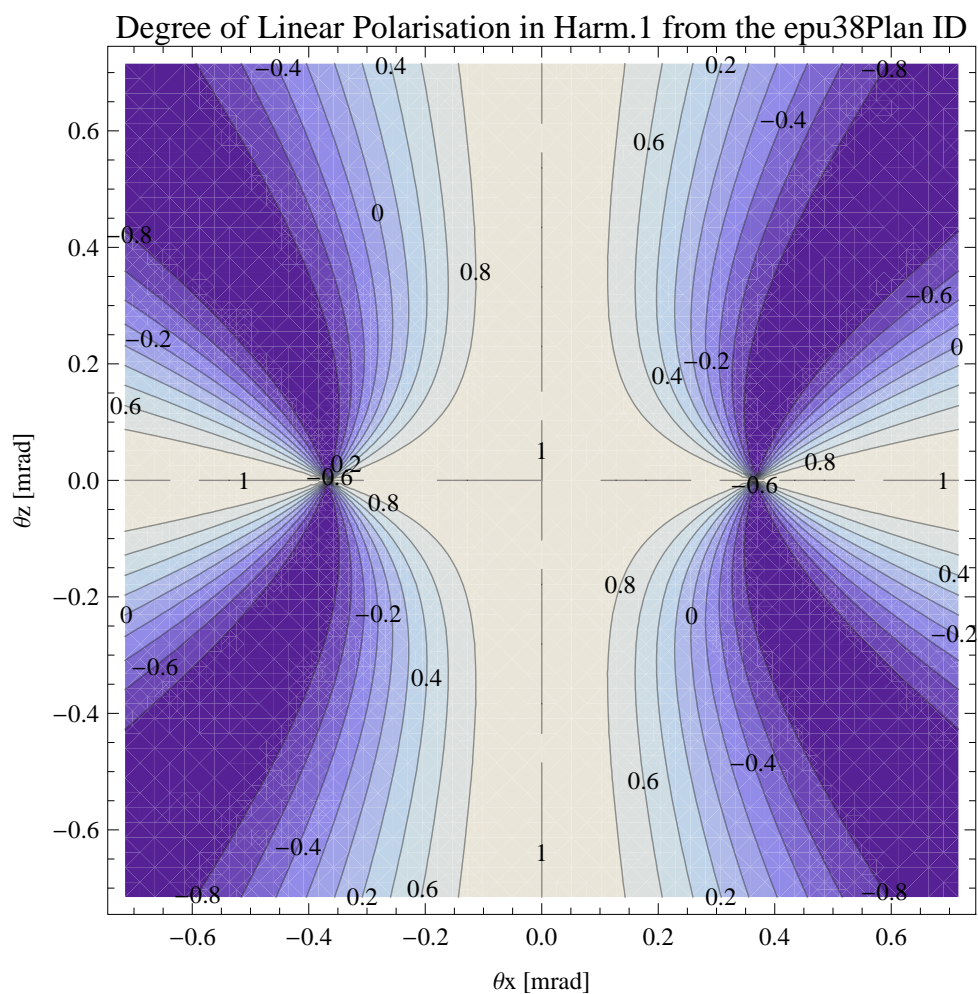


Figure 5.210: Map of linear polarisation in the fundamental harmonic of the synchrotron radiation emitted by the epu38Plan ID

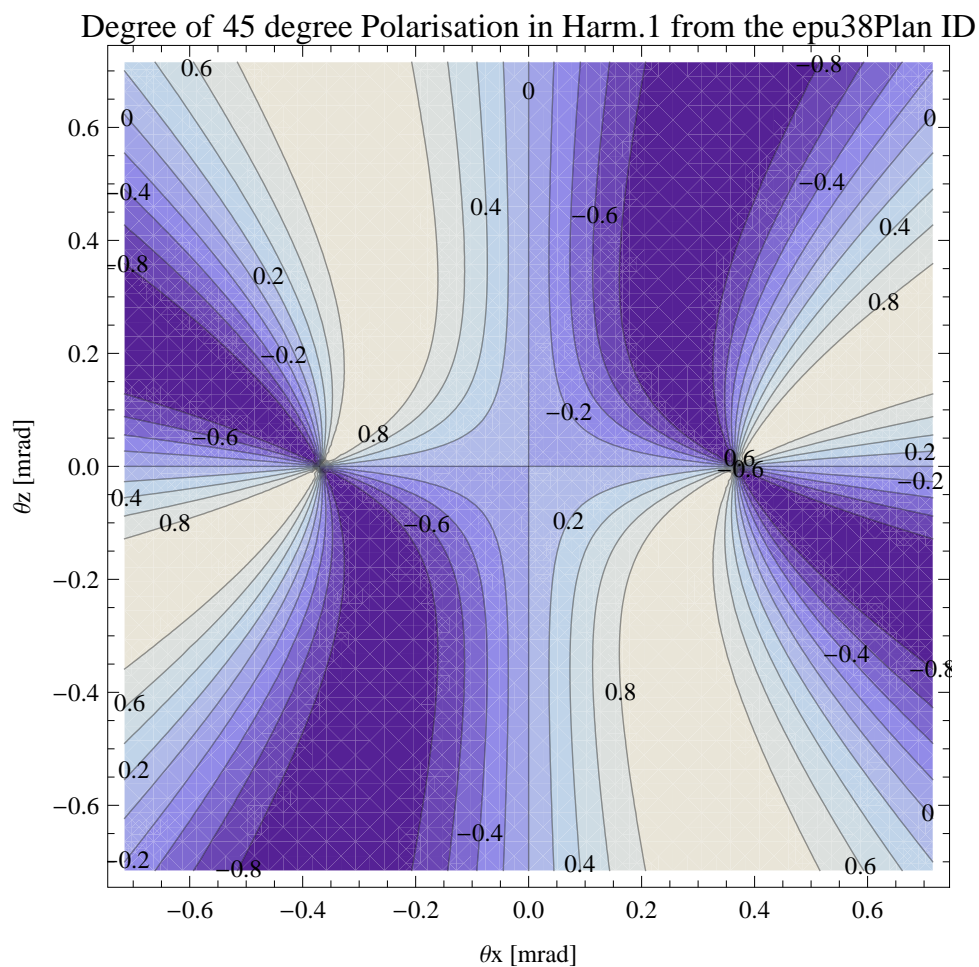


Figure 5.211: Map of 45 degree polarisation in the fundamental harmonic of the synchrotron radiation emitted by the epu38Plan ID

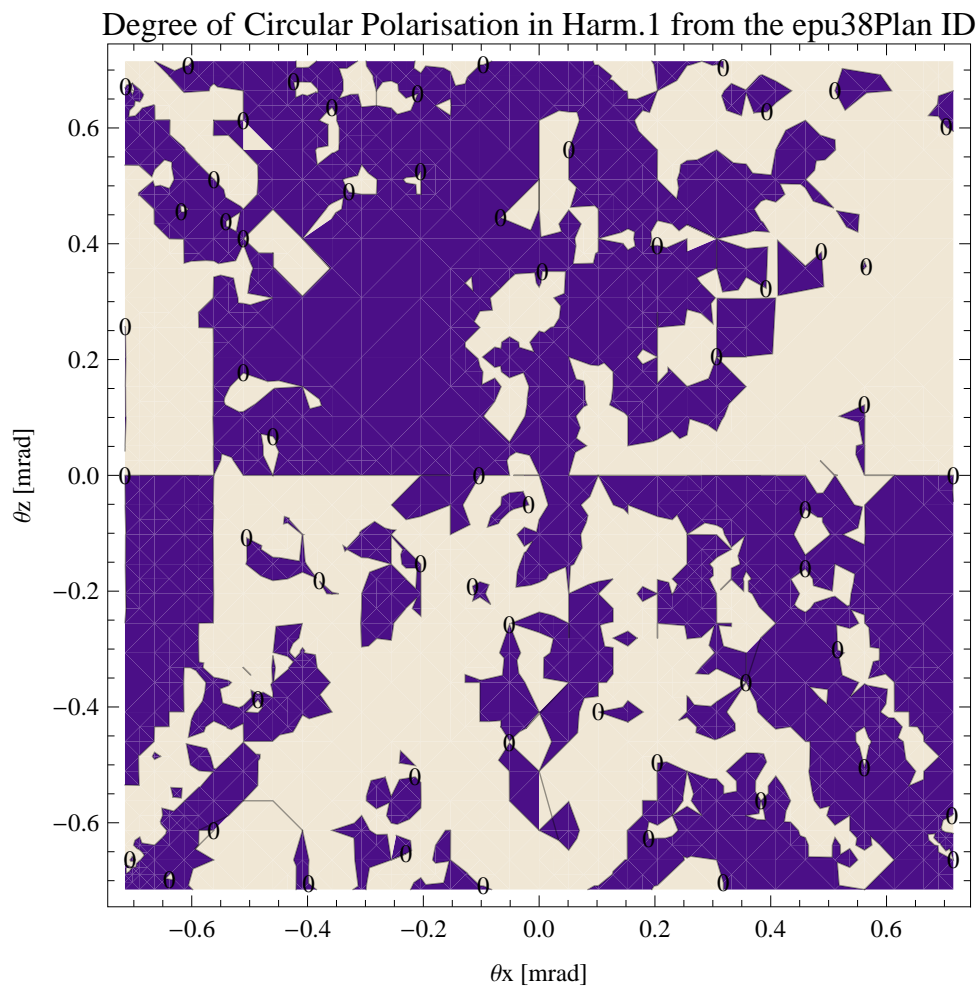


Figure 5.212: Map of circular polarisation in the fundamental harmonic of the synchrotron radiation emitted by the epu38Plan ID

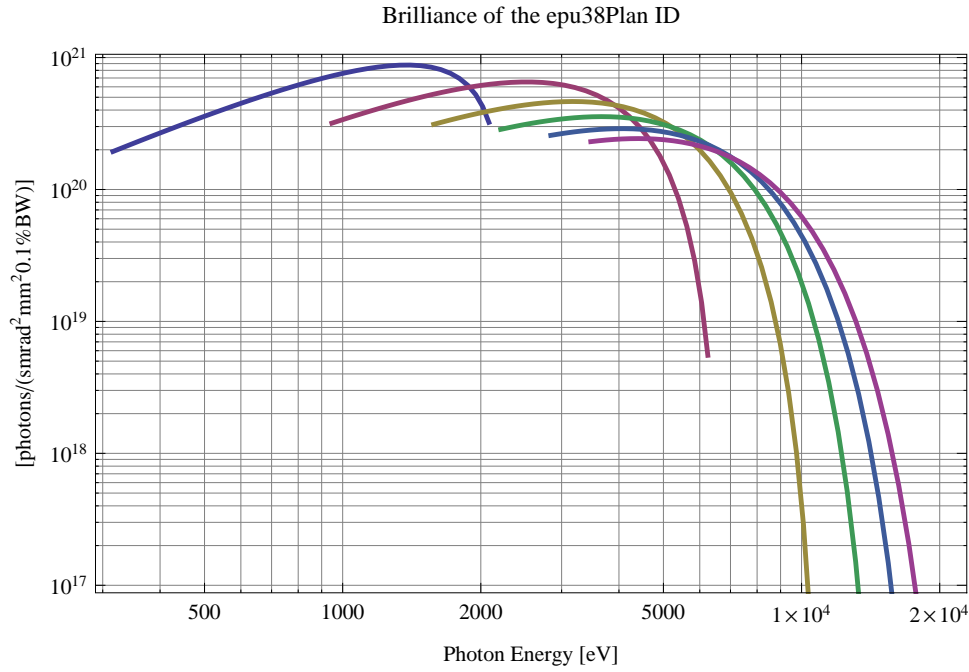


Figure 5.213: The brilliance at peak energy from the epu38Plan ID

The on axis brilliance at peak energy, the angular spectral flux, the flux in the harmonics, the power in the harmonics, the ratio of coherence, the coherent flux in the harmonics, and the power of coherent radiation in the harmonics from the epu38Plan ID have been calculated and the resulting plots are found in this section of the document. The beam parameters used for the calculation are 0.5 A of stored current,  $\beta_H = 9$  m,  $\varepsilon_H = 0.263$  nmrad,  $\beta_V = 4.8$  m,  $\varepsilon_V = 8$  pmrad, and an energy spread of 0.001.

The brilliance at peak energy and the angular spectral flux density from the epu38Plan ID for different harmonics at maximum K-value (3.500) are given in Table 5.38 and for minimum K-value (0.400) these values are given in Table 5.39.

Table 5.38: The brilliance at peak energy and the angular spectral flux density from the epu38Plan ID for different harmonics at maximum K-value (3.500)

Harmonic	Photon Energy [eV]	Brilliance [Ph./s/mrad <sup>2</sup> /mrad <sup>2</sup> /0.1%BW]	Angular Spectral Flux [Ph./s/mrad <sup>2</sup> /0.1%BW]
1	315.746	$1.94 \times 10^{20}$	$7.35 \times 10^{17}$
3	947.237	$3.18 \times 10^{20}$	$7.98 \times 10^{17}$
5	1578.73	$3.12 \times 10^{20}$	$6.84 \times 10^{17}$
7	2210.22	$2.85 \times 10^{20}$	$5.85 \times 10^{17}$
9	2841.71	$2.57 \times 10^{20}$	$5.05 \times 10^{17}$
11	3473.2	$2.3 \times 10^{20}$	$4.4 \times 10^{17}$



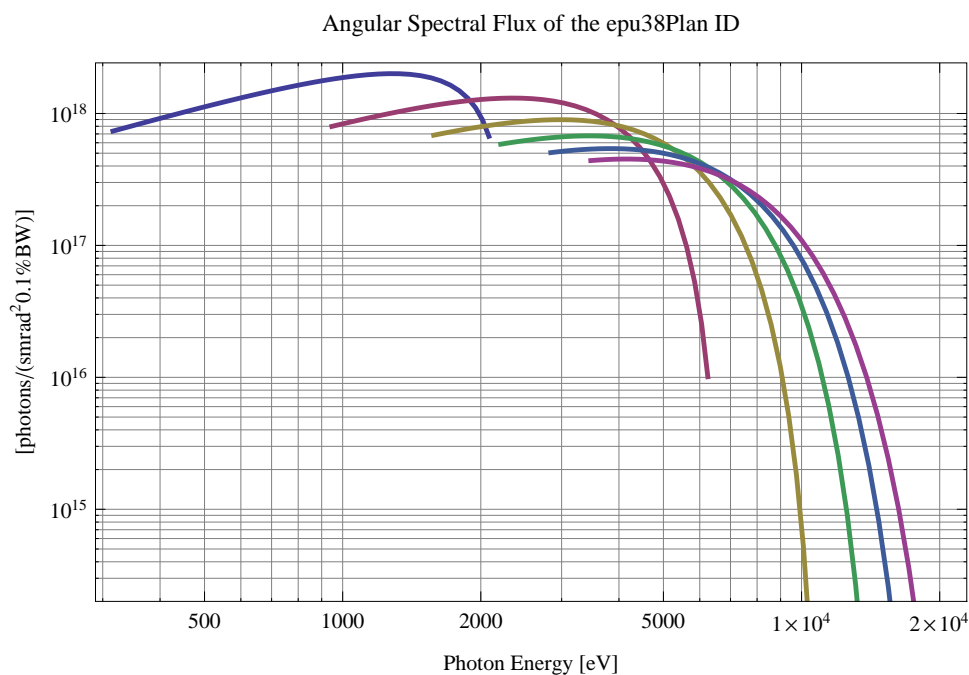


Figure 5.214: The angular spectral flux from the epu38Plan ID

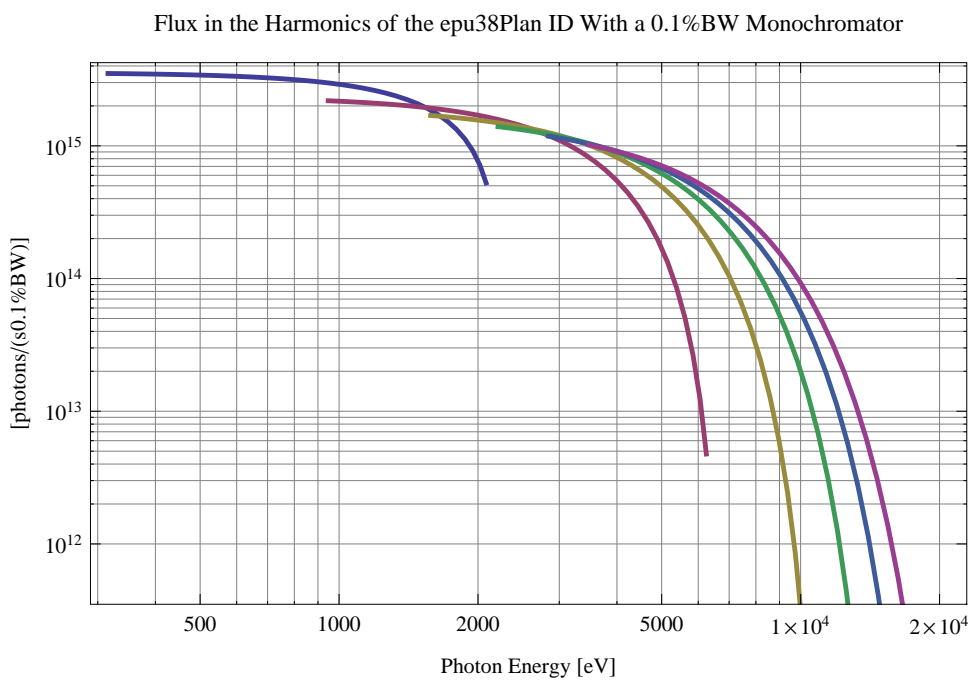


Figure 5.215: The flux of photons in the harmonics from the epu38Plan ID using a 0.1%BW monochromator

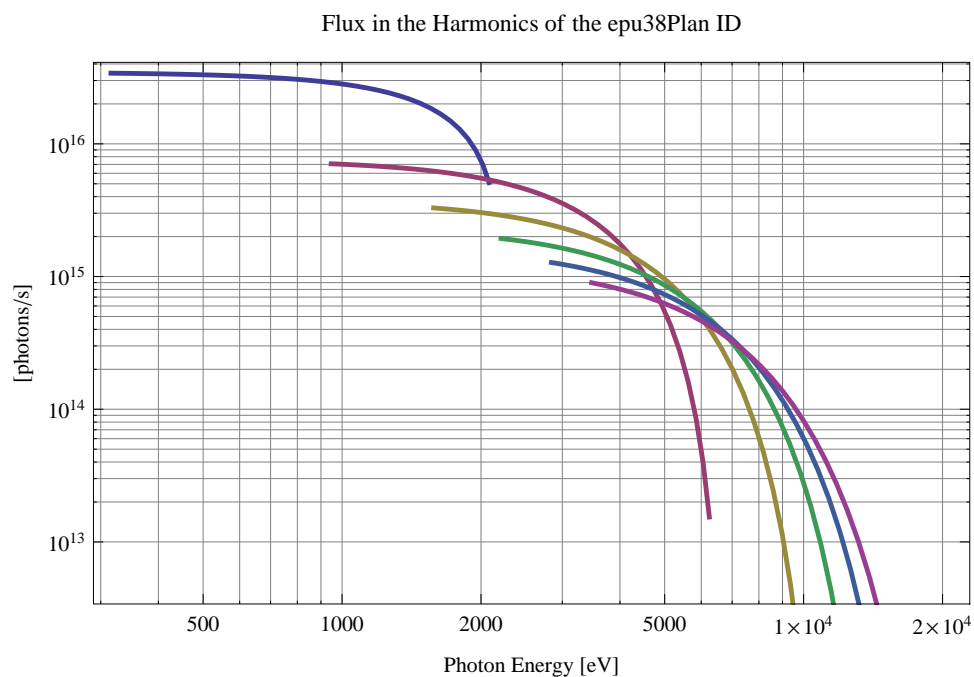


Figure 5.216: The flux of photons in the harmonics from the epu38Plan ID

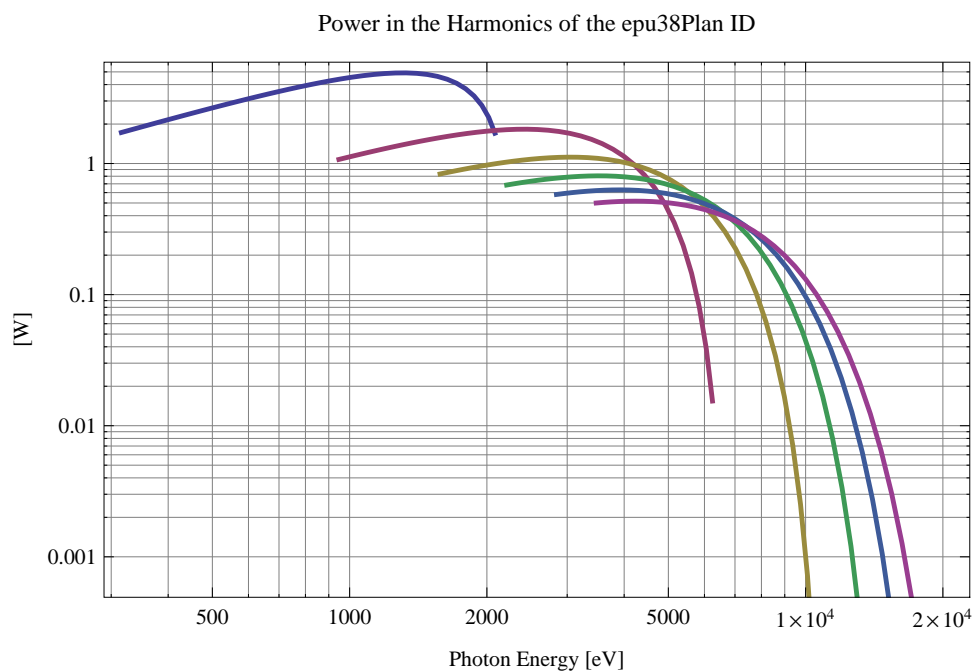


Figure 5.217: The power in the harmonics from the epu38Plan ID

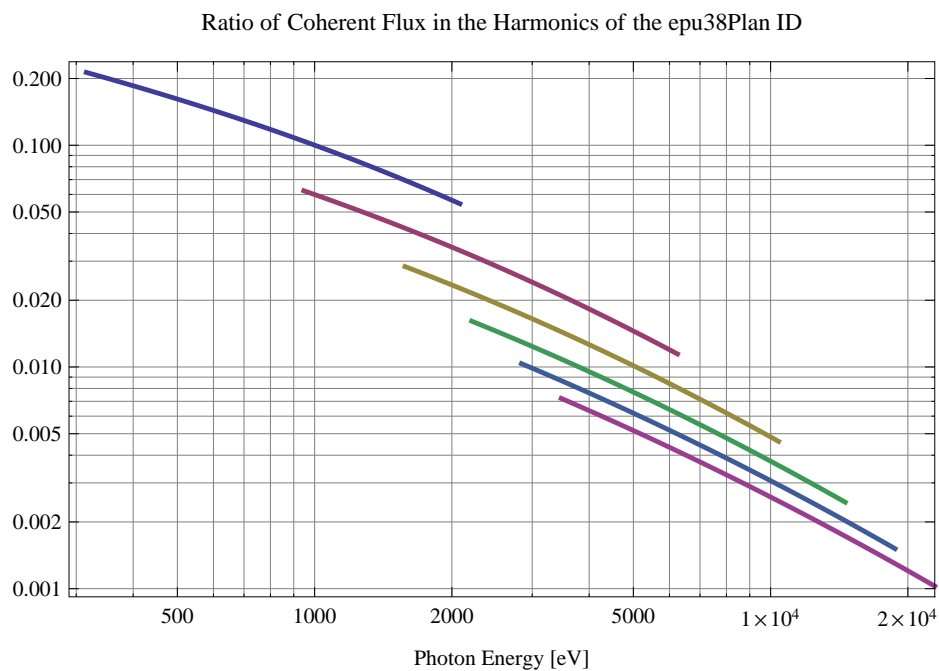


Figure 5.218: The ratio of coherent flux in the harmonics from the epu38Plan ID

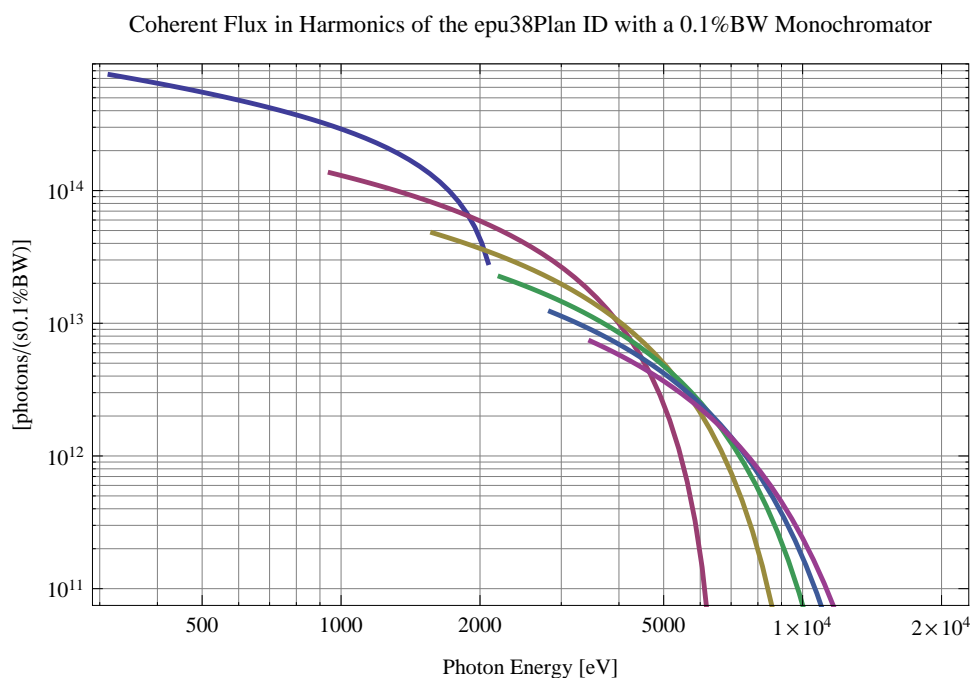


Figure 5.219: The coherent flux in the harmonics of the epu38Plan ID using a 0.1%BW Monochromator

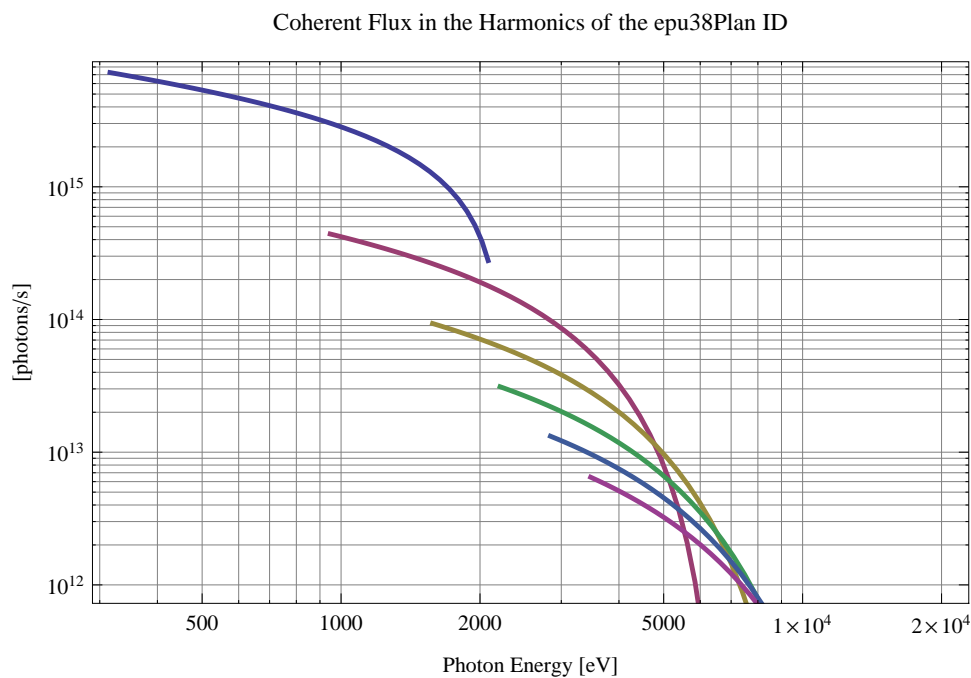


Figure 5.220: The coherent flux in the harmonics of the epu38Plan ID

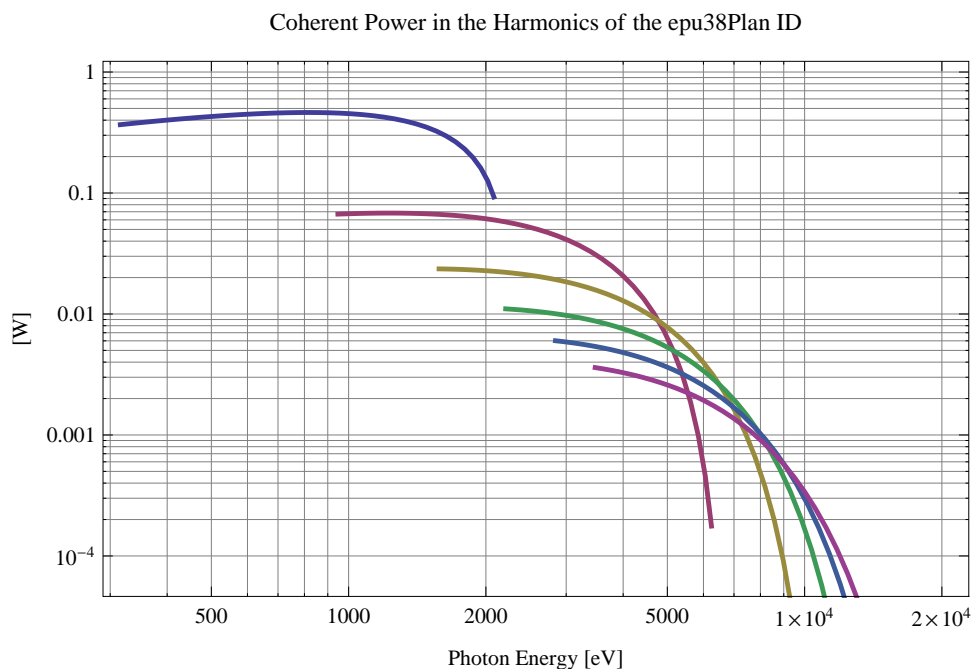


Figure 5.221: The power of coherent synchrotron radiation in the harmonics of the epu38Plan ID

Table 5.39: The brilliance at peak energy and the angular spectral flux density from the epu38Plan ID for different harmonics at minimum K-value (0.4)

Harmonic	Photon Energy [eV]	Brilliance [Ph./s/mrad <sup>2</sup> /mrad <sup>2</sup> /0.1%BW]	Angular Spectral Flux [Ph./s/mrad <sup>2</sup> /0.1%BW]
1	2082.54	$3.23 \times 10^{20}$	$6.72 \times 10^{17}$
3	6247.63	$5.54 \times 10^{18}$	$1.01 \times 10^{16}$
5	10412.7	$6.1 \times 10^{16}$	$1.09 \times 10^{14}$
7	14577.8	$6.35 \times 10^{14}$	$1.12 \times 10^{12}$
9	18742.9	$6.5 \times 10^{12}$	$1.15 \times 10^{10}$
11	22908.	$6.62 \times 10^{10}$	$1.17 \times 10^8$

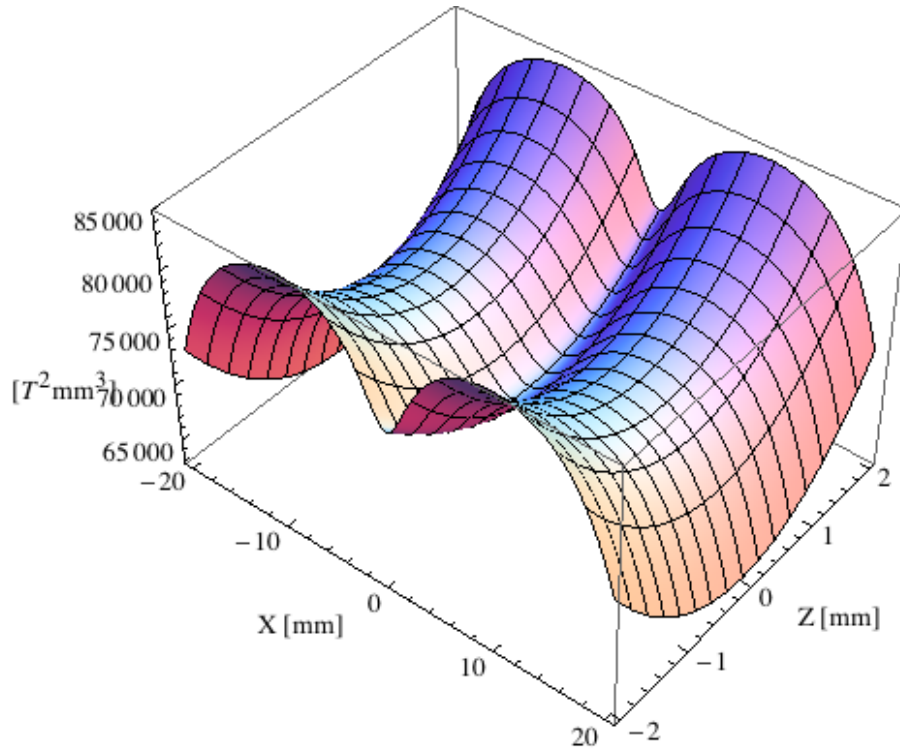


Figure 5.222: Focusing potential from the epu38Plan ID over the beam stay clear aperture.

### Influence from the epu38Plan ID on the optics of the stored beam

Figure 5.222 shows the focusing potential from the epu38Plan over the beam stay clear aperture of the ring aperture.

Figure 5.223 shows the kick map in the beam energy independent unit  $T^2 m^2$  of the kicks induced by the epu38Plan ID over the beam stay clear aperture.

Figure 5.224 shows the induced angular kick on the stored beam from the epu38Plan ID as a function of the vertical distance to the axis of the ID.

Figure 5.225 shows the induced angular kick on the stored beam from the epu38Plan ID as a function of the horizontal distance to the axis of the ID.

Figure 5.226 shows tune shift induced by the epu38Plan ID over the beam stay clear aperture. Note that the tune shift depends on the beam size at the ID.

Figure 5.227 shows the induced tune shift from the epu38Plan ID as a function of the vertical distance to the axis of the ID.

Figure 5.228 shows the induced tune shift from the epu38Plan ID as a function of the horizontal distance to the axis of the ID.

### Magnet model of the elliptically polarising undulator epu38Heli

The Radia [2] magnet model of the epu38Heli ID is shown in Figure 5.229. The length of the magnet model is 320.976 mm. The magnetic material in the model is NdFeb with a remanence of 1.28 T, a material similar to VACODYM 776 TP from Vacuumschmelze. Blocks with vertical magnetisation are blue and blocks with horizontal magnetisation are yellow. The block size is

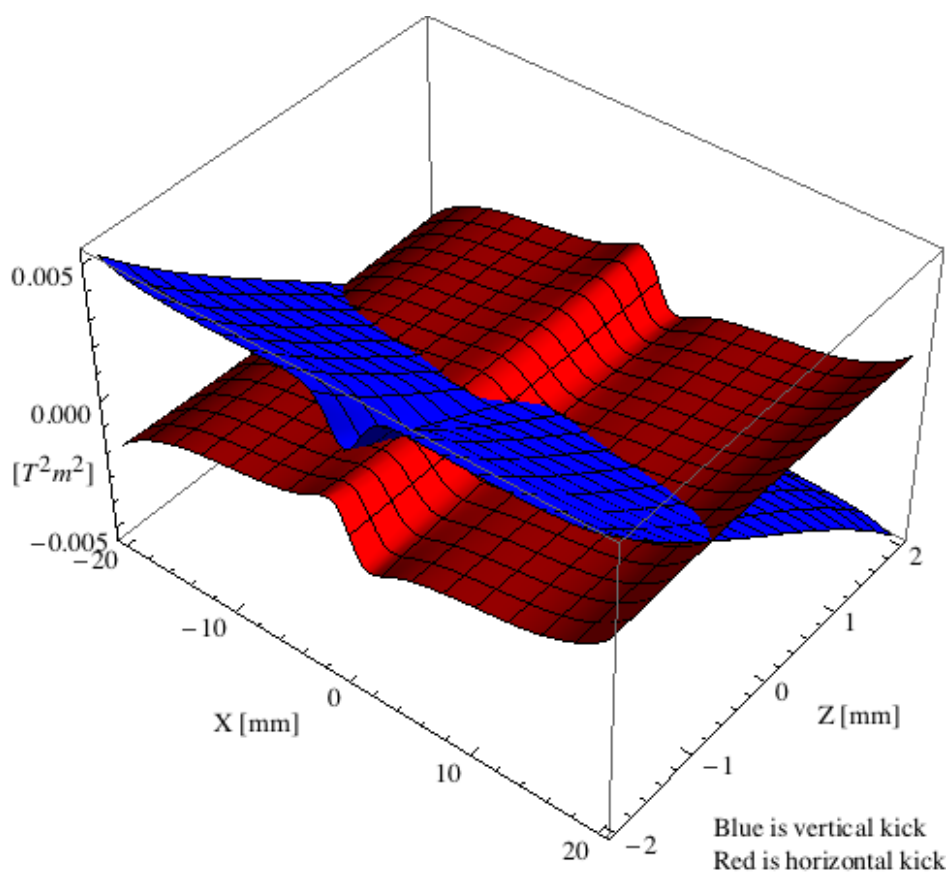


Figure 5.223: Kick map in the beam energy independent unit  $T^2m^2$  of the kicks induced by the epu38Plan ID over the beam stay clear aperture.

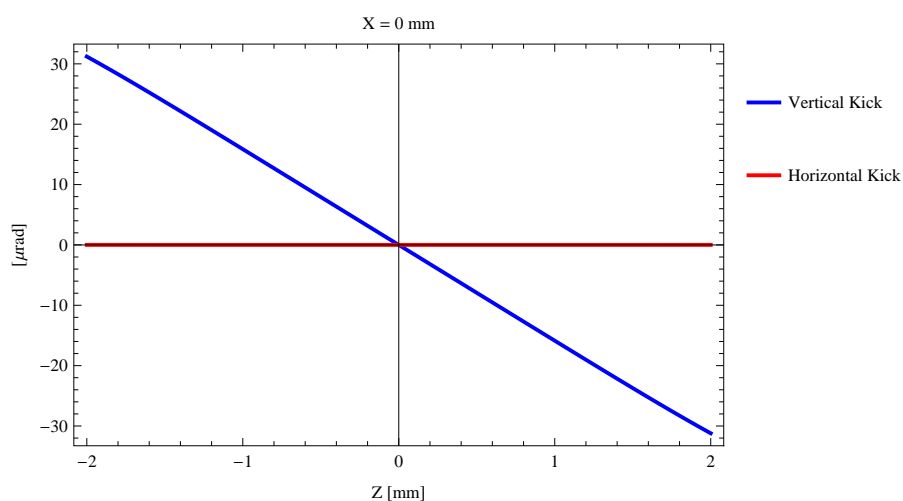


Figure 5.224: Induced angular kick on the stored beam from the epu38Plan ID as a function of the vertical distance to the ID axis.

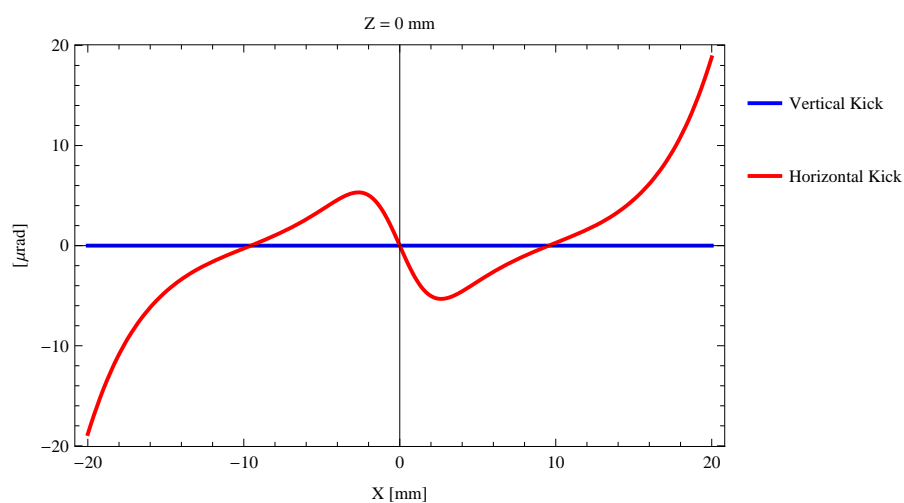


Figure 5.225: Induced angular kick on the stored beam from the epu38Plan ID as a function of the horizontal distance to the ID axis.

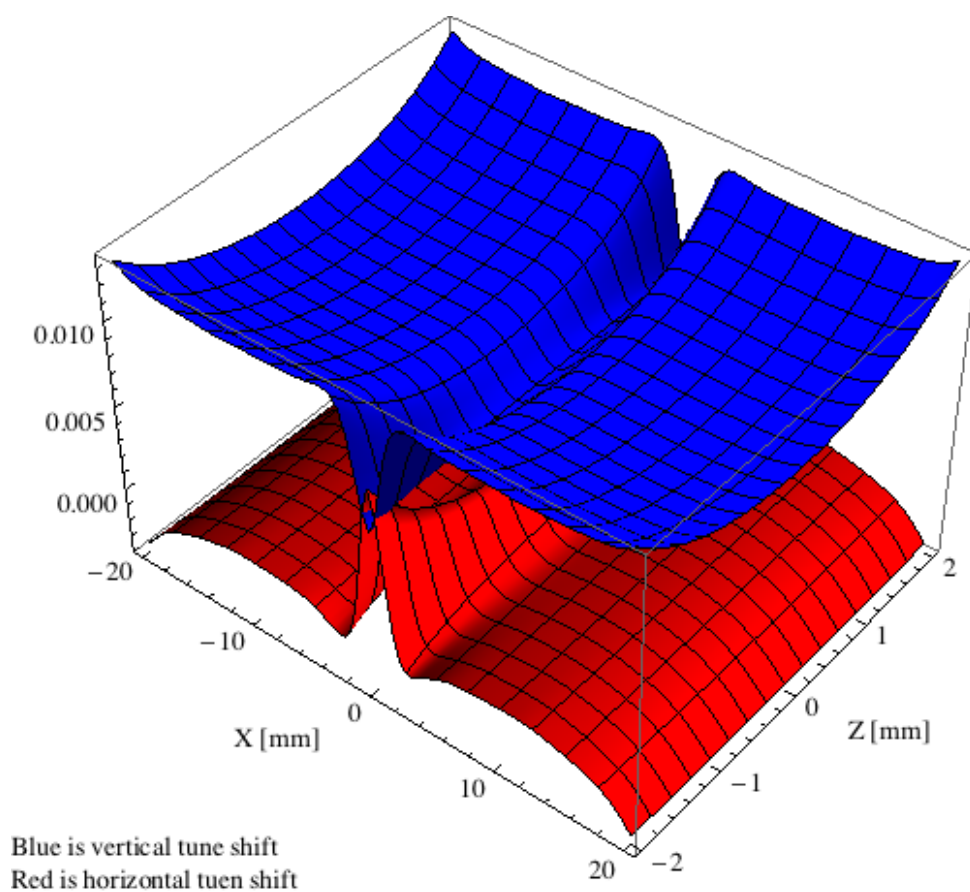


Figure 5.226: Tune shift induced by the epu38Plan ID over the beam stay clear aperture.



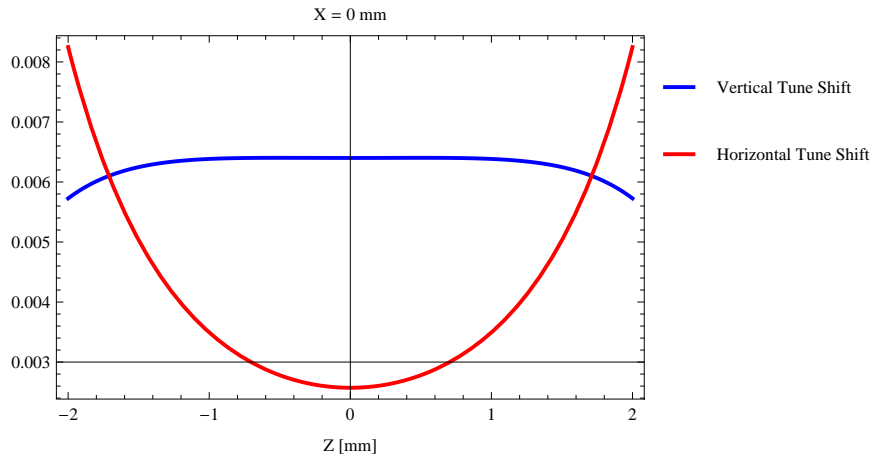


Figure 5.227: Induced tune shift from the epu38Plan ID as a function of the vertical distance to the axis of the ID.

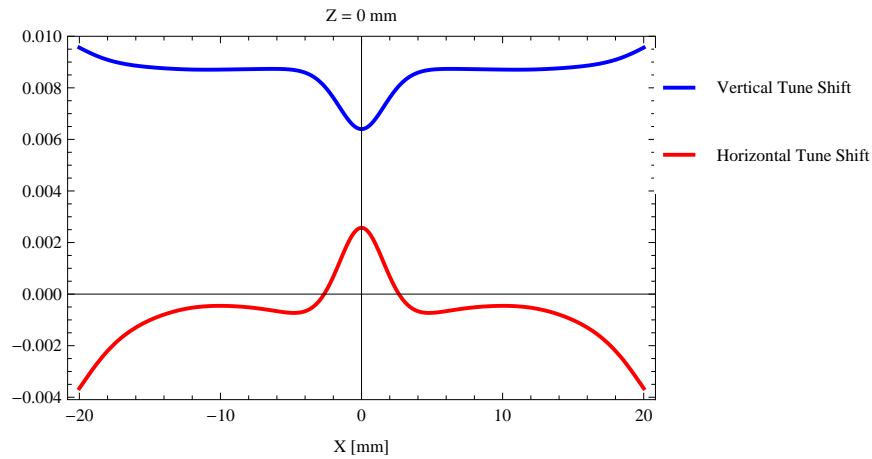


Figure 5.228: Induced tune shift from the epu38Plan ID on the stored beam from the ID as a function of the horizontal distance to the axis of the ID.

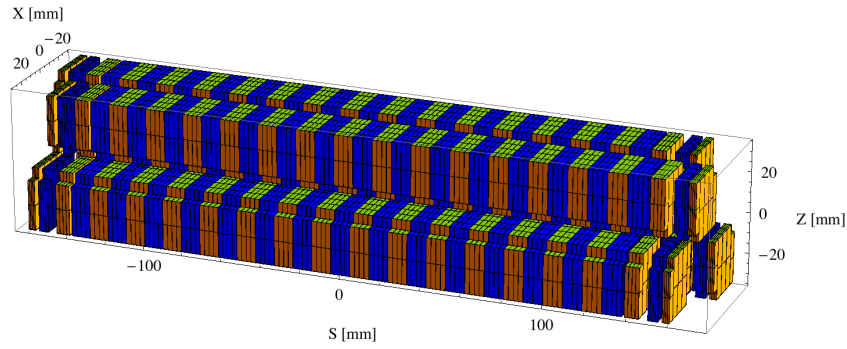


Figure 5.229: Magnetic model of the epu38Heli ID. The ID has been modelled with Radia [2]

$30 \times 30 \times 9.5 \text{ mm}^3$  and there is a 5. mm cut-out in two of the corners of the blocks. The total length of the epu38Heli ID is 3930.98 mm.

### Analysis of the magnetic field of the epu38Heli ID

The effective magnetic fields on axis and the fundamental photon energy of the epu38Heli ID are shown in Table 5.40. The higher harmonic contents in the magnetic field of an elliptically polarising undulator made of permanent magnets is negligible and the efficient field has about the same strength as the peak field.

Table 5.40: Effective Fields on axis and Fundamental Photon Energy of the epu38Heli ID

Undulator Period	38	mm
Undulator Gap	9	mm
Undulator Mode	Helical	
Undulator Phase	11.229	mm
Vertical Peak Field	0.585	T
Efficient Vertical Field	0.587	T
K <sub>x</sub> (from vert. field)	2.083	
Horizontal Peak Field:	0.590	T
Efficient Horizontal Field	0.587	T
K <sub>z</sub> (from hor. field)	2.083	
Photon Energy, Harm.1	0.421	keV
Emitted Power	7.713	kW
Total Length	3931.0	mm

### Synchrotron radiation from the epu38Heli ID

The power map of the emitted synchrotron radiation by the epu38Heli ID, assuming a 0.5 A filament beam with an energy of 3 GeV and undulator properties of the synchrotron radiation, is shown in Figure 5.234. The on-axis power density is  $1.644 \text{ kW/mrad}^2$

A map of the degree of linear polarisation of the fundamental harmonic of the synchrotron radiation emitted by the epu38Heli ID over the angle of observation is shown in Figure 5.235.

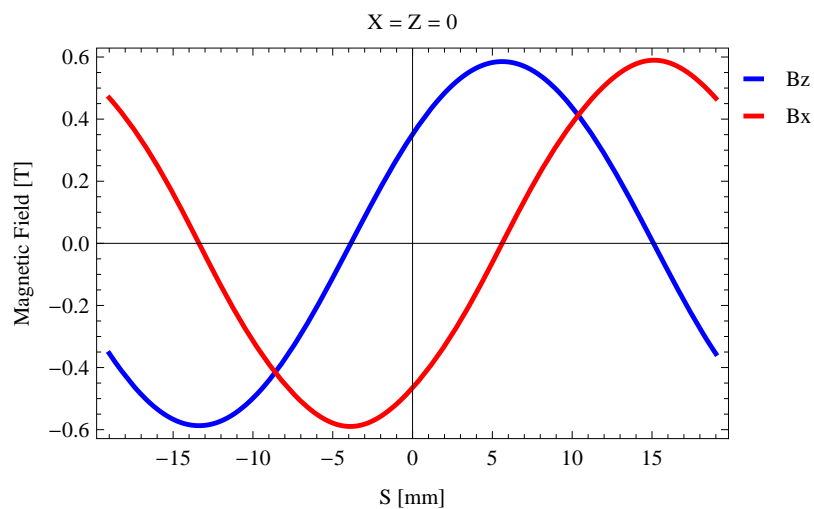


Figure 5.230: Vertical magnetic field in a central pole of the epu38Heli ID along the ID axis,  $X = Z = 0$

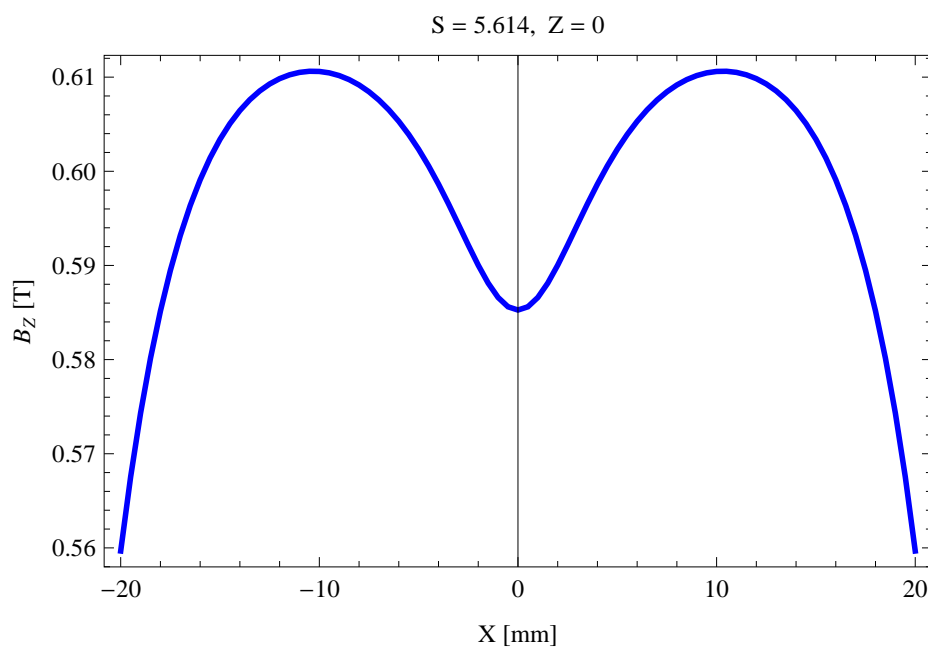


Figure 5.231: Vertical magnetic field in a central pole of the epu38Heli ID along the horizontally transverse direction to the ID axis,  $S = 5.614$ ,  $Z = 0$

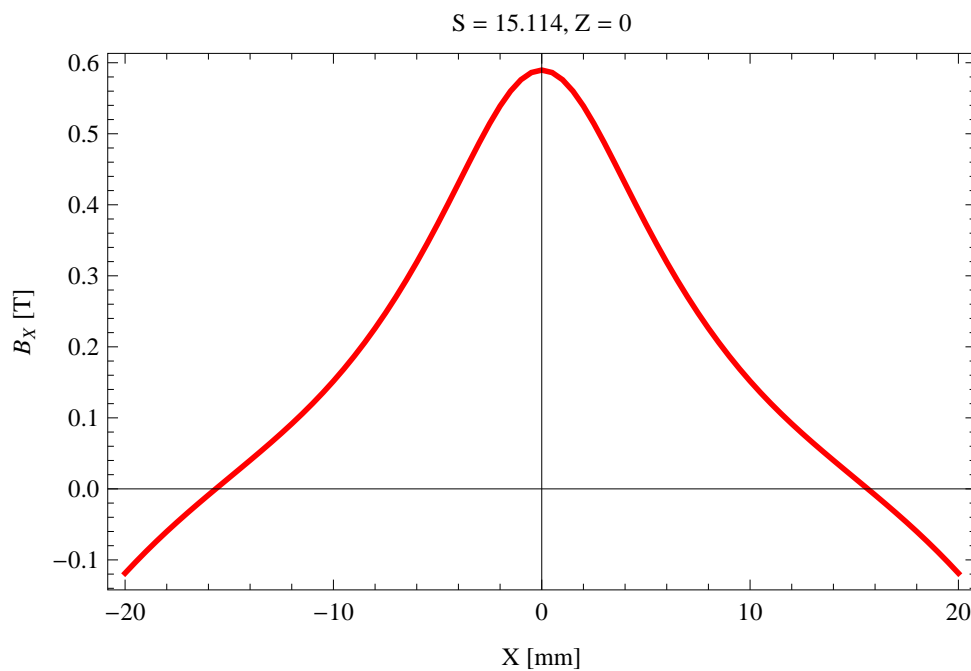


Figure 5.232: Horizontal magnetic field in a central pole of the epu38Heli ID along the horizontally transverse direction to the ID axis, S = 15.114, Z = 0

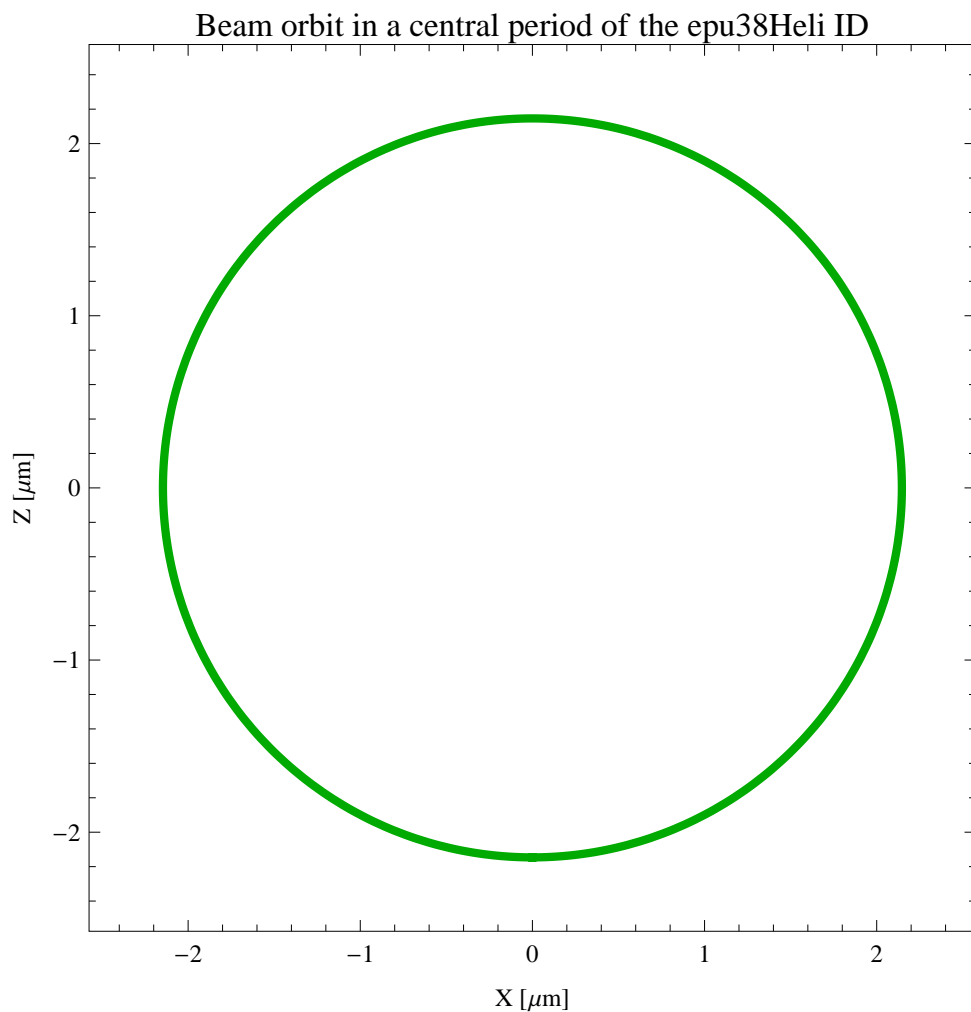


Figure 5.233: The beam orbit of the electron beam through a central period of the epu38Heli ID

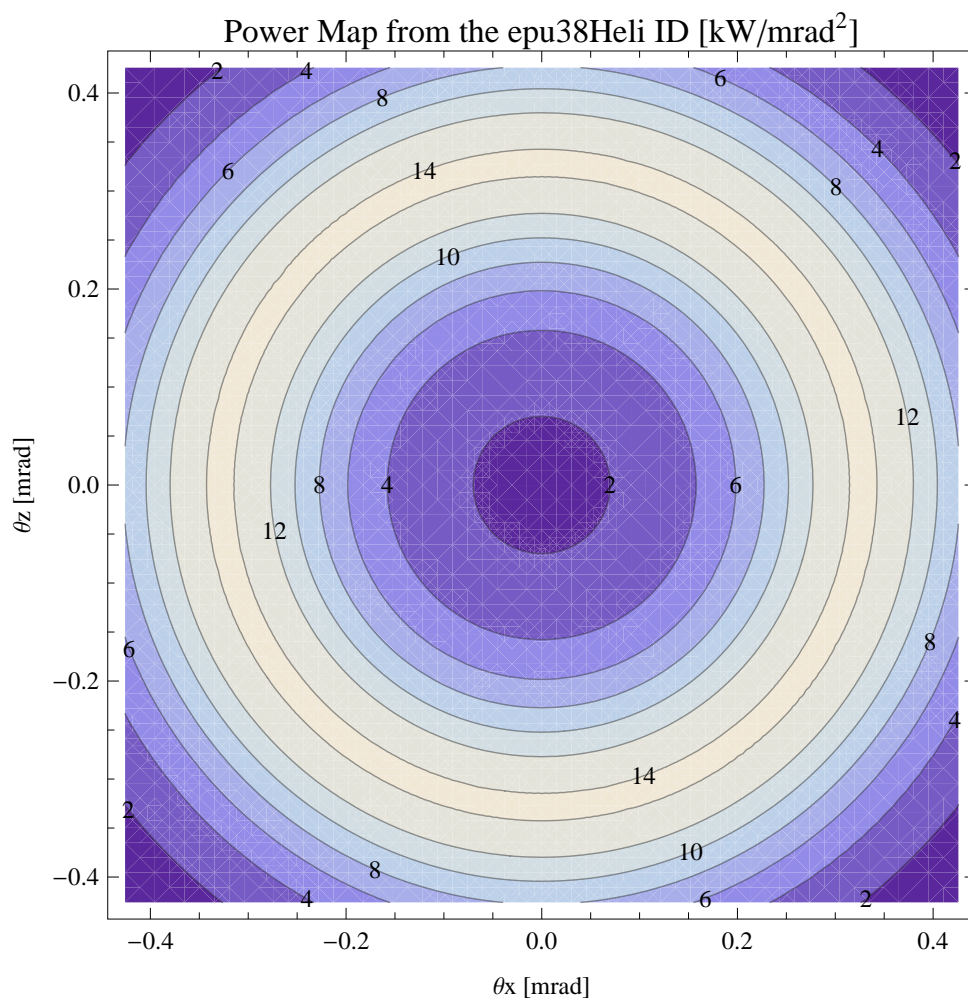


Figure 5.234: Map of the power distribution of the emitted synchrotron radiation by the epu38Heli ID

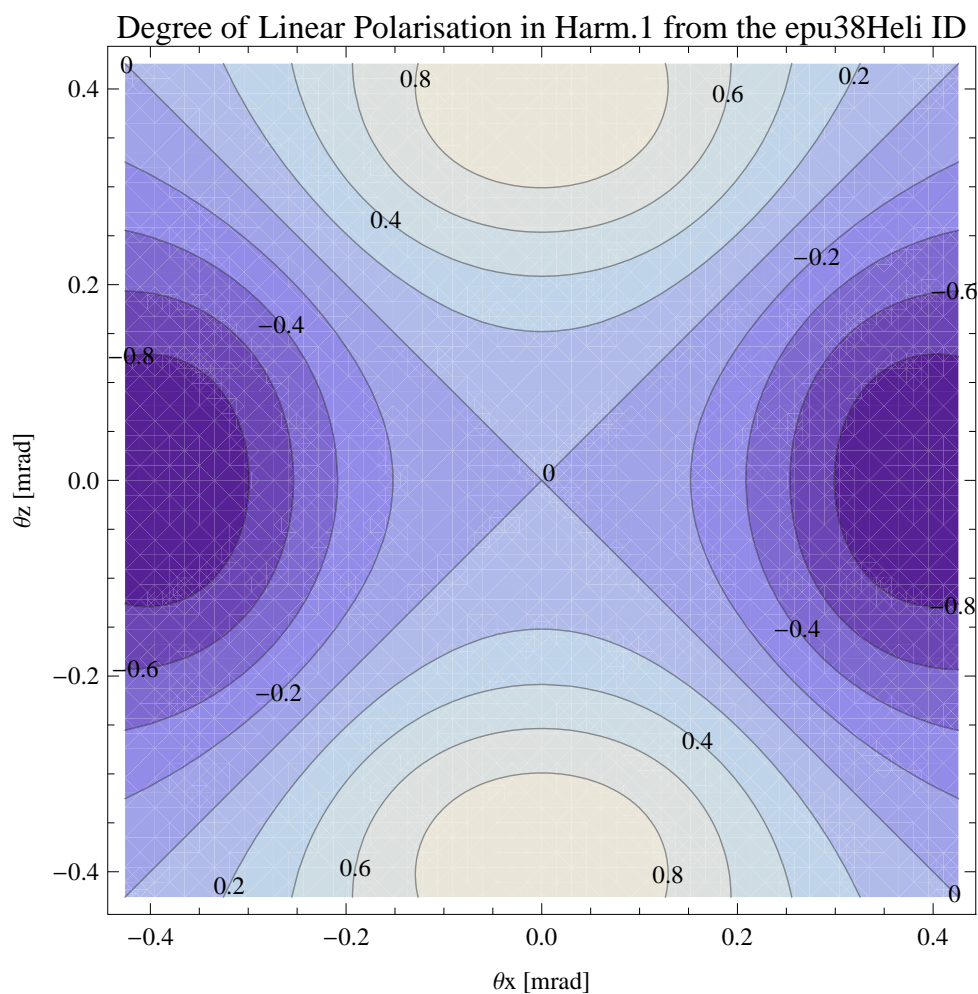


Figure 5.235: Map of linear polarisation in the fundamental harmonic of the synchrotron radiation emitted by the epu38Heli ID

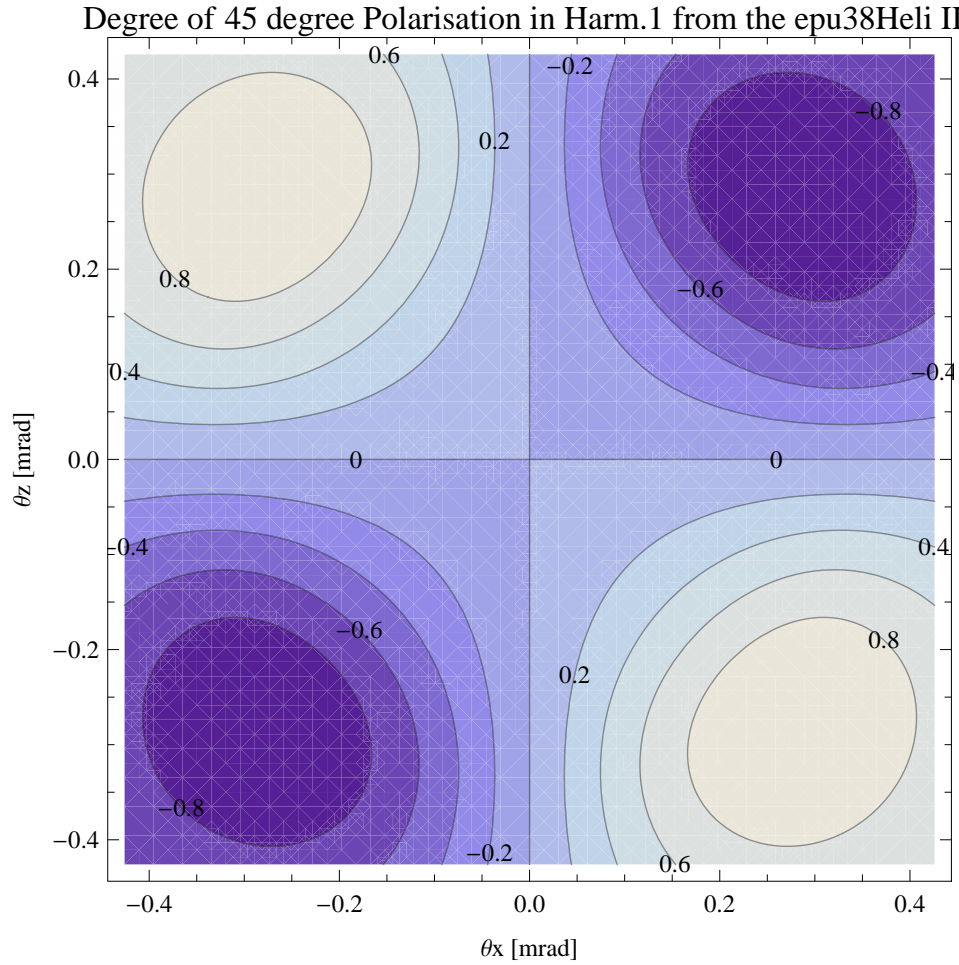


Figure 5.236: Map of 45 degree polarisation in the fundamental harmonic of the synchrotron radiation emitted by the epu38Heli ID

A map of the degree of 45 degree polarisation of the fundamental harmonic of the synchrotron radiation emitted by the epu38Heli ID over the angle of observation is shown in Figure 5.236.

A map of the degree of circular polarisation of the fundamental harmonic of the synchrotron radiation emitted by the epu38Heli ID over the angle of observation is shown in Figure 5.237.

The on axis brilliance at peak energy, the angular spectral flux, the flux in the harmonics, the power in the harmonics, the ratio of coherence, the coherent flux in the harmonics, and the power of coherent radiation in the harmonics from the epu38Heli ID have been calculated and the resulting plots are found in this section of the document. The beam parameters used for the calculation are 0.5 A of stored current,  $\beta_H = 9$  m,  $\varepsilon_H = 0.263$  nmrad,  $\beta_V = 4.8$  m,  $\varepsilon_V = 8$  pmrad, and an energy spread of 0.001.

The brilliance at peak energy and the angular spectral flux density from the epu38Heli ID for different harmonics at maximum K-value (2.946) are given in Table 5.41 and for minimum K-value (0.400) these values are given in Table 5.42.

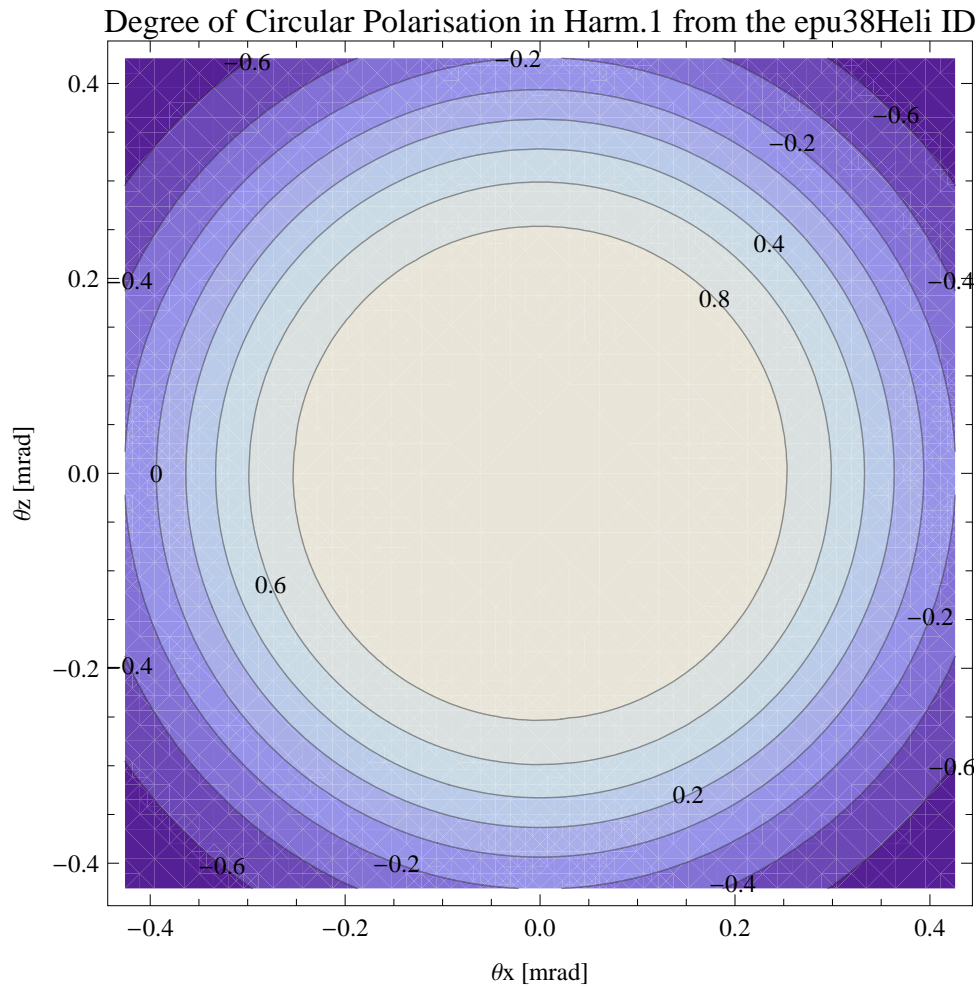


Figure 5.237: Map of circular polarisation in the fundamental harmonic of the synchrotron radiation emitted by the epu38Heli ID

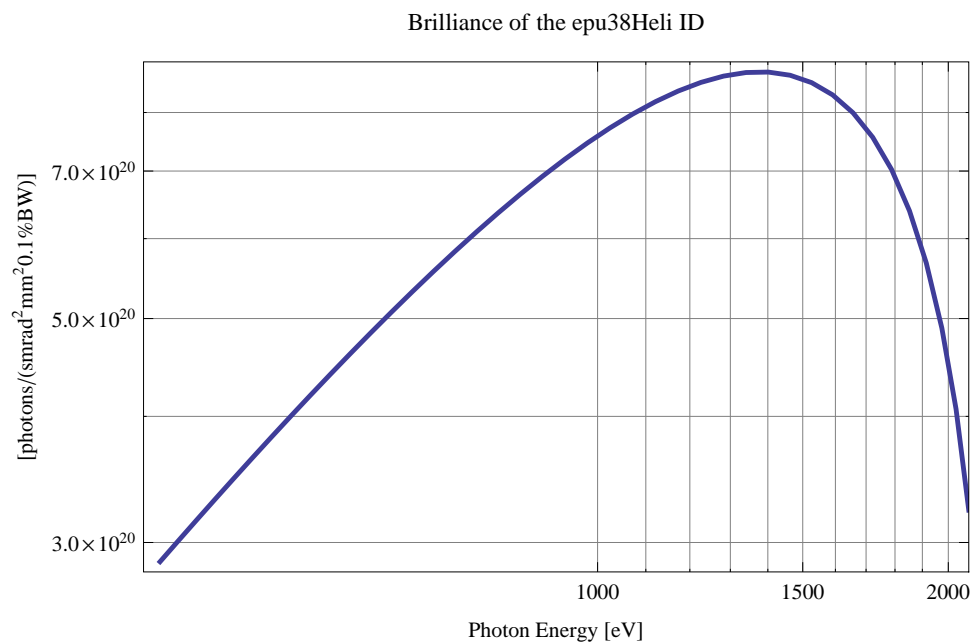


Figure 5.238: The brilliance at peak energy from the epu38Heli ID



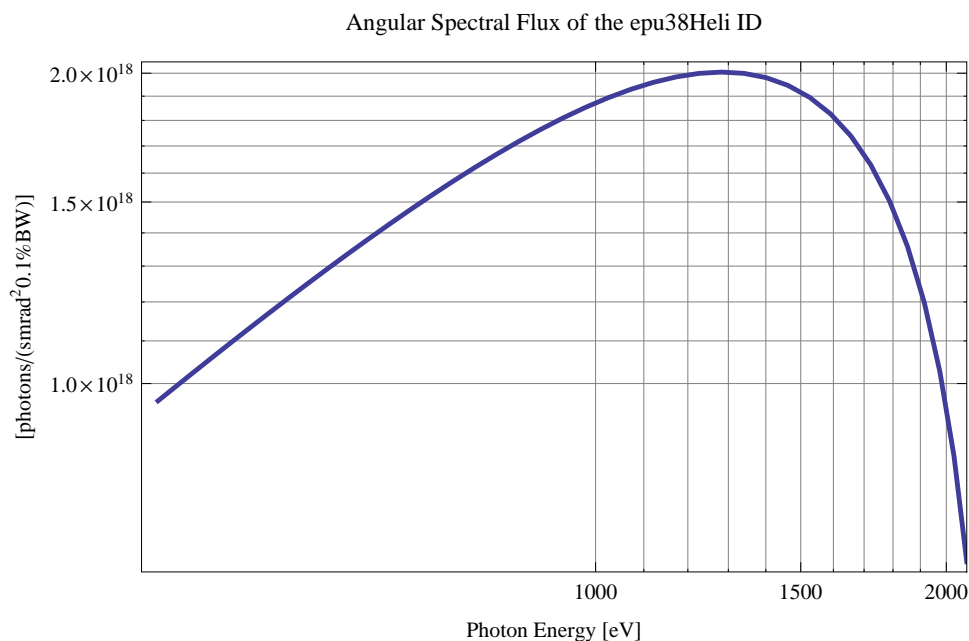


Figure 5.239: The angular spectral flux from the epu38Heli ID

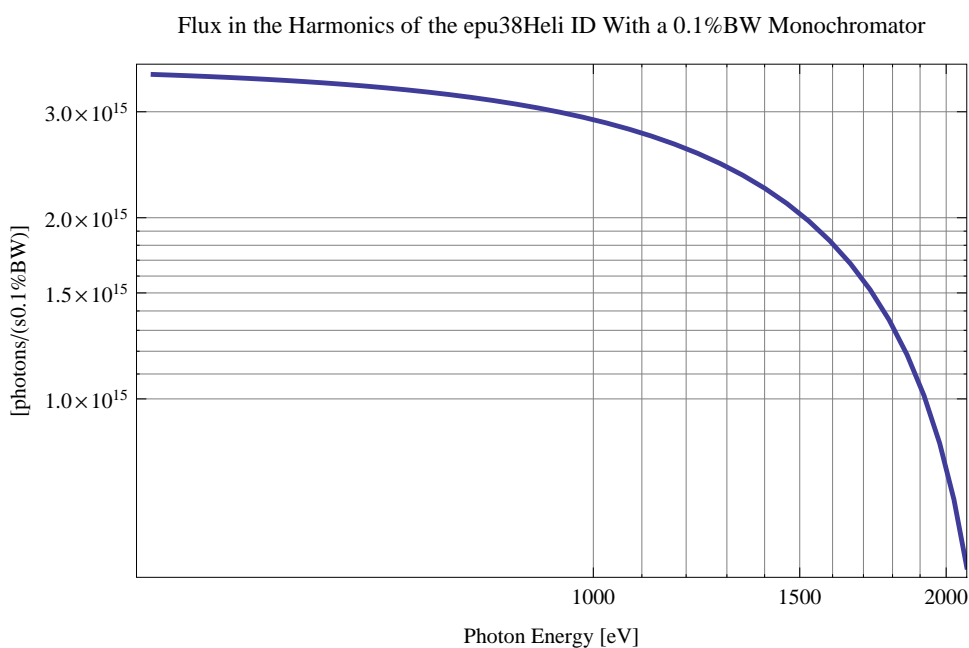


Figure 5.240: The flux of photons in the harmonics from the epu38Heli ID using a 0.1%BW monochromator

Table 5.41: The brilliance at peak energy and the angular spectral flux density from the epu38Heli ID for different harmonics at maximum K-value (2.946)

Harmonic	Photon Energy [eV]	Brilliance [Ph./s/mrad <sup>2</sup> /mrad <sup>2</sup> /0.1%BW]	Angular Spectral Flux [Ph./s/mrad <sup>2</sup> /0.1%BW]
1	421.151	$2.87 \times 10^{20}$	$9.62 \times 10^{17}$

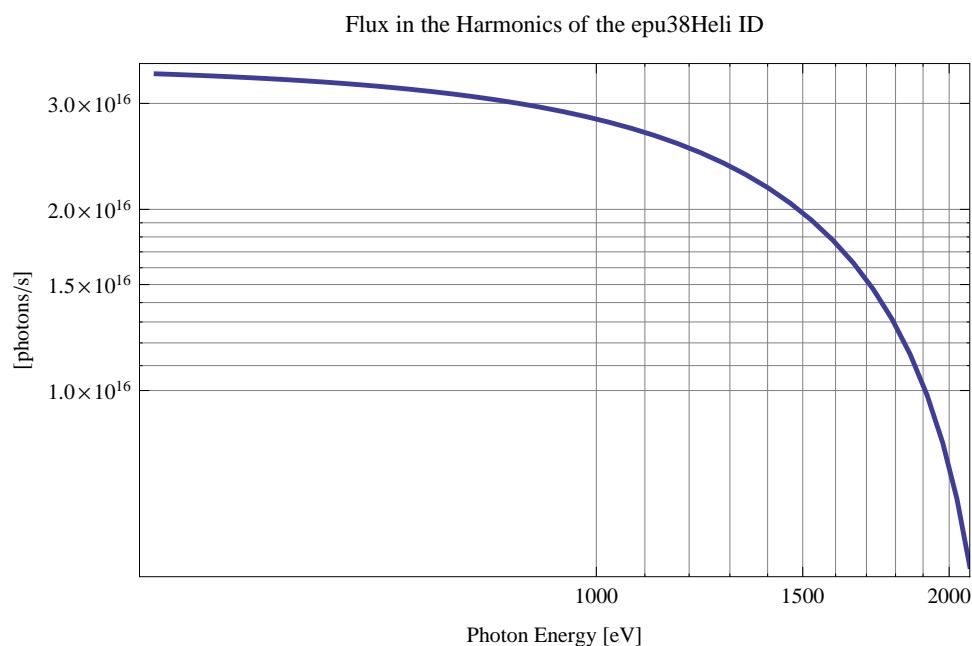


Figure 5.241: The flux of photons in the harmonics from the epu38Heli ID

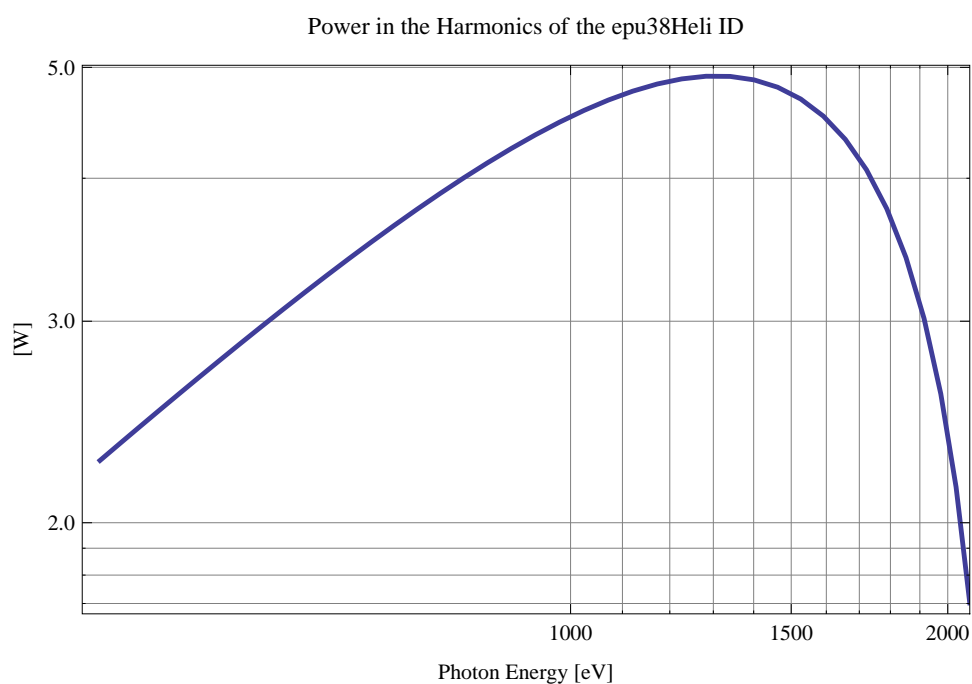


Figure 5.242: The power in the harmonics from the epu38Heli ID

Table 5.42: The brilliance at peak energy and the angular spectral flux density from the epu38Heli ID for different harmonics at minimum K-value (0.4)

Harmonic	Photon Energy [eV]	Brilliance [Ph./s/mrad <sup>2</sup> /mrad <sup>2</sup> /0.1%BW]	Angular Spectral Flux [Ph./s/mrad <sup>2</sup> /0.1%BW]
1	2082.54	$3.23 \times 10^{20}$	$6.72 \times 10^{17}$

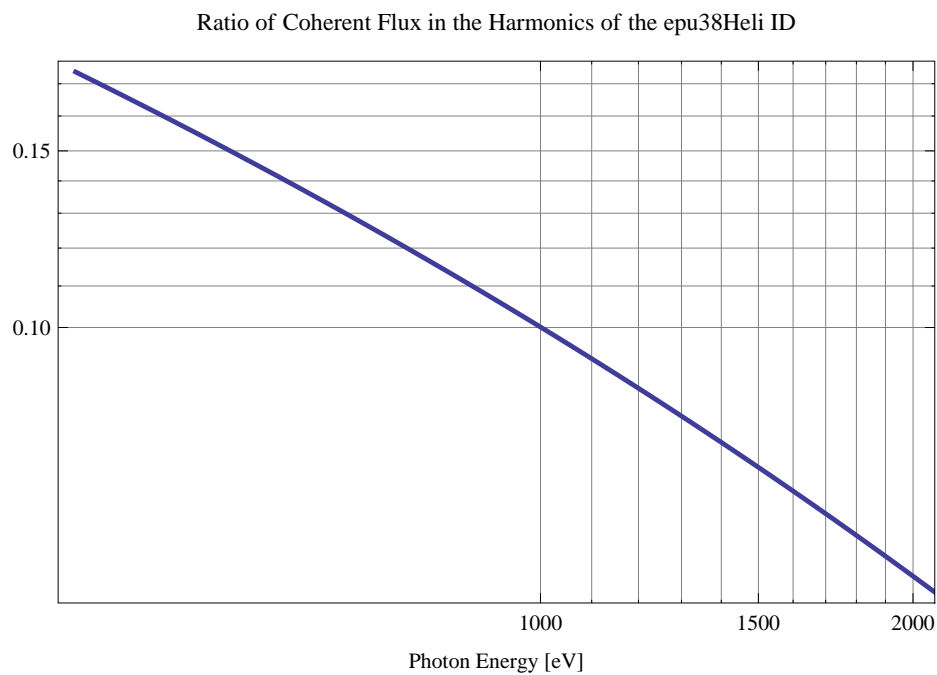


Figure 5.243: The ratio of coherent flux in the harmonics from the epu38Heli ID

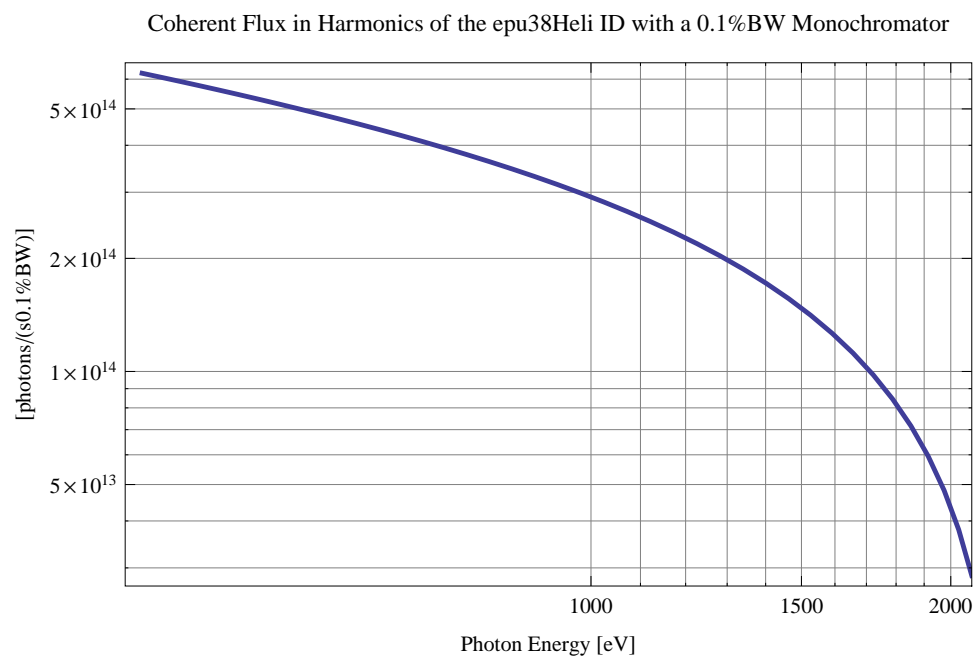


Figure 5.244: The coherent flux in the harmonics of the epu38Heli ID using a 0.1%BW Monochromator

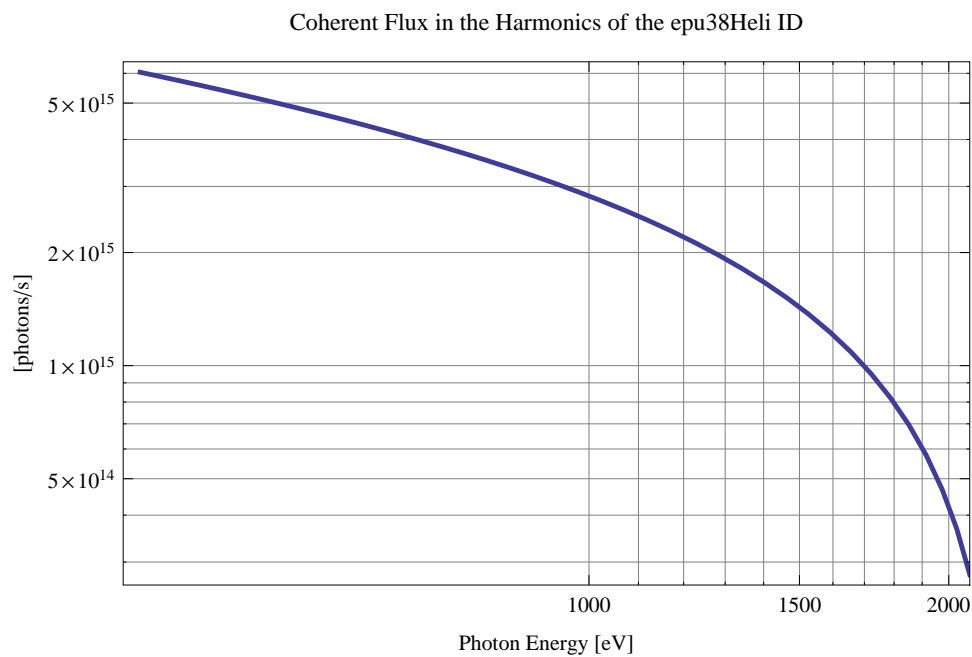


Figure 5.245: The coherent flux in the harmonics of the epu38Heli ID

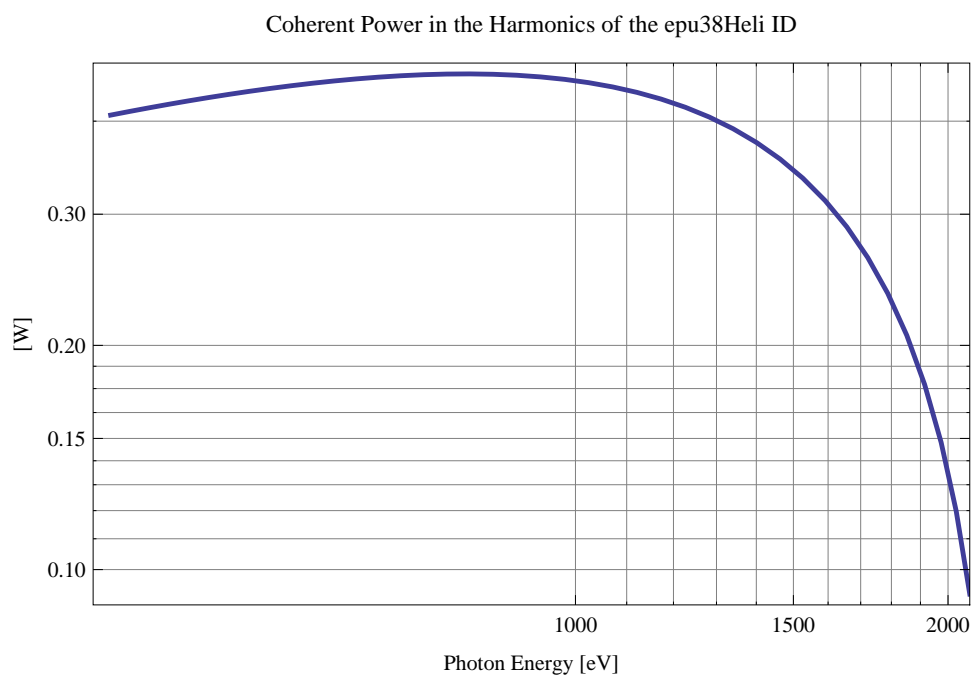


Figure 5.246: The power of coherent synchrotron radiation in the harmonics of the epu38Heli ID

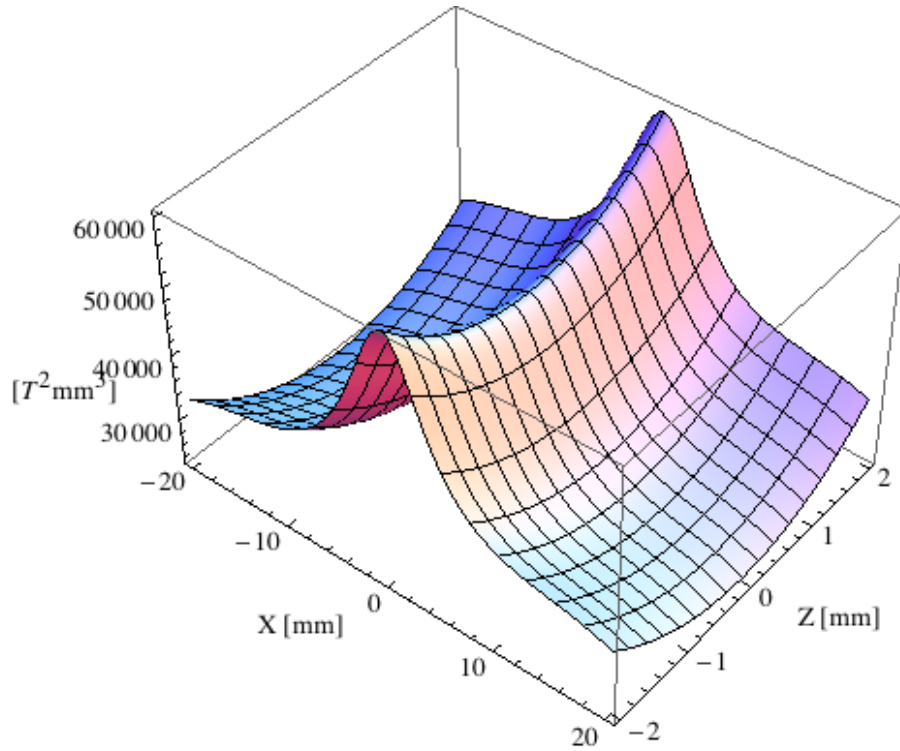


Figure 5.247: Focusing potential from the epu38Heli ID over the beam stay clear aperture.

### Influence from the epu38Heli ID on the optics of the stored beam

Figure 5.247 shows the focusing potential from the epu38Heli over the beam stay clear aperture of the ring aperture.

Figure 5.248 shows the kick map in the beam energy independent unit  $T^2 m^2$  of the kicks induced by the epu38Heli ID over the beam stay clear aperture.

Figure 5.249 shows the induced angular kick on the stored beam from the epu38Heli ID as a function of the vertical distance to the axis of the ID.

Figure 5.250 shows the induced angular kick on the stored beam from the epu38Heli ID as a function of the horizontal distance to the axis of the ID.

Figure 5.251 shows tune shift induced by the epu38Heli ID over the beam stay clear aperture. Note that the tune shift depends on the beam size at the ID.

Figure 5.252 shows the induced tune shift from the epu38Heli ID as a function of the vertical distance to the axis of the ID.

Figure 5.253 shows the induced tune shift from the epu38Heli ID as a function of the horizontal distance to the axis of the ID.

### Magnet model of the elliptically polarising undulator epu38Incl

The Radia [2] magnet model of the epu38Incl ID is shown in Figure 5.254. The length of the magnet model is 320.976 mm. The magnetic material in the model is NdFeb with a remanence of 1.28 T, a material similar to VACODYM 776 TP from Vacuumschmelze. Blocks with vertical magnetisation are blue and blocks with horizontal magnetisation are yellow. The block size is

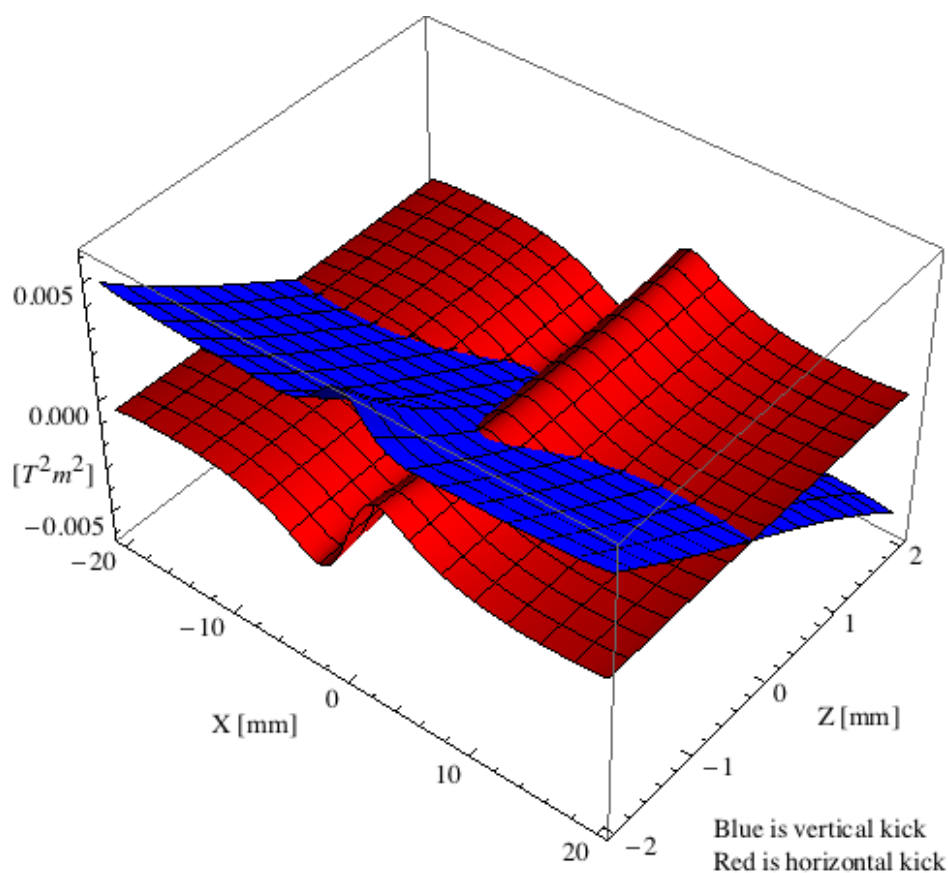


Figure 5.248: Kick map in the beam energy independent unit  $T^2m^2$  of the kicks induced by the epu38Heli ID over the beam stay clear aperture.

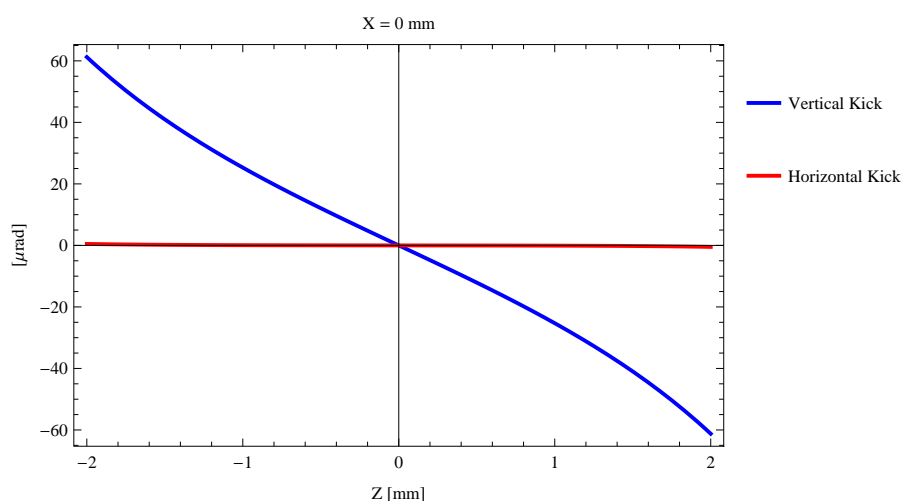


Figure 5.249: Induced angular kick on the stored beam from the epu38Heli ID as a function of the vertical distance to the ID axis.

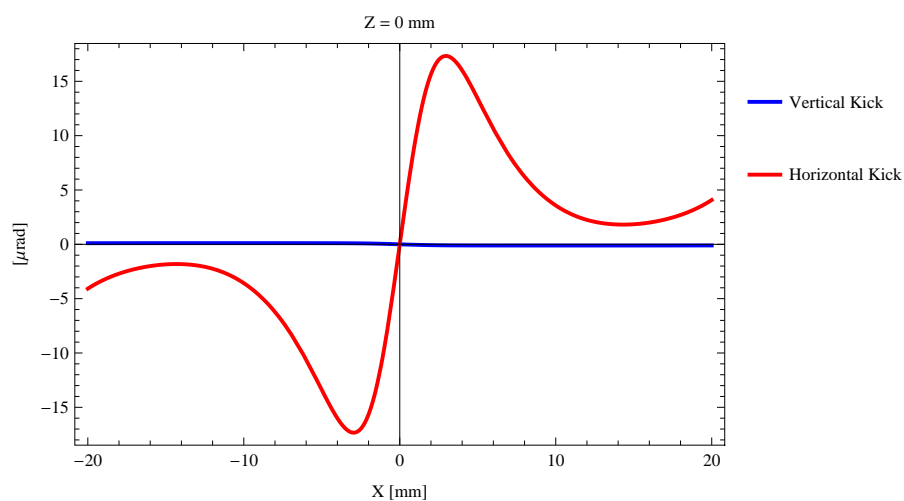


Figure 5.250: Induced angular kick on the stored beam from the epu38Heli ID as a function of the horizontal distance to the ID axis.

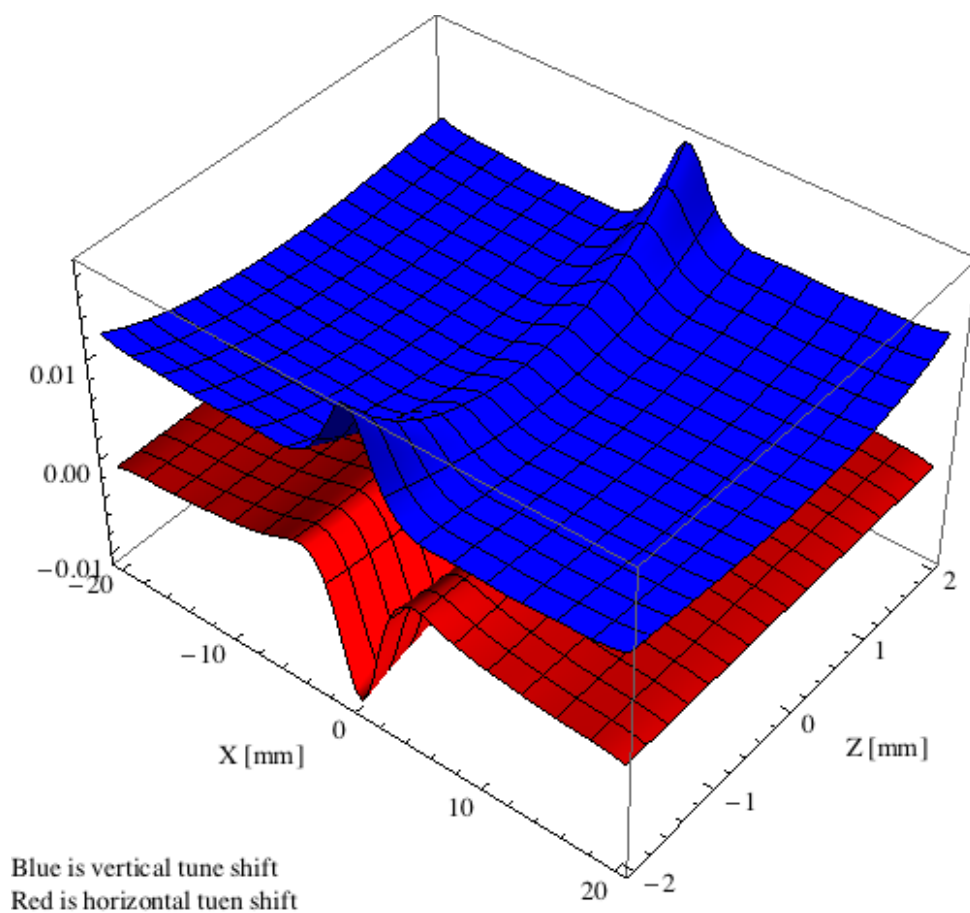


Figure 5.251: Tune shift induced by the epu38Heli ID over the beam stay clear aperture.

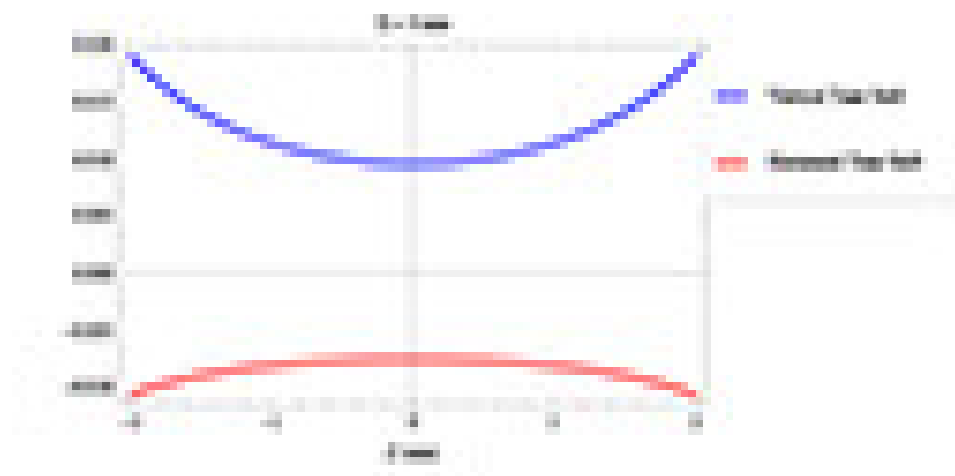


Figure 5.252: Induced tune shift from the epu38Heli ID as a function of the vertical distance to the axis of the ID.

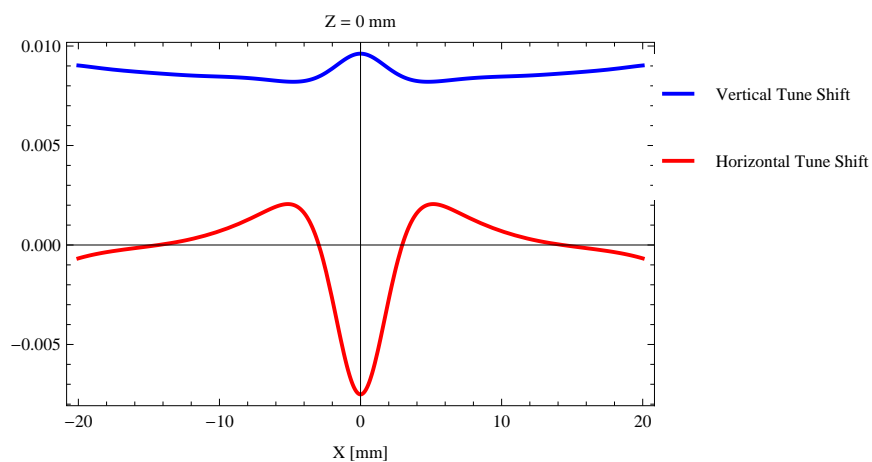


Figure 5.253: Induced tune shift from the epu38Heli ID on the stored beam from the ID as a function of the horizontal distance to the axis of the ID.



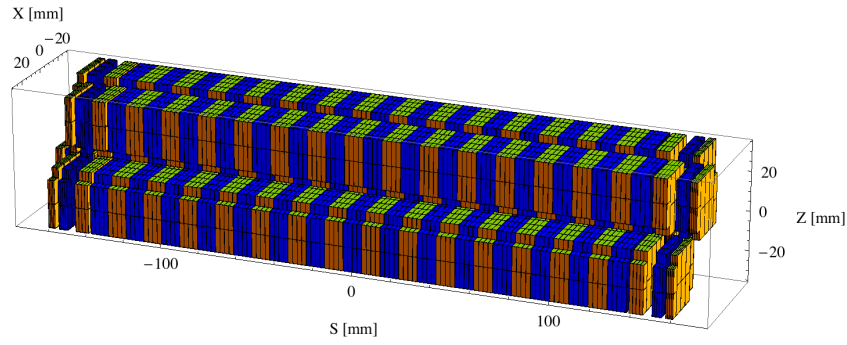


Figure 5.254: Magnetic model of the epu38Incl ID. The ID has been modelled with Radia [2]

$30 \times 30 \times 9.5 \text{ mm}^3$  and there is a 5. mm cut-out in two of the corners of the blocks. The total length of the epu38Incl ID is 3930.98 mm.

### Analysis of the magnetic field of the epu38Incl ID

The effective magnetic fields on axis and the fundamental photon energy of the epu38Incl ID are shown in Table 5.43. The higher harmonic contents in the magnetic field of an elliptically polarising undulator made of permanent magnets is negligible and the efficient field has about the same strength as the peak field.

Table 5.43: Effective Fields on axis and Fundamental Photon Energy of the epu38Incl ID

Undulator Period	38	mm
Undulator Gap	9	mm
Undulator Mode	Inclined	
Undulator Phase	10.373	mm
Vertical Peak Field	0.417	T
Efficient Vertical Field	0.419	T
K <sub>x</sub> (from vert. field)	1.487	
Horizontal Peak Field:	-0.416	T
Efficient Horizontal Field	0.420	T
K <sub>z</sub> (from hor. field)	1.491	
Photon Energy, Harm.1	0.699	keV
Emitted Power	3.939	kW
Total Length	3931.0	mm

### Synchrotron radiation from the epu38Incl ID

The power map of the emitted synchrotron radiation by the epu38Incl ID, assuming a 0.5 A filament beam with an energy of 3 GeV and undulator properties of the synchrotron radiation, is shown in Figure 5.259. The on-axis power density is  $26.124 \text{ kW/mrad}^2$

A map of the degree of linear polarisation of the fundamental harmonic of the synchrotron radiation emitted by the epu38Incl ID over the angle of observation is shown in Figure 5.260.

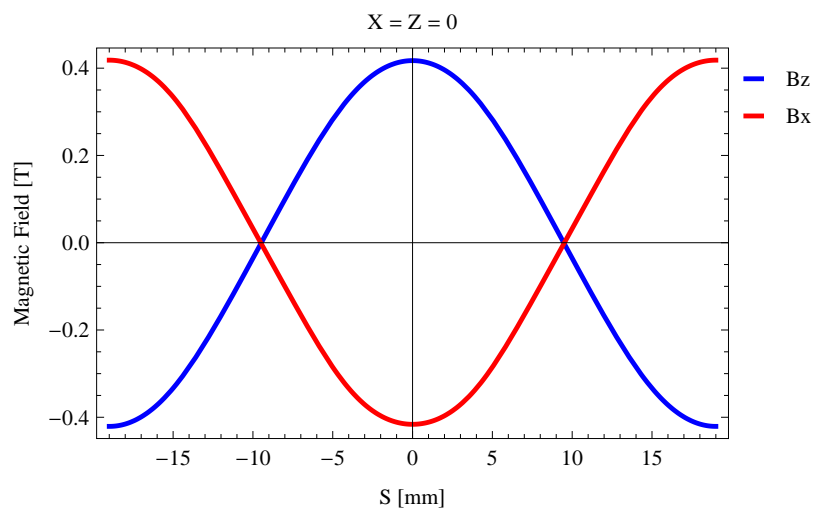


Figure 5.255: Vertical magnetic field in a central pole of the epu38Incl ID along the ID axis,  $X = Z = 0$

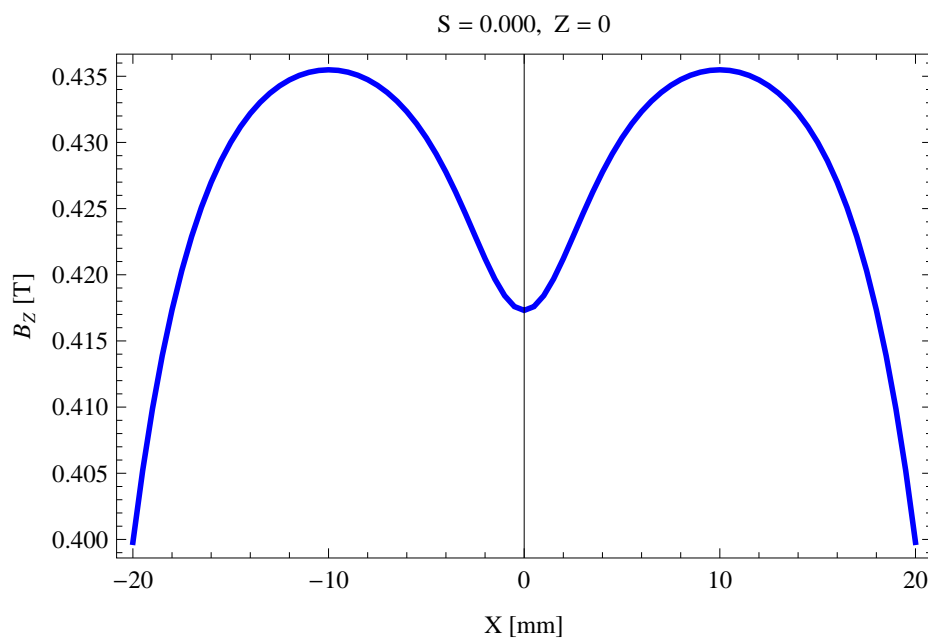


Figure 5.256: Vertical magnetic field in a central pole of the epu38Incl ID along the horizontally transverse direction to the ID axis,  $S = 0.000$ ,  $Z = 0$

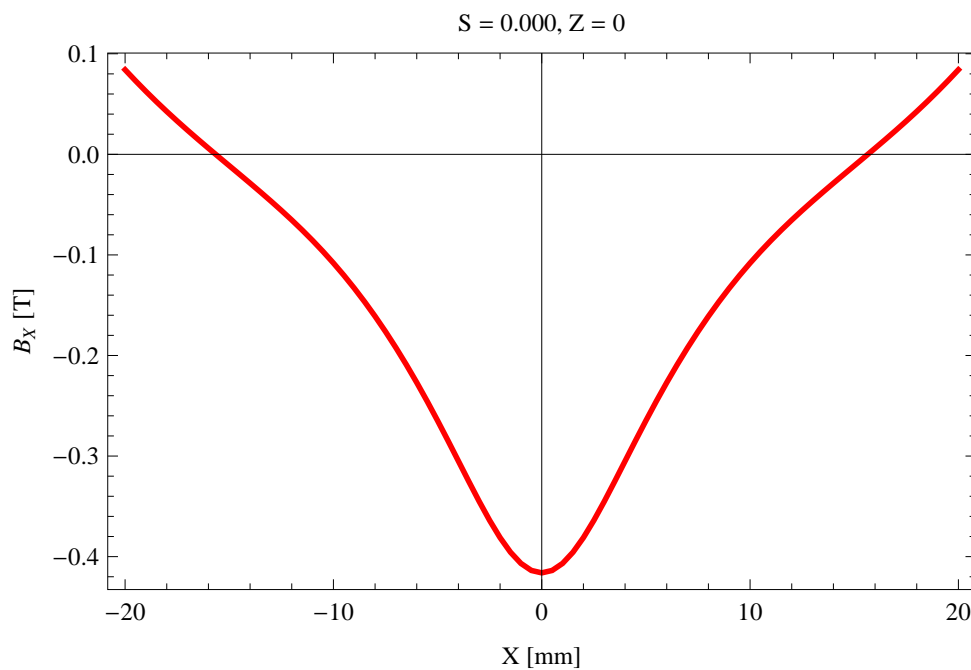


Figure 5.257: Horizontal magnetic field in a central pole of the epu38Incl ID along the horizontally transverse direction to the ID axis,  $S = 0.000$ ,  $Z = 0$

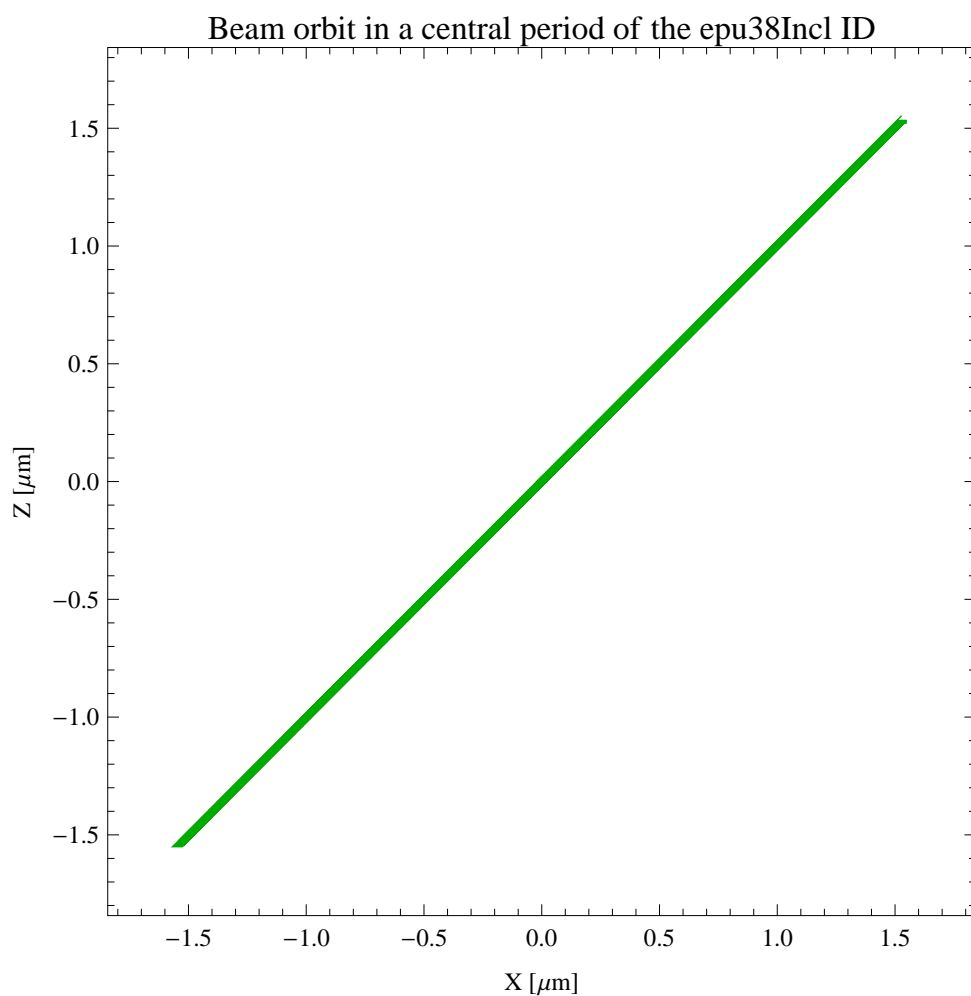


Figure 5.258: The beam orbit of the electron beam through a central period of the epu38Incl ID

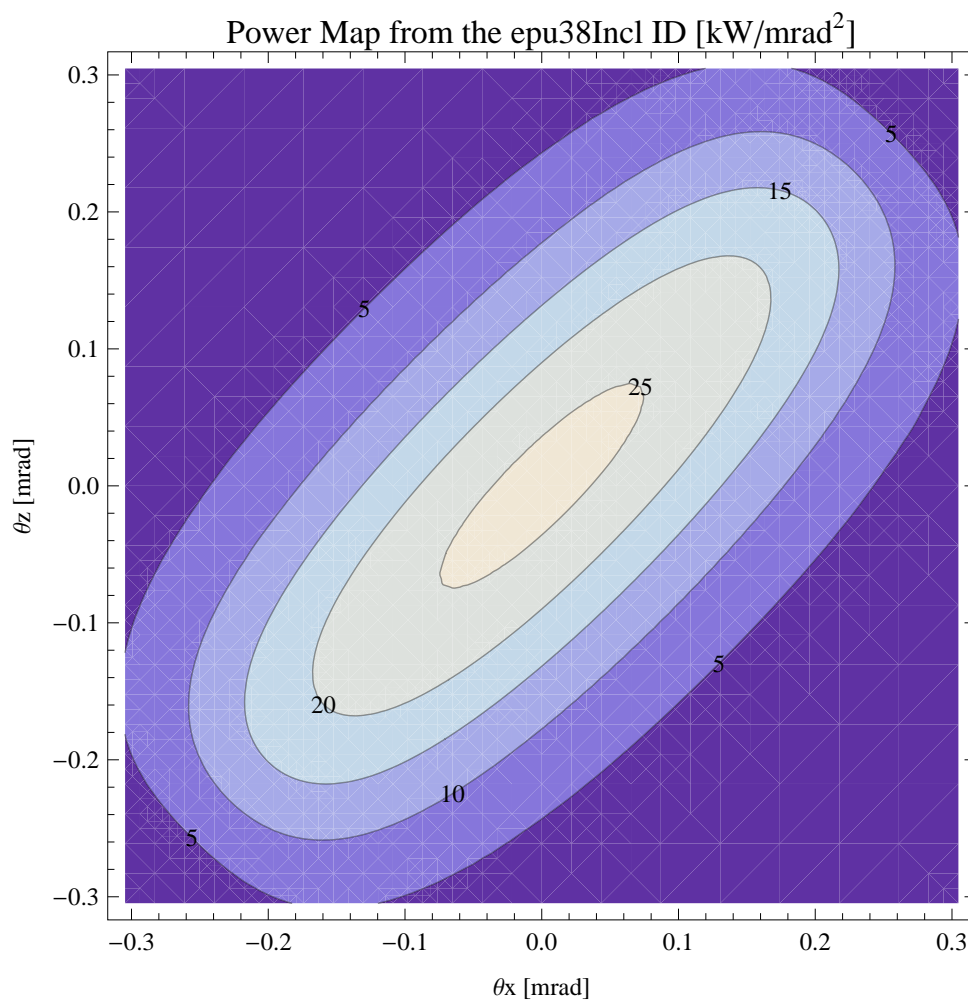


Figure 5.259: Map of the power distribution of the emitted synchrotron radiation by the epu38Incl ID

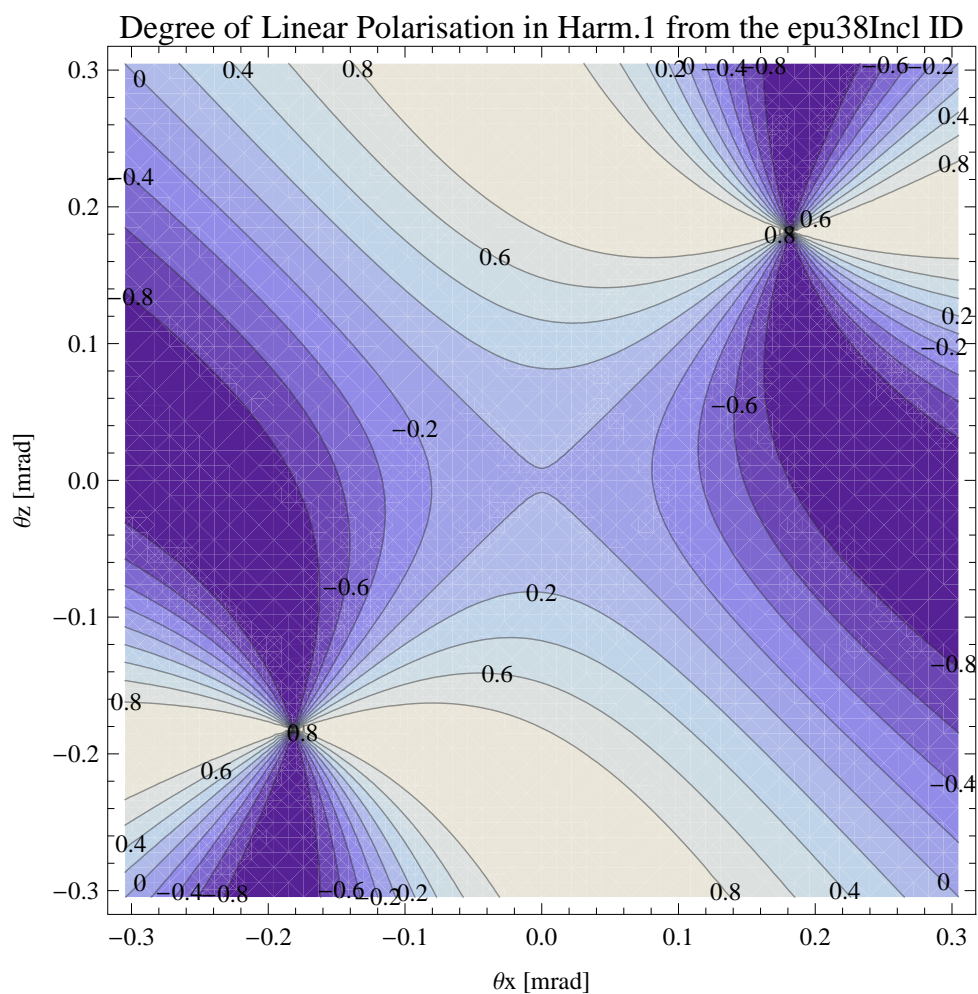


Figure 5.260: Map of linear polarisation in the fundamental harmonic of the synchrotron radiation emitted by the epu38Incl ID

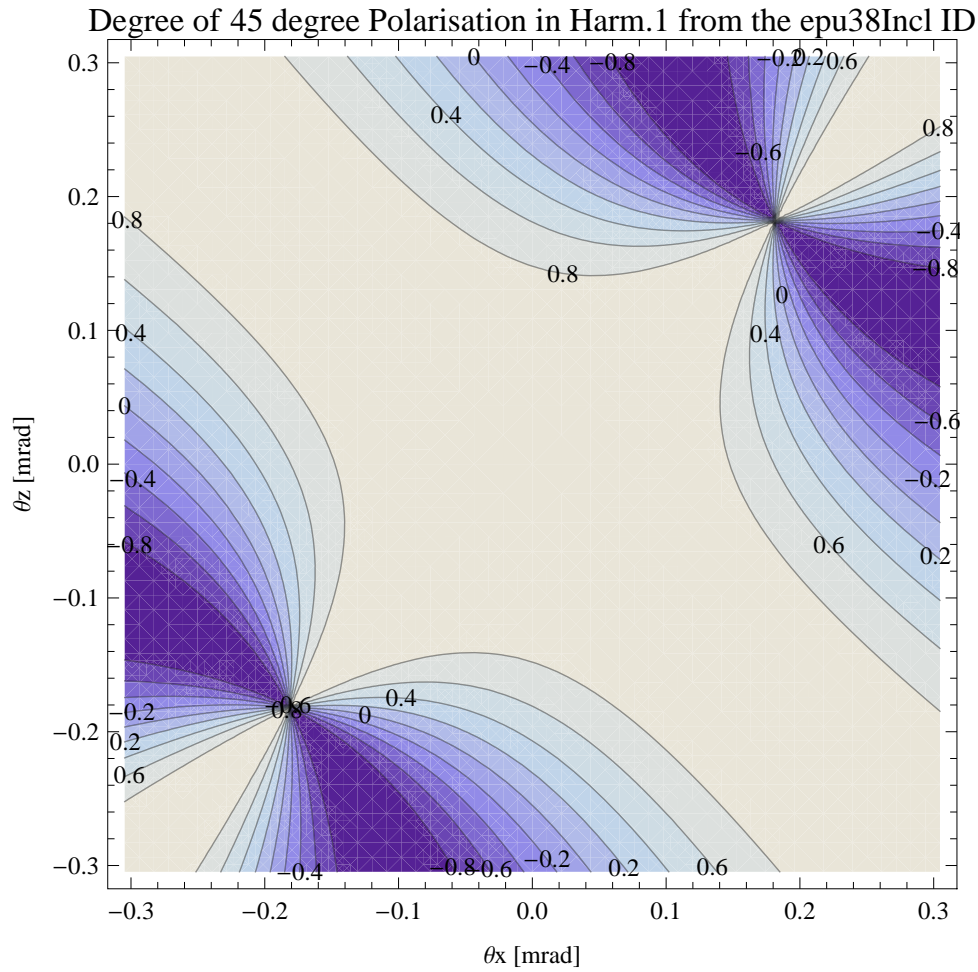


Figure 5.261: Map of 45 degree polarisation in the fundamental harmonic of the synchrotron radiation emitted by the epu38Incl ID

A map of the degree of 45 degree polarisation of the fundamental harmonic of the synchrotron radiation emitted by the epu38Incl ID over the angle of observation is shown in Figure 5.261.

A map of the degree of circular polarisation of the fundamental harmonic of the synchrotron radiation emitted by the epu38Incl ID over the angle of observation is shown in Figure 5.262.

The on axis brilliance at peak energy, the angular spectral flux, the flux in the harmonics, the power in the harmonics, the ratio of coherence, the coherent flux in the harmonics, and the power of coherent radiation in the harmonics from the epu38Incl ID have been calculated and the resulting plots are found in this section of the document. The beam parameters used for the calculation are 0.5 A of stored current,  $\beta_H = 9$  m,  $\varepsilon_H = 0.263$  nmrad,  $\beta_V = 4.8$  m,  $\varepsilon_V = 8$  pmrad, and an energy spread of 0.001.

The brilliance at peak energy and the angular spectral flux density from the epu38Incl ID for different harmonics at maximum K-value (2.106) are given in Table 5.44 and for minimum K-value (0.400) these values are given in Table 5.45.

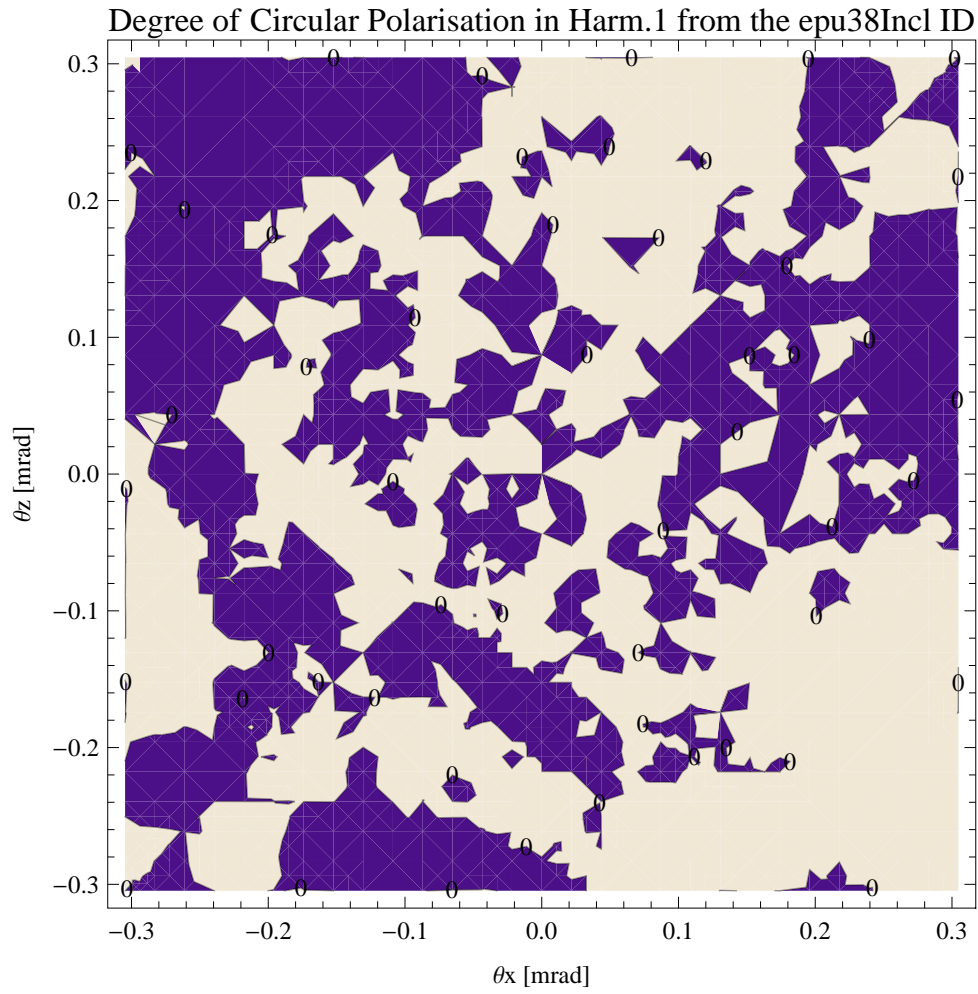


Figure 5.262: Map of circular polarisation in the fundamental harmonic of the synchrotron radiation emitted by the epu38Incl ID

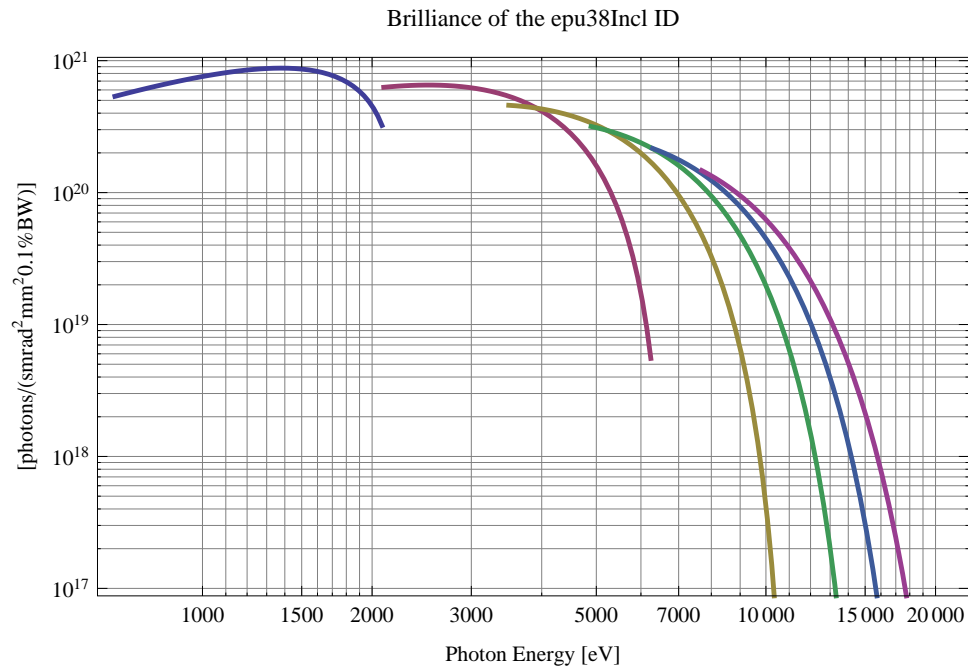


Figure 5.263: The brilliance at peak energy from the epu38Incl ID

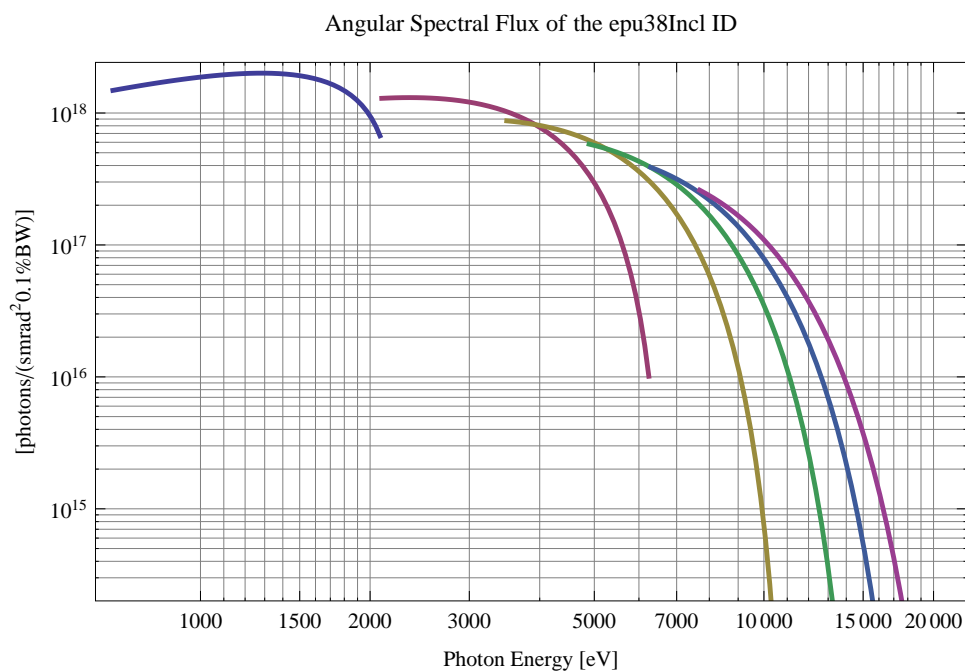


Figure 5.264: The angular spectral flux from the epu38Incl ID

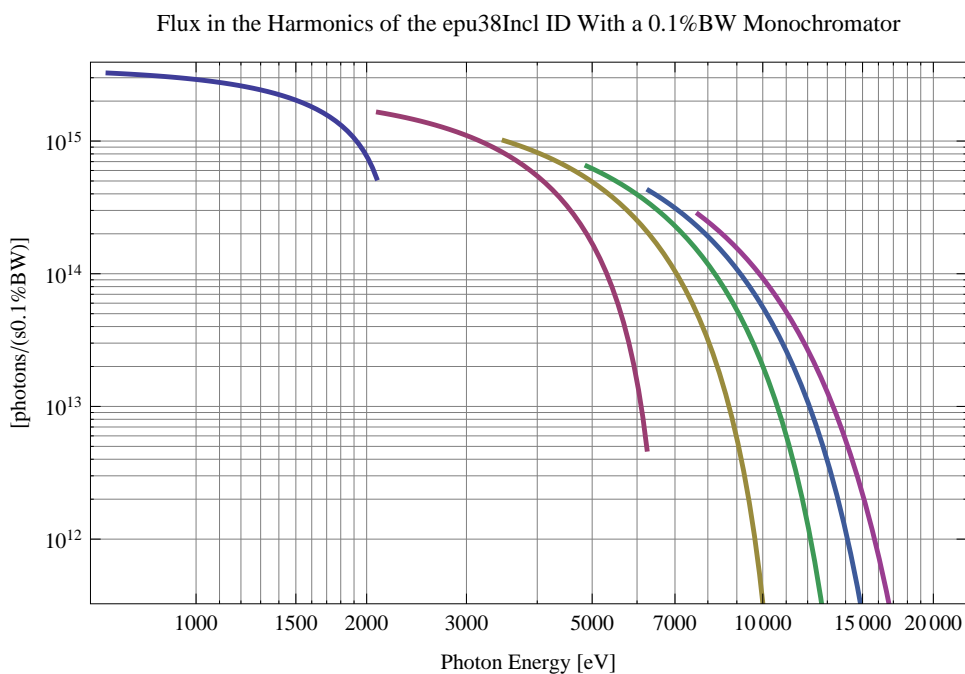


Figure 5.265: The flux of photons in the harmonics from the epu38Incl ID using a 0.1%BW monochromator



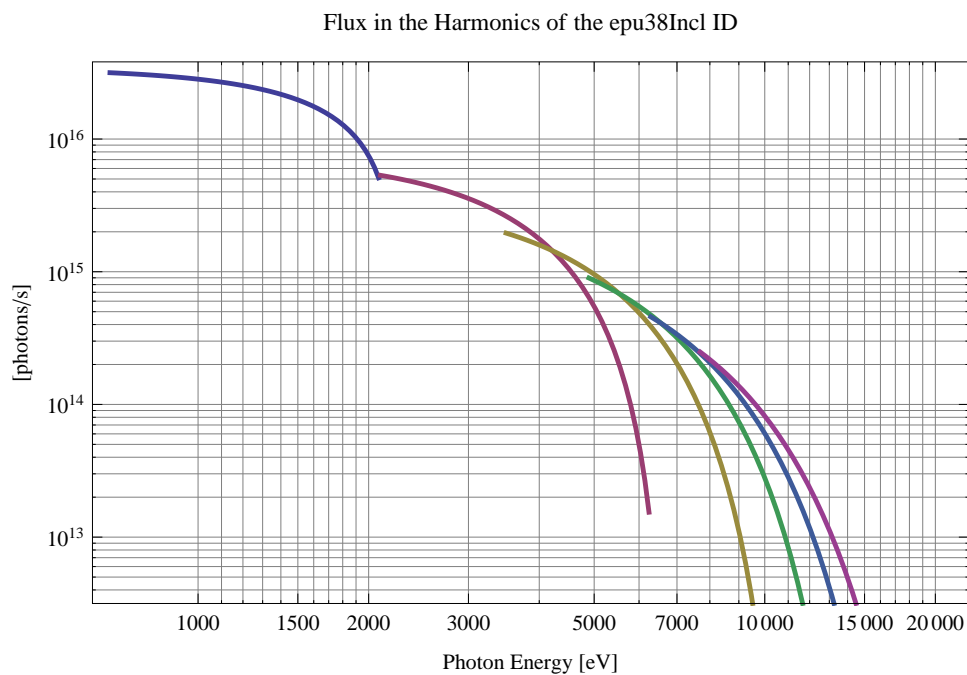


Figure 5.266: The flux of photons in the harmonics from the epu38Incl ID

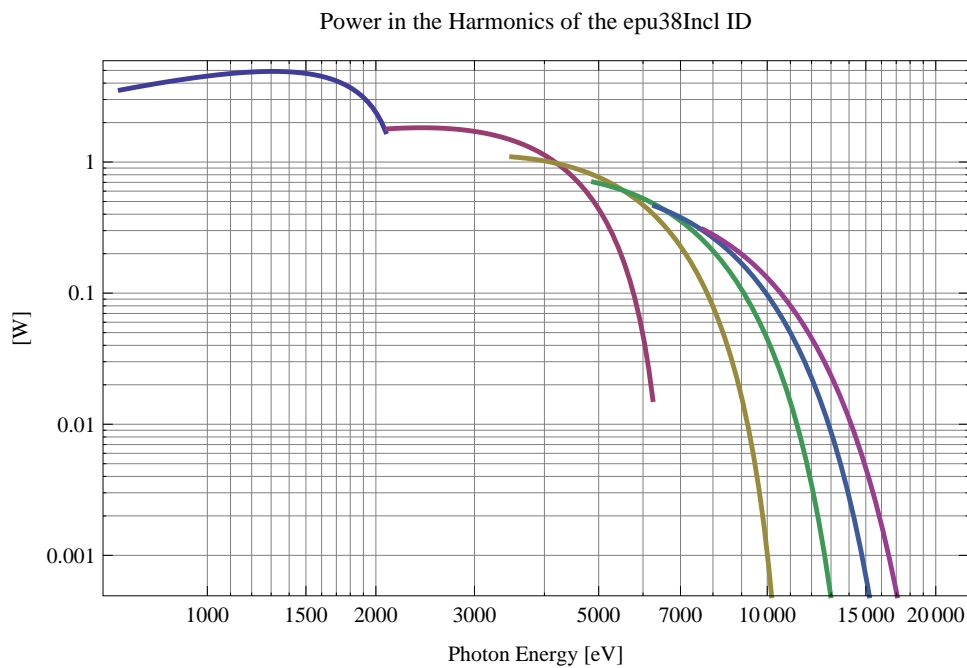


Figure 5.267: The power in the harmonics from the epu38Incl ID

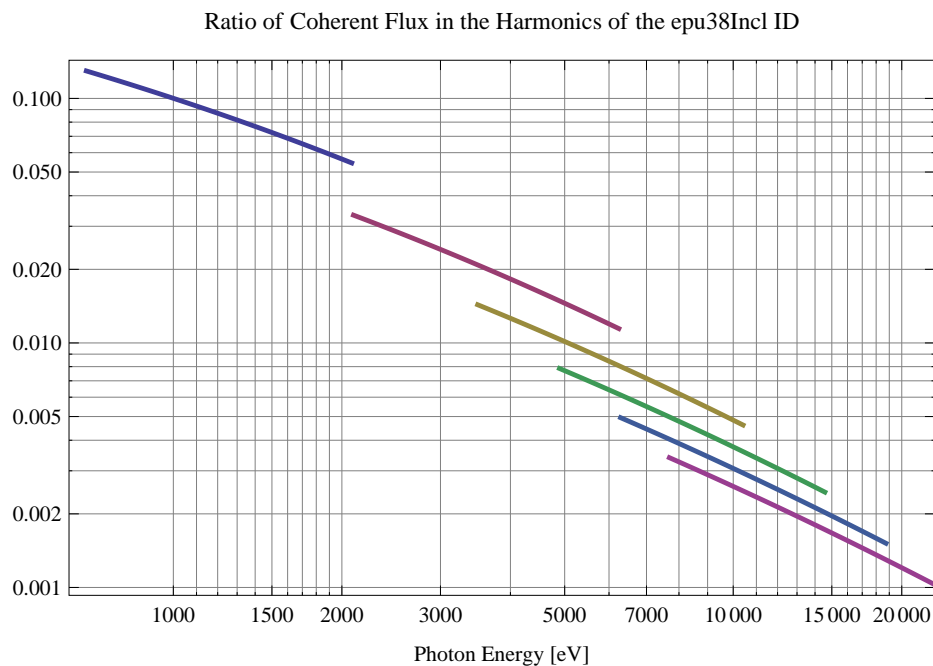


Figure 5.268: The ratio of coherent flux in the harmonics from the epu38Incl ID

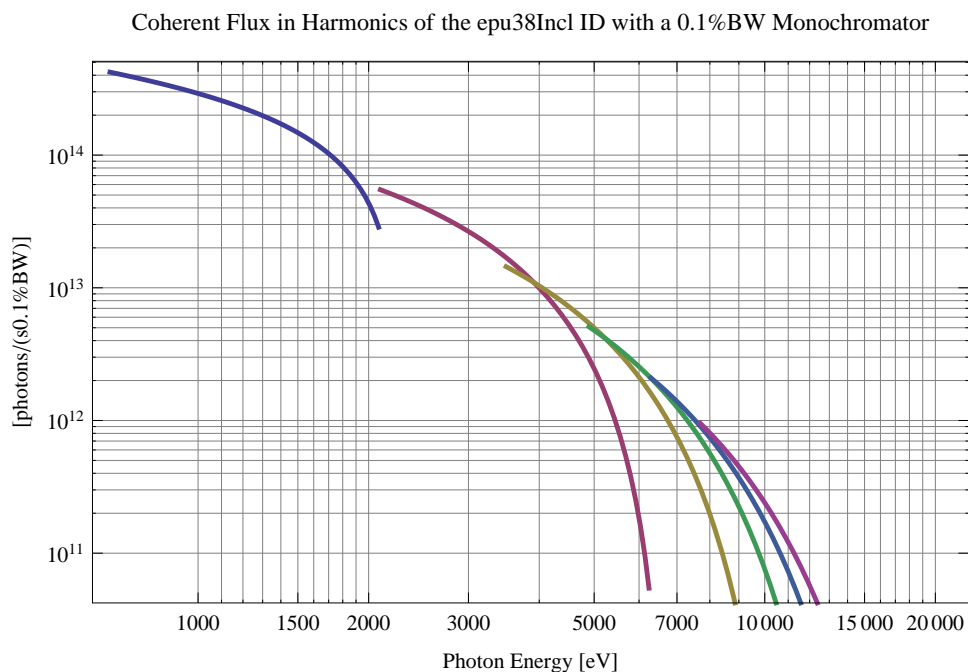


Figure 5.269: The coherent flux in the harmonics of the epu38Incl ID using a 0.1%BW Monochromator

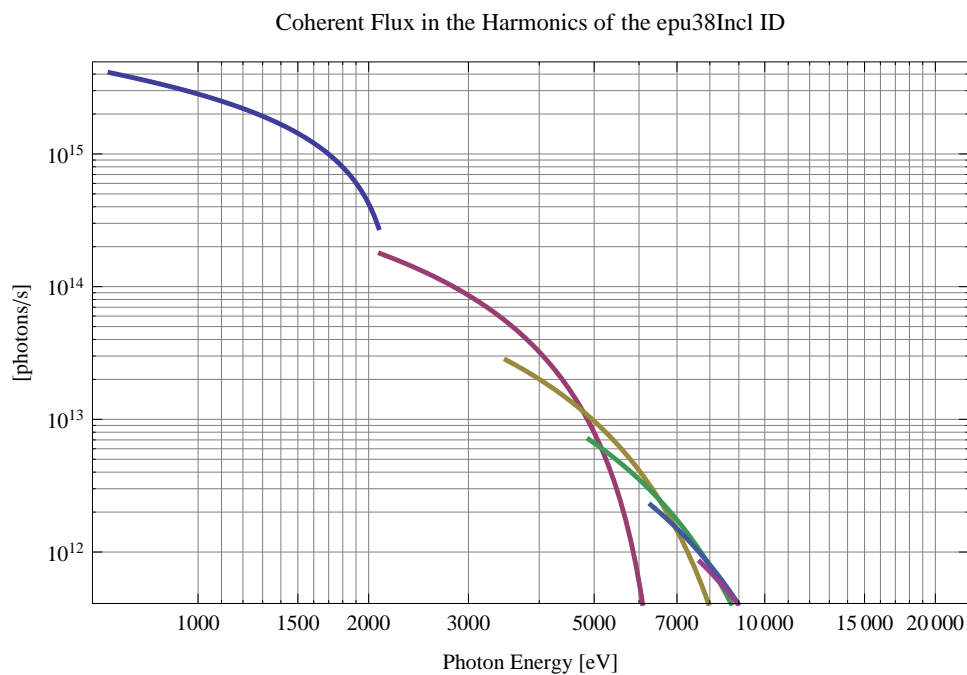


Figure 5.270: The coherent flux in the harmonics of the epu38Incl ID

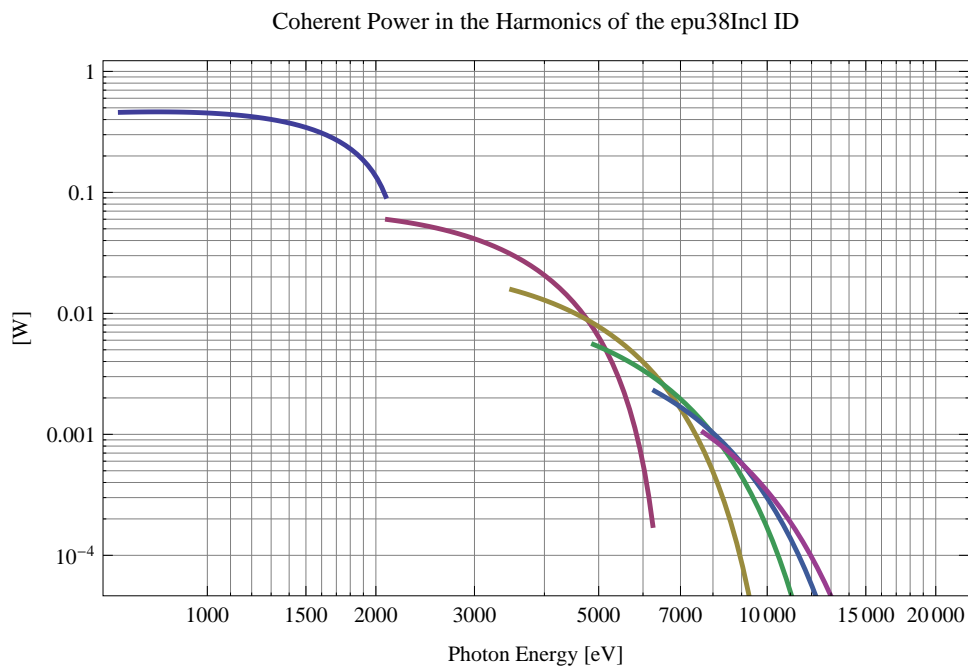


Figure 5.271: The power of coherent synchrotron radiation in the harmonics of the epu38Incl ID

Table 5.44: The brilliance at peak energy and the angular spectral flux density from the epu38Incl ID for different harmonics at maximum K-value (2.106)

Harmonic	Photon Energy [eV]	Brilliance [Ph./s/mrad <sup>2</sup> /mrad <sup>2</sup> /0.1%BW]	Angular Spectral Flux [Ph./s/mrad <sup>2</sup> /0.1%BW]
1	699.189	$5.37 \times 10^{20}$	$1.48 \times 10^{18}$
3	2097.57	$6.28 \times 10^{20}$	$1.29 \times 10^{18}$
5	3495.94	$4.59 \times 10^{20}$	$8.72 \times 10^{17}$
7	4894.32	$3.17 \times 10^{20}$	$5.81 \times 10^{17}$
9	6292.7	$2.16 \times 10^{20}$	$3.88 \times 10^{17}$
11	7691.08	$1.47 \times 10^{20}$	$2.6 \times 10^{17}$

Table 5.45: The brilliance at peak energy and the angular spectral flux density from the epu38Incl ID for different harmonics at minimum K-value (0.4)

Harmonic	Photon Energy [eV]	Brilliance [Ph./s/mrad <sup>2</sup> /mrad <sup>2</sup> /0.1%BW]	Angular Spectral Flux [Ph./s/mrad <sup>2</sup> /0.1%BW]
1	2082.54	$3.23 \times 10^{20}$	$6.72 \times 10^{17}$
3	6247.63	$5.54 \times 10^{18}$	$1.01 \times 10^{16}$
5	10412.7	$6.1 \times 10^{16}$	$1.09 \times 10^{14}$
7	14577.8	$6.35 \times 10^{14}$	$1.12 \times 10^{12}$
9	18742.9	$6.5 \times 10^{12}$	$1.15 \times 10^{10}$
11	22908.	$6.62 \times 10^{10}$	$1.17 \times 10^8$

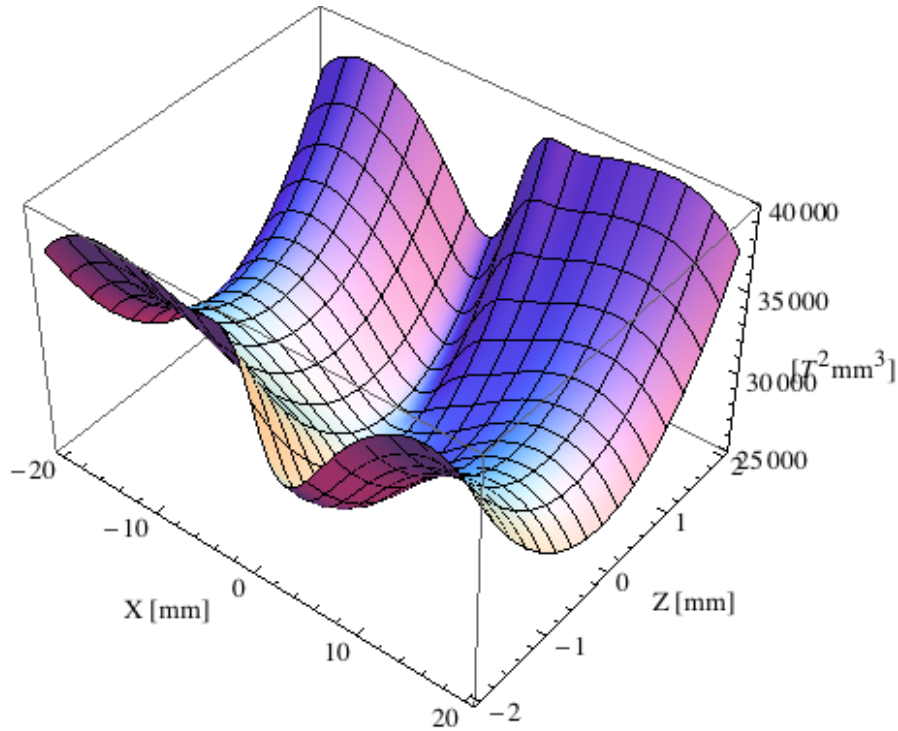


Figure 5.272: Focusing potential from the epu38Incl ID over the beam stay clear aperture.

### Influence from the epu38Incl ID on the optics of the stored beam

Figure 5.272 shows the focusing potential from the epu38Incl over the beam stay clear aperture of the ring aperture.

Figure 5.273 shows the kick map in the beam energy independant unit  $T^2 m^2$  of the kicks induced by the epu38Incl ID over the beam stay clear aperture.

Figure 5.274 shows the induced angular kick on the stored beam from the epu38Incl ID as a function of the vertical distance to the axis of the ID.

Figure 5.275 shows the induced angular kick on the stored beam from the epu38Incl ID as a function of the horizontal distance to the axis of the ID.

Figure 5.276 shows tune shift induced by the epu38Incl ID over the beam stay clear aperture. Note that the tune shift depends on the beam size at the ID.

Figure 5.277 shows the induced tune shift from the epu38Incl ID as a function of the vertical distance to the axis of the ID.

Figure 5.278 shows the induced tune shift from the epu38Incl ID as a function of the horizontal distance to the axis of the ID.

### Magnet model of the elliptically polaraising undulator epu38Vert

The Radia [2] magnet model of the epu38Vert ID is shown in Figure 5.279. The length of the magnet model is 320.976 mm. The magnetic material in the model is NdFeb with a remanence of 1.28 T, a material similar to VACODYM 776 TP from Vacuumschmelze. Blocks with vertical magnetisation are blue and blocks with horizontal magnetisation are yellow. The block size is

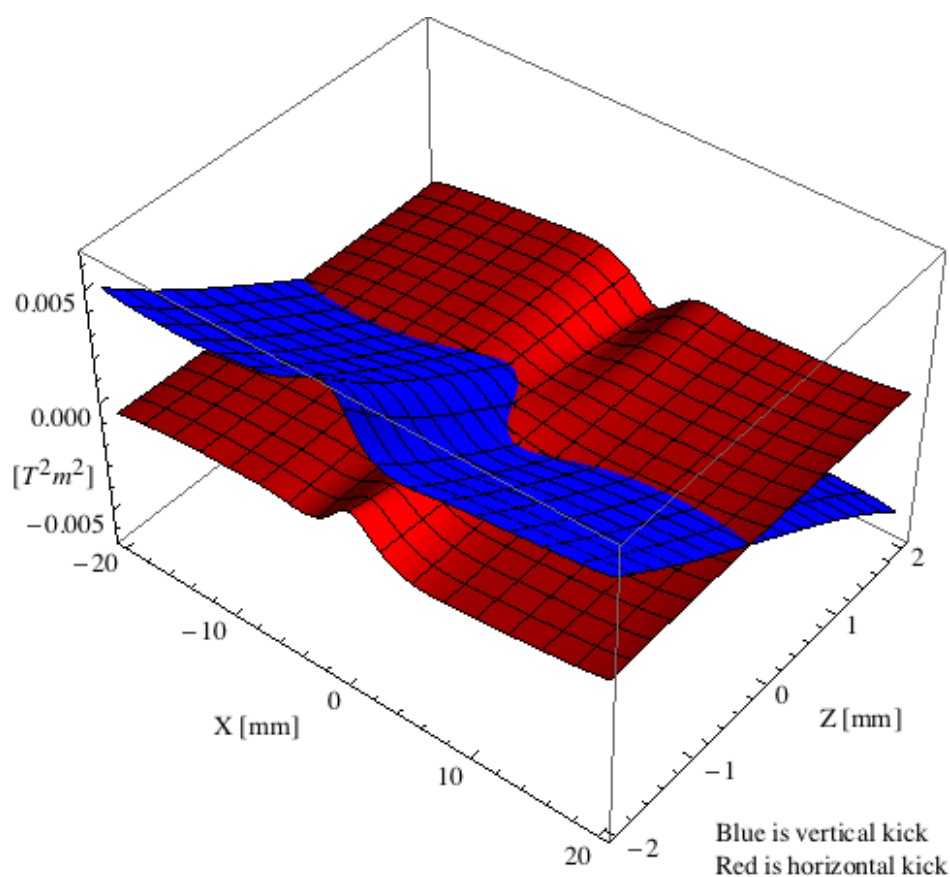


Figure 5.273: Kick map in the beam energy independent unit  $T^2m^2$  of the kicks induced by the epu38Incl ID over the beam stay clear aperture.

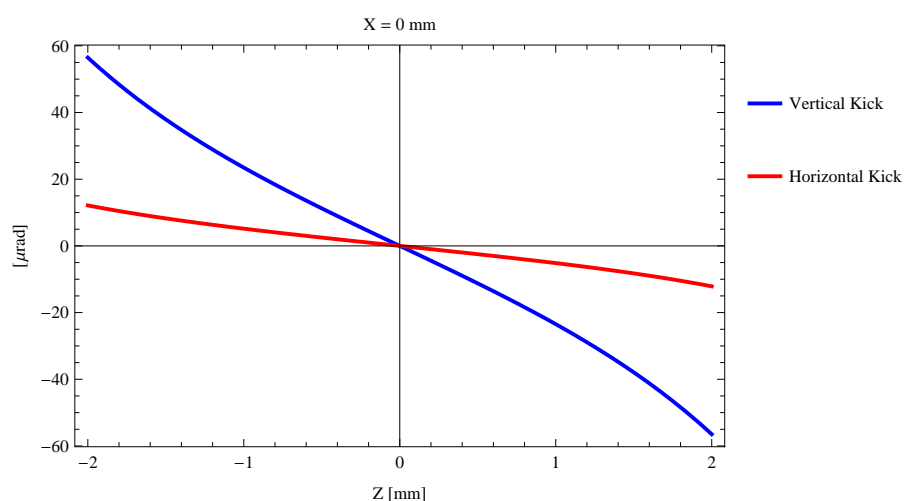


Figure 5.274: Induced angular kick on the stored beam from the epu38Incl ID as a function of the vertical distance to the ID axis.

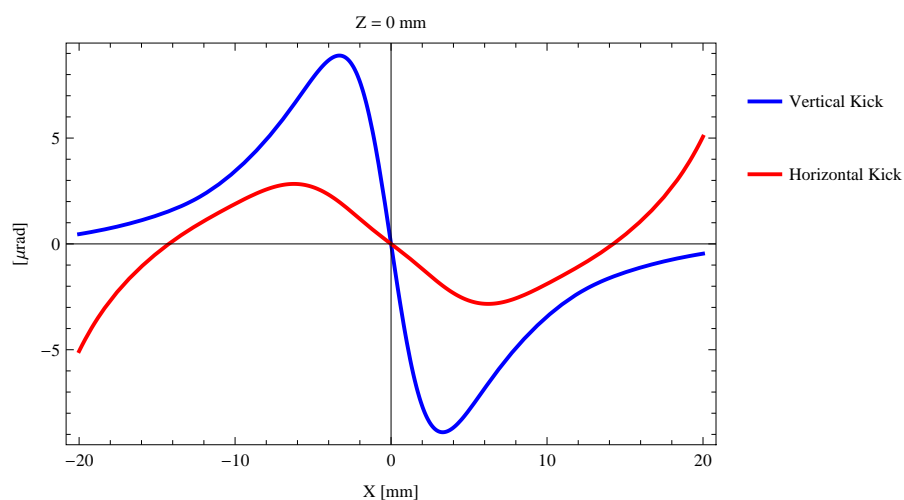


Figure 5.275: Induced angular kick on the stored beam from the epu38Incl ID as a function of the horizontal distance to the ID axis.

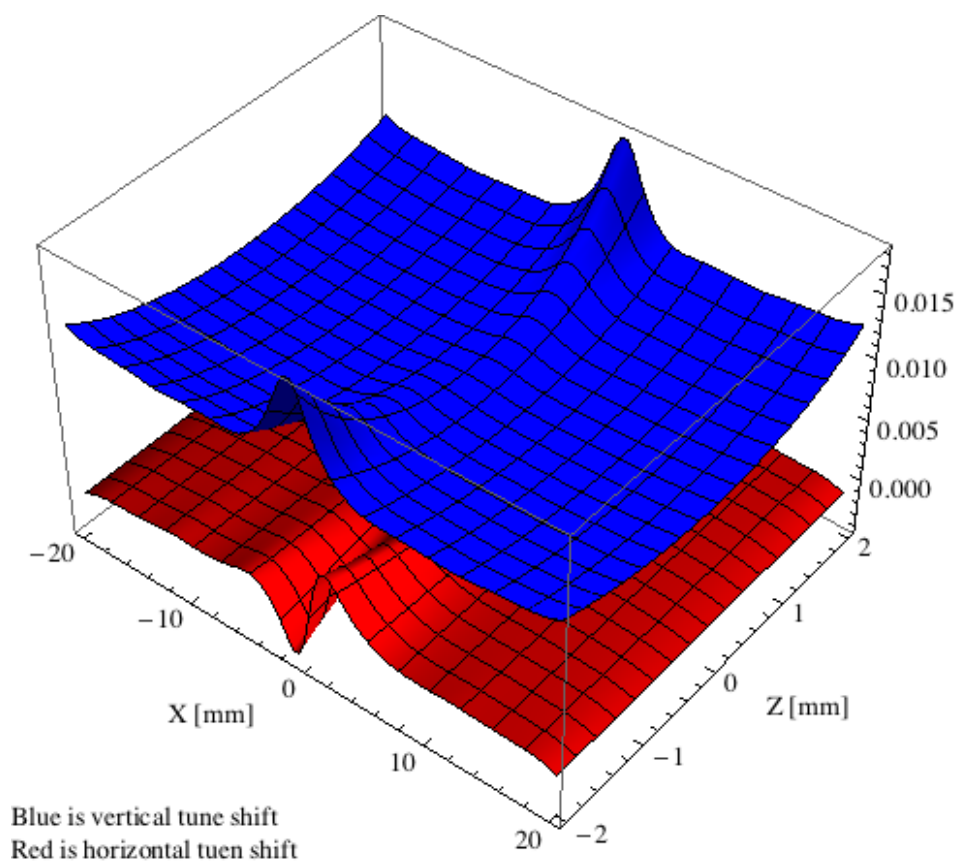


Figure 5.276: Tune shift induced by the epu38Incl ID over the beam stay clear aperture.

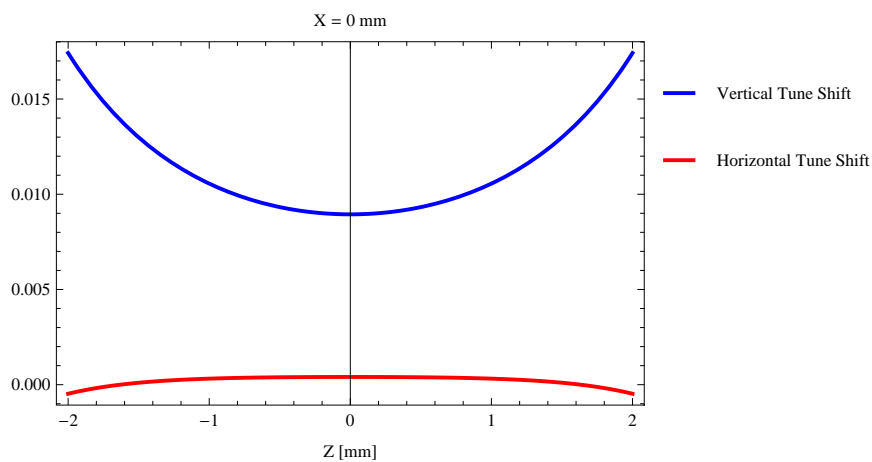


Figure 5.277: Induced tune shift from the epu38Incl ID as a function of the vertical distance to the axis of the ID.

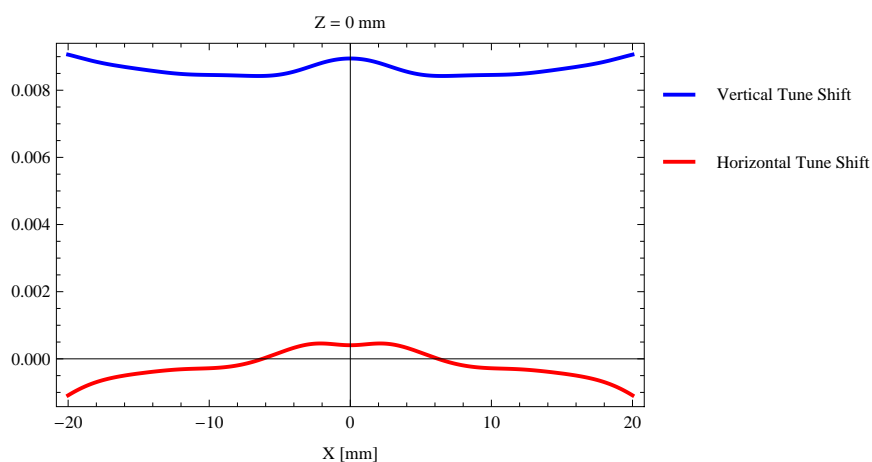


Figure 5.278: Induced tune shift from the epu38Incl ID on the stored beam from the ID as a function of the horizontal distance to the axis of the ID.



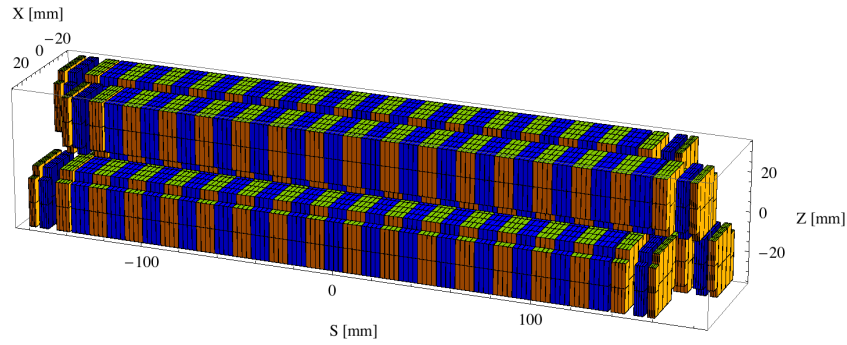


Figure 5.279: Magnetic model of the epu38Vert ID. The ID has been modelled with Radia [2]

$30 \times 30 \times 9.5 \text{ mm}^3$  and there is a 5. mm cut-out in two of the corners of the blocks. The total length of the epu38Vert ID is 3930.98 mm.

### Analysis of the magnetic field of the epu38Vert ID

The effective magnetic fields on axis and the fundamental photon energy of the epu38Vert ID are shown in Table 5.46. The higher harmonic contents in the magnetic field of an elliptically polarising undulator made of permanent magnets is negligible and the efficient field has about the same strength as the peak field.

Table 5.46: Effective Fields on axis and Fundamental Photon Energy of the epu38Vert ID

Undulator Period	38	mm
Undulator Gap	9	mm
Undulator Mode	Vertical	
Undulator Phase	19.000	mm
Vertical Peak Field	-0.001	T
Efficient Vertical Field	0.000	T
Kx (from vert. field)	0.000	
Horizontal Peak Field:	0.732	T
Efficient Horizontal Field	0.733	T
Kz (from hor. field)	2.602	
Photon Energy, Harm.1	0.513	keV
Emitted Power	6.013	kW
Total Length	3931.0	mm

### Synchrotron radiation from the epu38Vert ID

The power map of the emitted synchrotron radiation by the epu38Vert ID, assuming a 0.5 A filament beam with an energy of 3 GeV and undulator properties of the synchrotron radiation, is shown in Figure 5.283. The on-axis power density is  $32.461 \text{ kW/mrad}^2$

A map of the degree of linear polarisation of the fundamental harmonic of the synchrotron radiation emitted by the epu38Vert ID over the angle of observation is shown in Figure 5.284.

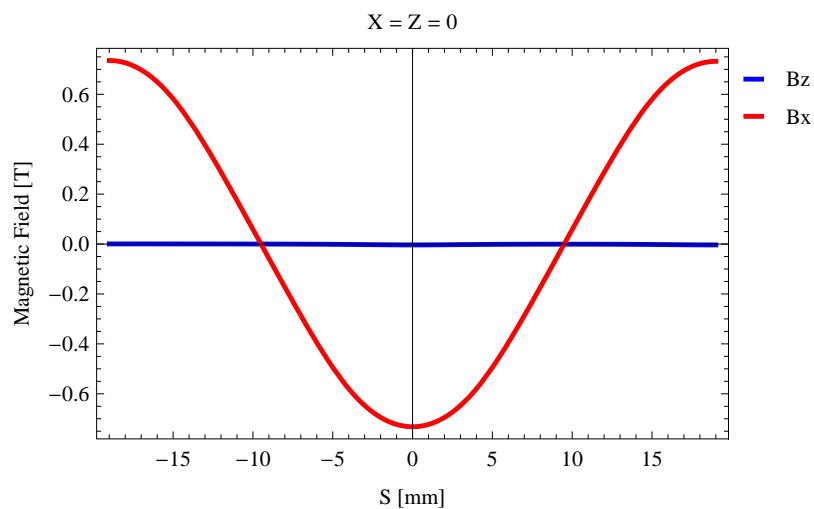


Figure 5.280: Vertical magnetic field in a central pole of the epu38Vert ID along the ID axis,  $X = Z = 0$

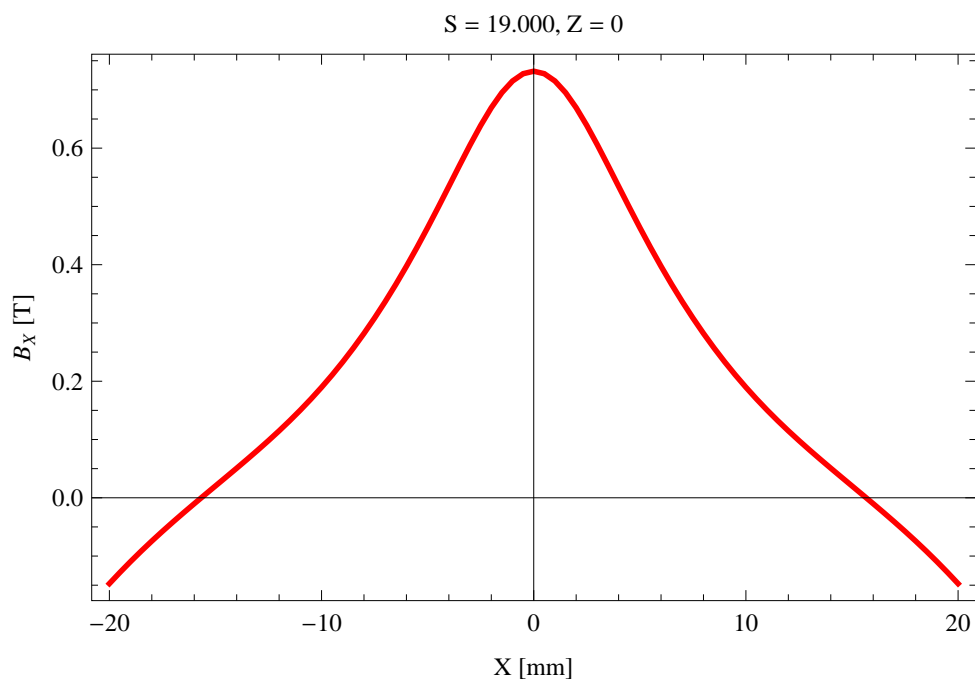


Figure 5.281: Horizontal magnetic field in a central pole of the epu38Vert ID along the horizontally transverse direction to the ID axis,  $S = 19.000$ ,  $Z = 0$

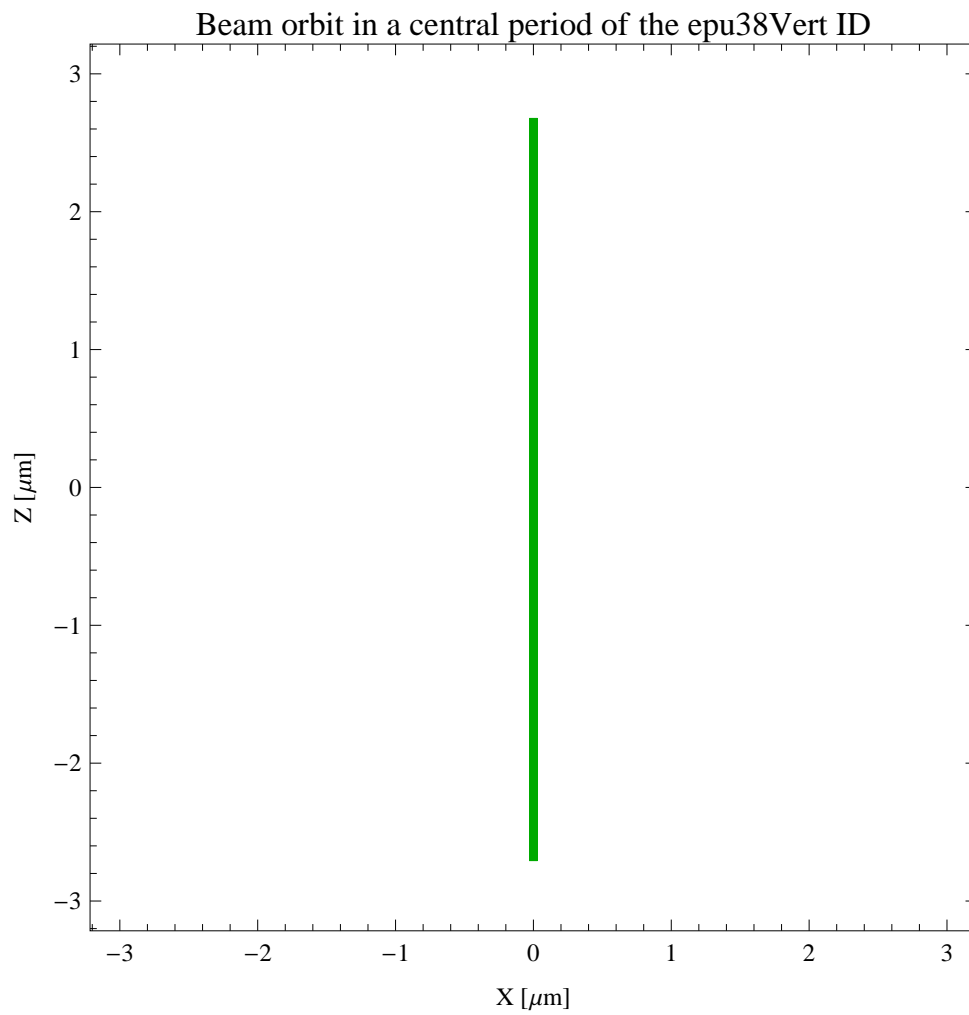


Figure 5.282: The beam orbit of the electron beam through a central period of the epu38Vert ID

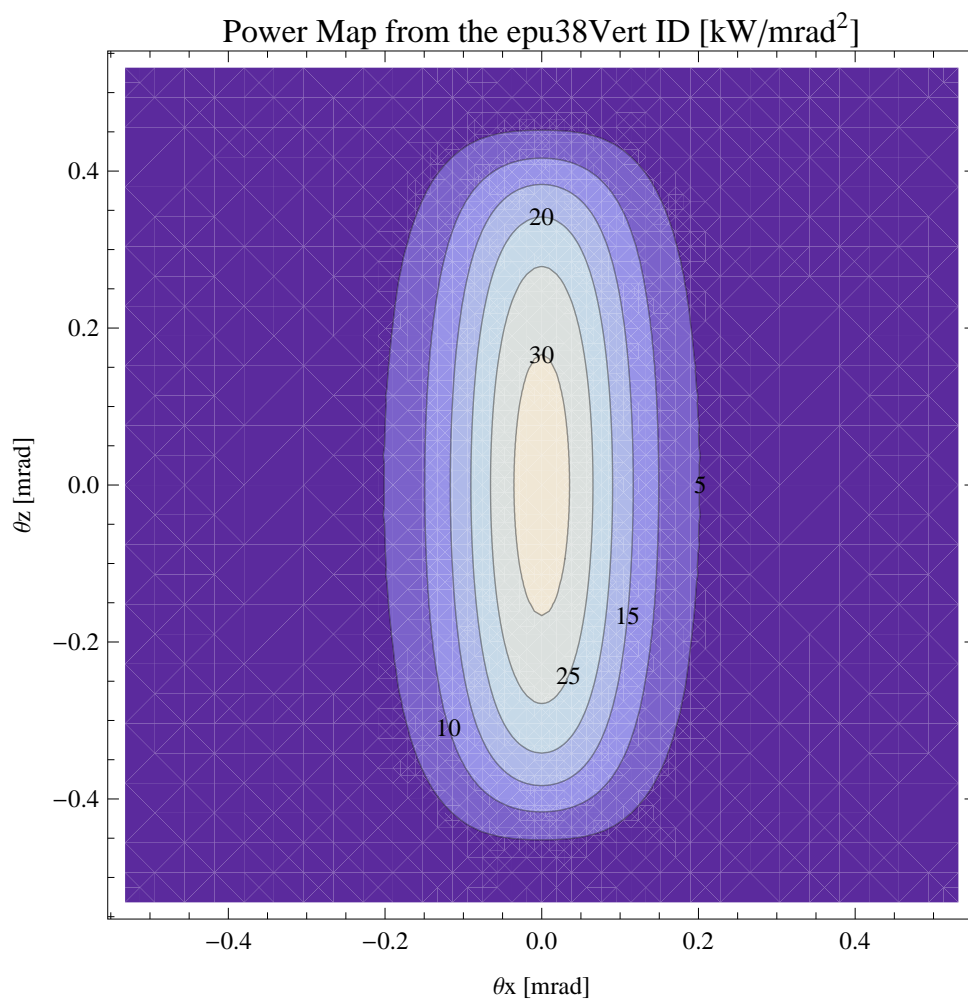


Figure 5.283: Map of the power distribution of the emitted synchrotron radiation by the epu38Vert ID

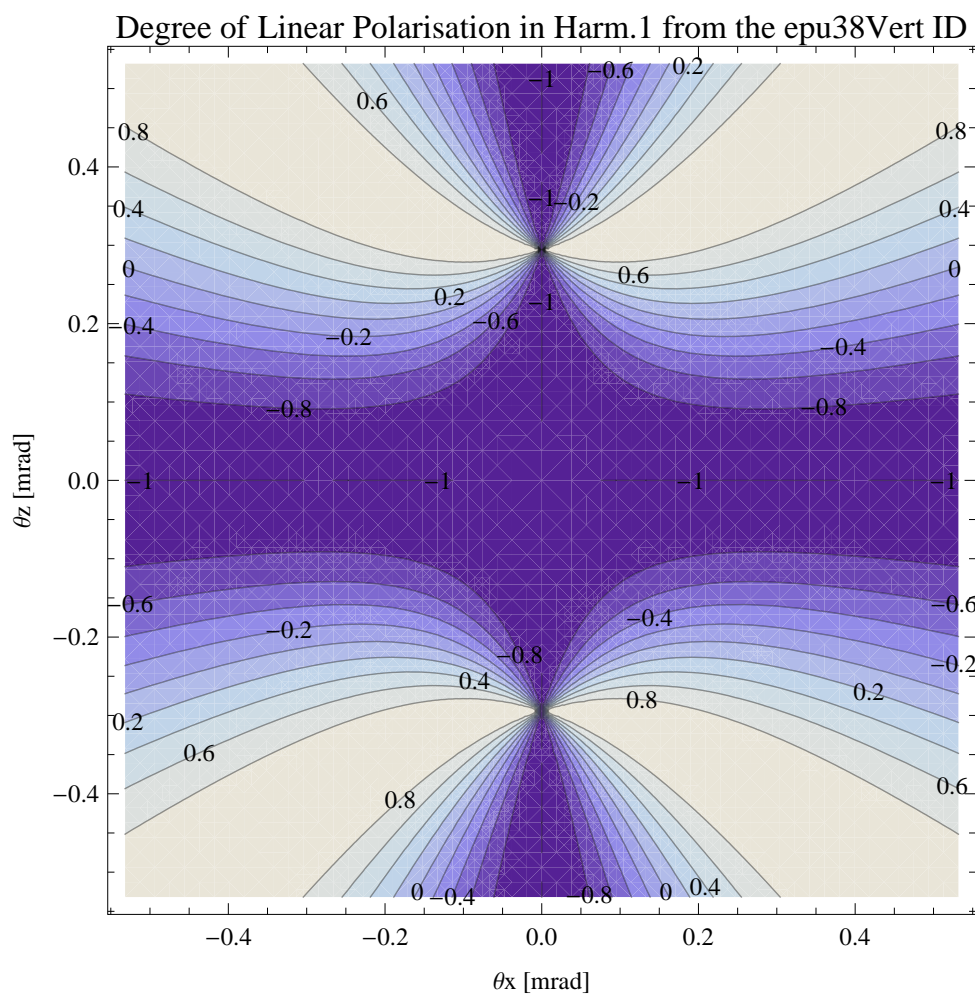


Figure 5.284: Map of linear polarisation in the fundamental harmonic of the synchrotron radiation emitted by the epu38Vert ID

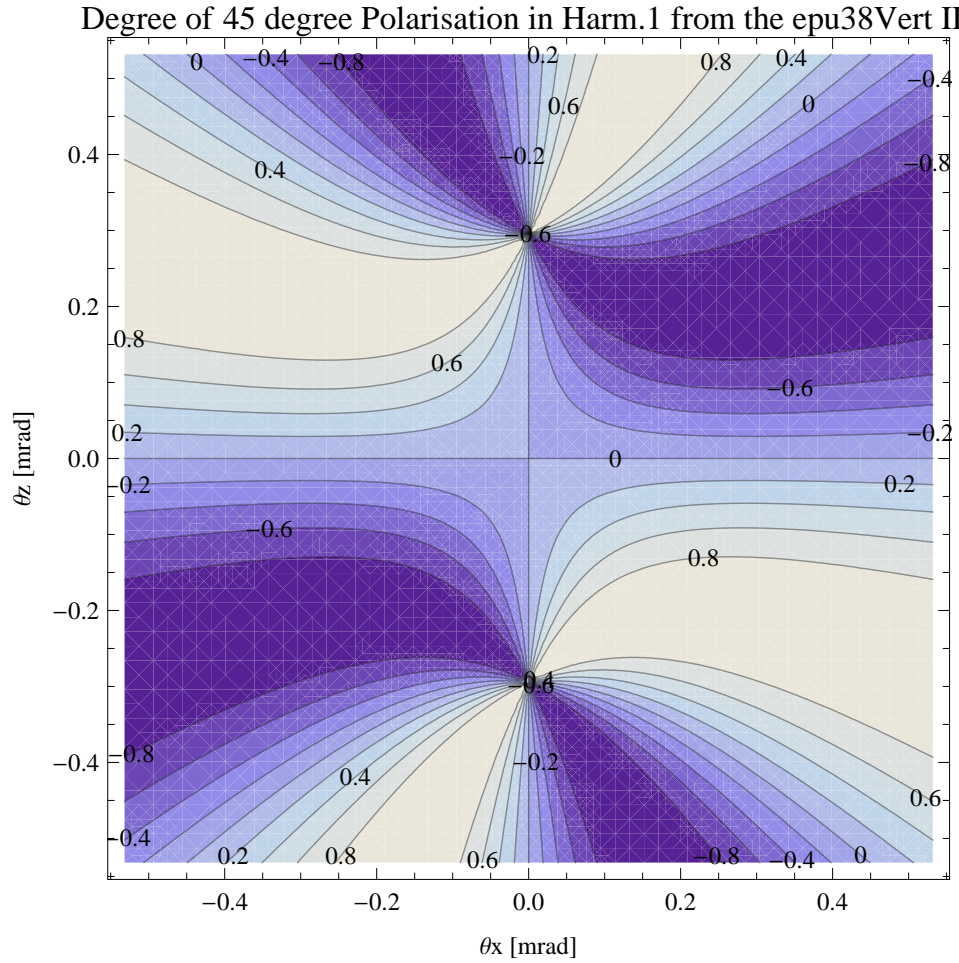


Figure 5.285: Map of 45 degree polarisation in the fundamental harmonic of the synchrotron radiation emitted by the epu38Vert ID

A map of the degree of 45 degree polarisation of the fundamental harmonic of the synchrotron radiation emitted by the epu38Vert ID over the angle of observation is shown in Figure 5.285.

A map of the degree of circular polarisation of the fundamental harmonic of the synchrotron radiation emitted by the epu38Vert ID over the angle of observation is shown in Figure 5.286.

The on axis brilliance at peak energy, the angular spectral flux, the flux in the harmonics, the power in the harmonics, the ratio of coherence, the coherent flux in the harmonics, and the power of coherent radiation in the harmonics from the epu38Vert ID have been calculated and the resulting plots are found in this section of the document. The beam parameters used for the calculation are 0.5 A of stored current,  $\beta_H = 9$  m,  $\varepsilon_H = 0.263$  nmrad,  $\beta_V = 4.8$  m,  $\varepsilon_V = 8$  pmrad, and an energy spread of 0.001.

The brilliance at peak energy and the angular spectral flux density from the epu38Vert ID for different harmonics at maximum K-value (2.602) are given in Table 5.47 and for minimum K-value (0.400) these values are given in Table 5.48.

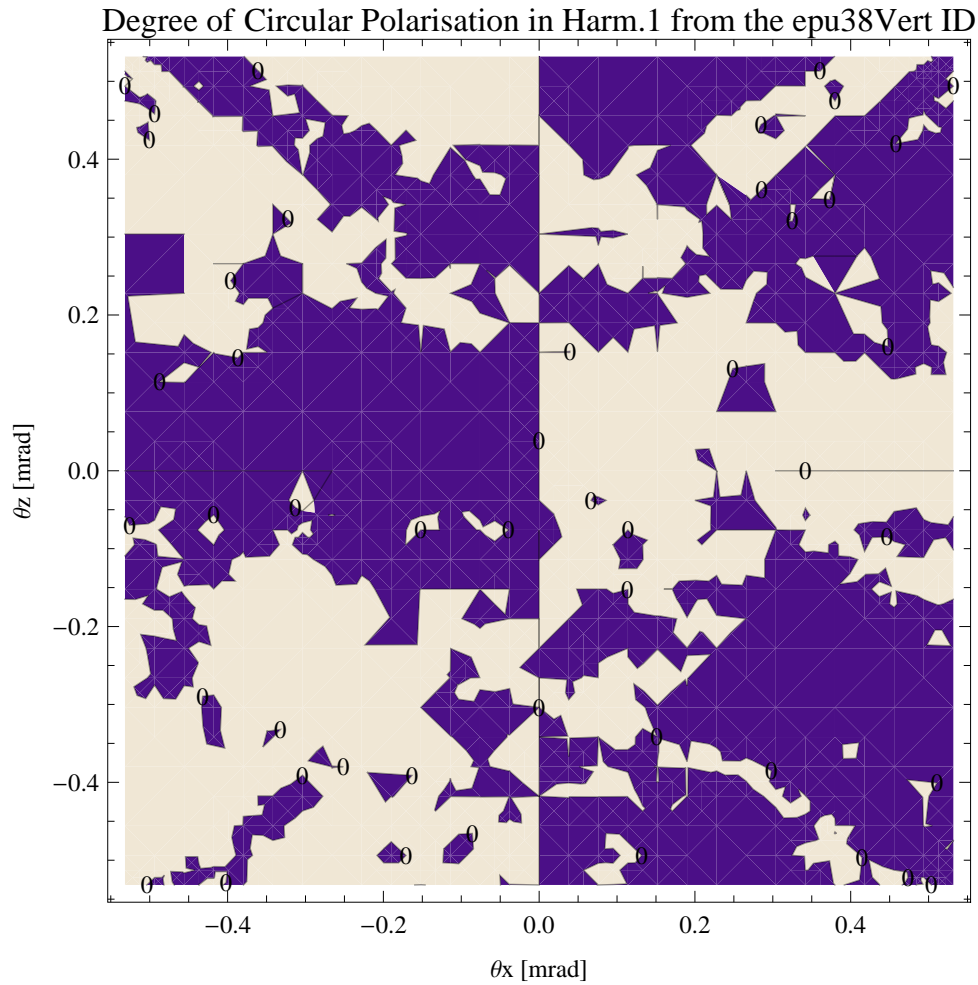


Figure 5.286: Map of circular polarisation in the fundamental harmonic of the synchrotron radiation emitted by the epu38Vert ID

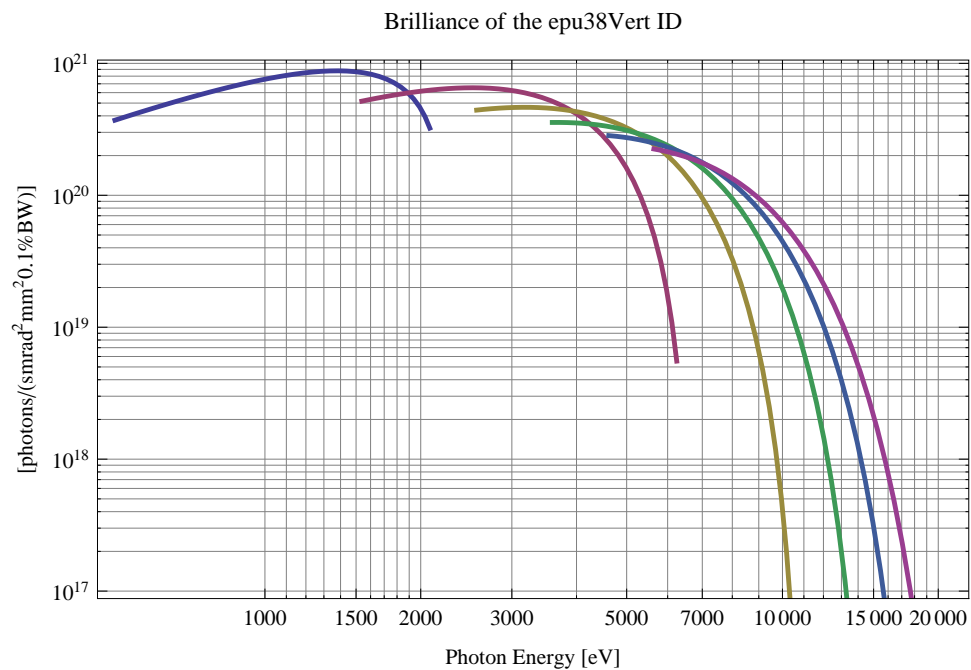


Figure 5.287: The brilliance at peak energy from the epu38Vert ID

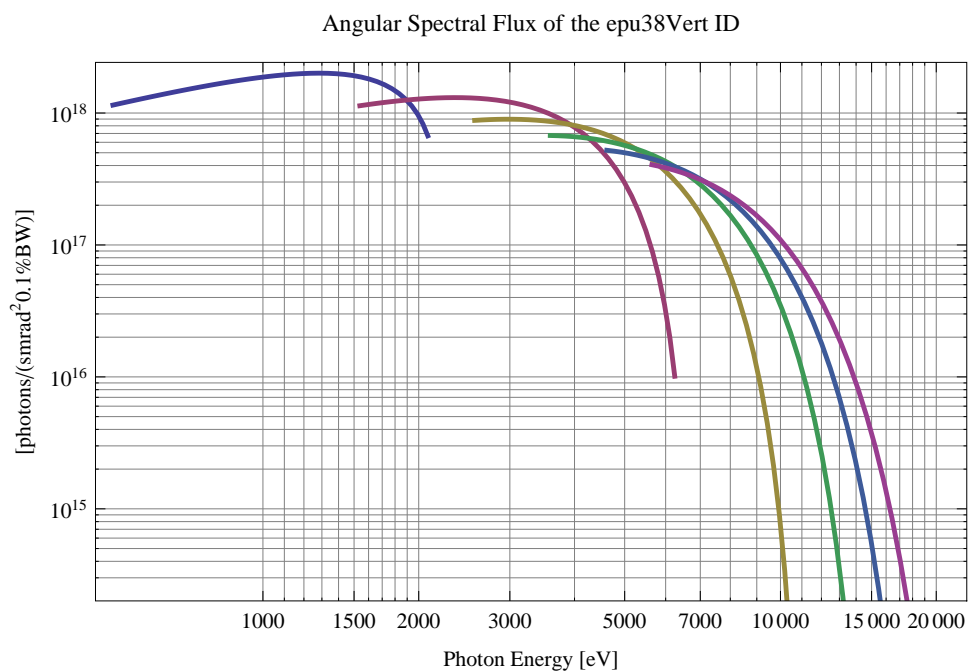


Figure 5.288: The angular spectral flux from the epu38Vert ID

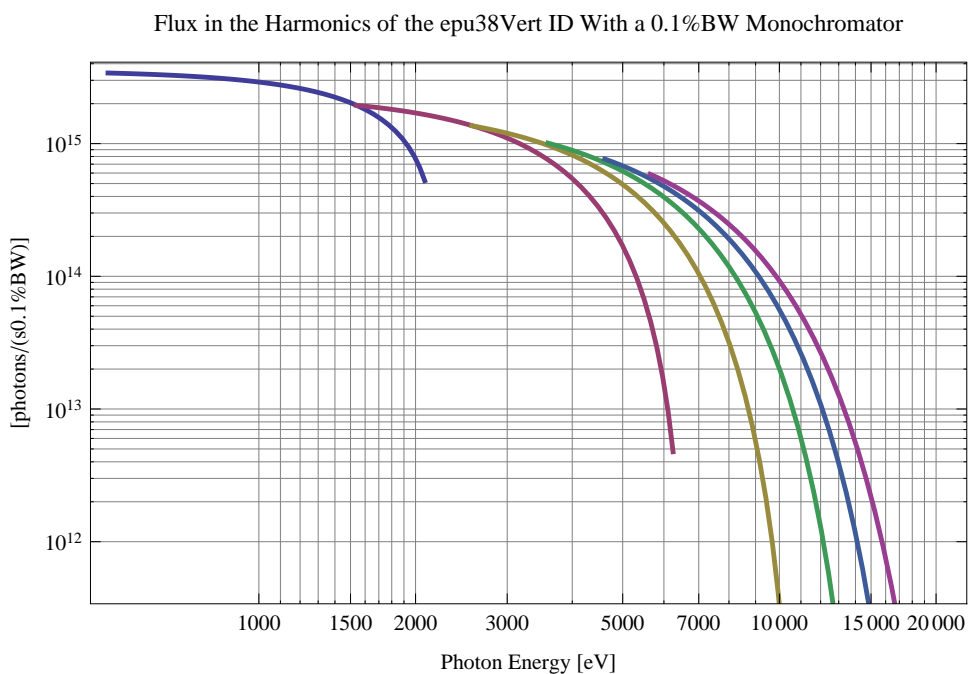


Figure 5.289: The flux of photons in the harmonics from the epu38Vert ID using a 0.1%BW monochromator



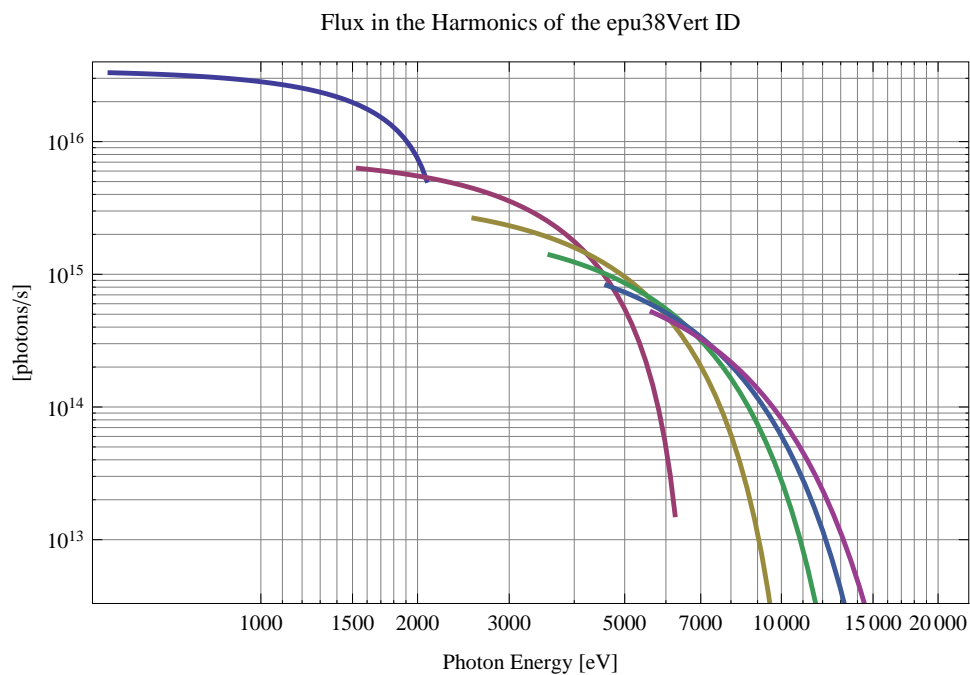


Figure 5.290: The flux of photons in the harmonics from the epu38Vert ID

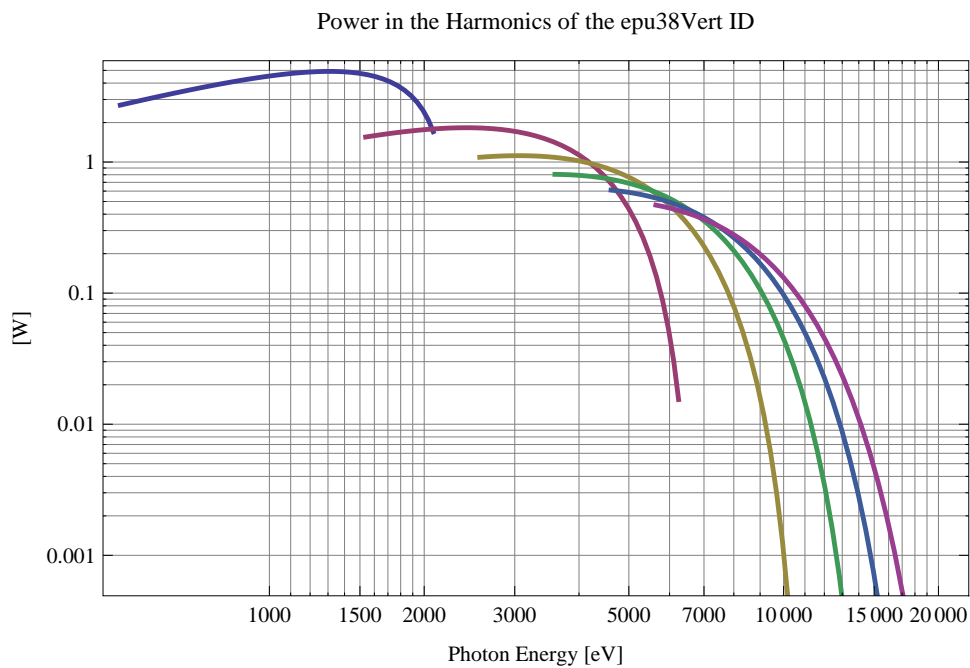


Figure 5.291: The power in the harmonics from the epu38Vert ID

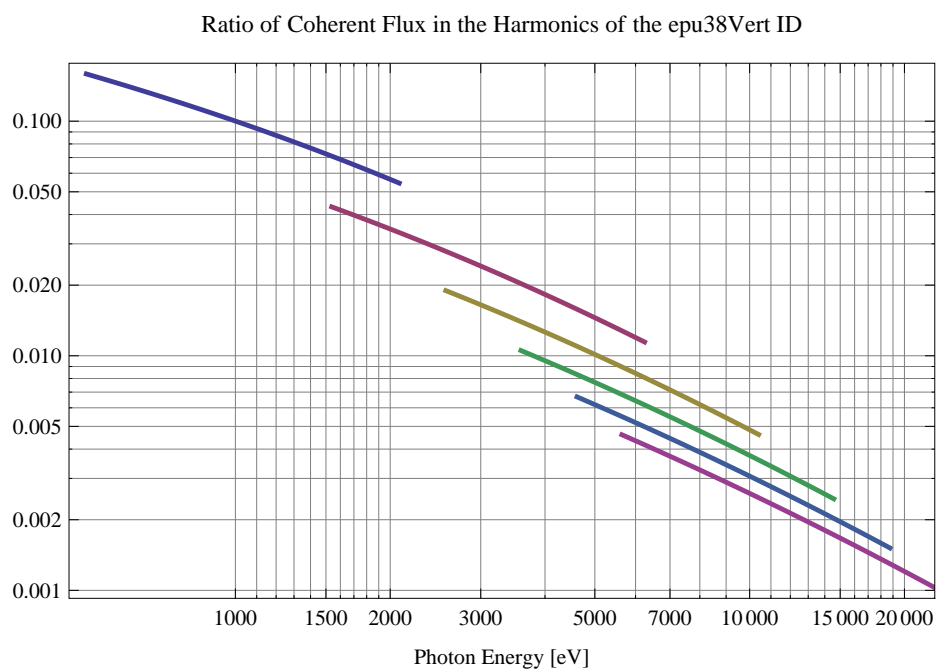


Figure 5.292: The ratio of coherent flux in the harmonics from the epu38Vert ID

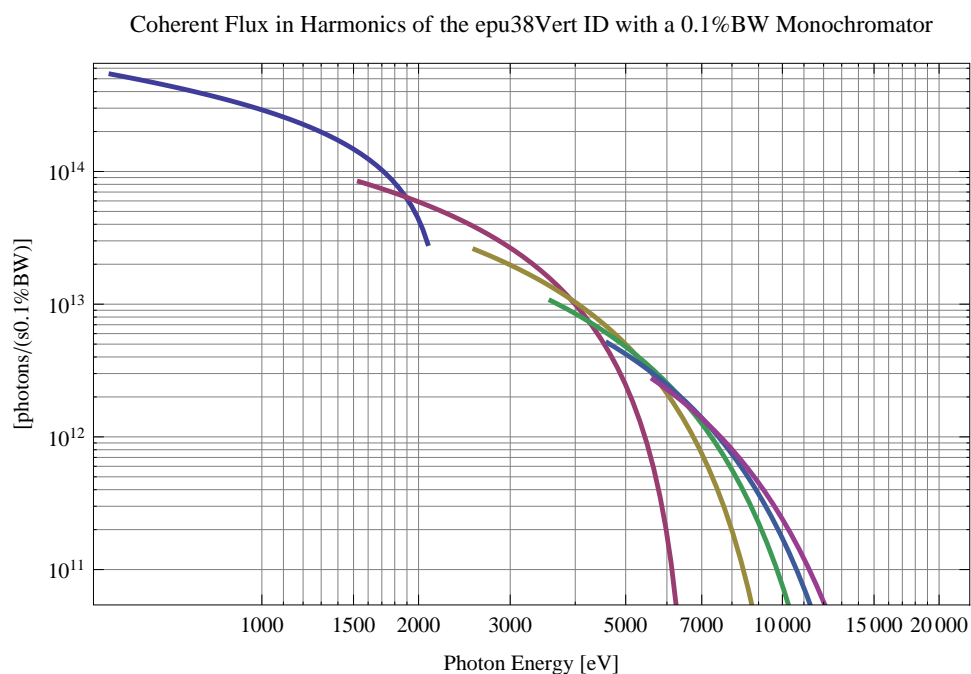


Figure 5.293: The coherent flux in the harmonics of the epu38Vert ID using a 0.1%BW Monochromator

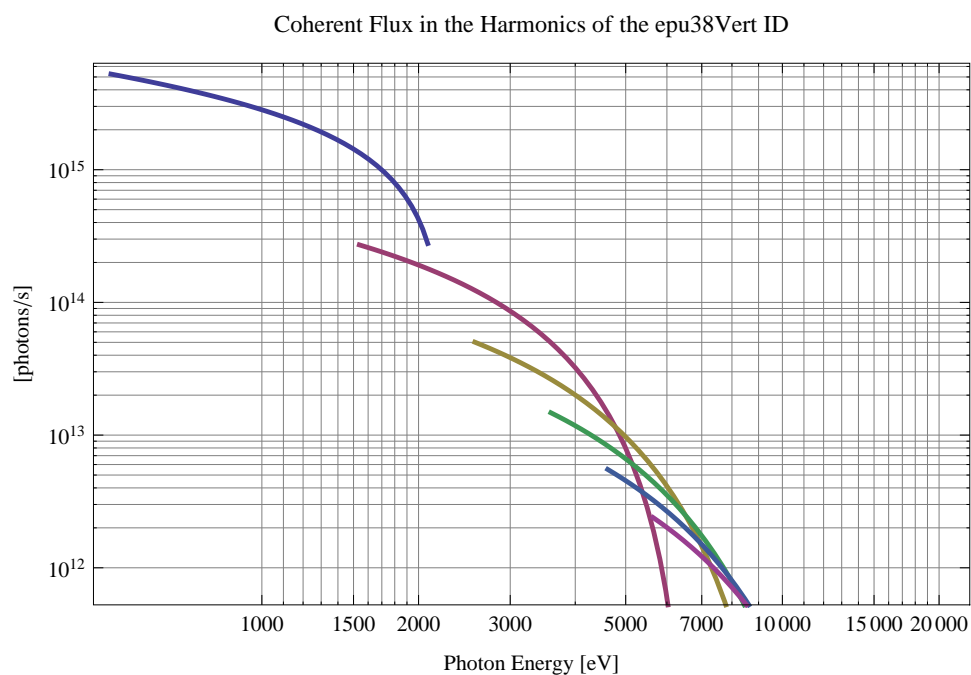


Figure 5.294: The coherent flux in the harmonics of the epu38Vert ID

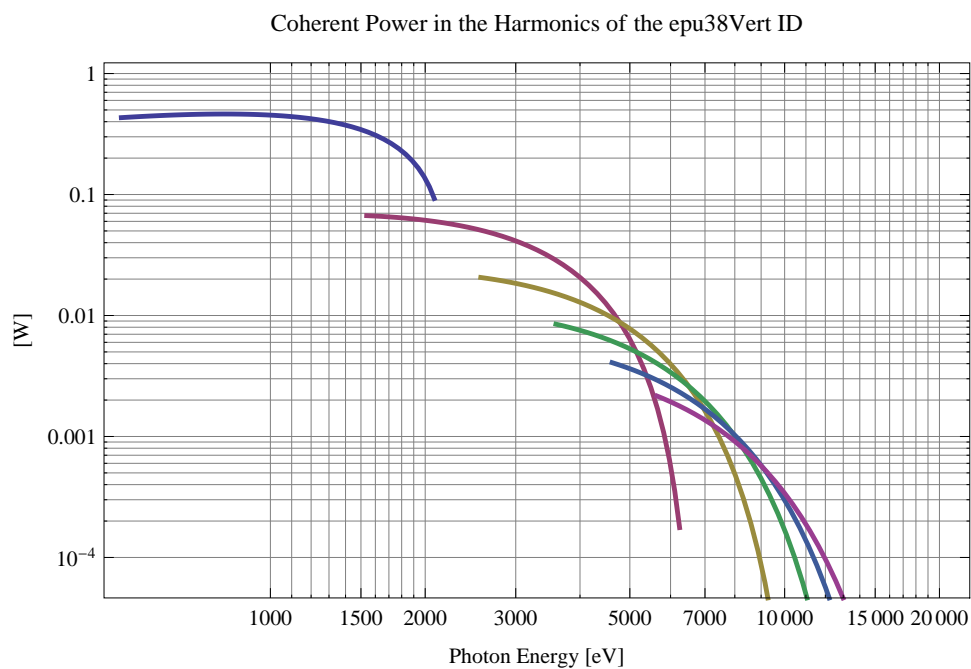


Figure 5.295: The power of coherent synchrotron radiation in the harmonics of the epu38Vert ID

Table 5.47: The brilliance at peak energy and the angular spectral flux density from the epu38Vert ID for different harmonics at maximum K-value (2.602)

Harmonic	Photon Energy [eV]	Brilliance [Ph./s/mrad <sup>2</sup> /mrad <sup>2</sup> /0.1%BW]	Angular Spectral Flux [Ph./s/mrad <sup>2</sup> /0.1%BW]
1	513.028	$3.71 \times 10^{20}$	$1.15 \times 10^{18}$
3	1539.08	$5.17 \times 10^{20}$	$1.14 \times 10^{18}$
5	2565.14	$4.42 \times 10^{20}$	$8.79 \times 10^{17}$
7	3591.19	$3.57 \times 10^{20}$	$6.76 \times 10^{17}$
9	4617.25	$2.83 \times 10^{20}$	$5.22 \times 10^{17}$
11	5643.3	$2.24 \times 10^{20}$	$4.06 \times 10^{17}$

Table 5.48: The brilliance at peak energy and the angular spectral flux density from the epu38Vert ID for different harmonics at minimum K-value (0.4)

Harmonic	Photon Energy [eV]	Brilliance [Ph./s/mrad <sup>2</sup> /mrad <sup>2</sup> /0.1%BW]	Angular Spectral Flux [Ph./s/mrad <sup>2</sup> /0.1%BW]
1	2082.54	$3.23 \times 10^{20}$	$6.72 \times 10^{17}$
3	6247.63	$5.54 \times 10^{18}$	$1.01 \times 10^{16}$
5	10412.7	$6.1 \times 10^{16}$	$1.09 \times 10^{14}$
7	14577.8	$6.35 \times 10^{14}$	$1.12 \times 10^{12}$
9	18742.9	$6.5 \times 10^{12}$	$1.15 \times 10^{10}$
11	22908.	$6.62 \times 10^{10}$	$1.17 \times 10^8$

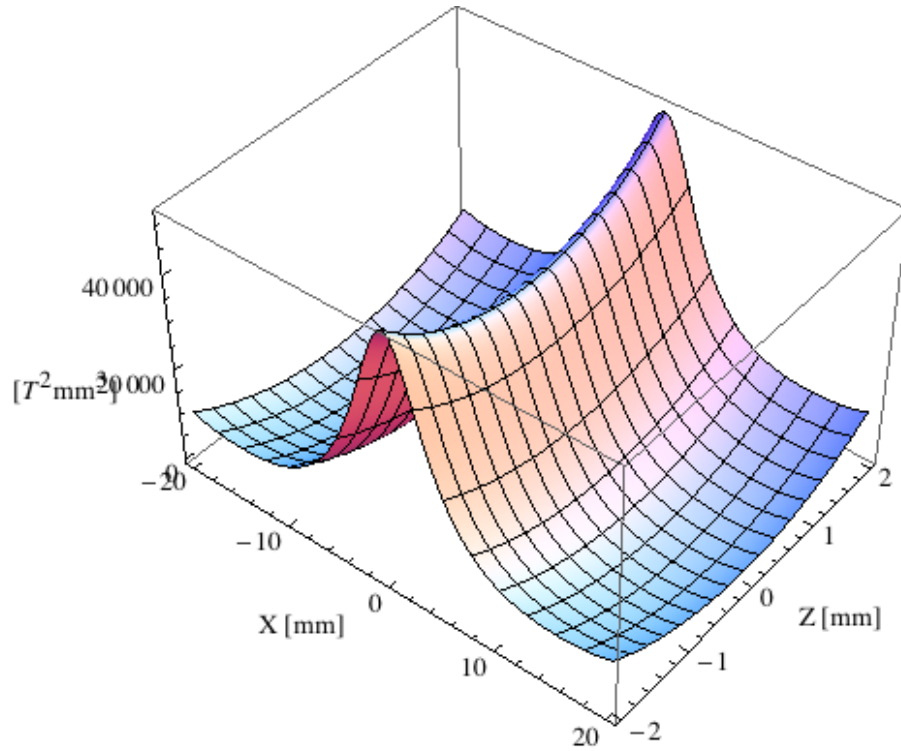


Figure 5.296: Focusing potential from the epu38Vert ID over the beam stay clear aperture.

### Influence from the epu38Vert ID on the optics of the stored beam

Figure 5.296 shows the focusing potential from the epu38Vert over the beam stay clear aperture of the ring aperture.

Figure 5.297 shows the kick map in the beam energy independent unit  $T^2 m^2$  of the kicks induced by the epu38Vert ID over the beam stay clear aperture.

Figure 5.298 shows the induced angular kick on the stored beam from the epu38Vert ID as a function of the vertical distance to the axis of the ID.

Figure 5.299 shows the induced angular kick on the stored beam from the epu38Vert ID as a function of the horizontal distance to the axis of the ID.

Figure 5.300 shows tune shift induced by the epu38Vert ID over the beam stay clear aperture. Note that the tune shift depends on the beam size at the ID.

Figure 5.301 shows the induced tune shift from the epu38Vert ID as a function of the vertical distance to the axis of the ID.

Figure 5.302 shows the induced tune shift from the epu38Vert ID as a function of the horizontal distance to the axis of the ID.

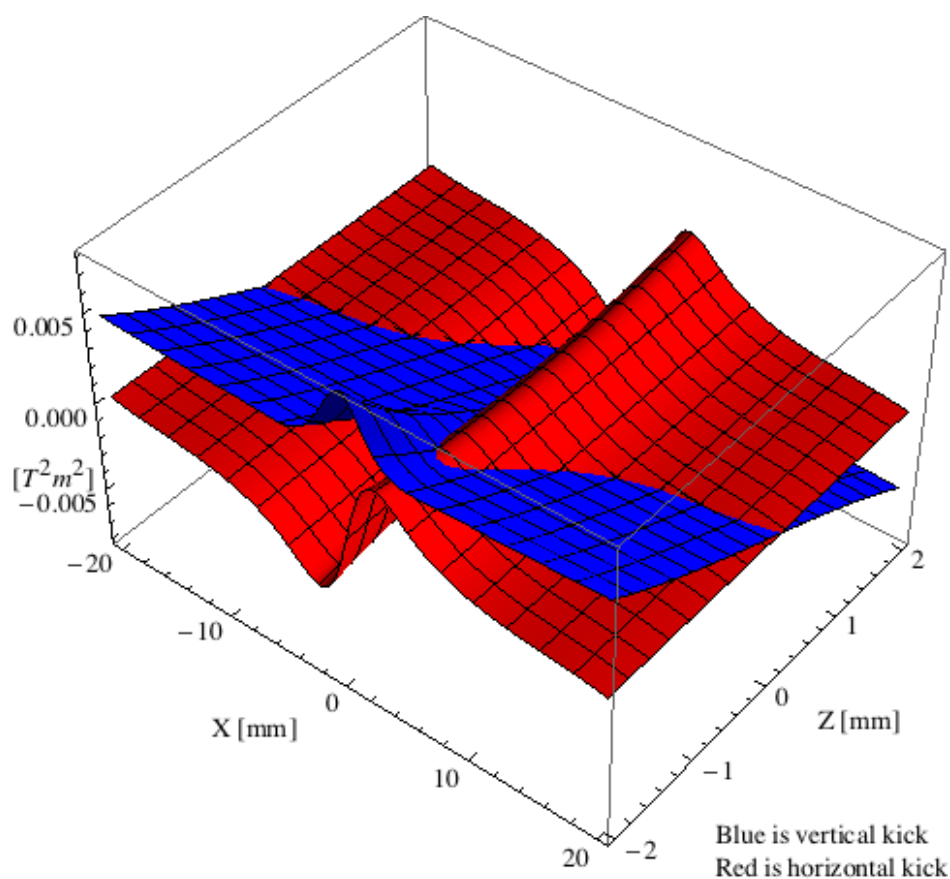


Figure 5.297: Kick map in the beam energy independent unit  $T^2m^2$  of the kicks induced by the epu38Vert ID over the beam stay clear aperture.

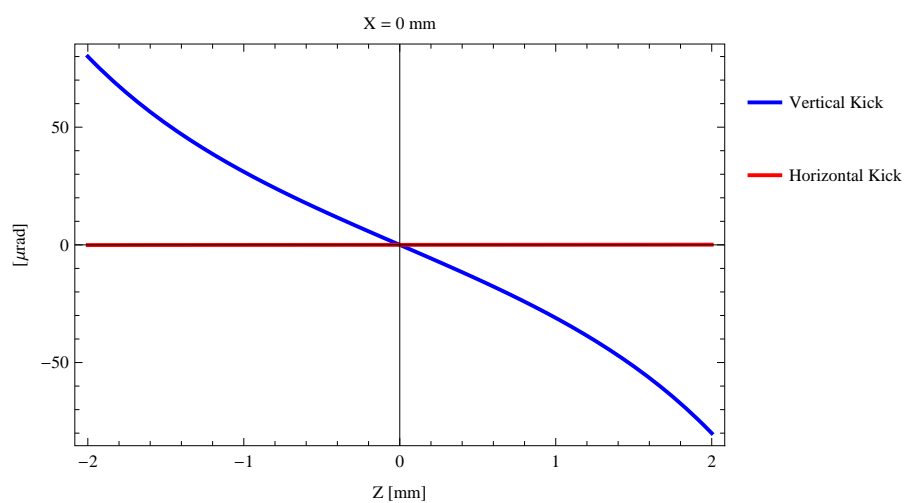


Figure 5.298: Induced angular kick on the stored beam from the epu38Vert ID as a function of the vertical distance to the ID axis.

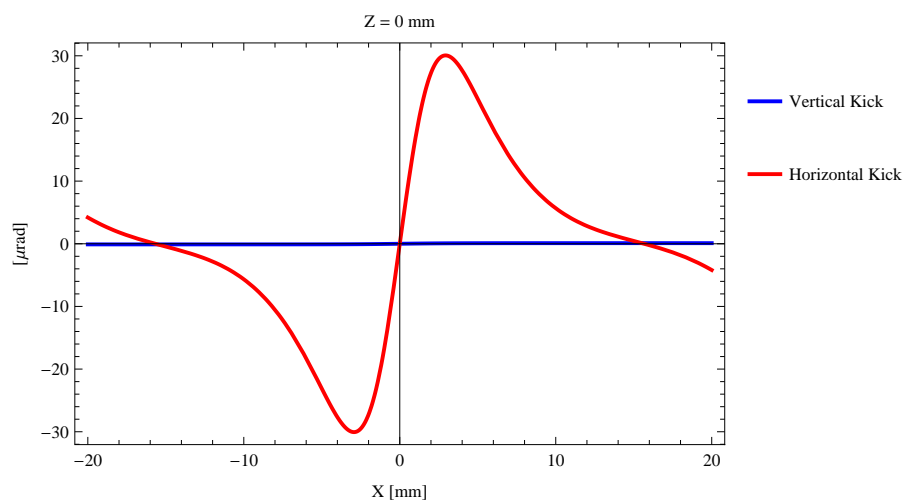


Figure 5.299: Induced angular kick on the stored beam from the epu38Vert ID as a function of the horizontal distance to the ID axis.

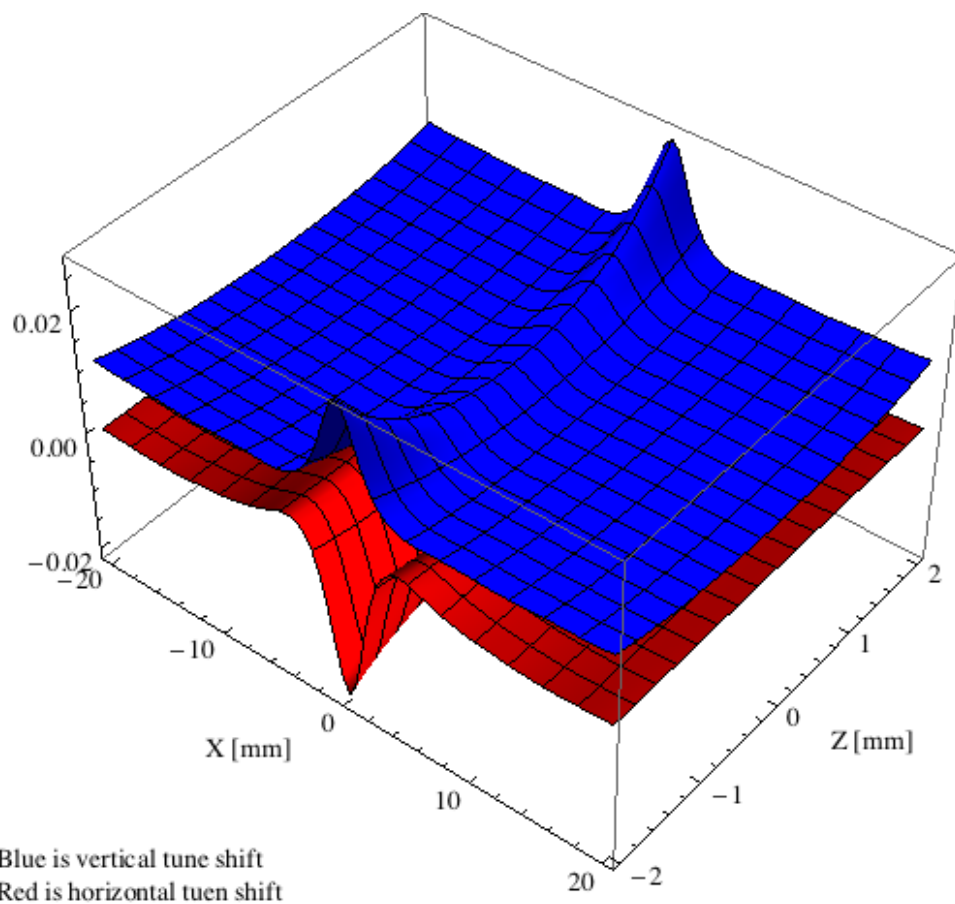


Figure 5.300: Tune shift induced by the epu38Vert ID over the beam stay clear aperture.

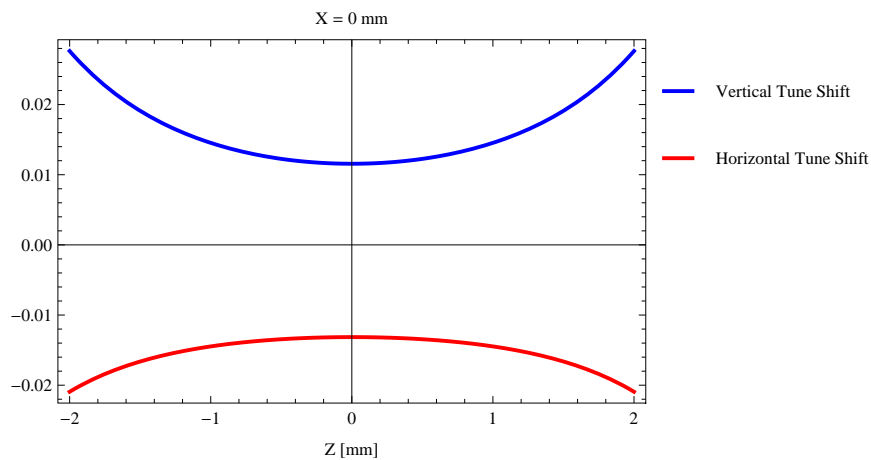


Figure 5.301: Induced tune shift from the epu38Vert ID as a function of the vertical distance to the axis of the ID.

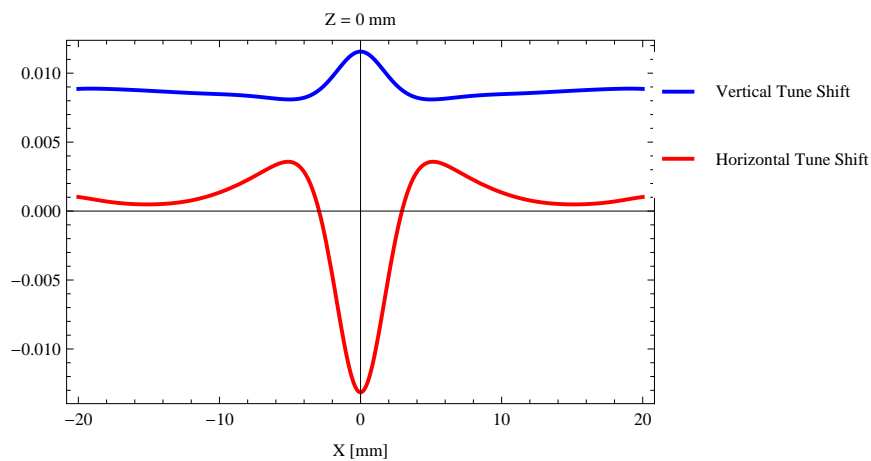


Figure 5.302: Induced tune shift from the epu38Vert ID on the stored beam from the ID as a function of the horizontal distance to the axis of the ID.



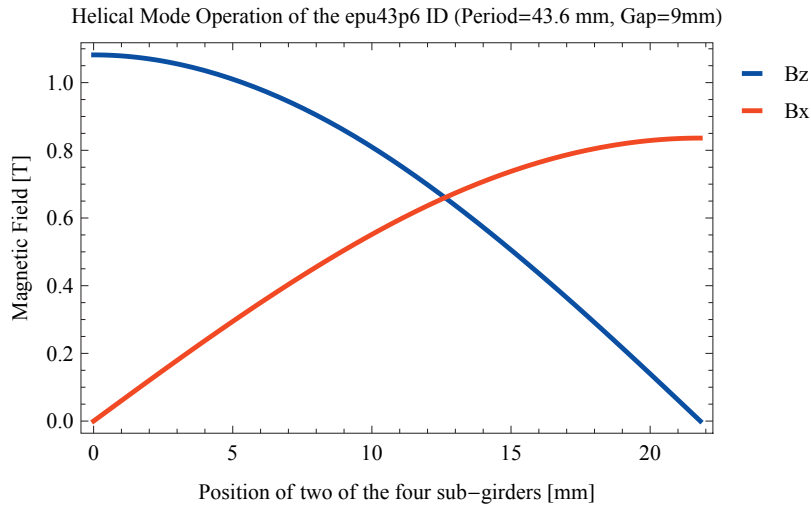


Figure 5.303: Vertical and horizontal magnetic field for the the epu43p6 ID when operating in the helical mode for different positions for two of the four sub-girders

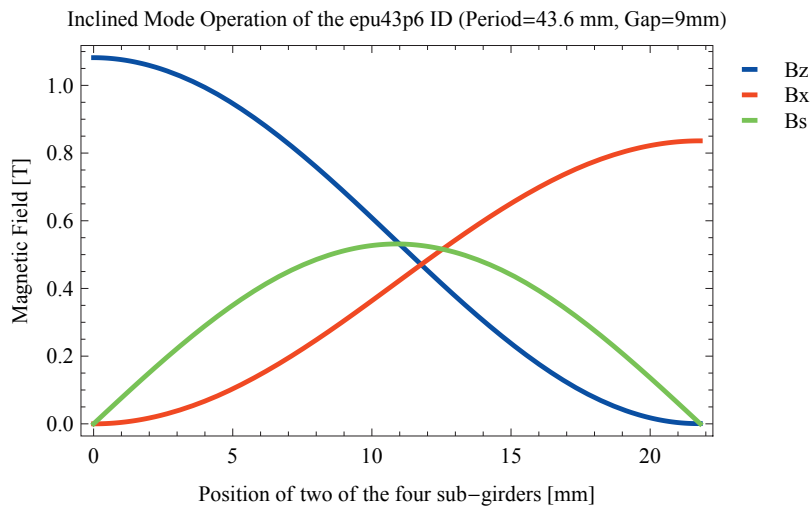


Figure 5.304: Vertical, horizontal, and longitudinal magnetic field for the the epu43p6 ID when operating in the inclined mode for different positions for two of the four sub-girders

### 5.3.8. The elliptically polarising undulator epu43p6

#### Modes of operation in the elliptically polarising undulator epu43p6

Horizontal polarisation of the emitted synchrotron radiation from the epu43p6 ID (Period=43.6 mm, Gap=9mm) is found in the planar mode when there is no movement of the sub-girders.

Circular polarisation is found in the elliptical mode of operation for a symmetric sub-grider movement of 12.6269 mm. Figure 5.303 shows the vertical and horizontal magnetic field for the epu43p6 ID when operating in the helical mode.

45 degree polarisation is found in the inclined mode of operation for an assymetric sub-grider movement of 11.7712 mm. Figure 5.304 shows the vertical and horizontal magnetic field for the epu43p6 ID when operating in the inclined mode.

The following sub-sections will cover four different situations: The epu43p6 operating in the

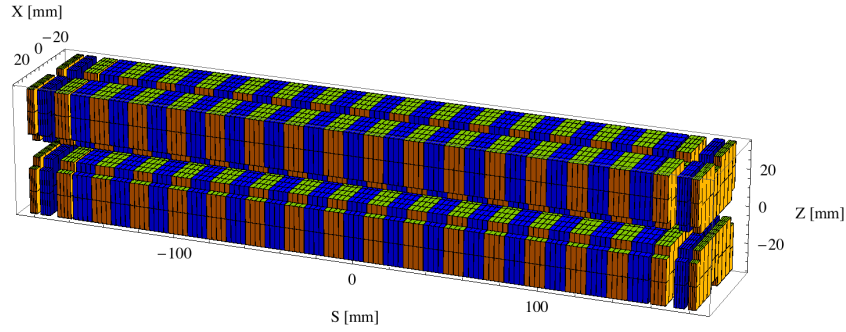


Figure 5.305: Magnetic model of the epu43p6Plan ID. The ID has been modelled with Radia [2]

planar mode for horizontal polarisation (epu43p6Plan); The epu43p6 operating in the helical mode for circular polarisation (epu43p6Heli), the epu43p6 operating in the inclined mode for 45 degree polarisation (epu43p6Incl); and The epu43p6 operating in the vertical mode for vertical polarisation (epu43p6Vert).

### Magnet model of the elliptically polarising undulator epu43p6Plan

The Radia [2] magnet model of the epu43p6Plan ID is shown in Figure 5.305. The length of the magnet model is 366.067 mm. The magnetic material in the model is NdFeb with a remanence of 1.28 T, a material similar to VACODYM 776 TP from Vacuumschmelze. Blocks with vertical magnetisation are blue and blocks with horizontal magnetisation are yellow. The block size is  $30 \times 30 \times 10.9 \text{ mm}^3$  and there is a 5 mm cut-out in two of the corners of the blocks. The total length of the epu43p6Plan ID is 3941.27 mm.

### Analysis of the magnetic field of the epu43p6Plan ID

The effective magnetic fields on axis and the fundamental photon energy of the epu43p6Plan ID are shown in Table 5.49. The higher harmonic contents in the magnetic field of an elliptically polarising undulator made of permanent magnets is negligible and the efficient field has about the same strength as the peak field.

### Synchrotron radiation from the epu43p6Plan ID

The power map of the emitted synchrotron radiation by the epu43p6Plan ID, assuming a 0.5 A filament beam with an energy of 3 GeV and undulator properties of the synchrotron radiation, is shown in Figure 5.309. The on-axis power density is  $42.128 \text{ kW/mrad}^2$

A map of the degree of linear polarisation of the fundamental harmonic of the synchrotron radiation emitted by the epu43p6Plan ID over the angle of observation is shown in Figure 5.310.

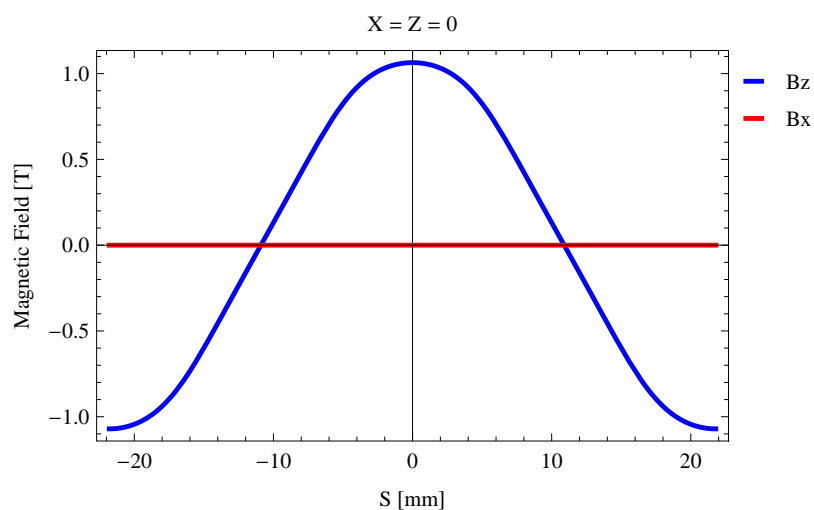
A map of the degree of 45 degree polarisation of the fundamental harmonic of the synchrotron radiation emitted by the epu43p6Plan ID over the angle of observation is shown in Figure 5.311.

A map of the degree of circular polarisation of the fundamental harmonic of the synchrotron radiation emitted by the epu43p6Plan ID over the angle of observation is shown in Figure 5.312.

The on axis brilliance at peak energy, the angular spectral flux, the flux in the harmonics, the power in the harmonics, the ratio of coherence, the coherent flux in the harmonics, and the power

Table 5.49: Effective Fields on axis and Fundamental Photon Energy of the epu43p6Plan ID

Undulator Period	43.6	mm
Undulator Gap	9	mm
Undulator Mode	Planar	
Undulator Phase	0.000	mm
Vertical Peak Field	1.064	T
Efficient Vertical Field	1.082	T
Kx (from vert. field)	4.406	
Horizontal Peak Field:	0.000	T
Efficient Horizontal Field	0.000	T
Kz (from hor. field)	0.000	
Photon Energy, Harm.1	0.183	keV
Emitted Power	13.137	kW
Total Length	3941.3	mm

Figure 5.306: Vertical magnetic field in a central pole of the epu43p6Plan ID along the ID axis,  $X = Z = 0$

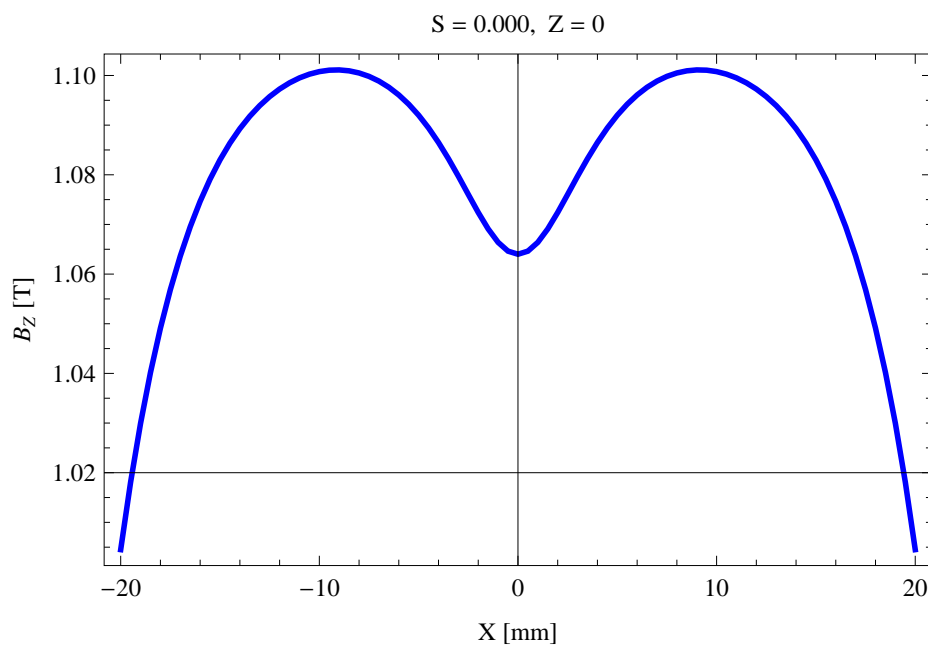


Figure 5.307: Vertical magnetic field in a central pole of the epu43p6Plan ID along the horizontally transverse direction to the ID axis,  $S = 0.000, Z = 0$

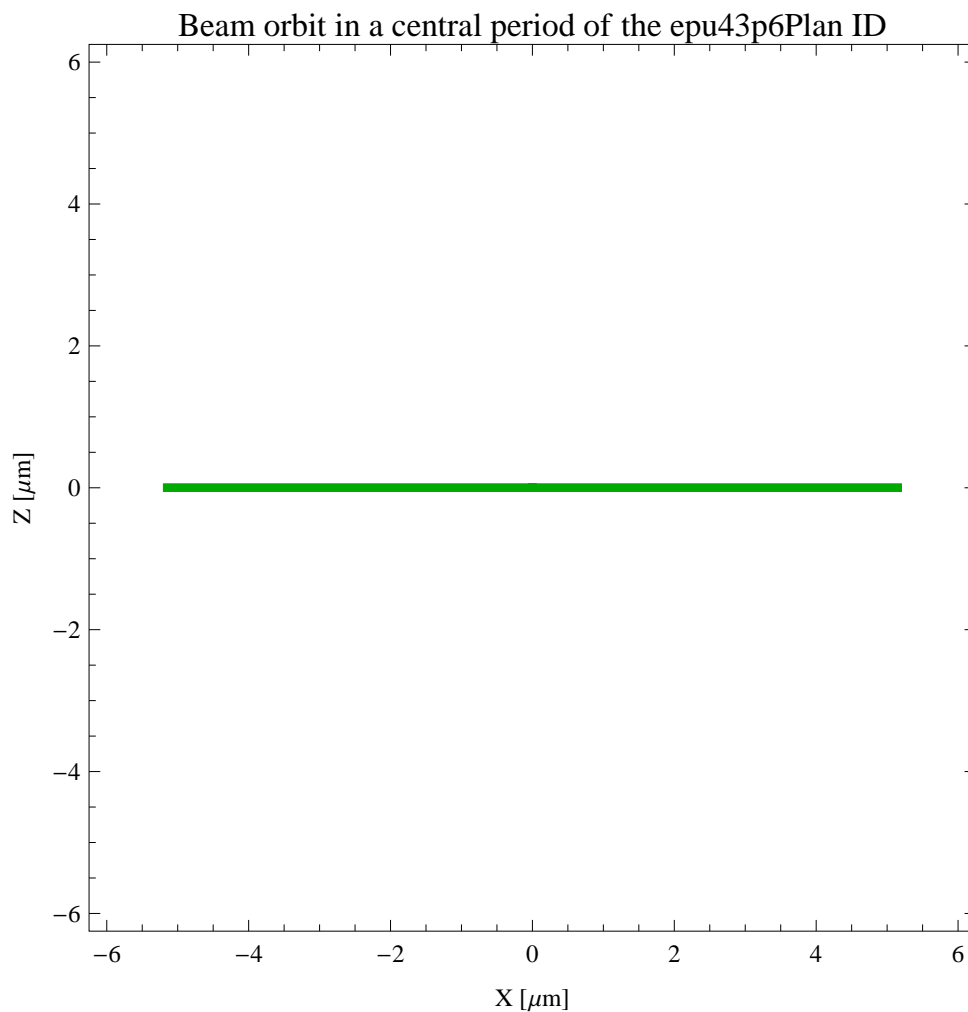


Figure 5.308: The beam orbit of the electron beam through a central period of the epu43p6Plan ID

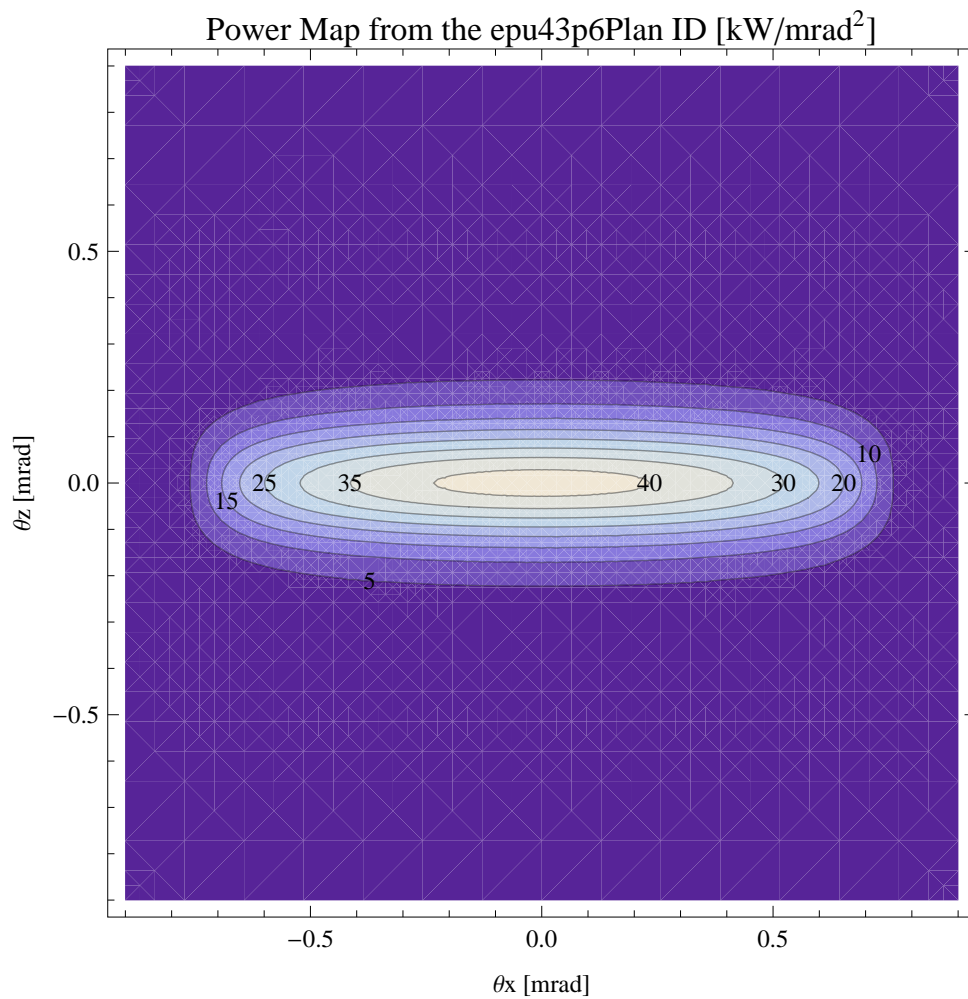


Figure 5.309: Map of the power distribution of the emitted synchrotron radiation by the epu43p6Plan ID

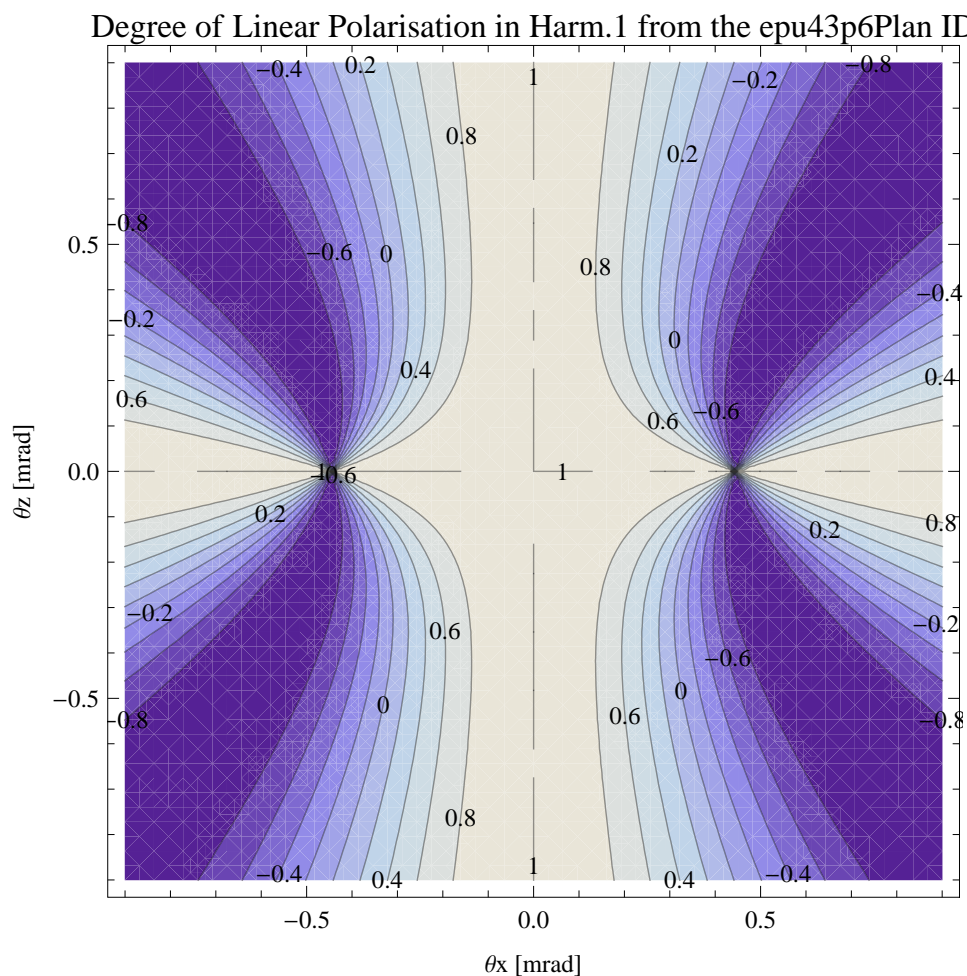


Figure 5.310: Map of linear polarisation in the fundamental harmonic of the synchrotron radiation emitted by the epu43p6Plan ID

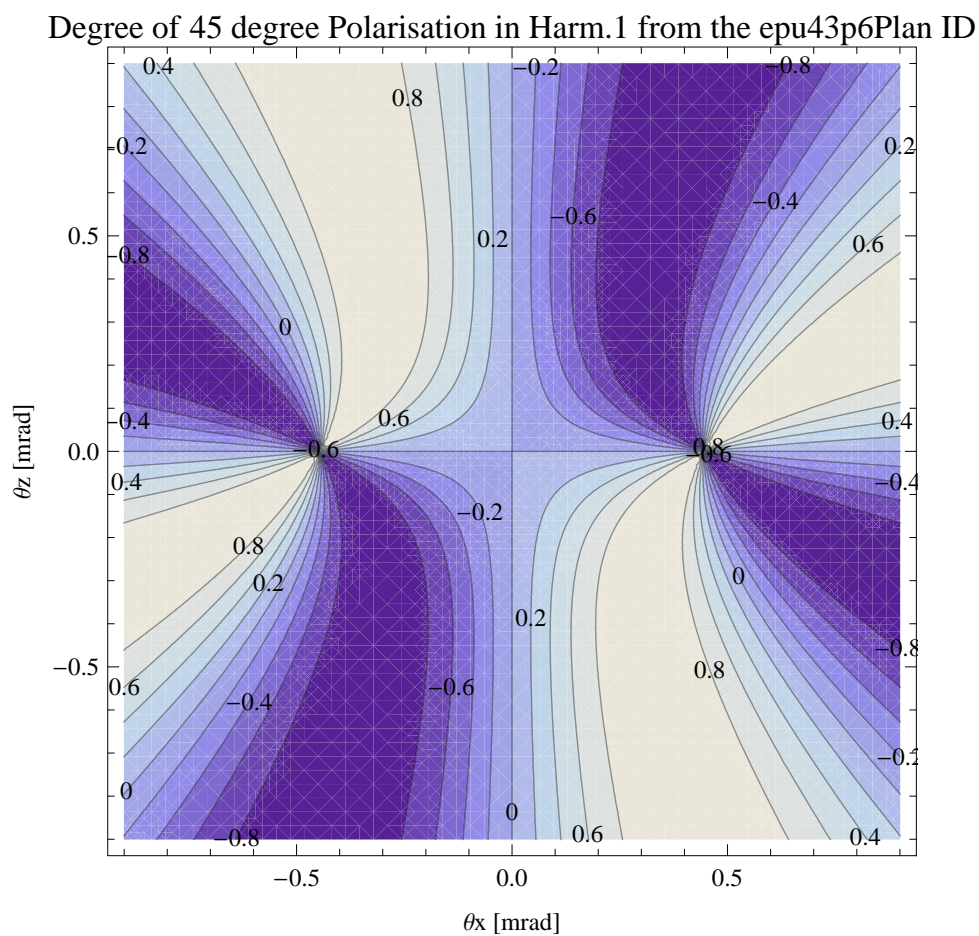


Figure 5.311: Map of 45 degree polarisation in the fundamental harmonic of the synchrotron radiation emitted by the epu43p6Plan ID

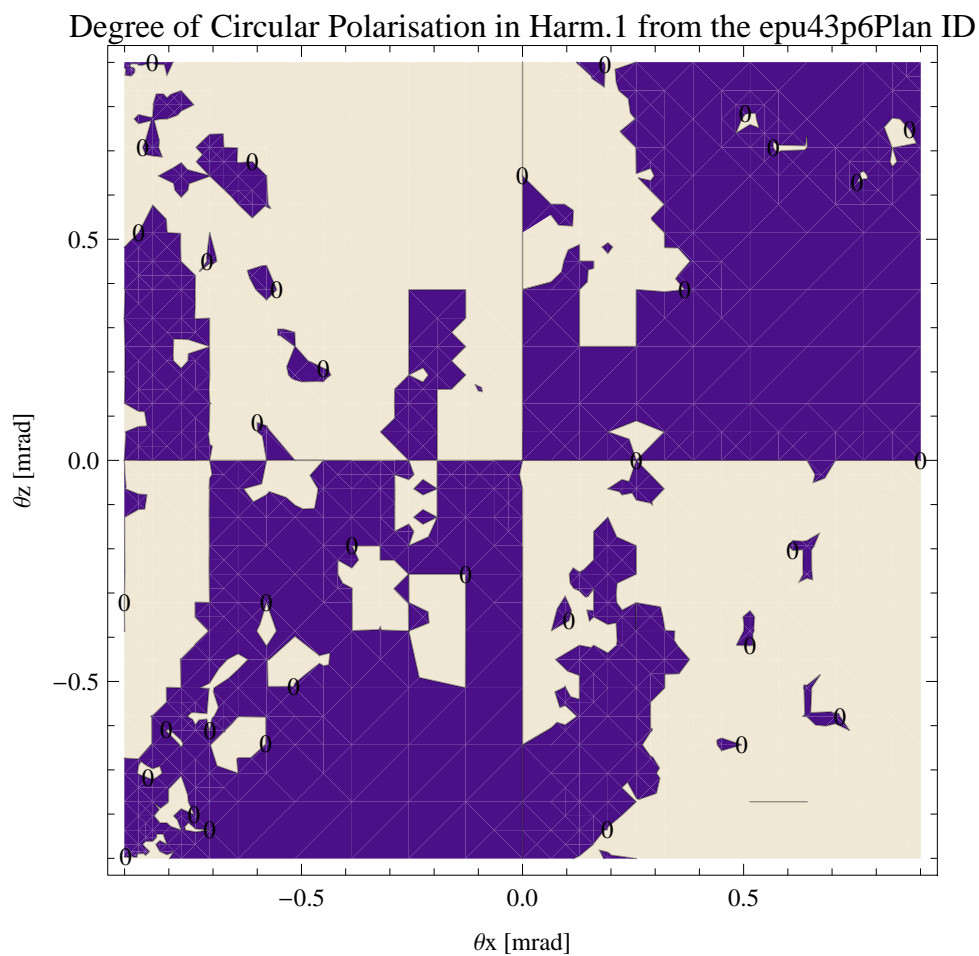


Figure 5.312: Map of circular polarisation in the fundamental harmonic of the synchrotron radiation emitted by the epu43p6Plan ID



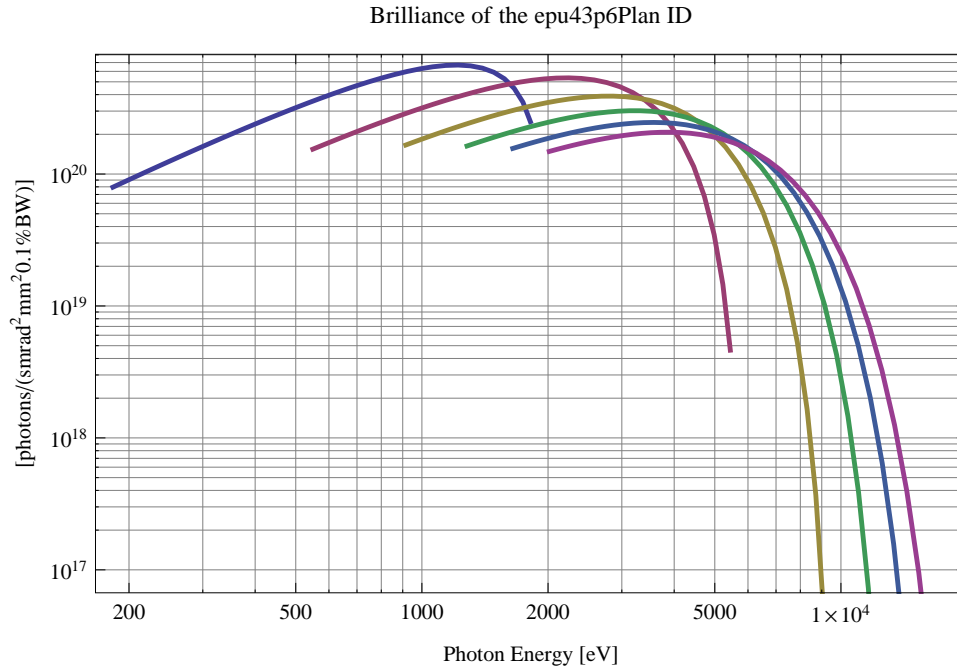


Figure 5.313: The brilliance at peak energy from the epu43p6Plan ID

of coherent radiation in the harmonics from the epu43p6Plan ID have been calculated and the resulting plots are found in this section of the document. The beam parameters used for the calculation are 0.5 A of stored current,  $\beta_H = 9$  m,  $\varepsilon_H = 0.263$  nmrad,  $\beta_V = 4.8$  m,  $\varepsilon_V = 8$  pmrad, and an energy spread of 0.001.

The brilliance at peak energy and the angular spectral flux density from the epu43p6Plan ID for different harmonics at maximum K-value (4.406) are given in Table 5.50 and for minimum K-value (0.400) these values are given in Table 5.51.

Table 5.50: The brilliance at peak energy and the angular spectral flux density from the epu43p6Plan ID for different harmonics at maximum K-value (4.406)

Harmonic	Photon Energy [eV]	Brilliance [Ph./s/mrad <sup>2</sup> /mrad <sup>2</sup> /0.1%BW]	Angular Spectral Flux [Ph./s/mrad <sup>2</sup> /0.1%BW]
1	183.08	$7.95 \times 10^{19}$	$3.91 \times 10^{17}$
3	549.241	$1.54 \times 10^{20}$	$4.68 \times 10^{17}$
5	915.401	$1.66 \times 10^{20}$	$4.24 \times 10^{17}$
7	1281.56	$1.63 \times 10^{20}$	$3.8 \times 10^{17}$
9	1647.72	$1.56 \times 10^{20}$	$3.42 \times 10^{17}$
11	2013.88	$1.48 \times 10^{20}$	$3.11 \times 10^{17}$

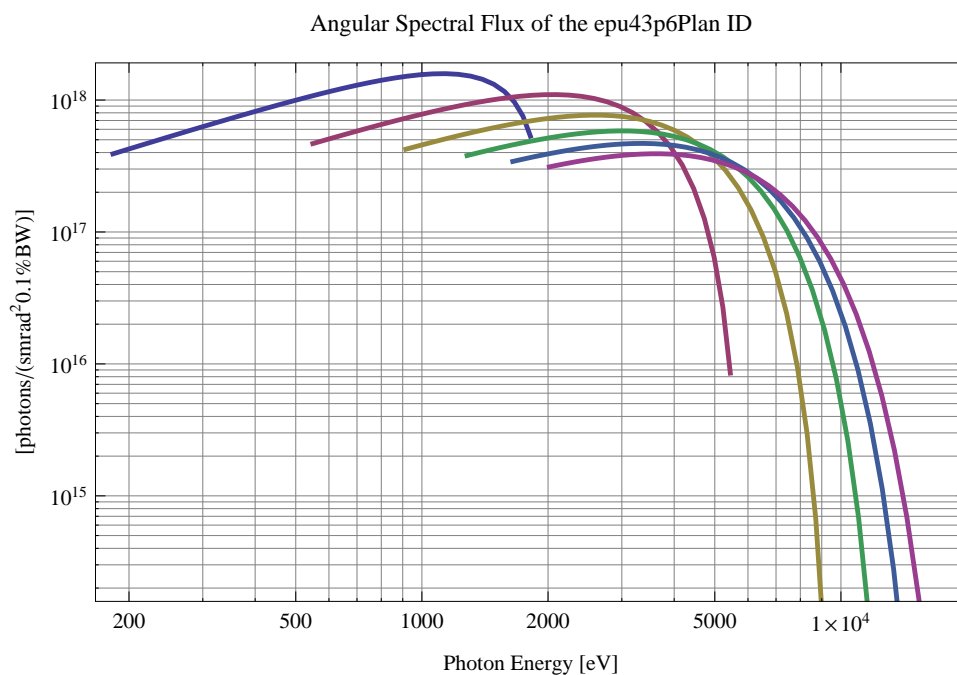


Figure 5.314: The angular spectral flux from the epu43p6Plan ID

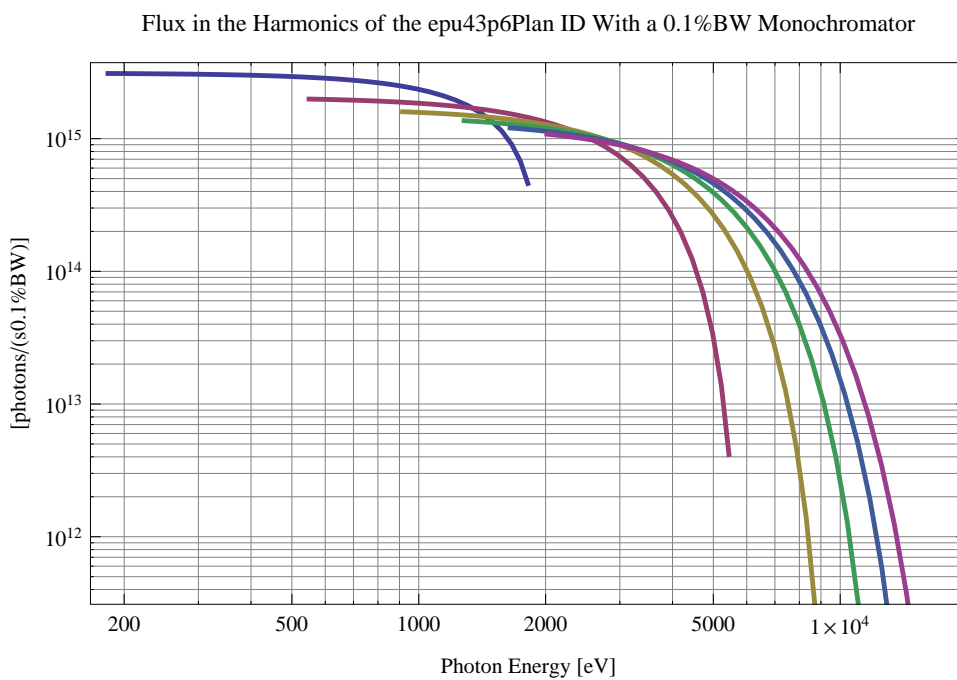


Figure 5.315: The flux of photons in the harmonics from the epu43p6Plan ID using a 0.1%BW monochromator

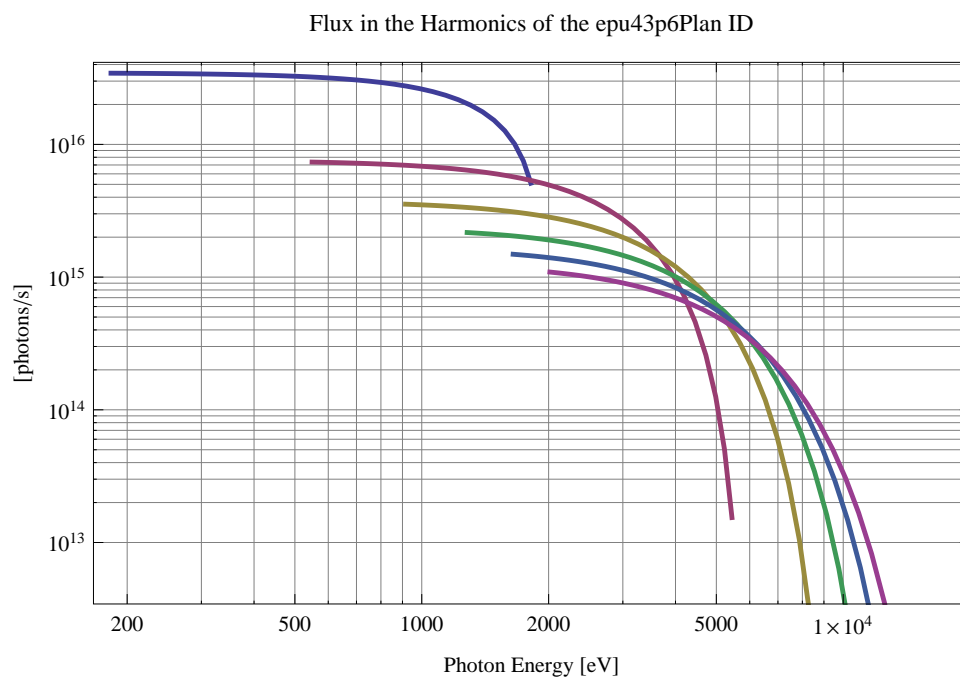


Figure 5.316: The flux of photons in the harmonics from the epu43p6Plan ID

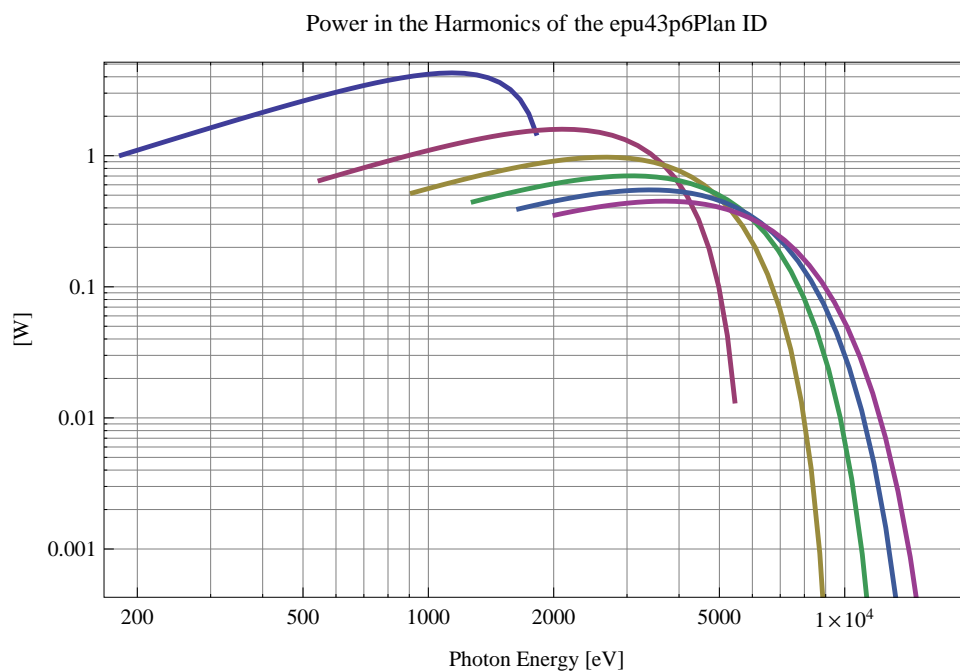


Figure 5.317: The power in the harmonics from the epu43p6Plan ID

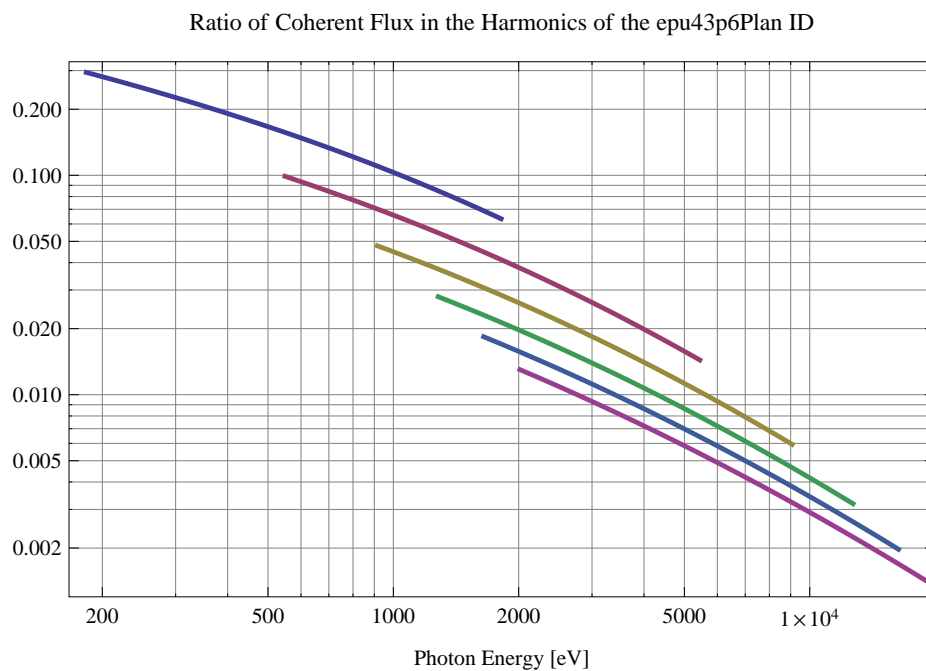


Figure 5.318: The ratio of coherent flux in the harmonics from the epu43p6Plan ID

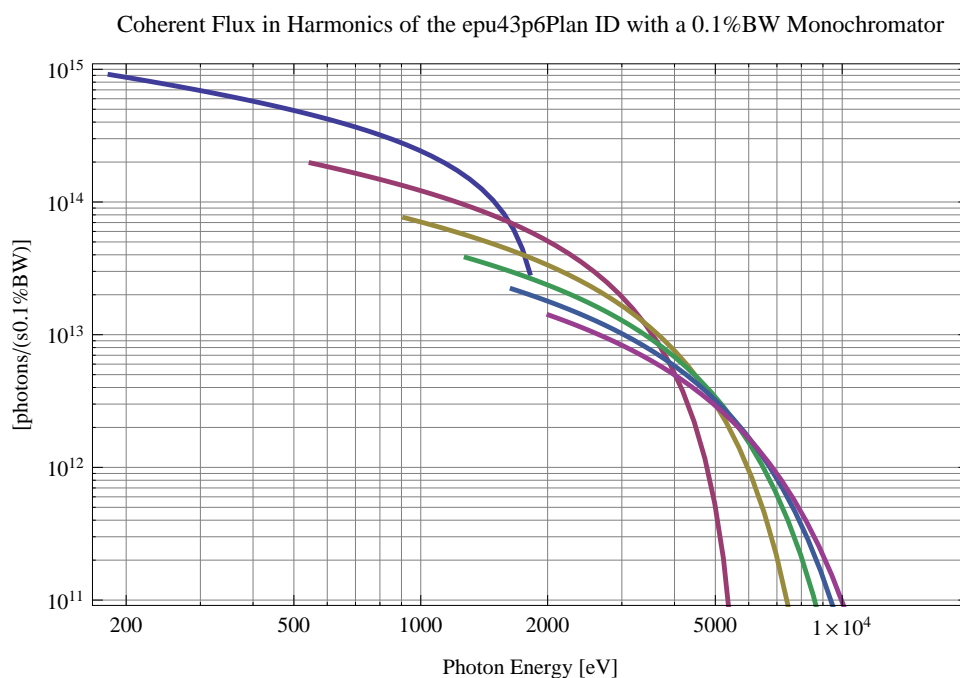


Figure 5.319: The coherent flux in the harmonics of the epu43p6Plan ID using a 0.1%BW Monochromator

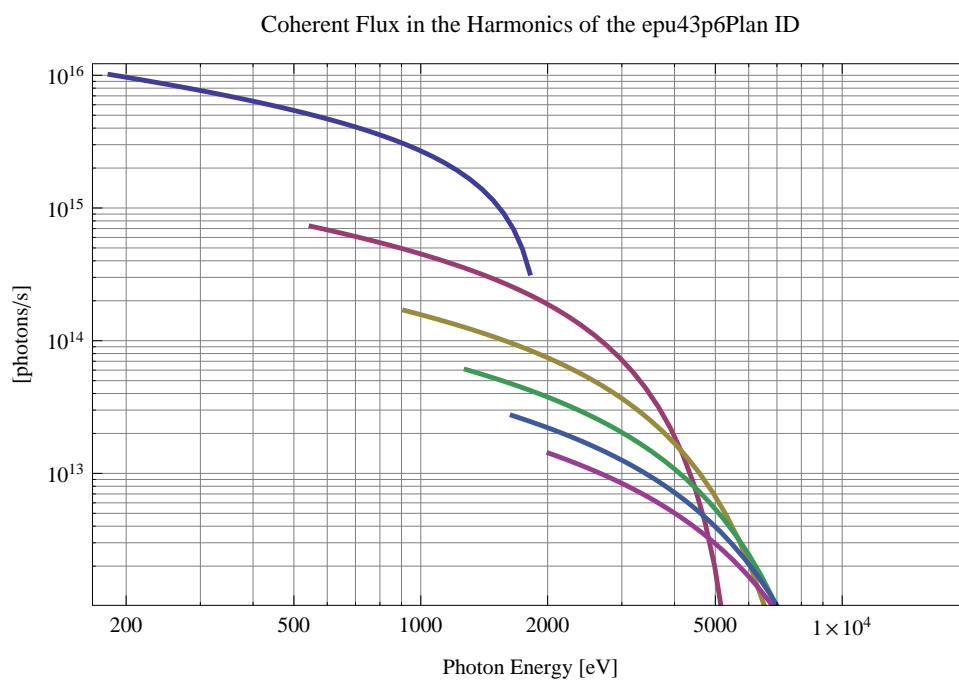


Figure 5.320: The coherent flux in the harmonics of the epu43p6Plan ID

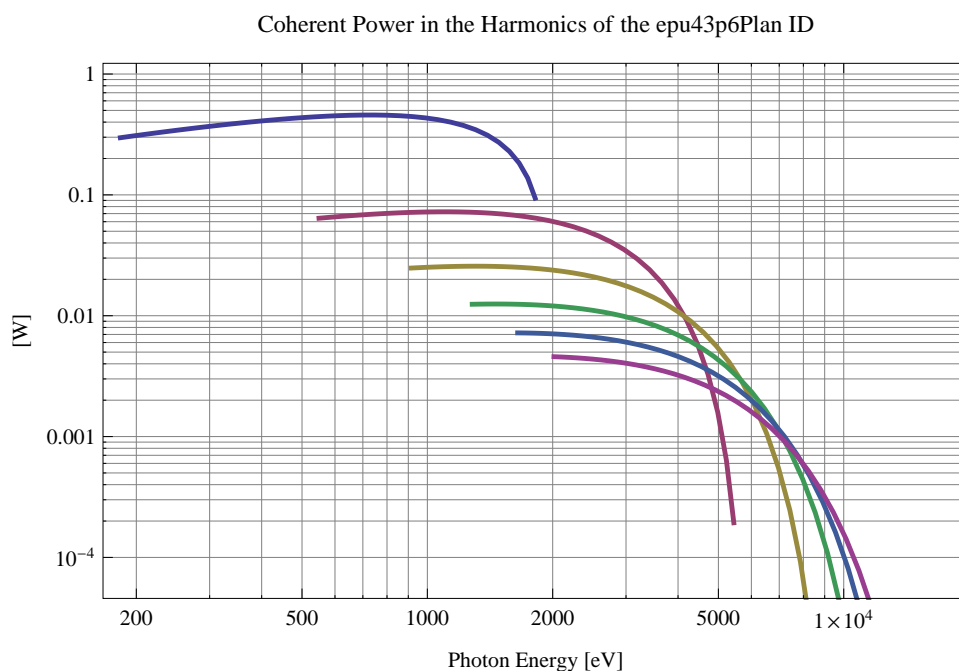


Figure 5.321: The power of coherent synchrotron radiation in the harmonics of the epu43p6Plan ID

Table 5.51: The brilliance at peak energy and the angular spectral flux density from the epu43p6Plan ID for different harmonics at minimum K-value (0.4)

Harmonic	Photon Energy [eV]	Brilliance [Ph./s/mrad <sup>2</sup> /mrad <sup>2</sup> /0.1%BW]	Angular Spectral Flux [Ph./s/mrad <sup>2</sup> /0.1%BW]
1	1815.06	$2.49 \times 10^{20}$	$5.33 \times 10^{17}$
3	5445.18	$4.62 \times 10^{18}$	$8.52 \times 10^{15}$
5	9075.31	$5.21 \times 10^{16}$	$9.34 \times 10^{13}$
7	12705.4	$5.46 \times 10^{14}$	$9.71 \times 10^{11}$
9	16335.5	$5.62 \times 10^{12}$	$9.94 \times 10^9$
11	19965.7	$5.74 \times 10^{10}$	$1.01 \times 10^8$

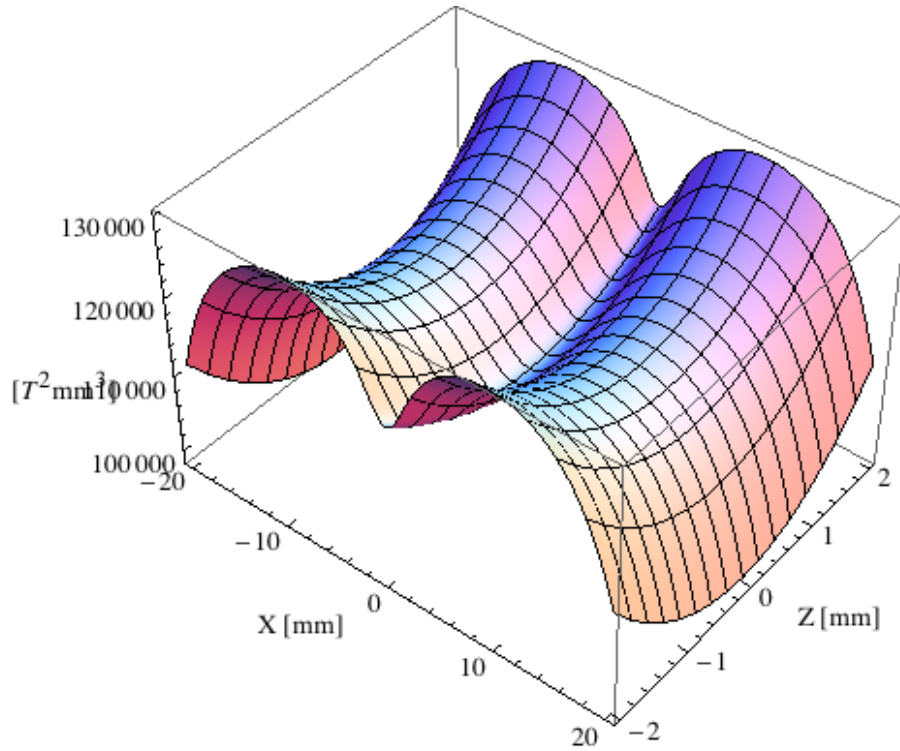


Figure 5.322: Focusing potential from the epu43p6Plan ID over the beam stay clear aperture.

### Influence from the epu43p6Plan ID on the optics of the stored beam

Figure 5.322 shows the focusing potential from the epu43p6Plan over the beam stay clear aperture of the ring aperture.

Figure 5.323 shows the kick map in the beam energy independent unit  $T^2 m^2$  of the kicks induced by the epu43p6Plan ID over the beam stay clear aperture.

Figure 5.324 shows the induced angular kick on the stored beam from the epu43p6Plan ID as a function of the vertical distance to the axis of the ID.

Figure 5.325 shows the induced angular kick on the stored beam from the epu43p6Plan ID as a function of the horizontal distance to the axis of the ID.

Figure 5.326 shows tune shift induced by the epu43p6Plan ID over the beam stay clear aperture. Note that the tune shift depends on the beam size at the ID.

Figure 5.327 shows the induced tune shift from the epu43p6Plan ID as a function of the vertical distance to the axis of the ID.

Figure 5.328 shows the induced tune shift from the epu43p6Plan ID as a function of the horizontal distance to the axis of the ID.

### Magnet model of the elliptically polarising undulator epu43p6Heli

The Radia [2] magnet model of the epu43p6Heli ID is shown in Figure 5.329. The length of the magnet model is 366.067 mm. The magnetic material in the model is NdFeb with a remanence of 1.28 T, a material similar to VACODYM 776 TP from Vacuumschmelze. Blocks with vertical magnetisation are blue and blocks with horizontal magnetisation are yellow. The block size is

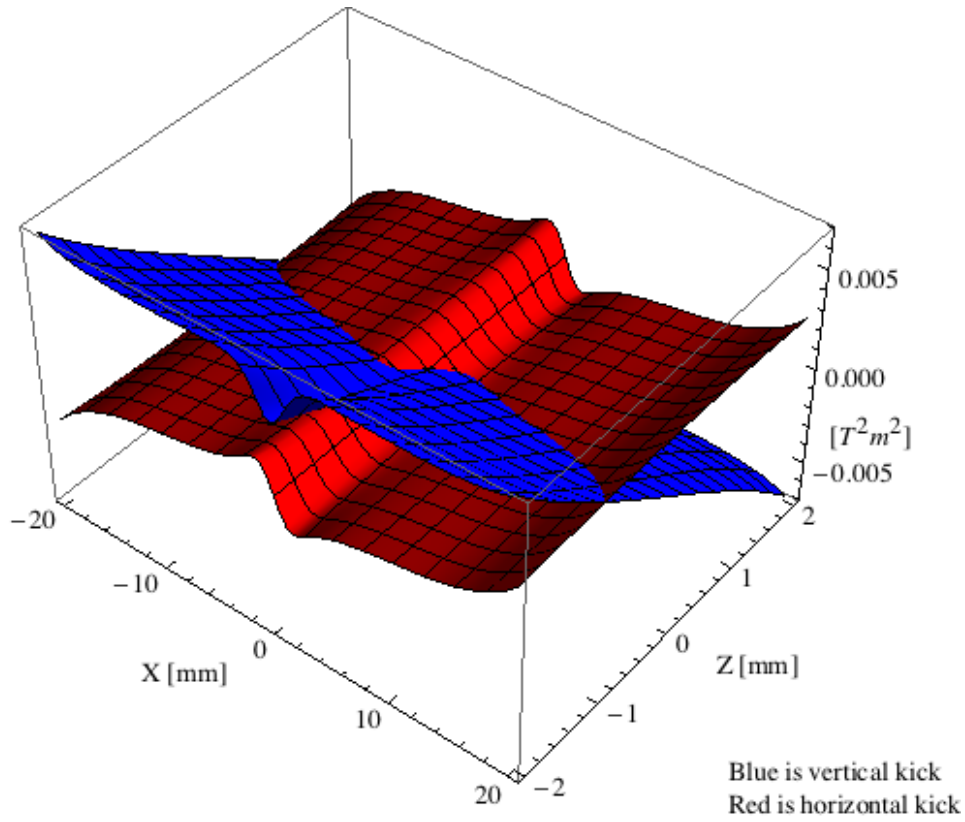


Figure 5.323: Kick map in the beam energy independent unit  $T^2 m^2$  of the kicks induced by the epu43p6Plan ID over the beam stay clear aperture.

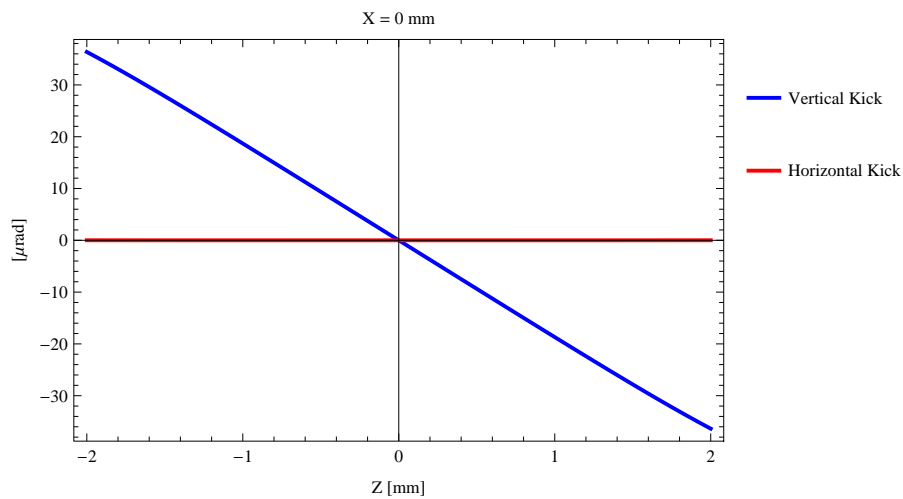


Figure 5.324: Induced angular kick on the stored beam from the epu43p6Plan ID as a function of the vertical distance to the ID axis.



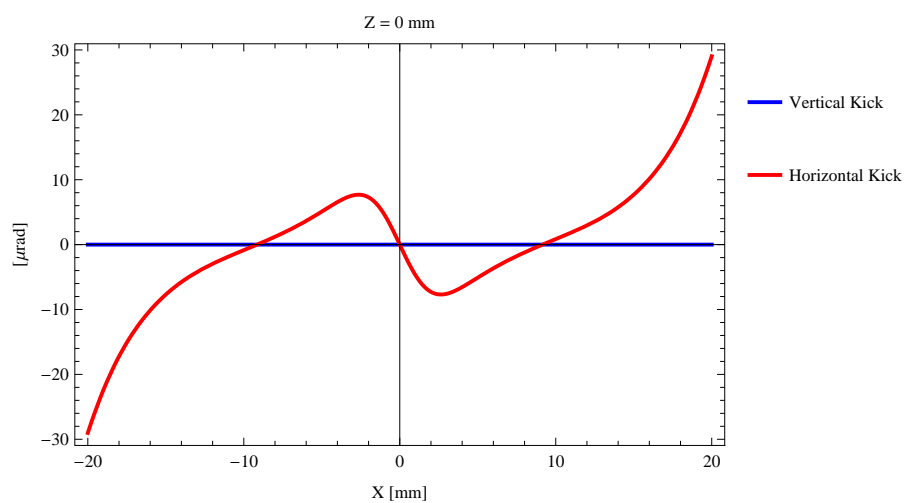


Figure 5.325: Induced angular kick on the stored beam from the epu43p6Plan ID as a function of the horizontal distance to the ID axis.

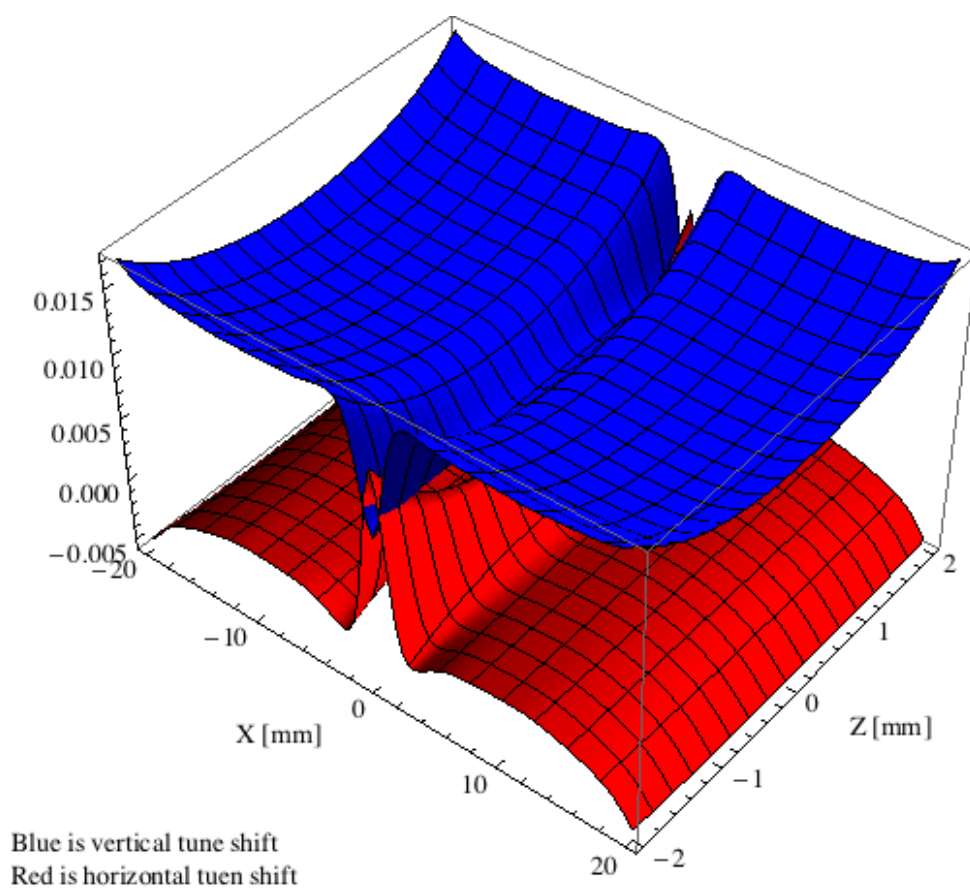


Figure 5.326: Tune shift induced by the epu43p6Plan ID over the beam stay clear aperture.

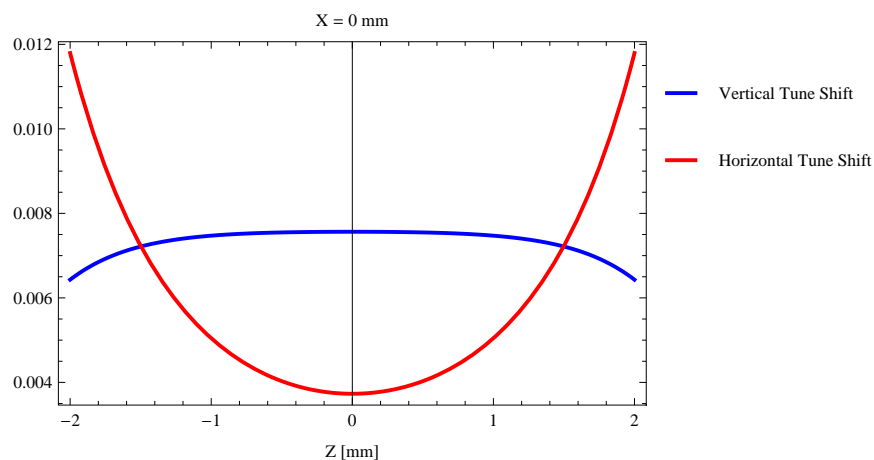


Figure 5.327: Induced tune shift from the epu43p6Plan ID as a function of the vertical distance to the axis of the ID.

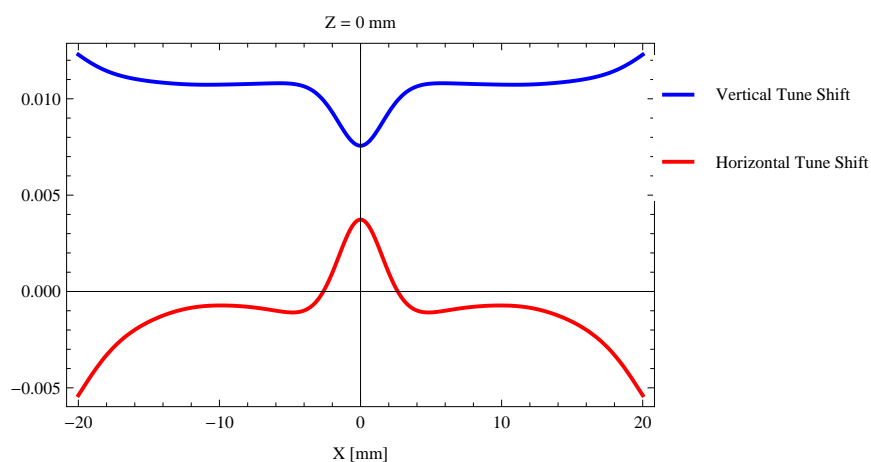


Figure 5.328: Induced tune shift from the epu43p6Plan ID on the stored beam from the ID as a function of the horizontal distance to the axis of the ID.

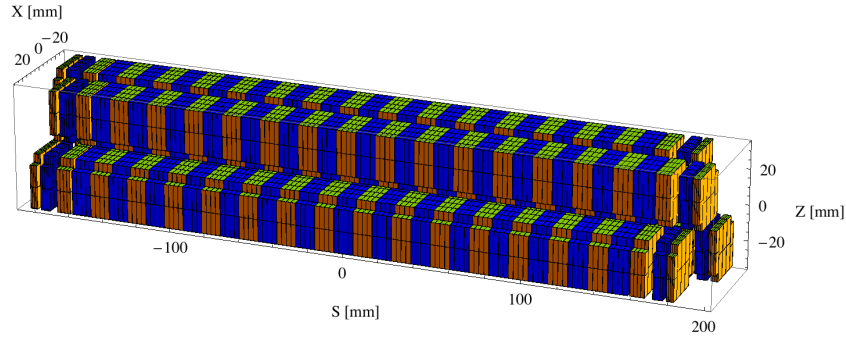


Figure 5.329: Magnetic model of the epu43p6Heli ID. The ID has been modelled with Radia [2]

$30 \times 30 \times 10.9 \text{ mm}^3$  and there is a 5. mm cut-out in two of the corners of the blocks. The total length of the epu43p6Heli ID is 3941.27 mm.

### Analysis of the magnetic field of the epu43p6Heli ID

The effective magnetic fields on axis and the fundamental photon energy of the epu43p6Heli ID are shown in Table 5.52. The higher harmonic contents in the magnetic field of an elliptically polarising undulator made of permanent magnets is negligible and the efficient field has about the same strength as the peak field.

Table 5.52: Effective Fields on axis and Fundamental Photon Energy of the epu43p6Heli ID

Undulator Period	43.6	mm
Undulator Gap	9	mm
Undulator Mode	Helical	
Undulator Phase	12.627	mm
Vertical Peak Field	0.660	T
Efficient Vertical Field	0.660	T
K <sub>x</sub> (from vert. field)	2.688	
Horizontal Peak Field:	0.665	T
Efficient Horizontal Field	0.660	T
K <sub>z</sub> (from hor. field)	2.688	
Photon Energy, Harm.1	0.238	keV
Emitted Power	9.776	kW
Total Length	3941.3	mm

### Synchrotron radiation from the epu43p6Heli ID

The power map of the emitted synchrotron radiation by the epu43p6Heli ID, assuming a 0.5 A filament beam with an energy of 3 GeV and undulator properties of the synchrotron radiation, is shown in Figure 5.334. The on-axis power density is 0.570 kW/mrad<sup>2</sup>

A map of the degree of linear polarisation of the fundamental harmonic of the synchrotron radiation emitted by the epu43p6Heli ID over the angle of observation is shown in Figure 5.335.

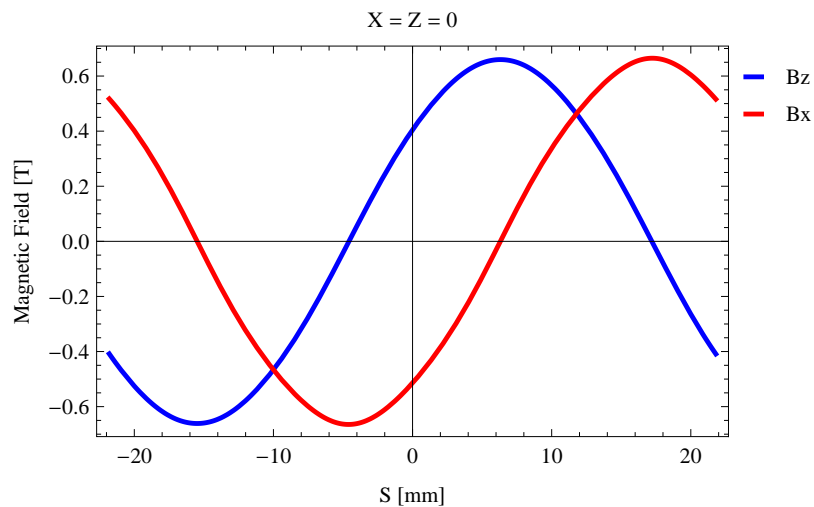


Figure 5.330: Vertical magnetic field in a central pole of the epu43p6Heli ID along the ID axis,  $X = Z = 0$

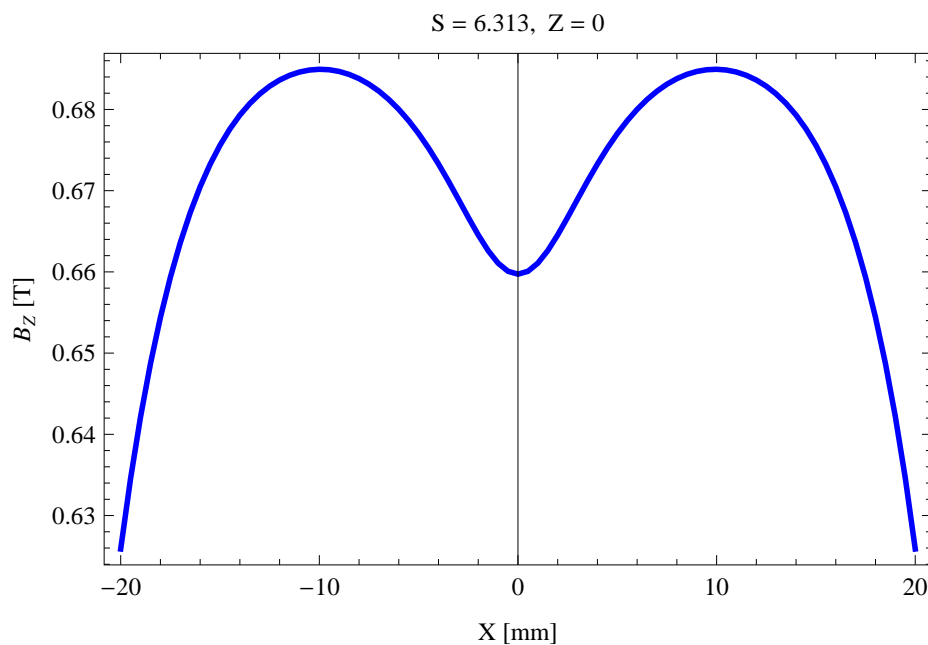


Figure 5.331: Vertical magnetic field in a central pole of the epu43p6Heli ID along the horizontally transverse direction to the ID axis,  $S = 6.313$ ,  $Z = 0$

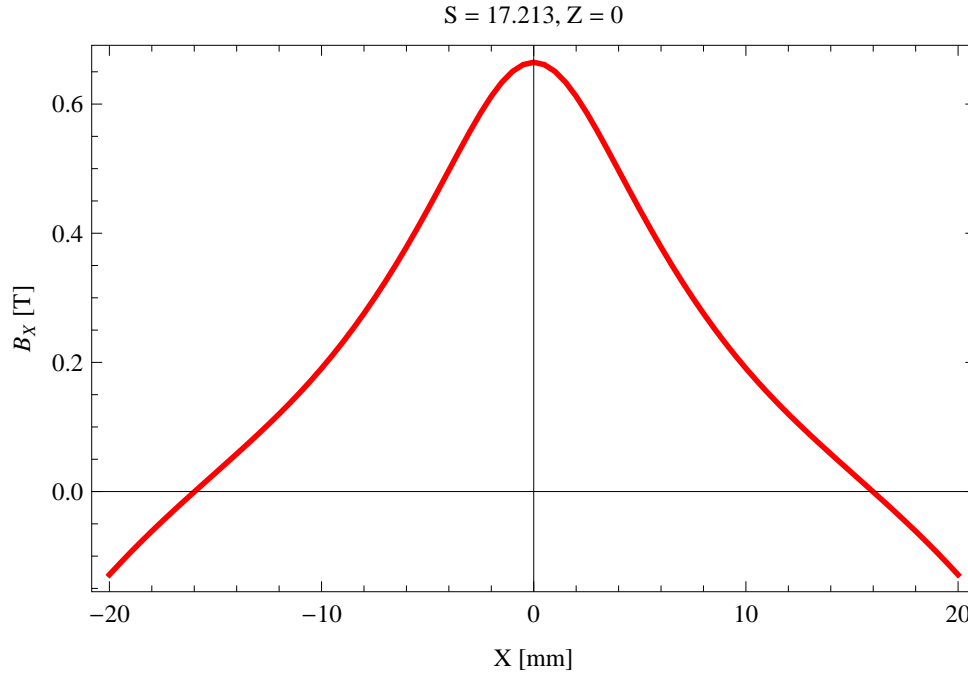


Figure 5.332: Horizontal magnetic field in a central pole of the epu43p6Heli ID along the horizontally transverse direction to the ID axis,  $S = 17.213$ ,  $Z = 0$

A map of the degree of 45 degree polarisation of the fundamental harmonic of the synchrotron radiation emitted by the epu43p6Heli ID over the angle of observation is shown in Figure 5.336.

A map of the degree of circular polarisation of the fundamental harmonic of the synchrotron radiation emitted by the epu43p6Heli ID over the angle of observation is shown in Figure 5.337.

The on axis brilliance at peak energy, the angular spectral flux, the flux in the harmonics, the power in the harmonics, the ratio of coherence, the coherent flux in the harmonics, and the power of coherent radiation in the harmonics from the epu43p6Heli ID have been calculated and the resulting plots are found in this section of the document. The beam parameters used for the calculation are 0.5 A of stored current,  $\beta_H = 9$  m,  $\varepsilon_H = 0.263$  nmrad,  $\beta_V = 4.8$  m,  $\varepsilon_V = 8$  pmrad, and an energy spread of 0.001.

The brilliance at peak energy and the angular spectral flux density from the epu43p6Heli ID for different harmonics at maximum K-value (3.801) are given in Table 5.53 and for minimum K-value (0.400) these values are given in Table 5.54.

Table 5.53: The brilliance at peak energy and the angular spectral flux density from the epu43p6Heli ID for different harmonics at maximum K-value (3.801)

Harmonic	Photon Energy [eV]	Brilliance [Ph./s/mrad <sup>2</sup> /mrad <sup>2</sup> /0.1%BW]	Angular Spectral Flux [Ph./s/mrad <sup>2</sup> /0.1%BW]
1	238.37	$1.17 \times 10^{20}$	$5.05 \times 10^{17}$

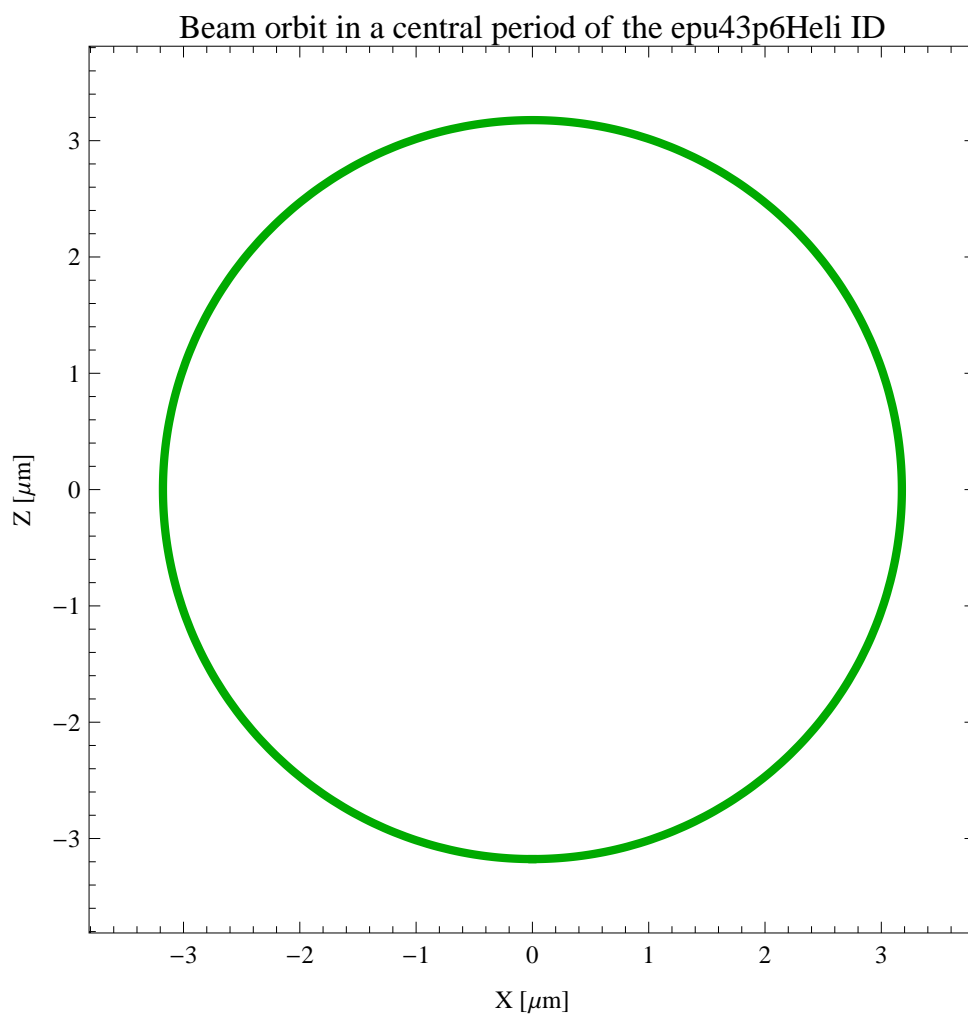


Figure 5.333: The beam orbit of the electron beam through a central period of the epu43p6Heli ID

Table 5.54: The brilliance at peak energy and the angular spectral flux density from the epu43p6Heli ID for different harmonics at minimum K-value (0.4)

Harmonic	Photon Energy [eV]	Brilliance [Ph./s/mrad <sup>2</sup> /mrad <sup>2</sup> /0.1%BW]	Angular Spectral Flux [Ph./s/mrad <sup>2</sup> /0.1%BW]
1	1815.06	$2.49 \times 10^{20}$	$5.33 \times 10^{17}$

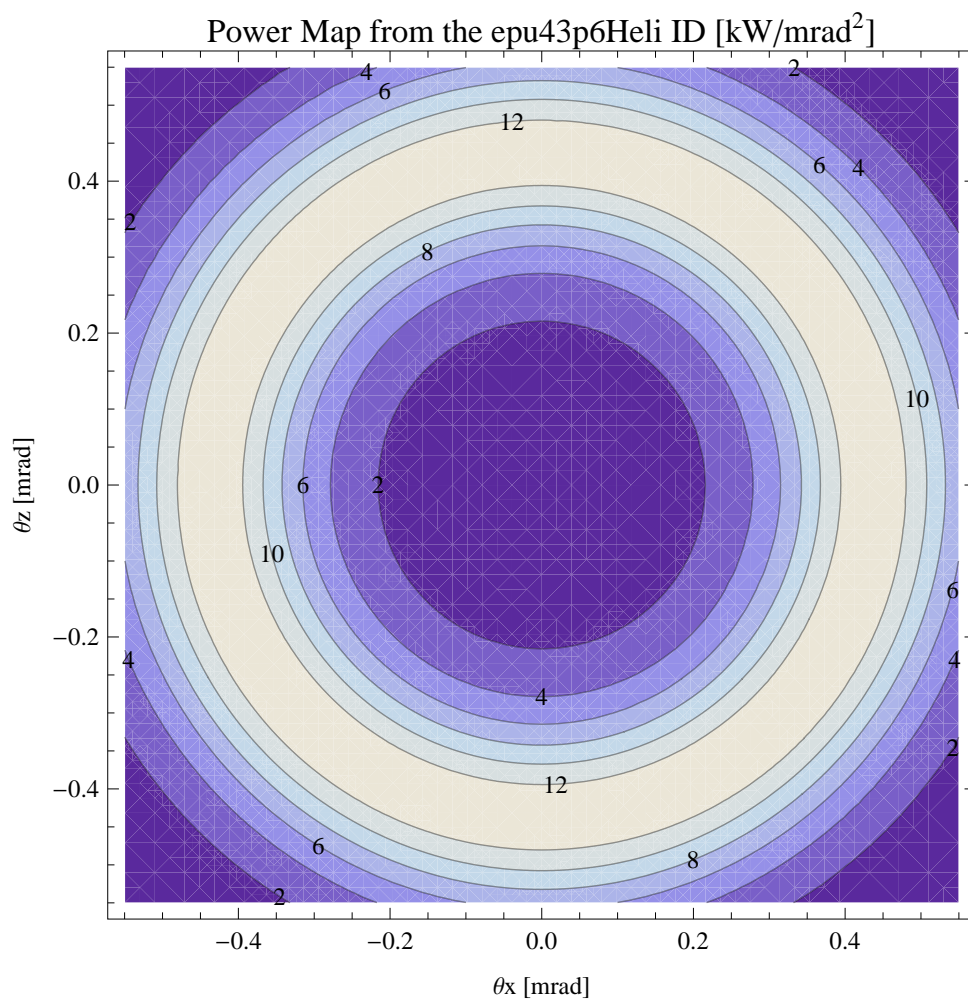


Figure 5.334: Map of the power distribution of the emitted synchrotron radiation by the epu43p6Heli ID

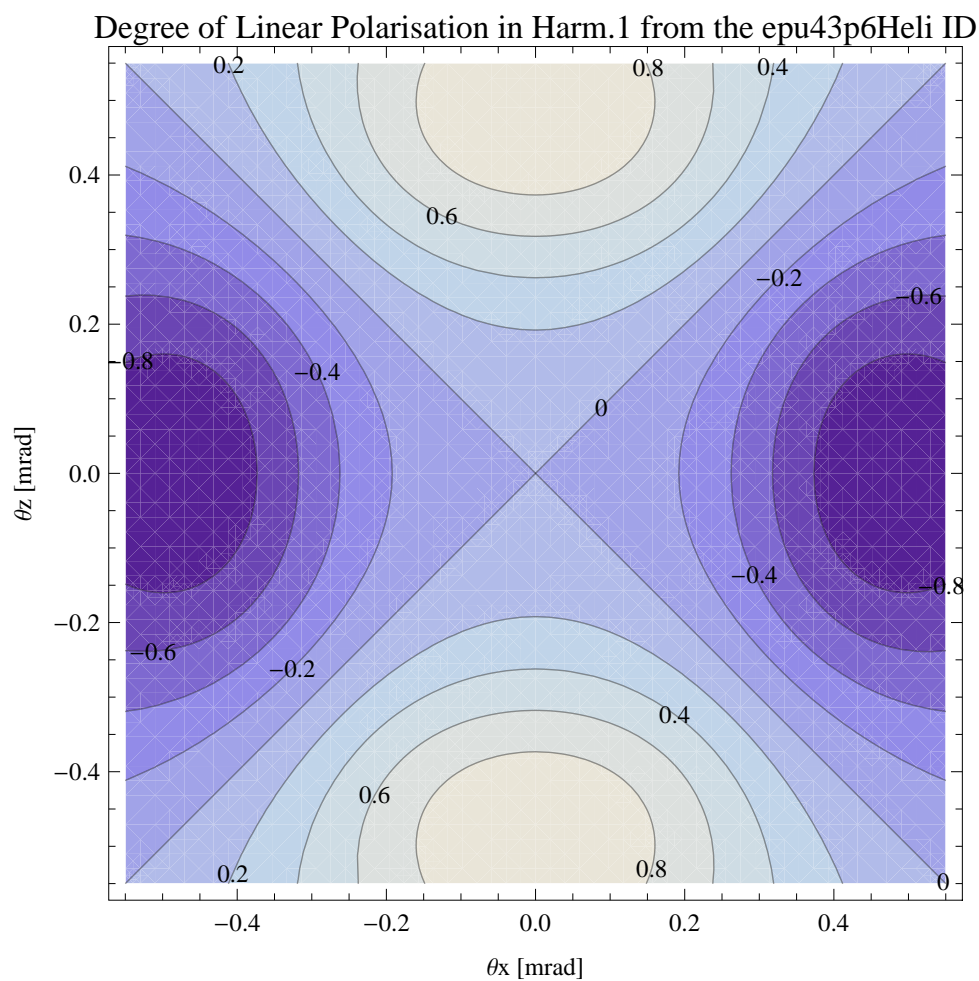


Figure 5.335: Map of linear polarisation in the fundamental harmonic of the synchrotron radiation emitted by the epu43p6Heli ID



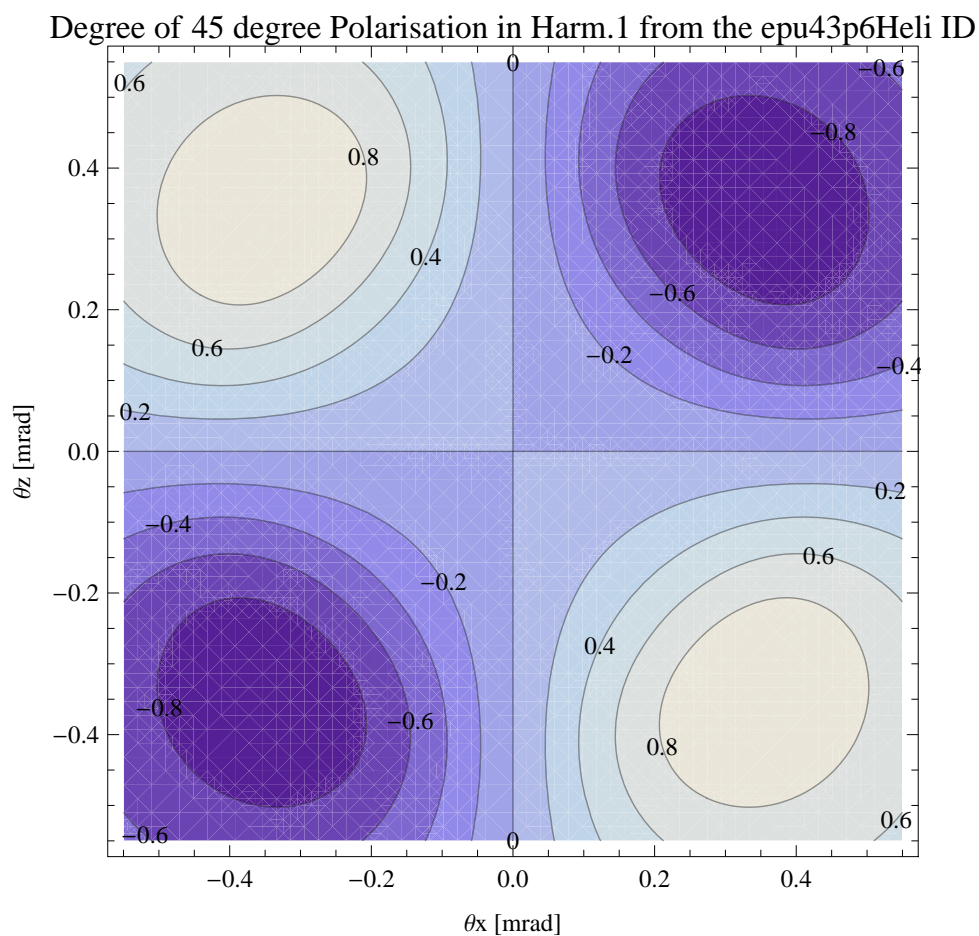


Figure 5.336: Map of 45 degree polarisation in the fundamental harmonic of the synchrotron radiation emitted by the epu43p6Heli ID

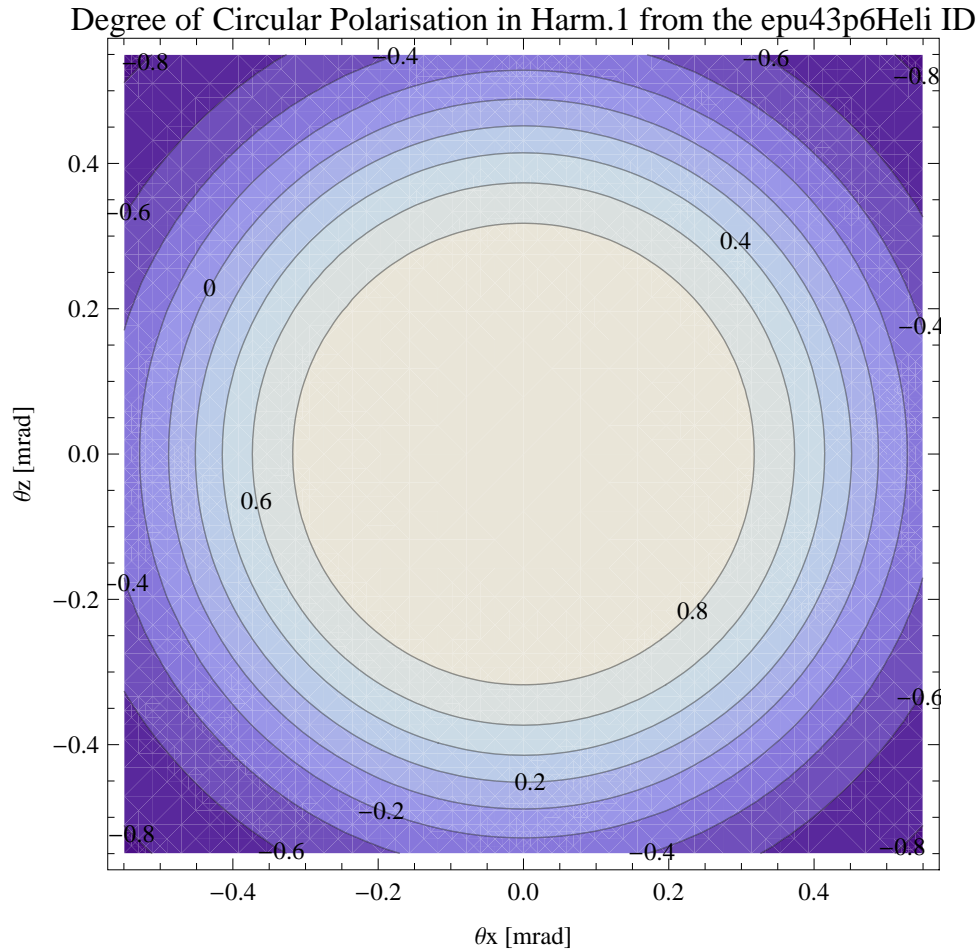


Figure 5.337: Map of circular polarisation in the fundamental harmonic of the synchrotron radiation emitted by the epu43p6Heli ID

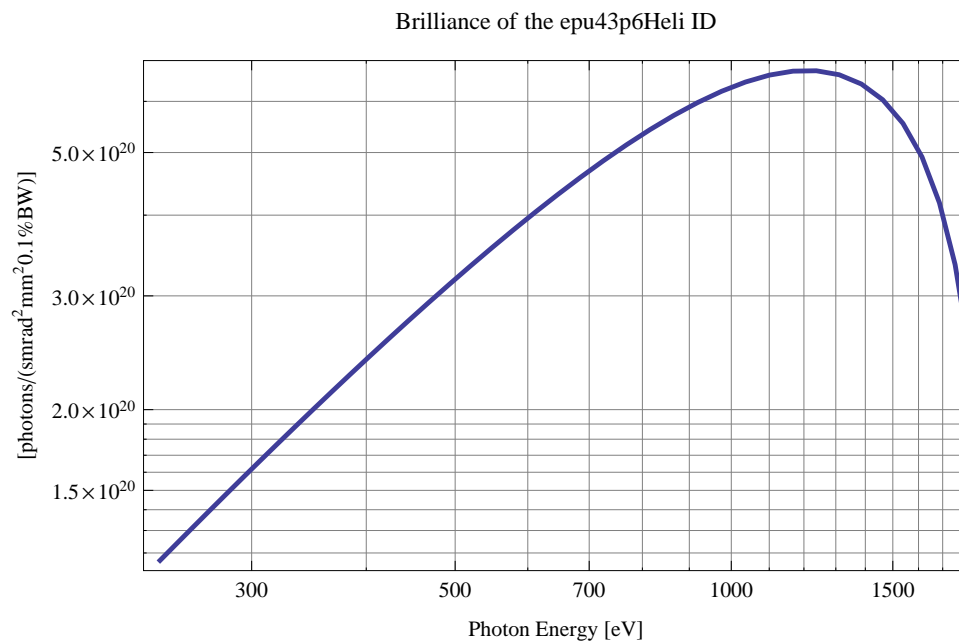


Figure 5.338: The brilliance at peak energy from the epu43p6Heli ID

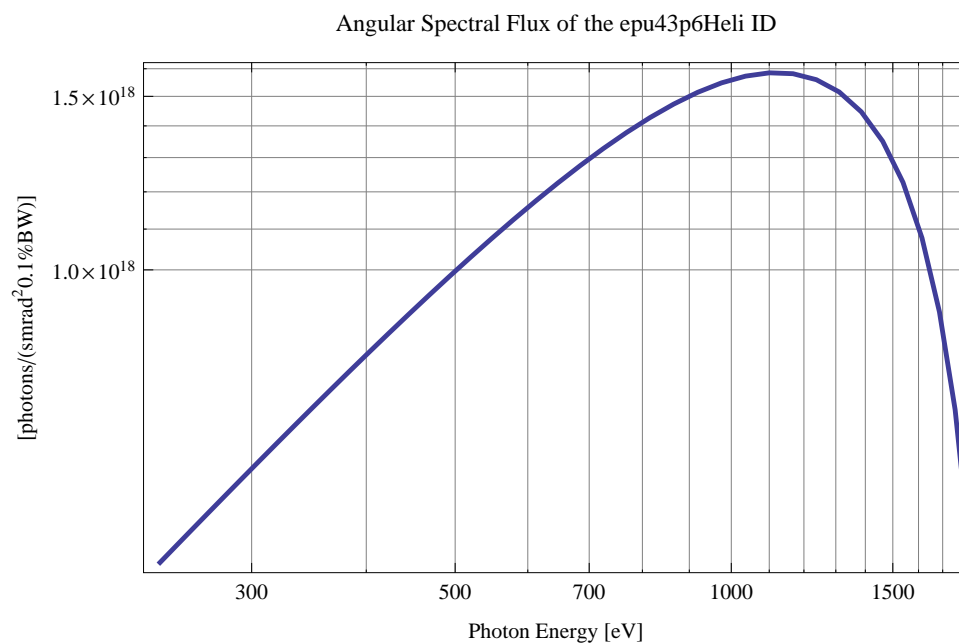


Figure 5.339: The angular spectral flux from the epu43p6Heli ID

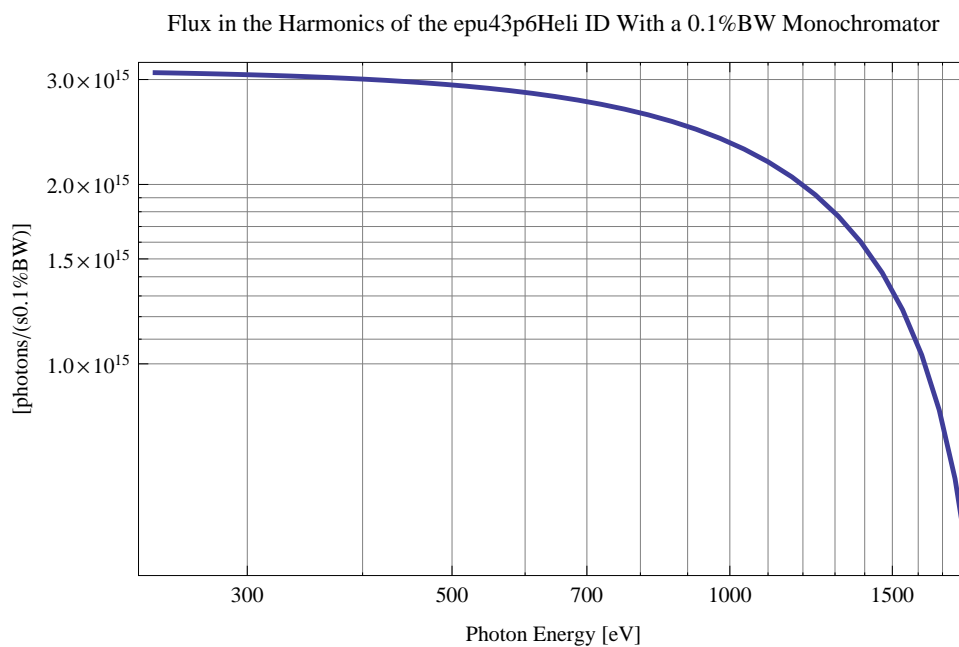


Figure 5.340: The flux of photons in the harmonics from the epu43p6Heli ID using a 0.1%BW monochromator

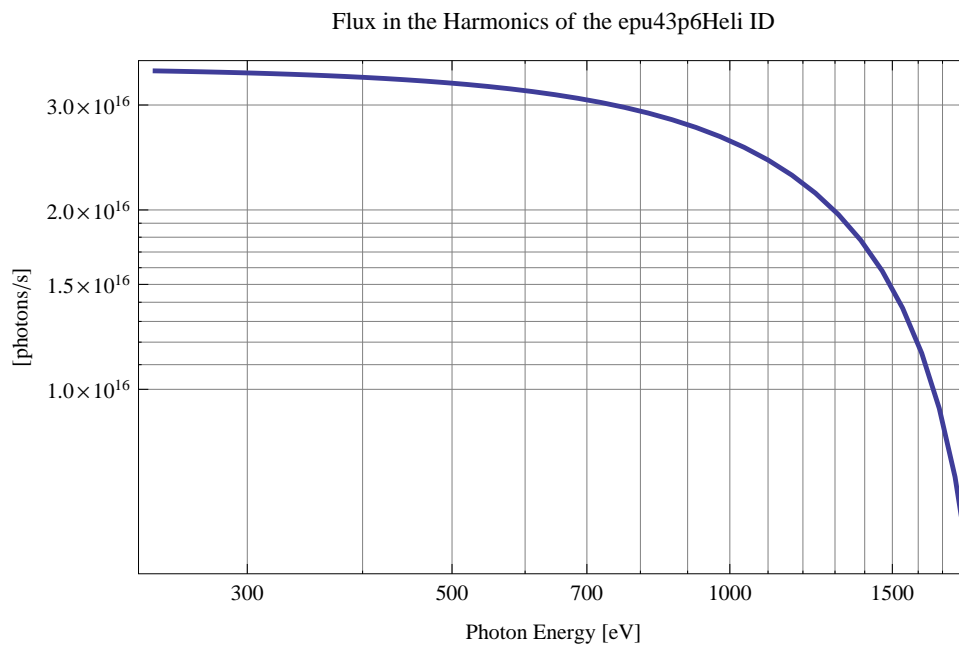


Figure 5.341: The flux of photons in the harmonics from the epu43p6Heli ID

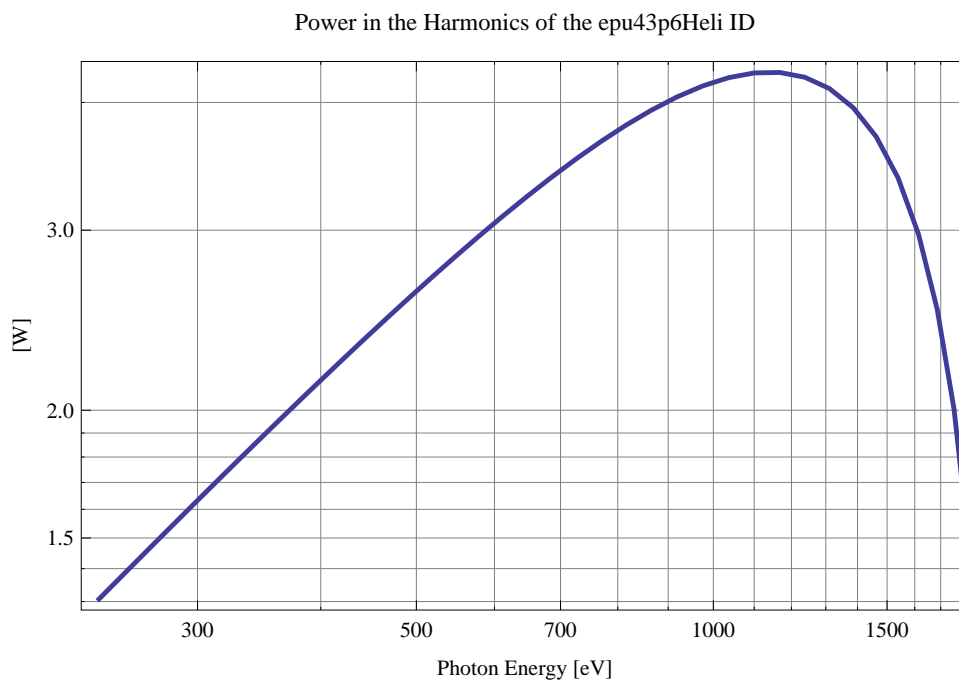


Figure 5.342: The power in the harmonics from the epu43p6Heli ID

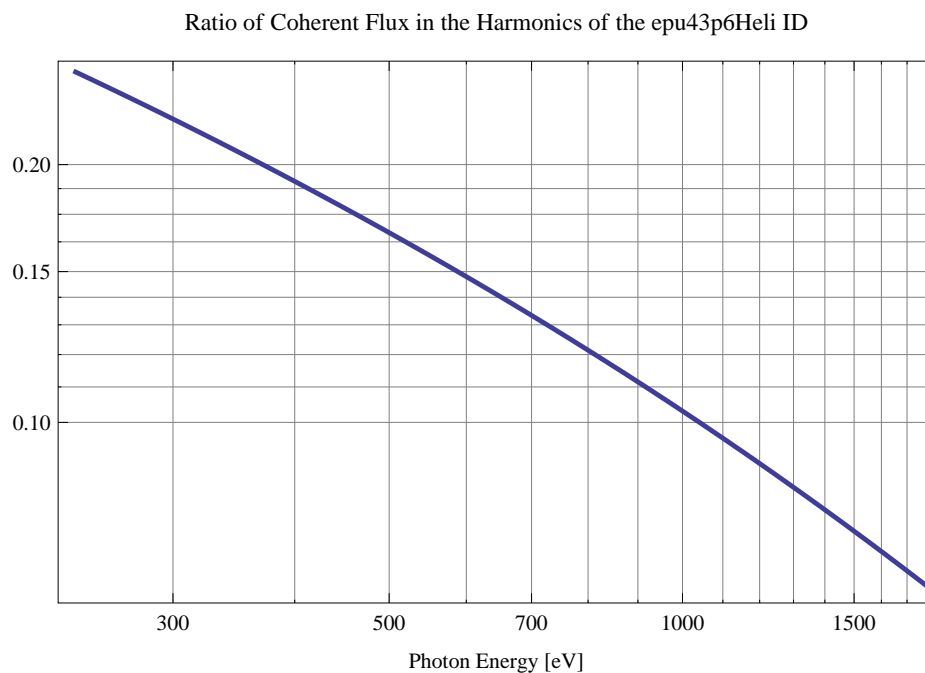


Figure 5.343: The ratio of coherent flux in the harmonics from the epu43p6Heli ID

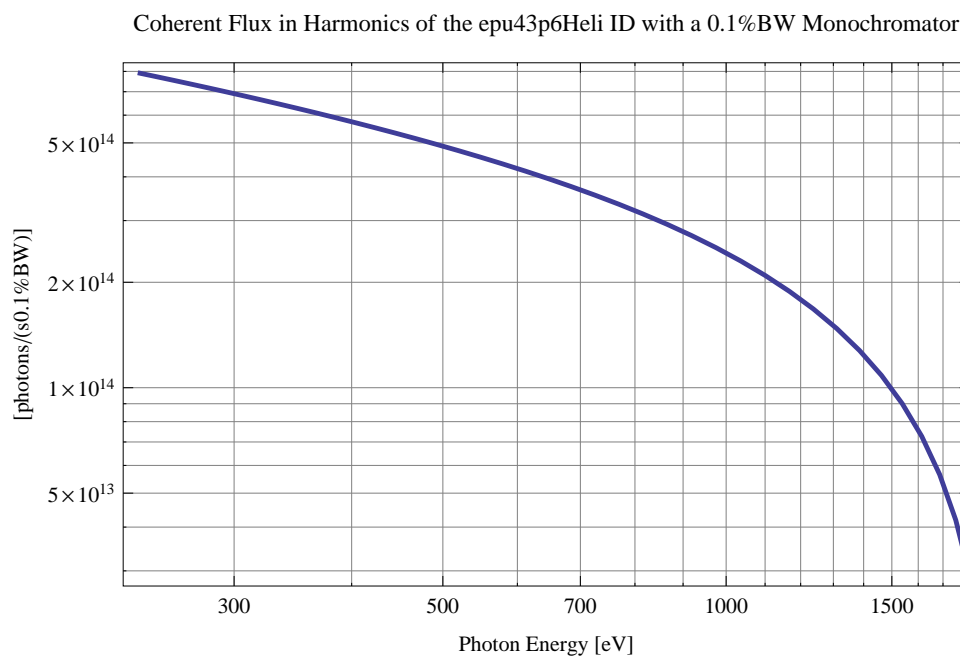


Figure 5.344: The coherent flux in the harmonics of the epu43p6Heli ID using a 0.1%BW Monochromator

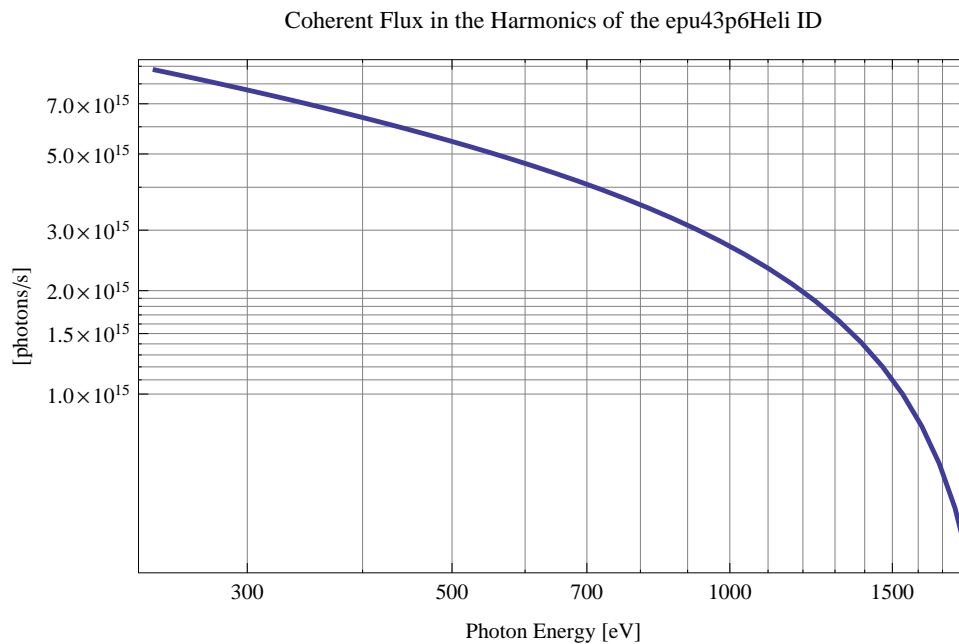


Figure 5.345: The coherent flux in the harmonics of the epu43p6Heli ID

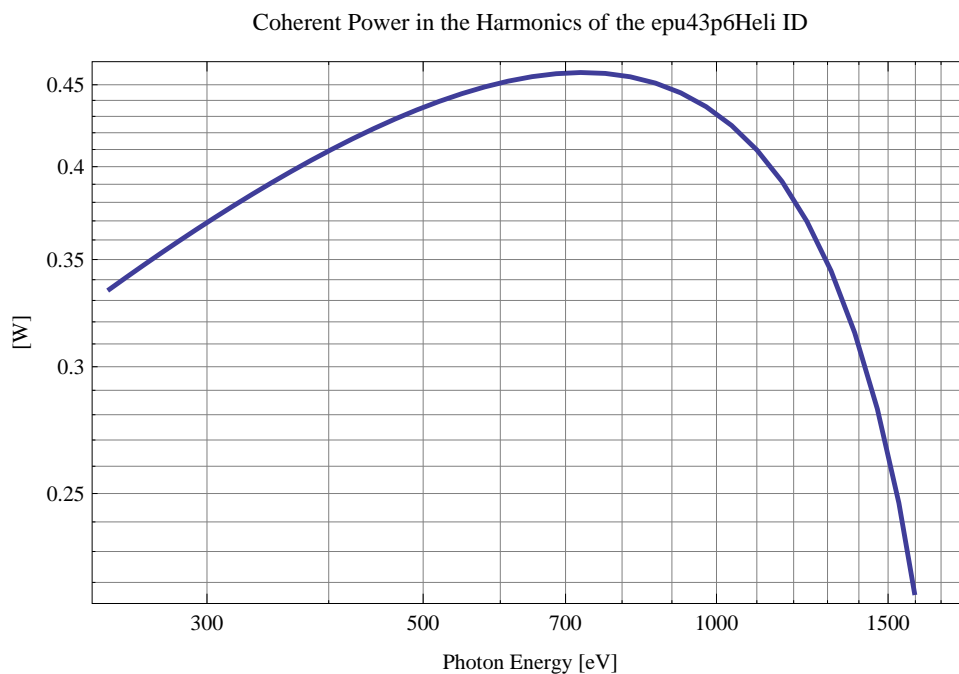


Figure 5.346: The power of coherent synchrotron radiation in the harmonics of the epu43p6Heli ID

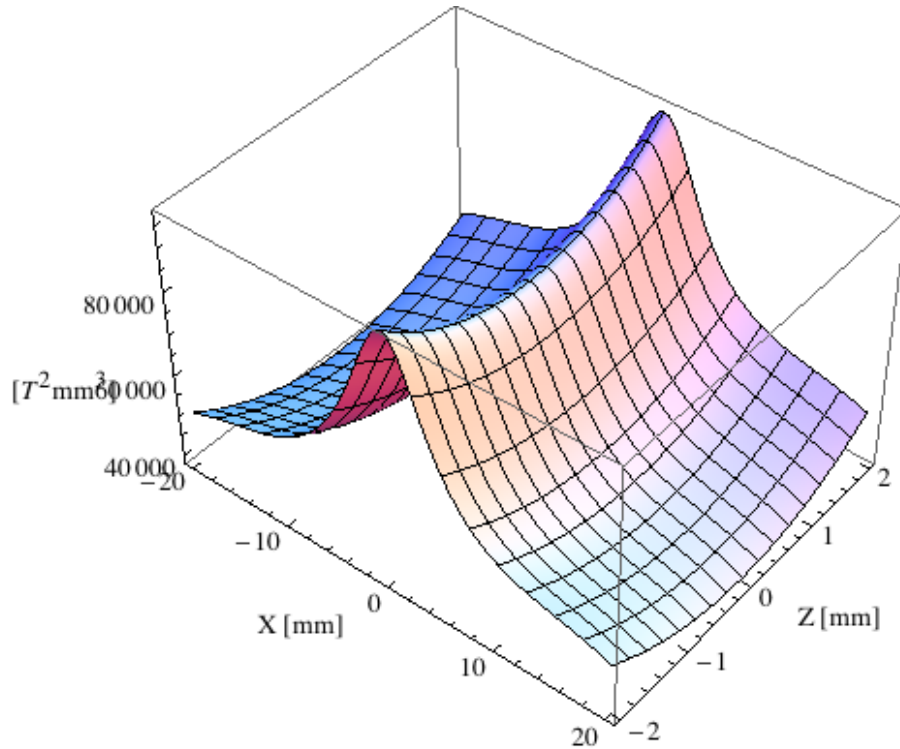


Figure 5.347: Focusing potential from the epu43p6Heli ID over the beam stay clear aperture.

### Influence from the epu43p6Heli ID on the optics of the stored beam

Figure 5.347 shows the focusing potential from the epu43p6Heli over the beam stay clear aperture of the ring aperture.

Figure 5.348 shows the kick map in the beam energy independent unit  $T^2 m^2$  of the kicks induced by the epu43p6Heli ID over the beam stay clear aperture.

Figure 5.349 shows the induced angular kick on the stored beam from the epu43p6Heli ID as a function of the vertical distance to the axis of the ID.

Figure 5.350 shows the induced angular kick on the stored beam from the epu43p6Heli ID as a function of the horizontal distance to the axis of the ID.

Figure 5.351 shows tune shift induced by the epu43p6Heli ID over the beam stay clear aperture. Note that the tune shift depends on the beam size at the ID.

Figure 5.352 shows the induced tune shift from the epu43p6Heli ID as a function of the vertical distance to the axis of the ID.

Figure 5.353 shows the induced tune shift from the epu43p6Heli ID as a function of the horizontal distance to the axis of the ID.

### Magnet model of the elliptically polarising undulator epu43p6Incl

The Radia [2] magnet model of the epu43p6Incl ID is shown in Figure 5.354. The length of the magnet model is 366.067 mm. The magnetic material in the model is NdFeb with a remanence of 1.28 T, a material similar to VACODYM 776 TP from Vacuumschmelze. Blocks with vertical magnetisation are blue and blocks with horizontal magnetisation are yellow. The block size is

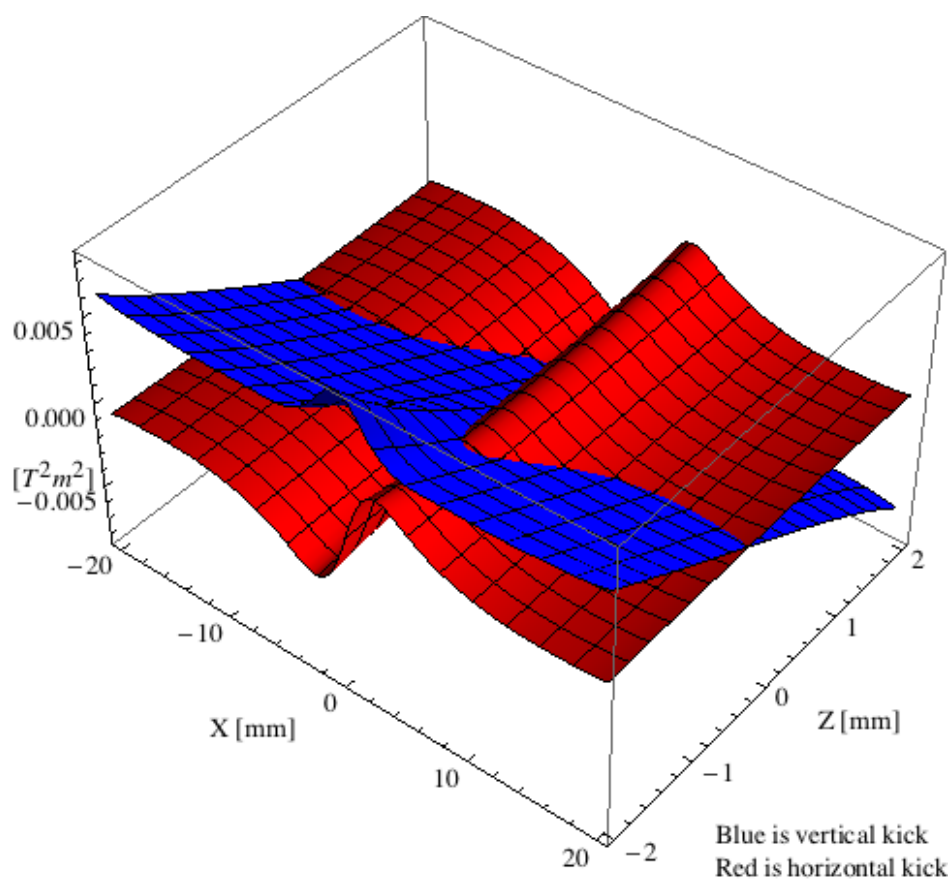


Figure 5.348: Kick map in the beam energy independent unit  $T^2m^2$  of the kicks induced by the epu43p6Heli ID over the beam stay clear aperture.

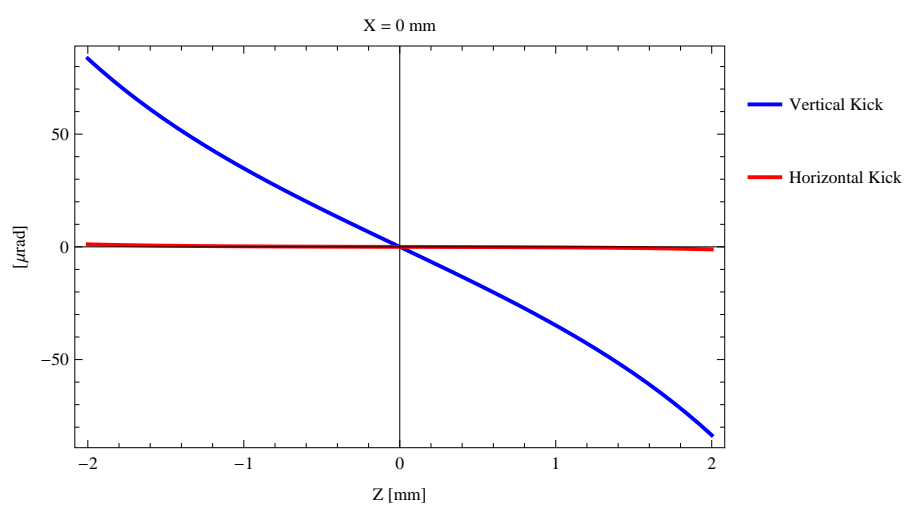


Figure 5.349: Induced angular kick on the stored beam from the epu43p6Heli ID as a function of the vertical distance to the ID axis.



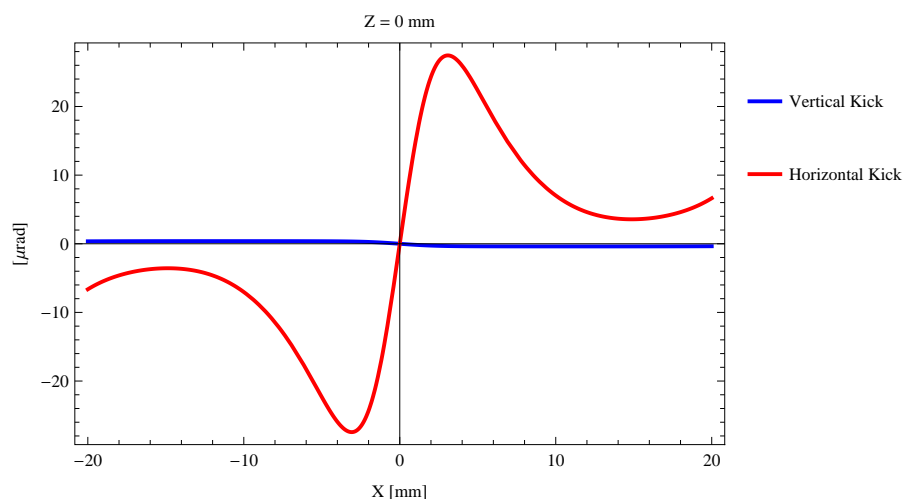


Figure 5.350: Induced angular kick on the stored beam from the epu43p6Heli ID as a function of the horizontal distance to the ID axis.

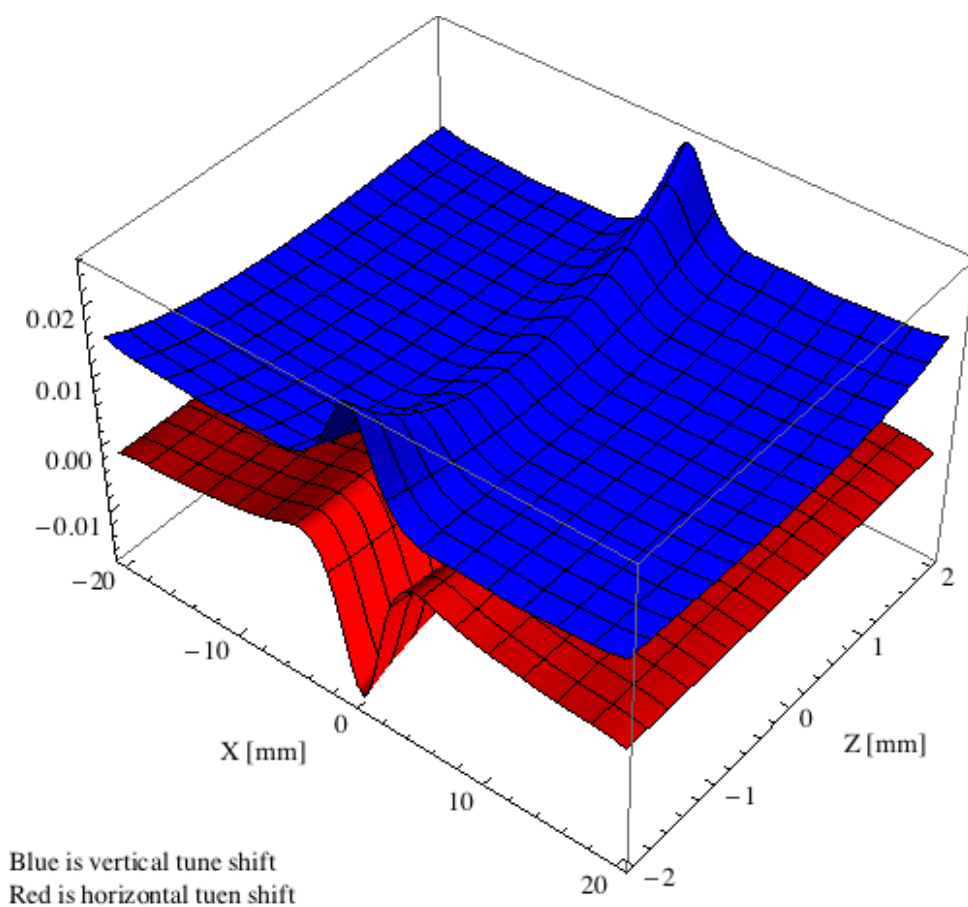


Figure 5.351: Tune shift induced by the epu43p6Heli ID over the beam stay clear aperture.

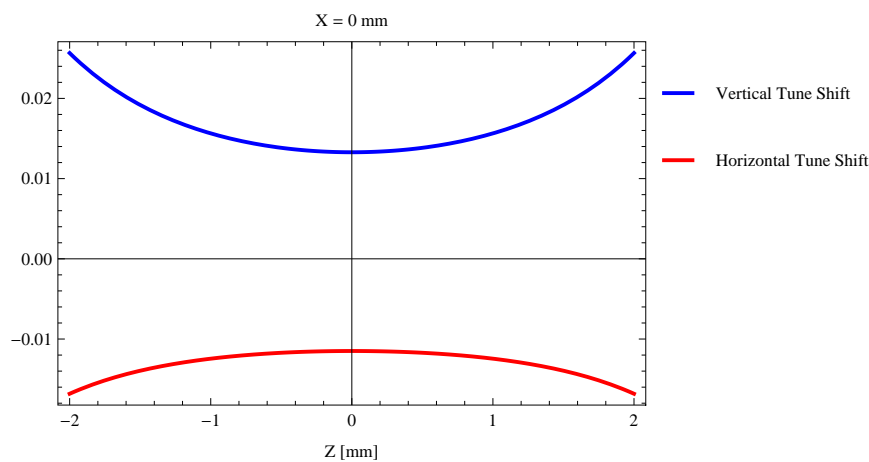


Figure 5.352: Induced tune shift from the epu43p6Heli ID as a function of the vertical distance to the axis of the ID.

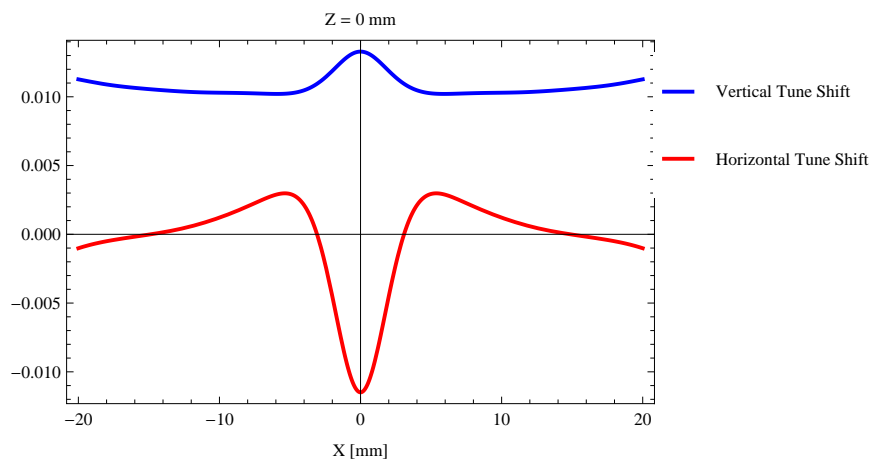


Figure 5.353: Induced tune shift from the epu43p6Heli ID on the stored beam from the ID as a function of the horizontal distance to the axis of the ID.

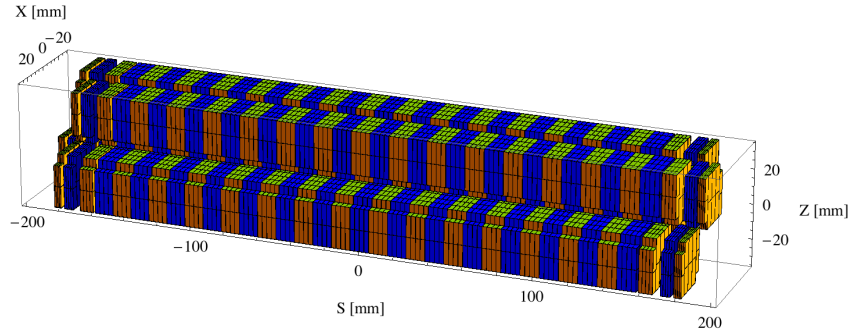


Figure 5.354: Magnetic model of the epu43p6Incl ID. The ID has been modelled with Radia [2]

$30 \times 30 \times 10.9 \text{ mm}^3$  and there is a 5. mm cut-out in two of the corners of the blocks. The total length of the epu43p6Incl ID is 3941.27 mm.

### Analysis of the magnetic field of the epu43p6Incl ID

The effective magnetic fields on axis and the fundamental photon energy of the epu43p6Incl ID are shown in Table 5.55. The higher harmonic contents in the magnetic field of an elliptically polarising undulator made of permanent magnets is negligible and the efficient field has about the same strength as the peak field.

Table 5.55: Effective Fields on axis and Fundamental Photon Energy of the epu43p6Incl ID

Undulator Period	43.6	mm
Undulator Gap	9	mm
Undulator Mode	Inclined	
Undulator Phase	11.771	mm
Vertical Peak Field	0.467	T
Efficient Vertical Field	0.470	T
Kx (from vert. field)	1.914	
Horizontal Peak Field:	-0.466	T
Efficient Horizontal Field	0.471	T
Kz (from hor. field)	1.918	
Photon Energy, Harm.1	0.420	keV
Emitted Power	4.968	kW
Total Length	3941.3	mm

### Synchrotron radiation from the epu43p6Incl ID

The power map of the emitted synchrotron radiation by the epu43p6Incl ID, assuming a 0.5 A filament beam with an energy of 3 GeV and undulator properties of the synchrotron radiation, is shown in Figure 5.359. The on-axis power density is  $25.734 \text{ kW/mrad}^2$

A map of the degree of linear polarisation of the fundamental harmonic of the synchrotron radiation emitted by the epu43p6Incl ID over the angle of observation is shown in Figure 5.360.

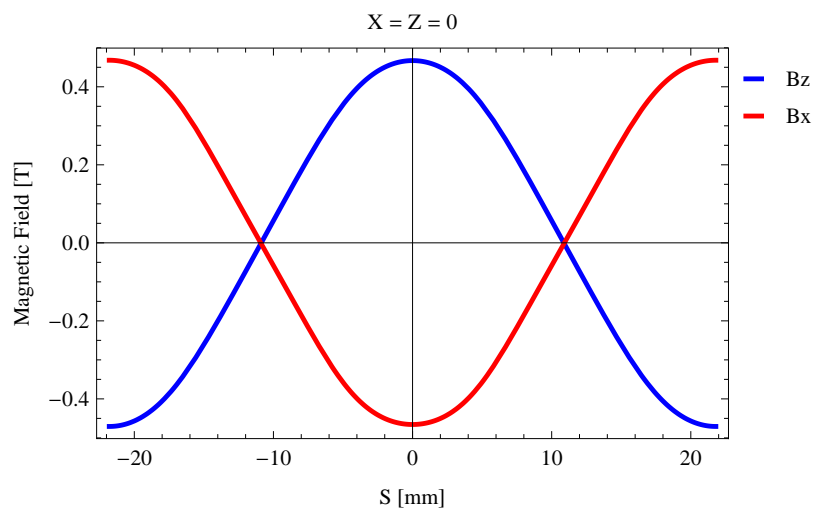


Figure 5.355: Vertical magnetic field in a central pole of the epu43p6Incl ID along the ID axis,  $X = Z = 0$

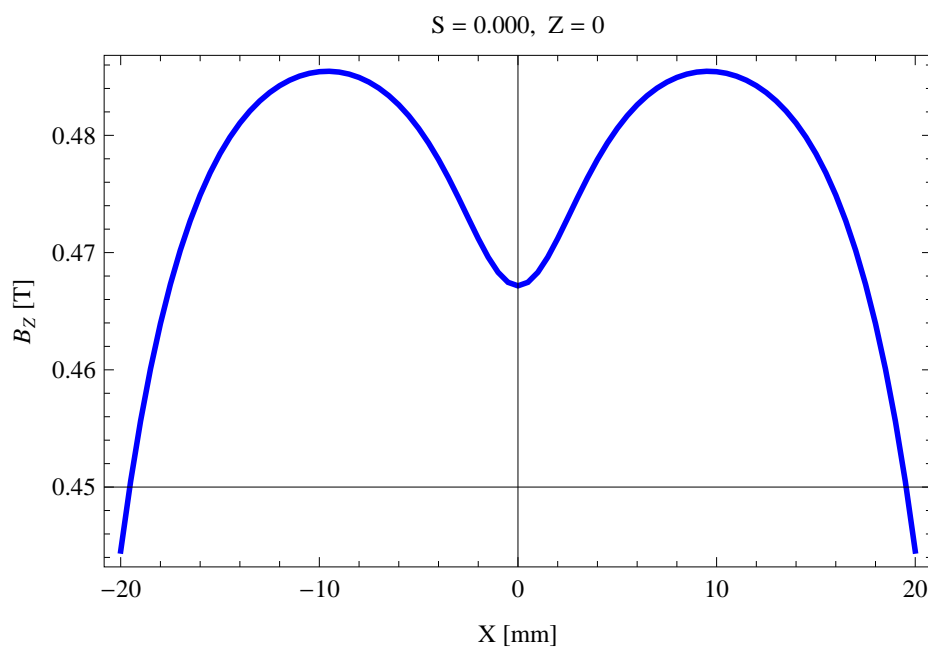


Figure 5.356: Vertical magnetic field in a central pole of the epu43p6Incl ID along the horizontally transverse direction to the ID axis,  $S = 0.000, Z = 0$

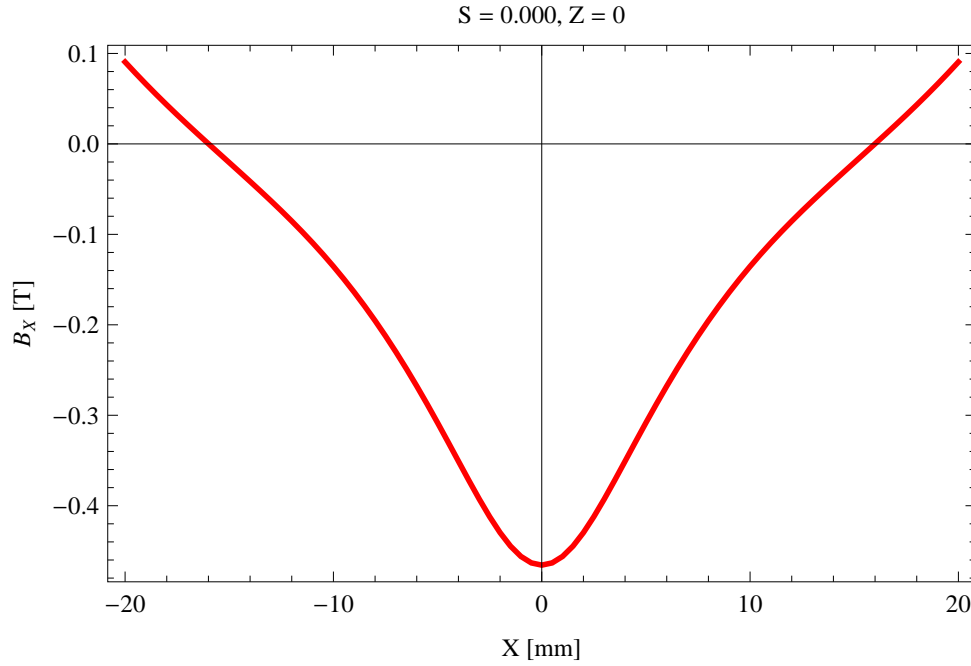


Figure 5.357: Horizontal magnetic field in a central pole of the epu43p6Incl ID along the horizontally transverse direction to the ID axis,  $S = 0.000$ ,  $Z = 0$

A map of the degree of 45 degree polarisation of the fundamental harmonic of the synchrotron radiation emitted by the epu43p6Incl ID over the angle of observation is shown in Figure 5.361.

A map of the degree of circular polarisation of the fundamental harmonic of the synchrotron radiation emitted by the epu43p6Incl ID over the angle of observation is shown in Figure 5.362.

The on axis brilliance at peak energy, the angular spectral flux, the flux in the harmonics, the power in the harmonics, the ratio of coherence, the coherent flux in the harmonics, and the power of coherent radiation in the harmonics from the epu43p6Incl ID have been calculated and the resulting plots are found in this section of the document. The beam parameters used for the calculation are 0.5 A of stored current,  $\beta_H = 9$  m,  $\varepsilon_H = 0.263$  nmrad,  $\beta_V = 4.8$  m,  $\varepsilon_V = 8$  pmrad, and an energy spread of 0.001.

The brilliance at peak energy and the angular spectral flux density from the epu43p6Incl ID for different harmonics at maximum K-value (2.710) are given in Table 5.56 and for minimum K-value (0.400) these values are given in Table 5.57.

Table 5.56: The brilliance at peak energy and the angular spectral flux density from the epu43p6Incl ID for different harmonics at maximum K-value (2.710)

Harmonic	Photon Energy [eV]	Brilliance [Ph./s/mrad <sup>2</sup> /mrad <sup>2</sup> /0.1%BW]	Angular Spectral Flux [Ph./s/mrad <sup>2</sup> /0.1%BW]
1	419.666	$2.55 \times 10^{20}$	$8.56 \times 10^{17}$
3	1259.	$3.97 \times 10^{20}$	$9.18 \times 10^{17}$
5	2098.33	$3.58 \times 10^{20}$	$7.39 \times 10^{17}$
7	2937.66	$2.99 \times 10^{20}$	$5.83 \times 10^{17}$
9	3776.99	$2.45 \times 10^{20}$	$4.62 \times 10^{17}$
11	4616.32	$1.99 \times 10^{20}$	$3.67 \times 10^{17}$

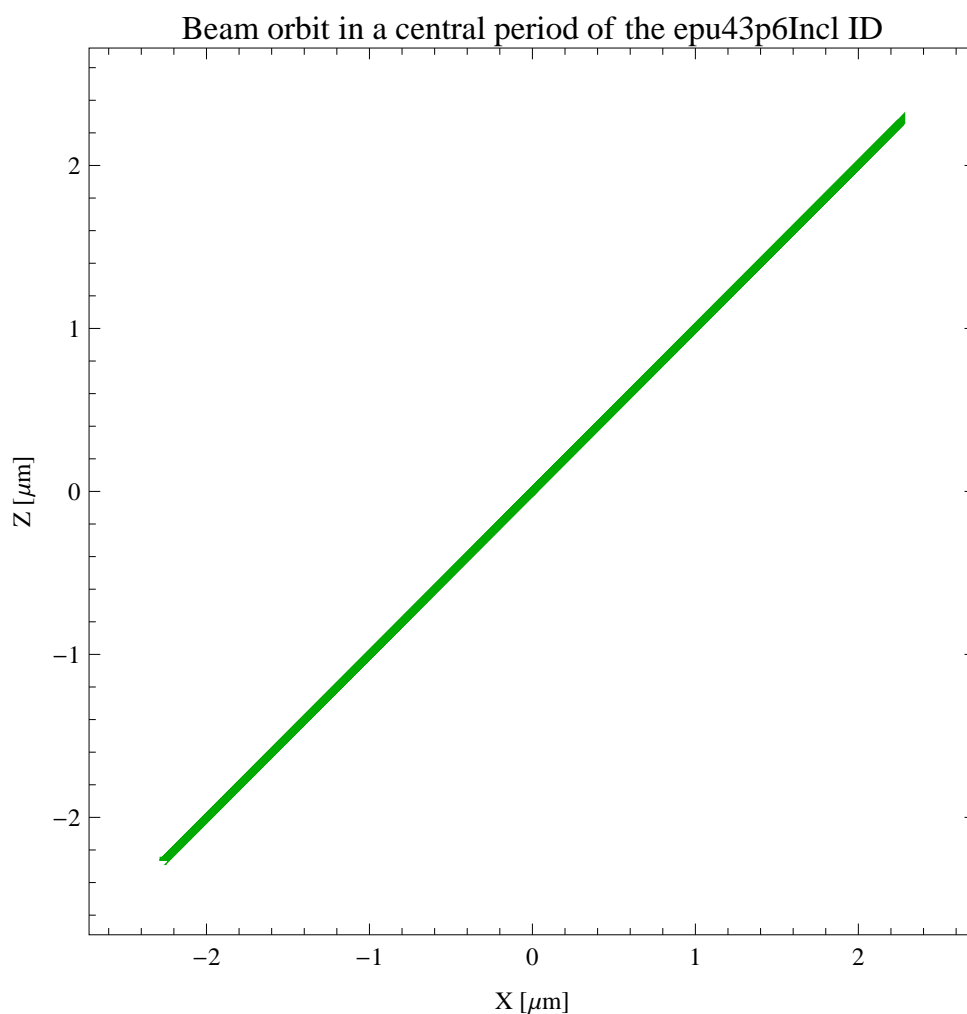


Figure 5.358: The beam orbit of the electron beam through a central period of the epu43p6Incl ID

Table 5.57: The brilliance at peak energy and the angular spectral flux density from the epu43p6Incl ID for different harmonics at minimum K-value (0.4)

Harmonic	Photon Energy [eV]	Brilliance [Ph./s/mrad <sup>2</sup> /mrad <sup>2</sup> /0.1%BW]	Angular Spectral Flux [Ph./s/mrad <sup>2</sup> /0.1%BW]
1	1815.06	$2.49 \times 10^{20}$	$5.33 \times 10^{17}$
3	5445.18	$4.62 \times 10^{18}$	$8.52 \times 10^{15}$
5	9075.31	$5.21 \times 10^{16}$	$9.34 \times 10^{13}$
7	12705.4	$5.46 \times 10^{14}$	$9.71 \times 10^{11}$
9	16335.5	$5.62 \times 10^{12}$	$9.94 \times 10^9$
11	19965.7	$5.74 \times 10^{10}$	$1.01 \times 10^8$

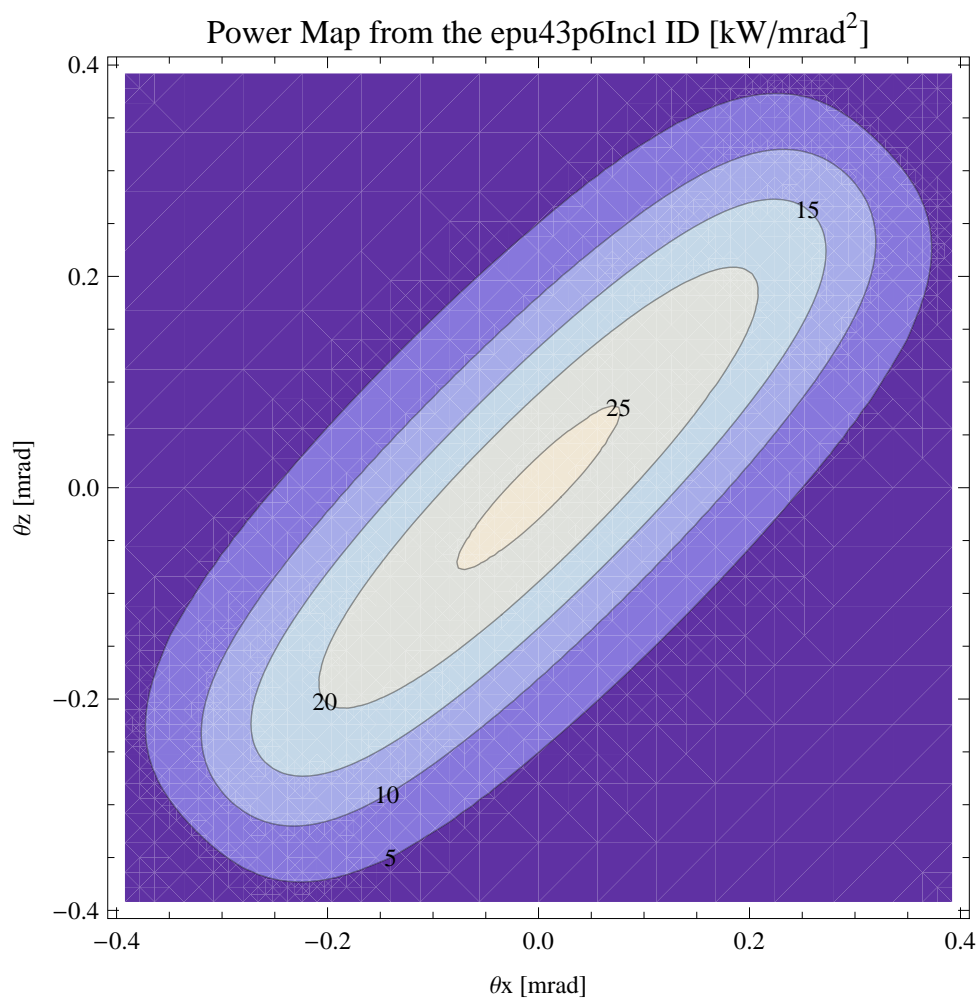


Figure 5.359: Map of the power distribution of the emitted synchrotron radiation by the epu43p6Incl ID

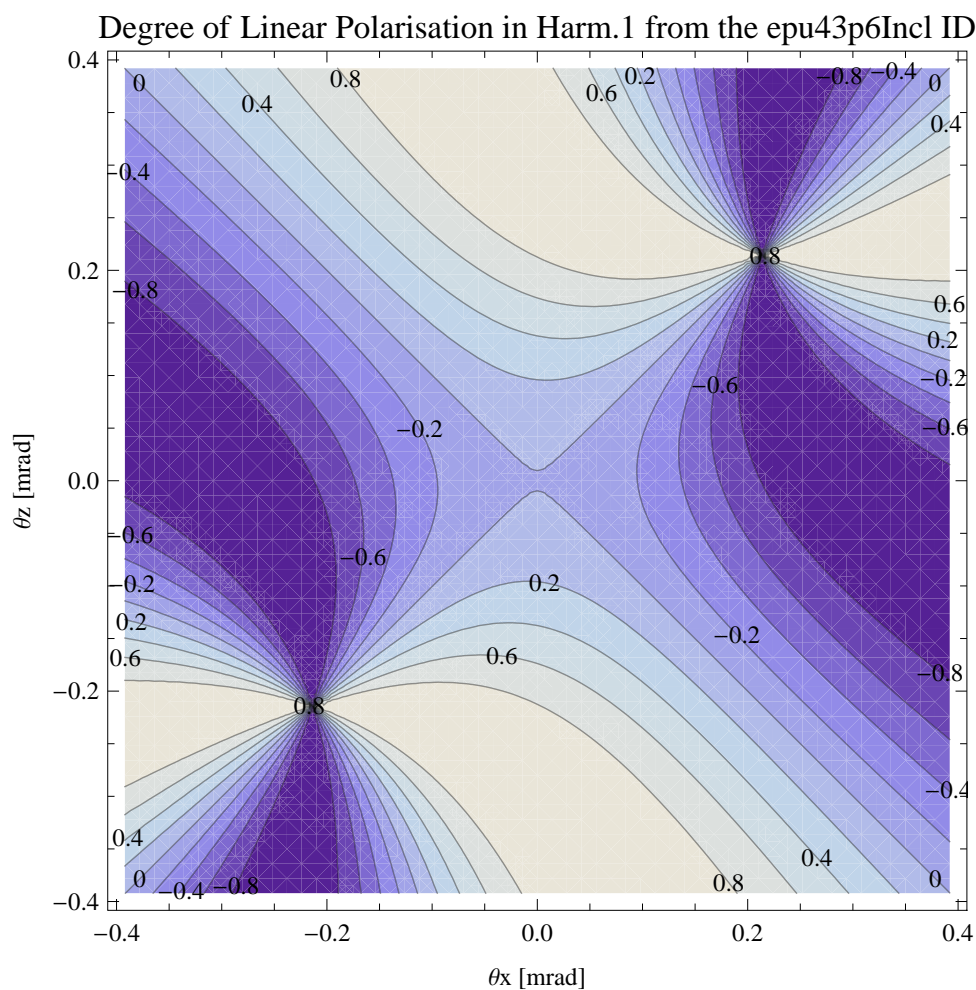


Figure 5.360: Map of linear polarisation in the fundamental harmonic of the synchrotron radiation emitted by the epu43p6Incl ID



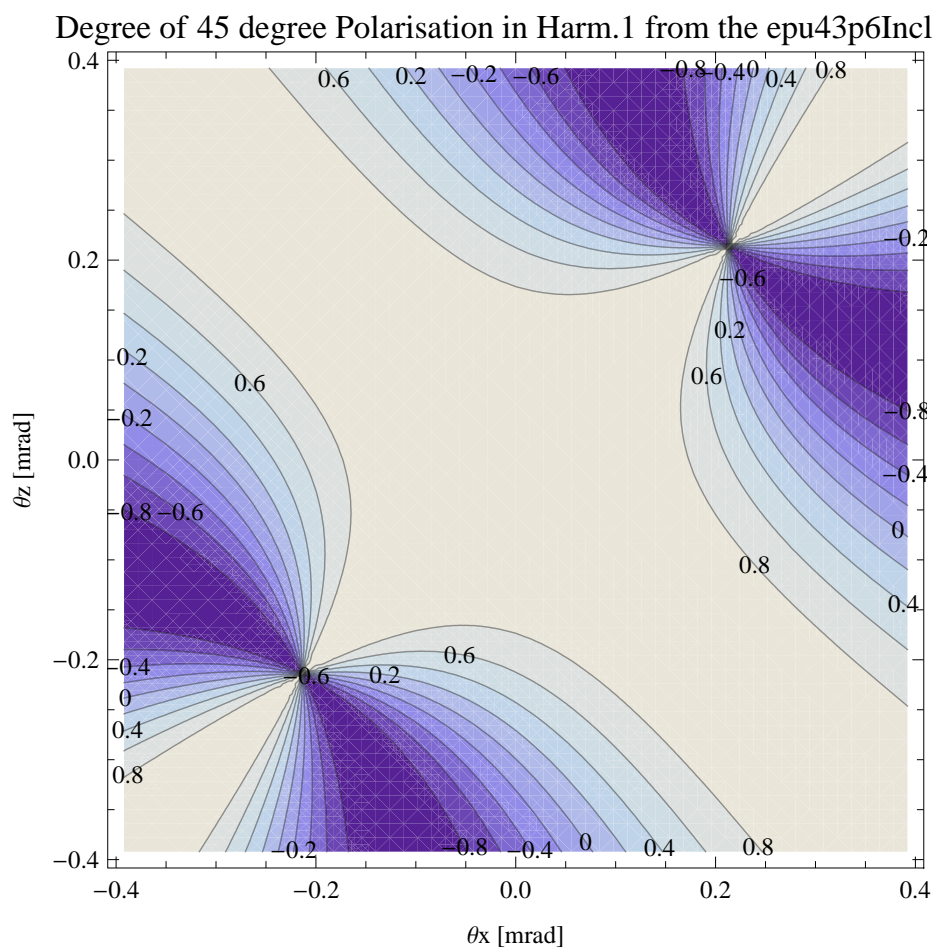


Figure 5.361: Map of 45 degree polarisation in the fundamental harmonic of the synchrotron radiation emitted by the epu43p6Incl ID

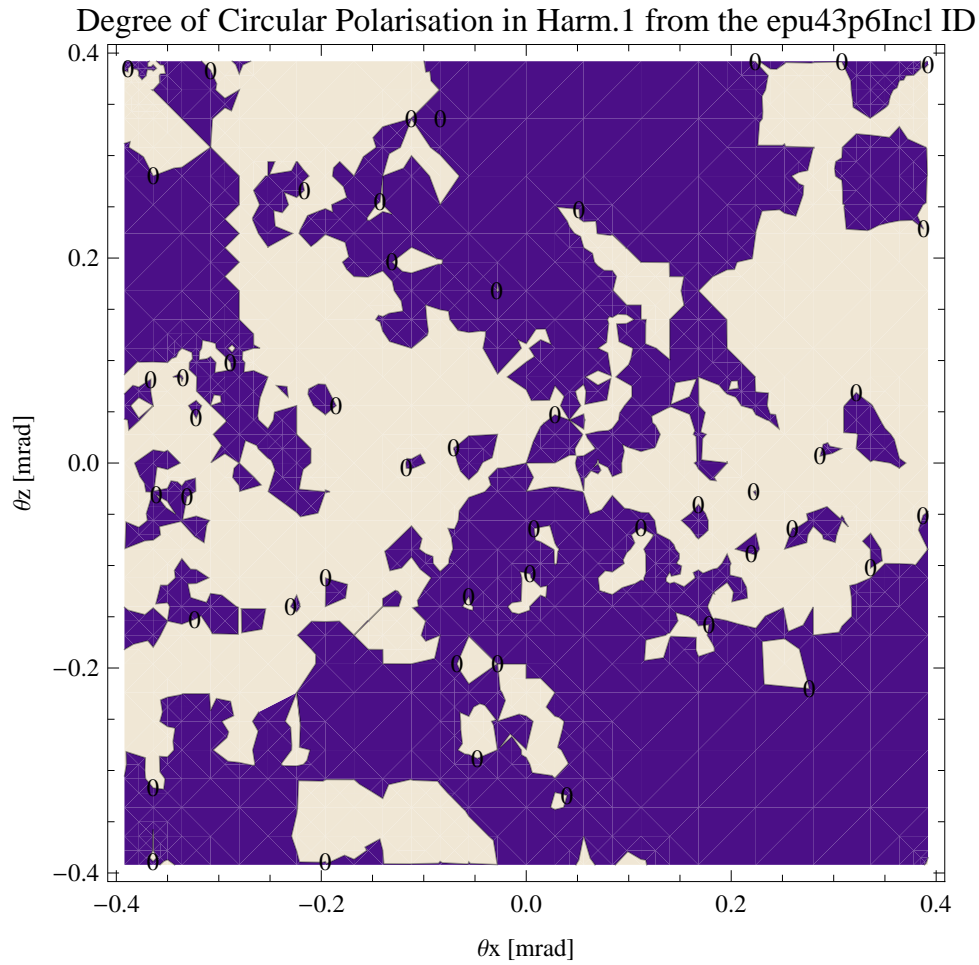


Figure 5.362: Map of circular polarisation in the fundamental harmonic of the synchrotron radiation emitted by the epu43p6Incl ID

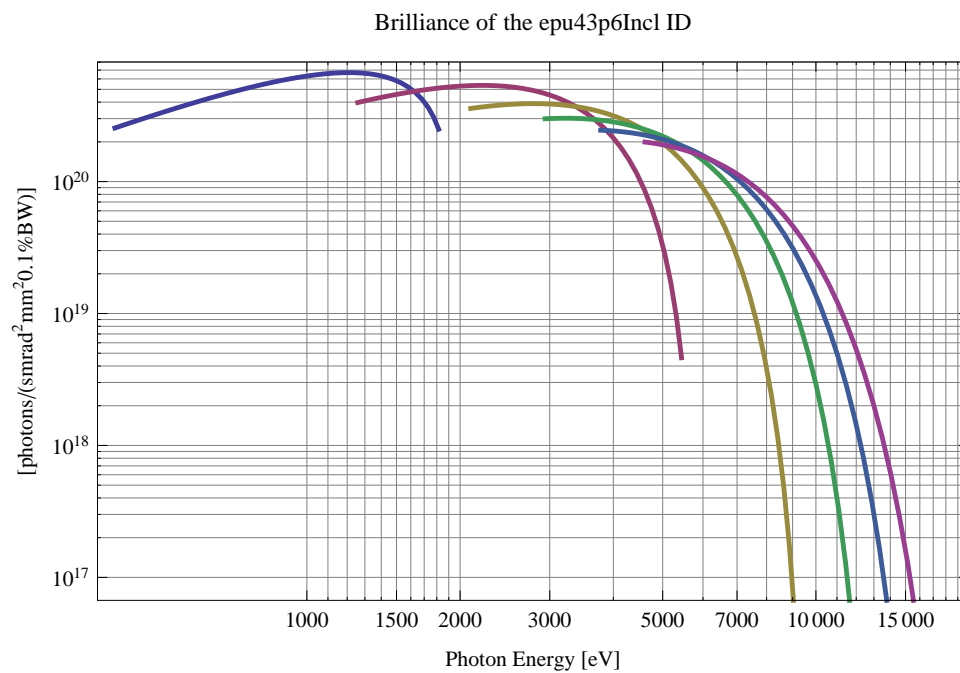


Figure 5.363: The brilliance at peak energy from the epu43p6Incl ID

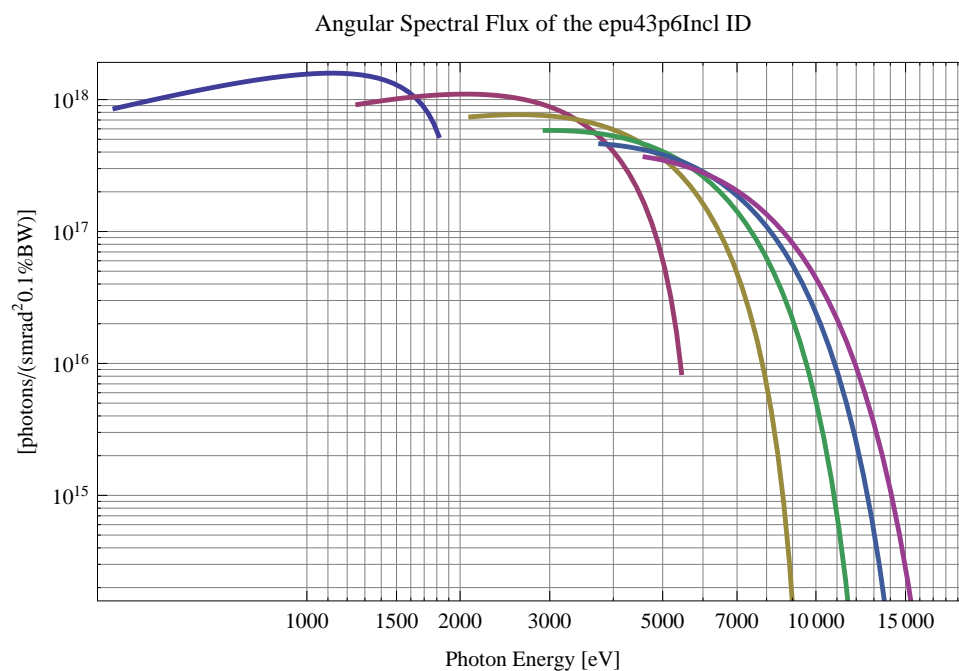


Figure 5.364: The angular spectral flux from the epu43p6Incl ID

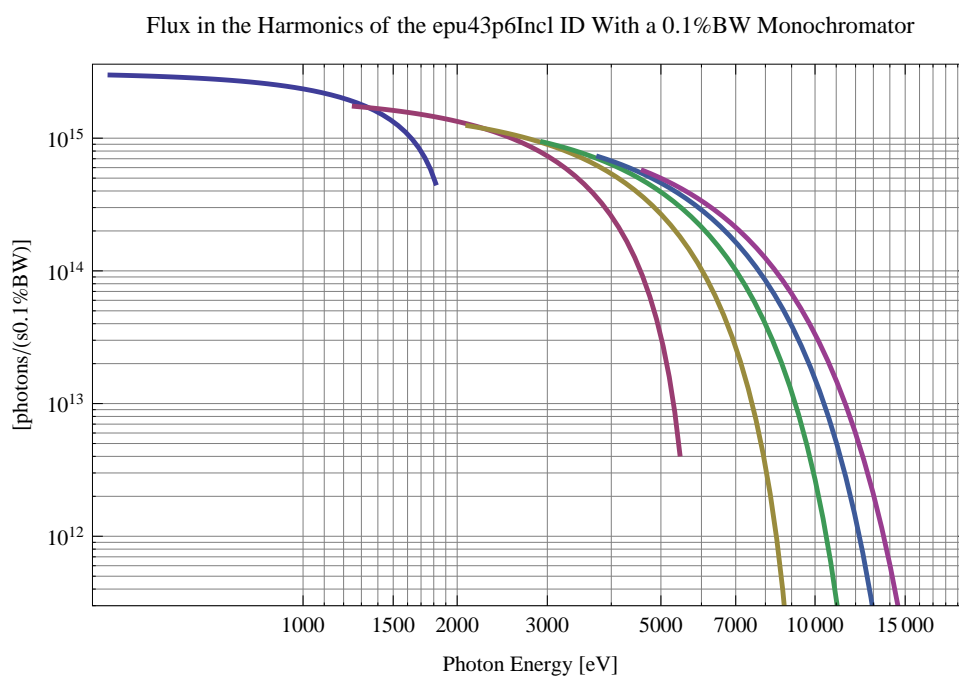


Figure 5.365: The flux of photons in the harmonics from the epu43p6Incl ID using a 0.1%BW monochromator

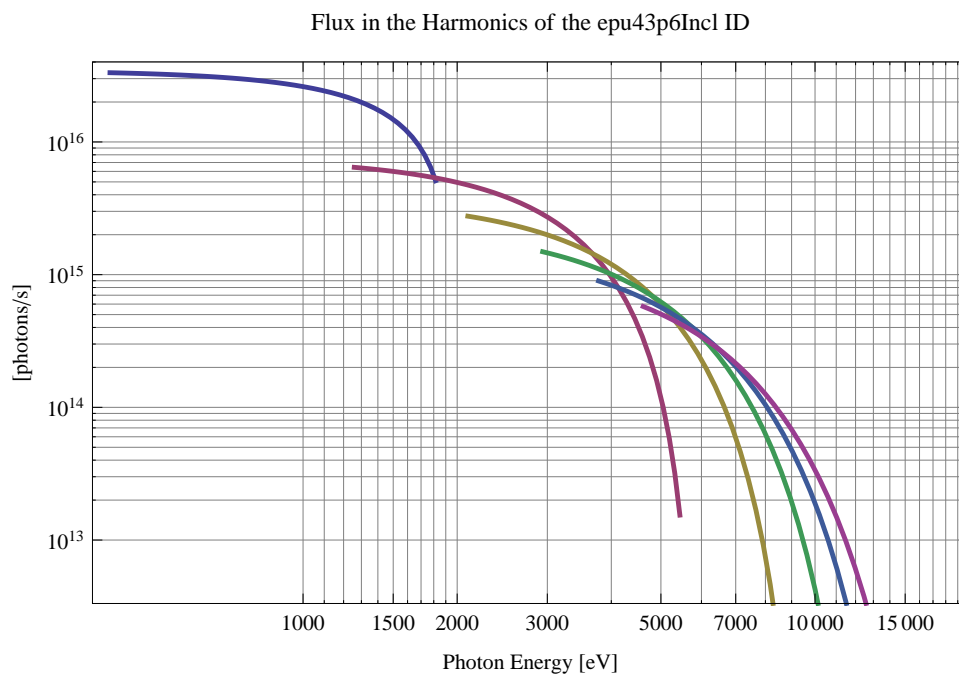


Figure 5.366: The flux of photons in the harmonics from the epu43p6Incl ID

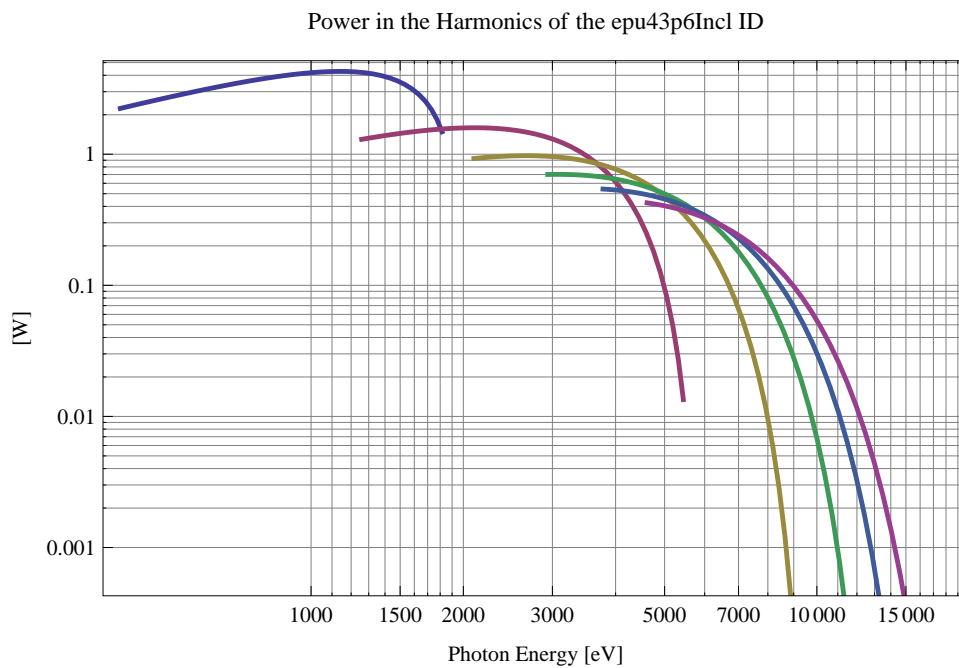


Figure 5.367: The power in the harmonics from the epu43p6Incl ID

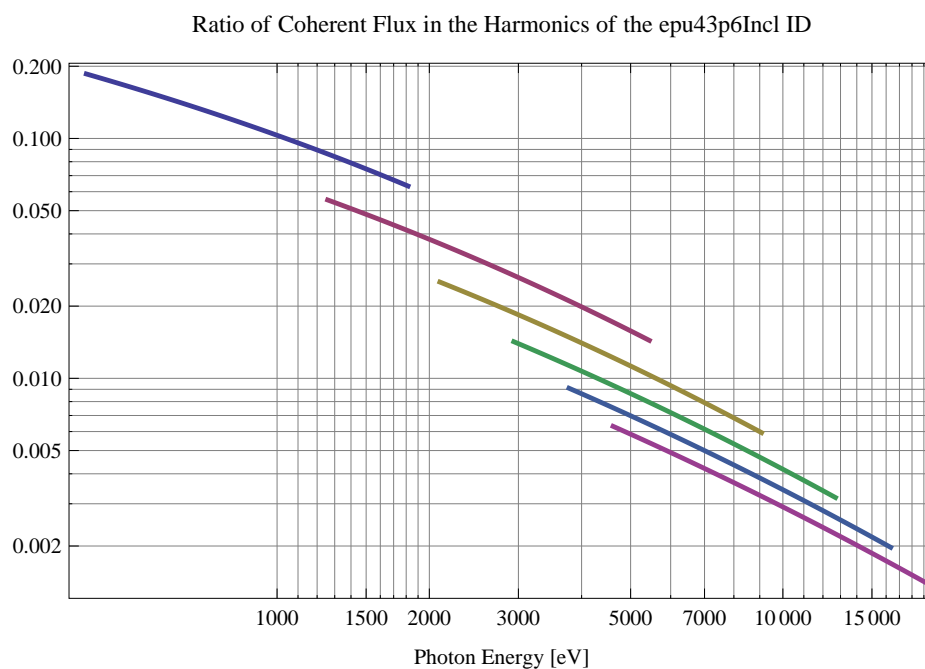


Figure 5.368: The ratio of coherent flux in the harmonics from the epu43p6Incl ID

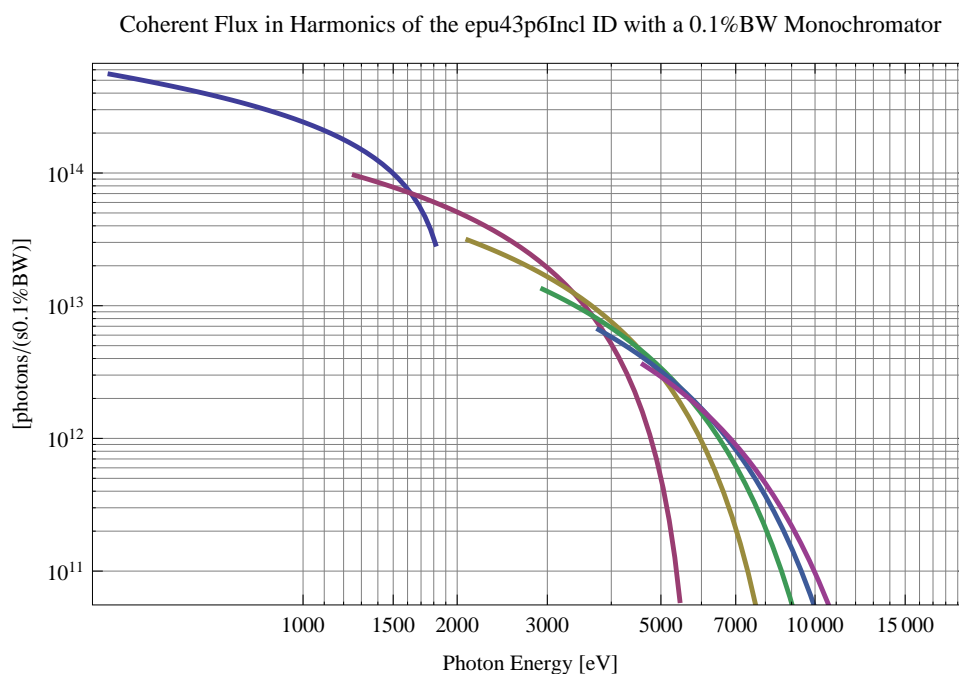


Figure 5.369: The coherent flux in the harmonics of the epu43p6Incl ID using a 0.1%BW Monochromator

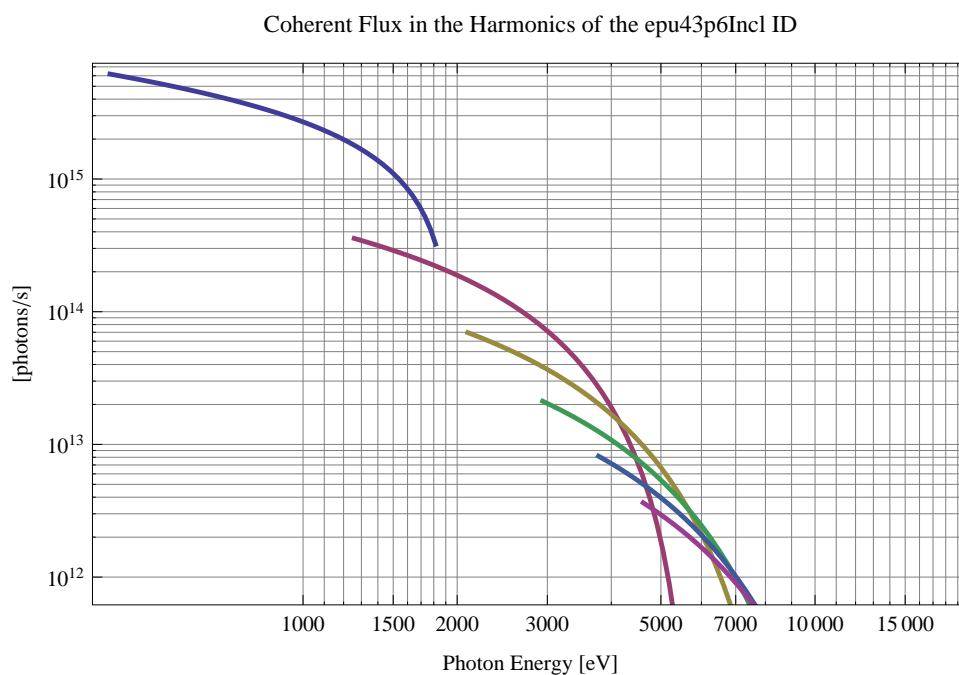


Figure 5.370: The coherent flux in the harmonics of the epu43p6Incl ID

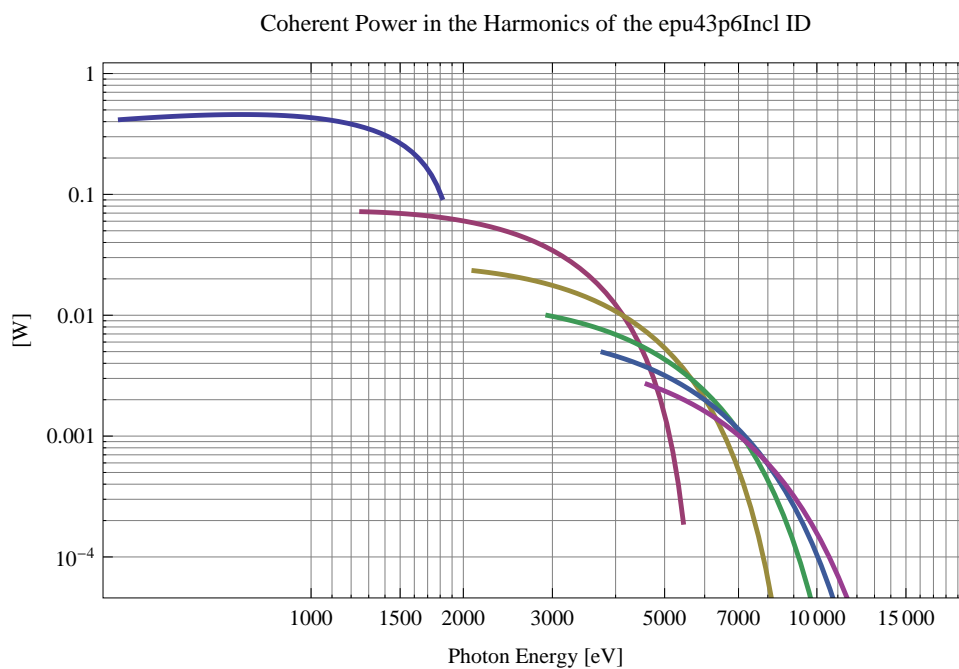


Figure 5.371: The power of coherent synchrotron radiation in the harmonics of the epu43p6Incl ID

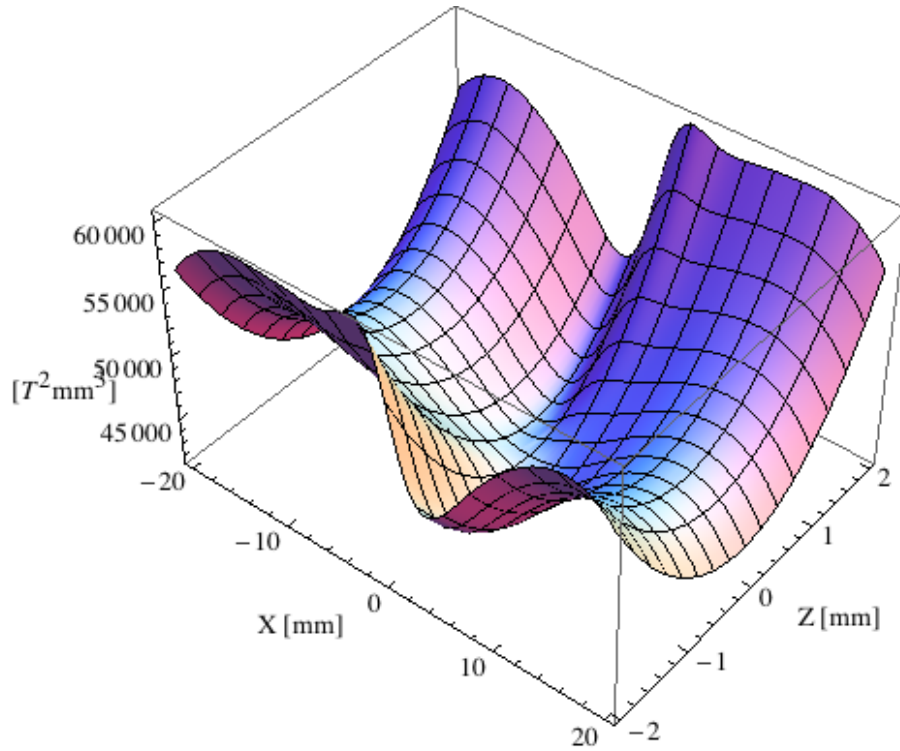


Figure 5.372: Focusing potential from the epu43p6Incl ID over the beam stay clear aperture.

### Influence from the epu43p6Incl ID on the optics of the stored beam

Figure 5.372 shows the focusing potential from the epu43p6Incl over the beam stay clear aperture of the ring aperture.

Figure 5.373 shows the kick map in the beam energy independent unit  $T^2 m^2$  of the kicks induced by the epu43p6Incl ID over the beam stay clear aperture.

Figure 5.374 shows the induced angular kick on the stored beam from the epu43p6Incl ID as a function of the vertical distance to the axis of the ID.

Figure 5.375 shows the induced angular kick on the stored beam from the epu43p6Incl ID as a function of the horizontal distance to the axis of the ID.

Figure 5.376 shows tune shift induced by the epu43p6Incl ID over the beam stay clear aperture. Note that the tune shift depends on the beam size at the ID.

Figure 5.377 shows the induced tune shift from the epu43p6Incl ID as a function of the vertical distance to the axis of the ID.

Figure 5.378 shows the induced tune shift from the epu43p6Incl ID as a function of the horizontal distance to the axis of the ID.

### Magnet model of the elliptically polarising undulator epu43p6Vert

The Radia [2] magnet model of the epu43p6Vert ID is shown in Figure 5.379. The length of the magnet model is 366.067 mm. The magnetic material in the model is NdFeb with a remanence of 1.28 T, a material similar to VACODYM 776 TP from Vacuumschmelze. Blocks with vertical magnetisation are blue and blocks with horizontal magnetisation are yellow. The block size is

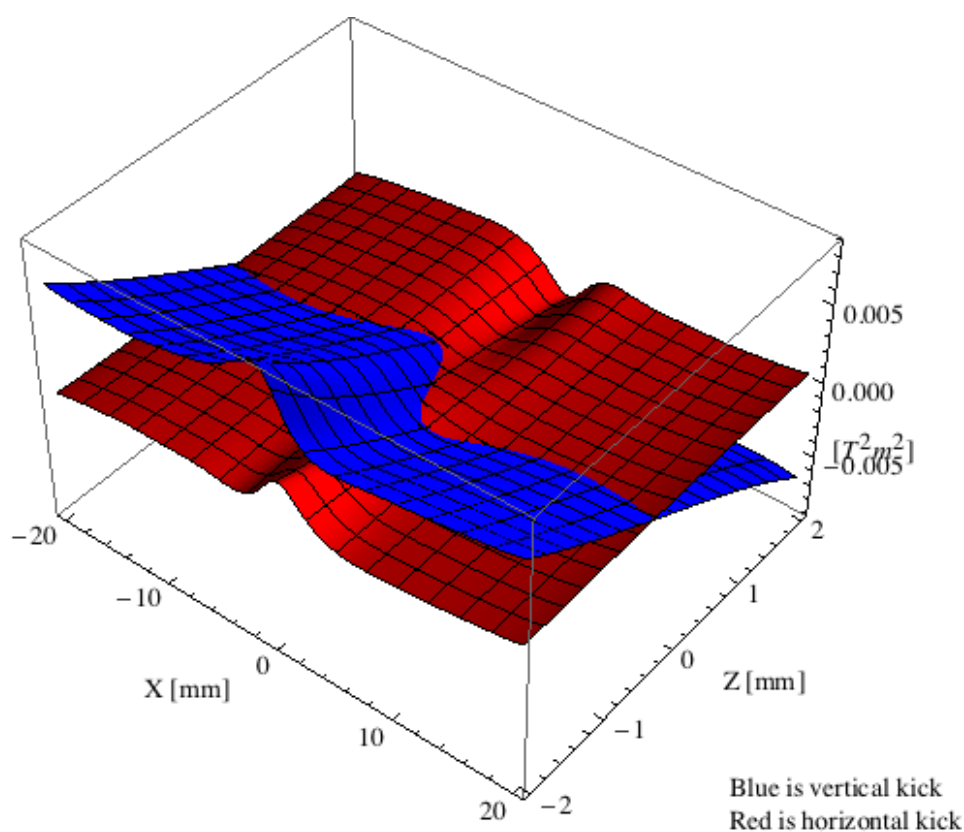


Figure 5.373: Kick map in the beam energy independent unit  $T^2m^2$  of the kicks induced by the epu43p6Incl ID over the beam stay clear aperture.

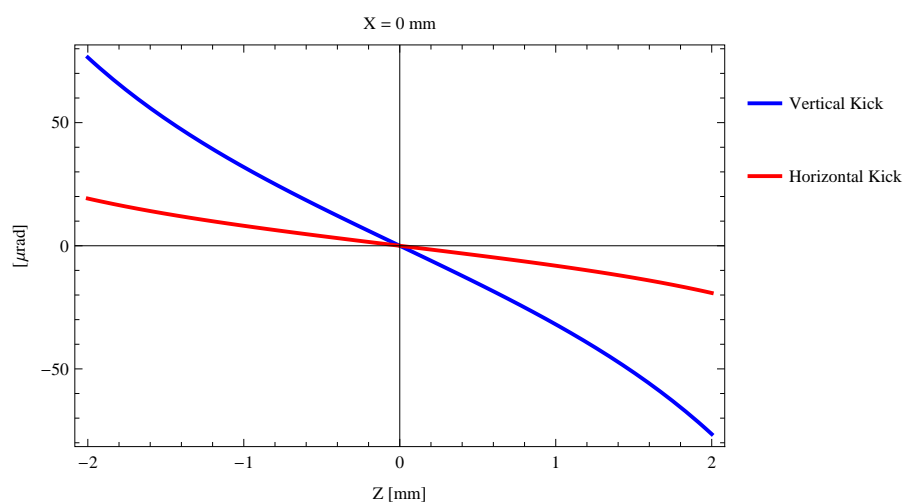


Figure 5.374: Induced angular kick on the stored beam from the epu43p6Incl ID as a function of the vertical distance to the ID axis.



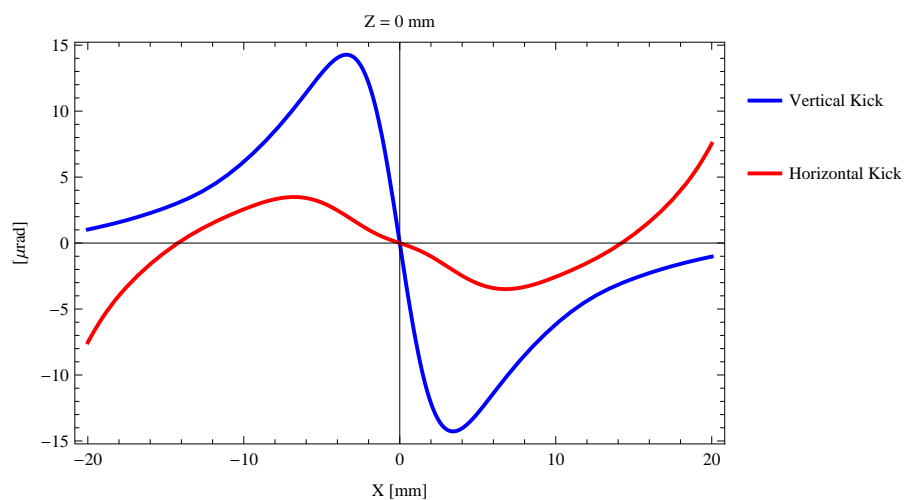


Figure 5.375: Induced angular kick on the stored beam from the epu43p6Incl ID as a function of the horizontal distance to the ID axis.

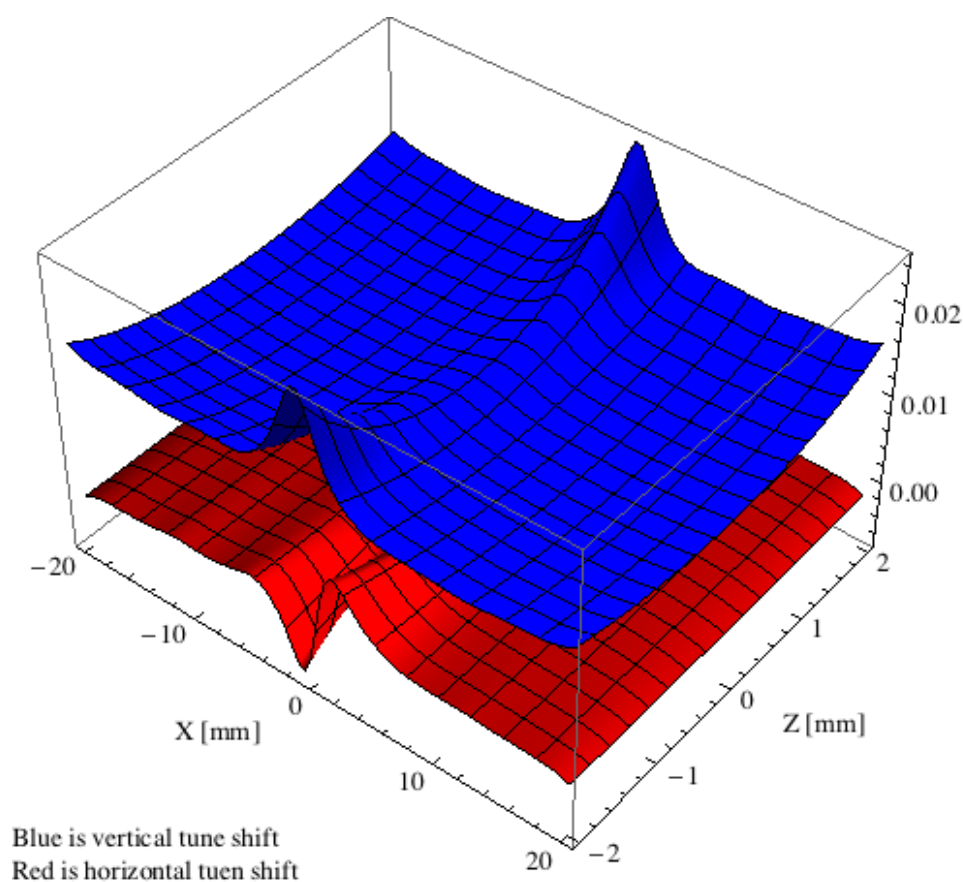


Figure 5.376: Tune shift induced by the epu43p6Incl ID over the beam stay clear aperture.

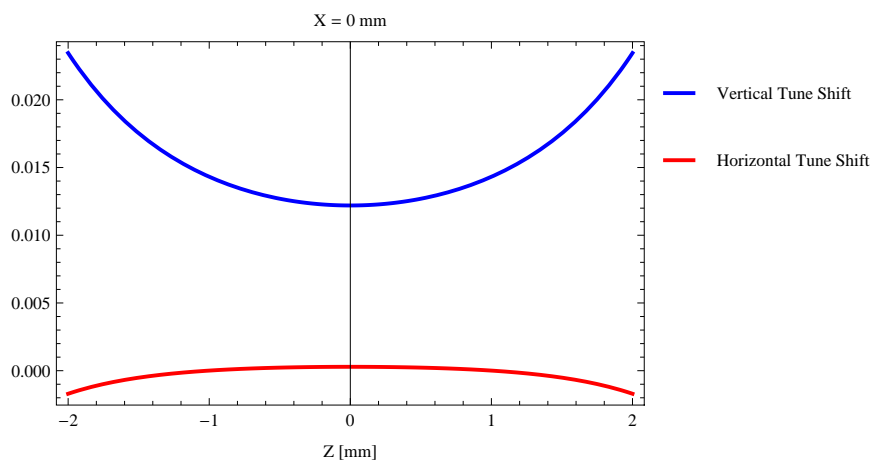


Figure 5.377: Induced tune shift from the epu43p6Incl ID as a function of the vertical distance to the axis of the ID.

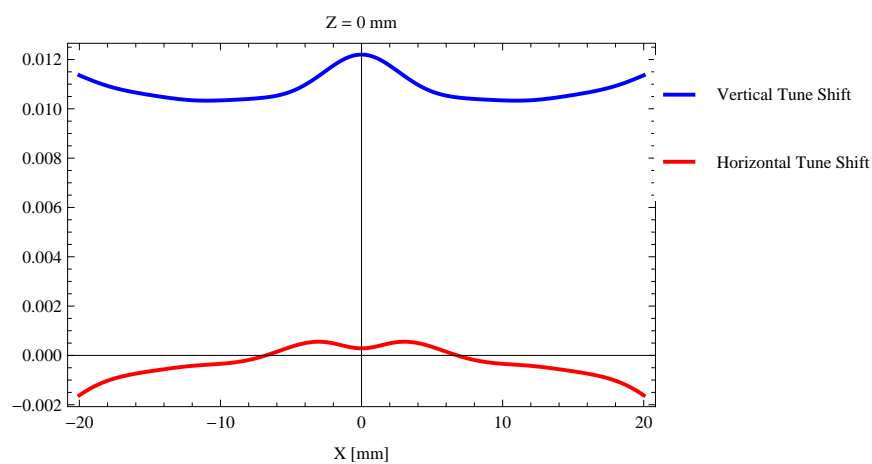


Figure 5.378: Induced tune shift from the epu43p6Incl ID on the stored beam from the ID as a function of the horizontal distance to the axis of the ID.

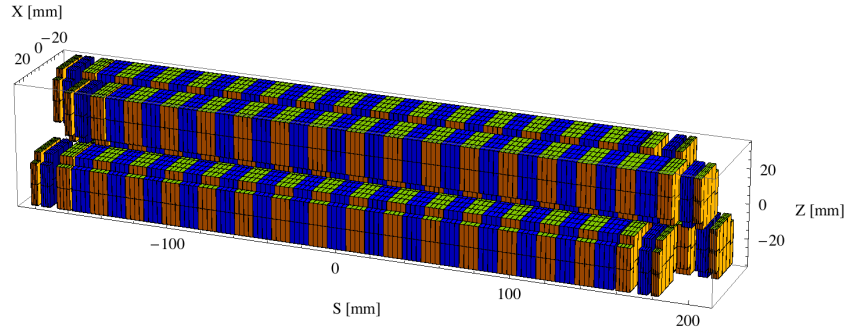


Figure 5.379: Magnetic model of the epu43p6Vert ID. The ID has been modelled with Radia [2]

$30 \times 30 \times 10.9 \text{ mm}^3$  and there is a 5. mm cut-out in two of the corners of the blocks. The total length of the epu43p6Vert ID is 3941.27 mm.

### Analysis of the magnetic field of the epu43p6Vert ID

The effective magnetic fields on axis and the fundamental photon energy of the epu43p6Vert ID are shown in Table 5.58. The higher harmonic contents in the magnetic field of an elliptically polarising undulator made of permanent magnets is negligible and the efficient field has about the same strength as the peak field.

Table 5.58: Effective Fields on axis and Fundamental Photon Energy of the epu43p6Vert ID

Undulator Period	43.6	mm
Undulator Gap	9	mm
Undulator Mode	Vertical	
Undulator Phase	21.800	mm
Vertical Peak Field	0.000	T
Efficient Vertical Field	0.000	T
Kx (from vert. field)	0.000	
Horizontal Peak Field:	0.835	T
Efficient Horizontal Field	0.836	T
Kz (from hor. field)	3.404	
Photon Energy, Harm.1	0.289	keV
Emitted Power	7.842	kW
Total Length	3941.3	mm

### Synchrotron radiation from the epu43p6Vert ID

The power map of the emitted synchrotron radiation by the epu43p6Vert ID, assuming a 0.5 A filament beam with an energy of 3 GeV and undulator properties of the synchrotron radiation, is shown in Figure 5.383. The on-axis power density is  $32.460 \text{ kW/mrad}^2$

A map of the degree of linear polarisation of the fundamental harmonic of the synchrotron radiation emitted by the epu43p6Vert ID over the angle of observation is shown in Figure 5.384.

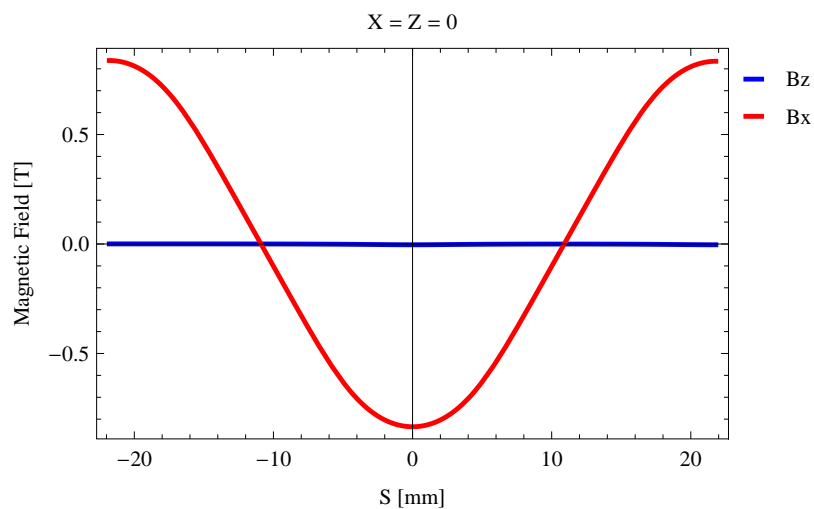


Figure 5.380: Vertical magnetic field in a central pole of the epu43p6Vert ID along the ID axis,  $X = Z = 0$

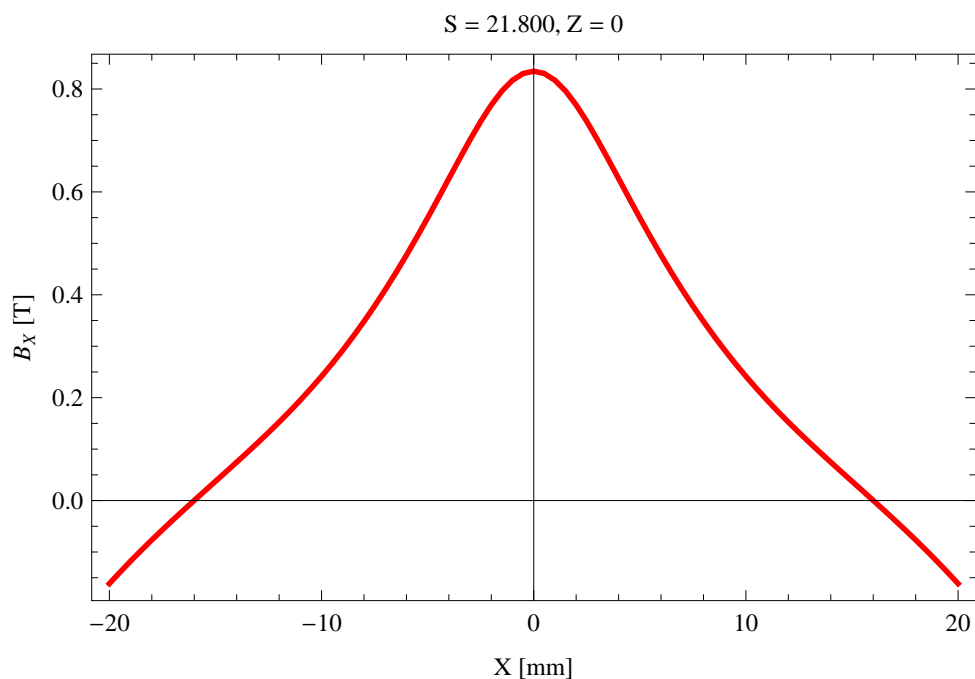


Figure 5.381: Horizontal magnetic field in a central pole of the epu43p6Vert ID along the horizontally transverse direction to the ID axis,  $S = 21.800$ ,  $Z = 0$

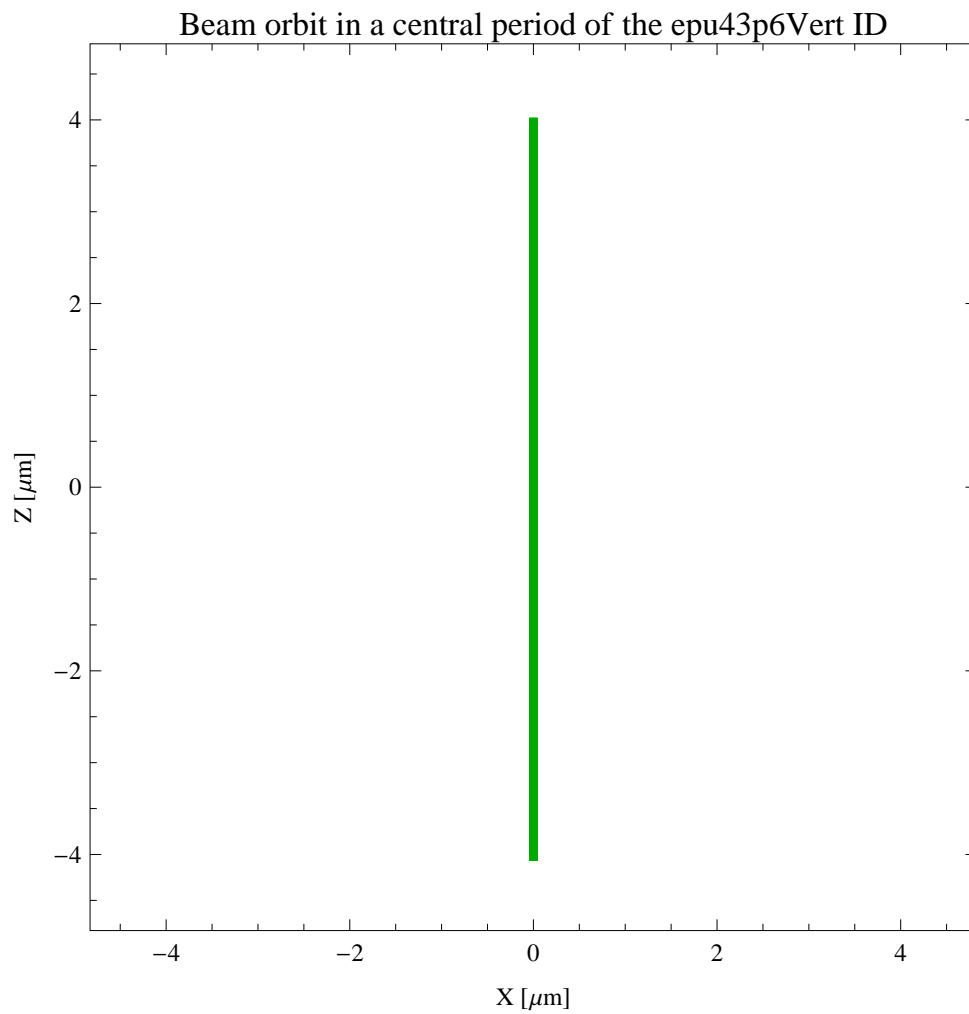


Figure 5.382: The beam orbit of the electron beam through a central period of the epu43p6Vert ID

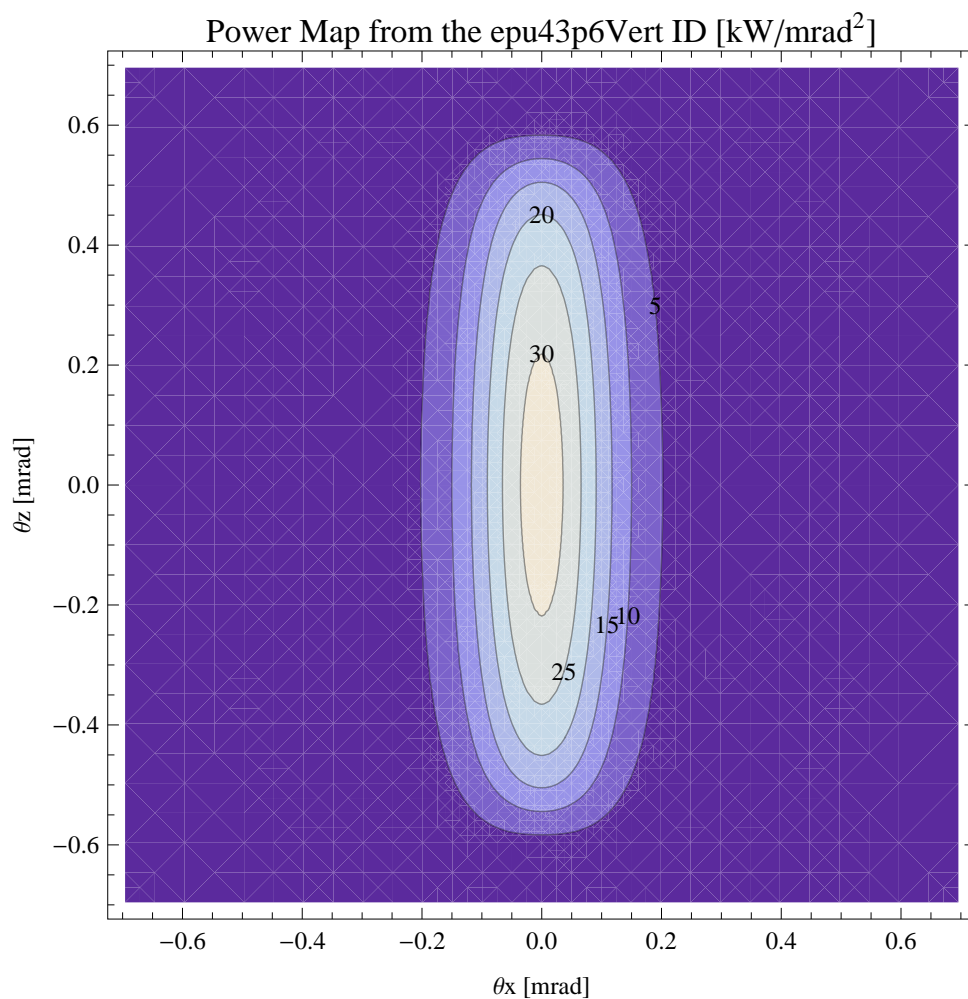


Figure 5.383: Map of the power distribution of the emitted synchrotron radiation by the epu43p6Vert ID

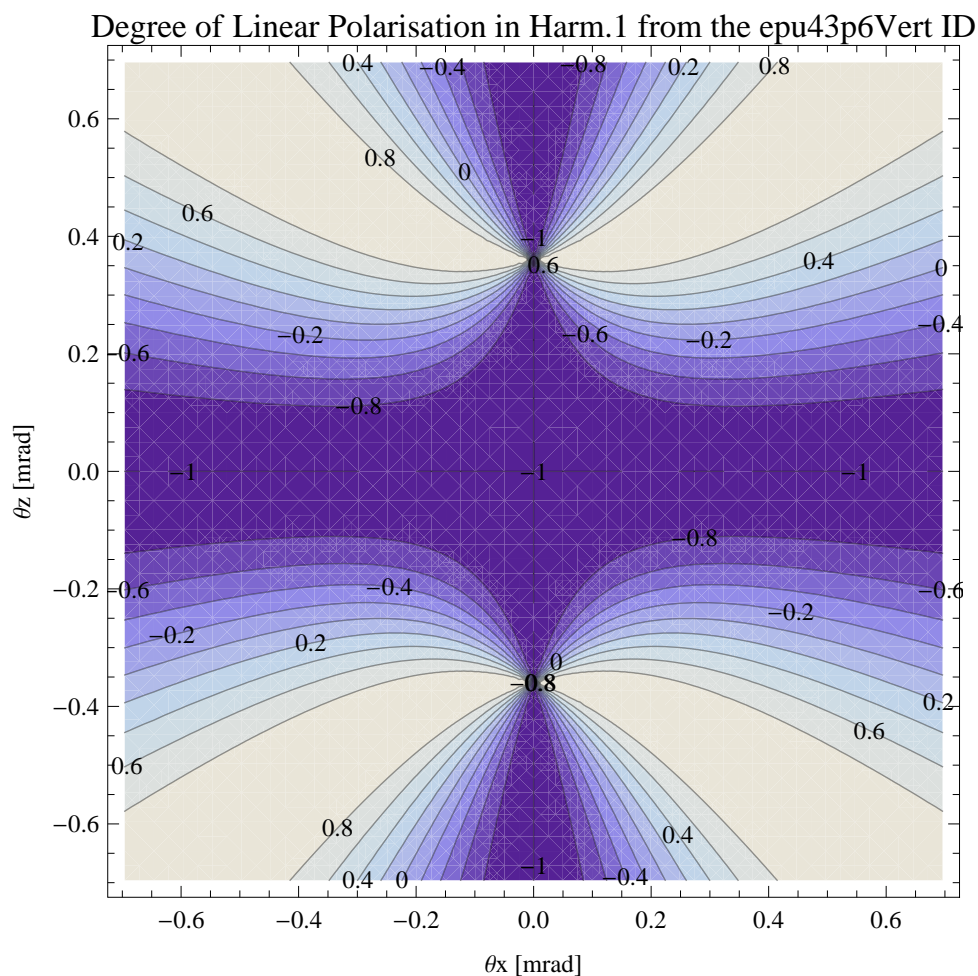


Figure 5.384: Map of linear polarisation in the fundamental harmonic of the synchrotron radiation emitted by the epu43p6Vert ID

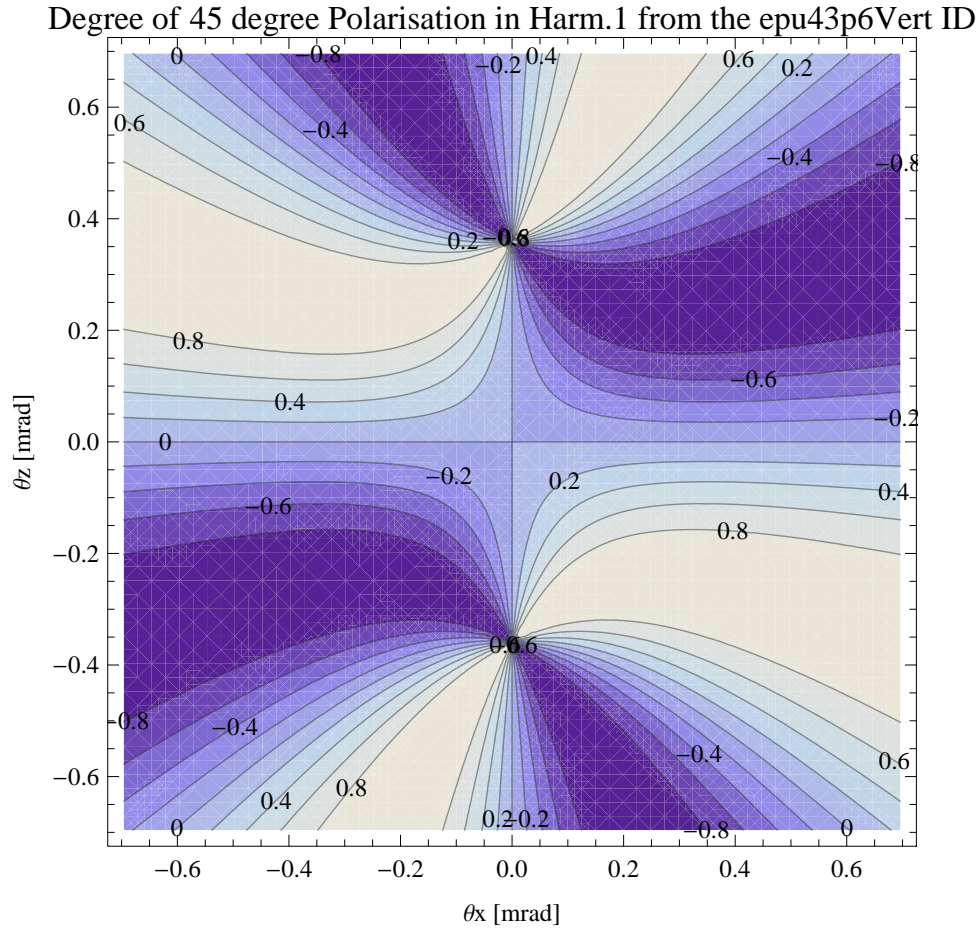


Figure 5.385: Map of 45 degree polarisation in the fundamental harmonic of the synchrotron radiation emitted by the epu43p6Vert ID

A map of the degree of 45 degree polarisation of the fundamental harmonic of the synchrotron radiation emitted by the epu43p6Vert ID over the angle of observation is shown in Figure 5.385.

A map of the degree of circular polarisation of the fundamental harmonic of the synchrotron radiation emitted by the epu43p6Vert ID over the angle of observation is shown in Figure 5.386.

The on axis brilliance at peak energy, the angular spectral flux, the flux in the harmonics, the power in the harmonics, the ratio of coherence, the coherent flux in the harmonics, and the power of coherent radiation in the harmonics from the epu43p6Vert ID have been calculated and the resulting plots are found in this section of the document. The beam parameters used for the calculation are 0.5 A of stored current,  $\beta_H = 9$  m,  $\varepsilon_H = 0.263$  nmrad,  $\beta_V = 4.8$  m,  $\varepsilon_V = 8$  pmrad, and an energy spread of 0.001.

The brilliance at peak energy and the angular spectral flux density from the epu43p6Vert ID for different harmonics at maximum K-value (3.404) are given in Table 5.59 and for minimum K-value (0.400) these values are given in Table 5.60.



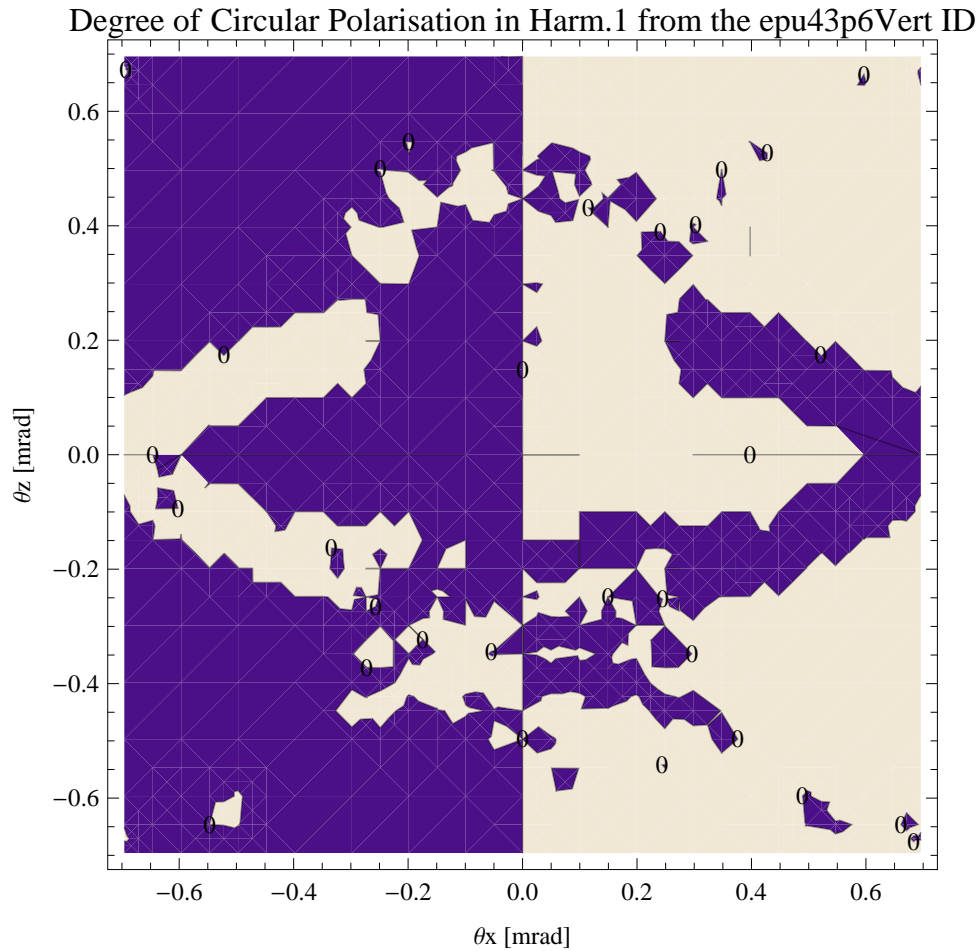


Figure 5.386: Map of circular polarisation in the fundamental harmonic of the synchrotron radiation emitted by the epu43p6Vert ID

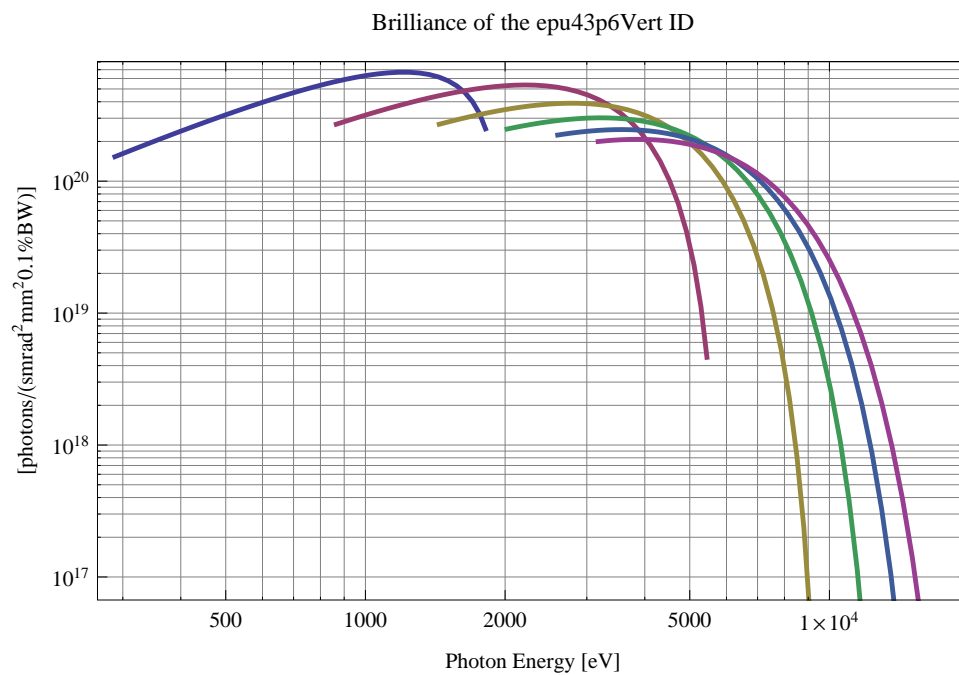


Figure 5.387: The brilliance at peak energy from the epu43p6Vert ID

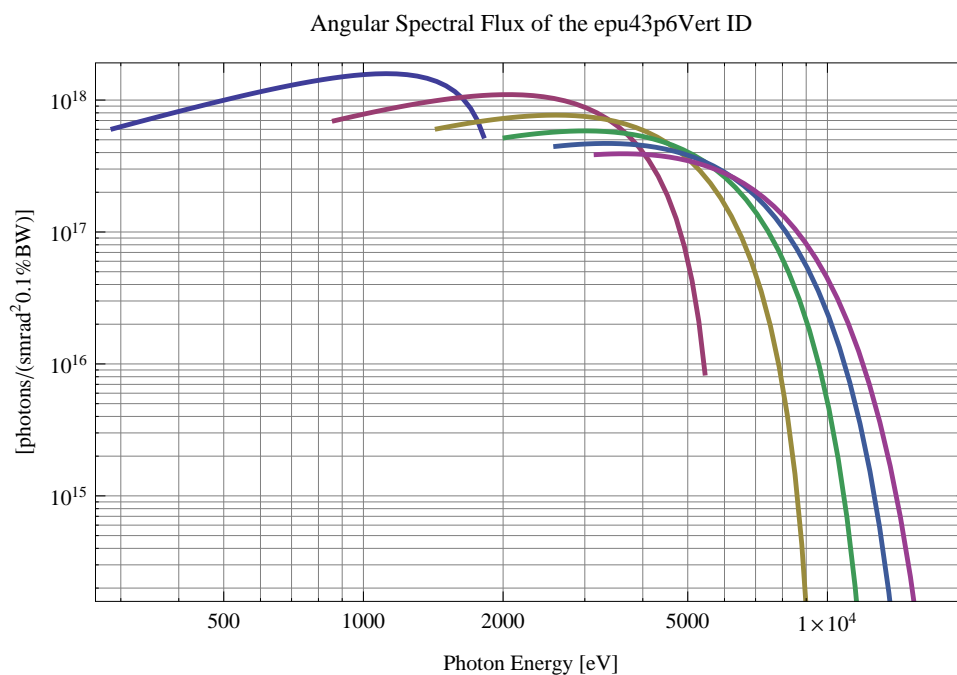


Figure 5.388: The angular spectral flux from the epu43p6Vert ID

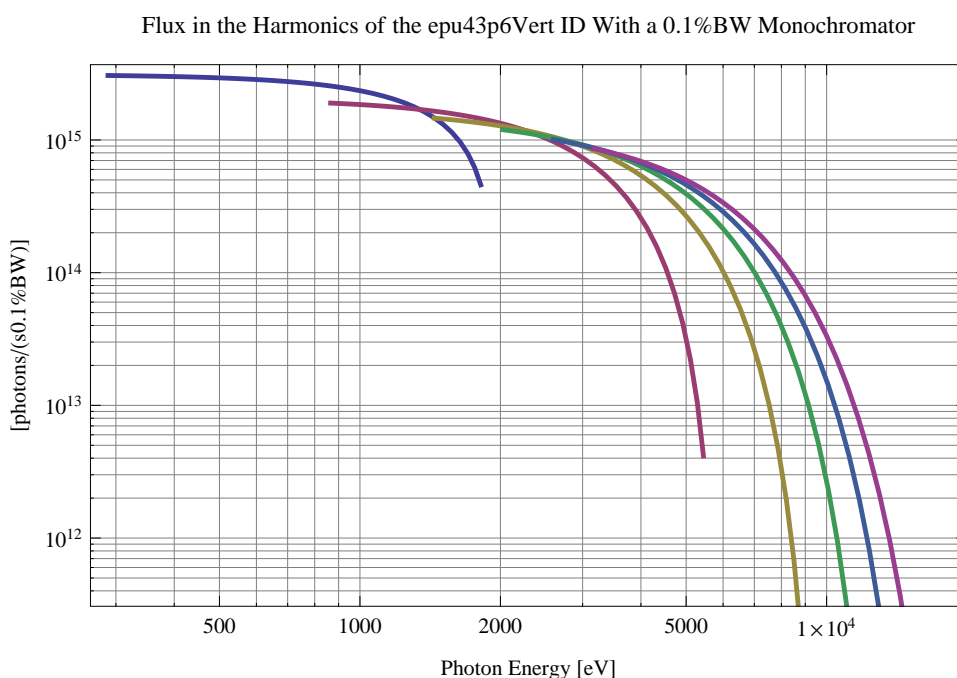


Figure 5.389: The flux of photons in the harmonics from the epu43p6Vert ID using a 0.1%BW monochromator

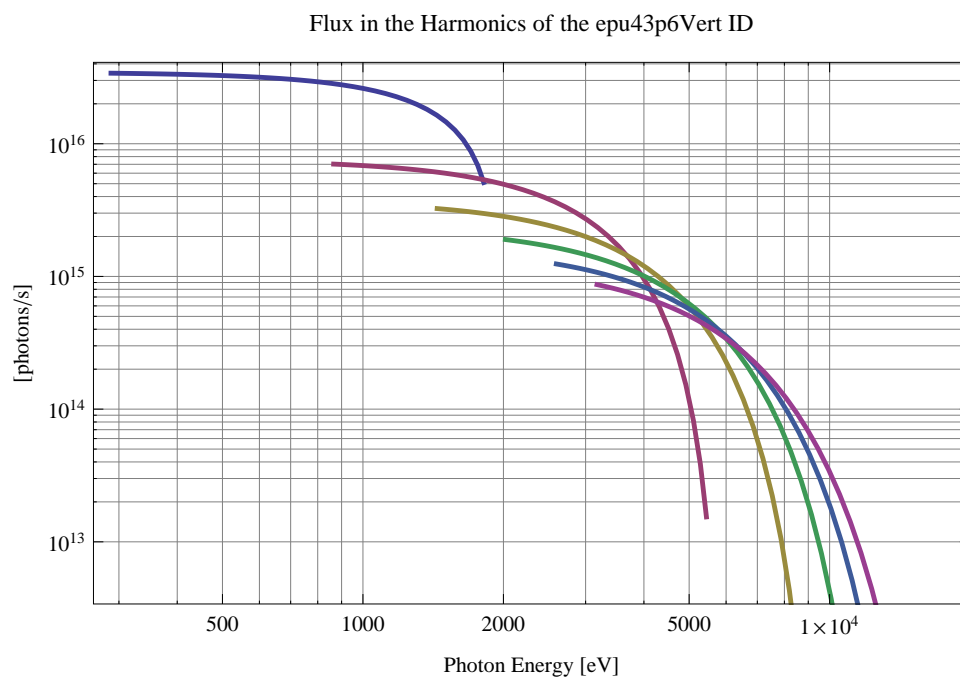


Figure 5.390: The flux of photons in the harmonics from the epu43p6Vert ID

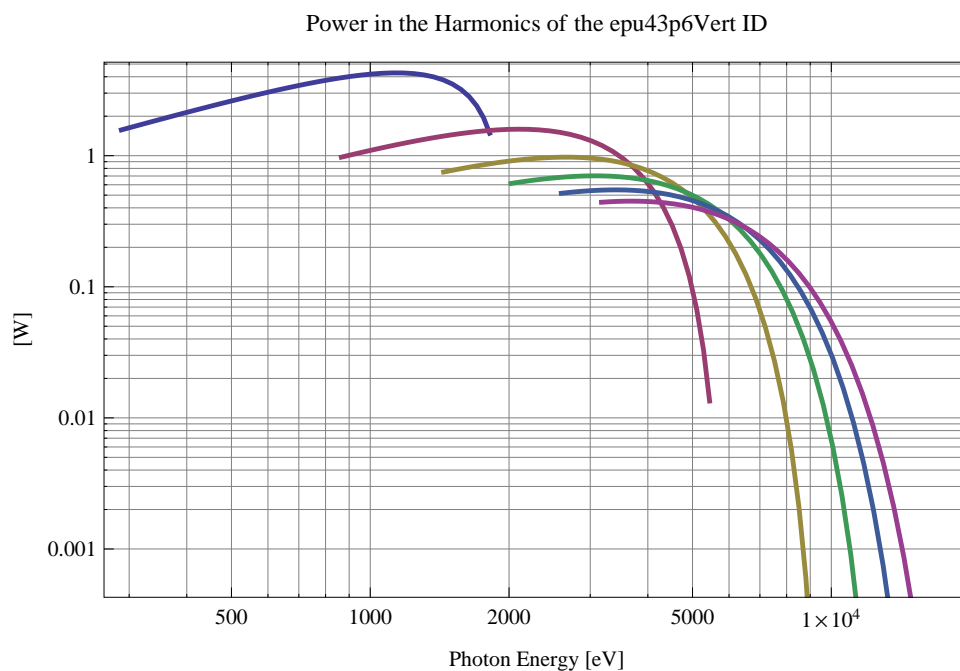


Figure 5.391: The power in the harmonics from the epu43p6Vert ID

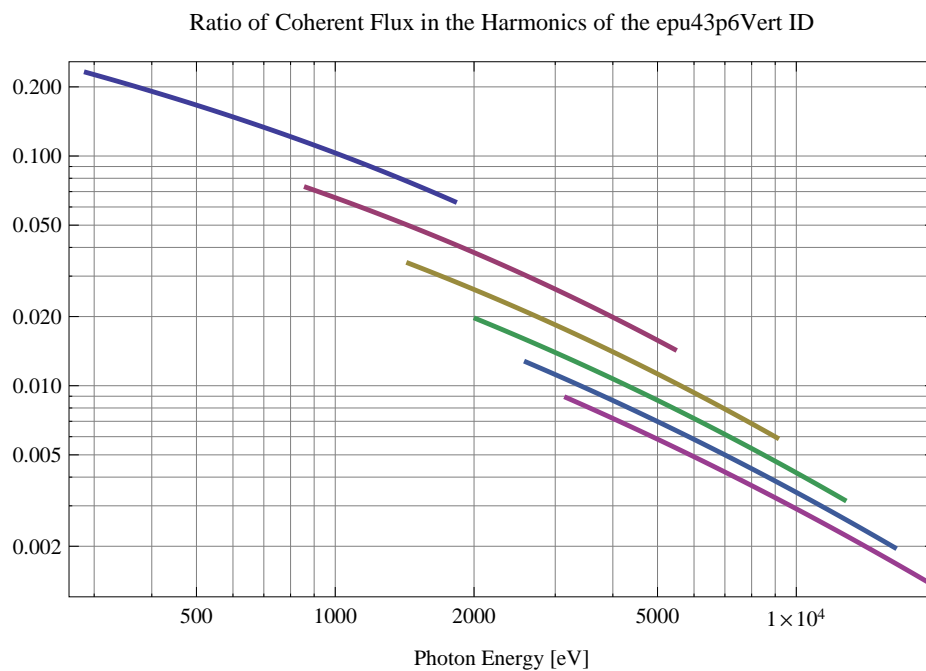


Figure 5.392: The ratio of coherent flux in the harmonics from the epu43p6Vert ID

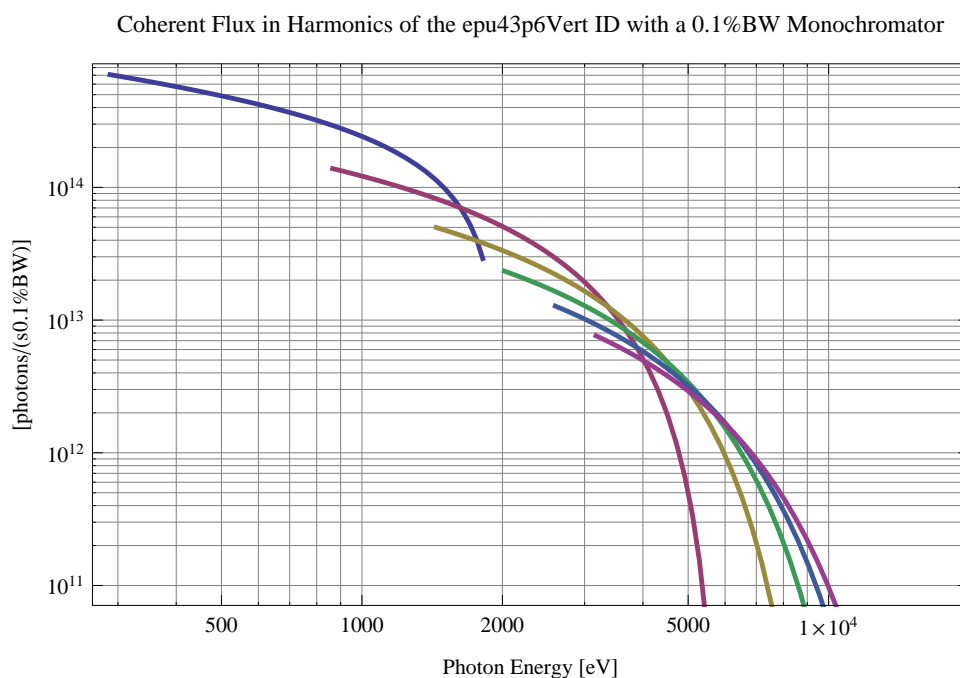


Figure 5.393: The coherent flux in the harmonics of the epu43p6Vert ID using a 0.1%BW Monochromator

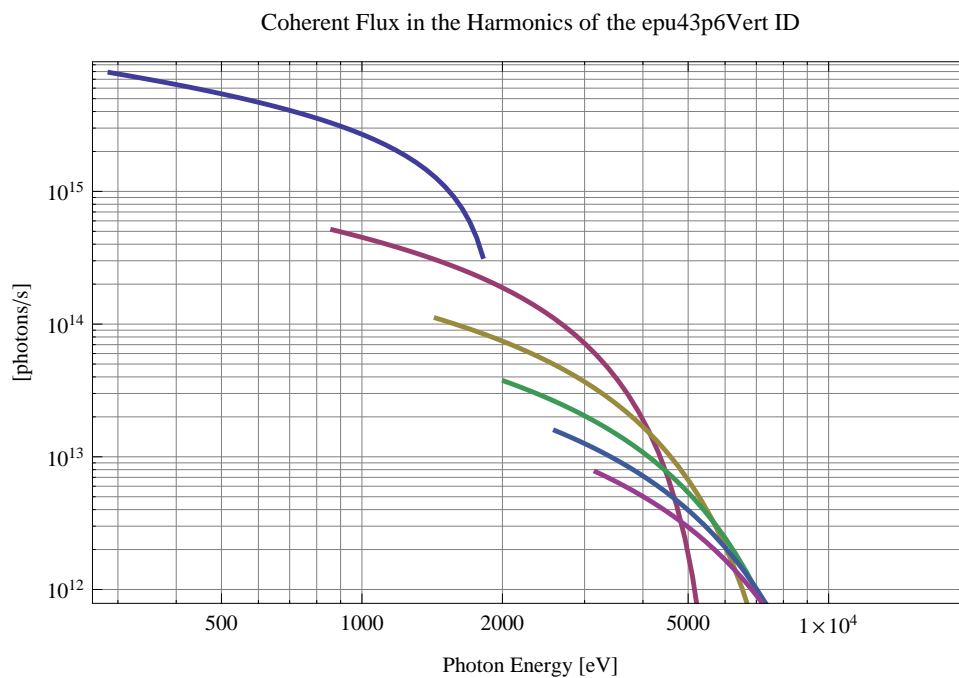


Figure 5.394: The coherent flux in the harmonics of the epu43p6Vert ID

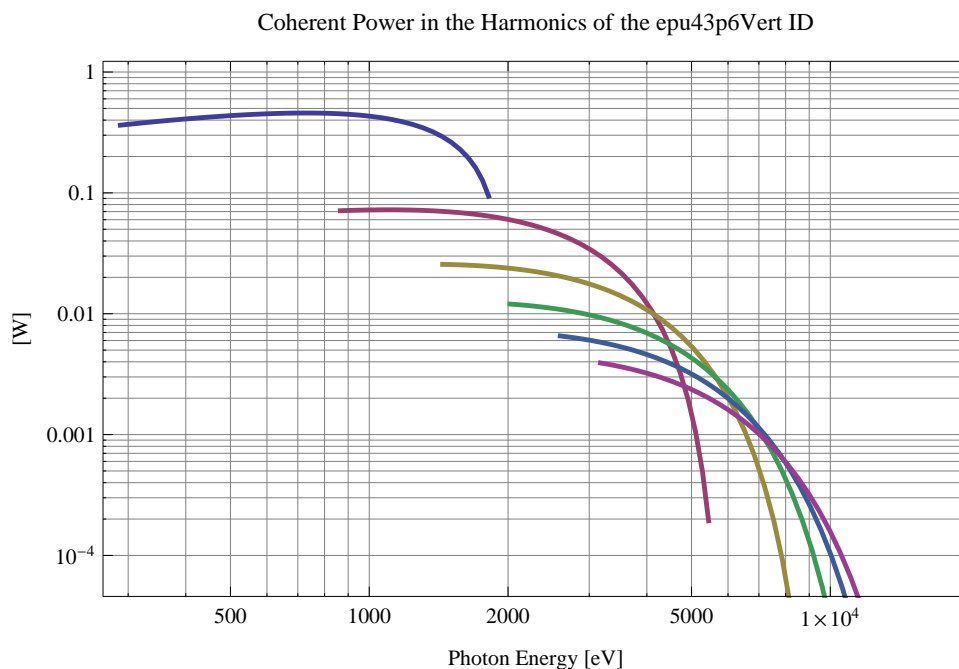


Figure 5.395: The power of coherent synchrotron radiation in the harmonics of the epu43p6Vert ID

Table 5.59: The brilliance at peak energy and the angular spectral flux density from the epu43p6Vert ID for different harmonics at maximum K-value (3.404)

Harmonic	Photon Energy [eV]	Brilliance [Ph./s/mrad <sup>2</sup> /mrad <sup>2</sup> /0.1%BW]	Angular Spectral Flux [Ph./s/mrad <sup>2</sup> /0.1%BW]
1	288.489	$1.53 \times 10^{20}$	$6.06 \times 10^{17}$
3	865.467	$2.7 \times 10^{20}$	$6.97 \times 10^{17}$
5	1442.44	$2.7 \times 10^{20}$	$6.05 \times 10^{17}$
7	2019.42	$2.48 \times 10^{20}$	$5.18 \times 10^{17}$
9	2596.4	$2.24 \times 10^{20}$	$4.46 \times 10^{17}$
11	3173.38	$2. \times 10^{20}$	$3.86 \times 10^{17}$

Table 5.60: The brilliance at peak energy and the angular spectral flux density from the epu43p6Vert ID for different harmonics at minimum K-value (0.4)

Harmonic	Photon Energy [eV]	Brilliance [Ph./s/mrad <sup>2</sup> /mrad <sup>2</sup> /0.1%BW]	Angular Spectral Flux [Ph./s/mrad <sup>2</sup> /0.1%BW]
1	1815.06	$2.49 \times 10^{20}$	$5.33 \times 10^{17}$
3	5445.18	$4.62 \times 10^{18}$	$8.52 \times 10^{15}$
5	9075.31	$5.21 \times 10^{16}$	$9.34 \times 10^{13}$
7	12705.4	$5.46 \times 10^{14}$	$9.71 \times 10^{11}$
9	16335.5	$5.62 \times 10^{12}$	$9.94 \times 10^9$
11	19965.7	$5.74 \times 10^{10}$	$1.01 \times 10^8$

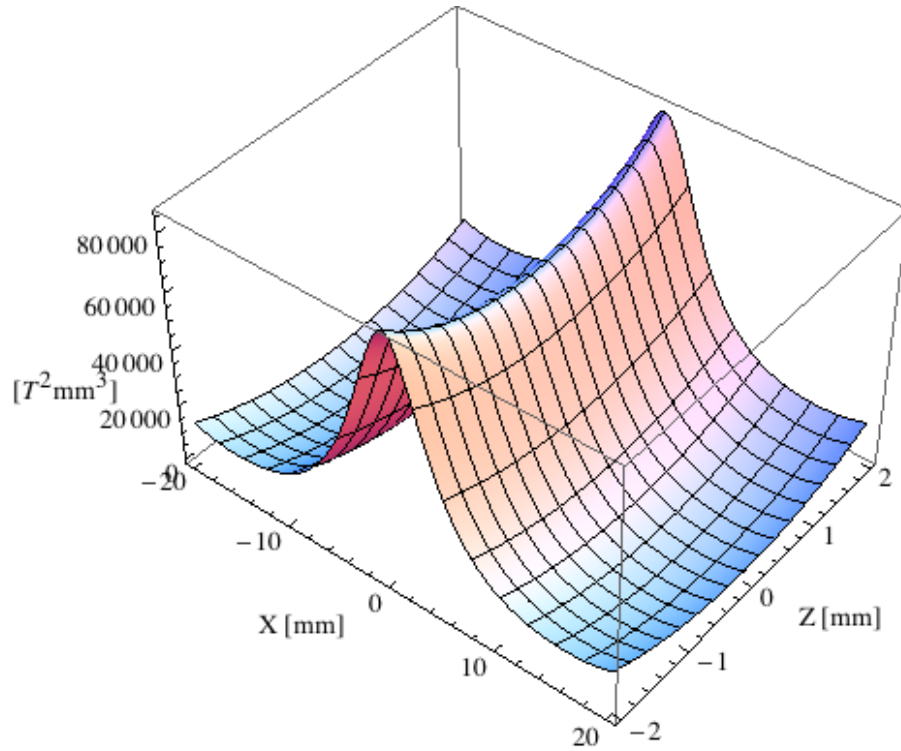


Figure 5.396: Focusing potential from the epu43p6Vert ID over the beam stay clear aperture.

### Influence from the epu43p6Vert ID on the optics of the stored beam

Figure 5.396 shows the focusing potential from the epu43p6Vert over the beam stay clear aperture of the ring aperture.

Figure 5.397 shows the kick map in the beam energy independent unit  $T^2 m^2$  of the kicks induced by the epu43p6Vert ID over the beam stay clear aperture.

Figure 5.398 shows the induced angular kick on the stored beam from the epu43p6Vert ID as a function of the vertical distance to the axis of the ID.

Figure 5.399 shows the induced angular kick on the stored beam from the epu43p6Vert ID as a function of the horizontal distance to the axis of the ID.

Figure 5.400 shows tune shift induced by the epu43p6Vert ID over the beam stay clear aperture. Note that the tune shift depends on the beam size at the ID.

Figure 5.401 shows the induced tune shift from the epu43p6Vert ID as a function of the vertical distance to the axis of the ID.

Figure 5.402 shows the induced tune shift from the epu43p6Vert ID as a function of the horizontal distance to the axis of the ID.

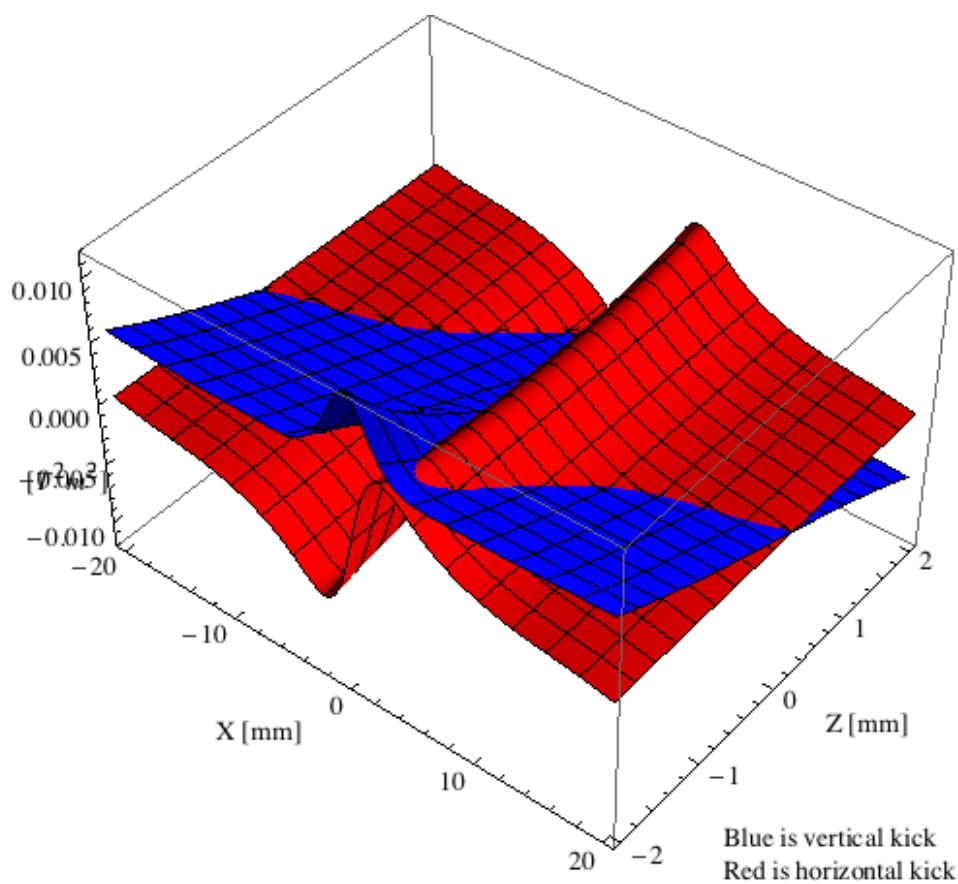


Figure 5.397: Kick map in the beam energy independent unit  $T^2m^2$  of the kicks induced by the epu43p6Vert ID over the beam stay clear aperture.

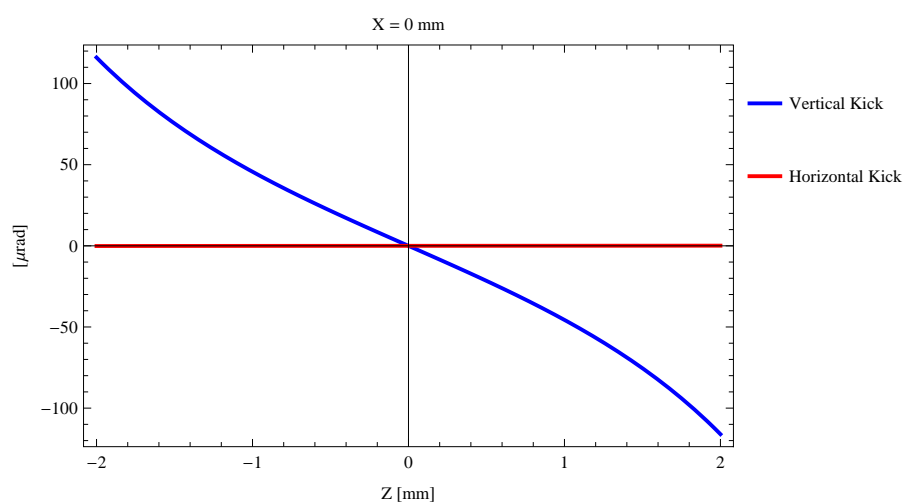


Figure 5.398: Induced angular kick on the stored beam from the epu43p6Vert ID as a function of the vertical distance to the ID axis.



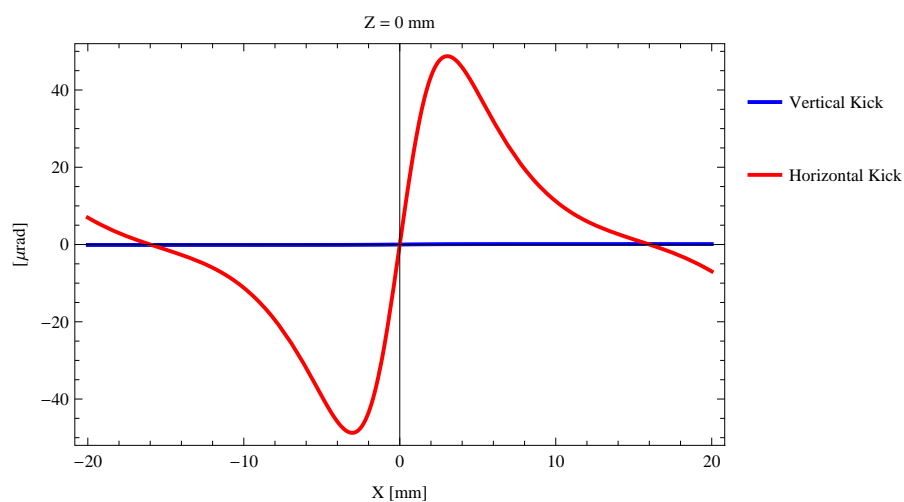


Figure 5.399: Induced angular kick on the stored beam from the epu43p6Vert ID as a function of the horizontal distance to the ID axis.

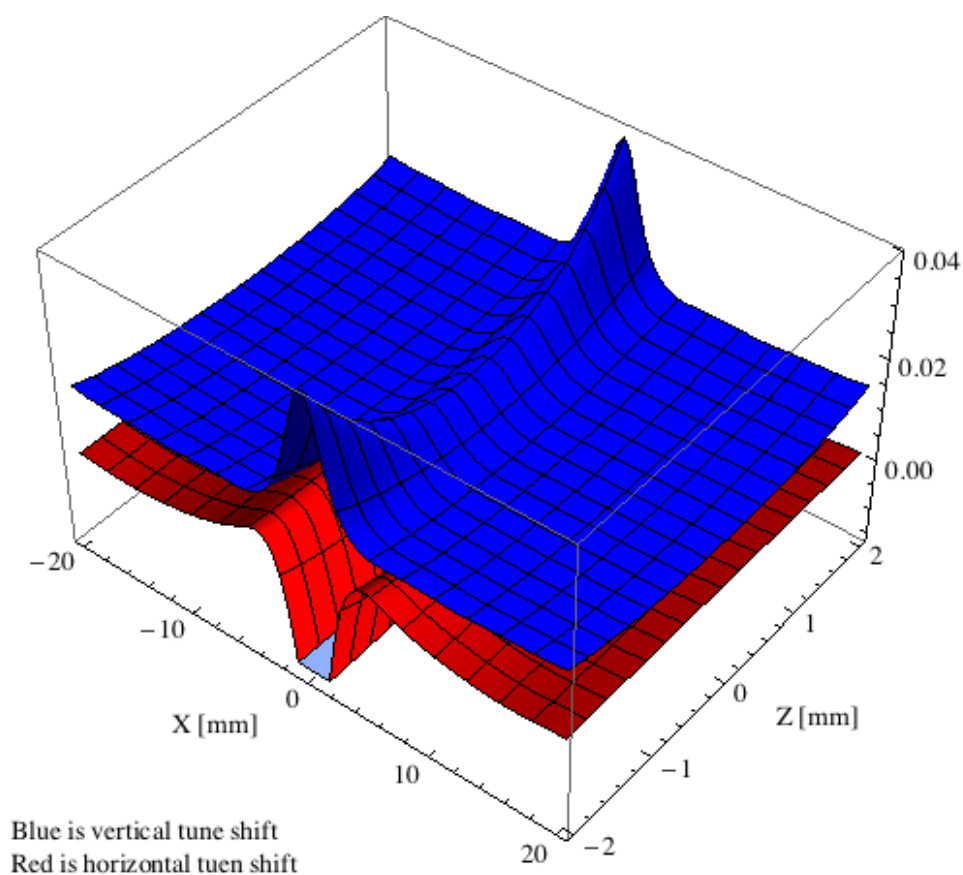


Figure 5.400: Tune shift induced by the epu43p6Vert ID over the beam stay clear aperture.

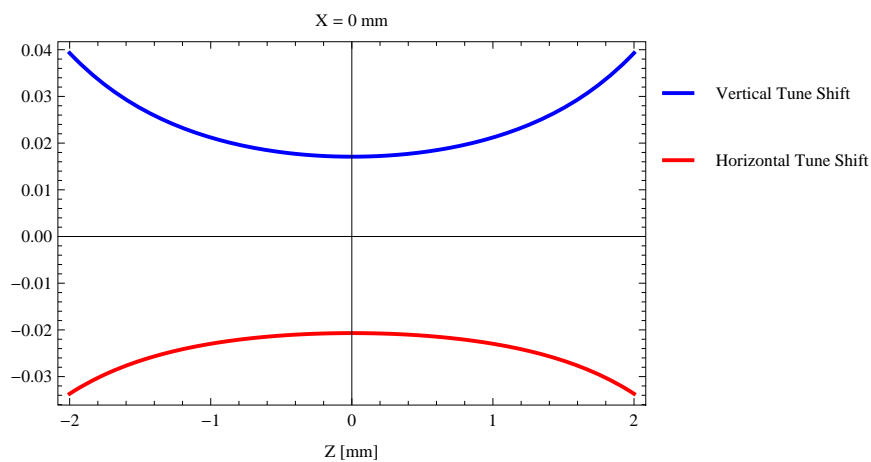


Figure 5.401: Induced tune shift from the epu43p6Vert ID as a function of the vertical distance to the axis of the ID.

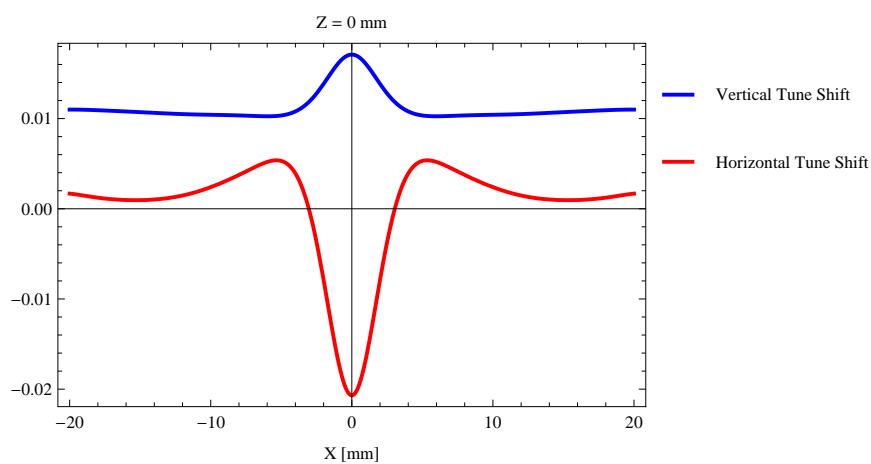


Figure 5.402: Induced tune shift from the epu43p6Vert ID on the stored beam from the ID as a function of the horizontal distance to the axis of the ID.

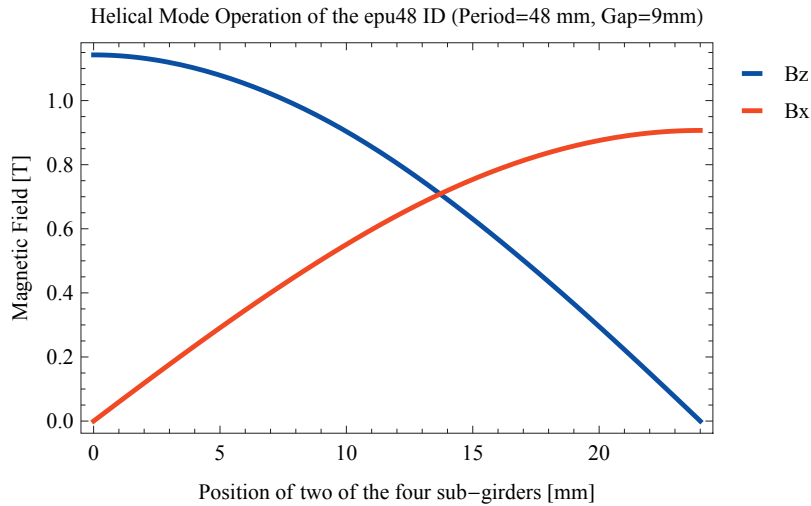


Figure 5.403: Vertical and horizontal magnetic field for the the epu48 ID when operating in the helical mode for different positions for two of the four sub-girders

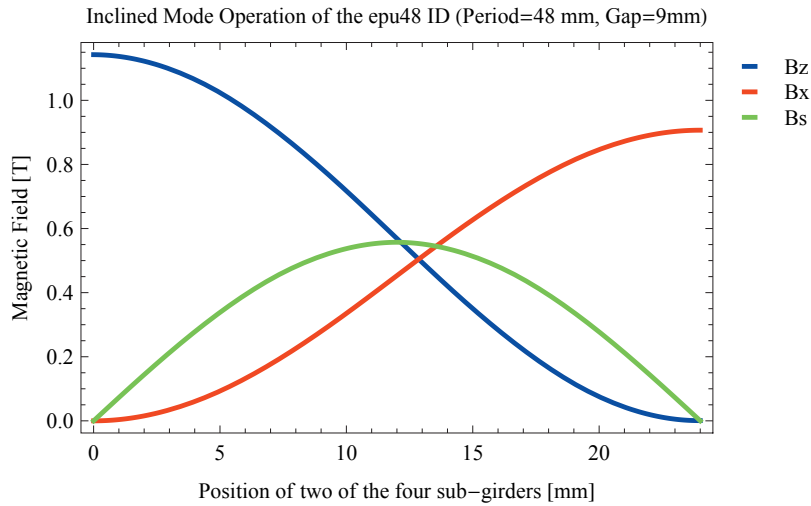


Figure 5.404: Vertical, horizontal, and longitudinal magnetic field for the the epu48 ID when operating in the inclined mode for different positions for two of the four sub-girders

### 5.3.9. The elliptically polarising undulator epu48

#### Modes of operation in the elliptically polarising undulator epu48

Horizontal polarisation of the emitted synchrotron radiation from the epu48 ID (Period=48 mm, Gap=9mm) is found in the planar mode when there is no movement of the sub-girders.

Circular polarisation is found in the elliptical mode of operation for a symmetric sub-grider movement of 13.7071 mm. Figure 5.403 shows the vertical and horizontal magnetic field for the epu48 ID when operating in the helical mode.

45 degree polarisation is found in the inclined mode of operation for an assymetric sub-grider movement of 12.8612 mm. Figure 5.404 shows the vertical and horizontal magnetic field for the epu48 ID when operating in the inclined mode.

The following sub-sections will cover four different situations: The epu48 operating in the pla-

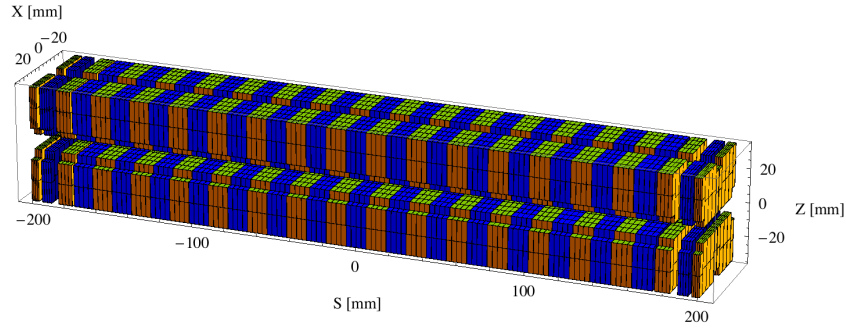


Figure 5.405: Magnetic model of the epu48Plan ID. The ID has been modelled with Radia [2]

nar mode for horizontal polarisation (epu48Plan); The epu48 operating in the helical mode for circular polarisation (epu48Heli), the epu48 operating in the inclined mode for 45 degree polarisation (epu48Incl); and The epu48 operating in the vertical mode for vertical polarisation (epu48Vert).

### Magnet model of the elliptically polarising undulator epu48Plan

The Radia [2] magnet model of the epu48Plan ID is shown in Figure 5.405. The length of the magnet model is 401.496 mm. The magnetic material in the model is NdFeb with a remanence of 1.28 T, a material similar to VACODYM 776 TP from Vacuumschmelze. Blocks with vertical magnetisation are blue and blocks with horizontal magnetisation are yellow. The block size is 30.x30.x12. mm<sup>3</sup> and there is a 5. mm cut-out in two of the corners of the blocks. The total length of the epu48Plan ID is 3905.5 mm.

### Analysis of the magnetic field of the epu48Plan ID

The effective magnetic fields on axis and the fundamental photon energy of the epu48Plan ID are shown in Table 5.61. The higher harmonic contents in the magnetic field of an elliptically polarising undulator made of permanent magnets is negligible and the efficient field has about the same strength as the peak field.

### Synchrotron radiation from the epu48Plan ID

The power map of the emitted synchrotron radiation by the epu48Plan ID, assuming a 0.5 A filament beam with an energy of 3 GeV and undulator properties of the synchrotron radiation, is shown in Figure 5.409. The on-axis power density is 40.045 kW/mrad<sup>2</sup>

A map of the degree of linear polarisation of the fundamental harmonic of the synchrotron radiation emitted by the epu48Plan ID over the angle of observation is shown in Figure 5.410.

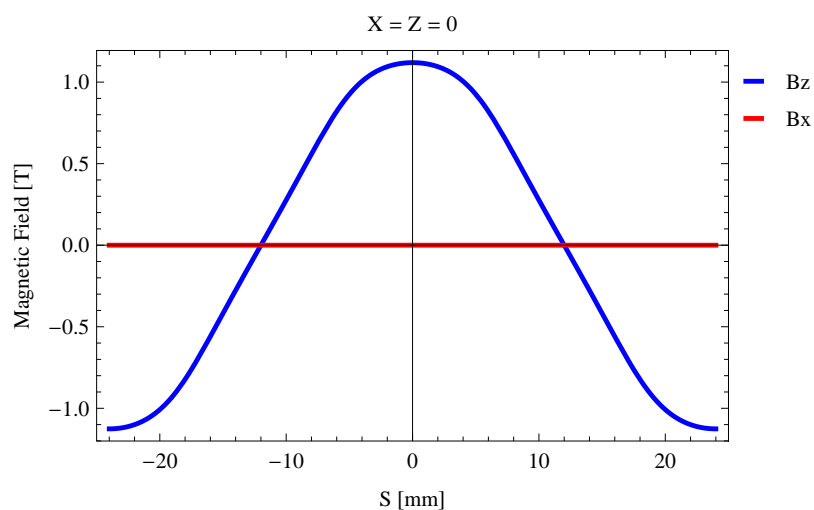
A map of the degree of 45 degree polarisation of the fundamental harmonic of the synchrotron radiation emitted by the epu48Plan ID over the angle of observation is shown in Figure 5.411.

A map of the degree of circular polarisation of the fundamental harmonic of the synchrotron radiation emitted by the epu48Plan ID over the angle of observation is shown in Figure 5.412.

The on axis brilliance at peak energy, the angular spectral flux, the flux in the harmonics, the power in the harmonics, the ratio of coherence, the coherent flux in the harmonics, and the

Table 5.61: Effective Fields on axis and Fundamental Photon Energy of the epu48Plan ID

Undulator Period	48	mm
Undulator Gap	9	mm
Undulator Mode	Planar	
Undulator Phase	0.000	mm
Vertical Peak Field	1.119	T
Efficient Vertical Field	1.143	T
Kx (from vert. field)	5.124	
Horizontal Peak Field:	0.000	T
Efficient Horizontal Field	0.000	T
Kz (from hor. field)	0.000	
Photon Energy, Harm.1	0.126	keV
Emitted Power	14.527	kW
Total Length	3905.5	mm

Figure 5.406: Vertical magnetic field in a central pole of the epu48Plan ID along the ID axis,  $X = Z = 0$

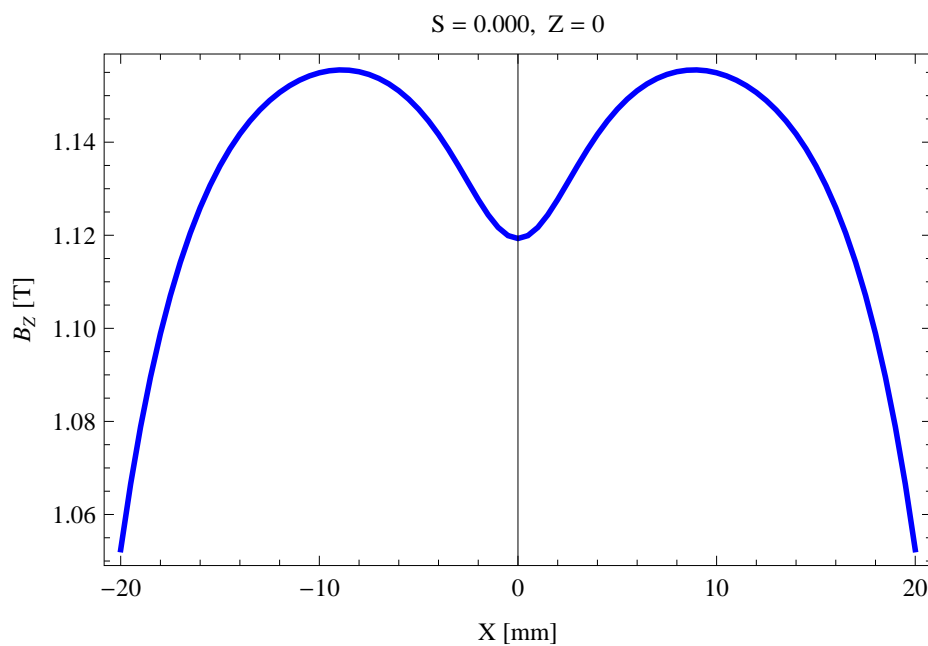


Figure 5.407: Vertical magnetic field in a central pole of the epu48Plan ID along the horizontally transverse direction to the ID axis,  $S = 0.000$ ,  $Z = 0$

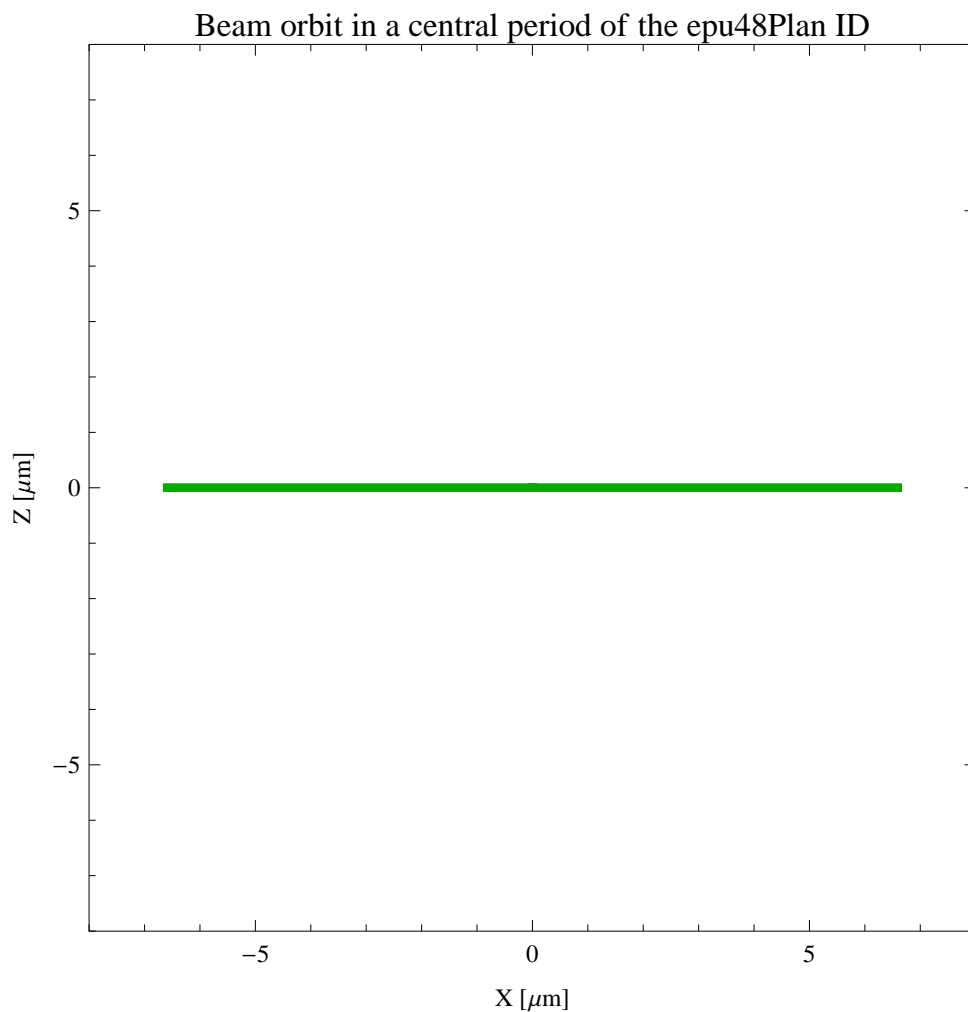


Figure 5.408: The beam orbit of the electron beam through a central period of the epu48Plan ID

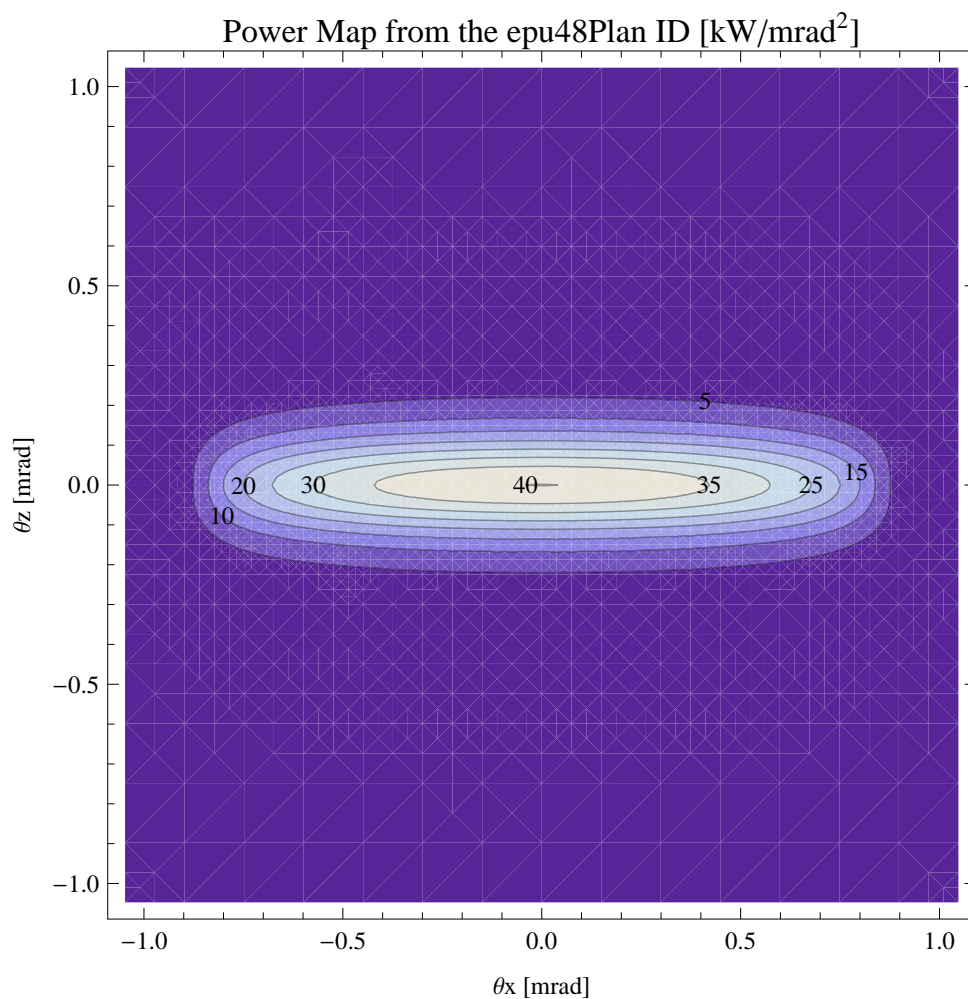


Figure 5.409: Map of the power distribution of the emitted synchrotron radiation by the epu48Plan ID

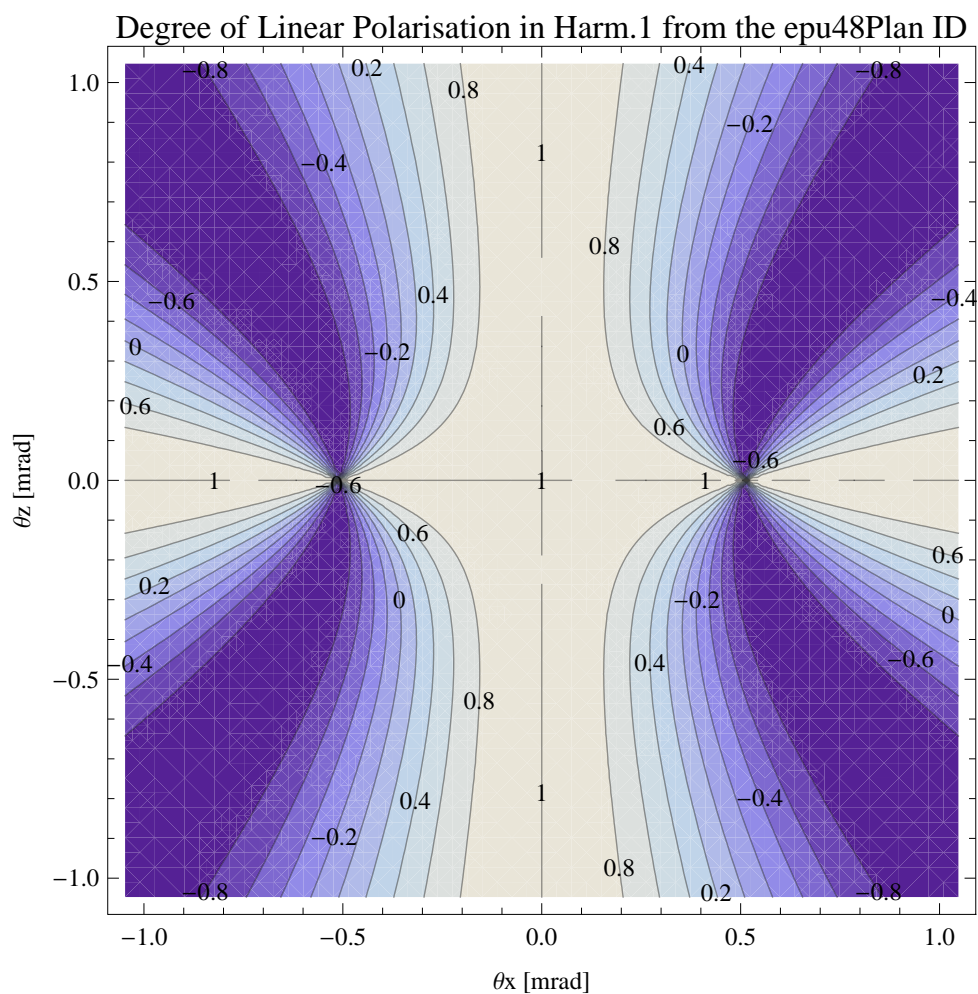


Figure 5.410: Map of linear polarisation in the fundamental harmonic of the synchrotron radiation emitted by the epu48Plan ID



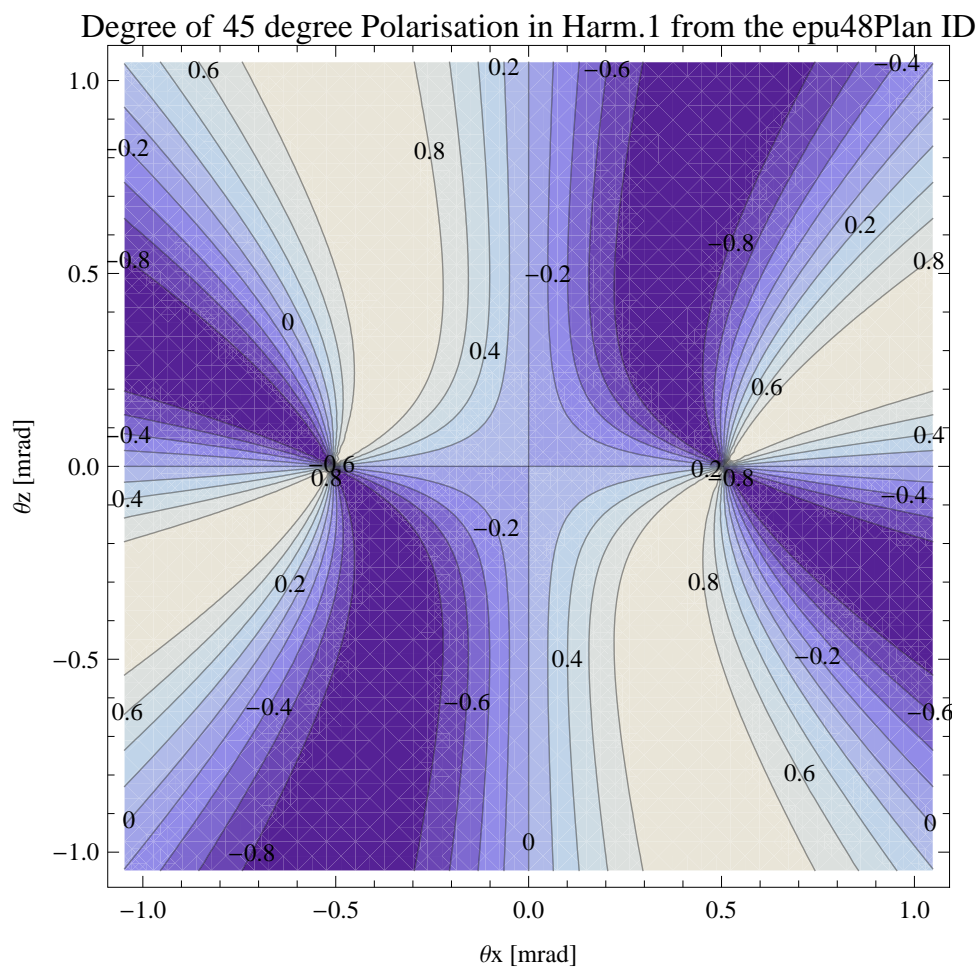


Figure 5.411: Map of 45 degree polarisation in the fundamental harmonic of the synchrotron radiation emitted by the epu48Plan ID

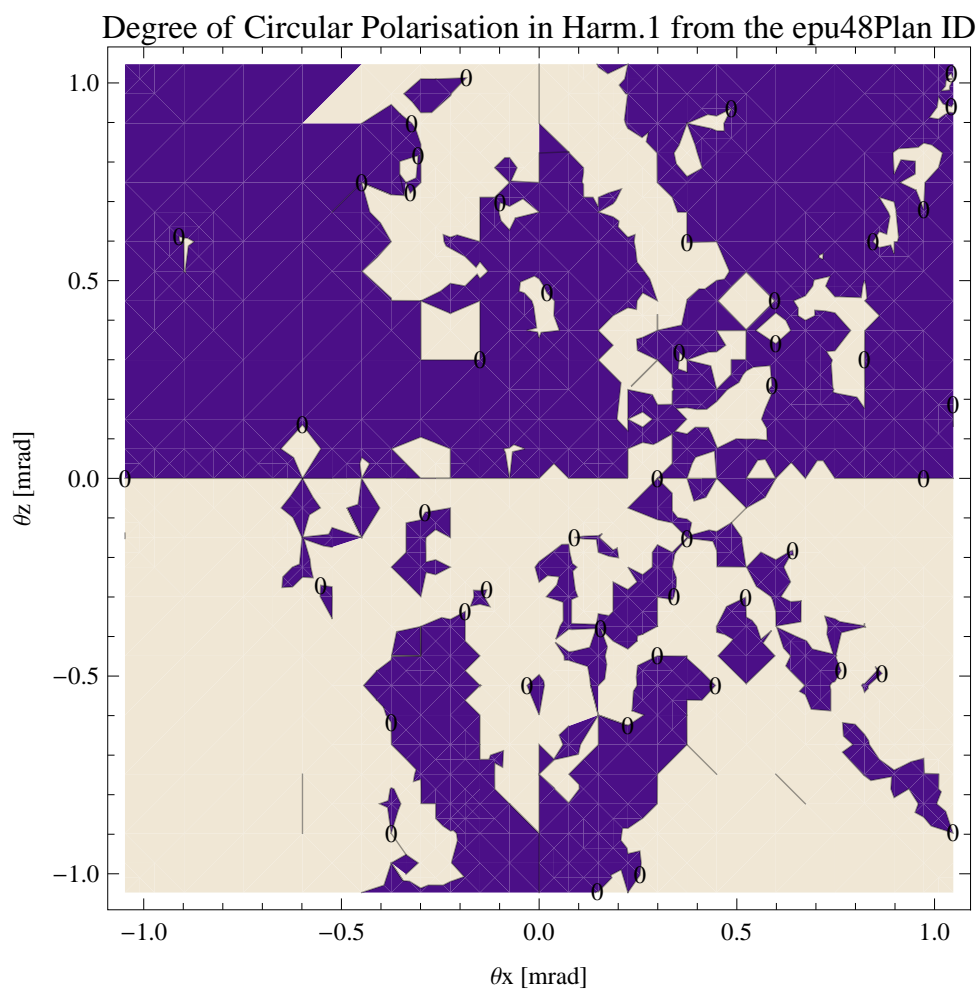


Figure 5.412: Map of circular polarisation in the fundamental harmonic of the synchrotron radiation emitted by the epu48Plan ID

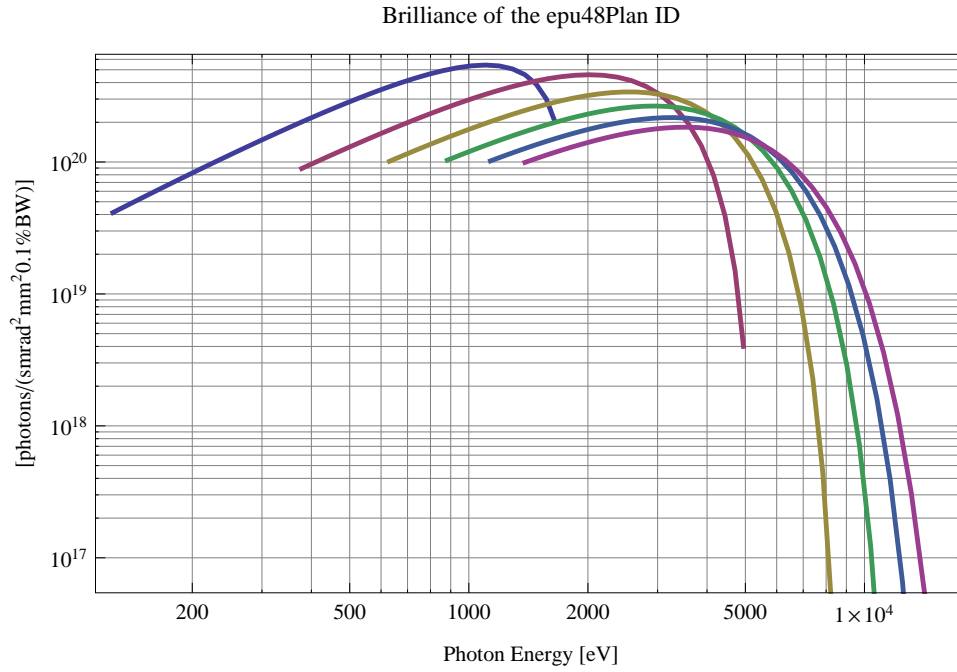


Figure 5.413: The brilliance at peak energy from the epu48Plan ID

power of coherent radiation in the harmonics from the epu48Plan ID have been calculated and the resulting plots are found in this section of the document. The beam parameters used for the calculation are 0.5 A of stored current,  $\beta_H = 9$  m,  $\varepsilon_H = 0.263$  nmrad,  $\beta_V = 4.8$  m,  $\varepsilon_V = 8$  pmrad, and an energy spread of 0.001.

The brilliance at peak energy and the angular spectral flux density from the epu48Plan ID for different harmonics at maximum K-value (5.124) are given in Table 5.62 and for minimum K-value (0.400) these values are given in Table 5.63.

Table 5.62: The brilliance at peak energy and the angular spectral flux density from the epu48Plan ID for different harmonics at maximum K-value (5.124)

Harmonic	Photon Energy [eV]	Brilliance [Ph./s/mrad <sup>2</sup> /mrad <sup>2</sup> /0.1%BW]	Angular Spectral Flux [Ph./s/mrad <sup>2</sup> /0.1%BW]
1	126.021	$4.14 \times 10^{19}$	$2.46 \times 10^{17}$
3	378.062	$8.92 \times 10^{19}$	$3.13 \times 10^{17}$
5	630.104	$1.01 \times 10^{20}$	$2.92 \times 10^{17}$
7	882.146	$1.03 \times 10^{20}$	$2.67 \times 10^{17}$
9	1134.19	$1.02 \times 10^{20}$	$2.45 \times 10^{17}$
11	1386.23	$9.93 \times 10^{19}$	$2.27 \times 10^{17}$

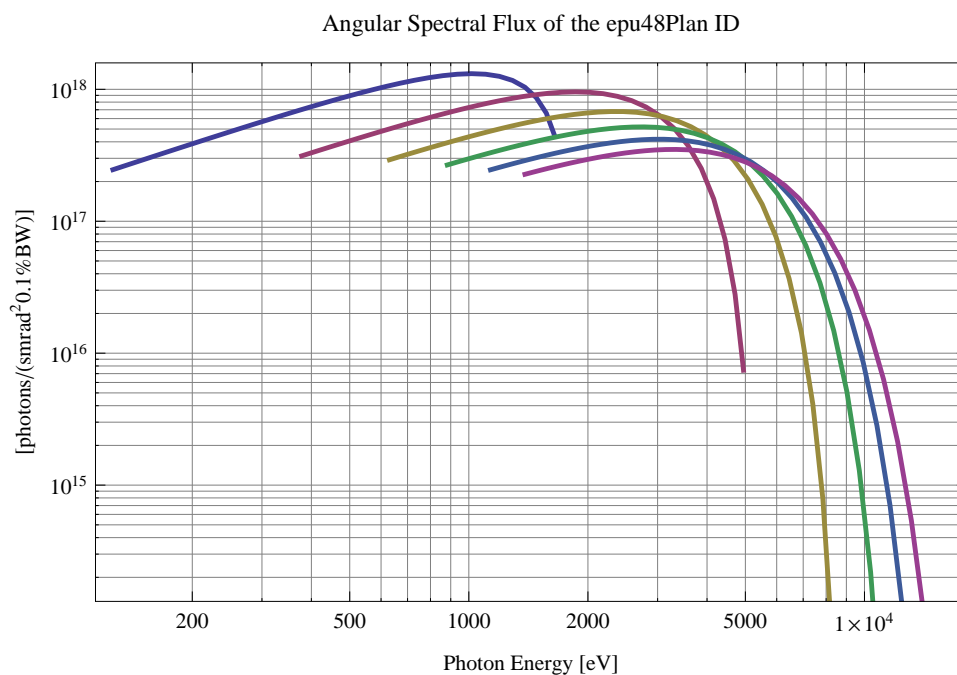


Figure 5.414: The angular spectral flux from the epu48Plan ID

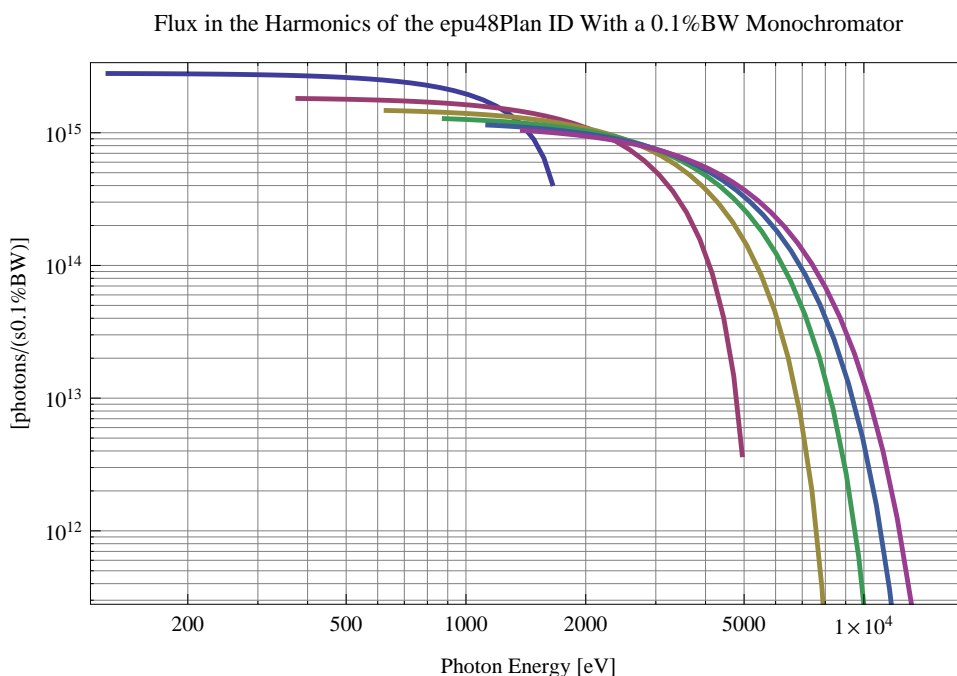


Figure 5.415: The flux of photons in the harmonics from the epu48Plan ID using a 0.1%BW monochromator

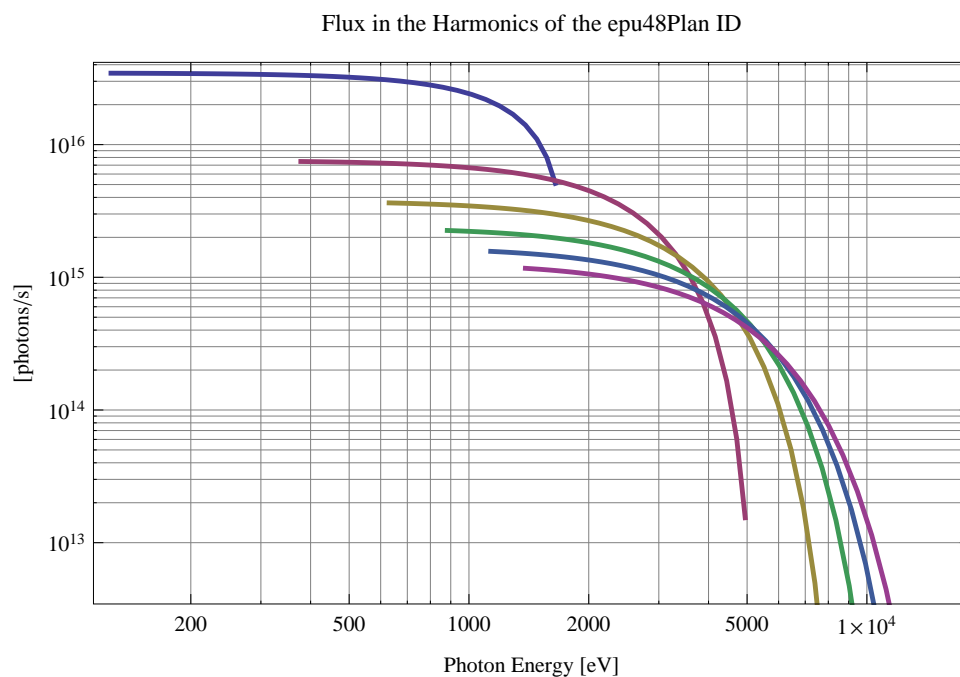


Figure 5.416: The flux of photons in the harmonics from the epu48Plan ID

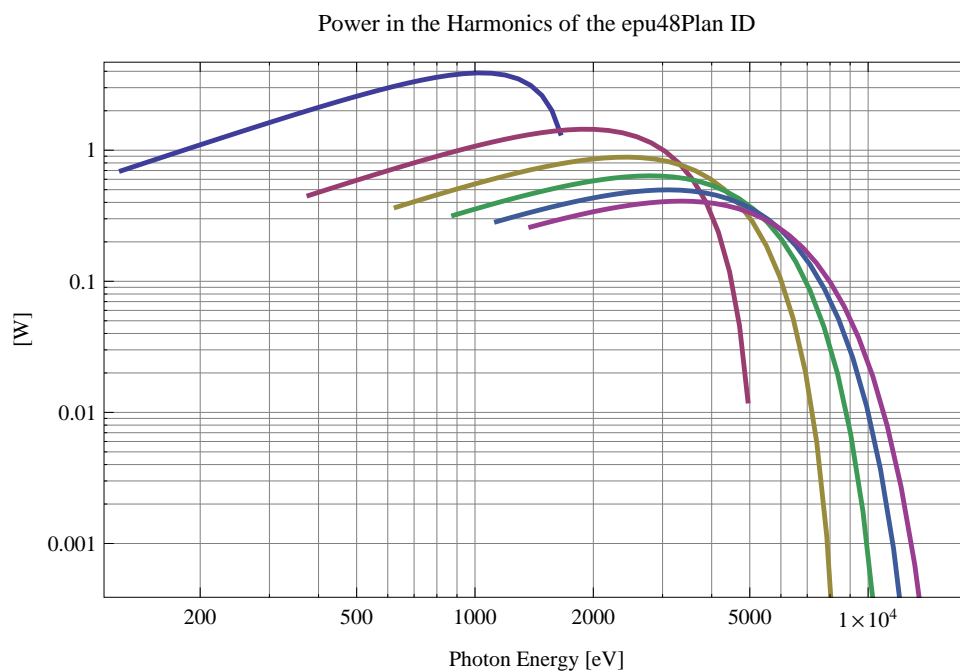


Figure 5.417: The power in the harmonics from the epu48Plan ID

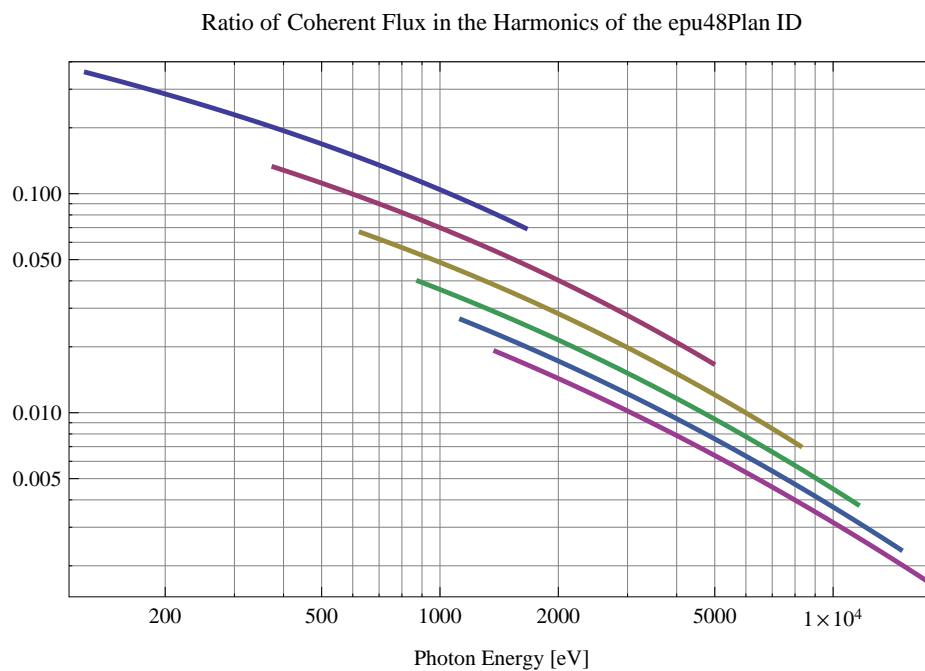


Figure 5.418: The ratio of coherent flux in the harmonics from the epu48Plan ID

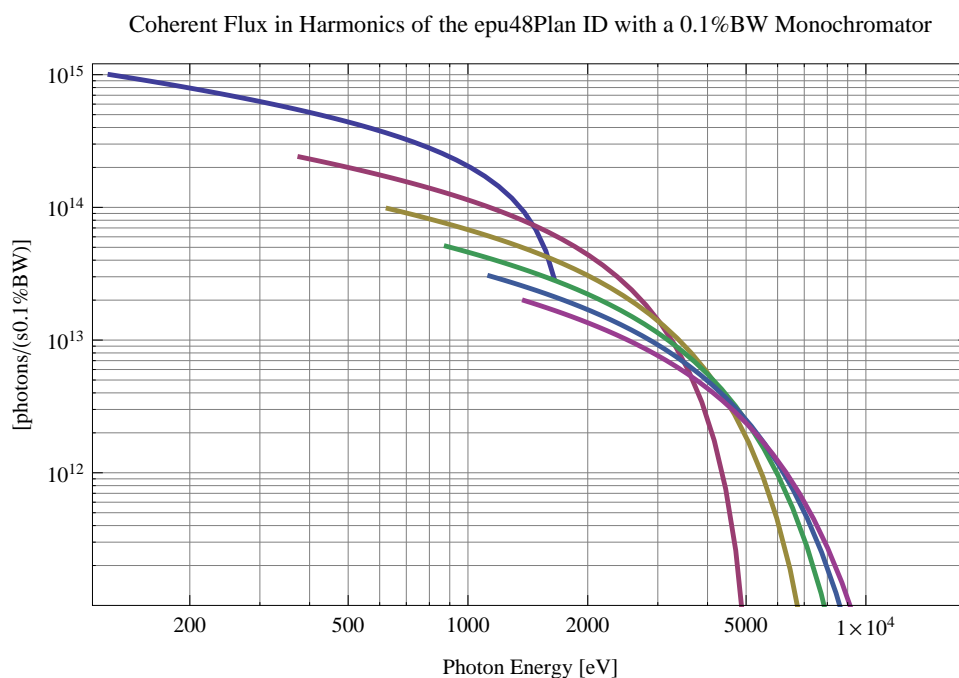


Figure 5.419: The coherent flux in the harmonics of the epu48Plan ID using a 0.1%BW Monochromator

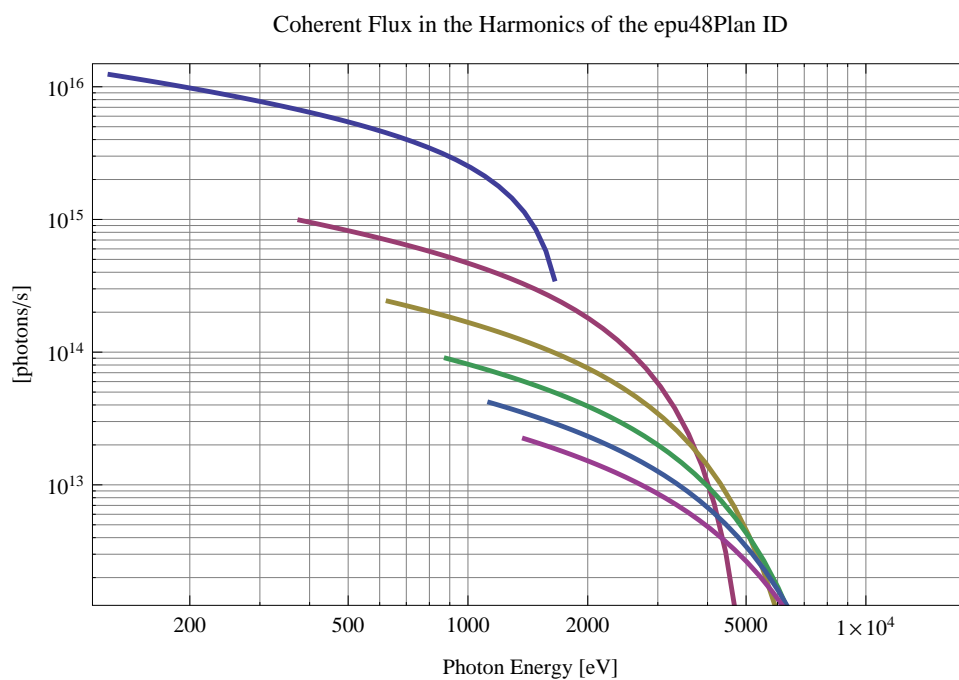


Figure 5.420: The coherent flux in the harmonics of the epu48Plan ID

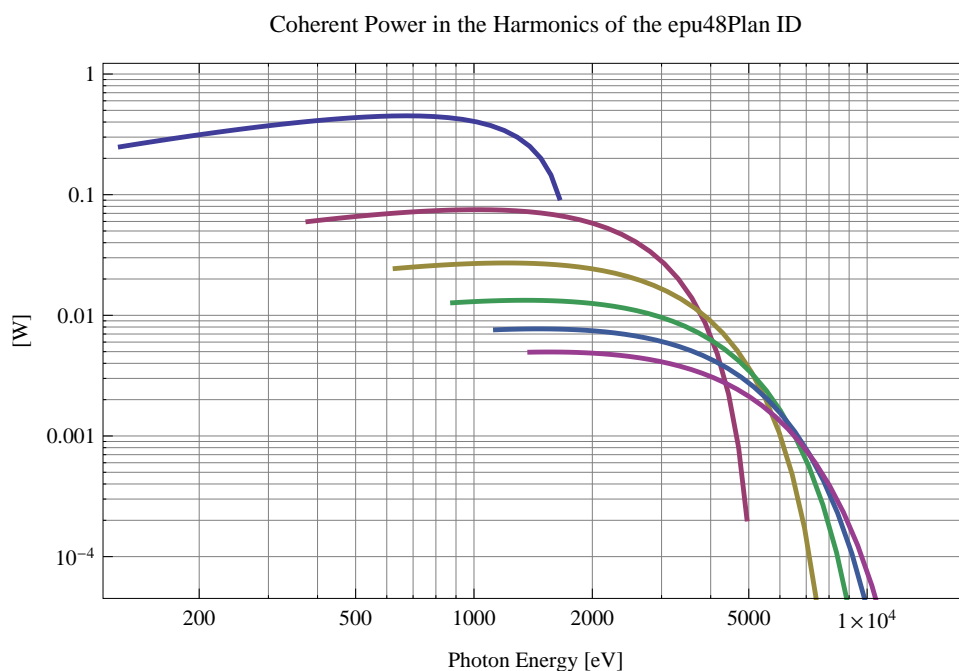


Figure 5.421: The power of coherent synchrotron radiation in the harmonics of the epu48Plan ID

Table 5.63: The brilliance at peak energy and the angular spectral flux density from the epu48Plan ID for different harmonics at minimum K-value (0.4)

Harmonic	Photon Energy [eV]	Brilliance [Ph./s/mrad <sup>2</sup> /mrad <sup>2</sup> /0.1%BW]	Angular Spectral Flux [Ph./s/mrad <sup>2</sup> /0.1%BW]
1	1648.68	$2.04 \times 10^{20}$	$4.43 \times 10^{17}$
3	4946.04	$4. \times 10^{18}$	$7.43 \times 10^{15}$
5	8243.4	$4.6 \times 10^{16}$	$8.27 \times 10^{13}$
7	11540.8	$4.86 \times 10^{14}$	$8.64 \times 10^{11}$
9	14838.1	$5.02 \times 10^{12}$	$8.88 \times 10^9$
11	18135.5	$5.13 \times 10^{10}$	$9.06 \times 10^7$



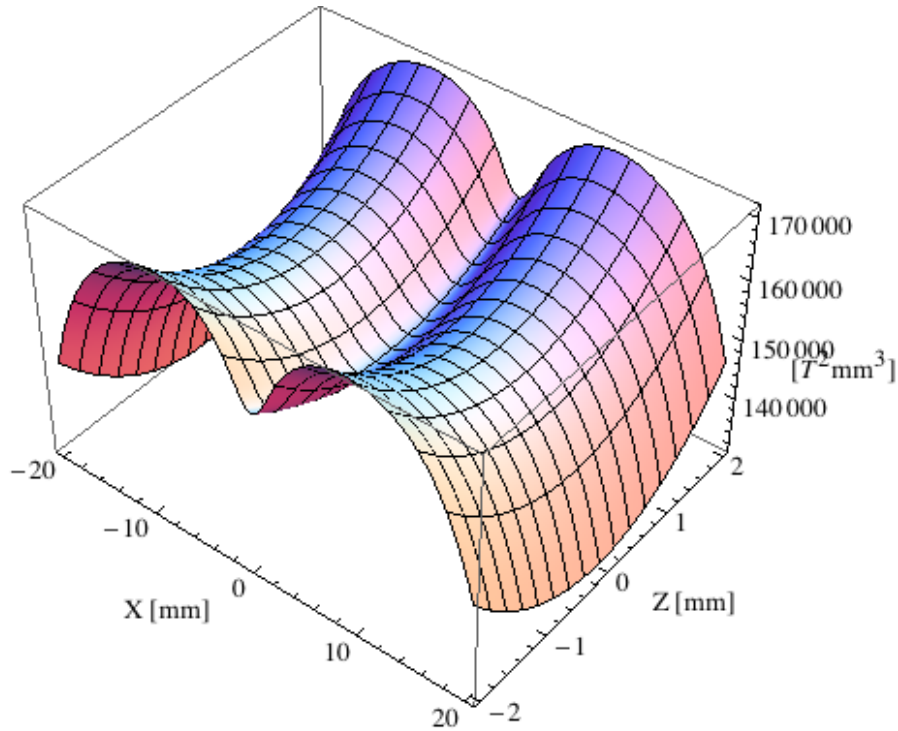


Figure 5.422: Focusing potential from the epu48Plan ID over the beam stay clear aperture.

### Influence from the epu48Plan ID on the optics of the stored beam

Figure 5.422 shows the focusing potential from the epu48Plan over the beam stay clear aperture of the ring aperture.

Figure 5.423 shows the kick map in the beam energy independant unit  $T^2 m^2$  of the kicks induced by the epu48Plan ID over the beam stay clear aperture.

Figure 5.424 shows the induced angular kick on the stored beam from the epu48Plan ID as a function of the vertical distance to the axis of the ID.

Figure 5.425 shows the induced angular kick on the stored beam from the epu48Plan ID as a function of the horizontal distance to the axis of the ID.

Figure 5.426 shows tune shift induced by the epu48Plan ID over the beam stay clear aperture. Note that the tune shift depends on the beam size at the ID.

Figure 5.427 shows the induced tune shift from the epu48Plan ID as a function of the vertical distance to the axis of the ID.

Figure 5.428 shows the induced tune shift from the epu48Plan ID as a function of the horizontal distance to the axis of the ID.

### Magnet model of the elliptically polaraising undulator epu48Heli

The Radia [2] magnet model of the epu48Heli ID is shown in Figure 5.429. The length of the magnet model is 401.496 mm. The magnetic material in the model is NdFeb with a remanence of 1.28 T, a material similar to VACODYM 776 TP from Vacuumschmelze. Blocks with vertical magnetisation are blue and blocks with horizontal magnetisation are yellow. The block size is

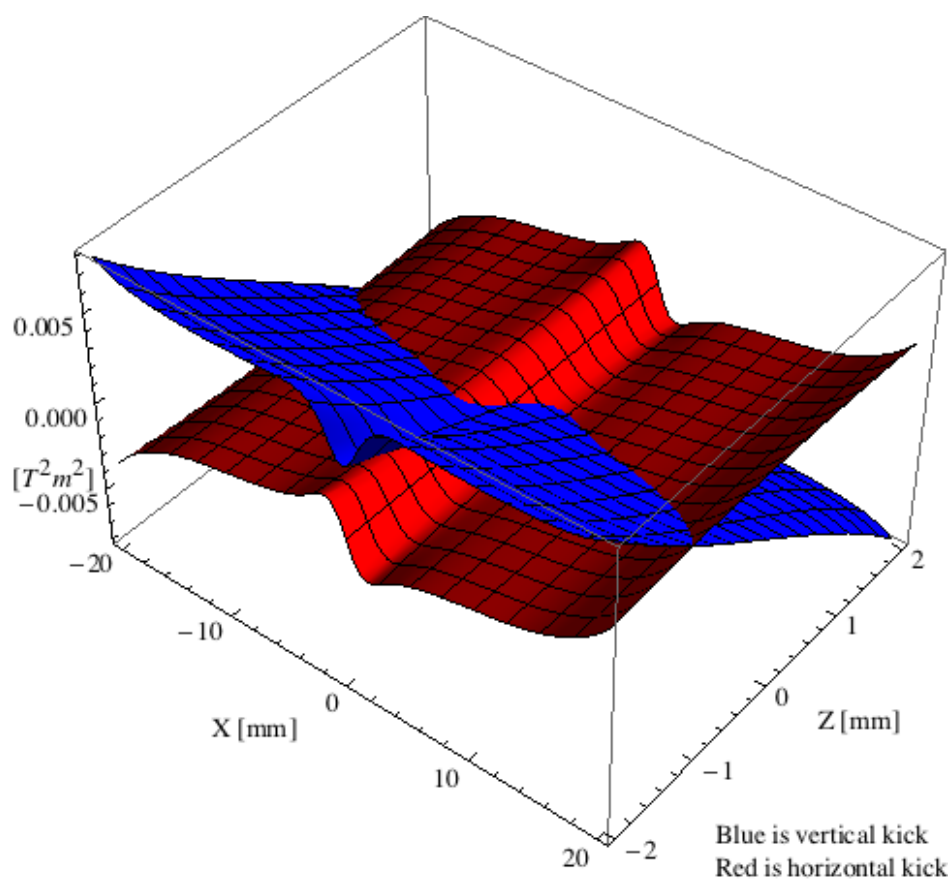


Figure 5.423: Kick map in the beam energy independent unit  $T^2m^2$  of the kicks induced by the epu48Plan ID over the beam stay clear aperture.

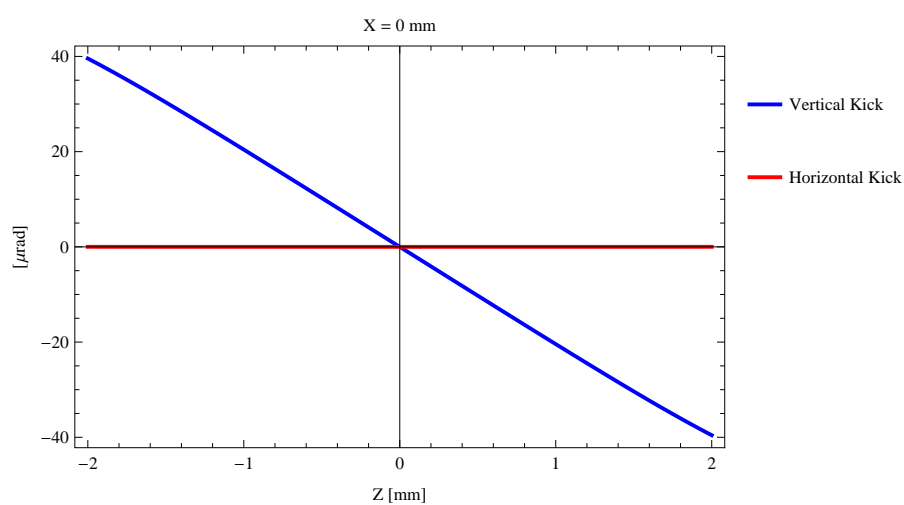


Figure 5.424: Induced angular kick on the stored beam from the epu48Plan ID as a function of the vertical distance to the ID axis.

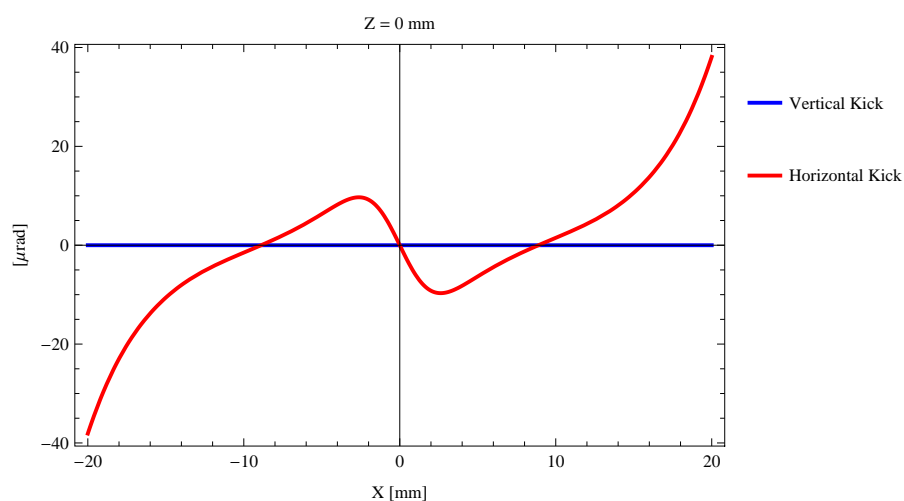


Figure 5.425: Induced angular kick on the stored beam from the epu48Plan ID as a function of the horizontal distance to the ID axis.

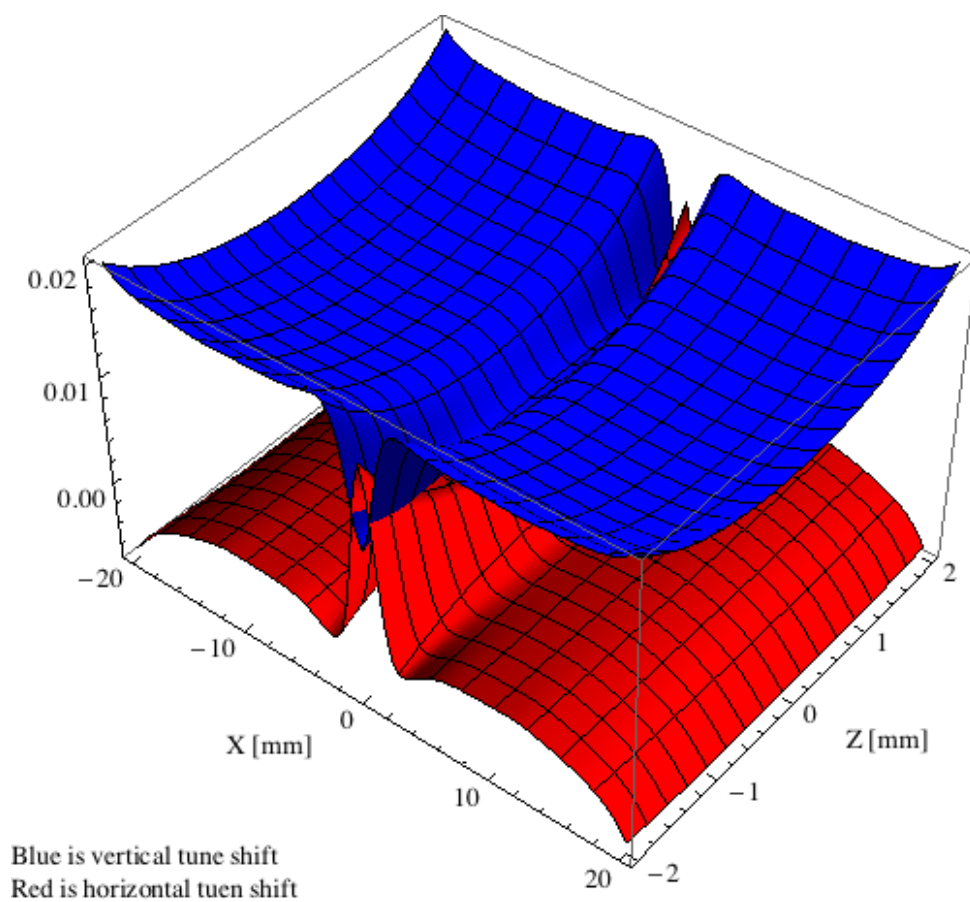


Figure 5.426: Tune shift induced by the epu48Plan ID over the beam stay clear aperture.

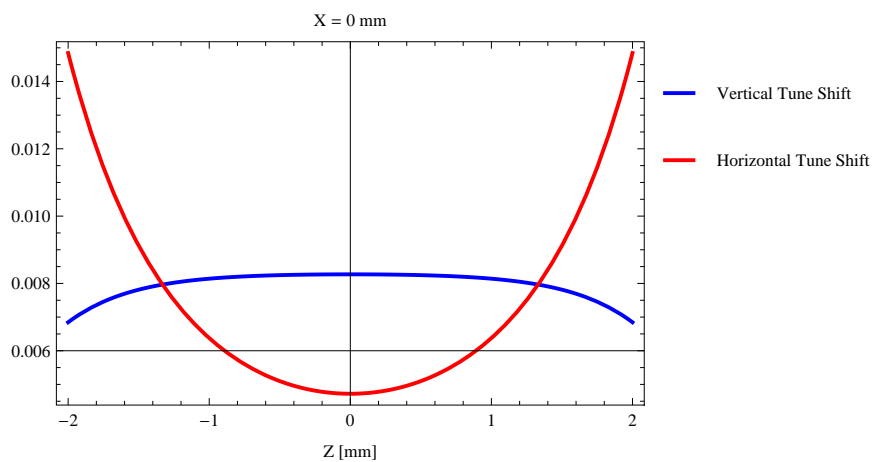


Figure 5.427: Induced tune shift from the epu48Plan ID as a function of the vertical distance to the axis of the ID.

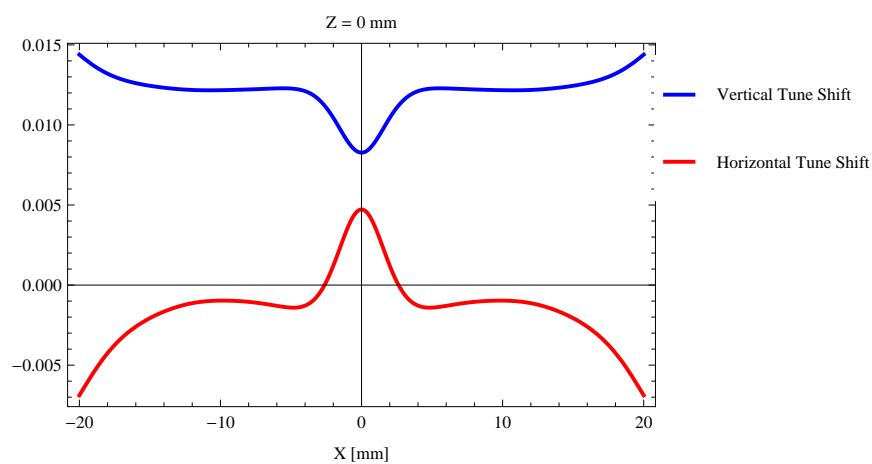


Figure 5.428: Induced tune shift from the epu48Plan ID on the stored beam from the ID as a function of the horizontal distance to the axis of the ID.

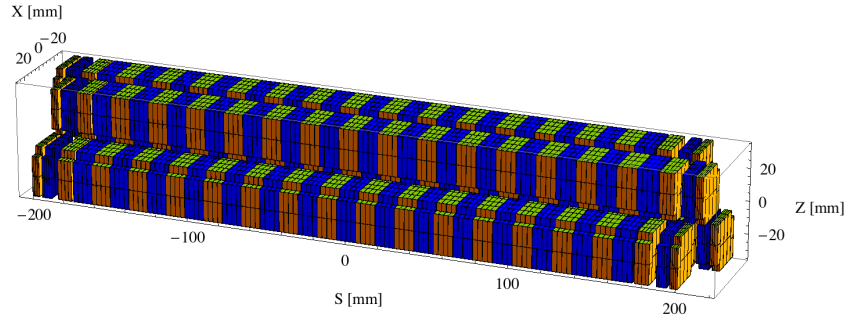


Figure 5.429: Magnetic model of the epu48Heli ID. The ID has been modelled with Radia [2]

$30 \times 30 \times 12 \text{ mm}^3$  and there is a 5. mm cut-out in two of the corners of the blocks. The total length of the epu48Heli ID is 3905.5 mm.

### Analysis of the magnetic field of the epu48Heli ID

The effective magnetic fields on axis and the fundamental photon energy of the epu48Heli ID are shown in Table 5.64. The higher harmonic contents in the magnetic field of an elliptically polarising undulator made of permanent magnets is negligible and the efficient field has about the same strength as the peak field.

Table 5.64: Effective Fields on axis and Fundamental Photon Energy of the epu48Heli ID

Undulator Period	48	mm
Undulator Gap	9	mm
Undulator Mode	Helical	
Undulator Phase	13.707	mm
Vertical Peak Field	0.710	T
Efficient Vertical Field	0.709	T
K <sub>x</sub> (from vert. field)	3.179	
Horizontal Peak Field:	0.715	T
Efficient Horizontal Field	0.709	T
K <sub>z</sub> (from hor. field)	3.179	
Photon Energy, Harm.1	0.160	keV
Emitted Power	11.179	kW
Total Length	3905.5	mm

### Synchrotron radiation from the epu48Heli ID

The power map of the emitted synchrotron radiation by the epu48Heli ID, assuming a 0.5 A filament beam with an energy of 3 GeV and undulator properties of the synchrotron radiation, is shown in Figure 5.434. The on-axis power density is 0.264 kW/mrad<sup>2</sup>

A map of the degree of linear polarisation of the fundamental harmonic of the synchrotron radiation emitted by the epu48Heli ID over the angle of observation is shown in Figure 5.435.

A map of the degree of 45 degree polarisation of the fundamental harmonic of the synchrotron radiation emitted by the epu48Heli ID over the angle of observation is shown in Figure 5.436.

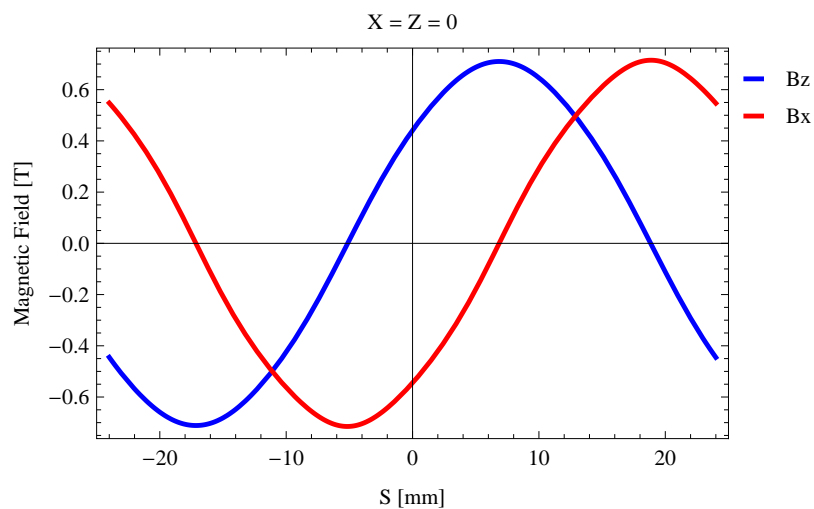


Figure 5.430: Vertical magnetic field in a central pole of the epu48Heli ID along the ID axis,  $X = Z = 0$

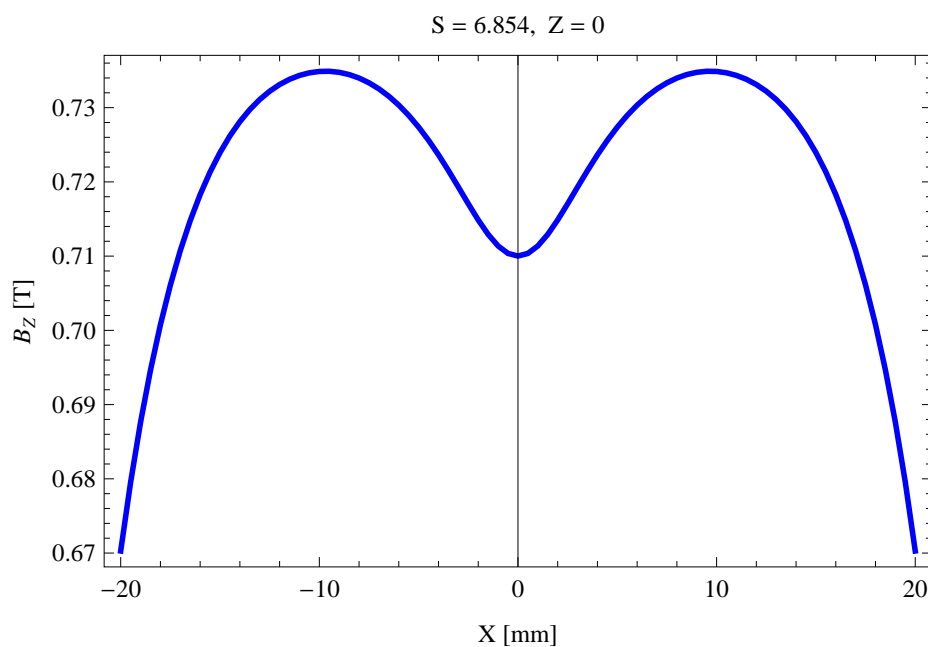


Figure 5.431: Vertical magnetic field in a central pole of the epu48Heli ID along the horizontally transverse direction to the ID axis,  $S = 6.854$ ,  $Z = 0$

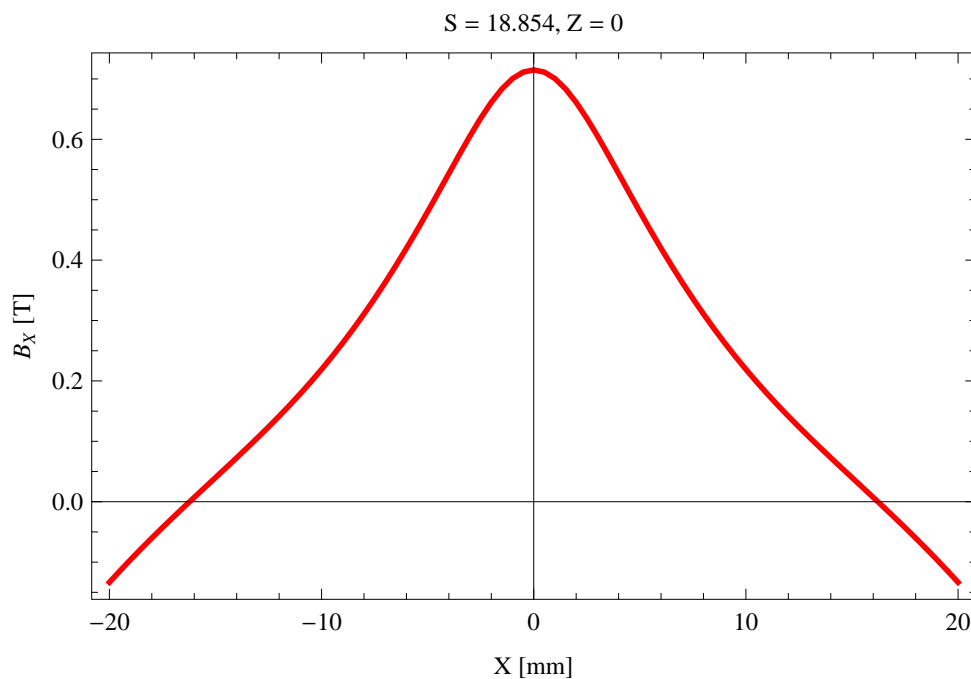


Figure 5.432: Horizontal magnetic field in a central pole of the epu48Heli ID along the horizontally transverse direction to the ID axis, S = 18.854, Z = 0

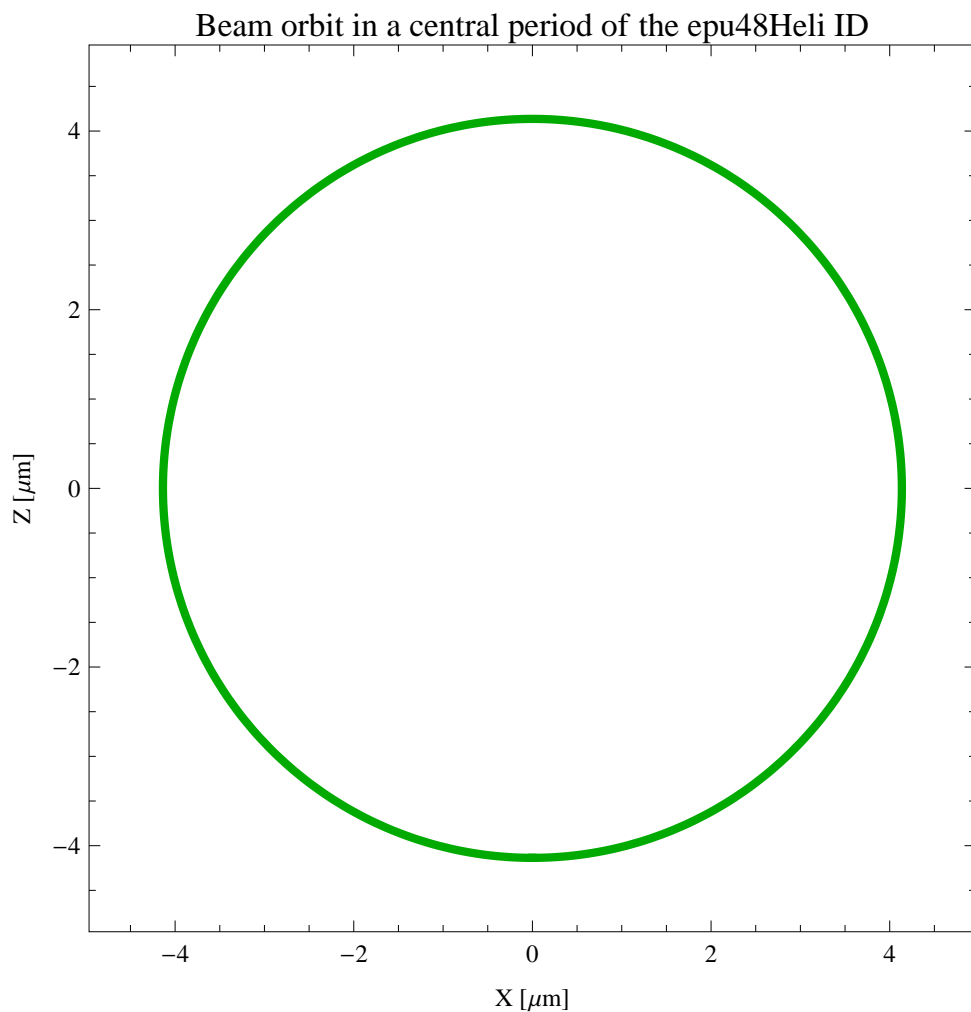


Figure 5.433: The beam orbit of the electron beam through a central period of the epu48Heli ID

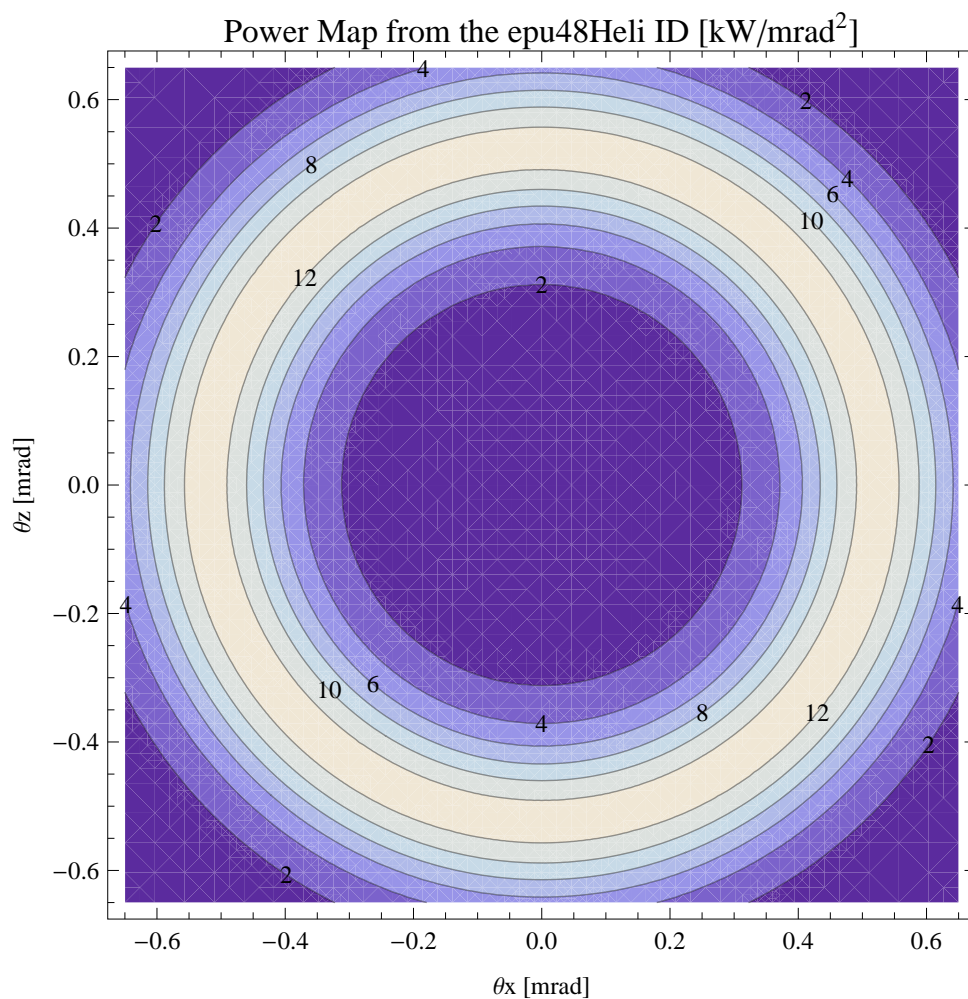


Figure 5.434: Map of the power distribution of the emitted synchrotron radiation by the epu48Heli ID



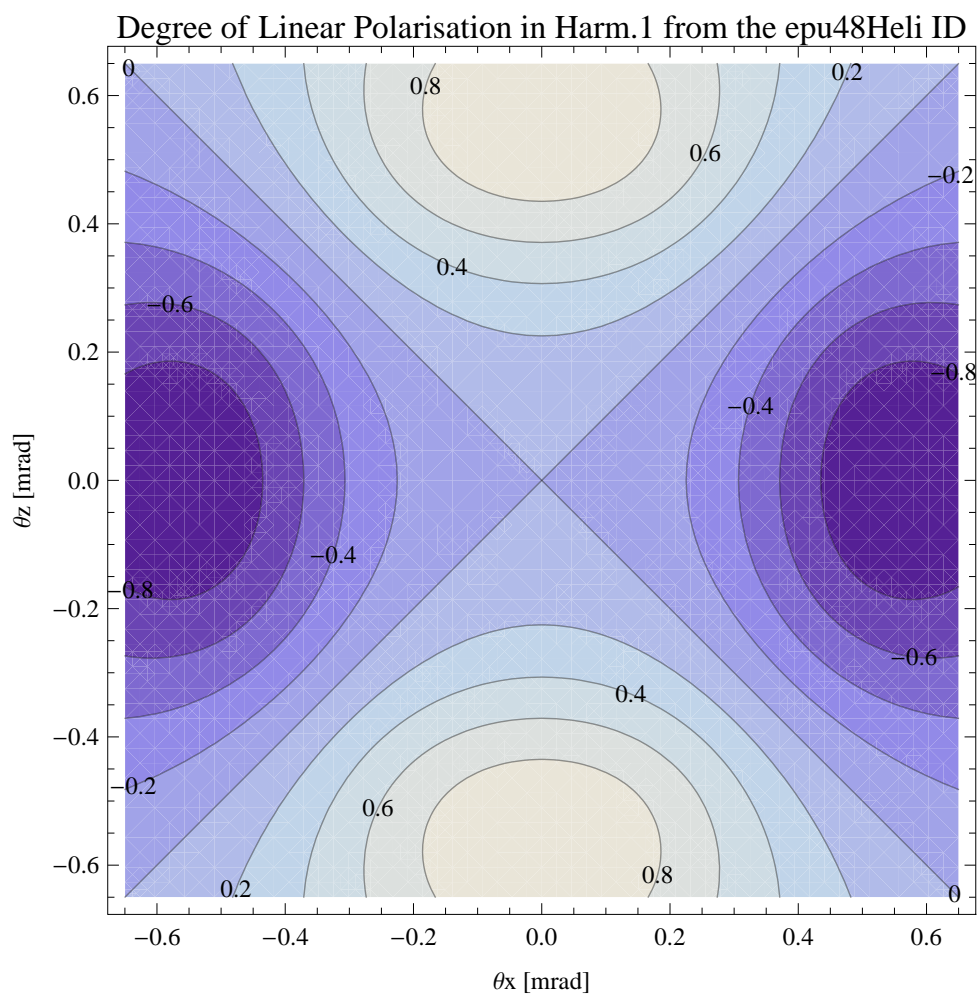


Figure 5.435: Map of linear polarisation in the fundamental harmonic of the synchrotron radiation emitted by the epu48Heli ID

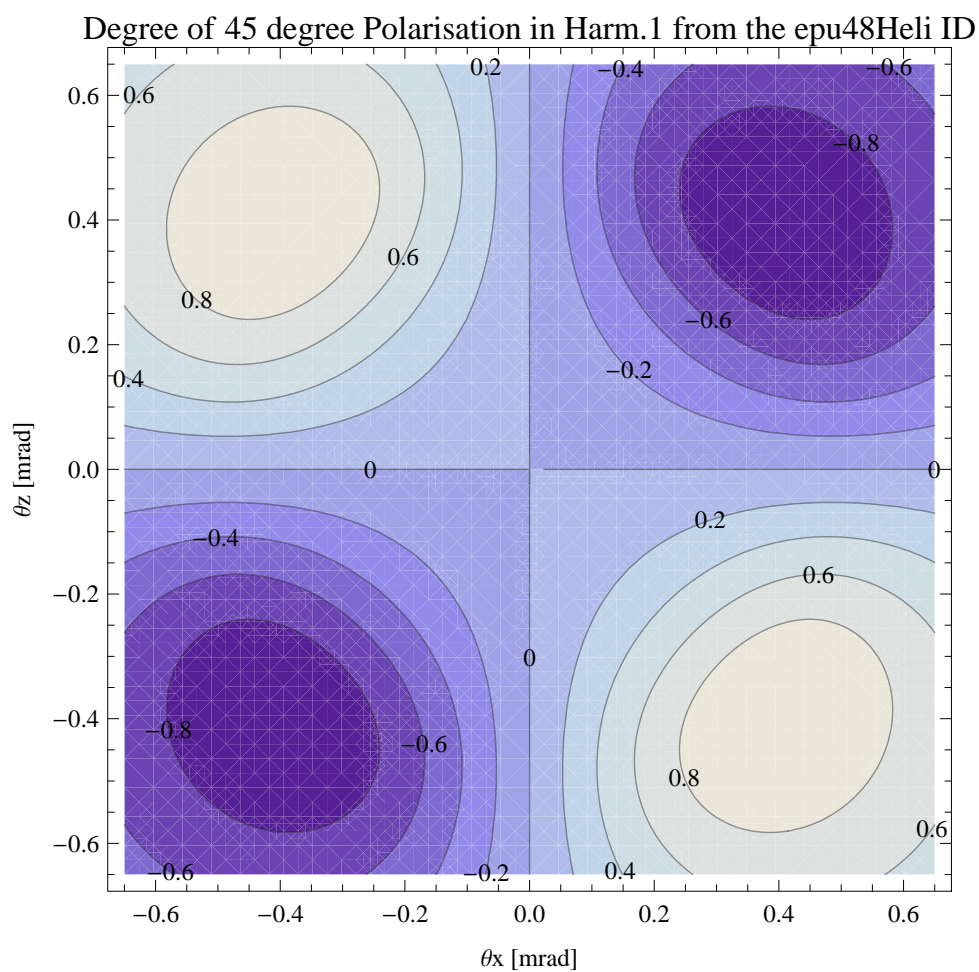


Figure 5.436: Map of 45 degree polarisation in the fundamental harmonic of the synchrotron radiation emitted by the epu48Heli ID

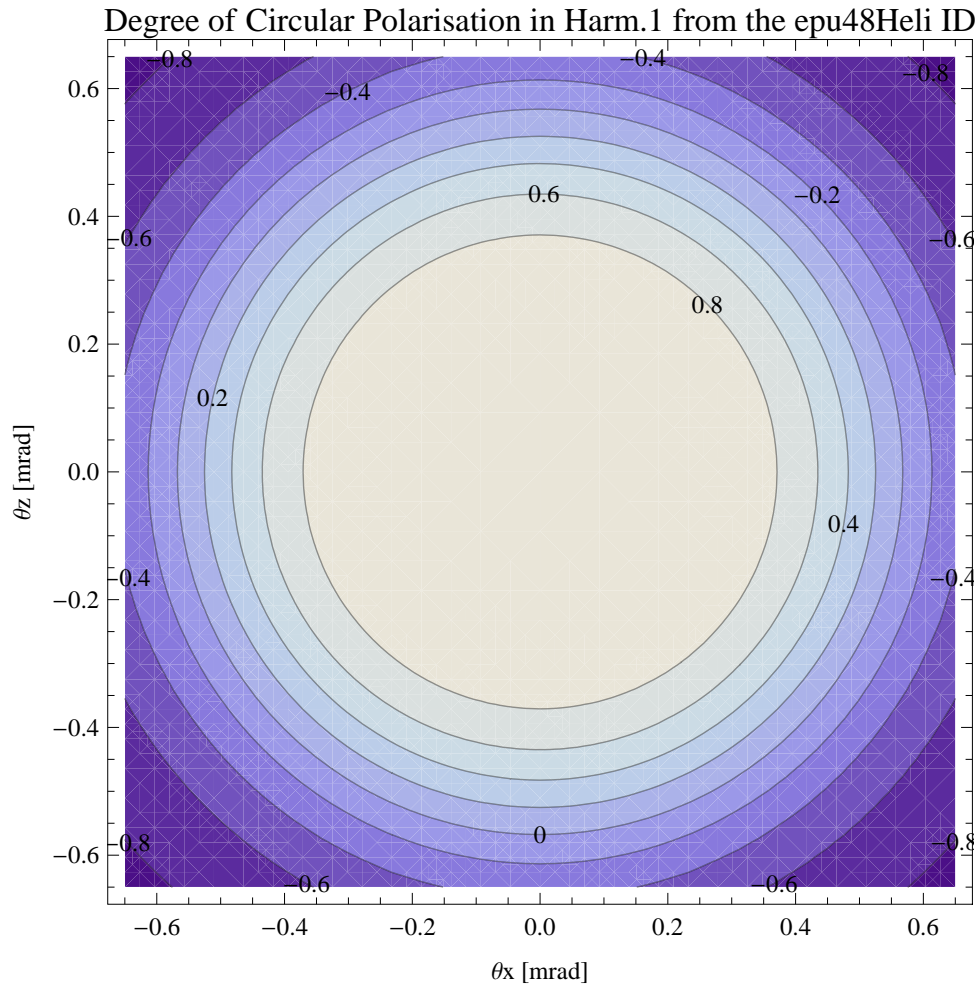


Figure 5.437: Map of circular polarisation in the fundamental harmonic of the synchrotron radiation emitted by the epu48Heli ID

A map of the degree of circular polarisation of the fundamental harmonic of the synchrotron radiation emitted by the epu48Heli ID over the angle of observation is shown in Figure 5.437.

The on axis brilliance at peak energy, the angular spectral flux, the flux in the harmonics, the power in the harmonics, the ratio of coherence, the coherent flux in the harmonics, and the power of coherent radiation in the harmonics from the epu48Heli ID have been calculated and the resulting plots are found in this section of the document. The beam parameters used for the calculation are 0.5 A of stored current,  $\beta_H = 9$  m,  $\varepsilon_H = 0.263$  nmrad,  $\beta_V = 4.8$  m,  $\varepsilon_V = 8$  pmrad, and an energy spread of 0.001.

The brilliance at peak energy and the angular spectral flux density from the epu48Heli ID for different harmonics at maximum K-value (4.495) are given in Table 5.65 and for minimum K-value (0.400) these values are given in Table 5.66.

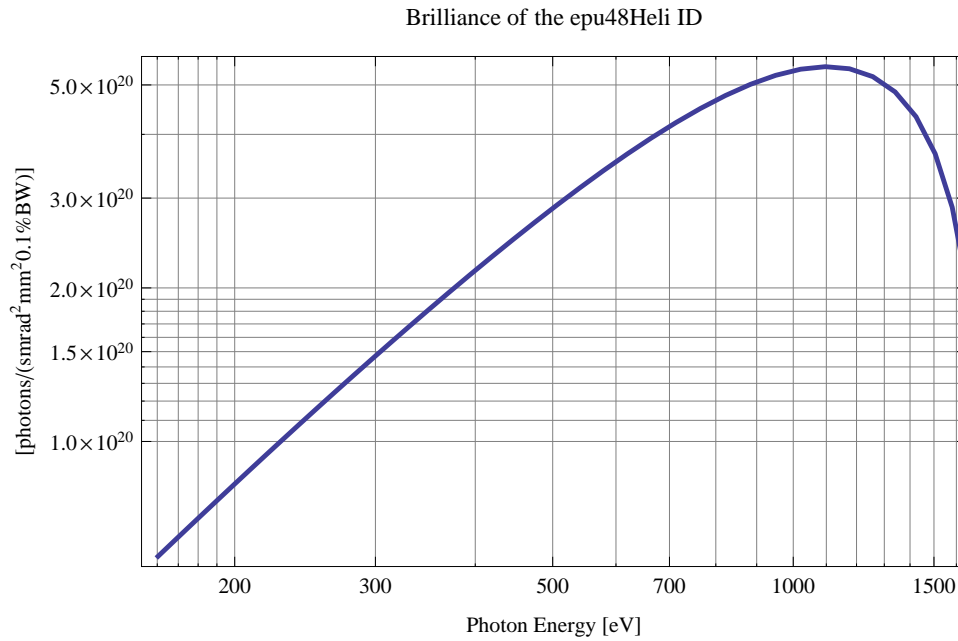


Figure 5.438: The brilliance at peak energy from the epu48Heli ID

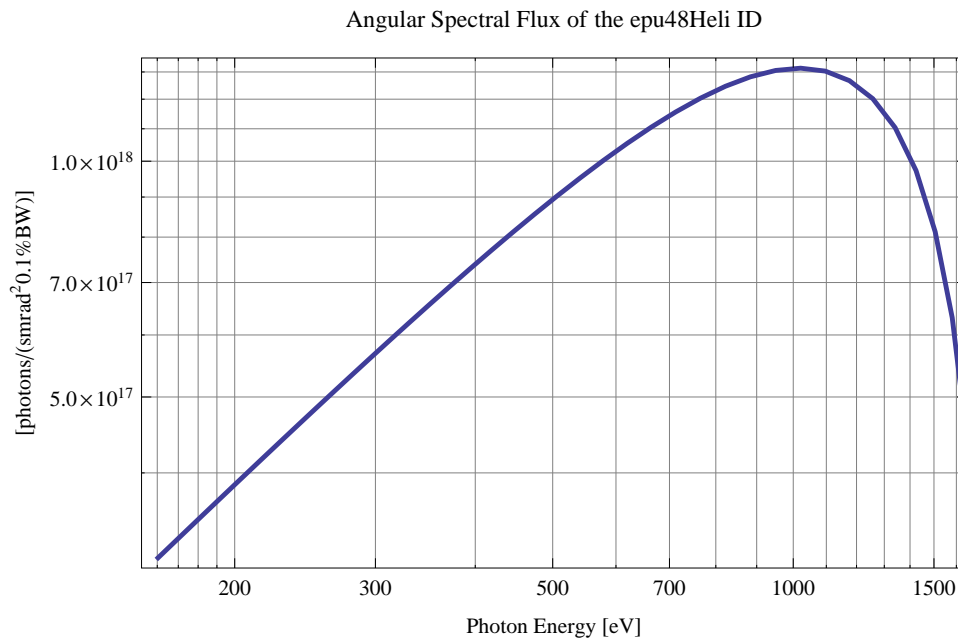


Figure 5.439: The angular spectral flux from the epu48Heli ID

Table 5.65: The brilliance at peak energy and the angular spectral flux density from the epu48Heli ID for different harmonics at maximum K-value (4.495)

Harmonic	Photon Energy [eV]	Brilliance [Ph./s/mrad <sup>2</sup> /mrad <sup>2</sup> /0.1%BW]	Angular Spectral Flux [Ph./s/mrad <sup>2</sup> /0.1%BW]
1	160.363	$5.95 \times 10^{19}$	$3.12 \times 10^{17}$

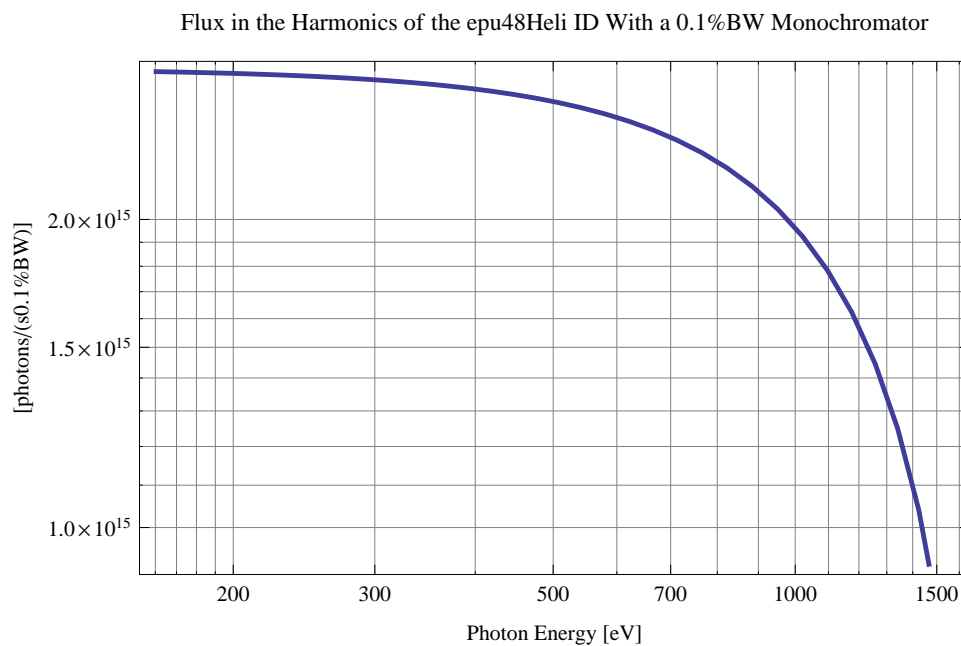


Figure 5.440: The flux of photons in the harmonics from the epu48Heli ID using a 0.1%BW monochromator

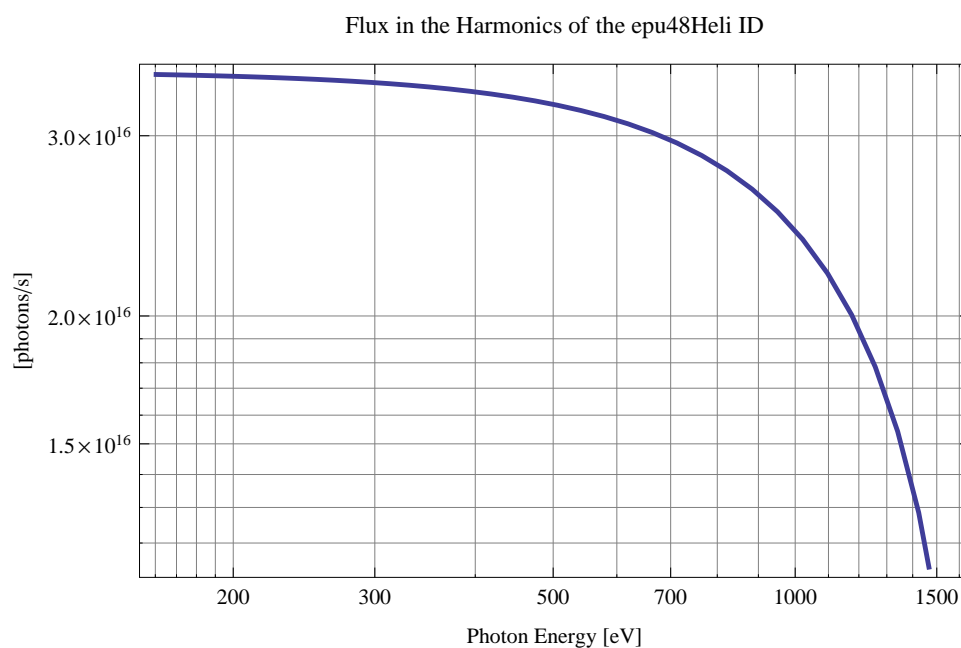


Figure 5.441: The flux of photons in the harmonics from the epu48Heli ID

Table 5.66: The brilliance at peak energy and the angular spectral flux density from the epu48Heli ID for different harmonics at minimum K-value (0.4)

Harmonic	Photon Energy [eV]	Brilliance [Ph./s/mrad <sup>2</sup> /mrad <sup>2</sup> /0.1%BW]	Angular Spectral Flux [Ph./s/mrad <sup>2</sup> /0.1%BW]
1	1648.68	$2.04 \times 10^{20}$	$4.43 \times 10^{17}$

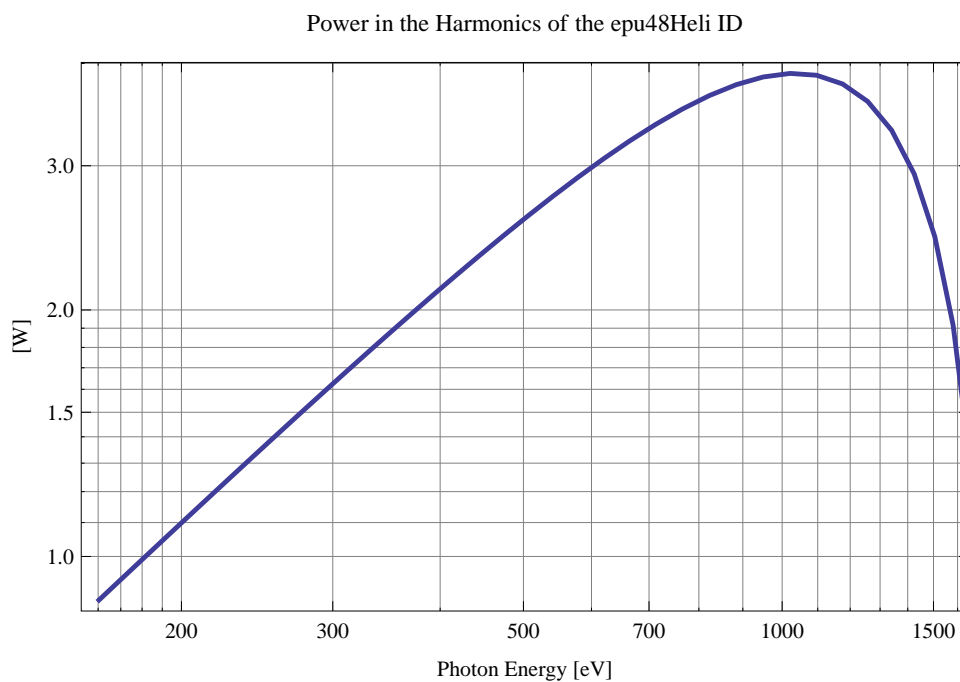


Figure 5.442: The power in the harmonics from the epu48Heli ID

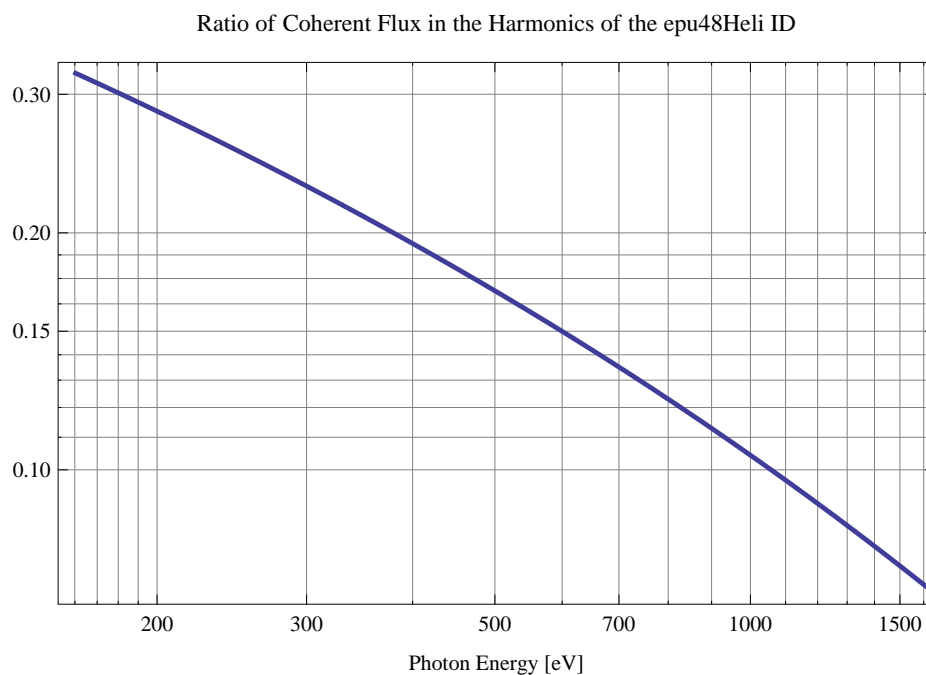


Figure 5.443: The ratio of coherent flux in the harmonics from the epu48Heli ID

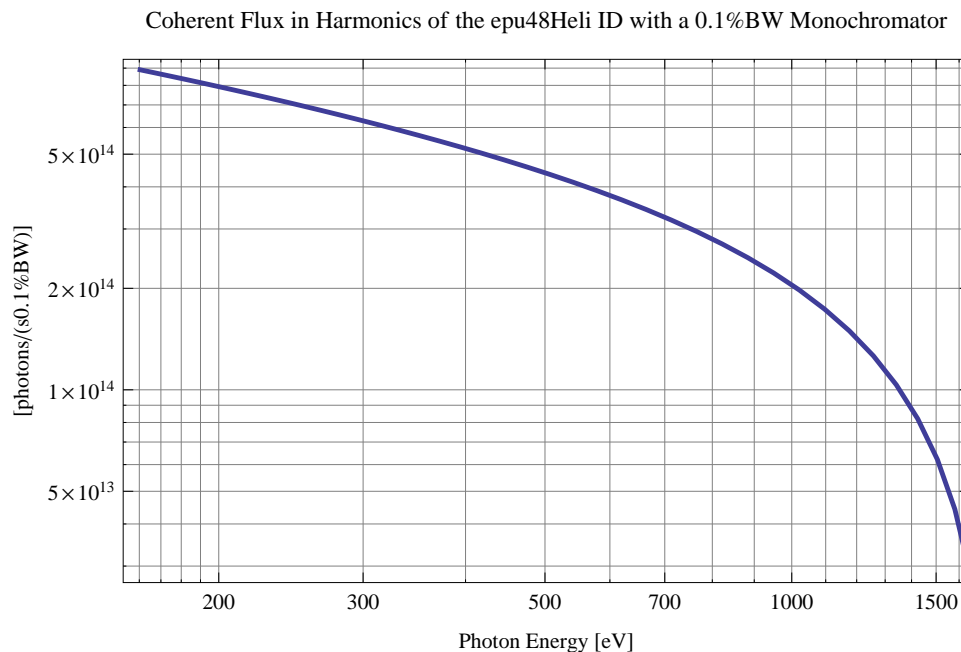


Figure 5.444: The coherent flux in the harmonics of the epu48Heli ID using a 0.1%BW Monochromator

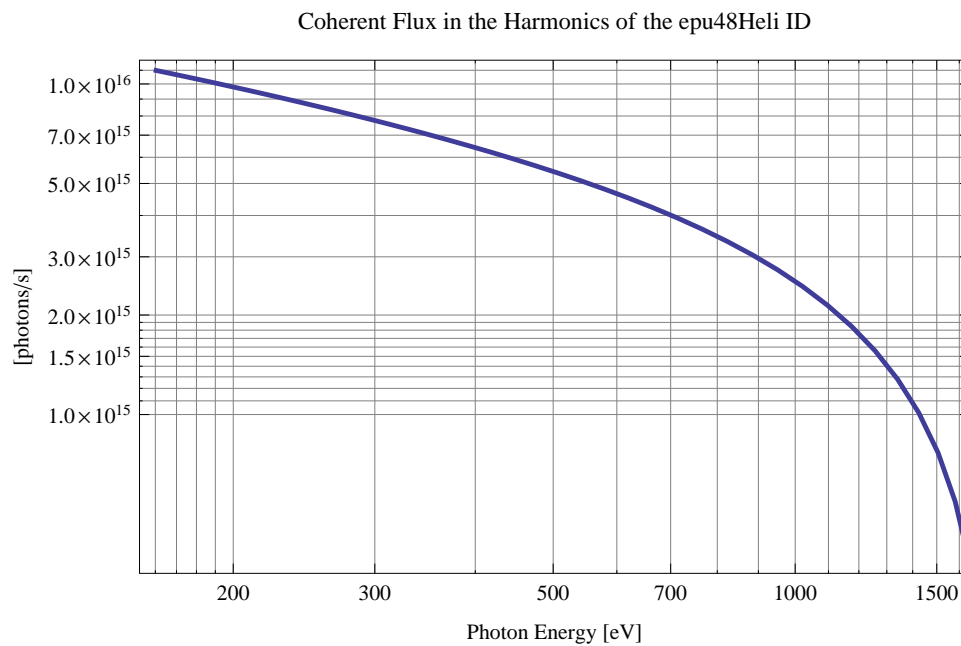


Figure 5.445: The coherent flux in the harmonics of the epu48Heli ID

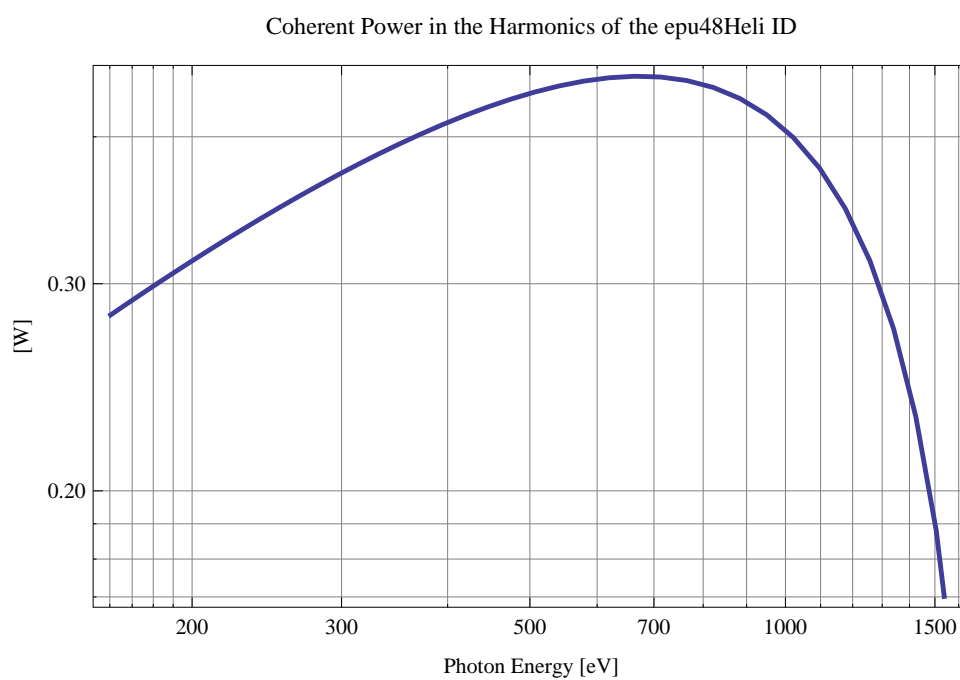


Figure 5.446: The power of coherent synchrotron radiation in the harmonics of the epu48Heli ID



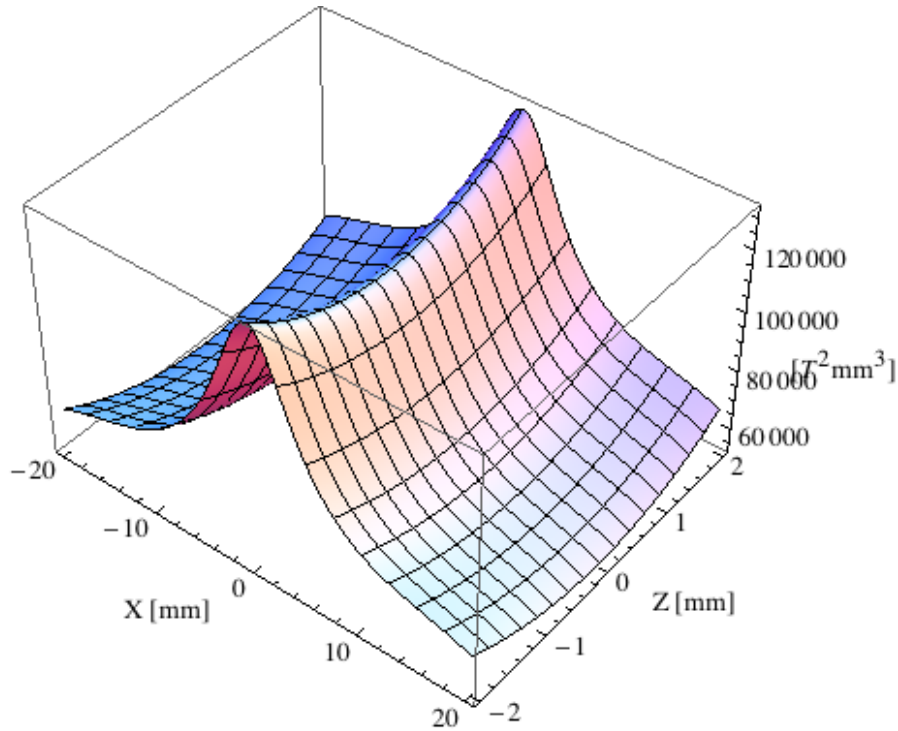


Figure 5.447: Focusing potential from the epu48Heli ID over the beam stay clear aperture.

### Influence from the epu48Heli ID on the optics of the stored beam

Figure 5.447 shows the focusing potential from the epu48Heli over the beam stay clear aperture of the ring aperture.

Figure 5.448 shows the kick map in the beam energy independant unit  $T^2 m^2$  of the kicks induced by the epu48Heli ID over the beam stay clear aperture.

Figure 5.449 shows the induced angular kick on the stored beam from the epu48Heli ID as a function of the vertical distance to the axis of the ID.

Figure 5.450 shows the induced angular kick on the stored beam from the epu48Heli ID as a function of the horizontal distance to the axis of the ID.

Figure 5.451 shows tune shift induced by the epu48Heli ID over the beam stay clear aperture. Note that the tune shift depends on the beam size at the ID.

Figure 5.452 shows the induced tune shift from the epu48Heli ID as a function of the vertical distance to the axis of the ID.

Figure 5.453 shows the induced tune shift from the epu48Heli ID as a function of the horizontal distance to the axis of the ID.

### Magnet model of the elliptically polaraising undulator epu48Incl

The Radia [2] magnet model of the epu48Incl ID is shown in Figure 5.454. The length of the magnet model is 401.496 mm. The magnetic material in the model is NdFeb with a remanence of 1.28 T, a material similar to VACODYM 776 TP from Vacuumschmelze. Blocks with vertical magnetisation are blue and blocks with horizontal magnetisation are yellow. The block size is

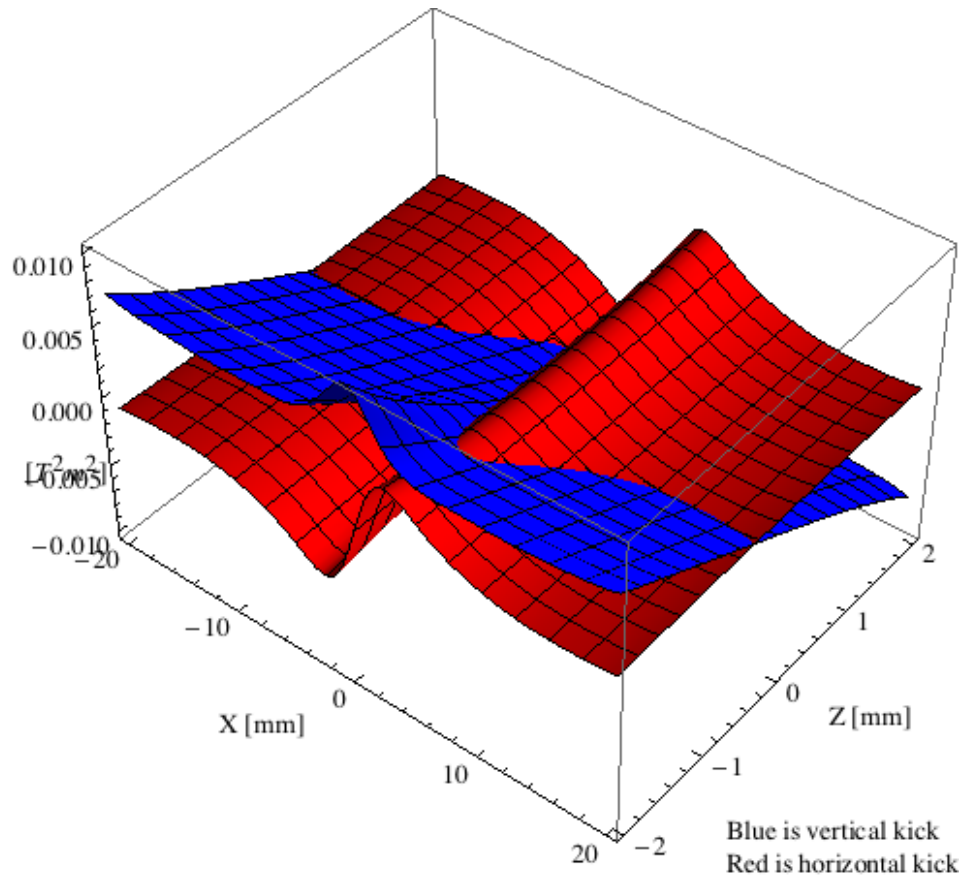


Figure 5.448: Kick map in the beam energy independent unit  $T^2 m^2$  of the kicks induced by the epu48Heli ID over the beam stay clear aperture.

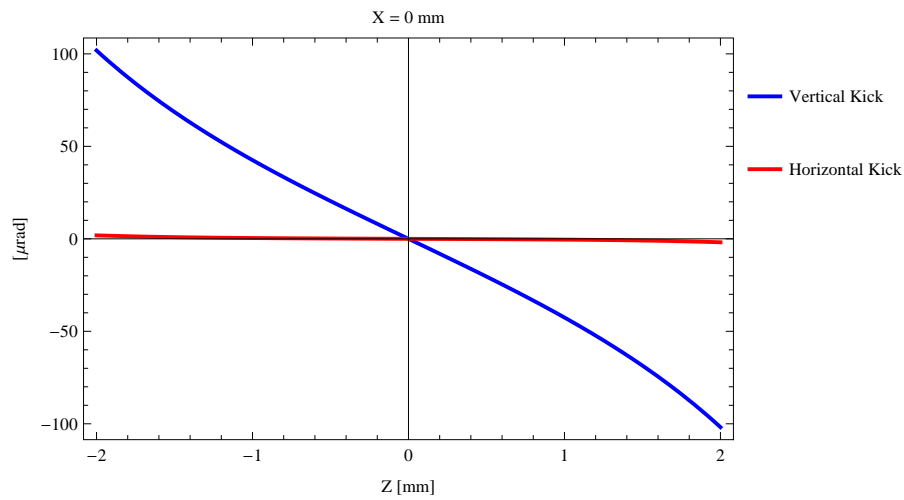


Figure 5.449: Induced angular kick on the stored beam from the epu48Heli ID as a function of the vertical distance to the ID axis.

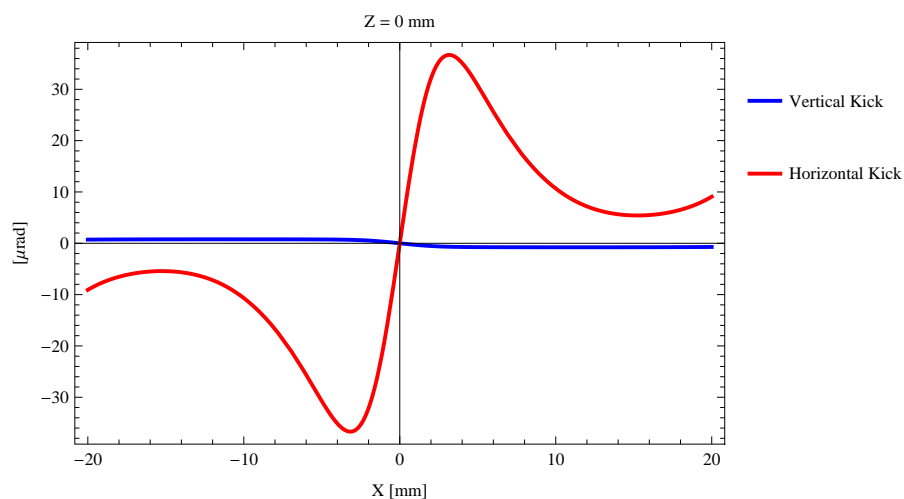


Figure 5.450: Induced angular kick on the stored beam from the epu48Heli ID as a function of the horizontal distance to the ID axis.

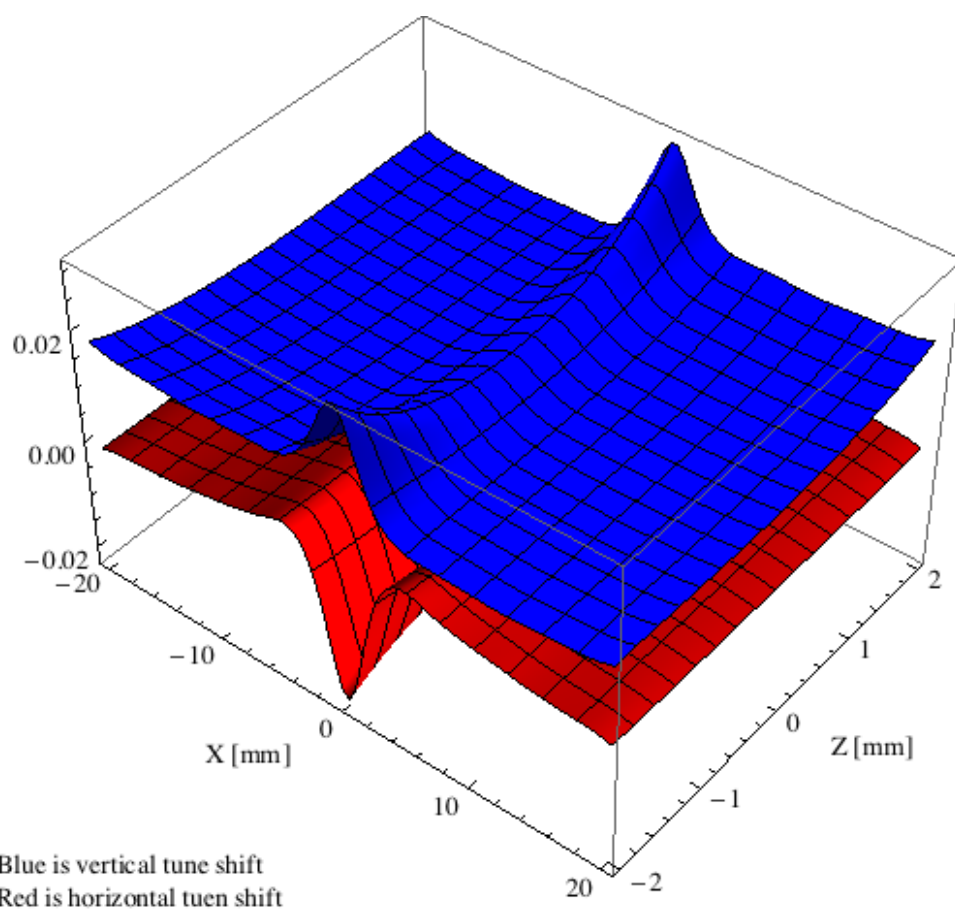


Figure 5.451: Tune shift induced by the epu48Heli ID over the beam stay clear aperture.

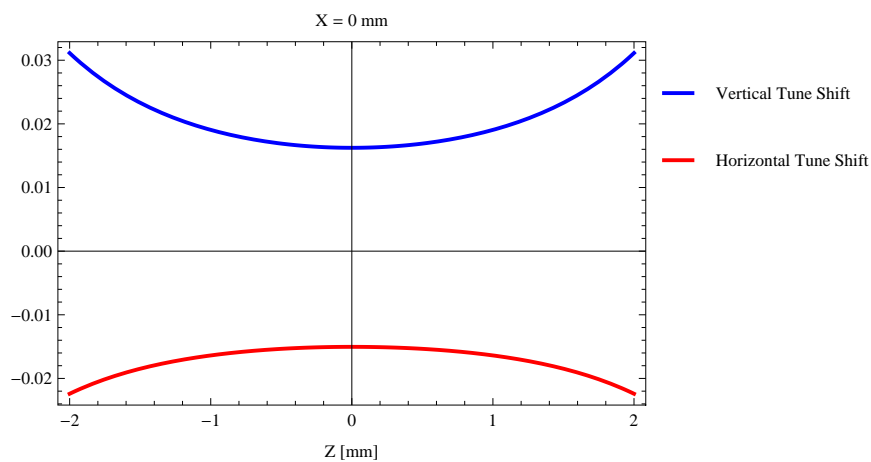


Figure 5.452: Induced tune shift from the epu48Heli ID as a function of the vertical distance to the axis of the ID.

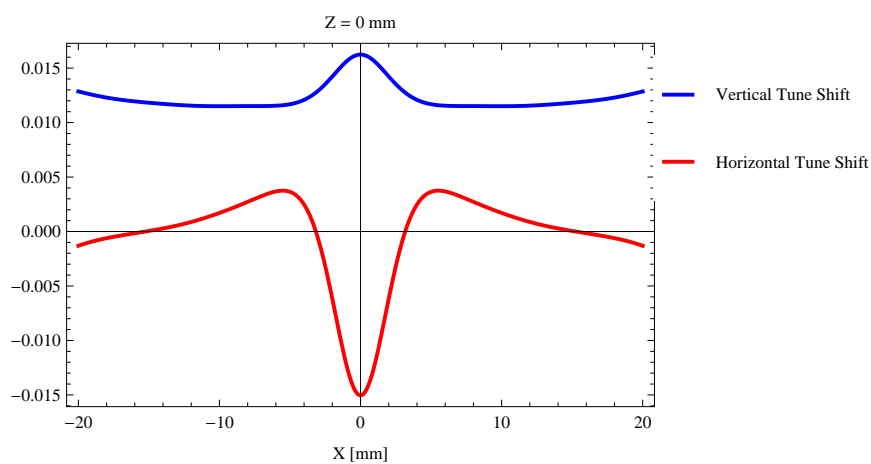


Figure 5.453: Induced tune shift from the epu48Heli ID on the stored beam from the ID as a function of the horizontal distance to the axis of the ID.

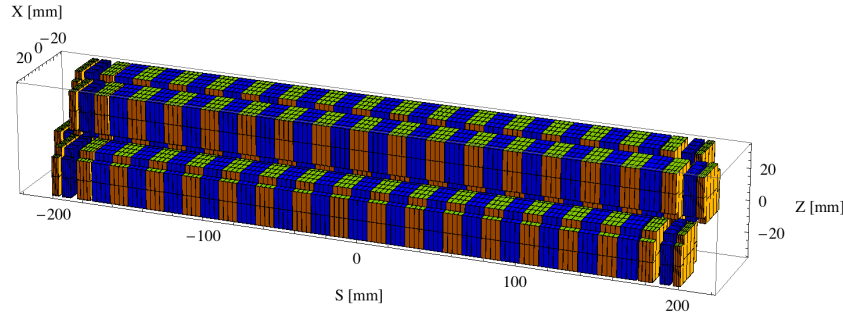


Figure 5.454: Magnetic model of the epu48Incl ID. The ID has been modelled with Radia [2]

$30 \times 30 \times 12 \text{ mm}^3$  and there is a 5. mm cut-out in two of the corners of the blocks. The total length of the epu48Incl ID is 3905.5 mm.

### Analysis of the magnetic field of the epu48Incl ID

The effective magnetic fields on axis and the fundamental photon energy of the epu48Incl ID are shown in Table 5.67. The higher harmonic contents in the magnetic field of an elliptically polarising undulator made of permanent magnets is negligible and the efficient field has about the same strength as the peak field.

Table 5.67: Effective Fields on axis and Fundamental Photon Energy of the epu48Incl ID

Undulator Period	48	mm
Undulator Gap	9	mm
Undulator Mode	Inclined	
Undulator Phase	12.861	mm
Vertical Peak Field	0.500	T
Efficient Vertical Field	0.504	T
K <sub>x</sub> (from vert. field)	2.260	
Horizontal Peak Field:	-0.498	T
Efficient Horizontal Field	0.505	T
K <sub>z</sub> (from hor. field)	2.264	
Photon Energy, Harm.1	0.291	keV
Emitted Power	5.660	kW
Total Length	3905.5	mm

### Synchrotron radiation from the epu48Incl ID

The power map of the emitted synchrotron radiation by the epu48Incl ID, assuming a 0.5 A filament beam with an energy of 3 GeV and undulator properties of the synchrotron radiation, is shown in Figure 5.459. The on-axis power density is 24.878 kW/mrad<sup>2</sup>

A map of the degree of linear polarisation of the fundamental harmonic of the synchrotron radiation emitted by the epu48Incl ID over the angle of observation is shown in Figure 5.460.

A map of the degree of 45 degree polarisation of the fundamental harmonic of the synchrotron radiation emitted by the epu48Incl ID over the angle of observation is shown in Figure 5.461.

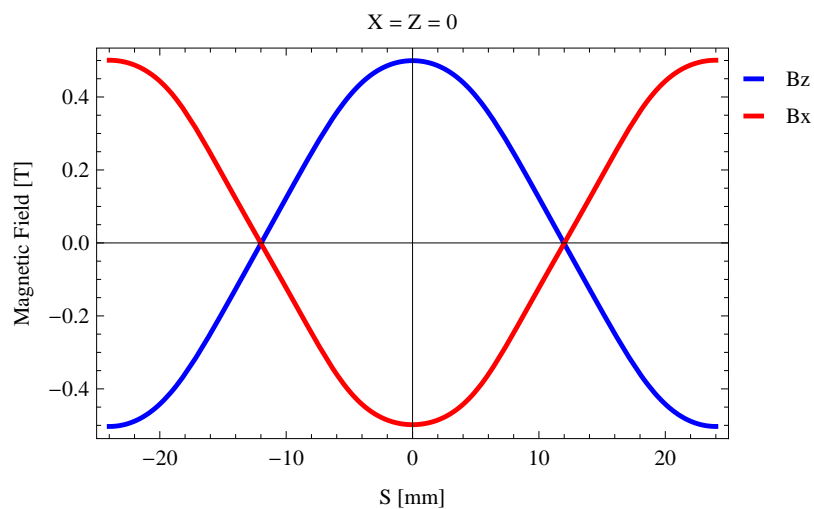


Figure 5.455: Vertical magnetic field in a central pole of the epu48Incl ID along the ID axis,  $X = Z = 0$

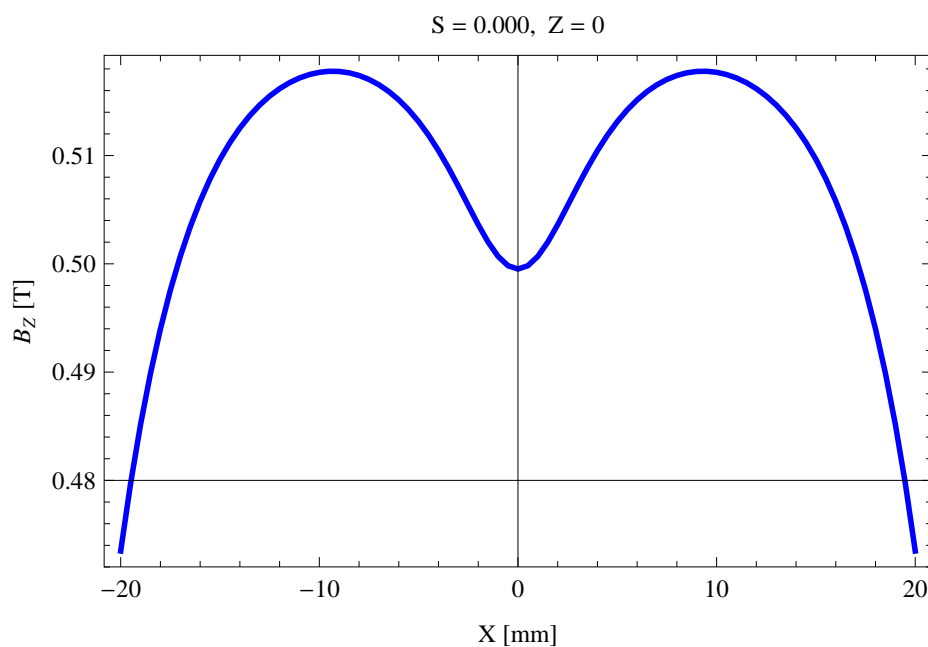


Figure 5.456: Vertical magnetic field in a central pole of the epu48Incl ID along the horizontally transverse direction to the ID axis,  $S = 0.000$ ,  $Z = 0$

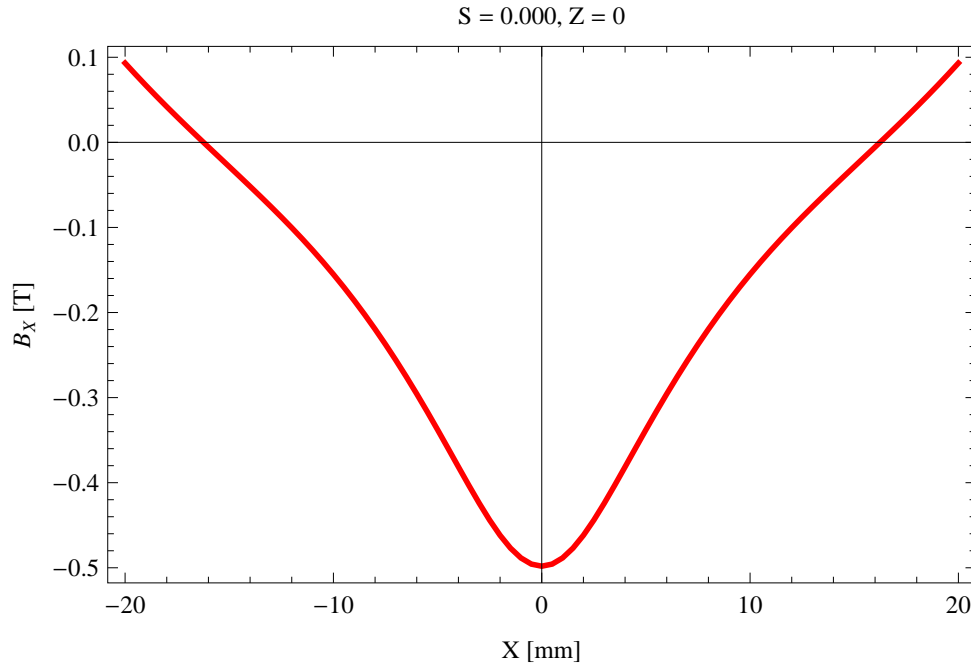


Figure 5.457: Horizontal magnetic field in a central pole of the epu48Incl ID along the horizontally transverse direction to the ID axis,  $S = 0.000$ ,  $Z = 0$

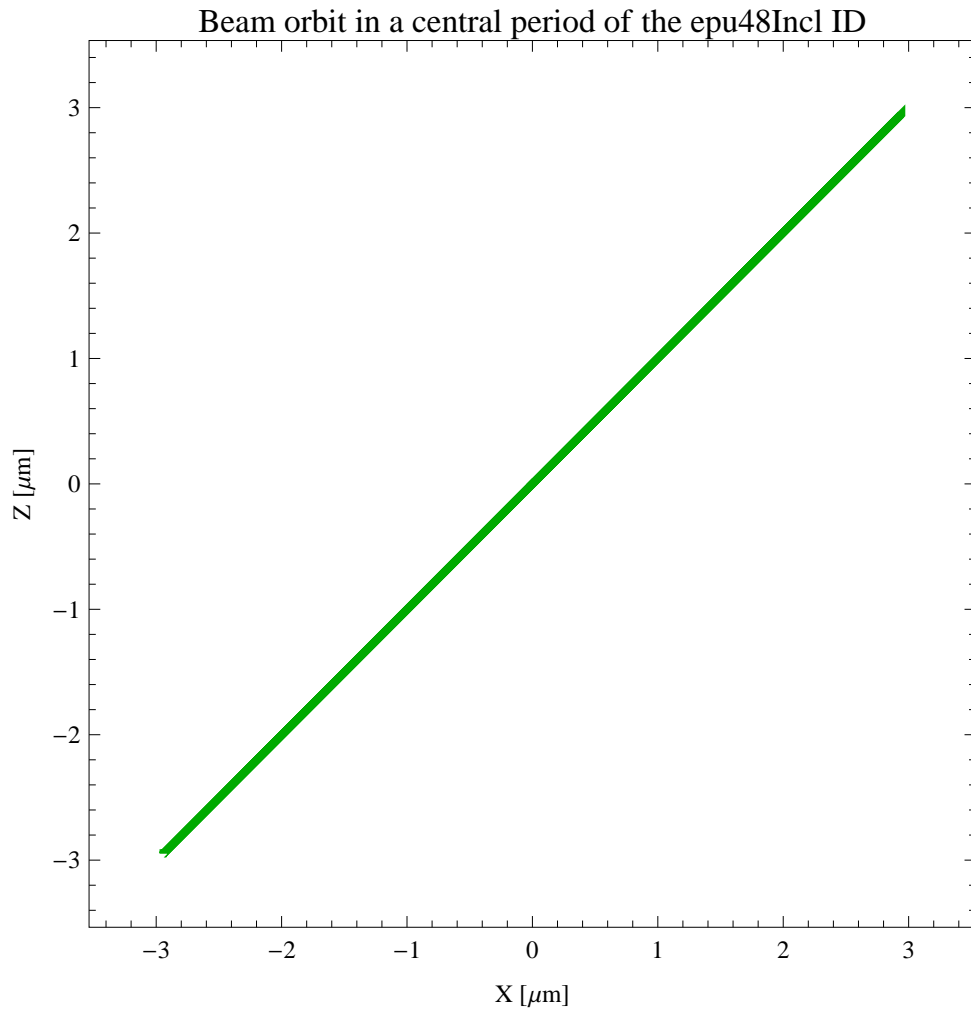


Figure 5.458: The beam orbit of the electron beam through a central period of the epu48Incl ID

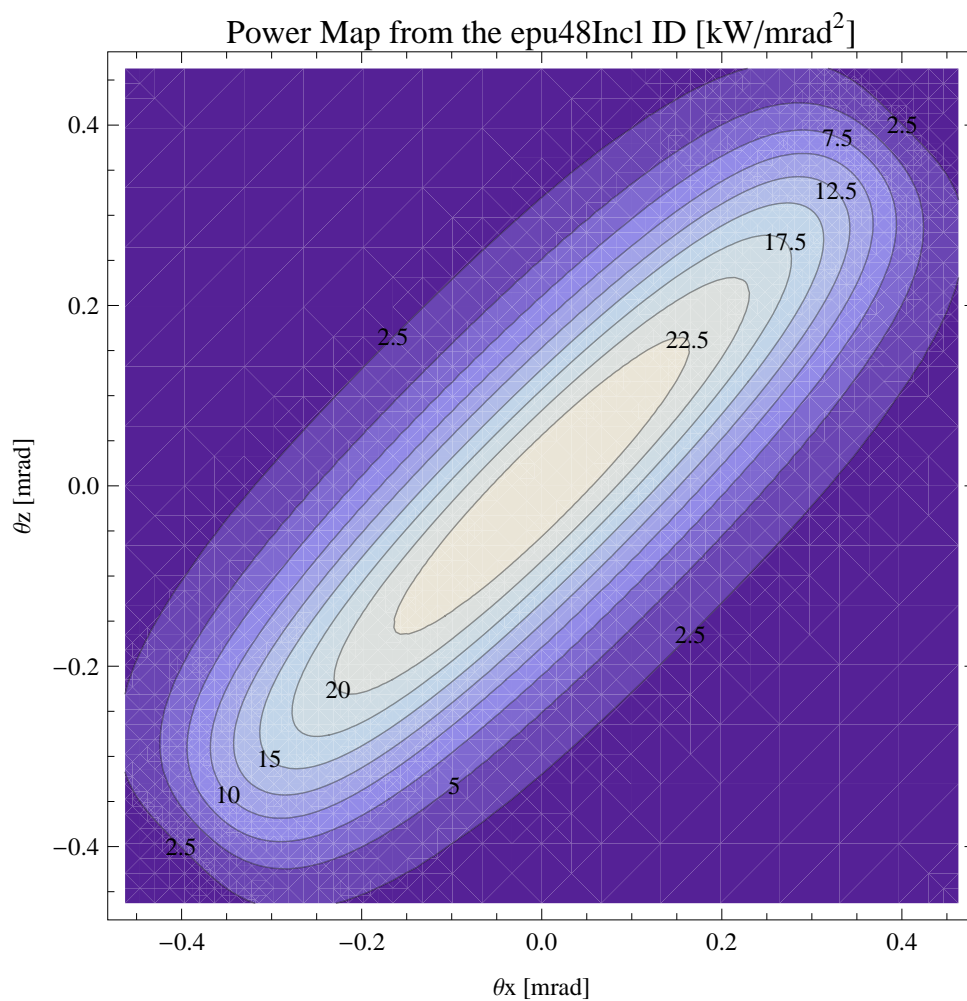


Figure 5.459: Map of the power distribution of the emitted synchrotron radiation by the epu48Incl ID



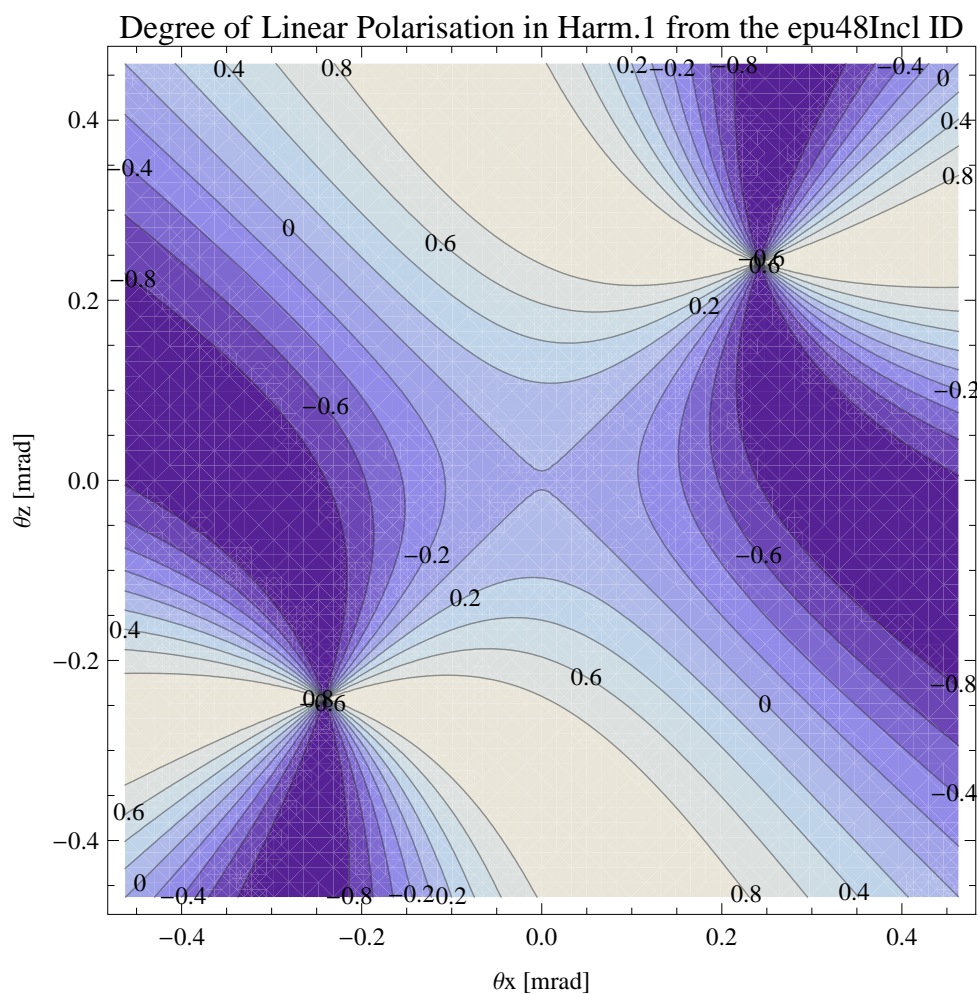


Figure 5.460: Map of linear polarisation in the fundamental harmonic of the synchrotron radiation emitted by the epu48Incl ID

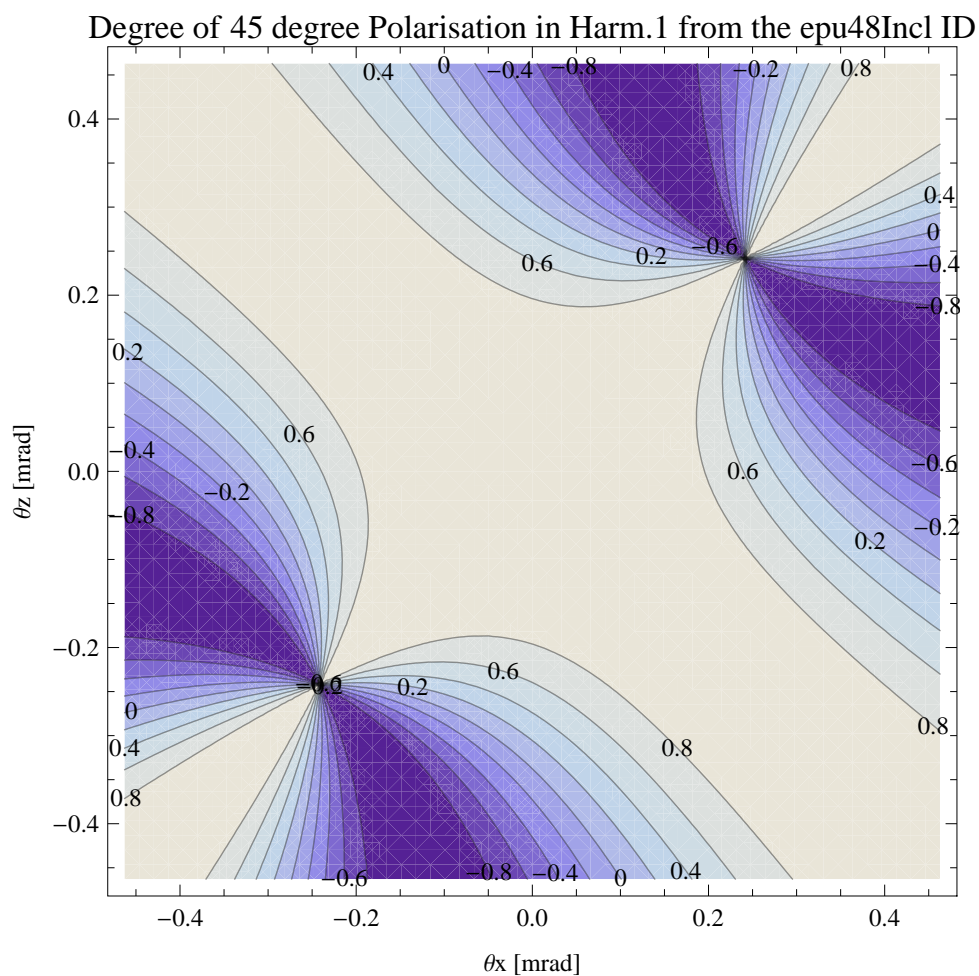


Figure 5.461: Map of 45 degree polarisation in the fundamental harmonic of the synchrotron radiation emitted by the epu48Incl ID

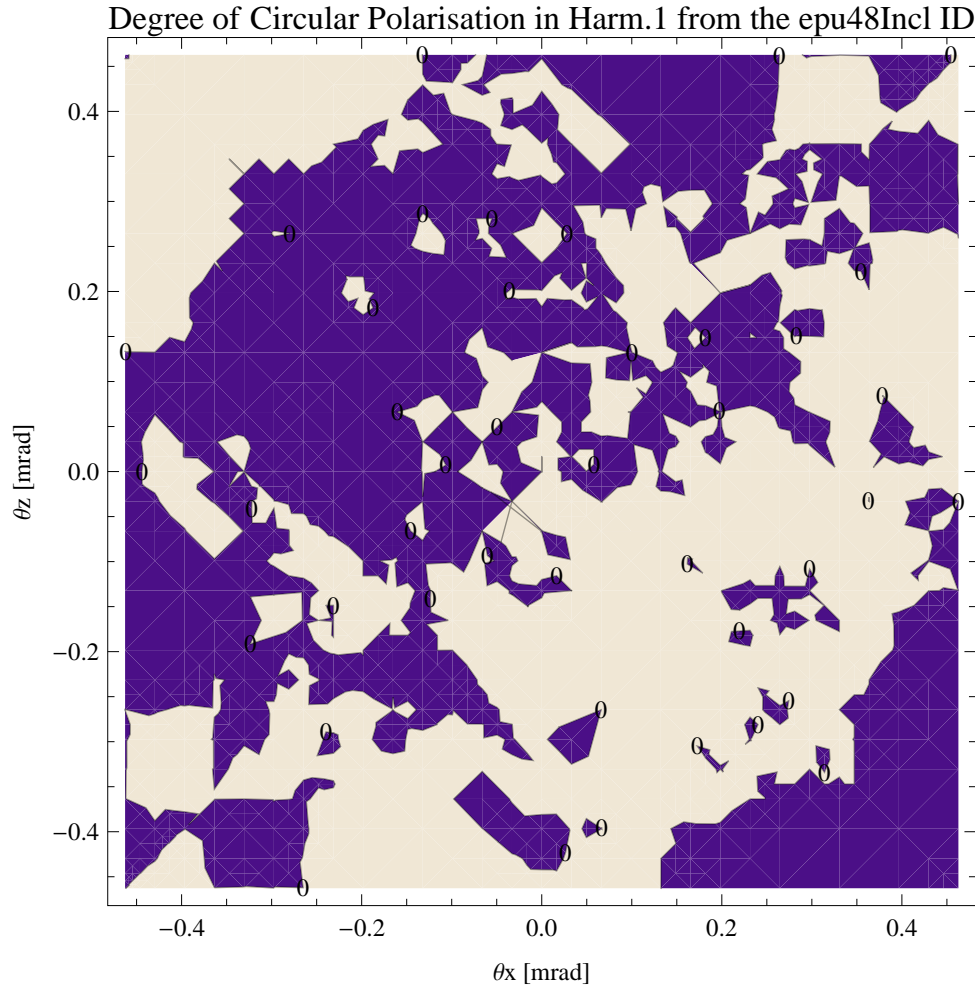


Figure 5.462: Map of circular polarisation in the fundamental harmonic of the synchrotron radiation emitted by the epu48Incl ID

A map of the degree of circular polarisation of the fundamental harmonic of the synchrotron radiation emitted by the epu48Incl ID over the angle of observation is shown in Figure 5.462.

The on axis brilliance at peak energy, the angular spectral flux, the flux in the harmonics, the power in the harmonics, the ratio of coherence, the coherent flux in the harmonics, and the power of coherent radiation in the harmonics from the epu48Incl ID have been calculated and the resulting plots are found in this section of the document. The beam parameters used for the calculation are 0.5 A of stored current,  $\beta_H = 9$  m,  $\varepsilon_H = 0.263$  nmrad,  $\beta_V = 4.8$  m,  $\varepsilon_V = 8$  pmrad, and an energy spread of 0.001.

The brilliance at peak energy and the angular spectral flux density from the epu48Incl ID for different harmonics at maximum K-value (3.199) are given in Table 5.68 and for minimum K-value (0.400) these values are given in Table 5.69.

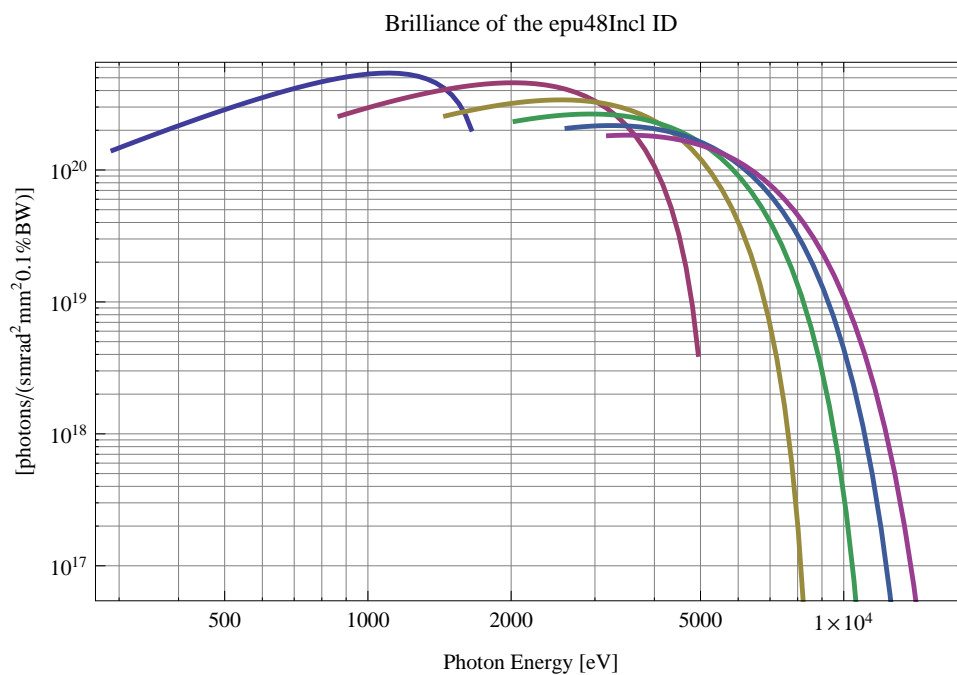


Figure 5.463: The brilliance at peak energy from the epu48Incl ID

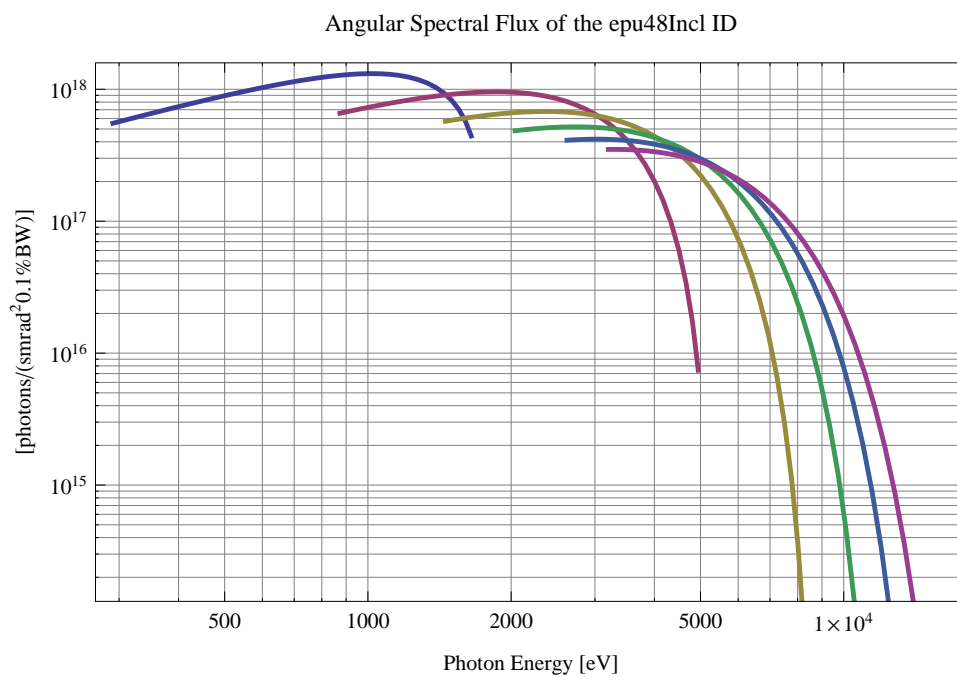


Figure 5.464: The angular spectral flux from the epu48Incl ID

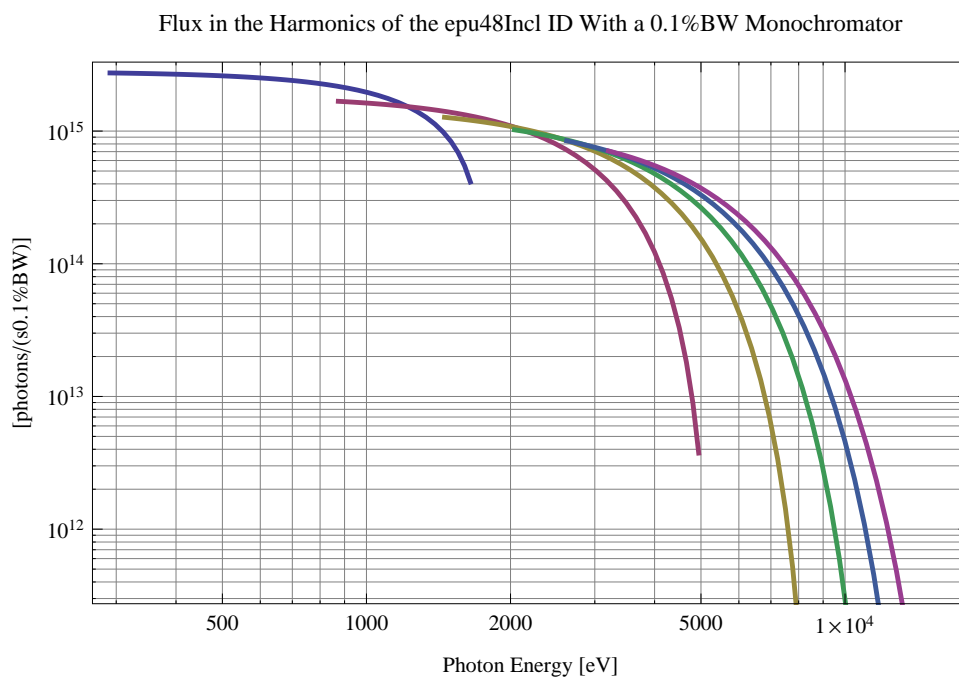


Figure 5.465: The flux of photons in the harmonics from the epu48Incl ID using a 0.1%BW monochromator

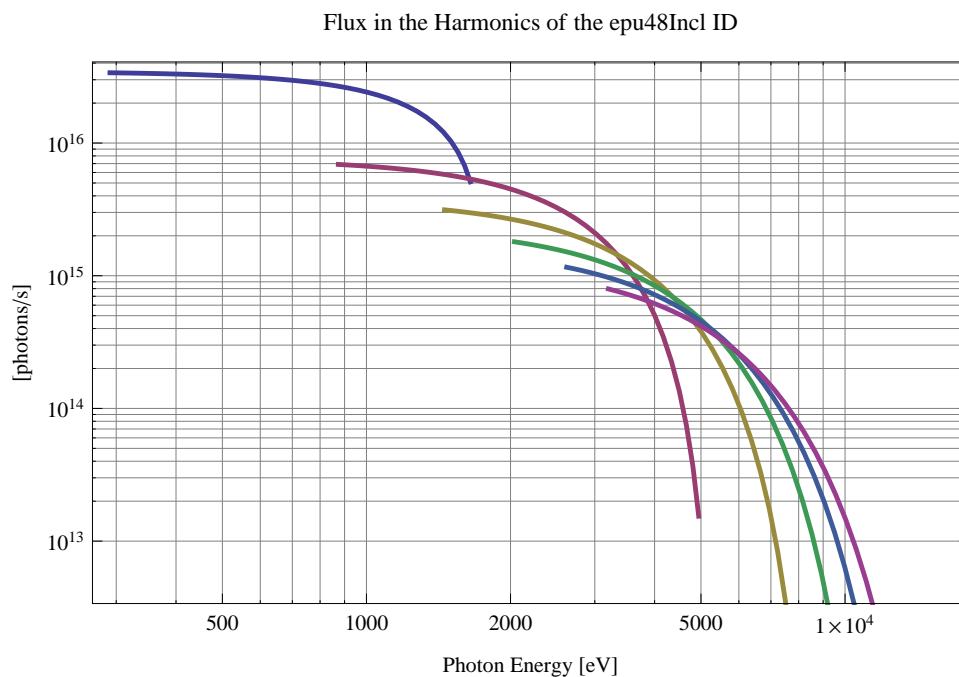


Figure 5.466: The flux of photons in the harmonics from the epu48Incl ID

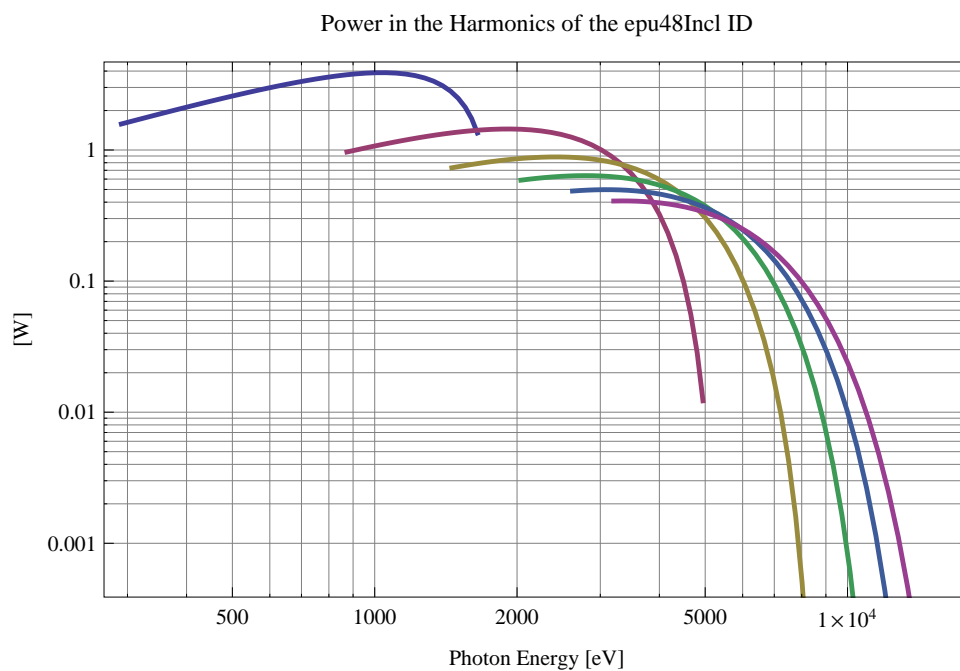


Figure 5.467: The power in the harmonics from the epu48Incl ID

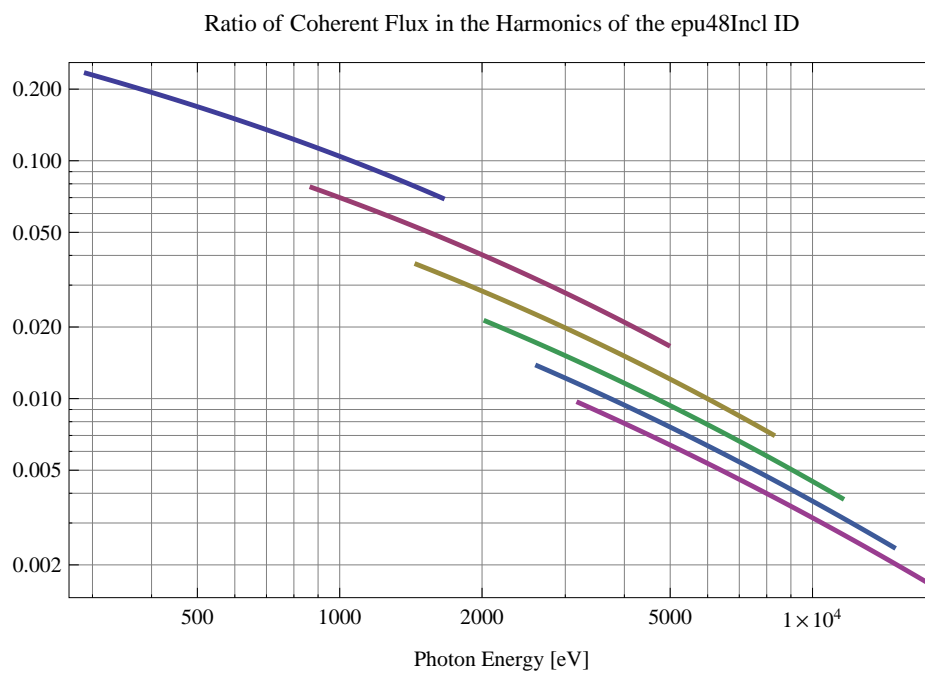


Figure 5.468: The ratio of coherent flux in the harmonics from the epu48Incl ID

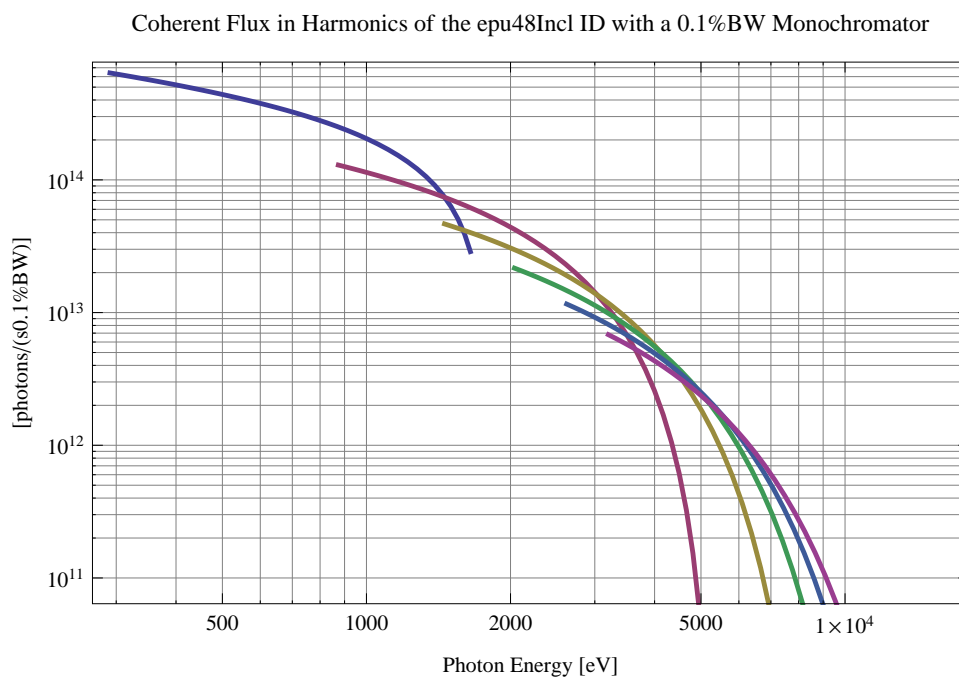


Figure 5.469: The coherent flux in the harmonics of the epu48Incl ID using a 0.1%BW Monochromator

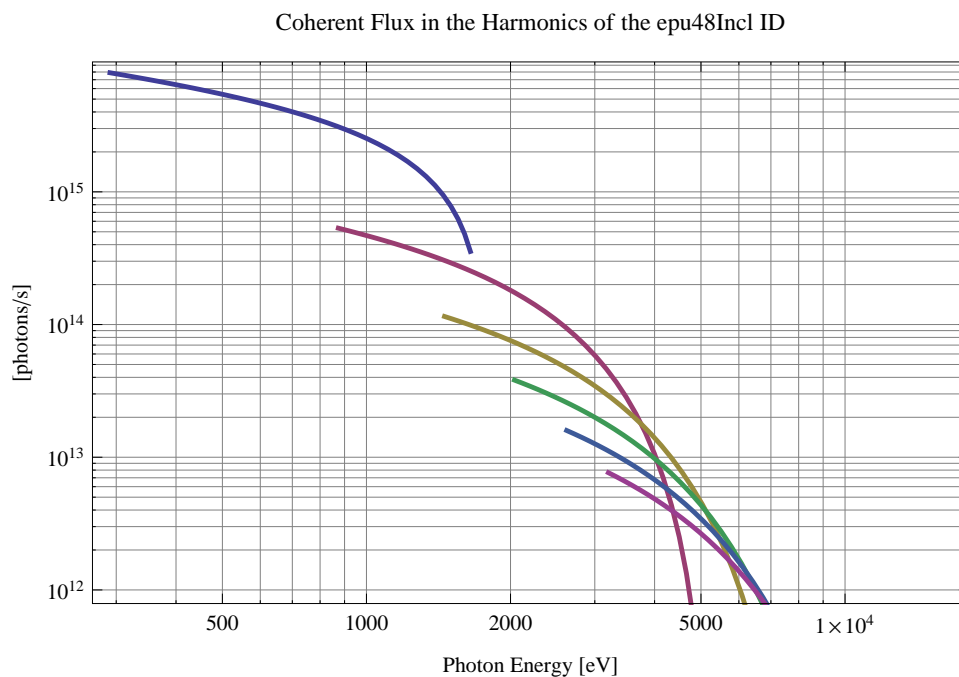


Figure 5.470: The coherent flux in the harmonics of the epu48Incl ID

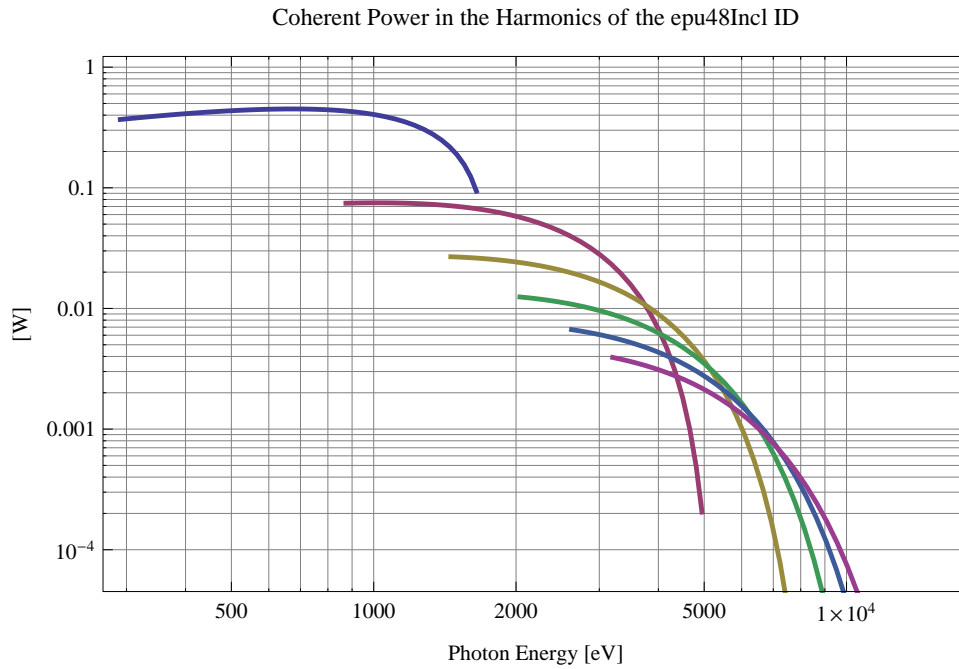


Figure 5.471: The power of coherent synchrotron radiation in the harmonics of the epu48Incl ID

Table 5.68: The brilliance at peak energy and the angular spectral flux density from the epu48Incl ID for different harmonics at maximum K-value (3.199)

Harmonic	Photon Energy [eV]	Brilliance [Ph./s/mrad <sup>2</sup> /mrad <sup>2</sup> /0.1%BW]	Angular Spectral Flux [Ph./s/mrad <sup>2</sup> /0.1%BW]
1	291.152	$1.41 \times 10^{20}$	$5.53 \times 10^{17}$
3	873.455	$2.57 \times 10^{20}$	$6.58 \times 10^{17}$
5	1455.76	$2.57 \times 10^{20}$	$5.72 \times 10^{17}$
7	2038.06	$2.34 \times 10^{20}$	$4.85 \times 10^{17}$
9	2620.36	$2.07 \times 10^{20}$	$4.11 \times 10^{17}$
11	3202.67	$1.82 \times 10^{20}$	$3.5 \times 10^{17}$

Table 5.69: The brilliance at peak energy and the angular spectral flux density from the epu48Incl ID for different harmonics at minimum K-value (0.4)

Harmonic	Photon Energy [eV]	Brilliance [Ph./s/mrad <sup>2</sup> /mrad <sup>2</sup> /0.1%BW]	Angular Spectral Flux [Ph./s/mrad <sup>2</sup> /0.1%BW]
1	1648.68	$2.04 \times 10^{20}$	$4.43 \times 10^{17}$
3	4946.04	$4. \times 10^{18}$	$7.43 \times 10^{15}$
5	8243.4	$4.6 \times 10^{16}$	$8.27 \times 10^{13}$
7	11540.8	$4.86 \times 10^{14}$	$8.64 \times 10^{11}$
9	14838.1	$5.02 \times 10^{12}$	$8.88 \times 10^9$
11	18135.5	$5.13 \times 10^{10}$	$9.06 \times 10^7$



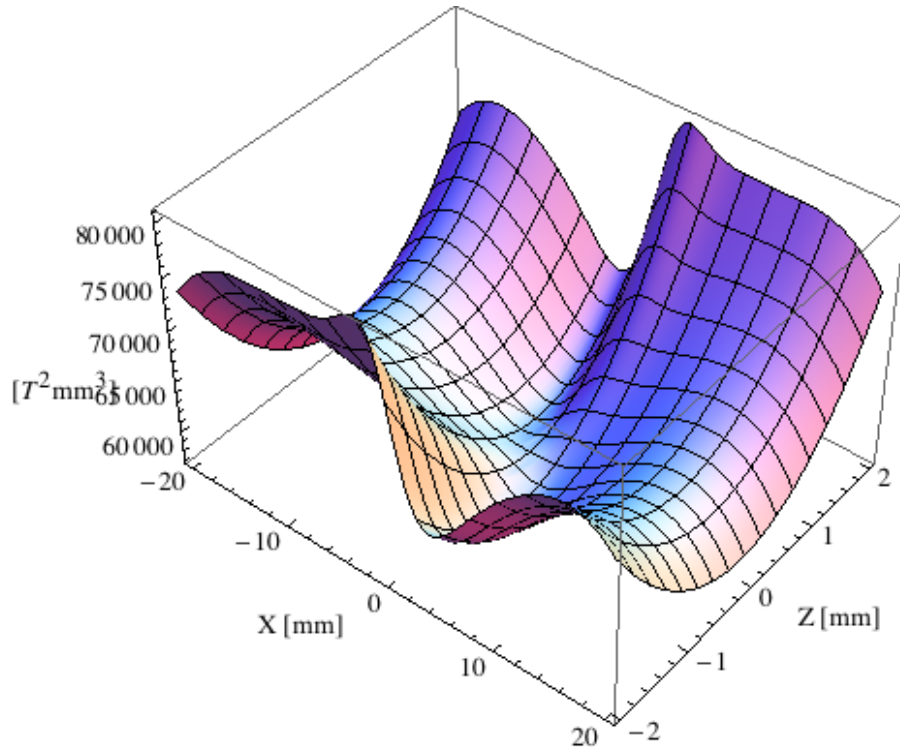


Figure 5.472: Focusing potential from the epu48Incl ID over the beam stay clear aperture.

### Influence from the epu48Incl ID on the optics of the stored beam

Figure 5.472 shows the focusing potential from the epu48Incl over the beam stay clear aperture of the ring aperture.

Figure 5.473 shows the kick map in the beam energy independent unit  $T^2 m^2$  of the kicks induced by the epu48Incl ID over the beam stay clear aperture.

Figure 5.474 shows the induced angular kick on the stored beam from the epu48Incl ID as a function of the vertical distance to the axis of the ID.

Figure 5.475 shows the induced angular kick on the stored beam from the epu48Incl ID as a function of the horizontal distance to the axis of the ID.

Figure 5.476 shows tune shift induced by the epu48Incl ID over the beam stay clear aperture. Note that the tune shift depends on the beam size at the ID.

Figure 5.477 shows the induced tune shift from the epu48Incl ID as a function of the vertical distance to the axis of the ID.

Figure 5.478 shows the induced tune shift from the epu48Incl ID as a function of the horizontal distance to the axis of the ID.

### Magnet model of the elliptically polarising undulator epu48Vert

The Radia [2] magnet model of the epu48Vert ID is shown in Figure 5.479. The length of the magnet model is 401.496 mm. The magnetic material in the model is NdFeb with a remanence of 1.28 T, a material similar to VACODYM 776 TP from Vacuumschmelze. Blocks with vertical magnetisation are blue and blocks with horizontal magnetisation are yellow. The block size is

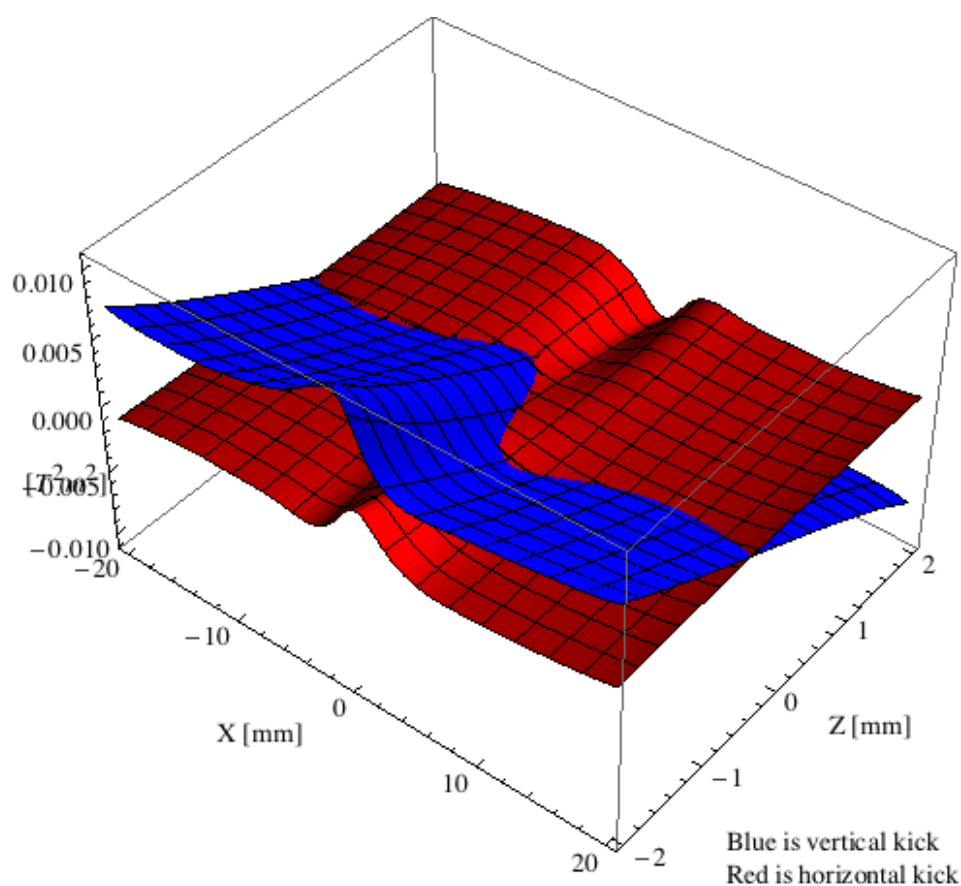


Figure 5.473: Kick map in the beam energy independent unit  $T^2m^2$  of the kicks induced by the epu48Incl ID over the beam stay clear aperture.

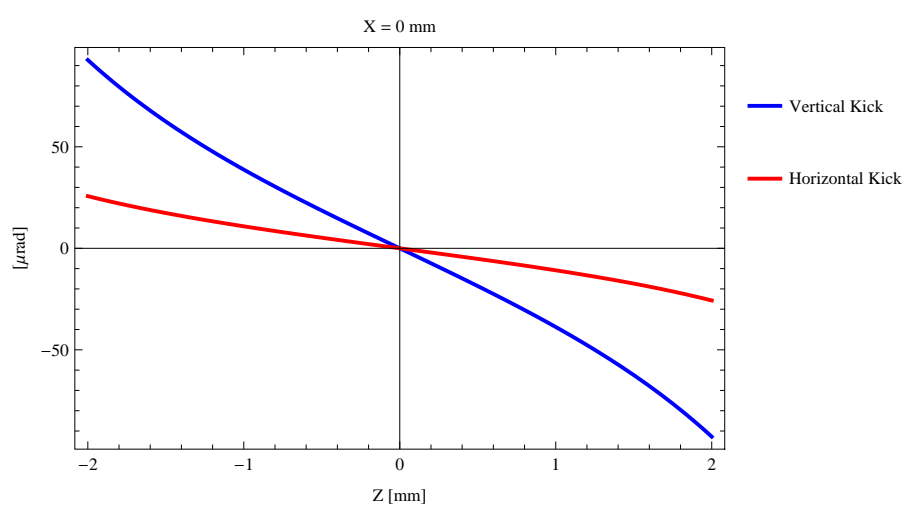


Figure 5.474: Induced angular kick on the stored beam from the epu48Incl ID as a function of the vertical distance to the ID axis.

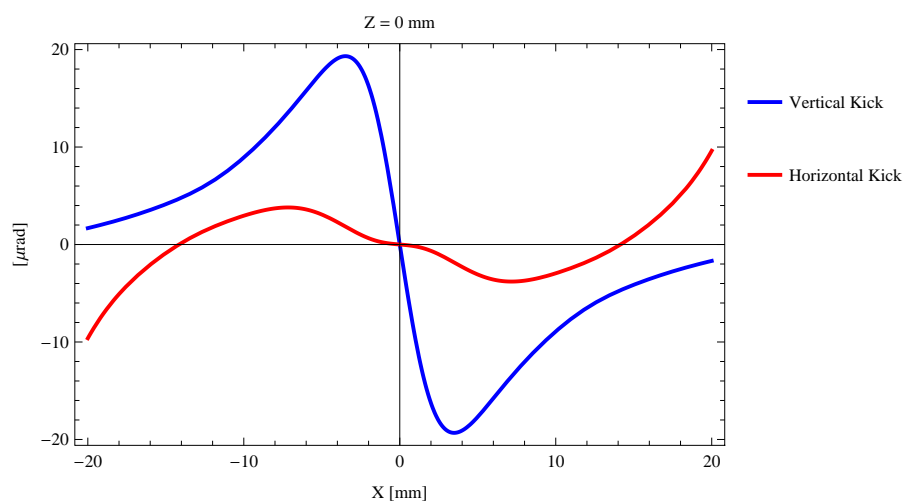


Figure 5.475: Induced angular kick on the stored beam from the epu48Incl ID as a function of the horizontal distance to the ID axis.

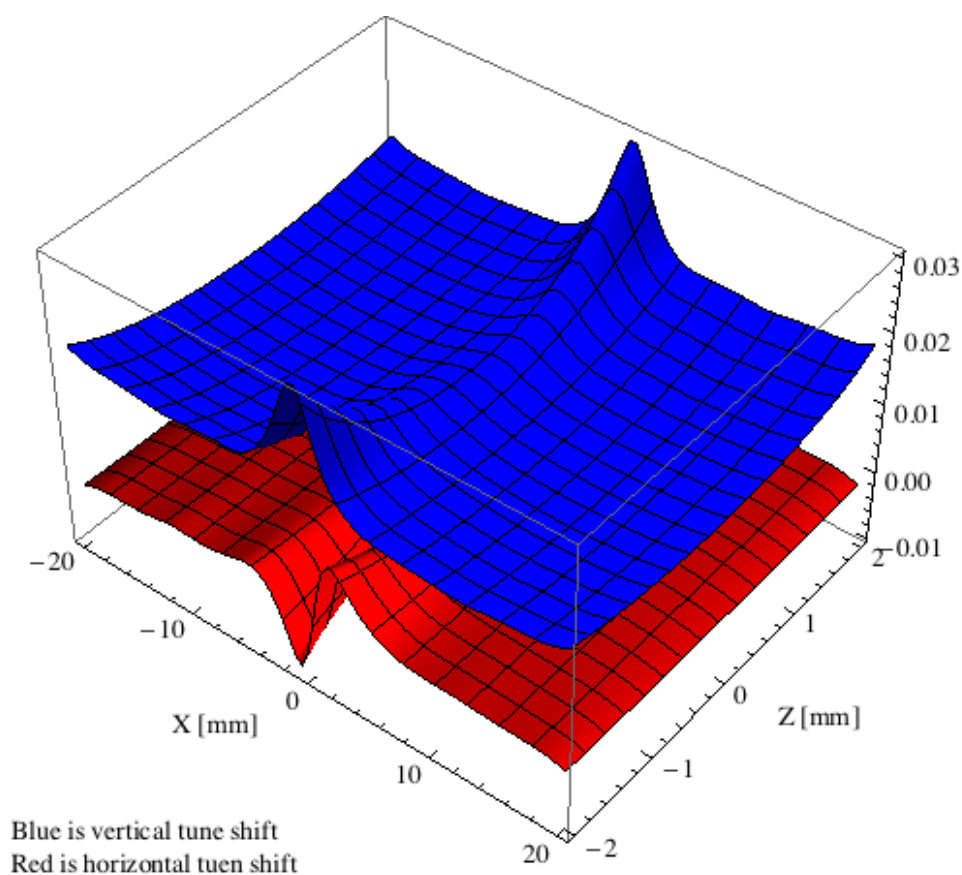


Figure 5.476: Tune shift induced by the epu48Incl ID over the beam stay clear aperture.

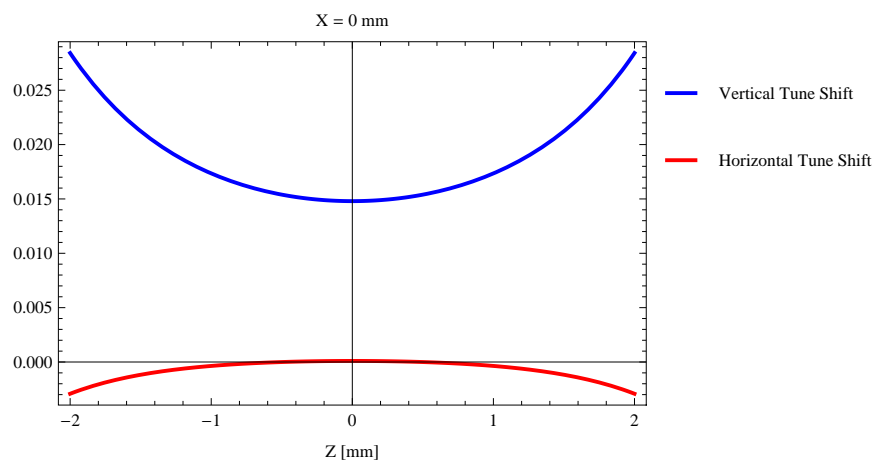


Figure 5.477: Induced tune shift from the epu48Incl ID as a function of the vertical distance to the axis of the ID.

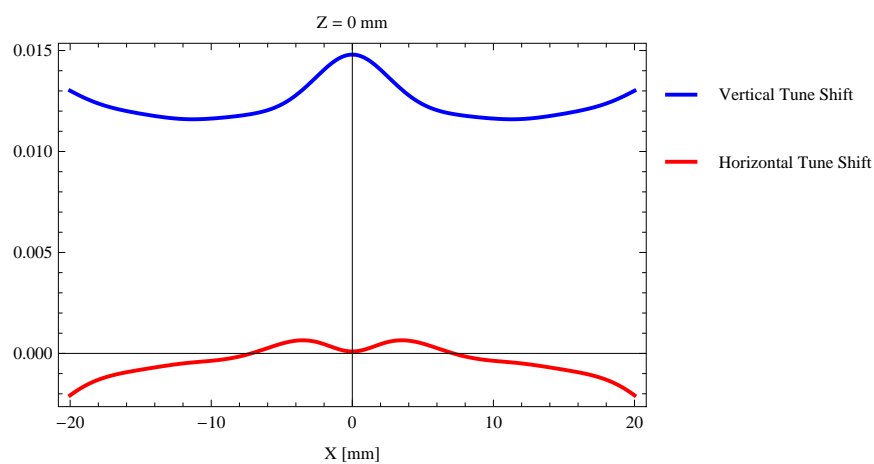


Figure 5.478: Induced tune shift from the epu48Incl ID on the stored beam from the ID as a function of the horizontal distance to the axis of the ID.

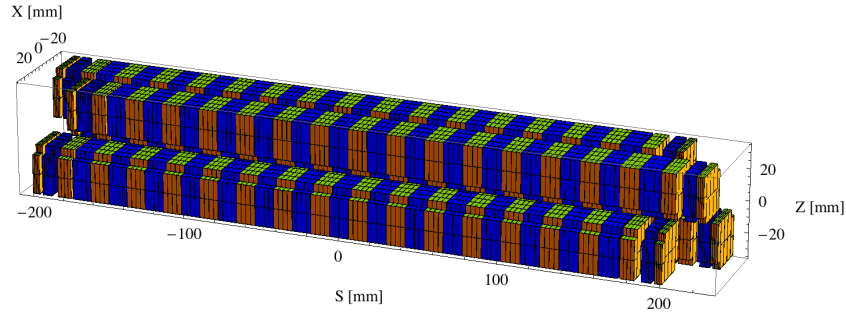


Figure 5.479: Magnetic model of the epu48Vert ID. The ID has been modelled with Radia [2]

30.x30.x12. mm<sup>3</sup> and there is a 5. mm cut-out in two of the corners of the blocks. The total length of the epu48Vert ID is 3905.5 mm.

### Analysis of the magnetic field of the epu48Vert ID

The effective magnetic fields on axis and the fundamental photon energy of the epu48Vert ID are shown in Table 5.70. The higher harmonic contents in the magnetic field of an elliptically polarising undulator made of permanent magnets is negligible and the efficient field has about the same strength as the peak field.

Table 5.70: Effective Fields on axis and Fundamental Photon Energy of the epu48Vert ID

Undulator Period	48	mm
Undulator Gap	9	mm
Undulator Mode	Vertical	
Undulator Phase	24.000	mm
Vertical Peak Field	0.000	T
Efficient Vertical Field	0.000	T
Kx (from vert. field)	0.000	
Horizontal Peak Field:	0.905	T
Efficient Horizontal Field	0.907	T
Kz (from hor. field)	4.066	
Photon Energy, Harm.1	0.192	keV
Emitted Power	9.147	kW
Total Length	3905.5	mm

### Synchrotron radiation from the epu48Vert ID

The power map of the emitted synchrotron radiation by the epu48Vert ID, assuming a 0.5 A filament beam with an energy of 3 GeV and undulator properties of the synchrotron radiation, is shown in Figure 5.483. The on-axis power density is 31.721 kW/mrad<sup>2</sup>

A map of the degree of linear polarisation of the fundamental harmonic of the synchrotron radiation emitted by the epu48Vert ID over the angle of observation is shown in Figure 5.484.

A map of the degree of 45 degree polarisation of the fundamental harmonic of the synchrotron radiation emitted by the epu48Vert ID over the angle of observation is shown in Figure 5.485.

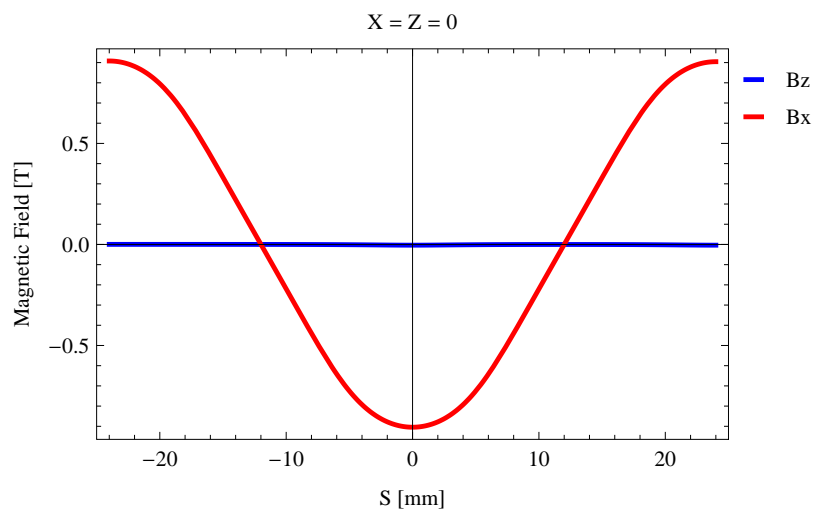


Figure 5.480: Vertical magnetic field in a central pole of the epu48Vert ID along the ID axis,  $X = Z = 0$

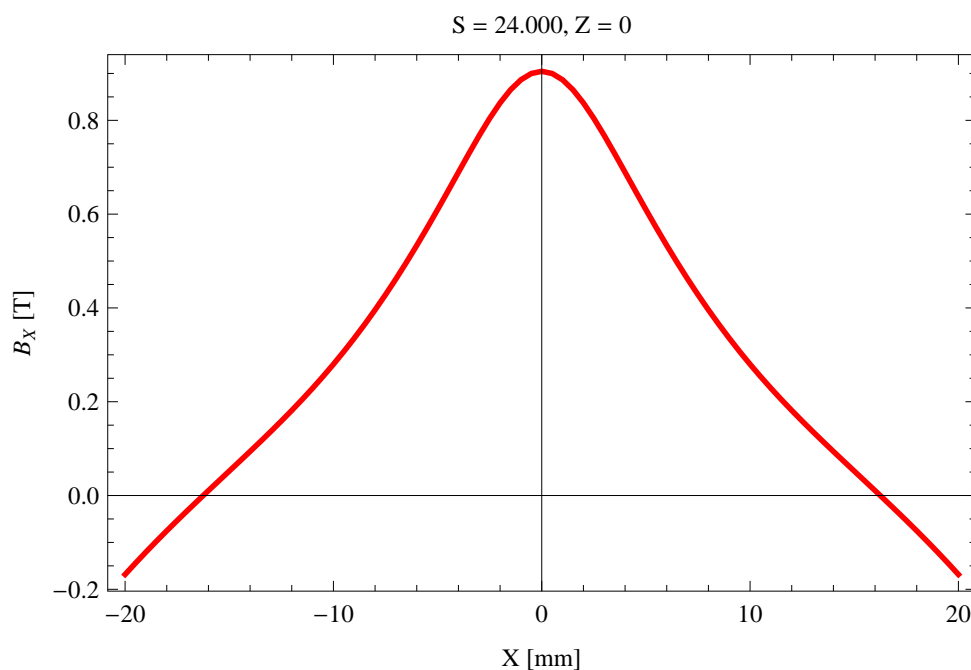


Figure 5.481: Horizontal magnetic field in a central pole of the epu48Vert ID along the horizontally transverse direction to the ID axis,  $S = 24.000, Z = 0$

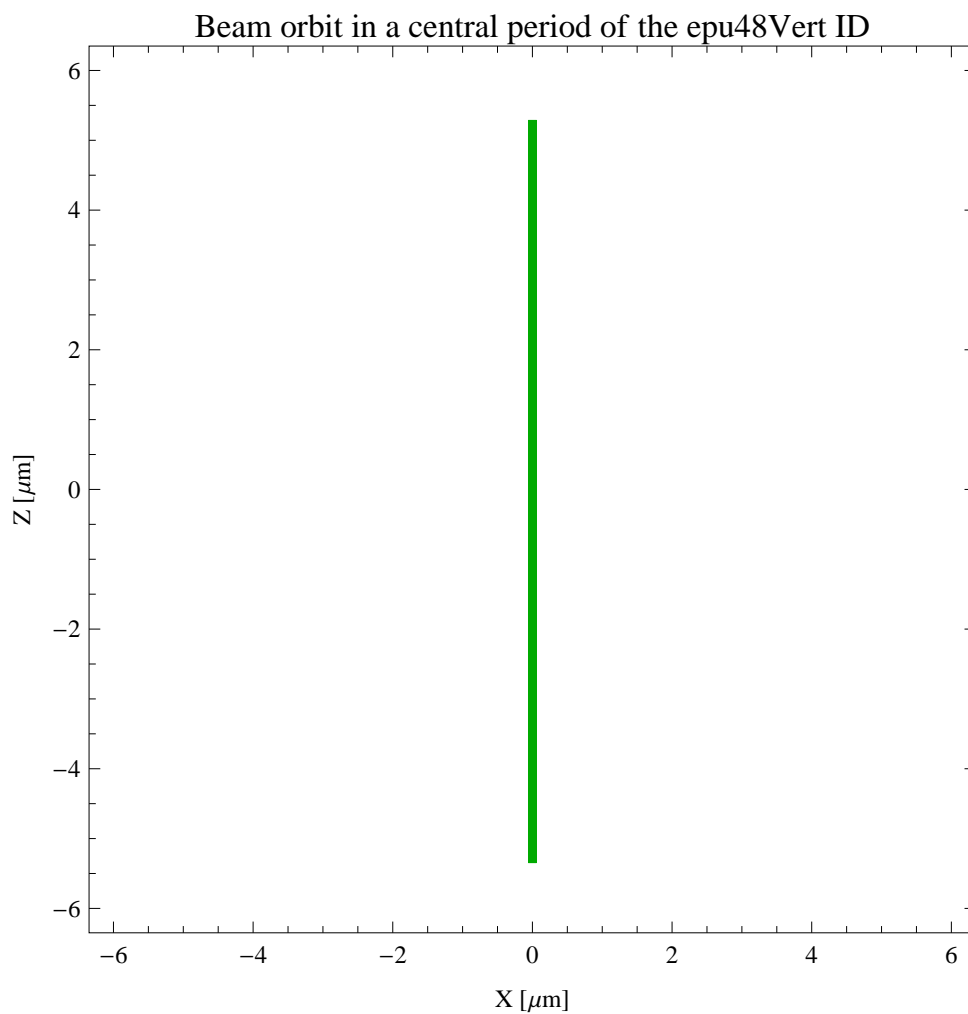


Figure 5.482: The beam orbit of the electron beam through a central period of the epu48Vert ID

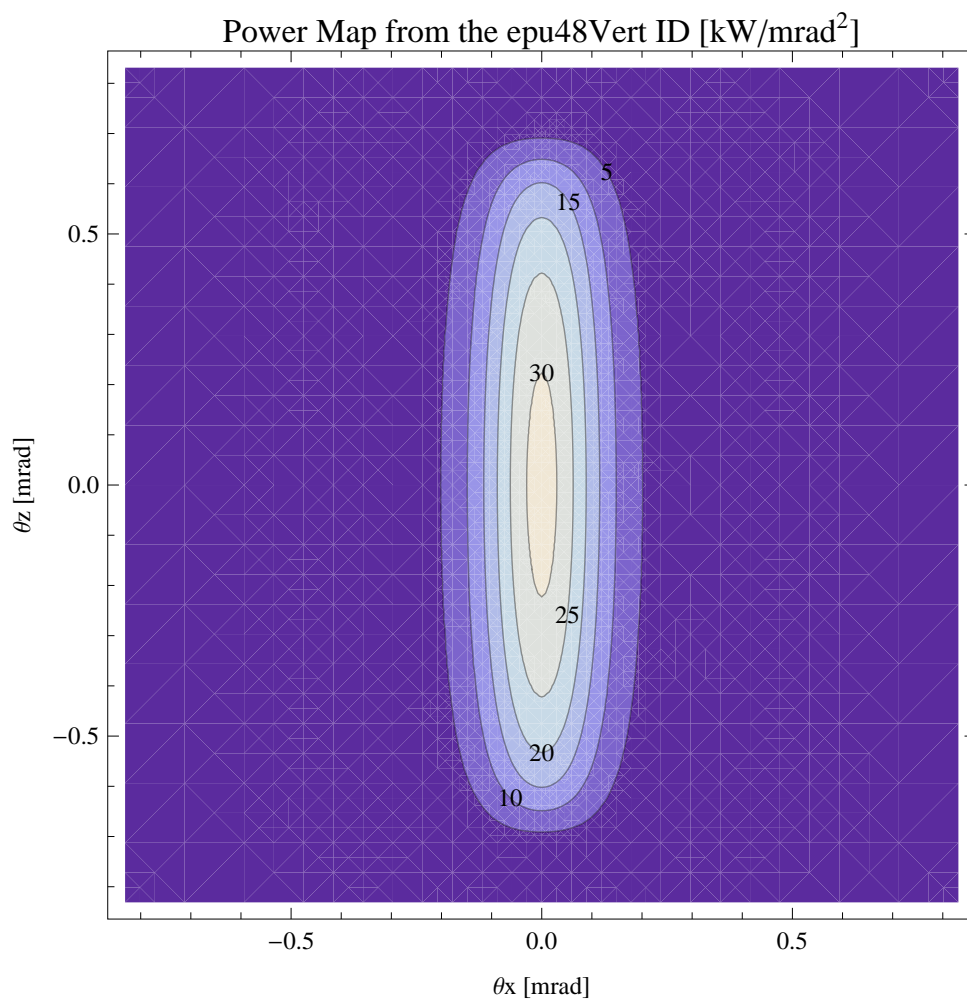


Figure 5.483: Map of the power distribution of the emitted synchrotron radiation by the epu48Vert ID



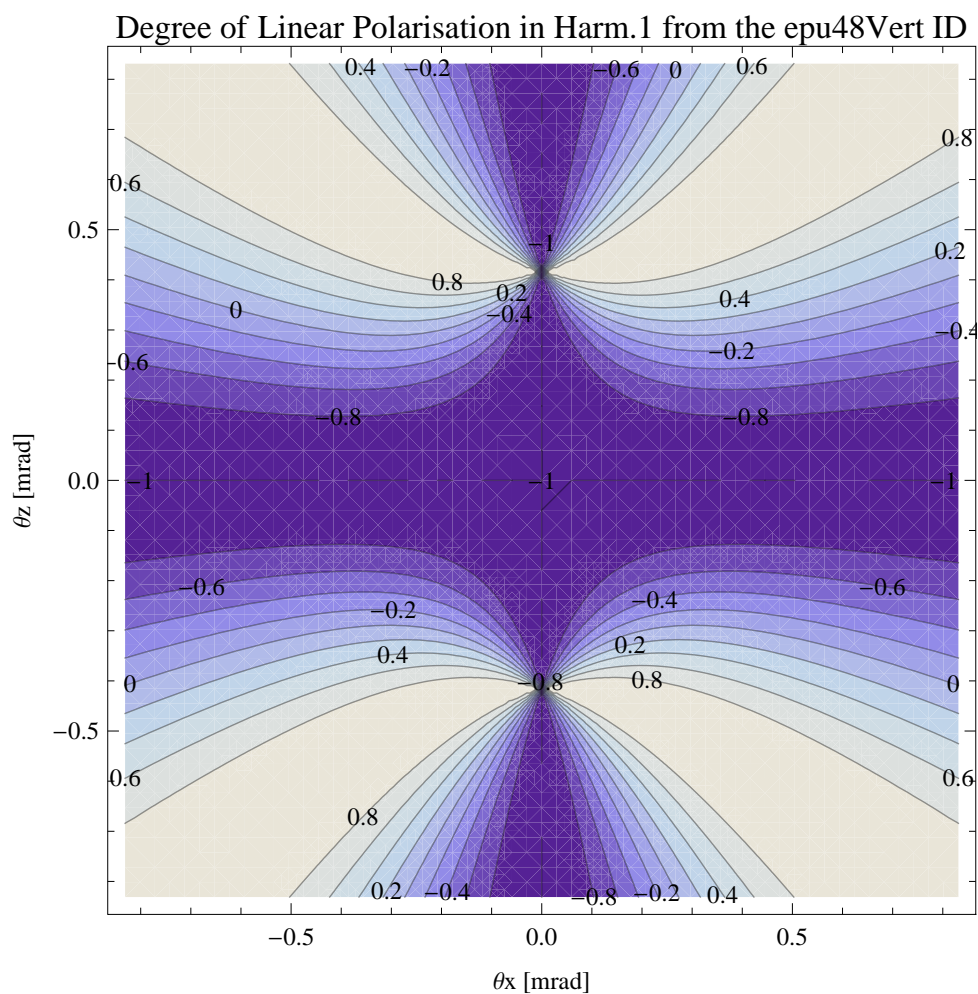


Figure 5.484: Map of linear polarisation in the fundamental harmonic of the synchrotron radiation emitted by the epu48Vert ID

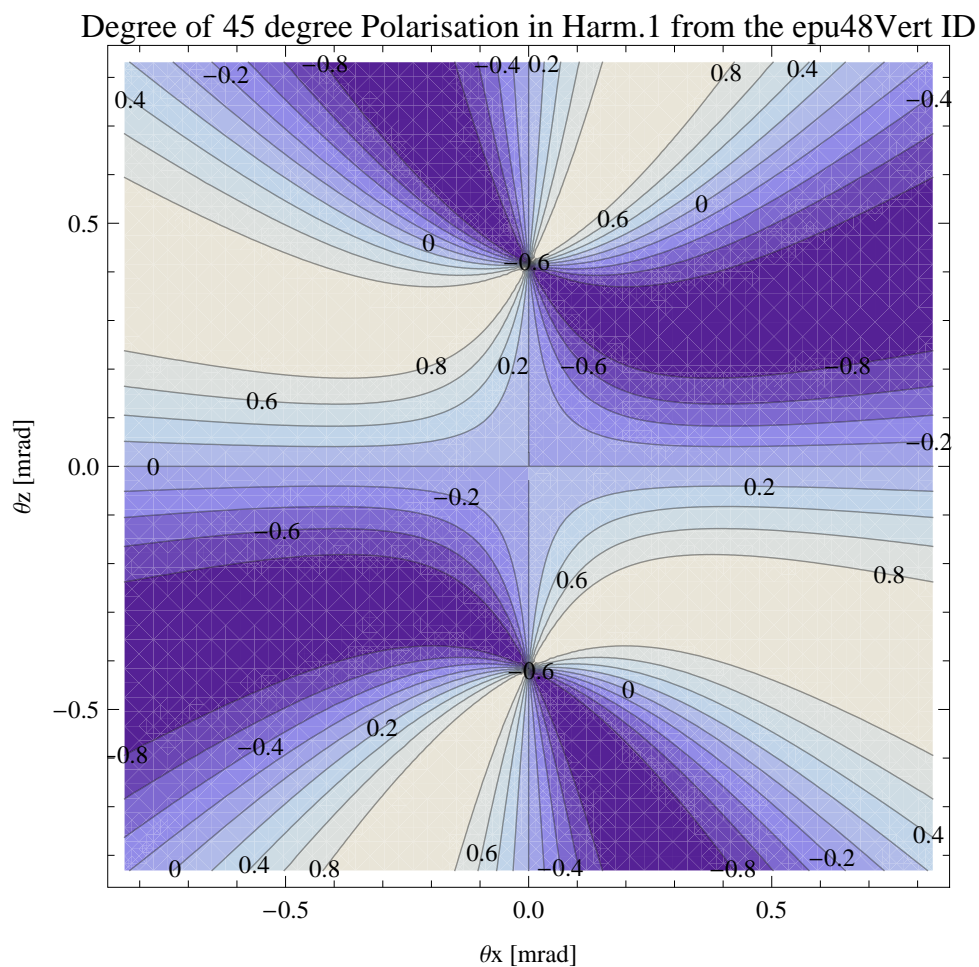


Figure 5.485: Map of 45 degree polarisation in the fundamental harmonic of the synchrotron radiation emitted by the epu48Vert ID

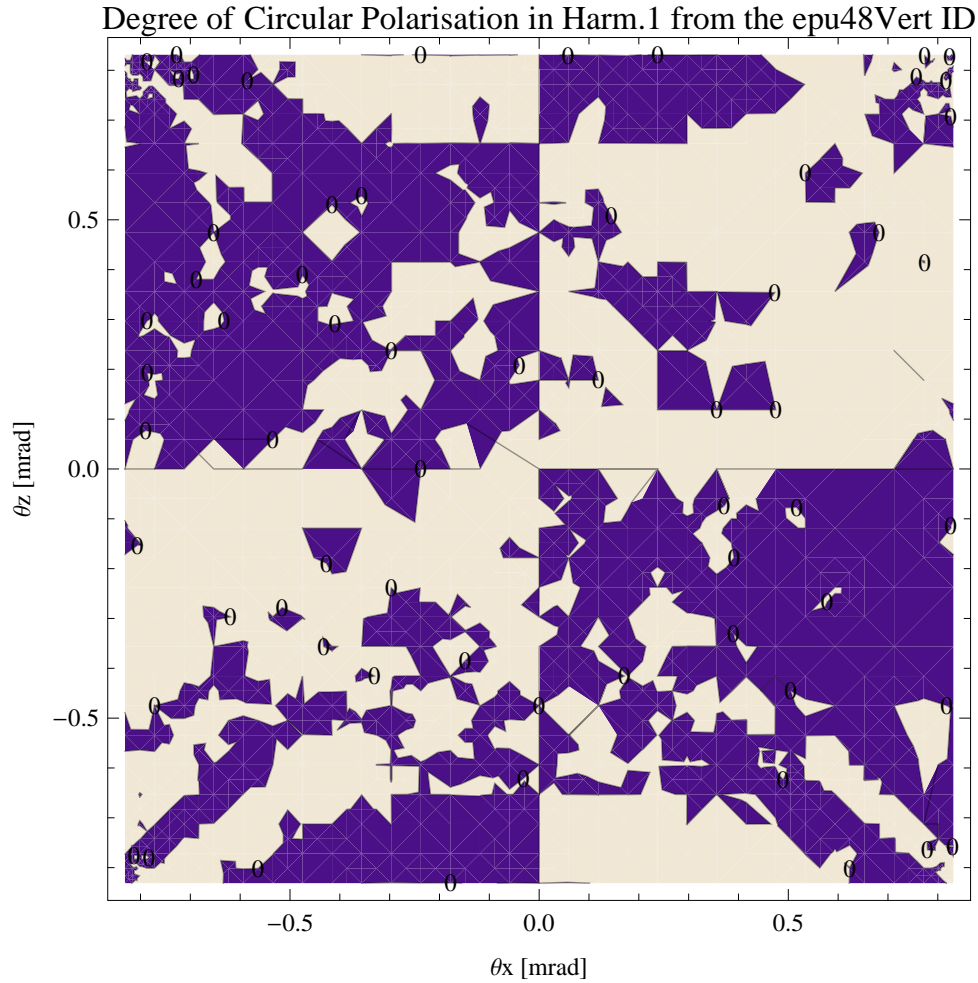


Figure 5.486: Map of circular polarisation in the fundamental harmonic of the synchrotron radiation emitted by the epu48Vert ID

A map of the degree of circular polarisation of the fundamental harmonic of the synchrotron radiation emitted by the epu48Vert ID over the angle of observation is shown in Figure 5.486.

The on axis brilliance at peak energy, the angular spectral flux, the flux in the harmonics, the power in the harmonics, the ratio of coherence, the coherent flux in the harmonics, and the power of coherent radiation in the harmonics from the epu48Vert ID have been calculated and the resulting plots are found in this section of the document. The beam parameters used for the calculation are 0.5 A of stored current,  $\beta_H = 9$  m,  $\varepsilon_H = 0.263$  nmrad,  $\beta_V = 4.8$  m,  $\varepsilon_V = 8$  pmrad, and an energy spread of 0.001.

The brilliance at peak energy and the angular spectral flux density from the epu48Vert ID for different harmonics at maximum K-value (4.066) are given in Table 5.71 and for minimum K-value (0.400) these values are given in Table 5.72.

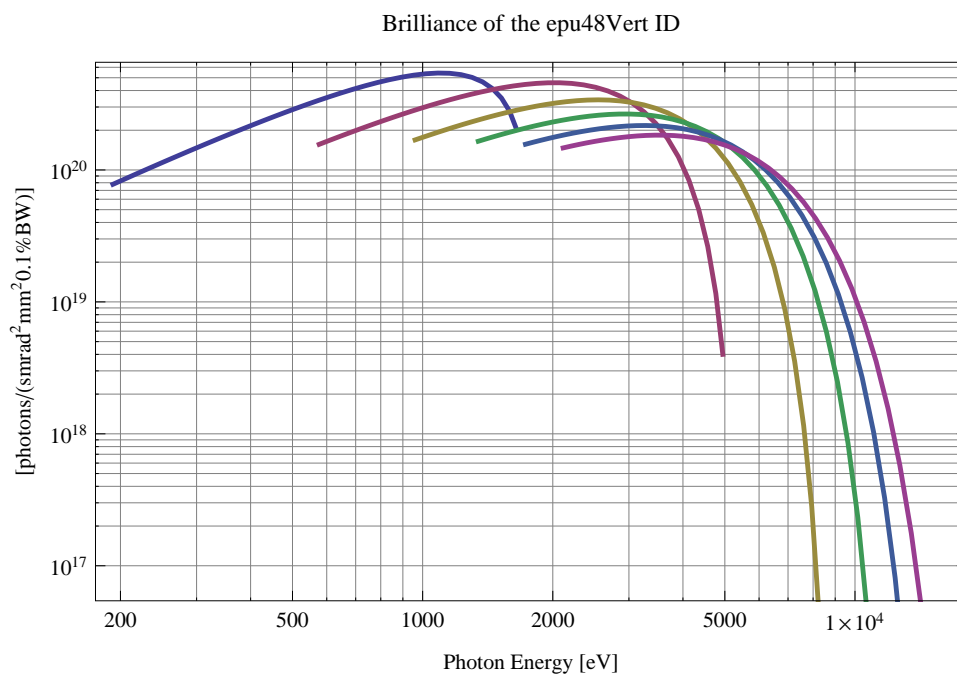


Figure 5.487: The brilliance at peak energy from the epu48Vert ID

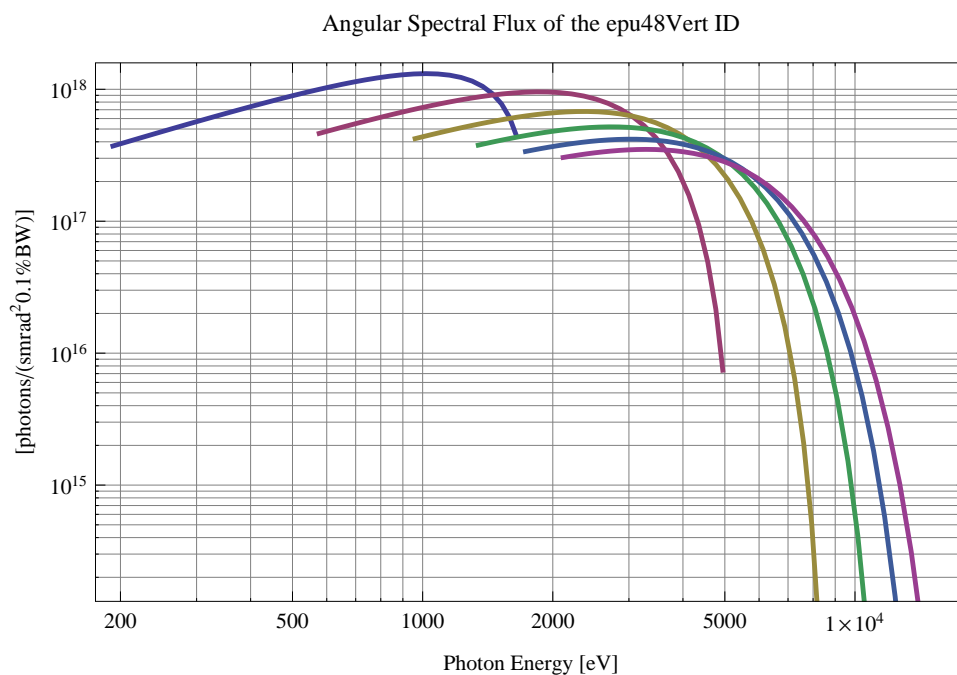


Figure 5.488: The angular spectral flux from the epu48Vert ID

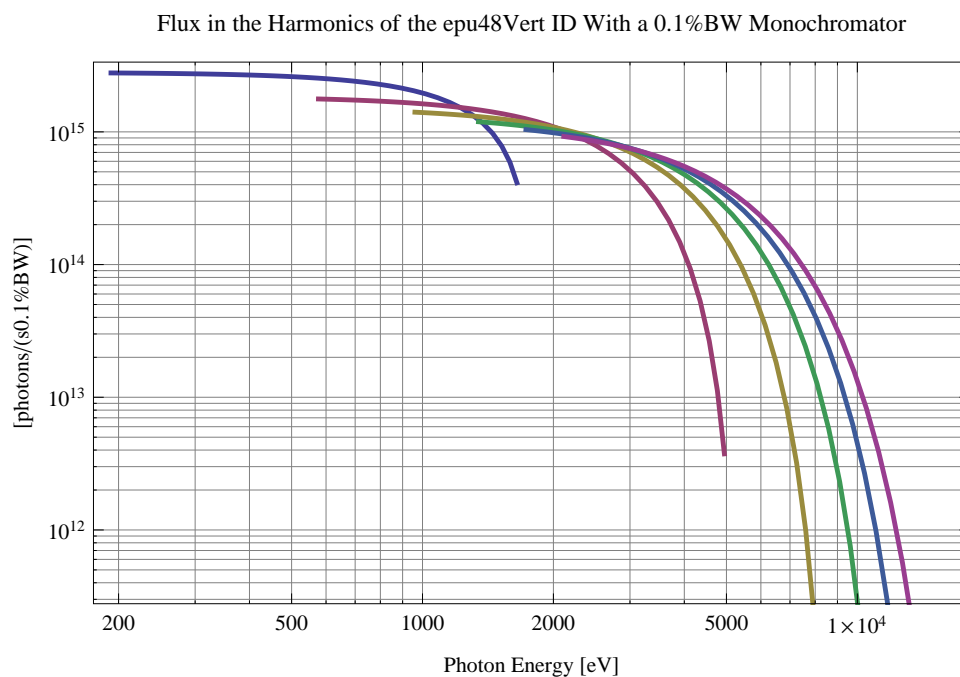


Figure 5.489: The flux of photons in the harmonics from the epu48Vert ID using a 0.1%BW monochromator

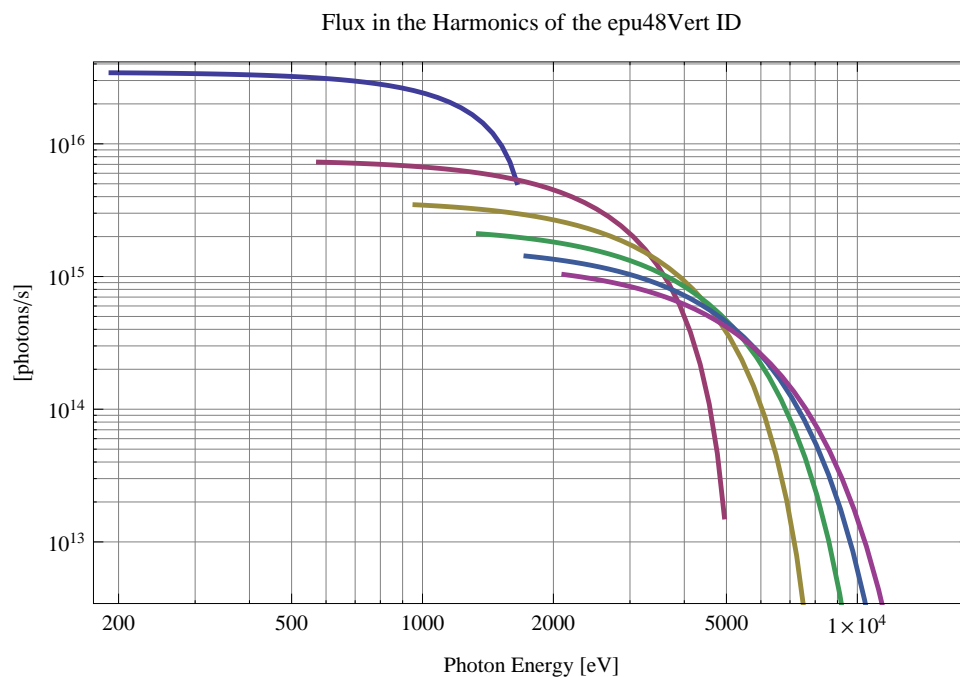


Figure 5.490: The flux of photons in the harmonics from the epu48Vert ID

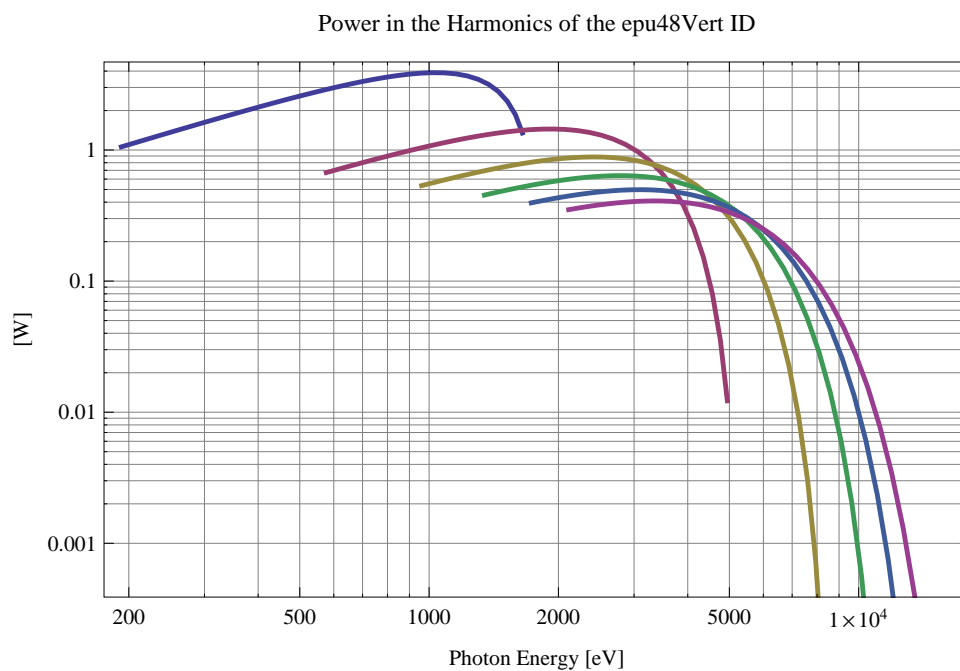


Figure 5.491: The power in the harmonics from the epu48Vert ID

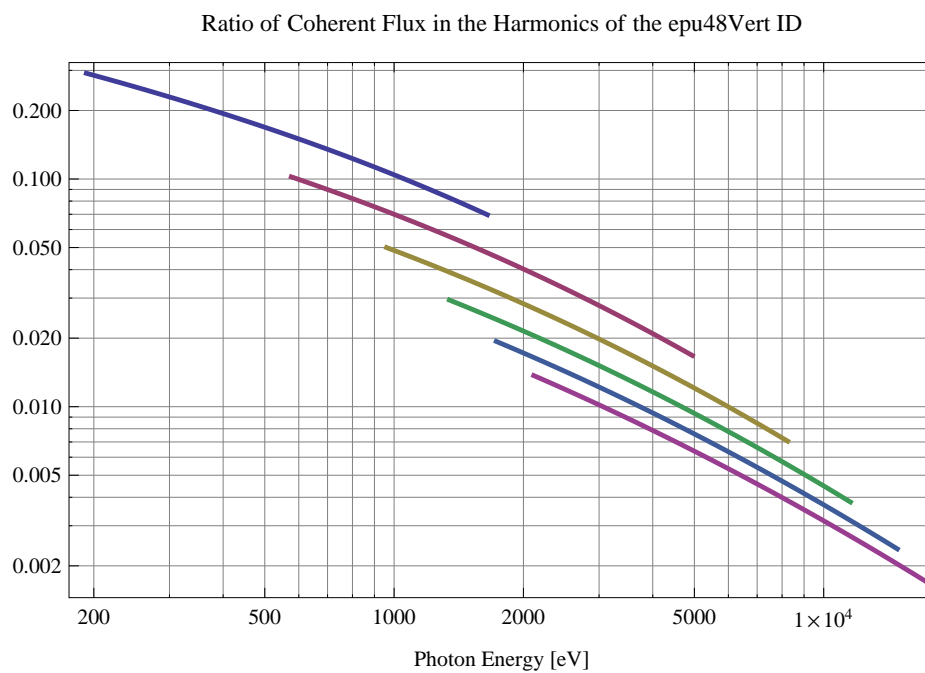


Figure 5.492: The ratio of coherent flux in the harmonics from the epu48Vert ID

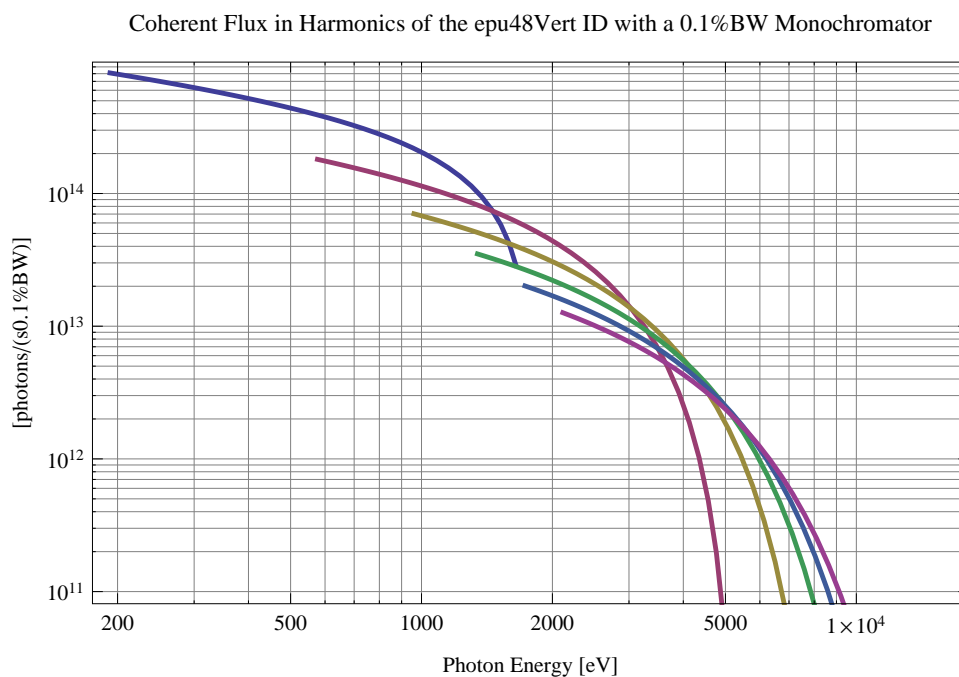


Figure 5.493: The coherent flux in the harmonics of the epu48Vert ID using a 0.1%BW Monochromator

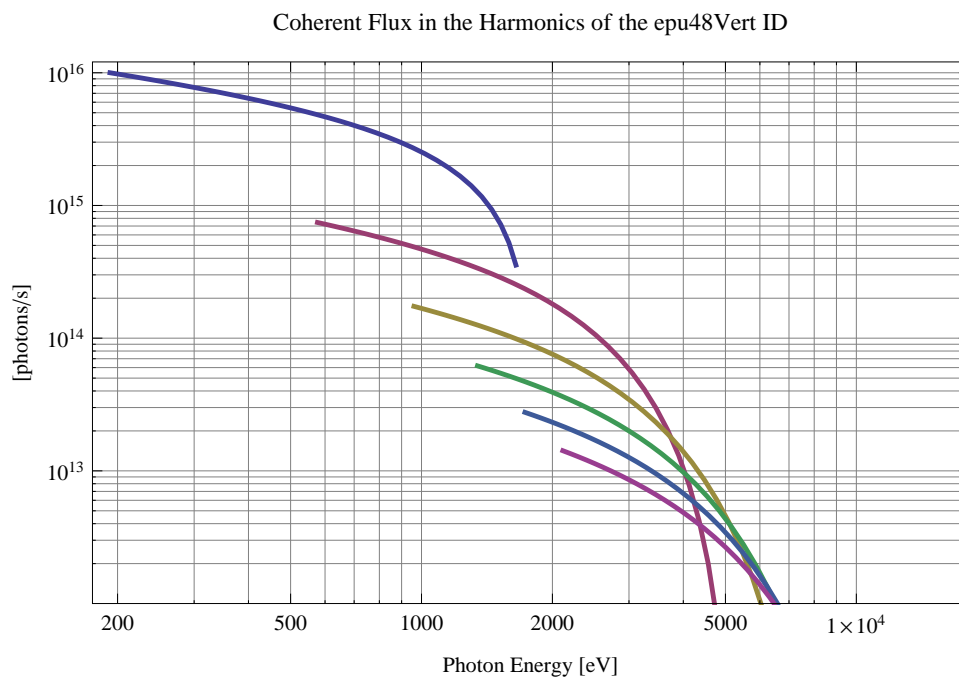


Figure 5.494: The coherent flux in the harmonics of the epu48Vert ID

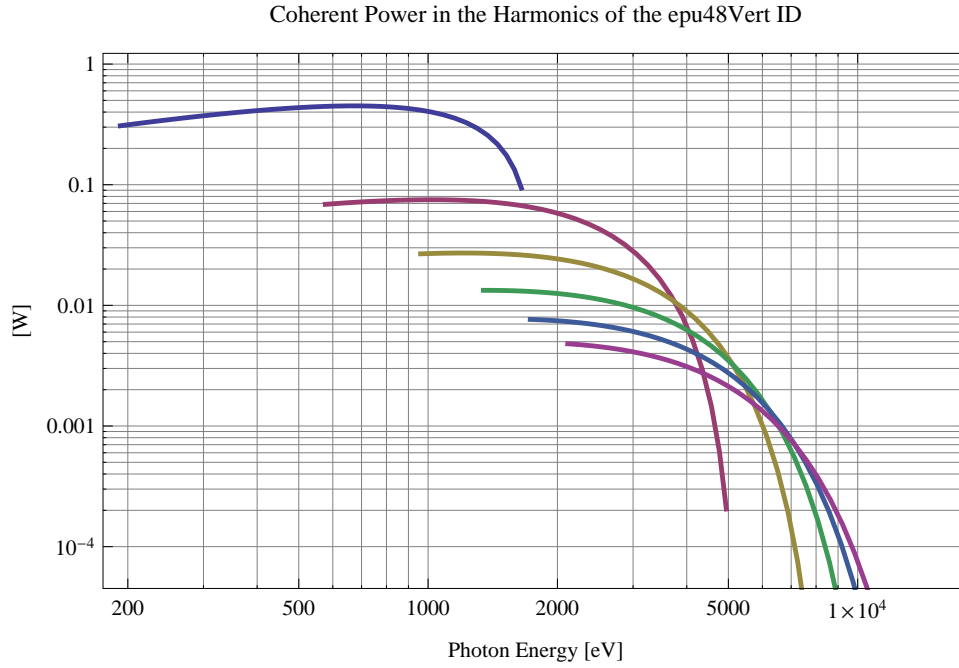


Figure 5.495: The power of coherent synchrotron radiation in the harmonics of the epu48Vert ID

Table 5.71: The brilliance at peak energy and the angular spectral flux density from the epu48Vert ID for different harmonics at maximum K-value (4.066)

Harmonic	Photon Energy [eV]	Brilliance [Ph./s/mrad <sup>2</sup> /mrad <sup>2</sup> /0.1%BW]	Angular Spectral Flux [Ph./s/mrad <sup>2</sup> /0.1%BW]
1	192.136	$7.78 \times 10^{19}$	$3.72 \times 10^{17}$
3	576.409	$1.56 \times 10^{20}$	$4.63 \times 10^{17}$
5	960.682	$1.69 \times 10^{20}$	$4.23 \times 10^{17}$
7	1344.95	$1.65 \times 10^{20}$	$3.77 \times 10^{17}$
9	1729.23	$1.57 \times 10^{20}$	$3.38 \times 10^{17}$
11	2113.5	$1.47 \times 10^{20}$	$3.04 \times 10^{17}$

Table 5.72: The brilliance at peak energy and the angular spectral flux density from the epu48Vert ID for different harmonics at minimum K-value (0.4)

Harmonic	Photon Energy [eV]	Brilliance [Ph./s/mrad <sup>2</sup> /mrad <sup>2</sup> /0.1%BW]	Angular Spectral Flux [Ph./s/mrad <sup>2</sup> /0.1%BW]
1	1648.68	$2.04 \times 10^{20}$	$4.43 \times 10^{17}$
3	4946.04	$4. \times 10^{18}$	$7.43 \times 10^{15}$
5	8243.4	$4.6 \times 10^{16}$	$8.27 \times 10^{13}$
7	11540.8	$4.86 \times 10^{14}$	$8.64 \times 10^{11}$
9	14838.1	$5.02 \times 10^{12}$	$8.88 \times 10^9$
11	18135.5	$5.13 \times 10^{10}$	$9.06 \times 10^7$



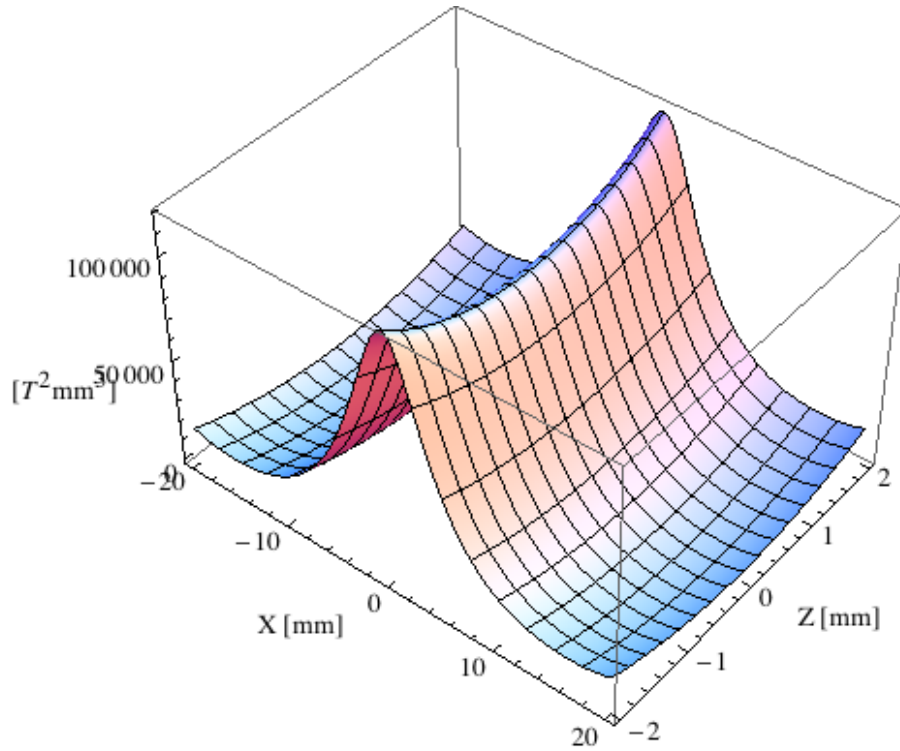


Figure 5.496: Focusing potential from the epu48Vert ID over the beam stay clear aperture.

### Influence from the epu48Vert ID on the optics of the stored beam

Figure 5.496 shows the focusing potential from the epu48Vert over the beam stay clear aperture of the ring aperture.

Figure 5.497 shows the kick map in the beam energy independent unit  $T^2 m^2$  of the kicks induced by the epu48Vert ID over the beam stay clear aperture.

Figure 5.498 shows the induced angular kick on the stored beam from the epu48Vert ID as a function of the vertical distance to the axis of the ID.

Figure 5.499 shows the induced angular kick on the stored beam from the epu48Vert ID as a function of the horizontal distance to the axis of the ID.

Figure 5.500 shows tune shift induced by the epu48Vert ID over the beam stay clear aperture. Note that the tune shift depends on the beam size at the ID.

Figure 5.501 shows the induced tune shift from the epu48Vert ID as a function of the vertical distance to the axis of the ID.

Figure 5.502 shows the induced tune shift from the epu48Vert ID as a function of the horizontal distance to the axis of the ID.

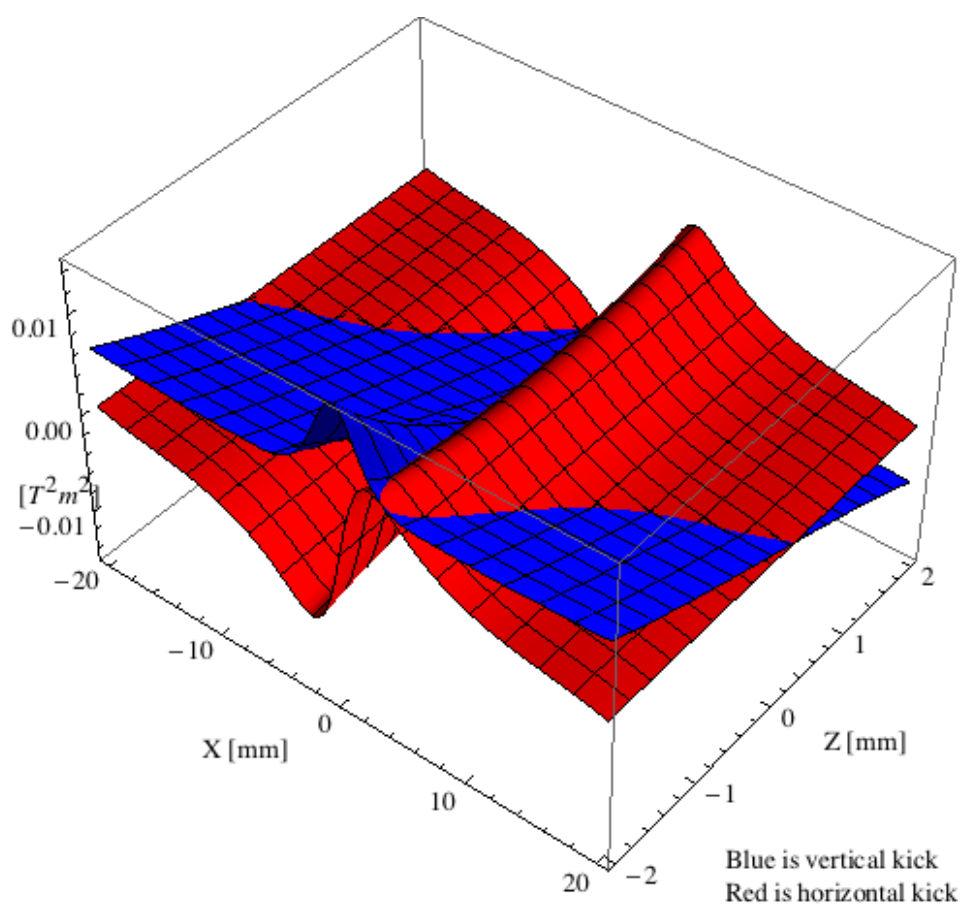


Figure 5.497: Kick map in the beam energy independent unit  $T^2 m^2$  of the kicks induced by the epu48Vert ID over the beam stay clear aperture.

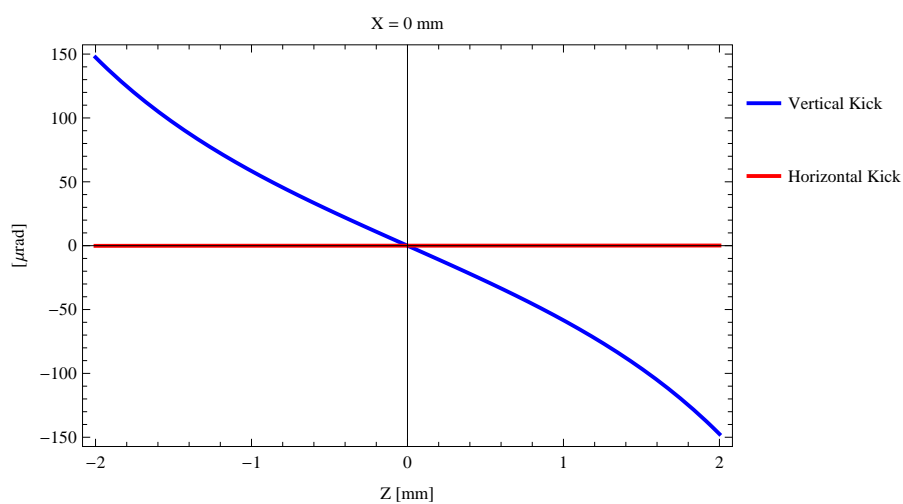


Figure 5.498: Induced angular kick on the stored beam from the epu48Vert ID as a function of the vertical distance to the ID axis.

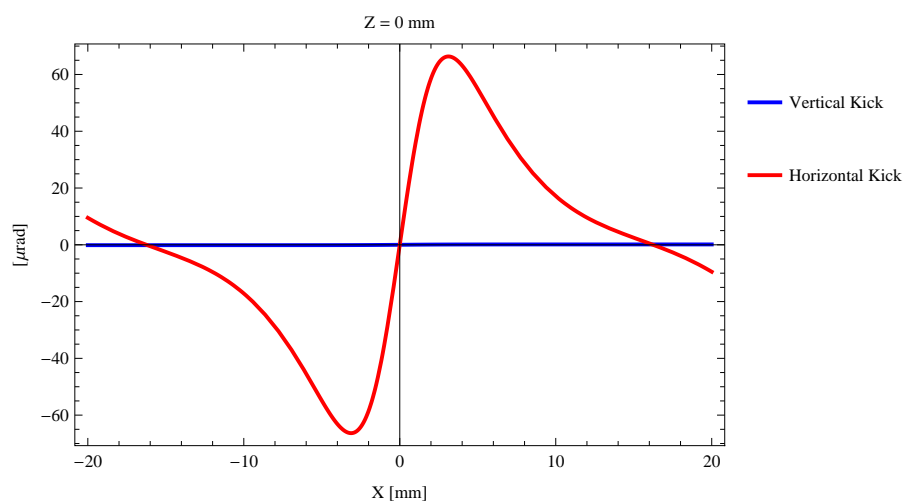


Figure 5.499: Induced angular kick on the stored beam from the epu48Vert ID as a function of the horizontal distance to the ID axis.

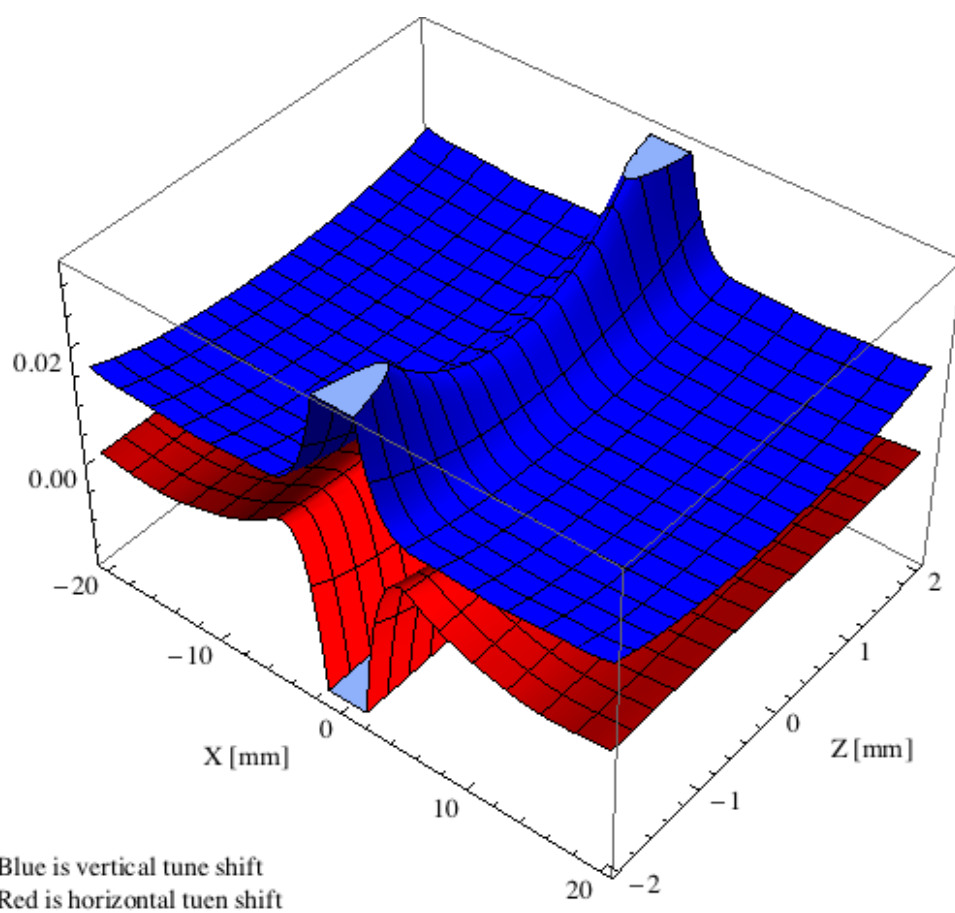


Figure 5.500: Tune shift induced by the epu48Vert ID over the beam stay clear aperture.

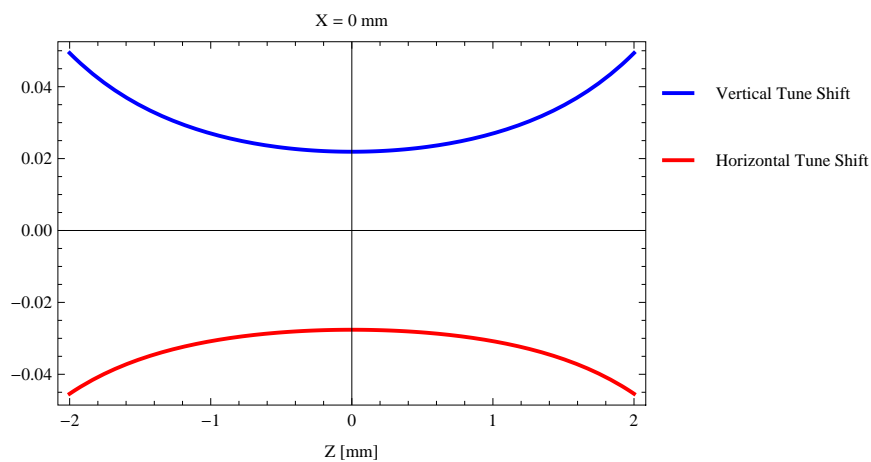


Figure 5.501: Induced tune shift from the epu48Vert ID as a function of the vertical distance to the axis of the ID.

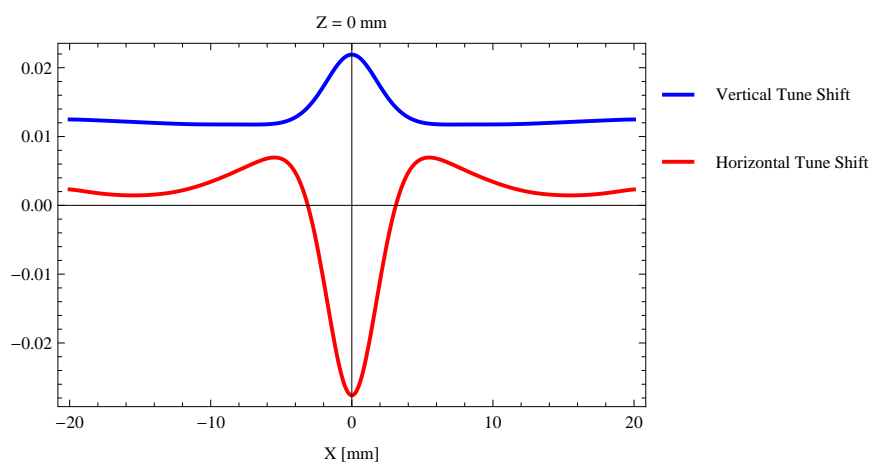


Figure 5.502: Induced tune shift from the epu48Vert ID on the stored beam from the ID as a function of the horizontal distance to the axis of the ID.

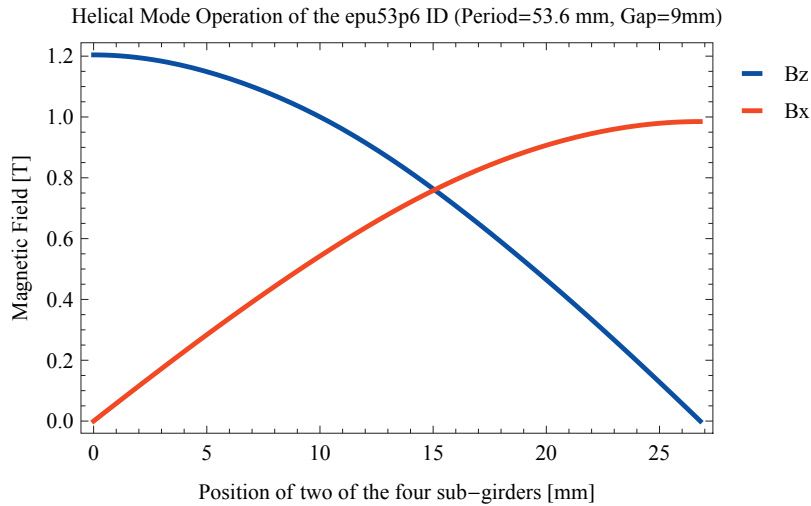


Figure 5.503: Vertical and horizontal magnetic field for the the epu53p6 ID when operating in the helical mode for different positions for two of the four sub-girders

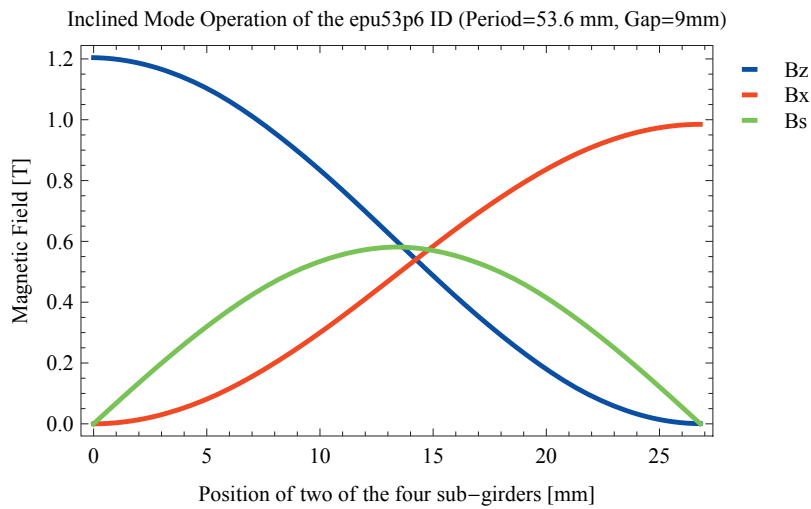


Figure 5.504: Vertical, horizontal, and longitudinal magnetic field for the the epu53p6 ID when operating in the inclined mode for different positions for two of the four sub-girders

### 5.3.10. The elliptically polarising undulator epu53p6

#### Modes of operation in the elliptically polarising undulator epu53p6

Horizontal polarisation of the emitted synchrotron radiation from the epu53p6 ID (Period=53.6 mm, Gap=9mm) is found in the planar mode when there is no movement of the sub-girders.

Circular polarisation is found in the elliptical mode of operation for a symmetric sub-grider movement of 15.0601 mm. Figure 5.503 shows the vertical and horizontal magnetic field for the epu53p6 ID when operating in the helical mode.

45 degree polarisation is found in the inclined mode of operation for an assymetric sub-grider movement of 14.2385 mm. Figure 5.504 shows the vertical and horizontal magnetic field for the epu53p6 ID when operating in the inclined mode.

The following sub-sections will cover four different situations: The epu53p6 operating in the

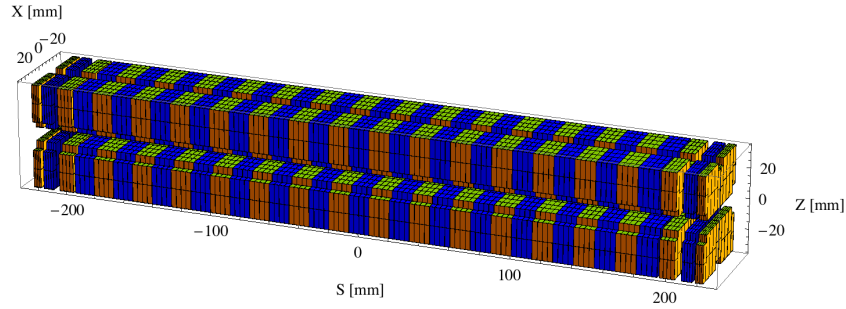


Figure 5.505: Magnetic model of the epu53p6Plan ID. The ID has been modelled with Radia [2]

planar mode for horizontal polarisation (epu53p6Plan); The epu53p6 operating in the helical mode for circular polarisation (epu53p6Heli), the epu53p6 operating in the inclined mode for 45 degree polarisation (epu53p6Incl); and The epu53p6 operating in the vertical mode for vertical polarisation (epu53p6Vert).

### Magnet model of the elliptically polarising undulator epu53p6Plan

The Radia [2] magnet model of the epu53p6Plan ID is shown in Figure 5.505. The length of the magnet model is 446.587 mm. The magnetic material in the model is NdFeb with a remanence of 1.28 T, a material similar to VACODYM 776 TP from Vacuumschmelze. Blocks with vertical magnetisation are blue and blocks with horizontal magnetisation are yellow. The block size is  $30 \times 30 \times 13.4 \text{ mm}^3$  and there is a 5. mm cut-out in two of the corners of the blocks. The total length of the epu53p6Plan ID is 3930.59 mm.

### Analysis of the magnetic field of the epu53p6Plan ID

The effective magnetic fields on axis and the fundamental photon energy of the epu53p6Plan ID are shown in Table 5.73. The higher harmonic contents in the magnetic field of an elliptically polarising undulator made of permanent magnets is negligible and the efficient field has about the same strength as the peak field.

Table 5.73: Effective Fields on axis and Fundamental Photon Energy of the epu53p6Plan ID

Undulator Period	53.6	mm
Undulator Gap	9	mm
Undulator Mode	Planar	
Undulator Phase	0.000	mm
Vertical Peak Field	1.173	T
Efficient Vertical Field	1.204	T
Kx (from vert. field)	6.028	
Horizontal Peak Field:	0.000	T
Efficient Horizontal Field	0.000	T
Kz (from hor. field)	0.000	
Photon Energy, Harm.1	0.083	keV
Emitted Power	16.222	kW
Total Length	3930.6	mm

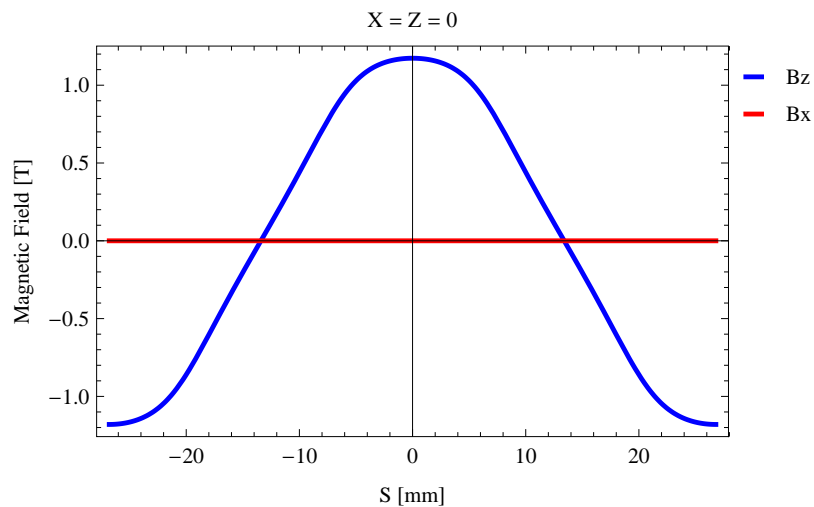


Figure 5.506: Vertical magnetic field in a central pole of the epu53p6Plan ID along the ID axis,  $X = Z = 0$

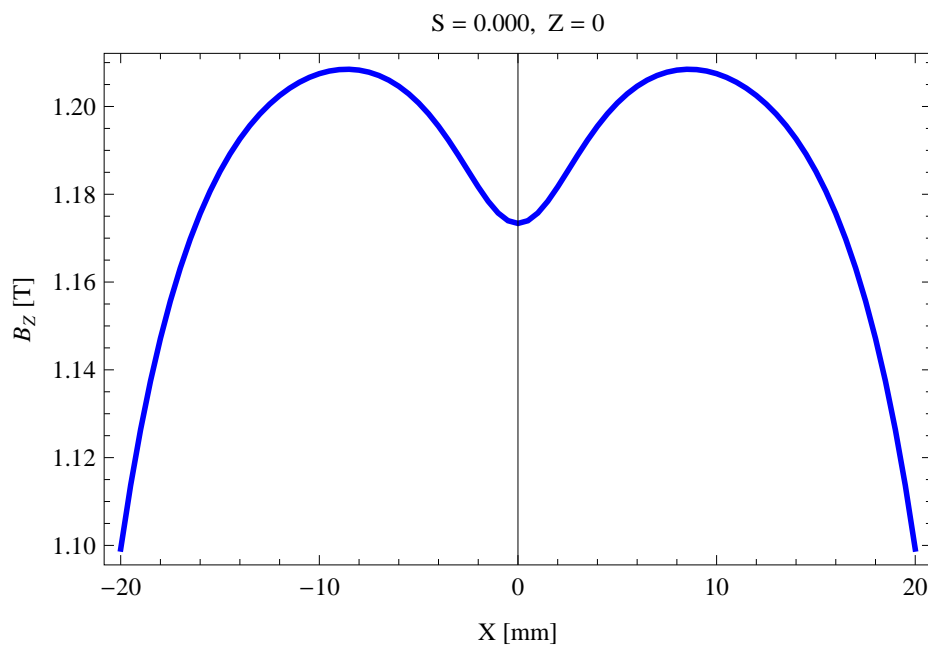


Figure 5.507: Vertical magnetic field in a central pole of the epu53p6Plan ID along the horizontally transverse direction to the ID axis,  $S = 0.000$ ,  $Z = 0$

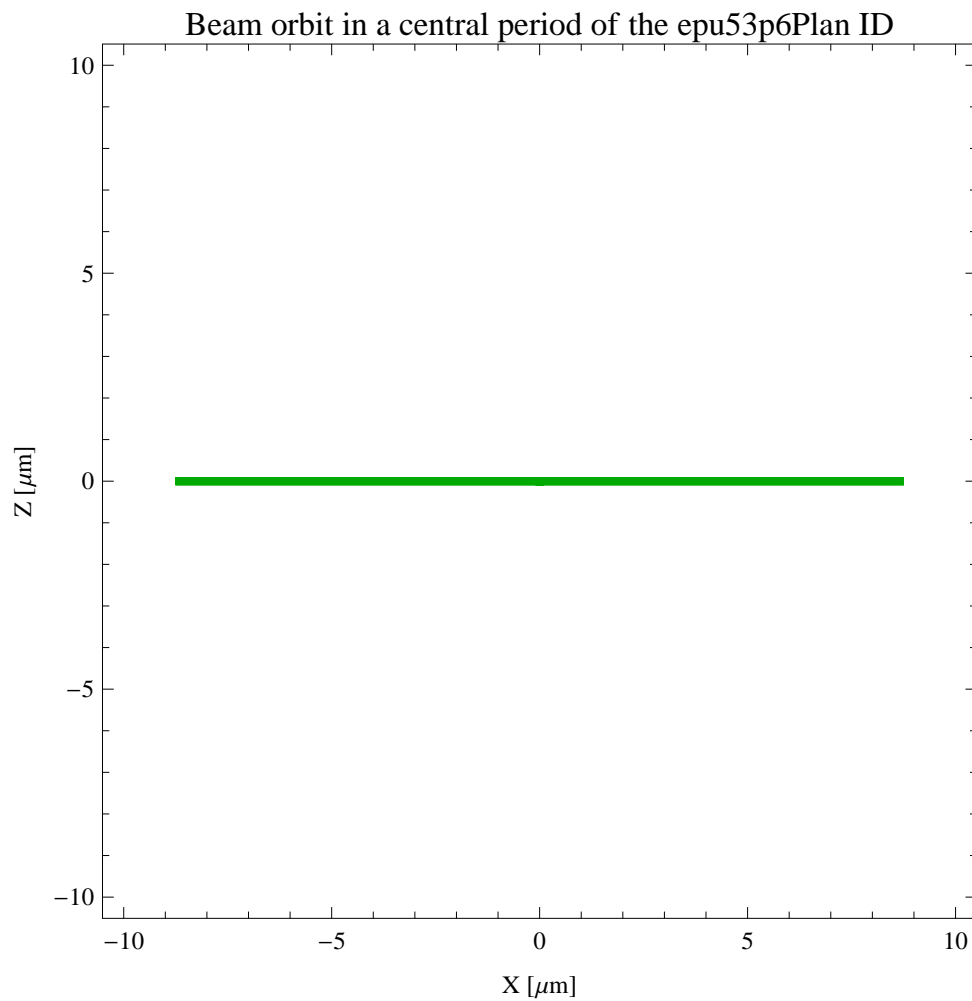


Figure 5.508: The beam orbit of the electron beam through a central period of the epu53p6Plan ID



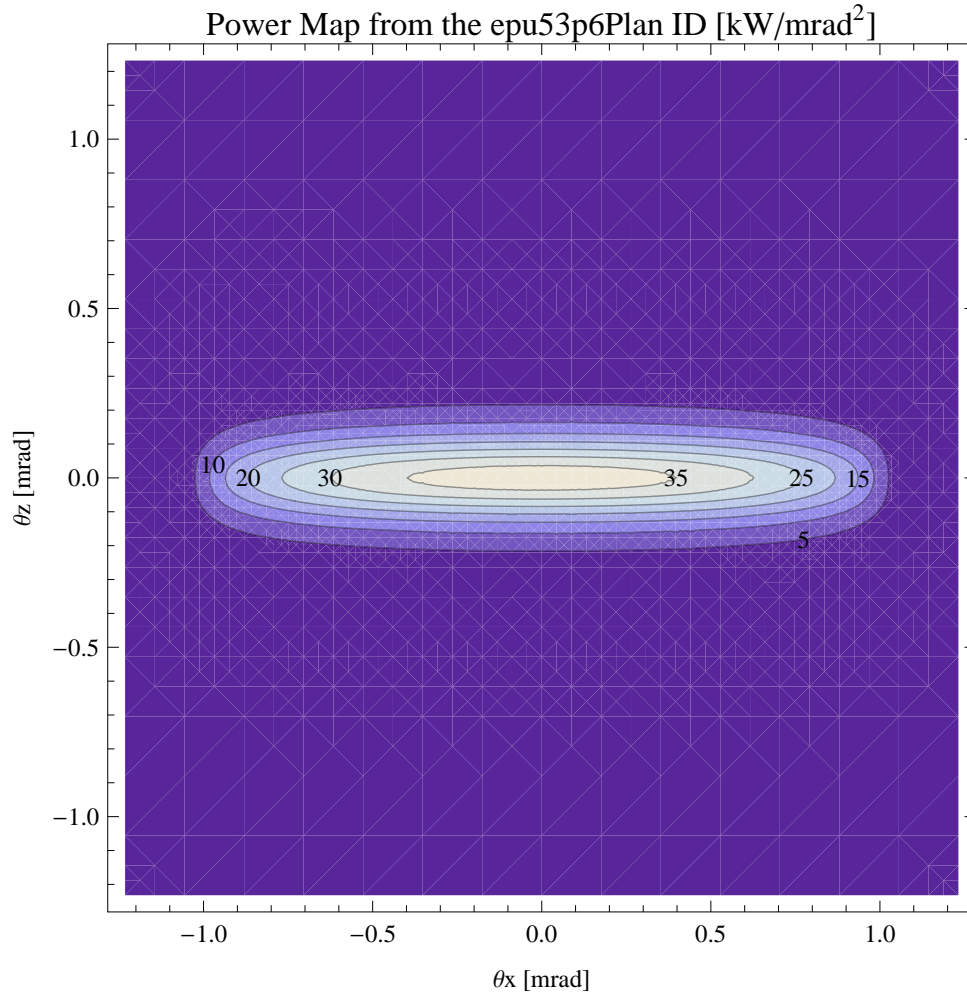


Figure 5.509: Map of the power distribution of the emitted synchrotron radiation by the epu53p6Plan ID

### Synchrotron radiation from the epu53p6Plan ID

The power map of the emitted synchrotron radiation by the epu53p6Plan ID, assuming a 0.5 A filament beam with an energy of 3 GeV and undulator properties of the synchrotron radiation, is shown in Figure 5.509. The on-axis power density is 37.995 kW/mrad<sup>2</sup>

A map of the degree of linear polarisation of the fundamental harmonic of the synchrotron radiation emitted by the epu53p6Plan ID over the angle of observation is shown in Figure 5.510.

A map of the degree of 45 degree polarisation of the fundamental harmonic of the synchrotron radiation emitted by the epu53p6Plan ID over the angle of observation is shown in Figure 5.511.

A map of the degree of circular polarisation of the fundamental harmonic of the synchrotron radiation emitted by the epu53p6Plan ID over the angle of observation is shown in Figure 5.512.

The on axis brilliance at peak energy, the angular spectral flux, the flux in the harmonics, the power in the harmonics, the ratio of coherence, the coherent flux in the harmonics, and the power of coherent radiation in the harmonics from the epu53p6Plan ID have been calculated and the resulting plots are found in this section of the document. The beam parameters used for the calculation are 0.5 A of stored current,  $\beta_H = 9$  m,  $\varepsilon_H = 0.263$  nmrad,  $\beta_V = 4.8$  m,  $\varepsilon_V = 8$  pmrad, and an energy spread of 0.001.

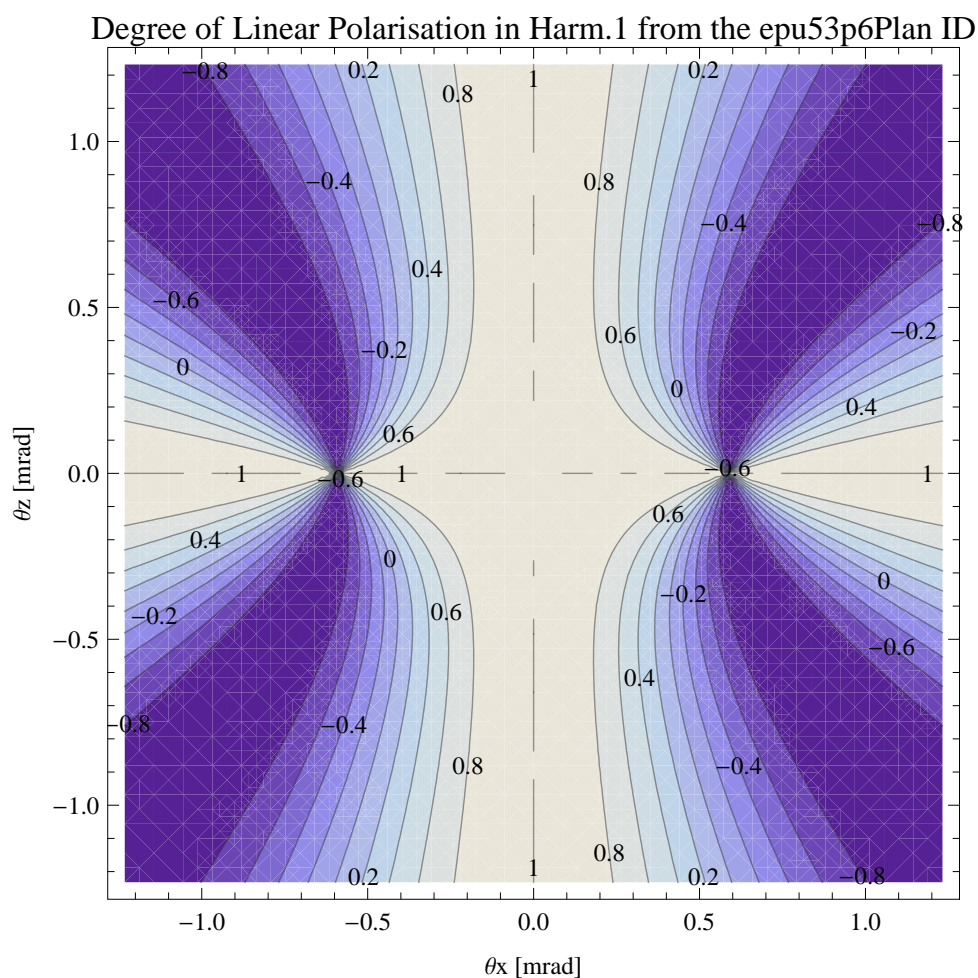


Figure 5.510: Map of linear polarisation in the fundamental harmonic of the synchrotron radiation emitted by the epu53p6Plan ID

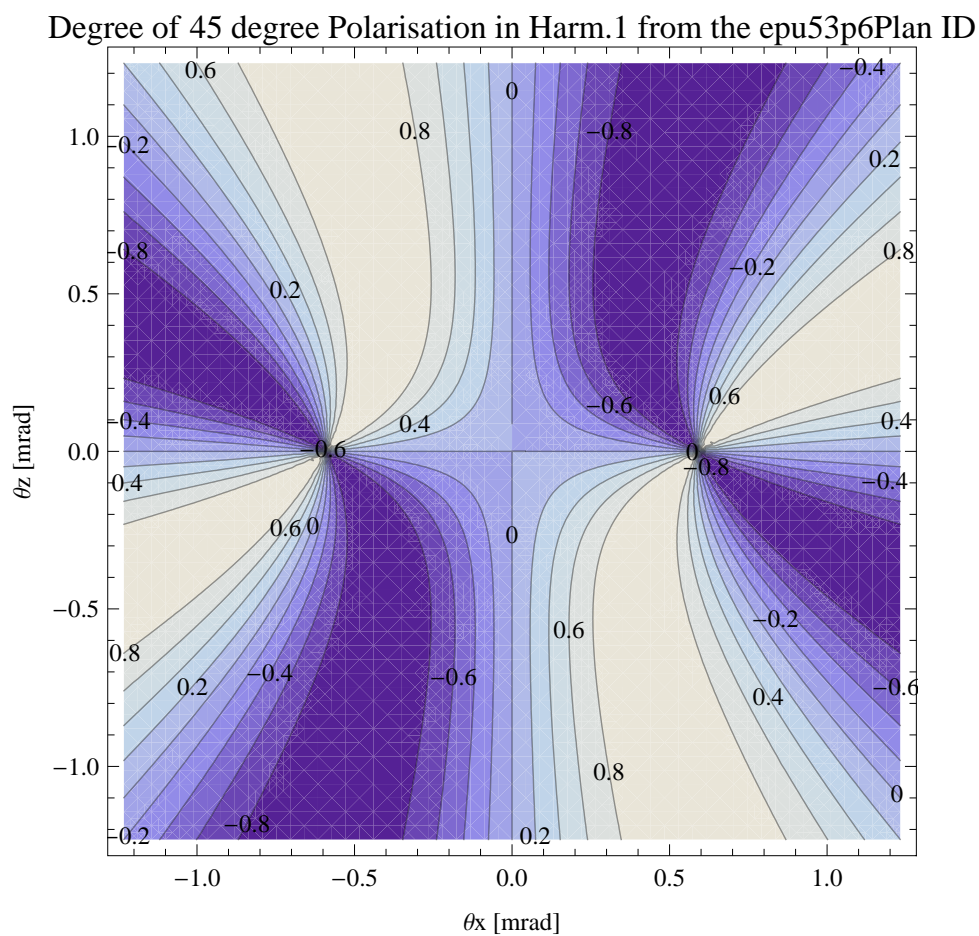


Figure 5.511: Map of 45 degree polarisation in the fundamental harmonic of the synchrotron radiation emitted by the epu53p6Plan ID

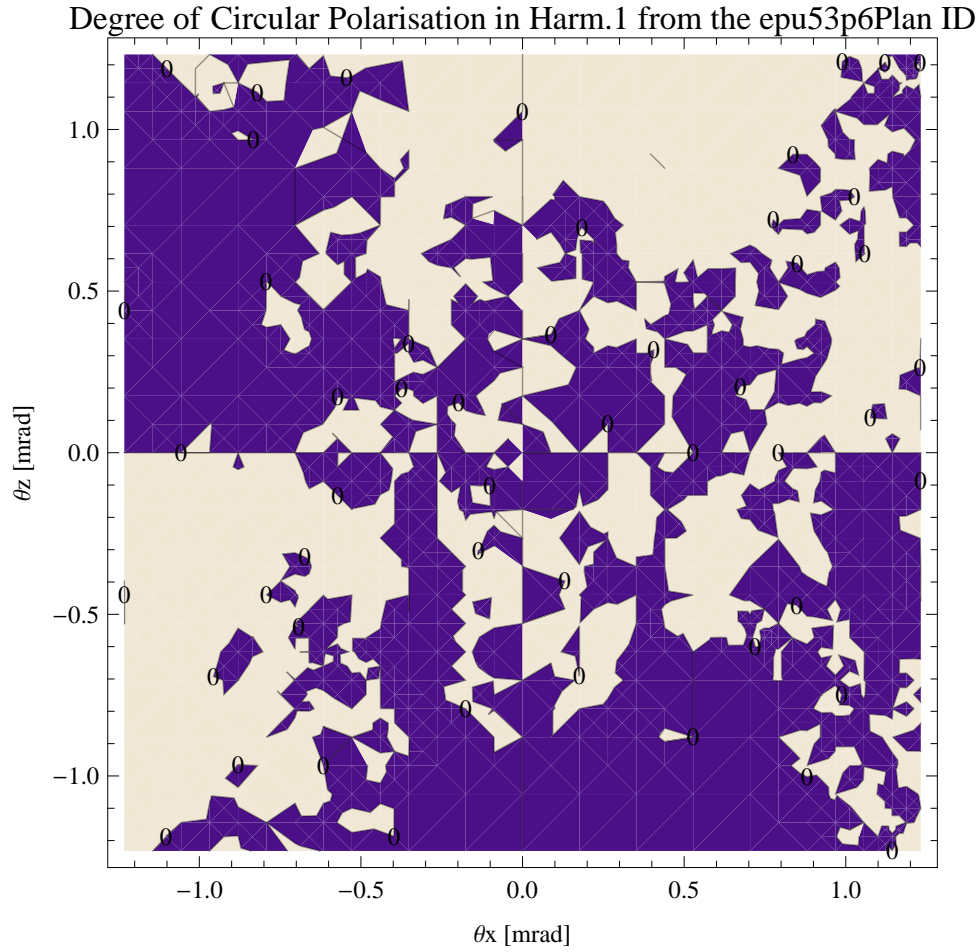


Figure 5.512: Map of circular polarisation in the fundamental harmonic of the synchrotron radiation emitted by the epu53p6Plan ID

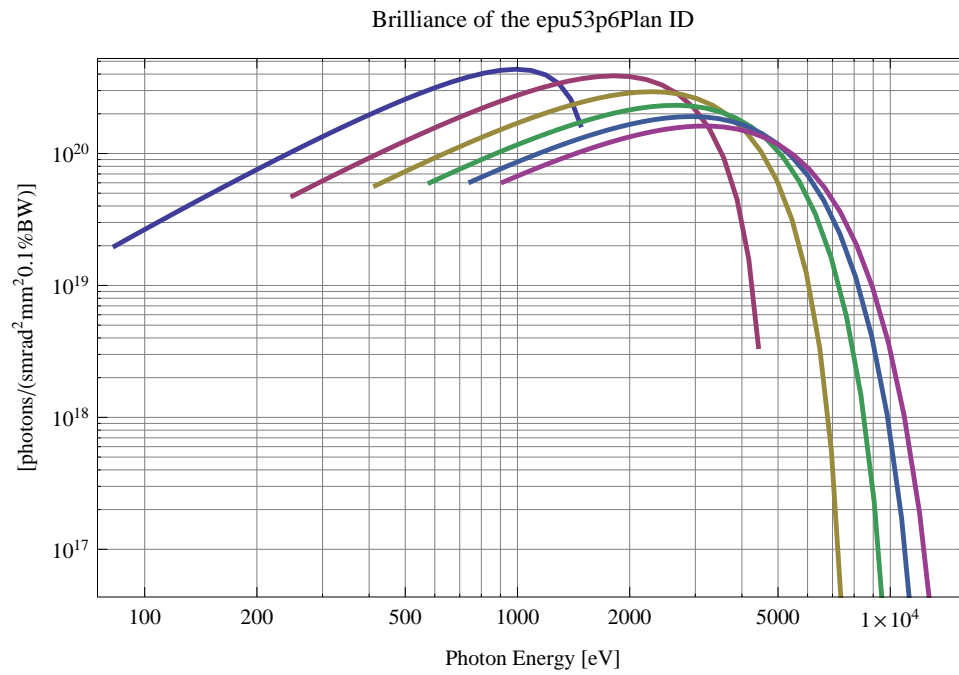


Figure 5.513: The brilliance at peak energy from the epu53p6Plan ID

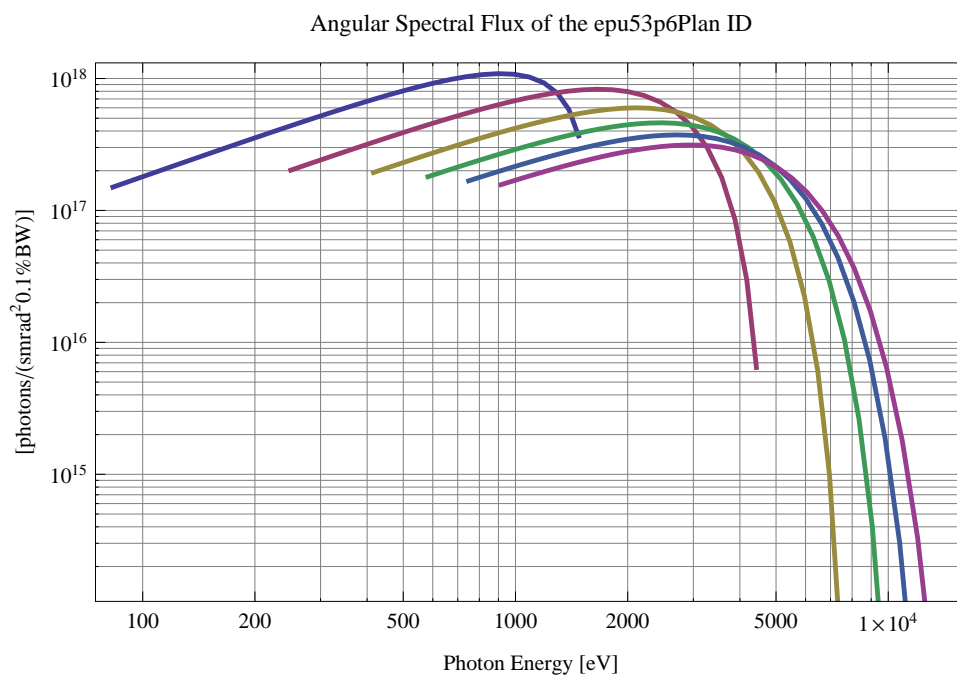


Figure 5.514: The angular spectral flux from the epu53p6Plan ID

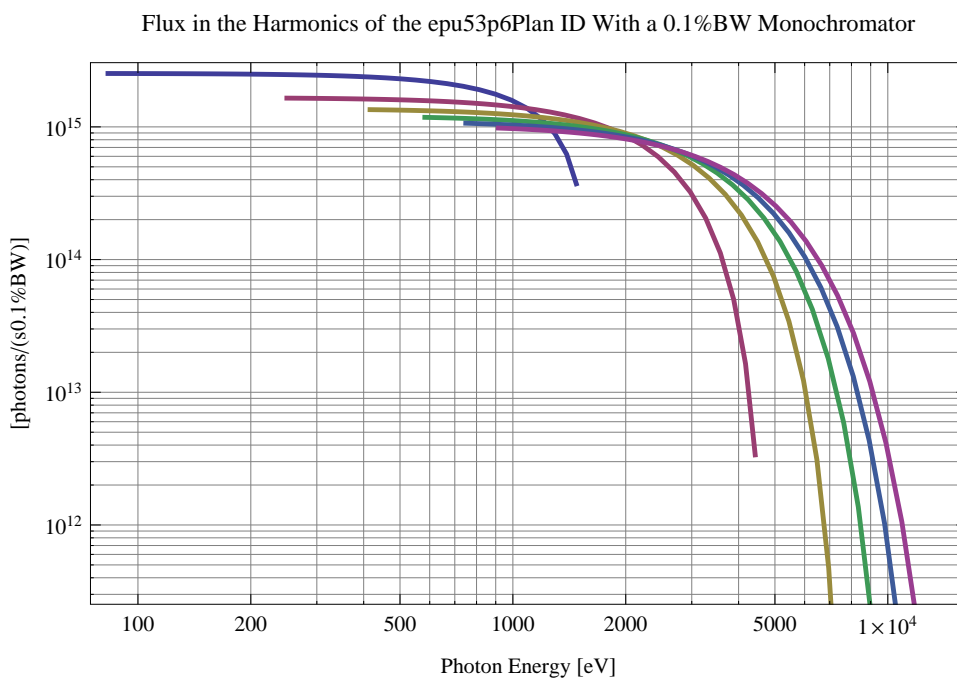


Figure 5.515: The flux of photons in the harmonics from the epu53p6Plan ID using a 0.1%BW monochromator

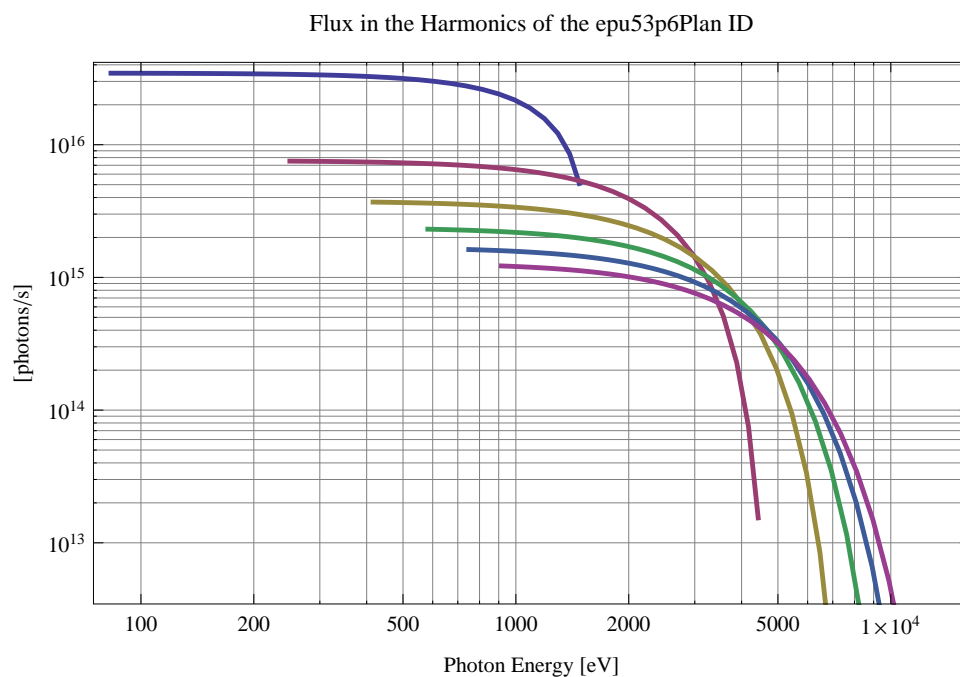


Figure 5.516: The flux of photons in the harmonics from the epu53p6Plan ID

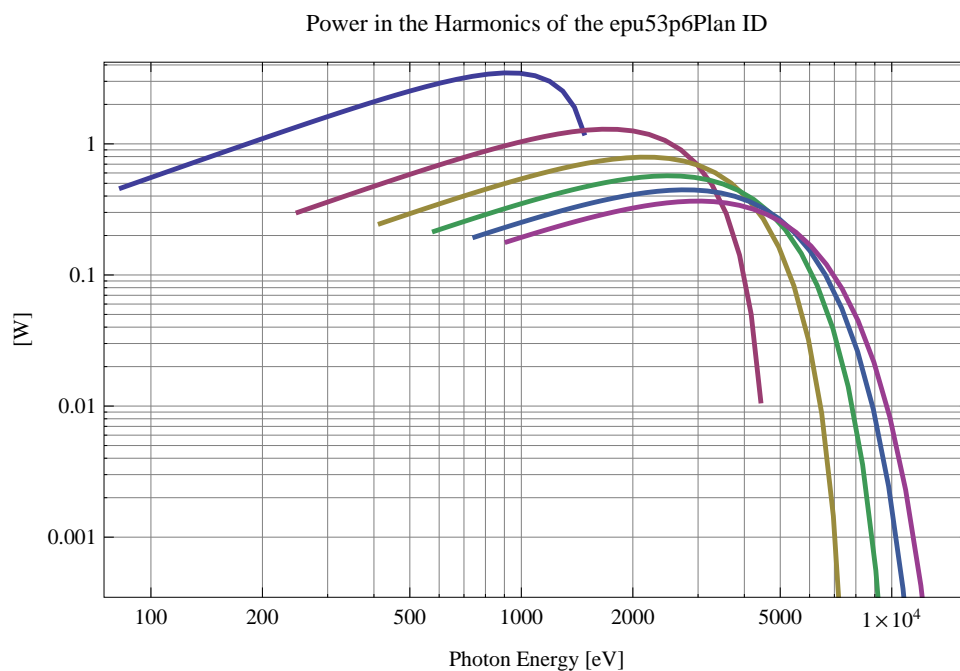


Figure 5.517: The power in the harmonics from the epu53p6Plan ID

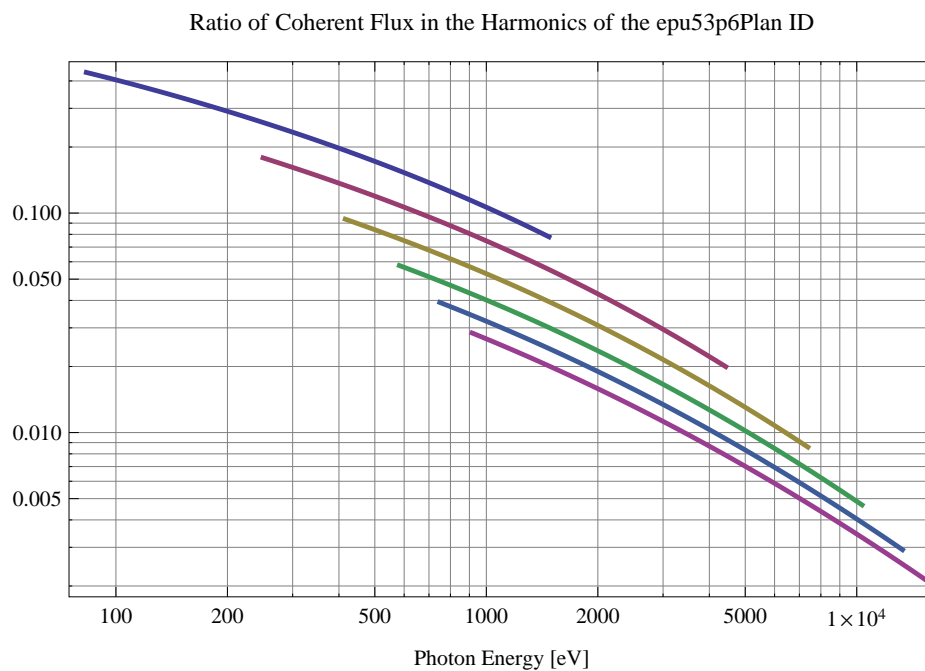


Figure 5.518: The ratio of coherent flux in the harmonics from the epu53p6Plan ID

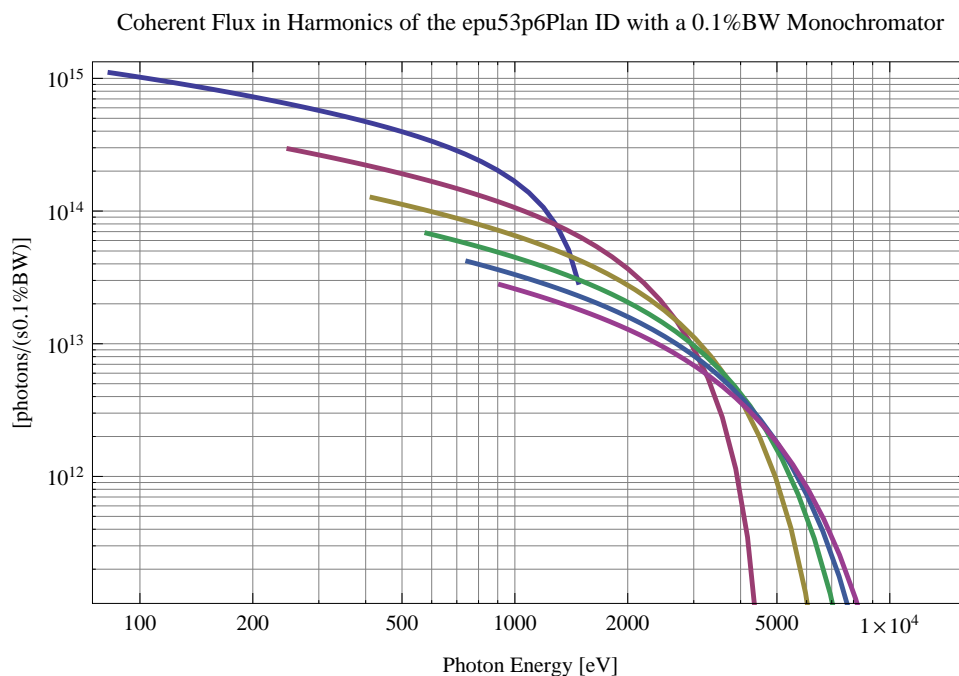


Figure 5.519: The coherent flux in the harmonics of the epu53p6Plan ID using a 0.1%BW Monochromator

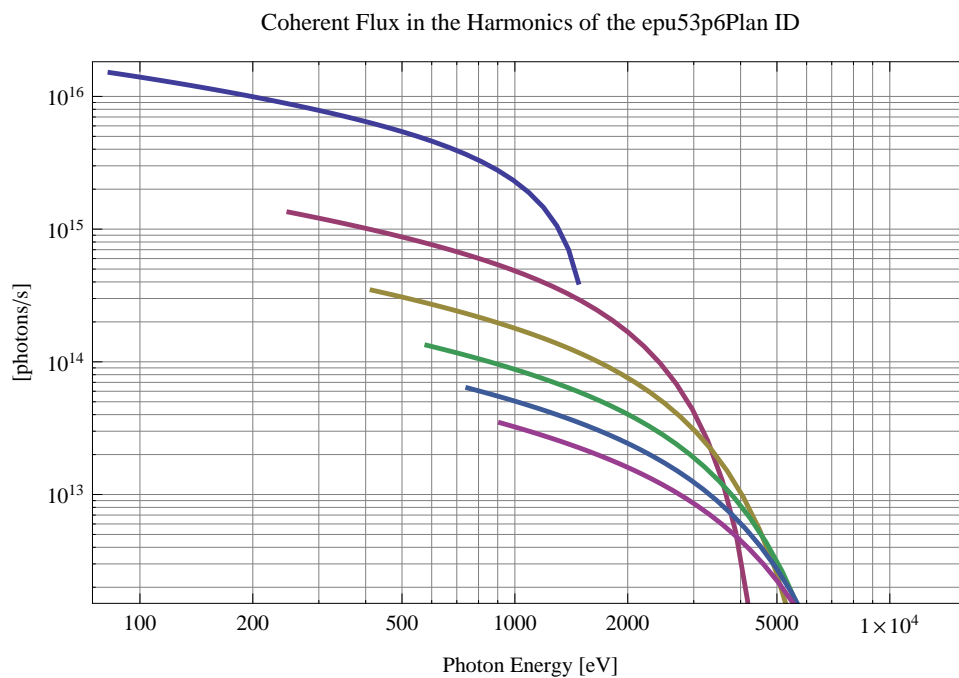


Figure 5.520: The coherent flux in the harmonics of the epu53p6Plan ID

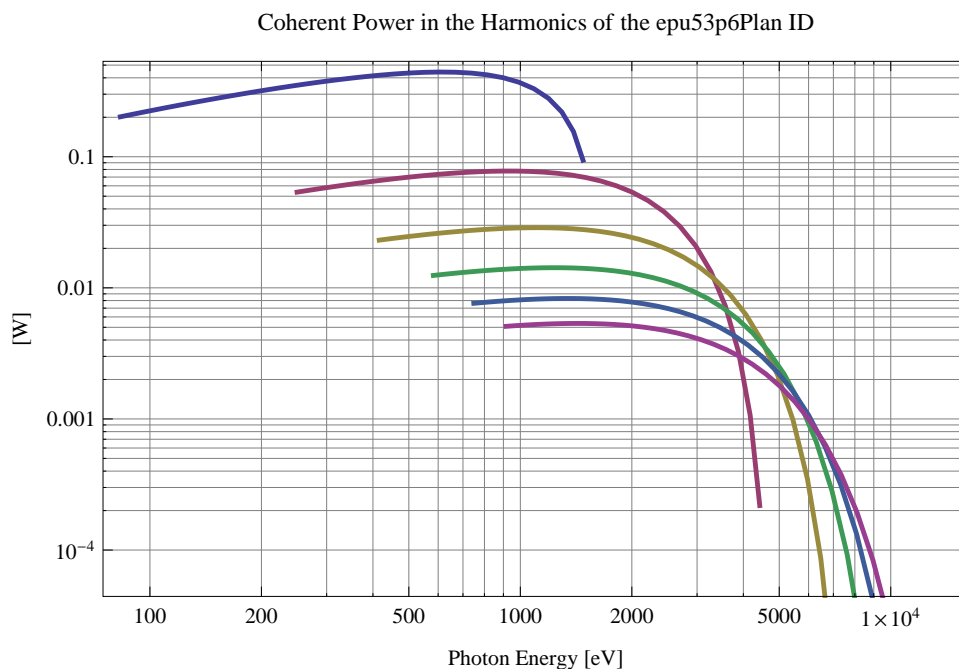


Figure 5.521: The power of coherent synchrotron radiation in the harmonics of the epu53p6Plan ID



The brilliance at peak energy and the angular spectral flux density from the epu53p6Plan ID for different harmonics at maximum K-value (6.028) are given in Table 5.74 and for minimum K-value (0.400) these values are given in Table 5.75.

Table 5.74: The brilliance at peak energy and the angular spectral flux density from the epu53p6Plan ID for different harmonics at maximum K-value (6.028)

Harmonic	Photon Energy [eV]	Brilliance [Ph./s/mrad <sup>2</sup> /mrad <sup>2</sup> /0.1%BW]	Angular Spectral Flux [Ph./s/mrad <sup>2</sup> /0.1%BW]
1	83.1989	$1.99 \times 10^{19}$	$1.5 \times 10^{17}$
3	249.597	$4.77 \times 10^{19}$	$2.02 \times 10^{17}$
5	415.994	$5.7 \times 10^{19}$	$1.94 \times 10^{17}$
7	582.392	$6.01 \times 10^{19}$	$1.8 \times 10^{17}$
9	748.79	$6.09 \times 10^{19}$	$1.68 \times 10^{17}$
11	915.188	$6.07 \times 10^{19}$	$1.57 \times 10^{17}$

Table 5.75: The brilliance at peak energy and the angular spectral flux density from the epu53p6Plan ID for different harmonics at minimum K-value (0.4)

Harmonic	Photon Energy [eV]	Brilliance [Ph./s/mrad <sup>2</sup> /mrad <sup>2</sup> /0.1%BW]	Angular Spectral Flux [Ph./s/mrad <sup>2</sup> /0.1%BW]
1	1476.43	$1.65 \times 10^{20}$	$3.68 \times 10^{17}$
3	4429.29	$3.44 \times 10^{18}$	$6.45 \times 10^{15}$
5	7382.15	$4.04 \times 10^{16}$	$7.31 \times 10^{13}$
7	10335.	$4.31 \times 10^{14}$	$7.7 \times 10^{11}$
9	13287.9	$4.47 \times 10^{12}$	$7.93 \times 10^9$
11	16240.7	$4.59 \times 10^{10}$	$8.11 \times 10^7$

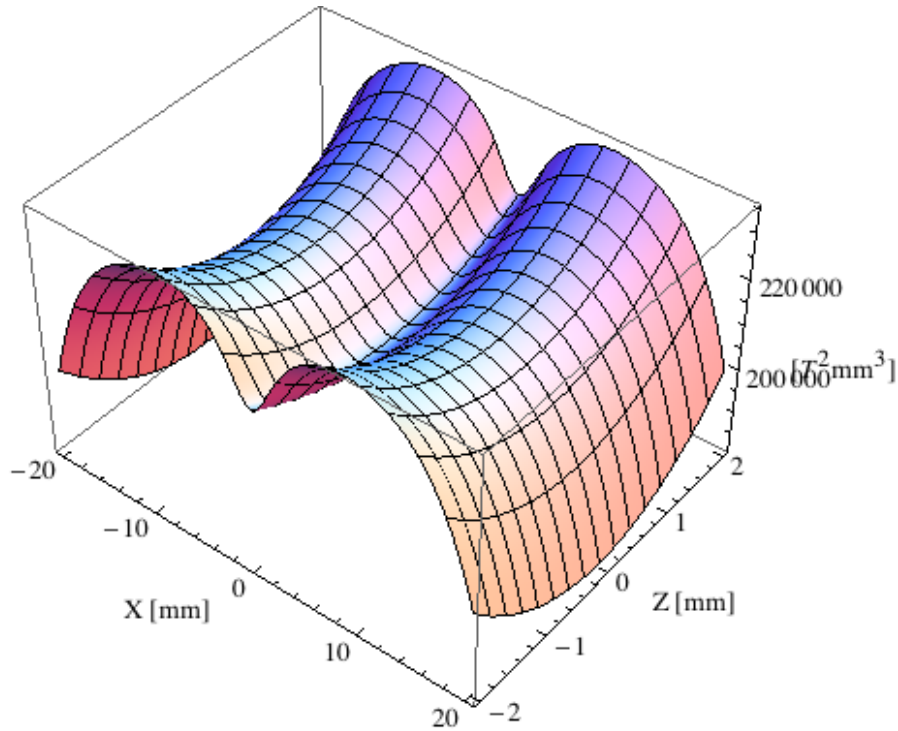


Figure 5.522: Focusing potential from the epu53p6Plan ID over the beam stay clear aperture.

### Influence from the epu53p6Plan ID on the optics of the stored beam

Figure 5.522 shows the focusing potential from the epu53p6Plan over the beam stay clear aperture of the ring aperture.

Figure 5.523 shows the kick map in the beam energy independent unit  $T^2 m^2$  of the kicks induced by the epu53p6Plan ID over the beam stay clear aperture.

Figure 5.524 shows the induced angular kick on the stored beam from the epu53p6Plan ID as a function of the vertical distance to the axis of the ID.

Figure 5.525 shows the induced angular kick on the stored beam from the epu53p6Plan ID as a function of the horizontal distance to the axis of the ID.

Figure 5.526 shows tune shift induced by the epu53p6Plan ID over the beam stay clear aperture. Note that the tune shift depends on the beam size at the ID.

Figure 5.527 shows the induced tune shift from the epu53p6Plan ID as a function of the vertical distance to the axis of the ID.

Figure 5.528 shows the induced tune shift from the epu53p6Plan ID as a function of the horizontal distance to the axis of the ID.

### Magnet model of the elliptically polarising undulator epu53p6Heli

The Radia [2] magnet model of the epu53p6Heli ID is shown in Figure 5.529. The length of the magnet model is 446.587 mm. The magnetic material in the model is NdFeb with a remanence of 1.28 T, a material similar to VACODYM 776 TP from Vacuumschmelze. Blocks with vertical magnetisation are blue and blocks with horizontal magnetisation are yellow. The block size is

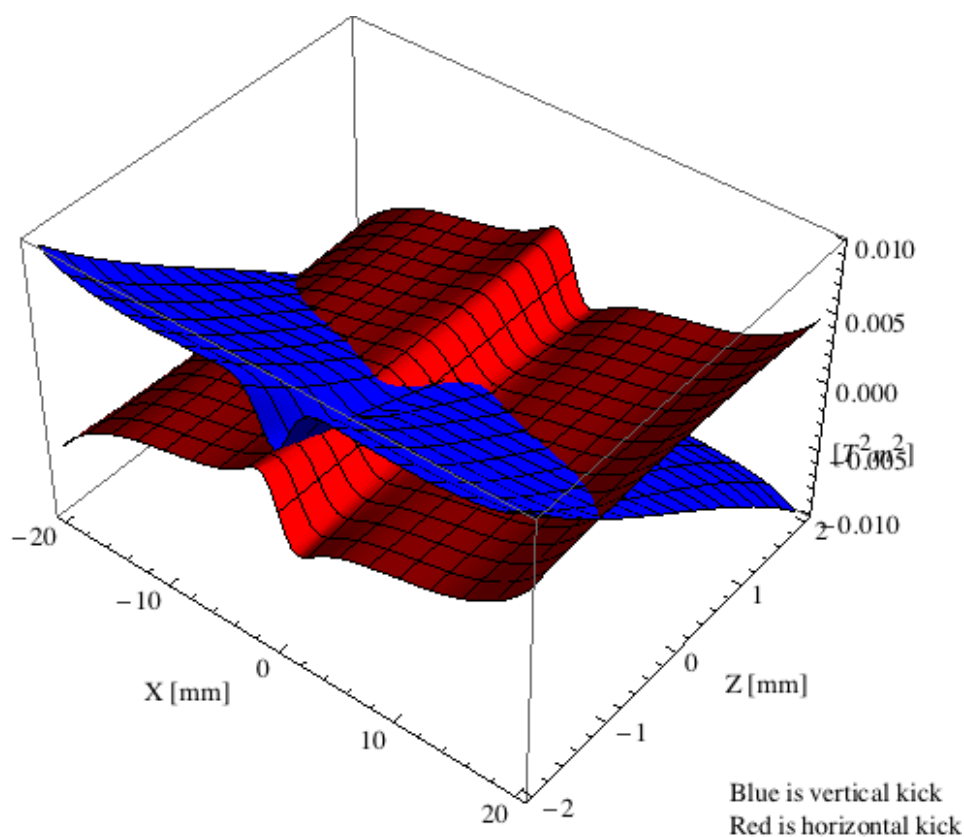


Figure 5.523: Kick map in the beam energy independent unit  $T^2m^2$  of the kicks induced by the epu53p6Plan ID over the beam stay clear aperture.

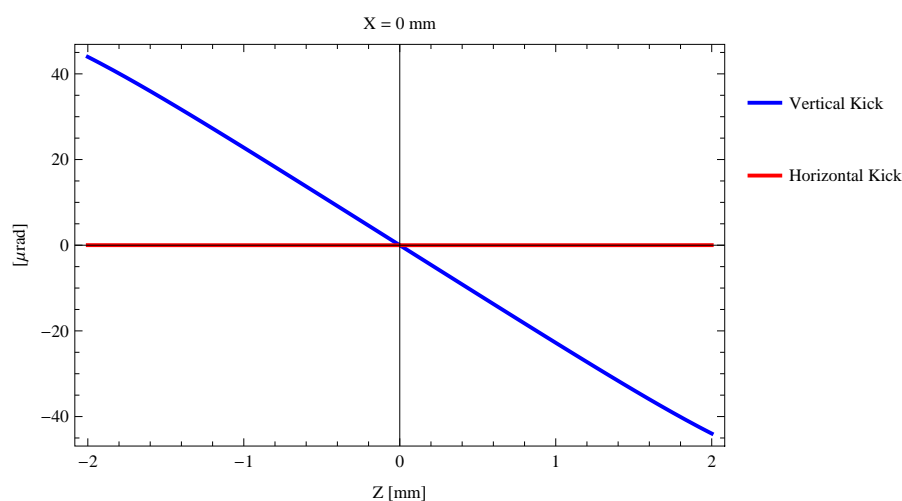


Figure 5.524: Induced angular kick on the stored beam from the epu53p6Plan ID as a function of the vertical distance to the ID axis.

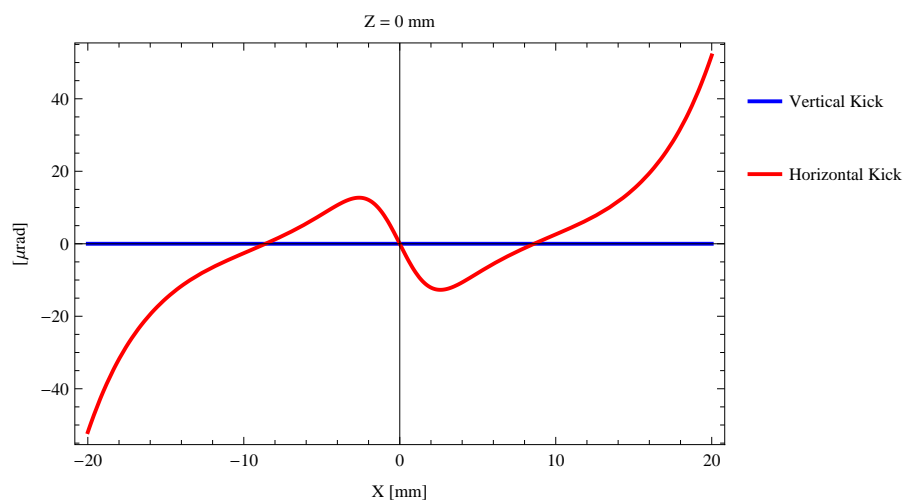


Figure 5.525: Induced angular kick on the stored beam from the epu53p6Plan ID as a function of the horizontal distance to the ID axis.

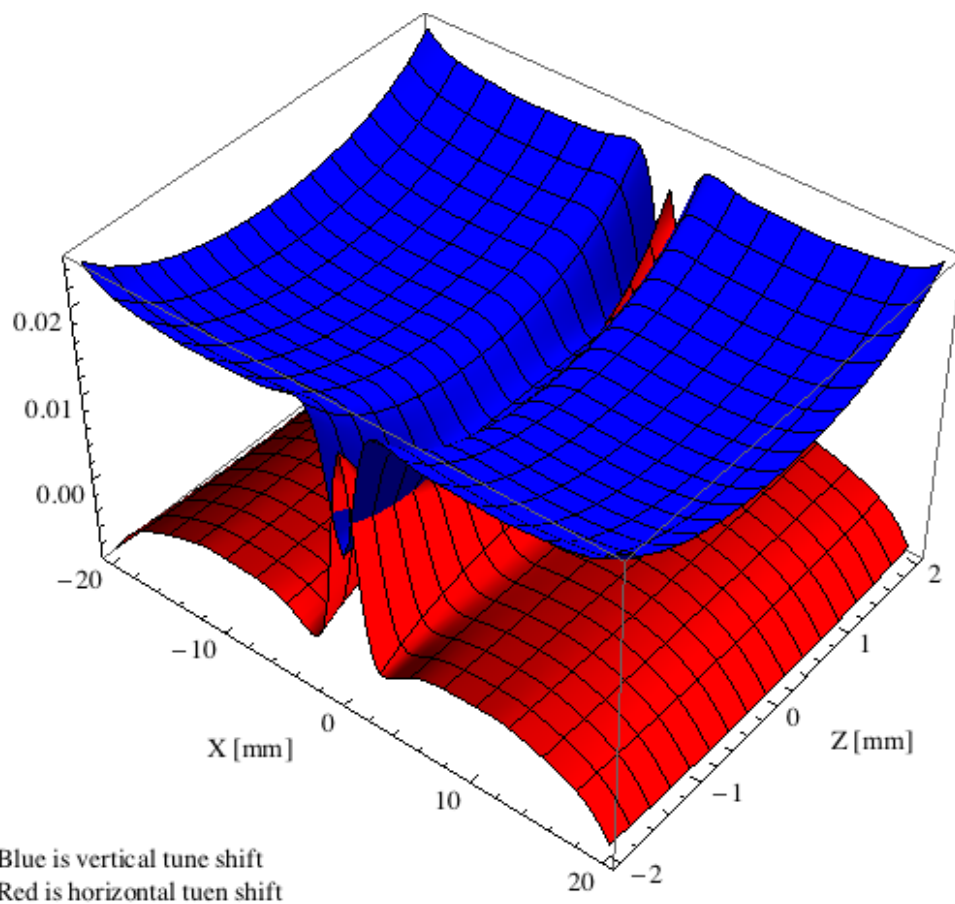


Figure 5.526: Tune shift induced by the epu53p6Plan ID over the beam stay clear aperture.

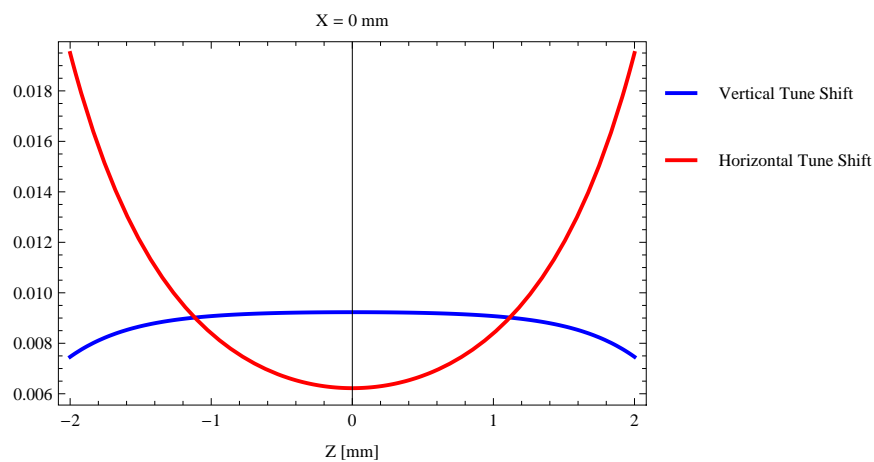


Figure 5.527: Induced tune shift from the epu53p6Plan ID as a function of the vertical distance to the axis of the ID.

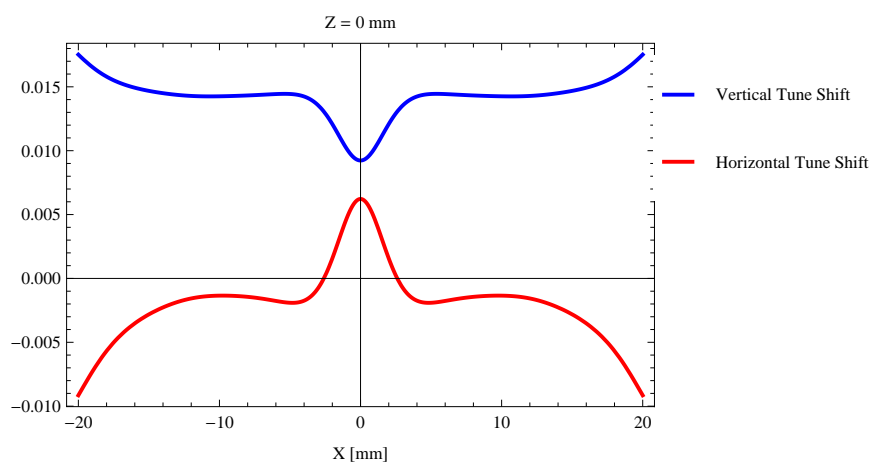


Figure 5.528: Induced tune shift from the epu53p6Plan ID on the stored beam from the ID as a function of the horizontal distance to the axis of the ID.

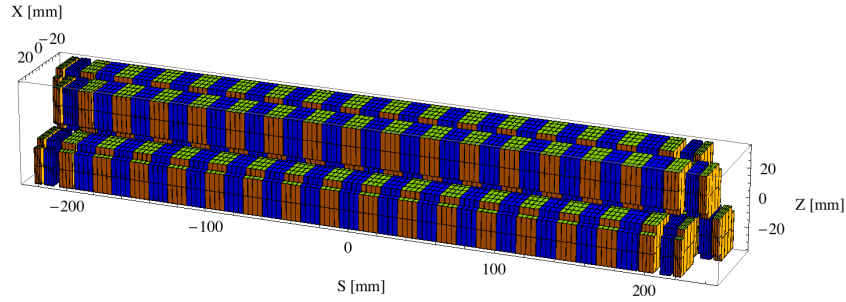


Figure 5.529: Magnetic model of the epu53p6Heli ID. The ID has been modelled with Radia [2]

$30 \times 30 \times 13.4 \text{ mm}^3$  and there is a 5. mm cut-out in two of the corners of the blocks. The total length of the epu53p6Heli ID is 3930.59 mm.

### Analysis of the magnetic field of the epu53p6Heli ID

The effective magnetic fields on axis and the fundamental photon energy of the epu53p6Heli ID are shown in Table 5.76. The higher harmonic contents in the magnetic field of an elliptically polarising undulator made of permanent magnets is negligible and the efficient field has about the same strength as the peak field.

Table 5.76: Effective Fields on axis and Fundamental Photon Energy of the epu53p6Heli ID

Undulator Period	53.6	mm
Undulator Gap	9	mm
Undulator Mode	Helical	
Undulator Phase	15.060	mm
Vertical Peak Field	0.765	T
Efficient Vertical Field	0.760	T
K <sub>x</sub> (from vert. field)	3.805	
Horizontal Peak Field:	0.769	T
Efficient Horizontal Field	0.760	T
K <sub>z</sub> (from hor. field)	3.805	
Photon Energy, Harm.1	0.103	keV
Emitted Power	12.928	kW
Total Length	3930.6	mm

### Synchrotron radiation from the epu53p6Heli ID

The power map of the emitted synchrotron radiation by the epu53p6Heli ID, assuming a 0.5 A filament beam with an energy of 3 GeV and undulator properties of the synchrotron radiation, is shown in Figure 5.534. The on-axis power density is  $0.113 \text{ kW/mrad}^2$

A map of the degree of linear polarisation of the fundamental harmonic of the synchrotron radiation emitted by the epu53p6Heli ID over the angle of observation is shown in Figure 5.535.

A map of the degree of 45 degree polarisation of the fundamental harmonic of the synchrotron radiation emitted by the epu53p6Heli ID over the angle of observation is shown in Figure 5.536.

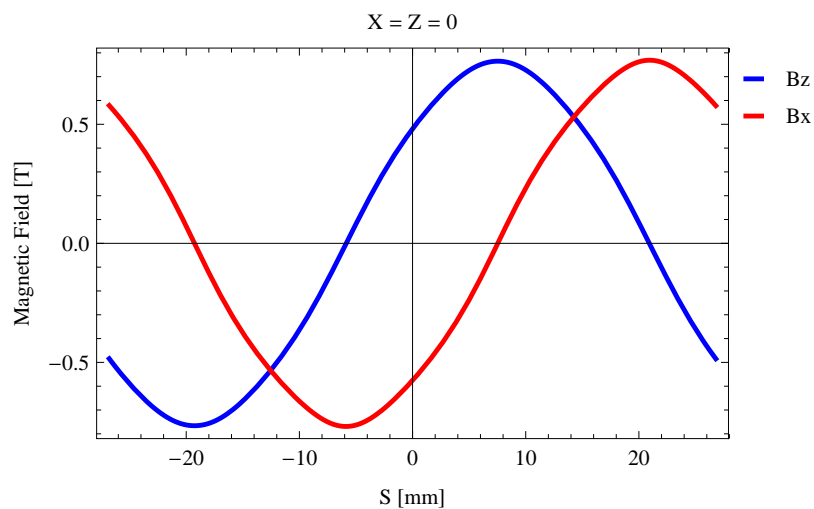


Figure 5.530: Vertical magnetic field in a central pole of the epu53p6Heli ID along the ID axis,  $X = Z = 0$

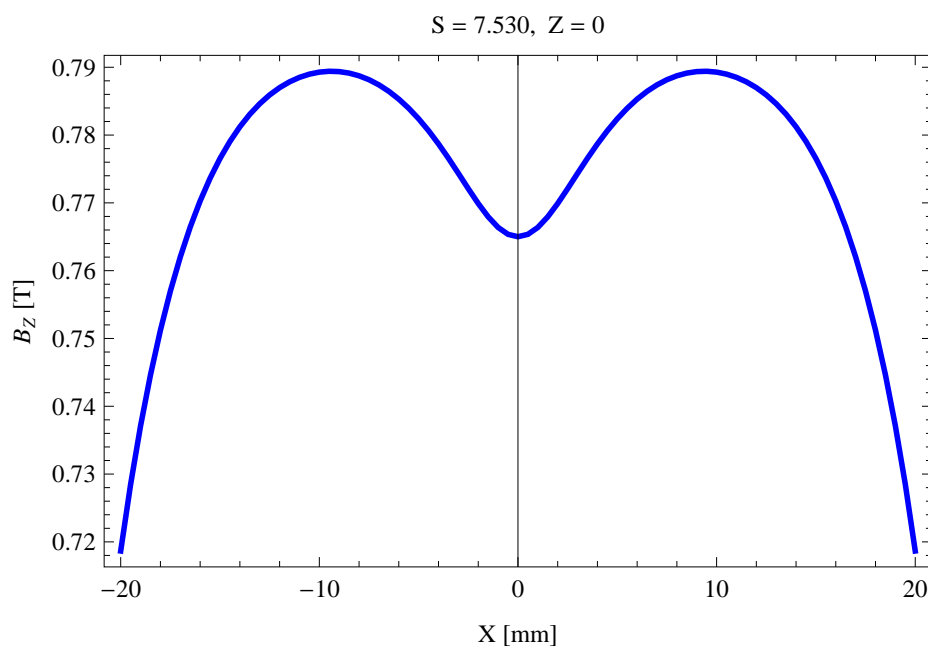


Figure 5.531: Vertical magnetic field in a central pole of the epu53p6Heli ID along the horizontally transverse direction to the ID axis,  $S = 7.530$ ,  $Z = 0$

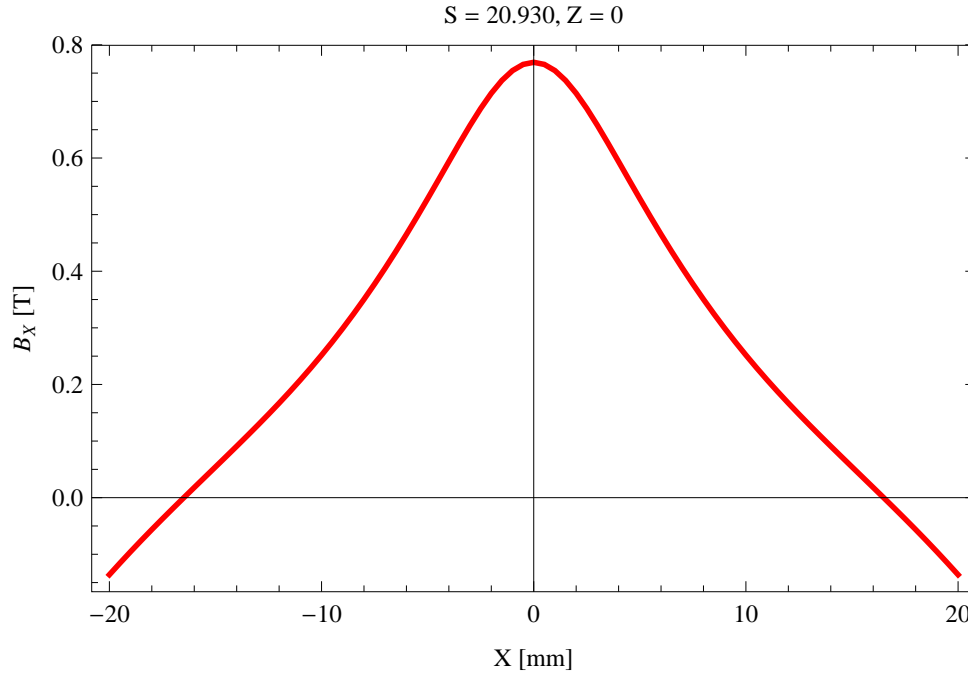


Figure 5.532: Horizontal magnetic field in a central pole of the epu53p6Heli ID along the horizontally transverse direction to the ID axis,  $S = 20.930$ ,  $Z = 0$

A map of the degree of circular polarisation of the fundamental harmonic of the synchrotron radiation emitted by the epu53p6Heli ID over the angle of observation is shown in Figure 5.537.

The on axis brilliance at peak energy, the angular spectral flux, the flux in the harmonics, the power in the harmonics, the ratio of coherence, the coherent flux in the harmonics, and the power of coherent radiation in the harmonics from the epu53p6Heli ID have been calculated and the resulting plots are found in this section of the document. The beam parameters used for the calculation are 0.5 A of stored current,  $\beta_H = 9$  m,  $\varepsilon_H = 0.263$  nmrad,  $\beta_V = 4.8$  m,  $\varepsilon_V = 8$  pmrad, and an energy spread of 0.001.

The brilliance at peak energy and the angular spectral flux density from the epu53p6Heli ID for different harmonics at maximum K-value (5.381) are given in Table 5.77 and for minimum K-value (0.400) these values are given in Table 5.78.

Table 5.77: The brilliance at peak energy and the angular spectral flux density from the epu53p6Heli ID for different harmonics at maximum K-value (5.381)

Harmonic	Photon Energy [eV]	Brilliance [Ph./s/mrad <sup>2</sup> /mrad <sup>2</sup> /0.1%BW]	Angular Spectral Flux [Ph./s/mrad <sup>2</sup> /0.1%BW]
1	103.033	$2.78 \times 10^{19}$	$1.86 \times 10^{17}$



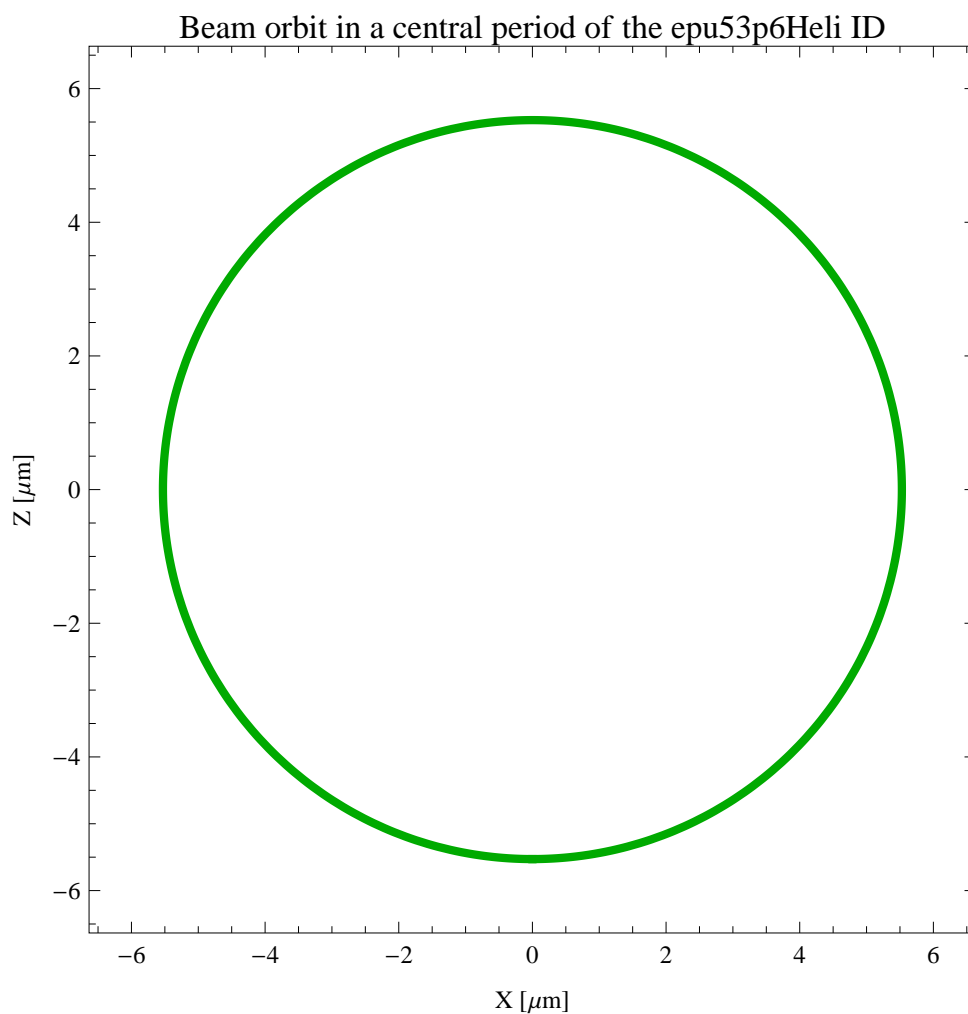


Figure 5.533: The beam orbit of the electron beam through a central period of the epu53p6Heli ID

Table 5.78: The brilliance at peak energy and the angular spectral flux density from the epu53p6Heli ID for different harmonics at minimum K-value (0.4)

Harmonic	Photon Energy [eV]	Brilliance [Ph./s/mrad <sup>2</sup> /mrad <sup>2</sup> /0.1%BW]	Angular Spectral Flux [Ph./s/mrad <sup>2</sup> /0.1%BW]
1	1476.43	$1.65 \times 10^{20}$	$3.68 \times 10^{17}$

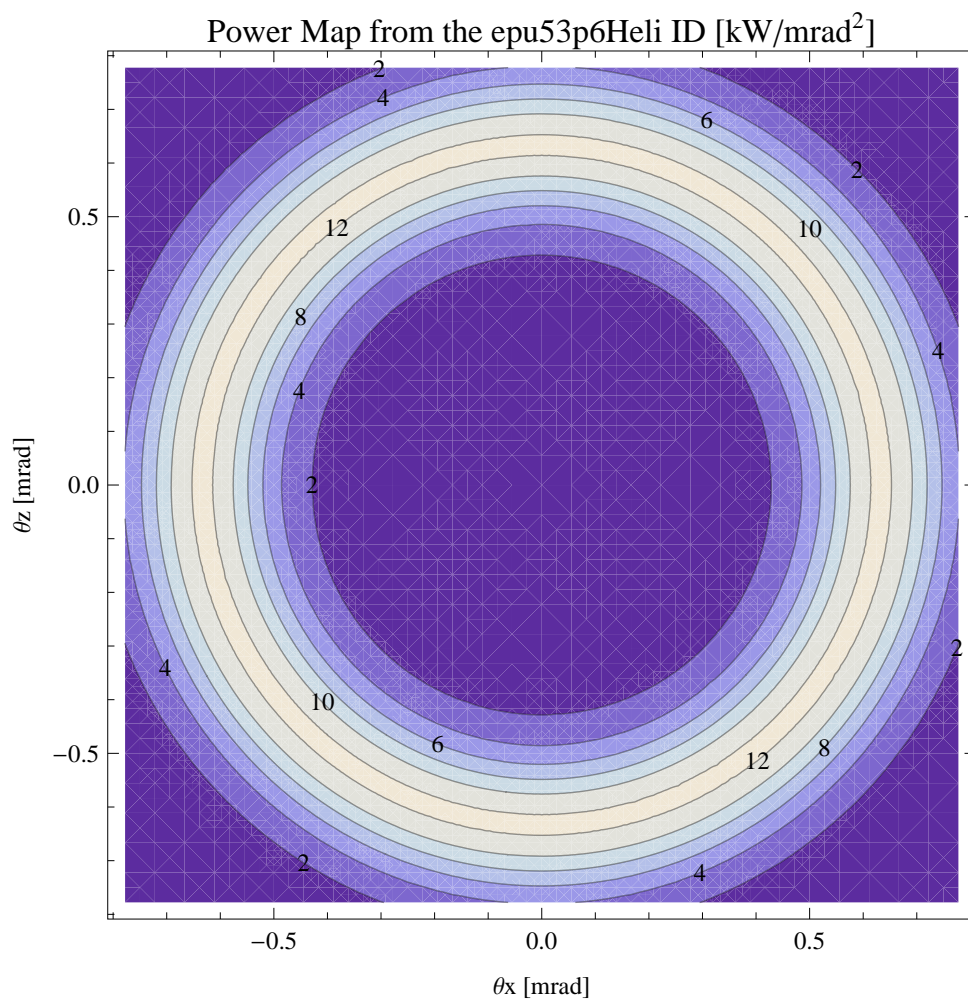


Figure 5.534: Map of the power distribution of the emitted synchrotron radiation by the epu53p6Heli ID

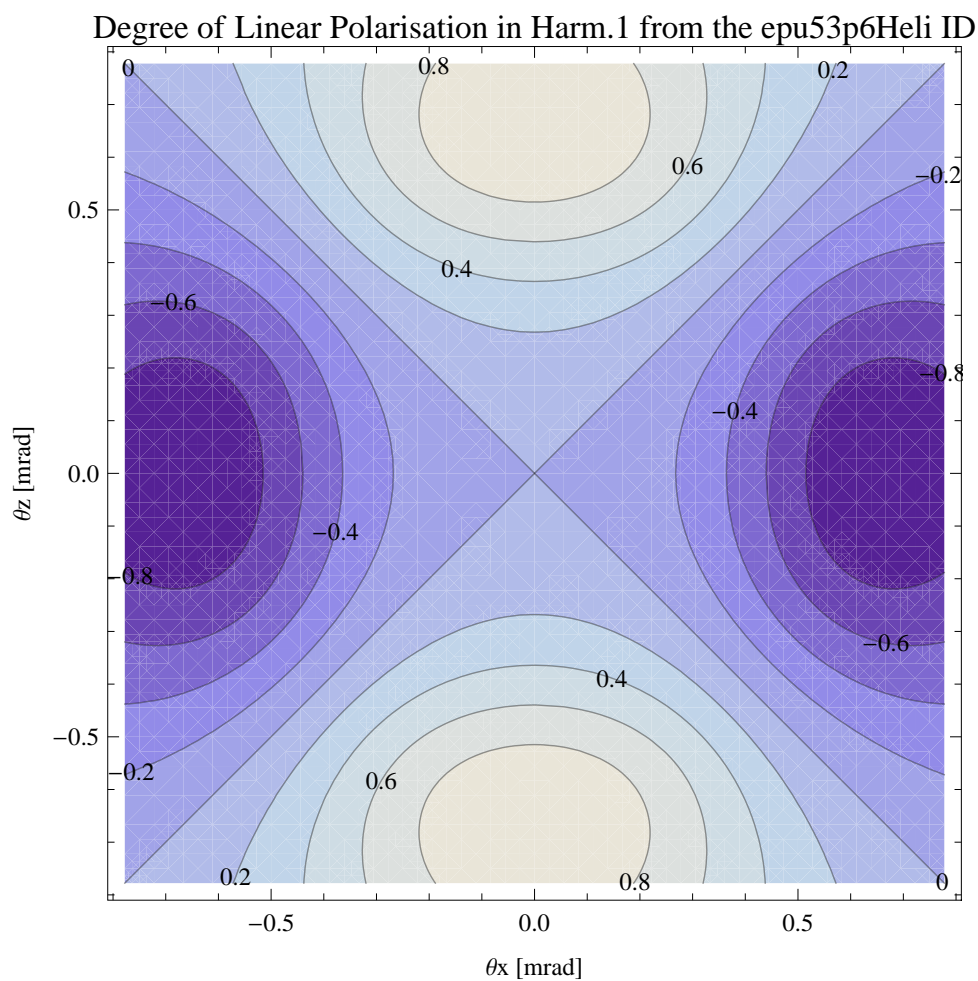


Figure 5.535: Map of linear polarisation in the fundamental harmonic of the synchrotron radiation emitted by the epu53p6Heli ID

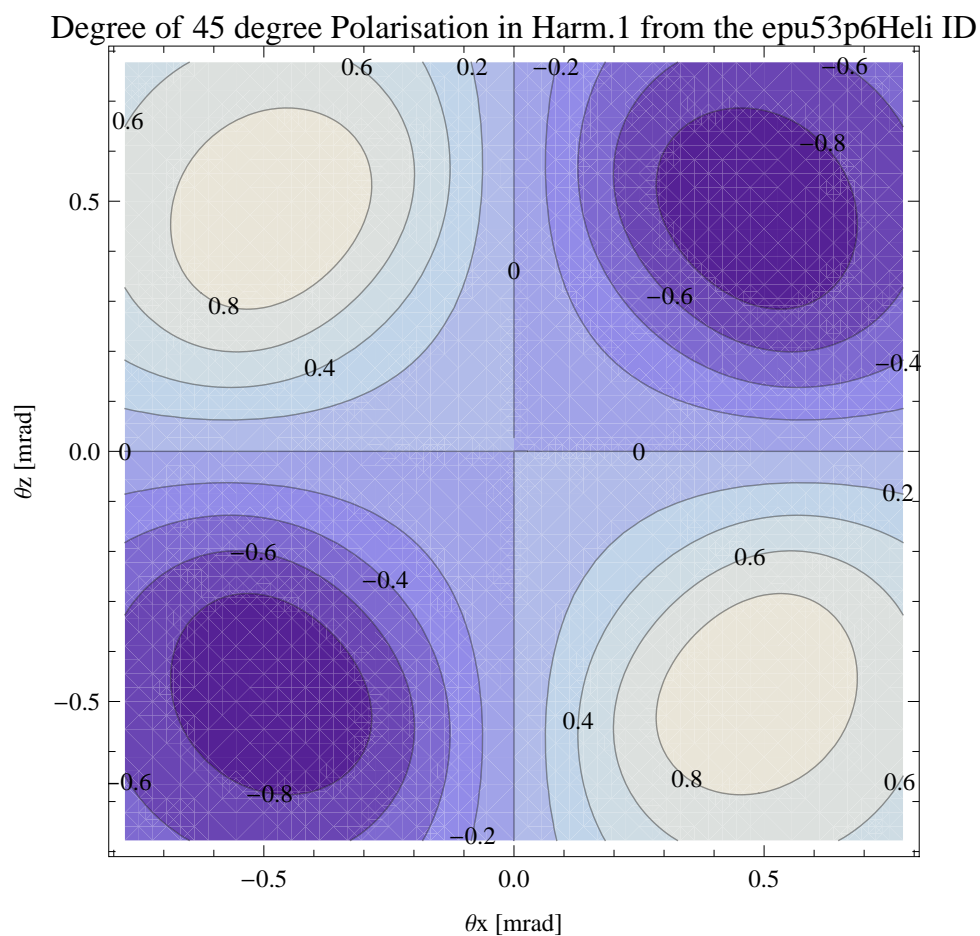


Figure 5.536: Map of 45 degree polarisation in the fundamental harmonic of the synchrotron radiation emitted by the epu53p6Heli ID

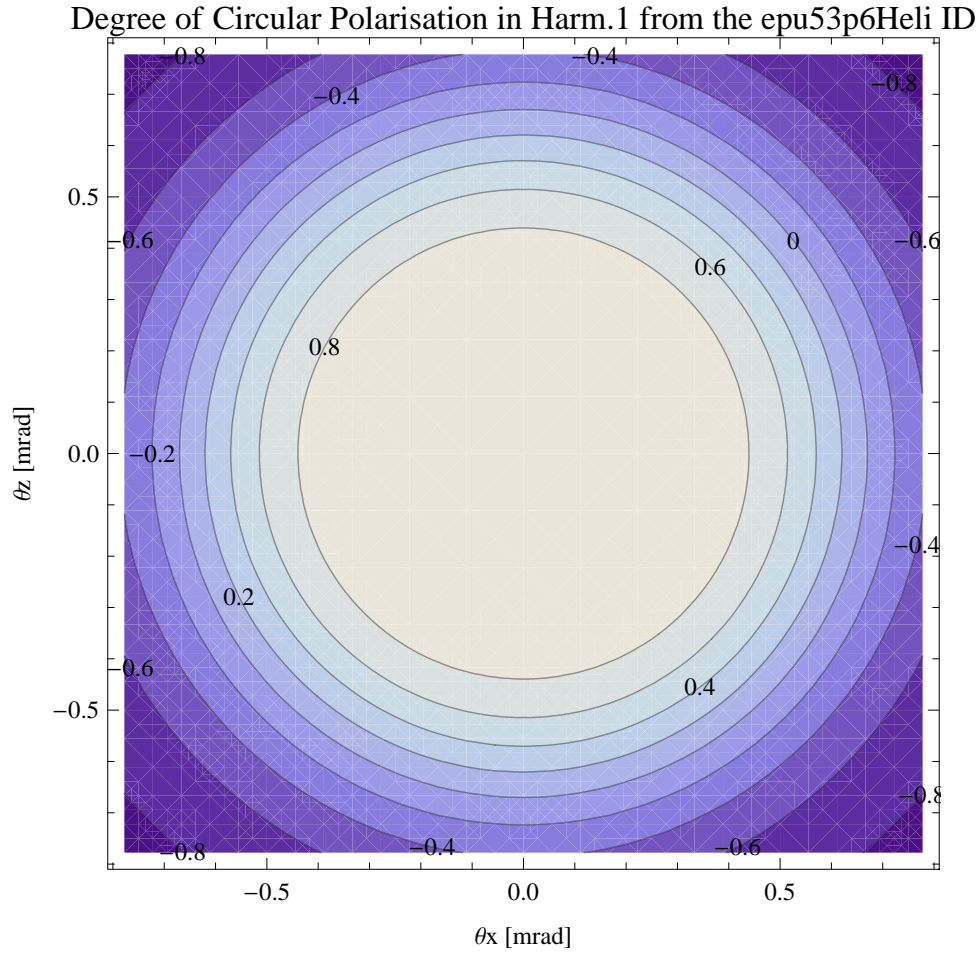


Figure 5.537: Map of circular polarisation in the fundamental harmonic of the synchrotron radiation emitted by the epu53p6Heli ID

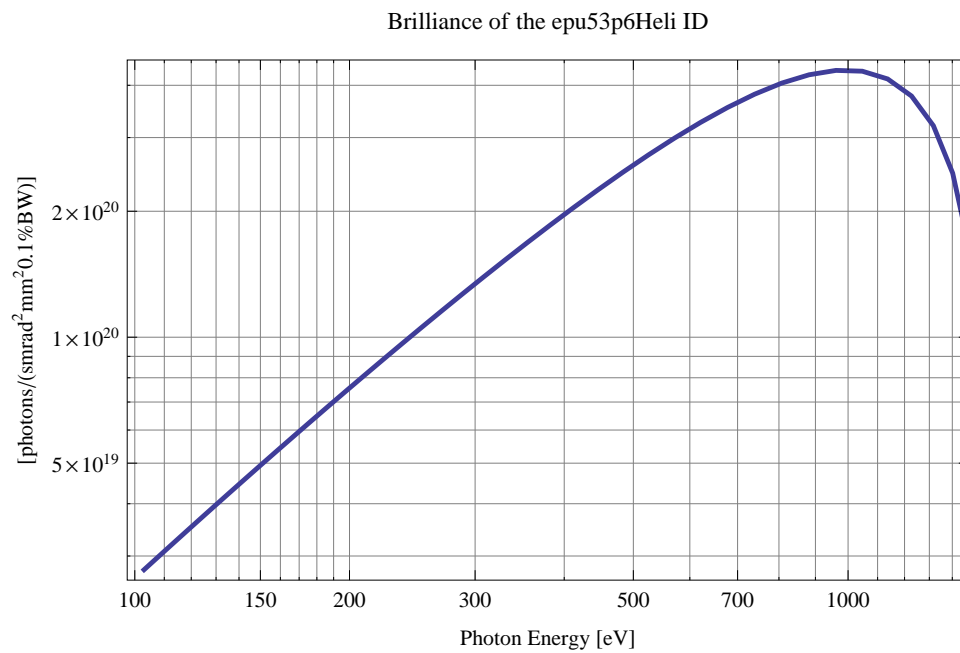


Figure 5.538: The brilliance at peak energy from the epu53p6Heli ID

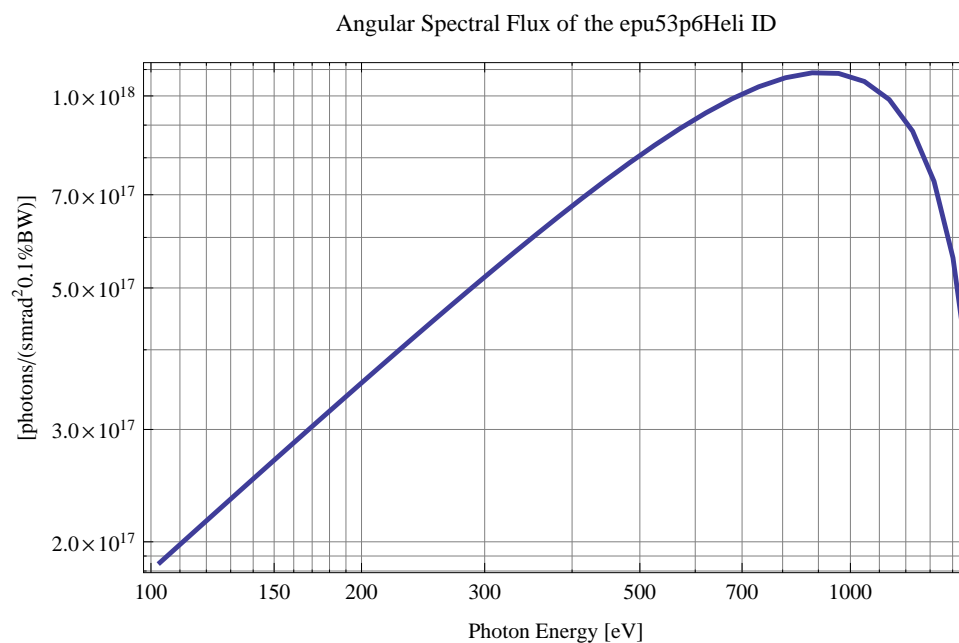


Figure 5.539: The angular spectral flux from the epu53p6Heli ID

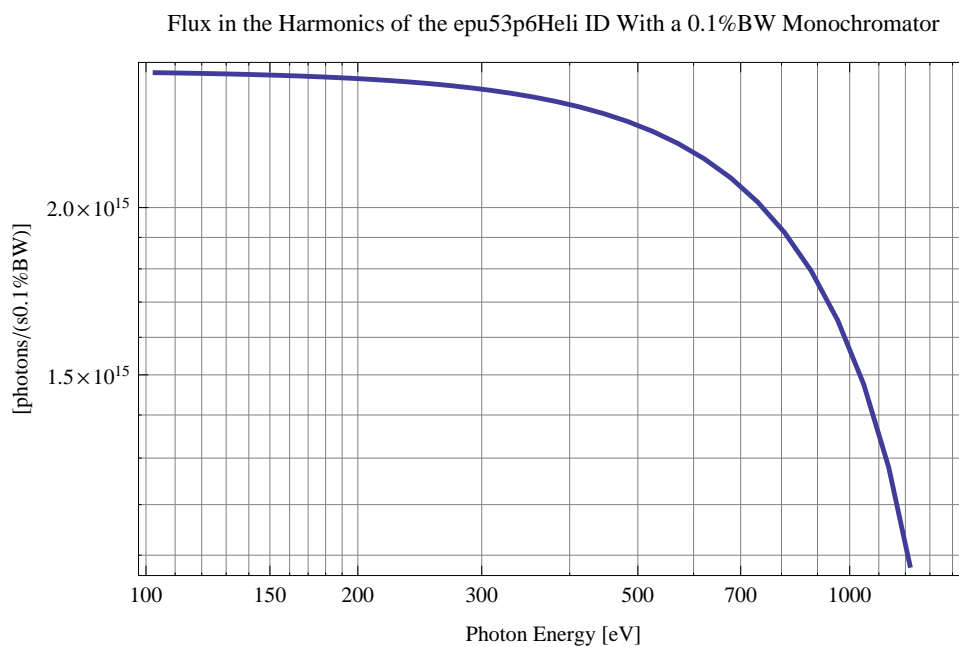


Figure 5.540: The flux of photons in the harmonics from the epu53p6Heli ID using a 0.1%BW monochromator

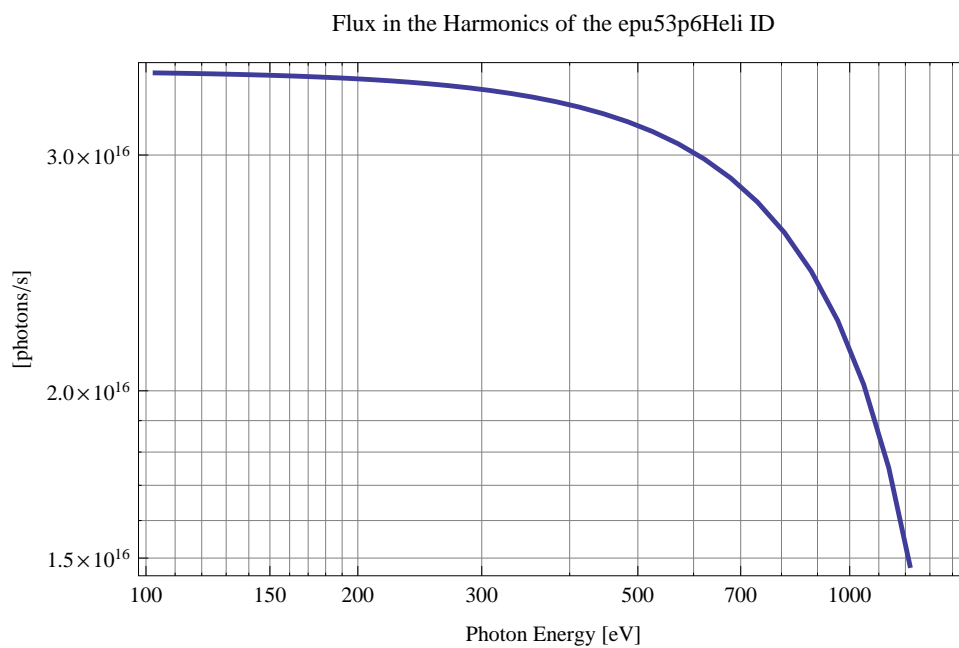


Figure 5.541: The flux of photons in the harmonics from the epu53p6Heli ID

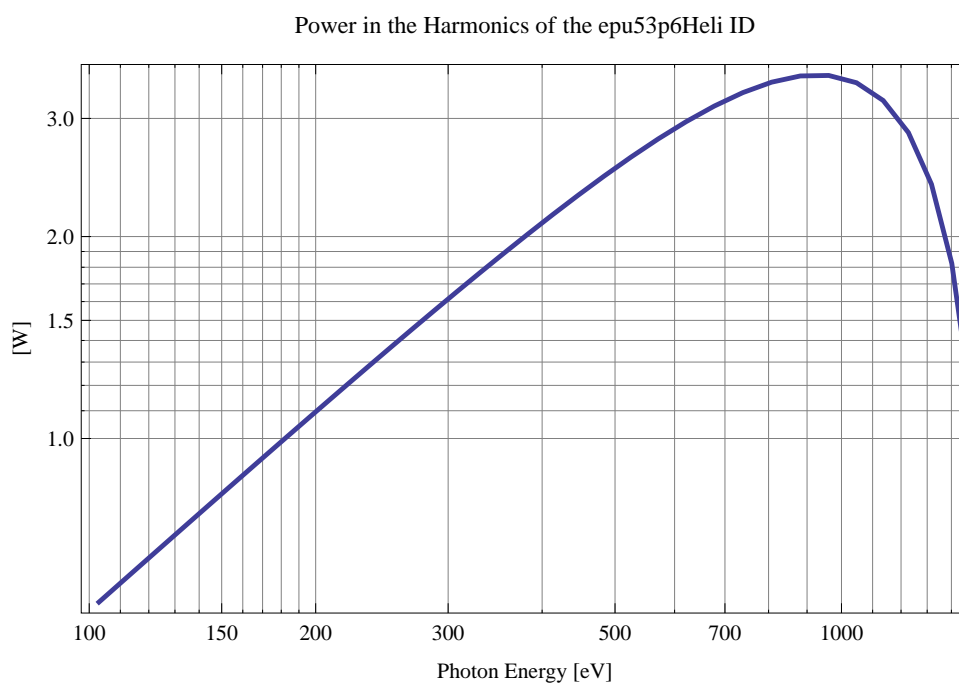


Figure 5.542: The power in the harmonics from the epu53p6Heli ID

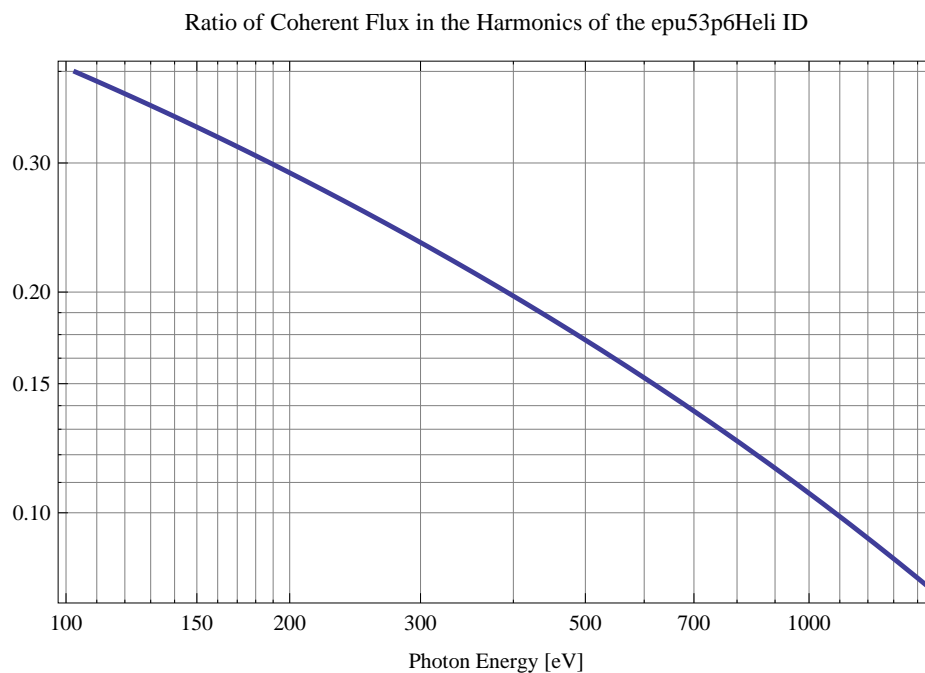


Figure 5.543: The ratio of coherent flux in the harmonics from the epu53p6Heli ID

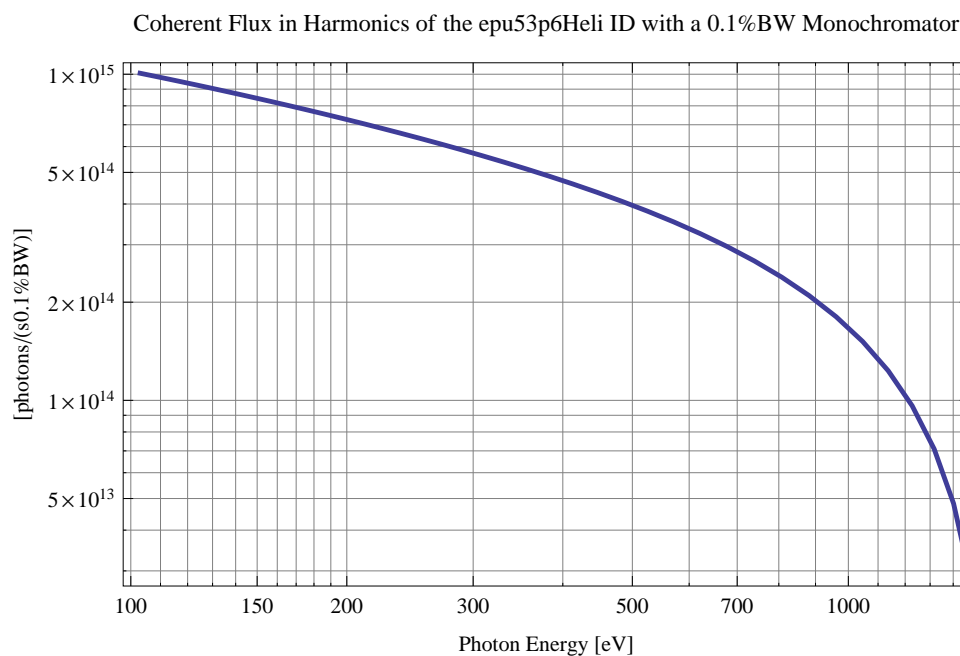


Figure 5.544: The coherent flux in the harmonics of the epu53p6Heli ID using a 0.1%BW Monochromator



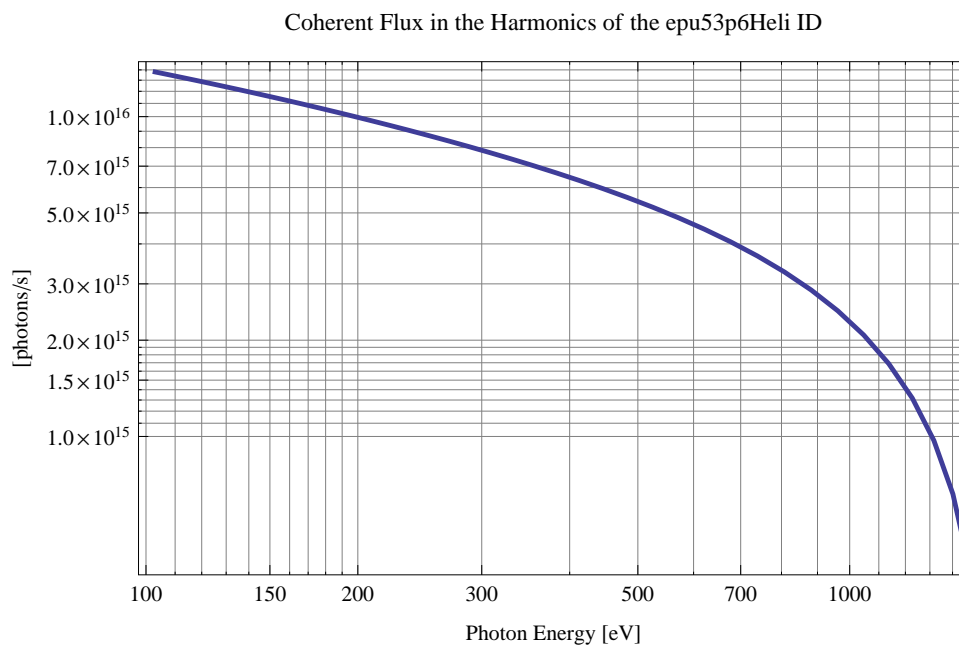


Figure 5.545: The coherent flux in the harmonics of the epu53p6Heli ID

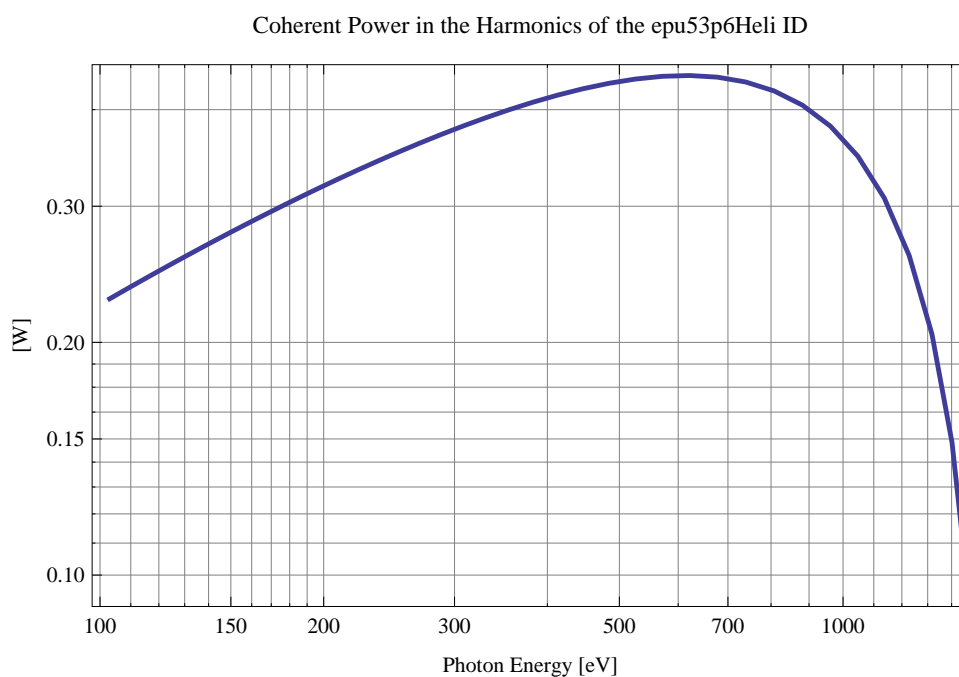


Figure 5.546: The power of coherent synchrotron radiation in the harmonics of the epu53p6Heli ID

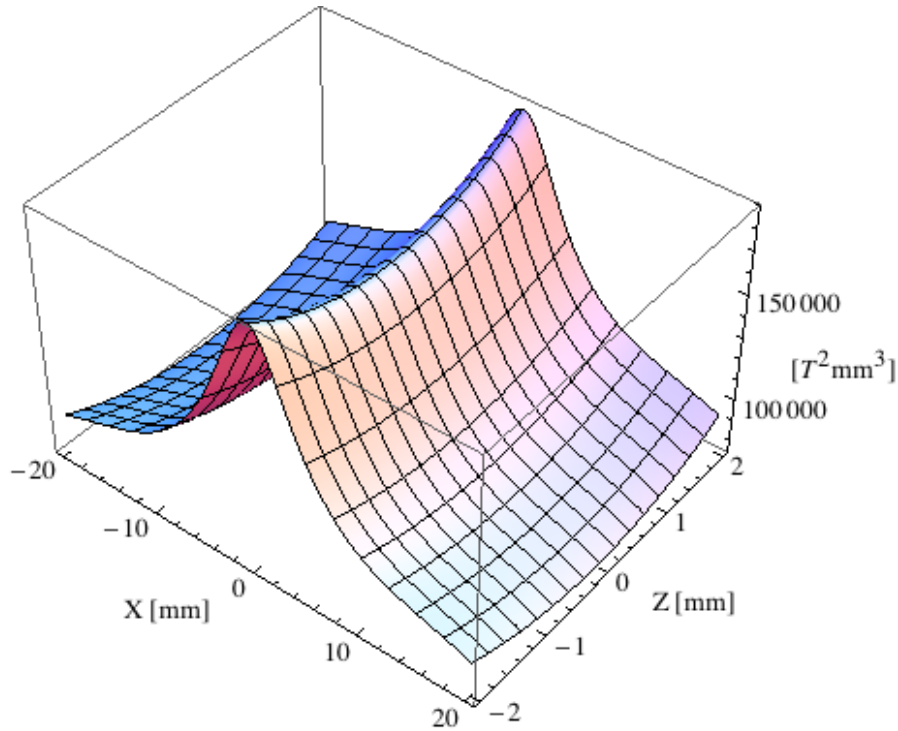


Figure 5.547: Focusing potential from the epu53p6Heli ID over the beam stay clear aperture.

### Influence from the epu53p6Heli ID on the optics of the stored beam

Figure 5.547 shows the focusing potential from the epu53p6Heli over the beam stay clear aperture of the ring aperture.

Figure 5.548 shows the kick map in the beam energy independent unit  $T^2 m^2$  of the kicks induced by the epu53p6Heli ID over the beam stay clear aperture.

Figure 5.549 shows the induced angular kick on the stored beam from the epu53p6Heli ID as a function of the vertical distance to the axis of the ID.

Figure 5.550 shows the induced angular kick on the stored beam from the epu53p6Heli ID as a function of the horizontal distance to the axis of the ID.

Figure 5.551 shows tune shift induced by the epu53p6Heli ID over the beam stay clear aperture. Note that the tune shift depends on the beam size at the ID.

Figure 5.552 shows the induced tune shift from the epu53p6Heli ID as a function of the vertical distance to the axis of the ID.

Figure 5.553 shows the induced tune shift from the epu53p6Heli ID as a function of the horizontal distance to the axis of the ID.

### Magnet model of the elliptically polarising undulator epu53p6Incl

The Radia [2] magnet model of the epu53p6Incl ID is shown in Figure 5.554. The length of the magnet model is 446.587 mm. The magnetic material in the model is NdFeb with a remanence of 1.28 T, a material similar to VACODYM 776 TP from Vacuumschmelze. Blocks with vertical magnetisation are blue and blocks with horizontal magnetisation are yellow. The block size is

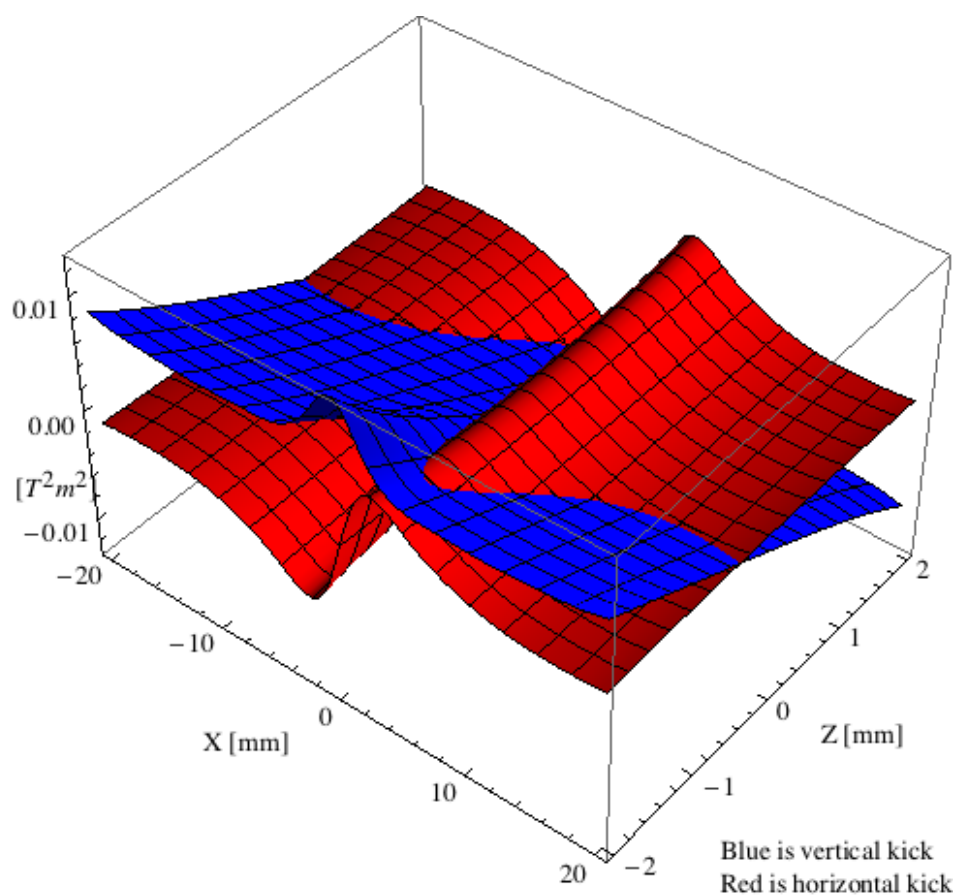


Figure 5.548: Kick map in the beam energy independent unit  $T^2m^2$  of the kicks induced by the epu53p6Heli ID over the beam stay clear aperture.

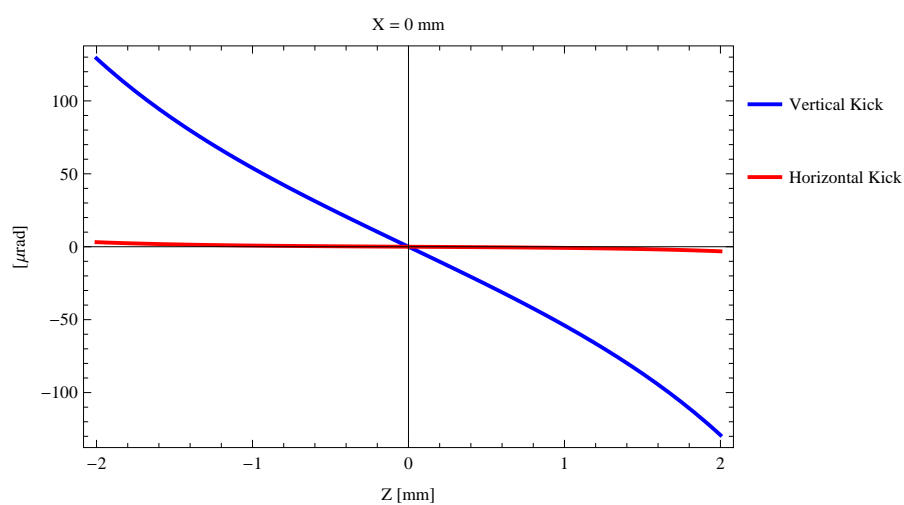


Figure 5.549: Induced angular kick on the stored beam from the epu53p6Heli ID as a function of the vertical distance to the ID axis.

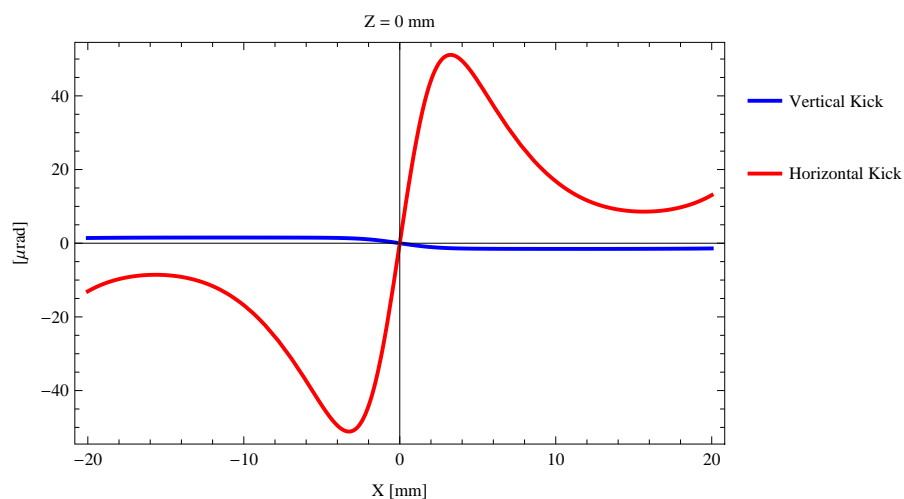


Figure 5.550: Induced angular kick on the stored beam from the epu53p6Heli ID as a function of the horizontal distance to the ID axis.

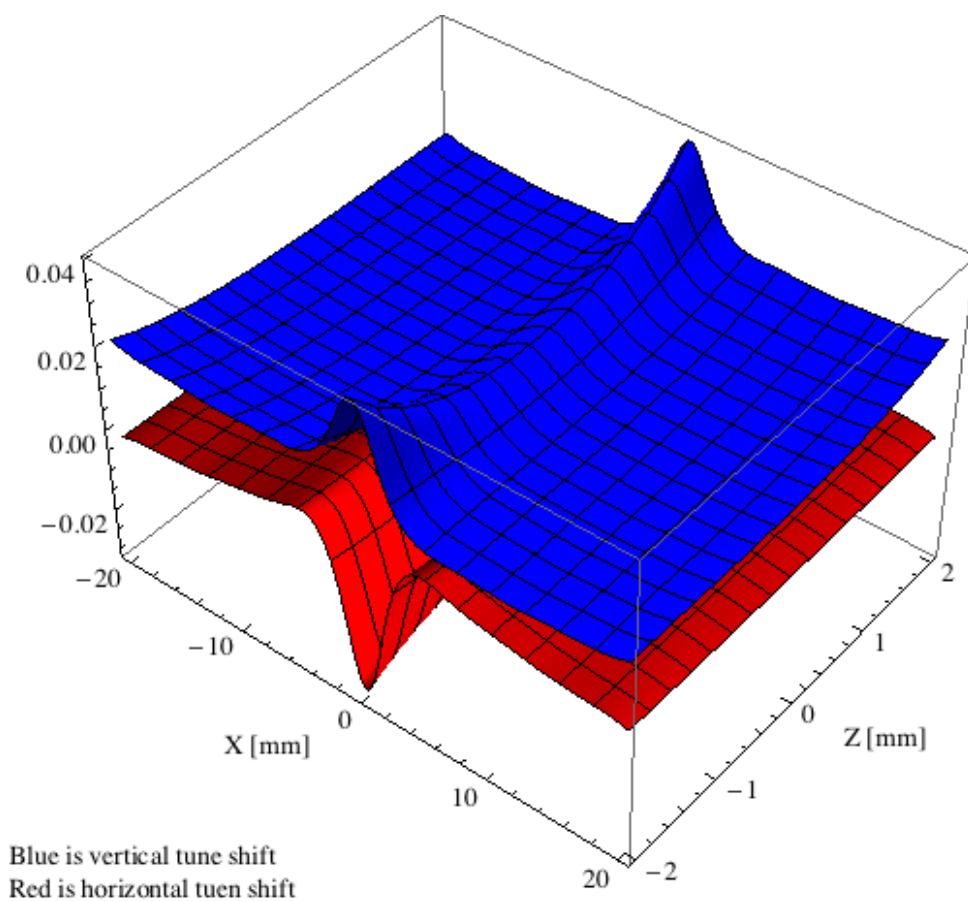


Figure 5.551: Tune shift induced by the epu53p6Heli ID over the beam stay clear aperture.

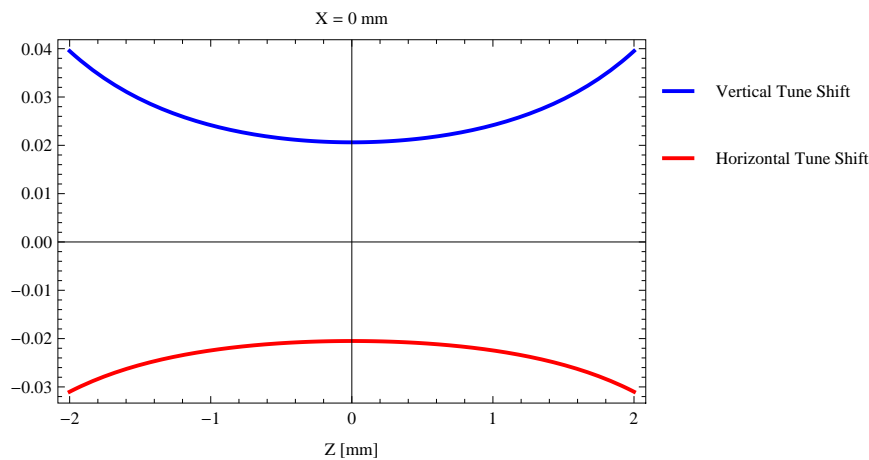


Figure 5.552: Induced tune shift from the epu53p6Heli ID as a function of the vertical distance to the axis of the ID.

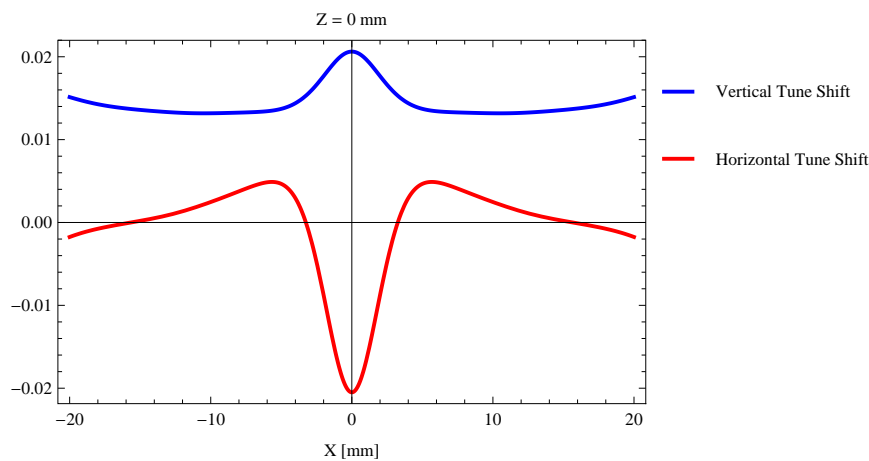


Figure 5.553: Induced tune shift from the epu53p6Heli ID on the stored beam from the ID as a function of the horizontal distance to the axis of the ID.

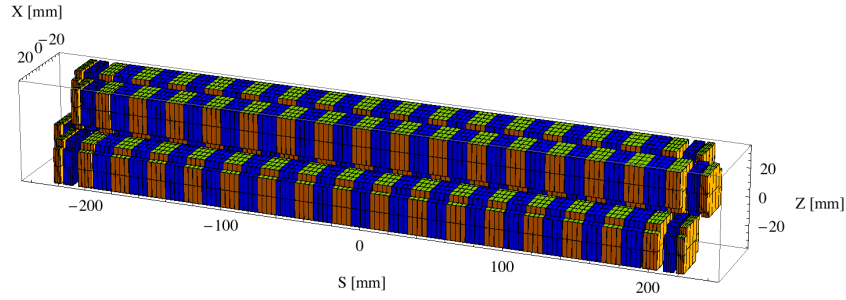


Figure 5.554: Magnetic model of the epu53p6Incl ID. The ID has been modelled with Radia [2]

$30 \times 30 \times 13.4 \text{ mm}^3$  and there is a 5. mm cut-out in two of the corners of the blocks. The total length of the epu53p6Incl ID is 3930.59 mm.

### Analysis of the magnetic field of the epu53p6Incl ID

The effective magnetic fields on axis and the fundamental photon energy of the epu53p6Incl ID are shown in Table 5.79. The higher harmonic contents in the magnetic field of an elliptically polarising undulator made of permanent magnets is negligible and the efficient field has about the same strength as the peak field.

Table 5.79: Effective Fields on axis and Fundamental Photon Energy of the epu53p6Incl ID

Undulator Period	53.6	mm
Undulator Gap	9	mm
Undulator Mode	Inclined	
Undulator Phase	14.239	mm
Vertical Peak Field	0.533	T
Efficient Vertical Field	0.540	T
Kx (from vert. field)	2.703	
Horizontal Peak Field:	-0.532	T
Efficient Horizontal Field	0.541	T
Kz (from hor. field)	2.708	
Photon Energy, Harm.1	0.192	keV
Emitted Power	6.539	kW
Total Length	3930.6	mm

### Synchrotron radiation from the epu53p6Incl ID

The power map of the emitted synchrotron radiation by the epu53p6Incl ID, assuming a 0.5 A filament beam with an energy of 3 GeV and undulator properties of the synchrotron radiation, is shown in Figure 5.559. The on-axis power density is  $24.045 \text{ kW/mrad}^2$

A map of the degree of linear polarisation of the fundamental harmonic of the synchrotron radiation emitted by the epu53p6Incl ID over the angle of observation is shown in Figure 5.560.

A map of the degree of 45 degree polarisation of the fundamental harmonic of the synchrotron radiation emitted by the epu53p6Incl ID over the angle of observation is shown in Figure 5.561.

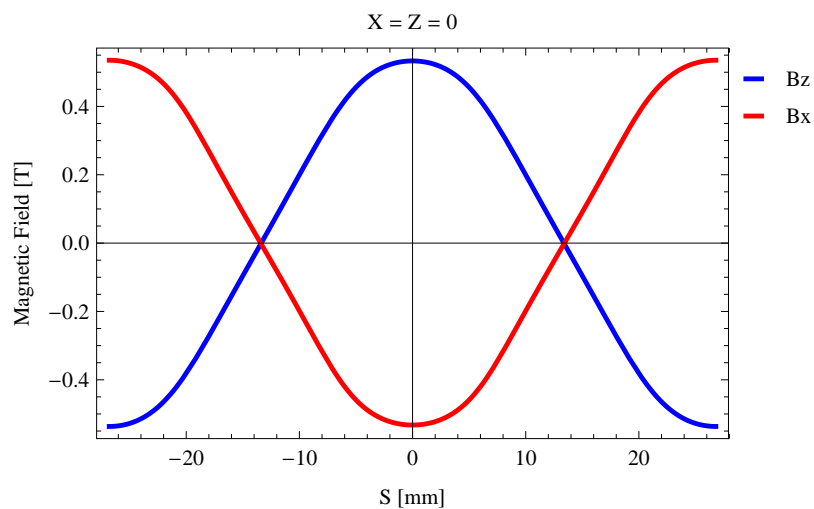


Figure 5.555: Vertical magnetic field in a central pole of the epu53p6Incl ID along the ID axis,  $X = Z = 0$

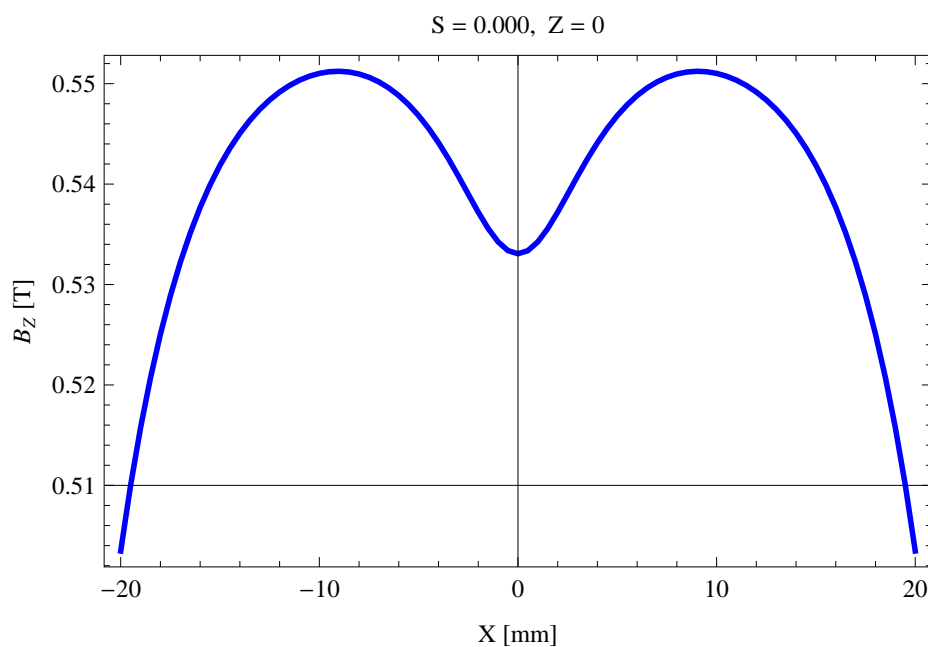


Figure 5.556: Vertical magnetic field in a central pole of the epu53p6Incl ID along the horizontally transverse direction to the ID axis,  $S = 0.000$ ,  $Z = 0$

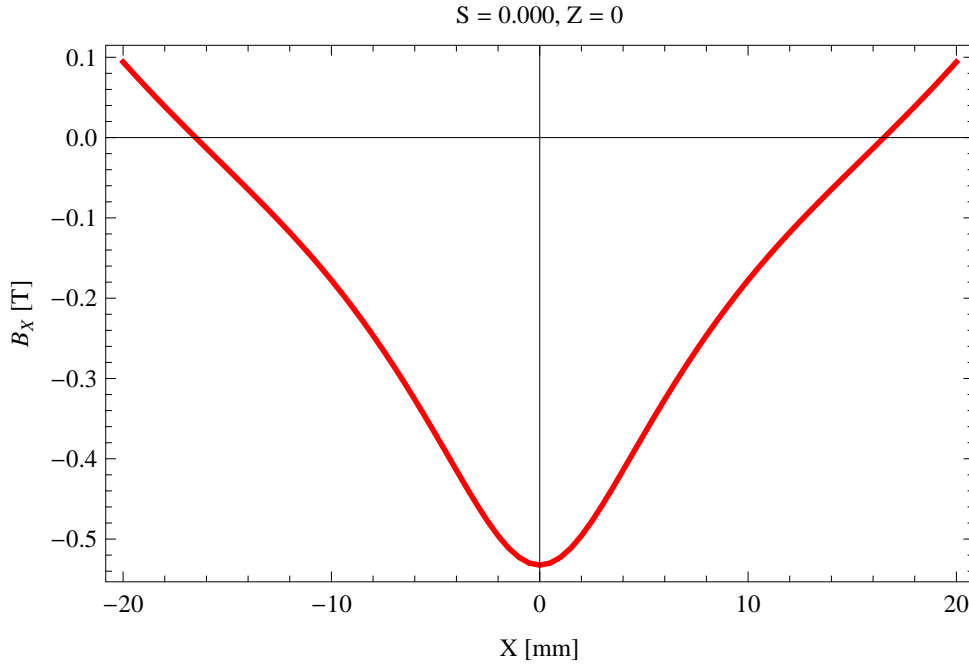


Figure 5.557: Horizontal magnetic field in a central pole of the epu53p6Incl ID along the horizontally transverse direction to the ID axis,  $S = 0.000$ ,  $Z = 0$

A map of the degree of circular polarisation of the fundamental harmonic of the synchrotron radiation emitted by the epu53p6Incl ID over the angle of observation is shown in Figure 5.562.

The on axis brilliance at peak energy, the angular spectral flux, the flux in the harmonics, the power in the harmonics, the ratio of coherence, the coherent flux in the harmonics, and the power of coherent radiation in the harmonics from the epu53p6Incl ID have been calculated and the resulting plots are found in this section of the document. The beam parameters used for the calculation are 0.5 A of stored current,  $\beta_H = 9$  m,  $\varepsilon_H = 0.263$  nmrad,  $\beta_V = 4.8$  m,  $\varepsilon_V = 8$  pmrad, and an energy spread of 0.001.

The brilliance at peak energy and the angular spectral flux density from the epu53p6Incl ID for different harmonics at maximum K-value (3.827) are given in Table 5.80 and for minimum K-value (0.400) these values are given in Table 5.81.

Table 5.80: The brilliance at peak energy and the angular spectral flux density from the epu53p6Incl ID for different harmonics at maximum K-value (3.827)

Harmonic	Photon Energy [eV]	Brilliance [Ph./s/mrad <sup>2</sup> /mrad <sup>2</sup> /0.1%BW]	Angular Spectral Flux [Ph./s/mrad <sup>2</sup> /0.1%BW]
1	191.612	$7.1 \times 10^{19}$	$3.41 \times 10^{17}$
3	574.835	$1.49 \times 10^{20}$	$4.41 \times 10^{17}$
5	958.058	$1.62 \times 10^{20}$	$4.06 \times 10^{17}$
7	1341.28	$1.58 \times 10^{20}$	$3.62 \times 10^{17}$
9	1724.5	$1.49 \times 10^{20}$	$3.22 \times 10^{17}$
11	2107.73	$1.39 \times 10^{20}$	$2.88 \times 10^{17}$



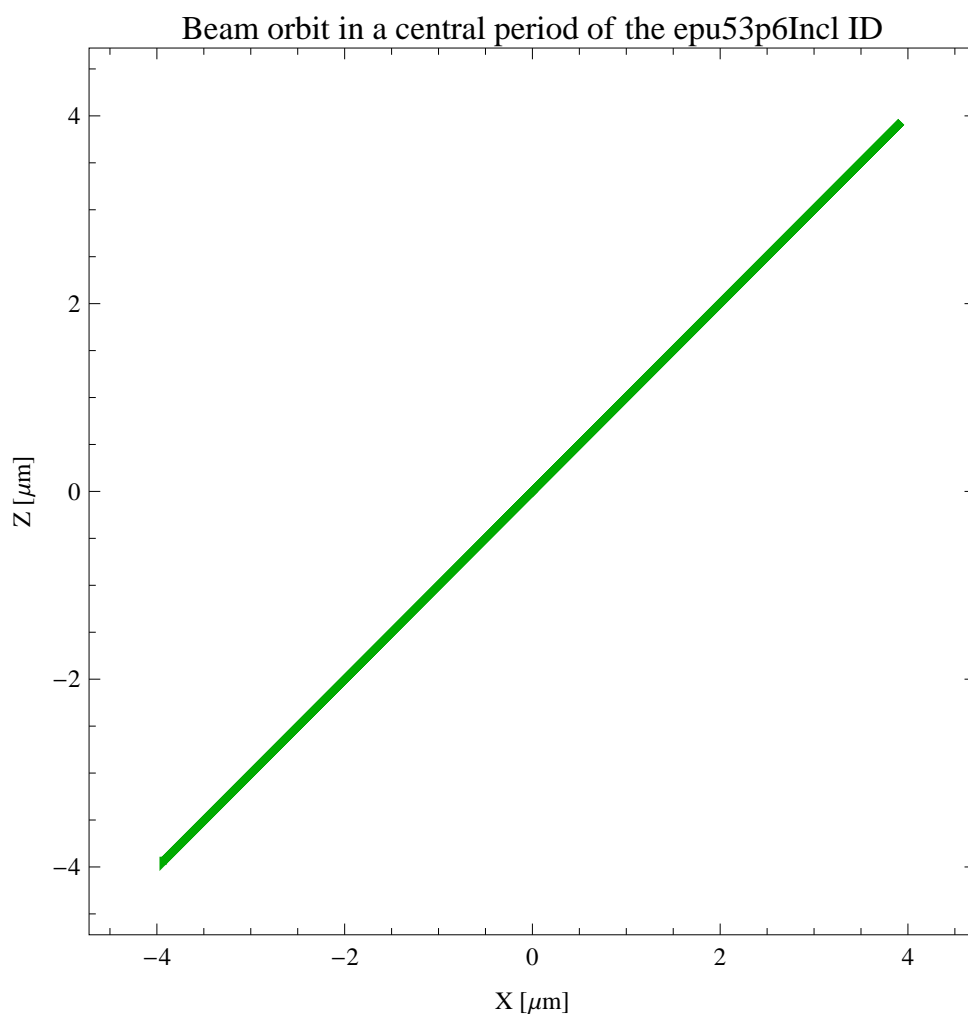


Figure 5.558: The beam orbit of the electron beam through a central period of the epu53p6Incl ID

Table 5.81: The brilliance at peak energy and the angular spectral flux density from the epu53p6Incl ID for different harmonics at minimum K-value (0.4)

Harmonic	Photon Energy [eV]	Brilliance [Ph./s/mrad <sup>2</sup> /mrad <sup>2</sup> /0.1%BW]	Angular Spectral Flux [Ph./s/mrad <sup>2</sup> /0.1%BW]
1	1476.43	$1.65 \times 10^{20}$	$3.68 \times 10^{17}$
3	4429.29	$3.44 \times 10^{18}$	$6.45 \times 10^{15}$
5	7382.15	$4.04 \times 10^{16}$	$7.31 \times 10^{13}$
7	10335.	$4.31 \times 10^{14}$	$7.7 \times 10^{11}$
9	13287.9	$4.47 \times 10^{12}$	$7.93 \times 10^9$
11	16240.7	$4.59 \times 10^{10}$	$8.11 \times 10^7$

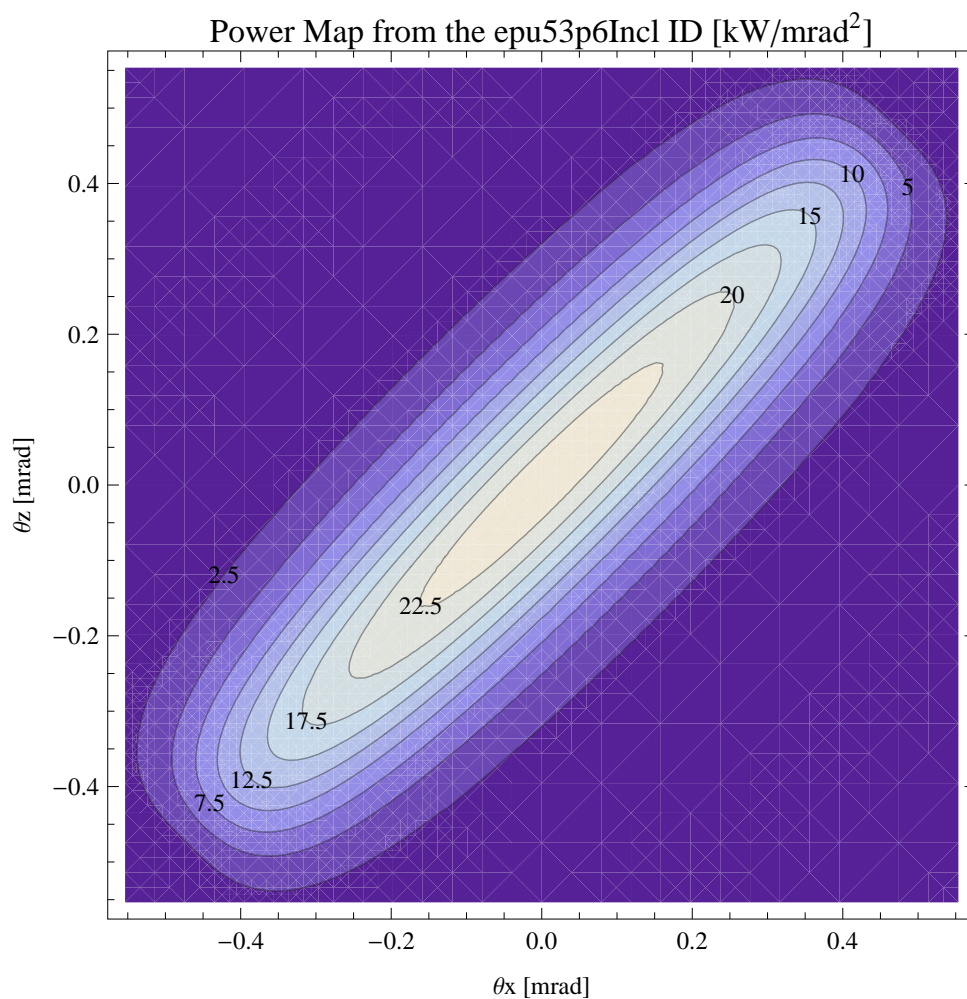


Figure 5.559: Map of the power distribution of the emitted synchrotron radiation by the epu53p6Incl ID

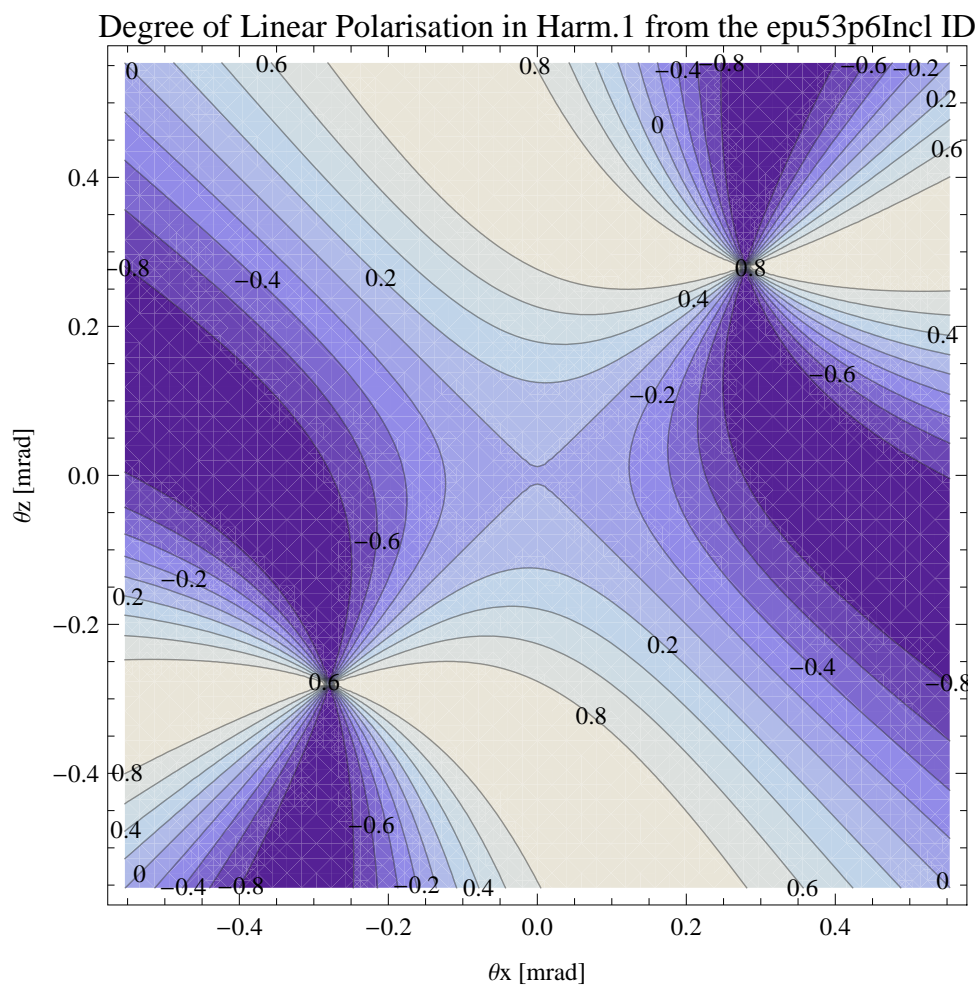


Figure 5.560: Map of linear polarisation in the fundamental harmonic of the synchrotron radiation emitted by the epu53p6Incl ID

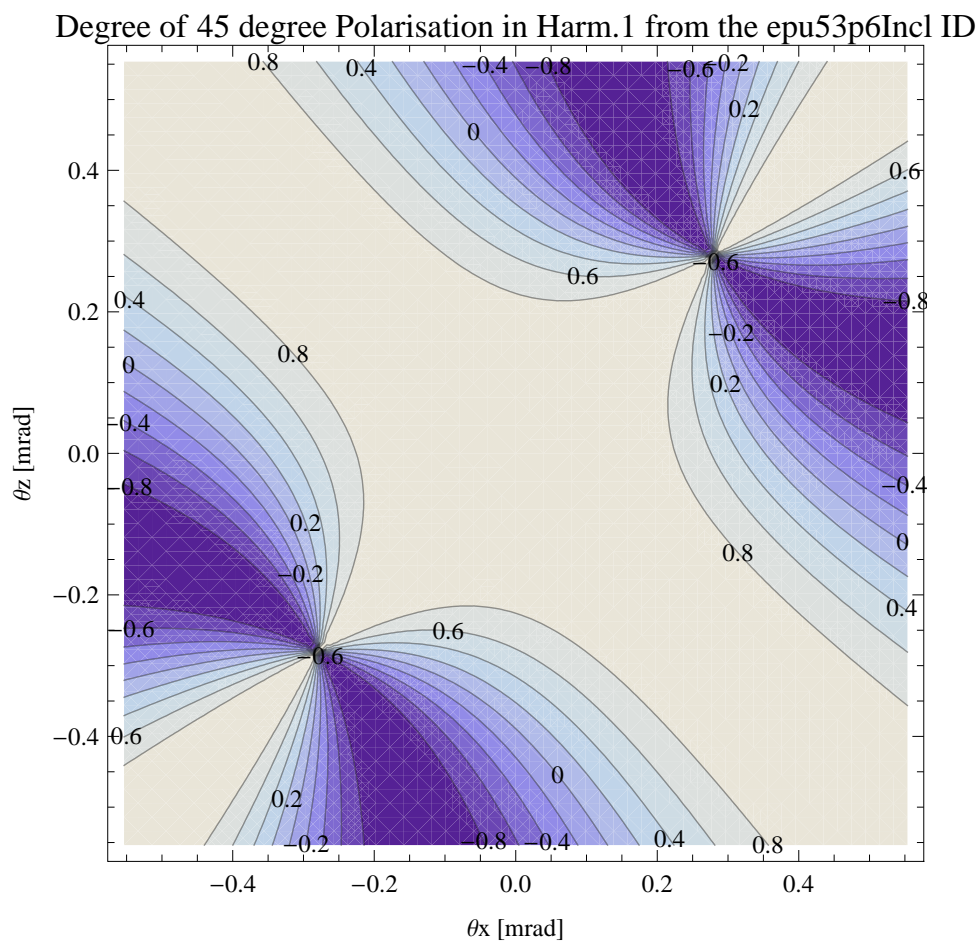


Figure 5.561: Map of 45 degree polarisation in the fundamental harmonic of the synchrotron radiation emitted by the epu53p6Incl ID

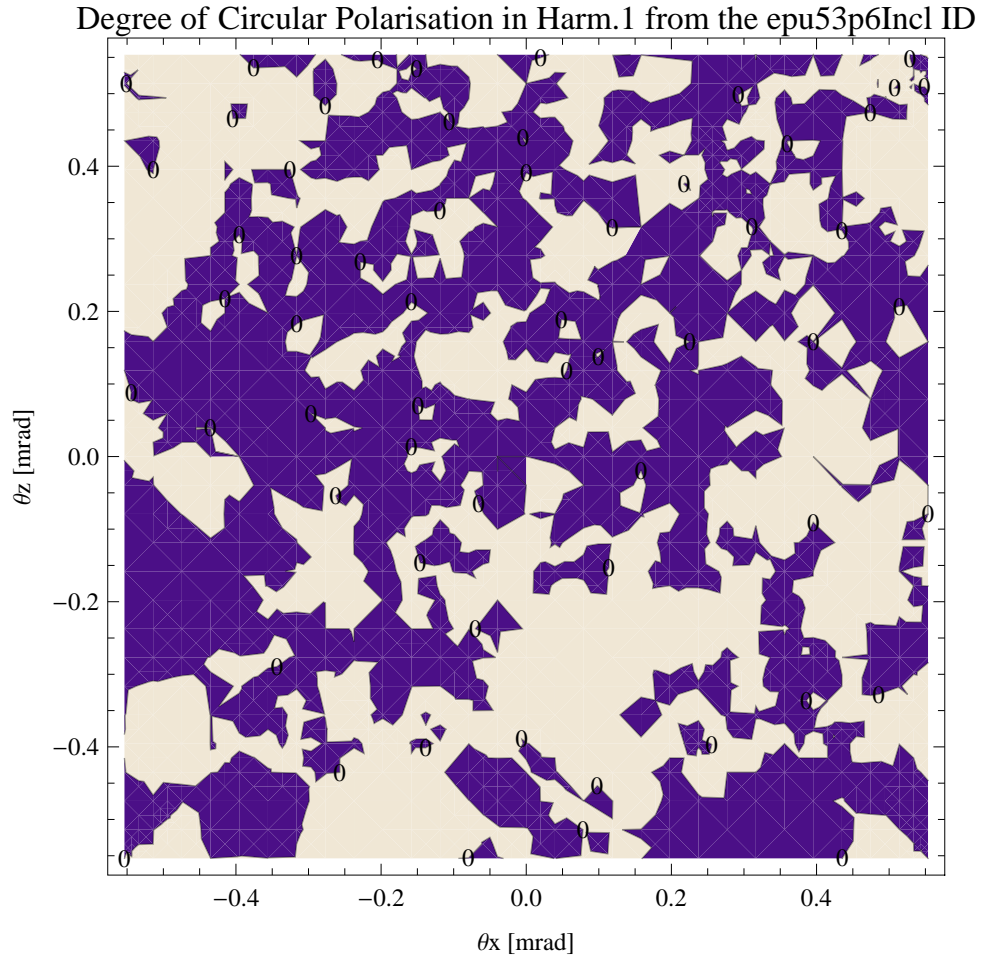


Figure 5.562: Map of circular polarisation in the fundamental harmonic of the synchrotron radiation emitted by the epu53p6Incl ID

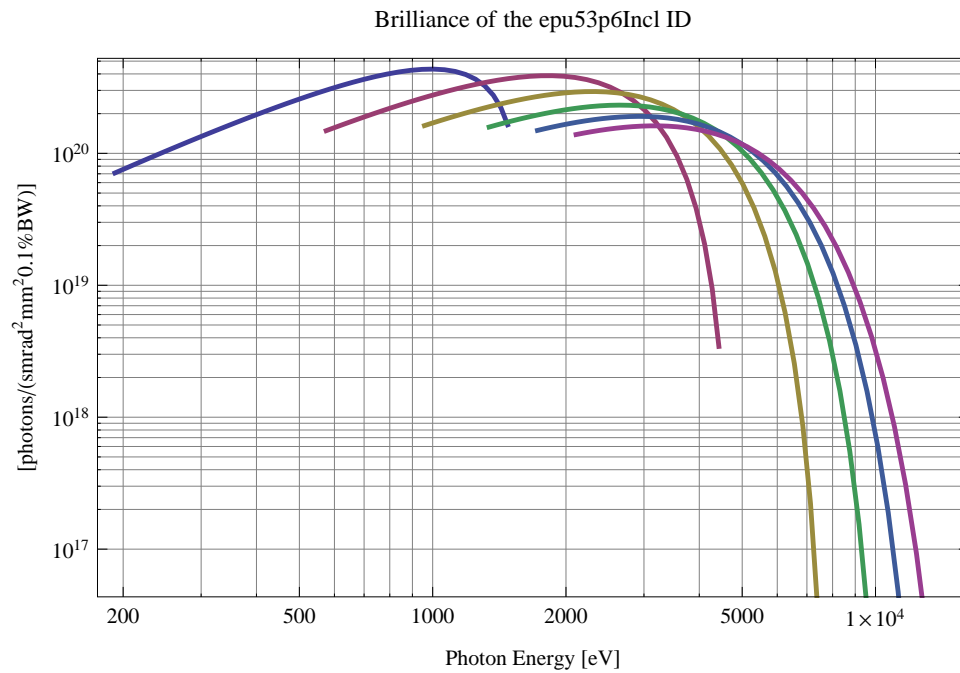


Figure 5.563: The brilliance at peak energy from the epu53p6Incl ID

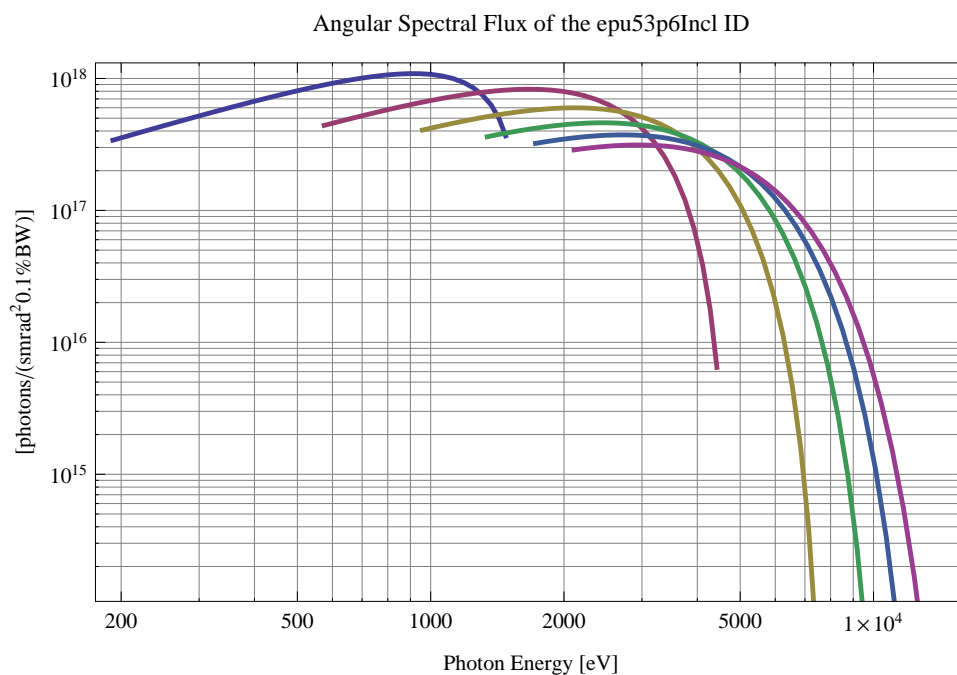


Figure 5.564: The angular spectral flux from the epu53p6Incl ID

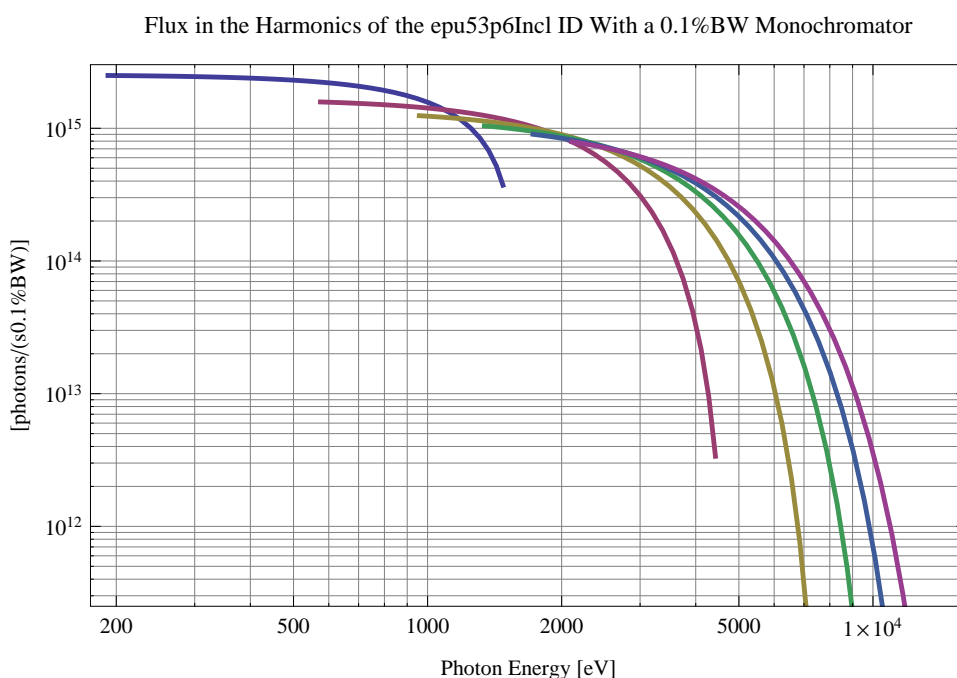


Figure 5.565: The flux of photons in the harmonics from the epu53p6Incl ID using a 0.1%BW monochromator

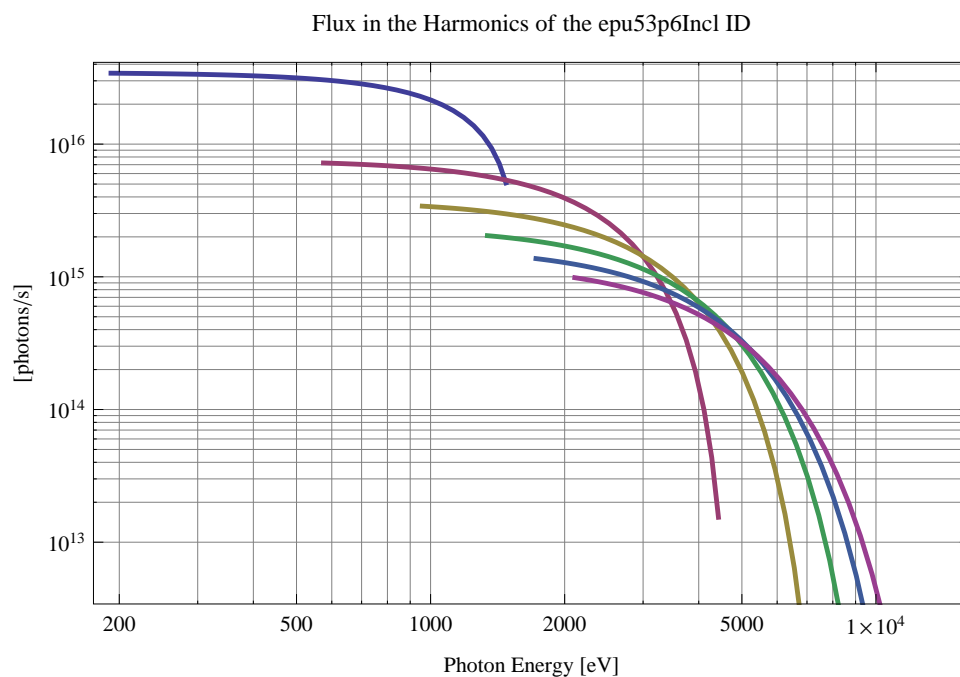


Figure 5.566: The flux of photons in the harmonics from the epu53p6Incl ID

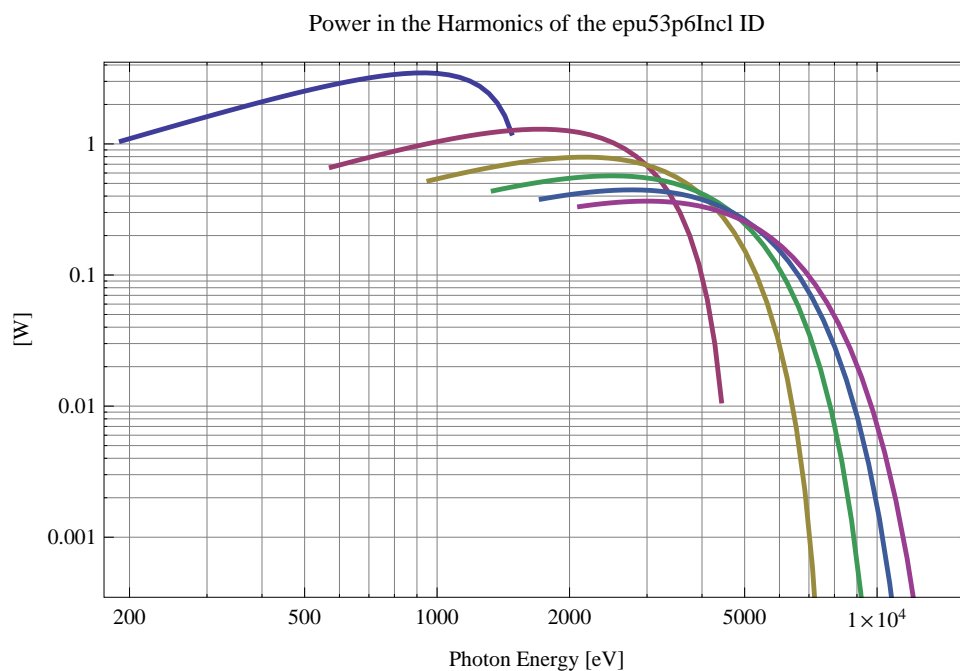


Figure 5.567: The power in the harmonics from the epu53p6Incl ID

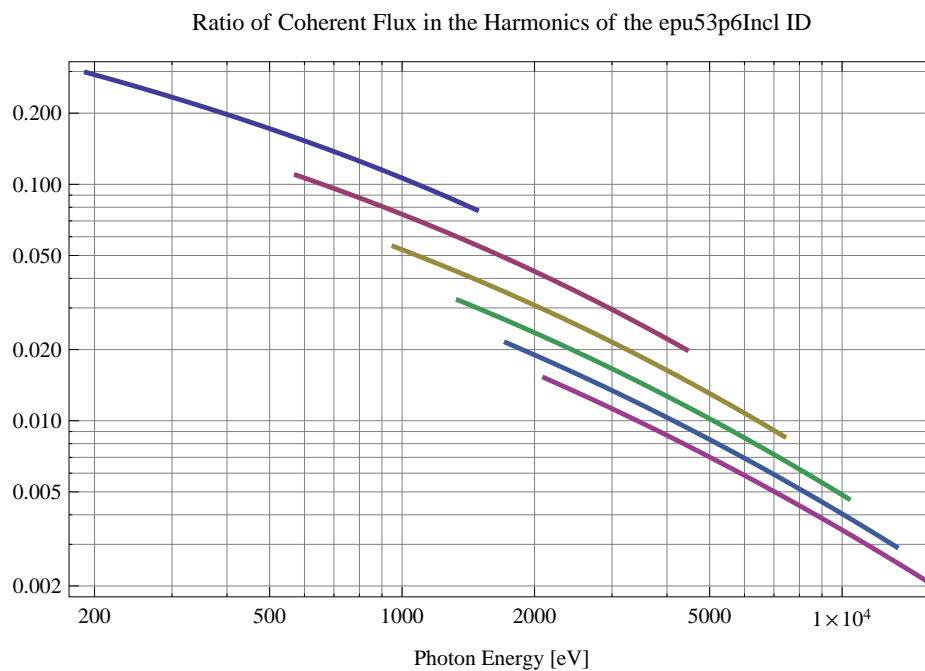


Figure 5.568: The ratio of coherent flux in the harmonics from the epu53p6Incl ID

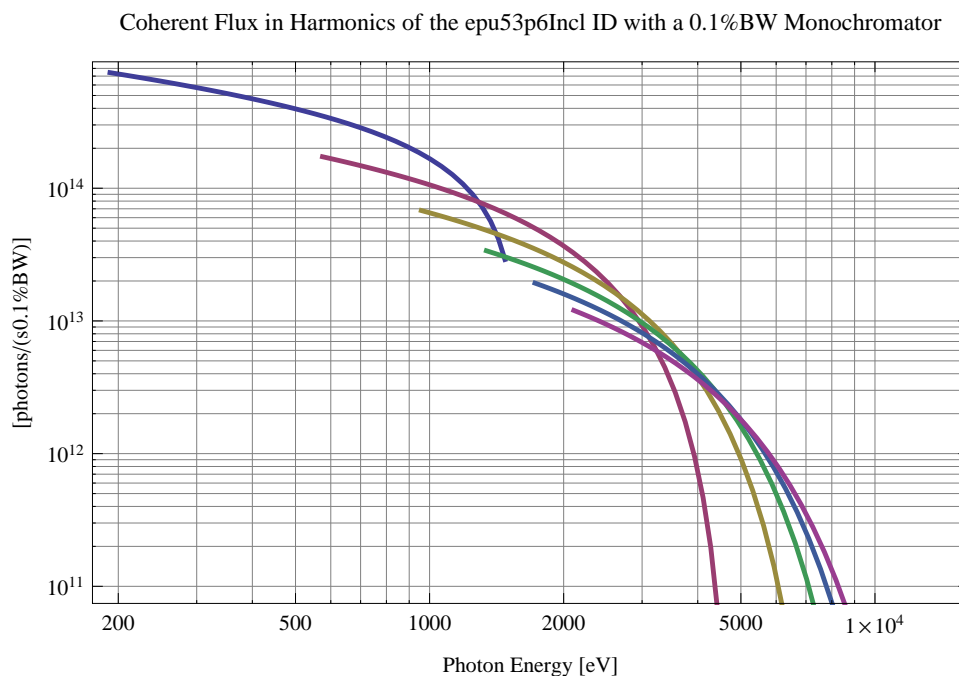


Figure 5.569: The coherent flux in the harmonics of the epu53p6Incl ID using a 0.1%BW Monochromator



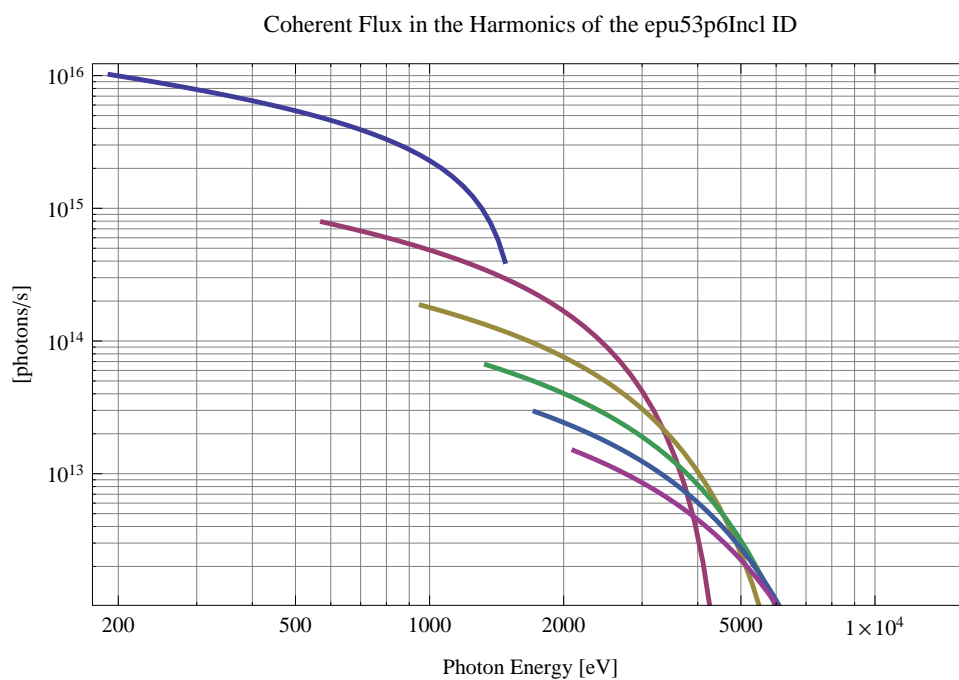


Figure 5.570: The coherent flux in the harmonics of the epu53p6Incl ID

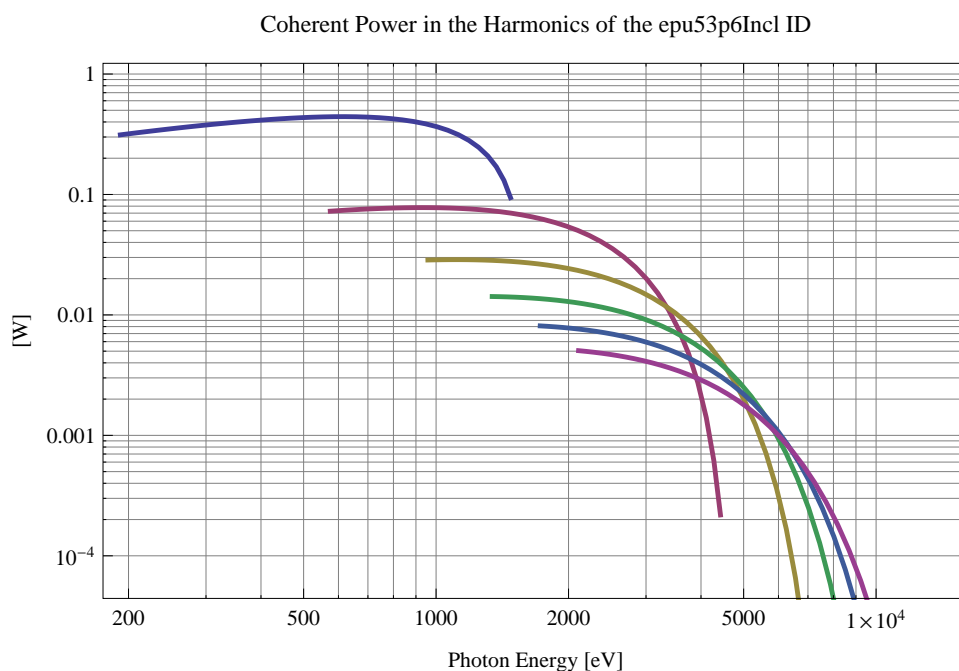


Figure 5.571: The power of coherent synchrotron radiation in the harmonics of the epu53p6Incl ID

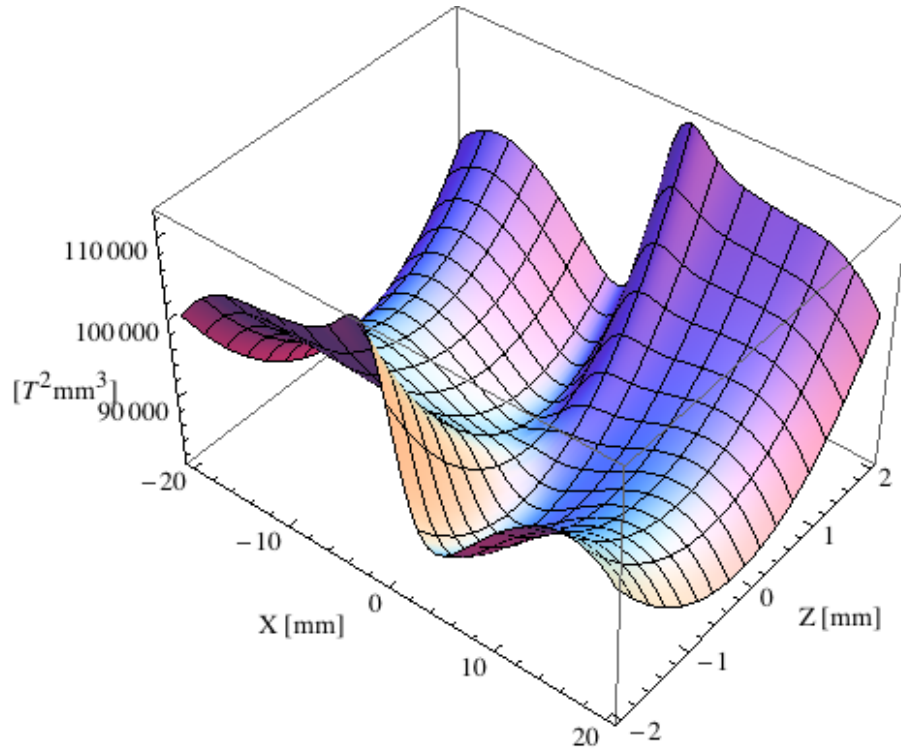


Figure 5.572: Focusing potential from the epu53p6Incl ID over the beam stay clear aperture.

### Influence from the epu53p6Incl ID on the optics of the stored beam

Figure 5.572 shows the focusing potential from the epu53p6Incl over the beam stay clear aperture of the ring aperture.

Figure 5.573 shows the kick map in the beam energy independent unit  $T^2 m^2$  of the kicks induced by the epu53p6Incl ID over the beam stay clear aperture.

Figure 5.574 shows the induced angular kick on the stored beam from the epu53p6Incl ID as a function of the vertical distance to the axis of the ID.

Figure 5.575 shows the induced angular kick on the stored beam from the epu53p6Incl ID as a function of the horizontal distance to the axis of the ID.

Figure 5.576 shows tune shift induced by the epu53p6Incl ID over the beam stay clear aperture. Note that the tune shift depends on the beam size at the ID.

Figure 5.577 shows the induced tune shift from the epu53p6Incl ID as a function of the vertical distance to the axis of the ID.

Figure 5.578 shows the induced tune shift from the epu53p6Incl ID as a function of the horizontal distance to the axis of the ID.

### Magnet model of the elliptically polarising undulator epu53p6Vert

The Radia [2] magnet model of the epu53p6Vert ID is shown in Figure 5.579. The length of the magnet model is 446.587 mm. The magnetic material in the model is NdFeb with a remanence of 1.28 T, a material similar to VACODYM 776 TP from Vacuumschmelze. Blocks with vertical magnetisation are blue and blocks with horizontal magnetisation are yellow. The block size is

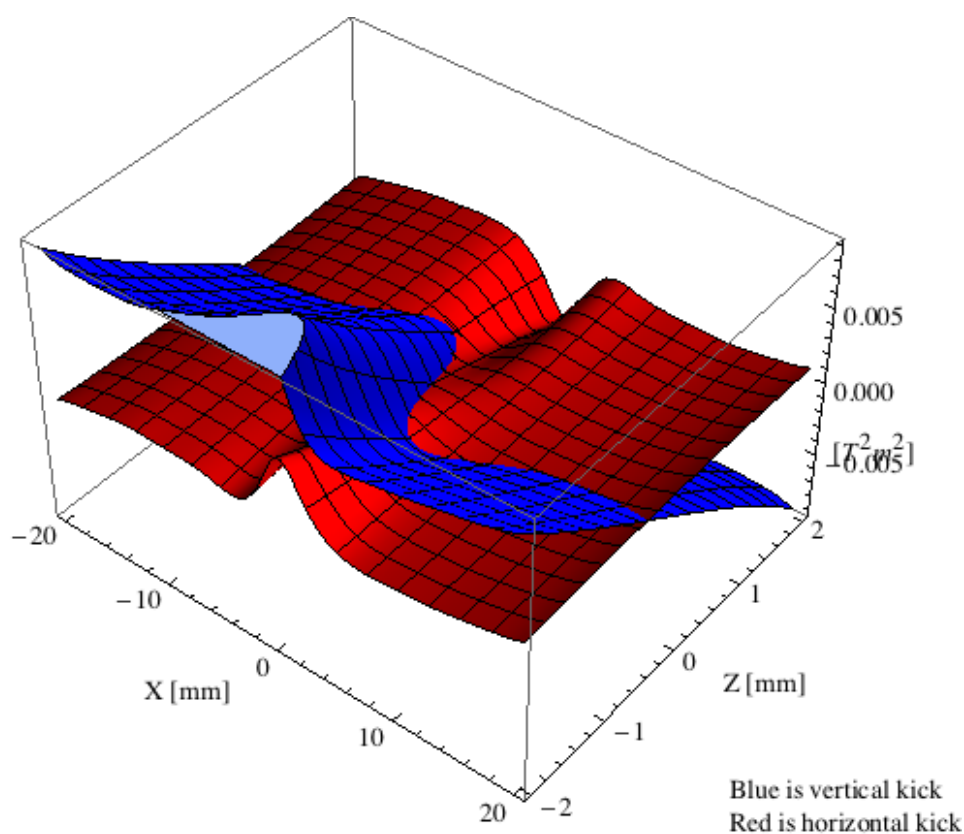


Figure 5.573: Kick map in the beam energy independent unit  $T^2m^2$  of the kicks induced by the epu53p6Incl ID over the beam stay clear aperture.

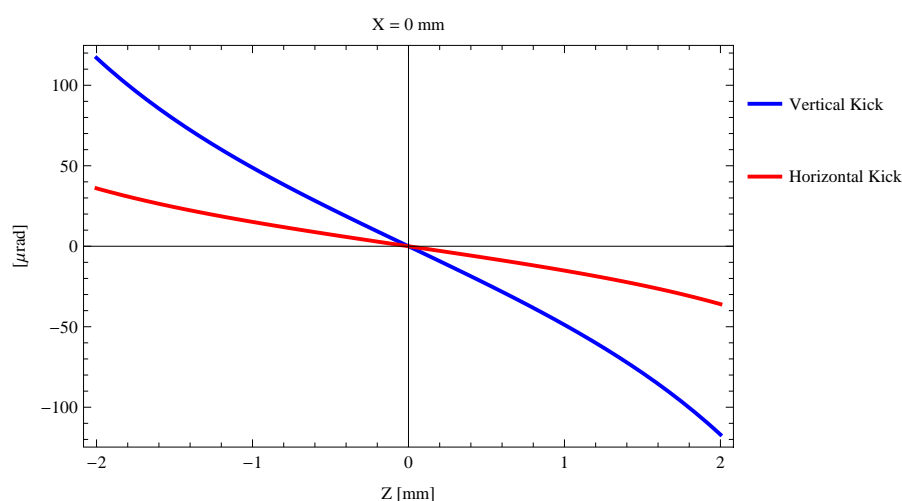


Figure 5.574: Induced angular kick on the stored beam from the epu53p6Incl ID as a function of the vertical distance to the ID axis.

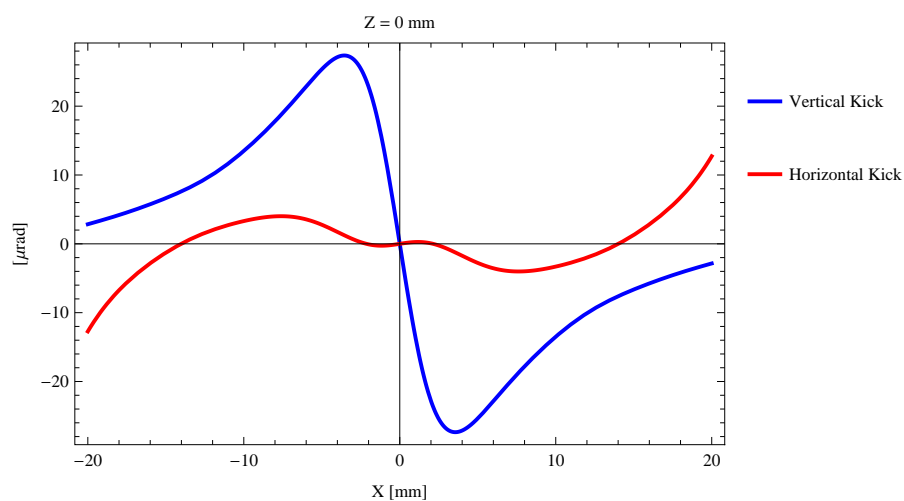


Figure 5.575: Induced angular kick on the stored beam from the epu53p6Incl ID as a function of the horizontal distance to the ID axis.

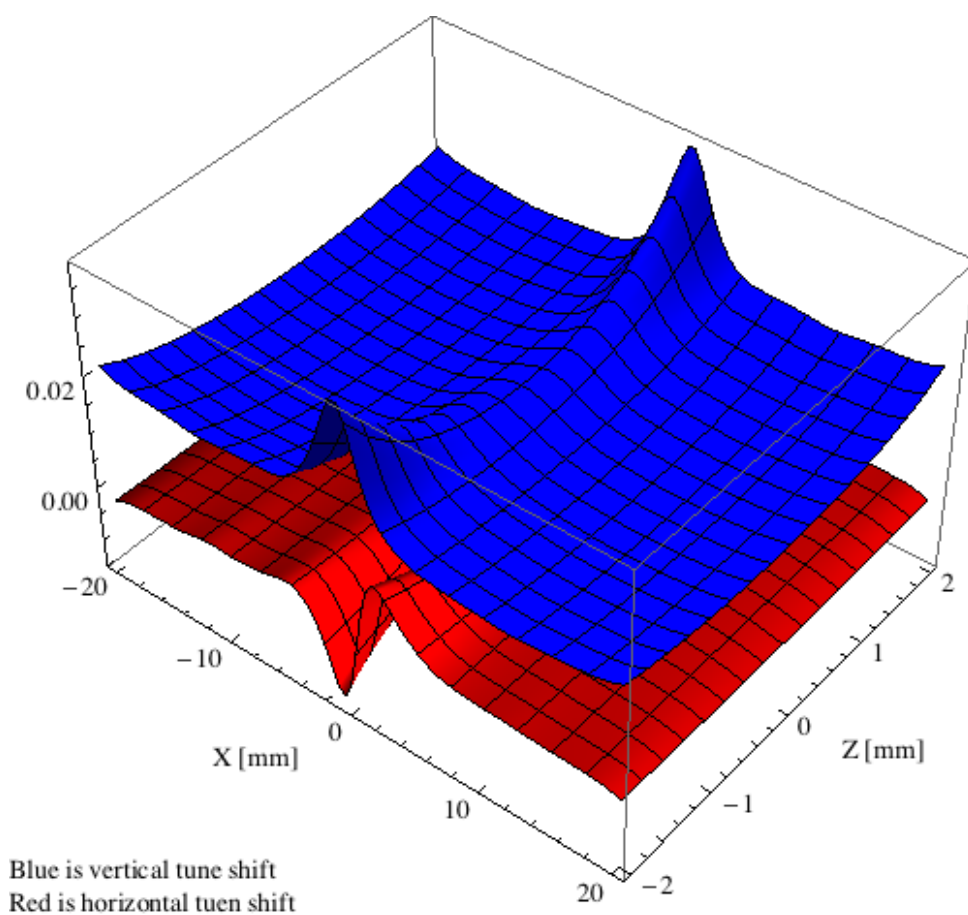


Figure 5.576: Tune shift induced by the epu53p6Incl ID over the beam stay clear aperture.

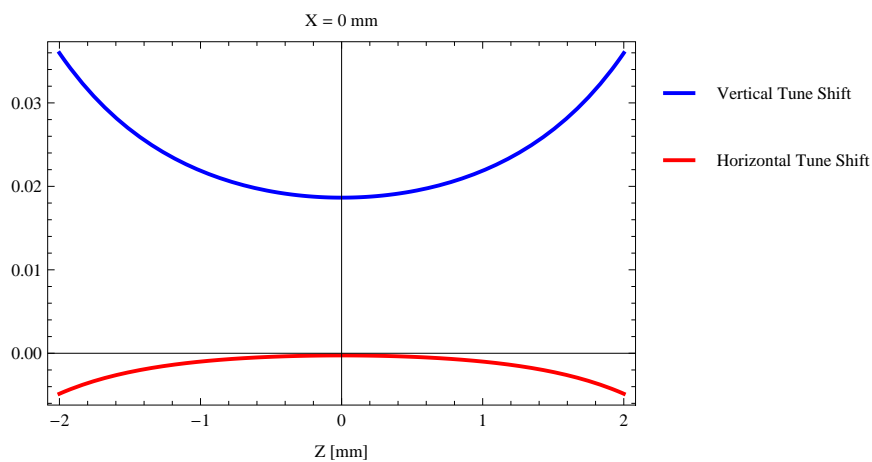


Figure 5.577: Induced tune shift from the epu53p6Incl ID as a function of the vertical distance to the axis of the ID.

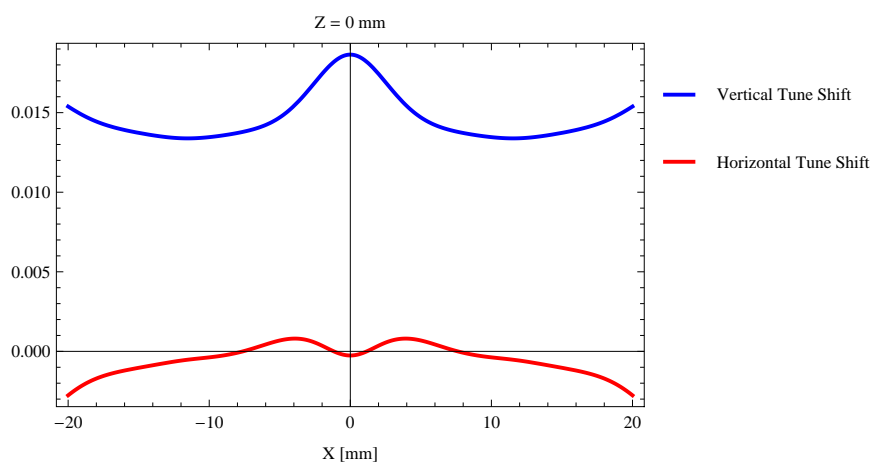


Figure 5.578: Induced tune shift from the epu53p6Incl ID on the stored beam from the ID as a function of the horizontal distance to the axis of the ID.

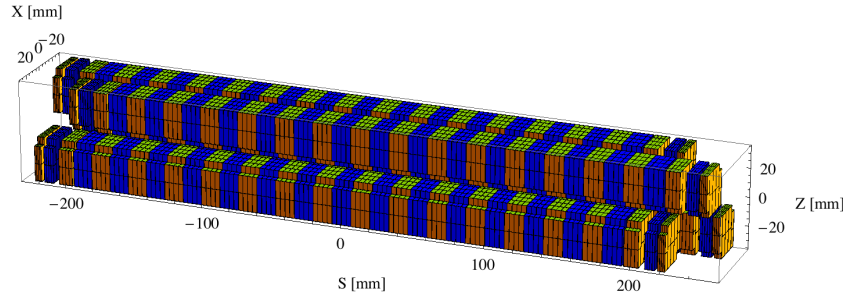


Figure 5.579: Magnetic model of the epu53p6Vert ID. The ID has been modelled with Radia [2]

$30 \times 30 \times 13.4 \text{ mm}^3$  and there is a 5. mm cut-out in two of the corners of the blocks. The total length of the epu53p6Vert ID is 3930.59 mm.

### Analysis of the magnetic field of the epu53p6Vert ID

The effective magnetic fields on axis and the fundamental photon energy of the epu53p6Vert ID are shown in Table 5.82. The higher harmonic contents in the magnetic field of an elliptically polarising undulator made of permanent magnets is negligible and the efficient field has about the same strength as the peak field.

Table 5.82: Effective Fields on axis and Fundamental Photon Energy of the epu53p6Vert ID

Undulator Period	53.6	mm
Undulator Gap	9	mm
Undulator Mode	Vertical	
Undulator Phase	26.800	mm
Vertical Peak Field	0.000	T
Efficient Vertical Field	0.000	T
Kx (from vert. field)	0.000	
Horizontal Peak Field:	0.981	T
Efficient Horizontal Field	0.985	T
Kz (from hor. field)	4.931	
Photon Energy, Harm.1	0.121	keV
Emitted Power	10.858	kW
Total Length	3930.6	mm

### Synchrotron radiation from the epu53p6Vert ID

The power map of the emitted synchrotron radiation by the epu53p6Vert ID, assuming a 0.5 A filament beam with an energy of 3 GeV and undulator properties of the synchrotron radiation, is shown in Figure 5.583. The on-axis power density is  $31.051 \text{ kW/mrad}^2$

A map of the degree of linear polarisation of the fundamental harmonic of the synchrotron radiation emitted by the epu53p6Vert ID over the angle of observation is shown in Figure 5.584.

A map of the degree of 45 degree polarisation of the fundamental harmonic of the synchrotron radiation emitted by the epu53p6Vert ID over the angle of observation is shown in Figure 5.585.

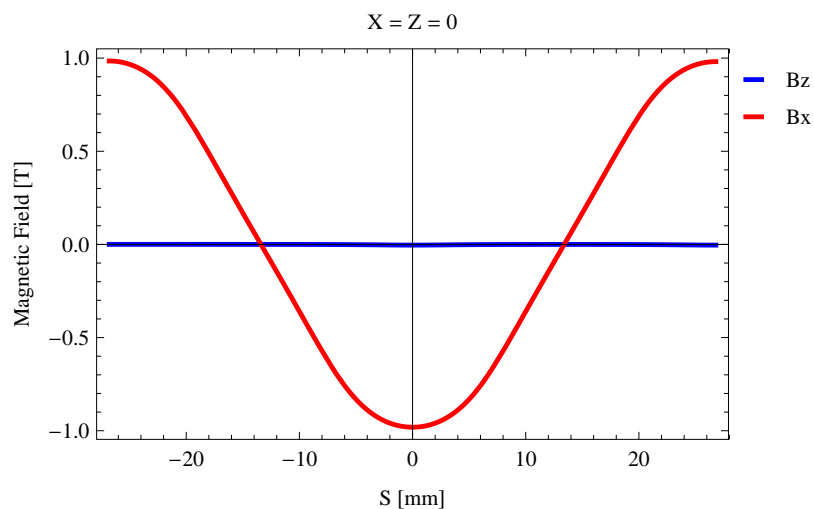


Figure 5.580: Vertical magnetic field in a central pole of the epu53p6Vert ID along the ID axis,  $X = Z = 0$

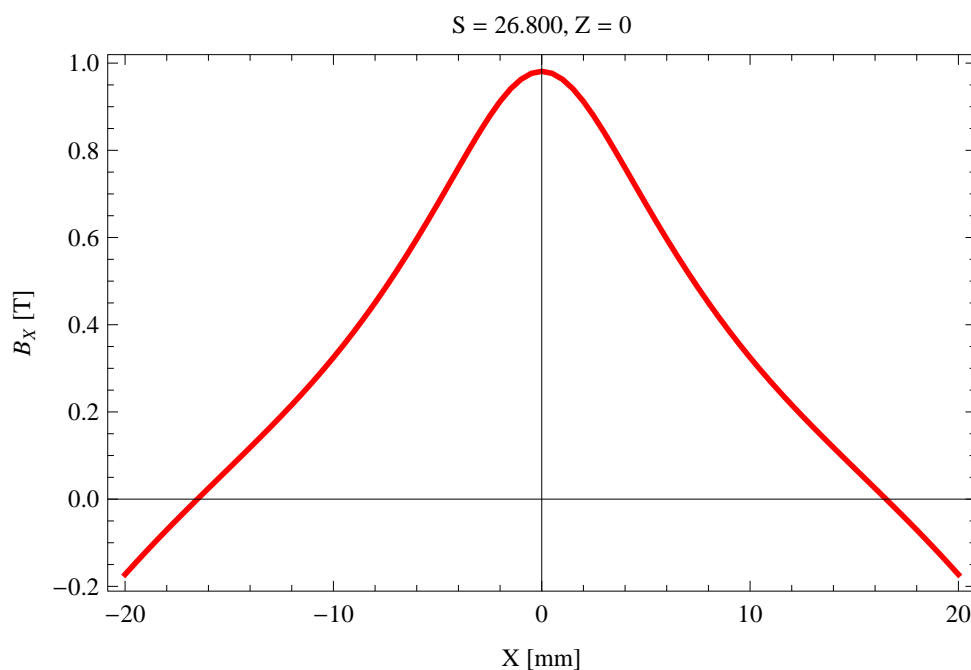


Figure 5.581: Horizontal magnetic field in a central pole of the epu53p6Vert ID along the horizontally transverse direction to the ID axis,  $S = 26.800$ ,  $Z = 0$

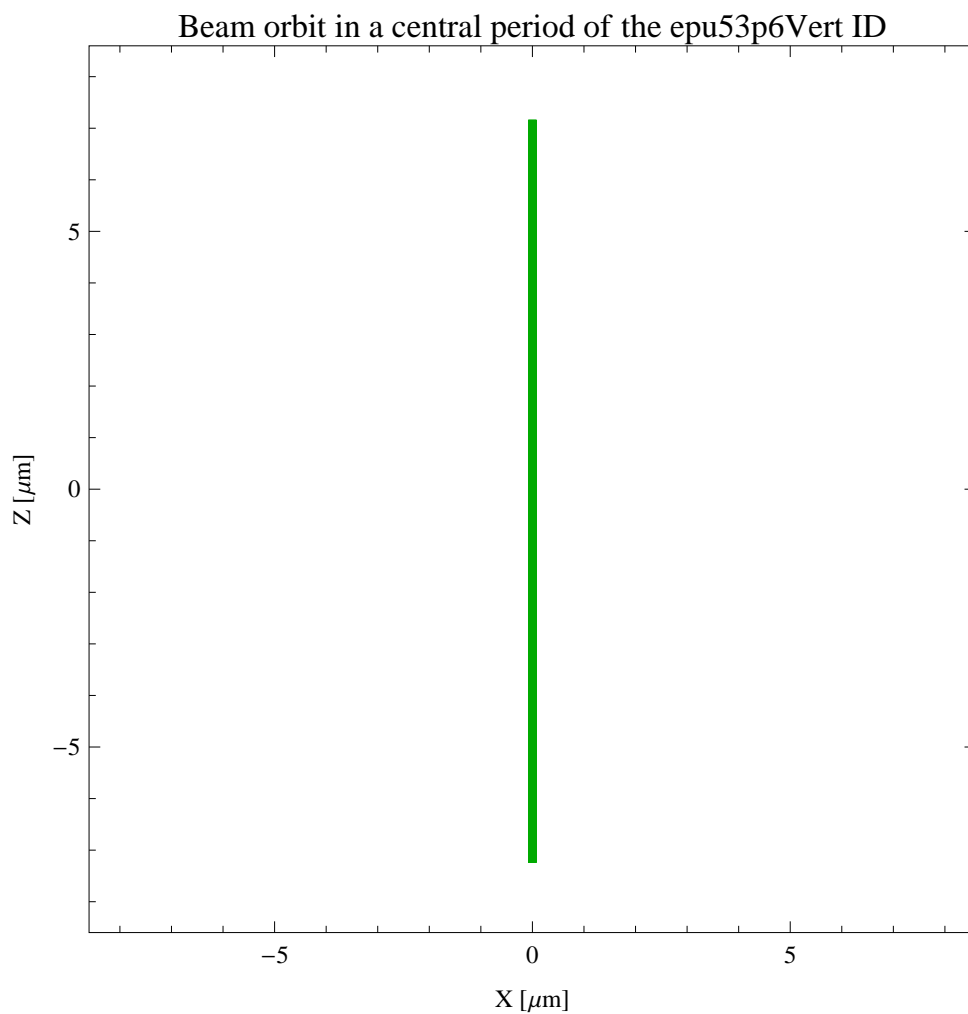


Figure 5.582: The beam orbit of the electron beam through a central period of the epu53p6Vert ID



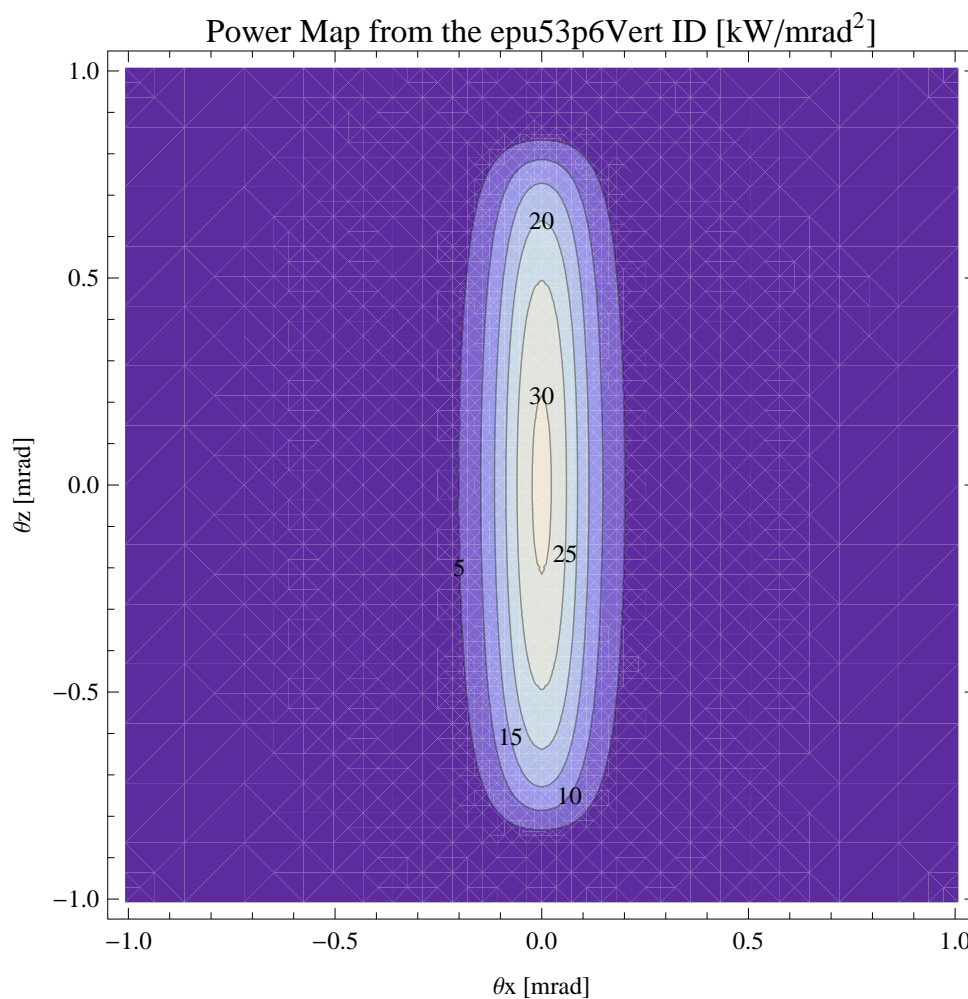


Figure 5.583: Map of the power distribution of the emitted synchrotron radiation by the epu53p6Vert ID

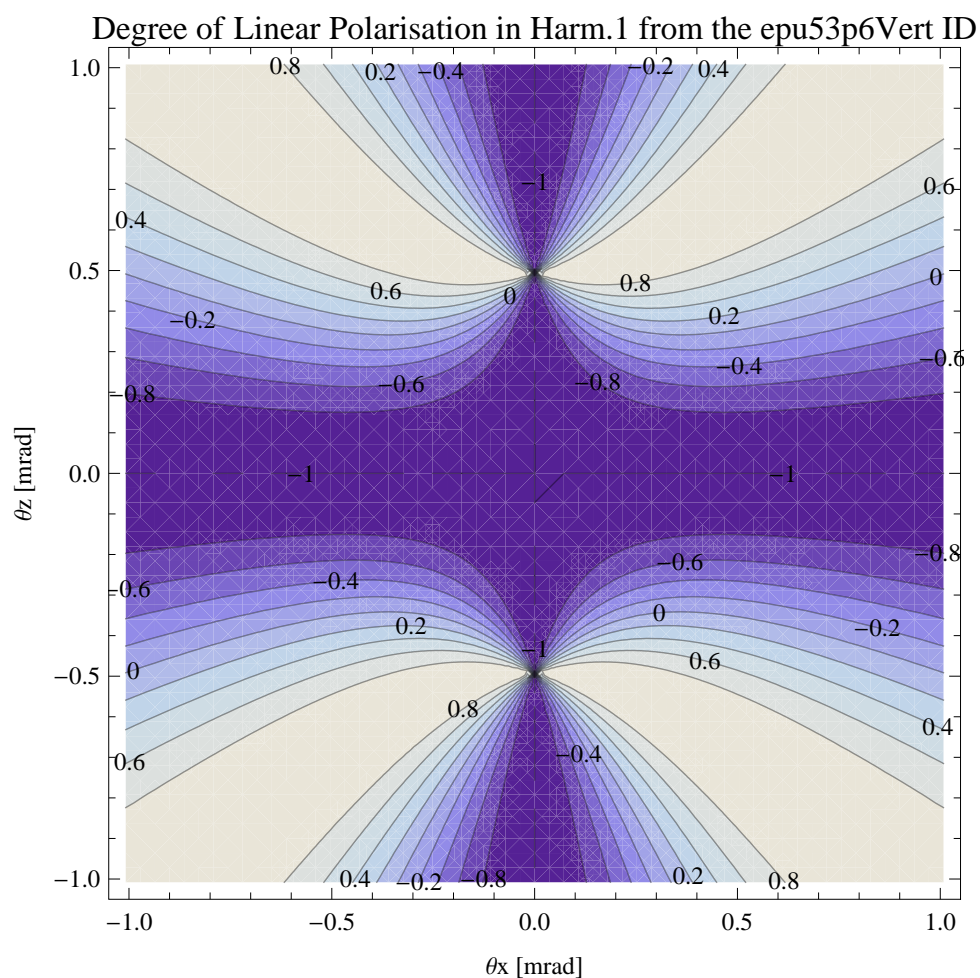


Figure 5.584: Map of linear polarisation in the fundamental harmonic of the synchrotron radiation emitted by the epu53p6Vert ID

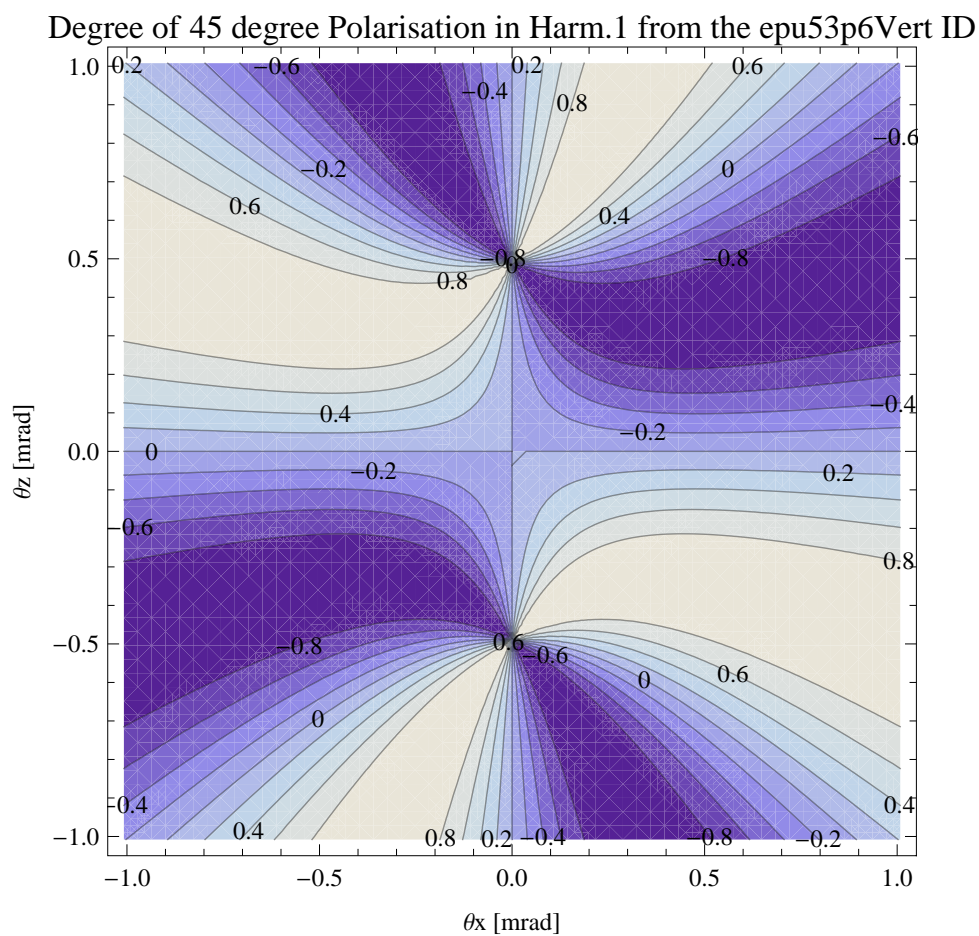


Figure 5.585: Map of 45 degree polarisation in the fundamental harmonic of the synchrotron radiation emitted by the epu53p6Vert ID

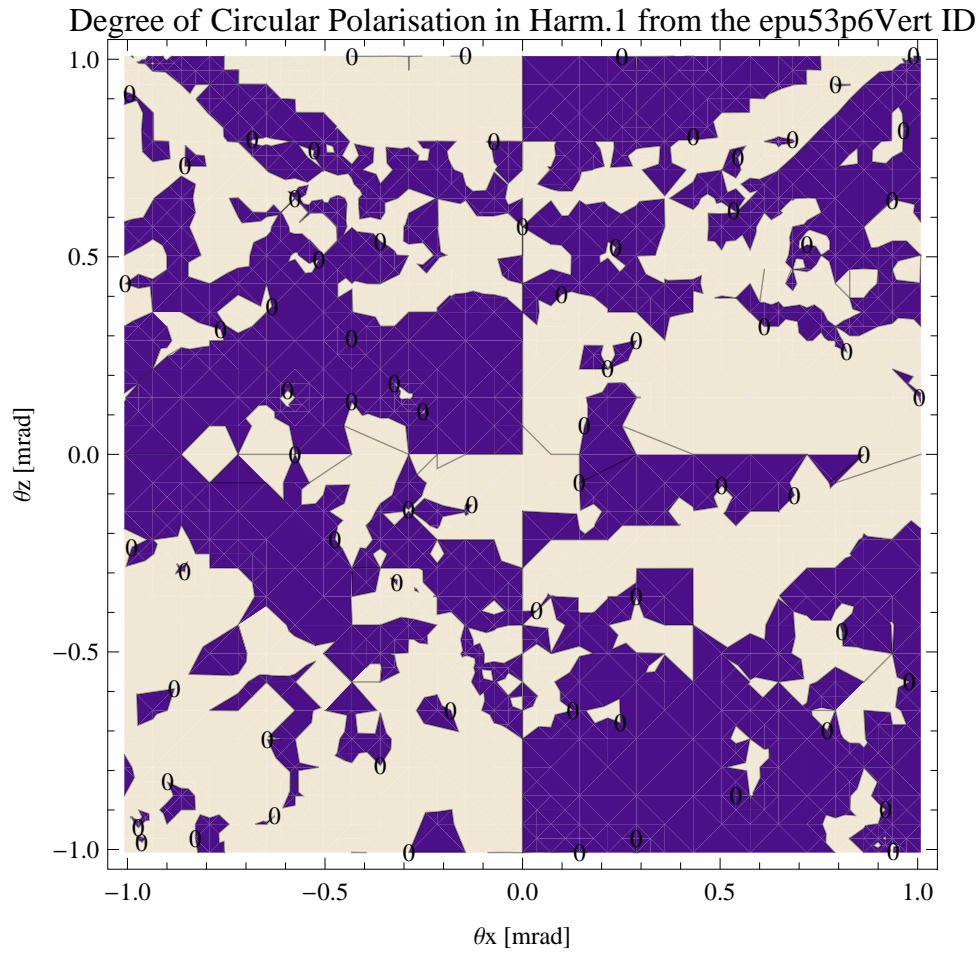


Figure 5.586: Map of circular polarisation in the fundamental harmonic of the synchrotron radiation emitted by the epu53p6Vert ID

A map of the degree of circular polarisation of the fundamental harmonic of the synchrotron radiation emitted by the epu53p6Vert ID over the angle of observation is shown in Figure 5.586.

The on axis brilliance at peak energy, the angular spectral flux, the flux in the harmonics, the power in the harmonics, the ratio of coherence, the coherent flux in the harmonics, and the power of coherent radiation in the harmonics from the epu53p6Vert ID have been calculated and the resulting plots are found in this section of the document. The beam parameters used for the calculation are 0.5 A of stored current,  $\beta_H = 9$  m,  $\varepsilon_H = 0.263$  nmrad,  $\beta_V = 4.8$  m,  $\varepsilon_V = 8$  pmrad, and an energy spread of 0.001.

The brilliance at peak energy and the angular spectral flux density from the epu53p6Vert ID for different harmonics at maximum K-value (4.931) are given in Table 5.83 and for minimum K-value (0.400) these values are given in Table 5.84.

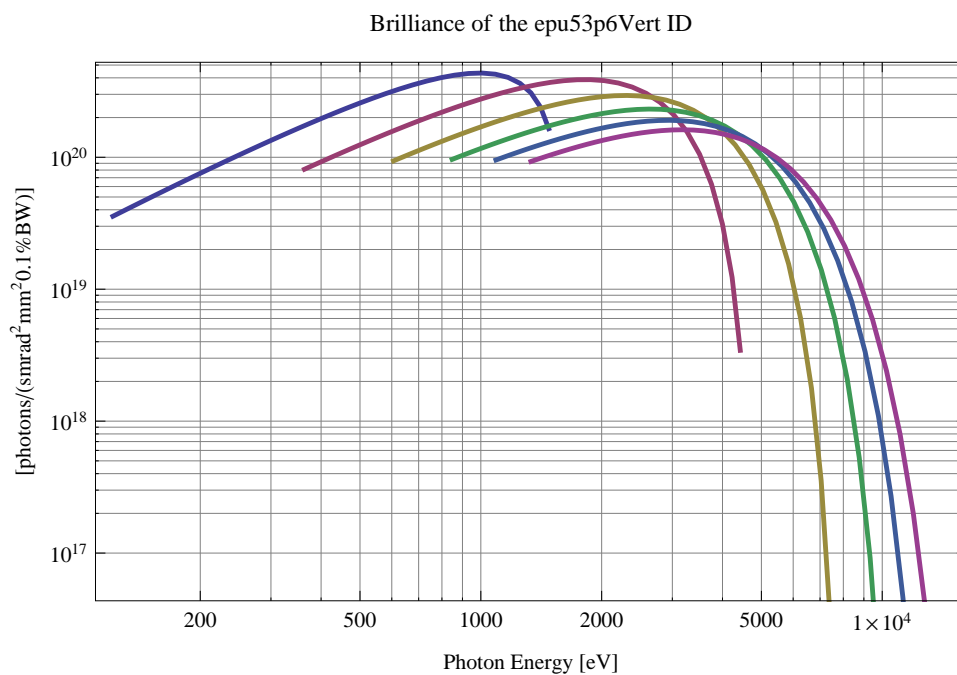


Figure 5.587: The brilliance at peak energy from the epu53p6Vert ID

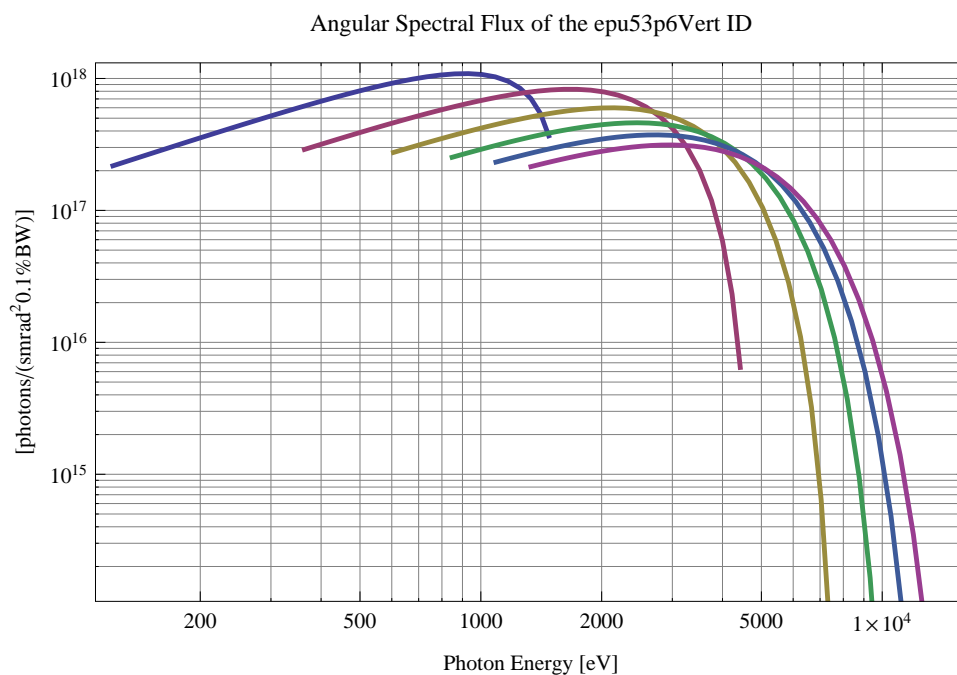


Figure 5.588: The angular spectral flux from the epu53p6Vert ID

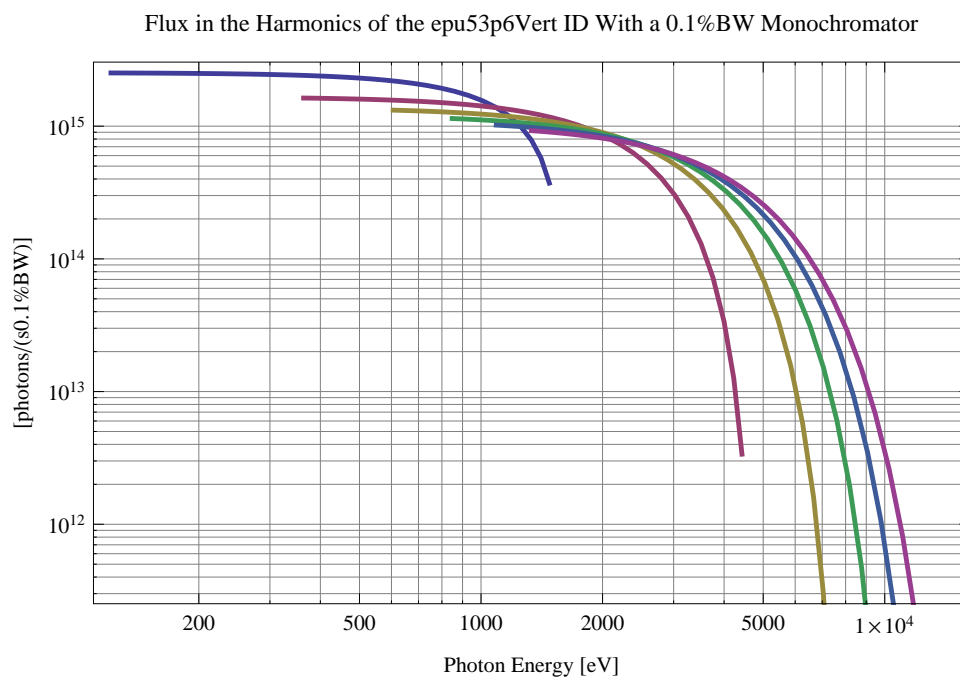


Figure 5.589: The flux of photons in the harmonics from the epu53p6Vert ID using a 0.1%BW monochromator

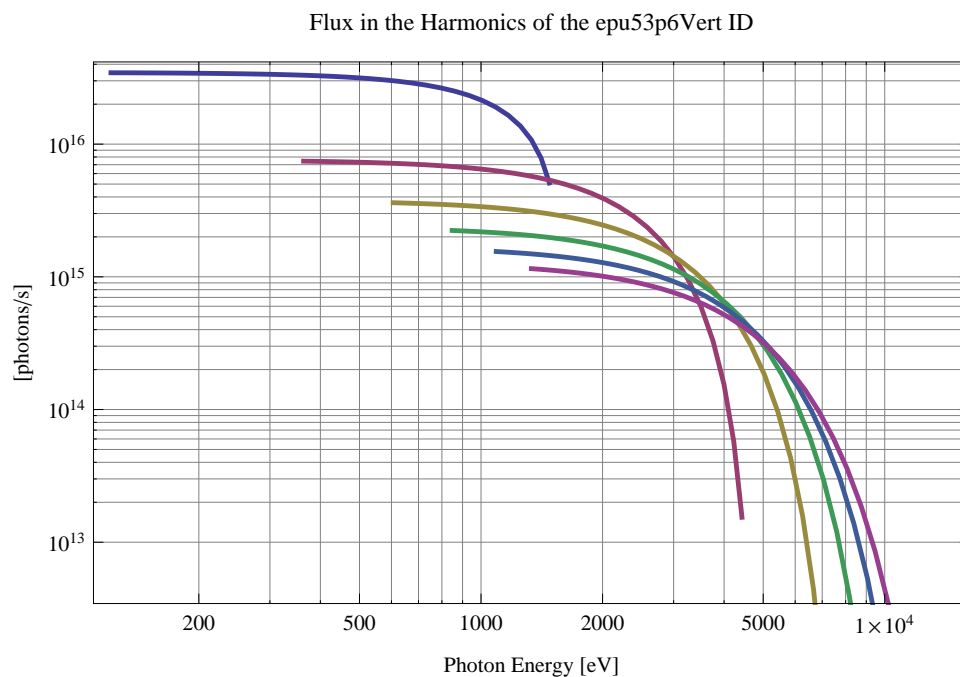


Figure 5.590: The flux of photons in the harmonics from the epu53p6Vert ID

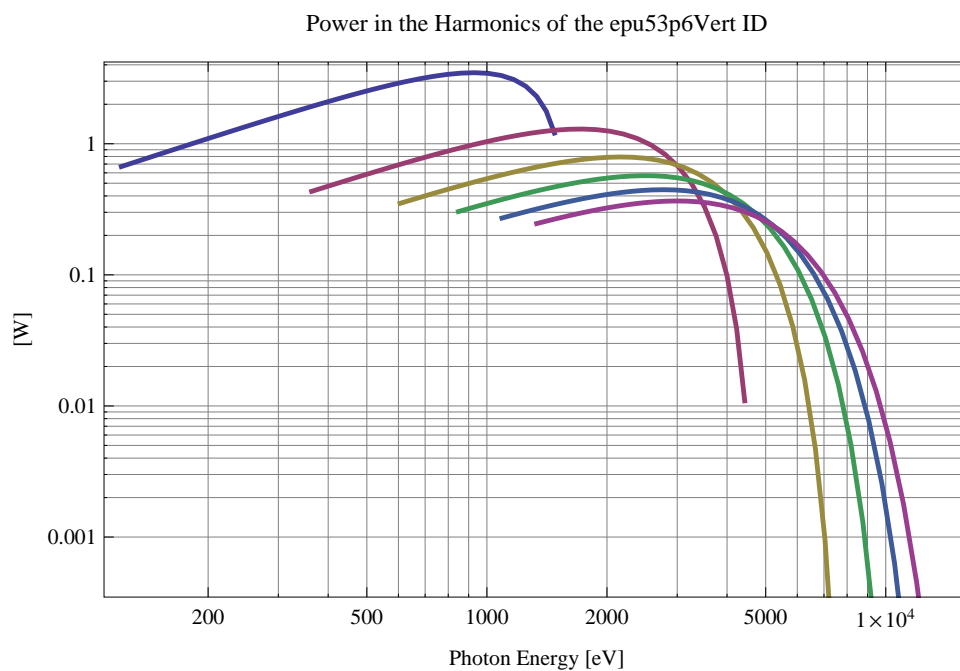


Figure 5.591: The power in the harmonics from the epu53p6Vert ID

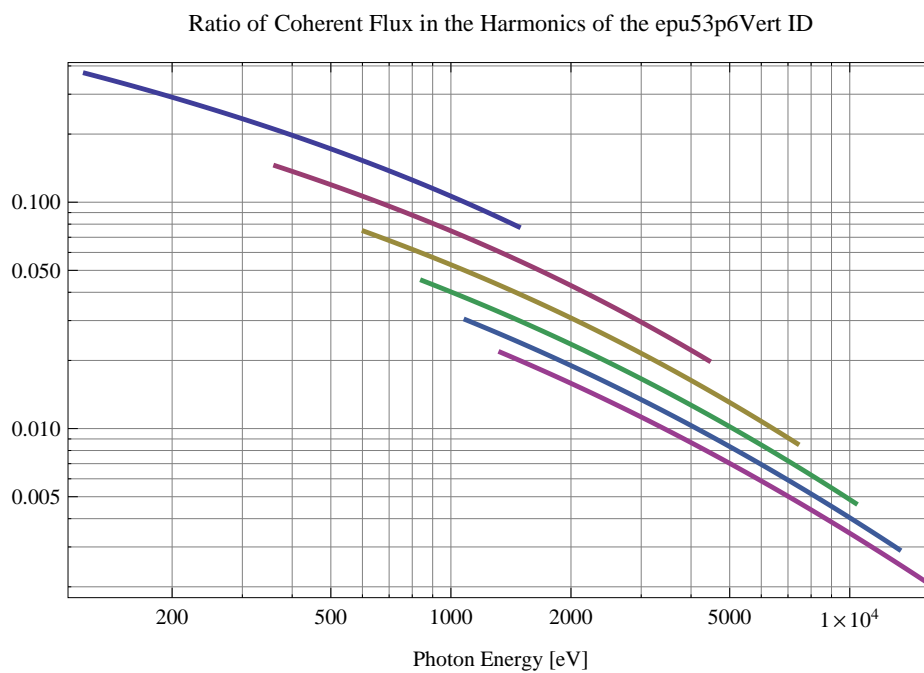


Figure 5.592: The ratio of coherent flux in the harmonics from the epu53p6Vert ID

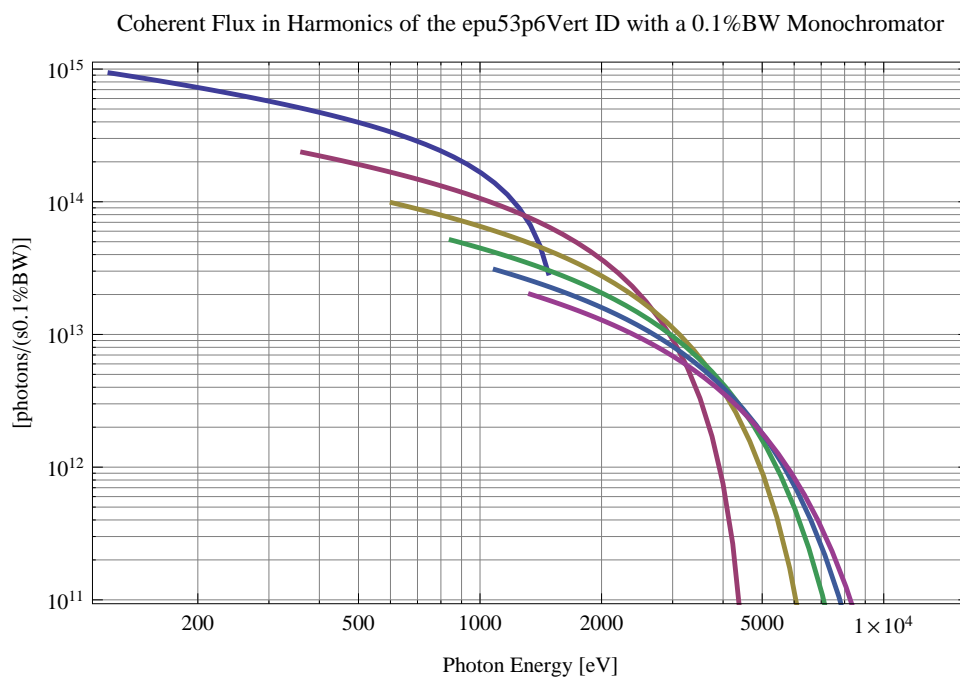


Figure 5.593: The coherent flux in the harmonics of the epu53p6Vert ID using a 0.1%BW Monochromator

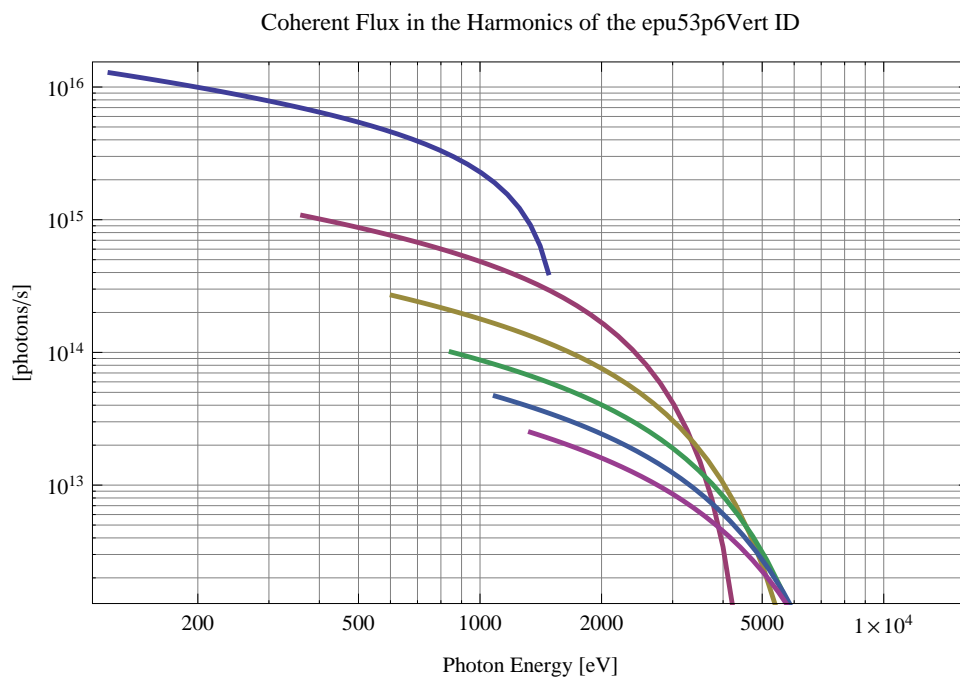


Figure 5.594: The coherent flux in the harmonics of the epu53p6Vert ID



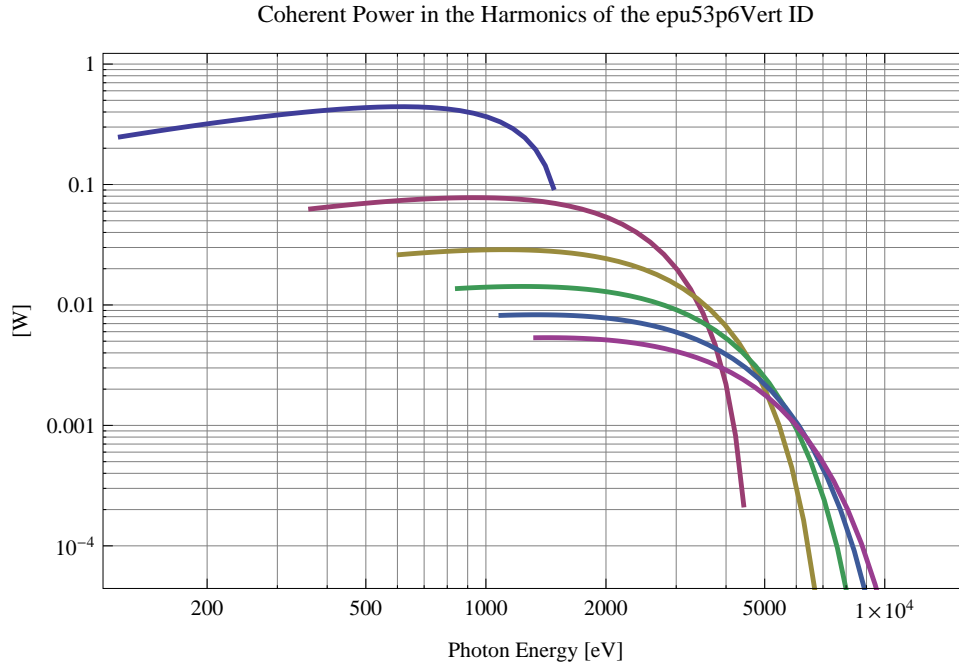


Figure 5.595: The power of coherent synchrotron radiation in the harmonics of the epu53p6Vert ID

Table 5.83: The brilliance at peak energy and the angular spectral flux density from the epu53p6Vert ID for different harmonics at maximum K-value (4.931)

Harmonic	Photon Energy [eV]	Brilliance [Ph./s/mrad <sup>2</sup> /mrad <sup>2</sup> /0.1%BW]	Angular Spectral Flux [Ph./s/mrad <sup>2</sup> /0.1%BW]
1	121.183	$3.57 \times 10^{19}$	$2.18 \times 10^{17}$
3	363.55	$8.11 \times 10^{19}$	$2.9 \times 10^{17}$
5	605.917	$9.39 \times 10^{19}$	$2.75 \times 10^{17}$
7	848.284	$9.64 \times 10^{19}$	$2.53 \times 10^{17}$
9	1090.65	$9.53 \times 10^{19}$	$2.32 \times 10^{17}$
11	1333.02	$9.29 \times 10^{19}$	$2.15 \times 10^{17}$

Table 5.84: The brilliance at peak energy and the angular spectral flux density from the epu53p6Vert ID for different harmonics at minimum K-value (0.4)

Harmonic	Photon Energy [eV]	Brilliance [Ph./s/mrad <sup>2</sup> /mrad <sup>2</sup> /0.1%BW]	Angular Spectral Flux [Ph./s/mrad <sup>2</sup> /0.1%BW]
1	1476.43	$1.65 \times 10^{20}$	$3.68 \times 10^{17}$
3	4429.29	$3.44 \times 10^{18}$	$6.45 \times 10^{15}$
5	7382.15	$4.04 \times 10^{16}$	$7.31 \times 10^{13}$
7	10335.	$4.31 \times 10^{14}$	$7.7 \times 10^{11}$
9	13287.9	$4.47 \times 10^{12}$	$7.93 \times 10^9$
11	16240.7	$4.59 \times 10^{10}$	$8.11 \times 10^7$

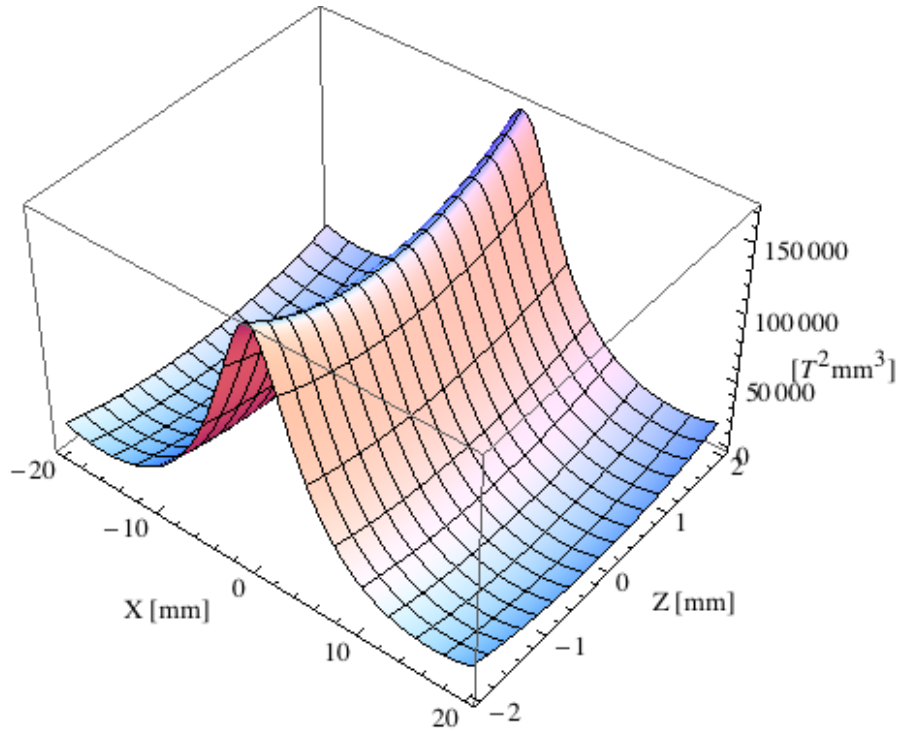


Figure 5.596: Focusing potential from the epu53p6Vert ID over the beam stay clear aperture.

### Influence from the epu53p6Vert ID on the optics of the stored beam

Figure 5.596 shows the focusing potential from the epu53p6Vert over the beam stay clear aperture of the ring aperture.

Figure 5.597 shows the kick map in the beam energy independent unit  $T^2 m^2$  of the kicks induced by the epu53p6Vert ID over the beam stay clear aperture.

Figure 5.598 shows the induced angular kick on the stored beam from the epu53p6Vert ID as a function of the vertical distance to the axis of the ID.

Figure 5.599 shows the induced angular kick on the stored beam from the epu53p6Vert ID as a function of the horizontal distance to the axis of the ID.

Figure 5.600 shows tune shift induced by the epu53p6Vert ID over the beam stay clear aperture. Note that the tune shift depends on the beam size at the ID.

Figure 5.601 shows the induced tune shift from the epu53p6Vert ID as a function of the vertical distance to the axis of the ID.

Figure 5.602 shows the induced tune shift from the epu53p6Vert ID as a function of the horizontal distance to the axis of the ID.

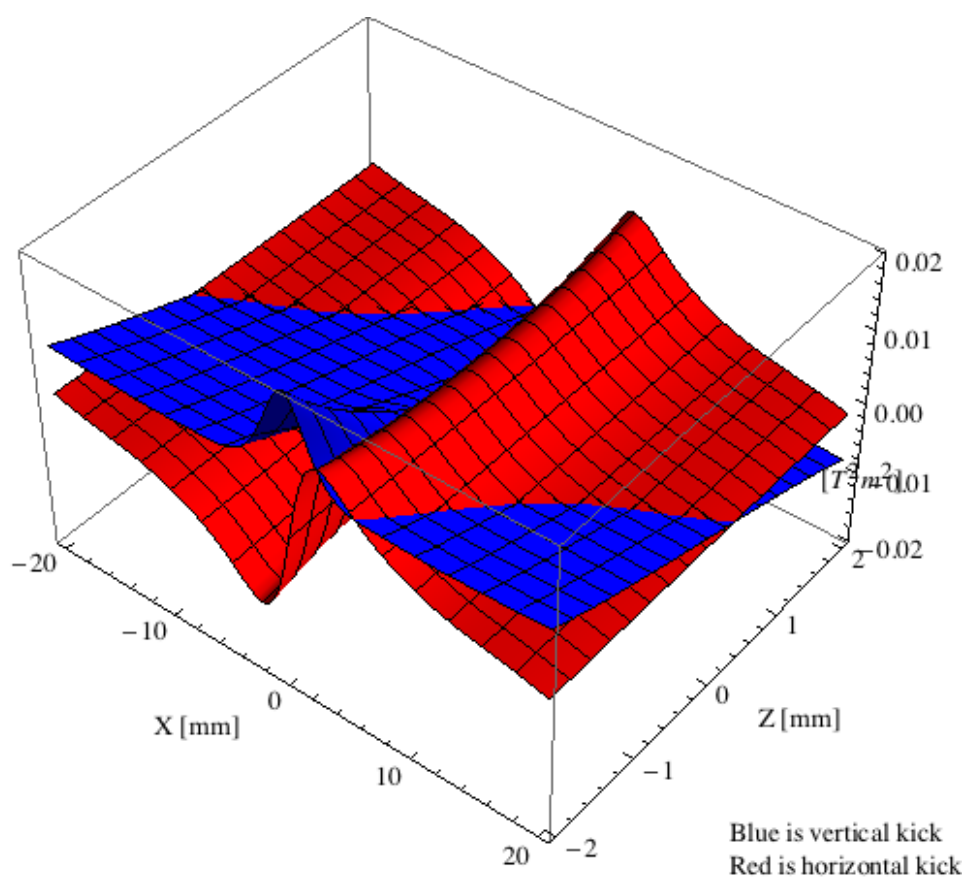


Figure 5.597: Kick map in the beam energy independent unit  $T^2m^2$  of the kicks induced by the epu53p6Vert ID over the beam stay clear aperture.

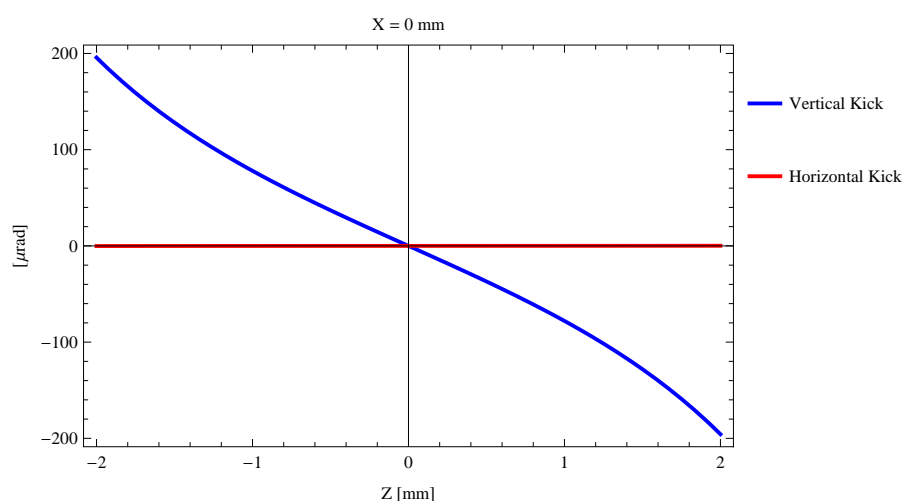


Figure 5.598: Induced angular kick on the stored beam from the epu53p6Vert ID as a function of the vertical distance to the ID axis.

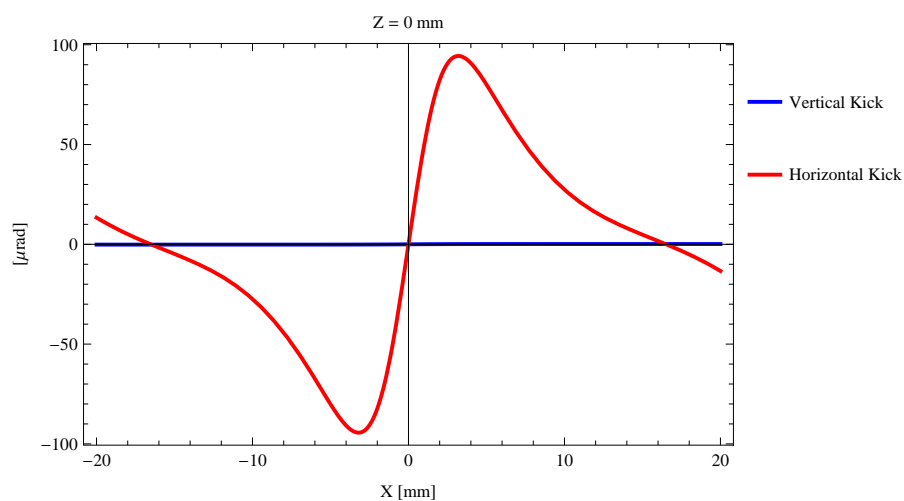


Figure 5.599: Induced angular kick on the stored beam from the epu53p6Vert ID as a function of the horizontal distance to the ID axis.

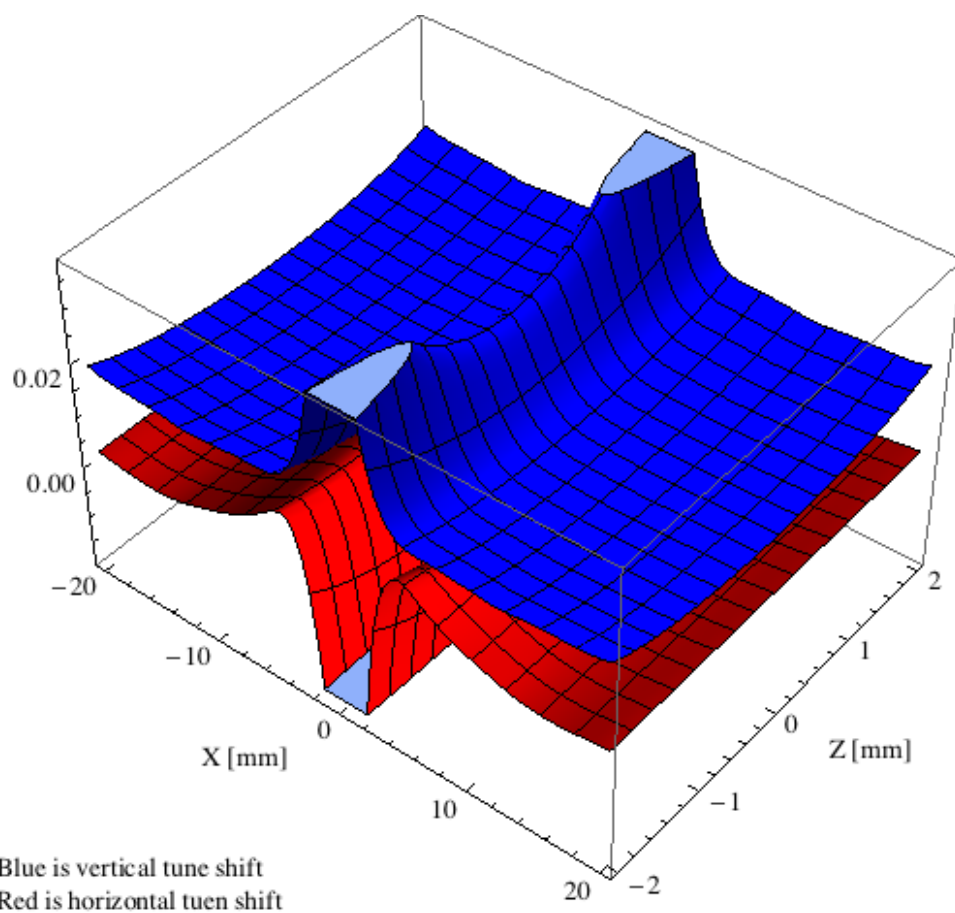


Figure 5.600: Tune shift induced by the epu53p6Vert ID over the beam stay clear aperture.

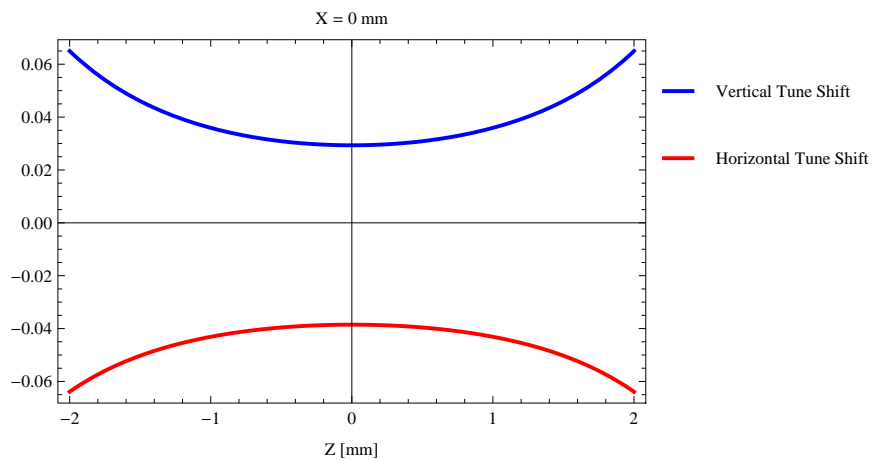


Figure 5.601: Induced tune shift from the epu53p6Vert ID as a function of the vertical distance to the axis of the ID.

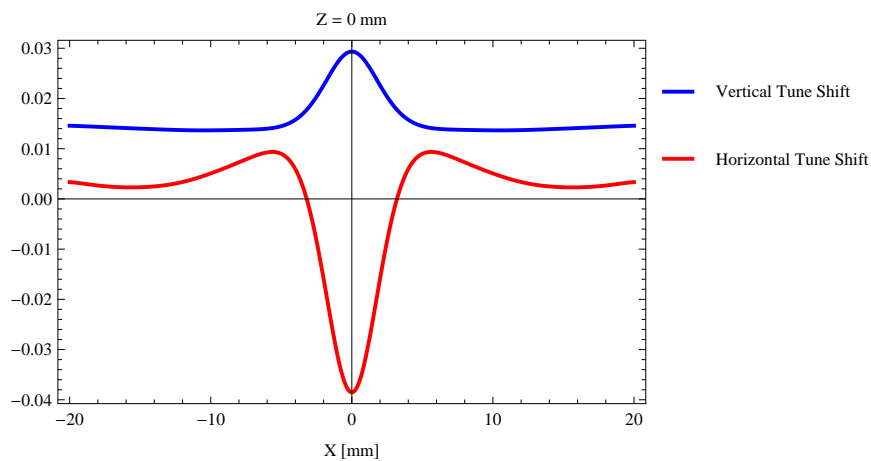


Figure 5.602: Induced tune shift from the epu53p6Vert ID on the stored beam from the ID as a function of the horizontal distance to the axis of the ID.

### 5.3.11. Summary of the magnet model calculations

In total 10 different IDs have been modelled.

The pmu18p5 is an in-vacuum undulator of hybrid type that will produces synchrotron radiation for the PX1, PX2 ,NANO-1 ,NANO-2 , SAXS/WAXS, and XDIF beamlines and there will be 6 IDs of this type.

The cpmu16 is an optional cryogenically cooled in-vacuum undulator of hybrid type for the NANO-1 and NANO-2 beamlines.

The pmu20 is an in-vacuum undulator of hybrid type that will produces synchrotron radiation for the XAFS and HIKE beamlines and there will be 2 IDs of this type.

The scw46 is superconducting wiggler that will produces synchrotron radiation for the MATERIAL and TOM beamlines and there will be 2 IDs of this type.

The wig80 is an optional wiggler of hybrid type for the MATERIAL and TOM beamlines.

The epuI1011 is an elliptically polarising undulator that will produces synchrotron radiation for the BL3-I1011 beamline and there will be 1 ID of this type.

The epu38 is an elliptically polarising undulator that will produces synchrotron radiation for the BL4-Gas and BL5-Spect beamlines and there will be 2 IDs of this type installed in the middle of a straight section.

The epu43p6 is an optional elliptically polarising undulator for the BL4-Gas and BL5-Spect beamlines.

The epu48 is an optional elliptically polarising undulator for the BL4-Gas and BL5-Spect beamlines.

The epu53p6 is is an optional elliptically polarising undulator for the BL4-Gas and BL5-Spect beamlines.

The served beamlines, lengths, magnetic gaps and period lengths of the modelled IDs are given in Table 5.85. The magnetic peak field and efficient field and the  $K_x$ -value of the modelled IDs are given in Table 5.86. The emitted synchrotron radiation power and on-axis power density of the modelled IDs are given in Table 5.87. The vertical and horizontal tune shifts of the modelled IDs are given in Table 5.88.

Table 5.85: The served beamlines, length, minimum magnetic gap and period lengths for the modelled IDs

Name	Beamline	Length [mm]	Gap [mm]	Period Length [mm]
pmu18p5	PX1,..., and XDIF	3783.25	4.2	18.5
cpmu16	NANO-1 and NANO-2	3800.	4.2	16
pmu20	XAFS and HIKE	3790.	4.2	20
scw46	MATERIAL and TOM	1969.48	12	46
wig80	MATERIAL and TOM	3990.7	7.8	80
epuI1011	BL3-I1011	2134.76	14	46.6
epu38	BL4-Gas and BL5-Spect	3930.98	9	38
epu43p6	BL4-Gas and BL5-Spect	3941.27	9	43.6
epu48	BL4-Gas and BL5-Spect	3905.5	9	48
epu53p6	BL4-Gas and BL5-Spect	3930.59	9	53.6

Table 5.86: The magnetic peak field and efficient field and the  $K_x$ -value of the modelled IDs

Name	Peak Field [T]	Efficient Field [T]	Efficient $K_x$ -value
pmu18p5	1.24131	1.11146	1.92049
cpmu16	1.2653	1.17275	1.75255
pmu20	1.3244	1.17294	2.19105
scw46	3.6952	3.63951	15.6368
wig80	2.38365	1.99185	14.8831
epl1011	0.707	0.712	3.09894
epl38	0.974	0.986	3.49951
epl43p6	1.064	1.082	4.40616
epl48	1.119	1.143	5.1243
epl53p6	1.173	1.204	6.02751

Table 5.87: The emitted synchrotron radiation power and on-axis power density of the modelled IDs

Name	SR Power [kW]	On-axis power density [kW/mrad <sup>2</sup> ]
pmu18p5	13.3062	97.1077
cpmu16	14.8798	119.221
pmu20	14.8454	95.8185
scw46	74.2747	67.2207
wig80	45.0781	51.2407
epl1011	3.08115	13.9582
epl38	10.8807	43.8925
epl43p6	13.137	42.1283
epl48	14.5269	40.0452
epl53p6	16.2224	37.9952

Table 5.88: The vertical and horizontal tune shifts of the modelled IDs

Name	Vertical Tune Shift	Horizontal Tune Shift
pmu18p5	$9.54426 \times 10^{-3}$	$-2.97452 \times 10^{-6}$
cpmu16	$1.06561 \times 10^{-2}$	$-1.75134 \times 10^{-6}$
pmu20	$1.06491 \times 10^{-2}$	$-2.76306 \times 10^{-6}$
scw46	$5.1373 \times 10^{-2}$	$-8.34116 \times 10^{-5}$
wig80	$3.29853 \times 10^{-2}$	$-2.06728 \times 10^{-4}$
epl1011	$1.65984 \times 10^{-3}$	$8.28077 \times 10^{-4}$
epl38	$6.40052 \times 10^{-3}$	$2.57193 \times 10^{-3}$
epl43p6	$7.56479 \times 10^{-3}$	$3.73107 \times 10^{-3}$
epl48	$8.27026 \times 10^{-3}$	$4.72219 \times 10^{-3}$
epl53p6	$9.23205 \times 10^{-3}$	$6.22184 \times 10^{-3}$

## 5.4. Influence from the insertion devices on the RF-system, the emittance, and the energy spread of the stored electron beam

The insertion devices in this report can be combined in 378 different ways, assuming that the IDs are either at minimum gap or not influencing the stored beam. For simplicity, only the horizontal polarisation mode of the elliptically polarising undulators has been included.

The influence on the RF-system parameters, the momentum acceptance, the emittance, and the energy spread of the stored beam for 378 different combinations, assuming that the IDs are either at minimum gap or not influencing the stored beam, are given in Table 5.89,  $P_g$  is the generator power,  $P_b$  is the beam loading,  $P_r$  is the reflected power, and the last three columns are the momentum acceptance, the change of emittance and the change of energy spread with a varying number of IDs in operation.

Table 5.89: The influence on the RF-system and the emittance and energy spread of the stored beam with a varying number of IDs in operation, assuming that the IDs are either at minimum gap or not influencing the stored beam

pmu18p5	pmu20	scw46	epu11011	epu38	$P_g$	$P_b$	$P_r$	$\delta_{rf}$	$\frac{\epsilon_{x,ID}}{\epsilon_{x,0}}$	$\frac{\sigma_{eID}}{\sigma_{e0}}$
#	#	#	#	#	kW	kW	kW	%	%	%
0	0	0	0	0	299	180	12	6.2	100.	100.
0	0	0	0	1	308	191	10	6.1	96.9	99.7
0	0	0	0	2	317	202	8	6.01	93.7	99.3
0	0	0	1	0	301	183	11	6.17	99.1	99.5
0	0	0	1	1	311	194	9	6.08	96.	99.2
0	0	0	1	2	320	205	8	5.99	92.8	98.9
0	0	1	0	0	364	254	3	5.56	84.8	142.3
0	0	1	0	1	374	265	2	5.47	81.6	142.1
0	0	1	0	2	384	276	1	5.37	78.5	141.8
0	0	1	1	0	367	257	2	5.54	83.9	142.
0	0	1	1	1	377	268	2	5.44	80.7	141.7
0	0	1	1	2	387	279	1	5.35	77.6	141.5
0	0	2	0	0	436	329	0	4.91	69.5	174.6
0	0	2	0	1	447	339	0	4.81	66.4	174.4
0	0	2	0	2	458	350	0	4.72	63.3	174.3
0	0	2	1	0	439	332	0	4.88	68.6	174.4
0	0	2	1	1	450	343	0	4.79	65.5	174.2
0	0	2	1	2	461	353	1	4.69	62.3	174.
0	1	0	0	0	311	195	9	6.07	95.8	100.7
0	1	0	0	1	321	206	8	5.98	92.6	100.4
0	1	0	0	2	330	217	6	5.89	89.5	100.
0	1	0	1	0	314	198	9	6.05	94.9	100.2
0	1	0	1	1	323	209	7	5.95	91.7	99.9
0	1	0	1	2	333	220	6	5.86	88.6	99.6
0	1	1	0	0	378	269	2	5.43	80.5	142.8
0	1	1	0	1	388	280	1	5.34	77.4	142.5
0	1	1	0	2	399	291	1	5.24	74.3	142.3
0	1	1	1	0	381	272	1	5.41	79.6	142.4
0	1	1	1	1	391	283	1	5.31	76.5	142.2
0	1	1	1	2	402	294	0	5.22	73.3	142.
0	1	2	0	0	451	343	0	4.78	65.3	175.



pmu18p5	pmu20	scw46	epuI1011	epu38	$P_g$	$P_b$	$P_r$	$\delta_{rf}$	$\frac{\epsilon_{x,ID}}{\epsilon_{x,0}}$	$\frac{\sigma_{eID}}{\sigma_{e0}}$
#	#	#	#	#	kW	kW	kW	%	%	%
0	1	2	0	1	462	354	1	4.68	62.2	174.8
0	1	2	0	2	473	365	1	4.58	59.	174.6
0	1	2	1	0	454	346	0	4.75	64.4	174.7
0	1	2	1	1	465	357	1	4.65	61.2	174.6
0	1	2	1	2	477	368	1	4.55	58.1	174.4
0	2	0	0	0	324	210	7	5.95	91.5	101.4
0	2	0	0	1	334	221	6	5.85	88.4	101.
0	2	0	0	2	343	231	5	5.76	85.2	100.7
0	2	0	1	0	327	213	7	5.92	90.6	100.9
0	2	0	1	1	336	224	6	5.83	87.5	100.6
0	2	0	1	2	346	235	4	5.73	84.3	100.2
0	2	1	0	0	392	284	1	5.3	76.3	143.3
0	2	1	0	1	402	295	0	5.21	73.2	143.
0	2	1	0	2	413	306	0	5.11	70.	142.8
0	2	1	1	0	395	287	1	5.28	75.4	142.9
0	2	1	1	1	405	298	0	5.18	72.2	142.7
0	2	1	1	2	416	309	0	5.09	69.1	142.5
0	2	2	0	0	466	358	1	4.64	61.1	175.4
0	2	2	0	1	478	369	1	4.54	57.9	175.2
0	2	2	0	2	489	380	2	4.44	54.8	175.
0	2	2	1	0	469	361	1	4.62	60.1	175.1
0	2	2	1	1	481	372	2	4.52	57.	175.
0	2	2	1	2	492	383	2	4.42	53.9	174.8
1	0	0	0	0	310	193	10	6.08	96.2	100.3
1	0	0	0	1	319	204	8	5.99	93.	100.
1	0	0	0	2	329	215	7	5.9	89.9	99.6
1	0	0	1	0	313	196	9	6.06	95.3	99.8
1	0	0	1	1	322	207	8	5.97	92.1	99.5
1	0	0	1	2	332	218	6	5.87	89.	99.2
1	0	1	0	0	376	268	2	5.45	80.9	142.5
1	0	1	0	1	387	278	1	5.35	77.8	142.3
1	0	1	0	2	397	289	1	5.26	74.7	142.
1	0	1	1	0	379	271	2	5.42	80.	142.2
1	0	1	1	1	390	282	1	5.33	76.9	141.9
1	0	1	1	2	400	292	0	5.23	73.8	141.7
1	0	2	0	0	449	342	0	4.79	65.7	174.8
1	0	2	0	1	460	353	1	4.69	62.6	174.6
1	0	2	0	2	472	364	1	4.59	59.4	174.4
1	0	2	1	0	452	345	0	4.76	64.8	174.5
1	0	2	1	1	464	356	1	4.67	61.7	174.3
1	0	2	1	2	475	367	1	4.57	58.5	174.1
1	1	0	0	0	323	208	7	5.96	91.9	101.
1	1	0	0	1	332	219	6	5.87	88.8	100.6
1	1	0	0	2	342	230	5	5.77	85.7	100.3
1	1	0	1	0	325	211	7	5.93	91.	100.5
1	1	0	1	1	335	222	6	5.84	87.9	100.2
1	1	0	1	2	345	233	5	5.75	84.8	99.8
1	1	1	0	0	390	282	1	5.32	76.7	143.
1	1	1	0	1	401	293	0	5.22	73.6	142.7

pmu18p5	pmu20	scw46	epuI1011	epu38	$P_g$	$P_b$	$P_r$	$\delta_{rf}$	$\frac{\epsilon_{x,ID}}{\epsilon_{x,0}}$	$\frac{\sigma_{eID}}{\sigma_{e0}}$
#	#	#	#	#	kW	kW	kW	%	%	%
1	1	1	0	2	412	304	0	5.13	70.4	142.5
1	1	1	1	0	393	286	1	5.29	75.8	142.6
1	1	1	1	1	404	296	0	5.2	72.7	142.4
1	1	1	1	2	415	307	0	5.1	69.5	142.2
1	1	2	0	0	465	357	1	4.66	61.5	175.2
1	1	2	0	1	476	368	1	4.56	58.3	175.
1	1	2	0	2	488	378	2	4.46	55.2	174.8
1	1	2	1	0	468	360	1	4.63	60.6	174.9
1	1	2	1	1	479	371	1	4.53	57.4	174.7
1	1	2	1	2	491	382	2	4.43	54.3	174.5
1	2	0	0	0	336	223	6	5.83	87.7	101.6
1	2	0	0	1	345	234	4	5.74	84.6	101.3
1	2	0	0	2	355	245	3	5.65	81.4	101.
1	2	0	1	0	339	226	5	5.81	86.8	101.2
1	2	0	1	1	348	237	4	5.71	83.7	100.9
1	2	0	1	2	358	248	3	5.62	80.5	100.5
1	2	1	0	0	405	297	0	5.19	72.5	143.5
1	2	1	0	1	415	308	0	5.09	69.3	143.2
1	2	1	0	2	426	319	0	5.	66.2	143.
1	2	1	1	0	408	300	0	5.16	71.6	143.1
1	2	1	1	1	418	311	0	5.06	68.4	142.9
1	2	1	1	2	429	322	0	4.97	65.3	142.7
1	2	2	0	0	480	372	1	4.52	57.2	175.6
1	2	2	0	1	492	382	2	4.42	54.1	175.4
1	2	2	0	2	503	393	3	4.32	51.	175.2
1	2	2	1	0	483	375	2	4.49	56.3	175.3
1	2	2	1	1	495	386	2	4.39	53.2	175.1
1	2	2	1	2	507	396	3	4.29	50.1	174.9
2	0	0	0	0	321	207	8	5.97	92.4	100.6
2	0	0	0	1	331	217	6	5.88	89.2	100.2
2	0	0	0	2	341	228	5	5.79	86.1	99.9
2	0	0	1	0	324	210	7	5.95	91.5	100.1
2	0	0	1	1	334	221	6	5.85	88.3	99.8
2	0	0	1	2	343	231	5	5.76	85.2	99.4
2	0	1	0	0	389	281	1	5.33	77.1	142.7
2	0	1	0	1	399	292	1	5.24	74.	142.5
2	0	1	0	2	410	303	0	5.14	70.9	142.2
2	0	1	1	0	392	284	1	5.3	76.2	142.4
2	0	1	1	1	402	295	0	5.21	73.1	142.1
2	0	1	1	2	413	306	0	5.11	69.9	141.9
2	0	2	0	0	463	355	1	4.67	61.9	175.
2	0	2	0	1	474	366	1	4.57	58.8	174.8
2	0	2	0	2	486	377	2	4.47	55.6	174.6
2	0	2	1	0	466	358	1	4.64	61.	174.7
2	0	2	1	1	478	369	1	4.54	57.9	174.5
2	0	2	1	2	489	380	2	4.44	54.7	174.3
2	1	0	0	0	334	221	6	5.85	88.1	101.3
2	1	0	0	1	344	232	5	5.75	85.	100.9
2	1	0	0	2	354	243	4	5.66	81.9	100.6

pmu18p5	pmu20	scw46	epu11011	epu38	$P_g$	$P_b$	$P_r$	$\delta_{rf}$	$\frac{\epsilon_{x,ID}}{\epsilon_{x,0}}$	$\frac{\sigma_{eID}}{\sigma_{e0}}$
#	#	#	#	#	kW	kW	kW	%	%	%
2	1	0	1	0	337	225	5	5.82	87.2	100.8
2	1	0	1	1	347	235	4	5.73	84.1	100.5
2	1	0	1	2	357	246	3	5.63	80.9	100.1
2	1	1	0	0	403	296	0	5.2	72.9	143.2
2	1	1	0	1	414	307	0	5.11	69.8	142.9
2	1	1	0	2	425	317	0	5.01	66.6	142.7
2	1	1	1	0	406	299	0	5.17	72.	142.8
2	1	1	1	1	417	310	0	5.08	68.8	142.6
2	1	1	1	2	428	321	0	4.98	65.7	142.4
2	1	2	0	0	479	370	1	4.54	57.7	175.3
2	1	2	0	1	490	381	2	4.44	54.5	175.2
2	1	2	0	2	502	392	3	4.34	51.4	175.
2	1	2	1	0	482	373	2	4.51	56.8	175.1
2	1	2	1	1	493	384	2	4.41	53.6	174.9
2	1	2	1	2	505	395	3	4.31	50.5	174.7
2	2	0	0	0	348	236	4	5.72	83.9	101.9
2	2	0	0	1	358	247	3	5.62	80.8	101.6
2	2	0	0	2	368	258	2	5.53	77.6	101.3
2	2	0	1	0	350	239	4	5.69	83.	101.5
2	2	0	1	1	360	250	3	5.6	79.8	101.1
2	2	0	1	2	370	261	2	5.5	76.7	100.8
2	2	1	0	0	418	311	0	5.07	68.7	143.7
2	2	1	0	1	429	321	0	4.97	65.5	143.4
2	2	1	0	2	440	332	0	4.88	62.4	143.2
2	2	1	1	0	421	314	0	5.04	67.7	143.3
2	2	1	1	1	432	325	0	4.95	64.6	143.1
2	2	1	1	2	443	335	0	4.85	61.5	142.9
2	2	2	0	0	494	385	2	4.4	53.4	175.7
2	2	2	0	1	506	396	3	4.3	50.3	175.6
2	2	2	0	2	518	407	4	4.2	47.1	175.4
2	2	2	1	0	498	388	3	4.37	52.5	175.5
2	2	2	1	1	509	399	3	4.27	49.4	175.3
2	2	2	1	2	521	410	5	4.17	46.2	175.1
3	0	0	0	0	333	220	6	5.86	88.6	100.9
3	0	0	0	1	343	231	5	5.77	85.4	100.5
3	0	0	0	2	353	242	4	5.67	82.3	100.2
3	0	0	1	0	336	223	6	5.83	87.6	100.4
3	0	0	1	1	345	234	4	5.74	84.5	100.1
3	0	0	1	2	355	245	3	5.65	81.4	99.7
3	0	1	0	0	402	294	0	5.22	73.3	142.9
3	0	1	0	1	412	305	0	5.12	70.2	142.7
3	0	1	0	2	423	316	0	5.02	67.	142.4
3	0	1	1	0	405	297	0	5.19	72.4	142.6
3	0	1	1	1	415	308	0	5.09	69.3	142.3
3	0	1	1	2	426	319	0	5.	66.1	142.1
3	0	2	0	0	477	368	1	4.55	58.1	175.1
3	0	2	0	1	488	379	2	4.45	54.9	174.9
3	0	2	0	2	500	390	3	4.35	51.8	174.7
3	0	2	1	0	480	372	1	4.52	57.2	174.9

pmu18p5	pmu20	scw46	epu11011	epu38	$P_g$	$P_b$	$P_r$	$\delta_{rf}$	$\frac{\epsilon_{x,ID}}{\epsilon_{x,0}}$	$\frac{\sigma_{eID}}{\sigma_{e0}}$
#	#	#	#	#	kW	kW	kW	%	%	%
3	0	2	1	1	492	382	2	4.42	54.	174.7
3	0	2	1	2	503	393	3	4.32	50.9	174.5
3	1	0	0	0	346	235	4	5.73	84.3	101.5
3	1	0	0	1	356	246	3	5.64	81.2	101.2
3	1	0	0	2	366	257	2	5.54	78.	100.9
3	1	0	1	0	349	238	4	5.7	83.4	101.1
3	1	0	1	1	359	249	3	5.61	80.3	100.7
3	1	0	1	2	369	260	2	5.52	77.1	100.4
3	1	1	0	0	416	309	0	5.08	69.1	143.4
3	1	1	0	1	427	320	0	4.99	65.9	143.2
3	1	1	0	2	438	331	0	4.89	62.8	142.9
3	1	1	1	0	419	312	0	5.06	68.2	143.
3	1	1	1	1	430	323	0	4.96	65.	142.8
3	1	1	1	2	441	334	0	4.86	61.9	142.6
3	1	2	0	0	493	383	2	4.41	53.8	175.5
3	1	2	0	1	504	394	3	4.31	50.7	175.3
3	1	2	0	2	516	405	4	4.21	47.6	175.1
3	1	2	1	0	496	386	2	4.39	52.9	175.2
3	1	2	1	1	508	397	3	4.29	49.8	175.1
3	1	2	1	2	520	408	4	4.18	46.7	174.9
3	2	0	0	0	360	250	3	5.6	80.1	102.2
3	2	0	0	1	370	260	2	5.51	76.9	101.9
3	2	0	0	2	380	271	1	5.41	73.8	101.6
3	2	0	1	0	363	253	3	5.58	79.2	101.7
3	2	0	1	1	373	264	2	5.48	76.	101.4
3	2	0	1	2	383	274	1	5.39	72.9	101.1
3	2	1	0	0	431	324	0	4.95	64.8	143.9
3	2	1	0	1	442	335	0	4.86	61.7	143.6
3	2	1	0	2	453	346	0	4.76	58.6	143.4
3	2	1	1	0	434	327	0	4.92	63.9	143.5
3	2	1	1	1	445	338	0	4.83	60.8	143.3
3	2	1	1	2	456	349	0	4.73	57.7	143.1
3	2	2	0	0	509	398	3	4.28	49.6	175.9
3	2	2	0	1	521	409	4	4.18	46.5	175.7
3	2	2	0	2	533	420	6	4.07	43.3	175.5
3	2	2	1	0	512	401	4	4.25	48.7	175.6
3	2	2	1	1	524	412	5	4.15	45.6	175.4
3	2	2	1	2	536	423	6	4.04	42.4	175.3
4	0	0	0	0	345	233	5	5.74	84.7	101.1
4	0	0	0	1	355	244	3	5.65	81.6	100.8
4	0	0	0	2	365	255	3	5.56	78.5	100.5
4	0	0	1	0	348	236	4	5.72	83.8	100.7
4	0	0	1	1	358	247	3	5.62	80.7	100.3
4	0	0	1	2	368	258	2	5.53	77.5	100.
4	0	1	0	0	415	307	0	5.1	69.5	143.1
4	0	1	0	1	426	318	0	5.	66.4	142.9
4	0	1	0	2	436	329	0	4.9	63.2	142.6
4	0	1	1	0	418	311	0	5.07	68.6	142.8
4	0	1	1	1	429	321	0	4.97	65.5	142.5

pmu18p5	pmu20	scw46	epu11011	epu38	$P_g$	$P_b$	$P_r$	$\delta_{rf}$	$\frac{\epsilon_{x,ID}}{\epsilon_{x,0}}$	$\frac{\sigma_{eID}}{\sigma_{e0}}$
#	#	#	#	#	kW	kW	kW	%	%	%
4	0	1	1	2	440	332	0	4.88	62.3	142.3
4	0	2	0	0	491	382	2	4.43	54.3	175.3
4	0	2	0	1	503	393	3	4.33	51.1	175.1
4	0	2	0	2	515	404	4	4.23	48.	174.9
4	0	2	1	0	494	385	2	4.4	53.4	175.
4	0	2	1	1	506	396	3	4.3	50.2	174.8
4	0	2	1	2	518	407	4	4.2	47.1	174.6
4	1	0	0	0	358	248	3	5.62	80.5	101.8
4	1	0	0	1	368	259	2	5.52	77.4	101.5
4	1	0	0	2	379	270	2	5.43	74.2	101.2
4	1	0	1	0	361	251	3	5.59	79.6	101.4
4	1	0	1	1	371	262	2	5.5	76.4	101.
4	1	0	1	2	381	273	1	5.4	73.3	100.7
4	1	1	0	0	429	322	0	4.97	65.3	143.6
4	1	1	0	1	440	333	0	4.87	62.1	143.4
4	1	1	0	2	452	344	0	4.77	59.	143.1
4	1	1	1	0	433	325	0	4.94	64.4	143.2
4	1	1	1	1	444	336	0	4.84	61.2	143.
4	1	1	1	2	455	347	0	4.74	58.1	142.8
4	1	2	0	0	507	397	3	4.29	50.	175.7
4	1	2	0	1	519	408	4	4.19	46.9	175.5
4	1	2	0	2	531	418	5	4.09	43.8	175.3
4	1	2	1	0	510	400	4	4.26	49.1	175.4
4	1	2	1	1	522	411	5	4.16	46.	175.2
4	1	2	1	2	534	421	6	4.06	42.8	175.
4	2	0	0	0	372	263	2	5.49	76.3	102.5
4	2	0	0	1	382	274	1	5.39	73.1	102.2
4	2	0	0	2	393	285	1	5.3	70.	101.9
4	2	0	1	0	375	266	2	5.46	75.3	102.
4	2	0	1	1	385	277	1	5.37	72.2	101.7
4	2	0	1	2	396	288	1	5.27	69.1	101.4
4	2	1	0	0	444	337	0	4.83	61.	144.1
4	2	1	0	1	456	348	0	4.74	57.9	143.8
4	2	1	0	2	467	359	1	4.64	54.7	143.6
4	2	1	1	0	448	340	0	4.81	60.1	143.7
4	2	1	1	1	459	351	1	4.71	57.	143.5
4	2	1	1	2	470	362	1	4.61	53.8	143.3
4	2	2	0	0	523	411	5	4.15	45.8	176.1
4	2	2	0	1	535	422	6	4.05	42.7	175.9
4	2	2	0	2	548	433	7	3.95	39.5	175.7
4	2	2	1	0	527	415	5	4.12	44.9	175.8
4	2	2	1	1	539	425	6	4.02	41.7	175.6
4	2	2	1	2	551	436	8	3.92	38.6	175.4
5	0	0	0	0	357	247	3	5.63	80.9	101.4
5	0	0	0	1	367	257	2	5.54	77.8	101.1
5	0	0	0	2	377	268	2	5.44	74.6	100.8
5	0	0	1	0	360	250	3	5.6	80.	101.
5	0	0	1	1	370	260	2	5.51	76.9	100.6
5	0	0	1	2	380	271	1	5.41	73.7	100.3

pmu18p5	pmu20	scw46	epu11011	epu38	$P_g$	$P_b$	$P_r$	$\delta_{rf}$	$\frac{\epsilon_{x,ID}}{\epsilon_{x,0}}$	$\frac{\sigma_{eID}}{\sigma_{e0}}$
#	#	#	#	#	kW	kW	kW	%	%	%
5	0	1	0	0	428	321	0	4.98	65.7	143.3
5	0	1	0	1	439	332	0	4.88	62.5	143.1
5	0	1	0	2	450	343	0	4.79	59.4	142.8
5	0	1	1	0	431	324	0	4.95	64.8	143.
5	0	1	1	1	442	335	0	4.86	61.6	142.7
5	0	1	1	2	453	346	0	4.76	58.5	142.5
5	0	2	0	0	505	395	3	4.31	50.4	175.5
5	0	2	0	1	517	406	4	4.2	47.3	175.3
5	0	2	0	2	529	417	5	4.1	44.2	175.1
5	0	2	1	0	509	398	3	4.28	49.5	175.2
5	0	2	1	1	521	409	4	4.18	46.4	175.
5	0	2	1	2	533	420	6	4.07	43.3	174.8
5	1	0	0	0	371	261	2	5.5	76.7	102.1
5	1	0	0	1	381	272	1	5.41	73.5	101.8
5	1	0	0	2	391	283	1	5.31	70.4	101.5
5	1	0	1	0	373	264	2	5.47	75.8	101.6
5	1	0	1	1	384	275	1	5.38	72.6	101.3
5	1	0	1	2	394	286	1	5.29	69.5	101.
5	1	1	0	0	443	336	0	4.85	61.4	143.8
5	1	1	0	1	454	347	0	4.75	58.3	143.6
5	1	1	0	2	465	357	1	4.65	55.2	143.3
5	1	1	1	0	446	339	0	4.82	60.5	143.4
5	1	1	1	1	457	350	0	4.72	57.4	143.2
5	1	1	1	2	469	360	1	4.62	54.3	143.
5	1	2	0	0	522	410	5	4.17	46.2	175.8
5	1	2	0	1	534	421	6	4.07	43.1	175.7
5	1	2	0	2	546	432	7	3.96	39.9	175.5
5	1	2	1	0	525	413	5	4.14	45.3	175.6
5	1	2	1	1	537	424	6	4.04	42.2	175.4
5	1	2	1	2	549	435	7	3.93	39.	175.2
5	2	0	0	0	385	276	1	5.37	72.4	102.8
5	2	0	0	1	395	287	1	5.28	69.3	102.5
5	2	0	0	2	405	298	0	5.18	66.2	102.1
5	2	0	1	0	387	279	1	5.35	71.5	102.3
5	2	0	1	1	398	290	1	5.25	68.4	102.
5	2	0	1	2	408	301	0	5.15	65.3	101.7
5	2	1	0	0	458	350	0	4.71	57.2	144.3
5	2	1	0	1	469	361	1	4.61	54.1	144.
5	2	1	0	2	481	372	2	4.52	50.9	143.8
5	2	1	1	0	461	354	1	4.69	56.3	143.9
5	2	1	1	1	473	364	1	4.59	53.2	143.7
5	2	1	1	2	484	375	2	4.49	50.	143.5
5	2	2	0	0	538	425	6	4.03	42.	176.2
5	2	2	0	1	550	436	8	3.92	38.8	176.
5	2	2	0	2	563	447	9	3.82	35.7	175.9
5	2	2	1	0	542	428	7	4.	41.1	176.
5	2	2	1	1	554	439	8	3.9	37.9	175.8
5	2	2	1	2	566	450	10	3.79	34.8	175.6
6	0	0	0	0	369	260	2	5.52	77.1	101.7

pmu18p5	pmu20	scw46	epu11011	epu38	$P_g$	$P_b$	$P_r$	$\delta_{rf}$	$\frac{\epsilon_{x,ID}}{\epsilon_{x,0}}$	$\frac{\sigma_{eID}}{\sigma_{e0}}$
#	#	#	#	#	kW	kW	kW	%	%	%
6	0	0	0	1	379	271	2	5.42	74.	101.4
6	0	0	0	2	390	282	1	5.33	70.8	101.1
6	0	0	1	0	372	263	2	5.49	76.2	101.2
6	0	0	1	1	382	274	1	5.39	73.1	100.9
6	0	0	1	2	393	285	1	5.3	69.9	100.6
6	0	1	0	0	441	334	0	4.86	61.9	143.5
6	0	1	0	1	452	345	0	4.76	58.7	143.3
6	0	1	0	2	464	356	1	4.66	55.6	143.
6	0	1	1	0	444	337	0	4.83	61.	143.2
6	0	1	1	1	456	348	0	4.74	57.8	142.9
6	0	1	1	2	467	359	1	4.64	54.7	142.7
6	0	2	0	0	520	408	4	4.18	46.6	175.6
6	0	2	0	1	532	419	6	4.08	43.5	175.4
6	0	2	0	2	544	430	7	3.98	40.4	175.2
6	0	2	1	0	523	411	5	4.15	45.7	175.3
6	0	2	1	1	535	422	6	4.05	42.6	175.2
6	0	2	1	2	548	433	7	3.95	39.4	175.
6	1	0	0	0	383	275	1	5.39	72.9	102.4
6	1	0	0	1	393	286	1	5.29	69.7	102.1
6	1	0	0	2	404	296	0	5.2	66.6	101.7
6	1	0	1	0	386	278	1	5.36	72.	101.9
6	1	0	1	1	396	289	1	5.26	68.8	101.6
6	1	0	1	2	407	300	0	5.17	65.7	101.3
6	1	1	0	0	457	349	0	4.73	57.6	144.
6	1	1	0	1	468	360	1	4.63	54.5	143.8
6	1	1	0	2	479	371	1	4.53	51.4	143.5
6	1	1	1	0	460	352	1	4.7	56.7	143.7
6	1	1	1	1	471	363	1	4.6	53.6	143.4
6	1	1	1	2	483	374	2	4.5	50.4	143.2
6	1	2	0	0	536	423	6	4.04	42.4	176.
6	1	2	0	1	549	434	7	3.94	39.3	175.8
6	1	2	0	2	561	445	9	3.84	36.1	175.6
6	1	2	1	0	540	426	6	4.01	41.5	175.7
6	1	2	1	1	552	437	8	3.91	38.3	175.5
6	1	2	1	2	565	448	9	3.81	35.2	175.4
6	2	0	0	0	397	290	1	5.26	68.6	103.1
6	2	0	0	1	408	300	0	5.16	65.5	102.7
6	2	0	0	2	418	311	0	5.06	62.3	102.4
6	2	0	1	0	400	293	0	5.23	67.7	102.6
6	2	0	1	1	411	303	0	5.13	64.6	102.3
6	2	0	1	2	422	314	0	5.04	61.4	102.
6	2	1	0	0	472	364	1	4.59	53.4	144.5
6	2	1	0	1	483	375	2	4.49	50.3	144.2
6	2	1	0	2	495	386	2	4.39	47.1	144.
6	2	1	1	0	475	367	1	4.56	52.5	144.1
6	2	1	1	1	487	378	2	4.47	49.3	143.9
6	2	1	1	2	498	389	3	4.37	46.2	143.7
6	2	2	0	0	553	438	8	3.9	38.2	176.4
6	2	2	0	1	566	449	9	3.8	35.	176.2

pmu18p5	pmu20	scw46	epu1011	epu38	$P_g$	$P_b$	$P_r$	$\delta_{rf}$	$\frac{\epsilon_{x,ID}}{\epsilon_{x,0}}$	$\frac{\sigma_{eID}}{\sigma_{e0}}$
#	#	#	#	#	kW	kW	kW	%	%	%
6	2	2	0	2	578	460	11	3.69	31.9	176.
6	2	2	1	0	557	441	8	3.87	37.2	176.1
6	2	2	1	1	569	452	10	3.77	34.1	175.9
6	2	2	1	2	582	463	12	3.66	31.	175.8

The RF-system parameters with 0 insertion devices installed are given in Table 5.90 and Figure 5.603 shows the phasor diagram with 0 insertion devices installed. The RF-system parameters with all insertion devices in operation and at minimum gap are given in Table 5.91 and Figure 5.604 shows the phasor diagram with all insertion devices in operation and at minimum gap.

Table 5.90: RF-system parameters with 0 insertion devices in operation

$P_g =$	298.81	kW
$P_{cy} =$	107.14	kW
$P_b =$	180.00	kW
$P_r =$	11.67	kW
$ V_{cy}  =$	1500.00	kV
$ V_b  =$	1244.60	kV
$ V_g  =$	1187.70	kV
$ V_{gr}  =$	2004.00	kV
$\psi =$	0.94	
$\beta =$	4	

Table 5.91: RF-system system parameters with all the insertion devices in operation and at minimum gap

$P_g =$	581.74	kW
$P_{cy} =$	107.14	kW
$P_b =$	462.92	kW
$P_r =$	11.68	kW
$ V_{cy}  =$	1500.00	kV
$ V_b  =$	1411.60	kV
$ V_g  =$	1879.50	kV
$ V_{gr}  =$	2796.20	kV
$\psi =$	0.83	
$\beta =$	4	



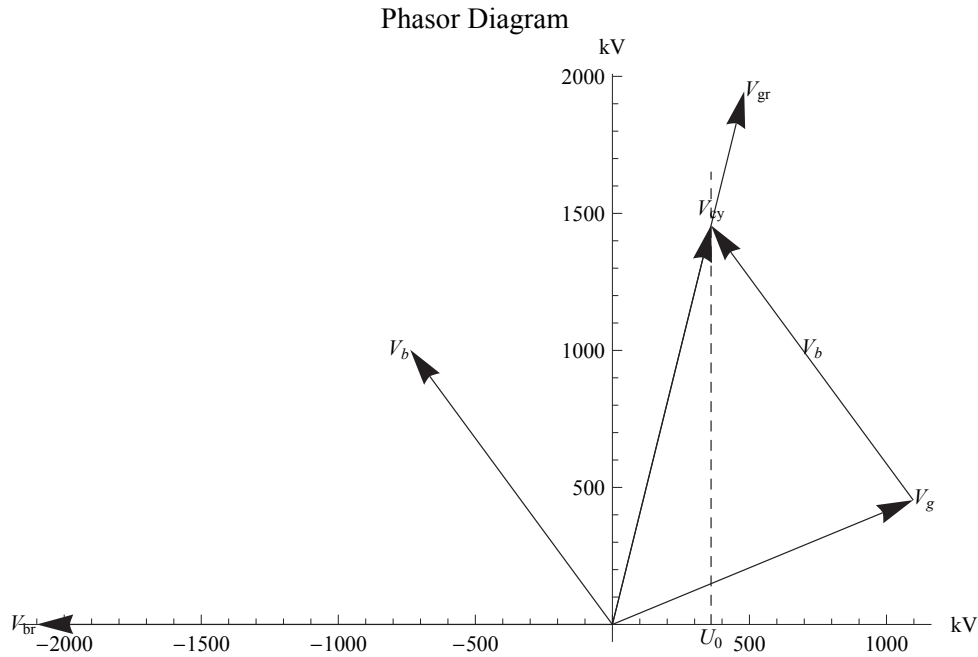


Figure 5.603: Phasor diagram with 0 insertion devices in operation

Table 5.92: The bare lattice beam parameters, with IBS and Landau cavities, in the middle of the straight sections of the MAX IV 3 GeV Ring [1]

Beam Energy	3.0	GeV
Beam Current	500	mA
Energy Spread (rms)	0.00077	
Horizontal Beta Function	9.00	m
Horizontal Emittance	0.372	nmrad
Vertical Beta Function	4.80	m
Vertical Emittance	0.008	nmrad

## 5.5. The influence on the brilliance and angular spectral flux from the number of IDs installed

The emittance of the stored electron beam will generally decrease with an increasing number of IDs in operations. The energy spread will on the other hand generally increase with an increasing number of IDs. IDs, in the form of e.g. damping wigglers, can hence be used to decrease the emittance of the stored beam. The damping wigglers will, if they are to be installed, occupy straight sections of the storage ring. The construction/purchasing of the damping will also represent a considerable capital cost.

In order to verify the benefit of running the accelerator with a large number of strong IDs, the numerical exercise of comparing the emittance and angular flux for the MAX IV 3 GeV storage ring with and without insertion devices has been carried out. The influence from the IDs on the emittance and energy spread has been estimated in Table 5.89. We will here compare the situation with 1 ID installed, the pmu18p5 in vacuum undulator, and all 13 IDs installed.

The bare lattice beam parameters in the middle of the straight sections the 3 GeV MAX-IV storage ring are given in Table 5.92 [1].

The beam parameters in the middle of the straight sections the 3 GeV MAX-IV storage ring with

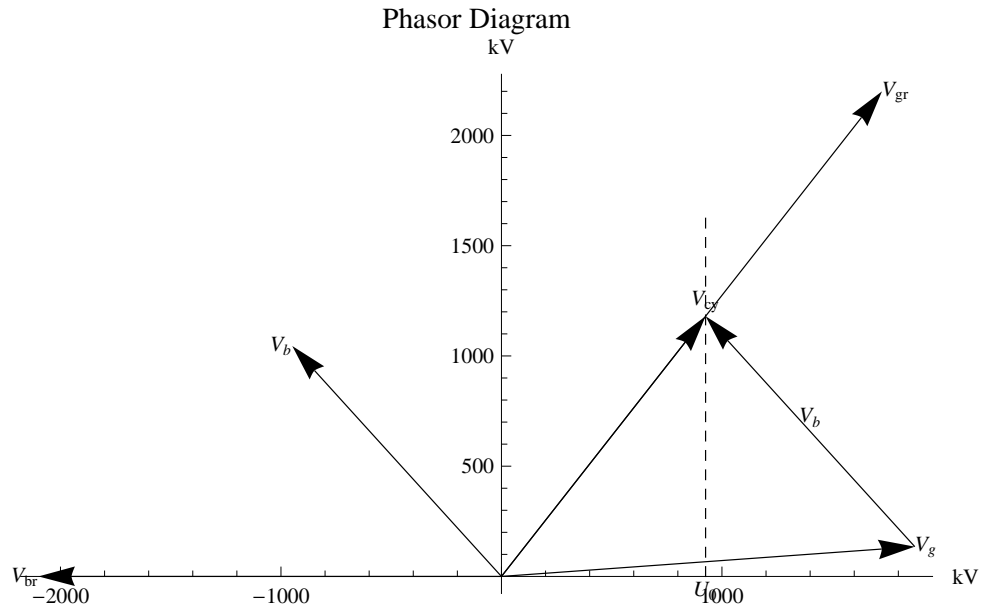


Figure 5.604: Phasor diagram with all the insertion devices in operation and at minimum gap

Table 5.93: The beam parameters, with IBS and Landau cavities, in the middle of the straight sections of the MAX IV 3 GeV Ring with 1 pmu18p5 installed and at minimum gap

Beam Energy	3.0	GeV
Beam Current	500	mA
Energy Spread (rms)	0.000772	
Horizontal Beta Function	9.00	m
Horizontal Emittance	0.358	nmrad
Vertical Beta Function	4.80	m
Vertical Emittance	0.008	nmrad

1 ID, pmu18p5, installed are given in Table 5.93 and for all IDs installed the beam parameters are given in Table 5.94.

The brilliance at peak energy of the emitted synchrotron radiation by pmu18p5 with 1 or 13 IDs installed is shown in Figure 5.605.

The angular spectral flux of the emitted synchrotron radiation by pmu18p5 with 1 or 13 IDs installed is shown in Figure 5.606.

The ratio of coherent flux in the harmonics of the emitted synchrotron by pmu18p5 with 1 or 13 IDs installed is shown in Figure 5.607.

Table 5.94: The beam parameters, with IBS and Landau cavities, in the middle of the straight sections of the MAX IV 3 GeV Ring with all IDs in Table 5.89 installed and at minimum gap

Beam Energy	3.0	GeV
Beam Current	500	mA
Energy Spread (rms)	0.001354	
Horizontal Beta Function	9.00	m
Horizontal Emittance	0.115	nmrad
Vertical Beta Function	4.80	m
Vertical Emittance	0.008	nmrad

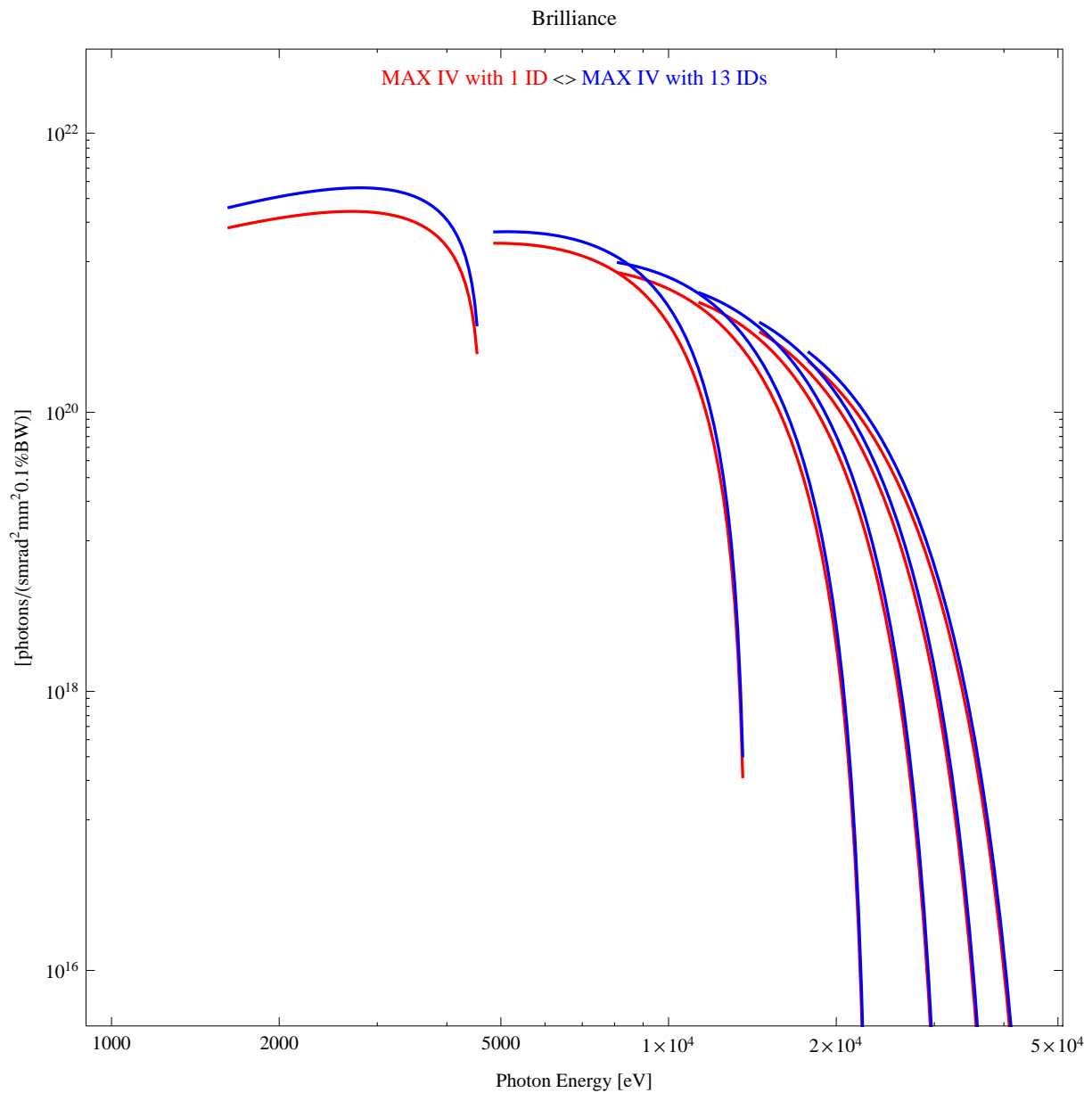


Figure 5.605: The brilliance at peak energy of the emitted synchrotron radiation by pmu18p5 with 1 or 13 IDs installed

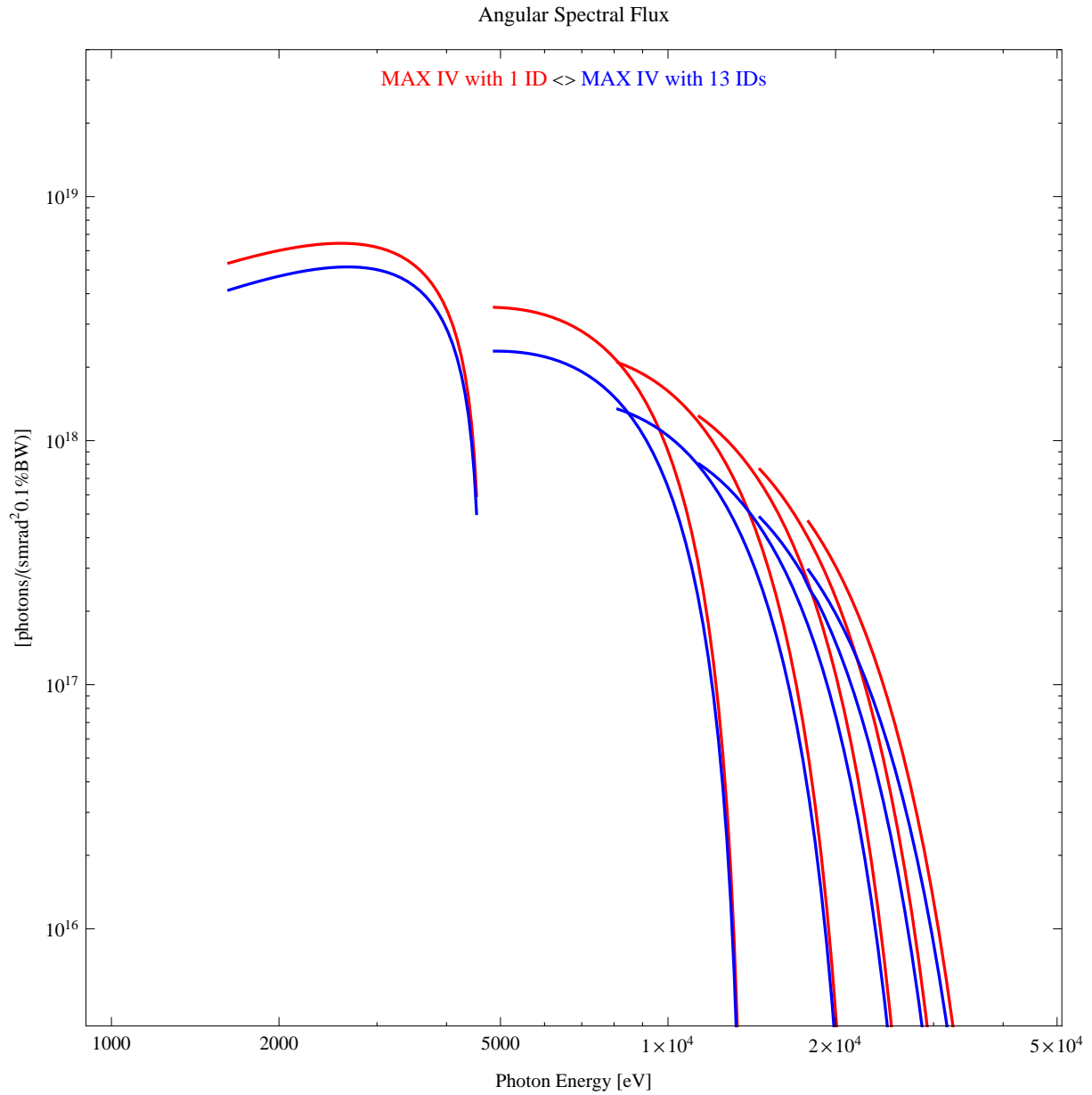


Figure 5.606: The angular spectral flux of the emitted synchrotron radiation by pmu18p5 with 1 or 13 IDs installed

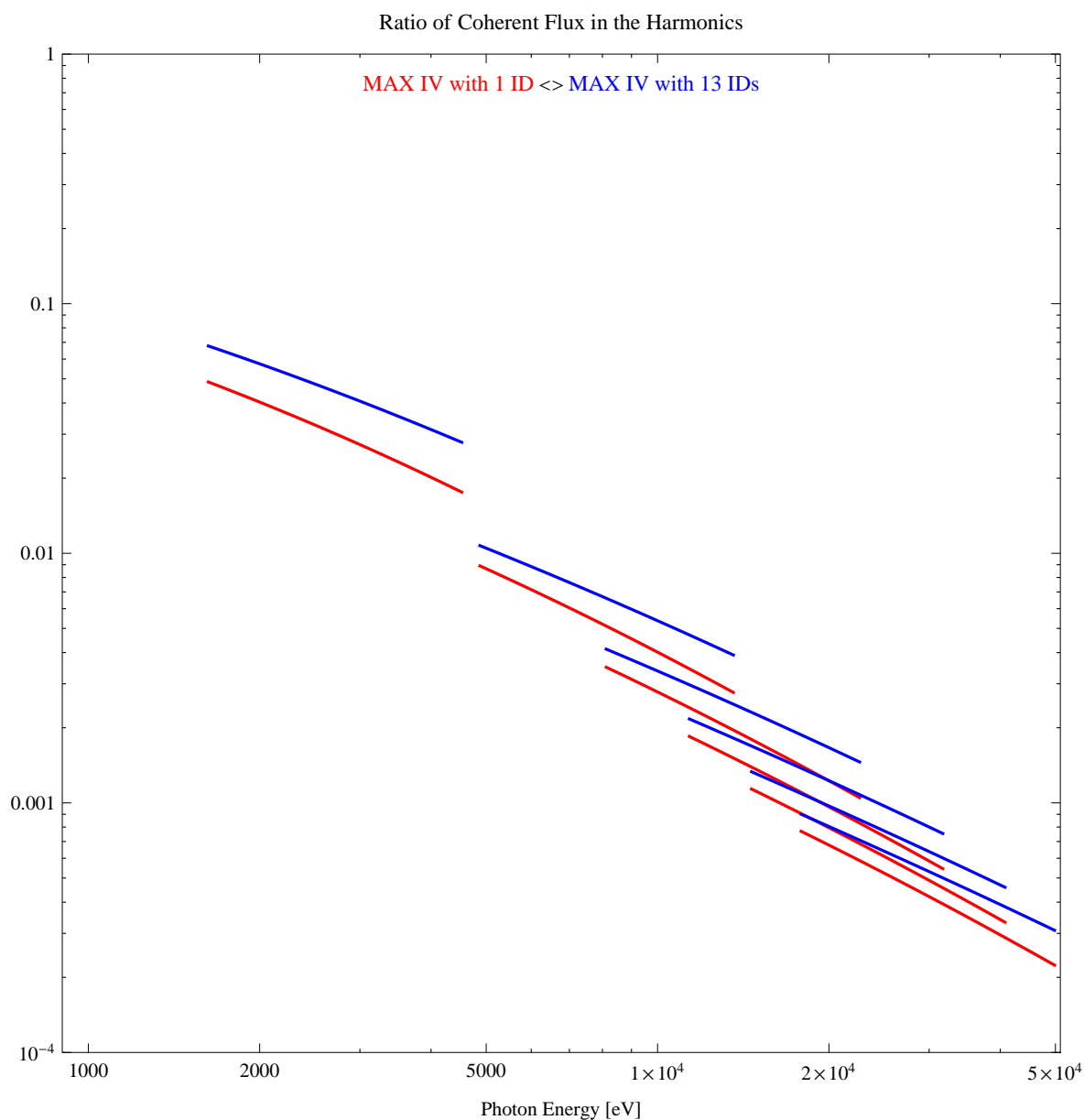


Figure 5.607: The ratio of coherent flux in the harmonics of the emitted synchrotron by pmu18p5 with 1 or 13 IDs installed

## 5.6. Comparison of specific undulators at different synchrotron radiation storage rings

The performance of specific undulators at a selection of existing and future synchrotron radiation storage rings has been compared.

The selection of undulators at the different synchrotron radiation storage rings NSLS II [4], PEP X [5, 6], PETRA III [7], ALS [8], Diamond [9], ESRF [10], Soleil [11], MAX II [12], and MAX IV 3 GeV Ring [13] is shown in Table 5.95, where  $E$  is the energy of the stored beam,  $I$  is the beam current,  $\sigma_\gamma$  is the energy spread in the beam,  $\varepsilon_H$  and  $\varepsilon_V$  are the horizontal and vertical emittance of the beam,  $\beta_H$  and  $\beta_V$  are the values of the horizontal and vertical beta-functions in the middle of the straight section,  $L_{ID}$  is the magnetic length of the insertion device,  $\lambda_0$  is the period length, and  $K_{max}$  is the maximum  $K$ -value of the undulator. It is assumed that the undulators are situated in the middle of a straight section with negligible dispersion.

The choice of undulators is targeted towards the shortest existing period length at the different synchrotron radiation storage rings. The minimum  $K$ -value for the undulators during the calculations is 0.2 and the maximum  $K$ -value is given in Table 5.95.

Table 5.95: Parameters used for the comparison of specific undulators at different light sources [4–13]

Facility	$E$ GeV	$I$ A	$\sigma_\gamma$ %rms	$\varepsilon_H$ pmrad	$\varepsilon_V$ pmrad	$\beta_H$ $m$	$\beta_V$ $m$	ID/BL	$L_{ID}$ $m$	$\lambda_0$ mm	$K_{max}$
MAX IV	3	0.5	0.1	263	8.	9	4.8	pmu18p5	3.8	18.5	1.92
NSLS II	3	0.5	0.1	550	8.	1.5	0.8	U19	3.	19.	2.03
PEP X	4.5	1.5	0.114	150	8.1	10.4	8	U23	3.5	23.	2.26
PETRA III	6	0.1	0.1	1000	10.	1.3	3	U29	5.	29.	2.2
ALS	1.9	0.4	0.1	6000	60.	11.2	4.2	U8	4.4	80.	5.98
diamond	3	0.3	0.11	2740	27.4	18	5	I03	1.98	21	1.69
ESRF	6	0.2	0.11	4000	24.	0.5	2.73	ID27	4	23	1.61
SOLEIL	2.75	0.3	0.1	3740	40	17.8	1.75	U20	1.8	20	1.92
MAX II	1.5	0.2	0.2	8840	880.	13	2.5	I1011	2.1	46.6	3.1

The brilliance at peak energy of the synchrotron radiation emitted at the rings and undulators in Table 5.95 is shown in Figure 5.608.

The angular spectral flux of the synchrotron radiation emitted at the rings and undulators in Table 5.95 is shown in Figure 5.609.

The flux of photons in the harmonics of the emitted synchrotron radiation at the rings and undulators in Table 5.95 using a 0.1%BW monochromator is shown in Figure 5.610.

The flux of photons in the harmonics of the emitted synchrotron radiation from the rings and undulators in Table 5.95 is shown in Figure 5.611.

The power in the harmonics of the emitted synchrotron radiation from the rings and undulators in Table 5.95 is shown in Figure 5.612.

The ratio of coherent flux in the harmonics of the emitted synchrotron radiation from the rings and undulators in Table 5.95 is shown in Figure 5.613.

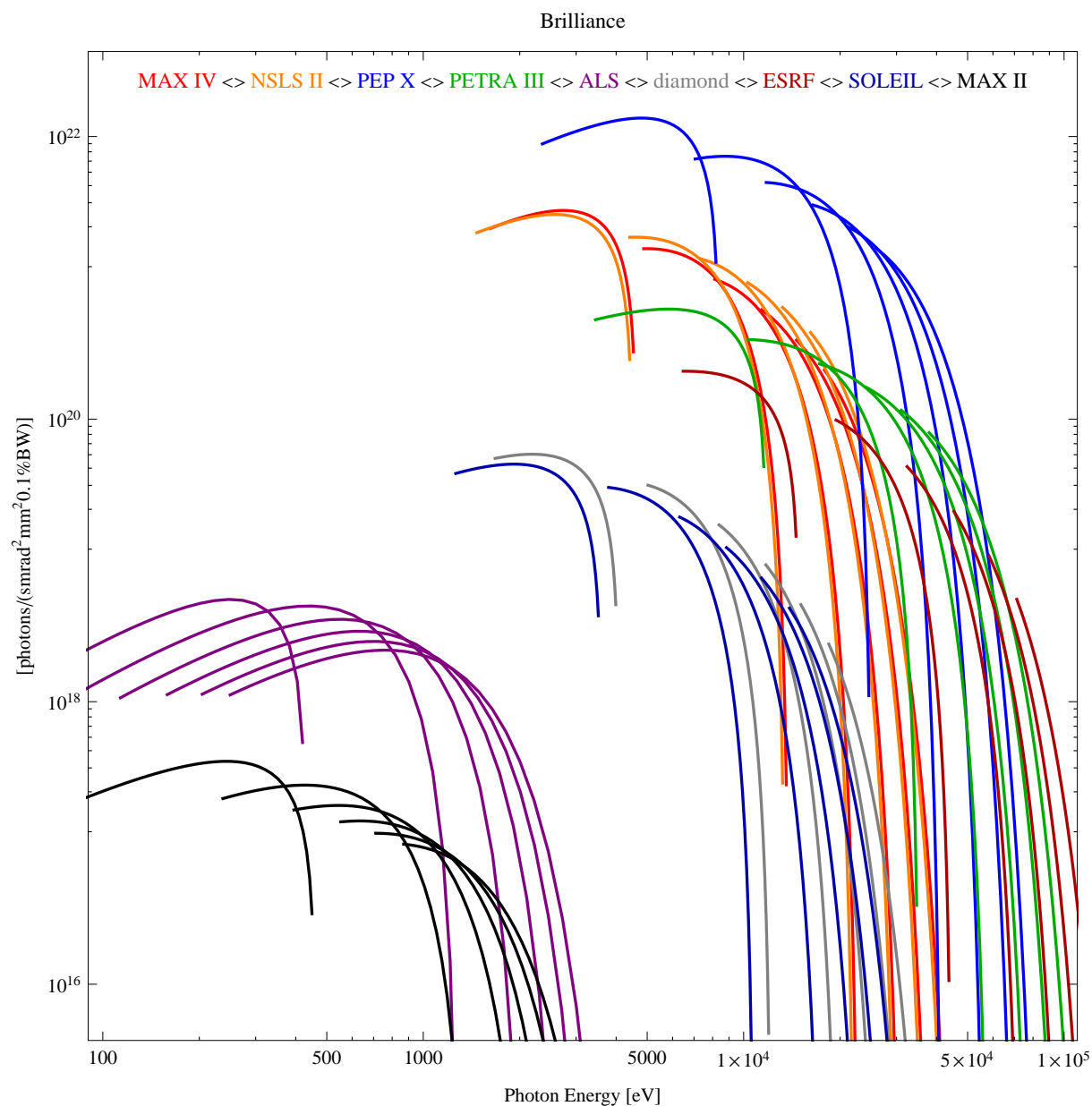


Figure 5.608: The brilliance at peak energy of the synchrotron radiation emitted at the rings and undulators in Table 5.95

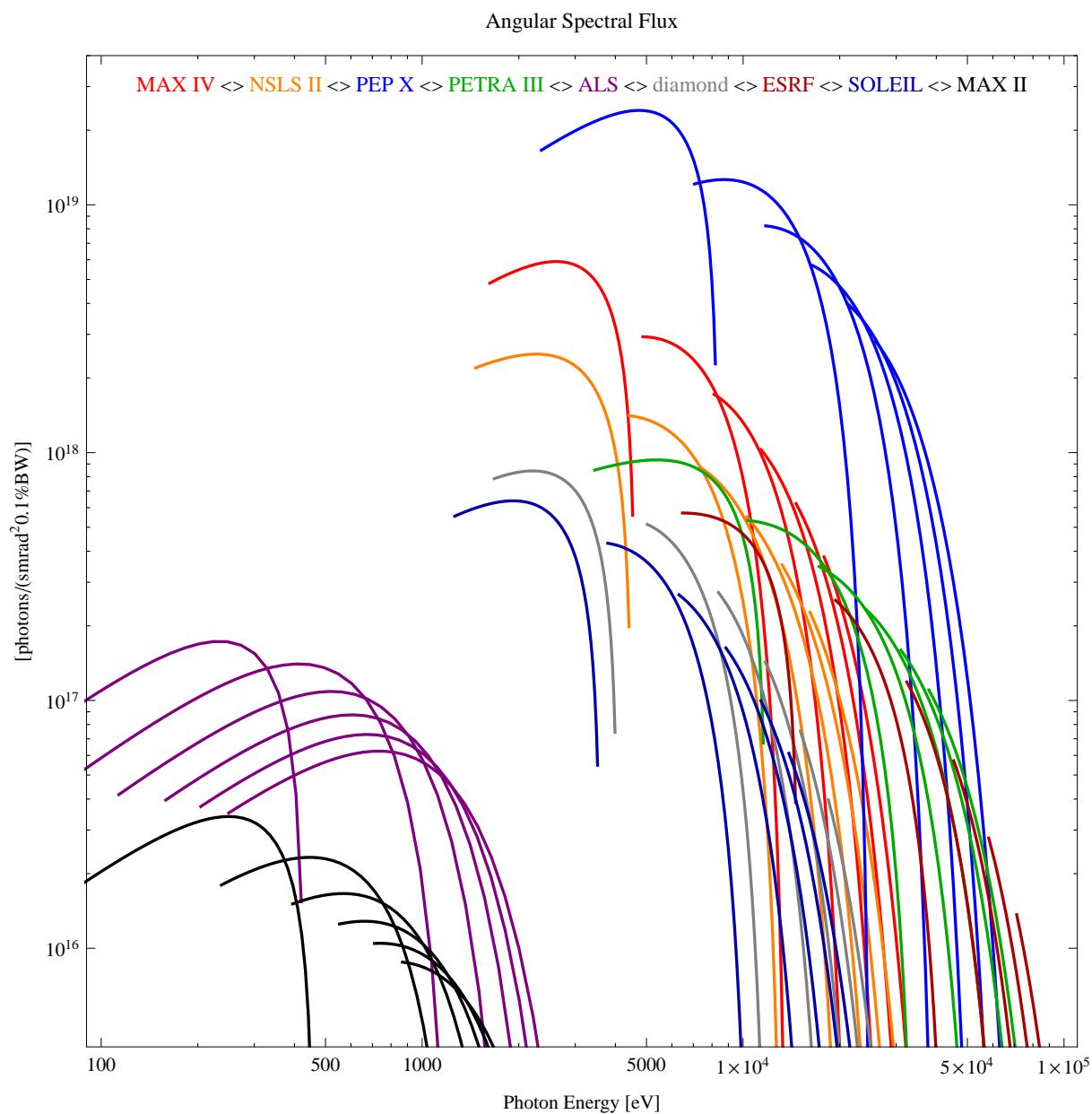


Figure 5.609: The angular spectral flux of the synchrotron radiation emitted at the rings and undulators in Table 5.95



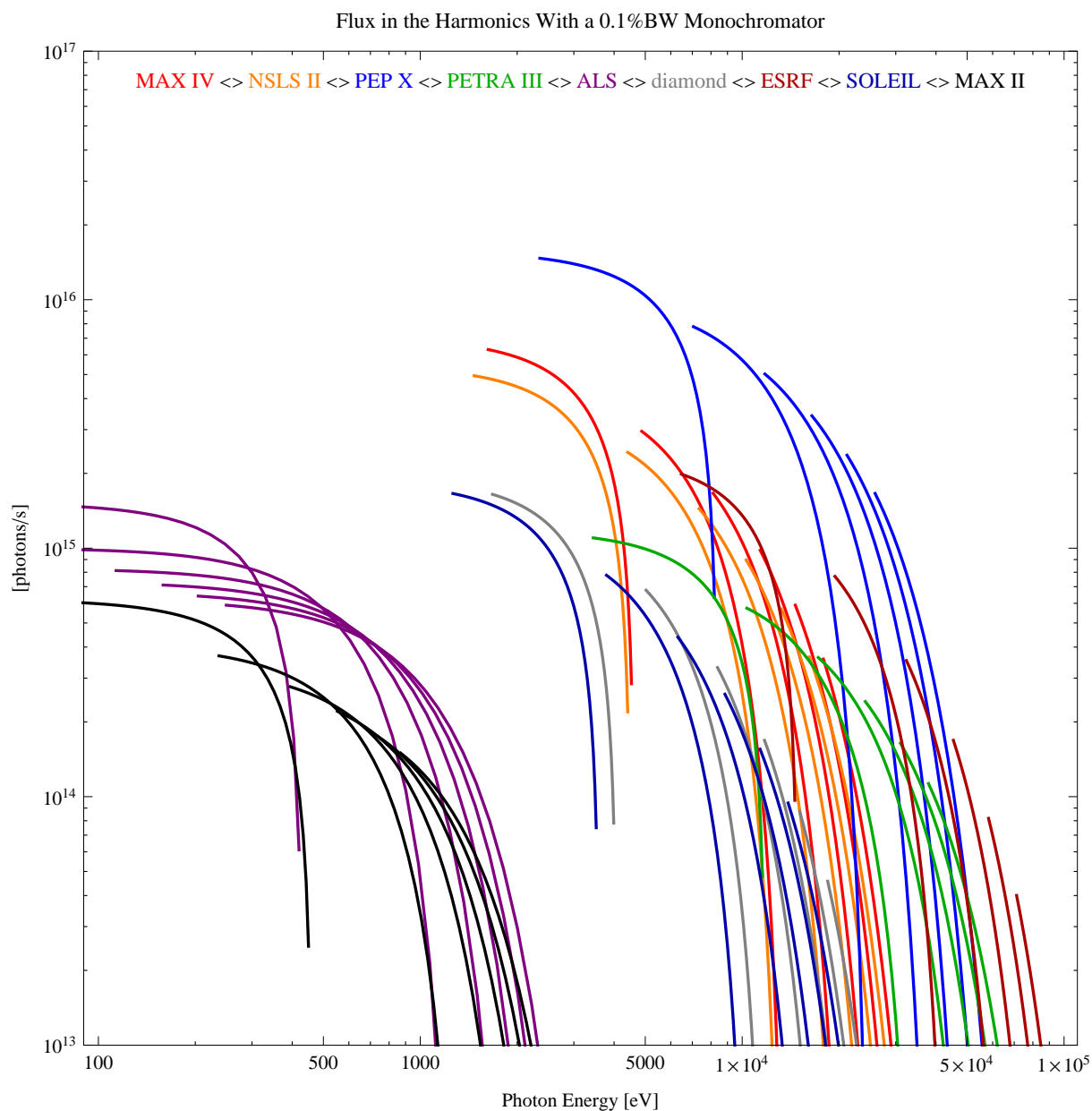


Figure 5.610: The flux of photons in the harmonics of the emitted synchrotron radiation at the rings and undulators in Table 5.95 using a 0.1%BW monochromator

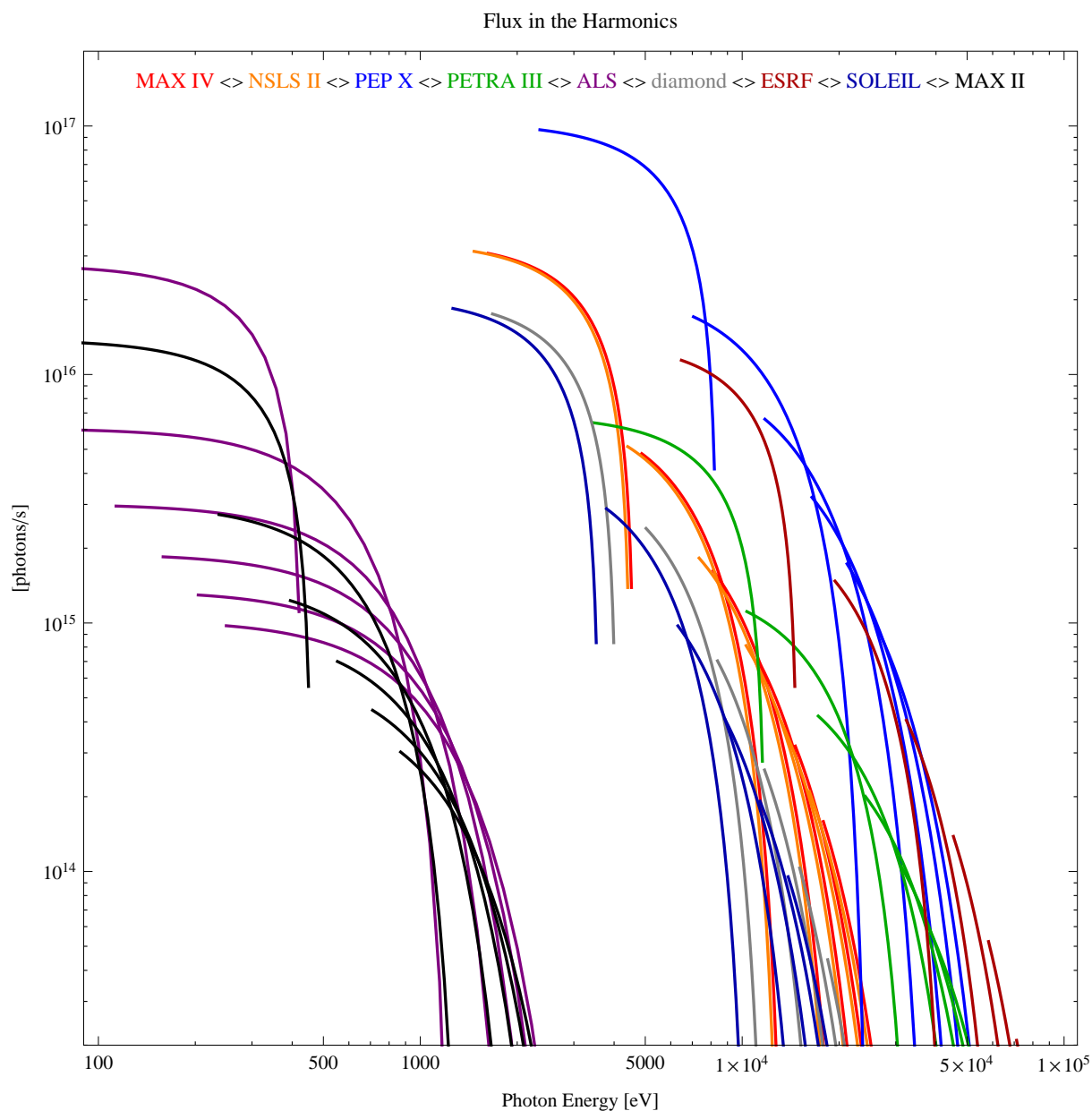


Figure 5.611: The flux of photons in the harmonics of the emitted synchrotron radiation from the rings and undulators in Table 5.95

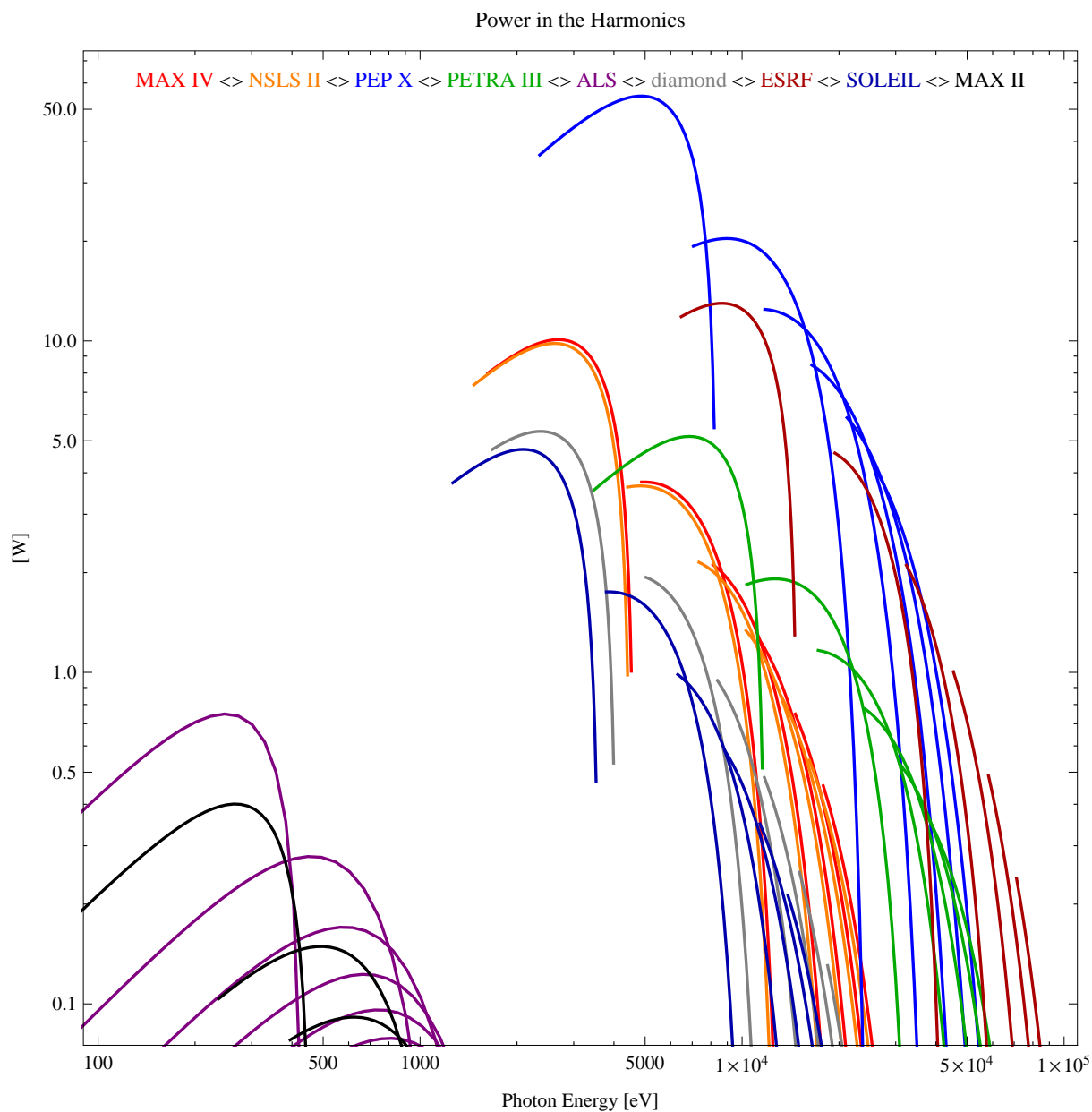


Figure 5.612: The power in the harmonics of the emitted synchrotron radiation from the rings and undulators in Table 5.95

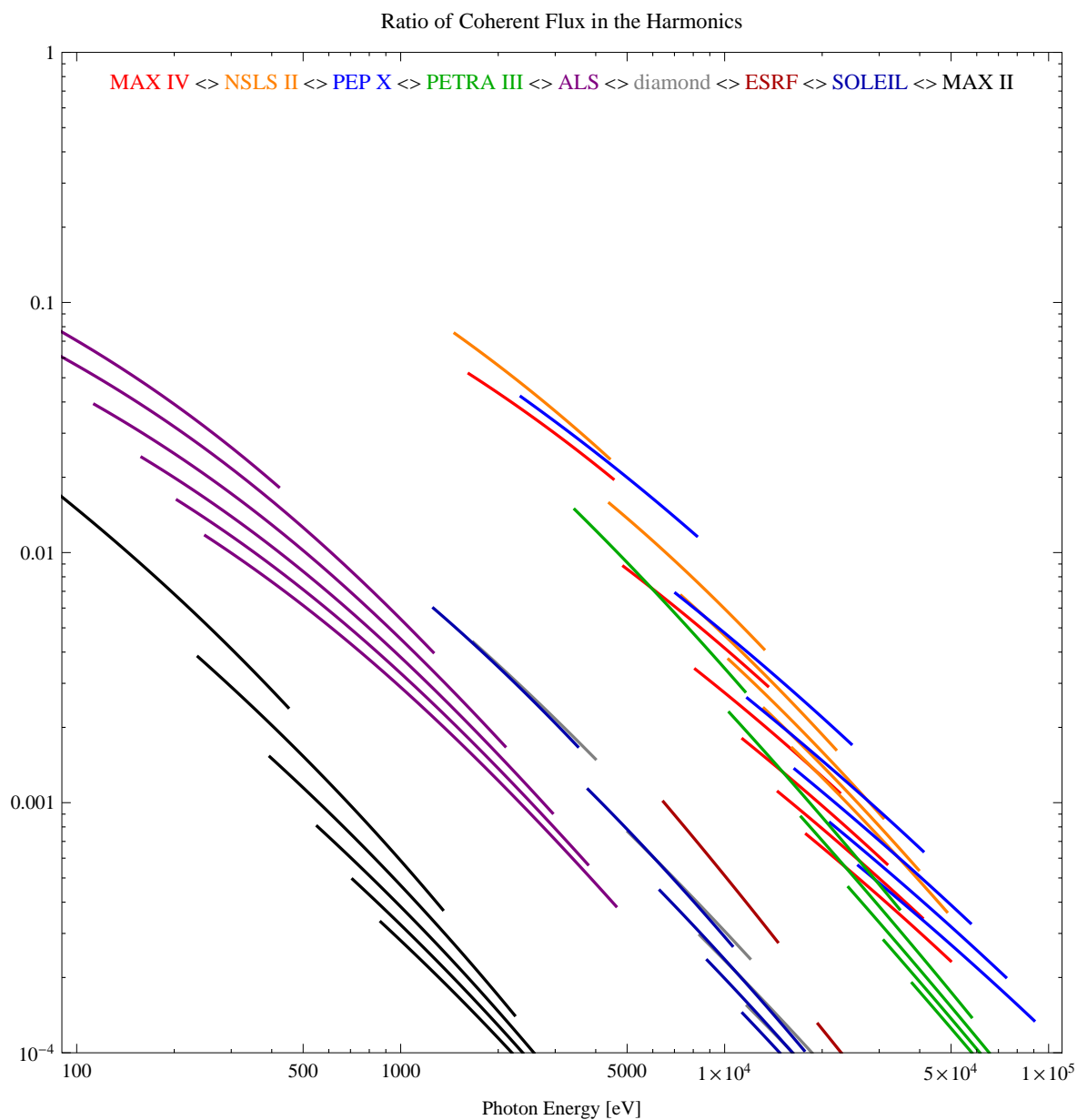


Figure 5.613: The ratio of coherent flux in the harmonics of the emitted synchrotron radiation from the rings and undulators in Table 5.95

The coherent flux in the harmonics of the rings and undulators in Table 5.95 using a 0.1%BW Monochromator is shown in Figure 5.614.

The coherent flux in the harmonics of the the rings and undulators in Table 5.95 is shown in Figure 5.615.

The power of coherent synchrotron radiation in the harmonics of the the rings and undulators in Table 5.95 is shown in Figure 5.616.

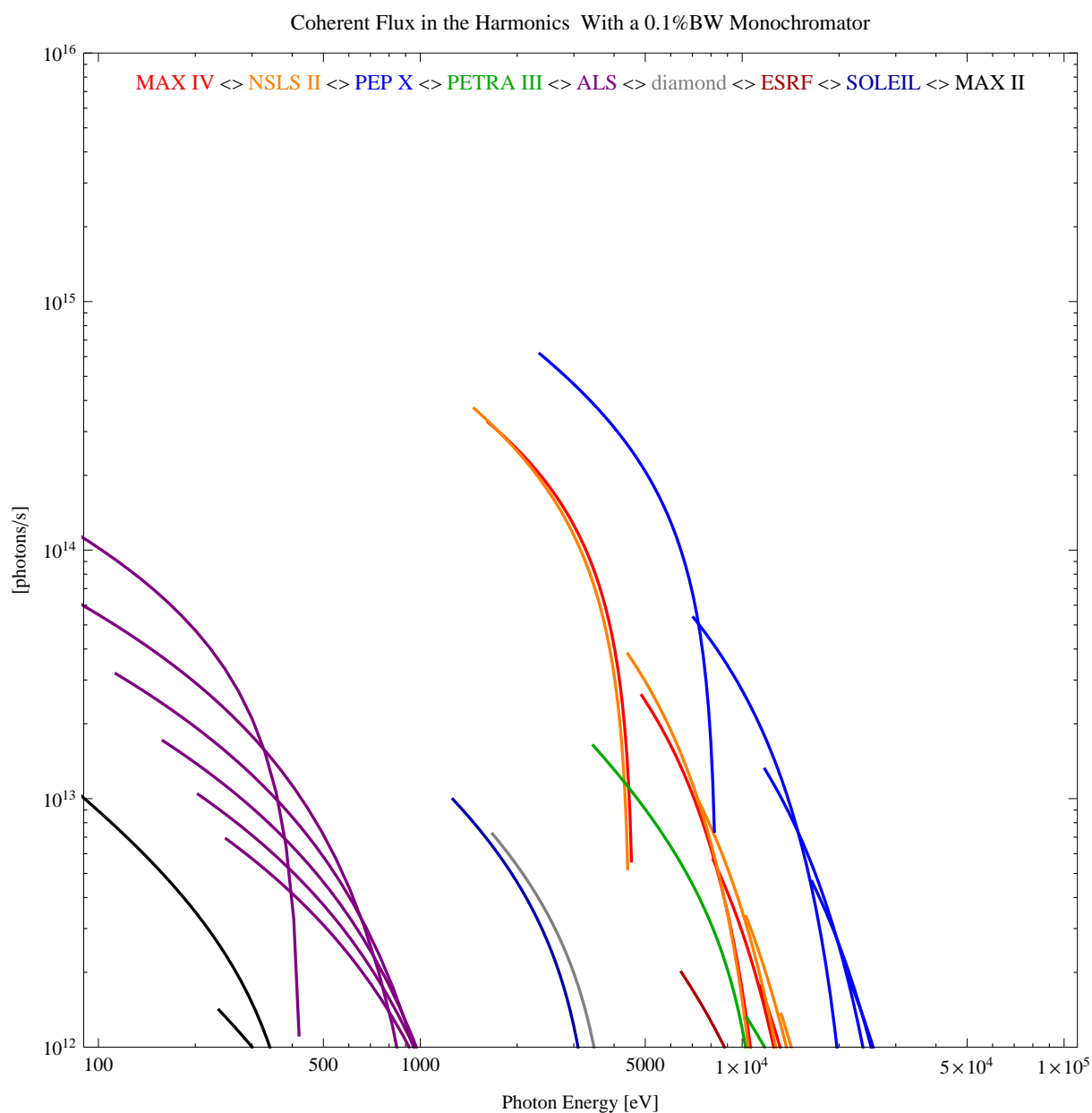


Figure 5.614: The coherent flux in the harmonics of the rings and undulators in Table 5.95 using a 0.1%BW Monochromator

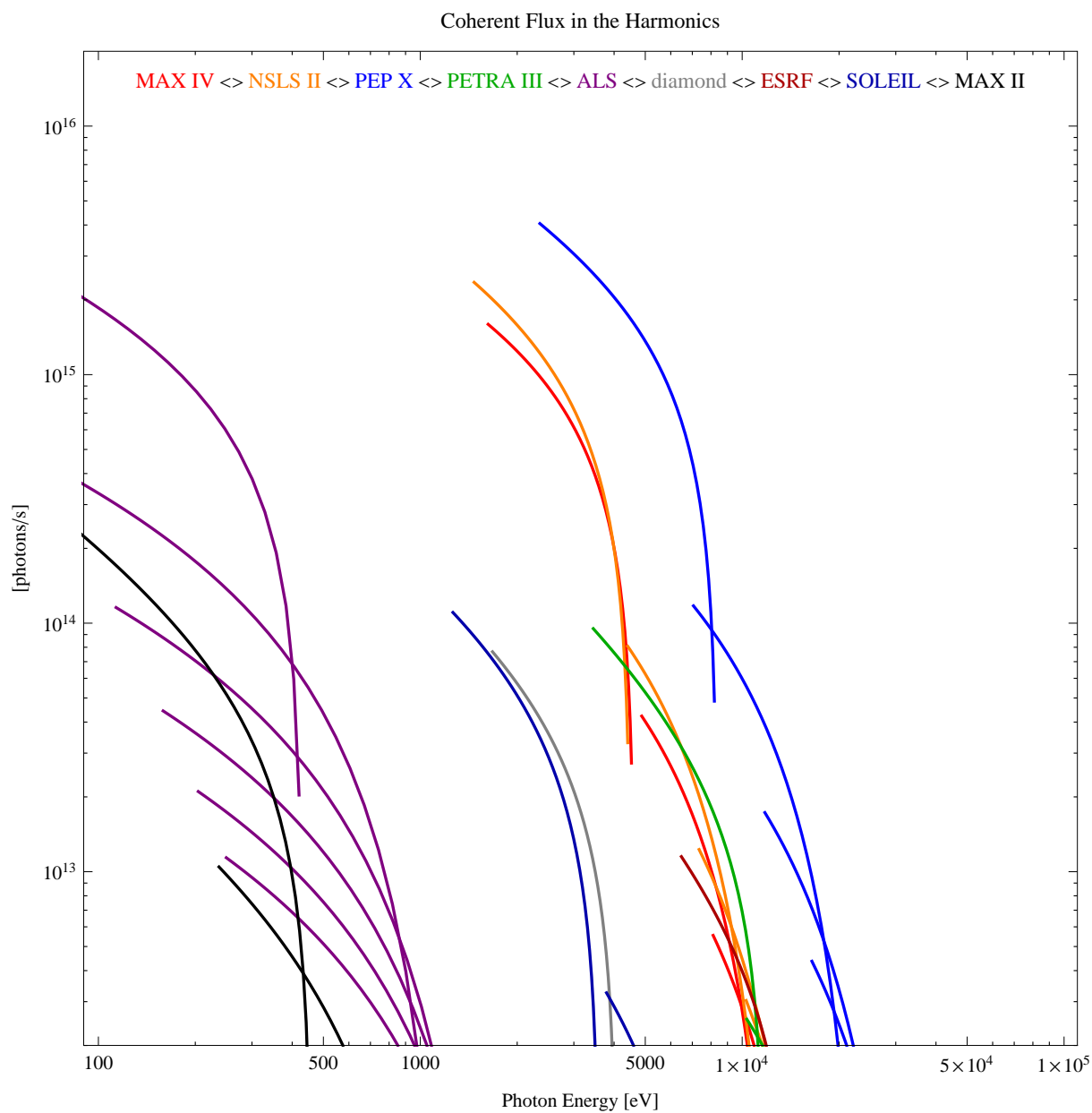


Figure 5.615: The coherent flux in the harmonics of the the rings and undulators in Table 5.95

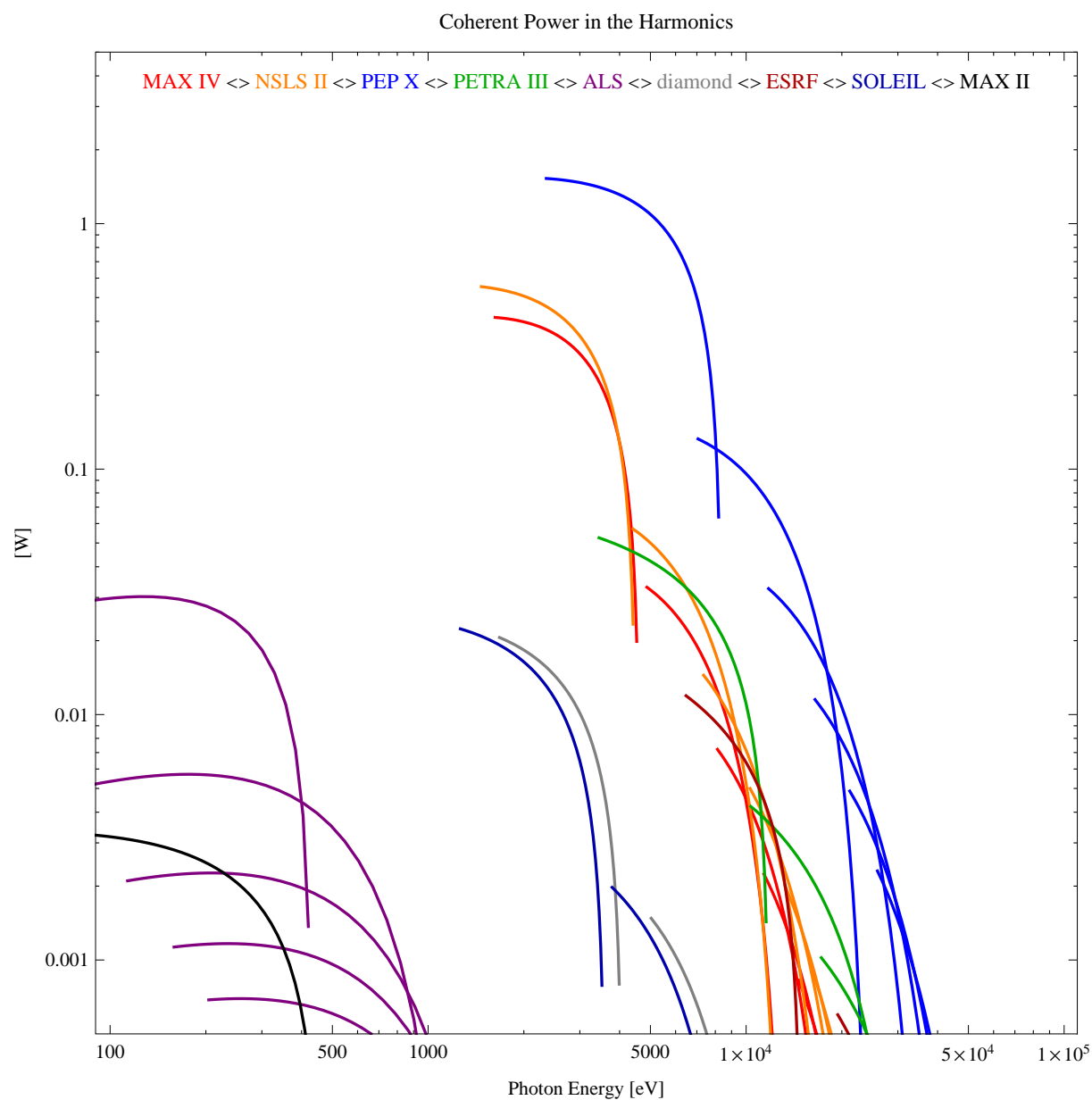


Figure 5.616: The power of coherent synchrotron radiation in the harmonics of the the rings and undulators in Table 5.95



## 5.7. Acknowledgement

---

vice during the work with the design of insertion devices and the calculations of the emitted synchrotron radiation.

I also would like to thank Oleg Chubar, Joël Chavanne, and Pascal Elleaume for providing the excellent software packages Radia [2] and SRW [14] as freeware to the accelerator and synchrotron radiation community.

I also would like to thank Takashi Tanaka and Hideo Kitamura for providing the excellent software package SPECTRA [15] as freeware to the synchrotron radiation community.

## 5.8. Appendix A: Synchrotron radiation

pressions for the synchrotron radiation produced by an ultra-relativistic electron beam passing through a sinusoidally periodic field with a large number of periods are given.

### 5.8.1. Synchrotron radiation from a single electron moving along an arbitrary trajectory

The scalar and vector potentials generated by an electron moving along an arbitrary trajectory (Liénard-Wiechert potential, SI-units) are given by [15–17]

$$\phi(\mathbf{r}, t) = \frac{e}{4\pi\epsilon_0 [R - \mathbf{v} \cdot \mathbf{R}/c]_{ret}} \quad (5.4)$$

$$\mathbf{A}(\mathbf{r}, t) = \frac{e\mathbf{v}}{4\pi\epsilon_0 c^2 [R - \mathbf{v} \cdot \mathbf{R}/c]_{ret}} \quad (5.5)$$

with

$$\mathbf{R} = \mathbf{r} - \mathbf{r}' \quad (5.6)$$

where  $\mathbf{r}$  is the vector from the origin to the observer,  $\mathbf{r}'$  is the vector from the origin to the electron,  $\mathbf{v}$  is the velocity of the electron,  $e$  is the electron charge,  $c$  is the speed of light, and  $\epsilon_0$  is the permittivity of vacuum. The subscript ‘ret’ denotes that the values in the square brackets should be calculated at the retarded time  $t'$  determined by

$$t' + R(t')/c = t \quad (5.7)$$

The electric  $\mathbf{E}(t)$  and magnetic  $\mathbf{B}(t)$  fields are given from the scalar and vector potential by

$$\mathbf{E}(t) = -\nabla\phi - \frac{\partial\mathbf{A}}{\partial t} \quad (5.8)$$

$$\mathbf{B}(t) = \nabla \times \mathbf{A} \quad (5.9)$$

The power density, or radiated power  $dP$  per unit area  $dS$  can be written as

$$\begin{aligned} \frac{dP}{dS} &= \epsilon_0 c \int_{-\infty}^{\infty} |\mathbf{E}(t)|^2 dt = \\ &= \frac{e^2 \gamma^4}{2\pi^2 \epsilon_0^2 c^2} \int_{-\infty}^{\infty} \left[ \frac{(\gamma\dot{\beta}_x)^2 + (\gamma\dot{\beta}_z)^2}{R^2 D^3} - \frac{4(\xi\gamma\dot{\beta}_x + \psi\gamma\dot{\beta}_z)^2}{R^2 D^5} + \frac{4c^2(\xi^2 + \psi^2)}{R^4 D^5} \right] dt \end{aligned} \quad (5.10)$$

with

$$\begin{aligned} D &= 1 + \xi^2 + \psi^2 \\ \xi &= \gamma n_x - \gamma\beta_x \\ \psi &= \gamma n_z - \gamma\beta_z \\ \mathbf{n} &= \mathbf{R}/R \end{aligned} \quad (5.11)$$

where  $\gamma$  is the Lorentz factor,  $\beta = v/c$  is relative velocity of the moving electron, and  $\mathbf{n}$  is a direction.

When calculating the spectral flux density of synchrotron radiation it is more convenient to be in the frequency domain and use the Fourier transform  $\mathbf{E}_\omega$  of the electric field [18]

$$\mathbf{E}_\omega = -\nabla\phi_\omega + i\omega\mathbf{A} \quad (5.12)$$

Using the retarded time (5.7), the following expression are obtained

$$\phi_\omega = \frac{e}{4\pi\epsilon_0} \int_{-\infty}^{\infty} \frac{1}{R(t')} \exp[i\omega t(t')] dt' \quad (5.13)$$

$$\mathbf{A} = \frac{e}{4\pi\epsilon_0 c} \int_{-\infty}^{\infty} \frac{\mathbf{v}(t')/c}{R(t')} \exp[i\omega t(t')] dt' \quad (5.14)$$

and by substitution of (5.13) and (5.14) into (5.12), we get

$$\mathbf{E}_\omega = \frac{e}{4\pi\epsilon_0} \mathbf{H} \quad (5.15)$$

where

$$\mathbf{H} = i\omega \int_{-\infty}^{\infty} \frac{1}{R(t')} \left[ \mathbf{v}(t')/c - \left( 1 + \frac{ic}{\omega R(t')} \right) \mathbf{n}(t') \right] \exp[i\omega t(t')] dt' \quad (5.16)$$

The angular spectral flux, also often spectral flux density, from the single electron is calculated as

$$\frac{d\Phi}{d\Omega} = \frac{d^2 P}{\hbar dS d\omega} = \frac{\epsilon_0 c}{\hbar \pi} |\mathbf{E}_\omega|^2 = \frac{\alpha}{4\pi^2} |\mathbf{H}|^2 \quad (5.17)$$

## 5.8.2. Polarisation of the emitted synchrotron radiation

The degree of polarization of the emitted synchrotron radiation are determined by the Stokes parameters

$$\begin{aligned} S_0 &= |H_x|^2 + |H_z|^2 \\ S_1 &= |H_x|^2 - |H_z|^2 \\ S_2 &= 2\text{Re}(H_x H_z^*) \\ S_3 &= 2\text{Im}(H_x H_z^*) \end{aligned} \quad (5.18)$$

There are 3 types of degree of polarization : linear (PL), circular (PC) and 45 - degree linear (PL45) polarization.

$$\begin{aligned} PL &= S_1/S_0 \\ PL45 &= S_2/S_0 \\ PC &= S_3/S_0 \end{aligned} \quad (5.19)$$

PL = +1 (-1) means that the electric vector of the photon beam lies on the horizontal (vertical) plane.

PL45 = +1 (-1) means that the electric vector lies on the plane tilted by 45 (135) degree from the horizontal plane.

PC = +1 (-1) means that the electric vector rotates counterclockwise (clockwise). Note counterclockwise polarization = right hand polarization = positive circular polarization and clockwise polarization = left hand polarization = negative circular polarization.

### 5.8.3. Angular spectral flux from periodic undulators with sinusoidal field and a filament current

Under the assumptions that the periodic field of the undulator is sinusoidal and the number of periods in the undulator is large a number of approximations can be done, as described in e.g. [17], and rather compact expressions for the angular spectral flux density can be derived.

The  $K$ -value is a fundamental parameter of an undulator and it is a unit-less parameter denoting the maximum deflection that the beam does in a period of the undulator in units of  $1/\gamma$ . The  $K$ -value for an undulator with a sinusoidal field with peak field  $B_0$  and period length  $\lambda_0$  is given by the relation (SI-units)

$$K = \frac{\lambda_0 B_0 e}{2\pi m_e c} \quad (5.20)$$

which in practical units is given by

$$K = 93.3737 \lambda_0 [\text{m}] B_0 [\text{T}] \quad (5.21)$$

A vertical periodical field in the undulator gives a horizontal  $K_x$ -value and a horizontal periodical field gives a vertical  $K_z$ -value. The motion of an electron in the filament along the undulator in the  $s$ -direction is given by

$$\begin{aligned} X(s) &= \frac{K_x \lambda_0}{2\pi\gamma} \sin(2\pi s/\lambda_0) \\ Z(s) &= \frac{K_z \lambda_0}{2\pi\gamma} \sin(2\pi s/\lambda_0 + \varphi) \end{aligned} \quad (5.22)$$

The oscillating electrons in the beam will emit synchrotron radiation at the fundamental frequency of the oscillation and also at higher harmonics of the fundamental oscillation frequency. The wavelength of fundamental harmonic is given by

$$\lambda_1 = \frac{\lambda_0}{2\gamma^2} (1 + K_x^2/2 + K_z^2/2 + \gamma^2 \theta_x^2 + \gamma^2 \theta_z^2) \quad (5.23)$$

where  $\theta_x$  and  $\theta_z$  are the horizontal and vertical angle out from the undulator axis in the  $s$ -direction. The emitted radiation can in the frequency domain be described by the lobe function

$$\mathbf{H}_n = \begin{bmatrix} H_{nx} \\ H_{nz} \end{bmatrix} = \frac{n}{\lambda_1} \int_0^{\lambda_0} \begin{bmatrix} \frac{K_x}{\gamma} \cos(2\pi s/\lambda_0) - \theta_x \\ \frac{K_z}{\gamma} \cos(2\pi s/\lambda_0 + \varphi) - \theta_z \end{bmatrix} e^{In\Psi} ds \quad (5.24)$$

where

$$\Psi = \frac{2\pi s}{\lambda_0} + \frac{-2\gamma\theta_x K_x \sin(\frac{2\pi s}{\lambda_0}) - 2\gamma\theta_z K_z \sin(\frac{2\pi s}{\lambda_0} + \varphi) + \frac{K_x^2}{4} \sin(\frac{4\pi s}{\lambda_0}) + \frac{K_z^2}{4} \sin(\frac{4\pi s}{\lambda_0} + 2\varphi)}{1 + K_x^2/2 + K_z^2/2 + \gamma^2\theta_x^2 + \gamma^2\theta_z^2} \quad (5.25)$$

The angular spectral flux, also often called spectral flux density, at the photon energy  $\epsilon$  from the harmonic  $n$  on axis for a filament current with zero energy spread and zero emittance is given by the expression

$$\frac{d\Phi_n}{d\Omega} = \alpha \frac{I}{e} N^2 (|H_{nx}|^2 + |H_{nz}|^2) \text{sinc} \left[ \pi N \left( \frac{\epsilon}{hc} \lambda_1 - n \right) \right]^2 \quad (5.26)$$

where  $\alpha$  is the fine structure constant,  $N$  is the number of periods in the undulator,  $I$  is the beam current, and  $\text{sinc}(x) = \sin(x)/x$ . The lobe function has in this expression been multiplied with the the interference factor with the  $\text{sinc}^2$  function. The interference factor has a sharper peak in the forward direction than the lobe function.

The angular spectral flux at a specific photon energy is given by the summation over all harmonics

$$\frac{d\Phi}{d\Omega} = \sum_{n=1}^{\infty} \frac{d\Phi_n}{d\Omega} \quad (5.27)$$

#### 5.8.4. On axis angular spectral flux from an undulator and a filament current

When the observer of the synchrotron radiation is on the undulator axis short expressions may be derived for the angular spectral flux and the brilliance.

The angular spectral flux, also often called spectral flux density, at the harmonic  $n$  on axis for a filament current with zero energy spread and zero emittance is given by the expression [17]

$$\frac{d\Phi_n}{d\Omega} = \alpha \frac{I}{e} N^2 \gamma^2 F_n \quad (5.28)$$

$F_n$  is function that involves Bessel functions of the first kind,  $J_n(z)$ .

$$F_n = \frac{n^2 K^2}{(1+K^2/2)^2} \left( J_{(n-1)/2} \left[ \frac{nK^2}{4+2K^2} \right] - J_{(n+1)/2} \left[ \frac{nK^2}{4+2K^2} \right] \right)^2 \quad \text{for } n = 1, 3, 5, \dots$$

$$F_n = 0 \quad \text{for } n = 2, 4, 6, \dots \quad (5.29)$$

where  $K$  is the  $K$ -value of the undulator.

### 5.8.5. On axis spectral flux in the central cone of radiation from an undulator and a filament current

The angle integrated angular spectral flux on axis at the harmonic  $n$   $\Phi_n$ , i.e. the spectral flux of photons in the central cone of harmonic  $n$ , from an undulator and a filament current is given by

$$\Phi_n = \frac{\pi}{2} \alpha \frac{I}{e} N Q_n \quad (5.30)$$

where  $Q_n$  is given by

$$\begin{aligned} Q_n &= \frac{nK^2}{1+K^2/2} \left( J_{(n-1)/2} \left[ \frac{nK^2}{4+2K^2} \right] - J_{(n+1)/2} \left[ \frac{nK^2}{4+2K^2} \right] \right)^2 & \text{for } n = 1, 3, 5, \dots \\ Q_n &= 0 & \text{for } n = 2, 4, 6, \dots \end{aligned} \quad (5.31)$$

To get the flux of photons passing a monochromator,  $\Phi_n$  should be multiplied with the FWHM bandwidth of the monochromator  $\frac{\Delta\lambda}{\lambda}$ , which usually is assumed to be 0.1 %. The total flux of photons in the cone is given by  $\Phi_n$  multiplied with the FWHM bandwidth of the undulator peak, which is  $\frac{1}{nN}$ .

### 5.8.6. On axis brilliance from an undulator and a filament current

The brilliance is the angular spectral flux divided by the source size and it is a quality measure of the emitted radiation. The brilliance  $\mathfrak{B}$  of the emitted radiation from a filament current is defined as  $\mathfrak{B} = \frac{4}{\lambda^2} \Phi$ , where  $\lambda$  is the wavelength of the radiation. The brilliance is invariant with respect to any linear transformation of the phase space of the radiation. The on axis brilliance  $\mathfrak{B}_n$  at the peak energy at harmonic  $n$  for a filament current is given by the expression

$$\mathfrak{B}_n = \frac{4}{(\lambda_1/n)^2} \frac{\pi}{2} \alpha \frac{I}{e} N Q_n \quad (5.32)$$

and  $\lambda_1$  is the wavelength of the fundamental harmonic on axis

$$\lambda_1 = \frac{\lambda_0}{2\gamma^2} \left( 1 + \frac{K^2}{2} \right) \quad (5.33)$$

The maximum brilliance for a filament beam is a factor of 2 larger than the brilliance at peak energy as explained in e.g. [17] and it is found at a slightly lower photon energy than the peak energy of the harmonic.

### 5.8.7. Approximative expressions for the on axis angular spectral flux and brilliance including the finite emittance and energy spread of the beam

For rapid calculations it may be useful to have approximative expressions for the angular spectral flux and brilliance. Below expressions that gives a numerical output within  $\pm 10\%$  of the numerical output of the calculations named "K-dependence  $\rightarrow$  Easy Calculation  $\rightarrow$  Brilliance @ Peak Energy " in Spectra [15] up to harmonic 15 are given. The broadening effect due to phase errors in the undulator is not included in the expressions below, which would make a difference at high harmonics. The highest harmonic used in the plots of this report is harmonic 11, which

requires an rms phase error in the undulator of 2 degrees or less in order to make it possible to neglect the broadening effect due to phase errors. An rms phase errors of 2 degrees or less is perfectly possible to obtain with the shimming techniques used today.

It is assumed that the undulator is installed in the middle of a straight section and that the beam size has its minimum in the centre of the undulator. The finite beam emittance, i.e. the beam size and divergence in the centre of the undulator, and the energy spread is described by the variables:

$\sigma_\gamma$	rms energy spread
$\sigma_x$	horizontal rms electron beam size [m]
$\sigma_{x'}$	horizontal rms electron beam divergence [rad]
$\sigma_z$	vertical rms electron beam size [m]
$\sigma_{z'}$	vertical rms electron beam divergence [rad]

The rms wavelength spread  $\sigma_\omega$  of the undulator peak from a filament beam is given by [19]

$$\sigma_\omega = \frac{0.360}{nN} \quad (5.34)$$

The energy spread  $\sigma_\gamma$  of a real beam will also give rise to a wavelength spread of the undulator peak and the induced wavelength spread is a factor 2 larger than the energy spread since the beam energy has a quadratic influence on the wavelength of the emitted synchrotron radiation. The total wavelength spread  $(\frac{\Delta\lambda}{\lambda})_{tot}$  is obtained by quadratic addition

$$\left(\frac{\Delta\lambda}{\lambda}\right)_{tot}^2 = (2\sigma_\gamma)^2 + \left(\frac{0.360}{nN}\right)^2 = \mu_\lambda^2 \sigma_\omega^2 \quad (5.35)$$

where  $\mu_\lambda$  is introduced as the broadening factor

$$\mu_\lambda = \sqrt{1 + \left(\frac{2\sigma_\gamma nN}{0.36}\right)^2} \quad (5.36)$$

To describe the source size including the broadening factor, the following total rms values are used

$$\begin{aligned} \sigma_{tx} &= \sqrt{\sigma_x^2 + (\lambda_1/n N \lambda_0)/(8\pi^2)} \\ \sigma_{tx'} &= \sqrt{\sigma_{x'}^2 + \mu_\lambda(\lambda_1/n)/(2N\lambda_0)} \\ \sigma_{tz} &= \sqrt{\sigma_z^2 + (\lambda_1/n N \lambda_0)/(8\pi^2)} \\ \sigma_{tz'} &= \sqrt{\sigma_{z'}^2 + \mu_\lambda(\lambda_1/n)/(2N\lambda_0)} \end{aligned} \quad (5.37)$$

An approximative value for the angular spectral flux  $\frac{d\Phi_n}{d\Omega}_{Real}$  at the peak energy at harmonic  $n$  for a real beam including finite beam emittance and energy spread is given by the expression

$$\frac{d\Phi_n}{d\Omega}_{Real} = \mathfrak{C}_n \alpha \frac{I}{e} N^2 \gamma^2 F_n \quad (5.38)$$

where  $\mathfrak{C}_n$  is a convolution over the energy spread and the angular divergence of the real beam

$$\mathfrak{C}_n = \frac{1.37}{(2\pi)^{3/2} \sigma_{tx'} \sigma_{tz'} \sigma_\gamma} \int_{-\infty}^{\infty} \int_{-\infty}^{\infty} \int_{-\infty}^{\infty} \exp \left[ - \left( \frac{\theta_x^2}{2\sigma_{tx'}^2} + \frac{\theta_z^2}{2\sigma_{tz'}^2} + \frac{\xi^2}{2\sigma_\gamma^2} \right) \right] \times$$

$$\times \text{sinc} \left[ \pi n N \left( -2\xi - \frac{\gamma^2 (\theta_x^2 + \theta_z^2)}{1 + \frac{K^2}{2}} \right) \right]^2 d\xi d\theta_x d\theta_z \quad (5.39)$$

The factor 1.37 in  $\mathfrak{C}_n$  is empirical and is found by comparing the numerical value of  $\frac{d\Phi_n}{d\Omega}_{Real}$  and the numerical output of Spectra.

An approximate value for the on axis brilliance  $\mathfrak{B}_{nReal}$  at the peak energy of harmonic  $n$ , including finite beam emittance and energy spread, is given by

$$\mathfrak{B}_{nReal} = \frac{1}{(2\pi)^2} \frac{1}{\sigma_{tx} \sigma_{tx'} \sigma_{tz} \sigma_{tz'}} \frac{\pi}{2} \alpha \frac{I}{e} N Q_n \quad (5.40)$$

The choice of calculating the brilliance at peak energy and not the maximum brilliance, which is found at a slightly lower photon energy, is that it is believed that in light sources with extremely low emittance it is of higher priority to use the narrow cone at the peak energy than the circular cone of synchrotron radiation at the peak brilliance.

### 5.8.8. Degree of spatial coherence in the emitted synchrotron radiation on axis

The degree of spatially coherent flux  $\mathfrak{R}_{coh}$  in the emitted synchrotron radiation on axis is given by

$$\mathfrak{R}_{coh} = \frac{((\lambda_1/n)/(4\pi))^2}{\sigma_{tx} \sigma_{tx'} \sigma_{tz} \sigma_{tz'}} \quad (5.41)$$

Where the phase space of spatially coherent light with the wavelength  $\lambda$  is defined to be  $\lambda/(4\pi)$ , in agreement with e.g. [20].

### 5.8.9. Flux of coherent photons on axis

The spatially coherent spectral flux  $\mathfrak{F}_{n,coh}$  from the harmonic  $n$  on axis is given by

$$\mathfrak{F}_{n,coh} = \mathfrak{R}_{coh} \frac{\pi}{2} \alpha \frac{I}{e} N Q_n \quad (5.42)$$

To get the flux of spatially coherent photons passing a monochromator,  $\mathfrak{F}_{n,coh}$  should be multiplied with FWHM bandwidth of the monochromator,  $\frac{\Delta\lambda}{\lambda}$  which usually is assumed to be 0.1 %. The longitudinal, or temporal, coherence length is in this case  $\frac{\lambda^2}{2\Delta\lambda}$  [20].

The flux in the cone itself is given by  $\mathfrak{F}_{n,coh}$  multiplied with the FWHM bandwidth of the undulator peak, which is  $\frac{1}{nN}$ . The longitudinal, or temporal, coherence length is in this case  $\frac{nN\lambda}{2}$  [20].



### 5.8.10. Numerical calculation of synchrotron radiation

The numerical calculation of the properties of synchrotron radiation is better carried out with dedicated software packages for synchrotron radiation calculations. Two excellent such software packages are Spectra [15] from Spring 8 in Japan or SRW [14] from the ESRF in France.

## 5.9. Appendix B: Modes of operation for elliptically polarising undulators

---

The magnetic structure of an elliptically polarising undulator (EPU) has a different configuration of the magnetic arrays compared to a standard flat field undulator.

The upper and lower girders are split in two halves along the vertical plane of the undulator axis giving in total four sub-girders, where the sub-girders can be moved individually to also give a horizontal magnetic field in addition to the vertical magnetic field that is normally found on the undulator axis.

If the horizontal field has an offset along the beam trajectory of a quarter of a period the EPU is running in the helical mode and if the magnetic fields in horizontal and vertical direction have the same magnitude, the EPU is producing synchrotron radiation with circular polarisation.

If the sub-girders are moved so that there is no offset between the horizontal and vertical magnetic field along the undulator axis, the EPU is operating in what is called the inclined mode and if the vertical and horizontal magnetic fields have the same magnitude, a state called 45 degree polarisation is obtained.

If the sub-girders are moved so that there is only a horizontal magnetic field component on axis, the EPU is operating is running in what is called the vertical mode.

The vertical mode can be reached in both inclined mode and helical mode with the difference that in the inclined mode the end sections are longer and the central section will be one period shorter. The two missing poles are added to the end sections of the EPU.

The maximum horizontal field in an EPU is weaker than the maximum vertical field and the horizontal field decays faster with increasing undulator than the vertical field.

The difference between flat field undulators and EPUs can also be demonstrated by looking at the symmetry planes of the magnetic structures as carried out by [21].

In a planar undulator two symmetry planes can be defined : a horizontal plane  $Z = 0$  in the magnetic mid plane, and a vertical plane  $X = 0$  that cuts the magnet arrays in the middle. The line  $X = 0, Z = 0$  is the magnetic center line or axis of the undulator.

An EPU in helical mode with a phase different from zero also has two symmetry planes  $X + Z = 0$  and  $X - Z = 0$ , and the line where the planes cut each other is the axis of the EPU.

An EPU in inclined plane mode has no symmetry planes.

The magnetic field lines must be perpendicular to a symmetry plane, and this requirement means there cannot be any longitudinal field component on the magnetic center line of an EPU in helical mode. In inclined plane mode all three field components will be present.

The movement of the sub-girders are called the phase,  $\psi$ , of the EPU and  $\psi$  is measured in the same units as the period length  $\lambda_0$ .

For the helical mode of operation the vertical and horizontal fields vary with the EPU phase  $\psi$  at constant gap,  $g$ , as

$$\begin{aligned} B_Z(g, \psi) &= B_Z(g) \cos \frac{\pi\psi}{\lambda_0} \\ B_X(g, \psi) &= B_X(g) \sin \frac{\pi\psi}{\lambda_0} \end{aligned} \quad (5.43)$$

where  $B_Z(g)$  and  $B_X(g)$  are the efficient vertical and horizontal magnetic fields found at  $\psi = 0$  and  $\psi = \lambda_0/2$ , respectively.

For the inclined plane mode of operation the fields over the central half period varies as

$$\begin{aligned} B_Z(g, \psi) &= B_Z(g) \cos^2 \frac{\pi\psi}{\lambda_0} \\ B_X(g, \psi) &= B_X(g) \sin^2 \frac{\pi\psi}{\lambda_0} \end{aligned} \quad (5.44)$$

The missing magnetic field in the inclined field shows up as a longitudinal field component.

For the circular phase in the helical mode and the 45 degree inclined plane phase in the inclined plane mode of operation the horizontal and vertical fields have equal strength.

The phases for circular and 45 degree inclined plane as functions of the EPU gap can hence be calculated by using

$$\begin{aligned} \psi_{Circular}(g) &= \frac{\lambda_0}{\pi} \arctan \frac{B_Z(g)}{B_X(g)} \\ \psi_{45Degree}(g) &= \frac{\lambda_0}{\pi} \arctan \sqrt{\frac{B_Z(g)}{B_X(g)}} \end{aligned} \quad (5.45)$$

An EPU will give rise to dynamic multipoles due to the strong field gradients out from the undulator axis and these dynamic multipoles may reduce the beam lifetime and injection efficiency in a storage ring dramatically if they are not compensated for. The neutralisation of the induced multipoles from an EPU is not trivial.

## 5.10. Appendix C: Influence from the insertion devices on the magnetic optics of the storage ring

### 5.10.1. Beam deflection

The insertion devices will be equipped with a set of air coils for each insertion device that will compensate for varying field integrals, which will deflect the beam, with gap of the insertion device. Feed forward tables for the air coils will be established during measurements with stored beam in the storage ring.

### 5.10.2. Simple approximations for focusing effect from planar field insertion devices

The main effect on the stored beam of flat field insertion devices is a vertical focusing effect. This focusing effect is inversely proportional to the square of the energy of the stored beam and is hence more pronounced in low energy storage rings.

The strength of the vertical focusing  $K_z$  is [22]

$$K_z = \frac{1}{2\rho^2} \quad (5.46)$$

where  $\rho$  is the radius of curvature in the field  $B_0$ , which is given by the relation  $\rho = E/(ceB_0) \approx E [\text{GeV}] / (0.3 B_0 [\text{T}])$ . The focusing effect is independent of the period length  $\lambda_0$ . The vertical focusing acts like a lens with the focal length  $F_z$  given by

$$\frac{1}{F_z} = LK_z = \frac{L}{2\rho^2} \quad (5.47)$$

where  $L$  is the total length of the insertion device. The (linear) vertical tune shifts induced is given by

$$\Delta\nu_z = \frac{\langle\beta_z\rangle L}{8\pi\rho^2} \quad (5.48)$$

The tune shift is directly proportional to the average vertical beta function,  $\langle\beta_z\rangle$ , at the wiggler. Hence the tune shift can be limited by providing a small  $\beta_z$  at the insertion device. The vertical focusing will, if it is not compensated for, distort the vertical beta function like

$$\left[ \frac{\Delta\beta_z}{\beta_z} \right] = \frac{\langle\beta_z\rangle L}{4\rho^2 \sin(2\pi\nu_z)} \quad (5.49)$$

The vertical focusing varies with the vertical aperture, i.e. it is nonlinear, and this gives rise to an amplitude dependent tune shift which might reduce the dynamic aperture of the storage ring. The tune shift with amplitude, which depends on the period length, is given by

$$\frac{d\Delta\nu_z}{dJ_z} = \frac{\pi\langle\beta_z^2\rangle L}{4\lambda_0^2\rho^2} \quad (5.50)$$

where  $J_z$  is the vertical action angle variable. Also in this case the effect of the nonlinear vertical focusing is reduced by reducing the beta function.

An undulator also has a transverse field roll-off varying with the horizontal position out from the undulator axis. This transverse field roll gives rise to a horizontal defocusing of the stored electron beam and give a change of the horizontal tune of the storage ring. The horizontal defocusing effect is in general low compared to the vertical focusing effect of the undulator.

The simple approximation described above is a somewhat poor approximation of the effect on the stored beam, especially for other insertion devices than flat field insertion devices with a negligible field roll off.

### 5.10.3. Focusing potential and kick maps for arbitrary types of periodic insertion devices

A better way to estimate the effect of an insertion device on the beam optics and dynamic aperture of a storage ring is to use the concept with kick-maps in the tracking calculations [23]. The kick-map describes the kick an electron would get when passing the undulator and the kick-map covers the full horizontal and vertical aperture of the insertion device.

The kick map is calculated from the potential function  $U(x, z)$ , which for a periodic insertion device with length  $L$  aligned to the longitudinal axis  $\hat{s}$  is given by

$$U(x, z) = L \int_{1 \text{ period}} \left[ \int_{-\infty}^s B_x(x, s', z) ds' \right]^2 + \left[ \int_{-\infty}^s B_z(x, s', z) ds' \right]^2 ds \quad (5.51)$$

In principle this an integration of the square of the angular deviation of the beam path over one undulator period.

The horizontal  $\Delta x'$  and the vertical  $\Delta z'$  angular kicks the electrons will get when the beam is passing through the undulator is then given by

$$\begin{aligned} \Delta x' &= - \left( \frac{e}{\gamma m_e c} \right)^2 \frac{1}{2} \frac{\partial U}{\partial x} \\ \Delta z' &= - \left( \frac{e}{\gamma m_e c} \right)^2 \frac{1}{2} \frac{\partial U}{\partial z} \end{aligned} \quad (5.52)$$

For tracking studies it is convenient to use kick maps where the energy dependent factor  $(e/(\gamma m_e c))^2$  has been omitted. A useful approximation is  $e/(\gamma m_e c) \approx 0.3/E [\text{GeV}]$ .

The kick maps with the unit  $\text{T}^2\text{m}^2$  can then be included in the line of elements in the tracking lattice and be used as a drift-kick-drift element.

The vertical and horizontal focusing/defocusing effects make the undulator works like a magnetic lens for the stored beam and the focal lengths of the insertion device is given by

$$\begin{aligned} \frac{1}{F_x} &= - \frac{\partial \Delta x'}{\partial x} = \left( \frac{e}{\gamma m_e c} \right)^2 \frac{1}{2} \frac{\partial^2 U}{\partial x^2} \\ \frac{1}{F_z} &= - \frac{\partial \Delta z'}{\partial z} = \left( \frac{e}{\gamma m_e c} \right)^2 \frac{1}{2} \frac{\partial^2 U}{\partial z^2} \end{aligned} \quad (5.53)$$

The tune shifts of the storage ring can be calculated from the focusing potential by using

$$\begin{aligned}\Delta\nu_x &= \frac{1}{4\pi} \frac{\langle\beta_x\rangle}{F_x} \\ \Delta\nu_z &= \frac{1}{4\pi} \frac{\langle\beta_z\rangle}{F_z}\end{aligned}\tag{5.54}$$

#### 5.10.4. Other methods

Instead of kick maps it is also possible to describe the influence from the insertion devices in a symplectic way with generating functions and include the generating function at the tracking calculations, as described in [24]. It is also possible to model the insertion device as a hamiltonian and use symplectic integration at the tracking calculations, as described in [25].

## 5.11. Appendix D: Influence from the insertion devices on the emittance and energy spread of the stored beam

The distribution of the electrons in an electron storage and the emittance will be determined by an equilibrium determined by the excitation, given by quantum excitation and intrabeam scattering (IBS), and the damping given by the emitted synchrotron radiation. The electron beam injected into the storage will after a damping time of typically 10-15 ms reach the equilibrium distribution.

### 5.11.1. Synchrotron radiation integrals, momentum compaction, emittance, and energy spread

The synchrotron radiation integrals,  $I_1 - I_5$ , determine the damping and quantum excitation. In the MAX IV 3 GeV ring the vertical emittance will be put by artificial means, e.g. a skew quadrupole, to a fixed value of 8 pmrad as explained in [1], where also the bare lattice emittance and energy spread of the MAX IV 3 GeV ring are given. It is hence only the horizontal emittance and the energy spread that are of interest here and the vertical part of the synchrotron radiation integrals can be neglected.

The synchrotron integrals, neglecting the vertical part, are [26]

$$I_1 = \int_0^C \frac{D_x}{\rho} ds \quad (5.55)$$

$$I_2 = \int_0^C \frac{1}{\rho^2} ds \quad (5.56)$$

$$I_3 = \int_0^C \frac{1}{|\rho^3|} ds \quad (5.57)$$

$$I_{4,x} = \int_0^C \frac{D_x(1 + 2\rho^2 k)}{\rho^3} ds \quad (5.58)$$

$$I_{5,x} = \int_0^C \frac{\mathcal{H}_x}{|\rho^3|} ds \quad (5.59)$$

where  $C$  is the circumference of the ring,  $D_x$  is the horizontal dispersion,  $\rho$  is the bending radius,  $k$  is the quadrupole strength of the magnets, and  $\mathcal{H}_x$  is given by

$$\mathcal{H}_x = \frac{1}{\beta_x} (D_x^2 + (\beta_x D'_x - \frac{1}{2} \beta'_x D_x)^2) \quad (5.60)$$

The radiation integrals for the lattice of the 528 m circumference 3 GeV storage ring without insertion devices are computed by the software packages [27, 28] used for designing the storage ring and the radiation integrals are:

$$\begin{aligned}
 I_{1,0} &= 0.1621534257 \\
 I_{2,0} &= 0.3157347208 \\
 I_{3,0} &= 0.01613875828 \\
 I_{4,x0} &= -0.2719069455 \\
 I_{5,x0} &= 1.448995144 \times 10^{-5}
 \end{aligned} \tag{5.61}$$

The momentum compaction  $\alpha$  is given by

$$\alpha = \frac{I_1}{C} \tag{5.62}$$

The energy loss per turn  $U_0$  is given by

$$U_0 = \frac{2}{3} r_e \frac{E^4}{(mc^2)^3} I_2 \tag{5.63}$$

where  $r_e$  is the classical electron radius,  $m$  is the electron mass, and  $E$  is the energy of the stored beam.

The horizontal electron beam emittance neglecting IBS,  $\epsilon_x$ , is given by

$$\epsilon_x = C_q \gamma^2 \frac{I_{5,x}}{I_2 - I_{4,x}} \tag{5.64}$$

where  $C_q$  is the quantum excitation constant defined by

$$C_q = \frac{55}{32\sqrt{3}} \frac{\hbar c}{m_e c^2} = 3.8319 \times 10^{-13} \text{m} \tag{5.65}$$

The energy spread neglecting IBS,  $\sigma_e$  is given by

$$\sigma_e^2 = C_q \gamma^2 \frac{I_3}{2I_2 + I_{4,x}} \tag{5.66}$$

### 5.11.2. Influence from insertion devices on the synchrotron radiation integrals, momentum compaction, emittance, and energy spread

What we are interested in here is the change of the horizontal emittance and the energy spread that is introduced by the insertion devices. The change of emittance and energy spread from the insertion devices are given by the relative change of the radiation integrals  $\Delta I_2, \Delta I_3, \Delta I_{4,x}, \Delta I_{5,x}$  by the relations [29]

$$\epsilon_{x,ID} = \epsilon_{x,0} \frac{1 + \Delta I_{5,x}/I_{5,x0}}{1 + (\Delta I_2 - \Delta I_{4,x})/(I_{2,0} - I_{4,x0})} \tag{5.67}$$

$$\sigma_{e,ID}^2 = \sigma_{e0}^2 \frac{1 + \Delta I_3/I_{3,0}}{1 + (2\Delta I_2 + \Delta I_{4,x})/(2I_{2,0} + I_{4,x0})} \tag{5.68}$$

The insertion devices are assumed to be installed in dispersion free straight sections and to have a sinusoidal field. The  $1/\rho$  factor for a sinusoidal field is

$$\frac{1}{\rho} = \frac{1}{\rho_0} \sin\left(\frac{2\pi s}{\lambda_0}\right) \tag{5.69}$$



where  $\rho_0$  is the bending radius at the undulator peak field, which is 8 m for a 1.25 T peak field in a 3 GeV storage ring, and  $\lambda_0$  is the undulator period length.  $D_x$  and  $D'_x$  in the undulator are the given by

$$D_x(s) = \frac{\lambda_0^2}{4\pi^2\rho_0} \sin\left(\frac{2\pi s}{\lambda_0}\right) \quad (5.70)$$

$$D'_x(s) = \frac{\lambda_0}{2\pi\rho_0} \cos\left(\frac{2\pi s}{\lambda_0}\right) \quad (5.71)$$

The integral  $I_{1,x}$  along the undulator length  $L$ , which will change the momentum compaction factor of the machine, is given by

$$\Delta I_{1,x} = \frac{L\lambda_0^2}{8\pi^2\rho_0^2} \quad (5.72)$$

The integral  $I_{2,x}$  along the undulator length  $L$ , which will change the amount of emitted synchrotron radiation, is given by

$$\Delta I_{2,x} = \frac{L}{2\rho_0^2} \quad (5.73)$$

The integral  $I_{3,x}$  along the undulator length  $L$ , which affects the energy spread, is given by

$$\Delta I_{3,x} = \frac{4L}{3\pi\rho_0^3} \quad (5.74)$$

The integral  $I_{4,x}$  along the undulator length will be a very small number compared to  $I_2$  along the undulator and the influence from  $I_{4,x}$  on the emittance, energy spread, and damping time change from IDs can be neglected.

Since  $\mathcal{H}_x$  in the  $I_{5,x}$  integral is dominated by the term  $\beta_x D'_x$  over the length  $L$  of the insertion device,  $\Delta I_{5,x}$  may be approximated by

$$\Delta I_{5,x} \approx \int_{-L/2}^{L/2} \beta_x \frac{D'_x(s)^2}{|\rho^3|} ds \approx \hat{\beta}_x \int_{-L/2}^{L/2} \frac{D'_x(s)^2}{|\rho^3|} \quad (5.75)$$

where  $\hat{\beta}_x$  is the average horizontal beta function in the insertion device. The relation

$$\frac{D'_x(s)^2}{|\rho^3|} = \frac{\lambda_0^2}{4\pi^2\rho_0^5} \cos^2\left(\frac{2\pi s}{\lambda_0}\right) \left| \sin^3\left(\frac{2\pi s}{\lambda_0}\right) \right| \quad (5.76)$$

makes it possible to get a finite number for  $\Delta I_{5,x}$ , which is

$$\Delta I_{5,x} \approx \hat{\beta}_x \frac{L\lambda_0^2}{15\pi^3\rho_0^5} \quad (5.77)$$

The beam is also excited by intrabeam scattering (IBS). A review of ways of calculating IBS can be found in [30]. From studying [30], it seems like the excitation due to IBS in the longitudinal and transverse directions follows the same scaling laws when installing IDs as the quantum excitation disregarding IBS. The exact relations for the IBS excitation requires further studies, which will be carried out in future versions of this report.

The influence from the installed IDs on the momentum compaction  $\alpha_0$ , emittance  $\varepsilon_{x,0}$ , and energy spread  $\sigma_{e0}$ , calculated with or without an IBS contribution, of the lattice without insertion devices are hence given by

$$\frac{\alpha_{ID}}{\alpha_0} = 1 + \frac{L \frac{\lambda_0^2}{8\pi^2 \rho_0^2}}{I_{1,0}} \quad (5.78)$$

$$\frac{\varepsilon_{x,ID}}{\varepsilon_{x,0}} \approx \frac{1 + (\hat{\beta}_x \frac{L \lambda_0^2}{15\pi^3 \rho_0^5}) / I_{5,x0}}{1 + (\frac{L}{2\rho_0^2}) / (I_{2,0} - I_{4,x0})} \quad (5.79)$$

$$\frac{\sigma_{eID}}{\sigma_{e0}} \approx \sqrt{\frac{1 + (\frac{4L}{3\pi\rho_0^3}) / I_{3,0}}{1 + (\frac{L}{\rho_0^2}) / (2I_{2,0} + I_{4,x0})}} \quad (5.80)$$

## 5.12. Appendix E: Beam loading of the radio frequency system from insertion devices

### 5.12.1. The network model of an RF system

The interaction between the radio frequency (RF) generator, cavity and beam is well described in [31] and this text is a short summary of the relations found in [31].

The accelerating cavity in an accelerator can be described by a parallel resonant circuit network model which is driven by an external rf-current current source  $I_g$  from a generator and the currents of the particle beam  $I_b$ . Figure 5.617 shows the network model.  $\beta$  is the coupling factor between the generator and cavity.

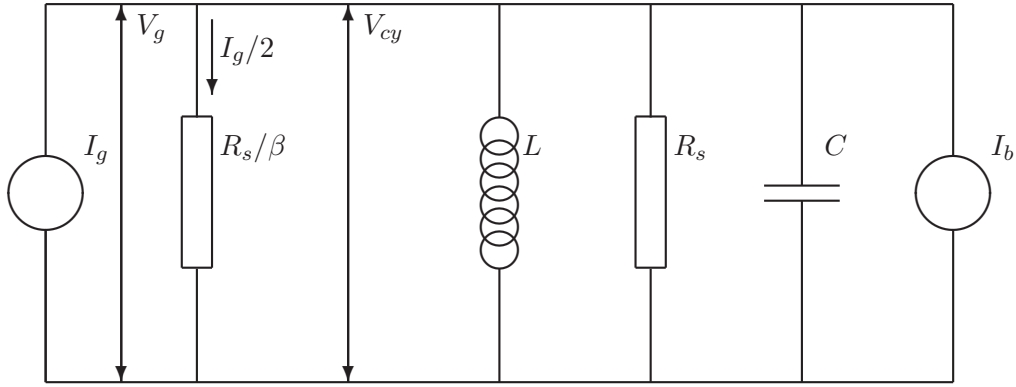


Figure 5.617: The network model of an accelerator cavity and the RF-generator

The resonance frequency  $\omega_r$  of the system is given the inductance  $L$  and capacitance  $C$ .

$$\omega_r = \frac{1}{\sqrt{LC}} \quad (5.81)$$

The losses in the cavity  $P_{cy}$ , the cavity peak field  $V_{cy}$  and the shunt impedance of the cavity  $R_s$  are related like

$$P_{cy} = \frac{V_{cy}^2}{2R_s} \quad (5.82)$$

The beam induced voltage at the cavity  $V_{br}$  at resonance by a beam with current  $I_b$  is given by

$$V_{br} = \frac{2I_b R_s}{1 + \beta} \quad (5.83)$$

The generator induced voltage at the cavity  $V_{gr}$  at resonance is given by

$$V_{gr} = \frac{2\sqrt{2\beta}}{1 + \beta} \sqrt{R_s P_g} \quad (5.84)$$

The losses  $U_0$ , measured in volts, during one turn of the electrons in the storage ring, gives the synchronous phase  $\psi_s$

$$\psi_s = \arcsin \frac{U_0}{V_{cy}} \quad (5.85)$$

The cavity is in normal operation not at resonance but it is side tuned to a slightly lower frequency than the resonance frequency, which gives a capacitance loaded system. Off resonance,

the generator voltage and current are no more in phase. The phase difference can be derived from the complex impedance  $Z$  of the network, which is the same seen from the generator as seen from the beam

$$\frac{1}{Z} = \frac{1 + \beta}{R_s} + i\omega C + \frac{1}{i\omega L} \quad (5.86)$$

The cavity detuning angle  $\psi$  and the generator angle  $\psi_g$  = at perfect phase matching, i.e. when the cavity and generator are in phase are given by

$$\psi = \arctan\left(\frac{V_{br}}{V_{cy}} \cos \psi_s\right) \quad (5.87)$$

$$\psi_g = \frac{\pi}{2} - \psi_s \quad (5.88)$$

The generator induced voltage  $V_g$  and the beam induced voltage  $V_b$  at the cavity are given by

$$V_g = V_{gr} \cos(\psi) e^{i\psi} \quad (5.89)$$

$$V_b = -V_{br} \cos(\psi) e^{i\psi} \quad (5.90)$$

The required power from the generator  $P_g$  is given by

$$P_g = \frac{(1 + \beta)^2}{8\beta R_S} |V_{gr}|^2 \quad (5.91)$$

The coupling factor  $\beta$  gives optimum coupling between the generator and the cavity for one specific beam loading situation only and in other situations there will be a reflected power  $P_r$  from the cavity given by.

$$P_r = P_g - P_{cy} - U_0 I_b \quad (5.92)$$

### 5.12.2. The phasor diagram for the RF system of the MAX IV 3 GeV ring a typical running situation

The complex vectors of  $V_b$ ,  $V_g$ , and  $V_{cy}$  can be shown in a phasor diagram. Figure 5.618 shows the phasor diagram for typical running situation for the MAX IV 3 GeV storage ring. The RF power levels for the same situation are given in Table 5.96. At the MAX IV 3 GeV storage ring, the coupling factor  $\beta$  will be fixed to 4 and there will be 6 cavities giving a total  $R_S$  of 10.5 MOhm and a total  $V_{cy}$  of 1.5 MV [32]. The energy loss per turn for the electrons with 4 wigglers installed is typically 570 keV.

Table 5.96: RF power distribution at a typical running situation

$P_g$	392.92	kW
$P_{cy}$	107.14	kW
$P_b$	285.00	kW
$P_r$	0.77	kW

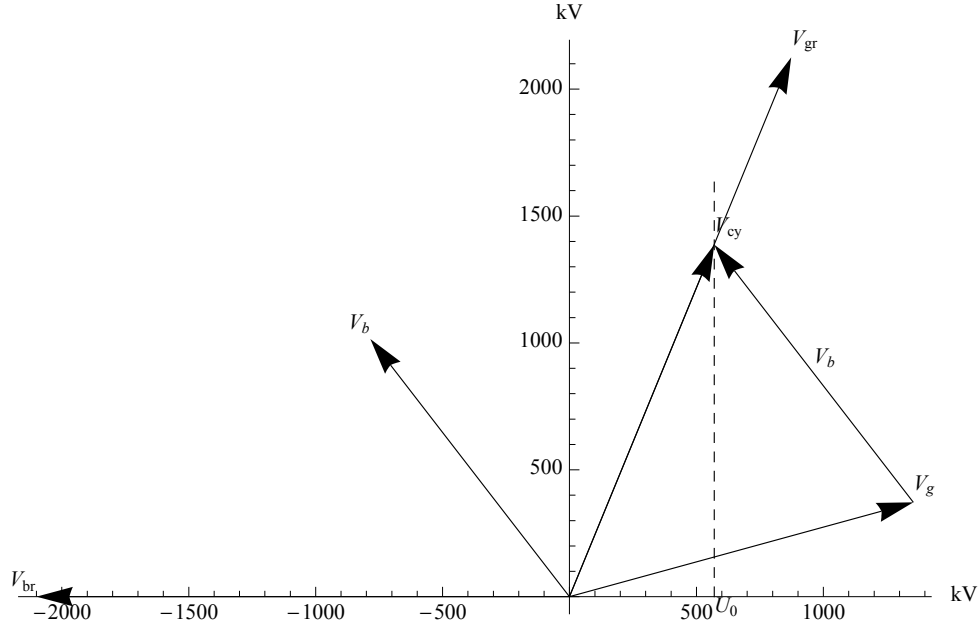


Figure 5.618: Phasor diagram for the beam-cavity-generator interaction in a typical running situation at the MAX IV 3 GeV storage ring

### 5.12.3. RF acceptance

The RF momentum acceptance  $\delta_{rf}$  of the system, which gives the maximum energy deviation for the electrons to stay within the RF-bucket, is given by

$$\delta_{rf} = \sqrt{\frac{V_{cy} \cos \psi_s}{\pi h |\gamma^{-2} - \alpha_c| E_0}} \sqrt{2 - (\pi - 2\psi_s) \tan \psi_s} \quad (5.93)$$

where  $\gamma$  is the relativistic factor of the beam with beam energy  $E_0$ ,  $\alpha_c$  is the momentum compaction, and  $h$  is the harmonic number of the ring. For the MAX IV 3 GeV storage ring  $h=176$ ,  $\gamma = 5871$ ,  $E_0 = 3 \times 10^9$  eV, and  $\alpha_c$  is varying with the number of IDs but it is in the region of  $3.07 \times 10^{-4}$ .

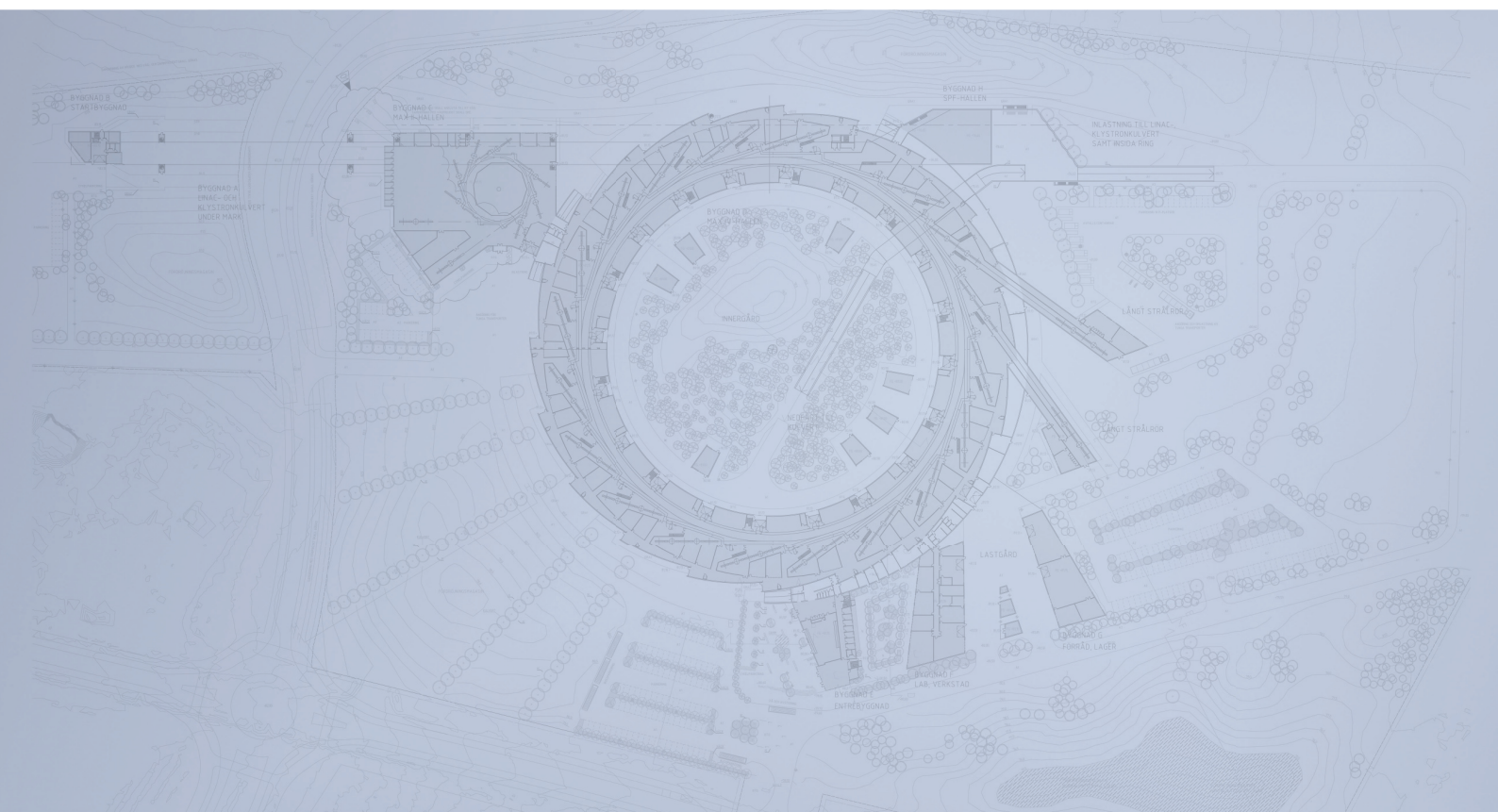
# Bibliography

---

- [1] S. C. Leemann, Å. Andersson, M. Eriksson, L.-J. Lindgren, E. Wallén, J. Bengtsson, and A. Streun. Beam dynamics for the MAX IV 3 GeV storage ring. *Phys. Rev. ST Accel. Beams*, 12:120701, 2009.
- [2] O. Chubar, P. Elleaume and J. Chavanne. *Journal of Synchrotron Radiation*, 5:481, 1998.
- [3] E. Wallén, J. Chavanne and P. Elleaume. Magnetic calculations of a superconducting undulator at the ESRF. *Nucl. Instr. And Meth. A.*, 541:630–650, 2005.
- [4] Summary of NSLS-II Source Properties, User Workshop July 17-18, 2007. <http://www.bnl.gov/nsls2/project/>.
- [5] R. Hettel, et al. CONCEPTS FOR THE PEP-X LIGHT SOURCE. *Proceedings of PAC09, Vancouver, BC, Canada*, page WE5RFP015, 2009.
- [6] K. Bane, et al. PEP-X Light Source at SLAC, Status Report, Revision 0, June 10, 2008.
- [7] K. Balewski, W. Brefeld, W. Decking, H. Franz, R. Rohlsberger, and E. Weckert. PETRAIII: A Low Emittance Synchrotron Radiation Source, Technical Design Report, February 29, 2004.
- [8] <http://www.als.lbl.gov/als/techspecs/insertdev.html>. ALS Photon Source Parameters.
- [9] <http://www.diamond.ac.uk/Home/Technology/Parameter.html>.
- [10] Reference and information should be updated.
- [11] <http://www.synchrotron-soleil.fr/>.
- [12] M. Sjöström, H. Tarawneh, E. Wallén, and M. Eriksson. Characterisation of the MAX II storage ring lattice. *Nucl. Instr. And Meth. A.*, 577:425D436, 2007.
- [13] MAX IV Detailed Design Report. In preparation. <http://www.maxlab.lu.se/maxlab/max4/index.html>.
- [14] O. Chubar and P. Elleaume. Accurate and efficient computation of synchrotron radiation in the near field region. *Proceedings of EPAC 1998*, pages 1177–1179, 1998.
- [15] T. Tanaka and H. Kitamura. SPECTRA: a synchrotron radiation calculation code. *Journal of Synchrotron Radiation*, 8:1221–1228, 2001.
- [16] J. D. Jackson. *Classical Electron Dynamics*, ISBN 0-471-30932-X.
- [17] H. Onuki and P. Elleaume. *Undulators, Wiggler and Their Applications*, ISBN 0-415-28040-0.
- [18] O. Chubar. *Rev. Sci. Instr.*, 66:1872–1874, 1995.
- [19] W. Joho. Radiation properties of an undulator, SLS-Note 4/95 (July 1995, rev. April 1996).

- [20] David Attwood. *Soft x-rays and extreme ultraviolet radiation, principles and applications*, Cambridge University Press 1999, ISBN 0 521 65214 6.
- [21] K. Ingvar Blomqvist. Magnetic Design of Two Elliptically Polarizing Undulators for the APRES Beam Line at the Canadian Light Source. October 15, 2006.
- [22] A. Ropert. *Cern Accelerator School proceedings CAS 98-04*, page 116.
- [23] P. Elleaume. A New Approach to the Electron Beam Dynamics in Undulators and Wigglers. *Proceedings of EPAC 92, Berlin*, pages 661–663, 1992.
- [24] J. Bhardt, M. Scheer, and G. Wustefeldt. Beam dynamics simulation tools for insertion devices at BESSY II. *Wiggler 2005 mini-workshop, LNF Frascati, Italy*, 2005.
- [25] Y. Wu, V. N. Litvinenko, and J. M. J. Madey. Lattice and dynamic aperture of the Duke FEL storage ring. *Proceedings of PAC 1993*, pages 218–220, 2005.
- [26] A. Chao, and M. Tigner. Construction of a Cryogenic Permanent Magnet Undulator at the ESRF.
- [27] OPA Lattice Design Code. <http://slsbd.psi.ch/~streun/opa/>.
- [28] J. Bengtsson. Tracy-2 User’s Manual. unpublished.
- [29] James A. Clark. The science and technology of undulators and wigglers, Oxford publishing, ISBN13: 9780198508557.
- [30] Kiyoshi Kubo, Sekazi K. Mtingwa, and Andrzej Wolski. Intrabeam scattering formulas for high energy beams. *Phys. Rev. ST Accel. Beams*, 8:081001, 2005.
- [31] Helmut Widemann. *Particle Accelerator Physics*, Third Edition, ISBN-13 978-3-540-49043-2 3rd ed. Springer Berlin Heidelberg New York, Chapter 16, pp.577-598.
- [32] Private communication with Å. Andersson September 14, 2009.

# Detailed Design Report



## Chapter 6 Stability and Tolerances

MAX IV Facility





## 6. Stability and Tolerances

---

<b>6.0</b>	<b>Stability and Tolerances (Vibrations, Settlements and Alignment)....</b>	<b>2</b>
<b>6.1.</b>	<b>Overall Stability Criteria .....</b>	<b>3</b>
6.1.1.	Dealing with Stability and Tolerances throughout this Report.....	3
6.1.2.	e-Beam Design Values .....	4
6.1.3.	e-Beam Position and Stability .....	5
<b>6.2.</b>	<b>Vibration Conventions .....</b>	<b>7</b>
6.2.1.	Tolerance Conventions and Basic Relations .....	7
<b>6.3.</b>	<b>Vibration Tolerances .....</b>	<b>10</b>
6.3.1.	Beamline Tolerances .....	10
6.3.2.	Accelerator Tolerances .....	11
6.3.3.	Summarizing Tolerances.....	15
<b>6.4.</b>	<b>Vibration Measurements .....</b>	<b>16</b>
6.4.1.	Early Measurements.....	16
6.4.2.	NGI Measurements .....	17
6.4.3.	Traffic .....	19
6.4.4.	Detailed Investigation PEAB/MAX-lab .....	20
<b>6.5.</b>	<b>Vibration Management .....</b>	<b>21</b>
6.5.1.	Passive Damping and Isolation .....	21
6.5.2.	Active Damping of Mechanical Vibrations.....	22
6.5.3.	Orbit Feedback.....	23
6.5.4.	Sources for Vibrations .....	25
6.5.5.	Civil Engineering.....	26
6.5.6.	Ring Girders .....	30
6.5.7.	Other Mechanical Structures .....	35
6.5.8.	Conclusions, Recommendations, Pointing at Solutions.....	35
<b>6.6.</b>	<b>Alignment, Positional Tolerances .....</b>	<b>36</b>
6.6.1.	MAX IV Rings .....	36
6.6.2.	Linac and e-beam Transport.....	36
6.6.3.	Beamlines .....	36
<b>6.7.</b>	<b>Conclusions .....</b>	<b>37</b>
<b>6.8.</b>	<b>References .....</b>	<b>38</b>



# MAX IV Facility



## 6.0. Stability and Tolerances (Vibrations, Settlements and Alignment)

---

In order to ensure that the facility will perform as expected in a cost effective way a lot of care has to be put into both

- Finding the proper tolerances
- Achieving these goals the proper way

This chapter deals with structural tolerances – both regarding alignment and stability. “Stability” covers vibrations, long term settlements and also thermal stability. Some issues are dealt with in other sections of this report.

Ground vibrations will displace the focusing magnets in a storage ring. These vibrations might be amplified by the magnet girders. The magnet lattice parameters define the amplification factor giving the displacement of the electron beam for a given magnet displacement. Also beamline components are affected by vibrations. In general it is possible to write down specifications for how much magnets or optical components are allowed to move, however there is no lower limit where one can say it is good enough, since less vibrations are always better. This is partly because new emerging technical possibilities will put even harder demands on stability.

**Because of the unknown future demands it is recommended that the present vibration level at the “green field” should not be significantly increased.**

Long term stability affected by settlements or thermal drift is a crucial task, especially in the first time phases for the facility. It might take a long time before the site gets into equilibrium. There is even a risk of periodic drift with seasons.

The list of mechanisms contributing to the amount of vibrations of ring and beamline components is long. All fields have to be analyzed and addressed. For beamline components even acoustic noise needs to be addressed.

The alignment of ring and beamline components is an important task to deal with since it also affects the performance.





# MAX IV Facility





## 6.1. Overall Stability Criteria

---

As starting point for writing down tolerances a quality analysis of our “product” (well defined photon beams) is needed. What does quality mean for the user? Some of the parameters are

- Continuous availability (no unplanned beam losses)
- Reached Design values
  - Resolving power
  - Flux
  - Polarization
  - Speed of systems (undulator, monochromator etc.)
- Stability
  - Flux
  - Position of light source
  - Direction of light beam
  - Source position (x,y,z)

Several parameters are interconnected and can be boiled down to a few machine parameters.

### 6.1.1. Dealing with Stability and Tolerances throughout this Report

The following table points at sections in the DDR where stability and tolerances are discussed.

<b>Ch1</b>		
<b>Ch2</b>		2.4. Lattice Errors and Correction 2.9. Diagnostics
<b>Ch3</b>		3.4. Lattice Errors and Correction 3.9. Diagnostics
<b>Ch4</b>		
<b>Ch5</b>		
<b>Ch6</b>	Vibration, General Comments Alignment, General Comments	6.5. Vibration Management, 6.6. Alignment, Positional Tolerances

Table 6.1: Switchboard to other chapters.

### 6.1.2. e-Beam Design Values

The electron beam performance parameters are directly connected to the achievable performance for the beamlines. Several of the first beamlines are designed for top performance and are thus taking advantage of the planned e-beam properties. Therefore it will have consequences if the design values are not met. Table values are chosen for the most demanding operation mode. An asterisk indicates at the center of the ID.

<b>MAX IV, 3 GeV</b>  <b>Damping wigglers included</b>	$\beta_x^*$	9 m
	$\beta_y^*$	4.8 m
	$\epsilon_x$	$\sim 300$ pm rad (includes damping wigglers, Landau cavities, and IBS)
	$\epsilon_y$	$\sim 8$ pm rad ( $1\text{\AA}$ diffraction limit, i.e. coupling 2.7 %)
	$\sigma_x^*$	$52\text{ }\mu\text{m}$ ( $\sigma_x'^* = 5.8\text{ }\mu\text{rad}$ )
	$\sigma_y^*$	$6\text{ }\mu\text{m}$ ( $\sigma_y'^* = 1.3\text{ }\mu\text{rad}$ )
<b>MAX IV, 3 GeV</b>  <b>Strong ID</b>	$\beta_x^*$	9 m
	$\beta_y^*$	$\geq 1$ m
	$\epsilon_x$	$\sim 3$ pm rad (includes damping wigglers, Landau cavities, and IBS)
	$\epsilon_y$	$300$ pm rad (includes damping wigglers, Landau cavities, and IBS), coupling 1 %
	$\sigma_x^*$	$52\text{ }\mu\text{m}$ ( $\sigma_x'^* = 5.8\text{ }\mu\text{rad}$ )
	$\sigma_y^*$	$2\text{ }\mu\text{m}$ ( $\sigma_y'^* = 1.7\text{ }\mu\text{rad}$ )
<b>MAX IV, 1.5 GeV</b>	$\beta_x^*$	5.66 m
	$\beta_y^*$	2.85 m
	$\epsilon_x$	6 nm rad (bare lattice)
	$\epsilon_y$ (1% coupling)	60 pm rad
	$\sigma_x^*$	$184\text{ }\mu\text{m}$ ( $\sigma_x'^* = 33\text{ }\mu\text{rad}$ )
	$\sigma_y^*$	$13\text{ }\mu\text{m}$ ( $\sigma_y'^* = 4.6\text{ }\mu\text{rad}$ )

Table 6.2: Design values.

The design values give a base for setting several tolerances.

### 6.1.3. e-Beam Position and Stability

The electron beam is the source for the beamlines. Fluctuations in the e-beam position will degrade the performance. If fluctuations in the e-beam are much smaller than the beam itself, it will not be noticed by the beamline. A tolerance for the fluctuations of 10 % RMS of the beam size seems reasonable.

Stability criterion rms	$\Delta y$
3 GeV	<200 nm, the lowest possible limit
1.5 GeV	<1.3 $\mu\text{m}$

Table 6.3: Vertical stability criterion.

Even if the electron beam is fulfilling this tolerance there could be problems for certain beamlines. For instance the infrared beamlines use Fourier interferometry which is very sensitive to harmonic fluctuations. Therefore the harmonic distribution of the fluctuations can be an issue. For IR the source size is far below the diffraction limit so in this case there is no problem.

Angular stability of the light is important as well for beamlines. Also here one can set a goal being a fraction of the angular distribution of a typical undulator photon beam. One problem with angular deviation is that sometimes it is necessary to baffle in on the beam. If the beam is then slowly varying in angle, the result is a variation in the flux on the sample. The tolerances from beamlines are not calculated so far. Here is a rough estimate of what should be possible to obtain from the rings.

Assuming an estimated sensitivity for the BPM heads of

Sensitivity rms	3 GeV ring	1.5 GeV ring
Vertical	200 nm	300 nm
Horizontal	300 nm	500 nm

Table 6.4: Assumed BPM sensitivity.

The vertical angular stability of an undulator beam from the 3 GeV ring is calculated to be

$$\frac{200\text{mm} \cdot \sqrt{2}}{4\text{m}} = 70\text{nrad}$$

rms. Using this method the expected stability is for both rings:

Angular stability rms	3 GeV ring	1.5 GeV ring
Vertical	70 nrad	140 nrad
Horizontal	110 nrad	240 nrad

Table 6.5 Expected angular stability.

The problem for beamlines regarding flux through apertures is generally on a very long time base, seconds. Fast fluctuations will often not be noticed as flux fluctuations. When doing long photon energy scan a fluctuation with a period length of several seconds will be disturbing if the flux varies with 1 % or so. More work has to be done in this area.

# MAX IV Facility



## 6.2. Vibration Conventions

---

This section describes some aspects on how to treat and present vibration data.

### 6.2.1. Tolerance Conventions and Basic Relations

When setting tolerances the first thing to do is to choose units. For beamlines one important number is the transverse stability of the electron beam. This is pointing at using position [m] as unit.

There are other ways to do this, for example manufacturers of sensitive equipment it is often chosen to use rms velocity (1) (2).

Criterion	RMS speed [ $\mu\text{m/s}$ ], measured in 1/3-octave band	Description of Use
<b>VC-A</b>	50	Adequate in most instances for optical microscopes to 400X, microbalances, optical balances, proximity and projection aligners, etc.
<b>VC-B</b>	25	Appropriate for optical microscopes to 1000X, inspection and lithography equipment including steppers) to 3 $\mu\text{m}$ line widths.
<b>VC-C</b>	12.5	A good standard for most lithography and inspection equipment (including electron microscopes) to 1 $\mu\text{m}$ detail size.
<b>VC-D</b>	6	Suitable in most instances for the most demanding equipment, including electron microscopes (TEMs and SEMs) and E-Beam systems, operating to the limits of their capability.
<b>VC-E</b>	3	A difficult criterion to achieve in most instances. Assumed to be adequate for the most demanding of sensitive systems, including long-path, laser-based small target systems, and other systems requiring extraordinary dynamic stability.

Table 6.6: Industry used Vibration Criterion (VC-) system.



It turns out that a lot of devices, that are vibration sensitive, have a flat floor in their tolerances measured in speed. This is the explanation for the choice. The criteria are set from the manufacturers based on measurements with the device positioned on a table where vibrations can be added and controlled.

There is a difference from being a lab floor, supporting a device, to long structures like an accelerator or a beamline, where the floor is actually a structural part of the device. Therefore the Vibration Criterion (VC-) system is not very suitable for the MAX IV facility.

The shutter time or measurement time in the experiments is generally not so short that the frequency of the oscillations matters. Vibrations of the source with frequencies more than 1 Hz will generally make the source look larger.

Due to the integration factor when going from speed to translation,  $1/f2\pi$ , a constant speed criterion is not strict enough in the low frequency region. Instead we use displacement as described below.

The spectral distribution of the vibration amplitudes are given by the Fourier transform of the time-dependent vibrations:

$$Y(f) = \int_{-T/2}^{T/2} y(t) e^{-2\pi i f t} dt$$

The power spectral distribution (PSD) is given by

$$S_y(f) = 2 \lim_{T \rightarrow \infty} \frac{1}{T} [Y(f)]^2$$

The PSD RMS displacement can then be calculated as

$$Y_{RMS}(f_1, f_2) = \sqrt{\int_{f_1}^{f_2} S_y(f) df}$$

This method is better when visualizing the results from vibration measurements. Since the translation amplitudes at high frequencies are smaller it is informative to integrate from high frequencies downwards.

# MAX IV Facility



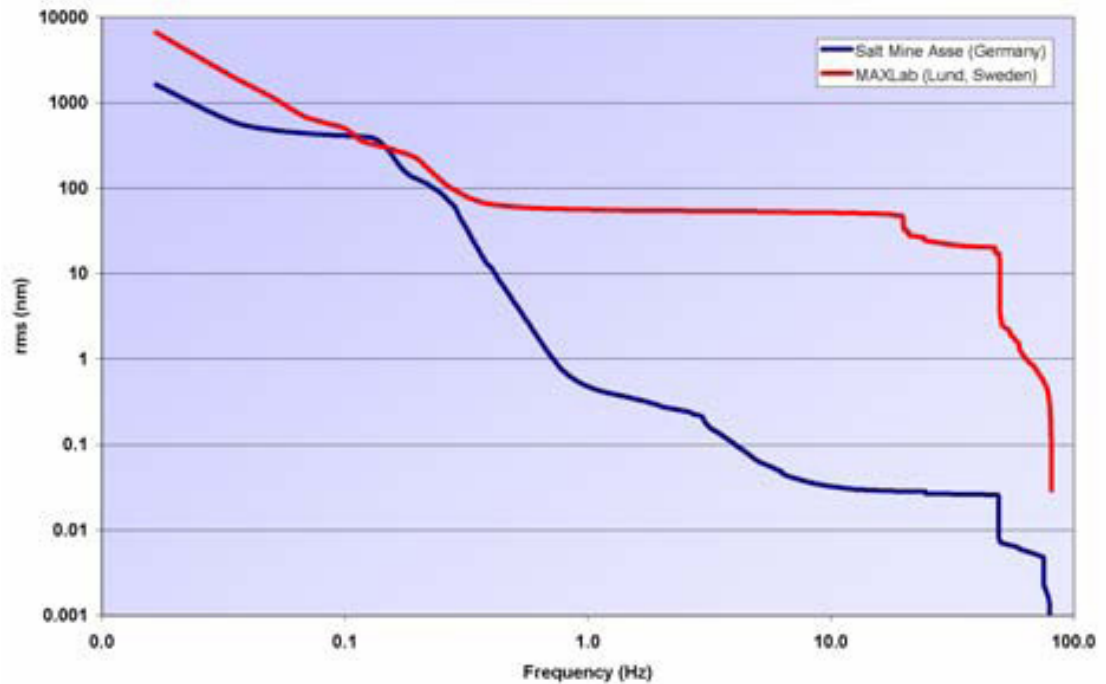


Fig. 6.1: Integrated vibration plot, MAX II floor 2006 (3).

The figure shows an example of an integrated graph showing the vibration level at the MAX II floor 2006 (red Curve). The RMS amplitude at frequencies over 1 Hz is in the order of 60 nm. There are large contributions from 50 Hz and 25 Hz. The blue curve shows the levels in a salt mine in Germany. As seen there is not much difference in the area below 0.5 Hz. The bump at 1/7 Hz is coming from sea waves hitting a shore somewhere.

## 6.3. Vibration Tolerances

### 6.3.1. Beamline Tolerances

The level of angular fluctuations and translations of optical components stemming directly from vibrations are generally not causing problems. It is the background vibration as a source for exciting natural Eigen modes in the mechanical systems which is the problem.

The general statement in the introduction on not to significantly increase the level from the “green field” level is valid here. By identifying the expected dominating frequencies it is possible to set demands on the natural frequencies of mechanical construction.

A typical spectrum from the MAX II floor is shown here.

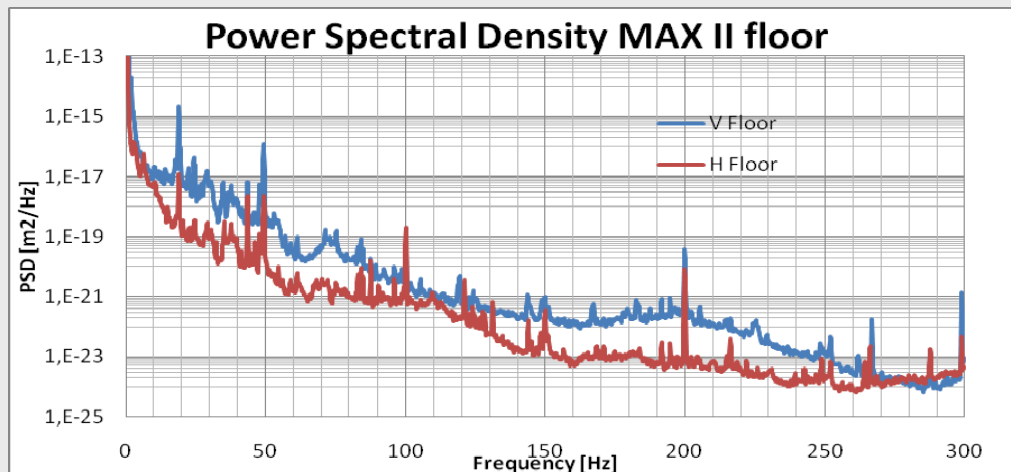


Fig. 6.2: Power Spectral Density, MAX II floor 2010.

As expected we see ca 50, 100 Hz etc. peaks from rotating machinery and transformers. The 18 Hz peak has been identified to come from the He compressor.

A general requirement for beamline components would be to not have deflection modes in the dispersion plane with natural frequencies below 55 Hz.

## 6.3.2. Accelerator Tolerances

The ground vibrations measured will often be amplified by structure resonances in the girders-magnet suspension system. The obvious goal is to get the mechanical amplification factor to 1. This section deals with the tolerances on mechanical vibrations set by the accelerator parts in order to fulfil the overall stability goal of 10 % of the e-beam size.

### 6.3.2.1. MAX IV 3 GeV

There is a significant difference between the bare lattice parameters and the parameters for specific Insertion Devices (ID). Furthermore the parameters depend on the chosen level of coupling. Therefore the smallest expected vertical beam size in a strong ID with low coupling is used for setting tolerances.

The smallest beam dimensions in the undulators are:

$$\sigma_{\text{hor}} = 52 \mu\text{m}, \sigma_{\text{vert}} = 2.0 \mu\text{m}$$

The maximum electron beam displacements to be accepted are taken to be 10 % of the RMS beam dimensions and we concentrate on the most demanding specification:

$$\Delta_{\text{vert}} < 0.20 \mu\text{m}$$

The vibrations of the magnets will induce vibrations of the electron beam with amplification. The amplification factors are here defined as the ratio between the closed orbit deviation at some point in the ring and the displacement of the magnet lenses in the ring. For the MAX IV 3.0 GeV ring lattice these were studied in two separate ways and the results were compared. The methodologies used were

#### **Analytical calculation:**

The uncorrelated amplification factor is used when assuming a random displacement of all magnet lenses with the same RMS value. This factor is used when calculating the closed orbit deviation due to misalignments. However, for vibrations the lens displacements in the same magnet block are assumed to be correlated and hence the amplification factor will differ for the correlated case. The difference is illustrated in Fig. 6.3 where the case of a Unit Cell magnet block is shown for a correlated displacement in the vertical direction.

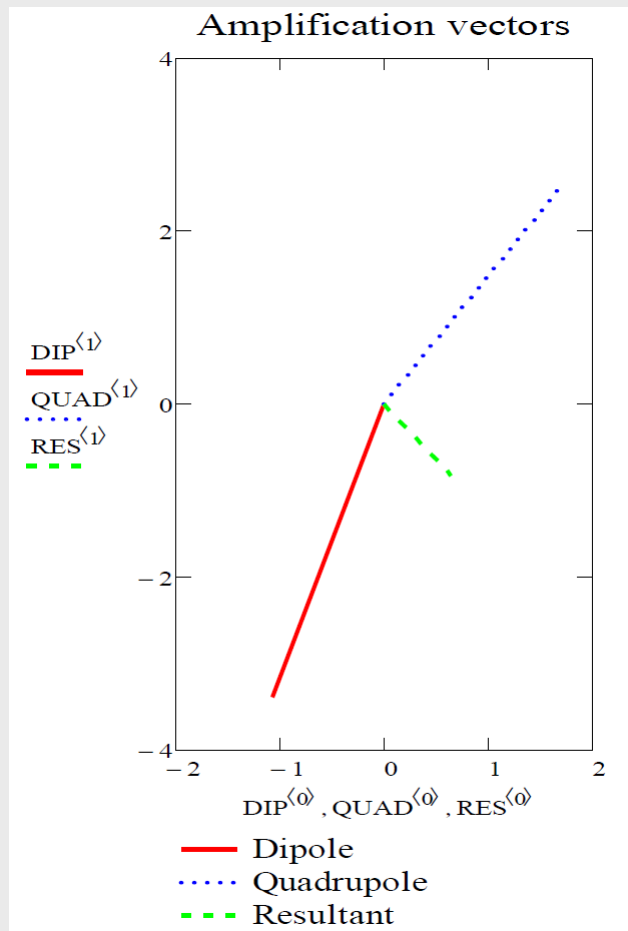


Fig. 6.3: Resultant amplification in a unit cell magnet block as sum of two contributions.

One vertically focusing dipole magnet and a vertically defocusing quadrupole are mounted on the same girder. The amplification due to the dipole displacement is shown in red, while the amplification due to the quadrupole displacement is blue dotted. The resulting amplification factor for the correlated displacement is the green-dotted vector.

The total uncorrelated amplification factor in the middle of the long straight section, when including the displacement of all magnet blocks, is **41**, which should be compared with **13** for the correlated case. The numbers are for the vertical direction.

#### Support response matrix:

A response matrix for small magnet block support shifts was calculated numerically using the full Accelerator Toolbox (AT) lattice. The amplification factors for the different BPMs in each achromat could then be obtained for different correlation cases by summation of elements in the response matrix with correlated shifts being treated as a single term in a quadratic sum.

Three cases were assumed:

- Uncorrelated support shifts due to vibrations. Results are shown in Table 6.7.
- Support shifts within the same magnet block are completely correlated, while shifts in different blocks are completely uncorrelated. Results are shown in Table 6.8.
- Support shifts within the same achromat are completely correlated, while shifts in different achromats are completely uncorrelated. Results are shown in Table 6.9.

PBM	Horizontal	Vertical
1	33.1929	23.3563
2	8.3303	31.2347
3	19.3608	16.8717
4	19.2362	17.7522
5	20.1211	18.5429
6	18.9187	18.5447
7	20.3842	17.7562
8	18.2286	16.8725
9	8.8618	31.229
10	32.9146	23.3525

Table 6.7: Amplification factors at each achromat BPM for uncorrelated vibrations at each magnet block support.

PBM	Horizontal	Vertical
1	29.2543	15.5559
2	6.8406	20.8681
3	16.7081	11.4045
4	16.1497	12.025
5	17.5737	12.4369
6	16.0054	12.4339
7	17.6581	12.0185
8	15.2299	11.4031
9	7.5467	20.8771
10	28.8897	15.5615

Table 6.8: Amplification factors at each achromat BPM where vibrations are perfectly correlated within the same magnet block and completely uncorrelated between supports at different magnet blocks.



PBM	Horizontal	Vertical
1	2.3082	3.569
2	1.1525	4.7838
3	1.8565	2.8871
4	1.7607	3.2551
5	1.5032	3.4918
6	1.5488	3.4994
7	1.8939	3.2711
8	1.6086	2.89
9	0.93856	4.7577
10	2.2557	3.5529

Table 6.9: Amplification factors at each achromat BPM where vibrations are perfectly correlated within the same achromat and completely uncorrelated between different achromats.

A comparison of the results can be done for the case of correlated shifts within the same magnet blocks. The analytical case yields **13** for the vertical direction in the center of the long straight, while the AT simulations yield **15.6** for the BPMs flanking the long straight. The difference is fully explained by the variation in  $\beta_y$ .

The same type of conclusion is drawn in (4). When taking into account the correlation of vibrations on girders it was possible to get a more realistic number for the effective amplification factor (from 45 to 8, with a measured value of 12).

Even between magnet blocks there will be a certain degree of correlation. The correlation between magnet blocks can be increased by making the floor and the underlying soil stiffer, increasing the wavelength of vibrations. The largest contributions to translation are coming from low frequencies and thus with longer wavelength.

We assume that we can reach an effective amplification of ca 10 at MAX IV and we thus set a vertical stability tolerance of **20-30 nm**.

### 6.3.2.2. MAX IV 1.5 GeV

For the 1.5 GeV ring the uncorrelated amplification factor is 38. The vertical beam size of  $1.3 \mu\text{m}$  sets then a stability criterion on uncorrelated motions to ca **34 nm**. Even here the correlated motions will reduce the effect.

### 6.3.2.3. Linac and Beam Transport Tolerances

In order to get some numbers for the tolerances regarding positioning some simulations has been done by moving some critical magnets from their nominal position. The magnets are in bunch compressor 1. The resulting displacements of the electron beam at the injection point for the 3 GeV ring and the Short Pulse Facility (SPF) have been used (using the preliminary design).

For use as injector for the 3 GeV ring a 200 nm displacement of the quadrupole magnets gives a displacement of the beam of 2.5  $\mu\text{m}$  which is ca 5 % of  $\sigma$ . This is about the acceptable fluctuations in order to keep a stable injection.

Also the effective emittance is increased. The angular fluctuation of the electron beam (from 200 nm amplitude vibration) is 1.3  $\mu\text{rad}$ . This will decrease the performance as a source for the SPF and especially for the future planned Free Electron Laser (FEL).

Due to the nature of a FEL the amplification of light is very dependent of the electron beam density. This could mean that the 5 % fluctuations of  $\sigma$  become 50 % for the FEL beam. The result will be a seriously unstable beam as seen from the user. Without having done a lot of calculations on this it seems realistic that a stability requirement for the magnets in the bunch compressor when used for the SPF and especially for the FEL should be in the order of **50-100 nm**. This is a maximum tolerance. Lower amplitudes will be better.

### 6.3.3. Summarizing Tolerances

The 3 GeV ring can have a vertical beam size as small as  $\sigma_{\text{vert}}=2.0 \mu\text{m}$ . Since the beam must be stable to within 10 % and because of the amplification by the lattice, the tolerance on the magnet stability is set to **20-30 nm rms**. The NSLS II has similar requirements (5).

The 1.5 GeV ring has a tolerance in vertical direction of **50 nm rms**.

The linac structure will have its tightest tolerances when used for FEL operation and the maximum tolerance is estimated to end up in the range **50-100 nm rms** vertical and horizontal. Tolerances will be tighter with new technical possibilities.

<b>3 GeV ring vertical</b>	20-30 nm
<b>1.5 GeV ring vertical</b>	Ca 50 nm
<b>Linac magnets, vertical and horizontal</b>	50-100 nm

Table 6.10: Summarized stability tolerances.

Estimating the effects of a certain level of vibrations is complicated. The correlation of vibrations is as important as the level itself. For the rings correlated vibrations are have smaller effects on the beam stability than uncorrelated.



# MAX IV Facility

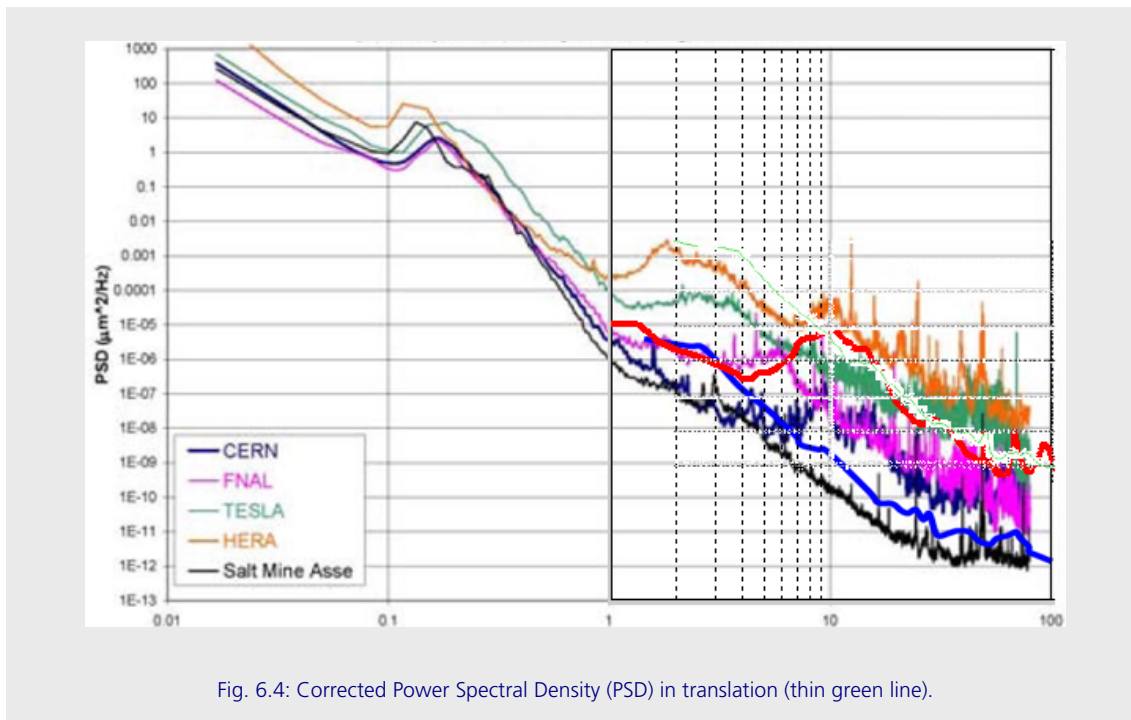


## 6.4. Vibration Measurements

The field at the MAX IV site has been characterized several times. The measurements show somewhat similar values (at least when they are corrected for errors). This section summarizes the results. New measurements are planned by the construction company PEAB in collaboration with MAX-lab.

### 6.4.1. Early Measurements

The first measurements showed very low (and unrealistic) vibration levels. A later report by NGI (6) (see next section), suggest a scaling error. After correction the measured levels are showing similar results. The results are shown here.



The thin green line is the corrected value and the red line is the NGI measured values. As seen, there is good correspondence between the measurements at frequencies down to 10 Hz.

### 6.4.2. NGI Measurements

The vibration level from NGI (Norges Geotekniske Institutt) report (6) is already shown as PSD in Fig.6.4 (red line). When the PSD is integrated from high to low frequencies one can see the RMS value of vibrations from a certain frequency and upwards:

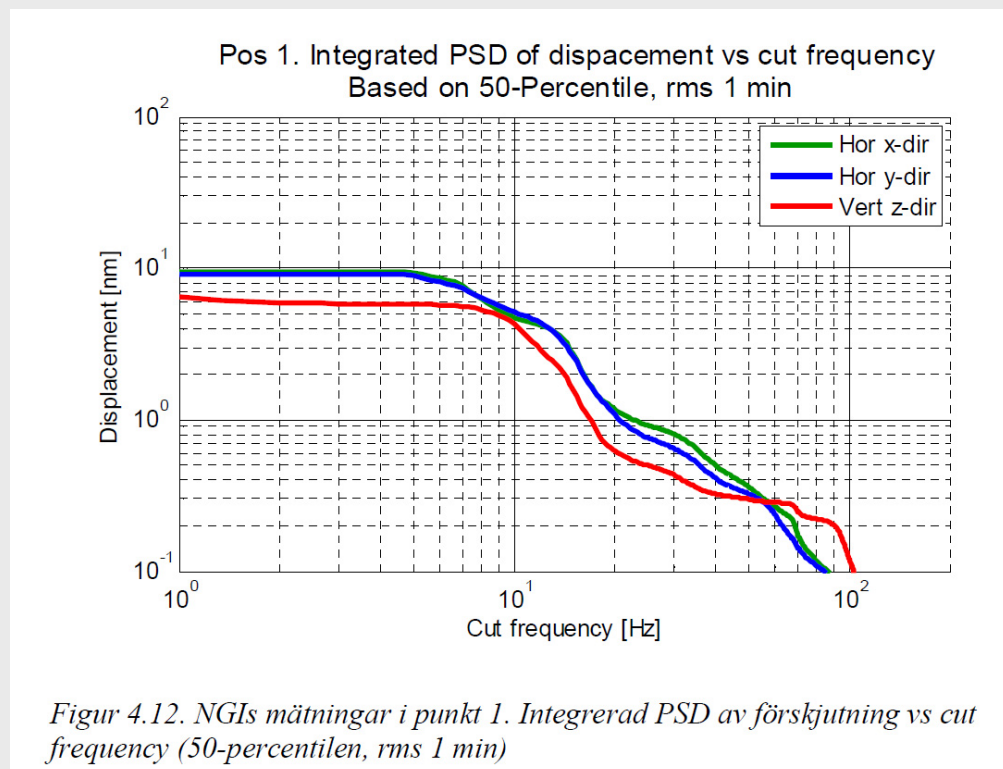


Fig 6.5: Integrated Displacement, averaged over a week.

These averaged values show very low vibration levels 5-10 nm RMS at frequencies over 7 Hz. The long time averaging does not show shorter disturbances.

Most experiments are sensitive to bursts of vibrations since they have time horizons in the area of minutes. It is therefore interesting to analyze not only the averaged values for a long period.

The following graph shows the level of the 1% worst minutes over one week.



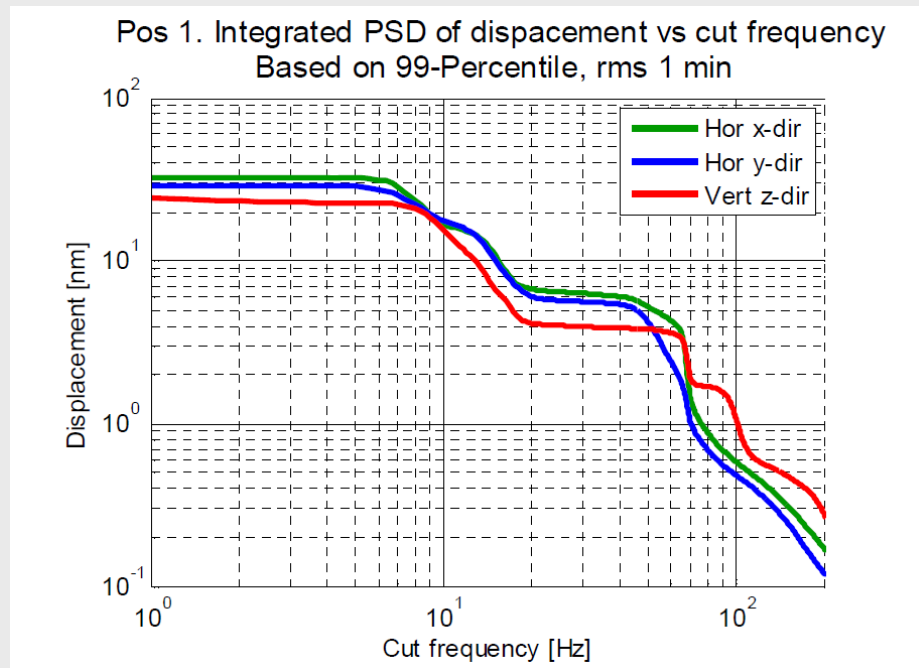


Fig. 6.6: Integrated displacement, 1% highest levels over a week.

As seen the levels are between 10 and ca 20 nm RMS (from 7 Hz and up).

The NGI report contains a graph with vibrations over several days with the vibration criteria outlined (See section 6.2.1):

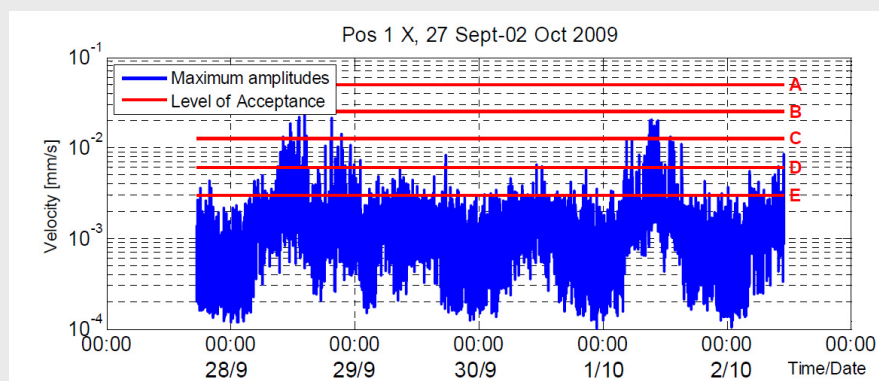


Fig. 6.7: Comparison between measured levels and VC- system levels.

This graph is only included for comparison since the velocity based Vibration Criterion (VC-A to VC-E) is less interesting for large scale facilities where translation amplitudes are more interesting.



### 6.4.3. Traffic

The vibrations from ordinary traffic on the local road and on the highway are already contained in the measurements in the previous section. In order to get information on the effect of more extraordinary traffic situations a series of measurements with a truck passing a 1" plank was performed.

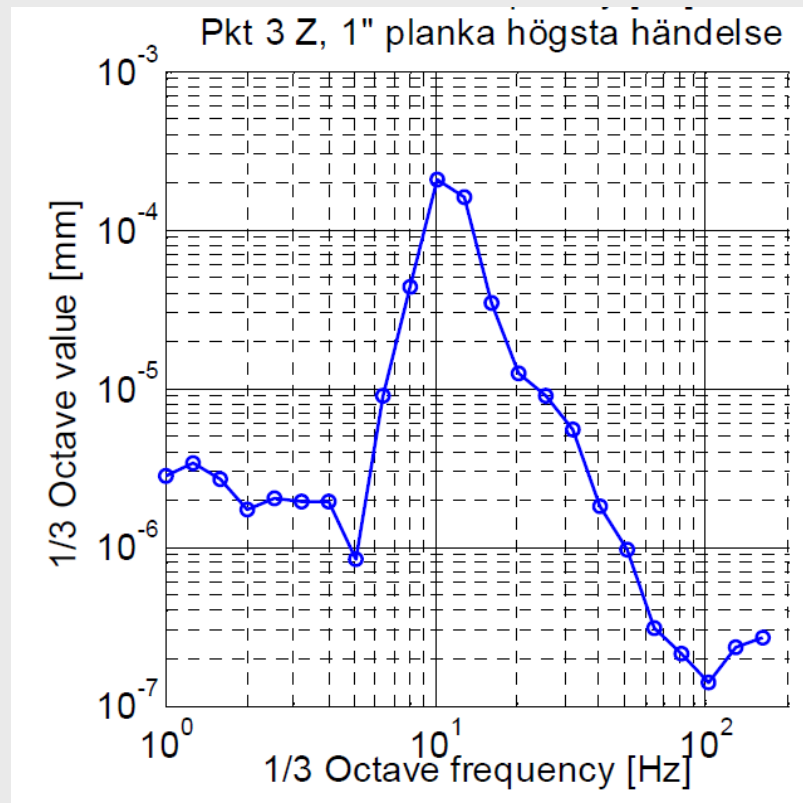


Fig. 6.8: Maximum vertical translation in 1/3 octave band at a distance of 55m from truck and plank, integrated over a 1s interval.

The report concludes that the level is 7 times higher than the 99 % background percentile. The highest amplitudes are at 10-12.5 Hz. The recommendations are to make sure the local roads are kept smooth and to avoid local traffic in the nearest vicinity of the facility.

It will not be possible to avoid local traffic close to the facility, since there will be several daily deliveries of goods. The Situation has been discussed with the construction company PEAB. It is decided to monitor vibrations induced by trucks at the facility and use the results to decide on speed limits.

#### 6.4.4. Detailed Investigation PEAB/MAX-lab

In order to get more qualified information it is decided to make a deeper investigation on the vibration level and on the ground/soil properties. These investigations were not finished at the deadline for this report.

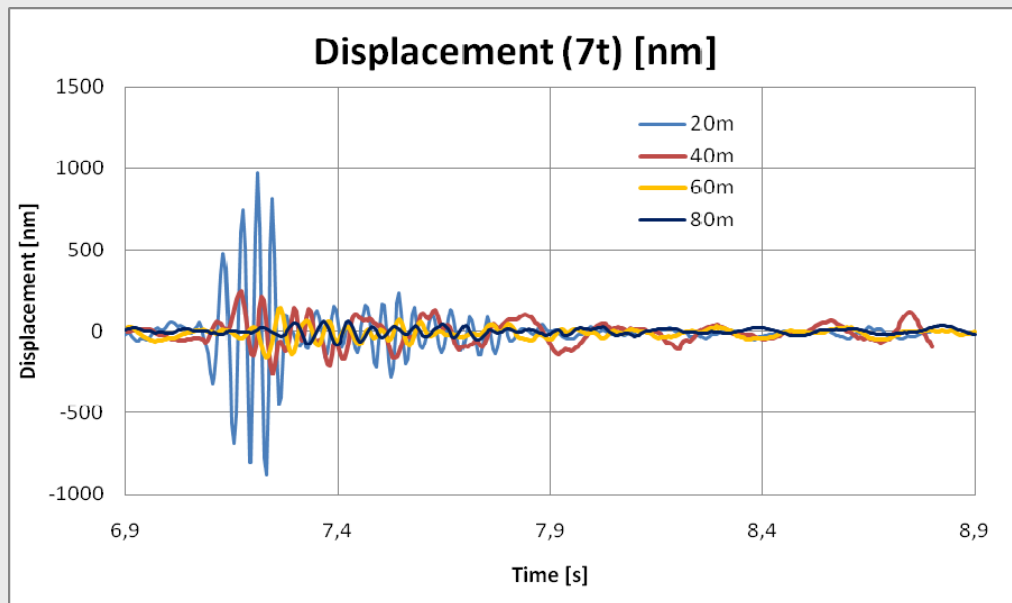
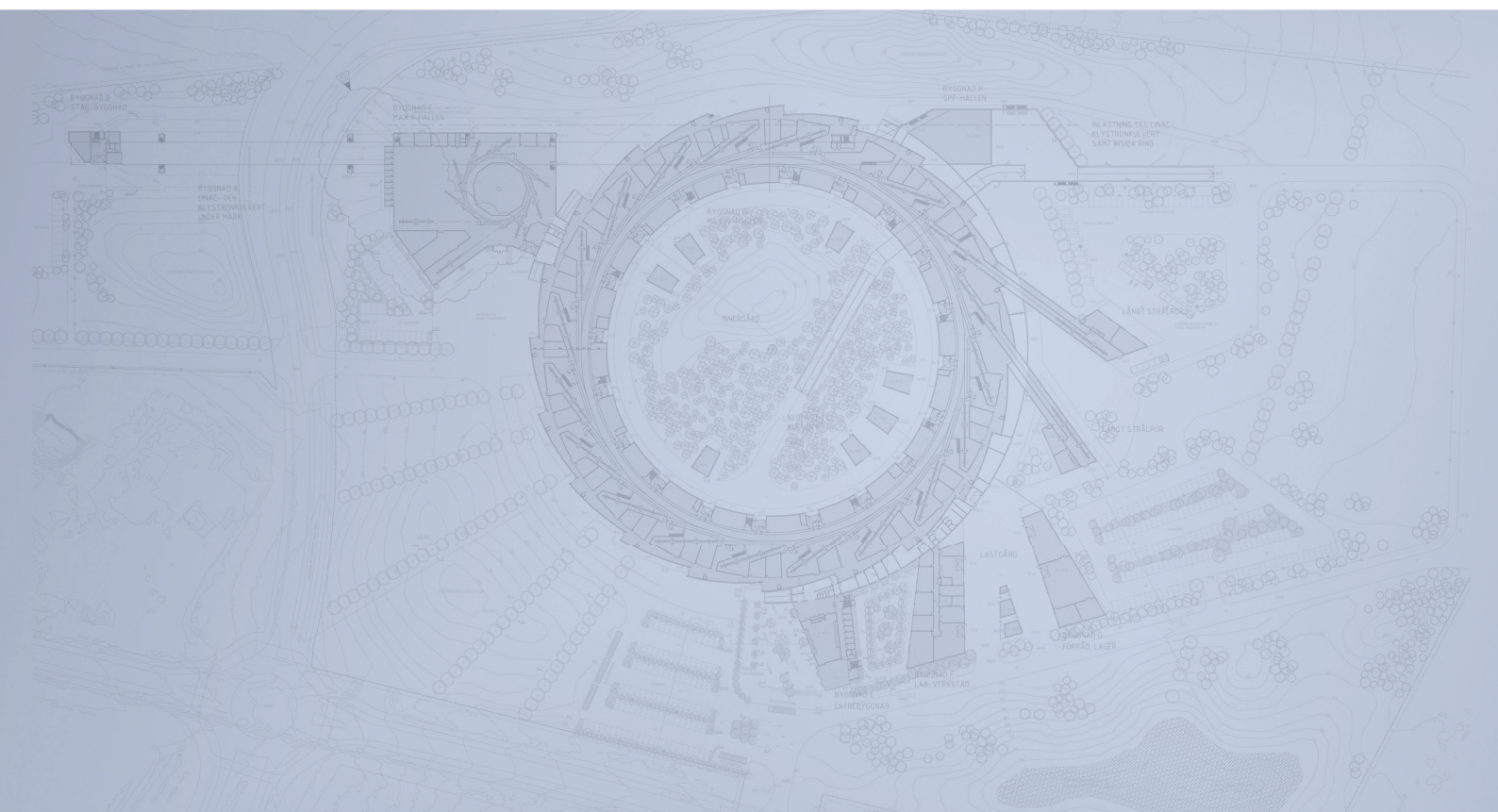


Fig. 6.9: Some preliminary field data.

The figure shows the displacement measured at different distances from a falling load with a force profile with max 70 kN. When the data is analyzed some numbers for the speed of waves and damping coefficient can be deduced. This is work in progress.



# Detailed Design Report



## Chapter 6 Stability and Tolerances 6.5. Vibration Management

**MAX IV Facility**



## 6.5. Vibration Management

---

The strategy for vibration management is to deal with vibrations in all design areas. This goes for sources of vibrations and design of buildings, girders and equipment so it is less sensitive to disturbances.

The ground vibrations could be divided into two classes; natural site vibrations and culturally induced vibrations. The natural vibrations are generally speaking of smaller importance, provided we haven't chosen a badly positioned site. Furthermore the building itself will tend to reduce the vibrations coming from the outside at frequencies above a few Hz (7), (8).

The cultural vibrations, induced by internal and external traffic, reciprocal machines, electric machinery, air-conditioning, water cooling system etc are generally dominant.

For a given impact or disturbance on a mechanical system the resulting translation amplitude of vibrations is dependent on the spring constant and the mass of the system. High spring constant is the goal. The effect of the mass is dual. High mass reduces amplitudes in the higher end of the spectrum. Lower mass increases the natural frequency and thus reduces amplitudes at low frequencies.

### 6.5.1. Passive Damping and Isolation

Damping and Isolation are often mistaken to be the same. Damping is taking out energy of vibrations by friction. At the relevant amplitudes and frequencies most materials are not very efficient at damping.

Isolation of machinery with a known spectral distribution is possible and will be carried out. The first principle is however to avoid machines inducing vibrations.

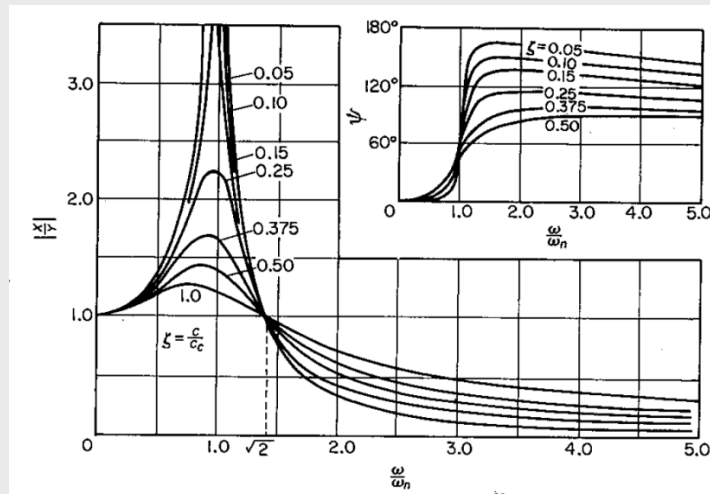


Figure 3.5-2. Plot of Equations (3.5-8) and (3.5-9).

Fig. 6.10: Isolation of oscillating forces (9).

By placing a vibrating device (frequency  $\omega$ ) in a system with low natural frequency ( $\omega_n$ ) the transmissibility of force  $\frac{F}{F_0}$  is reduced.  $\zeta$  is the damping factor, note that higher damping reduces the isolation effect.

An example of a planned initiative is to develop a new cart for transportable vacuum pumps. The cart should consist of a block (maybe concrete), placed with springs on a frame with wheels. By proper design it is possible to reduce the transfer of oscillating force to the floor.

Isolating buildings from external vibrations could be quite demanding, considering the wavelength of the low-frequency vibrations. Isolating floor from roof and outer walls is, however, a relatively simple means.

Damping of the floor could in fact be contra-productive. Damping materials are weak and thus might increase vibrations in the low-frequency part of the spectrum, which is responsible for the major contribution of the displacements.

The possibilities with damping with viscoelastic material as described in (10) will be investigated.

### 6.5.2. Active Damping of Mechanical Vibrations

So far there are no plans for active damping. For systems with specific frequencies it could be an option. Introducing more complexity to a mechanical system could however be counterproductive. Active damping of the electron beam is discussed in the following section.

### 6.5.3. Orbit Feedback

The stability of the beam trajectory in the accelerators is affected by a number of noise sources, of which mechanical vibrations is one. An additional source is magnet power supply stability, which modulated by magnet inductance and vacuum chamber eddy currents generate field fluctuations that can excite beam trajectory movement. A more significant source of trajectory movement is however Insertion Device (ID) gap changes in the storage rings.

In order to reduce beam trajectory movement relative to a reference orbit, orbit feedback is used at close to every active light source today. The feedback loops commonly uses BPMs as sensors and corrector magnets as actuators, although the feedback controller algorithms vary. The most common one is the standard PID controller.

As the references are defined in terms of BPM readings such systems will never be able to reduce beam trajectory movement to below that of the mechanical vibrations of the BPMs. Girder mechanical stability thus sets the noise floor.

For the 3.0 GeV storage ring, two orbit feedback systems are under design. One is a global system that will use all the available BPMs and corrector magnets in the ring to correct orbit deviations not only on the straight sections but also within the achromats. This system will be a relatively Slow Orbit Feedback (SOFB) and work at sampling/correction frequencies of 10 Hz. This will be sufficient to handle trajectory drifts over longer timescales, caused by for example temperature variations. "Global" refers to the calculation of the correction magnet settings: the effect of a corrector magnet system at every BPM is taken into account. This is in contrast to a "local" system where a closed bump of three corrector magnets is used to eliminate a trajectory deviation from the reference at a single BPM.

The second system under design for the 3.0 GeV storage ring is also global but will at least initially only use a subset of the available BPMs and corrector magnets in the ring: specifically the BPMs and corrector magnets flanking the long straight sections. It will however work at a significantly higher sampling/correction frequency of 10 kHz, allowing damping of trajectory vibrations with significantly higher frequencies. Preliminary simulation results for this Fast Orbit Feedback (FOFB) system show vibration amplification according to Figure X below. Note that even with a 10 kHz sampling rate, trajectory vibrations are only damped up to roughly 75-100 Hz. Apart from reducing stochastic noise, experience from other laboratories show that FOFB systems of this type are highly effective for damping trajectory movement due to ID gap changes.

For more in-depth information on the orbit feedback system for the 3.0 GeV storage ring, see chapter 2.4.5. It should be noted that trajectory feedback systems will also be used for the MAX IV injector and the 1.5 GeV storage ring but are currently in the design stage.



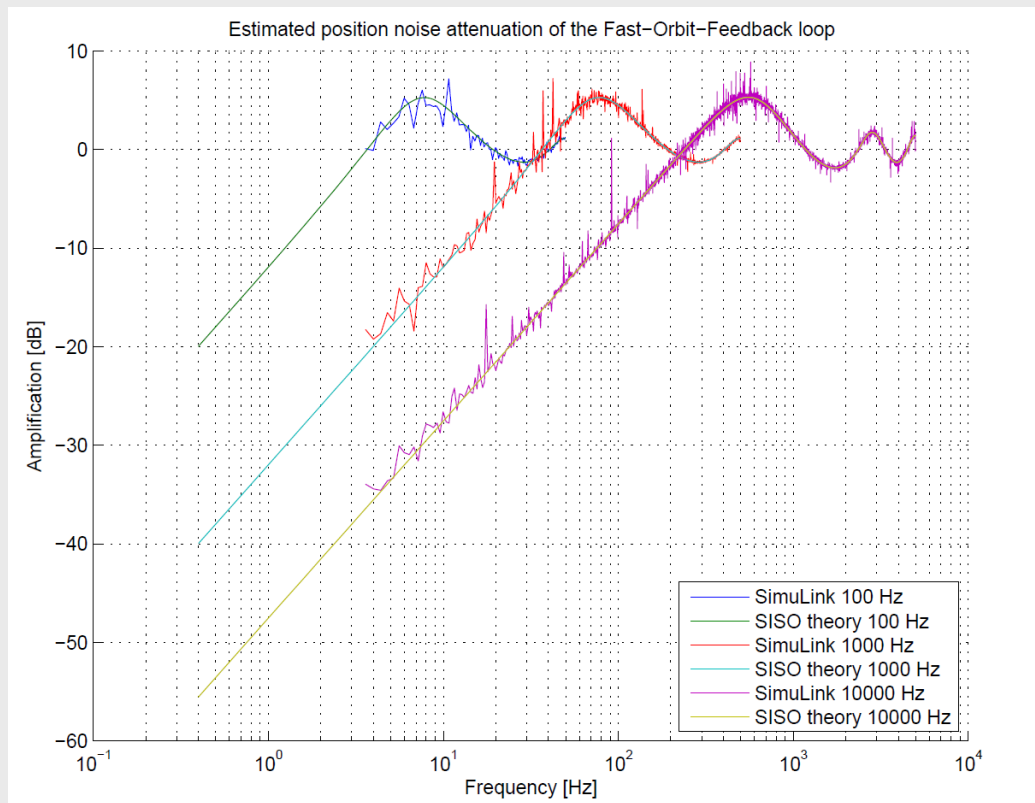


Fig. 6.11: Estimated Fast Orbit Feedback system amplification of stochastic beam orbit noise, assuming a Steel 304 vacuum chamber and a PID controller. Results are shown for three different sampling frequencies.

## 6.5.4. Sources for Vibrations

### 6.5.4.1. Acoustics

At least for beamlines the sound level in the experimental area plays an important role. The contribution from the sound level in the hall can be in the same order as the contribution from the manufacture errors on the beamline optics (11).

Most beamlines will be built in hutches. They can decrease the sound level but also act as resonators.

### 6.5.4.2. Cultural Noise

Most vibrations in present MAX-lab and possibly MAX IV are cultural noise. The sources for this are many.

Some functions can be placed outside the sensitive areas, maybe even far from the buildings. This can be transformer stations, heat pumps for cooling and UPS devices.

Many sources have to be placed inside the facility. In all cases vibrations have to be kept in mind. The technique of isolating sources is well known, so much can be done.

Sources that has to be managed are for example

- Pumps, vacuum and water
- Compressors
- Tubes with turbulent flow
- Fans
- Doors
- Internal traffic
- Power supplies and transformers

Internal traffic, walking people etc are sources that cannot be managed as easy. The solution is to make the building resistant.

### 6.5.4.3. External Sources

External sources have to be taken into account. Examples are

- Local and highway traffic
- External reciprocal and rotating equipment
- Transformers etc.

Since damping is not very effective at low frequencies and amplitudes, the quadratic law of radiation is the most effective means – put these sources as far as possible from the facility. Green field measurements show acceptable levels from present traffic. At present it is not possible to estimate max speed for trucks approaching the facility with deliveries. This will have to be determined by actual monitoring vibrations while a truck is moving in the area.

### 6.5.5. Civil Engineering

In order to give qualified input for the constructor of the buildings MAX-lab is collaborating with the Department of Construction Sciences, Division of Structural Mechanics and Division of Engineering Acoustics.

The goal of this collaboration is to find out how the buildings for MAX IV can be optimized for vibration management and to point out some tolerances for vibrating equipment.

The effects of various parameters have been investigated.

- Floor thickness
- Soil stiffness
- Effect of stiffening the system with piloting
- Slicing floor parts for isolation
- Walking loads
- Frequency sweeps for loads at various places

Also a scenario where a road with local traffic is crossing over the linac tunnel has been investigated.

A large stiff construction such as the facility floor will reduce external high frequency vibrations (7), (8). The reason is that the construction is larger than the wavelength of the vibrations. At low frequencies a stiff floor is also reducing the problem. The level of vibrations is not reduced but the construction increases the correlation of vibrations so that a larger part of the facility is rocking concurrently.

The following sections summarize the conclusions from the calculations. At the time for the work the knowledge on actual material properties has been limited. Therefore the calculations have not really been used to forecast the vibration level. The goal has instead been to investigate the effect of different ideas and parameter values. When doesn't it make any more sense to increase the floor thickness? What happens if we make a slit in the floor in order to isolate vibrations? Etc.

The work has been concentrated on the main floor and ring tunnel for the 3 GeV ring and the linac tunnel.

#### 6.5.5.1. 3 GeV Ring Floor and Tunnel

Since the 3 GeV ring is the most demanding when it comes to stability, special attention has been made here. Several calculations have been done on a FEM model of the floor and ring tunnel structure (12).

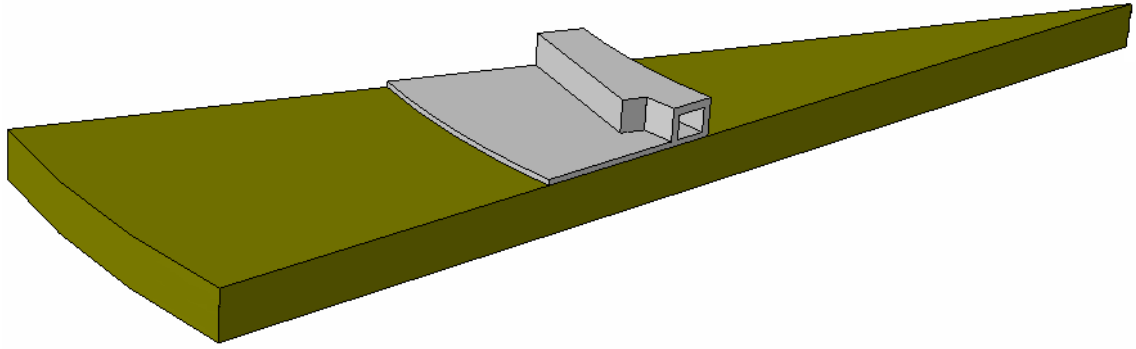


Fig.6.12: Segment of the FE-model.

Several parameter studies were performed. The effect of stiffness of the soil, thickness of the floor and also an idea of piloting under the floor was investigated. The number of pillars in the model was modulated by assuming a smeared out added stiffness to the soil.

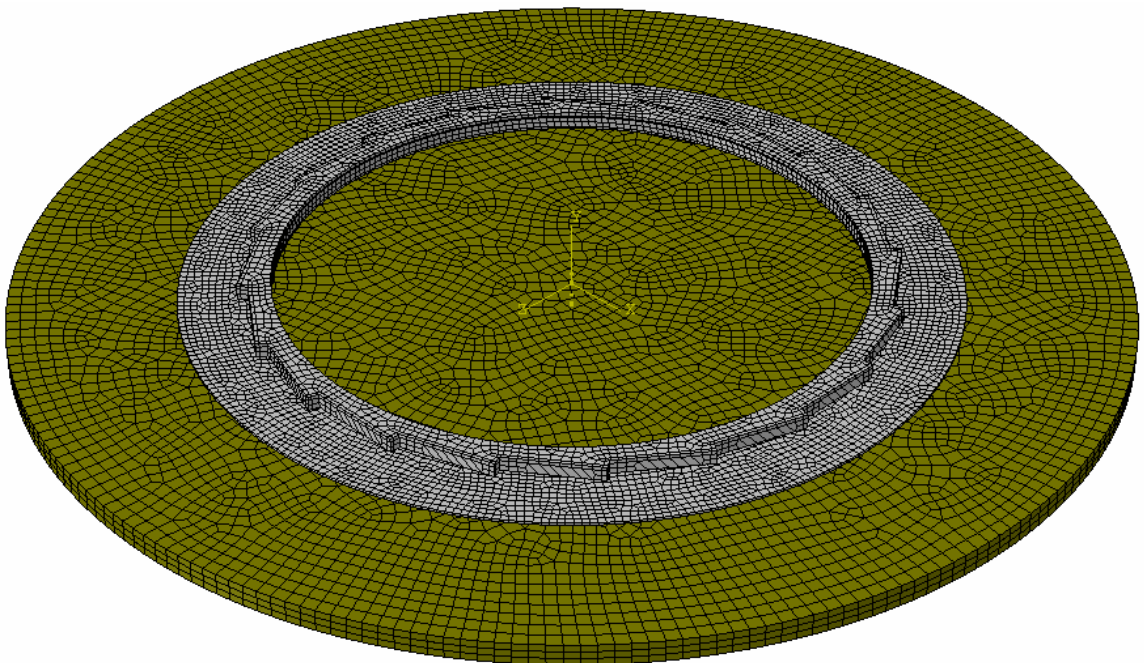


Fig. 6.13: Large scale model.

The conclusion from these studies is that the material properties of the soil and bedrock greatly influences the calculated results, much more knowledge in this area is needed in order to get credible results. However the work also shows that it is possible to find out where it doesn't make sense to increase floor thickness, number of pillars etc.

When we have better material knowledge this method will give us valuable information. If the pillar solution is chosen a detailed model with discrete pillars must be used.

In the analysis of effect of different loads, more work has to be done in order to get credible forecasts of the performance of the floor.

A study on the often used method of slicing the floor, from the idea of isolating vibrations from internal transport and walking, showed no or a small counterproductive effect. This was suspected, since experience from the MAX II floor points at that. The explanation is that the wavelengths of the vibrations are much longer than the floor thickness. Vibrations are going at least one wavelength deep and are thus traveling through the soil, rather than the floor. The floor acts more like a membrane. The counterproductive effect (larger amplitudes of vibrations) can be explained by the fact that the bending stiffness of the floor is decrease by the cut.

Recent studies with putting walking loads on top of the ring tunnel concludes that it might be necessary to use walking bridges from the office building, rather than letting people walk directly on the tunnel. More analysis will be done here when soil parameters are well known.

#### **6.5.5.2. The 1.5 GeV Ring**

The 1.5 GeV ring is more tolerant than the 3 GeV ring. So no special calculations have been done here. Some beamlines might have the same sensitivity as the 3 GeV beamlines, so the general vibration level should not be that different.

#### **6.5.5.3. The Linac Tunnel**

The most important task in the calculations on the linac tunnel has been to find out the effect of letting a local road cross the tunnel. Also the effect of a walking person in the service tunnel was analyzed (13), (14), (15).

For the road analysis a FEM model was build of a suggested solution consisting of a concrete construction designed to isolate the road from the linac tunnel.

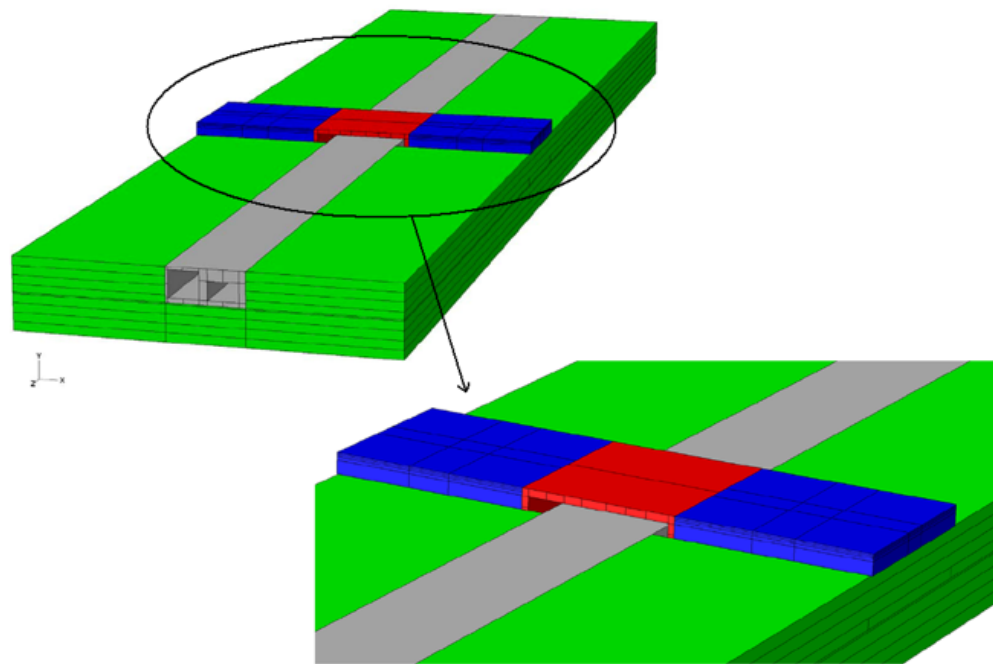


Fig. 6.14: Picture showing the FEM modeling of a “hidden bridge” over the tunnel.

Since the soil properties are not very well known, several values were tested.

The model for a modern bus was used on a very smooth road as well as on a road with some irregularities. The latter occurs when there are items on the road like twigs, stones, ice or when the road is not in optimal shape.

For the worst case of a bus on a smooth road, the dynamic deflection in the Linac tunnel was between 100 and 300 nm, dependent on frequency.

When introducing an irregularity on the road the maximum deflection was in the order of 1.5  $\mu\text{m}$  and the RMS value was 365 nm. This has to be compared to the estimated tolerance of 50-100 nm as described in section 6.3.2.3.

Only the dynamic part of the load from a bus was used. The effect of a “static” load with the whole mass of the bus was not investigated.

The conclusion was that it was considered a high risk for the project if the planned local road was allowed to cross. **Just at the deadline for this report it was decided by the city of Lund to relocate the road.**

Regarding effect of walking people we will have to wait for more precise material parameters for the soil and surroundings.

#### 6.5.5.4. Beamlines with Special Needs

Some beamlines will have special needs when it comes to vibrations. An example is the suggested nano-focusing beamline. Nano-focusing is done with high degree of demagnification when imaging the synchrotron source. When doing so, there will be a rather short distance between the last focusing optical component and the target. The tight tolerances are on the relative position of the last component and the target. This allows a “local” solution to the extreme stability demands.

#### 6.5.6. Ring Girders

The magnet suspension construction, the girders, will often exhibit Eigen-frequencies which amplify the vibrations. An ideal solution, but unpractical, solution would be to put the magnets on the floor. The suggested solution is to “bring the floor to the magnet”. By mounting the magnets on concrete block attached rigidly to the floor it should be possible to minimize amplification of the floor vibrations.

##### 6.5.6.1. Measurements on Prototypes

A prototype has been manufactured in an early stage. The latest measured values are presented here. The prototypes are positioned on the MAX II hall floor.

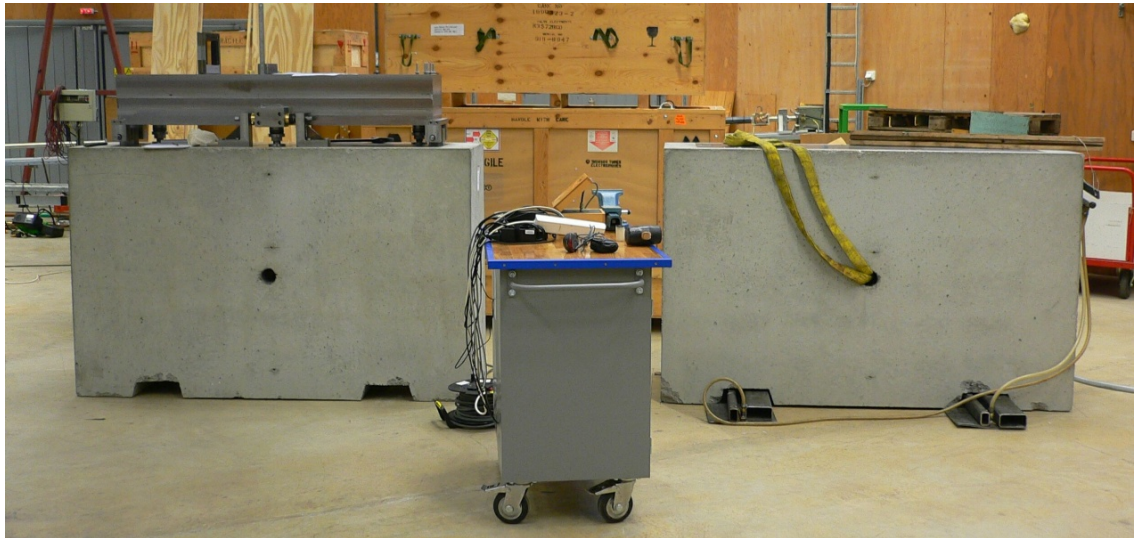


Fig. 6.15: Girder prototypes. The left is shown equipped with a magnet dummy. The concrete blocks are glued to the floor in the measurements.

In the vertical direction the vibration level on the magnet dummies is very similar to the level on the floor.



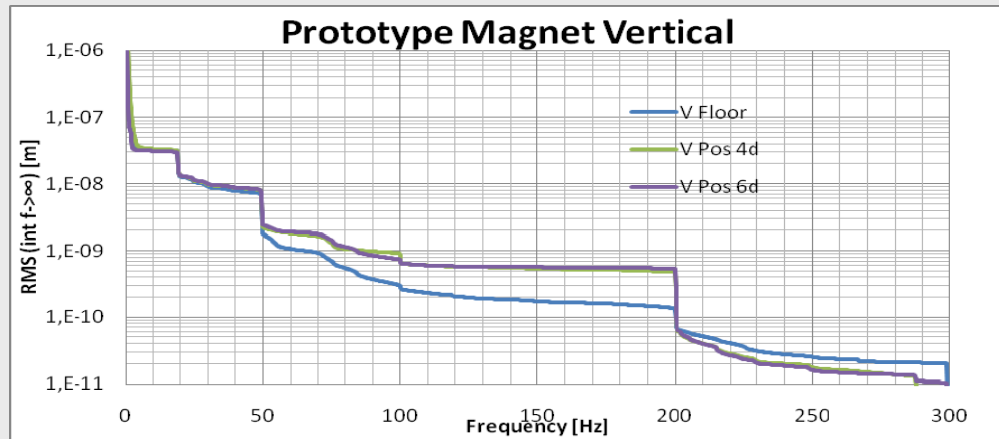


Fig. 6.16: Integrated vertical vibration level on two positions on magnet dummy and on floor.

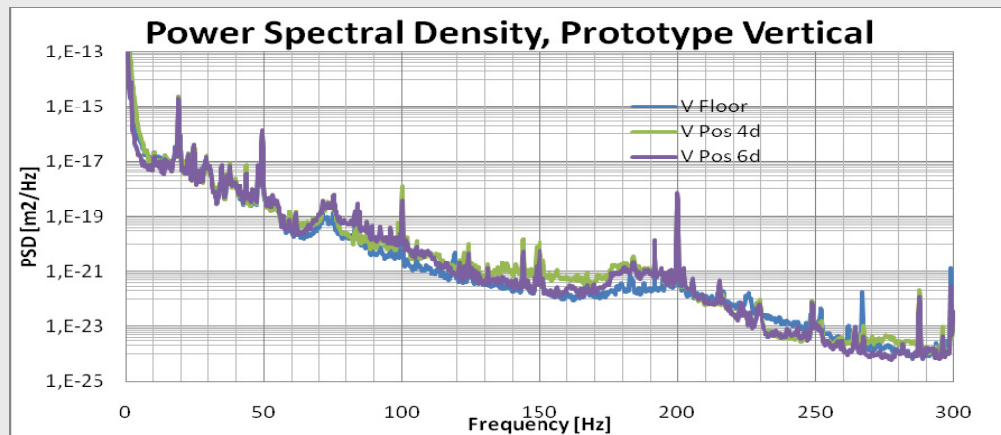


Fig. 6.17: PSD of translation on two positions on magnet dummy and on floor.

In order to judge how well the girder is performing the ratio between translation levels on the dummy and the floor are shown here.



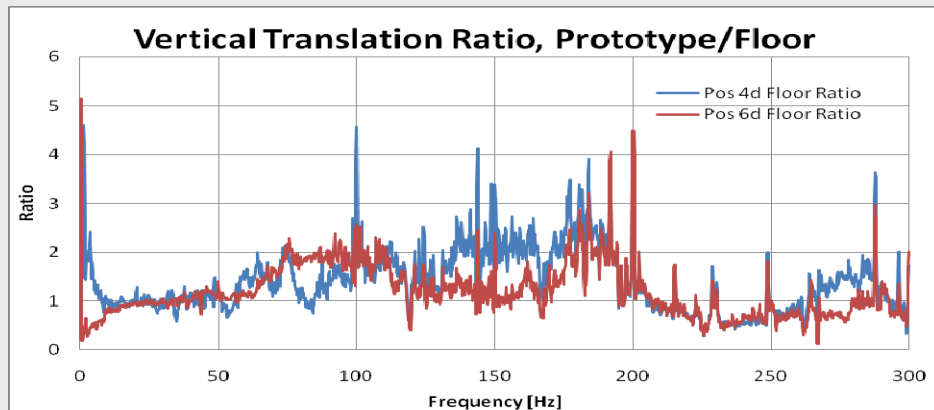


Fig. 6.18: Ratio between dummy and floor vibrations.

As seen the amplification factor is about unity at frequencies below 50 Hz. This is important since this is where we get highest contribution to the vibration amplitude.

The integrated horizontal (radial ring direction) vibration level on the magnet dummy is comparable to the vertical level. The ring is less sensitive to vibrations in the horizontal plane, but nevertheless the results are less impressive, since the floor vibrations are much lower.

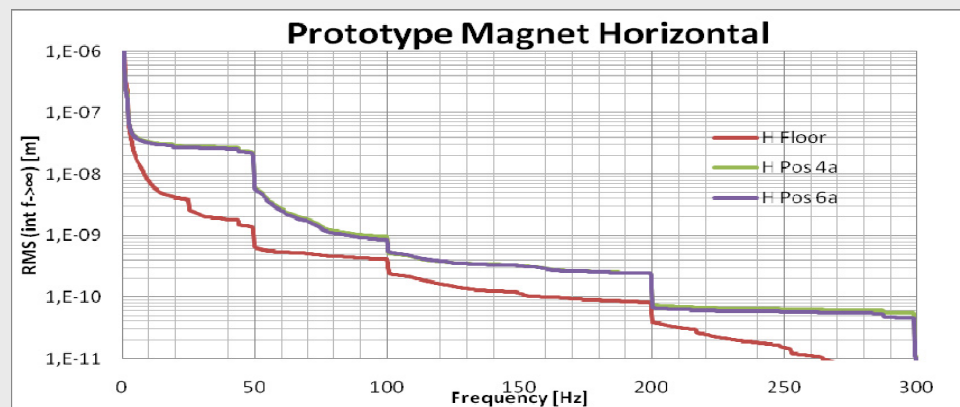


Fig. 6.19: Horizontal vibration level on magnet dummy and floor.

The amplification factor is shown here.

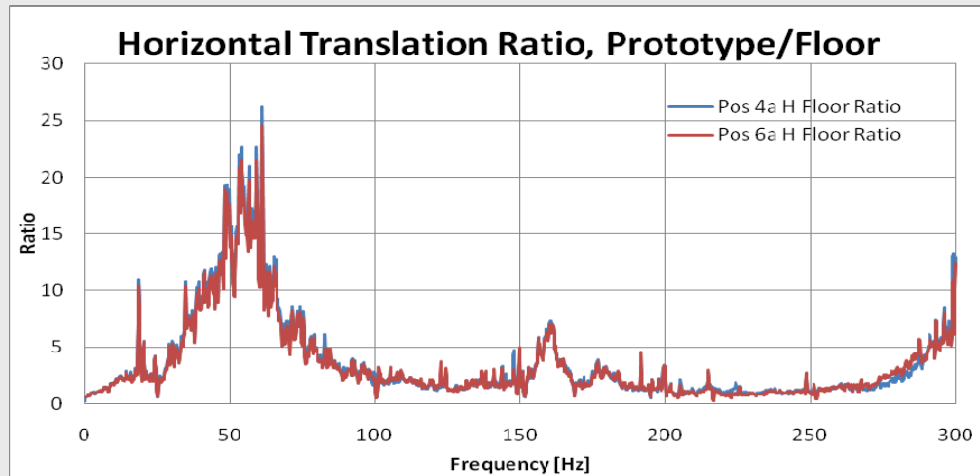


Fig. 6.20 Amplification factor from floor to Magnet dummy in horizontal direction.

The result will have to be analyzed further. The prototype girder is narrower at the bottom and taller than the planned girders for MAX IV. The magnets however will be longer and thus heavier so the new construction will probably not behave very differently if put on the same floor.

The MAX II floor where these measurements are done is 35 cm thick and the prototype girder is 65 cm at the bottom. The high amplification at 30-70 Hz might be explained by the floor and the underlying soil rather than the girder itself.

#### 6.5.6.2. Calculations and FEA Simulations

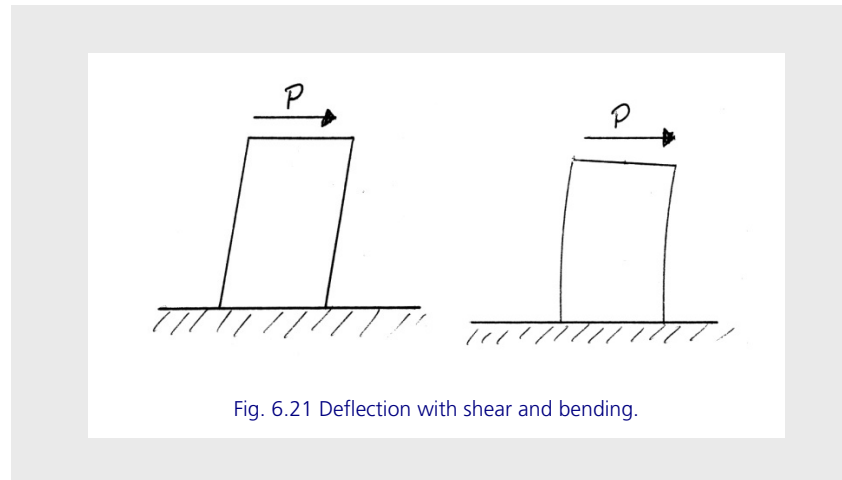
Some rough calculations have been done on the prototype system. The natural frequency  $f$  of a system consisting of a mass  $m$  on a spring with spring constant  $k$  is

$$f = \frac{1}{2\pi} \sqrt{\frac{k}{m}}$$

Deflection at the end of a beam with a force  $P$ , due to both shear and bending is

$$\Delta = \frac{PL^3}{3EI} \left( 1 + \frac{3E}{10G} \frac{h^2}{L^2} \right)$$

(16) where the second term gives the deflection due to shear.



$I$  is the area moment of inertia for the beam. For a rectangular cross section

$$I = \frac{bh^3}{12}$$

$b$  is width of the beam (length of block).

$P/\Delta$  becomes the spring constant  $k$ .  $L$  is the height of the block;  $h$  is the thickness.

$E$  and  $G$  are the modules of elasticity in tension/compression and in shear.

The ratio  $E/G$  is typical 2.5 for many materials. The contribution from shear is thus decreasing rapidly for ratios  $h/L < 1/2$ .

$L$  will not be many times larger than  $h$  in our case, so shear is contributing to the deflection.

The elastic properties for concrete (especially shear) are not so well described in literature. Concrete is not strong with shear forces, so  $G$  is generally not interesting for constructors.

[http://www.engineeringtoolbox.com/concrete-properties-d\\_1223.html](http://www.engineeringtoolbox.com/concrete-properties-d_1223.html) gives the ranges,  $E=14-41$  GPa and  $G=6-17$  GPa. The average values are  $E=28$  GPa,  $G=12$  GPa. The density of concrete is ca 2400 kg/m<sup>3</sup>.

For a uniform linear spring the contribution to the mass from the spring itself is 1/3 of the spring mass. This criterion is not totally right for the bending part, but the error will be at the conservative side, i.e. show a lower frequency. 1/3 of the block weight is approximately the same as the weight of the magnet dummy (573 and 593 kg/m respectively).

Using 1/3 of the block mass and the mass of the magnet the natural frequency should be in the order of **127 Hz**. Without magnet dummy the block has a frequency of ca 180 Hz.

A **FEM** calculation has been done using  $E=25$  GPa (17), showing a natural frequency for the lowest frequency bending mode for a concrete block with no magnet of **160 Hz**.

The two calculations show the same results, but the measurements show amplification of floor vibrations around 50 Hz. Even if the resulting vibrations are not alarming further investigations will have to be done on this issue. The rather thin floor at the site for the prototypes is a probable reason, but it will have to be investigated.

The choice of concrete type is obviously very important. It is possible to get concrete with  $E=40$  GPa. This is an obvious choice if not too expensive.

### 6.5.7. Other Mechanical Structures

The equipment must be constructed with vibrations in focus. As for ring girders, the main philosophy is to strive for higher natural frequencies. The philosophy with concrete blocks as stands will be used throughout the facility, both for accelerators and for delicate beamline equipment.

### 6.5.8. Conclusions, Recommendations, Pointing at Solutions

There are many ways to manage vibrations. All means will have to be used in order to reach the tolerances. The main content of vibrations on present MAX-lab is cultural.

The floor in the facility is part of the scientific equipment and should be designed for stiffness and high natural frequency. A solution suggested by PEAB, the construction company is to mix the soil, down to a depth of maybe 4 m, with cement or other stabilizing material in order to stiffen the underlying layers. This solution will be investigated soon with FEM after the deadline for this report.

Stands and girders for accelerators and beamlines have to be designed for high stiffness and natural frequencies. Special attention has to be made on the role of the floor thickness where stands are designed for high stiffness.

The same strategy has to be followed when designing mechanical mechanisms like moving beamline components etc. Especially Eigen-modes inducing oscillations of the light in the dispersion plane has to be addressed.

The floor and the building around will be isolated so that wind forces will not put strain on the floor.

All vibrating devices have to be placed and isolated in order to minimize transfer of forces and vibrations to the sensitive parts of the facility. Cooling water tubes might be put on “weak” joints to isolate. Turbulent flow can be avoided by increasing diameters of pipes, etc.

Local traffic in close vicinity to the facility should be limited in speed.



# MAX IV Facility



## 6.6. Alignment, Positional Tolerances

---

The tolerances for positioning components are discussed here. There are several sources for positional errors.

- Achievable precision during alignment
- Settling of buildings
- Thermal drift

Specification of tolerances has to be well thought through in order to avoid unnecessary costs and time consuming. Especially for the accelerators, there is a need for a diversified specification for the global scale and for finer, local, areas all the way down to internal positioning of magnet functions inside magnet units.

At the deadline there is not a full specification on the alignment tolerances. This section lists what is known.

### 6.6.1. MAX IV Rings

Between magnet block a tolerance 0.1 mm is foreseen to be acceptable. On a larger scale no calculations have been done so far. It seems realistic to be able to get down to a few mm on the diameter of the 3 GeV ring, 0.2 mm or better at the 1.5 GeV ring.

See section 2.4.3 for more information.

### 6.6.2. Linac and e-beam Transport

At the time for the deadline there are no numbers on the tolerances on alignment. When the lattice is ready it will be possible to calculate on this. This will be done in the nearest future. The method will probably be standard surveying methods in combination with beam based alignment.

### 6.6.3. Beamlines

Regarding beamline alignment there are no real tolerances set so far. The precision that can be achieved with normal surveying tools, such as autolevels, theodolites and laser trackers will work for most beamlines. Since specific beamlines are still not defined very detailed it is not possible to me more specific at this point. The same tools as for the accelerator alignment will be used and a relative precision of 100-200  $\mu\text{m}$  should be possible within the length of a 50 m long beamline.





# MAX IV Facility



## 6.7. Conclusions

---

- Due to the unknown future demands on the MAX IV facility the principle of caution is the overall goal: **It is recommended that the present vibration level at the “green field” should not be significantly increased.** The present levels are between 5 and 10 nm rms (from 10 Hz and up).
- The level of vibrations at the facility should be kept below 25 nm rms at frequencies higher than 10 Hz.
- The impact of vibrations on beamlines should be investigated deeper.
- All components that vibrate have to be designed, isolated or positioned in order to minimize their contribution to the cultural noise background.
- Beamline and accelerator components and their stands and girders should be designed with stiffness and high natural frequency as overall goal.
- The facility floor and underlying grade should be designed for high stiffness.
- Alignment tolerances are achievable with present modern surveying tools.
- More work is needed in several areas:
  - Effects of correlated vs. uncorrelated vibrations
  - Isolation of vibrating sources.
  - Testing viscoelastic damping pads.
  - Setting tolerances on alignment.
  - Analysis and tests on concrete girders and their connection to floor.
  - Reduction of vibrations from cooling water tubes
  - Analysis on beamline tolerances
  - Linac tolerances, vibrations, alignment and settlements
  - Get better material knowledge on the soil
  - Use better material parameters in new FEM calculations



# MAX IV Facility





## 6.8. References

---

1. “On generic vibration criteria for advanced technology facilities: with a tutorial on vibration data representation”, .: **Amick, H.** 1997, Vols. J. Inst. Env. Sci., 40(5), pp. 35-44.
2. “Centile spectra, measurement times, and statistics of ground vibration”. **Hal Amick, Michael Gendreau, & Nat Wongprasert.** Okayama University, Okayama, Japan : s.n., 2005, Presented at the Second International Symposium on Environmental Vibrations: Prediction, Monitoring, Mitigation and Evaluation (ISEV2005).  
[http://www.cganda.com/pdf/HA\\_MG\\_NW\\_Centile\\_Spectra\\_ISEV2005.pdf](http://www.cganda.com/pdf/HA_MG_NW_Centile_Spectra_ISEV2005.pdf).
3. **Ramila Amirikas, Alessandro Bertolini, Wilhelm Bialowons, Heiko Ehrlichmann.** *Measurement of a Magnet Girder in MAXLab.* 2006. EUROTeV-Report-2006-020.
4. *ANALYSIS OF BEAM ORBIT STABILITY AND GROUND VIBRATIONS AT THE DIAMOND STORAGE RING.* **R. Bartolini, H. Huang, J. Kay, I. Martin.** 2008, Proceedings of the EPAC08, Genoa, Italy, pp. 1980-1982. WEPC002.
5. [http://www.bnl.gov/nsls2/project/reviews/docs/CDR/Vibration\\_Analysis.pdf](http://www.bnl.gov/nsls2/project/reviews/docs/CDR/Vibration_Analysis.pdf).
6. **Rothschild, Karin.** *MaxLab IV – Mätning av vibrationer från omgivningen.* Oslo : NGI (Norges Geotekniske Institutt), 2009. 20091528-00-5-R.
7. “COMPARATIVE STUDY OF VIBRATION STABILITY AT OPERATING LIGHT SOURCE FACILITIES AND LESSONS LEARNED IN ACHIEVING NSLS II STABILITY GOALS”. **N. Simos, et al.** 2008, Proceedings of EPAC08, pp. 181-183.
8. *The Role of Buildings and Slabs-on-Grade in the Suppression of Low-Amplitude Ambient Ground Vibrations*”. **al., Hal Amick et.** Berkeley, CA : s.n., 2004, Vol. Proceedings of the 11th International Conference on Soil Dynamics & Earthquake Engineering (11th ICSDEE) & the 3rd International Conference on Earthquake Geotechnical Engineering (3rd ICEGE), pp. 877-881.
9. **Thomson, Willian Tyrell.** *Theory of Vibrations with Applications*, 2.ed. Sydney : George Allen & Unwin Ltd., 1981. p. 64. ISBN 0-04-620012-6.
10. *Reduction of Open-Loop Low Frequency Beam Motion at the APS.* **G. Decker, Y.G. Kang, S. Kim, D. Mangra, R. Merl, D. McGhee, S. Sharma.** Argonne : s.n., Vols. PROCEEDINGS OF THE 1995 PARTICLE ACCELERATOR CONFERENCE VOLUME 1 OF 5, p 303-305.
11. *Private communication.* **Rolf Follath, BESSY II/HZB, Berlin.**



12. **Persson, Peter.** *ANALYSIS OF VIBRATIONS IN HIGH-TECH FACILITY.*  
Lund : s.n., 2010. ISSN 0281-6679.
13. **Montero, Juan Negreira.** *Vibration Analysis of Underground Tunnel at High-Tech Facility.*  
Lund : s.n., 2010.
14. **J. Negreira, K. Persson, G. Sandberg, D. Bard.** *Vibration analysis of underground tunnel at high-tech facility (condensed report).* Lund : s.n., 2010.
15. **Jensen, B. N.** *On the suggested bridge over LINAC tunnel.* Lund : s.n., 2010.
16. **Popov, E. P.** *Mechanics of Materials, 2.ed.* Berkeley : Prentice/Hall International, Inc., 1987. p. 536.
17. **Vašina, Radovan.** *Transient response analysis on supporting blocks for bending.* 2009.

# MAX IV Facility



# Contents

---

<b>7.1.</b>	<b>General .....</b>	<b>4</b>
7.1.1.	Source Models and Attenuation Data .....	4
7.1.2.	Dose Limits .....	4
<b>7.2.</b>	<b>The Linac .....</b>	<b>6</b>
7.2.1.	Electron Losses .....	6
7.2.2.	The Linac Tunnel .....	7
7.2.3.	The Klystron Tunnel .....	12
<b>7.3.</b>	<b>The 3 GeV Ring .....</b>	<b>14</b>
7.3.1.	Introduction .....	14
7.3.2.	Comparison with Existing and Planned Facilities .....	14
7.3.3.	Electron Loss Scenario .....	15
7.3.4.	The MAX IV 3 GeV Storage Ring .....	16
7.3.5.	Heavy Concrete .....	19
7.3.6.	The Injection Area .....	19
7.3.7.	The Roof .....	19
7.3.8.	Other Laboratories .....	20
<b>7.4.</b>	<b>The Short Pulse Facility .....</b>	<b>21</b>
7.4.1.	The Bulk Shield .....	21
7.4.2.	The Experimental Area Access Maze .....	26
<b>7.5.</b>	<b>Environmental .....</b>	<b>29</b>
7.5.1.	Activation .....	29
7.5.2.	Skyshine .....	42
7.5.3.	Direct Exposure .....	45

<b>Bibliography .....</b>	<b>47</b>
<b>Appendix A. Source Models .....</b>	<b>50</b>
<b>Appendix B. Material Attenuation Lengths .....</b>	<b>54</b>
<b>Appendix C. Electron Losses.....</b>	<b>56</b>
<b>Appendix D. The Linac .....</b>	<b>57</b>
<b>Appendix E. The Short Pulse Facility .....</b>	<b>75</b>

# MAX IV Facility





## 7.1. General

---

### 7.1.1. Source Models and Attenuation Data

High energy electrons may interact with accelerator components and residual gas molecules in the vacuum tube. The electromagnetic radiation created is known as Bremsstrahlung with an energy distribution from zero to the energy of the electron. The radiation is extremely forward peaked. The Bremsstrahlung photons interact with accelerator components which results in the development of an electromagnetic shower built up of photons and electron-positron pairs. Neutrons are produced in photonuclear reactions in the accelerator components. Depending on the reaction mechanism and photon energy, the neutrons may be classified as low energy (about 2 MeV), medium and high energy. The medium and high energy neutrons are more likely to be emitted in the forward direction, whereas the low energy neutrons are emitted isotropically.

The effective dose equivalent rate  $H(\theta)$  (Sv h<sup>-1</sup>) at a distance  $r$  (m) from a point of loss  $L$  (kW) of electrons behind a shielding wall of thickness  $t$  is given by

$$H(\theta) = [L/r^2] \cdot \sum H_j(\theta) e^{-t/\lambda_j} \quad (1.1)$$

The sum is over the different types of radiation  $j$  and  $H_j(\theta)$  is the so called source term in units of Sv m<sup>2</sup> h<sup>-1</sup> kW<sup>-1</sup>,  $\theta$  is the angle between the electron direction and the dose point.  $\lambda_j$  is the material attenuation length for radiation of type  $j$ . If more than one shielding material is present, the expression will contain additional  $e^{-t/\lambda}$  factors. Equation 1.1 was implemented through out the report for analytical determinations of the dose rates except where explicitly stated otherwise.

There exists different expressions for the source terms  $H_j$ . Three of these



are examined in appendix A. They can differ by more than a factor of two which implies that the uncertainty in the results is at least as large. The model used in this report is from [15] but normalized to the 90° data in table 1.1.

Source term	Sv/kWh @ 1m and 90°
Bremsstrahlung	50
Neutrons < 25 MeV	10
Neutrons 25-100 MeV	1.2
Neutrons > 100 MeV	0.36

Table 1.1: The 90° source terms from [25]

The source terms in table 1.1 will be referred to as Brems (Bremsstrahlung), LEN (Low Energy Neutrons, < 25 MeV), MEN (Medium Energy Neutrons, 25-100 MeV) and HEN (High Energy Neutrons, > 100 MeV) in this report. The majority of the Bremsstrahlung photons emitted at 90° have energies below 10 MeV (see appendix A).

The shielding material attenuation lengths  $\lambda$  used in this report were mainly obtained from [16] and are listed in table 1.2.

Material	Brems- strahlung (cm)	Neutron (<25 MeV) (cm)	Neutron (25-100 MeV) (cm)	Neutron (>100 MeV) (cm)
lead	2.2	14	17	17
iron	4.7	13	18	18
heavy concrete	14	12	19	34
concrete	21	17	28	49
earth	44	21	56	56
polyethylene	69	6.2	61	61

Table 1.2: Attenuation lengths in cm for the shielding materials.

### 7.1.2. Dose Limits

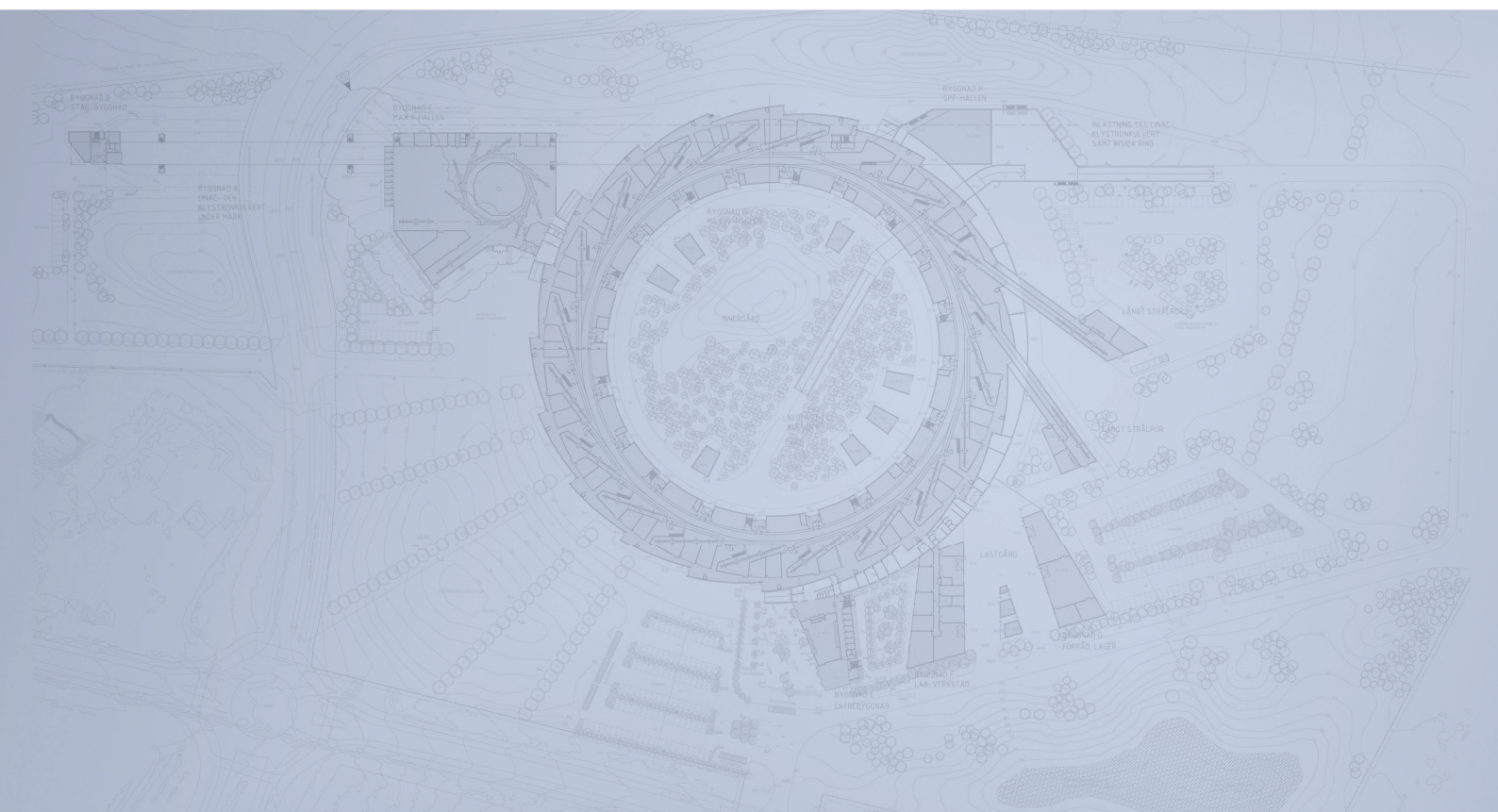
The dose limit for the general public is 1 mSv/year from facilities using ionizing radiation [23]. Since a given individual can be exposed to more than one source, the design annual dose limit for the public adopted for MAX IV is 100  $\mu$ Sv.

For radiation workers employed at the lab the probability that they should receive a dose of 6 mSv/year should be negligible (category B personnel)

[23]. The objective of the shielding design of the non-public areas of the facility is to ensure that employees receive doses less than 1 mSv/year which means (with an occupancy of 2000 h)  $1 \text{ mSv} / 2000 \text{ h} = 0.5 \text{ } \mu\text{Sv/h}$ . In addition to this, the doses resulting from system failures need to be taken into account. One of these is the case of a full beam loss at any point along the electron path.



# Detailed Design Report



## Chapter 7 MAX IV Shielding 7.2. The Linac

MAX IV Facility



## 7.2. The Linac

---

### 7.2.1. Electron Losses

The linac will be operated in two different modes. One is where it is used to fill or top-up the 3 GeV ring and this mode will always be active, i.e. its “duty” is 1. The linac can also be operated for the Short Pulse Facility (SPF) and will then run at full power. In this report, it is assumed that this mode will also be active all of the time. The different operating modes of the linac is summarized in the table 2.1

Mode	Rate (Hz)	Energy (GeV)	Charge (nC)	Power (W)	Duty
Fill/top-up	0.1	3.0	1	0.3	1.0
SPF	100	3.0	0.1	30	1.0

Table 2.1: Operating modes of the linac.

The projected electron losses in the linac tunnel and transport beam lines during normal operation will determine its required shielding. At this stage, no data concerning these losses exist for the MAX IV facility. Values from similar facilities found in literature range between 0.1% and 12%. This data is compiled in appendix C and the values adopted for MAX IV are provided in table 2.2

For the shielding design it is assumed that the losses occur at a single point. For example, in the linac tunnel ( $E > 0.2$  GeV) 1% of the electrons may be lost at any point. The minimum separation between these points, in order for the results presented in this section to be valid, will depend on the spatial width of the dose rate distribution resulting from a loss at a single point. The width is of the order of 10 m (see below) which means that different loss points need to be at least 10 m apart to prevent their

Location	Energy (GeV)	Loss (%)	Beam power @100Hz(W)	Loss power @100Hz(W)
linac	0-0.2	20	0-2	0-0.4
linac	0.2-3	1	2-30	0.02-0.3
transport/SPF	3	1	30	0.3

Table 2.2: Projected maximum losses at a single point during normal operation of the linac. The beam power and loss power is for the linac SPF mode

respective dose rate distributions from adding up (overlapping).

The charge of the electron beam will be measured at several points along the linac. It will thus be possible to determine the amount of charge lost between each of these points for every bunch of electrons accelerated by the linac. The data will be fed into the radiation protection interlock system and will regulate the frequency at which the linac operates. Both cavity BPMs (Beam Position Monitors) and toroids (current transformers) will be installed. The expected precision from a toroid system can be around 2 % [11].

As stated earlier, the shielding calculations are based on the assumption of a certain loss in Watts at a given location in the linac tunnel. The shielding results are valid as long as the loss is not exceeded. The loss of 1% of the beam at a given location at 100 Hz is equivalent to losing 100% at 1 Hz. Thus, the frequency of the linac should be adjusted such that the loss powers in table 2.2 are not exceeded.

### 7.2.2. The Linac Tunnel

MAX IV will be situated in the outskirts of Lund. Referring to figure 2.1, the linac runs in an underground tunnel which starts at location 1 and continues to location 4 where the electrons can be directed upwards to the 3 GeV ring. The electrons can also continue in the linac tunnel to the SPF located at 5. The area above the tunnel at locations 1,2 and 3 does not belong to the MAX IV facility and is freely accessible to the public. The circumference of the 3 GeV ring is 530 m and the length of the linac between locations 1 and 4 is approximately 300 m.

The bulk shielding calculation will be carried out for the linac tunnel at locations 1-4. The electron energy and the projected losses at a single point at these locations are provided in table 2.3 (refer also to table 2.2).

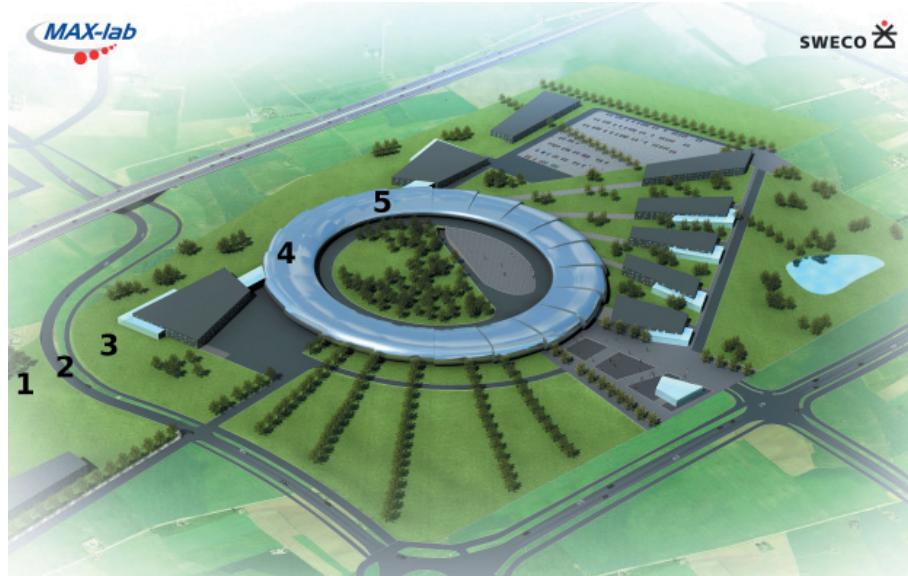


Figure 2.1: Overview of the MAX IV site.

Location	Energy (GeV)	Loss (%)	Loss @ 100 Hz (W)
1	0.2	20	0.4
2	1.0	1	0.1
3	1.5	1	0.15
4	3.0	1	0.3

Table 2.3: The electron energy and the projected losses at a single point for locations 1-4. The last column is the loss in Watts when the linac operates in SPF mode.



Figure 2.2 shows the tunnel layout at location 1. The linac is situated 130 cm off the floor in the linac tunnel and the electrons travel into the figure. The klystron tunnel runs parallel to the linac tunnel and contains the klystrons and other support systems. A layer of insulation surrounds the tunnels and prevents water from leaking in through the concrete. In the calculations that follow, it was assumed that the insulation has an attenuation coefficient of 0.0 cm. The rest of the material between the insulation and the ground level is earth. The vertical shield thickness above the linac is 50 cm of concrete, 20 cm of insulation and 380 cm of earth.

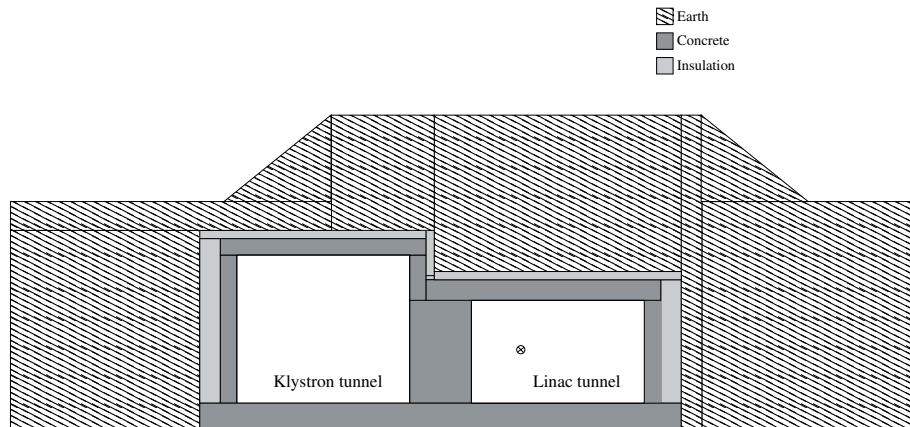


Figure 2.2: Crossection of the linac and klystron tunnels. The electrons travel into the figure.

Table 2.4 shows the tunnels at location 1 (corresponding to figure 2.2). The dose rates for Bremsstrahlung, low, medium and high energy neutrons were calculated on the grids g0-g4 which are offset 10 cm from the ground. The result of this calculation is also shown in table 2.4.

Referring to table 2.4,  $x$  is the coordinate going from right to left and equals 0.0 at the right edge of grid g4.  $z$  is the coordinate along the linac and equals 0.0 at the source point where the electron loss is assumed to occur. The geometry package in ROOT [19] was used to model the tunnels, for visualization and to calculate the length of the “trajectories” in the various materials. The distance between different points on the grids for which the dose rate was determined was typically 10 cm in both  $x$  and  $z$ .

For a given point on the grid, the distance to the source point was determined. Further, the angle between the trajectory connecting the source point and the point on the grid and the initial direction of the electrons was determined. Finally, the attenuation due to the materials along the tra-

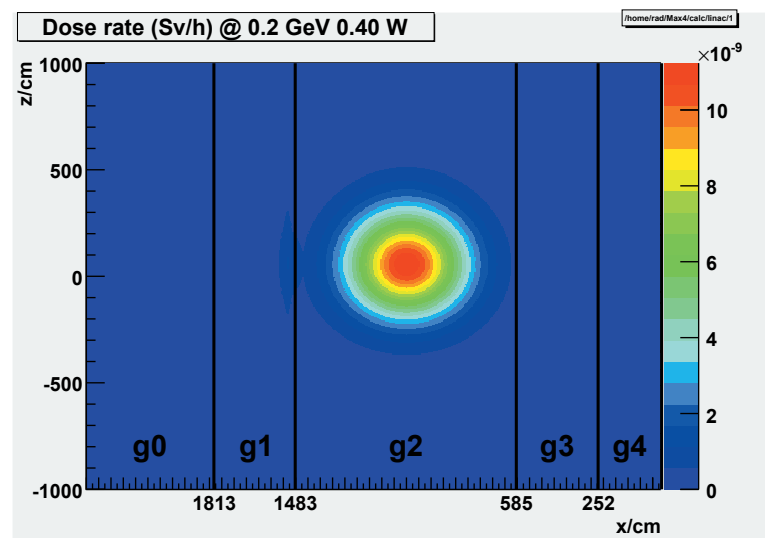
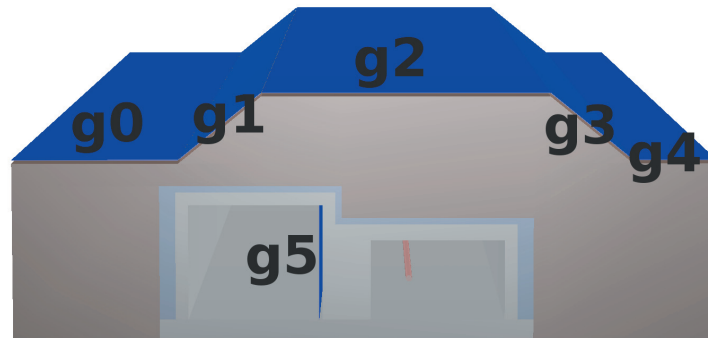


Table 2.4: Top: the linac and klystron tunnels at location 1 and the grids g0-g4 on which the dose rate was calculated. The electrons travel into the figure. Bottom: the corresponding dose rate on grids g0-g4.

jectory between the source point and the point on the grid was calculated. The dose rate is then given by equation 1.1 for the energy and loss power as given by table 2.3.

The maximum dose rate is around 10 nSv/h and the position of the maximum dose rate is at  $z=60$  cm which corresponds to an angle of approximately  $84^\circ$ . The dose rate has decreased to 5 nSv/h at  $z=270$  and at  $z=-140$  which means its Full Width at Half Maximum is 410 cm. At  $z=466$  and  $z=-330$  it has decreased to 1/10 of its maximum value making its width  $466 - (-330) = 796$  cm. As stated earlier, this width determines the minimum separation required between different loss points in order to prevent their dose rate distributions from adding up.

At a maximum dose rate of 10 nSv/h, the public can spend 10000 h at location 1 until the dose limit of 100  $\mu$ Sv is reached. The procedure above was carried out for locations 2, 3 and 4 and the detailed results are available in appendix D. Table 2.5 summarizes these results.

Location	Vertical shield	Dose rate ( $\mu$ Sv/h)	Dose limit (mSv)	Hours
1	50 cm concrete, 380 cm earth	0.010	0.1	10000
2	230 cm concrete	0.015	0.1	6700
3	150 cm concrete, 200 cm earth	0.005	0.1	20000
4	15 cm iron, 150 cm concrete	0.50	1.0	2000

Table 2.5: The dose rate, the dose limit and the number of hours required before the dose limit is reached for locations 1-4.

From table 2.5 it follows that the public can spend 6700 h per year above the tunnels. At location 4 iron had to be added in order to obtain an occupancy of 2000 h per year. The weight of the iron shield at location 4 is approximately 350 kg/m.

The dose rates for the case of full beam loss (100%) at locations 1-4, are arrived at by multiplying the dose rates in table 2.5 with 5 or 100, since the assumed loss was 20% at location 1 and 1% at locations 2-4. This, and the dose per linac cycle is provided in table 2.6. The electron charge detection system, described in section 2.1, will detect the low (0%) throughput and stop or reduce the frequency of the linac before the next cycle begins. At 100 Hz, there is 10 ms between the cycles which should be sufficient to accomplish this.

The dose rate distributions for distributed sources are also presented in appendix D. The calculation was carried out 100 times shifting the source point with approximately 50 cm along the linac between each calculation.

Location	Dose rate ( $\mu\text{Sv/h}$ )	Dose/cycle (pSv)
1	0.05	0.14
2	1.5	4.2
3	0.5	1.4
4	50	140

Table 2.6: The full beam loss (100% at a single point) dose rate and the dose per linac cycle for locations 1-4.

The strength of the source was normalized to 0.1 W/m which equals the available power divided by the length of the tunnel, 30 W/300 m.

### 7.2.3. The Klystron Tunnel

The thickness of the concrete wall separating the linac and klystron tunnels is 150 cm which is too thin for the projected electron losses. The dose rate in the klystron tunnel was calculated according to equation 1.1 on a grid offset 10 cm from the wall separating the linac and klystron tunnels (grid g5 in the top figure in table 2.4). The full result is available in appendix D and is summarized in table 2.7.

Location	Dose rate ( $\mu\text{Sv/h}$ )	Dose limit (mSv)	Hours
1	2.4	1.0	420
2	0.80	1.0	1200
3	1.2	1.0	830
4	2.7	1.0	370

Table 2.7: The dose rate, the dose limit and the number of hours required before the dose limit is reached in the klystron tunnel at locations 1-4.

From table 2.7 it follows the staff can spend 370 hours at location 4 until the dose limit is reached. However, these results assume a linac repetition rate of 100 Hz (30 W). At the fill/top-up repetition rate of 0.1 Hz (0.3 W), the dose rates decrease with a factor of 100 and access to the klystron tunnel is allowed.

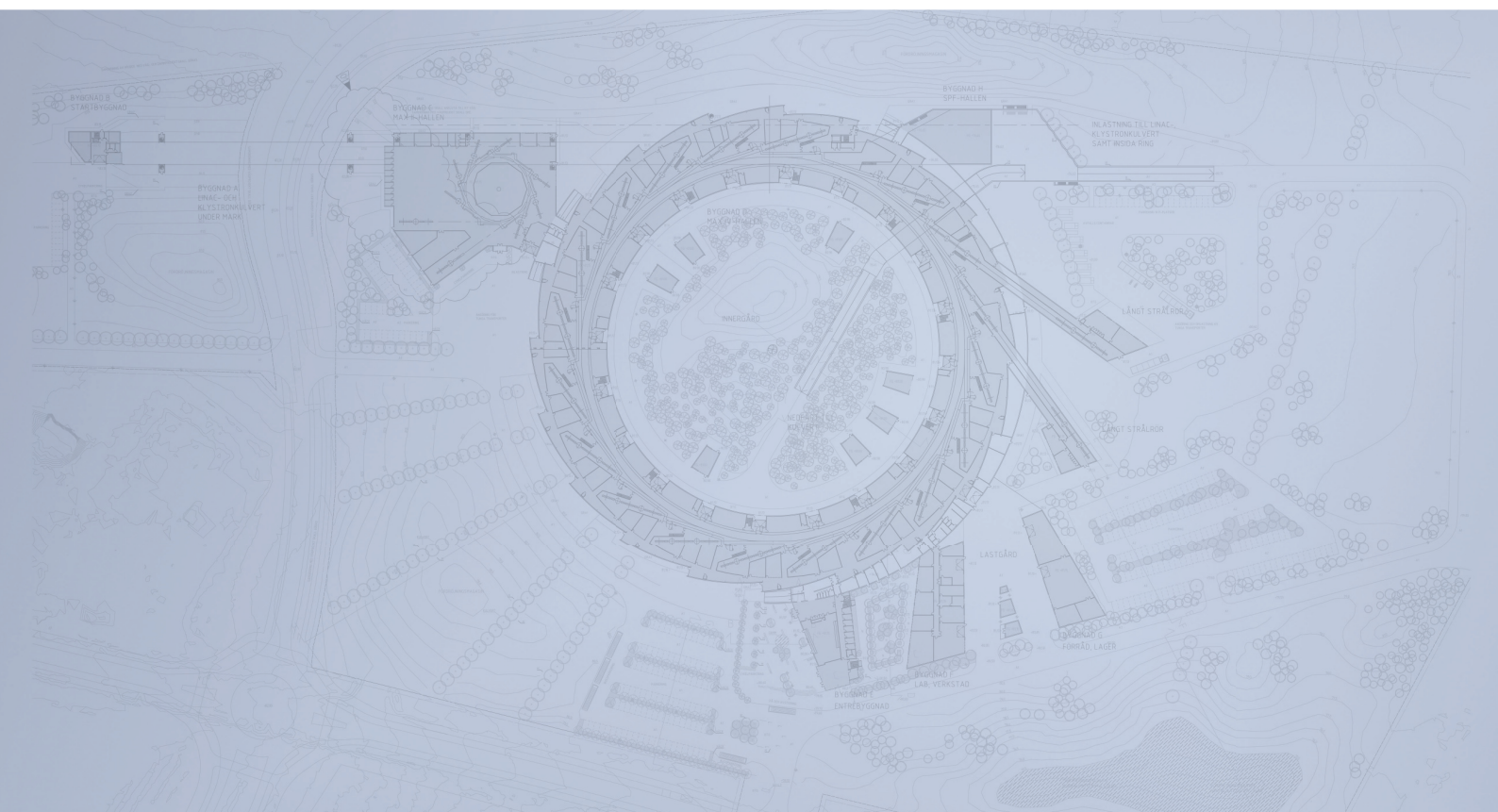
Further, the klystrons that are currently being considered for MAX IV will be equipped with integrated radiation shielding. Even if access will be restricted when the linac is running at 100 Hz, there might exist a need to access the klystron tunnel when the electron source (the gun) is off and just the klystrons are being “conditioned” at 100 Hz. The klystron shielding should sufficient to allow for this mode of operation.

The dose rates for the case of full beam loss (100%) at locations 1-4 in the klystron tunnel, are arrived at by multiplying the dose rates in table 2.7 with 5 or 100, since the assumed loss was 20% at location 1 and 1% at locations 2-4. This, and the dose per linac cycle is provided in table 2.8. The electron charge detection system, described in section 2.1, will detect the low (0%) throughput and stop or reduce the frequency of the linac before the next cycle begins.

Location	Dose rate ( $\mu\text{Sv/h}$ )	Dose/cycle (pSv)
1	12	33
2	80	220
3	120	330
4	270	750

Table 2.8: The full beam loss (100% at a single point) dose rate and the dose per linac cycle for locations 1-4 in the klystron tunnel.

# Detailed Design Report



## Chapter 7 MAX IV Shielding 7.3. The 3 GeV Ring

MAX IV Facility



## 7.3. The 3 GeV Ring

---

### 7.3.1. Introduction

The new MAX IV facility is planned to have a 3 GeV, 500 mA storage ring, with a circumference of 530 m. A full energy linear accelerator will be used as injector. The present chapter contains shielding estimates for the 3 GeV storage ring. In addition to this ring, a 1.5 GeV ring, similar to the existing MAX II ring, is being planned.

### 7.3.2. Comparison with Existing and Planned Facilities

Table 3.1 compares the properties of the MAX IV 3 GeV ring to other projects.

Facility	E (GeV)	I (mA)	circumference (m)
CLS	2.9	500	170.88
SPEAR 3	3.0	500	234.1
ALS	1.9	400	196.8
AS	3.0	400	210
DIAMOND	3.0	500	561.6
MAX IV 3 GeV	3.0	500	530
ALBA	3.0	400	268.8
NSLS-II	3.5	500	780
SOLEIL	2.75	500	354

Table 3.1: Properties of some synchrotron radiation facilities

The design parameters for MAX IV 3 GeV ring are similar to those of DIAMOND for the electron energy, stored current and circumference of the ring.



### 7.3.3. Electron Loss Scenario

The circumference of the 3 GeV ring is 530 m with 20 straight sections, one for injection and 19 for insertion devices (the length of one straight section is 5 m). A current of 500 mA corresponds to a stored energy of

$$S(J) = I(A) \cdot E_0(eV) \cdot \frac{l(m)}{c(m/s)} = 2.65 kJ \quad (3.1)$$

The number of electrons required to reach 500 mA in the 3 GeV ring is

$$n_e = \frac{I(A)}{1.60210^{-19}(As)} \cdot \frac{l(m)}{c(m/s)} = 5.5 \cdot 10^{12} \quad (3.2)$$

The linac electron bunches contain 1 nC or  $6.25 \cdot 10^9$  electrons. If the injection efficiency is 100 % then 880 bunches are required to fill the ring which will take 88 s at 10 Hz repetition rate. If we assume 4 injections per 24 h, the total number of electrons injected during 24 h are  $2.2 \cdot 10^{13}$ . These are also lost during 24 h. The loss in connection with the injection process has to be added.

Let us assume 50 % injection efficiency. The loss scheme assumed is shown in figure 3.1

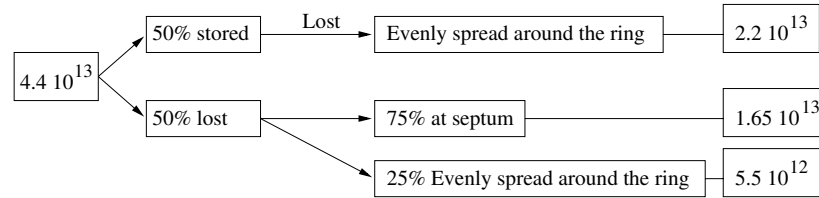


Figure 3.1: Loss scheme

With 20 straight sections we will loose  $(2.2 \cdot 10^{13} + 5.5 \cdot 10^{12})/20 = 1.38 \cdot 10^{12}$  in a sector of length  $530/20 = 26.5$  m. We will assume that the electrons may be lost at one single point along the section. This is a conservative estimate. In the calculations of the annual doses, we will use an occupancy of 2000 h. The loss numbers above are divided with 24 and multiplied with 2000. We get at septum  $(1.65 \cdot 10^{13} + 1.38 \cdot 10^{12}) \cdot 2000/24 = 1.49 \cdot 10^{15}$  and at any point along the storage ring sections we have  $1.38 \cdot 10^{12} \cdot 2000/24 = 1.15 \cdot 10^{14}$ . Each electron corresponds to  $4.81 \cdot 10^{-10}$  J. The loss at septum during 2000 h is assumed to be  $7.17 \cdot 10^5$  J. The loss at any given point along the storage ring is assumed to be  $5.53 \cdot 10^4$  J.

### 7.3.4. The MAX IV 3 GeV Storage Ring

Figures 3.2 and 3.3 illustrate the shielding design used in the calculations. In figure 3.2 the 1 m normal concrete shielding wall is shown at a position along the ring corresponding to the center of the long straight section. In figure 3.3 one sector of the ring is shown with the shielding wall being illustrated between the positions of the centers of two adjacent long straight sections. The distance between the centers is 26.5 m.

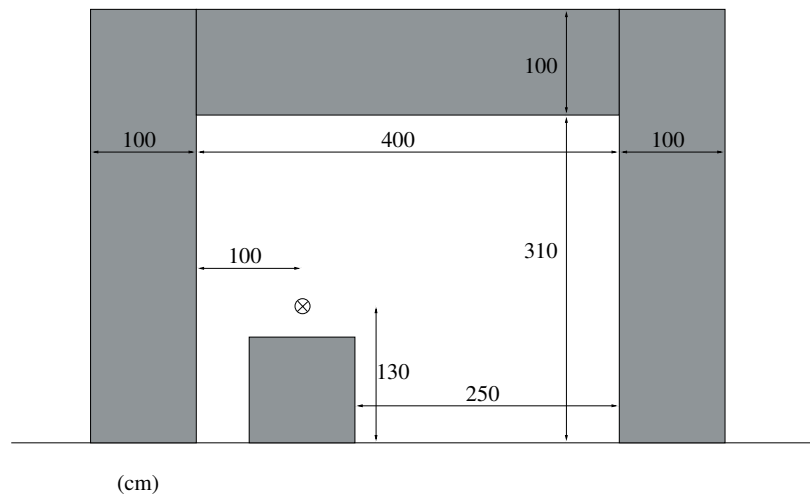


Figure 3.2: A cross section of the shielding. The left part of the shielding is towards the beam line area. The doses are calculated at a position 0.5 m outside the shielding wall.

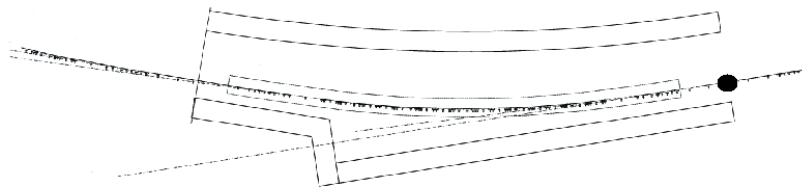


Figure 3.3: The shielding wall between the centers of two straight sections. The loss point is indicated by the solid circle.

The annual dose (2000 h) is shown in figure 3.4 as a function of the angle with respect to the direction of the electron beam. The shielding wall is 1 m ordinary concrete and the distance to the ratchet wall is about 20 m. The point of loss is in the center of the straight section and is indicated by the solid circle in figure 3.3. The ratchet wall is reinforced with 10 cm of lead

covering 3 degrees or 100 cm on both sides of  $0^\circ$ .

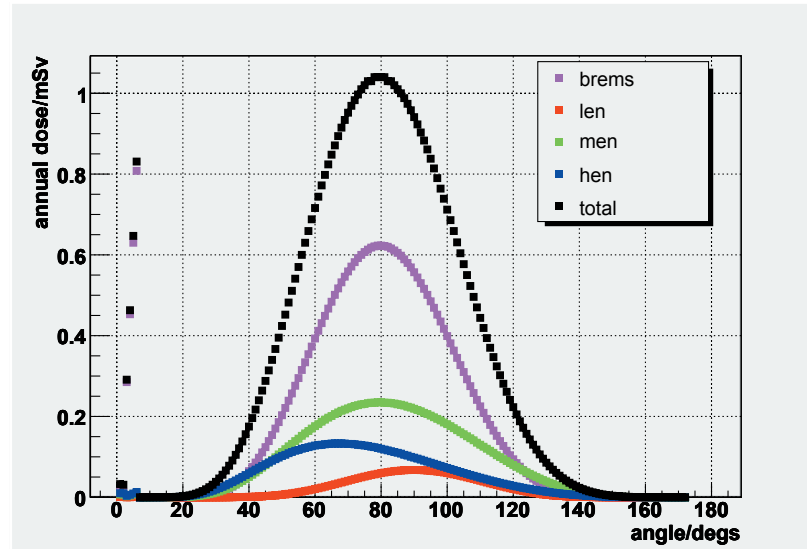


Figure 3.4: Annual dose outside a 1 m concrete shielding wall. The loss point is indicated by the solid circle in figure 3.3.

In figure 3.5 an alternative to the normal shielding wall is shown. In order to decrease the distance from the center of the long straight section to the ratchet wall to about 15 m, two parameters are changed. First, the shielding wall is moved closer to the concrete foundation housing the ring magnetic structure, second the 1 m concrete wall is replaced by a combination of iron and polyethylene over a distance of 6 m.

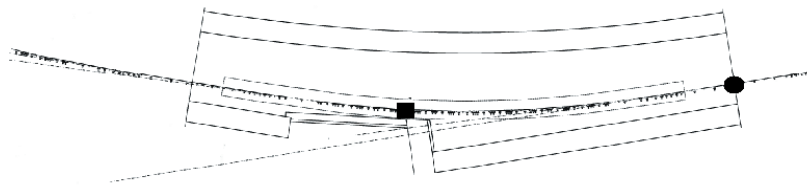


Figure 3.5: Alternative shielding wall. The two loss points are indicated by the solid circle and rectangle.

The annual dose (2000 h) for the alternative shielding is shown in figure 3.6 as a function of the angle with respect to the direction of the electron beam. The shielding wall is 1 m ordinary concrete and the distance to the ratchet wall is about 15 m. After that a shielding wall of 0.3 m iron and 0.1 m borated polyethylene is used. The point of loss is in the center of

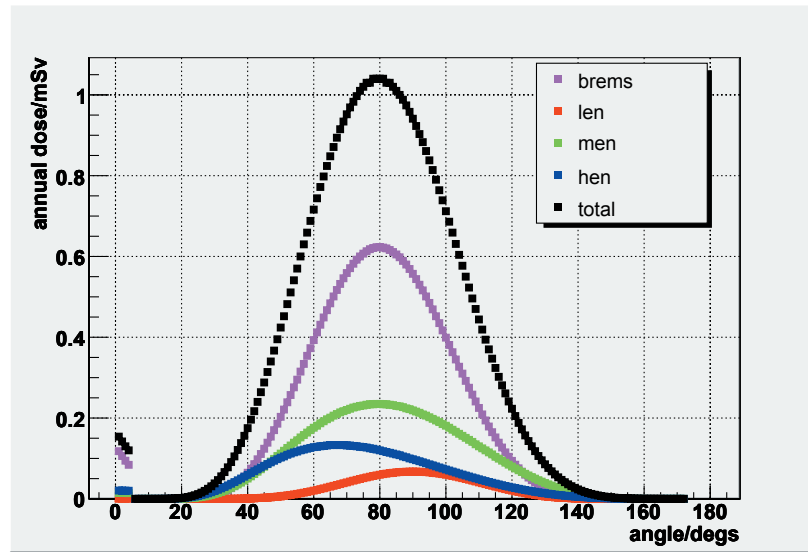


Figure 3.6: Annual dose outside the alternative shielding wall with the point of loss in the middle of the long straight section as indicated by the solid circle in figure 3.5.

the straight section as indicated by the solid circle. The ratchet wall is reinforced with 10 cm lead for angles below  $4^\circ$  corresponding to about 1 m on both sides of the forward direction.

With the shielding wall illustrated in figure 3.5, the distance from the center of the straight section to the shielding wall is about 15 m, however, the outside of the shielding wall after the ratchet wall has no effect for angles larger than  $0^\circ$  in the case of the loss of beam in the center of the long straight section.

If the point of loss is moved to where the modified shielding wall begins, indicated by the solid rectangle in figure 3.5, the dose distribution differs from that shown in figure 3.6 for angles smaller than  $90^\circ$ .

The annual dose (2000 h) for the alternative shielding is shown in figure 3.7 as a function of the angle with respect to the direction of the electron beam. The shielding wall is 1 m ordinary concrete and the distance to the ratchet wall is about 15 m. After that a shielding wall of 0.3 m iron and 0.1 m borated polyethylene is used. The point of loss is in the ring at the point where the iron-BPE shielding begins as indicated by the solid rectangle in figure 3.5. Notice that the occupancy time is 2000 h in the first optical hutch of the beamline which is probably a factor of 10 too much. The hutch will be interlocked when the beamline shutters located just before the ratchet wall are open and access will not be permitted.

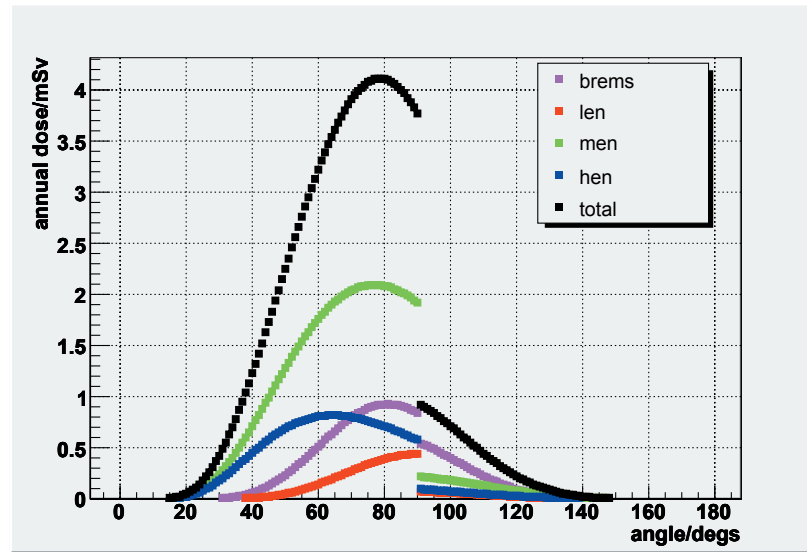


Figure 3.7: Annual dose outside the alternative shielding wall with the point of loss at a point where the alternative wall begins as indicated by the solid rectangle in figure 3.5.

### 7.3.5. Heavy Concrete

Using heavy concrete with a density of  $3.70 \text{ g/cm}^3$  for the normal shielding wall, the  $90^\circ$  annual dose is reduced to less than 0.5 mSv per year which scales with the Bremsstrahlung attenuation coefficients for heavy and normal concrete, see figure 3.8.

With heavy concrete, the thickness of the concrete shielding wall may be reduced to about 60 cm, for an annual dose of 1 mSv.

### 7.3.6. The Injection Area

As the details of the injection area are not known, we will simply use the normal ring shielding walls with an annual loss of  $7.17 \cdot 10^5 \text{ J}$ . With normal concrete, the wall thickness has to be increased to 1.7 m to limit the annual dose at  $90^\circ$  to 1 mSv. The ratchet wall requires about 2 m of concrete.

If heavy concrete is used, the thickness may be reduced to 1.3 m at  $90^\circ$  and 1.3 m for the ratchet wall.

### 7.3.7. The Roof

The thickness of the roof may be reduced due to the longer distance from the point of loss to the dose point. The distance at  $90^\circ$  will increase from

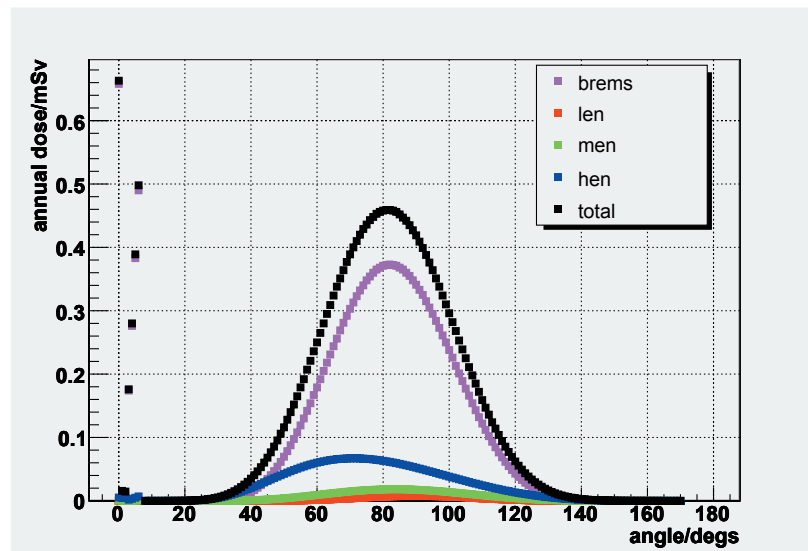


Figure 3.8: Annual dose outside the normal shielding wall consisting of heavy concrete with the point of loss at the center of the long straight section.

2.5 m to about 4 m. This implies a reduction in the dose to about 50 per cent of the values given above.

### 7.3.8. Other Laboratories

In table 3.2 the thickness of shielding walls at different laboratories are shown. The wall thickness for MAX IV 3 GeV ring seems quite similar to other storage rings, although CLS and DIAMOND are a bit different.

Facility	E (GeV)	S (J)	Side wall thickness (m)	Ratchet wall thickness (m)
CLS	2.9	826	0.46 con.	0.54 con.
SPEAR 3	3.0	1171	0.61 con.	0.91 con.
ALS	1.9	500	0.61 con.	0.61 con.
DIAMOND	3.0	2808	1.15 h.con.	1.65 h.con.
MAX IV 3 GeV	3.0	2650	1 con.	1 con.
ALBA	3.0	1075	1 con.	1 con.
NSLS-II	3.5	4550	1.2 con.	1.6 con.
SOLEIL	2.75	1622	0.7 h. con.	0.6 h. con. + lead

Table 3.2: Properties of some synchrotron radiation facilities (con. = concrete, h. con. = heavy concrete).



# MAX IV Facility





## 7.4 The Short Pulse Facility

---

### 7.4.1. The Bulk Shield

If the electrons are not directed upwards towards the 3 GeV ring, they can continue in the extension of the linac tunnel to the SPF. The electrons will pass through an undulator device, generating photons with energies in the region of 10 keV. These photons travel parallel to the electron beam up to point at which the electron beam is deflected by a dipole magnet towards the beam dump. Its important from an experimental point of view to minimize the distance between the undulator and the experimental area where the undulator photons are used. A 1 T magnet deflects the 3 GeV electron beam along a circle with a radius of 10 m. If the magnet extends between  $z=0$  and  $z=342$  cm, it deflects the beam by  $20^\circ$  ( $z$  is the coordinate along the electron path before the dump magnet). At  $z=570$  cm, the beam passes through the floor towards the beam dump. Figure 4.1 shows a schematic layout of the beam dump area. The magnet begins at point “A”, the beam dump is labeled “B”. The undulator (not shown) is situated upstream (to the left) of point “A” and the undulator photons continue along the straight dotted line to the experimental area at “C”.

The iron and concrete shielding in figure 4.1 was designed to accommodate various electron loss scenarios. Firstly, the dose rate above the beam dump at “E” should not exceed  $0.5 \mu\text{Sv/h}$  for a 30 W loss of electrons in the dump “B”. Secondly, personnel can access the experimental area at “C” even though the beam is on if the beam stoppers at “D” are blocking the photon beam. For that scenario, the dose rate at “C” should not exceed  $0.5 \mu\text{Sv/h}$  for a 30 W loss in the beam dump. Further, it is assumed that 1% of the electrons can be lost at a single point but since losses at different points can to some extent add up in the forward direction, a loss of 2% was assumed at the beginning of the magnet at “A”. The beam stoppers at “D” prevent radiation from entering the experimental area through the 5

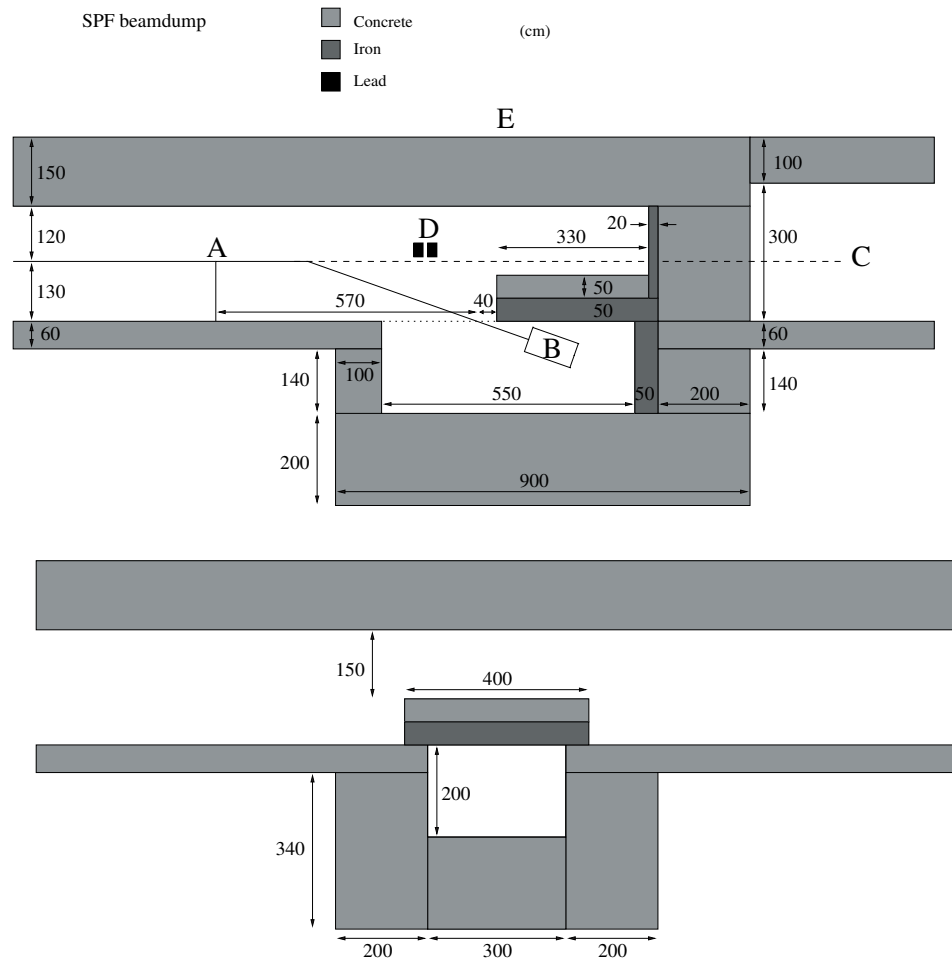


Figure 4.1: The SPF beam dump viewed along two cuts, parallel (top) and perpendicular (bottom) to the initial direction of the electrons. Refer to text for details.

cm diameter beamline opening but for larger angles ( $> 0.5^\circ$ ) the wall must be such that a loss of 0.6 W at “A” results in a dose rate below  $0.5 \mu\text{Sv/h}$  at “C”. Finally, considerations concerning activation of earth and air were also made and had an impact on the design of the beam dump. Details are given in chapter 5. A detailed layout of the beam dump is provided in figure 5.1. In the calculations that follow, attenuation due to the central core of the beam dump (labeled “C” in figure 5.1) was disregarded i.e. the source point of the analytical calculations was positioned in the center of the empty space previously occupied by the central core.

The dose rates were calculated on three grids g0, g1 and g2 for the loss scenarios described above. The grids were offset by 10 cm from the floors and walls and are shown in blue in figure 4.2.

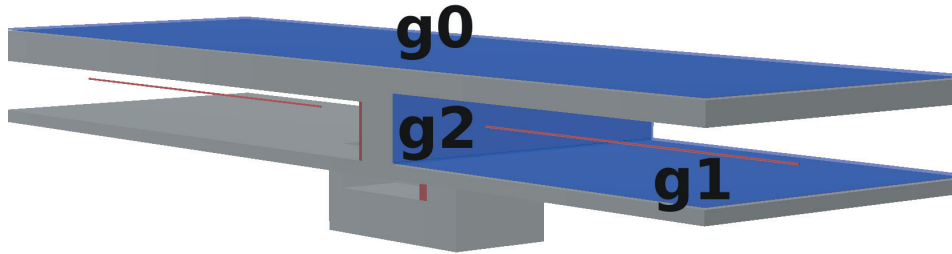


Figure 4.2: Upstream view of the three grids shown in blue on which the doses were calculated. g0 is located on the roof above the beam dump and g1 and g2 on the floor and wall in the SPF experimental area. One side of the beam dump pit and the earth surrounding it are not shown.

Figure 4.3 shows the dose rate on grid g0 for loss of 30 W in the beam dump. Looking upstream (as in figure 4.2), x runs from left to right. Z is the coordinate along the direction of the electrons. The source (the dump) is at  $x=0$ ,  $z=740$  at a  $20^\circ$  downward angle. The maximum dose rate is  $0.12 \mu\text{Sv/h}$  and is almost entirely due to neutrons.

Table 4.1 shows the dose rates on grids g1 and g2 for electron losses of 0.6 W at point “A” in figure 4.1 and for a 30 W loss in the beam dump at “B”. The left column shows the results for grid g1 and the right column for grid g2. For both g1 and g2, x runs from left to right (see figure 4.2) with the source at 0. Z for g1 is the coordinate along the floor with point “A” defining 0. Y for g2 is the height above the beamline.

The upper row shows the results for the case when 30 W of electrons are

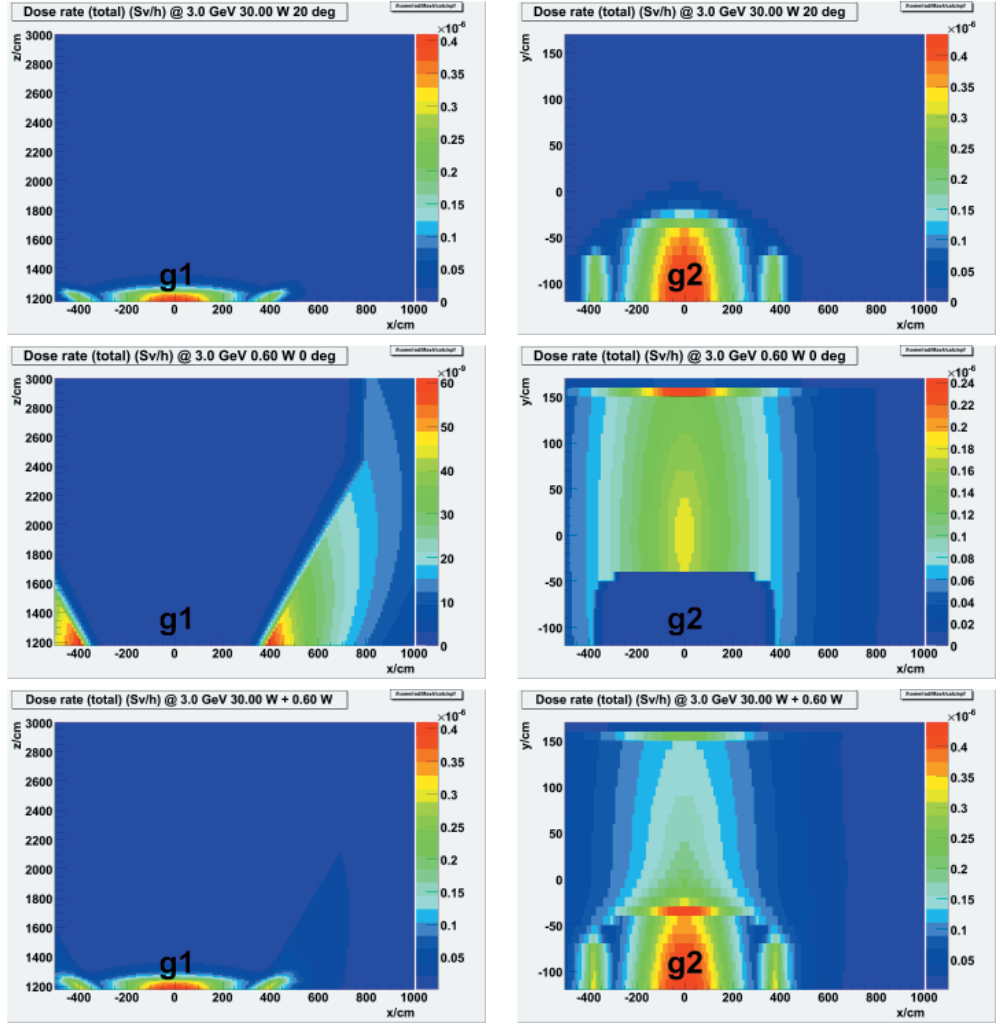


Table 4.1: The dose rates on grids g1 and g2 due to electron losses of 0.6 or/and 30 W. Refer to text for details.

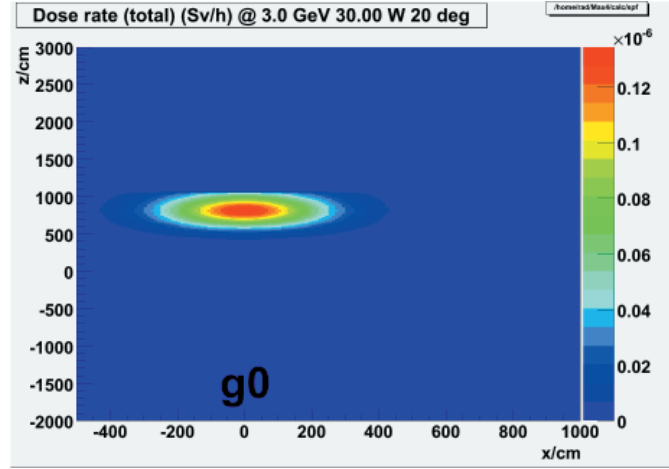


Figure 4.3: The dose rate on grid g0. Refer to text for details.

lost in the dump. The dose rate is  $0.4 \mu\text{Sv/h}$  at the intersection between the floor (g1) and wall (g2) and decreases as  $z$  and  $y$  increases. The middle row shows the dose rates when  $0.6 \text{ W}$  of electrons are lost at “A”. For both g1 and g2, the “shadow” of the concrete and iron shielding stacked on top of the beam dump pit is clearly visible. For g1 the maximum dose rate is  $60 \text{ nSv/h}$  and for g2 it is  $0.24 \mu\text{Sv/h}$  along a narrow band located at  $y=150$ . This band is due to the difference in ceiling heights between the SPF hall and the experimental area and corresponds to radiation passing above the  $20 \text{ cm}$  iron shield through the SPF ceiling into the experimental area (see figure 4.1). The bottom row shows the sum of the upper and middle row i.e. a situation in which  $30 \text{ W}$  of electrons are lost in the beam dump and  $0.6 \text{ W}$  are lost at point “A”.

The full set of results are available in appendix E the summary of which is in table 4.2.

Grid	Dose rate ( $\mu\text{Sv/h}$ )
g0	0.12
g1	0.40
g2	0.40

Table 4.2: The dose rate on grids g0, g1 and g2.

The dose rates for the case of full beam loss (100%) at point “A” are arrived at by multiplying the 2 % loss ( $0.60 \text{ W}$ ) dose rates with 50 (the middle row in table 4.1). This result, and the dose per linac cycle is provided in table 4.3. A electron charge detection system, similar to the system described

in section 2.1, will be installed in the SPF facility and will detect the low (0%) throughput and stop or reduce the frequency of the linac before the next cycle begins.

Grid	Dose rate ( $\mu\text{Sv/h}$ )	Dose/cycle (pSv)
g1	3	8
g2	12	33

Table 4.3: The full beam loss (100% at a single point) dose rates and the dose per linac cycle on grids g1 and g2.

### 7.4.2. The Experimental Area Access Maze

The previous section mostly dealt with the bulk shields located between the SPF hall and the experimental area where the undulator photons will be used for experiments. This section is about the Bremsstrahlung radiation which will enter the experimental area along with the undulator photons. There will be 4 experimental stations (beam lines) in the SPF hall with slightly different layouts. The beamline shown in figure 4.4 is the most critical in terms of radiation protection since it has the shortest length and width.

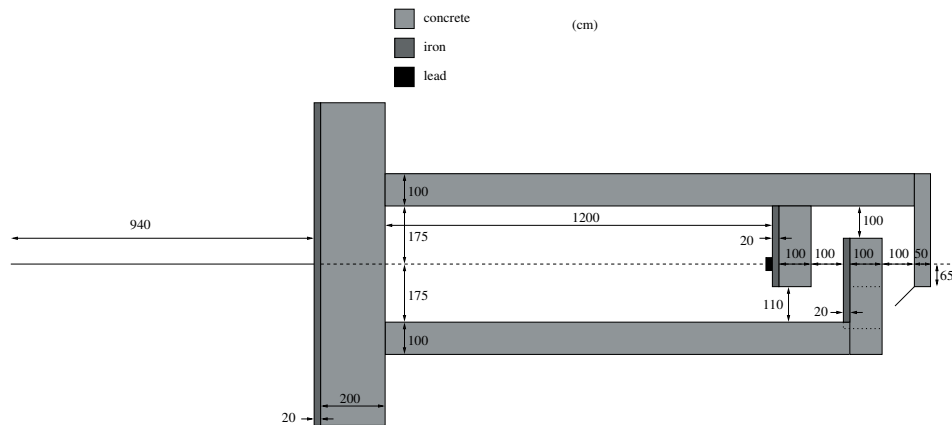


Figure 4.4: The layout of SPF experimental station number 4.

The experimental area is accessed through a maze which is closed off by a 5 mm iron door. The source of the Bremsstrahlung photons is located 940 cm from the 20 cm iron shield between the hall and the experimental area (location “A” in figure 4.1). The beamline is modeled as an iron tube with 3 mm thickness and an outer diameter of 50 mm. Lost electrons

will hit the inside of the tube with a small angle of incidence and generate Bremsstrahlung which can reach the experimental area. A “typical” angle of incidence in these scenarios is 1 mrad ( $0.057^\circ$ ), however the angle was investigated by Monte-Carlo methods [7] [8]. For angles in the range from 0 to 10 mrad, the energy of the photons and electrons entering the experimental area was determined. In these simulations the magnet deflecting the electrons  $20^\circ$  to the dump was represented as a 1 T magnetic field present between  $z=0$  (point “A”) and  $z=66$  cm. 66 cm is the distance required for the 3 GeV electron beam to be deflected 22 mm which is the inner radius of the beamline tube. For an angle of 1 mrad, the average sum of photon and electron energies was 100 MeV (per incident 3 GeV electron). This sum was found to decrease as the angle increased. Thus, the angle was set at 1 mrad.

As the undulator photons (and the Bremsstrahlung) enter the experimental area they will pass through various equipment such as mirrors and slits. This was modeled as a 30 cm long 5 cm diameter Silicon cylinder positioned directly in the beam as it emerges through the wall aperture in the experimental area. Table 4.4 shows the result of the FLUKA [7] [8] simulation of the experimental area.

The upper figure in table 4.4 shows the total dose rate in Sv/h, the middle figure the dose rate due to neutrons and the lower figure the dose rate due to muons. The dose rate at the maze entrance (at  $z=2750$ ) is approximately  $0.2 \mu\text{Sv/h}$  and about the same behind the 100 cm concrete wall at ( $z=1300$ ,  $x=-300$ ). The dose rate for a 100 % loss at point “A” is 50 times higher or about  $10 \mu\text{Sv/h}$ .



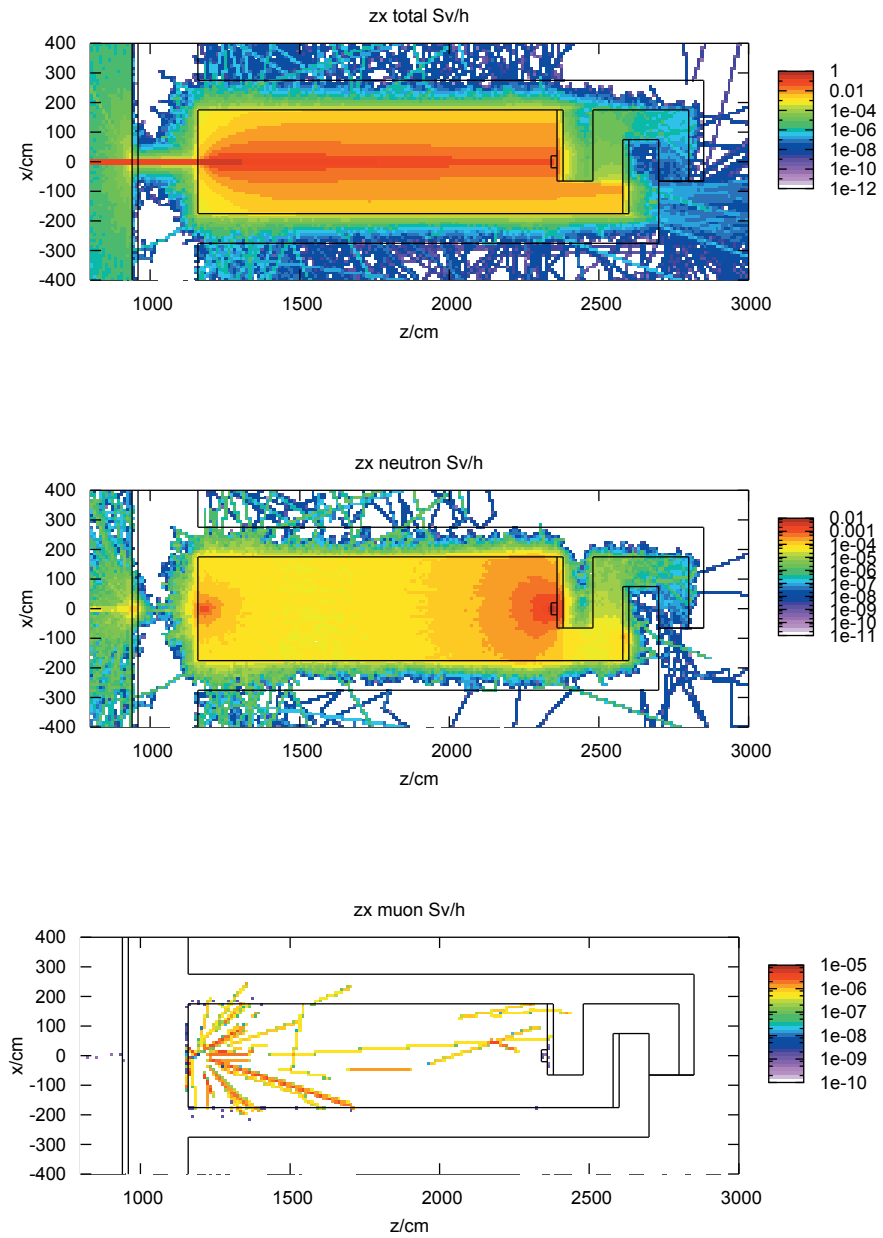
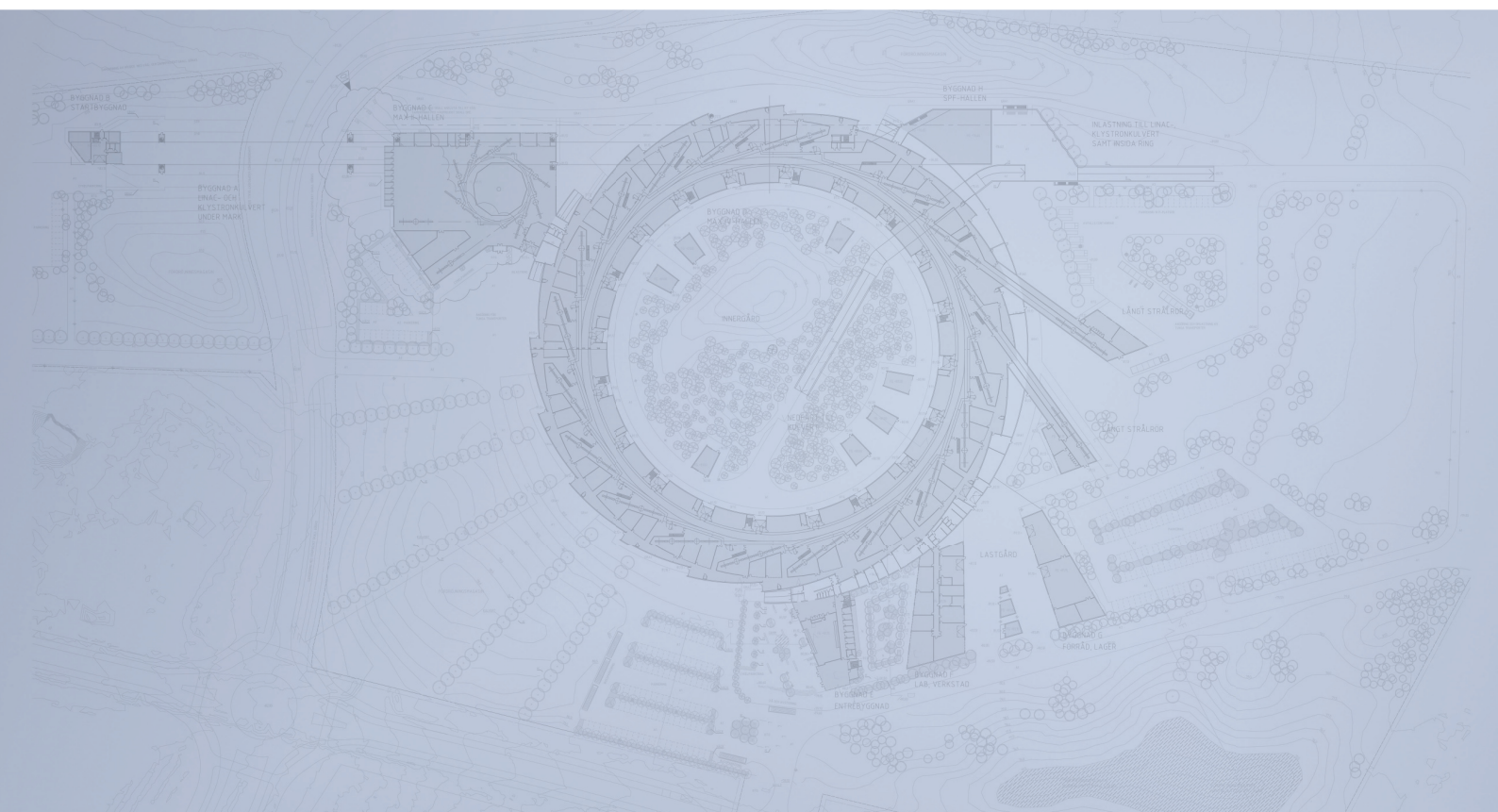


Table 4.4: The total (top), neutron (middle) and muon (bottom) dose rates in Sv/h for the SPF beamline for a 0.6 W loss of electrons at point “A” located at  $z=0$  (not shown).

# Detailed Design Report



## Chapter 7 MAX IV Shielding 7.5. Environmental

MAX IV Facility



## 7.5. Environmental

---

This chapter mostly covers effects which contribute to the general public dose. They are activation of the air and the earth and prompt radiation. The prompt radiation contributes both directly and indirectly through so-called sky-shine.

### 7.5.1. Activation

Every electron accelerated by the linac will eventually be stopped, either in a designated beam-dump or elsewhere. Photons and neutrons from the shower created when the electron is stopped can activate nuclei in the surrounding materials. The produced activity for a given isotope at time  $t$  is given by

$$S(t) = S_{sat}(1 - e^{-\lambda t}) \quad (5.1)$$

where  $\lambda$  is the decay constant and  $S_{sat}$  is the saturation activity. The saturation activity equals the rate at which the isotope is produced. If the isotope is produced in air and the air is vented, equation 5.1 changes to

$$S(t) = \frac{\lambda P}{\lambda + m}(1 - e^{-(\lambda+m)t}) \quad (5.2)$$

where  $m$  is the relative air exchange rate. The unvented saturation activity  $S_{sat}$  has been replaced by the production rate  $P$ .

In order to determine the activation of air and earth, assumptions regarding where the electrons are lost have to be made. The results that follow are based on the assumption that 20 % of the electrons are lost at 0.2 GeV and another 5 % are lost at 3.0 GeV at different locations before the electrons reach the designated beam-dump in the SPF hall. Since the beam power is 30 W in SPF mode, the power of the electrons lost at 0.2 GeV will be 0.4 W and 1.5 W at 3.0 GeV. To reduce the number of scenarios, the electrons lost at 0.2 GeV were added to the electrons lost at 3.0 GeV

increasing the power to 1.9 W. In order to account for the MAX IV 3 GeV ring which will be filled at an average power of 0.3 W, the losses at 3.0 GeV were again increased to 2.2 W.

Further, the electrons that are lost before reaching the beam-dump were assumed to hit an iron cylinder with a radius of 1.0 cm and a length of 10.0 cm. The designated beam-dump situated in the SPF hall is shown in figure 5.1 and consists of a 18 cm diameter iron core cylinder with a length of 35 cm surrounded by additional iron shielding. The electrons enter from the left along the arrow. The core cylinder is labeled “C” in the figure and its length corresponds to 20 radiation lengths (1.76 cm) and the diameter to 3 Moliere radii (1.40 cm) plus one Bremsstrahlung attenuation length (4.7 cm). Thus, the majority of the shower will develop in the core cylinder. The weight of the dump is approximately 2200 kg. An advantage of using iron instead of aluminum or graphite, is its lower yield of high energy neutrons. The yield is lower by almost a factor two [25] compared to aluminum and the shielding around the electron-dump is largely determined by the high energy neutrons. The disadvantage is that iron is more susceptible to activation than aluminum.

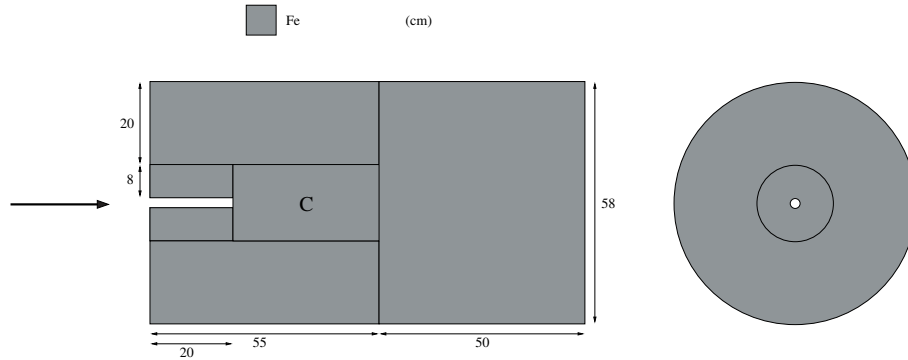


Figure 5.1: The SPF beam-dump.

The 30 W average power delivered to the dump will probably not require water cooling. However, local heating in the very first part of the core cylinder hit by the electrons, needs to be investigated further. If this is found to be a problem, one could either defocus the beam just before it strikes the dump or replace the first part of the core cylinder by carbon. Carbon (graphite) has a higher melting point and higher heat conductivity than iron and a lower  $Z$  and  $\rho$  which means the heat-load is distributed over a larger volume.

A schematic overview of the SPF hall and electron dump is shown in table 5.1. The upper figure shows the SPF hall with dimensions of 20 m  $\times$  38.5 m

and the pit where dump is located. The red volume is the volume in which the electrons are assumed to be lost if they do not reach the beam-dump. It was placed at beam height (130 cm) approximately in the middle of the hall. The earth layer with a thickness of 640 cm situated under the concrete floor is also visible. The hall was enclosed by 100 cm thick concrete walls on 3 sides but only one of these side walls are visible in the figure. Similarly, the 150 cm thick concrete ceiling has been removed when generating the figure. The wall separating the SPF hall from the experimental area is visible behind the beam-dump.

The lower figure shows the beam-dump area from below with the earth and one side of the pit removed. The beam dump area is also shown in figure 4.1.

The setup in table 5.1 was realized in the Monte Carlo program FLUKA [7] [8] where the full shower created by the electrons was simulated. In order to decrease the time of the simulation, the tracking of electrons and photons was aborted at 3 MeV which is well below the threshold of  $(\gamma, n)$  reactions. Neutrons were transported down to  $10^{-5}$  eV. The simulation recorded residual nuclei produced in inelastic interactions in the air and earth volumes. The chemical composition of the air and earth used in the simulation is listed in tables 5.2 and 5.3

The output of the simulation is the total number of a given isotope that was produced in air or earth divided by the total number of electrons. Many of the produced isotopes are stable or short lived and thus have no impact. According to [15], the isotopes of significance for air activation are  $^3\text{H}$ ,  $^7\text{Be}$ ,  $^{11}\text{C}$ ,  $^{13}\text{N}$ ,  $^{15}\text{O}$  and  $^{41}\text{Ar}$  and the results presented here will thus be limited to these. Further, the most important mechanism for the activity produced in the earth below the beam-dump to contribute to the public dose, is via the ground water. The produced isotopes in the earth thus need to be produced directly in the ground water or be soluble in it. According to [15], the most important isotopes found in ground water are  $^3\text{H}$  and  $^{22}\text{Na}$ . The “leach-out” of  $^3\text{H}$  is assumed to be 100 %, that is, all the  $^3\text{H}$  produced in the earth will be present in the ground water. For  $^{22}\text{Na}$  the leach-out is assumed to be 20 % [15].

As stated above, the simulation yields the total number of isotopes produced in the air and earth volumes. However, the concentration of  $^3\text{H}$  and  $^{22}\text{Na}$  in water is also of interest. The earth layer extends about 6 m below the concrete floor and 3 m below the beam-dump pit. From the attenuation properties of earth (table 1.2) it is clear that the expected yield of isotopes at a distance larger than 3 m is small. The reported concentrations of  $^3\text{H}$  and  $^{22}\text{Na}$  below takes the yield from the full earth volume but assumes it was produced in a volume extending 3 m from the concrete surrounding the beam-dump pit. This volume amounts to  $1033.8 \text{ m}^3$ .

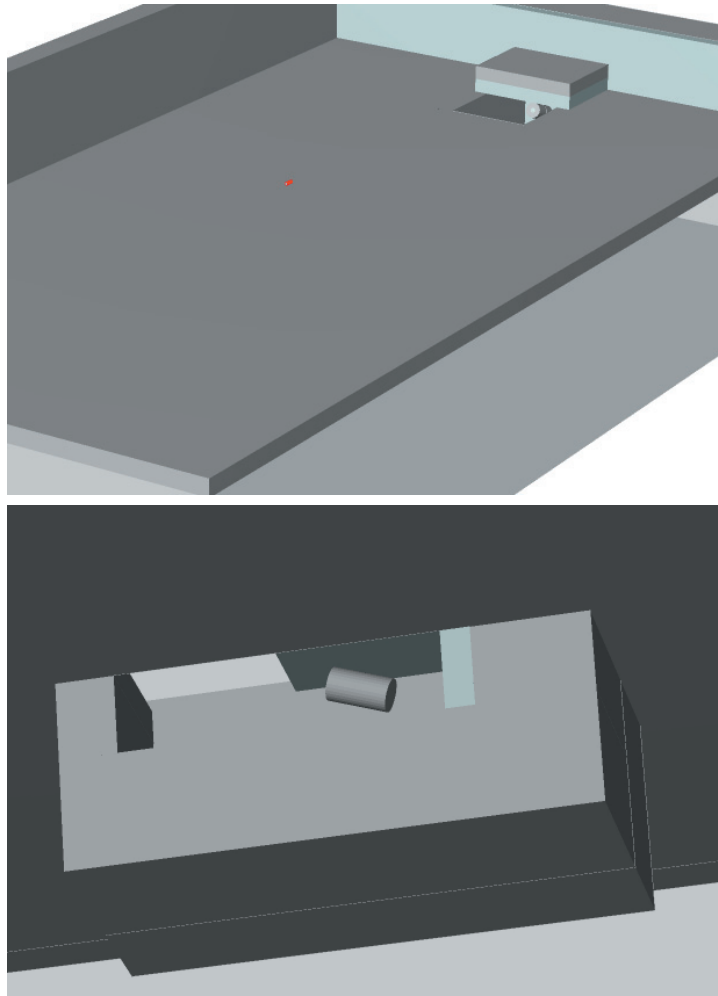


Table 5.1: The electron beam-dump in the SPF hall. The red volume in the middle of the upper figure is the volume in which the electrons are lost if they did not reach the beam dump. See also figure 4.1 for details.

Element	Weight fraction
C	0.000125
N	0.755
O	0.232
Ar	0.0128

Table 5.2: The chemical composition of air from [7] [8]

Element	Weight fraction
H	0.03
O	0.62
Mg	0.02
Al	0.04
Fe	0.02
Ca	0.04
Si	0.23

Table 5.3: The chemical composition of earth from [3].

Each simulation was divided into 5 runs in order to estimate the statistical error of the number of isotopes produced. The average statistical error is around 30 %.

#### 7.5.1.1. Results for ground water

Table 5.4 shows the number of isotopes produced in earth per incident electron for the two scenarios mentioned previously.

Isotope	Before dump/e	Dump/e
$^3\text{H}$	$3.2 \cdot 10^{-5}$	$6.4 \cdot 10^{-7}$
$^{22}\text{Na}$	$8.7 \cdot 10^{-6}$	$1.4 \cdot 10^{-7}$

Table 5.4: The relevant isotopes produced in earth per incident electron for the two scenarios considered.

Per electron, the isotope yields are higher when the electrons are stopped before the dump. This is to be expected and is a measure of the effectiveness of the dump.

For a loss of 2.3 W before the dump and 30 W in the dump the production rate per second of  $^3\text{H}$  and  $^{22}\text{Na}$  in earth can be determined. The total activities in the earth volume after one year and after 20 years follow from the half-lives of  $^3\text{H}$  and  $^{22}\text{Na}$  which are 12.3 and 2.60 years respectively. These results are presented in table 5.5. The concentration of  $^3\text{H}$  and  $^{22}\text{Na}$  in the water surrounding the beam-dump pit is arrived at through the following. The earth [3] has a density of  $1.8 \text{ g/cm}^3$  and contains 27 % water (by mass). The  $1033.8 \text{ m}^3$  volume surrounding the pit thus contains around  $502 \text{ m}^3$  water. The last column in table 5.5 has been arrived at assuming a leach-out of 100 % for  $^3\text{H}$  and 20 % for  $^{22}\text{Na}$ .



Isotope	Production rate ( $\text{s}^{-1}$ )	Activity 1 y./20 y. (Bq)	Water c. 1 y./20 y. (Bq/ $\text{m}^3$ )
$^3\text{H}$	$1.9 \cdot 10^5$	$0.11 \cdot 10^5 / 1.3 \cdot 10^5$	21/260
$^{22}\text{Na}$	$5.0 \cdot 10^4$	$1.2 \cdot 10^4 / 5.0 \cdot 10^4$	4.7/20

Table 5.5: The production rates and the total activity in the earth volume for  $^3\text{H}$  and  $^{22}\text{Na}$ . The last column contains the activity concentration in the water around the beam-dump pit.

To estimate the doses the public could receive due to the water activity presented in table 5.5, the following conservative approach was used. It is assumed that the water around the pit is not diluted during 20 years of 30 W operation and that a person then uses that water for drinking during one year. The amount of water used by a person during one year is estimated to be 3 liters/day  $\times$  365 days which equals  $1.1 \text{ m}^3$ . The  $^3\text{H}$  activity in that water is  $2.9 \cdot 10^2 \text{ Bq}$  and the  $^{22}\text{Na}$  activity 22 Bq. The conversion to doses is carried out using the coefficients in [24]. For  $^3\text{H}$  and  $^{22}\text{Na}$  the coefficients are  $1.8 \cdot 10^{-11}$  and  $3.2 \cdot 10^{-9} \text{ Sv/Bq}$ , respectively. The resulting doses for  $^3\text{H}$  and  $^{22}\text{Na}$  are 5.2 nSv and 70 nSv, respectively.

#### 7.5.1.2. Results for air

Table 5.6 shows the number of isotopes produced in air per incident electron for the two scenarios mentioned above.

Isotope	Half-life	Before dump/e	Dump/e
$^3\text{H}$	12.3 y	$2.0 \cdot 10^{-5}$	$7.2 \cdot 10^{-7}$
$^7\text{Be}$	53.1 d	$3.7 \cdot 10^{-6}$	$8.3 \cdot 10^{-8}$
$^{11}\text{C}$	20.4 min	$4.3 \cdot 10^{-6}$	$1.7 \cdot 10^{-7}$
$^{13}\text{N}$	9.97 min	$8.3 \cdot 10^{-6}$	$3.3 \cdot 10^{-7}$
$^{15}\text{O}$	122 s	$4.3 \cdot 10^{-6}$	$2.2 \cdot 10^{-7}$
$^{41}\text{Ar}$	109 min	$2.0 \cdot 10^{-5}$	$1.6 \cdot 10^{-5}$

Table 5.6: The relevant isotopes produced in air per incident electron for the two scenarios considered.

As for the earth, per electron, the isotope yields are higher when the electrons are stopped before the dump. As before, the production rate of these isotopes was determined for a 2.3 W loss before dump and a 30 W loss in the dump. The result is given in table 5.7.

In order to determine the activity per volume in the SPF hall and the released activity, it has been assumed that the volume of the hall is  $20 \text{ m} \times 38.5 \text{ m} \times 2.5 \text{ m} = 1925 \text{ m}^3$  (as it was in the simulation). The volume of the electron dump pit has to be added to this and is  $2 \text{ m} \times 3 \text{ m} \times 5.5 \text{ m} = 33 \text{ m}^3$ . Further, it is assumed that the ventilation is such that the entire

Isotope	Production rate ( $s^{-1}$ )
$^3\text{H}$	$1.4 \cdot 10^5$
$^7\text{Be}$	$2.3 \cdot 10^4$
$^{11}\text{C}$	$3.1 \cdot 10^4$
$^{13}\text{N}$	$6.0 \cdot 10^4$
$^{15}\text{O}$	$3.4 \cdot 10^4$
$^{41}\text{Ar}$	$1.1 \cdot 10^6$

Table 5.7: The isotope production rates in air per second.

volume of  $1958 \text{ m}^3$  is replaced every two hours, i.e. the relative ventilation rate  $m$  is

$$m = \frac{1}{2 \cdot 3600} = 1.4 \cdot 10^{-4} s^{-1} \quad (5.3)$$

and the ventilation rate is  $m \times 1958 \text{ m}^3 = 0.27 \text{ m}^3 s^{-1}$ . Figure 5.2 shows the air activity concentrations as a function of time.

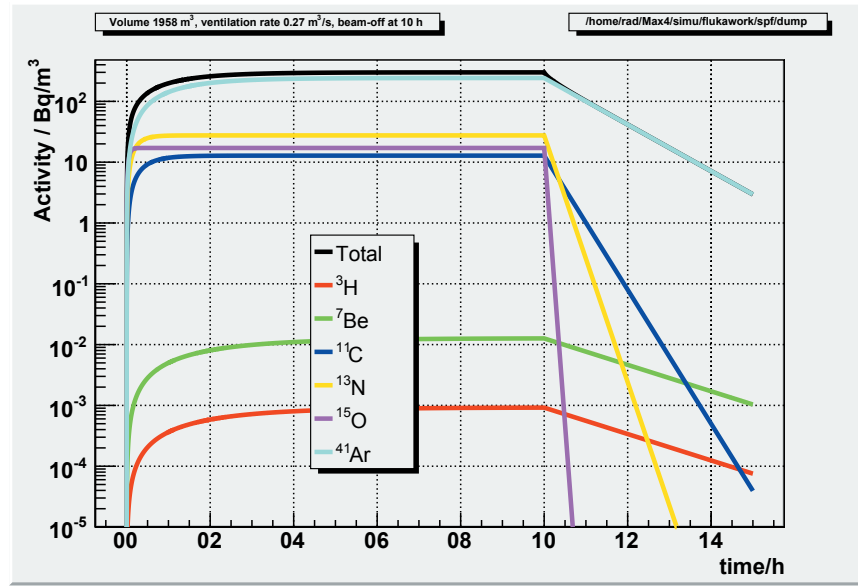


Figure 5.2: The air activity in the SPF hall. The activity is assumed to be zero when the beam is turned on. The beam is turned off after 10 h.

After 10 hours, corresponding to 5 ventilation cycles, the activities have effectively reached saturation. The short-lived (compared to the ventilation constant) isotopes,  $^{11}\text{C}$ ,  $^{13}\text{N}$  and  $^{15}\text{O}$ , reach saturation earlier and also decay faster when the beam is turned off. The air activity concentrations at saturation in the SPF hall can be determined from equation 5.2 or from figure 5.2. They are listed in table 5.8 together with release to the outside world

due to ventilation.

Isotope	Saturation activity (Bq/m <sup>3</sup> )	Release (Bq s <sup>-1</sup> )
<sup>3</sup> H	$9.3 \cdot 10^{-4}$	$2.5 \cdot 10^{-4}$
<sup>7</sup> Be	$1.3 \cdot 10^{-2}$	$3.5 \cdot 10^{-3}$
<sup>11</sup> C	$1.3 \cdot 10^1$	$3.5 \cdot 10^0$
<sup>13</sup> N	$2.8 \cdot 10^1$	$7.5 \cdot 10^0$
<sup>15</sup> O	$1.7 \cdot 10^1$	$4.7 \cdot 10^0$
<sup>41</sup> Ar	$2.4 \cdot 10^2$	$6.6 \cdot 10^1$
Total	$3.0 \cdot 10^2$	$8.2 \cdot 10^1$

Table 5.8: The saturation activity concentrations for isotopes produced in the SPF hall and the release due to ventilation.

The upper limit of the released activity to the outside world corresponds to when the linac constantly provides electrons to the SPF at 30 W. This results in a total released activity of 2.6 GBq per year.

Personnel who enter the SPF hall directly after the beam has been turned off will receive a dose due to the activated air. The dose is the sum of two contributions, due to inhalation and submersion.

Submersion is the external exposure due to the photons and electrons from the activated air. For each isotope, the dose rate is given by the product of the activity concentration (Bq/m<sup>3</sup>) and a coefficient  $h_{sub}$  (Sv/s / Bq/m<sup>3</sup>) [5].

The dose due to inhalation depends on in which organs the isotope is enriched, and on the physical and biological half-life of the isotope. The dose (committed dose) results from 50 year time integrals over the dose rate in the organs. The dose rate is given by the product of the inhalation rate (m<sup>3</sup>/h), the activity concentration (Bq/m<sup>3</sup>) and a coefficient  $h_{inh}$  (Sv/Bq) [24]. The inhalation rate is assumed to be 25 l/min or 1.5 m<sup>3</sup>/h. The coefficients, the resulting dose rates,  $D_{sub}$  and  $D_{inh}$ , and their sum are provided in table 5.9.

Personnel who enter the SPF hall after it has been running for at least 10 hours, which is sufficiently to achieve saturation activities, will, according to table 5.9, be exposed to a dose rate of 0.067  $\mu$ Sv/h. The dose rate will decrease both due to decay of the activated air and ventilation (see figure 5.2). The dose rate will decrease a factor of  $e$  during two hours due to ventilation only. The dose during two hours will thus be less than

$$0.067 \mu\text{Sv/h} \int_0^{2h} e^{-t/2} dt \quad (5.4)$$

Isotope	$h_{sub}$ (Sv/s / Bq/m <sup>3</sup> )	$h_{inh}$ (Sv/Bq)	$D_{sub}$ (Sv/h)	$D_{inh}$ (Sv/h)	$D$ (Sv/h)
<sup>3</sup> H	$3.3 \cdot 10^{-19}$	$1.8 \cdot 10^{-15}$	$1.1 \cdot 10^{-18}$	$2.5 \cdot 10^{-18}$	$3.6 \cdot 10^{-18}$
<sup>7</sup> Be	$2.4 \cdot 10^{-15}$	$4.8 \cdot 10^{-11}$	$1.1 \cdot 10^{-13}$	$9.2 \cdot 10^{-13}$	$1.0 \cdot 10^{-12}$
<sup>11</sup> C	$4.9 \cdot 10^{-14}$	$2.2 \cdot 10^{-12}$	$2.3 \cdot 10^{-9}$	$4.2 \cdot 10^{-11}$	$2.3 \cdot 10^{-9}$
<sup>13</sup> N	$4.9 \cdot 10^{-14}$	n/a	$4.9 \cdot 10^{-9}$	n/a	$4.9 \cdot 10^{-9}$
<sup>15</sup> O	$4.9 \cdot 10^{-14}$	n/a	$3.0 \cdot 10^{-9}$	n/a	$3.0 \cdot 10^{-9}$
<sup>41</sup> Ar	$6.5 \cdot 10^{-14}$	n/a	$5.7 \cdot 10^{-8}$	n/a	$5.7 \cdot 10^{-8}$
Total					$6.7 \cdot 10^{-8}$

Table 5.9: The dose rates due to submersion and inhalation of the activated air (at saturation) in the SPF hall directly after the beam has been turned off.

which equals  $0.085 \mu\text{Sv}$ . Entering the hall for two hours every day, 250 days per year, will thus result in a dose of about  $21 \mu\text{Sv}$ .

The activity released to the outside world due to ventilation,  $82 \text{ Bq/s}$ , will contribute both to the public dose and the MAX IV personnel dose. The activity concentration downwind from the exhaust will depend on the landscape and the atmospheric conditions. However, in [25], a simple model which only depends on the wind speed is presented. According to this model, the activity concentration  $q$  ( $\text{Bq/m}^3$ ) downwind of a release is given by

$$q = 18Q/uX^2 \quad (5.5)$$

where  $Q$  is the released activity in  $\text{Bq/s}$ ,  $u$  the wind speed ( $\text{m/s}$ ) and  $X$  the downwind distance ( $\text{m}$ ). This model does not account for the decay of the isotopes during the time it takes to reach the point of observation at  $X$ . Using the previously established relation between activity concentration and dose rate (tables 5.8 and 5.9), which states that  $300 \text{ Bq/m}^3$  corresponds to  $0.067 \mu\text{Sv/h}$ , and equation 5.5, the dose rate at various distances downwind of the exhaust can be determined. Table 5.10 shows the results for a wind speed of  $2 \text{ m/s}$ .

Distance (m)	Activity conc. (Bq/m <sup>3</sup> )	Dose rate (Sv/h)	Annual dose (Sv/y)
10	7.4	$1.7 \cdot 10^{-9}$	$1.5 \cdot 10^{-5}$
60	0.21	$4.7 \cdot 10^{-11}$	$4.1 \cdot 10^{-7}$
100	$7.4 \cdot 10^{-2}$	$1.7 \cdot 10^{-11}$	$1.5 \cdot 10^{-7}$
500	$3.0 \cdot 10^{-3}$	$6.7 \cdot 10^{-13}$	$5.9 \cdot 10^{-9}$

Table 5.10: The activity concentration and dose rates downwind of a release of  $82 \text{ Bq/s}$  for a wind speed of  $2 \text{ m/s}$ . The annual dose corresponds to  $24 \times 365$  hours.

Taking the changing wind direction into account will significantly decrease the annual doses in table 5.10.

### 7.5.1.3. Activation of the beam-dump

The iron in the SPF beam-dump is the most important material to consider in terms of activation. Activation will occur elsewhere, however, it is estimated that around 90 % of the electron power will be lost in the SPF beam-dump. Activation of the beam-dump (and other accelerator components) poses two problems. The first is the potential radiation hazard to personnel entering the area after the beam has been turned off. The second is the possible need to store the activated material as it decays after de-commissioning of the facility.

The Monte Carlo program FLUKA was again implemented to address these issues. The tracking of (prompt) photons and electrons was aborted at 3 MeV which is below the threshold of  $(\gamma, n)$  reactions. The threshold for the decay photons was 10 keV and for the decay electrons 100 keV. Since the attenuation length of a 10 keV photon in iron is around  $10 \mu\text{m}$  and the range of 100 keV electron around  $30 \mu\text{m}$  these thresholds will not influence the result. Table 5.11 shows the dose rate in the beam-dump area due to activation after different cool-down times (time since the beam was turned off). The activation in table 5.11 was preceded by a 10 year irradiation at 30 W and shows the dose rate down to  $0.01 \mu\text{Sv/h}$ .

In the upper figure in table 5.11 the dose rate directly after the beam has been turned off is around  $5 \mu\text{Sv/h}$  at a distance of 1m from the dump. Allowing for one day of cooling significantly improves the situation and will be required before entering the pit. After one year the activity has decreased even further and after 10 years it has effectively ceased (below  $1.0 \cdot 10^{-8} \text{ Sv/h}$ ).

As mentioned previously, the majority of the shower and thus the activation occurs in the volume labeled “C” in figure 5.1 of the beam-dump. The simulation shows that 96 % of the  $^{55}\text{Fe}$  and 87 % of the  $^{54}\text{Mn}$  is produced in the central core volume. Should there arise a need to access the pit for extended periods of time, the removal of the central core of the dump can be considered. Similarly, at de-commission, the activation is mostly concentrated to the central core and possibly only it needs to be stored separately. In both cases it is of interest to determine the dose rate distribution around the bare core volume after it has been irradiated. Table 5.12 shows the result of a FLUKA simulation of a 10 year 30 W irradiation of the bare core volume. The tracking of (prompt) photons and electrons was aborted at 3 MeV. The threshold for the decay photons and electrons was 3 keV. It should be noted that this was the actual geometry simulated, i.e. the core

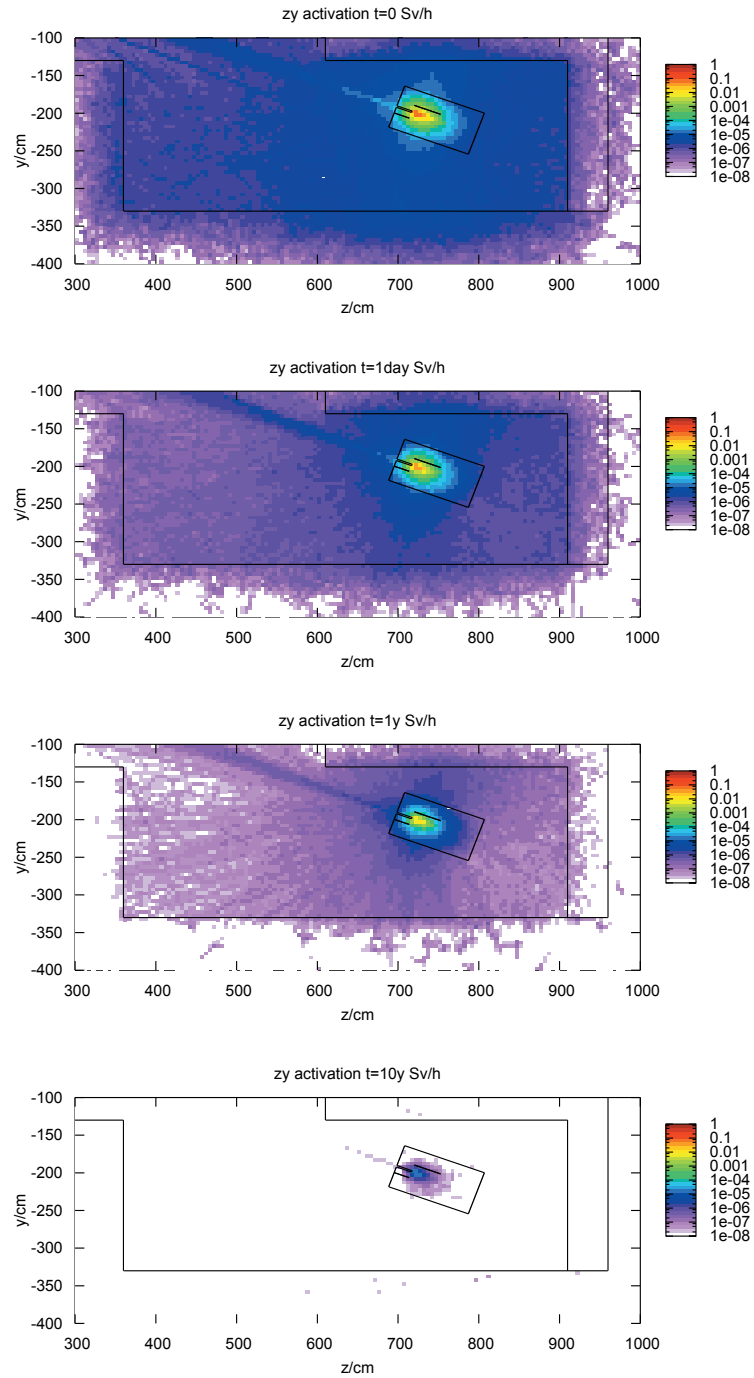


Table 5.11: The dose rate in the beam-dump pit due to activation after different cool-down times (directly after beam-off, 1 day, 1 year and 10

was not surrounded by other materials during the simulation.

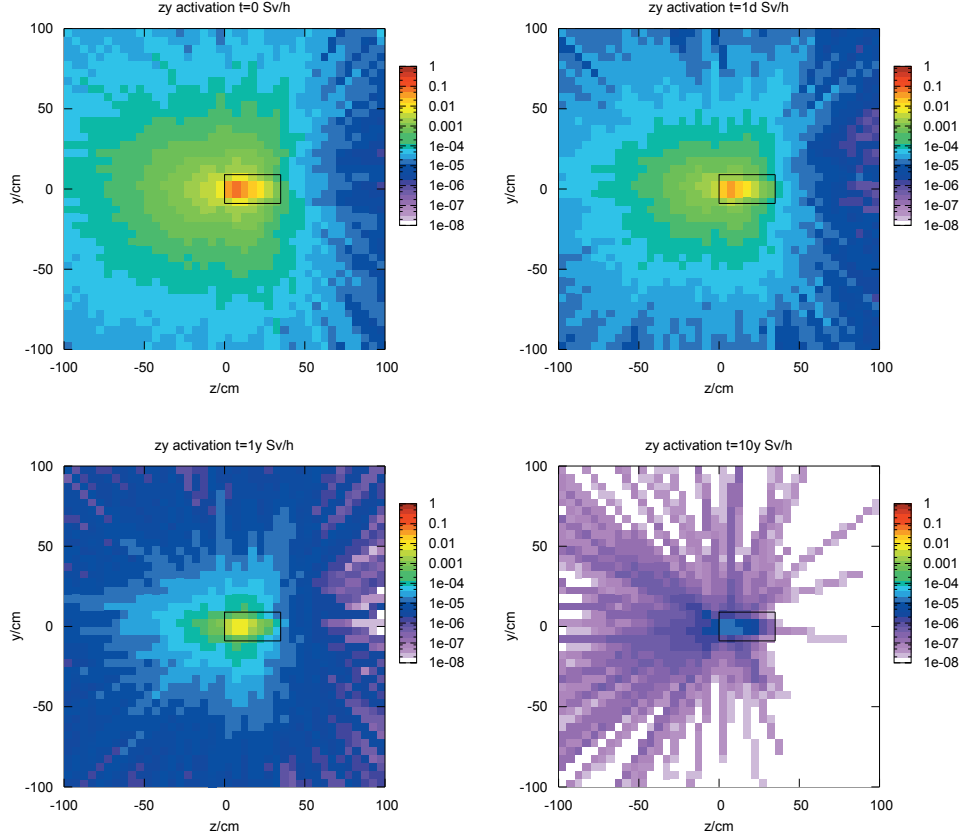


Table 5.12: The dose rate distribution due to activation of the beam-dump core at different cool-down times (directly after beam-off, 1 day, 1 year and 10 years). Refer to text for details.

From table 5.12 it follows that the dose rate at a distance of 1 m from the bare core is around  $80 \mu\text{Sv/h}$  directly after beam off. After 1 day it has decreased to about  $40 \mu\text{Sv/h}$ , after one year it is around  $8 \mu\text{Sv/h}$  and finally after 10 years it has decreased to about  $0.05 \mu\text{Sv/h}$ .

[1] investigates the isotopes produced when a 2.5 GeV electron beam hits thick targets of Al, Fe, Cu and Pb. The isotopes for which results are presented in [1] were also determined from the present FLUKA simulation and are listed in table 5.13.

Generally, the agreement between the present FLUKA simulation (column 4) and [1] (column 5) is good. The residual activity in the iron target

Isotope	Half-life	Production ( $e^{-1}$ )	Production ( $s^{-1}$ )	Ref. [1] (Bq)	Activity @ t=0 (Bq)	Activity @ t=10y. (Bq)	Activity @ t=20y. (Bq)
$^3\text{H}$	12.3 y	$2.0 \cdot 10^{-3}$	$1.2 \cdot 10^8$	$9.6 \cdot 10^7$	$5.4 \cdot 10^7$	$3.1 \cdot 10^7$	$1.7 \cdot 10^7$
$^{24}\text{Na}$	15.0 h	$4.3 \cdot 10^{-6}$	$2.7 \cdot 10^5$	$8.4 \cdot 10^5$	$2.7 \cdot 10^5$	0.0	0.0
$^{44}\text{Sc}$	3.93 h	$2.1 \cdot 10^{-4}$	$1.3 \cdot 10^7$	$1.7 \cdot 10^7$	$1.3 \cdot 10^7$	0.0	0.0
$^{46}\text{Sc}$	83.8 d	$1.6 \cdot 10^{-4}$	$1.0 \cdot 10^7$	$2.0 \cdot 10^7$	$1.0 \cdot 10^7$	0.0	0.0
$^{47}\text{Sc}$	3.35 d	$1.3 \cdot 10^{-4}$	$8.1 \cdot 10^6$	$8.7 \cdot 10^6$	$8.1 \cdot 10^6$	0.0	0.0
$^{48}\text{Sc}$	43.7 h	$2.9 \cdot 10^{-5}$	$1.8 \cdot 10^6$	$1.4 \cdot 10^6$	$1.8 \cdot 10^6$	0.0	0.0
$^{48}\text{V}$	16.0 d	$1.4 \cdot 10^{-3}$	$8.8 \cdot 10^7$	$6.9 \cdot 10^7$	$8.8 \cdot 10^7$	0.0	0.0
$^{48}\text{Cr}$	21.6 h	$5.3 \cdot 10^{-5}$	$3.3 \cdot 10^6$	$2.8 \cdot 10^6$	$3.3 \cdot 10^6$	0.0	0.0
$^{49}\text{Cr}$	42.3 min	$7.0 \cdot 10^{-4}$	$4.4 \cdot 10^7$	$3.3 \cdot 10^7$	$4.4 \cdot 10^7$	0.0	0.0
$^{51}\text{Cr}$	27.7 d	$5.6 \cdot 10^{-3}$	$3.5 \cdot 10^8$	$3.3 \cdot 10^8$	$3.5 \cdot 10^8$	0.0	0.0
$^{52}\text{Mn}$	5.59 d	$1.8 \cdot 10^{-3}$	$1.1 \cdot 10^8$	$8.7 \cdot 10^7$	$1.1 \cdot 10^8$	0.0	0.0
$^{54}\text{Mn}$	312 d	$1.9 \cdot 10^{-2}$	$1.2 \cdot 10^9$	$1.1 \cdot 10^9$	$1.2 \cdot 10^9$	$3.6 \cdot 10^5$	$1.1 \cdot 10^2$
$^{56}\text{Mn}$	2.58 h	$1.4 \cdot 10^{-3}$	$8.8 \cdot 10^7$	$1.8 \cdot 10^8$	$8.8 \cdot 10^7$	0.0	0.0
$^{52}\text{Fe}$	8.28 h	$7.5 \cdot 10^{-5}$	$4.7 \cdot 10^6$	$7.8 \cdot 10^6$	$4.7 \cdot 10^6$	0.0	0.0
$^{55}\text{Fe}$	2.73 y	$3.3 \cdot 10^{-1}$	$2.1 \cdot 10^{10}$	$1.9 \cdot 10^{10}$	$1.9 \cdot 10^{10}$	$1.5 \cdot 10^9$	$1.2 \cdot 10^8$
Total					$2.1 \cdot 10^{10}$	$1.5 \cdot 10^9$	$1.4 \cdot 10^8$

Table 5.13: Activation of the beam-dump core after 10 year operation at 30 W. The saturation activities from [1] were normalized to a 30 W beam. The three last columns contains the activation after 10 years of operation ( $t=0$ ), after a cool-down of 10 years and after a cool-down of 20 years.



after 10 year operation is  $2.1 \cdot 10^{10}$  Bq, however most isotopes are relatively short-lived. After a 10 year cool-down only  $^3\text{H}$ ,  $^{54}\text{Mn}$  and  $^{55}\text{Fe}$  remains.  $^3\text{H}$  decays by beta with a maximum energy of 18 keV and  $^{55}\text{Fe}$  by electron capture and emits a low energy photon and electron (5 keV) and do not contribute to the dose rate around the activated central core.  $^{54}\text{Mn}$  also decays by electron capture but to an excited state which in turn decays emitting a photon with an energy of 835 keV.

The Annual Limit on Intake (ALI) determines when activated material may be transferred from the production site to a local waste processing facility [22]. The relevant  $\text{ALI}_{\min}$ 's are  $1.1 \cdot 10^{13}$  Bq [ $^3\text{H}$  gaseous),  $3 \cdot 10^7$  Bq ( $^{54}\text{Mn}$ ) and  $7 \cdot 10^7$  Bq ( $^{55}\text{Fe}$ ). [22] further states that the sum of the activities, expressed in ALIs, should be less than 1 for each deposit. After a 20 year cool-down, this sum amounts to 1.7 and is dominated by  $^{55}\text{Fe}$ . Allowing for an additional 1.7 years of cool-down brings the sum down to 1.

### 7.5.2. Skyshine

The term skyshine refers to radiation observed at a point on the surface of the ground which arrives at that point after one or several large angle scattering events. Skyshine has two components, photons and neutrons, and may be observed at large distances from an accelerator. For both electron and proton accelerators, neutrons are the dominant component. The radiation is prompt and ceases when the accelerator is turned off.

Below, the skyshine from the MAX IV 3 GeV and 1.5 GeV storage rings is calculated as well as contributions from the beam dump in the SPF facility. For the 3 GeV ring the loss scheme described in chapter 3 is used. For the 1.5 GeV ring the source of radiation is approximated with one point in the center of the ring. The beam dump is also considered to be a point source. The skyshine dose rate due to neutrons is calculated with the method described in [16] based on a method developed by [17].

The shielding for the 3.0 GeV ring is illustrated in figure 3.2. The layout of the injection area is similar but with a concrete thickness of 1.7 m. For the purpose of the calculation of the skyshine contributions, we will use the same shielding for the 1.5 GeV ring as for the 3.0 GeV ring, i.e. 1 m concrete. The SPF beam dump is shown in figure 4.1.

The average distance traveled by the neutrons through the shielding at the different sources was determined using the method described in [14]. This resulted in an effective shield thickness increase of 10 % for the 3 GeV ring and 25 % for the SPF.

The neutron source terms (see equation 1.1) are composed of three con-

tributions, LEN (low energy neutrons), MEN (medium energy neutrons) and HEN (high energy neutrons). The neutron dose equivalent rates are dominated by high energy neutrons for the 3.0 GeV ring injection area and the SPF, as is shown in table 5.14.

Location	$H_{LEN}(90)$	$H_{MEN}(90)$	$H_{HEN}(90)$
1.5 GeV Ring	1.0	1.2	1.1
3.0 GeV Ring	1.0	1.5	2.5
3.0 GeV Ring inj.	1.0	6.1	25
SPF dump	1.0	150	2100

Table 5.14: The relative (to  $H_{LEN}(90)$ ) contribution of neutrons with different energies at the skyshine sources.

The neutron dose rates at the sources are given in table 5.15 below. These rates are used to calculate the skyshine contribution at various positions around the MAX IV facility.

Facility	Loss (W)	$H_n(90)$ ( $\mu\text{Sv/h}$ )
1.5 GeV Ring	0.022	0.13
3.0 GeV Ring sector	0.0076	0.054
3.0 GeV Ring inj.	0.10	0.090
SPF dump	30	0.081

Table 5.15: The neutrons dose rates at the skyshine sources.

The skyshine dose rates are obtained from

$$H_{sdr}(r) = \frac{a \cdot H_n(90)}{r^2} e^{-r/\lambda} \quad (5.6)$$

where  $r$  is the distance, in m, to the source point, i.e. the septum and 19 sectors of the 3.0 GeV ring, the 1.5 GeV ring and the SPF dump. The constant  $a = 7$ . The effective air attenuation factor is denoted  $\lambda$  which is taken to be 330 m. Equation 5.6 is valid when the distance to the source exceeds 100 m. Table 5.16 shows the result of the calculation for the area around MAX IV facility.

The top figure in table 5.16 shows an overview of the MAX IV site and the bottom figure the dose distribution due to skyshine during one year ( $24 \times 365$  h). The 19 section and the injection sources of the 3 GeV ring are visible as is the SPF and 1.5 GeV sources. The borders of the MAX IV site are indicated by the solid black lines. The dashed circles show where the distance to the source equals 100 m and equation 5.6 only applies outside of any such area. The annual dose from skyshine amounts to about  $2 \mu\text{Sv}$

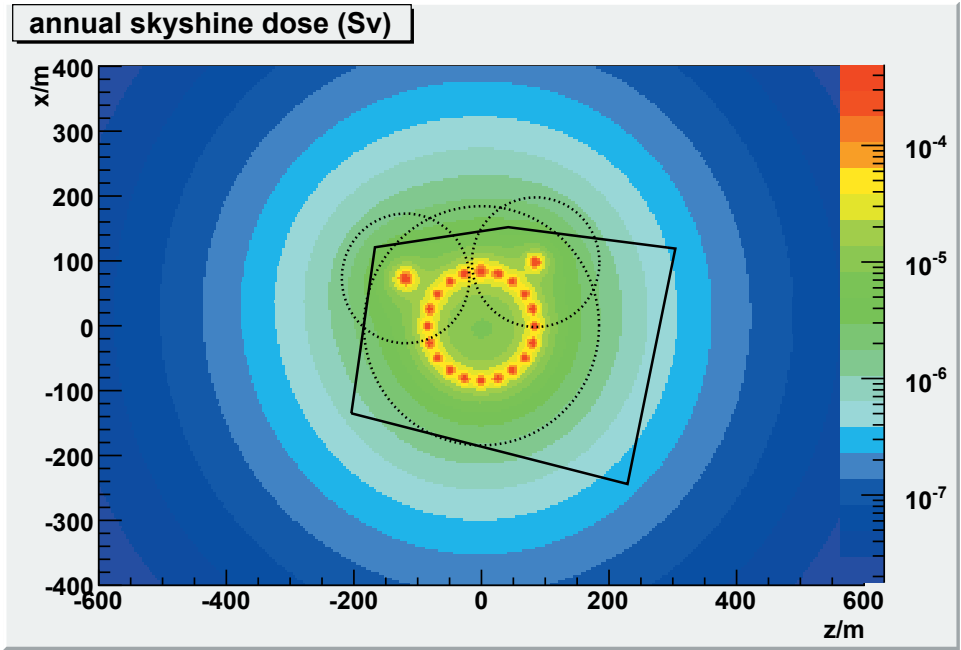
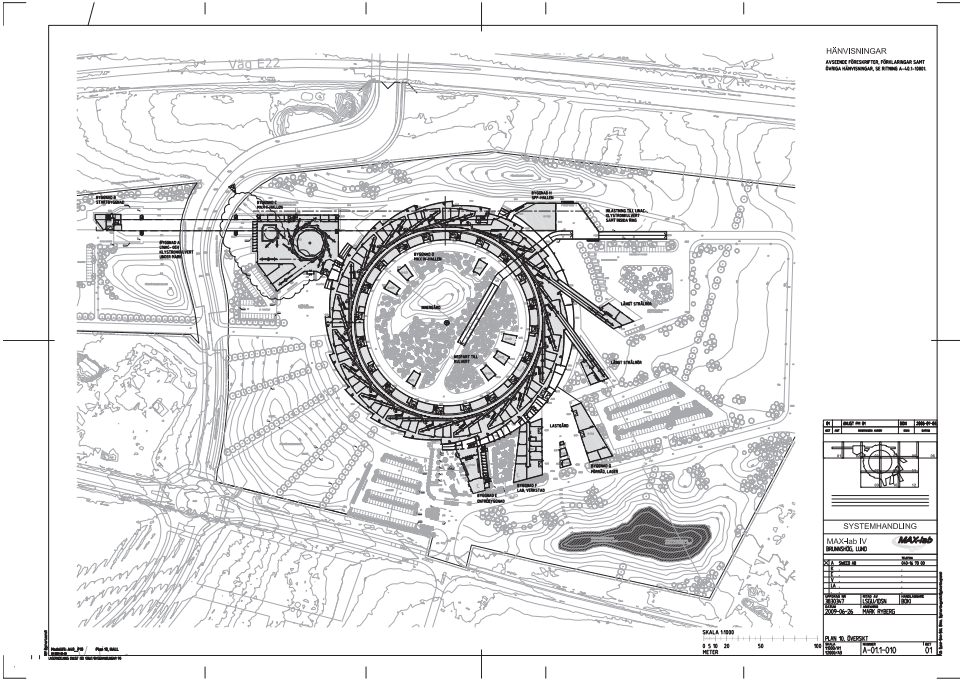


Table 5.16: Top: overview of the MAX IV site. Bottom: the skyshine dose rate during one year in Sv. Refer to text for details.

at the site borders.

### 7.5.3. Direct Exposure

The contribution from direct radiation at the MAX IV site border and beyond needs to be estimated. Only the 3 GeV ring is considered below since the SPF is situated below ground and thus there is no direct contribution from it. Further, the power of the 1.5 GeV ring is low compared to the 3 GeV ring and it is also not included here.

The 3 GeV ring is shielded to 1 mSv per 2000 h at a distance of 0.5 m from the shielding wall of the ring (see chapter 3). The shortest distance from the 3 GeV ring tunnel to the site border is 60 m. This is in the up direction in the top figure in table 5.16. The annual dose rate was determined as a function of the radial distance from the 3 GeV ring tunnel. A 0.0076 W loss of electrons at each of the 20 loss-points was assumed (the injection sector was replaced by an ordinary sector which is a reasonable approximation since it is also shielded to 1 mSv per 2000 h). For each point on the radial path and for each loss-point, the effective thicknesses of concrete and lead was calculated. The angle between the direction of the electrons and a line connecting the loss-point and the point on the radial path was determined. The geometry for which this was carried out is shown in figure 3.3. The dose rate per year ( $365 \times 24$  h) was determined using equation 1.1 and table 1.2. It was found that the result was slightly dependent on the location of the start point for the radial path, i.e. its location relative the closest loss-point and ratchet wall. Since the symmetry of the ring is 20 (there is  $18^\circ$  between two sectors) the calculation was repeated 18 times shifting the ring one degree clockwise each time and then taking the average. The result is shown in figure 5.3.

In the calculation above attenuation of the radiation in the building housing the ring tunnel and the air was disregarded. The annual dose at a location 60 m from the ring tunnel is  $40 \mu\text{Sv}$ .

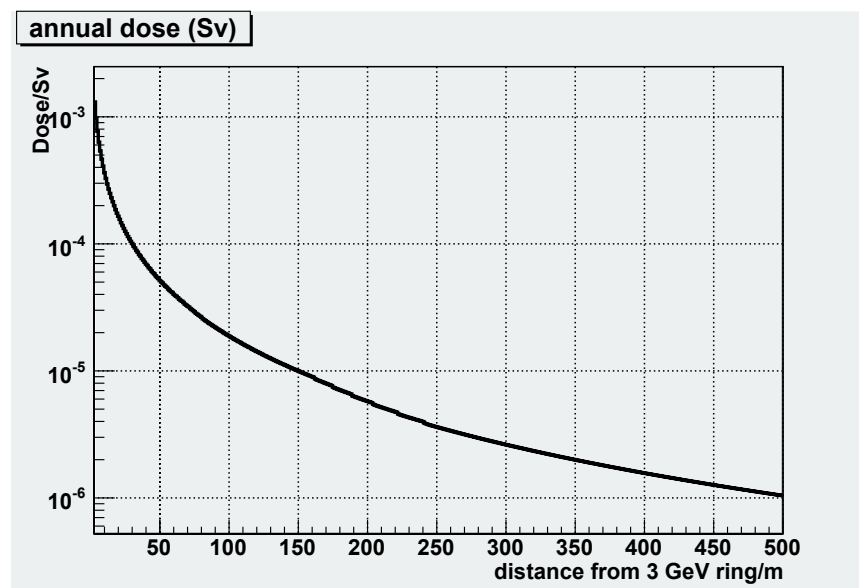


Figure 5.3: The annual dose due to direct radiation from the 3 GeV ring as a function of the distance to the ring tunnel. Refer to text for details.

---

## Bibliography

- [1] Radioactivity induced in a 2.5 GeV electron beam dump  
S. Ban *et al.*  
Radiation Protection Dosimetry, Vol 93, No. 3, pp. 231-236 (2001)
- [2] Calculation and design for SSRF's bulk shield  
K. M. Fang *et al.*  
Radiation Measurements 41 (2007) S256-S259
- [3] Soil, Groundwater and Cooling Water Activation at the TESLA Beam Dump  
N. Tesch  
Laboratory Note, DESY D3 - 114, March 2001  
Deutsches Elektronen-Synchrotron DESY
- [4] Radionuclide and radiation protection handbook 2002  
D. Delacroix *et al.*  
Radiation Protection Dosimetry Vol. 98 No 1, 2002
- [5] External Exposure to Radionuclides in Air, Water and Soil  
EPA-402-R-93-081  
Federal Guidance Report No. 12  
Keith F. Eckerman and Jeffrey C. Ryman  
Oak Ridge National Laboratory  
Oak Ridge, Tennessee 37831  
September 1993
- [6] Radiation Protection Studies for the ALBA Facility  
Ferran Fernandez and Xavier Queralt  
4th International Workshop on Radiation Safety at Synchrotron Radiation Sources
- [7] "The FLUKA code: Description and benchmarking"  
G. Battistoni, S. Muraro, P.R. Sala, F. Cerutti, A. Ferrari, S. Roesler, A. Fasso', J. Ranft,  
Proceedings of the Hadronic Shower Simulation Workshop 2006,  
Fermilab 6–8 September 2006, M. Albrow, R. Raja eds.,  
AIP Conference Proceeding 896, 31-49, (2007)

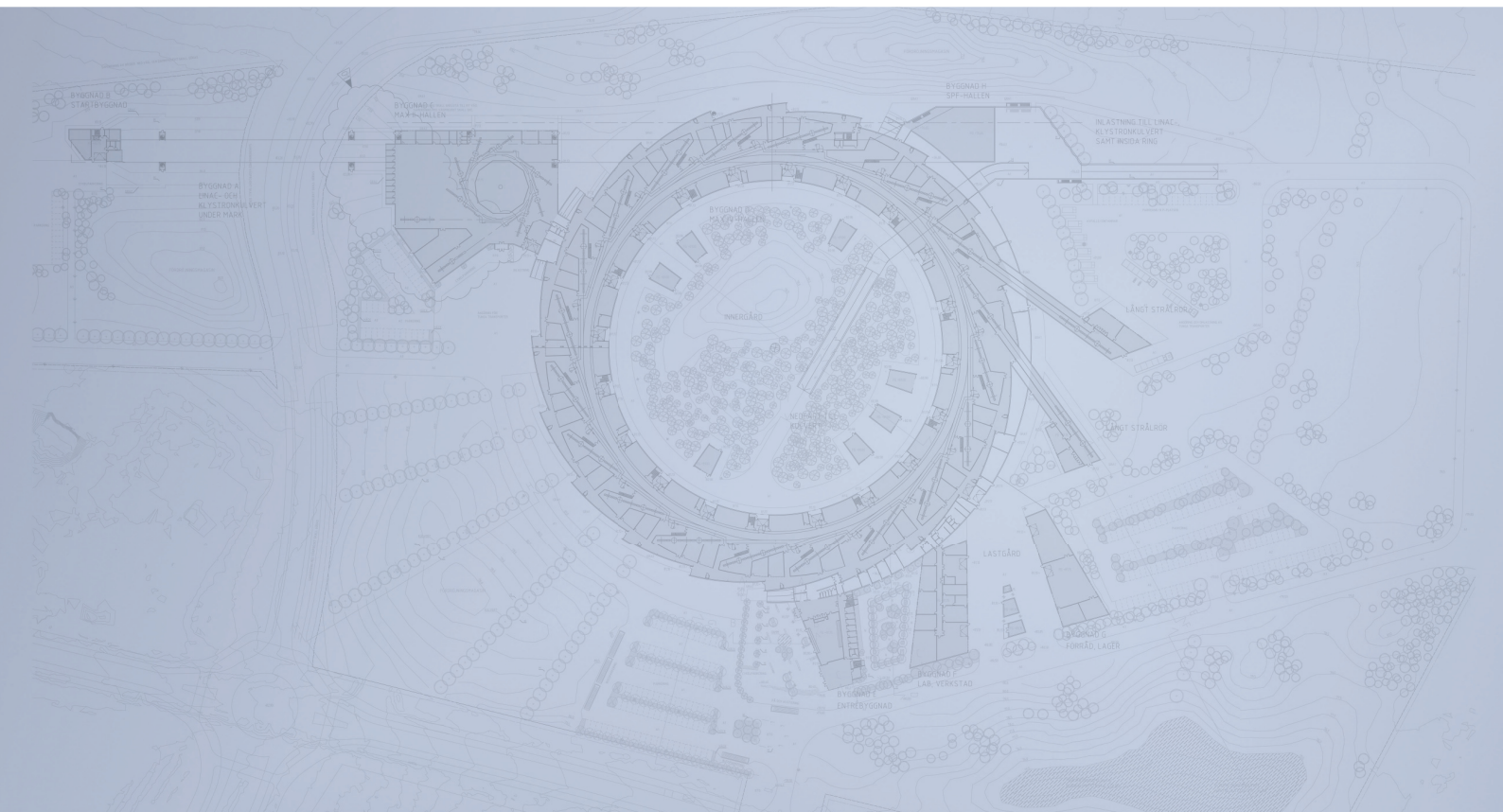
- [8] “FLUKA: a multi-particle transport code”  
A. Fassio<sup>1</sup>, A. Ferrari, J. Ranft, and P.R. Sala,  
CERN-2005-10 (2005), INFN/TC\_05/11, SLAC-R-773
- [9] PAL X-ray Free Electron Laser and Preliminary Radiological Considerations  
Hee-Seock Lee  
3rd International Workshop on Radiation Safety of Synchrotron Radiation Sources
- [10] Radiation safety aspects of the TESLA test facility. phase 2  
Albrecht Leuschner  
Radiation Measurements 41 (2007) S252-255
- [11] LCLS Physics Requirement Document 1.2-030  
Physics Requirements for the Injector and Linac Toroids and Faraday cups  
Stanford Linear Accelerator Center, USA.
- [12] 90 degrees Bremsstrahlung Source Term Produced in Thick Targets by 50 MeV to 10 GeV electrons  
X. S. Mao *et al.*  
SLAC-PUB-7722 (2000)
- [13] Radiation Protection Scheme for the LCLS Injector  
X. S. Mao *et al.*  
SLAC-PUB-12687 (2007)
- [14] Radiological Considerations for the Operation of the Advanced Photon Source Storage Ring - Revised.  
H. J. Moe, APS Report LS-295 (1997)
- [15] NCRP Report No. 144  
Radiation protection for particle accelerator facilities.  
National Council on Radiation Protection and Measurements, 2003
- [16] NSLS-II Preliminary Design Report (2007)  
Brookhaven National Laboratory
- [17] A. Rindi and R. H. Thomas  
Particle Accelerators Vol. 7 pp. 23 - 39 (1975)
- [18] Radiation safety aspects of the linac coherent light source project at SLAC  
S.H. Rokni *et al.*  
Radiation Measurements 41(2007) S247-S251
- [19] A Data Analysis Framework, root.cern.ch

- [20] SCSS X-FEL Conceptual Design Report (2005)  
RIKEN Harima Institute/SPRING-8
- [21] The SHIELD11 Computer Code  
W. R. Nelson and T. M. Jenkins  
SLAC-Report-737, 2005
- [22] SSMFS 2008:50, Swedish Radiation Safety Authority
- [23] SSMFS 2008:51, Swedish Radiation Safety Authority
- [24] SSI report 2000:05  
Doskoefficienter för beräkning av interna doser  
Swedish Radiation Protection Institute, 2000
- [25] A guide to radiation protection and radioactivity levels near high energy  
particle accelerators.  
A. H. Sullivan, Nuclear Technology Publishing, 1992
- [26] W. P. Swanson *et al.*, Aladdin Upgrade Design Study,  
Shielding  
University of Wisconsin Report (1985)





# Detailed Design Report



## Chapter 7 MAX IV Shielding Appendix

MAX IV Facility



# Appendix A

---

## Source Models

Different models for determining the dose equivalent rate are compared in the 4 figures below. The models are from [15], [21], [26] and [25].

The source terms,  $H_j$  (see eq. 1.1), were calculated for an electron energy of 3 GeV and shown as function of the angle. The figures show the terms due to Bremsstrahlung (Brems), Low Energy Neutrons (<25 MeV)(LEN), Medium Energy Neutrons (25 - 100 MeV)(MEN) and High Energy Neutrons (>100 MeV)(HEN). Figure A.5 show the relative strengths of the MEN and HEN source terms as a function of electron energy.

The approach in this report is to use the source terms given in [15] but normalized to the 90 deg data in [25]. The result of this approach is labeled “NCRP144 (Sullivan)” and represented by the black curves in the figures below.

The energy distribution of the Bremsstrahlung photons produced at 90° from thick targets was investigated in [12] by Monte-Carlo methods. It was found that 99.9% of the photons have energies below 10 MeV. The results for Aluminum, Copper and Lead are shown in figure A.6.

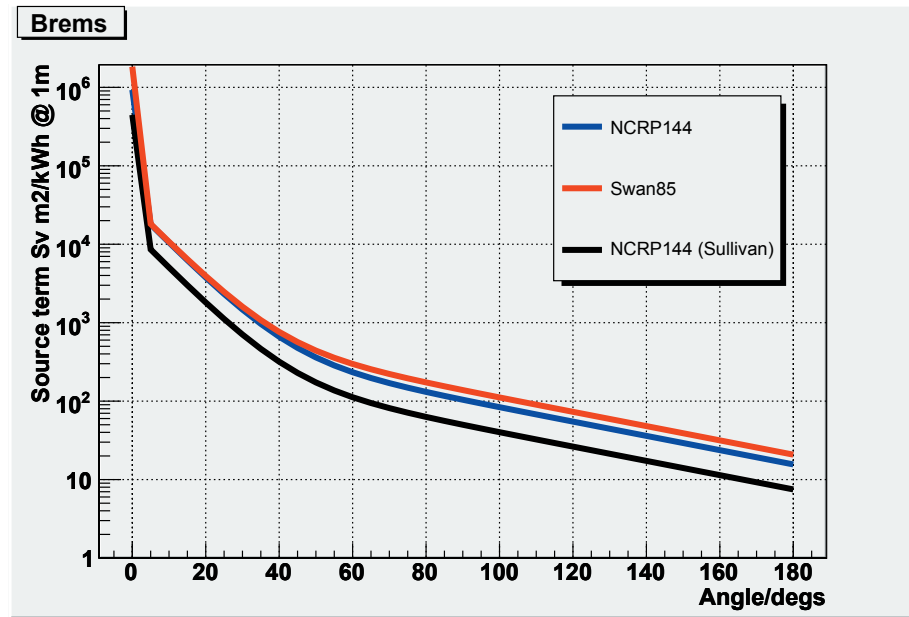


Figure A.1: The Bremsstrahlung source term as a function of the angle for 3 GeV electrons.

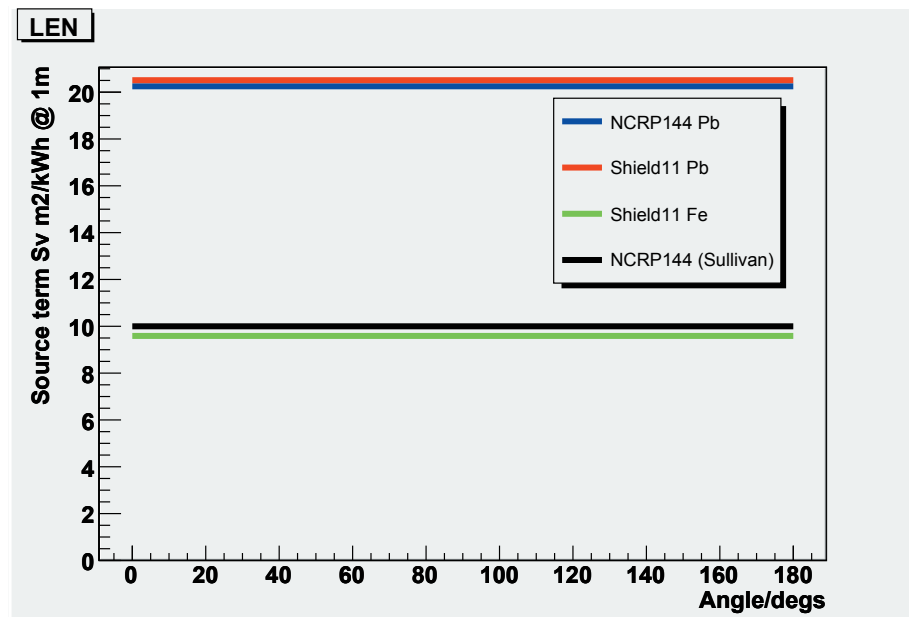


Figure A.2: The low energy neutron (<25 MeV) source term as a function of the angle for 3 GeV electrons

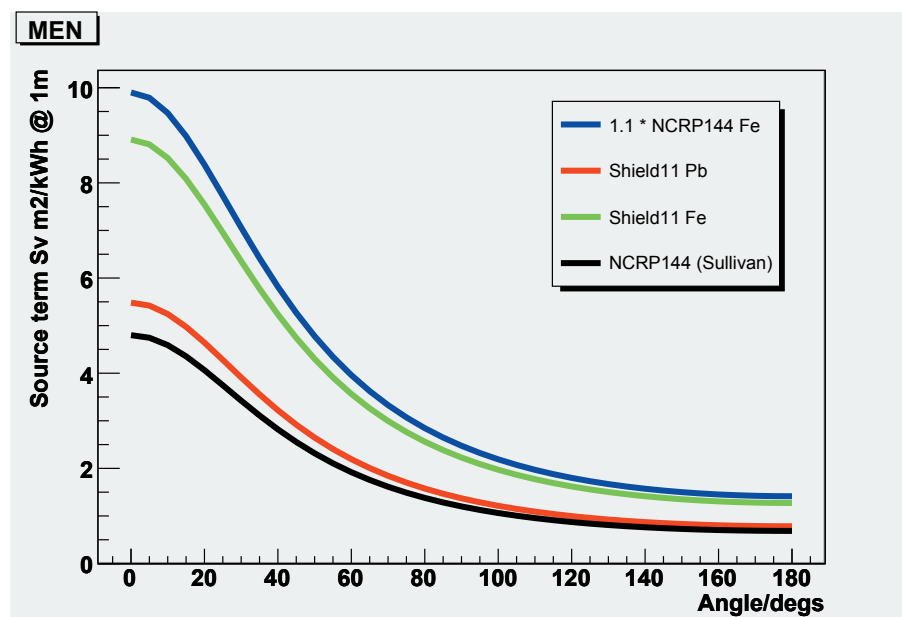


Figure A.3: The medium energy neutron (25-100 MeV) source term as a function of the angle for 3 GeV electrons. Note that the NCRP144 Fe term has been multiplied with 1.1 for clarity.

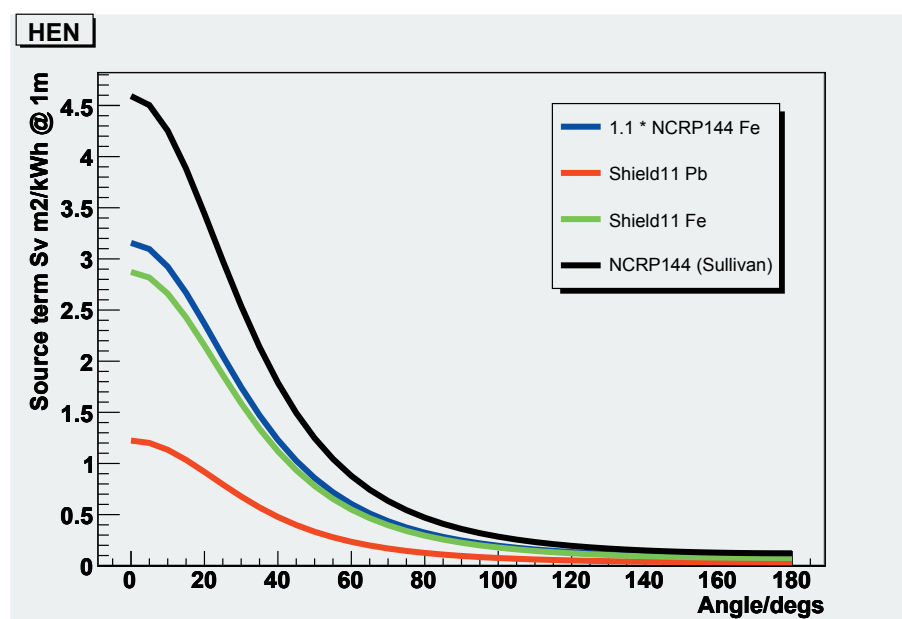


Figure A.4: The high energy neutron (>100 MeV) source term as a function of the angle for 3 GeV electrons. Note that the NCRP144 Fe term has been multiplied with 1.1 for clarity.

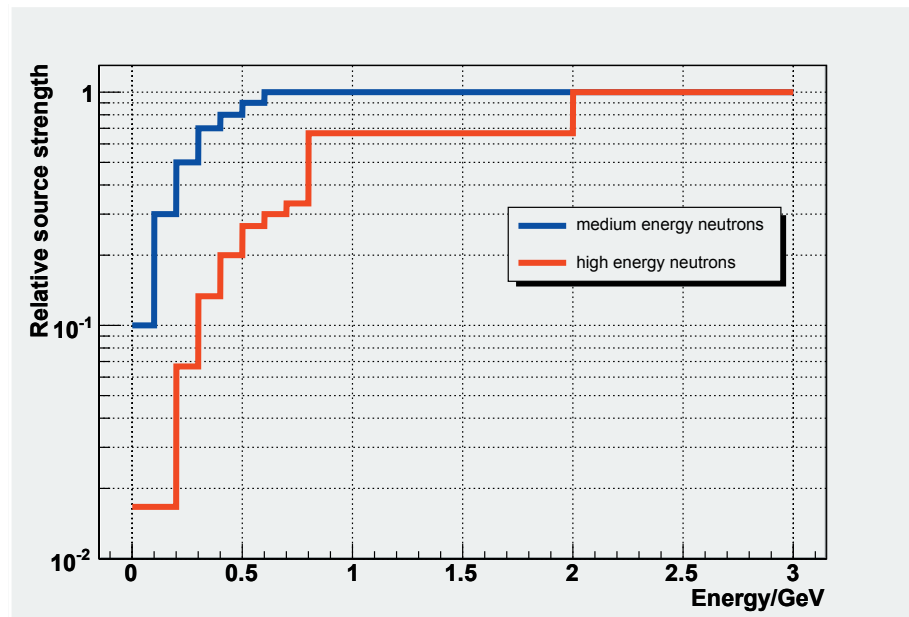


Figure A.5: Relative source terms for medium (MEN) and high (HEN) energy neutrons as a function of the electron energy [15].

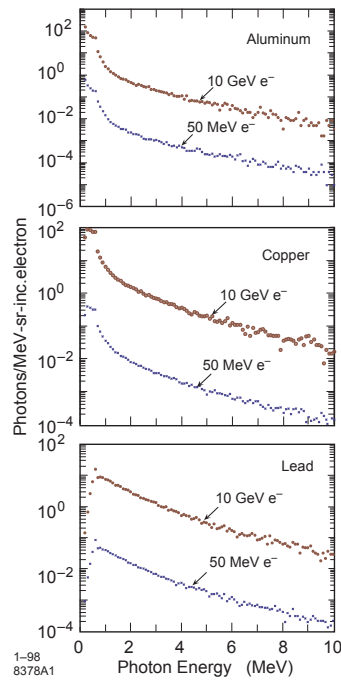


Figure A.6: The 90° thick target Bremsstrahlung spectra from [12].

## Appendix B

---

### Material Attenuation Lengths



Bremsstrahlung	[15]	[25]	[21]	[16]	[14]	
lead		2.4	2.1	2.2	2.1	2.2
iron		4.7	4.3	4.7	4.3	4.7
heavy concrete				14	14	14
concrete		21	18	21	21	21
polyethylene				69	75	69
earth				44		44
Low Energy Neutrons	[15]	[25]	[21]	[16]	[14]	
lead			8.5	14	14	14
iron	13	16	6.0	13	13	13
heavy concrete				12	12	12
concrete	13	18	13	17	17	17
polyethylene				6.2	6.8	6.2
earth				21		21
Medium Energy Neutrons	[15]	[25]	[21]	[16]	[14]	
lead			18	17	17	17
iron	18		18	18	18	18
heavy concrete					19	19
concrete	23	28	23	28	28	28
polyethylene				61	67	61
earth				56		56
High Energy Neutrons	[15]	[25]	[21]	[16]	[14]	
lead			18	17	17	17
iron	18	18	18	18	18	18
heavy concrete				34	34	34
concrete	51	43	51	49	49	49
polyethylene				61	67	61
earth				56		56

Table B.1: Material attenuation lengths in cm for Bremsstrahlung, Low Energy Neutrons (<25 MeV), Medium Energy Neutrons (25-100 MeV) and High Energy Neutrons (>100 MeV). The last column contains the values used in the present report.

# Appendix C

---

## Electron Losses

Table C.1 show electron losses (theoretical) from various facilities

Facility	Energy (GeV)	Loss (%)	Comment	Ref
ALBA	0.05	10	Linac	[6]
	0.10	10	Linac	[6]
NSLS-II	0.0-0.20	10	Linac (distributed)	[16]
PAL	3.0	10	Linac	[9]
LCLS	0.135	12	Linac	[13]
	14.35	0.1	Beamline	[18]
	14.35	0.6	Dumpline	[18]
SCSS	6.0	1	Linac	[20]
SSRF	0.001-0.010	32	Buncher	[2]
	0.010-0.100	8	Linac	[2]
TTF2	1.6	0.3	Linac	[10]

Table C.1: Electron losses at various facilities.

## Appendix D

---

### The Linac

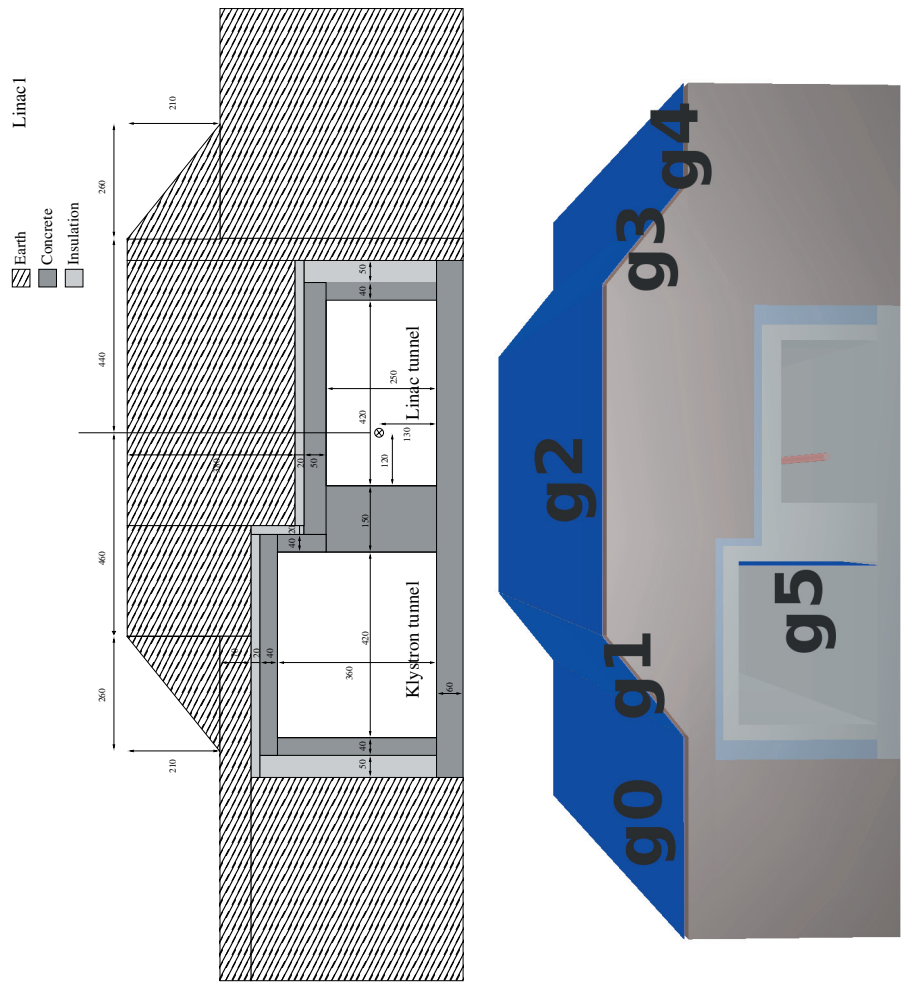


Table D.1: Crossection of the tunnels at location 1. Distances are given in cm. The electrons travel into the figure.

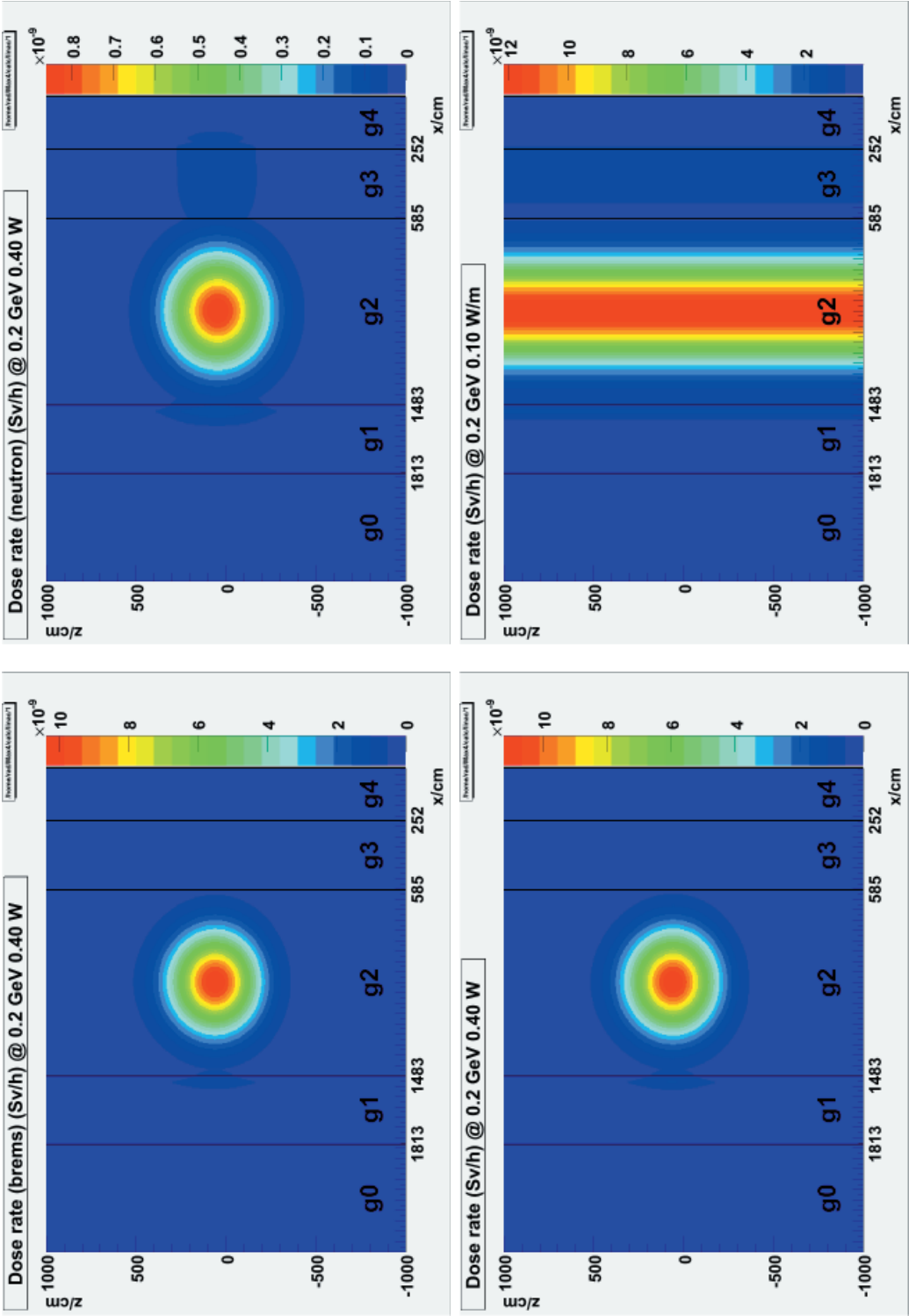


Table D.2: The dose rates on top of the tunnels at location 1.

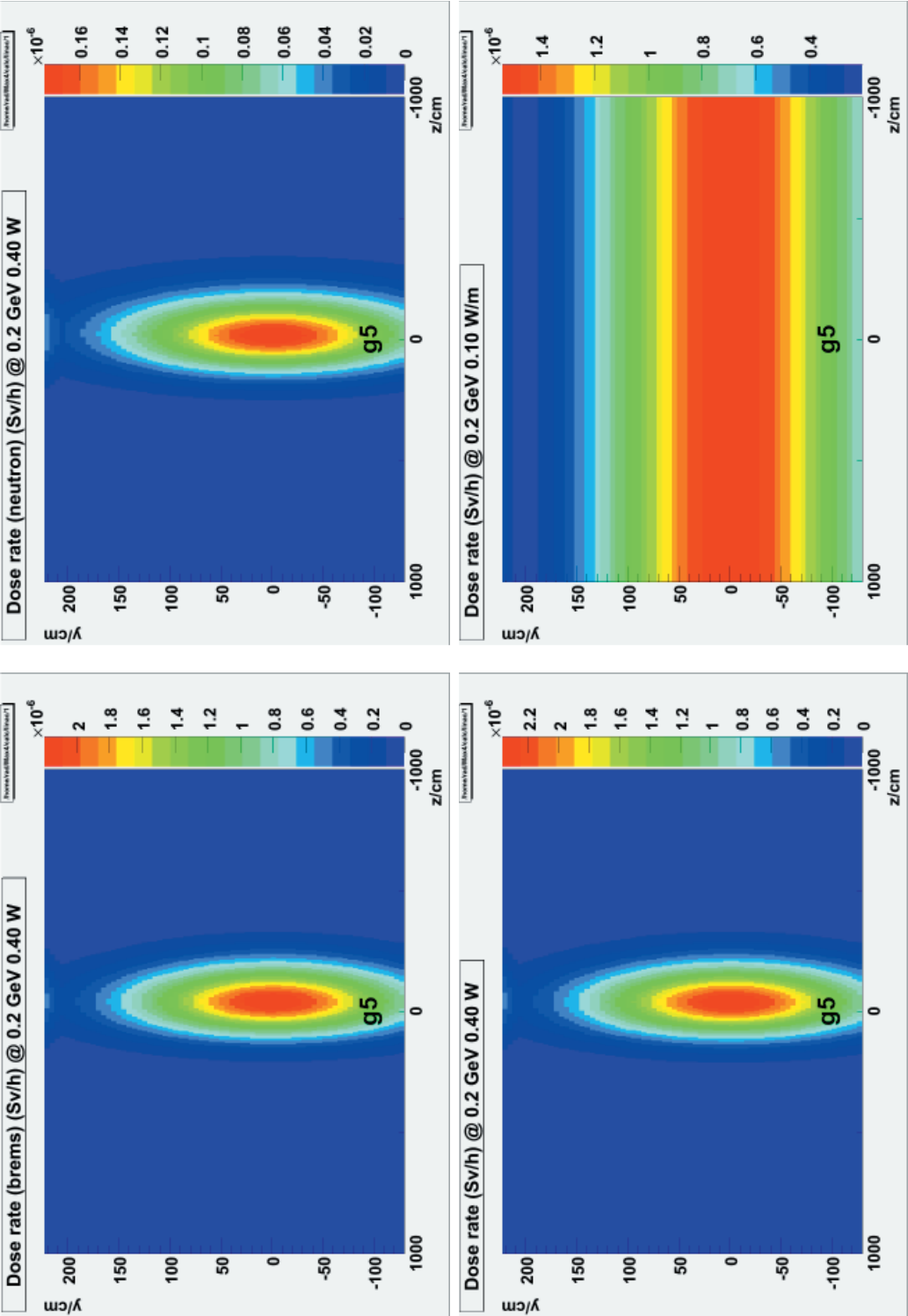


Table D.3: The dose rates in the klystron tunnel at location 1.

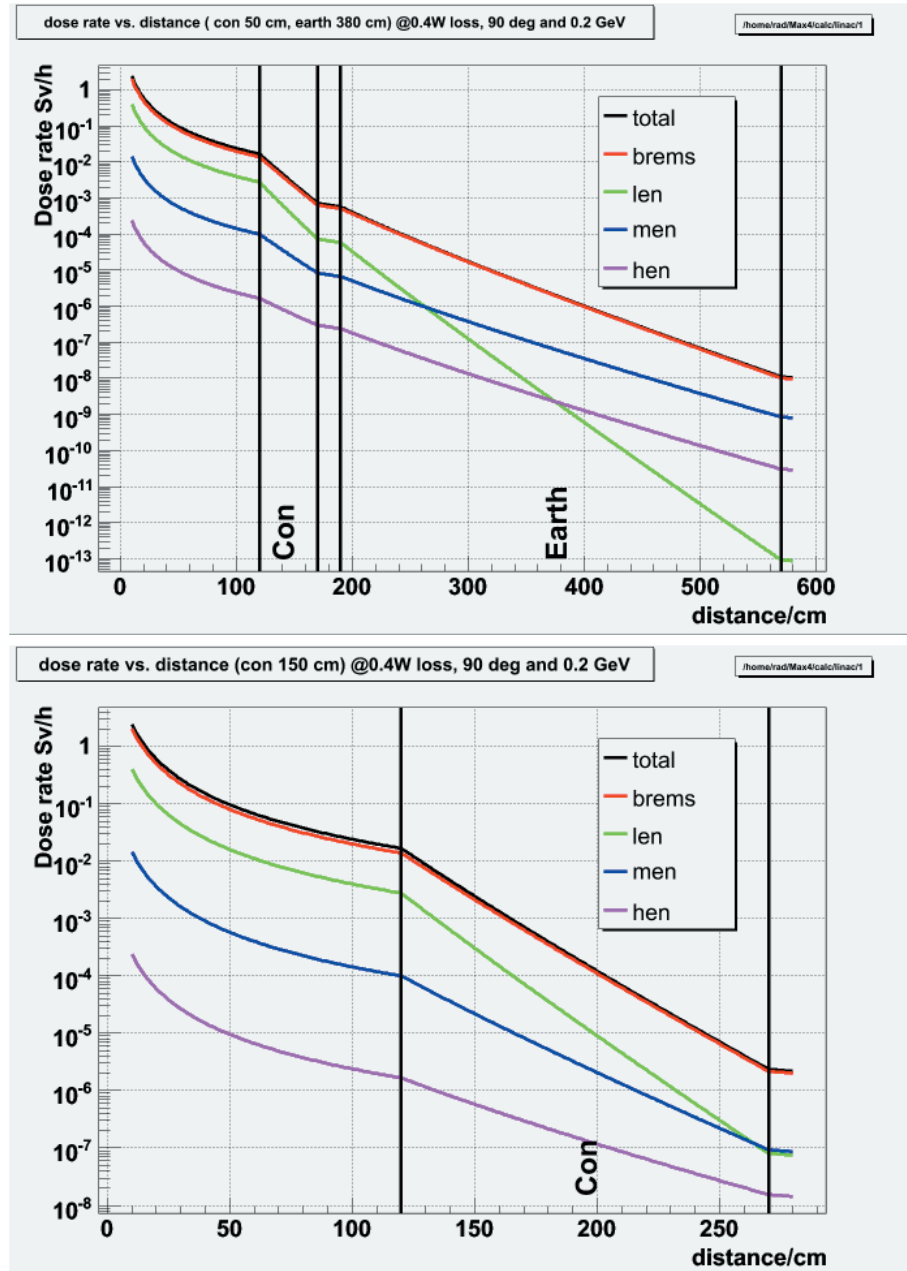


Table D.4: The components of the  $90^\circ$  dose rate at location 1. The top figure shows the components on the surface above the linac tunnel and the bottom figure the components in the klystron tunnel. The source is at 0 and the dose rate is not shown for the first 10 cm.

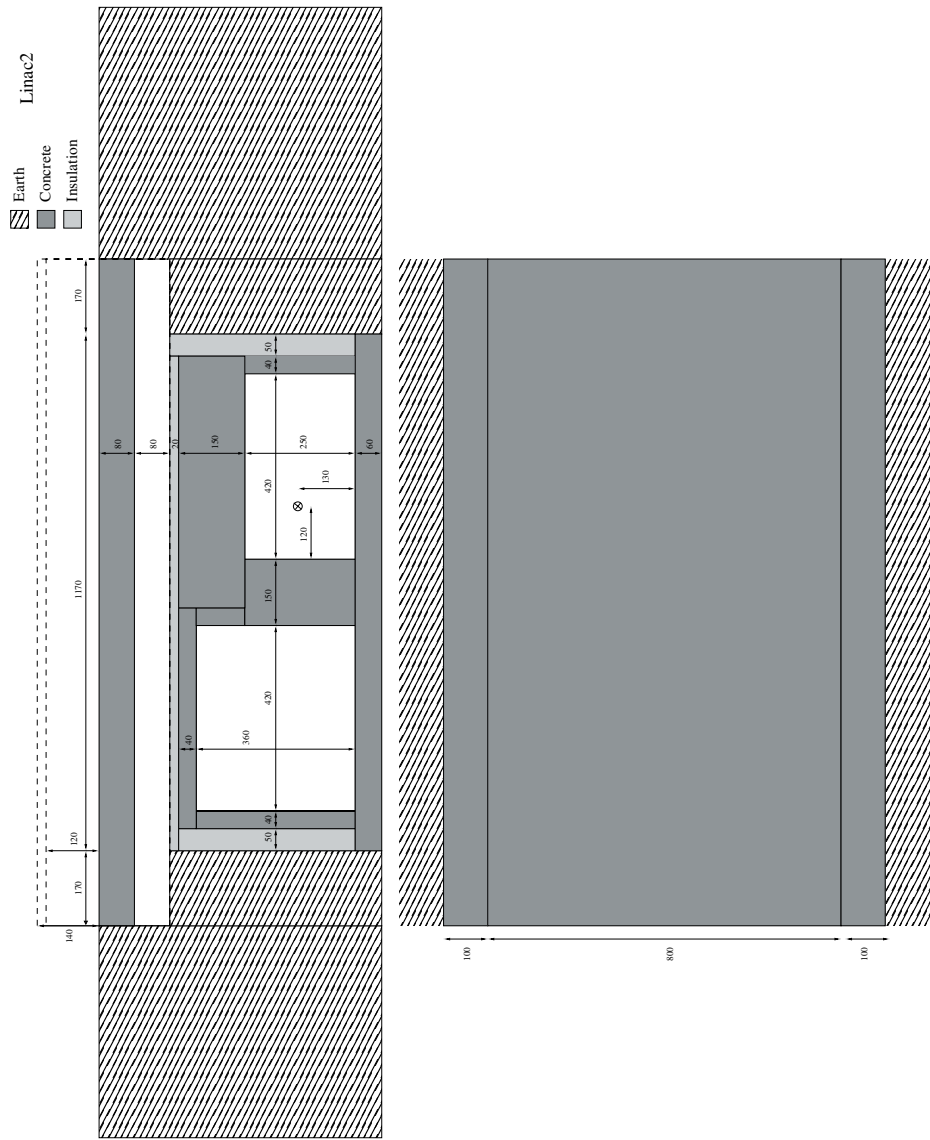


Figure D.5: Cross-section of the tunnels and the bridge at location 2. The bridge is also shown from above. Distances are given in mm. The electrons travel into the upper figure.



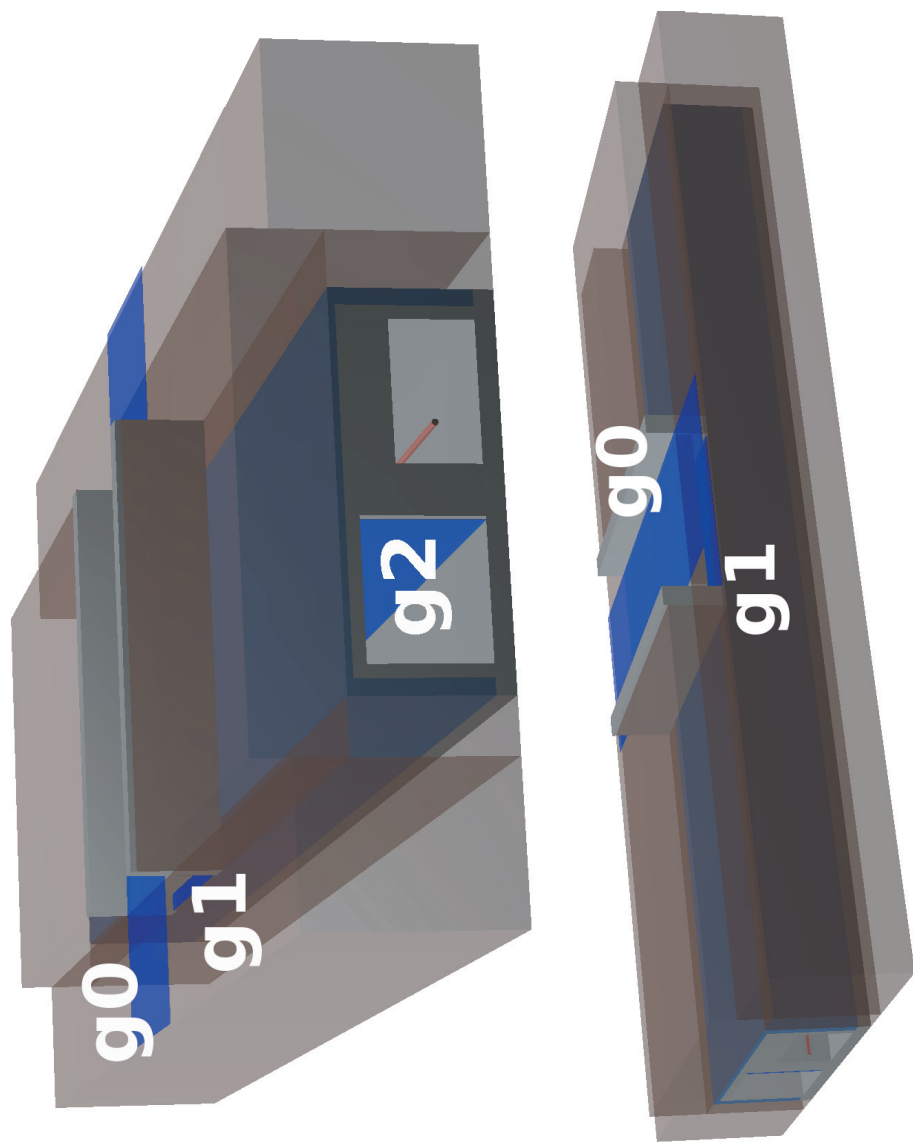


Table D.6: The tunnels and the bridge at location 2.

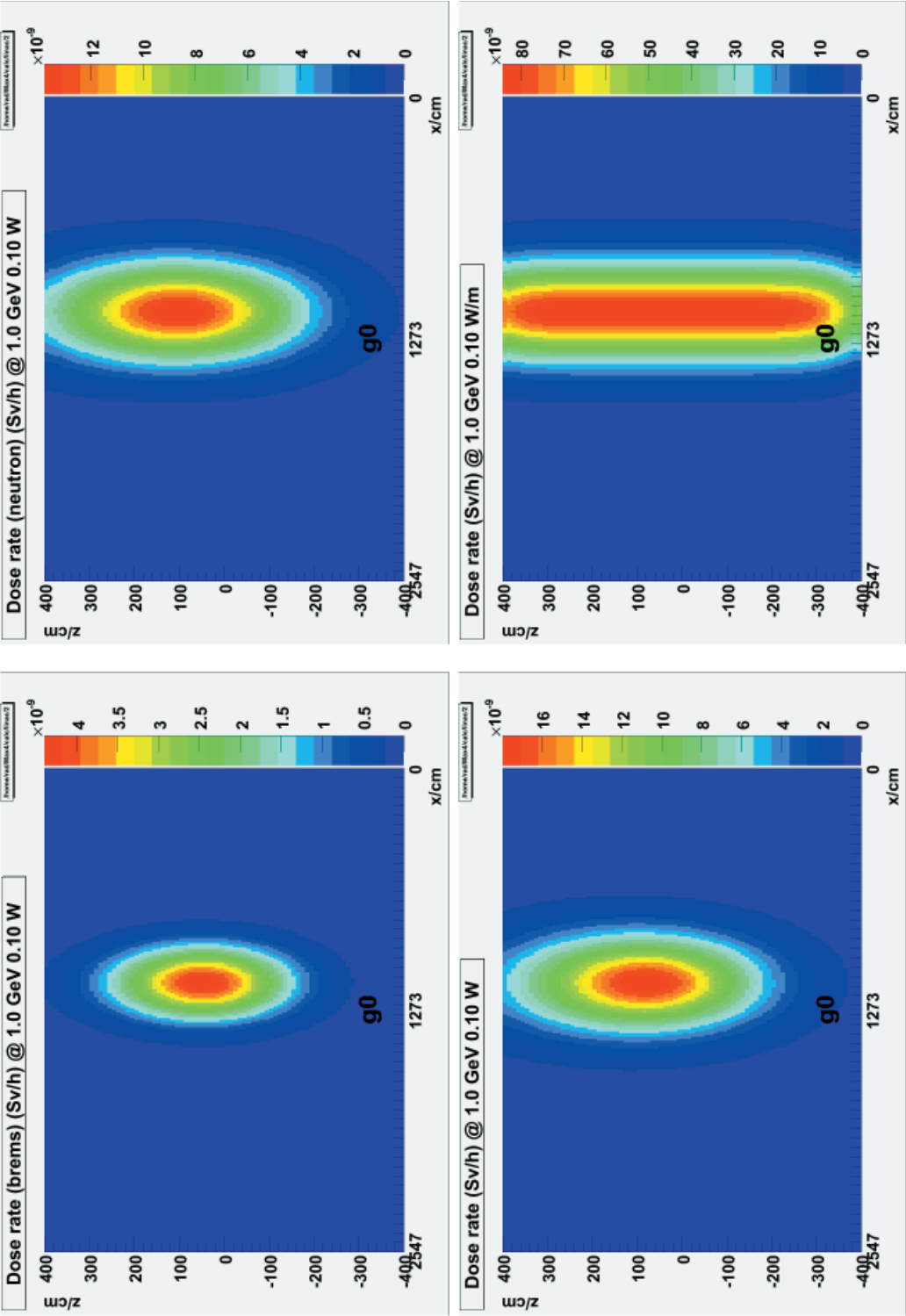


Table D.7: The dose rates on the bridge above the tunnels at location 2.

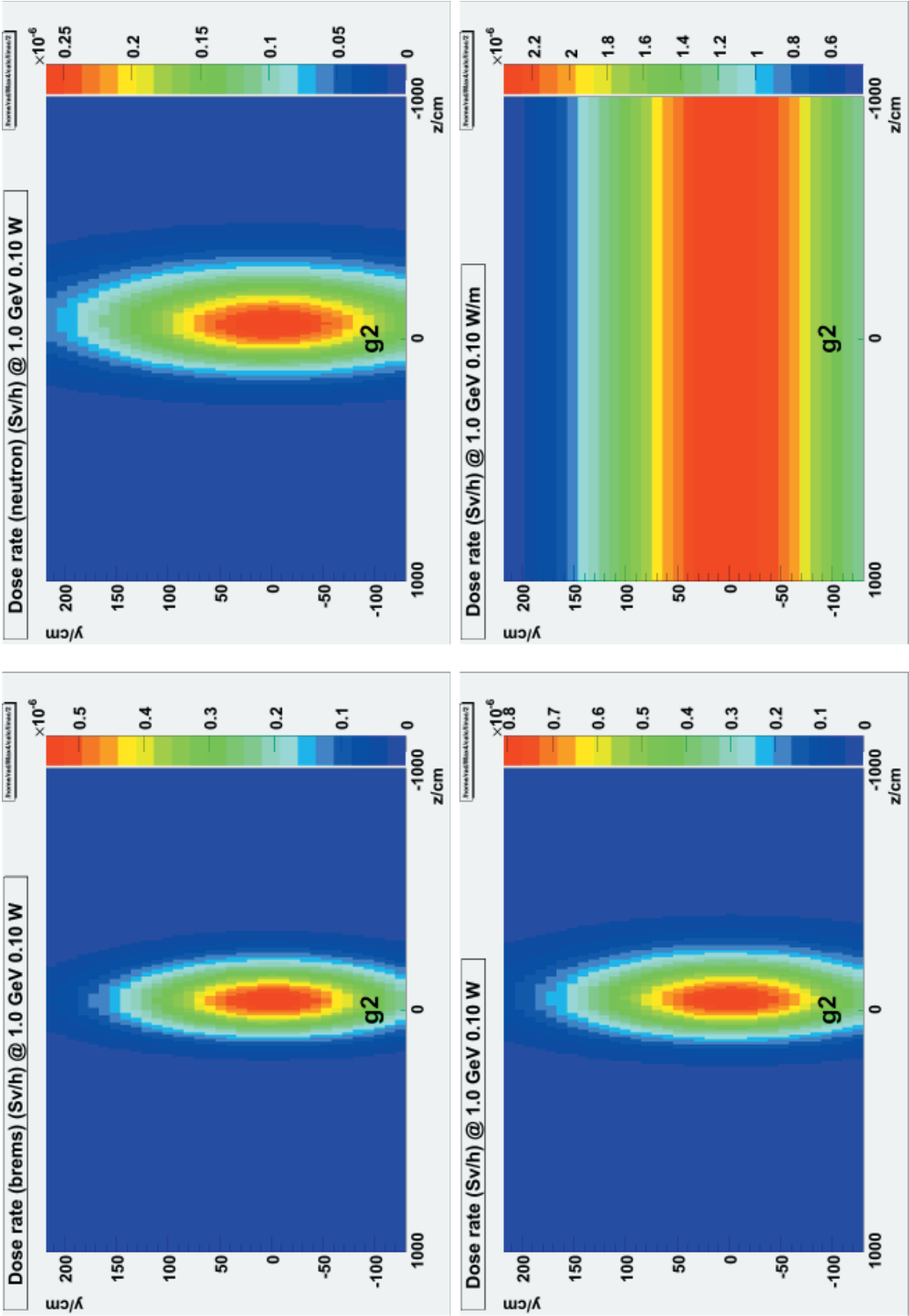


Table D.8: The dose rates in the klystron tunnel at location 2.

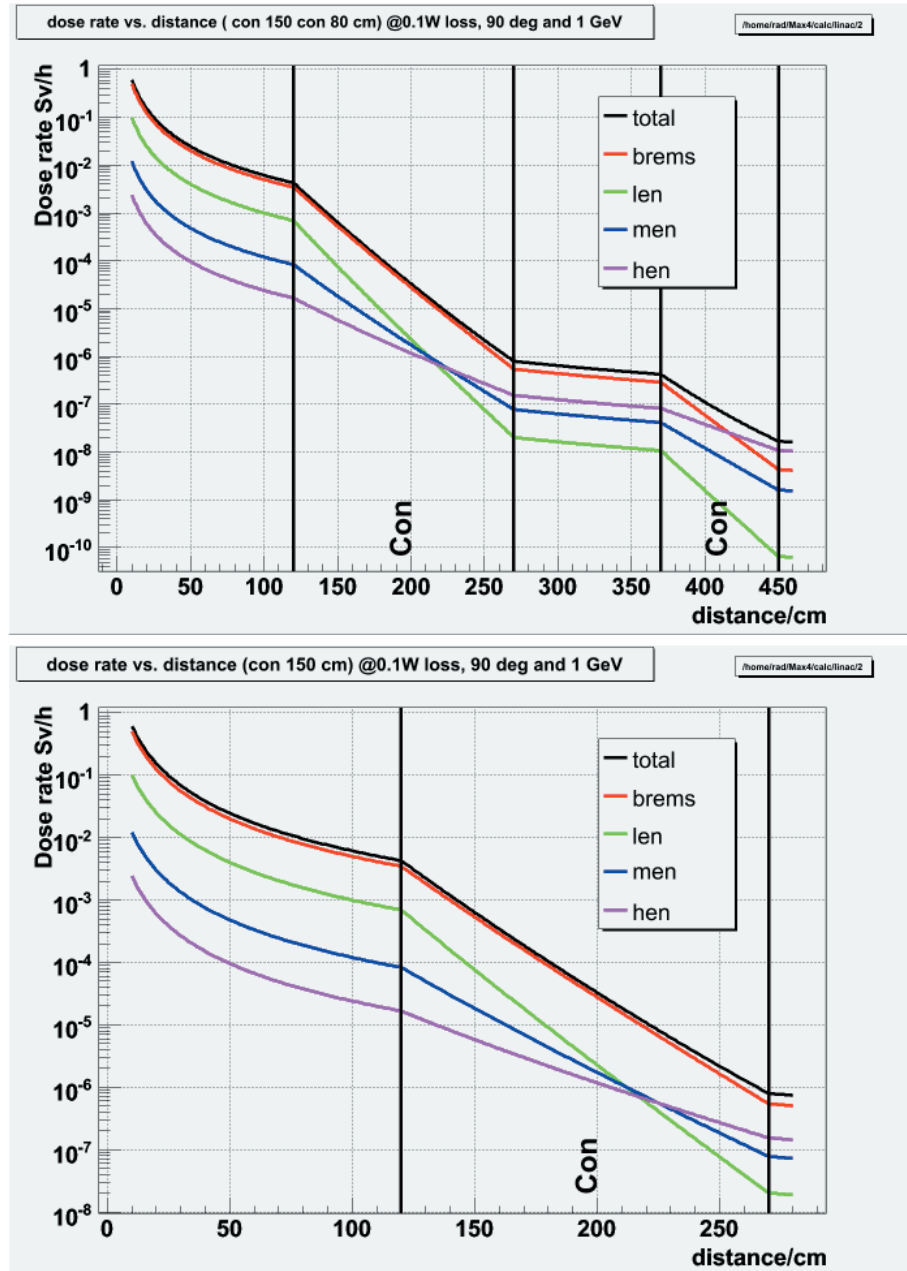


Table D.9: The components of the 90° dose rate at location 2. The top figure shows the components on the bridge above the tunnels and the bottom figure the components in the klystron tunnel. The source is at 0 and the dose rate is not shown for the first 10 cm.

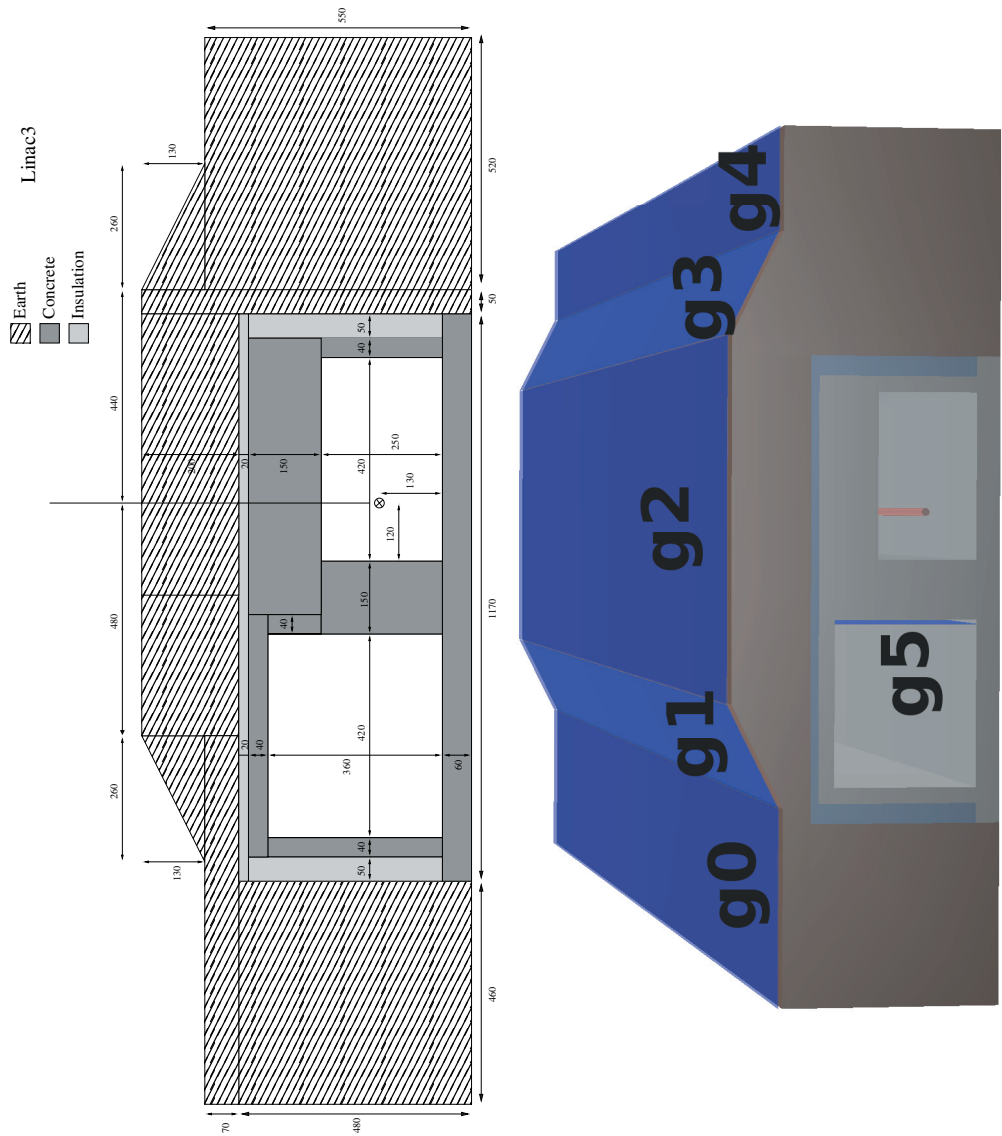


Table D.10: Crossection of the tunnels at location 3. Distances are given in cm. The electrons travel into the figure.

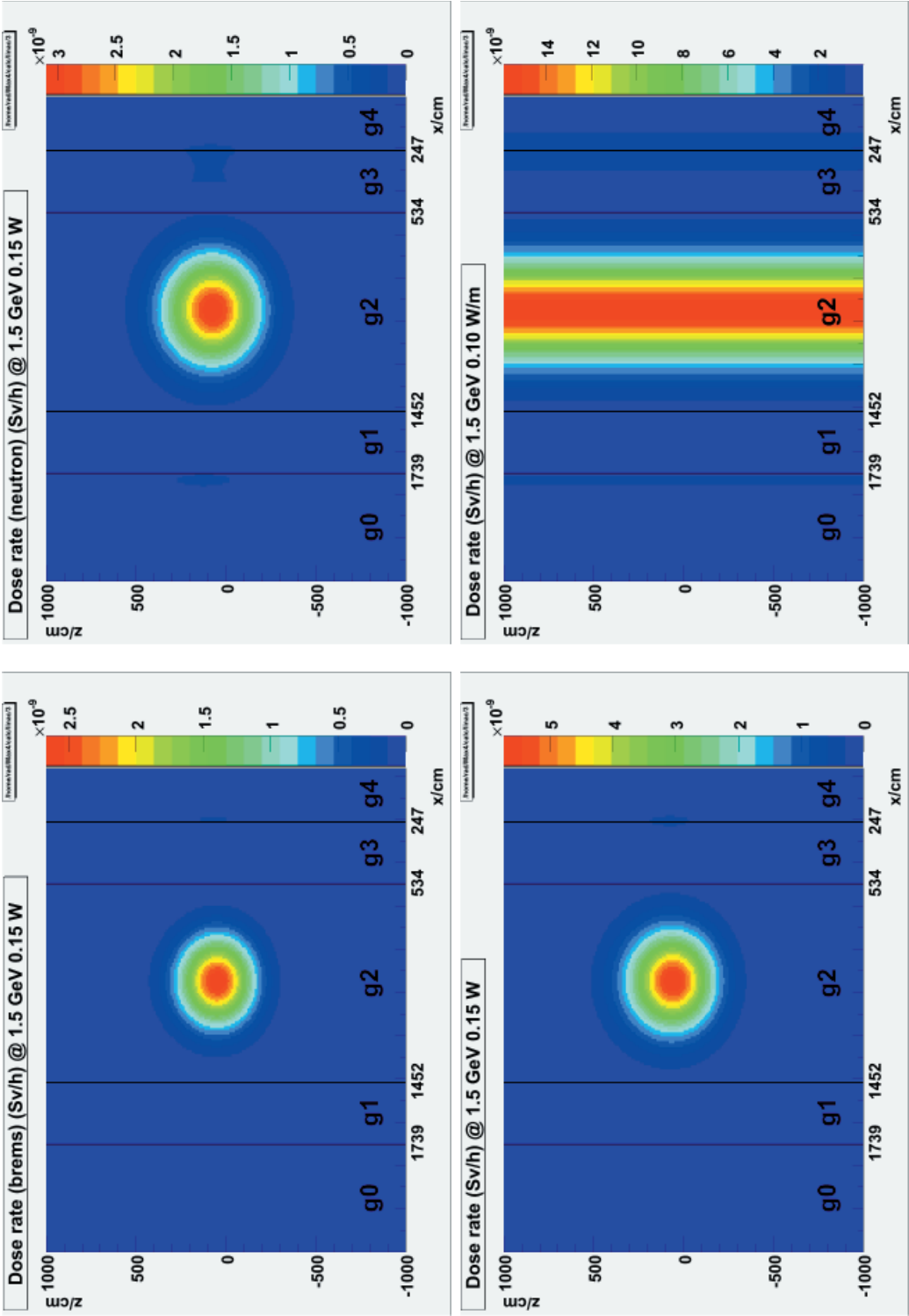


Table D.11: The dose rates on top of the tunnels at location 3.

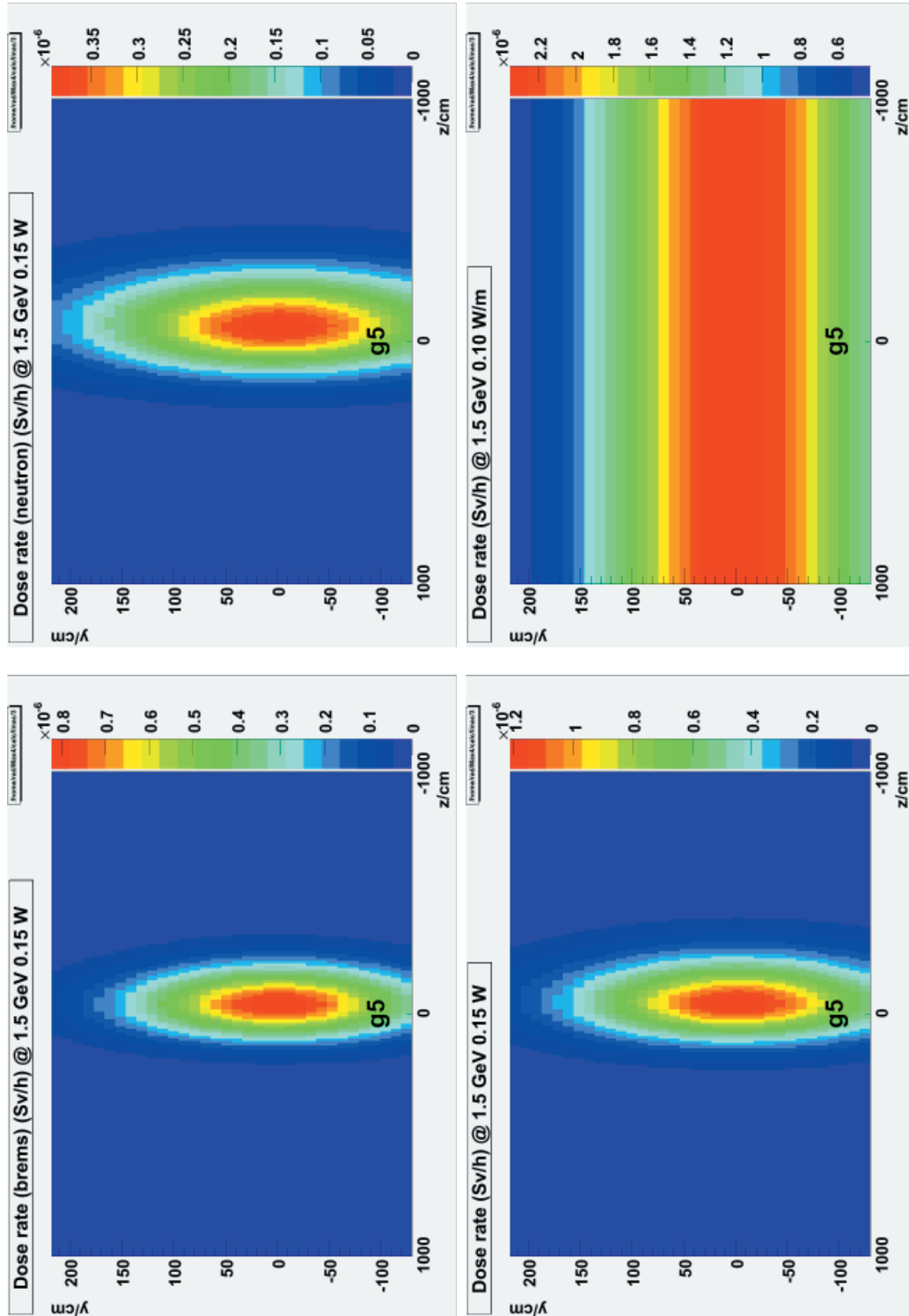


Table D.12: The dose rates in the klystron tunnel at location 3.

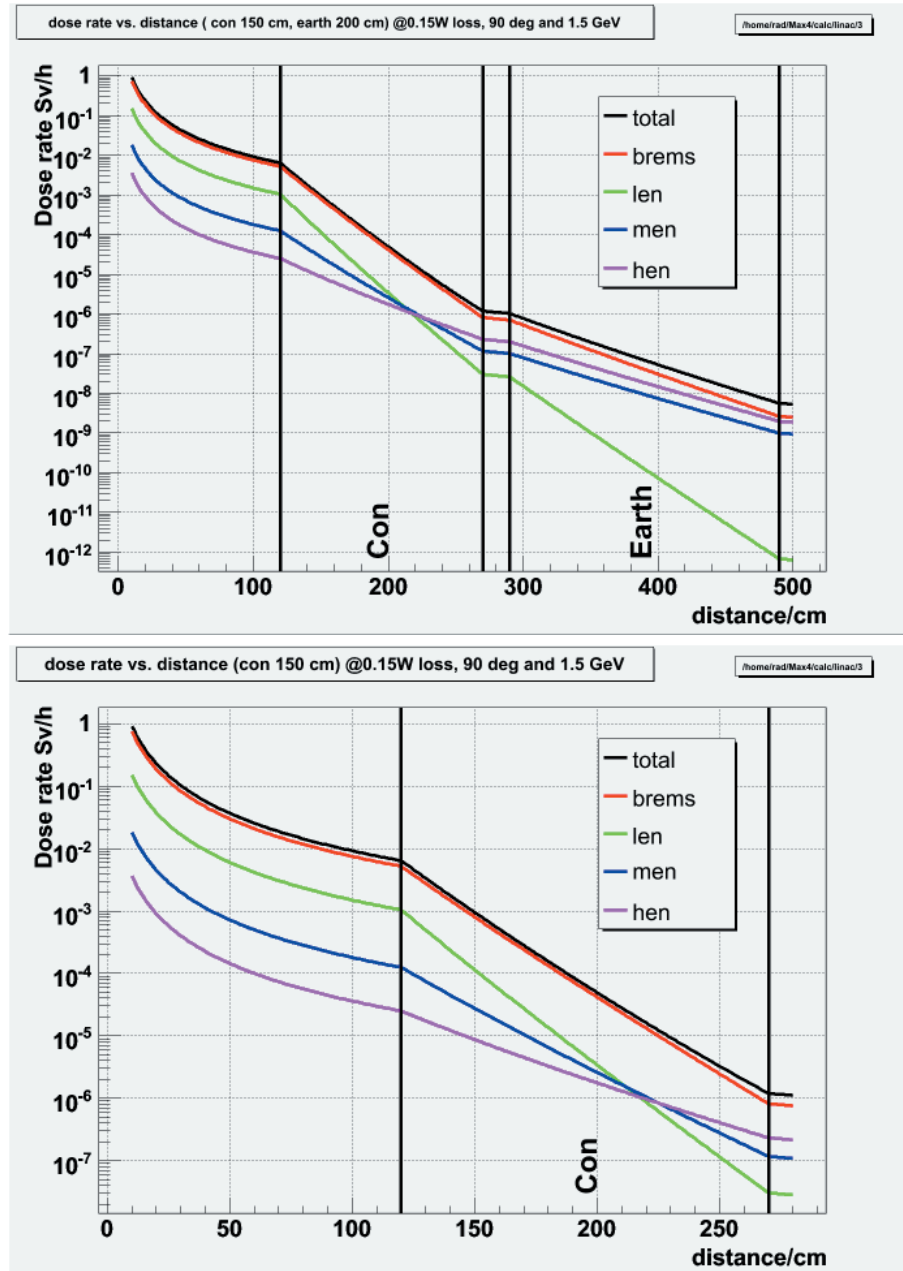


Table D.13: The components of the  $90^\circ$  dose rate at location 3. The top figure shows the components on the surface above the tunnels and the bottom figure the components in the klystron tunnel. The source is at 0 and the dose rate is not shown for the first 10 cm.



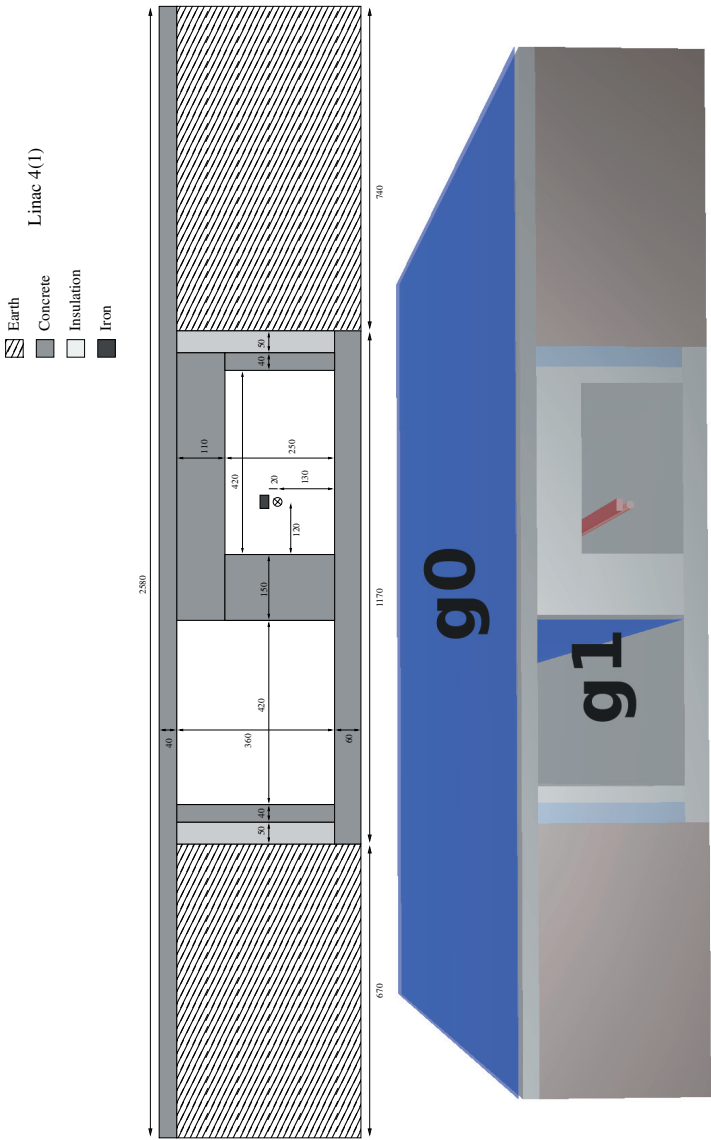


Table D.14: Crossection of the tunnels at location 4. Distances are given in cm. The electrons travel into the figure.

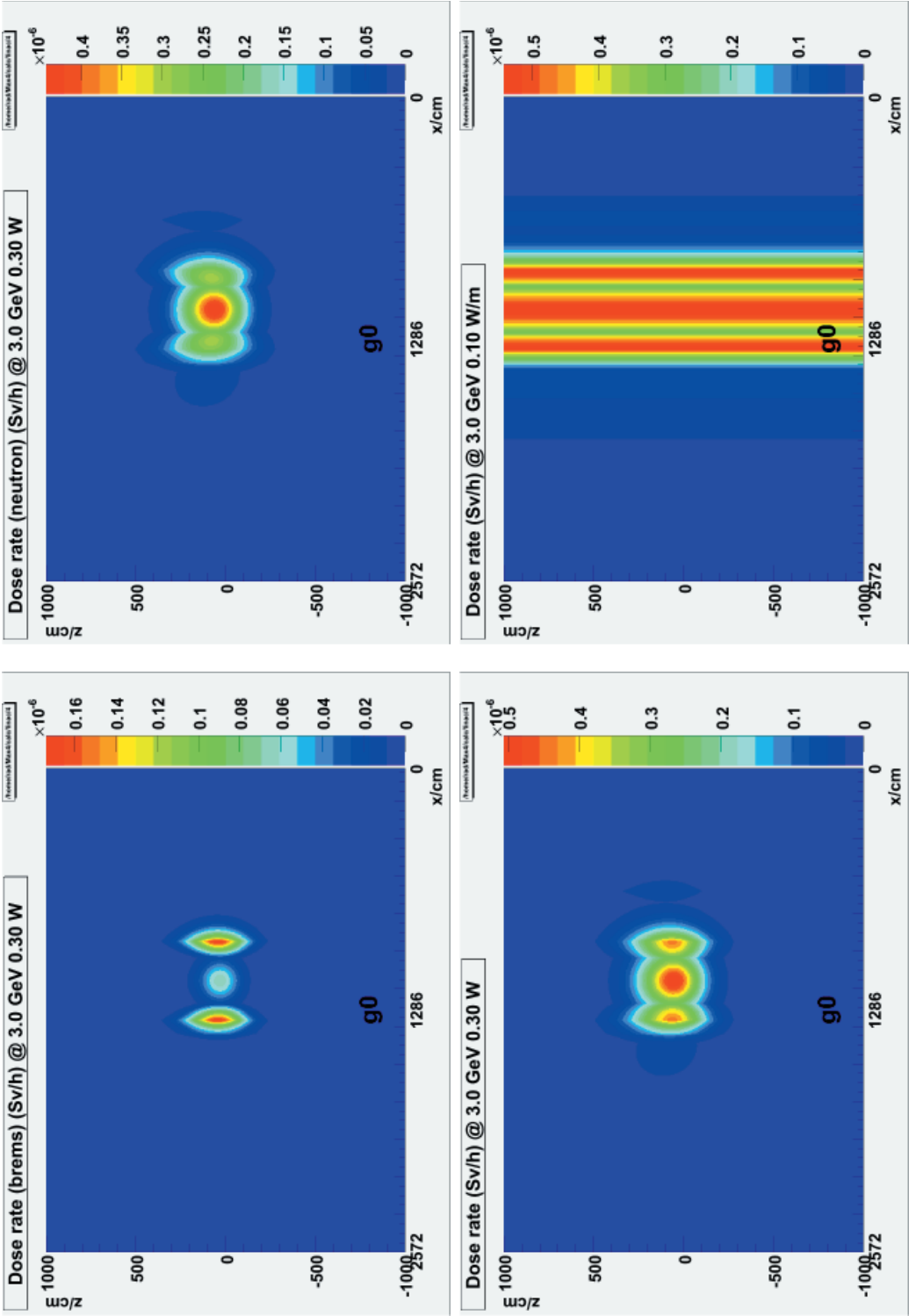


Table D.15: The dose rates on top of the tunnels at location 4.

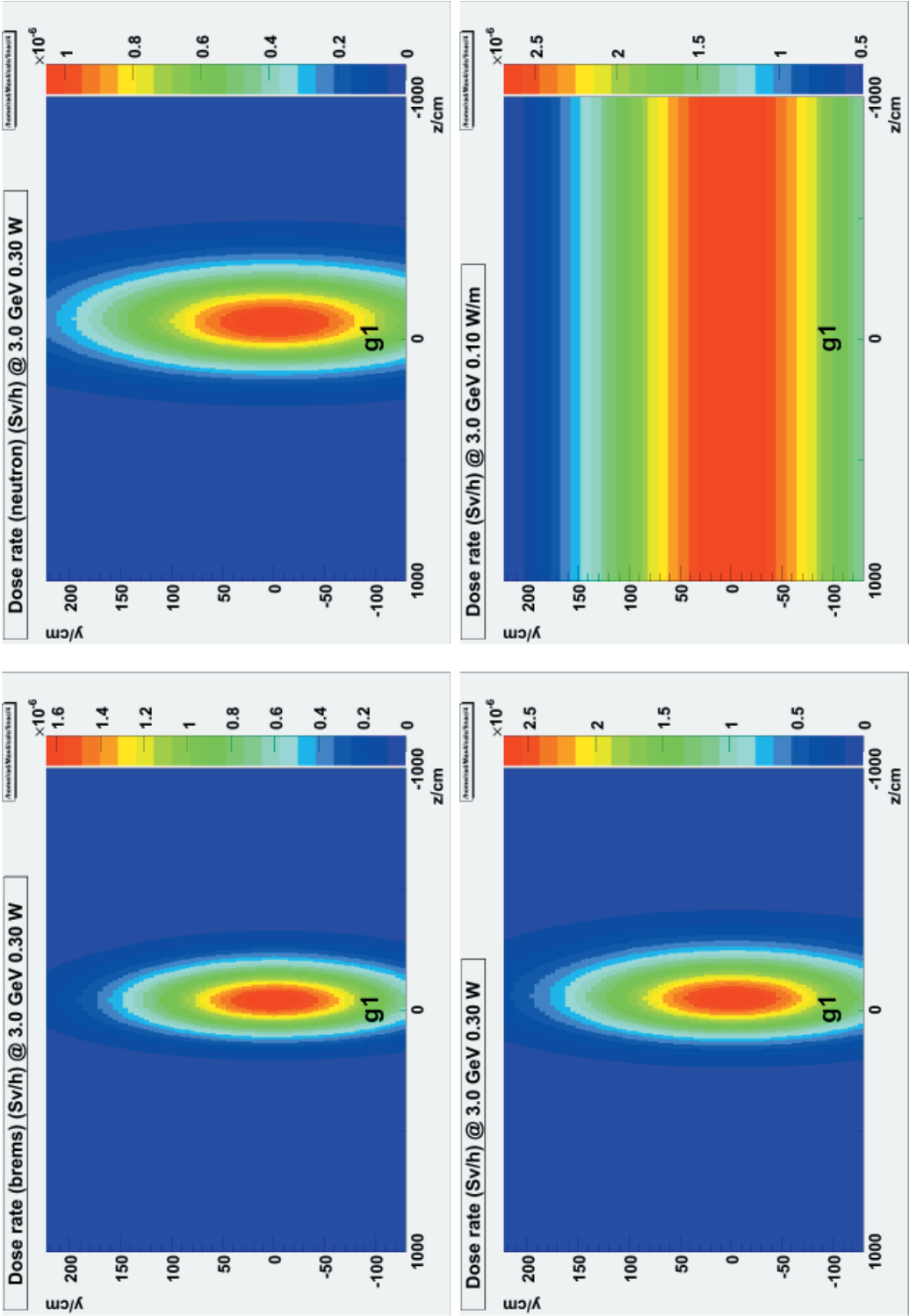


Table D.16: The dose rates in the klystron tunnel at location 4.

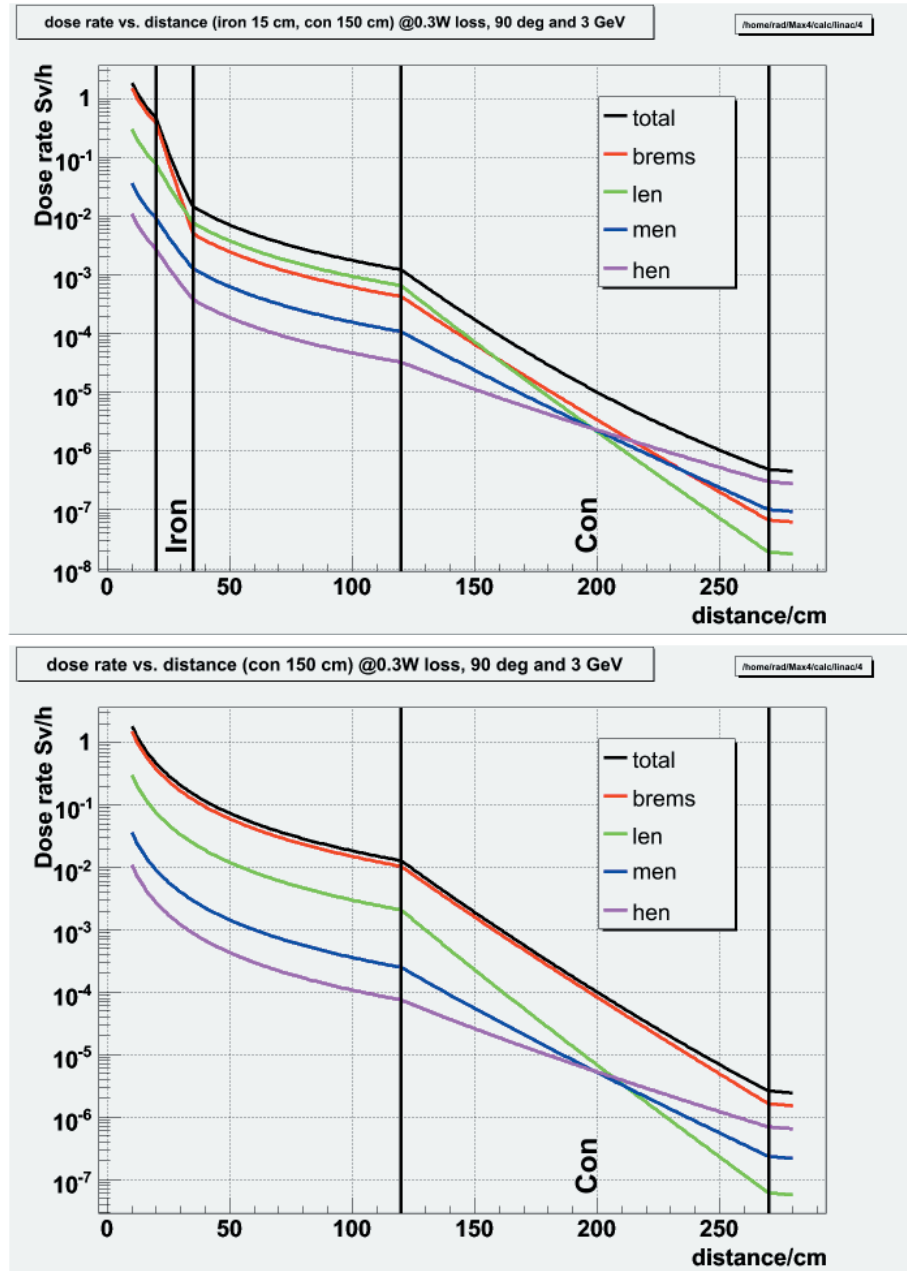


Table D.17: The components of the 90° dose rate at location 4. The top figure shows the components on the surface above the tunnels and the bottom figure the components in the klystron tunnel. The source is at 0 and the dose rate is not shown for the first 10 cm.

## Appendix E

---

### The Short Pulse Facility

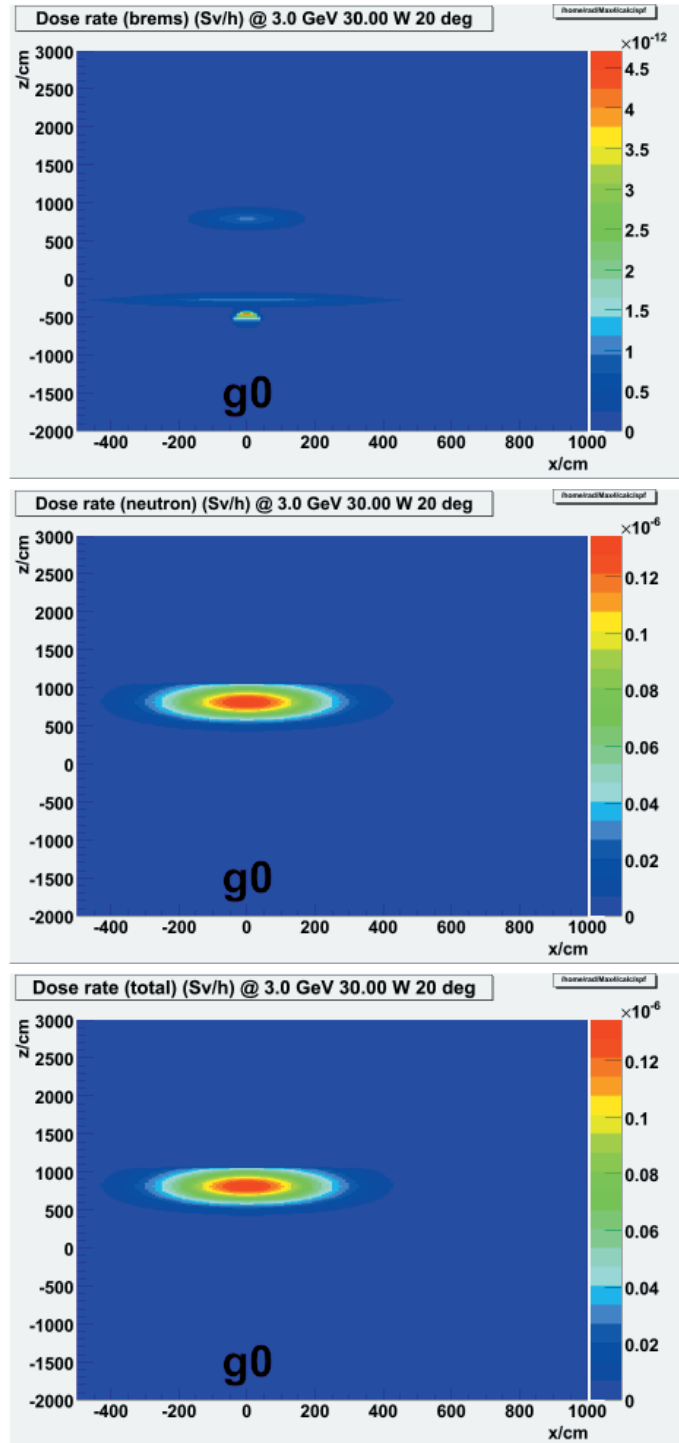


Table E.1: The SPF dose rates on grid g0 (on the roof above the beam dump) for a 30 W loss in the beam dump.

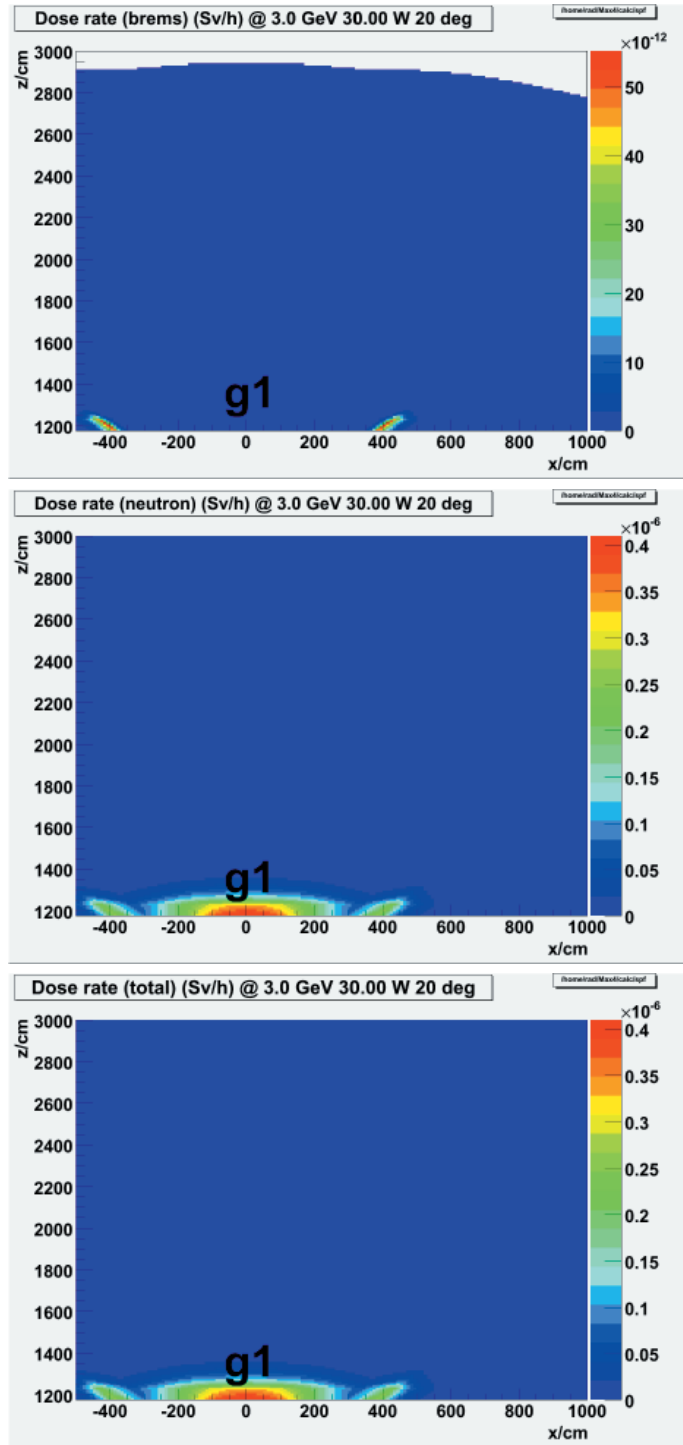


Table E.2: The SPF dose rates on grid g1 (on the floor of the experimental area) for a 30 W loss in the beam dump.

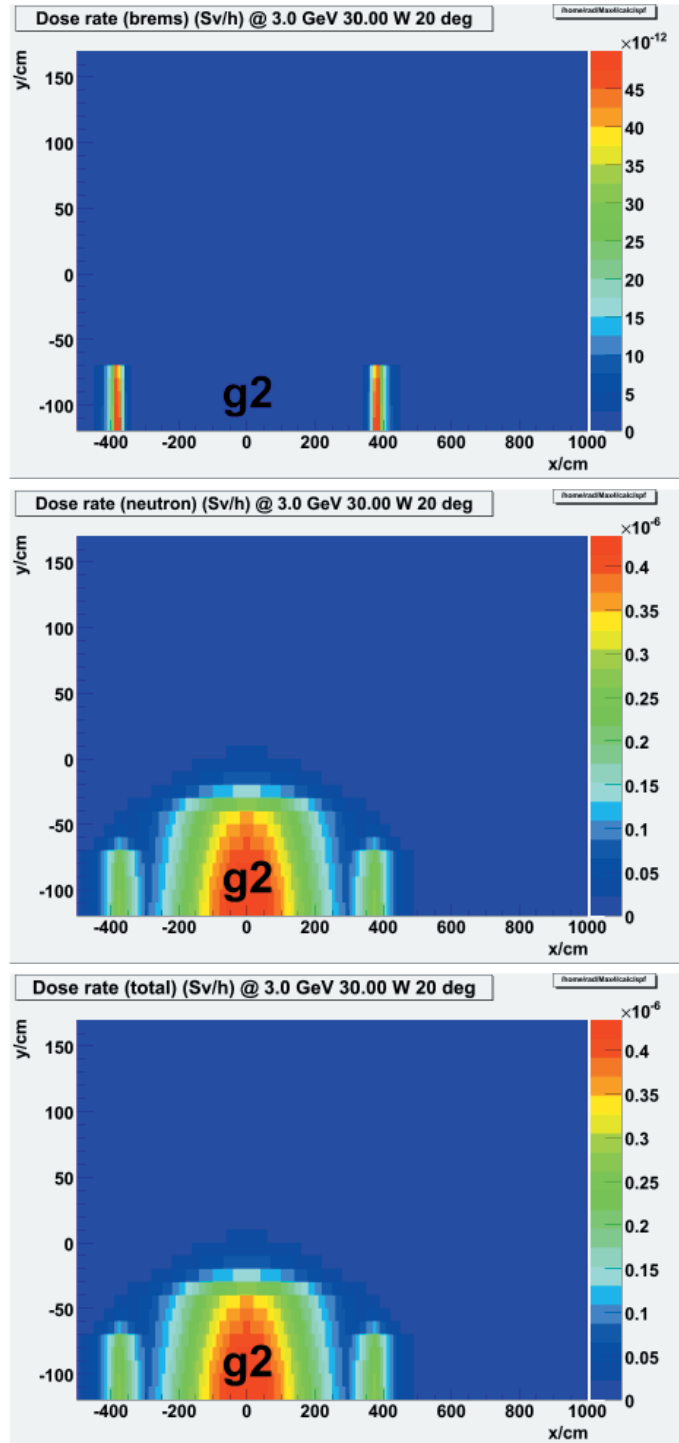


Table E.3: The SPF dose rates on grid g2 (on the wall towards the SPF hall) for a 30 W loss in the beam dump.



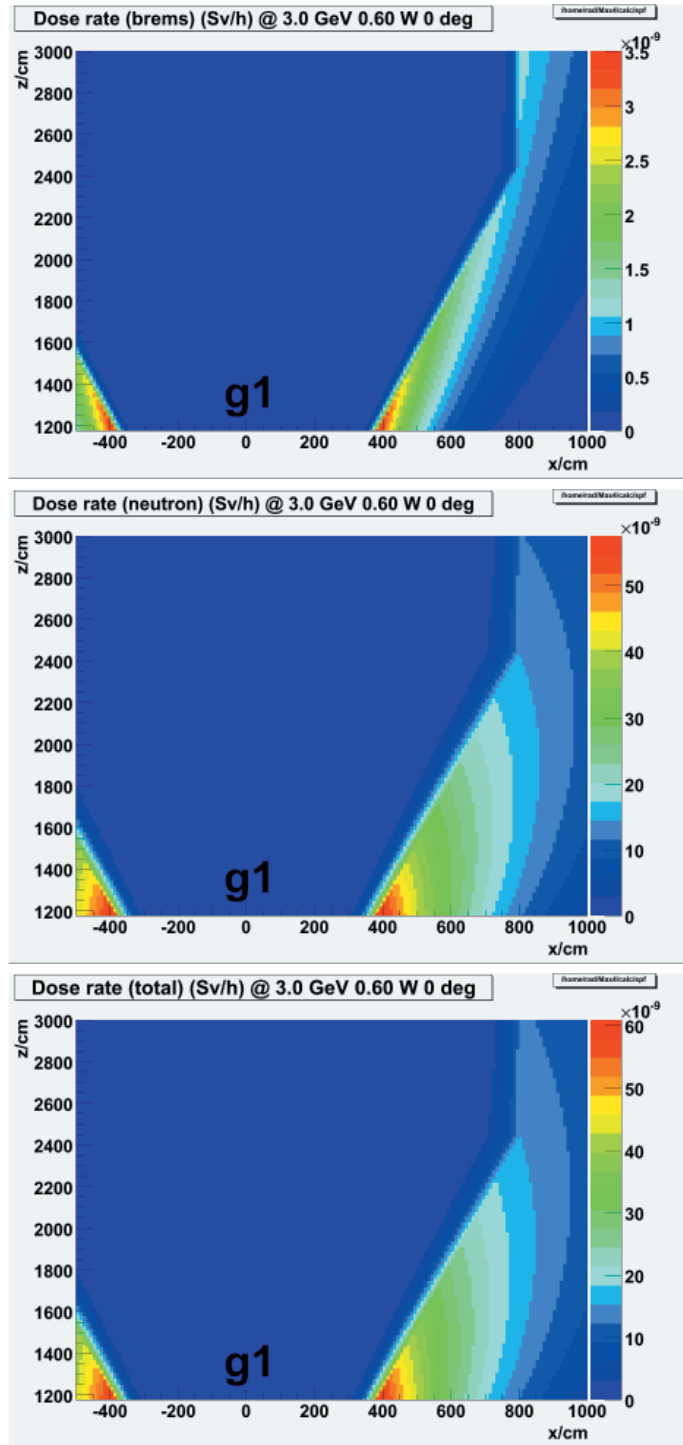


Table E.4: The SPF dose rates on grid g1 (on the floor of the experimental area) for a 0.6 W loss before the dump magnet.

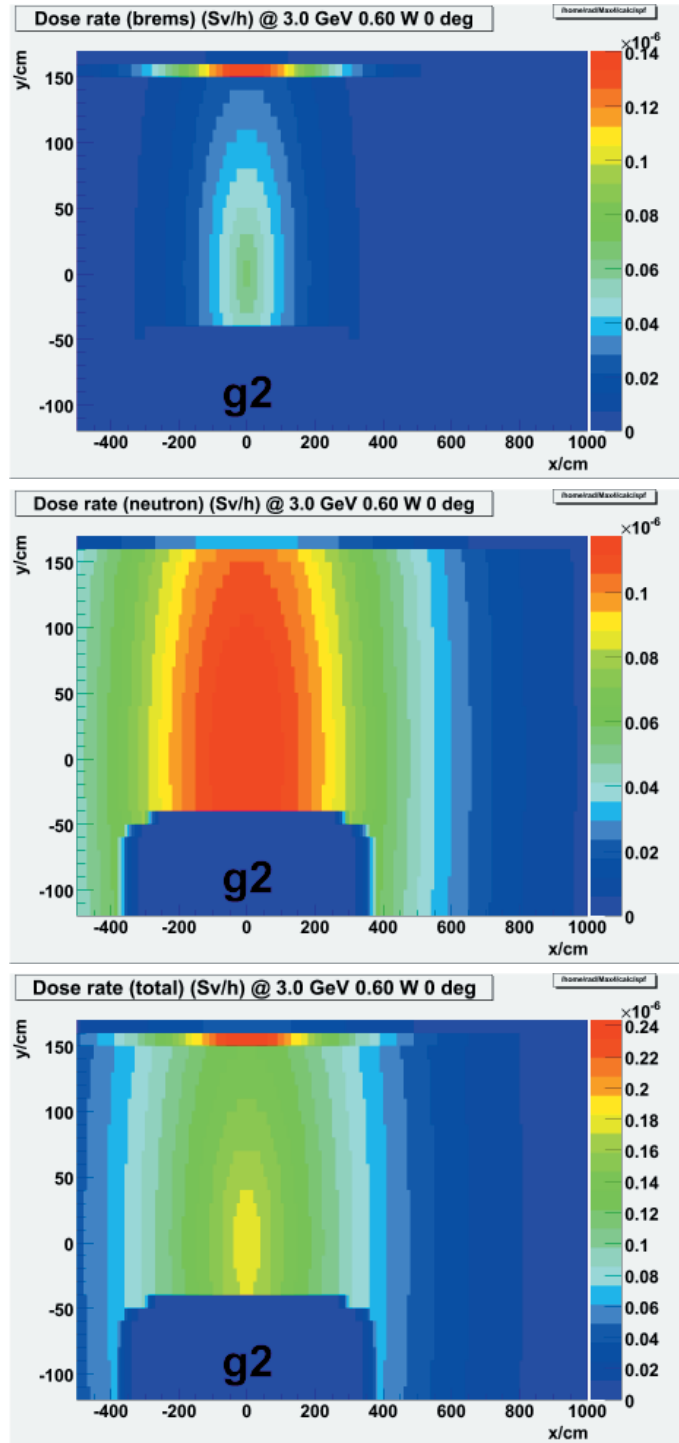


Table E.5: The SPF dose rates on grid g2 (on the wall towards the SPF hall) for a 0.6 W loss before the dump magnet.



# Detailed Design Report



## Chapter 8 Commissioning

**MAX IV Facility**



# Contents

---

<b>8.1.</b>	<b>Sub-system Commissioning Policy .....</b>	<b>4</b>
<b>8.2.</b>	<b>Time Plan .....</b>	<b>5</b>
<b>8.3.</b>	<b>Organization .....</b>	<b>6</b>
8.3.1.	Shifts .....	6
8.3.2.	Log .....	6
<b>8.4.</b>	<b>3.0 GeV Storage Ring Commissioning .....</b>	<b>7</b>
8.4.1.	Requirements on Equipment .....	8
8.4.2.	Beam Commissioning Plan .....	12
<b>8.5.</b>	<b>1.5 GeV Storage Ring Commissioning .....</b>	<b>19</b>
8.5.1.	Requirements on Equipment .....	20
8.5.2.	Beam Commissioning Plan .....	23
<b>8.6.</b>	<b>Injector Commissioning .....</b>	<b>25</b>
	 Appendix A: Acronyms .....	 26
	References .....	27

## 8. Commissioning

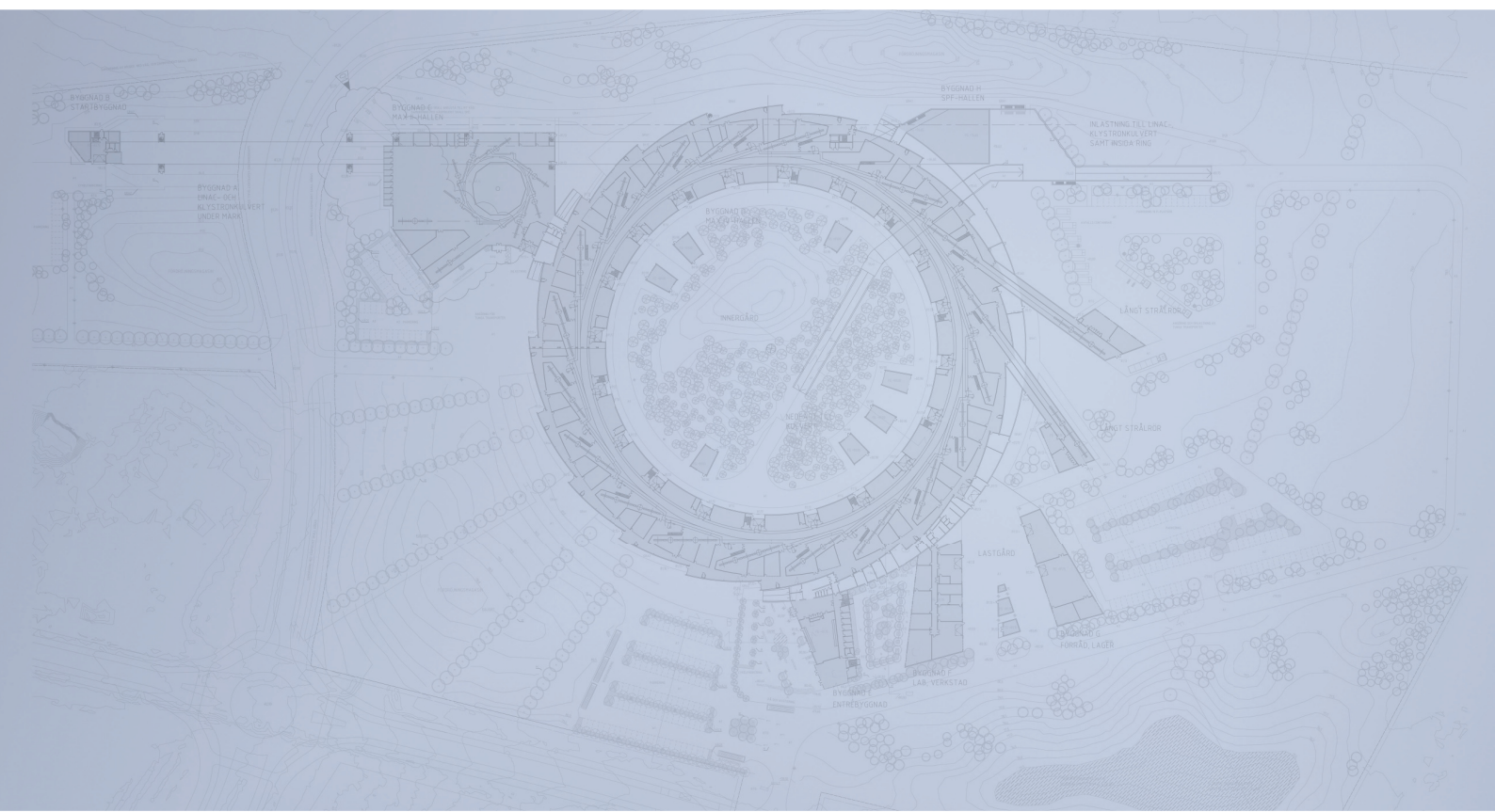
---

The scope and complexity of the MAX IV project is considerable, with a vast number of subsystems. In order for light source commissioning to be even minimally successful, i.e. achieve the primary goal of being able to deliver light to users, most if not all of these subsystems must function without error.

In this Detailed Design Report (DDR) chapter the aim is both to set out a plan for the beam commissioning of the MAX IV accelerators, i.e. the 3.0 GeV storage ring, the 1.5 GeV storage ring and the injector, as well as to state a commissioning policy for the different subsystems.



# Detailed Design Report



## Chapter 8 Commissioning

### 8.1. Sub-system Commissioning Policy

**MAX IV Facility**





## 8.1. Sub-system Commissioning Policy

---

**Modular commissioning approach:** each subsystem is commissioned separately. Once it has passed its individual performance criteria it is signed off on and control of the subsystem is passed to the main control system.

**Owner commissioning:** the group responsible for the design and construction of the subsystem also carries out the commissioning. This is to avoid additional people having to learn the design and construction in detail.

**Ready-to-use:** a subsystem that has finished commissioning must be available in the main control system with all necessary software ready and tested. An operator not familiar with the code should be able to use it.

It should be noted that as a consequence, *no accelerator subsystem can finish commissioning before the control system framework is in place*. In this regard, the control system will be the single most important accelerator component of the facility.



# Chapter 8

## Commissioning

### 8.2. Time Plan

# MAX IV Facility

# MAX IV Facility



## 8.2. Time Plan

---

Given the early stage of the project, the beam commissioning time plan is still in a state of flux. A preliminary time schedule is currently in development.



# MAX IV Facility





## 8.3. Organization

---

Given the complexity of the project there is a need for clearly defined routines during the beam commissioning. There will be several different groups taking shifts during the beam commissioning and communication between them is essential.

### 8.3.1. Shifts

At the time of writing, shift schedules and organization is not finalized and will receive more attention as the start of beam commissioning for the linear accelerator approaches. Factors to consider during planning are:

- The shift schedule should contain a contingency reserve in order not to unduly stress personnel
- The shift team composition should ensure that critical competences are available
- Key personnel may be needed elsewhere in the project during beam commissioning. Double booking should be avoided.
- Support for communication between shift teams

It should be noted that external factors may appear that will impose restrictions on the commissioning schedule. One such external factor that *may* need to be considered is the time schedule for construction work on the neighbouring European Spallation Source (ESS) facility, as such activity may generate vibrations and disturb various commissioning activities.

### 8.3.2. Log

There will be an online logbook available during commissioning. During and after each commissioning shift the responsible operator must fill out an entry including the following:

**Shift staff:** A list of staff present during the shift.

**Shift agenda:** This section should contain clearly defined goals for each shift, filled in at the start of a shift.

**Operation:** This section should give a cursory description of what is done during the shift. I.e., "10:45 - Magnets in Bunch Compressor 1 cycled".

**Summary:** A summary of the shift containing achieved goals, problems, tips for the next shifts and suggestions for improvements.

The logbook must be capable of storing both text and images. Ease of use should be prioritized as filling out the logbook should *not* be the major part of shift activity.

Furthermore, at the end of a shift a history list of control system commands executed should automatically be appended to the log. This is motivated by the human factor, i.e. compensating for the fact that some operators will perform operations such as cycling magnets more often than others: such information is not likely to get into the shift log despite the best efforts of the operators.



# MAX IV Facility



## 8.4. 3.0 GeV Storage Ring Commissioning

---

The commissioning will be divided into three main phases, according to the following list.

**Phase I** The initial goal of the storage ring commissioning is to *obtain stored beam of sufficient quality that beamline installation can use the synchrotron radiation for alignment*. For this to be reached, the following must be achieved:

- Radiation levels on the floor outside the storage ring shielding must be within acceptable limits ( $< 0.5\mu\text{Sv/h}$  daily average) in order for people to be able to work with beamline installation.
- Stored beam in decay mode, with sufficient current and lifetime to allow linear optics characterization.
- Stable orbit over the long term, i.e. orbit RMS variations in each Beam Position Monitor (BPM) flanking the straight sections are below 10% of the transverse beam size. This will require the Slow Orbit Feedback system to be operational.
- All BPMs calibrated against their respective multipoles to within  $10\mu\text{m}$ .

It should be noted that initially the insertion devices may only be closed/active during vacuum conditioning sessions as they would disturb characterization and correction of the storage ring optics.

**Phase II** In phase II the goal is to *reach the design parameters of the bare lattice, beam current excepted*. This will require:

- Correction of the bare lattice linear optics. The correction aims to:
  - Minimize betabeat in order to improve dynamic aperture and allow post-commissioning correction of the non-linear optics.
  - Adjust betatron coupling below 3%
  - Correct vertical dispersion to reduce emittance coupling.

**Phase III** During phase III the goal is to *reach the design parameters for the lattice with four damping wigglers included*. This will require:

- Correction of the machine functions to make the wigglers transparent.
- Reaching the target beam current of 500 mA. To achieve this target without compromising other parameters the following systems will likely prove necessary:
  - Passive 3rd order harmonic cavity to elongate bunches to fight Intra-Beam Scattering (IBS) and improve Touschek lifetime
  - Transverse Multi-Bunch Feedback to counteract current-dependent instabilities

**Post-commissioning** When phases I - III are finished the beam commissioning is over. Subsequent work on the storage ring will be focused on:

- Commissioning of the following sub-systems:
  - Pulsed multipole injection kicker
  - User top-up injection

- Fast Orbit Feedback
- Correction of the non-linear lattice
- Commissioning of beamline insertion devices. For the ring this requires:
  - Local optics correction for insertion device gap changes
  - Global tune correction

### 8.4.1. Requirements on Equipment

Before storage ring commissioning can commence, the requirements listed below must be fulfilled for the respective system.

#### 8.4.1.1 Injector

The injector and 3.0 GeV transfer line must be able to deliver a bunch train with the parameters specified in Table 8.1 to the 3.0 GeV ring septum magnet. Note that the bunch train will fit into one 100 MHz RF bucket.

If the bunch emittance criteria for the injector are met, matching of the transfer line optics to those of the ring will likely not be necessary. However, simulations are needed.

Table 8.1: Injector bunch train requirements for injection into the MAX IV 3.0 GeV ring.

Parameter	Value
Particle energy [GeV]	$3.0 \pm ?$
Charge (bunch train total) [pC]	$\geq 300$
Pulse length [ns]	$\leq 4$
Pulse/bucket delay [ns]	10
Bunch energy spread [%]	$\leq 1$
Repetition rate [Hz]	$\leq 10$
Emittance [ $\mu\text{m rad}$ ] <sup>1</sup>	
Horizontal	$\leq 7.1$
Vertical	$\leq 1.3$
Entry coordinates, ring system ( $x, y, s$ ) [mm]	( -13.5, 0, 1902 )
Entry angle, ring system ( $x', y'$ ) [mrad]	( 0, 0 )

The motivations behind the numbers in Table 8.1 are as follows:

**Energy:** The injector must deliver electrons with 3 GeV particle energy. The tolerance is determined by the ring energy acceptance for the *injected* beam. This number must be determined through tracking.

**Charge:** Judging from typical commercial BPM system, roughly 10 pC charge are needed for transfer line BPMs. The storage ring BPMs, operated in Turn-by-Turn mode, are less sensitive and will hence set the lower limit. The upper limit is in contrast not a hard limit, instead it determines how quickly the current may be stacked to reach the 500 mA target post-commissioning.

<sup>1</sup>Emittance is here defined as the area of the beam ellipse in phase space, divided by  $\pi$ . Note that this is *NOT* normalized for particle energy.

**Pulse length and delay:** At 100 MHz, the ring RF separatrix length is 5 ns. Taking the energy spread into consideration, pulse length should be limited to no more than 4 ns in order to avoid unnecessary injection losses. In order to control which RF bucket to inject into, control over bunch arrival time must allow time shifts of one RF period. These shifts must be possible to control electronically due to the need for filling pattern control. In order to be able to place the bunch train correctly into the RF bucket time greater precision is required: sub-ns delay precision is desired.

**Energy spread:** As the energy acceptance for the ring is considerably larger than what the linear accelerator is designed to deliver, meeting a 1% requirement should be a non-issue.

**Normalized emittance:** The dynamic acceptance for the 3.0 GeV ring at the septum is  $7.1 \mu\text{m rad}$  in the horizontal and  $1.3 \mu\text{m rad}$  in the vertical [1]. Again, the linear accelerator is designed to deliver bunches of significantly lower emittance [3] and meeting the stated requirement should be a non-issue.

#### 8.4.1.2 Timing system

Commissioning requirements on the timing system are still being investigated. For commissioning purposes, the following must be possible to adjust

- Injection trigger delays for
  - 3.0 GeV ring four-kicker bump
  - 3.0 GeV ring pulsed multipole magnet
  - 3.0 GeV injection line kicker magnet
  - Injector photocathode gun laser

#### 8.4.1.3 Control system

The MATLAB Middle Layer (MML) will be used for high-level control as it contains a large set of previously tested algorithms for storage ring commissioning, including but not limited to orbit control applications, response matrix measurements and BPM calibration routines.

Additionally, the TACO New Generation Objects (TANGO) interface for MATLAB will allow rapid prototyping of physics applications during commissioning should it be required.

As will be noted in section 8.6, MML does not support linear accelerators and there will be a need to develop high-level control applications for the commissioning.

#### 8.4.1.4 Storage ring magnets

**Calibration data** Main magnets in the storage ring will be set to nominal fields from the beginning of commissioning. Field calibration data (i.e. field multipole component strength as a function of coil current) should thus be available. As many magnets will not use individual power supplies but be powered in blocks, the relevant parameter will then be the variation of the average field of each block of magnets with the current.

**Cycling procedure** During machine tuning, a cycling procedure is required in order to obtain reproducible settings. The cycling procedure should be automated and implemented as part of the control system. In addition, the manufacturer should be required to use a standard cycling procedure during measurements.



#### 8.4.1.5 Diagnostics

Given the complexity of the 3.0 GeV storage ring, it is essential to have diagnostic systems ready and commissioned before beam commissioning of the ring can begin. This includes connection of the diagnostic systems to the main control system.

**Single pass BPMs, storage ring** Single pass BPMs will be required in order to guide the injected beam around the ring for the first time. The number of single pass BPMs available for commissioning will depend on budgetary constraints: in case only a few can be purchased they will be moved along the ring as the correct corrector magnet strengths are determined. The sum-signal from the BPMs can be used to measure lifetime. Calibration against current meters such as a DCCT will also allow BPMs to do current measurements. Initially the sum-signal may however be used to determine the timing for the pulsed sextupole magnet, in order to optimize the injection. This will however require time stamps for the single-pass BPM data. "First-turn" simulations for different scenarios, aiming to determine the most efficient correction strategy, are needed.

**Single pass BPMs, transfer line** To facilitate injection, at least two single pass BPMs are required on the transfer line from the linac to the septum. This will allow measurements of the bunch train angle and position at the septum location.

**Optical diagnostic beamline** The optical diagnostic beamline is required to be operational and able to provide, at a minimum, a direct video feed of the synchrotron radiation image. After the initial commissioning goal have been achieved it should be possible to calibrate the camera set-up and do emittance measurements. In addition, for the commissioning of the passive 3rd harmonic cavity accurate bunch-length measurements with a resolution of less than 30 ps would be helpful.

**Pinger magnet** Two operational pinger magnets are required as soon as stored beam has been achieved, one for each plane, at which point they will be used for tune measurements together with a single-pass BPM. It may be possible to use the pinger magnets for Transverse Multi-Bunch Feedback (TMBF) given orbit data from fast BPMs. At the time of writing, the design of the TMBF system for the 3.0 GeV storage ring is under development.

**Striplines** Two stripline units mounted in different short straight sections are required from the start of commissioning. One stripline in each unit should be available for tune measurements.

**Fast radiation monitors** More investigation is necessary.

**Fibre radiation monitors** More investigation is necessary. Information on the use of optical fibers as radiation monitors may be found in [6].

**Scrapers** More investigation is necessary.

**DCCT** The DCCT is required to be operational before commissioning can commence. Current measurements using BPM buttons is possible, but require calibration data from the DCCT.

#### 8.4.1.6 Machine protection systems

Safe current levels for the ring must be determined before commissioning begins, in order not to damage ring components.

**Vacuum chamber** Before the beam orbit is measured and brought to the correct location, local heating of the vacuum chamber may occur due to synchrotron radiation. This is not expected to be an issue for most of the achromat interiors, given that the Non-Evaporable Getter (NEG)-coated Cu vacuum chamber acts as an absorber. It may however occur in the straight section chambers and at the stainless steel sections where equipment such as BPMs and fast corrector magnets are located.

Gas desorption is expected to take place on two timescales both caused by vacuum chamber heating. On shorter time scales, direct exposure to Synchrotron Radiation (SR) will result in a fast increase in gas desorption which will be proportional to the current. On longer time scales, vacuum chamber heating due to energy deposition from the beam via both SR and RF will result in increasing thermal gas desorption.

A current level of 3 mA is safe from a vacuum system point of view even for large closed orbit deviations on the order of 4 mm, which corresponds to the expected orbit deviation due to misalignment models. Thus 3 mA beam current should not be exceeded before BPM calibration and orbit correction has finished, as the SR absorbers have been designed with the zero closed orbit in mind.

**Vacuum pumps** During commissioning there should be two pressure levels for the vacuum interlocks on ion pumps: these remain to be determined.

The first interlock should dump the beam through shutting off the RF in case gas desorption becomes too high. This is motivated by protection of the ion pumps from high currents and shorter lifespan.

The second interlock should be at a somewhat higher pressure and will close gate valves if triggered, in order to prevent contamination of neighbouring sections in case of a vacuum leak.

**Temperature monitors** During commissioning there will be the following concerns:

- Temporary use of higher-than-specified levels of coil current in the correction magnets could result in coil damage if the temperature rises too much. A safe level should be determined and temperature monitors installed on each corrector magnet. If safe temperature levels are exceeded for too long, the corrector magnet power supply should either shut down or decrease current to below specified maximum values.
- In case the coil cooling channels in the main magnet elements are clogged the magnets should be shut-down to protect them from overheating: this will require temperature monitors. Any stored beam should be dumped.
- Cooling water temperature should be monitored and equipped with interlocks to prevent components overheating.
- Sensitive regions of the vacuum chamber should be identified before commissioning and equipped with temperature monitors, for the following reasons
  - Initially the beam position will be unknown and regions not designed for such may be exposed to generated SR.
  - RF heating may occur of cavity-like vacuum chamber structures, such as bellows.

**Shut-down policy** In case the 3.0 GeV storage ring must be shut down due to a triggered interlock:

- the stored beam should be dumped via shutting off the RF: this should ensure that the beam is lost in a reproducible way and radiation shielding can be reinforced locally.
- the fast kicker magnet in the linac used to divert bunch trains into the transfer line to the 3.0 GeV ring should be disabled.

Further investigation is required regarding beamstoppers, injector control, beam loss locations for a beam dump via RF, et.c.

#### 8.4.1.7 Auxiliary systems

**Water cooling** Coil cooling channels should be flushed before the cooling system is assembled to avoid blockages.

#### 8.4.1.8 Accelerator alignment

Before beam commissioning of the storage ring can begin, alignment of the 140 magnet blocks must have finished and the ring tunnel temperature should be stable. For alignment and tunnel temperature tolerances, please refer to the DDR [4].

#### 8.4.1.9 Radiation protection

Currently the radiation protection for the MAX IV 3.0 GeV storage ring is designed for expected operational conditions, with no special attention to radiation levels during commissioning. Furthermore, during commissioning radiation measurements will take place continuously and the shielding reinforced where needed. As a consequence, until radiation levels have been confirmed to be within acceptable limits personnel access to sections of the laboratory main hall will be restricted. This may require ring commissioning to take place during out-of-office hours.

### 8.4.2. Beam Commissioning Plan

This chapter will present an outline of the beam commissioning plan for the 3.0 GeV storage ring. As the details of the ring design are still in a state of flux, modifications are highly likely. The commissioning procedure will be done serially in stages, up until a stored beam with corrected closed orbit has been achieved. At this point, some work can be done in parallel.

#### 8.4.2.1 Injection

The injection will be done using the standard four-kicker set-up. The pulsed multipole magnet will be available for the commissioning, but is not expected to be brought online until the 3.0 GeV storage ring has entered the post-commissioning phase. Having the pulsed multipole magnet available does however provide a backup option.

#### Possible problems:

- The four-kicker bump may not be balanced initially.
- Should an attempt be made to use a pulsed multipole magnet for injection during commissioning, the variation of the field with the trajectory offset from the magnetic centre will require some control of the beam location. However, injection kicker balancing will be a non-issue as there is only one magnet.

**Open questions:**

- Timing calibration of the four-kicker bump.
- Timing calibration of the pulsed multipole magnet.
- What are the experiences from commissioning a pulsed sextupole injection magnet at other facilities? What tuning was necessary?
- Commissioning a ring using a pulsed multipole injection magnet has never been done before: what would be the issues?
- Simulations of the injection procedure are needed.

**Radiation protection aspects:** Radiation emission is expected to be highly localized and concentrated to the septum and long straight exit and entrances due to the locally high  $\beta_x$  and the change in horizontal aperture. Simulations of the injection process will be required. All of the incoming charge will be lost during this stage: time-averaged radiation levels may be controlled using the injection repetition rate. Peak levels will be dependent on the bunch train current and are hence not adjustable below a certain limit given that sufficient charge is needed for the BPMs.

Beamline front-end beam stoppers should be closed and disabled manually during this stage.

**8.4.2.2 First turn**

At least 40 out of 200 BPMs will be equipped with electronics capable of making single-pass readings. These will be installed at the final locations, i.e. the four BPM heads closest to each long straight section. There will also be a minimum of 10 extra sets of single-turn electronics available to be moved around for commissioning purposes. Note that in order for the BPMs to sense the electron bunches the injector must deliver 300 pC bunch trains when attempting to achieve "First turn".

The procedure for beam trajectory guidance through each achromat during commissioning is still under investigation.

Post-commissioning, the 40 BPMs are expected to be sufficient for Fast Orbit Feedback (FOFB) on the long straights. Analysis and correction of the non-linear lattice by determination of resonance driving terms using the method detailed in [5] may however not be possible. Further investigation is required.

**Possible problems:**

- Aperture limitations should if present be possible to locate using the single-pass electronics.
- Magnet polarity errors are to be expected. Preventative measures to be taken during design include standardization of cabling, "fool-proof" connections and colour coding. Routines for installation may be considered. Available diagnostic methods during commissioning to identify polarity errors are:
  - Dipoles: polarity errors should make it impossible to get past the dipole in question. In case BPMs with single-turn electronics are installed everywhere identification becomes trivial, if not it will be possible to manually check the polarity in the tunnel.
  - Quadrupoles: deviation between ideal and measured trajectory should show which quad is not connected the right way. May be necessary to get fast BPM electronics on the entire achromat in order to get the orbit response.
  - Sextupoles: investigations into diagnostic methods are needed.

- Octupoles: investigations into diagnostic methods are needed. It is anticipated to be very difficult to identify a polarity error using beam diagnostics due to the high order of the octupole field.
- Poleface strips: for nominal optics no poleface strip current should be required. Once a stored beam is obtained the tune response may be used to identify polarity errors. Poleface strips should not prove necessary during "First turn".
- Corrector magnets: trajectory response should immediately give the polarity. No hardware correction will be necessary.
- Trim coils: investigations into diagnostic methods are needed.

#### Open questions:

- Will two single-turn BPMs in each achromat be sufficient without moving electronics around, given the expected misalignment model?
- Is it possible to use a k-variation technique to get a rough calibration of the BPMs against the quadrupoles even before stored beam is achieved?
- What kind of BPM-quadrupole offset can we expect during commissioning? In MAX II and MAX III several millimeters were observed.

**Radiation protection aspects:** While guiding the bunches around the ring to achieve first-turn the particle losses will be highly localized. The peak intensity will be proportional to the bunch charge, for which the lower limit is set by the BPM electronics. The dose will be proportional to both the bunch charge and the injector repetition rate, the latter of which will be adjusted in case unacceptably high radiation dose levels are measured. Radiation dose limits will depend on the presence of staff in the laboratory main hall.

Beamline front-end beam stoppers should be closed and disabled manually during this stage.

#### 8.4.2.3 Stored beam

Once the first turn has been achieved, the response for each corrector in the subsequent BPMs will be measured. The corrections are then altered until a few thousand turns are achieved, at which point the power to the RF cavities is switched on and current is stacked to a safe limit. The timing between the storage ring RF clock and the injector trigger will have to be adjusted in order to place the incoming 3 GHz bunch train in the correct 100 MHz RF bucket.

The total charge for the 3 GHz bunch train coming from the linear accelerator should be kept low while storing beam in order to avoid a high bunch charge in the ring. This will avoid filling a single bucket using just a few shots and reduce potential heating due to SR and impedance effects. In addition, filling pattern control should also be used with the same aim: to avoid high single bunch currents.

With stored beam, the following should be possible to measure:

- Tunes
- Chromaticity
- BPM offset relative sextupoles
- Bunch dimensions

#### Possible problems:

**Open questions:**

- A strategy is needed for bringing the cavities online. One at a time? Initially, one will be sufficient to store beam as the current will be rather low.
- How is the phase synchronization between cavities handled? Can this be done before there is beam?
- What is the safe current limit? Currently the vacuum system can take at least 3 mA beam current with unknown beam position.

**Radiation protection aspects:** Once beam is stored radiation levels will be due to both particle losses and synchrotron radiation, the latter of which will now become a significant radiation source with levels proportional to the stored beam current. Radiation levels will be monitored in the accelerator hall and the stored beam current limited if necessary to bring radiation levels to within safe limits.

Particle loss levels will initially be determined by the vacuum pressure as the vacuum lifetime is expected to dominate. Top-up operation with closed beamline front-ends may be used in order to reduce the time needed for vacuum chamber conditioning.

During measurements the machine will be in decay mode to reduce disturbances from injection. The risk for total beam loss at this stage is considerable as the closed orbit is unknown and several measurements adjust the closed orbit. Such losses are expected to be localized, rather than distributed around the circumference.

Beamline front-end beam stoppers should be closed and disabled manually during this stage.

**8.4.2.4 Orbit correction and BPM calibration**

The BPM will initially require calibration against the MAX IV multipoles: to do this the auxiliary coils of the SDend, SFi, SFo and SFm sextupole families as well as the OXX octupole family will be wired in the quadrupole configuration. This will allow determination of the BPM offsets relative to the respective quadrupole fields. The routines in the MML will be used for this where applicable, though some alteration due to the powering of auxiliary coils may be required. Once the BPM offsets have been measured, an MML orbit correction routine based on Singular Value Decomposition (SVD) will be used to correct the orbit to the measured multipole centers. This procedure is expected to be iterative, with several BPM calibration and orbit correction steps required until the closed orbit is satisfactory.

Initially only the slow global orbit feedback will be active: work on the FOFB will commence during the post-commissioning phase.

**Possible problems:**

- It may prove impossible to correct the orbit to measured multipole centers due to corrector magnet saturation. Accelerator Toolbox (AT) simulations indicate that for the "required case" for misalignments one to three correctors will reach saturation. Possible solutions, still to be fully investigated, include
  - powering some auxiliary coils as extra corrector magnets or physical adjustments of the magnet blocks.
  - temporarily running higher currents through the correction magnets, although resistive heating then becomes a problem and safe coil current limits would need to be determined.
- BPM and corrector magnet coils may have been connected incorrectly. It may be possible to identify which using Linear Optics from Closed Orbits (LOCO).

**Open questions:**

**Radiation protection aspects:** No additional radiation protection issues are foreseen during this stage. As the closed orbit is brought to the design orbit and the vacuum levels gradually improve, the radiation levels should if anything decrease for the same beam current. Due to machine measurements, the beam current is going to be limited in order to avoid any instabilities due to impedances.

Beamline front-end beam stoppers should be closed and disabled manually during this stage.

**8.4.2.5 Linear optics characterization and correction**

Once the design orbit has been achieved the next step is to analyze the linear lattice. This will be done both by response matrix analysis, i.e. LOCO, and direct measurement of beam sizes and dispersion at diagnostic beamlines. The following information is expected to become available:

- Linear machine functions
- Magnet gradient errors
- Emittance coupling, i.e. the ratio  $\kappa = \epsilon_y/\epsilon_x$  where  $\epsilon_i$  are the measured equilibrium emittances in the horizontal and vertical planes.
- Skew gradients
- BPM gain factors
- Corrector magnet strengths and coupling

Although not a linear effect, chromaticity will also be measured. At this point, if LOCO measurements have not been done previously, BPM gain factors and transverse coupling (due to head rotation, electronics, et.c.) will be obtained and BPM calibration can be finalized.

Work may then begin on correcting the linear lattice. As for the orbit correction, this is expected to be an iterative process. Once the gradient errors have been obtained in each iteration, the procedure for correcting them will vary between magnet families.

Reduction of gradient errors in the gradient dipoles will be handled by pole-face strips. The pole-face strips are currently being designed. The current design goal would allow a 3% change of the basic gradient strength. To also allow adjustment for randomly varying gradient errors in the gradient dipoles individual power supplies will be needed for the pole face strips, unless the random variations can be kept sufficiently low during the manufacturing process.

Reduction of gradient errors in the quadrupoles will be handled by shunt resistors and current adjustments. Systematic gradient errors will be eliminated by adjusting the power supply current, as blocks of quadrupole magnets within the same family will be powered in series. The magnets within these blocks will be balanced against each other internally using shunts, which will allow elimination of the random gradient errors.

Correction of chromaticity will be done using the SD and SFi/SFm/SFo sextupole families.

Correction of vertical dispersion can be done using auxiliary windings connected in the skew quadrupole configuration. The vertical dispersion may be measured by measuring the DC orbit response for an RF shift.



**Possible problems:** It may not be possible to measure correct beam sizes and emittances until good ring vacuum has been established. Currently, due to a large part of the ring circumference being NEG-coated, this is expected to require a significantly lower amount of vacuum conditioning than for traditional vacuum systems. Simulations indicate 2.5 Ah for a fully NEG-coated ring and 175 Ah for a traditional vacuum system, with the real value falling somewhere in between [2]. Response matrix measurements will likely not be affected by bad vacuum, apart from a decrease in the S/N ratio.

**Open questions:** LOCO does have some limitations: one such is an inability to fit two adjacent quadrupoles accurately. The LOCO performance for the 3.0 GeV lattice needs to be investigated.

**Radiation protection aspects:** Radiation levels during this activity should correspond to that of a stored beam, although vacuum levels may worsen immediately after each gradient error correction due to illumination of different sections of the vacuum chamber wall.

Beamline front-end beam stoppers may be open only if the stored beam is in decay mode. While front-end beam stoppers are open *injection into the ring must not take place*. The specific technical solutions to achieve this is under discussion: interlocks on both the injector kicker magnet and an injection line beam stopper have been suggested.

When a beamline front-end beam stopper is first opened with stored beam in the ring the radiation levels at the experimental station must first be measured and verified to be within safe limits before staff is allowed to work in the surrounding areas.

#### 8.4.2.6 Vacuum conditioning

Given the full energy injection top-up operation is expected to be immediately available if required for the purpose of vacuum conditioning. Furthermore, once the BPMs have been calibrated, the orbit corrected and the pulsed multipole magnet commissioned, top-up injection should have a negligible effect on the stored beam. However, it should be noted that such top-up operation is for machine conditioning only. Top-up injection for user operation will not be possible without additional effort on radiation protection, as running top-up with front-ends open may impact on the radiation levels in the experimental stations.

**Possible problems:**

**Open questions:**

**Radiation protection aspects:** Until the vacuum has reached target values the stored current should be maintained at safe levels from a machine and radiation protection viewpoint. Once vacuum conditions improve and the radiation shielding has been reinforced at any hot spots the current can be increased.

#### 8.4.2.7 Current stacking

In order to reach the target beam current and lifetime, the 3rd harmonic cavity, the damping wigglers and the TMBF will likely be required. The current will be increased while radiation levels and the beam spectrum are measured continuously, the latter in order to determine the onset of any current-related instability.

Once current-related instabilities appear, they may be combatted by either the TMBF or by increasing Landau damping through an increase of chromaticity. A high chromaticity optics setting should be prepared beforehand.

The 3rd harmonic cavities will be brought online one at a time in order to more easily determine the source of any resulting effect on the beam. In addition, bringing them online one at a time allows



conditioning at lower beam currents corresponding to the same power deposition as for the case with three cavities and 500 mA.

The four damping wigglers will be installed and compensated for at low beam currents in order to verify that they do not significantly disturb the orbit and introduce heat loads on sensitive parts of the vacuum chamber. The distortion of the linear optics will be compensated according to the scheme described in Ref. [1]. Once they function according to specifications and are transparent for the ring the current may be stacked up to the target 500 mA.

**Possible problems:** For the 3rd harmonic cavity, considerable outgassing is expected as it is initially tuned in and fields are excited. This must be done slowly in order to avoid vacuum issues. The intention is to tune each cavity in separately in order to more easily determine the source of any problem.

**Open questions:**

- The conceptual design for the TMBF system is not yet finished.
- It is currently unknown whether the damping wigglers will be fixed-gap or variable-gap devices, which has implications for the orbit and optics correction.

**Radiation protection aspects:** As the damping wigglers are installed significant amounts of synchrotron radiation will be generated on the relevant straight sections once the gaps are closed. During wiggler beam commissioning beamline front-ends should be manually shut and disabled in order to avoid any radiation protection issues at the beamline stations.

# Chapter 8

## Commissioning

### 8.5. 1.5 GeV Storage Ring Commissioning

#### MAX IV Facility

# MAX IV Facility



## 8.5. 1.5 GeV Storage Ring Commissioning

---

Due to the ongoing design work for the 1.5 GeV storage ring, the commissioning plan is preliminary and details are subject to change. It is emphasized that the commissioning plan for the 1.5 GeV storage ring is a *work in progress*.

The commissioning will be divided into three main phases, according to the following list.

**Phase I** The initial goal of the storage ring commissioning is to *obtain stored beam of sufficient quality that beamline installation can use the synchrotron radiation for alignment*. For this to be reached, the following must be achieved:

- Radiation levels on the floor outside the storage ring shielding must be within acceptable limits ( $< 0.5\mu\text{Sv/h}$  daily average) in order for people to be able to work with beamline installation.
- Stored beam in decay mode, with sufficient current and lifetime to allow linear optics characterization.
- Stable orbit over the long term, i.e. orbit RMS variations in each BPM flanking the straight sections are below 10% of the transverse beam size. This will require the Slow-Orbit Feedback system to be operational.
- All BPMs calibrated against their respective quadrupoles to within  $10\mu\text{m}$ .

It should be noted that initially the insertion devices may only be closed/active during vacuum conditioning sessions as they would disturb characterization and correction of the storage ring optics.

**Phase II** In phase II the goal is to *reach the design parameters of the bare lattice, beam current excepted*. This will require:

- Correction of the bare lattice linear optics. The correction aims to:
  - Minimize betabeat in order to improve dynamic aperture and allow post-commissioning correction of the non-linear optics.
  - Correct vertical dispersion to reduce emittance coupling.

**Phase III** During phase III the goal is to *increase the stored current to the design value*. To achieve this without compromising lifetime the following systems will likely prove necessary:

- Passive 3rd order harmonic cavity to elongate bunches for improved Touschek lifetime
- Transverse Multi-Bunch Feedback to counteract current-dependent instabilities

**Post-commissioning** When phases I - III are finished the beam commissioning is over. Subsequent work on the storage ring will be focused on:

- Commissioning of the following sub-systems:
  - User top-up injection
  - Fast Orbit Feedback
- Correction of the non-linear lattice
- Commissioning of beamline insertion devices. For the ring this requires:
  - Local optics correction for insertion device gap changes
  - Global tune correction

Table 8.2: Injector bunch train requirements for injection into the MAX IV 1.5 GeV ring.

Parameter	Value
Particle energy [GeV]	$1.5 \pm ?$
Charge (bunch train total) [pC]	$\geq 300$
Pulse length [ns]	$\leq 4$
Pulse/bucket delay [ns]	10
Bunch energy spread [%]	$\leq 3.0$
Repetition rate [Hz]	$\leq 10$
Emittance [ $\mu\text{m rad}$ ] <sup>2</sup>	
Horizontal	$\leq 17.7$
Vertical	$\leq 5.6$
Entry coordinates, ring system $(x, y, s)$ [mm]	(?, ?, ?)
Entry angle, ring system $(x', y')$ [mrad]	(0, 0)

### 8.5.1. Requirements on Equipment

Before storage ring commissioning can commence, the requirements listed below must be fulfilled for the respective system.

#### 8.5.1.1 Injector

The injector and 1.5 GeV transfer line must be able to deliver a bunch train with the parameters specified in Table 8.2 to the 1.5 GeV ring septum magnet. Note that the bunch train will fit into one 100 MHz RF bucket.

If the bunch emittance criteria for the injector are met, matching of the transfer line optics to those of the ring will likely not be necessary. However, simulations are needed.

The motivations behind the numbers in Table 8.2 are as follows:

**Energy:** The injector must deliver electrons with 1.5 GeV particle energy. The tolerance is determined by the ring energy acceptance for the *injected* beam. This number must be determined through tracking.

**Charge:** Judging from typical commercial BPM system, roughly 10 pC charge are needed for transfer line BPMs. The storage ring BPMs, operated in Turn-by-Turn mode, are less sensitive and will hence set the lower limit. The upper limit is in contrast not a hard limit, instead it determines how quickly the current may be stacked to reach the 500 mA target post-commissioning.

**Pulse length and delay:** At 100 MHz, the ring RF separatrix length is 5 ns. Taking the energy spread into consideration, pulse length should be limited to no more than 4 ns in order to avoid unnecessary injection losses. In order to control which RF bucket to inject into, control over bunch arrival time must allow time shifts of one RF period. These shifts must be possible to control electronically due to the need for filling pattern control. In order to be able to place the bunch train correctly into the RF bucket time greater precision is required: sub-ns delay precision is desired.

**Energy spread:** As the energy acceptance for the ring is considerably larger than what the linear accelerator is designed to deliver, meeting a 3% requirement should be a non-issue. However, note that significant energy jitter for the injector bunch train will reduce the acceptable energy spread.

---

<sup>2</sup>Emittance is here defined as the area of the beam ellipse in phase space, divided by  $\pi$ . Note that this is *NOT* normalized for particle energy.

**Normalized emittance:** The dynamic acceptance for the 1.5 GeV ring at the septum is  $17.7 \mu\text{m rad}$  in the horizontal and  $5.6 \mu\text{m rad}$  in the vertical [1]. Again, the linear accelerator is designed to deliver bunches of significantly lower emittance [3] and meeting the stated requirement should be a non-issue.

#### 8.5.1.2 Timing system

Commissioning requirements on the timing system are still being investigated. For commissioning purposes, the following must be possible to adjust

- Injection trigger delays for
  - 1.5 GeV ring four-kicker bump
  - 1.5 GeV ring pulsed multipole magnet
  - 1.5 GeV injection line kicker magnet
  - Injector photocathode gun laser

#### 8.5.1.3 Control system

The MML will be used for high-level control as it contains a large set of previously tested algorithms for storage ring commissioning, including but not limited to orbit control applications, response matrix measurements and BPM calibration routines.

Additionally, the TANGO interface for MATLAB will allow rapid prototyping of physics applications during commissioning should it be required.

As will be noted in section 8.6, MML does not support linear accelerators and there will be a need to develop high-level control applications for the commissioning.

#### 8.5.1.4 Storage ring magnets

**Calibration data** Main magnets in the storage ring will be set to nominal fields from the beginning of commissioning. Field calibration data (i.e. field multipole component strength as a function of coil current) should thus be available. As many magnets will not use individual power supplies but be powered in blocks, the relevant parameter will then be the variation of the average field of each block of magnets with the current.

**Cycling procedure** During machine tuning, a cycling procedure is required in order to obtain reproducible settings. The cycling procedure should be automated and implemented as part of the control system. In addition, the manufacturer should be required to use a standard cycling procedure during measurements.

#### 8.5.1.5 Diagnostics

It is essential to have diagnostic systems ready and commissioned before beam commissioning of the ring can begin. This includes connection of the diagnostic systems to the main control system. Currently the diagnostic systems for the 1.5 GeV ring are being designed. This section should thus be considered a work in progress.

**Single pass BPMs, storage ring** Single pass BPMs will be required in order to guide the injected beam around the ring for the first time. The number of single pass BPMs available for commissioning will depend on budgetary constraints: in case only a few can be purchased they will be moved along the ring as the correct corrector magnet strengths are determined. The sum-signal from the BPMs can be used to measure lifetime. Calibration against current meters such as a DCCT will also allow BPMs to do current measurements. "First-turn" simulations for different scenarios, aiming to determine the most efficient correction strategy, are needed.

**Single pass BPMs, transfer line** To facilitate injection, at least two single pass BPMs are required on the transfer line from the linac to the septum. This will allow measurements of the bunch train angle and position at the septum location.

**Optical diagnostic beamline** The optical diagnostic beamline is required to be operational and able to provide, at a minimum, a direct video feed of the synchrotron radiation image. After the initial commissioning goal have been achieved it should be possible to calibrate the camera set-up and do emittance measurements. In addition, for the commissioning of the passive 3rd harmonic cavity accurate bunch-length measurements with a resolution of less than 30 ps would be helpful.

**Pinger magnet** More investigation is necessary.

**Striplines** Two stripline units mounted in different short straight sections are required from the start of commissioning. One stripline in each unit should be available for tune measurements.

**Fast radiation monitors** More investigation is necessary.

**Fibre radiation monitors** More investigation is necessary. Information on the use of optical fibers as radiation monitors may be found in [6].

**Scrapers** More investigation is necessary.

**DCCT** The DCCT is required to be operational before commissioning can commence. Current measurements using BPM buttons is possible, but require calibration data from the DCCT.

#### 8.5.1.6 Machine protection systems

Currently no safety simulations have been made to determine safe levels of current for the ring. Such levels must be determined before commissioning begins, in order not to damage ring components.

**Vacuum chamber** The vacuum system for the 1.5 GeV storage ring is currently in design stage. More information will be added later.

**Vacuum pumps** The vacuum system for the 1.5 GeV storage ring is currently in design stage. More information will be added later.



**Temperature monitors** During commissioning there will be the following concerns:

- In case the coil cooling channels in the main magnet elements are clogged the magnets should be shut-down to protect them from overheating: this will require temperature monitors. Any stored beam should be dumped.
- Sensitive regions of the vacuum chamber should be identified before commissioning and equipped with temperature monitors. Initially the beam position will be unknown and such regions may be exposed to generated SR.

**Shut-down policy** In case the 1.5 GeV storage ring must be shut down due to a triggered interlock:

- the stored beam should be dumped via shutting off the RF: this should ensure that the beam is lost in a reproducible way and radiation shielding can be reinforced locally.
- the fast kicker magnet in the linac used to divert bunch trains into the transfer line to the 1.5 GeV ring should be disabled.

Further investigation is required regarding beamstoppers, injector control, beam loss locations for a beam dump via RF, etc.

#### 8.5.1.7 Auxiliary systems

**Water cooling** Coil cooling channels should be flushed before the cooling system is assembled to avoid blockages.

#### 8.5.1.8 Accelerator alignment

Before beam commissioning of the storage ring can begin, alignment of the magnet blocks must have finished and the ring tunnel temperature should be stable. For alignment and tunnel temperature tolerances, please refer to the DDR [4].

#### 8.5.1.9 Radiation protection

Currently the radiation protection for the MAX IV 1.5 GeV storage ring is in the design phase. This item will be expanded upon once more information becomes available.

### 8.5.2. Beam Commissioning Plan

This section will present an outline of the beam commissioning plan for the 1.5 GeV storage ring. As the details of the ring design are still being worked out material will be added in the respective subsections at a later time. The commissioning procedure will be done serially in stages, up until a stored beam with corrected closed orbit has been achieved. At this point, some work can be done in parallel.

#### 8.5.2.1 Injection

**Possible problems:**

**Open questions:**

**Radiation protection aspects:**



**8.5.2.2 First turn****Possible problems:****Open questions:****Radiation protection aspects:****8.5.2.3 Stored beam****Possible problems:****Open questions:****Radiation protection aspects:****8.5.2.4 Orbit correction and BPM calibration****Possible problems:****Open questions:****Radiation protection aspects:****8.5.2.5 Linear optics characterization and correction****Possible problems:****Open questions:****Radiation protection aspects:****8.5.2.6 Vacuum conditioning****Possible problems:****Open questions:****Radiation protection aspects:****8.5.2.7 Current stacking****Possible problems:****Open questions:****Radiation protection aspects:**

# MAX IV Facility



## 8.6. Injector Commissioning

---

Due to the ongoing design work for the MAX IV injector, the commissioning plan is preliminary and details are subject to change. It is emphasized that the commissioning plan for the injector is a *work in progress*.

# Appendix A

---

## Acronyms

<b>AT</b>	Accelerator Toolbox
<b>BPM</b>	Beam Position Monitor
<b>DDR</b>	Detailed Design Report
<b>ESS</b>	European Spallation Source
<b>FOFB</b>	Fast Orbit Feedback
<b>IBS</b>	Intra-Beam Scattering
<b>LOCO</b>	Linear Optics from Closed Orbits
<b>MML</b>	MATLAB Middle Layer
<b>NEG</b>	Non-Evaporable Getter
<b>SOFB</b>	Slow Orbit Feedback
<b>SR</b>	Synchrotron Radiation
<b>SVD</b>	Singular Value Decomposition
<b>TANGO</b>	TACO New Generation Objects
<b>TMBF</b>	Transverse Multi-Bunch Feedback

## References

---

- [1] Detailed design report on the MAX IV facility: Chapter 2.2. linear lattice. Technical report, 2010.
- [2] Detailed design report on the MAX IV facility: Chapter 2.8. vacuum system. Technical report, 2010.
- [3] Detailed design report on the MAX IV facility: Chapter 4.1. general description and design philosophy. Technical report, 2010.
- [4] Detailed design report on the MAX IV facility: Chapter 6.6. alignment, positional tolerances. Technical report, 2010.
- [5] R Bartolini, L H A Leunissen, Y Papaphilippou, F Schmidt, and A Verdier. Measurement of resonance driving terms from turn-by-turn data. oai:cds.cern.ch:387272. (CERN-SL-99-032-AP):3 p, Mar 1999.
- [6] H. Henschel, M. Körfer, J. Kuhnenn, U. Weinand, and F. Wulf. Fibre optic radiation sensor systems for particle accelerators. *Nuclear Instruments and Methods in Physics Research Section A: Accelerators, Spectrometers, Detectors and Associated Equipment*, 526(3):537 – 550, 2004.



# MAX IV Facility





## 9. Control System

---

<b>9.1.</b>	<b>Introduction .....</b>	<b>2</b>
9.1.1.	Requirements .....	2
<b>9.2.</b>	<b>Design.....</b>	<b>3</b>
9.2.1.	Guidelines .....	3
9.2.2.	Architecture.....	4
<b>9.3.</b>	<b>Hardware .....</b>	<b>6</b>
<b>9.4.</b>	<b>Connectivity .....</b>	<b>7</b>
9.4.1.	Field Bus .....	7
9.4.2.	Computer Network.....	7
<b>9.5.</b>	<b>Software.....</b>	<b>8</b>
9.5.1.	Programming Languages .....	8
9.5.2.	Software Repository and Deployment .....	8
9.5.3.	Databases .....	8
9.5.4.	Operating System.....	9



# MAX IV Facility



## 9.1. Introduction

---

The Machine Control System encompasses the end user interfaces and all that is necessary to control the hardware devices and consequently the physical parameters of the system.

The Control system should require little or no in-house development of new, cutting edge, solutions. Instead, most of the hardware and control software has already been implemented at other institutes and the trend in open nature and willingness to share means that solutions can easily be imported without the need to re-implement them. In some instances, little or no adaptation will be needed to arrive at a working solution. The work associated with deployment of the MAX IV Control System will mostly involve adaptation of existing technology.

### 9.1.1. Requirements

The requirements engineering process has to be flexible enough to meet the complexity challenges in a modern control system. During the development process, an open, light weight process needs to be applied due to the prototypical nature of a new light source facility, where requirements partially emerge. Despite the difficulty of foreseeing all the requirements, the success of out-sourcing projects of sub-systems heavily depends on requirements specification quality.

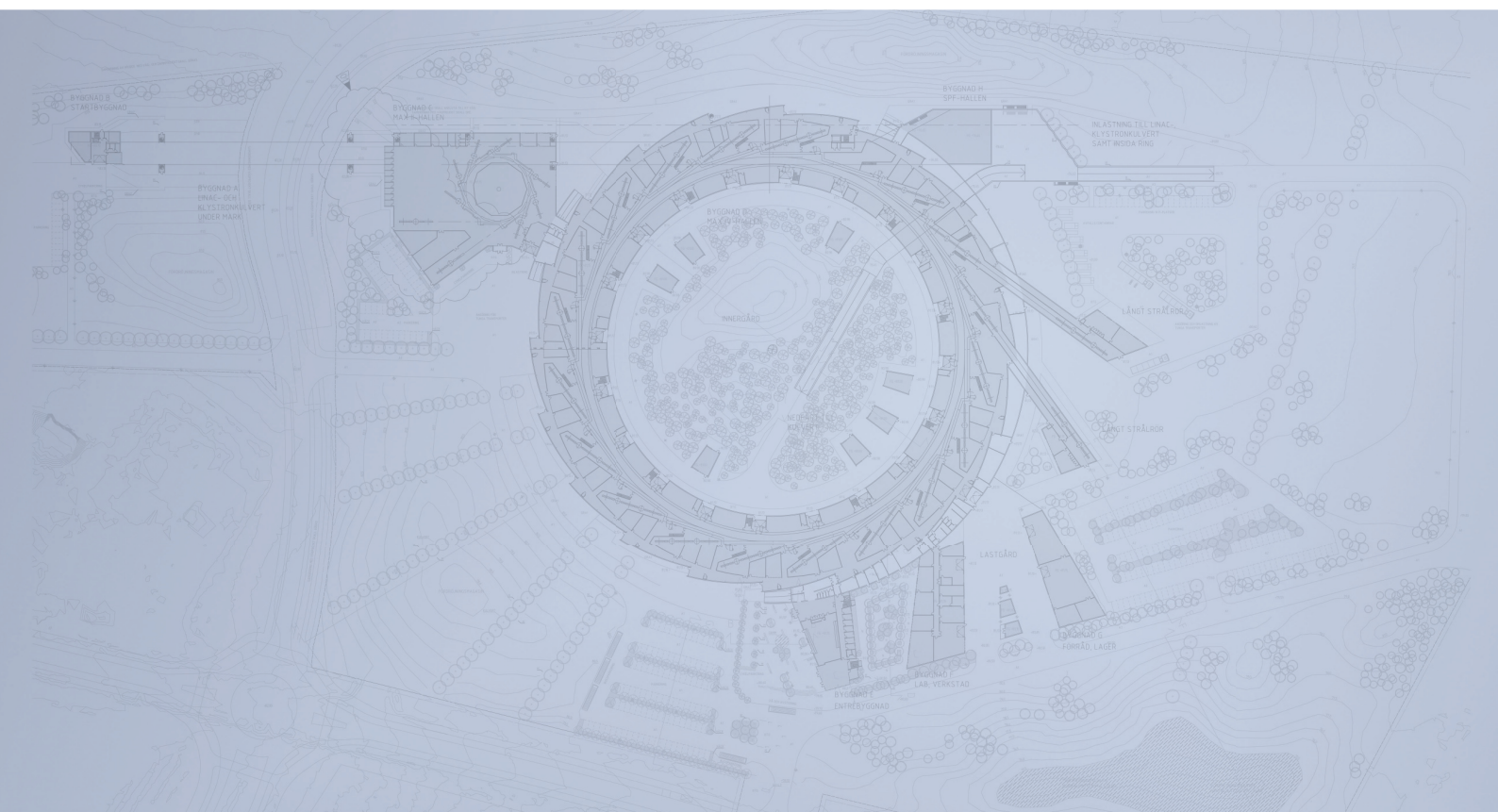
The requirements engineering process for the MAX IV Control System shall be oriented on the following issues:

- *ease of use*, in particular for persons who are not related to control system development
- suitability for *interdisciplinary communication*
- *prioritisation* of features and qualities in order to enable enough resources for the projects managers
- *validation* to ensure the actual user value of a system, its features etc
- *traceability* of requirements over time

The capture of the requirements will be different depending on the type of project. The simplest version being a text file with a use case description or in the Control Systems group a professional requirements tool to track all requirements.



# Detailed Design Report



## Chapter 9 Control System 9.2. The Design

**MAX IV Facility**





## 9.2. The Design

---

### 9.2.1. Guidelines

There are a number of design guidelines in the design of the Control System to make it cost and resource efficient, besides avoiding to re-invent the wheel as mentioned in the introduction,

- *Standardisation* of hardware and software systems

The effort to standardise systems results in a reduced number of system types which need to be developed and maintained by the support staff. This reduces the resources needed for development and maintenance or put in another way, given fixed resources, raises the level of the achievable goals.

- Develop *modular* solutions

The MAX IV facility has a long lifetime and during these years there will be new advances in technology. Developing modular, independent hardware and software systems will make it easier to upgrade to new technologies by being able to upgrade the system in modular parts.

- Use *open source* solutions

The building of an accelerator control system will involve connecting many, individual, smaller systems. Using an open source solution facilitates the integration since the source code is available to make adaptations where needed. Open source also reduces cost by avoiding license fees. This also favours collaboration with other institutes which might be less inclined to start a collaboration involving a proprietary product, not chosen by them, which requires an economic investment.

- *Enable users* (accelerator staff) to configure and operate the systems themselves

With suitable tools, the accelerator staff will be able to perform many tasks themselves which otherwise would have to be performed by the control system staff. Besides relieving the control system staff, this means that the work can be done more efficiently by the application experts.

### 9.2.2. Architecture

The architecture of the control system is shown in Figure 1. The integration layer for will be TANGO ([www.tango-controls.org](http://www.tango-controls.org)) used at research facilities such as ESRF, Soleil, ALBA, LMJ and FRM 2. Systems which require fast and/or real time control will be implemented at the electronics level and the integrative layer will connect for configuration or data acquisition (e.g. archiving of process variables). A local node, such as a Linux PC, will be used to connect to these systems instead of connecting directly from the integrative layer. This ensures that a potential network problem does not disturb the dedicated system. This solution with extra “shielding” should be used for the most critical devices (RF systems, accelerator protection systems).

In the TANGO layer, libraries or drivers should be used to connect to hardware. The use of libraries opens up more possibilities to share and collaborate with other facilities even if they do not use TANGO.

A number of services such as archiving and alarms will always be connected to the integrative layer. These are already developed within the TANGO community and should be used at MAX IV. At the top layer we find client applications in the form of graphical user interfaces, scripting and macro frameworks and bindings to data processing software. An example of the latter is the connection to Elegant made at Elettra and another the MAT-lab middle layer which makes it possible to use accelerator physics applications such as the Accelerator toolkit.

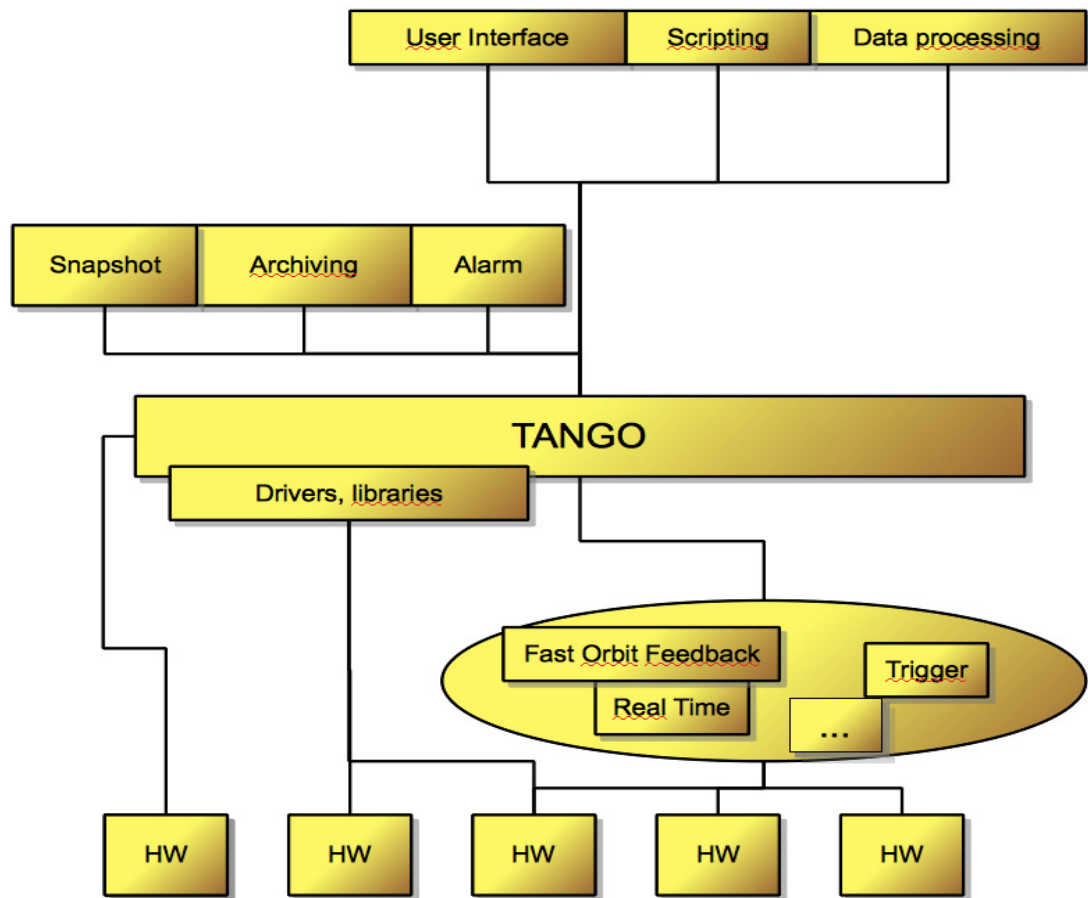


Figure 1: Architecture of the MAX IV Control System.



# MAX IV Facility



## 9.3. Hardware

---

The hardware divides into the following categories, each of which is subject to the design guidelines previously mentioned:

Computers and Peripherals – these are either control end stations with no direct hardware interfaced, or rack mounted machines with electronics connected to the bus. They may include the display and any other peripherals needed to perform the task for which they are intended.

Data Acquisition and Control Electronics – for controlling motion or digital/analogue I/O devices.

Monitoring sensors and Power drivers – for amplifying signals, requires the joint expertise of scientists and engineering groups.

All electronics and computers should fit in 19" cabinets. This provides a uniform, cost effective, environment where all equipment is cooled and protected.





# MAX IV Facility



## 9.4. Connectivity

---

### 9.4.1. Field Bus

There will be a number of different field buses in the MAX IV Control System. Each will require a certain amount of development effort and therefore this number should be kept as low as possible.

The preferred field bus will be Ethernet and failing that, other bus types can be accepted after discussion with the Control Systems group. All hardware must have a well documented protocol regardless of field bus.

### 9.4.2. Computer Network

The computer network (referred to as network) is the facility wide communication channel for the complete control system and will be designed for robustness and speed. The design will contain a redundant, high speed, backbone running through the MAX IV facility. Besides performance, the network needs to be secure and prevent unauthorised access.

It is highly desirable to be able to monitor the performance and status of the network equipment. This will facilitate preemptive maintenance of the system and also help when trouble shooting the control system. Key parameter from the network monitoring will be stored in the TANGO database.



# MAX IV Facility



## 9.5. Software

---

### 9.5.1. Programming Languages

The programming languages used in the control system is governed by the TANGO framework. This includes C/C++, Java and Python and although it is not limited to this it will be enough to solve most of high and low level tasks. In addition, we will provide bindings to other high level applications like Igor Pro and MAT-lab if required by the accelerator staff.

### 9.5.2. Software Repository and Deployment

There will be a central software repository for all source code used in the control system. It will track dependencies between different software and use versioning to track changes.

Build routines will be a part of the deployment workflow and there will be a binary repository of stable releases.

### 9.5.3. Databases

All devices within the TANGO layer are stored in a MySQL database. It contains the addresses for the devices and its configuration parameters. The database can be populated manually, but most of the entries of new devices will be done automatically using scripting. There are a number of solutions available to perform this task within the TANGO community.

The TANGO archiving system will be used to store all process variables into a separate database. Ideally, this should also include information from the infrastructure like room temperature and compressed air pressure.



### 9.5.4. Operating System

Our preferred platform will be GNU/Linux in the Control System. This provides a low cost with high availability and good remote management. There are many flavors of GNU/Linux and we will try to minimise the number used at MAX IV.

It is not always possible to have only one operating system because some applications require a different platform. This will have to be managed and given no other option this will be accepted in the control system.

# Chapter 10

## Short Pulse Facility

# MAX IV Facility



## 10. Short Pulse Facility

---

<b>10.1. Overview and Layout.....</b>	<b>2</b>
10.1.1. Lattice and Components.....	2
10.1.2. SPF Undulators .....	2
10.1.3. Science .....	2



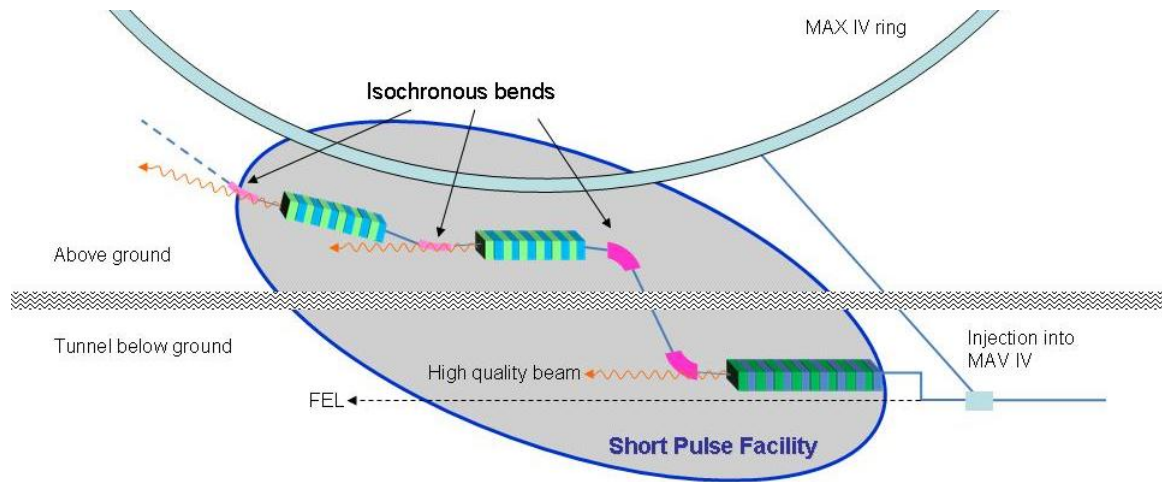
# MAX IV Facility





## 10.1. Overview and Layout

---



### 10.1.1. Lattice and Components

### 10.1.2. SPF Undulators

### 10.1.3. Science

#### 10.1.3.1. Scientific Scope and Motivation for Accelerator Parameters

The purpose of the SPF is to measure atomic rearrangements in molecules and solids using time-resolved X-ray diffraction. The initial dynamics is the most fundamental and therefore the work which will get the most attention. The pulse duration needed to do the job is thus coupled to atomic vibration and the pulse duration will be coupled to the mass of the atoms.

As examples of light and heavy system we can look at germanium with an optical phonon frequency of 100 fs and diamond with an optical phonon frequency of 25 fs.

Hence it is OK to start work at SPF using 100 fs pulse duration, but provisions to go down to 25 fs should be made.



This crude estimate is the relevant one for bondbreaking processes such as chemical reactions and phase-transitions.

A pulseduration below 5 fs will not be needed for this research field at all and a pulse duration between 5-25 fs is only needed if we wish to image atomic motion with a spatial motion better than the vibration amplitude.

In the UV/VUV range the situation is different. An FEL with 1 fs temporal resolution would be of great importance for studying electronic motion in atoms.

#### **10.1.3.1.1. Target Parameter for Pulse Duration**

Minimum requirement: 100 fs

A few years after start 25 fs

FEL (phase II) – As short as possible

#### **10.1.3.1.2. Target Parameter for Bunch Current**

A variable bunch current enabling the experimentalist to trade off intensity for pulse duration is optimal. We have assumed a 8-10 m long cold undulator with a 17 mm period.

The scientific case has been made for 1 nC bunch through the undulator which would be a good target. A factor of 2 lower value does not compromise the scientific case, but a factor 10 would probably impact liquid scattering studies.

Being able to run 10 nC pulses with 1-2 ps duration would allow for studies of caging dynamics in photo-induced reactions in liquids.

#### **10.1.3.1.3. Target Parameter for Pre-Post Pulses**

There are no fundamental arguments but this topic was discussed during the workshop in connection with MAX-lab annual meeting 2007. The full European expertise in the field was there. Experiences from SPPS-SLAC showed that:

Minimum requirement: 99% of electrons inside a 1 ps window.

Target parameter: 99.9 % of electrons inside a 1 ps window.

This gives a contrast of 1/100 respectively 1/1000. Please note that it is not in power but rather in energy which gives a more strict requirement.

### **10.1.3.2. Beamline Design and Requirements on Accelerator**

The undulator beamline at the MAX IV SPF is designed to provide 100 fs bursts of X-rays enabling the real-time study of atomic motion. The X-ray source is coupled to a synchronised femtosecond laser. This enables the study of photo-induced process in samples ranging from single crystals to small molecules in a solvent. Letters of intent from 50 researchers from 14 European laboratories have been signed showing the importance of such an infrastructure. A workshop was held in connection with the MAX-lab users

meeting October 2007. The meeting had 87 participants including a majority of the researchers behind the LOP's. At this time the design for the facility was discussed with the user community and the parameters for the facility was finalized. A more complete document can be obtained from Prof. J. Larsson on request.

#### 10.1.3.2.1. Modifying the Injector

The injector for the MAX IV ring will be modified in order to provide short pulses. It will be equipped with a laser-driven electron gun. The design from FERMI, Frascati, Rome will be used in a collaborative effort with the Frascati team. Two stages of bunch compression will be implemented. A magnetic chicane will provide the course compression and a 9 GHz cavity will facilitate fine-tuning providing clean 100 fs pulses.

#### 10.1.3.2.2. Timing and Synchronisation

To monitor the laser synchronisation to the X-rays, Electro-optical sampling (EOS) or other method with similar capability should be implemented in order to time-stamp each shot (postsynchronisation) User-controlled synchronisation in the hutch is also needed. This includes diagnostic with different degrees of complexity and temporal resolution. Experience from SPPS (SLAC) shows the need of user-controlled timing diagnostics (if EOS drifts.)

Key numbers for the timestructure are:

- **Pulse duration:** 100fs
- **Jitter:** <1 ps (it will be a gradual improvement until 30 fs is reached 10-15 fs rms)
- **(Post-) synchronisation:** 30 fs
- **Contrast:** 99% of pulse energy in 1 ps

#### 10.1.3.3. Discussion about Pump Lasers

The main laser for the photocathode as well as for the user area are cryocooled KHz Ti:Sap amplifiers (1kHz, 10 mJ@800 nm). The appeal of this solution is amplitude stability due to the fact that CW pumplasers for amplifiers can be used. This is important for non-linear conversion schemes. OPA's + mixing with 0.2-10 micron wavelength range together with THz generation will cover the needs of the physics and chemistry community. KHz rep rates are also required and useful for atomic physics community. Linac can operate at 1 kHz at lower energies.

The facility should also make provisions to include 200 Hz 20-30 mJ/pulse lasers which are based on CW diode pumped Nd-lasers at a later stage.

#### 10.1.3.4. Insertion Device

An undulator providing the highest number of photons per pulse should be used. Superconducting undulators has not reached the degree of maturity needed in order to

incorporate such a device in the first stage. The present thinking is to aim for an undulator which is cryogenically cooled. There was a discussion on the photon energy. The experience from ESRF is that 15 keV is a good photon energy for diffraction. The undulator period should be as small as technically possible.

#### **10.1.3.4.1. Optics**

Offset mirrors for harmonic suppression will be needed, in addition we will use Be-lenses and zone-plates for microfocusing.

For monochromatisation, several options needed. A set of three on the fly interchangeable monochromators is proposed (Si 111), (InSb 111) and (Multilayer optics with 1% bw).

#### **10.1.3.4.2. Wavelength Range**

2 keV- 20 keV

#### **10.1.3.4.3. Sample Environment**

The user needs are diverse and that a single sample environment is insufficient to cover a broad user base. A set-up which could handle vacuum, liquids, atomic and molecular physics, liquid-helium temperatures etc would be extremely complex and not user friendly. The way to address this will be coupled to the management of the project.

We will provide a beamline with a 4-C diffractometer for experiments in air allowing for sample cooling with a cryo-stream. The laboratory thus supplies the basic sample environment above and that the users are given the possibility to build their own set-ups which are interchangeable.

# Detailed Design Report



## Chapter 11 The Linac Test Beam (LTB)

**MAX IV Facility**



## 11. The Linac Test Beam (LTB)

---

A linac test beam (LTB) is planned for in the experimental area of the Short Pulse Facility (SPF) assuming that an electron beam line will be available. According to the present layout of the SPF area, an electron beam travelling some 70 m from a bending magnet to the standard beam dump construction is foreseen. Behind the beam dump cavity, a shielding wall, with a collimator opening, makes it possible to transport an electron beam or a photon beam into an experimental area 25 m long and 4 m wide. The LTB may be used in a wide range of applications in e.g. accelerator physics, radiation protection physics, detector tests, beam diagnostics, material test. Either the electron beam can be used in the 100 m<sup>2</sup> cave or a photon beam may be produced. In the case of an external electron beam with an average current of 20 nA, the intensity will probably have to be reduced due to radiation safety issues. An external electron beam in the cave requires an additional beam dump inside the cave. Photons may be produced by several methods e.g. Compton scattering (CS), Coherent Bremsstrahlung (CB), Channeling Radiation (CHR), Transition Radiation (XTR), Parametric X-rays (PXR) or the Smith-Purcell Effect (SP).

The LTB will allow tests of different components to be placed in the linac or the rings. Both electrons, X-rays from XTR or bremsstrahlung are of interest. These beams could also prove valuable in connection with a possible FEL facility. Accelerator components and target materials may be tested with the pulsed beam. A 200 fs electron pulse with 0.1 nC corresponds to a peak current of 500 A and focused to a radius  $\rho$  of a few  $\mu\text{m}$  produces a strong magnetic field  $B \approx 1080/(\rho/\mu\text{m})$  T [1]. The very short and high current bunches may be used not only to study the performance of the detector itself, but also of the electronics, largely stressed by high repetition rates and radiation doses. DAQ systems will suffer from the same issues, since they will acquire the impressive data through-puts of the future experiments. The possibility to have a test facility inside the laboratory is also very important for future developments in diagnostics devices for the accelerator complex itself. Such a facility will be a natural site for R&D, otherwise impossible to perform on other accelerators. The tendency in high energy physics and nuclear physics suggest that a few, large experiments will be implemented, needing a large amount of tests in order to optimize frontiers detectors, electronics, and data acquisition systems (DAQ). Much more than in the past, it will be necessary to perform accurate tests to check the device, show the reliability, and measure the aging due to large radiation damages, produced by hadrons and high charge beams of next accelerators machines [2].

Radiation safety codes and the input to radiation safety calculations may be experimentally tested. Source terms and shielding materials attenuation lengths may be measured and probably improve quality of shielding calculations.

A test beam facility can be a very useful and effective for students or young researchers, especially when the laboratory is close to many university centers. The LTB allows young physicist and engineers to work on small-scale set-ups, but with the full complexity with regards to detectors, electronics and DAQ systems. The LTB may also prove valuable in connection with educational programs, for projects and theses work.

## References

- [1] Interaction of Electron Pulses from the MAX-Linac Facility with Condensed Matter, H. Backe, Science at MAX IV in Lund, Linac Test Beam for Diagnostic and Research, October 31, 2007, Lund, Sweden
- [2] Summary report for 20 MAX IV user meeting discussion section “Test Beam Facility and diagnostics”, G. Mazzitelli, Science at MAX IV in Lund, Linac Test Beam for Diagnostic and Research, October 31, 2007, Lund, Sweden

